

VOL-II

305
2

**POST CENTENARY GOLDEN JUBILEE
OF UNIVERSITY OF CALCUTTA, INDIA**

PROCEEDINGS

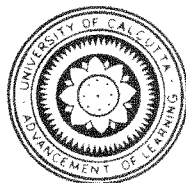
of

International Conference on Modeling and Simulation, MS'07 India

Theme: Control, Instrumentation, Embedded System Engineering and General Applications

December 3-5, 2007 Kolkata, India

Organised by



University of Calcutta, Department of Applied Physics, India

In Association with



AMSE, France

Co-organized by



The Institution of Engineering and
Technology (UK)

Technical Collaborators



IEEE (USA), Kolkata, India



IETE, Kolkata, India

ewk-H0464-2-07166016

POST CENTENARY GOLDEN JUBILEE OF UNIVERSITY OF CALCUTTA, INDIA

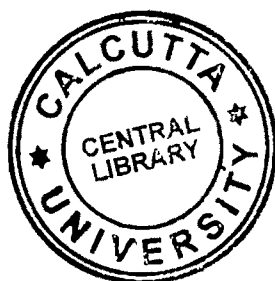
*Proceedings
of
International Conference
Modeling And Simulation, MS'07 INDIA*

Theme : Control, Instrumentation, Embedded System Engineering and General Applications



December 3-5, 2007 Kolkata, India

Organised by



Department of Applied Physics, University of Calcutta, India

**In association with
AMSE : International Association for Modeling and Simulation
Technique in Enterprise, France**

**Co-organiser
IET, Calcutta Branch**

**Technical collaborator
IEEE (USA), Kolkata Chapter, IETE, Kolkata Centre**

Professor Asis Kumar Banerjee
VICE-CHANCELLOR
University of Calcutta



87/1, College Street
Senate House
Kolkata-700 073
Telephone Nos. 2241-3288/0071/4984
Fax No. 91-33-2241-3288
E-mail : vc@caluniv.ac.in

November 7, 2007

FOREWORD

The University of Calcutta, established on January 24, 1857, is devoted to advancement of learning and is presently celebrating its Postcentenary Golden Jubilee. The Department of Applied Physics was established in 1925 as a Department of the University for the purpose of carrying out post graduate studies and research in Electrical Technology and allied Sciences. Since then it has produced a number of eminent teachers and pioneer technologists of national and international fame.

This Department organizes various types of academic activities in order to unravel new technologies before professionals and students throughout the year. The present Conference is an example. To address some critical issues in the areas of Control and Instrumentation, the Department resolved to take a venture in a broader spectrum in which they could obtain the association of AMSE, International Association for Modeling and Simulation Technique in Enterprise, France, a leading professional body engaged in dissemination of technology throughout the globe.

With the fast changing and competitive global industrial environment, engineers in the power and process sectors are confronted with unprecedented uncertainty in efficient operation of an industry. Unification of control technologies and restructuring and deregulation of power sectors have made things more complicated. Control and instrumentation constitute the lifeline of an industry and it is the use of state-of-the-art technology in these matters that can eradicate this uncertainty.

Professor Asis Kumar Banerjee
VICE-CHANCELLOR
University of Calcutta



87/1, College Street
Senate House
Kolkata-700 073
Telephone Nos. 2241-3288/0071/4984
Fax No. 91-33-2241-3288
E-mail : vc@caluniv.ac.in

Embedded systems technology has attempted to add to modern control and instrumentation techniques a new dimension. This technology, as a concept and in its numerous technological incarnations, is arguably one of the most influential transformations which have shaped our society in the recent past. No one can deny that it is gaining its relevance in every sphere of life. Rapid advances in computer and communication technologies have bolstered it. It is thus natural for the Department of Applied Physics to wish to explore the extent and diversity of developments in these technological arenas.

To achieve this goal the Department has, in association with AMSE: International Association for Modeling and Simulation Technique in Enterprise, France, planned to organize this Three-Day International Conference on "Modeling And Simulation" with the theme "Control, Instrumentation, Embedded System Engineering and General Applications" during 3-5 December, 2007 at Kolkata, India. The Conference will explore the deep-rooted linkages between existing and emerging concerns faced by the engineers in these and related fields. It will try to develop appropriate strategies and decision making tools and create awareness of the best practices in the fields of technology, management and general applications.

The Conference Proceedings, containing rich contributions from eminent experts in the relevant fields, aims at giving ample opportunity to the scientists, academicians, technologists and engineers to take stock of technological advancements in relevant areas, understand future trends and deliberate on other related issues of technical and social consequences.

I wish the Conference all success and I am confident that the Proceedings will be a lasting contribution to knowledge.

A. K. Banerjee
Asis Kumar Banerjee

PREFACE

With the advent of modern technologies, industries are having recourse to newer processes for efficient and zero breakdown running of a plant. On the other hand, power sector with its restructured environment has also started utilizing the advancement of technology in the different aspects of power and energy sectors. Control and instrumentation are the life lines of efficient operation of a plant or a system. Embedded systems technology combined with advanced computer and communication technologies has enriched modern control and instrumentation techniques. It is thus necessary to explore the extent and diversity of development in these technological arenas.

To discuss the rapid developments in the areas of control, instrumentation and embedded system engineering, Department of Applied Physics, University of Calcutta, India in association with AMSE, France and co-organised by IET, Calcutta Branch is going to organize an international conference on December 3-5, 2007 where speakers from all over India and abroad will present their original research works.

183 research papers, authored by eminent engineers, scientists, technologists and research workers, screened out from about 330 submissions, are included in this proceedings. Nine Invited Speeches, delivered by eminent national and international speakers, have also been included. All the papers and the invited speeches will be presented in 24 technical sessions and three plenary sessions. It should be mentioned that a number of good submissions could not be included due to space and time constraints for which the organizers apologize. The areas covered are,

- Control Theory
- Monitoring and control of power system components
- Process control and instrumentation
- Power Quality, HVDC and FACTS Technology
- Modern Protection, Instrumentation and Control
- Electro-optic Devices and Optical Communication
- Transmission and Distribution System Automation
- Application of Artificial Intelligence, Neural Network and Fuzzy Control Techniques
- Power Electronics and Drives
- Power System Dynamics, Control and Optimization
- Electric Power Market, Deregulation and restructuring
- Power System Modeling and Simulation
- Wind Power and Other Renewable Power, DG and Interconnection
- Modern Communication for Metering, Control and Protection
- Neural networks and Genetic Algorithms
- Embedded system engineering and Expert systems
- Pattern recognition and image processing
- Knowledge based decision systems
- Application for economy, finance, sociology, medicine and others
- General application of Modeling and Simulation; Case studies and Experimental results

The organizers have taken all efforts to make the proceedings error free. But still some errors might have crept in for which they apologize in anticipation. It is hoped that the readers will enjoy these volumes.

ACKNOWLEDGEMENT

Organizing Committee of MS'07 India would like to place on record its gratitude to the esteemed participants, engineers, scientists, technologists and research workers, for their valued technical contributions and participation.

Members of the international advisory committee and national organizing committee have contributed significantly in organizing the conference and also for this publication. The members of the Publication Sub-committee are grateful to the reviewers of the papers who have made tremendous efforts to maintain the time schedule and standard of the publication.

The committee also thanks the Superintendent of Calcutta University press along with his enthusiastic working force to publish these volumes within a short time.

It is a pleasure to acknowledge all supports, financial and moral, provided by the Associator, Co-organizer, Technical Collaborators, Sponsors and Advertisers without which this event could not come into reality.

The committee also puts on record the co-operations provided by the staff members of the conference secretariat, those of the Department of Applied Physics and those of the venue, different agencies and many more.

**International Conference
on
Modeling And Simulation, MS'07 INDIA**

Co-organiser

The Institution of Engineering and Technology, Kolkata Section

Technical Collaborator

Institute of Electrical & Electronics Engineers, Kolkata Section

The Institution of Electronics and Telecommunication Engineers, Kolkata Centre

SPONSORS

All India Council for Technical Education, Government of India

Department of Science and Technology, Government of India

Council of Scientific and Industrial Research, Government of India

Department of Information Technology (DIT), Government of India

Science and Technology Department, Government of West Bengal

Defence Research & Development Organisation, Government of India

University Grants Commission

Technical Education Quality Improvement Programme, TEQIP, UCT-CU

West Bengal State Electricity Distribution Company Limited, India

RTDS Technologies Inc., Canada

Usha Intercontinental (India), New Delhi, India

TATA Consultancy Services, Kolkata, India

Tech Mahindra Limited, Kolkata, India

Century Transformers Pvt. Limited, Kolkata, India

RAHUL Foundation, Kolkata, India

YOKOGAWA India Limited, India

Rockwell Automation

M. N. Dastur & Company (P) Limited, Kolkata, India

Principal Patrons

Professor Asis Kumar Banerjee,
Vice Chancellor,
University of Calcutta, India

Professor Jaime Gil Aluja
President, AMSE, Spain

Patrons

Professor Tapan Kumar Mukherjee
Pro Vice Chancellor,
University of Calcutta, India

Professor Suranjan Das
Pro Vice Chancellor,
University of Calcutta, India

Professor Christian Berger-Vachon
General Secretary, AMSE, France

International Advisory Committee

Chairman: D. K. Basu, Former Vice Chancellor, Burdwan University, India

- A Ogulu, University of Kwa Zulu-Natal, South Africa
A. R. Thakur, Vice Chancellor, WBUT, India
Aladin Zayegh, Victoria University of Technology, Australia
Andrew Forsyth, The University of Manchester, UK
Andrzej Horodecki, Lublin Technical University, Poland
Asoke K Nandi, The University of Liverpool, UK
B. B. Chaudhuri, ISI, Kolkata, India
Brad Lehman, Northeastern University, Boston, USA
C. S. Jha, Professor Emeritus, IIT, Delhi, India
D. P. Kothari, IIT, New Delhi
D. Sanyal, IET, Kolkata, India
Dragutin Debeljkovic, University of Belgrade, Belgrade Serbia
Francesco Carlo Morabito, University of Reggio Calabria, Italy
Frederico Gonzalez Santoyo, University of Michoacan, Mexico
Hamlaoui Abdessalam, University of Malaya, Kuala Lumpur
Jeno Kovacs, University of Oulu, Finland
K. Bhattacharyya, IEEE, Kolkata, India
K. C. Mukhopadhyay, IET, Kolkata, India
Li Ge, National University of Defense Technology, China
M. A. Kashem, University of Tasmania, Australia
Malcolm R Irving, Brunel University, Uxbridge, UK
N. R. Banerjee, Vice Chancellor, Bengal Engineering and Science University, India
P. Banerjee, IETE, Kolkata, India
Petr Stemberk, Czech Technical University, Czech Republic
P. N. Ghosh, Vice Chancellor, Jadavpur University, India
R. N. Lahiri, IET, Kolkata, India
Raed Abu Zitar, Philadelphia University, Jordan
S. Bhattacharyya, IIM, Kolkata, India
S. K. Sanyal, IEEE, Kolkata, India
S. N. Mishra, Sikkim, India
T. K. De, IETE, Kolkata, India

GENERAL CHAIR

A. K. Mukhopadhyay
Ex-Vice Chancellor, Tripura University, India and
Sir R. B. Ghosh Chair Professor of Department of Applied Physics,
University Of Calcutta, India

ORGANISING COMMITTEE

Chairman

G. Sarkar
Head and Labonyamoyee Das Chair Professor of Department Of Applied Physics, University Of Calcutta,
India

General Secretary

S. Sengupta, Applied Physics, University Of Calcutta, India

Joint Convenors

M. Mitra and J. N. Bera, Applied Physics, University Of Calcutta, India

Members

S. K. Bandyopadhyay, Registrar, CU, India
S. Sen, Dean, FET, CU, India
S. Sarkar, Secretary, UCSTA, CU, India
T. K. Mitra, Applied Physics, CU, India
Balaram Bhattacharyya, Applied Physics, CU, India
S. Phaujdar, Applied Physics, CU, India
S. C. Kar, Applied Physics, CU, India
R. Brahmachari, Applied Physics, CU, India
S. C. Bera, Applied Physics, CU, India
C. Dey, Applied Physics, CU, India
S. Chowdhury, Applied Physics, CU, India
R. Gupta, Applied Physics, CU, India
K. K. Mazumdar, UCT-CU, India
M. K. Sengupta, UCT-CU, India

Technical Committee

Chairman: K. K. Bandyopadhyay, Applied Physics, CU, India
Convenor: S. Chattopadhyay, Applied Physics, CU, India

Finance Committee

Chairman: S. K. Sen, Applied Physics, CU, India
Convenor: S. Phaujdar, Applied Physics, CU, India

Publication Committee

Chairman: A. Deb, Applied Physics, CU, India
Convenor: S. C. Kar, Applied Physics, CU, India

Event Management Committee

Chairman: S. K. Sen, Applied Physics, CU, India
Convenor: R. Gupta, Applied Physics, CU, India

Reception, Hospitality and Travel Management Committee

Chairman: S. Chowdhury, Applied Physics, CU, India
Convenor: C. Dey, Applied Physics, CU, India

CONTENTS

VOL I

	Page No.
<i>Foreword</i>	<i>i</i>
<i>Preface</i>	<i>iii</i>
<i>Acknowledgement</i>	<i>iv</i>
<i>Sponsors</i>	<i>v</i>
<i>Committee</i>	<i>vi</i>
Technical Session 1A: Power System Stability	
1. An Offline Simulation Method to Identify The Weakest Bus And its Voltage Stability Margin in a Multibus Power Network <i>Kabir Chakraborty, Sangita Das Biswas</i>	1
2. A Review of Analytical Techniques for Determination of Voltage Stability in a Multi-bus Power System <i>Suman Saha, Abhijit Chakroborti, C. K. Chanda, A .B. Chowdhury</i>	6
3. Bulk Power System Reliability Evaluation Using Fuzzy Logic <i>K. Thippeswamy, V. K. Keshavan</i>	11
4. Stability Investigation of Power System and Its Stabilization by a Coordinated Application of Power System Stabilizers in Multi-machine Systems <i>N. Albert Singh, F. Shamila, K. A. Muraleedharan and K. Gomathy</i>	16
5. Incorporating Static Synchronous Series Compensator in Optimal Reactive Power Allocation for Improving Voltage Stability Margins <i>P. Kanta Rao and K. Vaisakh</i>	21
6. Analysis of Voltage Control Stability Indices of Radial Distribution in Modern Power System <i>S. Sao, Sriniwasa Rao. Gorantla, M.V. Ramesh</i>	28
7. Assessment of Voltage Stability in Longitudinal Power Supply System <i>S. Haider nee Dey, A. Chakrabarti, A. De</i>	33
8. Single Cycle Mathematical Model for Harmonic Power in d-q Plane <i>Surajit Chattopadhyay, Madhuchhanda Mitra, Samarjit Sengupta</i>	38
Technical Session 1B: Process Control	
9. A Novel approach for the Design of Stabilizing PI Controllers <i>M. Siva Kumar, B. J. J Raju , A.Sarada Devi, P. Naga Manasa</i>	43
10. Improving Automation Benefits of Process Control System Using Performance Evaluation by Statistical Analysis <i>S. G. Hingmire, S. G. Karad, . D. S. Karanjkar</i>	47
11. Performance of Orifice Plates in Transient Cavitating Flow: Experimental Study <i>K. S. Sumam, S.G. Thampi, N. Sajikumar</i>	52
12. Design of H _∞ based Robust Controller for AVR System <i>V. Mukherjee, Bijoy K. Mukherjee, and S.P. Ghoshal</i>	56
13. Study of Energy Losses of a High Capacity Boiler and Design of Flue Gas Heat Recovery Unit for the Optimum Efficiency of a Thermal Power Plant <i>S. C. Bera, M. S. Bhowmick</i>	61
14. A Report on Modification of Burner Management System of a Steam Generation Unit in Naphtha and Natural Gas based Fertilizer Plant <i>S. C. Bera , M. S. Bhowmick</i>	66
15. Position Control System of a Motorized Valve in a Process Plant using PLC <i>S. Chattopadhyay, S. Pal, U. Chakraborty, S. C. Bera</i>	70
Technical Session 1C: Power Electronics Simulation	
16. Design, Analysis and Simulation of DC-to-DC Flyback Converter <i>R. A. Gupta, Rajesh Kumar, Saurabh Goyal, Parikshit Yadav</i>	75
17. Modelling of a 3-Phase Current Controlled Inverter With Observer-Feedback and Decoupling <i>Dipanwita Gangopadhyay, K.Selvajyothi, P.A.Janakiraman</i>	80

18.	Switch Mode Rectifier With Improved Power Factor & High Quality Input Waveforms <i>P. K. Gujarathi, M. V. Aware</i>	85
19.	Simulation and Design of An Active Power Filter for SCR Converter <i>Prabal Deb, Shilpi Bhattacharya, Sujit K. Biswas</i>	89
20.	SiC based Buck Boost Converter <i>Vineeta Agarwal, Neeraj Verma</i>	94
21.	Simulation of a Novel Zero Voltage Transition (ZVT) Technique Based Boost Power Factor Correction (PFC) Converter with EMI Filter <i>P. Ram Mohan, M. Vijaya Kumar, O. V. Raghava Reddy</i>	99
22.	Design and Simulation of 30 Watt Phase Modulated Converter <i>Rajesh Babu Kollipara, P. K. Chaturvedi, K. C. Pradhan</i>	104
Technical Session 1D: GA and its Application		
23.	Qualitative GA Based Identification and Control of 2DOF Inverted Pendulum <i>Altреза Rezazade, Mohsen Modarres</i>	110
24.	An Object Oriented Neural Network Model Optimized by Genetic Algorithm for Microwave FETs <i>Anil Ahlawat, Rajesh Tyagi, Sujata Pandey, Manoj Pandey</i>	115
25.	Genetic Algorithm Driven Modeling of Defect States in Poly-Thiophene (PT) and Poly-Selenophene (PS) under Zero Band-Gap Constraint <i>Rahul Sharma, S. P. Bhattacharyya</i>	119
26.	Optimum Design of Stewart Platform By Using Genetic Algorithm <i>R. Kaviani, A. Rastgo</i>	124
27.	Optimization of Surface Roughness in End Milling of Stainless Steel (SS 304) Using Genetic Algorithm <i>Anayet U Patwari, A.K.M. Nurul Amtn, and Ishtiyag M. Hossain</i>	129
28.	Genetic Algorithm Based Tabu Search Method for Solving the Unit Commitment Problem with Cooling – Banking Constraints <i>C. Christofer Asir Rajan</i>	133
29.	Automated Active Filter Design using Genetic Algorithm <i>Rupaban Subadar, Swanirbhar Majumder</i>	138
Technical Session 2A: FACTS		
30.	Dynamic Stability Analysis of Power System Using Thyristor Controlled Series Capacitor <i>P. Bera, D. Das, T. K. Basu</i>	143
31.	Simulation and Modeling of GA Optimized Distribution Static Compensator for Power Quality Improvement <i>Deepika Masand, Shailendra Jain, Gayatri Agnihotri</i>	147
32.	Improvement of Voltage Stability Margins with OPF Incorporating Static Series Synchronous Compensator <i>L. R. Srinivas, K. Vaisakh</i>	153
33.	Multi-Area Unit Commitment Using Dynamic Programming Approach and Checking of Dynamic Stability <i>Rambabu.Ch</i>	158
34.	Ratings of FACTS Devices for Power Flow Control in Power System Network <i>Subrata Majumdar, P. K. Chattopadhyay, A. K. Chakrabarty</i>	163
35.	Design of STATCOM Controller Based on State Predominant Approach <i>R. K. Pandey, Akashdeep Agrawal</i>	167
36.	Normal Form Analysis of Stressed Power System Incorporating STATCOM <i>Ramtin Hadidi Ahad Kazemi</i>	172
37.	A Homogeneous Model of SSSC in Power Network <i>R. K. Pandey, N. K. Singh</i>	177
38.	SSSC Based Power Oscillation Damping Controller <i>R. K. Pandey, N. K. Singh</i>	182

Technical Session 2B: Biomedical Signal Processing		
39.	Erythrocyte Shape Investigation and Analysis using Image Processing Technique Umalakshmi A, Rajeshwari S, Sandhya Rao, Shilpa G. S, Manjunatha M, Mallikarjuna Swamy <i>M. S, Mallikarjun S. Holi</i>	187
40.	Computer based Investigation of Hearing Disorders through Distortion Product Otoacoustic Emission Analysis <i>Jyothiraj V.P, Suresh Kumar A</i>	192
41.	Diagnosis Of Eye Diseases Using Medical Imaging. <i>Sheeba O, Suresh Kumar A.</i>	196
42.	Effect of Fractal Image Compression on Screening for Diabetic Retinopathy. <i>David. J, Suresh Kumar. A, Harsha. A</i>	201
43.	Protein Secondary Structure Prediction through Combination of Decisions from Multiple MLP classifiers <i>Piyali Chatterjee, Subhadip Basu, Mahantapas Kundu, Mita Nasipuri, Dipak Kumar Basu</i>	206
44.	Study of EEG Signals under Photoc Stimulation <i>Mohandas K P, Rameshkumar P</i>	211
45.	ECG Signal Processing for Analysis of Abnormalities based on QT Interval-A Novel Approach <i>Madhuchhanda Mitra, Saurabh Pal, Swantirbhar Majumder</i>	216
46.	Rough Set Based Classification of Myocardial Infarction <i>Sucharita Mitra, M. Mitra, and B. B. Chaudhuri</i>	219
47.	Pattern Grammar and Histogram Based ECG Features Extraction <i>Sucharita Mitra, M.Mitra, and B.B. Chaudhuri</i>	224
Technical Session 2C: Modeling and Simulation		
48.	First-Principles Modeling and Simulation of the Electronic and Magnetic Properties of C_8 , Si_8 and MnC_7 , $MnSi_7$ <i>T. Benabdesselam, A. Tadjer, and B. Bouhafs</i>	229
49.	Symmetry Through Group and Linear Transformations <i>Samir Zaki Mohamed Mehrez</i>	234
50.	Mathematical Modeling for Predicating the Mechanical Properties of Plain-Weft Knitted Fabric <i>H. R. Karimi, A. A. A. Jeddi, A. Rastgoo</i>	238
51.	A Simulation Model For Partial Discharge with Stochastic Features <i>P. Das</i>	243
52.	Developed Model of Exciter Mechanism in Vibrating Screen and its Influence on the Efficiency of Grading Particle in Iron Ore Production Line <i>A. Rastgoo, H. Sohanian, A. Aram</i>	247
53.	Modulus of Highest Eigenvalue of a Polynomial <i>J. R. P. Gupta, Yogesh V. Hote, D. Roy Choudhury</i>	251
54.	Heat And Mass Transfer with Interaction Effects Analysis between an External flow and a Capillary Porous Body <i>S. Larbi, M. Malki, H. Belhaneche</i>	255
55.	Extension Classification Method and Its Application <i>Yang Chunyan</i>	260
56.	Computation of Optimum Expansion Coefficients in Generalized Block Pulse Function Domain <i>Anish Deb, Gautam Sarkar, Nabanita Nath Chowdhury</i>	265
57.	An Approach to Detect Cause of Over Current in Power System Network Using Real Time Digital Simulation <i>A. K. Dhara, S. Chowdhury, J .N. Bera, S. C. Kar, S. Sengupta</i>	269
Technical Session 2D: Fuzzy Logic Applications		
58.	An approach for translation of Fuzzy Petri nets to Ladder Logic Diagrams <i>P.R. Venkateswaran, Jayadev Bhat, S. Meenatchisundaram</i>	273
59.	An Approach to Relate and Optimize Metal Forming Process Parameters by Fuzzy Logic <i>S.L. Mahmood, Fazlathunnessa, M. H. Banna, M. Raju Hossain</i>	277

60.	Selection of Membership Functions in the Prediction of Shoot Length of Mustard Plant at Maturity <i>Satyendra Nath Mandal, J. Pal Choudhury, Dillip De and S. K. Mukherjee</i>	282
61.	Behavior Modelling Based Fuzzy Controller for Combustion Control of Utility Boiler <i>T. R. Rangaswamy</i>	288
62.	Numerical Solution of Takagi-Sugeno Fuzzy Model Based State Equations via Block Pulse Functions <i>B.M. Mohan, Vertika Singh</i>	293
63.	Fuzzy ARTMAP Technique for Quality Evaluation of Tea using Electronic Nose <i>Dibyendu Bhattacharyya, Anil Kumar Bag, Bipan Tudu, Nabarun Bhattacharyya, Rajib Bandhopadhyaya</i>	297
64.	An Intelligent Approach for Multi-Sensor Data Validation and Fusion Using Fuzzy Logic <i>S. Saha, U. Kar and J. Sil</i>	302
65.	A Ziegler-Nichols PID Controller With Auto tuning Feature <i>Chandhal Dey, Rajani K. Mudl</i>	307
Technical Session 3A: Sensors and Transducers		
66.	Modelling & Simulation of Laser Material Processing and Predicting Melt Pool Geometry and Temperature Distribution <i>M A Sheikh</i>	312
67.	Simulation of Loopless Deflection Routing Algorithms in Label Switched Optical Networks using SimEvents <i>G Pavan Kumar, Vinod Chandra</i>	317
68.	Metal Oxide Gas Sensor under UV radiation : Theory and Experiment <i>Sunita Mishra, Indrajeet Boiragi, C Ghanshyam</i>	320
69.	Modeling and Simulation of SMART CMOS MEMS Pressure Sensor <i>C. RoyChaudhuri, N.Futane, H.Saha</i>	324
70.	Study of an IC Based Flow Transducer <i>S. C. Bera, N. Mandal</i>	329
71.	Study of Electrode Polarisation Impedence Type Transducer for The Measurement of Flow Rate of a Conducting Liquid <i>S. C. Bera, B.Chakraborty, N. Mandal, R. Sarkar</i>	332
72.	Study of a Magneto-Optic Element as a Displacement Sensor <i>S. Chakraborty, S.C. Bera</i>	336
Technical Session 3B: Control Theory		
73.	Design of H ⁻ -Optimal Robust Controller for a Singularly Perturbed System <i>Debasish Mondal</i>	339
74.	The Gauss-Hermite Filter and the Central Difference Filter for Bearing Only Tracking. <i>Manas Kumar Bera, Saurabh Pal</i>	344
75.	Robust Control of Inverted Pendulum System by Convex Optimization: An LMI Approach <i>Sharmistha Mandal, A. Sutradhar</i>	349
76.	Microprocessor based Identification of Sampled Data System with/without Hold Device using a Set of Sample-and-Hold and Dirac Delta Functions <i>Anindita Senguptaa, Anish deb, Sudipta Mandal</i>	354
77.	Robust control of stochastic system via Lyapunov Approach and Linear Matrix Inequalities (LMIs) <i>Selma Ben Attia, Salah Salhi, M.Ksouri</i>	359
78.	New Approach for Static Output Feedback Problem <i>Neila Bédout, Salah Salhi, M.Ksouri</i>	363
79.	A Parameter Plane Design Methodology for Two-Loop Lateral Missile Autopilot <i>Mousiki Kar (Deb), Kalyankumar Datta, Shyamal Kumar Goswami</i>	368
Technical Session 3C: Induction Machines		
80.	Eigen-Frequency Improvement of Induction Machine Using PI Controller <i>S. Ekram, A. K. Sen, B. Sarkar</i>	373
81.	A New Integrated Motor Starter for Induction Motor	377

	<i>J. P. Tewari, R. K. Singh, Naveen Nischal Chava</i>	
82.	Current and Vibration Analysis of Induction Motor for Detection of Broken Rotor bar <i>B. Kundu, P.P. Pal, P. Chattopadhyay, G. Bandyopadhyay</i>	380
83.	Decoupled Control of Linear Induction Motor <i>S. N. Mahendra, K. Chaudhary, Akshay K Rathore, Pankaj Chaudhary</i>	384
84.	Fault Identification of An Induction Motor by Fractal Analysis Technique <i>Dilip Dey, P. B. Duttagupta, S. Sengupta</i>	389
85.	Multi-Class Fault Identification of Induction Motor by Using Support Vector Machine <i>Dilip Dey, P. B. Duttagupta, S. Sengupta</i>	393
86.	Diagnosis of Fault Due to Unbalanced Rotor of an Induction Motor by Analysis of Vibration and Motor Current Signatures <i>Subrata Karmakar, S.K. Ahamed, M.Mitra, S. Sengupta</i>	399

Technical Session 3D: General Applications-I

87.	The Motion of Spherical Shock Waves in Self-gravitating Heat Conducting Medium <i>R. P. Yadav, Ratnesh Kumar, Virendra K. Gangwar</i>	404
88.	Sizing and Optimization Of Hybrid Renewable Power System <i>S. C. Gupta, Y. Kumar, Gayatri Agnihotri</i>	407
89.	Performance Comparison of a PV Powered Water-Pumping System with and without Maximum Power Point Tracker <i>Abu Tariq, M. S. Jamil Asghar</i>	412
90.	Modeling and Analysis of Particle Movement in a Common Enclosure Gas Insulated Bus Duct Under Unbalanced Voltages <i>G. V. Nagesh Kumar, J. Amarnath, B. P. Singh</i>	417
91.	Maximum Power Point Tracking Using Perturb and Observe Algorithm <i>Vineeta Agarwal, Alok Kumar Vishwakarma, B.K. Pandey</i>	422
92.	Open Circuit VMPPT with current compensation for low power photovoltaic cell <i>Vineeta Agarwal, Alok Kumar Vishwakarma, B.K. Pandey</i>	427
93.	An Approach for Attribute Data Measurement from a Network of Electrical Equipments as an Application of GIS <i>Epsita Das, Susmita Kundu, J. N. Bera, R. Bramhachari</i>	431

Author Index

VOL II

Technical Session 4A: Power Electronics Applications

94.	Automated Control Of Electric Locomotives <i>SrinivasaRao, Gorantla, S. Sao, M. V. Ramesh</i>	435
95.	Role of Electromagnetic and Radio Frequency Noise Suppressor for High Frequency Inverter Operated Induction Heating Equipment <i>Nitai Pal, Pradip Kumar Sadhu, Dilip Kumar Mitra, Rupendranath Chakrabarti</i>	440
96.	Performance Analysis of H.F. Mirror Inverter for Energy Efficient Induction Cooking Appliance Range <i>Pradip Kumar Sadhu, Nitai Pal, Rupendranath Chakrabarti, T. K. Chatterjee</i>	444
97.	Design of Speed Control of DC Series Motor using Fuzzy PID Controller <i>Barwal Shweta and K.K Garg</i>	449
98.	Microcontroller Based High Frequency Inverter <i>M. G. Wanl, V. K. Sharma, R. D. Kharadkar</i>	453
99.	A Constant Switching Frequency Hysteresis Current Controller for Single-Phase Voltage-Source Inverters <i>M. Ahmadi, H. Heydari, and A. Rahmati</i>	456
100.	Predictive Current Control of an Inverter-Fed a 25kA Current Injection Transformer System <i>M. Ahmadi, H. Heydari, A. Rahmati</i>	461
101.	Fuzzy Logic Based Extended Dynamic Braking of Electric Locomotive <i>R. S. Bhalpal, Rajesh Gupta</i>	466

Technical Session 4B: Biomedical Instrumentation		
102.	Real Time Data Acquisition System for Three Axis Force Measurements of Needle Insertion into Soft Tissue, its Modeling and Simulation <i>Debajit Bharali, Sohini Roy, Ajay K. Yagati, Sunil Kumar, Sujoy K. Guha</i>	471
103.	Automated Detection and Classification of Cerebral Palsy Gait using Support Vector Machines <i>M. Shiva Kumar, M. Sukumar</i>	476
104.	Single Channel Computerized ECG Recorder and Extraction of Relevant Parameters from the ECG-A DSP Based Approach <i>Monisha Chakraborty, Bipan Tudu, Debashis Das</i>	479
105.	Effect of Stimulus Parameters and Spontaneous Otoacoustic Emissions on Transient Evoked Otoacoustic Emission Measurement for Hearing Screening <i>Sukesh Kumar A, Jyothiraj V. P</i>	483
106.	Stochastic Model of Haematopoiesis <i>Probit Kumar Dhar, Abhik Mukherjee, Durjoy Majumder</i>	488
107.	Design And Simulation of Signal Generator For A New Noninvasive RF Heartbeat Detection System <i>S. Shabu, Roshna.R</i>	493
108.	A Methodology for Studying the Characteristics of Expansion of Stent Like Structures in a Hyper Elastic Artery Model <i>Naveen Kumar KU, Sujesh Sreedharan, CG Nandakumar, Muraleedharan CV</i>	498
Technical Session 4C: Electric Drives		
109.	ANN - Based Current Control of A Voltage Source PWM Inverter <i>R. Arulmozhiyal, K. Baskaran</i>	503
110.	A Simulink Based Dynamic Modeling and Analysis of High Performance Induction Motor Drive <i>Rajesh Kumar, R. A. Gupta, S. V. Bhangale</i>	507
111.	A PFC Based High Performance Induction Motor Drive <i>Rajesh Kumar, R. A. Gupta, S. V. Bhangale</i>	512
112.	Constant v/f Control of Combined Inverter-Induction Motor Drive <i>S. P. Muley, M. V. Aware</i>	517
113.	Observer-Based Sensorless Control of A Vector Controlled Five-Phase Induction Motor Drive <i>M. Rizwan Khan, Atif Iqbal, Mukhtar Ahmad</i>	521
114.	Simulation of Space Vector Theory Based Variable Speed Operation of a PMSM Drive System Using Predictive Current Control <i>A. Lekshmi, R. Sankaran, S. Ushakumari</i>	528
115.	New Current Control of PMSM Drives in Synchronously Rotor Reference Frame <i>M. Kadjoudj, M.E. Benbouzid, and C. Ghemai</i>	533
116.	Modelling of PWM-Inverter fed Induction Motor Drive and Simulation Analysis of Motor Terminal Overvoltages <i>B. Basavaraja, D. V. S. S. Siva Sarma</i>	538
117.	Speed Control of DC Drives for Controlling Tension of Steel Strips in Steel Strip Manufacturing Industries <i>S. K. Sen, B. R. Das, S. Banerjee, S. K. Basak, S. K. Mondal</i>	542
Technical Session 5A: Power System		
118.	Power Vector Coordinated Multilateral Trades <i>Sudha Balagopalan, S Ashok and KP Mohandas</i>	547
119.	High Speed Fault Identification in A HVDC System Using Wavelet Modulus Maxima <i>M. Sushama, Ch. Prasanth Babu, A. Jaya Lakshmi, G. Tulasi Ram Das</i>	552
120.	Design of an Optimum Controller for DVR to Compensate Unbalanced Voltage Sag <i>M. R. Shakarmai, A. Kazemi, B. Mahdian</i>	556
121.	On Line Three Phase Power Factor Estimation under Nonsinusoidal Unbalanced and Time Varying Condition <i>Arghya Sarkar, K. K. Mazumdar, S. Sengupta</i>	561
122.	Power Factor Control of Distribution System by Using DSTATCOM <i>J. Ramanjaneya Reddy, S. Jagadish Kumar, CH. Siva Kumar</i>	566

123.	A PC based simulated frequency relay for real time protection of power system <i>T. K. Sengupta, A. Das, A. K. Mukhopadhyay</i>	570
124.	A Novel Particle Swarm Optimized AGC for Restructured Three Area Power System <i>Ranjit Roy, S. P. Ghoshal</i>	575
125.	Development Of a Numeric Adaptive Relay For Transformer Overload Protection <i>Pratap Chandra Karfa, J.K. Das, K. Das (Bhattacharya)</i>	580
126.	Study For Monitoring And Control Of Power System Parameters Using Geographical Information System <i>Susmita Dey (Chaudhuri), Anushree Roy, Sumana Chowdhuri, Jitendra Nath Bera</i>	585
Technical Session 5B: Transmission and Distribution		
127.	Fuzzy System Approach to Power Purchase in a Power Pool of A Deregulated Power System. <i>Ajoy K Chakraborty, C. K. Roy, P. B. Duttagupta</i>	589
128.	Feeder Reconfiguration and Capacitor Placement for Loss Reduction of Distribution System Using Genetic Algorithm <i>P. V. Prasad, S. SivaNagaraju, N. Sreenivasulu</i>	594
129.	A New Approach to Calculate Frequency Dependent Impedance of Grounding Electrodes <i>S. M. Shahrtash, N. Ramezani</i>	598
130.	An offline Simulation Study of Security Analysis of a Multibus Power System Using Load-Flow Based Technique <i>Sangita Das Biswas, Kabir Chakraborty, Tanima Bhattacharya, Bishakha Nandi</i>	605
131.	Voltage Sag and Unbalance Mitigation in Distribution Systems Using Multi-level UPQC <i>H. R. Toodeji, S. M. Ale Emran, N. Farokhnia, H. Askartan, S. H. Fathi, G. B. Gharehpetian, M. Abedi</i>	610
132.	Electromagnetic Field Effect on Metallic Particle Contamination in a Common Enclosure Gas Insulated Bus duct <i>G. V. Nagesh Kumar, J. Amarnath, B. P. Singh, K. D. Srivatsava</i>	616
133.	PD Detection and Location in Cable Networks Based on Traveling Waves Indices <i>S. M. Shahrtash, F. Haghjoo</i>	621
134.	Reduced Order LQG Controller for Distribution Static Compensator used for Load Voltage Control of Distribution System <i>Rajesh Gupta, Arindam Ghosh</i>	628
135.	Concept and Benefits of Microgrid System with Modeling and Simulation <i>Prasenjit Basak, S.P. Chowdhury, and S. Chowdhury</i>	633
136.	Assessment of Transmission Line Losses through Power Flow Tracing in a Deregulated Multi-Bus Power System <i>Ashim Kumar Dey, Narendra Nath Sinha, J.K.Das, S. Sengupta</i>	637
Technical Session 5C: VHDL and Embedded System		
137.	Simulation of Random Early Detection Algorithm Using VHDL <i>Nilay Khare, Kavita Khare</i>	642
138.	An Efficient Simulator for Power Grid Analysis in VLSI Chips <i>Vishnu Vardhan, Sandeep K. Dey, Susmita Sur-Kolay, Debasis Mitra, Bhargab B. Bhattacharya</i>	646
139.	VHDL Simulation of A Memory Efficient, High Speed Huffman Decoder: Extension to FPGA Implementation <i>Bijoy Kumar Upadhyaya, P. Venkateswaran, S. K. Sanyal, R. Nandi</i>	651
140.	Hardware/Software Partitioning Problem in Embedded System Design Using Particle Swarm Optimization Technique <i>Amit Konar, Alakananda Bhattacharya</i>	656
141.	A CPLD Based Gold Code Generator <i>S. Chattopadhyay, S. K. Sanyal</i>	660
142.	Protection from Buffer Overflow with External Hardware in an Embedded System <i>Asim Dalta, S. Sengupta</i>	664
143.	Transmission of ECG Signal Using Microcontroller Based Wireless Bi-phase Modulation Technique <i>R. Gupta, C. Das, A. Mondal, J. N. Bera, M. Mitra, T. K. Mitra</i>	669

Technical Session 6A: ANN		
144.	Type Identification of Unknown Thermocouple Using Probabilistic Neural Network <i>Palash Kundu, Gautam Sarkar</i>	673
145.	Application of Neuro-Fuzzy Controller in HVAC System <i>A. K. Pal</i>	678
146.	Voltage Stability Evaluation using Artificial Neural Networks <i>P. Aruna Jeyanthi, D. Devaraj, N. Albert Singh</i>	683
147.	Electrical Fault Supervision in Induction Motors Using Neural Networks and Multiple Models Approach <i>IDER Zahir, Mendil Boubekour</i>	688
148.	ANN Application for Identification of Minimal Loss Feeder Reconfiguration <i>P. L. MuthuKarthik, P. S. Venkataramu, T. Ananthapadmanabha</i>	694
149.	Nonlinear Dynamic Time Series Modeling using Genetically Optimized Evolving Fuzzy Neural Network <i>Jayashri Vajpai, Arun JB</i>	699
Technical Session 6B: General Application-II		
150.	Effect of Axial Magnetic Field on Temperature Variation of Self-Gravitating Gas Atmosphere Perturbed by Strong Shock Wave <i>R. P. Yadav, Virendra K. Gangwar, Sandeep Bharti, Satyendru Prakash, P. S. Rawat</i>	704
151.	Temperature Rise in the Cell Phone User's Head <i>R. Seetharaman, N. Kumaravel</i>	710
152.	Simulation And Analysis Of Micro-Resonators Using Sugar <i>S. Meenatchisundaram, G. Uma, M. Umapathy, B. S. Sathyanarayana, P. R. Venkateswaran</i>	712
153.	An Analytical Approach to Study Dynamics of Beat-up Mechanism of a Loom <i>A. Rastgoo, A. Mirdehghan</i>	717
154.	Three Dimensional Free Vibration Analysis of Transradially Isotropic Thermoelastic Sphere <i>J. N. Sharma, Nivedita Sharma</i>	722
155.	Direct Simulation of Forced Convection in Porous Media <i>Mohammad Hassan Rahimian, Abdullah Abasiun</i>	726
Technical Session 6C: Electrical Machines		
156.	Damping of Low Frequency Oscillations in Alternators using Neuro Fuzzy Logic Controller <i>F. Shamila, N. Albert Singh, K. A. Muraleedharan, K. Gomathy</i>	731
157.	Simulation of an Adjustable Speed Synchronous Motor fed from Sinusoidal Currents <i>Soumya Ray, Kaushik Mukherjee, Nikhil Mondal, Sujit K. Biswas</i>	736
158.	The Superiority of Interleaved Windings in a 25kA Current Injection Transformer <i>S. M. Pedramrazi, H. Heydari</i>	741
159.	Low Cost Controller for Switched Reluctance Motor <i>A.K. Dhakar, Amitava Das</i>	746
160.	PC Based Remote Speed Control and Condition Monitoring of DC Motor <i>S. Chowdhuri, J.N. Bera, G. Sarkar, S. Phoujdar</i>	751
Technical Session 7A: Electronics and Software Based Applications		
161.	Amplitude Control in Sinusoidal Oscillator <i>H. Mechergui, A. Haddouk</i>	755
162.	Quality Control In Distributed Software Systems <i>Rusakov M. A.</i>	761
163.	An Efficient Architecture for Low Density Parity Check Code Decoder <i>Saheeda P. A.</i>	764
164.	VLSI Architecture for Implementing Hearing Aid Algorithms <i>P A Saheeda, Reena M Roy</i>	768
165.	A Soft Computing Paradigm for Handwritten Digit Recognition with Application to Bangla Digits <i>Nibaran Das, Ram Sarkar, Subhadip Basu, Mahantapas Kundu, Mita Nasipuri,</i>	771

	<i>Dipak Kumar Basu</i>	
166.	Efficient Nanodevices for Advanced Ultradense VLSI Systems <i>Subir Kumar Sarkar, T. Datta, Ankush Ghosh, J. C. Singh, G. Prakash, Debasis Samanta</i>	775
167.	Communication Security through Cryptography and Performance Evaluation of Three Encryption/Decryption algorithms <i>Awadhesh Kumar Singh</i>	778
168.	A Novel Design Of Low Power Low Voltage Full Adder Using 14 MOSFETS <i>Manash Chanda, Swapnadipt De, Amrit Ghosh, Devmalya Banerjee, Pijush Biswas</i>	782
Technical Session 7B: Image Processing		
169.	Statistical-Mechanical Modeling of Digital Halftoning <i>Jun-ichi Inoue, Yohei Saika, Masato Okada</i>	786
170.	Illumination Normalization Using DCT Coefficients Re-scaling and Adaptive Histogram Equalization for Face Recognition <i>Virendra P. Vishwakarma, Sujata Pandey, M. N. Gupta</i>	791
171.	Robust Face Recognition with PCA using Cascaded Correlation Neural Networks <i>J. Dheeba, N. Herald Anantha Rufus, N. Albert Singh</i>	796
172.	Face Recognition Using Back Propagation Algorithm <i>V.S. Dixit, Shweta Kundra Bhatta</i>	800
173.	An Application Module Using Eigenfaces for Face Recognition <i>S. Tripath, R. Agrawal, M. K. Saini, A. K. Jain, S. Basu, R. Ramchandani, A. Gupta</i>	805
174.	Equivalence between Two Layout-Variant Document Images Without Reading <i>P. Nagabhushan, Sahana D. Gowda</i>	809
175.	Wavelet And Dct-Based Image Coding & Reconstruction For Low Resolution Implementation <i>Swanirbhar Majumder, Md. Anwar Hussain</i>	814
Technical Session 7C: Communication and Microwave		
176.	Microstrip Leaky-Wave Antenna With Arbitrary Metallic Strip Radiating Characteristics <i>Z. Mekkioui, H. Baudrand</i>	819
177.	Modeling of Process of Interaction of The Enterprises on The Basis of A Web-Services by Means of Java-Technologies <i>G. Jurnatova</i>	822
178.	Performance Analysis of Neuro-Predictive Controller for Nonlinear Chemical Process <i>S. Paruya</i>	824
179.	Study of the Microwave Absorption Behaviour of Ceramic Material at X-Band Frequencies <i>S. K. Srivastava</i>	829
180.	Secure Communication in Power System Using Chaos Masking <i>Kabir Chakraborty, K.S.Sherpa, and S.Sengupta</i>	832
181.	A New Demodulation Scheme for AM Signals based on Sliding DFT <i>P. Sumathi, P. A. Janaktraman</i>	836
182.	Demonstration of Highly Efficient Transmission in Sixty Degree Sharply Bend Waveguide Based on Photonic Crystal at 1.5 μm Wavelength <i>L. Dekkiche, R. Naoum</i>	840
183.	Effect of Demodulator Filter Roll-off Factor on the Quality of QPSK Modulated Mobile Communication System <i>S. Chattopadhyay, S. K. Sanyal</i>	844
Invited Speeches		
184.	The Role of Measurement Automation on Accident Prevention and Industrial Safety <i>T. K. Mitra</i>	849
185.	The Changing Face of Power Electronics <i>Sujit K. Biswas</i>	851
186.	Beyond CMOS: Problems and Prospects of Nanodevices for VLSI Circuits <i>Subir Kumar Sarkar</i>	855
187.	Mobile GIS, Communication & Concurrent Safety for Intelligent Transport Systems	859

	<i>Rabindranath Bera</i>	
188.	HVDC-Link Modeling in OPF using Newton's Method: HDVC-LCC <i>Enrique Acha</i>	864
189.	Indian Electricity Sector <i>D Sanyal</i>	873
190.	Utility applications of a RTDS® Simulator <i>Paul Forsyth, Rick Kuffel</i>	877
191.	Modelling the auditory system: an interesting challenge <i>Christian Berger-Vachon</i>	882
192.	Patteren Recognition: A Universal Problem Solving Discipline <i>B B Chaudhuri</i>	883
<i>Author Index</i>		

Technical Session 4A

Power Electronics : Applications

Automated Control of Electric Locomotives

SrinivasaRao.Gorantla¹ · S.Sao² · M.V.Ramesh³

¹ Vignan's engineering college ,Vadlamudi Email:srinivas_gorantla@rediffmail.com
² Vignan's engineering college ,Vadlamudi Email:drsao53@yahoo.co.in
³ P.V.P.S.Institute of technology ,Vijayawada Email:vmaddukuri@yahoo.com

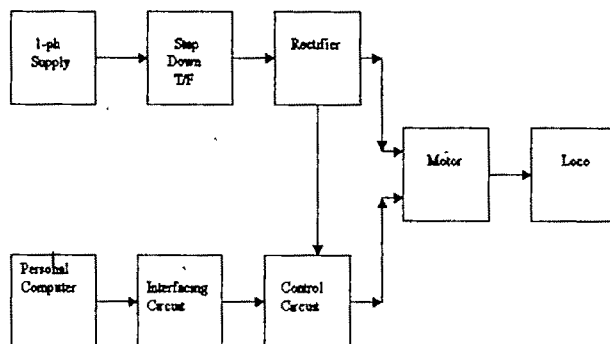
Abstract: Trains are uniquely susceptible to collision because of running on fixed rails, they are not capable of avoiding a collision by steering away, as a road vehicle; furthermore, trains cannot decelerate rapidly, and are frequently operating at high speeds whereby the train cannot be stopped instantly to avoid collision with it. Whenever there is a mix up in the discharge of signals by the crew in the base, it becomes rather difficult for the train crew to take control of the train at desire consequences. In order to avoid such mishaps this project deals with the control of the locomotive from the base itself and that too with the help of personal computer(PC). A program was written in 'C'. With the help of an interfacing circuit and control circuit the locomotive is controlled from the base itself. The functions include 1.Start 2. Stop 3.Forward 4.Reverse 5. Speed control

Key words— Electric locomotive , Electronic control circuit ,Personnel computer ,Interfacing circuit

I. INTRODUCTION

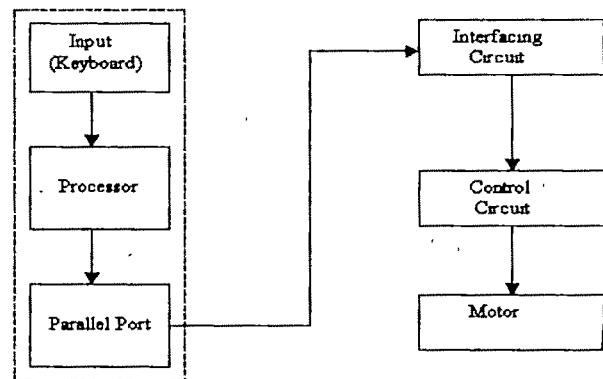
THE project deals with the control of locomotive with the help of PC. The loco is controlled with the help of control circuit, which is interfaced with the personal computer. It has the functions of start, stop, forward, reverse, base speed, low speed, and medium speed. There is two-way control one with personal computer and the other manually.

Block Diagram of the Project

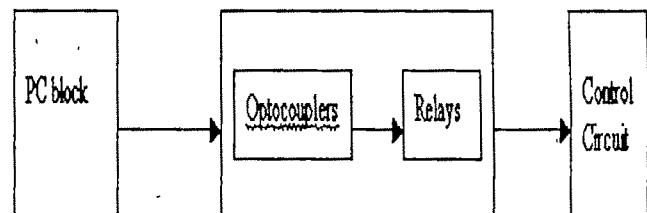


II. BLOCKS IN THE PROJECT

PC Block: We have come along way since the early days of computers, when ENIAC known as the first generation of computers was the state of the art occupies thousands of feet of floor space. Constructed largely of vacuum tubes, it was slow, prone to breakdown, and performed a limited number of instructions. When the transistor was invented, computers shrank in size and increased in power, leading to the second generation of computers. Third generation computers came about with the invention of the integrated circuits, which allowed hundreds of transistors to be packed on a small piece of silicon. LSI technology has created the fourth generation of computers that we use today.



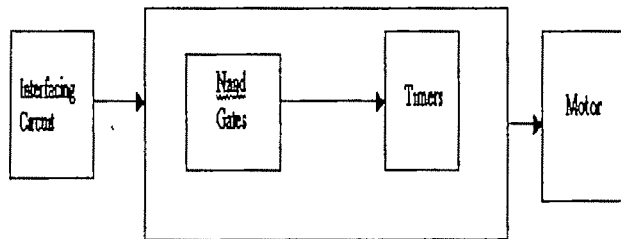
Interfacing block



When the signal from the pc block reaches to opto-coupler the LED in the opto-coupler gets turned into ON state and this emits the light which switches the Darlington pair which is also in the opto-coupler ON thus providing the path for the supply to reach the electromagnetic switch or relays that it gives signal to the control circuit. When the signal is turned

OFF from the D connector the transistors are switched into off state and the relay gets deactivated and again there is no signal to the control circuit

Control Circuit Block



The control circuit block is connected to the motor which when receives signals from the interfacing circuit starts working and according to the NAND gates and timer operations is used to start, stop, move the motor in reverse and forward direction. This also requires voltage of 12V.

Signaling Systems

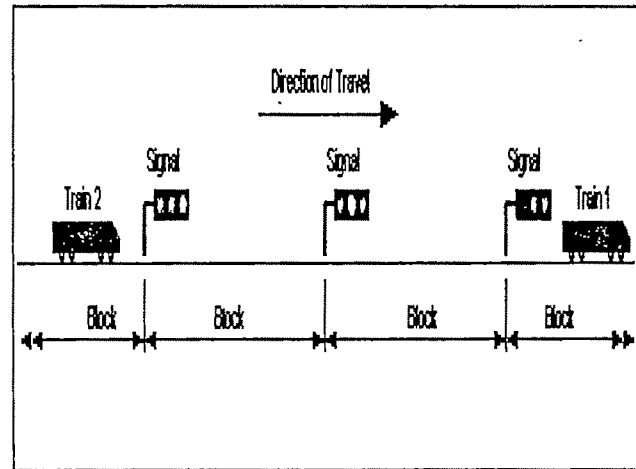
Signaling is one of the most important parts of the many which make up a railway system. Train movement safety depends on it and the control and management of trains depends on them. Over the years many signaling and train control systems have been evolved so that today a highly technical and complex industry has developed. Here is an attempt to explain, how we can control the locomotive with the help of computer. Railway signaling is a system used on railways to control traffic safely, for example, to prevent trains from colliding. Most forms of train control involve messages being passed from those in charge of the rail network or portions of it (e.g., a stationmaster) to the crew; these are known as 'signals'.

Time Table Operation

The simplest form of operation, in terms of equipment at least, is operation according to a timetable. Everything is laid down in advance and every train crew knows the timetable. Trains can only operate in pre-arranged time periods, during which they have 'possession' of the track and no other train can operate. When trains are operating in opposing directions on a single-line railroad meets are scheduled, where each train must wait for the other at a point they can pass. Neither is permitted to move until the other has arrived. The timetable system has several disadvantages. The first is that there is no positive confirmation that the tracks ahead clear; only that it should be clear. This system does not allow for breakdowns and other such problems. The second problem is the timetable system's inflexibility; trains cannot be added or delayed; trains cannot be rescheduled.

Block Systems: In the very early days of railways, on a double-tracked railway lines, where trains traveled in one direction on the same stretch of track, a means was needed to space out the trains to ensure that they did not collide. In the early days of railways, men were employed to stand next to the line at certain intervals with a stop watch. If a train had passed the man a short while ago, the following train was expected to slow down or to stop to allow sufficient space to develop

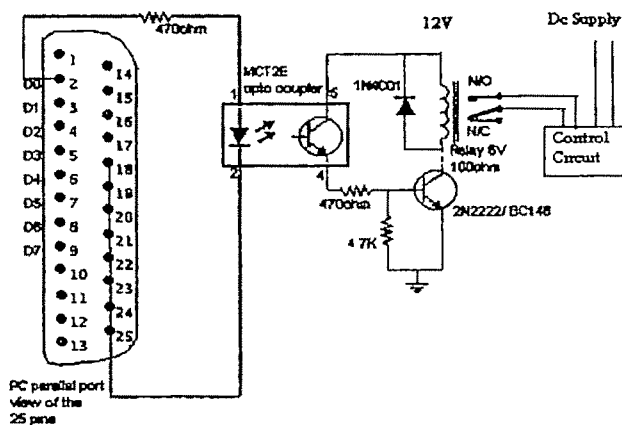
between the trains, to prevent a collision. The system was flawed, however, as the watchman had no way of knowing whether the preceding train had cleared the tracks ahead. And so, if the preceding train broke down or stopped for some reason, the following train would have no way of knowing, and collide with it rear-on. Accidents of this type were common in the early days of railways.



When a track signal block is occupied, the signal which the train has just passed automatically turns from green (yellow) to red, the signal behind that one automatically turns yellow to warn following trains of the red signal, and the signals behind that one can show green. If any train is following behind, the yellow signal will warn it to slow down in order to stop at the next signal. If, however, the train in front has passed into the next block, the following train and clears two blocks; the following train will come across a green signal

Interfacing Circuit

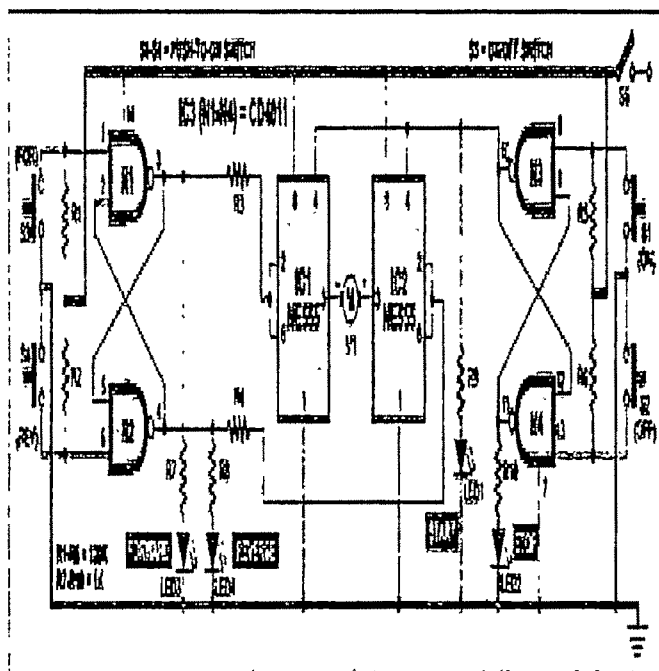
The circuit shown in figure below is used to control a single electrical appliance through parallel port of a personal computer. It consists of an opto coupler I.C. which totally isolates the load and the parallel port of the computer and also drives the relay which operates on a different voltage level of 12V D.C. Where as the output from parallel port is 5V or 0V D.C



Control Circuit

Using this circuit, you can control the rotation of a DC micro

motor simply by pressing two push-to-on switches momentarily. The circuit is built around two NE555 ICs (IC1 and IC2) and a quad-NAND IC CD4011 (comprising NAND gates N1 through N4). The NE555 ICs (IC1 and IC2) are configured as inverting buffers. IC CD4011 (IC3) NAND gates are configured as bistable flip-flop.



The DC motor to be controlled is connected between the outputs (pin 3) of IC1 and IC2. Closing switch S5 provides power to the circuit. Now when you press switch S1 momentarily, pin 10 of IC3 goes high, while its pin 11 goes low. Since pin 10 of IC3 is connected to reset pin 4 of IC1 and IC2, the high output at pin 10 of IC3 will enable IC1 and IC2 simultaneously. When switch S2 is pressed, pin 10 of IC3 goes low, while its pin 11 goes high. The low logic at pin 10 disables both IC1 and IC2. Switches S3 and S4 are used for forward and reverse motion of the motor in conjunction with switch S1. If you press switch S3 after pressing switch S1, pin 3 of IC3 goes high, while its pin 4 goes low. The motor now starts rotating in the forward direction. However, if you press switch S4 after pressing switch S1, the motor will rotate in reverse direction.

Parallel Port

PC parallel port can be very useful I/O channel for connecting your own circuits to PC. The PC's parallel port can be used to perform some very amusing hardware interfacing experiments. The port is very easy to use when you first understand some basic tricks. This document tries to show those tricks in easy to understand way. The Parallel Port is the most commonly used port for interfacing home made projects. This port will allow the input of up to 9 bits or the output of 12 bits at any one given time, thus requiring minimal external circuitry to implement many simpler tasks. The port is composed of 4 control lines, 5 status lines and 8 data lines. It's

found commonly on the back of your PC as a D-Type 25 Pin female connector. [4]

Hardware Properties

Below is a table of the "Pin Outs" of the D-Type 25 Pin connector. D-Type 25 Pin Connector.

Pin No (D-Type 25)	Pin No	SPP Signal	Direction In/out	Register	Hardware Inverted
1	1	nStrobe	In/Out	Control	Yes
2	2	Data 0	Out	Data	
3	3	Data 1	Out	Data	
4	4	Data 2	Out	Data	
5	5	Data 3	Out	Data	
6	6	Data 4	Out	Data	
7	7	Data 5	Out	Data	
8	8	Data 6	Out	Data	
9	9	Data 7	Out	Data	
10	10	nAck	In	Status	
11	11	Busy	In	Status	Yes
12	12	Paper-Out / Paper-End	In	Status	
13	13	Select	In	Status	
14	14	nAuto-Linefeed	In/Out	Control	Yes
15	32	nError / nFault	In	Status	
16	31	nInitialize	In/Out	Control	
17	36	nSelect-Printer / nSelect-In	In/Out	Control	Yes
18-25	19-30	Ground	Gnd		

The above table uses "n" in front of the signal name to denote that the signal is active low. e.g. nError. If the printer has occurred an error then this line is low. This line normally is high, should the printer be functioning correctly. The "Hardware Inverted" means the signal is inverted by the Parallel card's hardware. Such an example is the busy line. If +5v (Logic 1) was applied to this pin and the status register read, it would return back a 0 in Bit 7 of the Status register..

Port Addresses

The Parallel Port has three commonly used base addresses. These are listed in table below. The 3BCh base address was originally introduced used for Parallel Ports on early Video Cards. This address then disappeared for a while, when Parallel Ports were later removed from Video Cards. They has now reappeared as an option for Parallel Ports integrated onto motherboards, upon which their configuration can be changed using BIOS.

LPT1 is normally assigned base address 378h, while LPT2 is assigned 278h. However this may not always is the case as explained later. 378h & 278h have always been commonly used for Parallel Ports. The lower case h denotes that it is in hexadecimal. These addresses may change from machine to machine. PC parallel port is 25-pin D-shaped female connector in the back of the computer. It is normally used for connecting computer to printer, but many other types of hardware for that port are available today. Not all 25 are needed always. Usually it can be done with only 8 output pins (data lines) and signal ground. Those output pins are adequate for many purposes.

Opto-Coupler

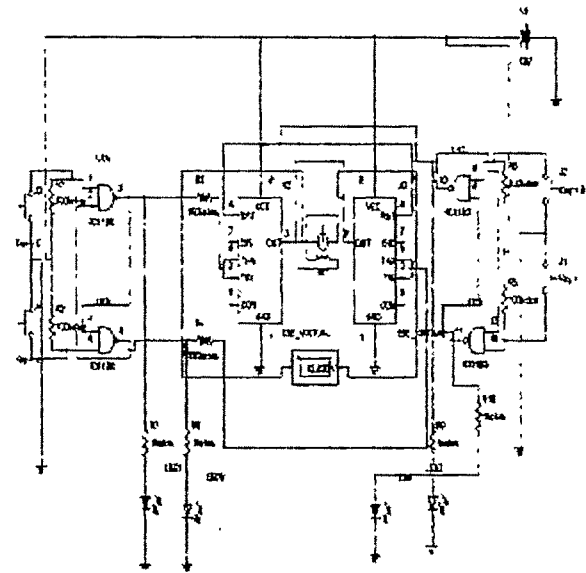
There are many situations where signals and data need to be transferred from one subsystem to another within a piece of electronics equipment, or from one piece of equipment to another, without making a direct ohmic electrical connection because the source and destination are at different voltages levels, which is operating from 3v Dc but being used to control a triac, which is switching 240V AC. In such situations the link between the two must be an isolated one, to protect the microprocessor from over voltage damage We have used multisim software to simulate the control circuit. Here we can see that the green led is on which indicates that the motor has started and the orange led shows that it is moving in the forward direction, which is further supported by the voltage appearing in the voltmeter, which is 12 volts There are many things that Multisim just does better than most schematic capture and simulation packages. Ease of use - it's one of the most important features. Together with exceptional value, this is why Design Bar, which gives you shortcuts to the logical steps of the entire design flow, to our intuitive, modelless schematic captures and immediate simulation results.

Design Bar

Like all the other toolbars in Multisim, the Design Bar can be resized and docked anywhere. By default, it's found near the top-middle of the screen. The first button of the Design Bar shows and hides the Component Toolbar, which is initially shown and docked to the left, and is made up of a series of intuitively organized Parts Bins.

Placing a Component

Here's where ease-of-use shows up next. To place a component on the circuit window, click or roll your mouse over a Parts Bin in the Component Toolbar. Clicking the second button down opens the component window & select the required component.

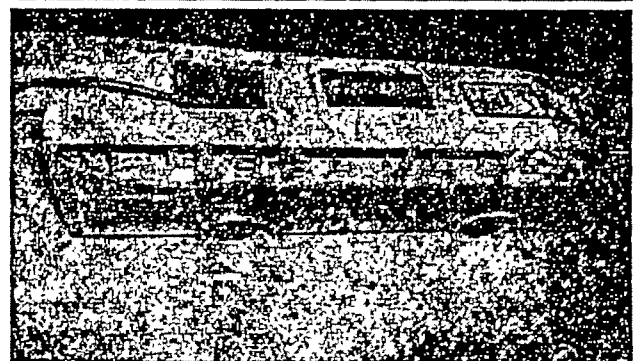
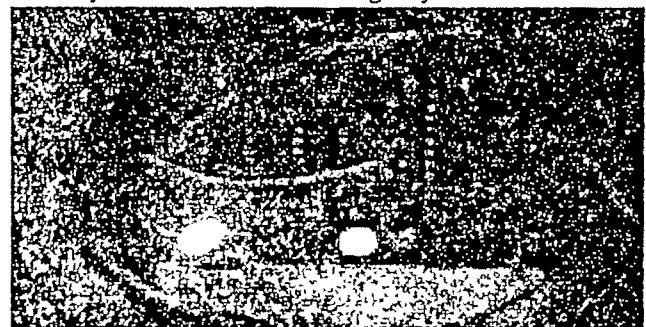


Spice simulation of Hardware circuit

Advantages: 1. The time of switching action is less. 2. The Program is a Command User Interface, but a common man can also use this without any difficulty. 3. The Circuit is very simple, fault identification and rectification is easy, it is a matter of replacing the malfunctioning IC. 4. The ICs used in this circuit are easily available in the local markets. 5. The circuit doesn't require any separate casing; it can be easily assembled inside the locomotive. The circuit is assembled and connected to a parallel port of the personal Computer

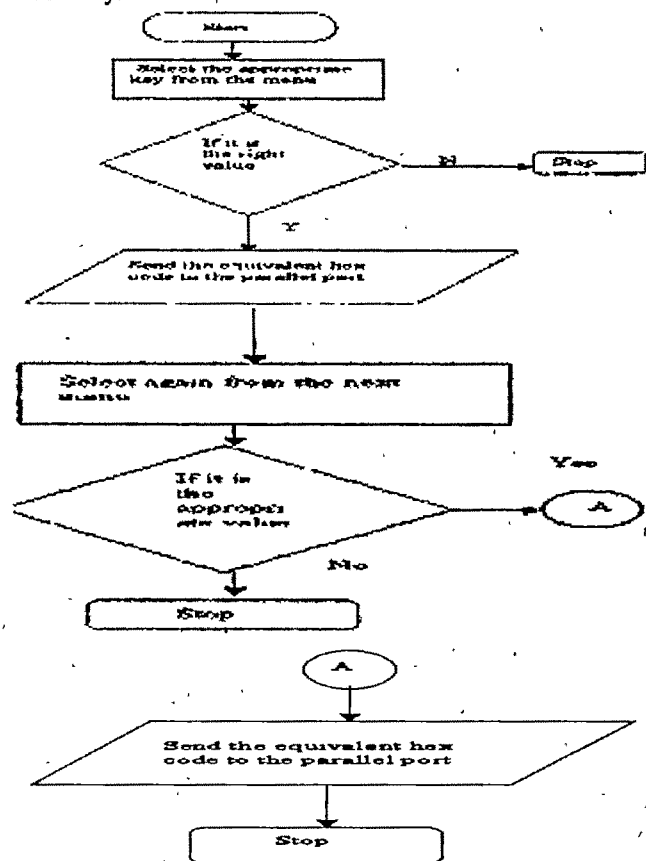
III .HARDWARE IMPLEMENTATION OF THE PROJECT

Hardware part of this project is implemented and tested in the laboratory and found that its working very well.



IV ALGORITHM

The following algorithm is used for realizing this project in the laboratory.



V..CONCLUSION

The circuit is assembled and connected to a parallel port of the personal Computer. On executing the application program the required function is executed which may be start, stop, forward, reverse, base speed, low speed, medium speed. This is a basic approach in the developing many flexible, user friendly, and fast acting system, which can be used for controlling the locomotive from the base itself. This project can be implemented in any base as it can control the movement of locomotive whenever required. The way to extend the project is to place a camera on the loco, which gives us the total view of the track ahead, which helps us, all the more in controlling the loco from the base itself.

ACKNOWLEDGMENT

G.Srinivasa Rao. Would like to thank Dr.G.kesava Rao, Professor, for Dept of Electrical & Electronics Engineering Vignana's Engineering college vadlamudi for his participation in technical discussions. He also thanks president of this institution for providing facilities in completing this project. He also thanks Head of the institution and Head of the department of Electrical & Electronics Engineering in Vignana's Engineering college, vadlamudi for providing facilities in completing this project.

REFERENCES

- [1] A microprocessor system for traction control Crawshaw, G. Davis, C. Cybulski, E.Cordon, M Wilson, R.M. Brush Electr. Machines, Loughborough
- [2] Locomotive drive control P.Mercorelli, P.terwiesch and D.Pattichizzo
- [3] Electronic Devices & Circuits- By Robert Boylestad
- [4] The Pentium Microprocessor - By James L. Antonakos
- [5] Mechanical Engineering Magazine ; Copyright 1998 by The American Society of Mechanical Engineers Drive Circuit Basics, Industrial Circuits Applications Notes, (<http://library.net/pdflib/pdf/drive.pdf>).
- [6] Automatic vehicle classification instrument based on multiple sensor information fusion Weiming Liu; Xueping Zhao; Jingfang Xiao; Youlong Wu Information Technology and Applications, 2005. ICITA 2005. Third International Conference on Volume 1, Issue , 4-7 July 2005 Page(s): 379 - 382 vol.1
- [7] MATLAB/PSB based modeling and simulation of 25 kV AC railway traction system - a particular reference to loading and fault conditions Shenoy, U.J.; Sheshadri, K.G.; Parthasarathy, K.; Khincha, H.P.; Thukaram, D. TENCON 2004. 2004 IEEE Region 10 Conference Volume C, Issue , 21-24 Nov. 2004 Page(s): 508 - 511 Vol. 3
- [8] Intelligent transportation SYSTEMS <http://www.ieee.org/its> IEEE ITS COUNCIL NEWSLETTER Editor: Prof. Alberto Broggi, broggi@ce.unipr.it Vol. 3, No. 3, July 2001
- [9] IEEE ICMA 2007 Conference Plenary Talk 1 Intersections between Mechatronics and Robot Manipulators of the Future William R. Hamel, Ph.D. Professor and Head Mechanical, Aerospace, and Biomedical Engineering University of Tennessee Knoxville, TN 37966, U.S.A.
- [10] Tracking Tremor Frequency in Spike Trains Using the Extended Kalman Filter Sunghun Kim and James McNames Proceedings of the 2005 IEEE Engineering in Medicine and Biology 27th Annual Conference Shanghai, China, September 1-4, 2005
- [11] IEEE Transactions on Industrial Electronics Volume 35, Number 1, Feb 1988
- [12] Expert Systems: Working Systems and the Research Literature By Bruce G. Buchanan Department of Computer Science Stanford University Stanford, CA 94305 october 1985
- [13] An automation system for radiocommunications to electric locomotives in a mine Transportable simulator trains control center operators
- [14] Waight, J.G.; Nodehi, K.; Bose, A.; Dobrowolski, E.; Wasley, R.G. Computer Applications in Power, IEEE Volume 5, Issue 2, Apr 1992 Page(s):23 - 28
- [15] Transportable simulator trains control center operators Waight, J.G. Nodehi, K.; Bose, A.; Dobrowolski, E.; Wasley, R.G. Computer Applications in Power, IEEE Volume 5, Issue 2, Apr 1992 Page(s):23 - 28
- [16] Locomotive "total systems" simulation using SIMULINK Mathew, R.; Flinders, F.; Oghanna, W. Electric Railways in a United Europe, 1995., International Conference on Volume , Issue , 27-30 Mar 1995 Page(s):202 - 206 R. W. Lucky, "Automatic equalization for digital communication," *Bell Syst. Tech. J.*, vol. 44, no. 4, pp. 547-588, Apr. 1965.
- [17] Developments in Rail Simulators and Computer Based Training to increase training efficiency and effectiveness Duncan Ward - Sydac Pty Ltd Paul Tyler - Sydac Pty Ltd Pat Wilson - Delphic Consultants Michael Eichinger - Sydac Pty Ltd
- [18] Use of power semiconductors to control locomotive traction motors in the French national railways Nourvion, F. Proceedings of the IEEE Volume 55, Issue 8, Aug. 1967 Page(s): 1441 - 1448
- [19] Automatic control system for trains Document Type and Number: United States Patent 20040015275 W. D. Doyle,
- [20] Modeling hybrid electric HMMWV power system performance Fish, S.; Savoie, T.; Vanicek, H. Magnetics, IEEE Transactions on Volume 37, Issue 1, Jan 2001 Page(s):480 - 484
- [21] Hybrid Electric Vehicle Design Based On A Multi-Objective Optimization Evolutionary Algorithm (Walter J. Karplus Summer Research Grant Report 2005) Lingfeng Wang Department of Electrical and Computer Engineering Texas A&M University College Station, Texas 77843.

Role of Electromagnetic and Radio Frequency Noise Suppressor for High Frequency Inverter Operated Induction Heating Equipment

Nitai Pal¹, Pradip Kumar Sadhu², Dilip Kumar Mitra³, Rupendranath Chakrabarti⁴

¹ Electrical Engineering Department, Indian School of Mines University, Dhanbad - 826004 e-mail : nitai_pal@rediffmail.com

² Electrical Engineering Department, Indian School of Mines University, Dhanbad - 826004 e-mail : pradip_sadhu@yahoo.co.in

³ Electrical Engineering Department, Indian School of Mines University, Dhanbad - 826004

⁴ Electrical Engineering Department, Jadavpur University, Kolkata - 700032 e-mail : rupen_chakrabarti@yahoo.co.in

Abstract—United states and international standards for Electromagnetic Interference (EMI) and Radio Frequency Interference (RFI) have been established which requires the manufacture of electronic equipment to minimize the radiated and conducted interference of their equipment to acceptable levels. In the United States the guiding document is the FCC Docket 20780 [3], while internationally the West Germany Verband Deutscher Elektrotechniker (VDE) safety standards have been widely accepted. It is very important to understand that both the FCC [3,4] and VDE [1,2] standards exclude subassemblies from compliance to the rules; rather, the final equipment, where the switching power supply is used, must comply with the EMI-RFI specification. Rightly so, since even if the switching power supply has an input filter, this filter is matched to the power supply when passive loads are powered, and its characteristics and suppression capabilities may drastically change when used to power active electronic circuits. This is an attempt made by the authors to introduce the reader to the conducted RFI problem and give some suggestions for minimizing it, whether it is applied in a power supply unit (e.g. SMPS) or a high frequency inverter operated induction-heating equipment.

Key words—EMI, RFI, FCC, VDE, High frequency switching, LC Filter.

I. INTRODUCTION

EMI and RFI are created whenever there are spikes in Electronic signals. These interferences occur in almost all types of electronic circuits having sharp rising and falling edges in current and voltage waveforms. In switching power supplies, the MOSFET switches will create these EMI or RFI noises. These should be filtered to comply with the Federal Communications Commission (FCC) and CE requirements and also to prevent interference in proper functioning of different electronic circuits. Common mode line filters are used to block these noises on the power lines. The international standards for

EMI-RFI have been well established. The manufactures of electronic equipment are asked to minimize the radiated and conducted interference of their equipment to acceptable levels. An attempt has been made by the researcher to introduce here the problem of conducted RFI and then to put forward some means for minimization when applied for a power supply or for a final system of radio-frequency mirror inverter scheduled to supply induction heating equipment.

Both FCC and VDE are concerned with the suppression of RFI generated by equipment connected to the a.c. mains and mend for high-frequency digital circuitry. The VDE has subdivided its RFI regulations into two categories, the first being unintentional high frequency generation by equipment with rated frequencies from 0 to 10kHz., i.e., VDE -0875 and VDE-0879, and the second deals with intentional high frequency generation by equipment for frequencies above 10kHz., i.e., VDE0871 and VDE0872. The FCC on the other hand includes in its RFI regulations all electronic devices and systems which generate and use timing signals or pulse at a rate greater than 10kHz. Fig.1 summarizes the RFI requirements for FCC and VDE. The EMI-RFI regulations of FCC closely follow those of the VDE. The FCC class-A specification covers business, commercial and industrial environment. Compliance to the specified EMI emission in dB-μV can be met by any equipment meeting VDE-0875/N [1] or VDE-0871/A.C [2]. On the other hand, FCC class-B requirements cover residential environment and are more stringent than those of class-A. Both FCC conducted EMI-RFI specifications, however, cover the frequency range from 450kHz to 30MHz. The VDE regulations extend below 450kHz range. In fact the VDE frequency range for EMI-RFI conducted emission covers a spectrum from 10kHz to 30MHz. Fig. 2 shows the FCC and VDE curves for conducted RFI emissions.

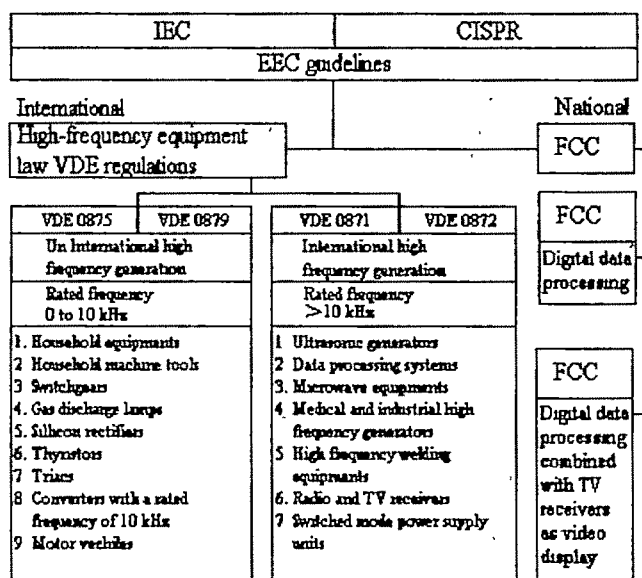


Fig. 1 : Summary of EMI-RFI requirements of FCC and VDE

Although the prescribed circuits will suppress the generated RFI to acceptable levels, yet it is important to understand that if the packaging or layouts of the power supply changes then even the assigned filter may not work properly. To elaborate on this claim let us consider a power transistor or a power rectifier handling high-frequency. Let it be directly mounted on the chassis of the power supply with only a mica insulator in between the two, and if the chassis is connected to the ac ground conductor, the generated RF-noise will be coupled to the ground conductor thus upset the effectiveness of the particular mains filter. It has been shown that a TO-3 switching transistor working at 20kHz, with a 200V input and mounted on a ground heat sink through a mica insulator, will generate an RF-current of 1mA at 1MHz. A solution to the above problem is to sandwich a metal shield in between the heat sink and insulator and to return the shield to the dc ground. This technique effectively "shorts out" the capacitance created by the mica insulator and thereby reduces the radio frequency noise currents. Power supply and system layouts are very important in reducing or eliminating RFI-EMI problems. The designer should take care in analyzing all potential problems before choosing the appropriate line filter.

II. RFI SOURCES IN SWITCHING POWER SUPPLIES

Every switching power supply is a source of RFI generation because of the very fast rise and fall times of current and voltage inherent in all converter operations. The main sources of switching noise are the switching transistors, the main rectifier, the output diodes, the protective diodes for transistors and of course the control unit itself. Now, depending upon the topology of the converter used, the RFI noise at the mains input may move from bad to worse levels. Fly back converters, which by design have a triangular input current waveforms, generate less conducted RFI noise than converters with

rectangular input current waveforms such as feed-forward or bridge converters. Fourier analysis shows that the amplitude of the high frequency harmonics of a triangular current waveform drop at a rate of 40dB/decade as compared to a 20dB/decade drop for a comparable rectangular current waveform.

III. PERMISSIBLE RFI EMISSION

The challenge of packaging electronic hardware to ensure electromagnetic compatibility (EMC) is becoming increasingly difficult. In U.S., the governing standard for regulating the containment of emissions is given by FCC Part 15, class-A and B. These FCC classes establish the levels of EMI containment permissible for various types of electronic equipment and these are expressed in allowable dB across a range of frequencies. An FCC class-A certification on radiation limits of digital devices is for business use while the class-B is for residential use. The class-B stipulation is more stringent in order to avoid interference with TV and other home reception systems. These stipulations are meant to put a limit on the amount of radiated emissions from electronic gadgets such as radios, televisions, ATM machines, radar equipment and other such devices.

The FCC class-B is generally meant for areas where emissions must be kept low like near an airport, hospitals and residential areas and also other places where it is more stringent on the level of allowed radiated emissions. In recent times EMC has taken on greater importance with the increasing use of electronics in security related applications.

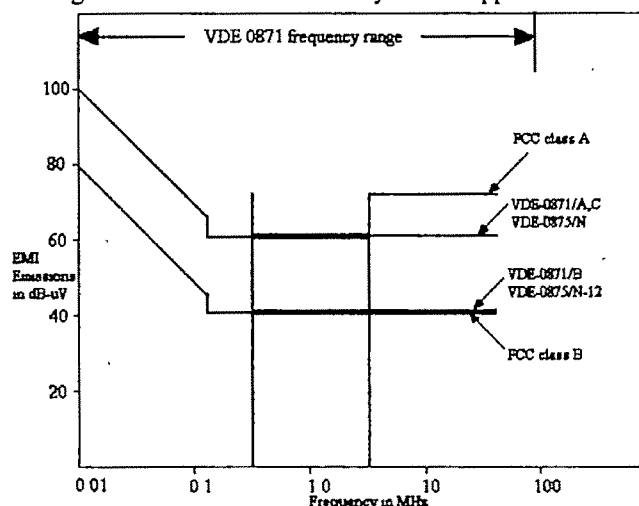


Fig. 2 : FCC and VDE regulation curves showing maximum permissible RFI-emission in dB-μV on conducted noise

EMC is of critical concern since its application provides network security. One can imagine the importance of preventing interference in network security applications. With too much interference the signal integrity may be impaired leading to breakdown of security system. The case study illustrates the various areas of concern and the modifications employed to ensure class-B compliance. Fig. 2 shows the

maximum possible RFI emission on conducted noise.

IV. AC INPUT LINE FILTER FOR RFI SUPPRESSION

The most common method of noise suppression at the switching power supply ac mains is the utilization of an LC filter for differential and common mode RFI suppression. Normally a coupled inductor is inserted in series with each ac line. while capacitors are placed between the lines, called X-capacitor (C_x) and between each line and the ground conductor, called Y-capacitor (C_y). The values of the capacitance and inductance may be within the following range for most of the suppressing systems.

$$C_x = 0.1 \text{ to } 2\mu\text{F}$$

$$C_y = 2200\text{pF to } 0.033\mu\text{F}$$

$$L = 1.8\text{mH at } 25\text{A to } 47\text{mH at } 0.3\text{A}$$

Fig. 3(a) depicts an input a.c. line filter for a standard switching power supply. During the selection of filter components it is important to ensure that the resonant frequency of the input filter is lower than the working frequency of the power supply. On the other hand, filtering conducted noise becomes much easier as the working frequency of the power supply is increased. The resistor R across the ac line of the filter is a discharge resistor for the X-capacitor. Its employment is recommended by the safety specifications of the VDE-0806 and IEC-380. In fact IEC-380 states that if the RFI X-capacitor is above 0.1uf, a discharge resistor of the following value is required in the circuit.

$$R = t / (2.21 C)$$

where, $t = 1\text{sec.}$ and C is the sum of the X-capacitors in μF .

Further reduction of the symmetrical and asymmetrical interference voltages can be accomplished by the insertion of an extra line choke L_2 as shown in fig. 3(b) but this in turn causes a reduction in the charging current of X-capacitors. Fig. 3(c) [5, 6, 8, 10, 11] and fig. 3(d) [5, 7, 9] depict standard radio-frequency mirror inverter circuits which are used for induction heating for industrial and domestic equipment respectively. Both these inverter circuits take a.c. power either through the line filter circuit of fig. 3(a) or through the line filter circuit of fig. 3(b).

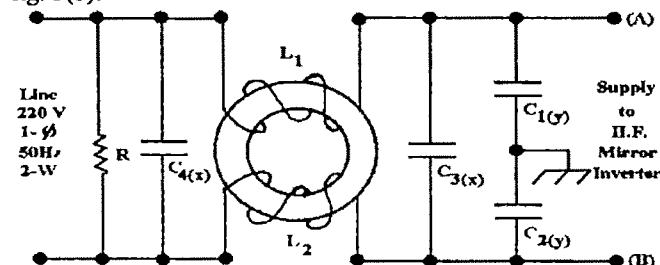


Fig. 3(a) : An input ac line filter of mirror-inverter power supply for RFI noise suppression using one line choke

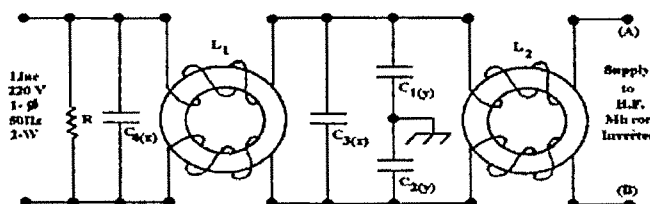


Fig. 3(b) : Improved ac line filter incorporating two line chokes

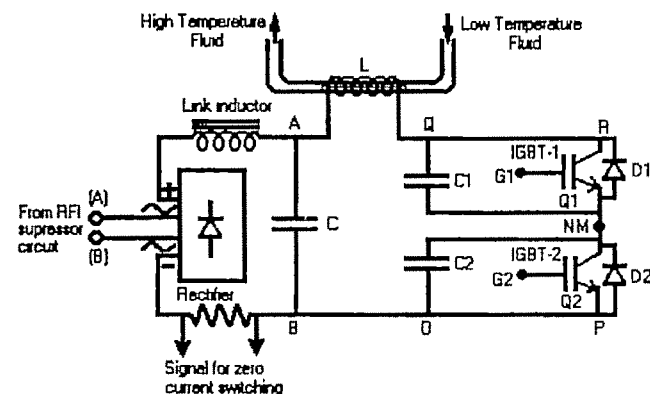


Fig. 3(c) : Radio-frequency mirror-inverter circuit for industrial application

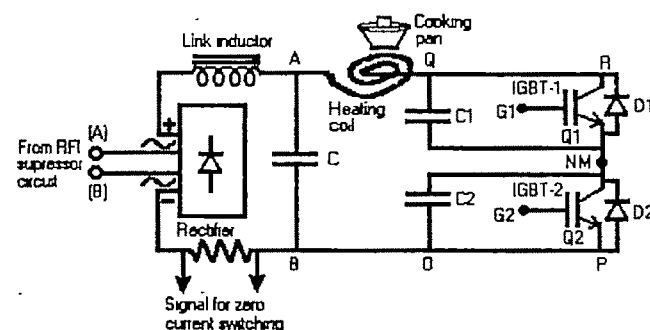


Fig. 3(d) : Radio-frequency mirror-inverter circuit for domestic application

V. CONCLUSION

Although the described circuits will suppress the generated RFI to acceptable levels, it is important to understand that if the power supplies packaging or layout changes, a certain filter may or may not work properly. To elaborate on this claim, if power transistor or power rectifier which uses high frequency waveform is directly mounted on the chassis of the power supply, with only a mica insulator between the two, and if the chassis is connected to the ac ground conductor, generated RF noise will be coupled into the ground conductor, thus upsetting the effectiveness of the particular mains filter. It has been shown that a TO-3 switching transistor working at 20kHz with a 200v Input, mounted on a ground heat sink through a mica insulator, will generate an RF current of 1mA at 1 MHz. A solution is to sandwich a metal shield between the insulator and to return the shield to the dc ground. This technique

effectively "shorts out" the capacitor created by the mica insulator, reducing RF noise currents. Power supply and systems layout are very important in reducing or eliminating RFI-EMI problems. The designer should take care in analyzing all potentials problems before the proper line filter is chosen.

REFERENCES

- [1] VDE-0875/6.77 = Specifications for the radio interferences suppression of equipment, machine and system with operation frequencies from 0 to 10 kHz.
- [2] VDE -0871/6.78 = Regulations for the radio frequency interference suppression of high frequency apparatus and installations.
- [3] FCC docket20780 = First report and order for technical standards for computing equipment, part 15. Subpart j
- [4] Docket 80-284,FCC 81-69 = FCC methods of measurement of radio noise emission from computing devices.
- [5] "An improved inverter circuit arrangement" by P.K.Sadhu, R.N.Chakrabarti, S.P.Chowdhury Patent Number 69/cal/2001, Patent Office - Government of India
- [6] "A new generation fluid heating using BJT and IGBT"-by Prof. Pradip Kumar Sadhu, Dr. R. N. Chakrabarti, Dr. S. P. Chowdhury - Published in "Journal of the institution of engineers" volume-82 March , 2002, P. P 273 -280
- [7] "A cooking apparatus using high frequency induction heating"- by P.K Sadhu, R.N.Chakrabarti, S.P Chowdhury. Patent Number 68/cal/2001, Patent Office- Government of India.
- [8] "A new generation microprocessor based radio-frequency operated induction heating for sterilization and boiler plant"-by Prof. Pradip Kumar Sadhu, Dr. S. K. Mukherjee, Dr. R. N. Chakrabarti, Dr. S. P. Chowdhury and Dr. B. M. Karan. - Published in "IEEMA Journal" volume XXII number 2 February 2002, P. P 36 - 48.
- [9] "A new generation microprocessor based series resonant inverter for induction heating cooking appliances"-by Prof. Pradip Kumar Sadhu, Dr. S. K. Mukherjee, Dr. R. N. Chakrabarti, Dr. S. P. Chowdhury and Dr. B. M. Karan. - Published in "Industrial Engineering Journal" volume xxx number 9 september ,2001, P. P 10 -15.
- [10] "Microprocessor-based energy efficient sterilization for surgical instrument using a new generation inverter topology"- published in the Journal of Energy, Heat & Mass Transfer, Regional Centre for Energy, Heat and Mass Transfer for Asia and the Pacific, Madras IIT, Madras; Vol 23, Number 1, March 2001, P.P. - 39-53, Authors:- Pradip Kumar Sadhu, Prof (Dr.) S. K. Mukherjee, Prof.(Dr.)R. N. Chakrabarti, Dr. S. P. Chowdhury, Dr. B. M. Karan.
- [11] "High efficient contamination free clean heat production"- published in the Indian Journal of Engineering & Materials Sciences, National Institute of Science Communication, New Delhi; Vol-9, June 2002, P.P. -172-176, Authors:- Pradip Kumar Sadhu, Prof (Dr.) S. K. Mukherjee, Prof.(Dr.)R. N. Chakrabarti, Dr. S. P. Chowdhury, Dr. B. M. Karan

Performance Analysis of H.F. Mirror Inverter for Energy Efficient Induction Cooking Appliance Range

Pradip Kumar Sadhu¹, Nitai Pal², Rupendranath Chakrabarti³, T. K. Chatterjee⁴

¹Electrical Engineering Department, Indian School of Mines University, Dhanbad - 826004 e-mail : pradip_sadhu@yahoo.co.in

²Electrical Engineering Department, Indian School of Mines University, Dhanbad - 826004 e-mail : nitai_pal@rediffmail.com

³Electrical Engineering Department, Jadavpur University, Kolkata - 700032 e-mail : rupen_chakrabarti@yahoo.co.in

⁴Electrical Engineering Department, Indian School of Mines University, Dhanbad - 826004 e-mail : tkeism@yahoo.com

Abstract—Induction cooking appliance range is a very practical device and can be used for any cooking application. It cooks food in a safer and more energy-efficient manner. Protecting the world's environment and conserving resources are of major concern today and the induction cooking appliance range is probably the most environment friendly cooking device compare to other available cooking device in the market. It releases no fumes or chemicals into the air and uses no irreplaceable fossil fuels. Several variables have been considered to determine the amount of heat energy required for a specific application like the degree of temperature change required, the mass, the specific heat and the coupling efficiency of the coil design. The paper outlines the testing of the equivalent model using Pspice simulation.

Key words— Pspice, Resonant, soft switching, duty ratio, IGBTs, Litz wire.

I. INTRODUCTION

INDUCTION cooking appliance range is one of the applications of induction heating. The induction cooking appliance range, while not yet a part of most households, becoming increasingly acceptable as a useful, energy-efficient method of preparing food. It is designed to replace ordinary stove-plates (Fig.1a & 1b). The induction cooking appliance ranges are available in a variety of forms, from full-sized four-hob ranges to portable one-hob hot plates. The conventional electric hot plates are very popular with catering businesses, as they are much cheaper and safer to operate than comparable butane units. They cook food quickly, are easy to use and are easy to clean. Induction cooking appliance ranges can be used with any type of food.

Table – 1 shows that an induction cooking appliance range is a highly efficient device and cut down the power bills drastically. Other tests show that induction cooking is faster

than using gas, halogen or a microwave oven. Although microwave ovens offer almost same overall efficiency with induction cooker, but it does not maintain the Indian style of cooking (frying food material with vegetable oil). The induction cooking appliance range more expensive than electric or gas hotplates but less expensive than microwave oven.

TABLE – I : EFFICIENCY OF VARIOUS COOKING SYSTEMS

Sl No	Cooking Methods	Efficiency
1.	Induction Heating Cooking	90%
2.	Microwave oven	90%
3.	Halogen Heating Cooking	58%
4.	Electric Resistive Heating	47%
5.	Gas Cooking (L.P.G.)	40%

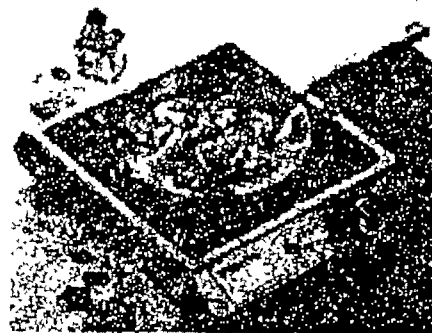


Fig.1 (a): Conventional electric hot plate

II. REQUIREMENT OF COMPONENTS FOR INDUCTION-EFFICIENT PAN

- 18/10 stainless steel is non-reactive to food and easy to clean,
- 18/10 stainless steel is used for superior bond,
- Magnetic stainless steel is used for efficient induction,
- 18/10 stainless steel resists pitting and rusting,
- Teflon made platform is used for cooking range because it passes maximum magnetic flux as well as withstand high temperature.

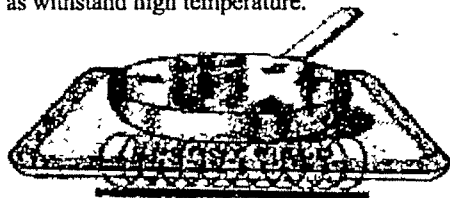


Fig. 1 (b): Diagram of an induction cooking appliance range

III. BASIC ASPECTS

A. Working principle of induction cooking appliance range

Each hob contains one or more coils made up of ferro-magnetic material. When an alternating current is passed through these coils, a magnetic field of the same frequency is produced. If a magnetic material based pan is placed on the hob, the magnetic field induces a current in the pan. The internal resistance of the pan causes heat to be dissipated, following the Joule effect. Thus it is the pan itself and not the cooker that heats up and cooks the food. Once the pan is removed from the cooker, the energy transfer stops. The result is a flameless method of cooking in which it is almost impossible to start a fire by forgetting to turn off the stove. Since there is no transfer of heat energy between the hob and the pan, the heat transfer takes place from the pan to the food and thus less heat is lost into the air, resulting in a more efficient means of cooking.

B. Practical induction cooking appliance range

The switching frequency may be varied between 20 kHz to 50 kHz, as this is the frequency range of practical induction cooking appliance ranges. Frequencies should be ultrasonic but not high enough to produce communication interference. An accurate design of the induction coil is necessary for induction cooking appliance ranges in respect of both the inductance and resistance of the coil. Since the practice in induction cooking appliance ranges is to place a ferrite disc underneath the coil, as shown in Fig. 2(b), the inductance and ac resistance of the heat-coil must be calculated by taking the presence of both the ferrite disc and the work piece into

account.

(a) Material characteristics of cooking pan, (b) Size & shape of cooking pan and (c) Positioning on coil of cooking pan are the key factors for the work piece.

(a) Power output, (b) Frequency and (c) Utility requirements are the key factors for power supply.

(a) Diameter, (b) Shape and (c) Number of turns are the key factors for induction coil.

IV. CIRCUIT DESCRIPTION AND OPERATION

Two IGBTs with internal anti-parallel diodes are mounted in the same module. In order to minimize the reactive loading, series and parallel compensating capacitors are used in the output circuit. An isolated gate drive is needed, but only a small isolation transformer will serve the purpose due to 50% duty ratio. A spiral heating coil made up of Litz as shown in Fig. 2(a) is used for induction cooking.

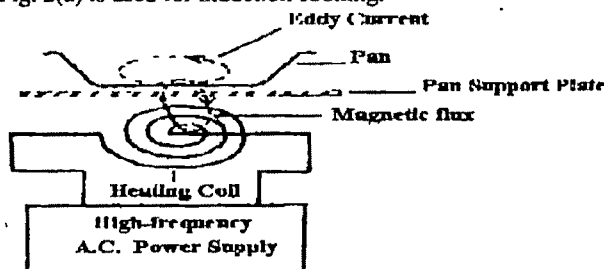


Fig.2(a): Basic circuit for Induction Heating

A thermal insulator Fig.2(b) is placed between the cooking vessel and the heating coil to protect the coil from overheating and also to support the vessel. The vessel must be made up of a material for which the product of resistivity and relative permeability is high enough to yield an acceptable efficiency. In order to obtain maximum coupling, the spacing between the vessel and the coil should be kept as small as possible, but at the same time it should be large enough for adequate support, airflow and insulation. A ferrite disc may be used to enhance the coupling, but with additional cost.



Fig.2(b): Structure of coil

A complete design can be done on the basis of the following assumptions:

- (i) The spacing between the coil and the vessel is same throughout.
- (ii) The heating coil has the same inner and outer diameter, irrespective of the number of turns.
- (iii) The cooking vessel remains unchanged.
- (iv) The key to a successful induction cooking appliance range is to select a well-suited inverter with optimal design (Fig.3). For present work, series h. f. mirror inverter is chosen.

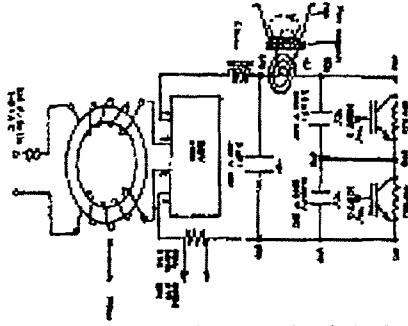


Fig. 3: Series h. f. mirror inverter circuit for induction cooking appliance range

Notations:

- x_{cw} → Spacing between the vessel and the coil
 $V_{d(rms)}$ → Fixed grid voltage (rms)
 $V_{d(p)}$ → Fixed grid voltage (peak)
 $V_{d(avg)}$ → Fixed grid voltage (average)
 V_{sp} → Spike voltage
 $V_{B(p)}$ → Peak voltage of bridge rectifier
 $V_{C(p)}$ → Peak voltage of input capacitor
 $V_{Cr(p)}$ → Peak voltage of resonant capacitor
 $V_{Cr(rms)}$ → RMS voltage of resonant capacitor
 $V_{S(p)}$ → Peak voltage of switches (IGBTs)
 $I_{B(avg)}$ → Average current of bridge rectifier
 $I_{Lr(p)}$ → Peak current of heating coil
 $I_{S(avg)}$ → Average current of switches (IGBTs)
 N → Number of turns of heating coil
 R_{cp}, L_{rp} → Resistance & leakage inductance of primary (heating coil)
 R_{cs}, L_{ls} → Resistance & leakage inductance of secondary (cooking vessel)
 P_{max} → Maximum power output
 R_{en} → Total equivalent resistance as referred to secondary
 L_{en} → Total equivalent inductance as referred to secondary
 R_i → Internal resistance of induction coil
 L_r → Series inductance of induction coil
 D_1, D_2 → Inner & outer diameter of induction coil
 C_r → Resonant capacitance
 C_i → Input capacitance
 f_r → Oscillating frequency of heating coil
 $f_{o(min)}$ → Minimum switching frequency f_s
 Z_0 → Characteristic impedance
 Q → Quality factor

V. LOAD CHARACTERISTICS

A circular heating coil^[1,2] with 37 turns, having an outer diameter of 175.5 mm and an inner diameter of 43.5mm have been used. The induction-heating load can be seen as a transformer with a short-circuited secondary, and will be

referred to as the load transformer. The heating coil and the cooking vessel can be represented by an equivalent series inductance (L_r) and resistance (R_i), assuming negligible magnetizing inductance. The power transformer is designed by assuming the primary to secondary turns ratio given by-

$$N = V_{in,min} / (2 V_{out}) \quad (1)$$

The characteristic impedance of the series resonant network is given as a function of input voltage and output power as:

$$Z_0 = \eta V_{in,min}^2 / 2 \pi P_{out} \quad (2)$$

Where, η is the efficiency of the inverter.

The resonant capacitor is

$$C_R = 1 / 2 \pi f Z_0 \quad (3)$$

and the resonant inductor is

$$L_R = Z_0 / (2 \pi f) \quad (4)$$

Where, f is the frequency of operation.

The parameters of the equivalent circuit in effect of normalization of R_i and L_r with respect to N are denoted by R_{en} and L_{en} ^[5,6] where

$$R_i = R_{cp} + N^2 R_{cs} \quad (5)$$

$$L_r = L_{rp} + N^2 L_{cs} \quad (6)$$

$$R_{en} = R_i / N^2 = (R_{cp} / N^2) + R_{cs} \quad (7)$$

$$L_{en} = L_r / N^2 = (L_{rp} / N^2) + L_{cs} \quad (8)$$

VI. INVERTER DESIGN

An analytical model has been used to investigate the operation of the inverter, assuming ideal reactive and semiconductor components. It is known that the normalized power is a function of the normalized switching frequency and that the maximum power (P_{max}) is obtained when f_s is equal to f_0 . Therefore, C_r should be so chosen that f_s of the test circuit is equal to the desired minimum switching frequency ($f_{s,min}$) of the inverter. The frequency f_0 and f_s are only significantly different at low values of Q where,

$$Q = Z_0 / R_i \quad (9)$$

$$Z_0 = \sqrt{L_r / C_r} \quad (10)$$

$$f_0 = (2\pi \sqrt{L_r C_r})^{-1} \quad (11)$$

$$f_r = (f_0^2 - (R_i / (4\pi L_r))^2)^{0.5} \quad (12)$$

$$f_r = f_0 (1 - (2Q)^{-2})^{0.5} \quad (13)$$

For the solution of $f_{s(min)}$, power is the main criteria and therefore, $f_{s(min)}$ is chosen to be equal to f_0 . It may be noted that the switching frequency range increases as the quality factor decreases for a certain power range, which is undesirable. If x_{cw} , f_0 , C_i , C_r and P_{max} are chosen, L_r , R_i , Z_0 and Q can be calculated using equations (2), (9), (10) and (11).

Table – II : Calculation of circuit parameters

Sl. No.	Variable	Method obtained	Value
1.	$V_d(\text{rms})$	Fixed grid voltage	220 V
2.	$V_d(p)$	$\sqrt{2} V_d(\text{rms})$	311 V
3.	$V_d(\text{avg})$	$2 V_d(p) / \pi$	198 V
4.	L_r	$(4 \pi^2 f_0^2 C_r)^{-1}$	51.7 μH
5.	Z_0	$\sqrt{L_r / C_r}$	11.37 Ω
6.	R_{cn}	$0.203 V_d(\text{avg})^2 / N^2 P_{max}$	5.81 m Ω
7.	R_1	$R_{cn} N^2$	7.95 Ω
8.	Q	Z_0 / R_1	1.43

where the following values are to be noted:

$P_{max} = 1000 \text{ w}$; $f_r = 35 \text{ kHz}$; $C_i = 5 \mu\text{F}$; $C_r = 0.4 \mu\text{F}$ (all chosen); $N = 37$; $f_0 = 24.6 \text{ to } 33.3 \text{ kHz}$; $D_1 = 43.5 \text{ mm}$; $D_2 = 175.5 \text{ mm}$ (all values taken due to practical considerations).

Table – III

Calculation of required power semiconductor switch ratings

Sl. No.	Variable	Method obtained	Value
1.	$V_B(p)$	$V_d(p)$	311 V
2.	$I_B(\text{avg})$	$0.901 P_{max} / V_d(\text{rms})$	4.1 A
3.	$V_{CI}(p)$	$V_d(p) + V_{sp}$	315.1 V
4.	$V_{Cr}(p)$	$(0.637Q + 0.5)V_d(p)$	438.8 V
5.	$V_{Cr}(\text{rms})$	$0.451Q V_d(\text{avg})$	121.7 V
6.	$I_{Lr}(p)$	$0.45 V_d(p) / R_1$	17.6 A
7.	$V_S(p)$	$V_d(p) + V_{sp}$	315.1 V
8.	$I_S(\text{avg})$	$0.203 V_d(\text{avg}) / R_1$	5.1 A
9.	$I_S(\text{off})$	$(0.113 \exp(-0.263Q + 0.321)) V_d(\text{avg}) / R_1$	2.66 A

VII. PSPICE CIRCUIT FOR SIMULATION

A circuit as shown in Fig.5 is designed using the values (refer to tables II and III) for the purpose of simulation by PSPICE.

A. Simulated Results

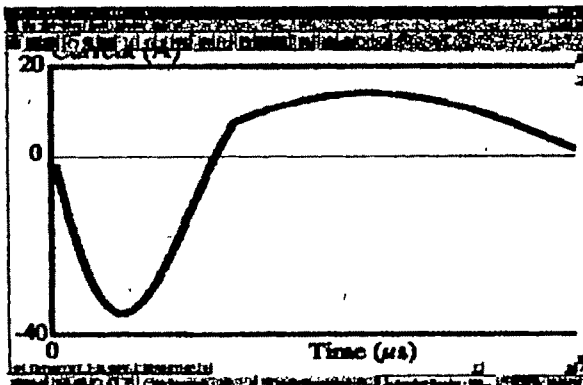


Fig. 4 : Induction-coil current as obtained by Koertzen, Wyk, and Ferreira in reference [4]

Currents through various elements of the circuit in Fig. 5 are obtained. The current through L_1 shows (fig.6) matches with the induction-coil current which has been obtained by Koertzen, Wyk, and Ferreira in reference [4].

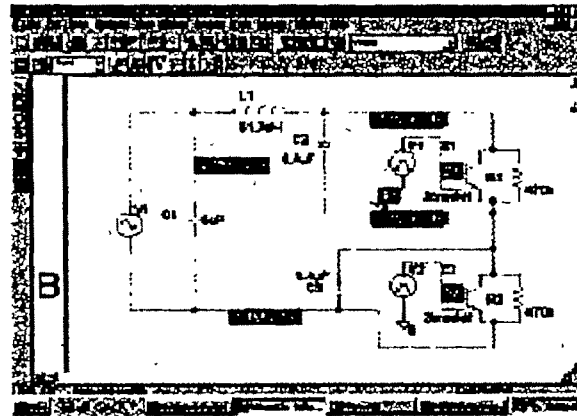


Fig. 5 : PSPICE circuit

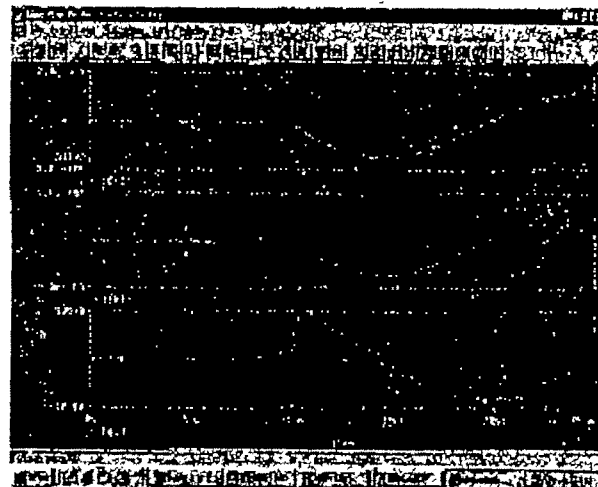


Fig. 6: Currents through L_1 , R_1 & R_2

VIII. CONCLUSION

In order to reduce the components and complexity of the control circuit, it becomes essential to employ modified half-bridge inverter circuit. The fact, that the output current can be maintained constant, irrespective of the load on the inverter, is an extremely desirable feature required for induction-heated home appliances like rice-cooker, hot-plates, drier, etc. because the secondary load is changed according to the size and thickness of the utensils.

REFERENCES

- [1] P.K.Sadhu, R.N.Chakrabarti, S.P.Chowdhury.- "An improved inverter circuit arrangement" - Patent Number 69/cal/2001, Patent Office – Government of India.

- [2] P.K.Sadhu, R.N.Chakrabarti, S.P.Chowdhury.-"A cooking apparatus using high frequency induction heating:"- Patent Number 68/cal/2001, Patent Office- Government of India.
- [3] Koertzen, Wyk, Ferreira - "Design of the half-bridge, Series resonant converter for Induction Cooking" - pp. 729-735, 0-7803-2730-6/95, 1995, IEEE.
- [4] Koertzen, Wyk, Ferreira - "An investigation of the analytical computation of inductance and ac resistance of the heat-coil for induction cookers" - pp.1113-1118, 0-7803-0634-0/92, 1992, IEEE.
- [5] Koertzen, Wyk, Ferreira - "Single shot surface heating series resonant converter with ZCS and an uncontrolled DC link voltage"- pp.1957-1963, 0-7803-3008-0/95,1995, IEEE.
- [6] Narendranath Jana, Dr. Pradip Kumar Sadhu, Prof. (Dr.) R. N. Chakrabarti - "A novel high-frequency mirror inverter for industrial induction heating"- Published in "Industrial Engineering Journal" volume XXXIII, Number 11, November-2004, P. P 25 -29.
- [7] Prof. Pradip Kumar Sadhu, Dr. S. K. Mukherjee, Dr. R. N. Chakrabarti, Dr. S. P. Chowdhury and Dr. B. M. Karan - "A new generation microprocessor based series resonant inverter for induction heating cooking appliances" - Published in "Industrial Engineering Journal" volume XXX, Number 9, September-2001, P. P 10 -15.
- [8] P. K. Sadhu, S. K. Mukherjee, R.N. Chakrabarti, S. P. Chowdhury and B. M. Karan, "Microprocessor - based energy efficient sterilization for surgical instrument using a new generation inverter topology" - Journal of Energy, Heat & Mass Transfer, Asia and the Pacific; Vol 23, Number 1, March 2001, P.P. - 39-53.
- [9] Dr. P.K. Sadhu, Dr. R. N. Chakrabarti, Mrs. N. L. Nath, Naveen.K. Batchu, Smrita Kumari, Kumari Rimjhim, "Analysis of a series resonant superimposed inverter applied to induction heating" - Journal of Institution of Engineers (I); Vol 84, March 2004, P.P. - 214-217.
- [10] Prof. Pradip Kumar Sadhu, Dr. R. N. Chakrabarti, Dr. S. P. Chowdhury - "A new generation fluid heating using BJT and IGBT" - Published in "Journal of the institution of engineers" volume-82 March , 2002, P P 273 -280.
- [11] Prof. Pradip Kumar Sadhu, Dr. S. K. Mukherjee, Dr. R. N. Chakrabarti, Dr. S. P. Chowdhury and Dr. B. M. Karan. - "A new generation microprocessor based radio-frequency operated induction heating for sterilization and boiler plant" - Published in "IEEMA Journal" volume XXII Number 2, February 2002, P. P 36 - 48.
- [12] P. K. Sadhu, S. K. Mukherjee, R.N. Chakrabarti, S. P. Chowdhury and B. M. Karan, "High efficient contamination free clean heat production" - Journal of Engineering & Material Sciences, National Institute of Science Communication, New Delhi; Vol 9, June 2002, P.P. - 172-176.

Design of Speed Control of DC Series Motor using Fuzzy PID Controller

Barwal Shwetla and K.K Garg

Department of Electrical Engineering, Panjab Engineering College, Chandigarh ,India (e-mail: shwetla_nith@yahoo.co.in)

Abstract: The use of fuzzy proportional integral controller for the speed control of DC series motor was studied. The results were compared with classical PI controller output. Results of simulation on the plant demonstrated that the proposed fuzzy controller was able to overcome disadvantages of usual PI-controller - sensitiveness to inertia variation and sensitiveness to variation of the range of reference speed alteration.

Key words: fuzzy logic controller (FLC), proportional integral (PI) controller

I. INTRODUCTION

IN the recent years, fuzzy logic controllers, especially PID type fuzzy controllers are being widely used in industrial processes owing to their heuristic nature associated with simplicity and effectiveness for both linear and nonlinear systems. In fact, for single- input single- output systems, most of fuzzy logic controllers have been essentially of PD type, PI type or PID type with nonlinear gains. Because of the nonlinearity of the control gains, fuzzy PID controllers possess the potential to achieve better system performance over conventional PID controllers provided the nonlinearity is suitably utilized [1].

Pure fuzzy control applications have been more an exception than the rule. In most cases the fuzzy controller output served as reference parameters, such as gains that are provided to a conventional controller instead of to driving actuators in the process directly. Because fuzzy controller could be regarded as a nonlinear characteristic field controller, it had no internal dynamic aspects. So, any dynamic property must be implemented by an appropriate preprocessing of the measured input data [2].

Classification chart of Fuzzy PID Controller in view of control actions have been given in Fig.1 [3].

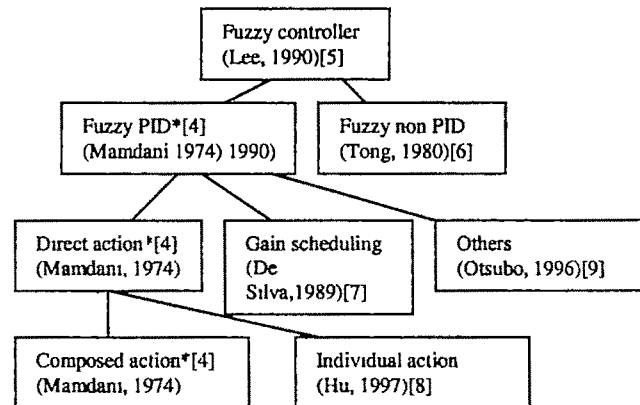


Fig. 1 Classification chart The main reference source is given in the parentheses. The asterisk indicates the commonly-used type of controllers compared with its counterparts.

There have been several types of control systems that use FLC as an essential system component. The majority of applications during the past two decades belonged to the class of fuzzy PID controllers. These fuzzy controllers could further be classified into three types: the direct action (DA) type, the gain scheduling (GS) type and a combination of DA and GS types. The majority of fuzzy PID applications belonged to the DA type where the fuzzy PID controller placed within the feedback control loop computed the PID actions through fuzzy inference. In GS type controllers, fuzzy inference has been used to compute the individual PID gains and the inference was either error driven self-tuning [4] or performance-based supervisory tuning [5]. In addition to the common Mamdani-type PI structure, several other structures using one-input or three-input controllers have been reported. Therefore, it became clear from the studies that the majority of these applications belonged to the class of two-input fuzzy PID type structures. Some two -input fuzzy structures are given below.

1) Fuzzy Proportional-Derivative (fuzzy-PD) control which generated a control output from the error and the change rate of error and was a position type control. [10]

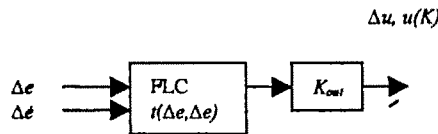


Fig. 2: Fuzzy PD controller diagram

2) Fuzzy proportional integral (fuzzy PI) control which generated incremental control output from the error and the change rate of error and was a velocity type control. [10]

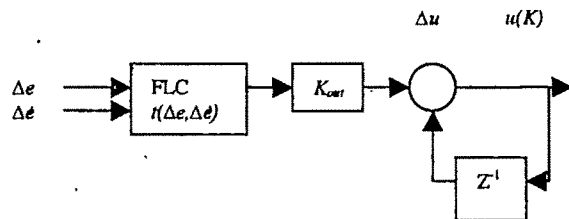


Fig. 3: Fuzzy PI controller diagram

II FUZZY CONTROLLER FOR DC SERIES MOTOR DRIVE

A.. DC Series Motor

DC series motor has been best suited for certain applications such as vehicle, crane, hoist, and similar drives where large starting torque at low speeds was required.

The differential equations (1) and (2) governing the performance of DC series motor were the following:

$$e_a = R_a i_a + L_a \frac{di_a}{dt} + K_{af} i_a \omega + K_{re} \omega \quad (1)$$

$$K_{af} i_a^2 = J \frac{d\omega}{dt} + B\omega + T_L \quad (2)$$

Where, R_a =armature resistance, L_a =armature inductance, K_{af} =armature voltage constant, K_{re} =residual magnetism voltage constant, J =moment of inertia, B = friction coefficient, T_L =load torque, e_a =motor terminal voltage, i_a =armature current and ω =motor speed. The above equations were nonlinear because of the product and square terms involving the variables.

A linear model or transfer function for the series motor could be derived by applying small signal perturbation techniques. This model would then be used in the analysis of a closed loop system incorporated the series motor. The analysis was valid for small disturbances around a given steady state operating point [11].

Fig 4. Overall transfer function of the DC series motor was modified to the form:

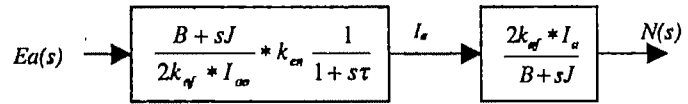


Fig. 4 transfer function block dig. of DC series motor

B. Fuzzy Controller

In this section, the design procedure of Fuzzy PI speed and current controllers have been presented. A typical FLC consisted of three basic components, namely Input signal fuzzification, a fuzzy engine, and output signal defuzzification. The fuzzification block transformed the continuous input signal into linguistic fuzzy variables. The fuzzy engine handled rule inference where human experience could easily be injected through linguistic rules. The defuzzification block transformed the fuzzy control actions to continuous (crisp) signals which could be applied to the physical plant. The knowledge base included fuzzy sets, which were defined on the interval of the inputs and the outputs of the FLC, and a rule base, which was constructed from fuzzy implications. [12]

The Figure 5 described the fuzzy PI controlled DC motor drive [12] where speed from motor (M) was read through tachogenerator (T) and compared with reference speed given at the input. The error was then processed through controllers to get desired speed response [11].

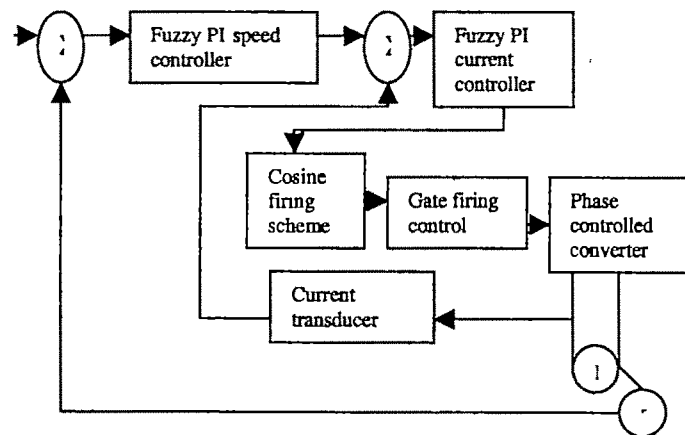


Fig. 5 Fuzzy PI controller in DC motor drive

III STEPS

A.. Fuzzification

The motor variables to be controlled were the speed ω and the armature current i_a . In the proposed PI fuzzy speed controller, the input variables were defined as the error $e_s(k)$ and the error change $\Delta e_s(k)$:

$$e_s(k) = \omega_r(k) - \omega(k) \quad (3)$$

$$\Delta e_s(k) = e_s(k) - e_s(k-1) \quad (4)$$

Equations similar to (3) and (4) could be defined for the PI fuzzy current controller:

Where, $\omega_r(k)$ was the reference speed signal, $\omega(k)$ was the actual motor speed, $i_{ar}(k)$ was the reference current signal (generated from the speed controller) and $i_a(k)$ was the armature current all at the k^{th} sampling interval.

The error and error change for both speed and current were scaled using appropriate scaling factors. These scaled input data were then converted into linguistic variables which were viewed as labels of fuzzy sets. In this paper, the following linguistic variables have been used for the input variables viz., Positive Medium (PM), Negative Medium (NM), Positive Small (PS), Negative Small (NS), Zero (Z), Positive Big (PB), Negative Big (NB).

A fuzzy set was defined by assigning the grade of membership values to each element of the universe of discourse. There were many types of membership functions, e.g., the bell-shaped, the triangular-shaped, the trapezoidal-shaped, etc. The choice of membership function shape is mainly dependent on the designer preference. For simplicity, the triangular-shaped functions had been used [8].

In the universe of discourse, the numbers for the afore mentioned linguistic variables range viz., NB $\{-1.33, -1.0, -0.66\}$, NM $\{-1.0, -0.66, -0.33\}$, NS $\{-0.66, -0.33, 0\}$, Z $\{-0.33, 0, 0.33\}$, PS $\{0, 0.33, 0.66\}$, PM $\{0.33, 0.66, 1.0\}$, PB $\{0.66, 1.0, 1.33\}$. were anticipated by the range of error from the graph derived with applying PI in the simple DC series motor drive.

B. Fuzzy Control Rules

The fuzzy control rules were developed based on intuition and experience instead of the availability of the system model. The structure of a general rule would be written as 'If $e(k)$ is W and $\Delta e(k)$ is Q Then $\Delta u(k)$ is C', where $\Delta u(k)$ was the change in control input (which was the output of the fuzzy controller) and W, Q and C were the fuzzy subsets defined over the universe of discourse of e , Δe and Δu , respectively. The linguistic variables used for the output signal $\Delta u(k)$ and their associated numbers were, Positive Very Big (PVB) (0.8, 1.0, 1.2), Positive Big (PB) { 0.6, 0.8, 1.0}, Positive Medium (PM) (0.4, 0.6, 0.8), Positive Small (PS) { 0.2, 0.4, 0.6, 1}, Zero (Z) { -0.2, 0.0, 0.2 }, Negative Small (NS) {-0.6, -0.4, -0.2}, Negative Medium (NM) { -0.8, -0.6, -0.4}, Negative Big (NB) { -1.0, -0.8, -0.6} and Negative Very Big (NVB) {-1.2, -1.0, -0.8}. The following observations were used to determine the fuzzy control rules:

1) If both the error (e) and the error change (Δe) are zero then the control settings should be kept at its present value (i.e. $\Delta u = 0$).

2) If the error is positive and increasing (i.e. Δe is positive), then positive control input (Δu positive) should be used to reduce the error to zero.

3) If the error is negative and decreasing (i.e. Δe is negative), then negative control input is used (Δu negative) to minimize the error.

4) If the error is positive and decreasing (or negative increasing), then small or zero control input is required.

According to the above observations, the fuzzy control rules were selected. Since both the speed and current loops must satisfy the needs of fast transient response with minimum overshoot and they have essentially first order characteristics, then, intuitively the same fuzzy control rules should be valid for both loops. For example these rules were given in Table I, the element in the fifth column and third row read: If $e(k)$ is PS and $\Delta e(k)$ is NS Then $\Delta u(k)$ is Z.

Fig. 6 Fuzzy control rules Chart for speed and current controllers

$\frac{e}{\Delta e}$	NB	NM	NS	Z	PS	PM	PB
NB	NVB	NVB	NVB	NB	NM	NS	Z
NM	NVB	NVB	NB	NM	NS	Z	PS
NS	NVB	NB	NM	NS	Z	PS	PM
Z	NB	NM	NS	Z	PS	PM	PB
PS	NM	NS	Z	PS	PM	PB	PVB
PM	NS	Z	PS	PM	PB	PVB	PVB
PB	Z	PS	PM	PB	PVB	PVB	PVB

Fig. 6 Rule matrix

D. Defuzzification

Basically, a defuzzification scheme could be viewed as a mapping from a space of fuzzy control actions defined over an output universe of discourse into a space of crisp control actions. The aim of a defuzzification strategy was to produce a crisp fuzzy action that best represented the possibility distribution of an inferred fuzzy control action. Bisector method was used here.

Once a crisp value of $\Delta u(k)$ is determined, the control signal $u(k)$ could be evaluated from the recursive formula

$$u(k) = \Delta u(k) + u(k-1) \quad [12].$$

III SIMULATION STUDY

In order to illustrate the effectiveness of the proposed fuzzy controllers, digital simulation of the drive system has been performed. The parameters of the drive system were as follows: $K_{res} = 0.027$ H, $K_{ar} = 0.027$ V.sec.rad, $R_a = 1$, $L_a = 0.032$ H, $J = 0.0465$ kg-m², $B = 0.004$ N.m.s/rad, k_t =tacho constant =0.057V.sec/rad, k_r =current transducer constant = 0.5 V/A, cosine firing scheme constant = 25. The steady state operating point was α_o 25.8, $e_{ao} = 102.6$ V, $\omega_o = 155.4$ rad/sec, $i_{ao} = 18.7$ A and $T_{Lo} = 10$ N.m. For the sake of comparison, classical PI speed and current controllers were also designed and simulated with the drive system.

The parameters of these controllers have been found to be: t_d = speed controller time delay = 0.5 sec., t_i = current controller time delay = 0.01 sec., k_s = speed controller gain = 1.2 and k_i = current controller gain = 0.01 [14].

The drive system was simulated with classical and fuzzy control loops for reference speed = 188.4 rad/sec (corresponds to 1800 rpm).

Comparison was made for the settling time and maximum overshoot of speed response for both types of controllers (Table I, II). It was evident that the transient behavior of the fuzzy controlled drive was better than that of the conventional PI controlled drive.

Software tool used for simulation is MATLAB.

IV. COMPARATIVE TABLES FOR CONCLUSION

Table I. Step input of 188.4 rad/sec

controller	Fuzzy PI	Classical PI
Maximum peak	178 rad/s	290 rad/s
Settling time	4 sec	5.5 sec
Steady state speed	178 rad/s	178 rad/s

Table II. Increasing step input range to 200 rad/sec

controller	Fuzzy PI	Classical PI
Maximum peak	190 rad/s	307.5 rad/s
Settling time	4.5 sec	5.1 sec
Steady state speed	190 rad/s	189.2 rad/s

Table III. Current response for step = 188.4 rad/sec

controller	Fuzzy PI	Classical PI
Maximum peak	10.75 A	25.7 A
Settling time	3 sec	5.5 sec
Steady state current	10.75 A	11 A

Table IV. Voltage response for step = 188.4 rad/sec

controller	Fuzzy PI	Classical PI
Maximum peak	157 volts	292 Volts
Settling time	3.5 sec	4.21 sec
Steady state Voltage	157 volts	157 volts

Table V. Application of step torque 5 Nm/sec at 3sec and input 188.4 rad/sec

parameters	Fuzzy PI	Classical PI
Steady state speed	179 rad/s	179 rad/s
Dip in speed curve at 3 sec	1 rad/sec	5 rad/sec

1) The results of response of fuzzy PI for the case of current, voltage and speed was better than PI controller.

2) By increasing the step range the response was better, and the oscillations were negligible in case of fuzzy PI.

3) The dip due to the application of torque was more in case of PI controllers.

4) The settling time and maximum peak for current voltage and speed response was lesser in the case of fuzzy PI controller.

In addition to this the following observations were also made; 1) The value of the change-of-control increment decreased when the error decreased, 2) The value of the change-of-control increment increases when the change-of-error decreases.

According to the above conclusion the fuzzy controller that provides robust control for the DC speed drive had been designed. The results of the simulation on the plant demonstrate that the proposed fuzzy controller was able to overcome the disadvantages of the usual PI-controller – sensitiveness to inertia variation and sensitiveness to variation of the range of the reference speed alteration.

Therefore, the above conclusions showed superiority of fuzzy over PI.

V. REFERENCES

- [1] Chen Liu*, Jian-Xin Xu** and Chang-Chieh Hang** 'Comparison Between a Fuzzy PID Controller and a Kind of Nonlinear PID Controller' by Proceedings of the 36th Conference on Decision & Control San Diego, California USA December 1997.
- [2] PID Control Toolset User Manual PID Control Toolset User Manual national instruments November 2001 Edition Part Number 322192A-01[34]-[36]
- [3] K.L. Lo and M.O. Sadegh, Systematic method for the design of a full-scale fuzzy PID stability controller for svc to control power system, IEE Proceedings online no.200330125
- [4] E. H. Mamdani, "Application of fuzzy algorithms for simple dynamic plant," Proc Inst. Elect. Eng., vol. D-121, pp. 1585-1588, 1974
- [5] C. C. Lee, "Fuzzy logic in control systems: Fuzzy logic controller-part I and part II," IEEE Trans. Syst., Man, Cybern., vol. 20, pp. 404-435, 1990
- [6] R. M. Tong, "Evaluation of fuzzy models derived from experimental data," Fuzzy Sets Syst., vol. 4, pp. 1-12, 198
- [7] C.W. de Silva and A. G. J. MacFarlane, Knowledge-Based Control with Application to Robots, Berlin: Springer-Verlag, 1989.
- [8] B.-G. Hu, G. K. I. Mann, and R. G. Gosine, "Theoretic and genetic designs of a three-rule fuzzy PI controller," Proc Sixth IEEE Int. Conf. Fuzzy Syst., pp. 1489-1496, July 1-5, 1997.
- [9] R. Katata, D. de Geest, and A. Titli, "Fuzzy controller design, evaluation Parallel and hierarchical combination with a PID controller," Fuzzy Sets Syst., vol. 71, pp. 113-129, 1995
- [10] B.-G. Hu, G. K. I. Mann, and R. G. Gosine, "Theoretic and genetic designs of a three-rule fuzzy PI controller, IEEE transactions on fuzzy systems, vol. 9, no. 5, October 2001
- [11] P. C. Sen, Thyristor DC Drives, John Wiley, 1981, pages 340-356
- [12] Hasan A. Yousef and Hanan hl Khalil, A Fuzzy Logic -Based Control of series DC Motor Drives, IEEE (Catalog Number 95TH18081)

Microcontroller Based High Frequency Inverter

M.G.WANI¹, V.K.SHARMA¹, R.D.KHARADKAR²

¹ Maharashtra Academy of Engineering, Alandi (D), Pune e-mail: mgwanisr@rediffmail.com

² G.H.Raisoni Institute of Engineering & Science, Wagholi, Pune email: r_kharadkar@yahoo.com

Abstract— As a pilot project a 12V D.C to 220V/50Hz, 250W system is developed, using micro controller which provides the switching control of the converters as well as protection features like battery drain, short circuit, over voltage and under voltage can be implemented easily. This eliminates the need for additional analog control circuitry. It uses step up conversion topology and 50 KHz operating frequency, which further reduces the system size.

Key words— High Frequency, Inverter, Microcontroller, SMPS, and UPS.

I. INTRODUCTION

The present power supply scenario is marred by frequent power cuts, load shedding and low voltage supplies. But power supply dependence in industries and increasing use of electrical and electronics appliances in homes have made uninterrupted power supply a modern day necessity. This has inflated the demand of inverters in both industries and households. The increase in demand has also called for more power efficient and portable designs. Major chunk of the requirement is met using storage batteries and DC to AC Inverters. Presently 220V/ 50Hz power generation is met using transformer of metals & metal alloys with inherent loss factor of 10 %. However they are heavy in weight, bulky in volume.

To overcome these issues use of high frequency ferrite core transformers provides weight reduction by one fifth of conventional inverters, one third of volumetric reduction along with 25 to 35% cost and the 10% improvement in efficiency. Lower cost of ferrites and growth of ferrite technology will lead to further reduction in cost and more power efficient designs.

Growing dependence of households on inverters calls for more economical, light weight, efficient and portable designs. Switching power supplies are more power efficient. Inverters using switching power supplies are in great demand as they are more compact, more power efficient and low cost.

The inverter design, developed in this work, uses switching technology hence meets all the above requirements needed by the consumers.

II. HARDWARE

The block schematic of the proposed scheme is shown in Fig.1. The various blocks of Fig.1 are explained below.

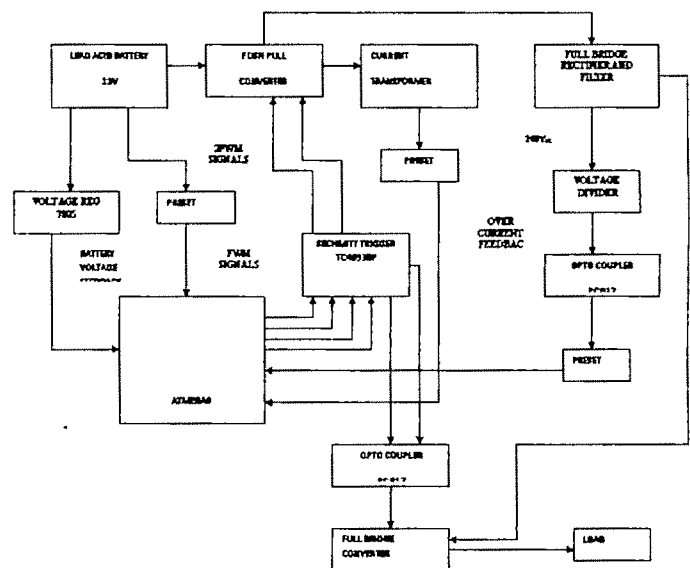


Fig. 1. Block diagram of Microcontroller Based High Frequency Inverter

A. Lead Acid Battery

Supplies d.c voltage from 10.5 to 13.6 volts to the push pull converter.

B. Push Pull converter

Steps up the dc voltage received on the primary side by a ratio of 31:1. The output obtained is a square wave with average value = 262V.

Duty cycle of PWM signal given to input switches of converter is varied from 64% to 84% to maintain an average value of 262V on the secondary of push pull transformer.

Auxiliary windings on the secondary side have 3 turns. Average value of 13V is obtained on the Output of the auxiliary winding. This auxiliary voltage supplies the dc voltage required by the three optocouplers (LM 817) in the circuit.

C. Full Bridge Rectifier and Filter

Removes the high voltage spikes present in the output of push pull converter. The output obtained is square wave with rolled ends with average value of 260V.

D. Full Bridge converter

Receives input from the full bridge rectifier and filter. The switching frequency is 50 Hz with a duty cycle of 85%. The output is square wave with rolled ends at a frequency of 50Hz and average value 220V.

E. Optocoupler

Three optocouplers (PC 817) are used in the circuit. One optocoupler is used in the feedback circuit to the microcontroller it isolates the microcontroller from the analog voltage being fed back from the output of full bridge rectifier and filter. Other two optocouplers are used to isolate the transistors used in the drive circuitry of full bridge converter switches from the fast rising signals received from the Schmitt trigger.

F. Schmitt Trigger

Signals from pin numbers 18, 19, 14 and 15 of microcontroller are fed to it. It decreases the rise and fall time of the signals obtained from microcontroller to a few nanoseconds (50ns to 990ns).

III. CONTROL SCHEME

The detailed circuit diagram of block schematic shown in Fig.1 is presented in Fig.2. The various circuits used in the proposed scheme include control circuit for microcontroller, power supply inverter configuration isolator circuit, output stage etc.

It receives battery voltage input on pin no 23 after the voltage is stepped down by the voltage divider and preset. The preset is set such that a battery voltage of 10.5V is stepped down to 2V. If the battery voltage goes below 2V then the microcontroller stops giving PWM signal to the push pull converter. Microcontroller receives over and under voltage feedback on pin no 24. A.C voltage output of push pull converter is converted to d.c using full bridge rectifier and filter. This high voltage output (317Vpk to 410Vpk) is converted to dc with an average value of 260V. It is stepped down using voltage divider and preset such that 310V is stepped down to 1.5V and 409V stepped down to 1.96V. The voltage feedback is stepped down and varied linearly from 1.5V to 1.96V. Depending on the feedback received microcontroller varies the duty cycle of PWM signal given to mosfet switches of the push pull converter. This duty cycle is varied from 64% to 84%. Pin nos 18 and 19 give PWM signal at a frequency of 50Khz. The duty cycle of this signal varies from 64% to 84% depending on the feedback received on pin no 24 (as explained above). If the feedback signal on pin no 24 is not in the specified boundary (1.5V to 1.96V) then the

PWM signal from pin no 18 and 19 to push pull switches is stopped (i.e. duty cycle made 0%).

PWM signals from pin no 18 and 19 have a delay of 10 μ s between them. Pin number 25 receives feedback from a current transformer connected at the output of the secondary of the push pull converter transformer. The output of the current transformer is stepped down using a preset. This stepped down voltage is feedback to the microcontroller pin no 25. Preset is so adjusted that 2V corresponds to full load current. For feedback more than 2V PWM signal given to the push pull switch is stopped (i.e. duty cycle=0).

Pin numbers 14 and 15 give Signal of frequency = 50Hz. The duty of this signal is 85%. This signal is given to the mosfet switches of full bridge converter. The signals from pin no 14 and 15 have a time delay of 10ms.

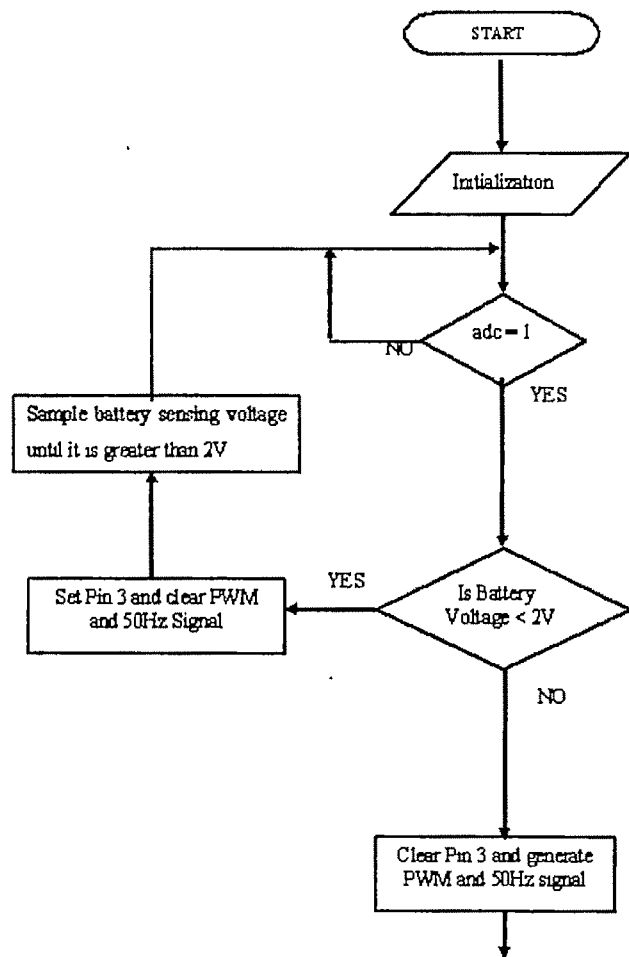


Fig 2. Flow chart for generating switching signals

IV. SOFTWARE

The flow chart for developing the control scheme is shown is self explanatory flow chart. The microcontroller generates the triggering signal for MOSFET, Shut down, over current,

battery voltage sensing. The flow chart is converted into assembly language of microcontroller.

V. TESTING AND RESULTS

Signals from pin numbers 18, 19, 14 and 15 of microcontroller are fed to it. It decreases the rise and fall time of the signals obtained from microcontroller to a few nanoseconds (50 ns to 990ns.) The hardware of the proposed scheme is developed and integrated with software control through microcontroller. The testing of the prototype is conducted in laboratory test bench. The system is switched on by press button switch on no load. The output voltage of 220 V a.c. is available and is recorded through a digital voltmeter. The system is switched off. A resistive load is connected.

VI. CONCLUSION

As a pilot project we have developed a 12V d.c. to 220V/50Hz, 250W system. We have added protection features like short circuit, over voltage, under voltage and battery drain protection. The protection circuitry is implemented using a

micro controller ATmega8. The use of micro controller for providing protection makes the protection circuit more compact and corrective measures sharper compared to that provided by an analog circuit. The circuit is tested for 250 watt load and the result was satisfactory. The micro controller also provides the switching control of the converters. This eliminates the need for additional analog control circuitry. It uses step up conversion topology and 50 KHz operating frequency, which further reduces the system size.

REFERENCES

- [1] Mehdi Ferdowsi, Ali Emadi, Mark Telefus, Curtis Davis, "Pulse regulation control techniques for flyback converter", IEEE Transactions on power electronics, July 2005.
- [2] Mohan, Undeland and Robbins, "Power Electronics Converters, Applications and Design", John Wiley & Sons, 2001.
- [3] Abraham. I. Pressman, "Switching Power Supply Design", McGraw Hill International, 1999.
- [4] Ito, Y., and Kawauchi, S.: 'Microprocessor-based robust digital control for UPS with three-phase PWM inverter', IEEE Trans. Power Electron., 1995, 10, (2), pp. 196-204

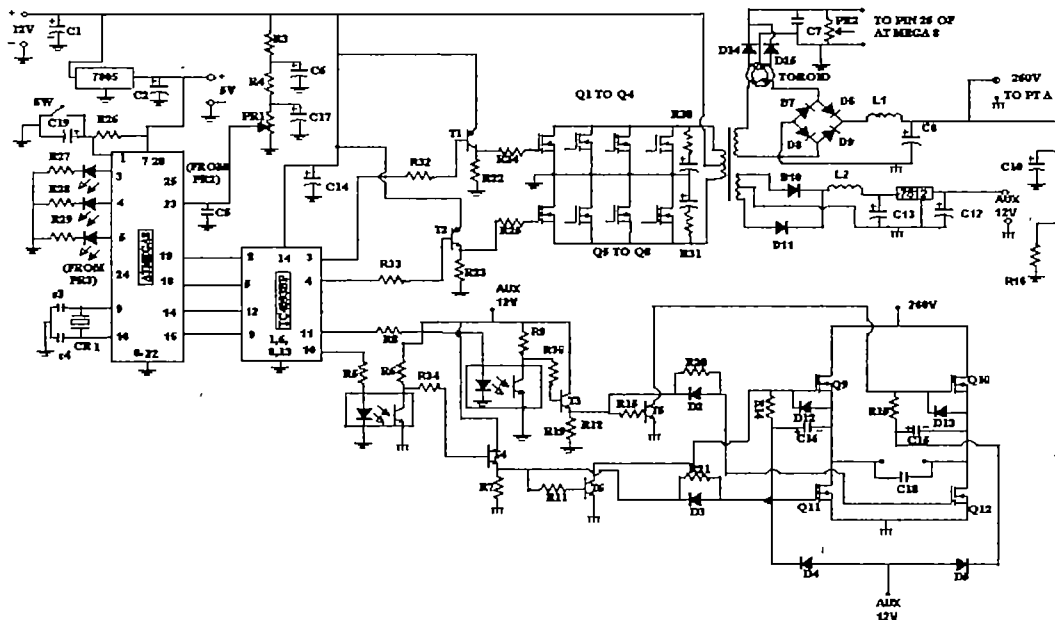


Fig. 3 System Circuit diagram

G2166016

A Constant Switching Frequency Hysteresis Current Controller for Single-Phase Voltage-Source Inverters

M. Ahmadi, H. Heydari, and A. Rahmati

Center of Excellence for Power System Automation and Operation
Electrical Engineering Department, Iran University of Science & Technology, Tehran, Iran
mohsen_a57@yahoo.co.uk, heydari@iust.ac.ir, and rahmati@iust.ac.ir

Abstract— Hysteresis current controllers having fixed bands are used in inverters of high-performance applications. The switching frequency of such controllers varies over the fundamental period of the modulating signal. The maximum switching frequency of these controllers is high. To limit the maximum switching frequency within the limit of inverter switches, fixed carrier lockouts are usually incorporated. The incorporation of carrier lockouts causes current distortion, and load currents do not confine within the predetermined band. In this paper, two new controllers are proposed. These controllers have a variable-band hysteresis comparator that varies with the slope of current's error. Performances of the proposed controllers are compared with the performance of the conventional fixed-band controller.

Key words— Hysteresis Current Control, Constant Switching Frequency and Voltage-Source Inverter.

I. INTRODUCTION

VOLTAGE source inverters (VSI's) having current controllers provide high dynamic performance of ac drives [1]. A variety of current-control methods have been reported in the literature. In general, the current-controlled pulse-width modulation (PWM) schemes can be roughly classified into the following categories [1]–[3].

1) Hysteresis Controller: It is simple to implement and has robust current control performance against load and source parameter changes. However, the resulting inverter output harmonic spectrum distributed characteristic depends largely on the variations of load and input voltage.

2) Ramp-Comparison Controller: The switching frequency of the inverter is fixed, but its current tracking control performance is sensitive to the variation of motor back EMF,

and the current tracking magnitude and phase errors inherently exist

3) Predictive Controller: The next switching-state vector for achieving good current tracking control is determined via prediction and optimization. The lookup table method is usually utilized to realize this kind of switching control approach. The current control response might be slower than other types of current controllers due to the extra processing time [1].

The hysteresis current control is one of the simple and extensively used methods [4]. In this method, hysteresis comparators are used to impose a fixed dead band or hysteresis around the reference current. The switching frequency varies during the fundamental period and exceeds the limit of the inverter switches at certain conditions. To limit the maximum switching frequency, lockout circuits are usually incorporated [5]. An adaptive hysteresis-band current control may be used to maintain a fixed modulation frequency [6], [7], [8], [9]. However, the implementation is complex and difficult. Reduction in switching frequency can be done by using the zero state of inverter [10]. In all these controllers, the switching frequency is load dependent. Another hysteresis current controller employs a band, which sinusoidally varies with the fundamental period of the inverter [12]. In this type of controller, the switching frequency is very high near the zero crossing points of the reference wave. Introduction of lockouts to this type of controller shows improved performance compared to the fixed-band controllers [12].

Switching frequency of the fixed-band controller is less than the sinusoidal-band controllers, but spectral behavior of sinusoidal-band controller is better. The two methods can be combined to have advantages of both types in one controller.

In this paper, two new variable-band Hysteresis techniques are proposed to reduce the upper limit of switching frequency and improving the spectral distribution of output current. These controllers use the derivative of current error to increase

the hysteresis band and thus reducing the switching frequency.

The current controllers proposed in this paper can be used for any type of VSI irrespective of the type of application. The basis of modulation of the controllers is derived from the hysteresis-band current controllers.

II. FIXED-BAND HYSTERESIS CURRENT CONTROLLER CHARACTERISTICS

Fig.1 shows a single-phase inverter with a fixed-band hysteresis comparator. The output current is compared with the reference current. When the current error exceeds the hysteresis band, the suitable switching commands are produced to keep the output current in the predetermined error band, as shown in Fig.2.

In the fixed-band hysteresis controller, the switching frequency varies during the fundamental period and exceeds the limit of the inverter switches at certain conditions.

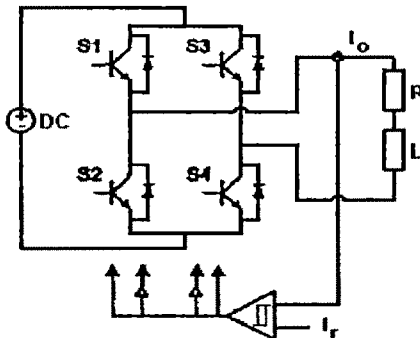


Fig.1 Hysteresis current controlled Single-phase inverter

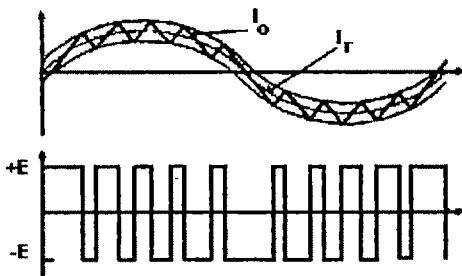


Fig 2 Output current (upper) and output voltage (lower) under fixed-band hysteresis controller

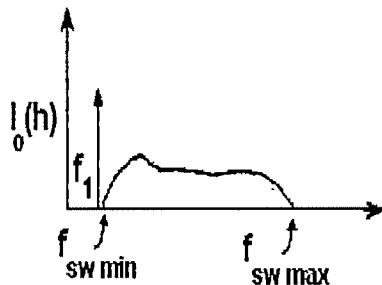


Fig.3 Output current harmonic distribution in fixed-band hysteresis current controller

Moreover, the output current harmonic distribution varies

in different conditions and has not a well-defined shape. Fig.3 shows the harmonic distribution of output current.

III. PROPOSED VARIABLE-BAND HYSTERESIS CONTROLLER

In a fixed-band hysteresis controller, when the difference between slopes of output current and reference current is high, the output current rapidly reaches the error band and hence switching frequency goes high.

The proposed current controller, increase the hysteresis band, proportional to the absolute slope of current error. Therefore, the switching frequency remains below a certain value. Fig.4 shows the basic scheme of proposed controller.

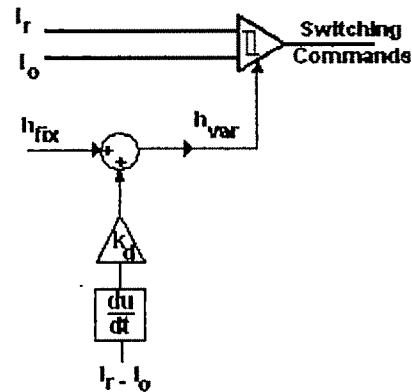


Fig 4 Basic scheme of proposed variable-band hysteresis

Simulations show that an integral compensator can improve the performance of proposed controller. As shown in Fig.5, current error is fed to an integral compensator and compensator's output is subtracted from fixed hysteresis band.

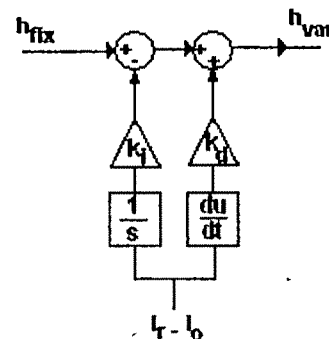


Fig 5: Improved variable-band hysteresis current Controller

IV. PERFORMANCE EVALUATION OF PROPOSED CURRENT CONTROLLERS

A. Fixed-Band Hysteresis Controller

In order to compare fixed-band hysteresis controller with proposed controllers, computer simulations have been conducted. The reference current amplitude is 25kA. Fig.6 shows output current of this controller. Fig.7 shows switching

frequency and harmonic distribution of output current in fixed-band hysteresis controller. As shown in Fig.7-a, switching frequency varies in a broad range of frequencies. The average switching frequency is 5 KHz and output current THD is 2.2%. Fig.7-b shows harmonic distribution of output current. As shown in Fig.7-b, output current has high amplitude harmonics about average switching frequency and other harmonics are randomly distributed

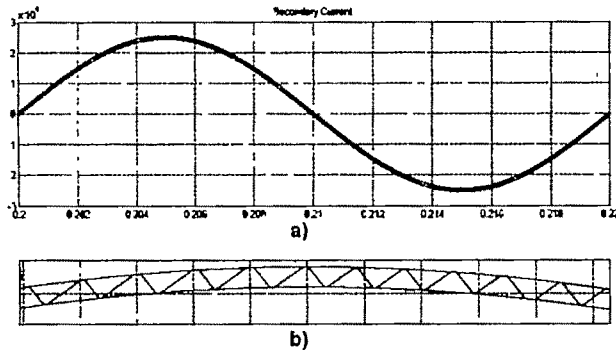


Fig.6 Fixed-band hysteresis controller output current: a) One period b) Detailed view

V. PROPOSED HYSTERESIS CONTROLLER

The simulation results of proposed current controller are shown in Fig.8 to Fig.11. The average switching frequency is 4.7 KHz and the output current THD is 2.6%. As shown in Fig.9-a, the hysteresis band is variable. Fig.9-b shows the current error. As shown in Fig.10, the proposed current controller has good performance in switching frequency regulation and harmonic distribution shaping. Due to switching frequency regulation, the harmonic distribution is in a well-defined shape, like PI controller's harmonic distribution [1]. To examine the switching frequency regulation, simulation is conducted in different conditions: first, with 50% decrease in load inductance and resistance, second, in case of a step change in amplitude of reference current. Fig.11 shows simulation results in these conditions. According to Fig.11, the proposed controller has a good performance in switching frequency regulation, in various system conditions.

In order to observe the effect of derivative coefficient k_d on frequency regulation, simulations are conducted with different values for k_d . Fig.12 shows the simulation results for two different values for k_d . Fig.12-a shows the switching frequency of inverter with a smaller k_d and Fig.12-b shows the switching frequency of inverter with a greater k_d . As one can see, appropriately choosing of k_d leads to regulated switching frequency at desired value.

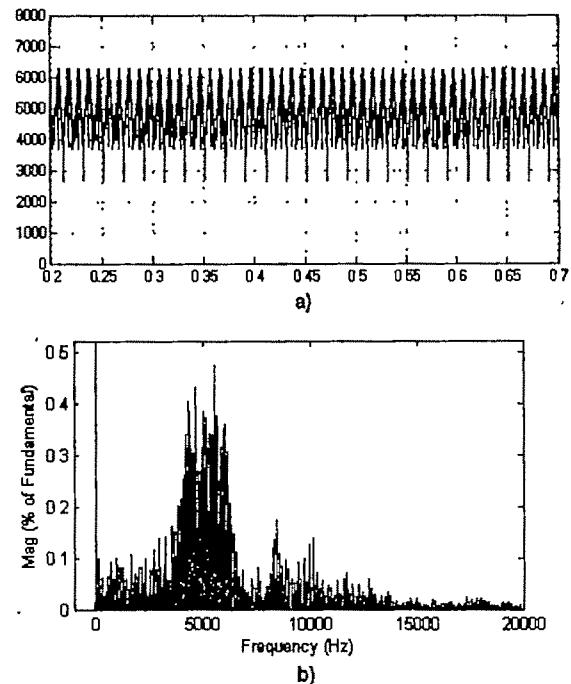


Fig 7 Fixed-band hysteresis controller. a) Switching frequency b) Harmonic distribution

VI. IMPROVED HYSTERESIS CONTROLLER

Fig.5 shows the scheme of improved proposed controller. Simulation shows same results in switching frequency regulation, but a great reduction about 75% in output current THD, for improved controller. Fig.13 shows output current and Fig.14 shows harmonic distribution of improved current controller. Fig.15 shows harmonic distribution of output current with a different value for integral coefficient k_i . As one can see, a better THD is achieved with tuning of integral coefficient.

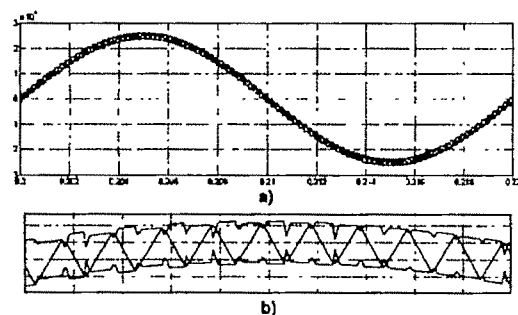


Fig.8 Proposed controller output current: a) One period b) Detailed view

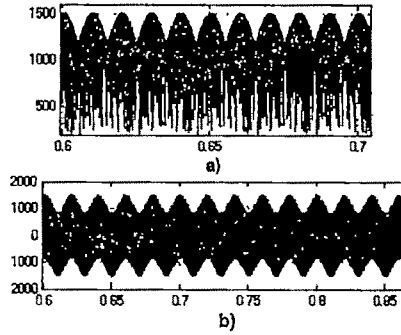


Fig 9 Proposed variable-band hysteresis controller: a) Hysteresis band b) Current error

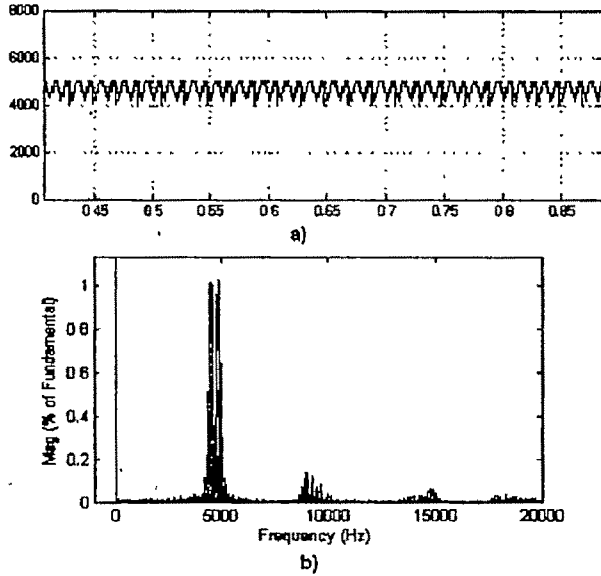


Fig.10 Proposed variable-band hysteresis controller a) Switching frequency b) Harmonic distribution

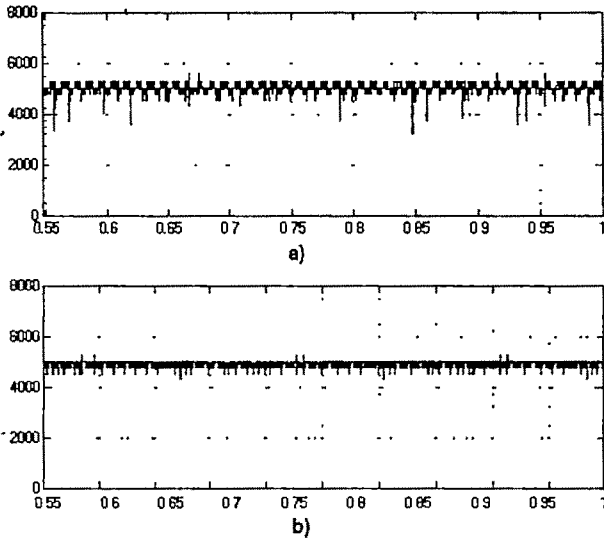


Fig.11 switching frequency of proposed controller a) 50% decrease in load b) 50% decrease in reference amplitude

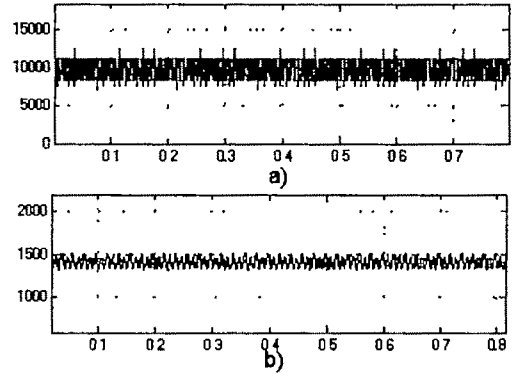


Fig.12 Inverter switching frequency with two different derivative coefficients

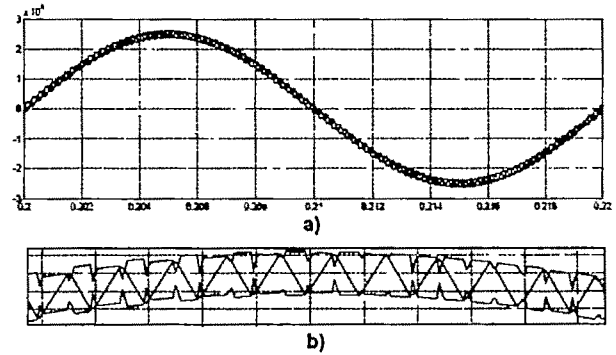


Fig.13 Improved controller output current: a) One period b) Detailed

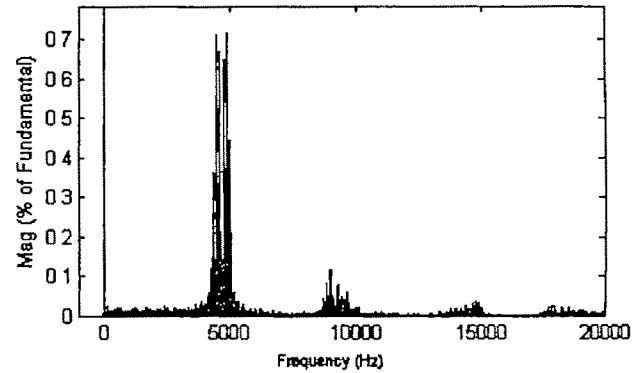


Fig.14: Improved current controller harmonic distribution

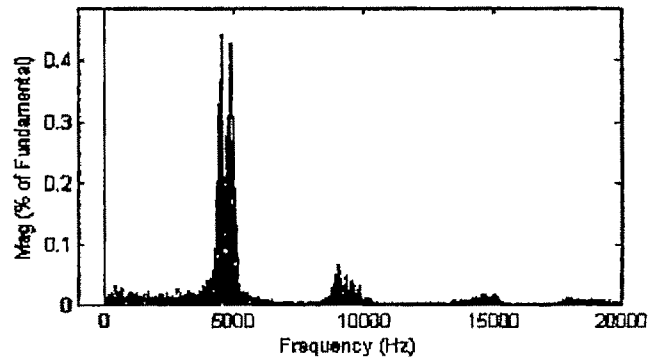


Fig.15 Improved current controller harmonic distribution with tuned integral coefficient

VII. COMPARISON BETWEEN DIFFERENT CONTROLLERS

Table 1 shows a comparison between simple Hysteresis current controller and two proposed current controllers. As one can observe, the advantage of two proposed controllers is in their regulated switching frequency and their disadvantage is in necessity of derivative and integral coefficients tuning.

Table 1 Comparison between Controllers

	Current Tracking	Fixed Switching Frequency	Load Dependency
Hysteresis Controller	Good	No	No
First Proposed Controller	Good	Yes	Yes
Second Proposed Controller	Good	Yes	Yes

VIII. CONCLUSION

Hysteresis current-controlled PWM possesses the robustness characteristics of bang-bang control, but suffers from the major disadvantage of non-constant switching frequency. This paper introduces two variable-band hysteresis current controllers for voltage source inverters. The regulation in switching frequency is achieved without additional lockout circuits since the switching frequency is regulated with suitable variation of hysteresis band according to current error slope. The output current has a harmonic distribution independent from load and system conditions. The improved controller provides a smaller current THD and has same switching regulation and harmonic distribution characteristics.

ACKNOWLEDGMENT

The authors gratefully acknowledge the support of the Tehran Regional Electric Company; Energy Ministry, Iran for this research.

REFERENCES

- [1] D. M. Brod and D. W. Novotny, "Current Control of VSI-PWM Inverters", *IEEE/IAS 1984 Annual Meeting*, 1984, pp. 418-425.
- [2] J. Holtz, "Pulse Modulation: A Survey", *IEEE Trans. Ind. Electron.*, vol. 39, 1992, pp. 410-420.
- [3] M. P. Kazmierkowski and L. Malesani, "Current control techniques for Three-Phase Voltage-Source PWM Converters: A Survey", *IEEE Trans. Ind. Electron.*, vol. 45, 1998, pp. 691-703.
- [4] P. Enjeti, P. D. Ziogas, L. F. Lindsay, and M. H. Rashid, "A Novel Current Controlled PWM Inverter for Variable Speed AC Drives", *IEEE/IAS 1986 Annual Meeting*, 1986, pp. 235-243.
- [5] A. B. Plunckett, "A Current Controlled PWM Transistor Inverter Drive", *IEEE/IAS 1979 Annual Meeting*, 1979, pp. 785-792.
- [6] H. Le-Huy and L. A. Dessaint, "An Adaptive Current Controller for PWM Inverters", *Annual Meeting of IEEE/IAS*, 1986, pp. 610-616.
- [7] B. K. Bose, "An Adaptive Hysteresis-Band Current Control Technique of a Voltage Fed PWM Inverter for Machine Drive System", *IEEE Trans. Ind. Electron.*, vol. 37, no. 5, 1990, pp. 402-408.
- [8] L. Malesani, L. Rossetto, P. Tomasin, A. Zucatto, "Digital Adaptive Hysteresis Current Control With Clocked Commutations and Wide Operating Range", *IEEE Transactions on Industry Applications*, Vol. 32, 1996, pp. 316-325.
- [9] L. Malesani, P. Mattavelli and P. Tomasin, "Improved Constant-Frequency Hysteresis Current Control of VSI Inverters with Simple Feed Forward Bandwidth Prediction", *IEEE Transaction in Industrial Application*, No.33 Vol.5, 1997, p. 1194-1202.
- [10] Dahono, P.A. Krisbiantoro, I., "A Hysteresis Current Controller for Single-Phase Full-Bridge Inverters", *Proceedings 4th IEEE International Conference on Power Electronics and Drive Systems*, Vol 1, 2001, pp. 415-419.
- [11] N. H. Rashidi, "Improved and Less Load Dependent Three-Phase Current Controlled Inverter with Hysteresis Current Controller", *IEEE Trans. Industrial Electronics*, vol. 42, no. 3, 1995, pp. 325-330.
- [12] A. Tripathi and P. C. Sen, "Comparative Analysis of Fixed and Sinusoidal Band Hysteresis Current Controllers for Voltage Source Inverters", *IEEE Trans Industrial Electronics*, vol. 39, no. 1, 1992, pp. 63-73.

Predictive Current Control of an Inverter-Fed a 25kA Current Injection Transformer System

M. Ahmadi, H. Heydari, and A. Rahmati,

Center of Excellence for Power System Automation and Operation
Electrical Engineering Department, Iran University of Science & Technology, Tehran, IRAN
mohsen_a57@yahoo.co.uk, heydari@iust.ac.ir, and rahmati@iust.ac.ir

Abstract—This paper proposes two digital current control technique of a single-phase voltage-source inverter. The key feature of these methods is minimization of the current error at every sampling point with no predetermined current error tolerance such as a hysteresis band. In the first technique, In order to make the current trajectory until the next sampling point as close as possible to a predicted current command, one of the two non-zero voltages in conjugation with the zero voltage is appropriately selected by the controller.

In the second technique, a zero-voltage vector is inserted once a sampling period to adjust the current vector velocity and to move the current to the closest position to the predicted current command. The proposed method achieves a dead-beat response without the predetermined current error tolerance and uses a simple model of transformer in prediction process. Resultant data obtained from computer simulations prove feasibility of the second proposed technique

Key words—Current Injection Transformer, Predictive Current Control, Constant Switching Frequency and Inductance Estimation

I. INTRODUCTION

CURRENT Injection Transformers (CITs) are within the major groups of standard type test equipments in electrical industry. The CITs are used to testing equipments such as circuit breakers, that must carry short-circuit current. Testing can assure that the tested product meets or exceeds performance standards.

In the case of an inverter-fed CIT, we must use a current-controlled PWM method to control the output current of the CIT. Current-controlled inverters have extensively been used in many applications such as ac servomotor controllers, switched ac-dc rectifiers, active filters and so forth [1][2]. Basically, these kinds of inverters have current feedback loops to regulate phase currents detected with Hall-effect CTs. The most common and conventional techniques to regulate the currents are a proportional-integral (PI) element based scheme

and a hysteresis comparator based scheme. The former has an advantage over the latter in terms of generation of optimum pulse-width-modulated (PWM) patterns but has drawbacks in a current response and a steady-state error. The latter has both advantages and disadvantages vice versa; hence it is rather difficult for these techniques to satisfy all requirements at the same time without sacrificing any of the performance indexes described above. In order to overcome such dilemma, several proposals have been made on the basis of sophisticated but complicated approaches. One of the approaches is a method using a spatial circular area as a current error tolerance, which can restrict the current error vector within the predetermined circular area [3]. Another is a dead-beat control based algorithm, which achieves an excellent current response with only one sampling time delay [4]. Also, other several papers have reported modified hysteresis comparator based solutions [5].

In many applications, current control is useful as part of a larger control structure. In the case of an injection transformer, a current controller may be used to control the desired output current. The application that is the focus in this paper is the control of an injection transformer, although the results have broader relevance.

This paper proposes two digital current control techniques, which features minimization of current error at every sampling point with no predetermined current error tolerance, such as a hysteresis bands. The second proposed method is a kind of dead-beat control. On-line identification of the load parameter is introduced to the controller to solve problems associated with a parameter mismatch. In this paper, a theoretical aspect of the proposed techniques is described and computer simulations are presented to examine feasibility of the methods.

II. CURRENT INJECTION SYSTEM

Fig.1 shows the current injection system. The Injection transformer is an inverter-fed transformer that injects desired current to the load. The transformer is fed by a current

controlled single-phase voltage-source inverter. Fig.2 shows simplified inverter-transformer system.

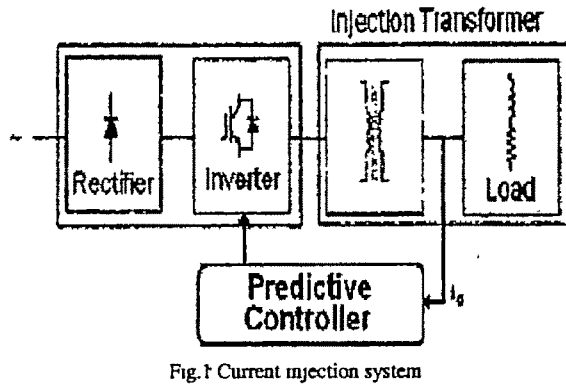


Fig.1 Current injection system

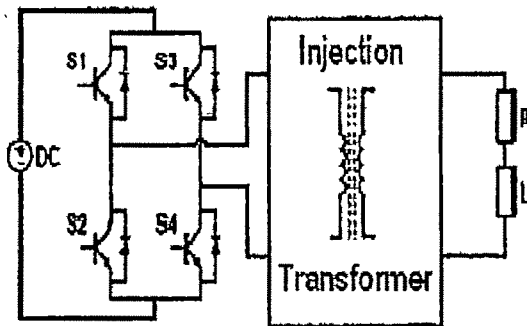


Fig.2 Simplified model of current injection system

III. PREDICTIVE CURRENT CONTROL

A. Minimum-Error Predictive Controller

In this section a predictive method is described that is based on output current sampling at instant t and calculation of output current at instant $t+1$ (the next sampling instant). According to inverter's voltage levels, $+E$, 0 and $-E$, three different current trajectories would be achieved, as shown in Fig.3. These three trajectories have three different values at instant $t+1$. Thus, three different current errors would be achieved at instant $t+1$. The control algorithm chooses the voltage level that produce minimum current error, during the sampling period. At instant $t+1$, these steps repeat for instant $t+2$ and so on. Therefore, the switching frequency upper limit is $1/2T$ where, T is sampling period.

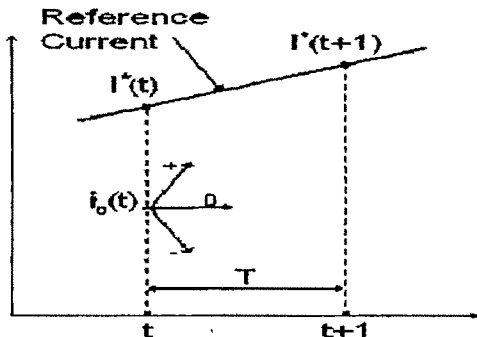


Fig.3 Current trajectories according to inverter output voltages

Calculations are based on transformer and load's model, hence more accurate model results more accurate current tracking. Fig.4 shows the control algorithm flowchart.

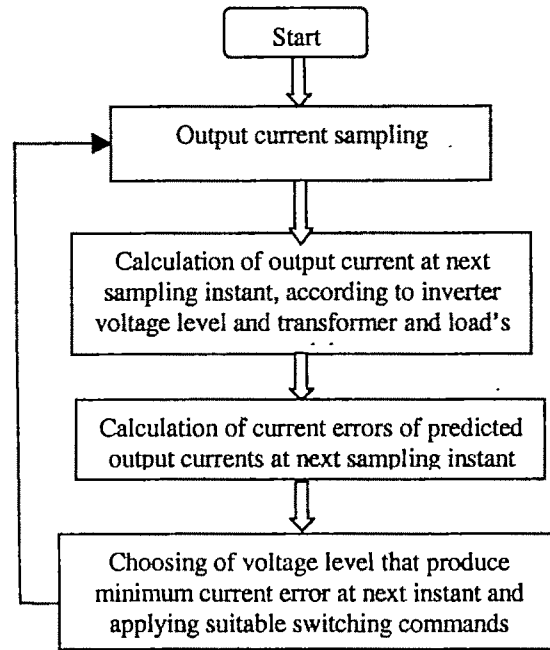


Fig.4 Flowchart of minimum-error method

B. Deadbeat Current Control

The objective of previous control method was reducing current error at next sampling instant. In this section, control algorithm tries to zero the current error at next sampling instant. Thus, we can categorize this method as deadbeat control. To implement the control algorithm, suppose a simple inductance model of transformer and load, thus:

$$i_o(t+1) = i_o(t) + \frac{V}{L}T \quad (1)$$

Where L is the equal inductance of transformer and load and V is applied voltage. To set current error to zero at next sampling instant, following equation must be valid:

$$i_o(t+1) = i^*(t+1) \quad (2)$$

Where, $i^*(t+1)$ is the value of reference current at the next sampling instant and has a known value. Combining (2) with (1) results:

$$V = \frac{L[i^*(t+1) - i_o(t)]}{T} \quad (3)$$

The voltage V that is computed from (3), has a different value from the voltage levels that inverter can produce. Thus, one must use zero level voltage together a non-zero voltage level, to approximate the reference voltage V , as shown in Fig.5. According to Fig.5, we have:

$$T_1 = \frac{V}{E}T \quad (4)$$

$$T_2 = T - T_1 \quad (5)$$

From (4), the durations of non-zero voltage, T_1 , and zero voltage, T_2 , is calculated. The duration of applying zero-

voltage is set between two half-duration of non-zero voltage, to reduce the current ripple [6]. Fig.6 shows the flowchart of this control method.

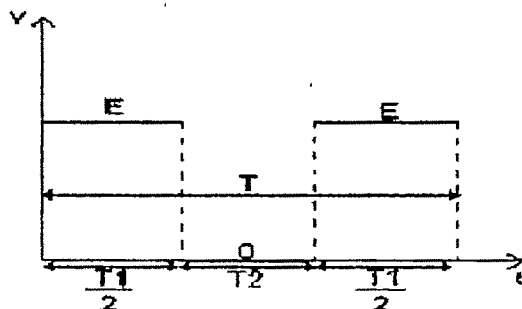


Fig 5 Durations of applying zero and non-zero voltages

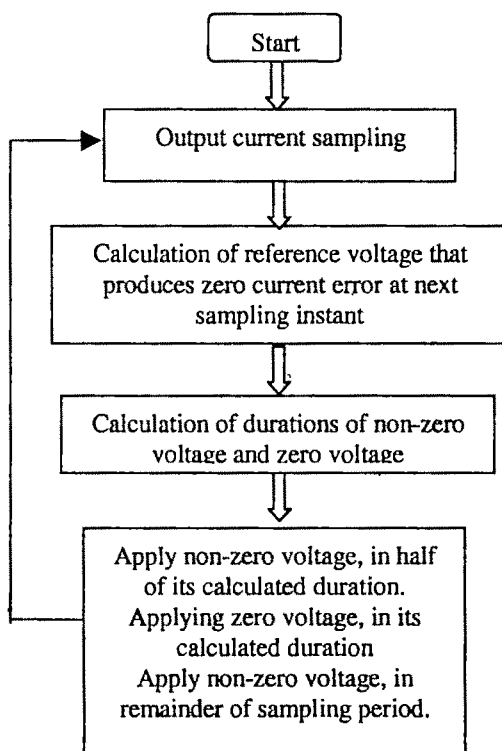


Fig.6 Flowchart of deadbeat method

C. Inductance Estimation

As, a single inductance is used to model the transformer and load, there would be some errors in current tracking. Using a more accurate model leads to a better current tracking. In this paper, an inductance estimation technique is employed as an alternative approach. The inductance may be estimated from the measured currents and past applied voltages. Simulations approved the usefulness of this technique.

IV. SIMULATION RESULTS

Several simulations were performed to examine the feasibility of two proposed control techniques.

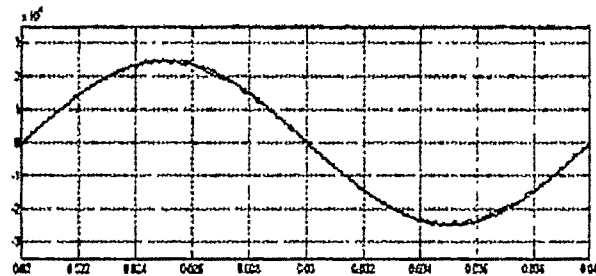


Fig.7 Minimum error controller: output current

V. PROCEDURE FOR PAPER SUBMISSION

A. Simulation Results of Minimum-Error Controller

The sampling period is set to 10 KHz. Fig.7 shows the output and reference currents. Fig.8 shows inverter's output voltage and output current's error. In this method, only the upper limit of switching frequency is controllable. Practically, switching frequency of inverter is less than half of sampling frequency. If in each sampling period, control algorithm chooses a different voltage level of inverter, the upper limit of switching frequency (i.e. $1/2T$) is reached. If at two or more sampling period, control algorithm chooses last voltage level, then the switching frequency reduces. Fig.9 shows the switching frequency of this method. The upper limit of switching, as shown in Fig.9, is 5KHz. Fig.10 shows the harmonic contents of output current.

Fig.11 shows the current error and switching frequency of inverter, during a step decrease of reference current amplitude. Since current error's amplitude remains unchanged; the output current ripple increases and the switching frequency largely decreases.

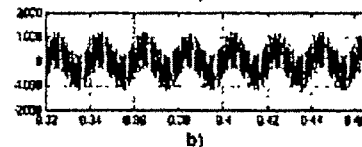
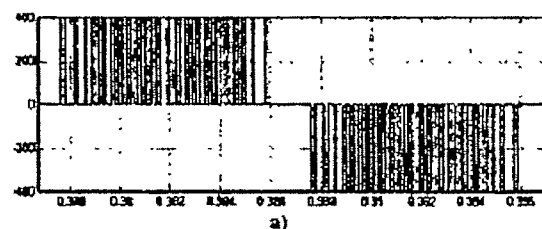


Fig.8 Minimum-error controller: a) Inverter voltage b) Current error

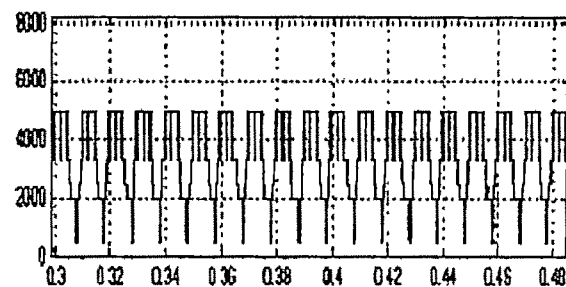


Fig 9 Minimum-error controller: switching frequency



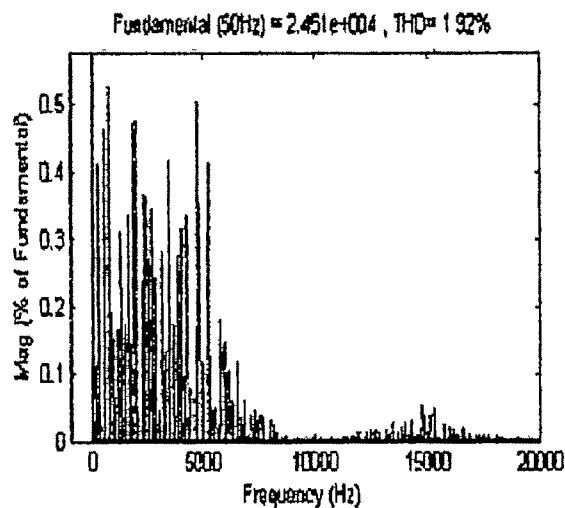


Fig 10. Minimum-error controller output current's harmonic contents

B. Simulation results of deadbeat controller

The sampling period is set to 5KHz. Fig.12 and Fig.13 shows the output current and voltage, respectively.

As shown in Fig.12, at the peak of reference current, output current can't reach to zero error. This is because of use of inaccurate model of transformer. As shown in Fig.13, an optimum PWM pattern is achieved.

Fig.14 and Fig.15 show the switching frequency of inverter and harmonic contents of output current, respectively. As shown in Fig.14, the switching frequency is regulated about sampling frequency. The constant switching frequency results the well distributed harmonic contents, as shown in Fig.15. The main harmonic contents are concentrated at switching frequency. As shown in Fig.16, the switching frequency remains at desired frequency. This is a great advantage over the last control algorithm.

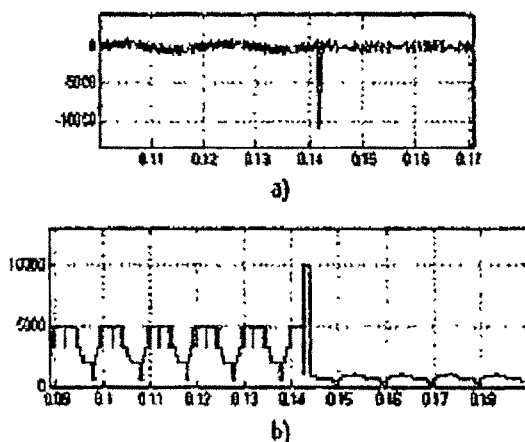


Fig.11 Minimum-error controller. a) Current error b) Switching frequency during step change in reference amplitude

C. Simulation of Inductance Estimation

Simulations are conducted to examine the effect of inductance estimation technique on current tracking. Fig.17 shows the output current when the inductance estimation technique is used.

As shown in Fig.17, the inductance estimation technique improves the current tracking.

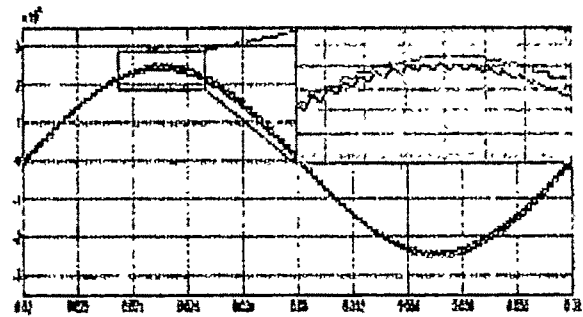


Fig.12 Deadbeat controller: output current

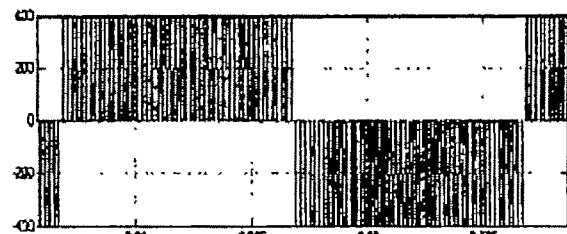


Fig.13 Deadbeat controller: inverter voltage

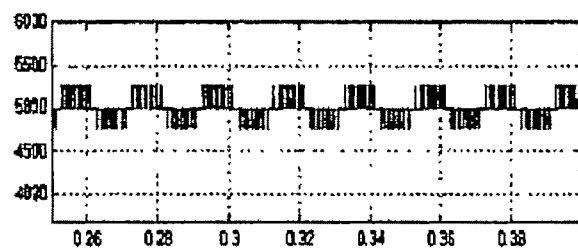


Fig.14 Deadbeat controller: switching frequency

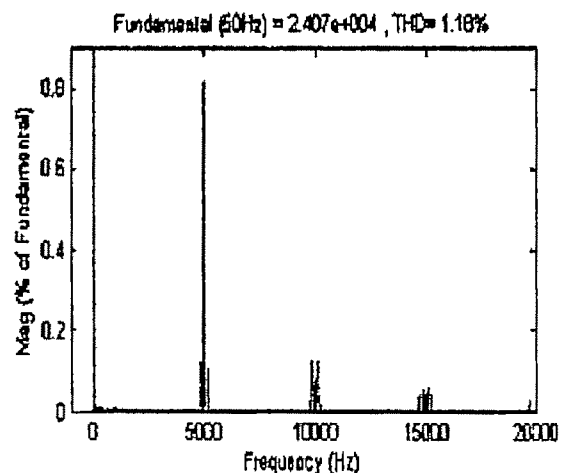


Fig 15 Deadbeat controller: output current harmonic contents

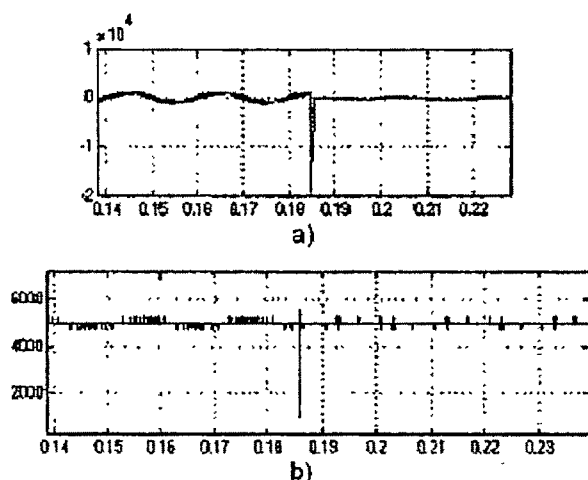


Fig.16. Deadbeat controller: a) Current error b) Switching frequency during step change in reference amplitude

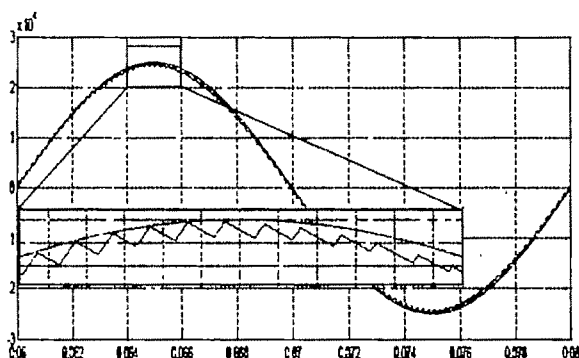


Fig.17 Output current of deadbeat controller with inductance estimation

REFERENCES

- [1] J. Holtz, "Pulse-Width Modulation for Electric Power Conversion", *IEEE Proc.*, Vol.82, No.8, 1994, pp. 1194-1214, 1994.
- [2] M. P. Kazmierkowski, and L. Malesani, "Current Control Techniques for Three-Phase Voltage-Source PWM Converters: A Survey", *IEEE Transaction on Industrial Electronics*, Vol.45, No.5, 1998, pp. 691-703.
- [3] J. Holtz, and S. Stadtfeld, "A Predictive Controller for the Stator Current Vector of AC Machines Fed from a Switched Voltage Source", *Conference Record of 1983 IPEC-Tokyo*, 1983, pp. 1665-1675.
- [4] T. Kawabata, T. Miyashita, and Y. Yamamoto, "Deadbeat Control of Three-Phase PWM Inverter", *IEEE Transaction on Power Electronics*, Vol 5, No.1, 1990, pp. 21-28.
- [5] B. K. Bose, "An Adaptive Hysteresis-Band Current Control Technique of a Voltage-Fed PWM Inverter for Machine Drive System", *IEEE Transaction on Industrial Electronics*, Vol.37, No.5, 1990, pp. 402-408.
- [6] Mahdavi, J., Agah, A., Ranjbar, A.M. and Toliyat H. A., "Extension of PWM Space Vector Technique for Multilevel Current-Controlled Voltage Source Inverters", *IEEE, Proceedings of the 25th Annual Conference of the Industrial Electronics Society, IECON '99*, Vol.2, 1999, pp. 583-588.

VI. CONCLUSION

This paper compared two digital current control strategies. The second and preferred strategy makes it possible to minimize the current error at every sampling point. The most unique point of the proposed method is to restrict automatically the current error vector within a minute band with no predetermined error tolerance, e.g., a hysteresis band. The method achieves optimum PWM patterns and a quick current response. Also, it has been clarified that the most conspicuous spectrum of the current harmonics can be observed at the inverter switching frequency. An inductance estimation technique is employed to compensate model inaccuracy. Operation of the proposed techniques has been examined with computer simulations and feasibility of second algorithm is verified.

ACKNOWLEDGMENT

The authors gratefully acknowledge the support of the Tehran Regional Electric Company; Energy Ministry, Iran for this research.

Fuzzy Logic Based Extended Dynamic Braking of Electric Locomotive

R. S. Bajpai¹ and R. Gupta²

¹Department of Electrical Engineering, S. R. M College of Engineering & Management, Lucknow, email: rsbajpai16@rediffmail .com.

²Department of Electrical Engineering, MNNIT, Allahabad, email: rajeshgupta@mnnit.ac in

Abstract— In this paper fuzzy logic based extended dynamic braking of electric locomotives is suggested for the braking control of locomotives equipped with traction drives. Controller design for the locomotive is carried out with two input, i.e., speed and distance and one output, i.e., braking effort using fuzzy logic algorithms. Commonly, conventional controllers are used for the above control. But these controllers give poor control performance due to uncertainty and unpredictability of traffic dynamics. Fuzzy logic based controllers proposed in this paper convert the linguistic strategy based upon the expert knowledge into an automatic braking control. An attempt is made to obtain higher braking torque at lower speed by using extended range of dynamic braking. Extended range is obtained by cutting out the breaking resistance in three stages. Fuzzy logic controller is designed by taking the advantage of extended range of dynamic braking and result obtained are superior to conventional scheme.

Key words—Extended range, Dynamic braking, Fuzzy logic, Locomotive.

I. INTRODUCTION

THE speed control system is required principally as a safety feature to prevent trains exceeding speed restrictions or passing signals at danger. This system will assist drivers of higher speed trains to reduce speed before exceeding the target points. This system can be used on lines with various types of traffic, high speed intercity, high density suburban, low density rural, various types of freight and parcel trains. Here aim is to apply train braking to achieve the desired target limit of the speed.

In this paper, a new class of control, called intelligent control using the principle of fuzzy logic has been proposed for smooth and effective braking control for the locomotives, which has enhanced dynamic braking characteristics. Intelligent control is the most sophisticated control, and it emulates the decision making capabilities of human beings. Application of fuzzy control can meet the fascinating challenges over the loco control system i.e. interlocking stations, automatic speed and braking controls. Fuzzy

controller is designed using high speed protection control equation, to prepare the rule base using Mamdani fuzzy inference system. The major advantage of fuzzy logic control [2] is its simplicity along with its robustness to components and system variations as well as to input and output measurement noise.

When the speed of train is zero, the electric braking [1] effort become zero and then the holding brake can be applied. If the measured value of speed has an error and the holding brake is applied at non zero speed, following problems may arise.

1. Passenger experiences jerking at the moment before the train comes to standstill.
2. The train is unable to stop within a designated distance.

To solve these problems it is important to know the speed in the vicinity of zero. While for jerk control, it is necessary to establish the error in speed and to correct this error. To achieve this goal it is proposed to use DC series motor in electric locomotive using fuzzy logic controller with extended range of dynamic braking. It is demonstrated through the simulation results that fuzzy logic controller [3] is superior to conventional controller among several key parameter, including accuracy in stopping at platforms, rider comfort and energy conservation. Tests indicate that dynamic braking with extended range is capable in reducing the speed of locomotive to a minimum speed of 12 km/h without using any other braking system. The case study illustrated in this paper refers to the Indian railway system.

II. DYNAMIC BRAKING

The dynamic brake uses the electric motors of the traction power system to generate current during braking, which is absorbed into a resistor known as rheostatic braking. Ideally, the dynamic brakes should be used as much as possible to reduce wear on brake pads (or blocks) and there are often circumstances when the dynamic brake can provide all the braking required. During dynamic braking, the motor series field windings have no connection with the armature, the traction motor works as separately excited shunt generators. Twisting effort is provided by push of the train against the locomotives. These action turns the locomotive wheels through the motor axle gearing and this turn the traction motor

armature. The torque produced by the armature acts to resist the forward movement of the train. This results in the slowing down of train. The current generated by the motor armature during dynamic braking is dissipated through the resistance grid in the form of heat. To remove heat from the grid resistor, air is blown through blower motor. The rate of cooling of resistor grid through blower motor depends upon the amount of current generated by the traction motor during dynamic braking.

A. Extended Dynamic Braking

In this the driver remotely controls the braking system. The series field of all the traction motors is disconnected from the armature and gets connected across alternator rectifier output. The armature of these traction motors also get connected across braking resistor of 0.5Ω . In the locomotives equipped with dynamic braking, the maximum braking effort normally drops off rapidly at track speed below 26 km/h. Fig 1 shows the curve for the maximum braking effort vs. loco speed. In this figure the line AB corresponds to the constant traction motor current of 800 A, and is controlled by armature current control reactor. The armature current is less than the field current until the maximum braking effort is attained at point B. The maximum braking effort is limited by the adhesion factor of 17 %. The line BC shows adhesion limit. Beyond the maximum braking efforts, line CD corresponds to constant armature current of 800 A, and is controlled by excitation control. At higher speed, the line EF corresponds to the limitation of armature current to 600 A. It can be seen from above graph that the maximum braking efforts of 21 tones is available between speed 37-25 km/h.

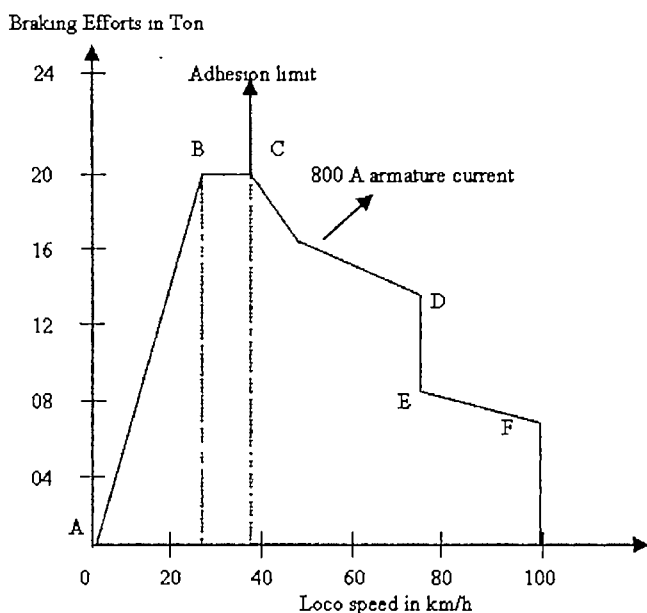


Fig. 1 Extended dynamic braking

It is evident that the maximum dynamic braking effort is available up to 25 km/h in loco and it decreases rapidly at lower speeds. In order to provide the higher braking efforts at lower speed the point B has to be shifted towards point B1 as shown in Fig. 2. This could be achieved by shorting out the

portions of grid resistances. It could be seen from Fig. 2 that in the extended range, the maximum dynamic brake efforts is available from 37 to 12 km/h by shifting point B to B1.

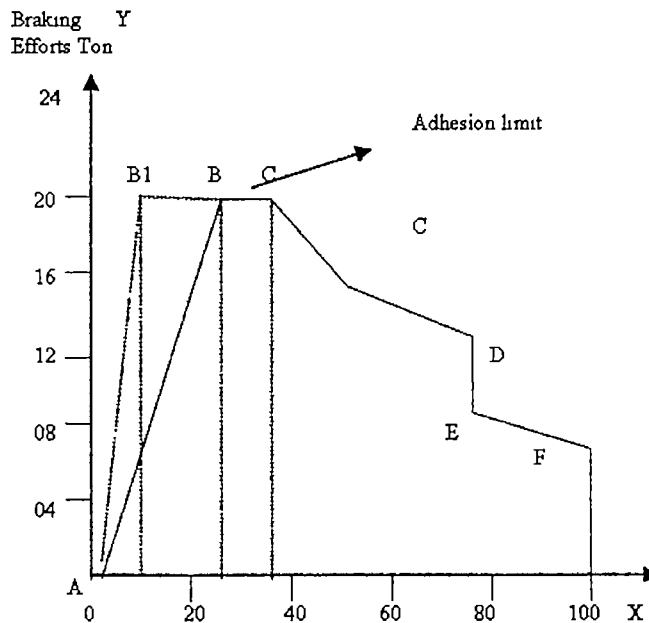


Fig 2 Loco speed in km/h

B. Full Extended Braking Range

To overcome the limitation of permanent shorting of grids, the grid resistances are shorted in stages and yield full dynamic braking. The existing dynamic braking of the locomotive is retained up to track speed of 26 km/h by using 0.5Ω grid resistance for each motor. Dynamic braking performance using extended range of dynamic braking for three stages is shown in Fig. 3 and illustrated as below.

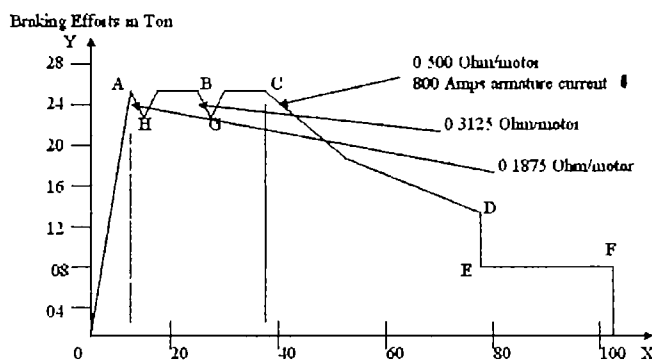


Fig. 3 Loco speed in km/h

STAGE I: Maximum braking efforts is achieved with the existing resistance value of 0.5Ω /motor. The normal dynamic braking with constant armature current is achieved with the existing system. The maximum braking effort is limited by the adhesion line BC between 26-37 km/h.

STAGE II: At point G, the speed is around 23 km/h. Further increase in braking efforts is achieved by shorting 75% of the resistance of one grid. The total resistance of braking grid will now become 0.3125 ohm/motor . The grid current will be

limited to 800 A.

STAGE III: At point H the speed is around 15 km/h. Further increase in braking effort is achieved by shorting one complete grid and 75 % of one grid/motor. The total resistance of braking grid will now become 0.1875 Ω /motor. Braking effort would again rise and maximum braking effort could be achieved at point A at a loco speed of 12 km/h as shown in Fig. 3.

III. HIGH SPEED PROTECTION AND CONTROL

In [7] automatic train protection (ATP) is used to prevent trains from speeding, i.e. train speed < maximum safe speed of the block. Tracks are divided into blocks, and only one train could occupy one block at a time. There is a maximum safe speed for each block, and it equals to the target speed assigned in the previous block, i.e., maximum safe speed for next block = target speed assigned in the present block. The basic rule is given by

$$v_t^2 = v^2 - 2(D_b + I)B_d \quad (1)$$

where, v is the present speed of train, v_t is the target speed, D_b is the deceleration of the train on level track, B_d is braking distance to reduce train speed from v to v_t and I is the deceleration due to inclination of the track. Rearranging (1), the deceleration braking efforts is given by

$$D_b = \left(\frac{v^2 - v_t^2}{2B_d} \right) - I \quad (2)$$

However if the gradient is zero in (2), it will reduce as

$$D_b = \left(\frac{v^2 - v_t^2}{2B_d} \right) \quad (3)$$

IV. APPLICATION OF FUZZY LOGIC

Use of fuzzy logic has avoided the knowledge [3] of a precise mathematical model of the system. The operation of fuzzy logic controller does not rely on the accuracy of the model, but on the rule base of fuzzy controller.

A. Fuzzy Controller

Fig 4 illustrates the operation of a fuzzy logic control system. The input to the fuzzy system is the output of the process, which enters via input interfaces. This input information would then go through the fuzzy logic process, where the processor would compare the input data to a database to obtain an output from the fuzzy logic processing.

This involves the execution of IF-THEN rules [4]. An input's grade specifies how well it fits into a particular graphic input data set. The output of a fuzzy controller is also defined by grades. These output grades determines the appropriate output value for the control element.

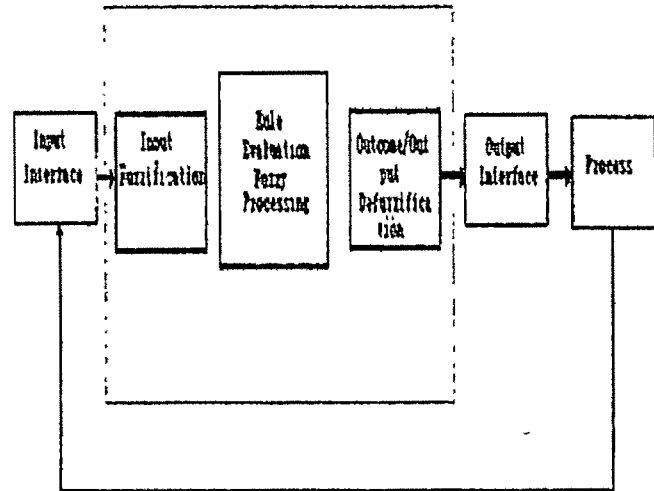


Fig. 4 Fuzzy logic controller

B. Fuzzy Logic Control Components

A fuzzy logic controller's control process consists of three main components, or actions, that must be completed sequentially to determine the appropriate output value. These components are:

- Input fuzzification
- Rule evaluation or fuzzy processing
- Output defuzzification

In this application, speed and distance are fed back to the fuzzy logic controller [8] via nonlinear saturator. This saturator allows to pass the input values within the specified ranges. The two input variables, i.e., speed and distance are allowed to pass the values between 0 to 100 km/h and 1 to 6 km respectively. These ranges can be varied to specific requirement and will be fed to the system through relays. Relays are controlled by programmed module used with fuzzy logic controller. The controller is allowed to receive the input values within the maximum speed and above the minimum required speed, via gate controlled switches. Operation of these switches can be controlled through microprocessor based programmed module. Fuzzy logic controller output is connected to motor field circuit through signal conversion and power electronic switch as shown in Fig 5. Signal conversion block converts the input signal into equivalent voltage source. Power electronic switches are set to operate during braking operation only.

It is found that fuzzy logic braking control is more effective since it is capable of providing required braking efforts to reduce the speed of locomotives from different speeds and braking distances to desired speed and braking distances.

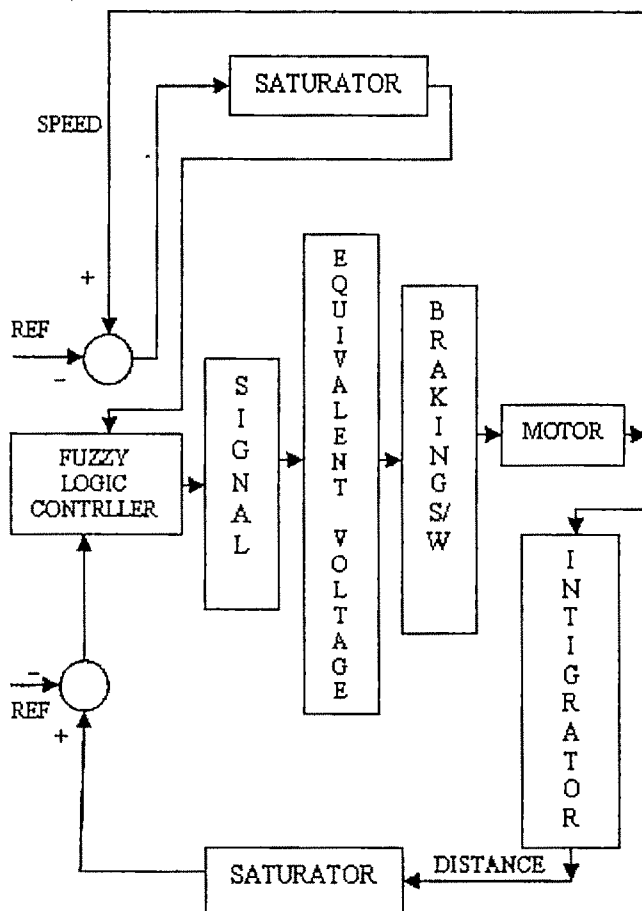


Fig. 5. Simulink model

The braking distance is fuzzified into the four ranges, as very near (VN), near (N), far (F) and very far (VF). The membership function corresponding to braking distance is shown in Fig. 6.

Membership Function

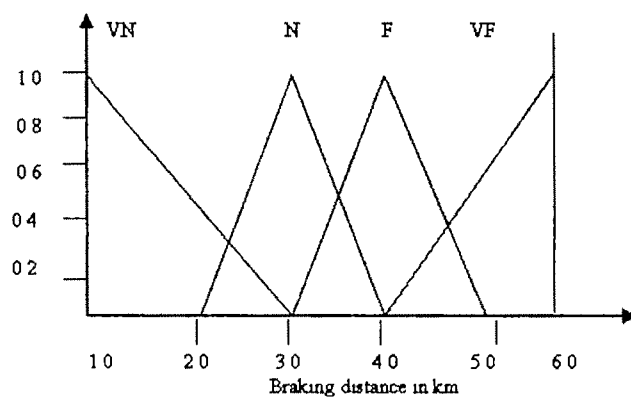


Fig. 6 Fuzzification of distance

Similarly, the range of speed is also fuzzified into four ranges as, very low (VL), low (L), high (H) and very high (VH). The corresponding membership plot is shown in Fig. 7.

Membership Function

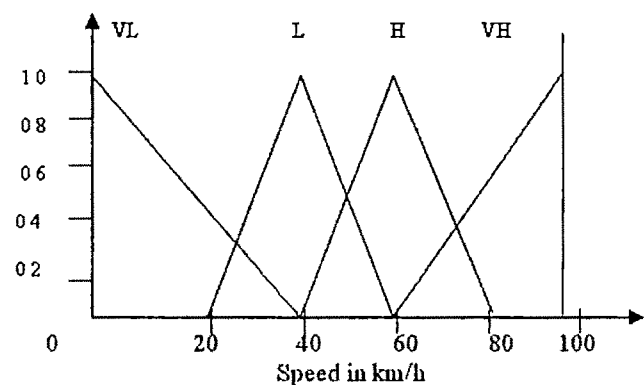


Fig. 7 Fuzzification of speed

The output membership function are fuzzified into the four levels as, ATTENTION, ALERT, WARNING and REMOTE. The corresponding membership function plot is shown in the Fig.8.

Membership Function

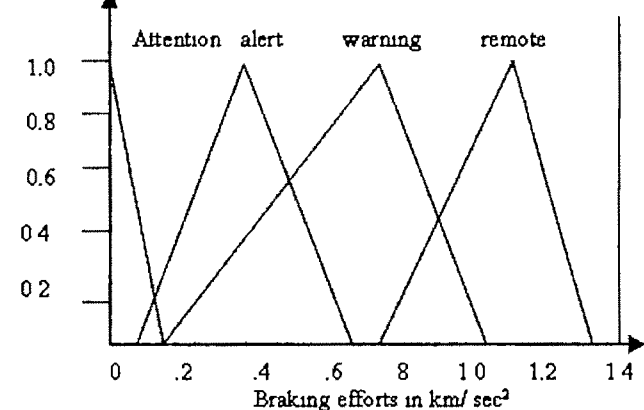


Fig. 8 Fuzzification of output braking effort

The rule-base relating fuzzified input and output is given in Table. 1.

Table 1 Rule-base for fuzzy-controller

Speed Distance	VN	N	F	VF
VH	REMOTE	REMOTE	WARNING	WARNING
H	REMOTE	WARNING	WARNING	WARNING
L	WARNING	WARNING	ALERT	ALERT
VL	WARNING	ALERT	ALERT	ATTENTION

C. Simulation Results

The various simulation results are reflected in following tables. Table 2 shows the various stages of extended range of braking. Table 3 shows the braking comparison and braking results are shown in Table. 4, Table. 5 and Table. 6.

Table 2 Stages of extended range of braking

Events	Loco Speed In Km/h	Braking Efforts/ Traction Motor	
		Before Transition ohm	After Transition ohm
01	23	0.500	0.3125
02	12	0.3125	0.1875

Table 3 Braking comparison

Types Of Dynamic Brake	Speed Range Of Max Dynamic Braking Efforts
Normal Dynamic Brake	37-26 km/h
Extended Range Of Dynamic Brake	37-12 km/h

Table 4 Braking results of conventional control system

Speed required (In KMPH)		Distance Travelled (In KMs)	Braking Current (In Amps)	Braking Voltage (In Volts)
From	To			
110	50	4.0	750-800	350-400
110	50	4.3	500-700	200-300
110	50	5.3	700-800	325-400
110	50	4.0	500-700	250-300
110	50	3.9	750-800	350-400
110	50	4.2	500-650	250-300

Table 5. Braking results without fuzzy logic and extended braking

Speed required (In KMPH)		Distance Travelled (In km)	Braking Current (In Amp)	Braking Torque (In n.m)
From	To			
110	12	4.8	750-425	2.5×10^4 - 1.4×10^4
90	12	4.0	450-225	1.5×10^4 - 75×10^4

Table 6 Braking results using fuzzy logic and extended braking

Desire d Distance In km	Speed required (In km/h)		Distance Travelled (In km)	Braking Current (In Amp)	Braking Torque (In n.m)
	From	To			
6	110	12	5.8	800-550	4.2×10^4 - 2.8×10^4
1	110	12	1.4	900-620	6.8×10^4 - 3.0×10^4
6	90	12	5.5	700-430	3.4×10^4 - 1.7×10^4
1	90	12	1.2	800-450	6.5×10^4 - 1.6×10^4

V. CONCLUSION

Simulation is carried out in MATLAB/SIMULINK for different speed and distance from 110 km/h to 12 km/h speed. These desired results may require increased requirement of braking torque and hence heat dissipation. This can be taken care of by blower fans connected to resistance grid. This work also considered the extended dynamic braking scheme, which has the enhanced braking torque characteristics. This scheme has the advantage of higher braking torque at lower speed. As per the simulation conducted the max braking torque of

6.8×10^4 Nm is obtained at 12 km/h speed. This paper concludes that the fuzzy logic controller used with extended range of dynamic braking, facilitate the action of pneumatic brake at lower speed say 12 km/h as compared to 26 km/h using conventional braking. This reduces the wear and tear of the traction wheels.

APPENDIX

The total six traction motors are mounted on each locomotive. Table 7 shows the specification of DC series motor, proposed to be used for locomotives.

Table 7. Specification of DC series motor

Type Of Motor	DC Series Motor
Model	HS 15250 A
Type	Forced Ventilation
Field	Series Field With Commutating Poles
Minimum Field Strength	40 %
Insulation	Class "H"
Continuous Rating	630 kw, 750 V, 900 Amps, 895 RPM
Reduction Gear	Single Reduction (64/40)
No Of Pole	6
Armature Winding Resistance	0.00953 ohm
Series Field Winding Resistance	0.00880 ohm
Mutual Inductance	0.052 H
Moment Of Inertia	31 Kg-m ³
Armature Inductance	0.00002 H
Field Winding Inductance	0.00002 H
Armature Core Diameter	500 mm
Armature Core Length	480 mm
Weight Of Armature	1010 Kg
Loco Wheel Diameter	1093 mm

REFERENCES

- [1] Masahiro Ashiya, "Application of pure electric braking", *Proc IEEE-IAS*, pp 415-418, 1997.
- [2] Ali Nabi and Masoud Valizadeh, "Development of a brake control system using fuzzy logic", *IEEE proceedings*, PP 1345-1350, 2006.
- [3] B. Cakir, N. Abut, "DC Motor Control by Using Computer Based Fuzzy Technique", *IEEE Proceedings*, PP 391-395, 1999.
- [4] Gerhard A. Thelen and Y.H. Tse, "An Automatic Speed Enforcement System For Heavy Freight Trains, Rail Corporation Philadelphia, Pennsylvania, PP 31-39, 1988.
- [5] Antsaklis PJ, "Defining Intelligent Control", (*Report of the Task Force on Intelligent Control*), *IEEE Control Systems*, Vol-14, No-3, PP 4-5 and 58-66, 1994.
- [6] Antsaklis PJ, Passino KM, Wang SJ, "An Introduction to Autonomous Control System", *IEEE Control System Magazine*, Vol-11, No-4, PP 5-13, 1991.
- [7] Leach M, "Automatic Train Protection", "Railway Control Systems", A Project Report Of The Institution Of Railway Signal Engineers, A & C Black, London, PP 258-280, 1990
- [8] Lee CC, "Fuzzy Logic In Control System, Fuzzy Logic Controller Part I And II", *IEEE Transactions On systems*, Vol-20, No-2, PP 404-435, 1990.

Technical Session 4B

Biomedical Instrumentation

Real Time Data Acquisition System for Three Axis Force Measurements of Needle Insertion into Soft Tissue, its Modeling and Simulation

Debajit Bharali^{1,2}, Sohini Roy^{1,3}, Ajay K Yagati¹, Sunil Kumar¹, Sujoy K Guha¹

¹School of Medical Science and Technology, Indian Institute of Technology, Kharagpur-721302, West Bengal

²Department of Electronics and Communication, Tezpur University, Tezpur-784028, Assam

³Department of Biomedical Laboratory Sciences and Management, Vidyasagar University, Midapore-721102, West Bengal

Abstract - Needle insertion in soft tissue has attracted considerable attention in recent years due to its application in minimally invasive percutaneous procedures such as radio-frequency ablation and brachytherapy. It requires controlled insertion force for accuracy in percutaneous procedure and also to provide tactile effect in robotic needle insertion. There can be a variety of force that act on needle, including friction, cutting forces/ internal stiffness and collisions with interior structures. The stiffness force is pre-puncture, and friction and cutting forces are post-puncture. It is difficult to maneuver the needle toward the target due to soft insertion site and slight deflection or uncontrolled movement can cause great trauma to the adjacent tissue. In order to overcome this, we have designed a MATLAB® based real time data acquisition system for reducing counter puncture of tissue or blood vessel. Finite Element Modeling of soft tissue deformation has also been performed using ANSYS 8.0. Modeling experiments involved a linear elastic material with Young's modulus of 2.53 kPa and Poisson's ratio of 0.48 to indicate near incompressibility. A fast algorithm for interactive needle insertion with force feedback, without loss of model detail or degradation in global response has been developed. These needle mechanics measurements and simulations are of interest for the development of physically-based virtual planning and training systems that are aimed at reducing the incidence of complications in clinical practice.

Keywords: Needle Insertion, simulation, modeling, percutaneous intervention.

I. INTRODUCTION

TODAY medical science uses many percutaneous procedures for minimal invasive surgeries, such as radio-frequency ablation and brachytherapy. The real time data acquisition of the needle insertion three axis forces into soft tissue can help medical professionals to perform these percutaneous procedures using robotics i.e., using haptic interface. Most of the percutaneous procedure is performed in soft tissues, so the insertion need to be accurate, therefore we have designed a three axis force sensor to sense the force along all three co-ordinate axis on the needle while insertion and a robotic manipulator which can translate in three directions. To validate this, we have simulated the model of a soft tissue using ANSYS software.

II. EXPERIMENTAL SET-UP

We designed a three axis force sensor for the measurement of triaxial force at the needle tip. The three axis force sensor was designed using piezoresistive strain gauges. The external casing was made of polymer. The strain gauges were attached to the crossed beam stainless steel cantilevers. Figure 1 shows the schematic diagram of the designed three-component force sensor with four strain gages (S1 ~ S4). The tactile sensor size was 10x10cm with spatial resolution of about 1cm. The rated capacity of sensor for Fx, Fy, Fz components was 10N and the rated capacity of force sensor was 0.3N. Thickness of the membrane was kept as large as possible within the elastic limits of the membrane and sensing material for maximum sensitivity. Using the strain distributions at locations of strain gages, the solution of the decoupling method for obtaining three force components signals can be represented by

For Fz loading, using strain gage signal S1, S2, S3 and S4,

$$\Delta V_{F_z} = \Delta V_{s1} + \Delta V_{s2} + \Delta V_{s3} + \Delta V_{s4} \quad (1)$$

For Fx loading, using strain gage signal S1 and S3,

$$\Delta V_{F_x} = \Delta V_{s1} - \Delta V_{s3} \quad (2)$$

For Fy loading, in a similar way,

$$\Delta V_{F_y} = \Delta V_{s2} - \Delta V_{s4} \quad (3)$$

Here ΔV means the change of voltage for strain gage.

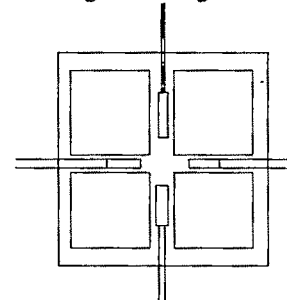


Figure 1: Schematic diagram of the three axis force sensor

The cantilever structure was made by the thin stainless steel film with a size of 2cm X 3cm X 0.1mm and its Young's modulus was 240 GPa. The spring coefficient of the sensor is

estimated as 1600 N/m. If we install a glass tool (weight: 67 mg), the resonance frequency of the sensor tip is estimated as 730 Hz. We made four pairs of bridge circuits.. Here, V1, V2, V3, and V4 are output voltage in each bridge circuits, respectively. We calculate Vx, Vy, and Vz as follows.

$$V_{Fz} = V_{S1} + V_{S2} + V_{S3} + V_{S4} \quad (4)$$

$$V_{Fx} = V_{S1} - V_{S3} \quad (5)$$

$$V_{Fy} = V_{S2} - V_{S4} \quad (6)$$

The output voltage vector V is written as follows by the applied moments Mx and My, force Fz, and matrix C.

$$V = CF \quad (7)$$

where,

$$V = [V_x \ V_y \ V_z]$$

$$F = [M_x \ M_y \ F_z]$$

$$C = \begin{bmatrix} C_{xx} & C_{xy} & C_{xz} \\ C_{yx} & C_{yy} & C_{yz} \\ C_{zx} & C_{zy} & C_{zz} \end{bmatrix}$$

Here, the compliant matrix C can be identified by a simple calibration experiment by measuring different kinds of loads. Then, the force on the tip is calculated by the following equation.

$$F_t = MC^{-1}V \quad (8)$$

where,

$$F_t = [F_x \ F_y \ F_z]$$

$$M = \text{diag} \left[\frac{1}{l} \ \frac{1}{l} \ l \right]$$

where, l is the length of tool.

We calibrated the complaint matrix by the experiment as follows:

$$C = \begin{bmatrix} 1.240 & -0.058 & 0.543 \\ 0.120 & 0.771 & 0.660 \\ 0.013 & 0.001 & 0.621 \end{bmatrix}$$

The three axis needle insertion manipulator [1] was designed to detect the actual position of the needle insertion i.e. the position of the vein and to measure the forces on a surgical needle during insertion into soft tissue. The needle insertion device has three powered (linear motion) axes. The z-axis motor drives a carriage up and down, so that it goes towards and away from the arm that is strapped in under it. This carriage is used to hold either a blunt probe (for finding a vein) on a syringe and needle combination. A single axis piezo-resistive force sensor is mounted on the carriage to measure the force on the probe or needle. The x-axis motor moves the carriage across the width of the arm. This enables the probe to press in a series of places along the width of the arm. The y-axis motor moves the whole robot along the length of the arm. This was designed to compensate for the slight difference between where the probe has identified a vein, and where the needle enters the skin, once the robot has been tilted.

Software to control the robot was written in Matlab on a PC running Windows XP. This procedure implemented a state machine, which had two phases: one to identify the position of the vein and a second one to insert the needle correctly. Safety

issues were of high importance. The robot was designed so that the needle insertion motion was physically constrained so as not to push the needle beyond a maximum depth of 20 mm. Also, all the axes could be operated by hand in the event of a power failure. Various software devices were implemented to check the behavior of the robot and to default to a safe condition in the event of an error.

Kinematics involved with the design of the force controller is explained in Figure 2.

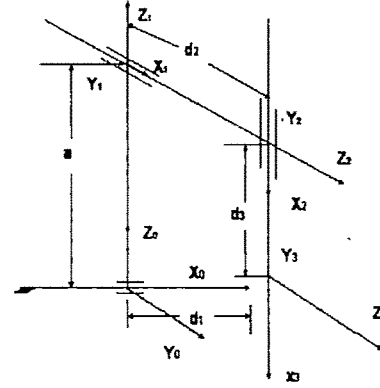


Figure 2: Kinematics of the three axis robotic needle insertion device. Where, a is the height of the fixed shaft in the robot. d1, d2 and d3 are the translational displacement in X, Y and Z direction respectively.

Kinematics equation of the three axis robotic insertion device are given as below

$$Z_0 = a - d_3(t) \quad (9)$$

$$Y_0 = d_2(t) \quad (10)$$

$$X_0 = d_1(t) \quad (11)$$

The computer controller consists of a host computer, motor drivers, amplifiers and filters, power and safety systems and necessary connection equipment. The software executes on a Microsoft Windows XP platform, Pentium (R) 4, 3.0 GHz processor based computer. The software for recording the insertion forces on the tissue is written in MATLAB. It is desirable to run the data collection at as fast a rate as possible in order to capture sudden changes in forces. A good rate for these experiments is 2 kHz because the puncture phenomena we want to capture occur at a slower rate. The control program is written using MATLAB® software.

To operate the program, the following sequence should be followed:

- First enable the robotic manipulator, and adjust the force sensor to zero output voltage. The robotic needle insertion device is loaded with the imaging probe.
- The device translate in the X direction using the stepper motor of that direction along the length of the tissue sample and then along Y axis using stepper motor along the breadth of the tissue sample to detect the position of needle insertion.
- After the position of the needle insertion is detected the imaging probe is replaced by a bevel shaped needle.
- Choose the linear motion of the needle (upward and downward) by connecting the stepper motor for the

external power supply and the control of the motor were done manually.

- v. Once the force transducer were started gathering the data, continues even if the motor stops the computer will display a force output.

III. MODELING & SIMULATION OF SOFT TISSUE

Theory of Finite Element Modeling (FEM):

The FEM, which uses a numerical procedure to obtain a discrete approximation in both static and dynamic problems, is well suited to the solution of the governing equation

$$\left(\mu_1 + \mu_2 \frac{\partial}{\partial t} \right) u_{,x} + \left((\mu_1 + \lambda_1) + (\mu_2 + \lambda_2) \frac{\partial}{\partial t} \right) u_{,x} = \rho \frac{\partial^2 u}{\partial t^2} \quad (13)$$

where λ_1 and μ_1 are the longitudinal and shear elastic modulus respectively, and λ_2 and μ_2 are the longitudinal and shear viscous modulus respectively.

Equations that govern the dynamic response of a medium are derived by requiring the work of the external vibration forces to be absorbed by the work of internal, inertial and viscous forces for small admissible motions. For a single element, the equilibrium equation for the harmonic vibration case is expressed as [2]:

$$(-\omega^2 [m] + i\omega [c] + [k]) \{d\} = \{r\} \quad (14)$$

where $[m]$, $[c]$ and $[k]$ are the element mass, damping and stiffness matrices respectively, $\{d\}$ and $\{r\}$ are the element grid displacement and force vectors respectively, ω is the angular frequency of vibration and i is the imaginary unit. The $[m]$, $[c]$ and $[k]$ matrices depend on ρ , (λ_2, μ_2) , and (λ_1, μ_1) respectively. After assembly of elements, the governing equations in FEM are derived from equation (14)

$$(-\omega^2 [M] + i\omega [C] + [K]) \{D\} = \{R\} \quad (15)$$

Where, $[M]$, $[C]$ and $[K]$ are the assembled element mass, damping and stiffness matrices respectively and $\{D\}$ and $\{R\}$ are the assembled element grid displacement and force vectors respectively.

In the case of harmonic vibration, the grid displacement and force are expressed as

$$D = A e^{i(\omega t + \theta)}, \quad R = B e^{i(\omega t + \phi)} \quad (16)$$

where A and θ are the displacement amplitude and phase vectors respectively, and B and ϕ are the force amplitude and phase vectors respectively. After substituting equation (16) into equation (15), the governing equations in the frequency domain can be obtained as

$$\begin{bmatrix} -\omega^2 M + K & -\omega C \\ \omega C & -\omega^2 M + K \end{bmatrix} \begin{Bmatrix} A \cos \theta \\ A \sin \theta \end{Bmatrix} = \begin{Bmatrix} B \cos \phi \\ B \sin \phi \end{Bmatrix} \quad (17)$$

Although Poisson's ratio and the damping coefficient are also unknown, for the purposes they will be assumed to be constant. Values of Poisson's ratio should fall between 0 and 0.5, with $\nu = 0.5$ for an incompressible material.

Based on measurements of stress/strain relationships in soft tissue phantoms, we have chosen to ignore damping for the time being. Under conditions where ωC is very small compared with $-\omega^2 M + K$, damping can indeed be ignored and equation (17) can be simplified to

$$[-\omega^2 M + K] \{A \cos \theta\} = \{B \cos \theta\} \quad (18)$$

The basic principle behind the iterative approach is as follows: given an assumed Young's modulus, solution of equation (18) will result in theoretical estimates of the vibration displacements. These are then compared with the measured data and Young's modulus is iteratively updated until convergence within a specified constraint is achieved. The range of Young's modulus values is given by $E_{min} < E_e < E_{max}$, where E_{min} and E_{max} are the minimum and maximum expected values, and E_e is the estimated value. Typically, Young's modulus for living soft tissue ranges from 1 kPa to 200 kPa for strains of less than 5% [3, 4].

Defining,

$$\Delta A = \Sigma (A_e - A_m) \text{ and } ssd = \Sigma (A_e - A_m)^2 \quad (19)$$

$$\Delta E = E_{max} - E_{min},$$

where A_e and A_m are the estimated and the measured amplitude respectively, the steps of implementation are as follows:

- i. Initialize values of E_{min} and E_{max} .
 - ii. Assume an estimated Young's modulus $E_e = (E_{min} + E_{max})/2$.
 - iii. Solve equation (19) for amplitude, A_e , and calculate ΔA .
 - iv. Update E_{min} and E_{max} in the following way:
 - a. If $\Delta A > 0$, then set $E_{min} = E_e$ and keep E_{max} .
 - b. If $\Delta A < 0$, then set $E_{max} = E_e$ and keep E_{min} .
- Repeat steps 2, 3 and 4 until $\Delta E/E_e < \text{threshold}$ or until M iterations.

The threshold may be set to any value less than half the expected error and the maximum iteration number, M , is arbitrary. For the purposes of our work, the threshold was set to 2% and M to 13.

IV. RESULTS

Needle insertion consists of four events: initial puncture, insertion, relaxation, and withdrawal.

The needle insertion procedure consists of six steps:

- i. **Tissue compression:** needle is inserted through soft tissue and pushes against the target membrane.
- ii. **Membrane puncture:** needle punctures the target membrane.
- iii. **Insertion:** needle moves deeper into the target.
- iv. **Tissue settling:** when the needle stops moving, the tissue settles to a stable state.
- v. **Retraction:** needle is removed.
- vi. **Equilibrium:** tissue returns to a stable state.

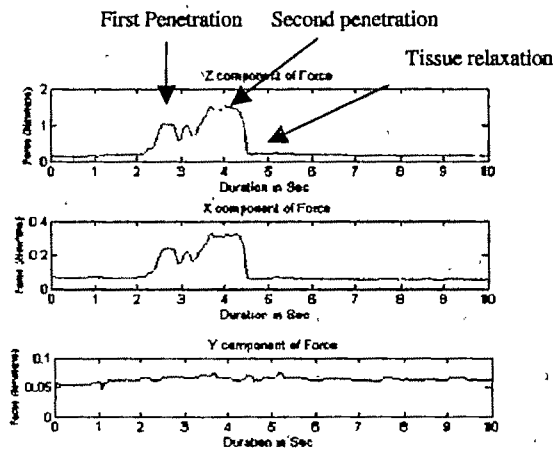


Figure 3: Force measured during needle insertion into soft tissue in puncture event in the first trial (45° inclined).

In order to model the needle insertion forces accurately, it is necessary to separate the data into its components. Below Figure 3 and 4 shows various components of the force having the pre-puncture, puncture and removal phases of the needle in to a test vessel.

The main event is designated by a peak in force after a steady rise, followed by a sharp decrease. Subsequent variations in the force are due to the friction, cutting forces/internal stiffness as well as collisions with the puncture of interior structures. The force data collected is a sum of stiffness, friction, and cutting forces. The stiffness force is pre-puncture, and the friction and cutting forces post-puncture.

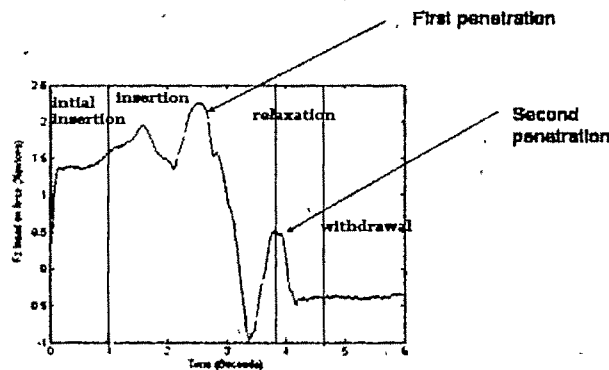


Figure 4: Fz (axial) force measured during one insertion showing the various insertion events.

The total force is thus represented by the following equation,

$$f_{\text{needle}}(z) = f_{\text{stiffness}}(z) + f_{\text{friction}}(z) + f_{\text{cutting}}(z) \quad (7.1)$$

3D Finite Element Model of the soft tissue

Needle deflection and tissue deformation are major problems encountered for accurate needle insertion and attempts have been made in the present study to model them. Modeling of soft tissue deformation due to needle insertion has been studied earlier by several authors [5, 6, 7 and 8]. Modeling of soft tissue deformation due to needle insertion is done with the

help of ANSYS software. We have considered the Young's modulus and Poisson's ratio of the soft tissue to be 2.53 kPa and 0.48 respectively. These needle mechanics measurements and simulations are of interest for the development of physically-based virtual planning and training systems that are aimed at reducing the incidence of complications in clinical practice

(A) With Mesh FEM model of soft tissue using ANSYS:

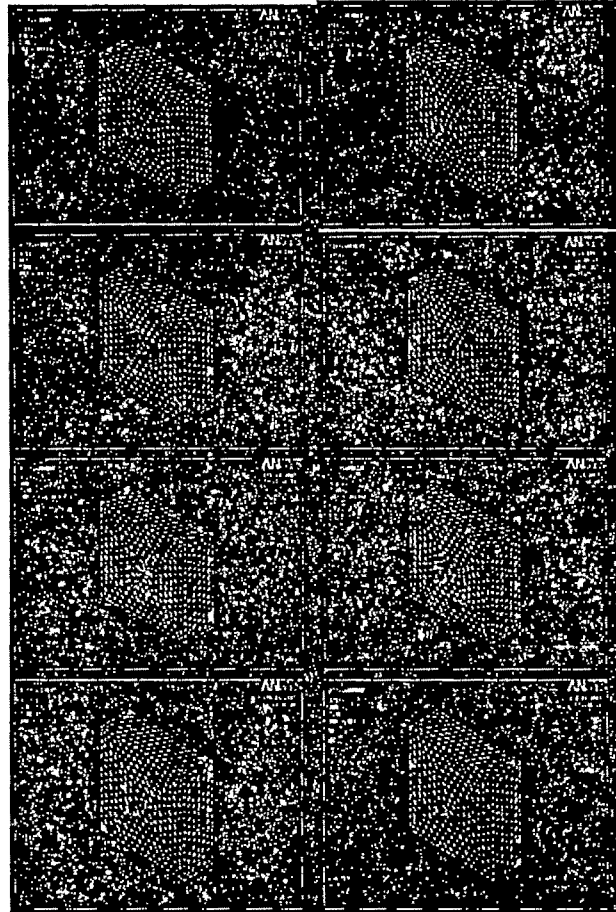


Figure 5: with mesh 3D FEM of soft tissue deformation due to needle insertion.

Figure 5 shows the series of images obtained by FEM modeling of insertion of needle into soft tissue. The figure clearly shows the deformation of sample when a force of certain strength is applied on it. These results were then analyzed on the solid model of the tissue. Figure 6 shows the tissue deformation on application of force over it. The change in color is due to the stress applied on the tissue. The red color indicates more deformation when compared with blue which is completely relaxed and normal. With this model we are able to tell exactly how the sample will behave on application of particular amount of force over it in specific time period.

(B) Without mesh 3D FEM of the soft tissue deformation due to needle insertion

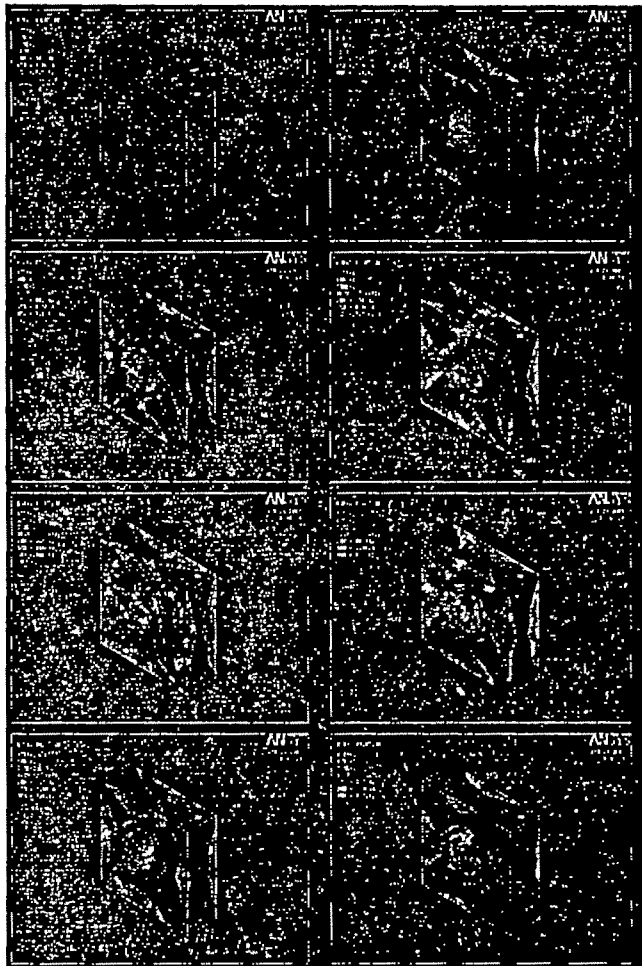


Figure 6: without mesh 3D FEM of Soft tissue deformation due to needle insertion

Conclusion:

During any surgical procedure it is necessary for a surgeon to carefully avoid the damage to adjacent tissues. Present study describes an automatic instrument (force feedback controlled)

through which it may be possible to limit the amount of damage caused to the tissue involved as well as to adjacent tissues during any surgical procedure. This instrument provides real-time force measurement of needle insertion that can then be used to guide the needle. We have measured the forces of needle insertion on several synthetic vessels, having similar physical properties as soft tissues. Further, we have also modeled the needle insertion forces and also simulated a model of soft tissue deformation during needle insertion. This method requires measurement of forces during surgery especially the forces that surgeon applies to the vessel. This measurement can then be delivered to the surgeon to increase his awareness of the operating field. Further investigations are being carried out in order to determine the most beneficial method of delivering the real-time data gathered by our instrument to the surgeon. Although this article only studied the vessel properties in a research setting, we see great potential for this instrument in the clinical application.

References:

- [1] N. Hata, F. Ohara, R. Hashimoto, M. Hashizume and T. Dohi, "Needle Guiding Robot with Five-Bar Linkage for MR-Guided Thermoablation of Liver Tumor," *Medical Image Computing and Computer-Assisted Intervention - MICCAI 2004*, vol. 3217, pp. 1611-1619.
- [2] R. D. Cook, D. S. Malkus and M. E. Plesha, "Concepts and Application of Finite Element Analysis" (New York: Wiley), pp. 368-370, 1989.
- [3] M. Radmacher, "Measuring the elastic properties of biological samples with the AFM," *IEEE Eng. Med. Biol.*, vol. 16, pp. 47-57, 1997.
- [4] T. A. Krouskop, T. M. Wheeler, F. Kallel, B. S. Garra and T. Hall, "Elastic modulus of breast and prostate tissues under compression," *Ultrason. Imaging*, vol. 20, pp. 260-274, 1998.
- [5] P. N. Brett, A. J. Harrison and T. A. Thomas, "Schemes for the identification of tissue types and boundaries at the tool point for surgical needles," *IEEE Trans. Inform. Technol. Biomed.*, vol. 4, pp. 30-36, 2000.
- [6] Brouwer, J. Ustin, L. Bentley, A. Sherman, N. Dhruv, and F. Tendick, "Measuring in vivo animal soft tissue properties for haptic modeling in surgical simulation," *Med. Meets Virtual Reality*, vol. 9, pp. 69-74, 2001.
- [7] S. P. DiMaio and S. E. Salcudean, "Needle insertion modeling and simulation," in *Proc. IEEE Int. Conf. Robotics Automat.*, pp. 2098-2105, 2002.
- [8] J. Rosen, B. Hannaford, M. MacFarlane, and M. Sinanan, "Force controlled and teleoperated endoscopic grasper for minimally invasive surgery—Experimental performance evaluation," *IEEE Trans. Biomed. Eng.*, vol. 46, pp. 1212-1221, 1999.

Automated Detection and Classification of Cerebral Palsy Gait using Support Vector Machines

M. Shiva Kumar¹ and M.Sukumar²

¹Research Scholar, J S S Research Foundation, S.J.C.E Campus, Mysore-570 006. e-mail: msbiet@rediffmail.com

²Professor & Head, Department of Instrumentation Technology, S J.C.E, Mysore-570006. e-mail: m_sukumar@rediffmail.com

Abstract- Cerebral palsy (CP) is a group of motor problems and physical disorders that result from a brain injury or abnormal brain development that may occur during fetal growth, at the time of birth, or within the first 2 or 3 years of a child's life. Gait analysis of children suffering from Cerebral Palsy (CP) will be helpful for diagnosis as well as for proper evaluation of the treatment outcomes. This paper explains the use of Support Vector Machines (SVM) for automated detection and classification of children with CP using two basic temporal-spatial gait parameters (Stride length and Cadence) as input features. Dataset used for classification using SVM method consists of 68 normal healthy children and 88 children suffering from Spastic Diplegia form of cerebral palsy. SVM Classifier was able to classify the children groups with an overall accuracy of 60% , Sensitivity 20%, Specificity 100%. Classification accuracy improved significantly when the gait parameters were normalized by the individual leg length and age, leading to an overall Accuracy, Sensitivity, and Specificity all close to 100%. Classifier's performance as functions of regularization and kernel parameters was also investigated.

Key words : Cerebral palsy, Gait, Support Vector Machines.

I. INTRODUCTION

WALKING, an important activity of daily living, is a mode of bipedal locomotion in which a period of double support, when both feet are in contact with the ground, is followed by a period in which the body is supported by one lower limb while the other is swung forward [1]. The pattern of how a person walks is called gait. Gait analysis is routinely used in clinical settings for the assessment of walking performance. One such important application of gait analysis is in the assessment of cerebral palsy (CP) patients.

Attempts to classify cerebral palsy children based on gait measurements have been primarily qualitative [2], [3] and are therefore of limited scientific relevance. Many treatments are designed to improve gait patterns in children with cerebral palsy (CP), but due to the heterogeneity of children with this diagnosis, evaluation of treatment effects in this population is problematic [4], [5]. Therefore, the need exists for a quantitative, objective technique to clearly identify (or differentiate) subgroups of children with CP in order to assess the outcome of surgical or therapeutic interventions.

Automated recognition and classification of the CP gait characteristics could offer many potential benefits, especially for the diagnosis, assessment and evaluation of the treatment

outcomes. Support Vector Machine, which is a supervised machine classifier, provides the output values in the range "0 to 1" (0 being normal and 1 pathological). Thus, the classifier output could be used to gauge the movement of the "overall performance" during an intervention within the spectrum of normal and pathological conditions. For example, during the course of a certain treatment / rehabilitation intervention, if the classifier's output shift towards zero, then it would indicate that the intervention has improved the overall gait function of the individual by being closer towards the normal healthy group.

SVM is a relatively new machine-learning tool and has emerged as a powerful technique for learning from data and solving classification and regression problems [6]. This has been particularly effective for binary classification applications. Applications of the SVM in gait pattern detection and classification has been so far limited to the classification of young and elderly gait patterns [7] despite their demonstrated high success rates in other biomedical areas (e.g., [8]). In this paper, we explore the classification ability of SVM in normal and CP children using gait data provided by O'Malley *et al.* in [9].

II. GAIT DATA ACQUISITION AND NORMALIZATION TECHNIQUES

Gait features used in this study for training and testing the SVM classifier were taken from the published gait data by O'Malley *et al.* [9].

A Gait Measurement and Feature Selection

The data set includes 88 children with spastic diplegia form of CP (age between 2 to 20 years, mean=9.9 years) and 68 children of neurologically intact control group (age between 2 to 13 years) with no history of motor pathology.

In their work [9], O'Malley *et al.* provided four feature values: Stride length, Cadence, Leg length and Age. In this work for classification purposes, we considered all four features but particularly interested in stride length and cadence. One of the main aims was to investigate how the normalization proposed by O'Malley *et al.* [10] on stride length and cadence, performs in distinguishing CP from normal children when applied to a classifier, i.e SVM. These two features are particularly significant as they are considered to be the fundamental gait parameters [11]. These are also found to be more sensitive indicators of the degree of motor

involvement among children with CP than other parameters, such as kinematics focused on single joints [12]. These features are statistically independent when normalized by the respective leg length and age, and are easy to interpret as well as clinically useful [9].

B Normalization of Gait Data

One of the major difficulties in using the temporal-distance parameters to differentiate gait patterns in children is the effect of age and leg length [13]. In order to have a reasonable number of samples, it is necessary to collect data from children of many different ages and leg lengths and therefore a proper normalization technique is required. One of the advantages of this technique is that it allows the normalization of a data set using a model based on the data set itself or a model based on a reference data set. Here, there are two data sets, 68 neurologically intact children in a control group and 88 children with CP. The control group was normalized using a model based on themselves. The children with CP are normalized using the model for the control group. Using this approach, any trends in the neurologically intact children for leg length and age are removed. For the children with CP any trends that would be expected in a neurologically intact population are removed, thus leaving any pathological trends [14]. This would not be achieved if the children with CP were normalized using a model based on themselves.

For the control group, stride length was normalized with respect to leg length according to

$$NSL_N = SL_N - (a_0 + a_1 LL_N + a_2 (LL_N)^2 + \dots + a_k (LL_N)^k) + \overline{SL_N} \quad (1)$$

where NSL_N is the normalized stride length of the control group children, SL_N is the stride length of the control group children, LL_N is the leg length of the control group children, $a_0, a_1, a_2, \dots, a_k$ are the parameters of the k^{th} order polynomial model which describes the stride length/leg length relationship for the control group children and $\overline{SL_N}$ is the average stride length of the control group children. For children with CP the stride length was normalized with respect to leg length according to

$$NSL_{CP} = SL_{CP} - (a_0 + a_1 LL_{CP} + a_2 (LL_{CP})^2 + \dots + a_k (LL_{CP})^k) + \overline{SL_N} \quad (2)$$

where NSL_{CP} is the normalized stride length of the children with CP, SL_{CP} is the stride length of the children with CP and LL_{CP} is the leg length of the children with CP. For the control group children cadence was normalized with respect to age according to

$$NCAD_N = CAD_N - (b_0 + b_1 AGE_N + b_2 (AGE_N)^2 + \dots + b_k (AGE_N)^k) + \overline{CAD_N} \quad (3)$$

where $NCAD_N$ is the normalized cadence of the control group children, CAD_N is the cadence of the control group children, AGE_N is the age of the control group children, $b_0, b_1, b_2, \dots, b_k$ are the parameters of the k^{th} order polynomial model which describes the cadence/age relationship for the control group children and $\overline{CAD_N}$ is the average cadence of the control group children.

For the children with CP, cadence was normalized with respect to age according to

$$NCAD_{CP} = CAD_{CP} - (b_0 + b_1 AGE_{CP} + b_2 (AGE_{CP})^2 + \dots + b_k (AGE_{CP})^k) + \overline{CAD_N} \quad (4)$$

Where $NCAD_{CP}$ is the normalized cadence of the children with CP, CAD_{CP} is the cadence of the children with CP and AGE_{CP} is the age of the children with CP.

C Testing a Classifier

Once a binary classifier is trained with the known gait data and the corresponding target associations (CP children=1, normal children=0), response to an unseen gait data from a new subject can be interpreted to belong to one of the categories. The following three measures (accuracy, sensitivity, and specificity) [15], [16] were used to assess the performance of the classifier:

$$\text{Accuracy} = \frac{TP + TN}{TP + FP + TN + FN} \times 100\% \quad (5)$$

$$\text{Sensitivity} = \frac{TP}{TP + FN} \times 100\% \quad (6)$$

$$\text{Specificity} = \frac{TN}{TN + FP} \times 100\% \quad (7)$$

Where TP is the number of true positives, i.e the classifier identifies a CP gait that was labeled as CP; TN is the number of true negatives, i.e., classifier identifies a normal gait that was labeled as normal; FP is the number of false CP identification; and FN is the number of false normal identification. Accuracy indicates overall detection accuracy for both normal and CP gait patterns. Sensitivity is defined as the ability of the classifier to accurately recognize a CP gait pattern whereas Specificity would indicate the classifier's ability not to generate a false detection.

III. MACHINE CLASSIFIER: SUPPORT VECTOR MACHINES

It belongs to a category of universal feedforward network which is a linear machine introduced by Vapnik. The Support Vector Machines (SVM) is an approximate implementation of the method of structural risk minimization. The SVM can provide a good generalization performance on pattern classification problems despite the fact that it does not incorporate problem-domain knowledge. This attribute is unique to SVM [17].

SVM can be used for the classification of both the linearly separable and nonseparable patterns. Support Vectors are those data points that satisfy the following equation precisely even if $\xi_i > 0$.

$$d_i(W^T X_i + b) \geq 1 - \xi_i, i = 1, 2, \dots, N \quad (8)$$

where X_i is the input vector, W is an adjustable weight vector, $\{\xi_i\}_{i=1}^N$ is the set of nonnegative scalar variables and b is the bias.

The idea of SVM hinges on two mathematical operations namely :

1. Nonlinear mapping of an input vector into a high-dimensional feature space that is hidden from both the input and output.
2. Construction of an optimal hyperplane for separating the features discovered in step1.



Fig. 1. Nonlinear Mapping $\Psi(\cdot)$ from the input space to the feature space.

Operation 1 is performed in accordance with Cover's theorem on the separability of patterns. Consider an input space made up of non-linearly separable patterns. Cover's theorem states that such a multidimensional space may be transformed into a new feature space where the patterns are linearly separable with high probability, provided two conditions are satisfied. First, the transformation is non-linear. Second, the dimensionality of the feature space is high enough. These two operations are embodied in operation 1.

Operation 2 exploits the idea of building an optimal separating hyperplane. The separating hyperplane is now defined as a linear function of vectors drawn from the feature space rather than the original input space.

IV. EXPERIMENTAL RESULTS

The performance of the SVM is influenced by regularization parameter and also the parameters that defines the SVM kernel functions. Analysis was conducted for values of regularization parameter (C) from 10^{-4} to 10^5 and parameters of the kernel functions namely Radial Basis Function (RBF) kernel and Linear Kernel. The SVM was implemented using SVM Torch developed by Vapnik.

In order to improve the performance of the SVM for classification, raw data (stride length and cadence) was normalized using the leg length and age. The polynomial coefficients used for normalization were adopted from [9]. $a_0 = 0.28$ m, $a_1 = 1.31$ m, $SL_N = 1.02$ m, $b_0 = 174.07$ steps/min, $b_1 = -7.04$ steps/min.yr, $b_2 = 0.22$ steps/min.yr² and $CAD_N = 136.84$ steps/min.

Table 1. Overall Accuracy, Sensitivity and Specificity of SVM classifier for various kernel functions.

Kernel type	Performance measure	Stride length and Cadence (Raw)	Stride length and Cadence (Normalized)
RBF	Accuracy	60	100
	Sensitivity	20	100
	Specificity	100	100
Linear	Accuracy	80	100
	Sensitivity	80	100
	Specificity	100	100

V. DISCUSSION

The present paper is aimed 1) to know whether SVM can be used as a machine classifier to distinguish the CP data from that of normal children using the SVM Torch developed by Vapnik; 2) the effectiveness of the polynomial normalization proposed by O'Malley et al. [10] was also tested to know whether the performance of the SVM improves with the normalization of the raw data. Results of this analysis suggest that SVM is capable of classifying the children with CP with significantly high accuracy rate (nearly 100%).

REFERENCES

- [1] Saud Al-Obaidi, James C. Wall, Alia Al-Yaqoub and Muneera Al-Ghanim, "Basic gait parameters: A comparison of reference data for normal subjects 20 to 29 years of age from Kuwait and Scandinavia," *Journal of Rehabilitation Research and Development*, Vol. 40, No. 4, pp. 361-366, July/August 2003
- [2] T. F. Winters, J. G. Gage, and R. Hicks, "Gait patterns in spastic hemiplegia in children and young adults," *J. Joint Bone Surg.*, vol. 69A, pp. 437-441, 1987.
- [3] M. M. Hoffer, E. Feiwell, R. Perry, R. J. Perry, and C. Bonnett, "Functional ambulation in patients with myelomeningocele," *J. Bone Joint Surg.*, vol. 55, pp. 137-148, 1973.
- [4] H. G. Watts, "Gait laboratory analysis for preoperative decision making in spastic cerebral palsy. Is it all it's cracked up to be?," *J. Paediatr Orthop.*, vol. 14, pp. 703-704, 1994.
- [5] J. G. Gage, "The role of gait analysis in the treatment of cerebral palsy," *J. Paediatr. Orthop.*, vol. 14, pp. 701-702, 1994.
- [6] V. N. Vapnik, *The Nature of Statistical Learning Theory*. New York: Springer, 1995.
- [7] R. K. Begg, M. Palaniswami, and B. Owen, "Support vector machines for automated gait classification," *IEEE Trans. Biomed. Eng.*, vol. 52, no. 5, pp. 828-838, May 2005.
- [8] G. Valentini, "Gene expression data analysis of human lymphoma using support vector machines and output coding ensembles," *Artif. Intell. Med.*, vol. 26, no. 3, pp. 281-304, 2002.
- [9] M. J. O'Malley, M. F. Abel, D. L. Damiano, and C. L. Vaughan, "Fuzzy clustering of children with cerebral palsy based on temporal-distance gait parameters," *IEEE Trans. Rehab. Eng.*, vol. 5, no. 4, pp. 300-309, Dec. 1997.
- [10] M. J. O'Malley, "Normalization of temporal-distance parameters in paediatric gait," *J. Biomech.*, vol. 29, no. 5, pp. 619-625, 1996.
- [11] V. T. Inman, H. J. Ralston, and F. Todd, *Human Walking*. Baltimore, MD: Williams & Wilkins, 1981.
- [12] D. L. Damiano and M. F. Abel, "Relationship of gait analysis to gross motor function in cerebral palsy," *Develop. Med. Child Neurol.*, vol. 38, pp. 389-396, 1996.
- [13] D. H. Sutherland, R. A. Olshen, E. N. Biden, and M. P. Wyatt, *The Development of Mature Walking*, Mac Keith Press, 1988.
- [14] R. D. Stevenson, R. P. Hayes, L. V. Cater, and J. A. Blackman, "Clinical correlates of linear growth in children with cerebral palsy," *Develop. Med. Child Neurol.*, vol. 36, pp. 135-142, 1994.
- [15] K. Chan, T. W. Lee, P. A. Sample, M. H. Goldbaum, R. N. Weinreb, and T. J. Sejnowski, "Comparison of machine learning and traditional classifiers in glaucoma diagnosis," *IEEE Trans. Biomed. Eng.*, vol. 49, no. 9, pp. 963-974, Sep. 2002.
- [16] C. C. Pang, A. R. Upton, G. Shine, and M. V. Kamath, "A comparison of algorithms for detection of spikes in the electroencephalogram," *IEEE Trans. Biomed. Eng.*, vol. 50, no. 4, pp. 521-526, Apr. 2003.
- [17] S. Haykin, *Neural Networks - A Comprehensive Foundation*: Prentice-Hall, 1999.

Single Channel Computerized ECG Recorder and Extraction of Relevant Parameters from the ECG-A DSP Based Approach

Monisha Chakraborty¹, Bipan Tudu², and Debashis Das³

¹School of Bio-Science & Engineering,
Jadavpur University, Kolkata, India, email: monishack@school.jdpu.ac.in

²Instrumentation and Electronics Engineering,
Jadavpur University, Kolkata, India, email: bt@ice.ju.ac.in

³Biomedical Engineering,
Jadavpur University, Kolkata, India, email: das_debashis123@rediffmail.com

Abstract— In the present work, attempt has been made to develop a single channel computerized Electrocardiogram (ECG) recorder for the extraction of the relevant parameters of the ECG signal using Digital Signal Processing (DSP) based peak detection algorithms. The relevant parameters identified are P, Q, R, S and T peaks. From the corresponding sample number of those peaks the durations PR, QRS, ST, PT, TT, PQ, QT, RR intervals and heart rate are determined to get the details of the ECG.

In this analysis, tachogram is also obtained and from the tachogram the power spectral components in the low frequency range (0.03Hz to 0.15 Hz) and high frequency range (0.18 Hz to 0.4 Hz) are extracted for the determination of the frequency domain heart rate variability parameter, the well known low to high frequency power (LF/HF) ratio to get an estimation of the cardiac autonomic function. The data acquisition and the entire signal processing are done on MATLAB® platform. To carry out this study, electrocardiographic signals of 25 cases have been considered. This technique gives the details of ECG signal for fast interpretation.

Key words— Digital Signal Processing (DSP), Electrocardiogram (ECG), Low to high frequency power (LF/HF) ratio, Single channel computerized Electrocardiogram (ECG) recorder, Tachogram.

I. INTRODUCTION

ELECTROCARDIOGRAM (ECG) is a graphic recording of the time-variant voltages produced by the myocardium during the cardiac cycle. Fig. 1 below shows the waveform of the normal electrocardiogram [1].

The relevant parameters of the Electrocardiogram, P, QRS and T waves reflect the rhythmical electrical depolarization and repolarization of the myocardium

associated with the contractions of the atria and ventricles. The shape and duration of each feature of the ECG are significant diagnostic parameters. The normal values for amplitudes and durations of important ECG parameters are available in literature [2].

Heart rate is another important diagnostic parameter. The normal value of heart rate lies in the range of 60 to 100 beats per minute. A slower than this rate is called bradycardia and a rate higher than this is known as tachycardia [2].

The uneven space between the cycles indicates an arrhythmia. If the PR interval is greater than 0.2 sec, it indicates blockage of the AV node. If one or more features of the ECG are missing, a heart block of some sort might be indicated [2].

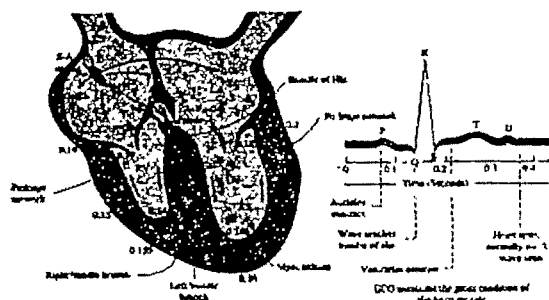


Fig. 1: Electro-conduction system of the heart and resulting ECG waveform

Analysis of both the spacing of the deflections and the morphology can diagnose malfunctions of specific parts of the heart and some diseases. The ECG pattern under the normal

condition of the human heart shows a periodic nature with R waves occurring at regular intervals of time.

Real time detection of QRS complexes is an important task in analysis of ECG signals. Problems which plague QRS detection include baseline shift, power line interference, muscle noise and other artifacts. The literature [3] reported several different methods to perform this task. A more detailed overview of current techniques and comparisons of them are reported in the literature [4]. The most common techniques are thresholding, transformations and morphological approaches.

Heart Rate Variability (HRV) is a cardiac measure that can be derived from the ECG. It is studied for the estimation of the cardiac autonomic function. HRV seems to be a marker of both dynamic and cumulative load. As a dynamic marker of load, HRV appears to be sensitive and responsive to acute stress. Under laboratory conditions, mental load-including complex decisions and public speech tasks have been shown to lower HRV. As a marker of cumulative wear and tear, HRV has also been shown to decline with the aging process. Although resting heart rate does not change significantly with advancing age, there is a decline in HRV, which has been attributed to a decrease in efferent vagal tone and reduced beta-adrenergic responsiveness. Regular physical activity has been shown to raise HRV, presumably by increasing vagal tone.

Reduced HRV has thus been used as a marker of reduced vagal activity. However, because HRV is a cardiac measure derived from the ECG, it is not possible to distinguish reduced central vagal activity from reduced peripheral activity [5].

Heart rate variability represents one of the most promising markers. The apparently easy derivation of this measure has popularized its use. As many commercial devices now provide automated measurement of HRV, the cardiologist has been provided with a seemingly simple tool for both research and clinical studies [6].

Non-linear properties of the R-R interval sequence have also attracted significant attention and are being studied by several different groups of specialists who have the possibility of combining the input from advanced mathematical theories and data from physiologic and clinical studies [7]-[8].

Clinical relevance of heart rate variability was first appreciated in 1965 when Hon and Lee [9] noted that fetal distress was preceded by alterations in inter-beat intervals before any appreciable change occurred in the heart rate itself. Sayers and others focused attention on the existence of physiological rhythms imbedded in the beat-to-beat heart rate signal [10]-[13].

During the 1970s, a number of simple bedside tests of short-term RR differences were reported to detect autonomic neuropathy in diabetic patients [14]. The association of higher risk of post-infarction mortality with reduced HRV was reported in literature in 1977 [15]. In 1981, power spectral analysis of heart rate fluctuations were reported to quantitatively evaluate beat to beat cardiovascular control [16]. These frequency domain analyses contributed to the understanding of the autonomic background of RR interval fluctuations in the heart rate record [17]-[18]. The clinical importance of HRV became apparent in the late 1980s when it

was confirmed that HRV was a strong and independent predictor of mortality following an acute myocardial infarction [19]-[21]. With the availability of new, digital, high frequency, 24-hours multi-channel electro-cardiographic recorders, HRV has the potential to provide additional valuable insight into physiological and pathological conditions and to enhance risk stratification.

II. EXPERIMENTAL SET-UP

The experimental set-up used in our work included an ECG amplifier interfaced to the PC by means of windows 16-bit sound card. The ECG electrodes were connected to the subject in lead-II configuration. The data acquisition and the entire signal processing were done on MATLAB® platform. The sampling rate was set at 200sps. In this paper, DSP based peak detection algorithms were utilized for the identification of the relevant parameters like P, Q, R, S and T peaks. From the corresponding sample number of those peaks the durations PR, QRS, ST, PT, TT, PQ, QT, RR intervals and heart rate were determined to get the details of the ECG.

In this work, tachogram was also obtained and from the tachogram the power spectral components in the low frequency range (0.03Hz to 0.15 Hz) and high frequency range (0.18 Hz to 0.4 Hz) were extracted for the determination of the frequency domain heart rate variability parameter, the low to high frequency power (LF/HF) ratio. Thus all the parameters obtained from this work would give the details of the ECG for fast interpretation. ECG signal captured through the data acquisition system is shown in Fig. 2.

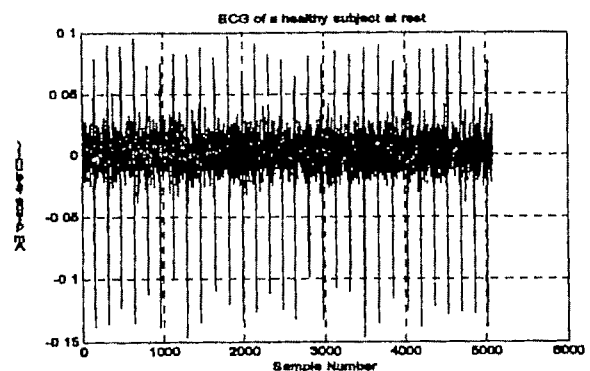


Fig. 2: ECG Signal captured through the data acquisition system

III. DATA ANALYSIS AND RESULTS

We have used DSP based peak detection algorithms for the identification of the relevant ECG parameters. The data acquisition and the entire signal processing were done on MATLAB® platform. The sampling rate was set at 200sps. The compact form of the computational methodology is shown in the Figure 3.

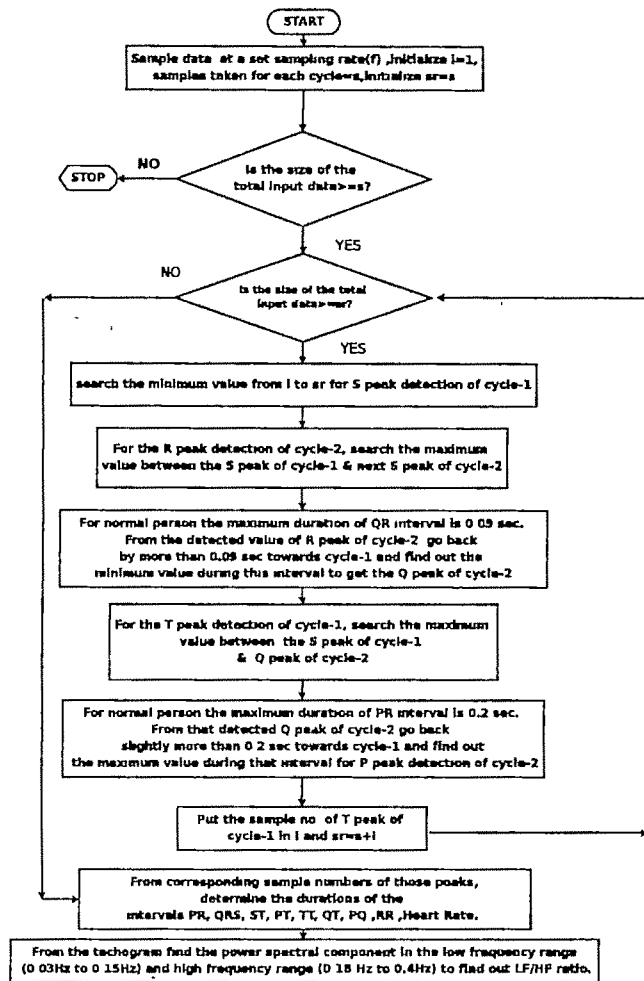


Figure 3: Compact form of the methodology

Using the above technique, the relevant peaks and time durations of ECG signal have been successfully computed. Identified peaks and obtained time durations, are tabulated in Table 1 and 2 respectively as sample results.

Table I: Peaks identified from the recorded ECG for obtaining the time-durations

No. of samples	P-peak (mV)	Q-peak (mV)	R-peak (mV)	S-peak (mV)	T-peak (mV)
1	2.07	1.90	2.85	1.57	2.50
2	2.13	1.92	2.96	1.62	2.54
3	2.15	1.93	2.86	1.57	2.53
4	2.10	1.86	2.90	1.53	2.54
5	2.17	1.90	2.95	1.56	2.55

Table II: Time durations obtained from the recorded ECG

No. of Samples	PR (sec)	QRS (sec)	ST (sec)	PT (sec)	TT (sec)	QT (sec)	PQ (sec)	Heart Rate (Bpm)	LF/HF Ratio
1	0.1150	0.0561	0.2100	0.3589	0.9917	0.2700	0.0860	60.0273	0.21885
2	0.1404	0.0529	0.2216	0.3910	0.9515	0.2742	0.1162	63.1001	0.0695
3	0.1552	0.0564	0.2221	0.4054	0.9184	0.2784	0.1273	65.4843	0.0811
4	0.1500	0.0529	0.2297	0.4066	0.7940	0.2828	0.1233	76.4505	0.0160
5	0.1300	0.0564	0.2235	0.3818	0.9190	0.2798	0.1023	65.6934	0.027

IV. CONCLUSION

The purpose for the identification of the peaks in the present study is to locate the corresponding sample number for finding the intermediate time-durations between the peaks. These time durations as obtained from the present work matches well with the standard results reported in the literature. From the present study RR intervals have been obtained and these are utilized for the determination of the LF/HF ratio which is a well known indicator of HRV which in turn gives an estimation of the cardiac autonomic function. Thus, the present work is an approach for the development of Single Channel Computerized ECG Recorder which can identify and extract the relevant parameters from the ECG signal to give a fast indication about the status of the signal.

REFERENCES

- [1] J. J. Carr, J. M. Brown, *Introduction to Biomedical Equipment Technology*. Fourth Edition, Pearson Education Asia, Chapter-2-Heart and Circulatory System, 2000, pp. 19.
- [2] L. Cromwell, F.J. Weibell, E.A. Pfeiffer, *Biomedical Instrumentation and Measurements*. Second Edition, Prentice Hall of India Private Limited, 1980, ch 6
- [3] J. Darrindton, "Towards real time QRS detection: A fast method using minimal pre-processing," *Biomedical Signal Processing and Control I*, pp. 169-176, 2006.
- [4] B.-U. Köhler, C. Hennig, and R. Orglmeister, "The principles of software QRS detection," *IEEE Eng. Med. Biol.*, 2002.
- [5] I. Kawachi, G.A. Colditz, A. Ascherio, E.B. Rimm, E. Giovannucci, M.J. Stampfer, W.C. Willett, Prospective study of phobic anxiety and risk of coronary heart disease. *Circulation* 1994a, vol. 89: pp. 1992-1997.
- [6] ———, Heart Rate variability: Standards of measurement, physiological interpretation and clinical use, Task Force of the European Society of Cardiology and North American Society of Pacing and Electrophysiology. *European Heart Journal*, vol. 17, pp. 354-381, 1996.
- [7] M.G. Signorini, S. Cerutti, et al., "Non-linear dynamics of cardiovascular variability signals," *Meth Inf Med*, vol. 33, pp.81-84, 1994.
- [8] A. Voss, J. Kurths, H.J. Kleiner, A. Witt, N. Wessel, "Improved analysis of heart rate variability by methods of non-linear dynamics," *Electrocardiol*, vol. 28, pp. 81-88, 1995.
- [9] E.H. Hon, S.T. Lee, "Electronic evaluations of fetal heart rate patterns preceding fetal death, further observations," *Am J Obstet Gynec*, vol. 87, pp. 814-826, 1965
- [10] B. M. Sayers, "Analysis of heart rate variability," *Ergonomics*, vol. 16, pp. 17-32, 1973
- [11] J. Penaz, J. Roukenz, H.J. Van Der Waal, *Spectral analysis of some spontaneous rhythms in the circulation*. In: Dietschel H, Tiedt N, eds Leipzig Biokibernetik, Karl Marx Univ, 1968, pp. 233-41.
- [12] H. Luczak, W.J. Loring, "An analysis of heart rate variability," *Ergonomics*, vol. 16, pp. 85-97, 1973.
- [13] J.A. Hirsh, B. Bishop, "Respiratory sinus arrhythmia in humans, how breathing patterns modulates heart rate," *Am J Physiol*, vol. 241, pp. 620-629, 1981.
- [14] D.J. Ewing, C.N. Martin, R.J. Young, B.F. Clarke, "The value of cardiovascular autonomic function tests: 10 years experience in diabetes," *Diabetic care*, vol. 8, pp. 491-498, 1985.
- [15] M.M. Wolf, G.A. Varigos, D. Hunt, J.G. Sloman, "sinus arrhythmia in acute myocardial infarction," *Med J Australia*, pp. 252-253, 1978
- [16] S. Akselrod, D. Gordon, F.A. Ubel, D. C. Shannon, A.C. Barger, R.J. Cohen, "Power spectral analysis of heart rate fluctuation a quantitative probe of beat to beat cardiovascular," *control science*, vol. 213, pp. 220-222, 1981.
- [17] M. Pomeranz, R.J.B. Macaulay, M.A. Caudil, "Assessment of autonomic function in humans by heart rate spectral analysis," *Am J Physiol*, vol. 248, pp. 151-153, 1985.
- [18] M. Pagani, F. Lombardi, S. Guzzetti et. al., "Power spectral analysis of heart rate and arterial pressure variabilities as a marker of sympatho-vagal interaction I man and conscious dog," *Circ Res*, vol. 59 pp. 178-193, 1986.
- [19] R.E. Kleiger, J.P. Miller, J.T. Bigget, A.J. Mos and Multi-center Post infarction Research Group, "Decreased heart rate variability and its association with increased mortality after acute myocardial infarction," *Am J Cardiol*, vol. 59, pp. 256-262, 1987.
- [20] M. Malik, T. Farrel, T. Cripps, A.J. Camm, "Heart rate variability in relation to prognosis after myocardial infarction: Selection of optimal processing techniques," *Eur Heart J*, vol. 10, pp. 1060-1074, 1989
- [21] J.T. Bigger, J.I. Fleiss, R.C. Stenman, I.M. Rolnitzky, R.F. Kleiger, I.N. Rottman, "Frequency domain measures of heart period variability and mortality after myocardial infarction," *Circulation*, vol. 85, pp. 164-171, 1992

Effect of Stimulus Parameters and Spontaneous Otoacoustic Emissions on Transient Evoked Otoacoustic Emission Measurement for Hearing Screening

Sukesh Kumar A¹ and Jyothiraj V. P²

¹ Dept of Electronics and Communication Engineering, College of Engineering, Trivandrum, Kerala, India
e-mail: sureshkumarcet@yahoo.com.

² Dept. of Electronics and Communication Engineering, College of Engineering, Trivandrum, Kerala, India. e-mail: vpr27@yahoo.com

Abstract—Transient evoked otoacoustic emissions (TEOAEs) are low intensity acoustic signals produced by the movement of outer hair cells on the organ of corti in the cochlea, when the auditory periphery is stimulated by acoustic click or tone burst. The aim of this study is the experimental evaluation of TEOAE responses from neonatal to adult subjects and to find the influence of stimulus parameters, subject characteristics and spontaneous otoacoustic emissions (SOAEs) on TEOAE responses. TEOAE responses are recorded from 43 hearing subjects using OAE measurement setup. SOAEs are also measured immediately after TEOAE recording. Both linear and nonlinear techniques are used for recording TEOAE responses. Digital signal processing techniques are applied for the analysis of TEOAEs in the presence of noise and stimulus artifact and in extracting information from OAE recording. The signal to noise ratio (SNR) of the recorded microphone signal is very low and therefore signal averaging is used for improving SNR. The nonlinear technique is applied to reduce stimulus artifact. TEOAE responses are analyzed under different stimulus parameters and SOAEs. The presence of SOAEs affects both spectra and level of TEOAE responses. Both ear side and gender difference are also affected the TEOAE response. Measuring of TEOAE is noninvasive. By analyzing the properties of TEOAE responses it is possible to find subjects suffering from noise induced hearing loss, to estimate the influence of ototoxic drugs to hearing and hearing screening.

Key words—Hearing screening, SOAE, Stimulus, TEOAE.

I. INTRODUCTION

IN 1978, Dr. David Kemp demonstrated that a healthy cochlea generated very low levels of acoustic emissions during the normal hearing process; such emissions are referred to as the otoacoustic emissions (OAEs) [1] and acts like active positive

feedback signals within a healthy inner ear. Outer hair cells (OHCs) of the organ of corti in the cochlea are thought to be the active source in the generation of this energy. The generated signal propagates through middle ear and into ear canal, where they can be measured with sensitive microphone placed in the outer ear canal. One of the most attractive features of OAE's is their tight relation to the cochlear status: OAEs are universally present to various degrees in all healthy cochlea, where as they are not generally observed or are greatly reduced in ears with mild hearing losses. This aspect together with the extreme facility to perform the test and the high reproducibility had made the OAEs an increasingly widespread application in diagnosis of hearing impairments.

OAEs are classified according to the type of acoustic stimulation to induce them. SOAEs are narrow band and low level signals which are produced without acoustic stimulation and appears in about 30 to 70% of normal hearing ears [2]. Fig. 1. shows the typical SOAE waveform recorded from normal hearing human ear. The spectrum of SOAE shows typically one or more pure tone like signals, at frequencies which are reported to be very stable over the time while their amplitudes may change. SOAEs are generally not observed in frequency regions with sensorineural hearing loss exceeding 30 dB. Majority of SOAEs from adult ears fall within the frequency region 1 KHz to 2 KHz with mean amplitude -3 to 0 dB SPL, which probably reflects the contribution of middle ear resonance characteristics. Multiple SOAEs from a single ear are common, and female subjects are more likely to have multiple SOAEs than male subjects. Distortion product OAEs (DPOAEs) are produced by simultaneous stimulation with two primary tones at frequencies f_1 and f_2 ($f_2 > f_1$) and most prominent distortion product is cubic difference tone at $2f_1 - f_2$ with the frequency ratio f_2/f_1 which is chosen to be 1.22 [3]. TEOAE responses are generated by movement of outer hair

cells on the organ corti, when the auditory periphery is stimulated by acoustic click or tone burst. TEOAEs are present in 100% of normal hearing subjects, but are usually absent or reduced in ears with mild hearing loss [4].

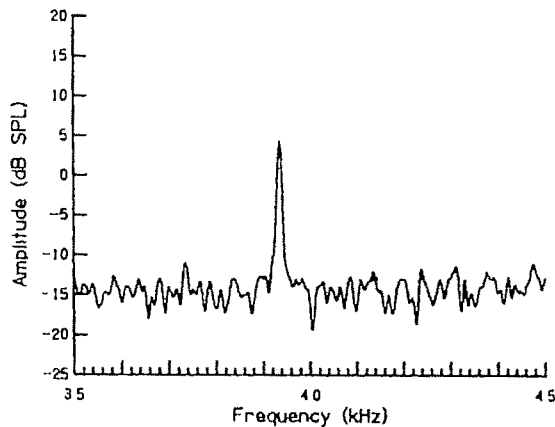


Fig. 1 Example of SOAE recorded from normal hearing human ear.

The primary value of TEOAE is that their presence indicates the preneural cochlear receptor mechanism responds sound in normal way. Various studies confirm the fact that TEOAEs are generated only in subjects with hearing level (HL) better than 20-40 dBHL [5]. The TEOAE is separated from the stimulus artifact by the time delay due to different travelling time for the direct coupled stimulus compared to the travelling time for the stimulus to reach into the cochlea and for the responding emissions to reach the microphone. The stimulus used are either impulse (duration 80 μ s), considered as broad band stimulus (click evoked OAE) or short tone bursts which are considered as narrow band stimuli. Broad band stimuli activate a large part of the basilar membrane and that the OAE response reflects outer hair cell activity from all activated parts of the basilar membrane simultaneously [6]. Frequency analysis of the response is assumed to give selective information about the functions of the outer hair cells (OHC) at different parts of the basilar membrane [7]. Narrow band stimulus activates more selective parts of the cochlea. TEOAE typically exhibit a non stationary, frequency dependent behaviour in which high frequency components occur at short latencies where as low frequency components occur at longer latencies [8]. Time frequency analysis has recently been considered for analyzing the non stationary, frequency dependent behaviour of TEOAE signals employing techniques such as Wigner-Ville distribution or wavelet transform. The aim of this study is the experimental evaluation of TEOAE responses from neonatal to adult subjects (both normal and hearing impaired) and to find the effect of stimulus parameters and SOAEs on TEOAE measurement for diagnosis of hearing impairment and hearing screening. This work is an extension of authors earlier work [9].

II. MATERIALS AND METHODS

A. TEOAE Measurement System

The schematic of computer based TEOAE measurement system is shown in Fig. 2. which includes a computer, DSP

system and a probe. The TEOAEs are collected by a probe that is sealed in the ear canal. The probe consists of a miniature microphone and a speaker. The speaker is used to present acoustic stimulus to elicit TEOAEs. The digital signal processing system in the instrument generates a series of clicks through a digital to analog converter (DAC). These tones are presented to ear via speaker tube located in the probe. A microphone in the probe measures the sound in the ear canal and transmits the conditioned signal to analog to digital converter (ADC) [10].

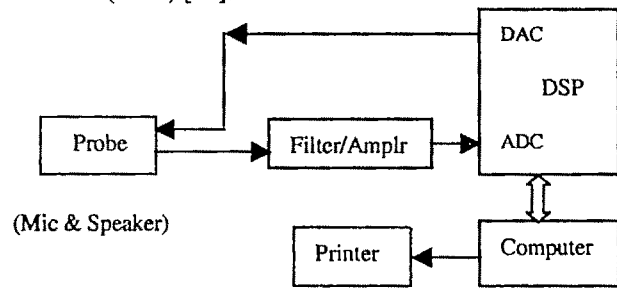


Fig. 2. Schematic of computer based TEOAE measurement system.

The digital signal processing system uses FFT to filter the signal into narrow frequency bands and detect any emission present. The level of these emissions can be compared with the level of noise. The sound pressure level (SPL), frequency of the test tones and the averaging time used to process the signals can be determined by the tester through the adjustable setting maintained in memory within the OAE instrument. The click stimulus is constituted by an electrical pulse with 80 μ s duration which is fed to the speaker. The stimulus is presented at a rate of 50 Hz, leaving a 20 ms recording time between each stimulus time.

B. TEOAE Response Acquisition and Analysis

A total of 43 (26 normal and 17 hearing impaired) TEOAE responses are recorded and analyzed using the methods proposed by Kemp [5, 11]. In non linear measurement technique uses four stimuli consisting of three identical clicks and a fourth click of opposite polarity and three times the amplitude of each of the preceding click. The four responses are summed to subtract the linear components and produce non linear components of OAE response, which is shown in Fig. 3.

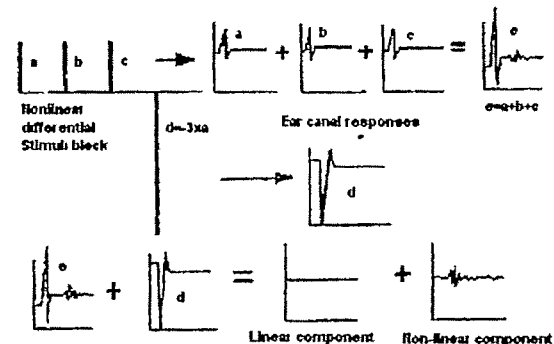


Fig. 3. Illustration of the non-linear stimulus method.

The advantage of this non linear measurement technique is that it completely eliminates any component of the transient response that is not associated with non linear mechanical process within the cochlea. However, in the process of cancelling, the linear response part of the cochlear response is also eliminated. The linear measurement technique used four identical clicks of the same polarity and amplitude. Using the linear stimulus mode, linear and non linear components elicited from the cochlea are recorded. In the present study, both linear and non linear methods are applied consecutively for each of different click intensities from 40-80 dB SPL. TEOAE recording window is selected from 2.5ms to 20 ms with four time windows (2.5-5ms, 5-10ms, 10-15ms, 15-20ms) are evaluated. Repeated stimulation and averaging are used to improve the SNR. The time-frequency representations are used to analyze the relationship between frequency components and latencies [12]. SOAEs are recorded immediately after TEOAE recording without probe removal and stimulus.

III. RESULTS AND DISCUSSIONS

The analysis of TEOAE have provided with many opportunities to explore details of auditory function. They have contributed to tremendous advances in the understanding of how normal and disordered systems function. Details of the TEOAE response characteristics from neonatal to adult (both normal and hearing impaired) subjects are collected and compared with ear dynamic characteristics. The proposed nonlinear stimulus mode effectively reduces the influence of stimulus artifacts; however, for higher click intensities, total elimination of artifact could not proved. Fig. 4. gives the TEOAE/Stimulus characteristics for different time windows of linear and nonlinear TEOAE modes. The wave shapes of both linear and nonlinear TEOAEs and corresponding characteristics showed a high inter subject variability. For time window $\geq 10-15$ ms, there is no significant difference between two modes as shown in Fig. 4(b). For shorter time windows (2.5-5ms, 5-10ms), there is a clear reduction in TEOAE amplitude as shown in Fig. 4(a).

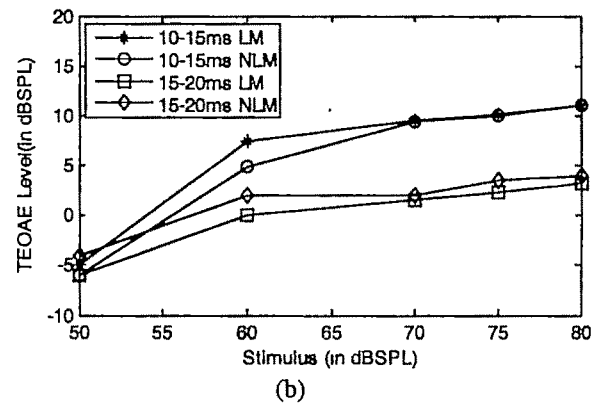
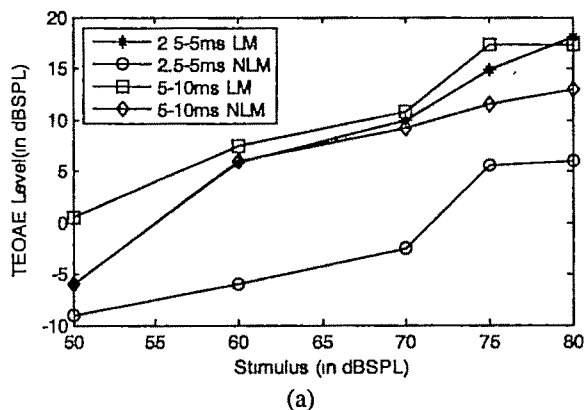


Fig. 4. TEOAE-Stimulus Characteristics for different time windows of linear mode(LM) and nonlinear mode(NLM) (a) 2.5-5ms and 5-10ms windows (b) 10-15ms and 15-20ms windows.

From the analysis of TEOAE data from neonatal to adult subjects, it is found that TEOAE level of newborns are considerably larger than those obtained in normal adults as shown in Fig. 5(a). If subjects have sensorineural hearing loss, TEOAE responses are present at the higher level of stimulus, but not at the lower level as shown in Fig. 5(b). In normal hearing subjects, amplitude of TEOAE response decreases with an increase of age.

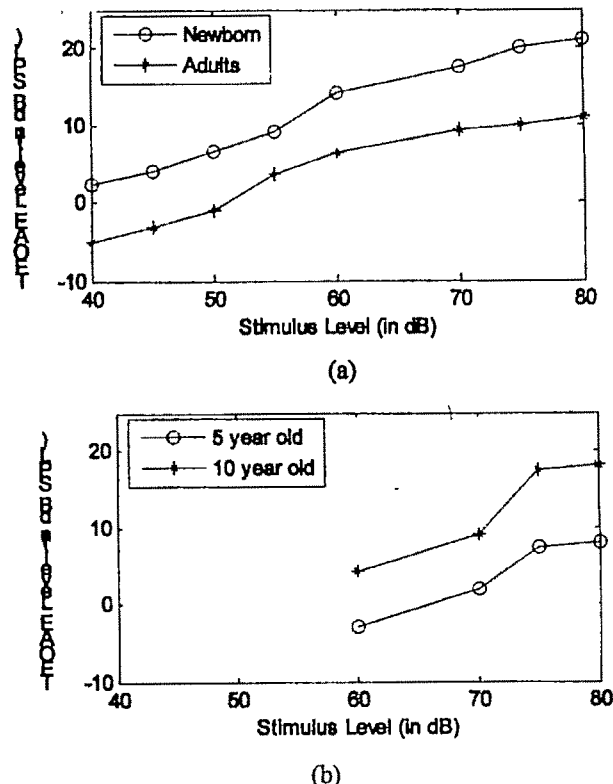


Fig. 5. TEOAE input output function of (a) Normal newborns and adults(b) Children with sensorineural hearing loss: 10 yr old boy at 1 KHz and 5 yr old girl at 500Hz- (both having 40 dB hearing loss).

In neonates the presence of SOAE is often clearly evident in the TEOAE. TEOAE in neonates are about 8 dB higher in level than adults and their frequency spectra skewed toward higher frequencies. If an SOAE can be recorded from the ear, the TEOAE obtained from that ear is likely to be more robust than from an ear without SOAE. The prevalence of SOAE may be correlated with the finding that TEOAEs recorded from the children and adults are larger in woman than in men as shown in Fig. 6. and are larger in the right ear than in left ear.

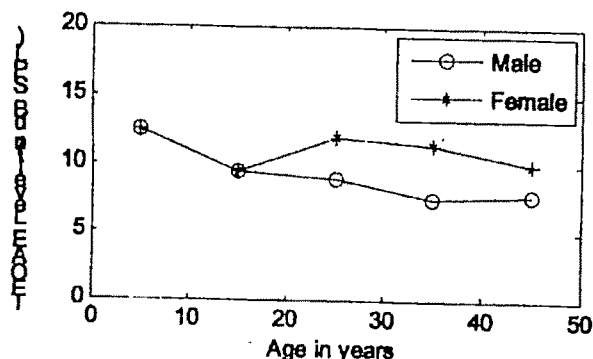


Fig. 6. Average TEOAE response level in hearing subjects grouped by age and gender.

Fig. 7. demonstrates the variation of TEOAE latency with respect to stimulus frequency for different stimulus intensities (1) with 70dB and (2) with 80 dB stimulus. In normal hearing ears the latency of TEOAEs depend on frequency and intensity of the stimulus. In the time frequency analysis, TEOAE exhibited non stationary frequency dependent behavior, in which higher frequency components occur at short latencies where as low frequency components occur at longer latencies and latency decreases with increase of stimulus intensity level.

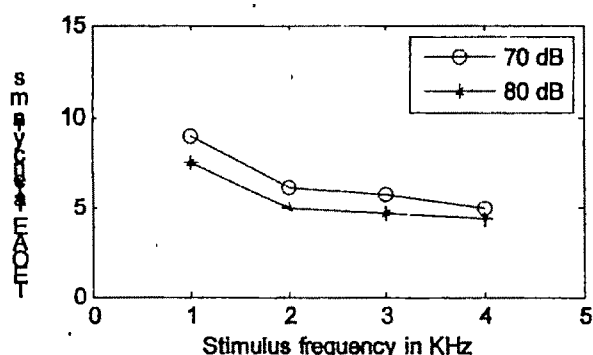


Fig. 7. TEOAE latency with respect to stimulus frequency for different stimulus intensities

The outcome of the study that have designed to determine the cutoff levels of hearing that can be identified with TEOAEs are shown in Fig *8.

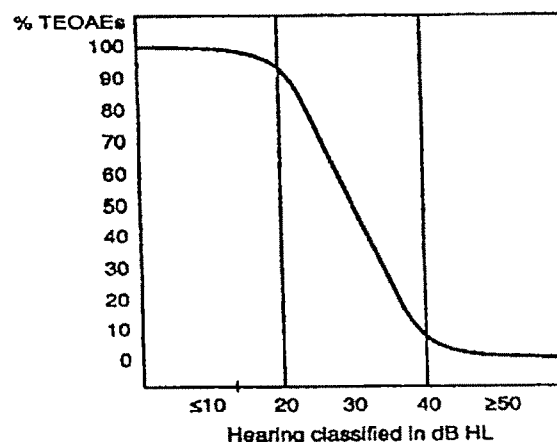


Fig. 8. Schematic representation of average pure tone results associated with percentage of TEOAEs present.

When all hearing levels from 0.2 to 6KHz are better than 20dBHL, TEOAEs are present 99% of ears. When all hearing levels from 0.2 to 6 KHz are poorer than 40dBHL, TEOAEs are absent in 100% of ear with peripheral hearing loss. TEOAEs are highly reproducible. The temporal and spectral properties of TEOAE are unique for each subject. The percentage of reproducibility is a good measure for differentiating normal from impaired ears. The above data provide the basis for using TEOAEs in the identification of hearing loss in screening programs. For such purposes, an overall parameter, such as percentage of reproducibility, response level, or a combination of measures, are calculated from the TEOAE and used to determine the presence or absence of hearing loss.

IV. CONCLUSION

The measurement of cochlear function TEOAEs have proven to have high sensitivity and reasonable specificity for hearing impairment diagnosis, especially when used for infant screening. Hearing level and middle ear mobility are the controlling factors affecting TEOAE status. It is a potential tool to predict the hearing problems. If those are detected at earlier period, the patient can be saved from impairment.

ACKNOWLEDGMENT

The authors are grateful to the Director, Kerala ENT Research Foundation (KERF), Kollam, Kerala and the Director, National Institute of Speech and Hearing (NISH), Trivandrum, Kerala for being provided the facility to carry out the above work.

REFERENCES

- [1] D. T Kemp, *Otoacoustic emissions in perspective*, Thieme Medical publishers, New York, 1978, pp 1-20
- [2] M. J. Penner, L. Glotzbach, and T Huang, "Spontaneous otoacoustic emissions. Measurement and data," *Hearing Research*, 68, pp. 229-237, 1993

- [3] F. P. Harris, Lonsbury, and B. L. Maertlin., "Acoustic distortion product in human systematic changes in amplitude as a function f2/f1 ratio," *Journal of Acoustic Society of America*, 85, 1989, pp 280-286.
- [4] D. T. Kemp, "Otoacoustic emissions, travelling wave cochlear mechanism", *Hearing Research*, 22, pp. 94-104, 1986.
- [5] B. Prier, 1996, "Click and tone-burst evoked otoacoustic emissions in normal and hearing impaired ears", *Journal of Acoustic Society of America*, 99, pp. 3077-3086
- [6] R. Probst, Lonsbury, B. L. Martin, and G. K. Martin, 1991, "A review of otoacoustic emissions", *Journal of Acoustic Society of America*, 89, pp. 2027-2067.
- [7] G. Tognola, F. Grandori, and P. Ravazzani, 1999, "Time-frequency analysis of click-evoked otoacoustic emissions in noise-induced hearing loss", *Proceeding of the first joint BMES/EMBS Conference Serving Humanity, Advancing Technology*, Oct 13-16.
- [8] D. T. Kemp, 1978, "Stimulated acoustic emissions from within the human auditory system", *Journal of Acoustic Society of America*, 64, no 5, pp. 1386-1391
- [9] V. P. Jyothiraj, and A. Suresh Kumar, "Detection and analysis of otoacoustic emissions for diagnosis of hearing disorders," presented at the 2004 16th Kerala science congress, Kozhikode, Kerala.
- [10] Minghui Du, F. H. Y. Chan, F. K. Lam, and Jun Ren, 1998, "Design consideration of a multi-function otoacoustic emission measurement system", *Proceedings of the 20th Annual International Conference of the IEEE Engineering in Medicine and Biology Society*, 20, no. 4, pp 1928-1931.
- [11] M. Whitehead, B. Stagner, and G. Martin, 19, "Measurement of otoacoustic emissions for hearing assessment," *IEEE Eng. Med. Biol.*, 13, pp. 213-224.
- [12] Zhengguo Zhang, "Time frequency analysis of TEOAE signals," *Proceedings of the 20th Annual International Conference of the IEEE Engineering in Medicine and Biology Society*, 20, no. 3, 1998, pp. 1520-1522.

Stochastic Model of Hematopoiesis

Probir Kumar Dhar^{1,3}, Abhik Mukherjee², Durjoy Majumder³

¹Department of ECE, BCET, Durgapur, West Bengal, India

²Department of CST, BESU, West Bengal, India

³Bioinformatics, PD School of Information Technology, BESU, West Bengal, India,
e-mail: durjoy@pdsit.becdu.ac.in, majumder103@yahoo.co.in,

Abstract - Hematopoiesis is a complex process by which all the blood cells of the peripheral blood are formed. With the advent of the molecular techniques, it has been shown that different biomolecules are activated in a coordinated and time dependent fashion for the development of different blood cells of specific lineage. Overall the proof has been done with the linear and isolated system. In recent times much emphasis is given to the quantification of system parameters. For understanding the dynamical process of any biological system it is important. But due to instrumental limitations this becomes a difficult task. It has been shown that minor variation in the initial parametric value in the systems equation may cause a large deviation of the system output in the long run. This implies that the biological phenomenon is complex. Hence, translation to those molecular events to the clinical scenario seems impossible. Moreover, no generalized model is available in the literature, by which clinicians and patients can be benefited. Even the prediction from the dynamics at the morphological stages is not available. We have developed a systems model based on discrete equation and incorporated a stochastic component to it. Our model shows that minor variation as well as incorporation of a minor stochastic component to that model equation may exhibit different hematological diseases. Incorporation of the controllability criterion has an advantage in the assessment of different therapeutic outcome. This mathematical model reinforces the necessity of expert domain knowledge in translating the parametric value so that individual patient could be benefited. And we hope that this model will provide the necessary help to the hematologists in the assessment of different therapeutic options.

Key words: Hematopoiesis, stochastic model, leukemia

I. INTRODUCTION

Hematopoiesis is a complex process of blood cells development. Different biomolecules viz., cytokines, cell signaling molecules and transcription factors synergistically act to control different cell(s) viz., erythrocytes (RBC), leukocytes (WBC) and thrombocytes (platelets) development of the hematopoietic system [1]. Any alteration of these molecules may lead to development of hematological diseases (HD). As phenotypes of differentiated lineages reflect the sets of genes expressed therein as well as the receiving signals by the cytokines, therefore the black box modeling could have an implication in the understanding of hematopoietic dynamics [2]. Under normal condition, the cytokine erythropoietin (EPO) regulates the erythrocyte production by increasing the production of primitive erythroid precursors and finally an increase in the numbers of circulating erythrocytes that takes place some days later [3-4]. In the production of white blood

cells, granulocyte colony stimulating factor (G-CSF) has been demonstrated to be very important [5]. Thrombopoietin (TPO) regulates platelet production, by controlling the production and maturation of megakaryocytes. These are platelet precursor cells that give rise to 1000 – 5000 platelets each [6-8].

Previously several mathematical models of hematopoiesis have been proposed. Different authors substantially identified different controlling variables whose alteration leads to the manifestation of HD. It has been shown that oscillations and delay in the stem cell compartment are important and drive several periodic HD [9-11] such as cyclical neutropenia (CN), periodic chronic myelogenous leukemia (PCML), cyclical thrombocytopenia, and periodic hemolytic anemia. CN and PCML are of special interest as oscillations in all three cell lines occur with the same oscillation period [12]. Using G0 stem cell model it was possible to explore the oscillations at the neutrophil level but not at the platelet level. Using integrated mathematical model it was possible to duplicate various features of CN. These have been addressed in the unified model of PCML and could be fitted well with the insertion of maturation delay time rather than only in the proliferation phase of a single discrete cell line [13-14]. Based on the simulations, authors substantially argued that the critical model parameters include amplification rate in the leukocyte line, differentiation rate from the stem cell compartment into the leukocytic line and rate of apoptosis in the stem cell compartment. By using differential delay equation it has been shown that oscillation in CN is due to the slow periodic oscillations in the stem cell level [15]. With a decoupled model of stem cell, addition of stochastic perturbation with noise term(s) at the differentiation/multiplication or apoptosis rate of stem cell level, it was also possible to introduce fluctuations in the cell number [16].

A four compartmental mathematical model has been developed by Michor *et.al.* to understand the treatment dynamics of chronic myeloid leukemia [17]. RQ-PCR based data (of BCR-ABL) points has been fitted to the mathematical model for the evaluation of developing imatinib resistance mutation. In this approach quantitative evaluations as well as numerical estimates of the turn-over rates of leukemic progenitors and differentiated cells are possible. Authors also concluded that the treatment failure is due to harbouring of resistance mutations increase with disease progression as a consequence of increased stem cell burden and multiple drug therapy is suggested to be especially important for the patients who were diagnosed with advanced and rapidly growing disease.

However the models developed earlier are based on data that are difficult to get and its translation into clinical scenario is practically impossible. In recent times, different biological parametric estimation procedures including the RQ-PCR have been criticized by a section of the scientific community [18]. Firstly the limitation is at the instrument level, as majority of the instruments have the reliability of data within 15% of coefficient of variation (CV) [19]. Secondly, there is a large variation of a particular parameter even at the smaller population level and a very small perturbation at the initial factor may produce a large drift during a given time course [20]. Therefore, for prediction of a therapeutic outcome of a treatment strategy, it may not be possible to apply the population level data to the individual cases and hence, it requires a model which can translate the data into a cost-effective and easy to handle model.

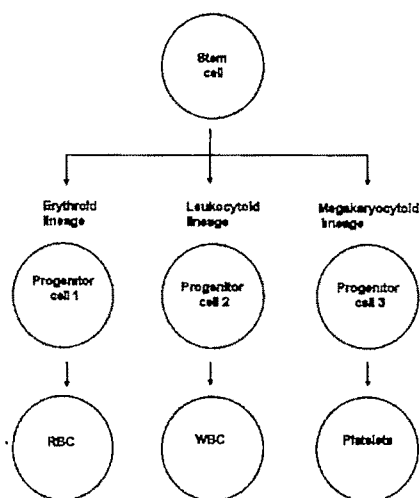


Fig 1. Schematic representation of hematopoiesis.

II. PROPOSED SYSTEM MODEL

A. Hematopoiesis model formulation

Like others we have also assumed the unified model of hematopoiesis and examine the same model by adding a stochastic component to its different parametric variables. The model has been schematically presented in Fig 1. In the model it is assumed that stem cell(s) is/are differentiated into the precursor cells of three lineages namely, erythroid (p1), leukocytoid (p2) and megakaryocytoid (p3) lines. Precursor cells of each lineage then differentiated into the corresponding mature cells – RBC (b1), WBC (b2) and platelets (b3). For simplification of the model, all sorts of precursor cells of each of the lineage are being considered as only progenitor/precursor cells. Thus this sort of model is a unidirectional model as described by others [13-14, 17] and thus, stem cells are being coupled with the cells of the peripheral blood. However in contrast to the previous models all parametric variables for simulation purposes are taken as the absolute cell numbers per cubic millimeter, the unit used in the conventional Neubauer hemocytometre chamber or by the cell counter. We also considered the whole leukocytic lineages

instead of only neutrophil lineage [14, 17]. The parameters which are being considered in the model have been shown in Table 1.

B. System equation

The dynamical equation of the model is based on the difference equation. The system of equations is being iterated for 750 days. Hence the system equation of cells of any maturation stage (compartmentalization) can be written as:

$$N(t) = (N(t-1) + r(t-1) \times N(t-1)) - (a(t-1) \times N(t-1)) \quad (1)$$

$$N(t) = (N(t-1) + r(t-1) \times N(t-1) + dr(t-1) \times N(t-1)) - a(t-1) \times N(t-1) \quad (2)$$

Here N stands for number of cells at an instant of time t , which depends on the factors of multiplication rate (r), apoptosis rate (a) and also on the number of differentiated cells from the precursor cells. Both a and r are functions of time. However, for the stem cell compartment the factor of differentiation (dr) is a subtractive term. Equation (1) will be used when there is a time delay in differentiation. In the subsequent cellular stage, maturation of cells will be governed by Equation (1) when the precursor cells are in the process of differentiation and the moment differentiation is completed, it will be governed by Equation (2). Cells at the matured stage will not go through any further process of differentiation.

C. Settings of Variables for the Hematopoiesis

The values have been set taking into consideration the hematopoietic process for a normal individual and are presented in Table 1. The values of cell numbers are presented in terms of absolute cell number per cubic millimeter and multiplication rate (doubling time), differentiation rate, time delay in differentiation, apoptosis rate are all in number of cells per days. For setting of parametric values we have either directly used the data mentioned in the references [6, 11-15, 17] or have made logical transformation of that data. With the setting of these values, the absolute cell number of different progenitor and mature cells in the peripheral blood remain almost static (Fig 2-3). From the study of the hematopoietic dynamics, the absolute number of total progenitors and mature cells could be evaluated at any time point.

III. ANALYTICAL STUDIES OF THE MODEL

A. Identification of the sensitive parameter

It is acknowledged that in different hematological disorders, parametric value changes. To identify the sensitive parameter and the impact of that parameter in the development of hematological disorder in the long run, simulation study would be helpful. Hence it is necessary to identify the influence of each parameter in the dynamics of the hematopoiesis. It is also acknowledged that in several hematological disorders different combinations of parameters may be altered. When diseases are identified there is a large deviation of the parametric mean in the diseased person in comparison to the normal. However, it is not known whether or not the minor variation in the value of different hematological parameters and their persistence within the system would influence the systems behavior even though the values are within the normal population variance.

Table 1. Parameters and value used for initialization in the model. After each parametric symbol r , a , dr and dt stands for multiplication rate, apoptosis rate, differentiation rate and differentiation delay time.

Symbols used	Value used for normalization
Stem cell	
s	14 cells/cu.mm.
sr	0.065 cells/day
sa	0.032 cells/day
sdr	0.033 cells/day
sdt	14 days
Progenitor 1	
$p1$	4×10^2 cells/ cu.mm.
$p1r$	0.013 cells/day
$p1a$	0.01339 cells/day
$p1dr$	$1-(p1r+p1a)$ cells/day
$P1dt$	2 days
Progenitor 2	
$p2$	1×10^2 cells/ cu.mm.
$p2r$	0.0345 cells/day
$p2a$	0.0359 cells/day
$p2dr$	$1-(p2r+p2a)$ cells/day
$P2dt$	7 days
Progenitor 3	
$p3$	1×10^2 cells/ cu.mm.
$p3r$	0.075 cells/day
$p3a$	0.0802 cells/day
$p3dr$	$1-(p3r+p3a)$ cells/day
$P3dt$	3 days
Erythrocytes	
$b1$	5×10^6 cells/ cu.mm.
$b1a$	0.00007747 cells/day
Leukocytes	
$b2$	1×10^4 cells/ cu.mm.
$b2a$	0.012999996 cells/day
Platelets	
$b3$	5×10^5 cells/ cu.mm.
$b3a$	0.00017 cells/day

B. Stochastic variation.

Any sort of biological observation is noisy and has been represented as the mean value with a variance. This is due to three reasons; one, non-homogeneous nature of the biological sample; two, variation due to the detection system; and thirdly, the experimental error. Conventional clinical testing consists of data at a discrete sequence of time but within two consecutive sequences of times the parametric value may have a large deviation from its mean value. The

loss of these data may influence the systems output in the long run. Incorporation of minor stochastic component within standard deviation of the mean value of the parametric variable(s) gives the simulation study a more realistic flavor.

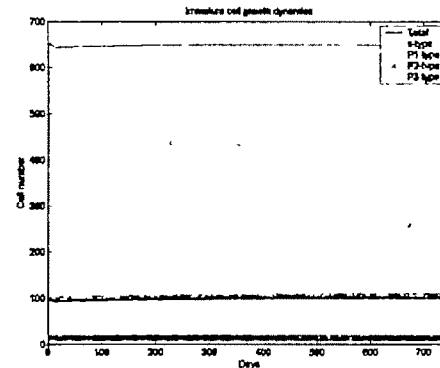


Fig 2. Dynamics of progenitor cells for a normal individual as simulated with the parametric values mentioned in Table 1.

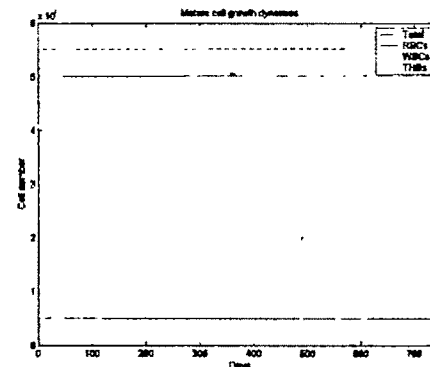


Fig 3. Dynamics of mature cells for a normal individual as simulated with the parametric values mentioned in Table 1.

IV. SYSTEM SIMULATION

A. Identification of the sensitive parameter

The simulation study has been done using MATLAB. To test the systems sensitivity and influence of the parametric variables in the manifestation of different hematological disorders, rigorous simulation exercises have been carried out. The value of the variables has been changed within 10% of the setting values. Simulation results suggest that change in parametric values of peripheral blood compartment have almost no impact on the dynamics of the overall system. On the other hand, minor variations, even within the 10% of the mean value of any parameter in the bone marrow (immature cells) compartment have considerable impact on the overall system dynamics. In this compartment multiplication rate, apoptotic rate, differentiation rate have much influence on the systems dynamics within a shorter time period whereas, differentiation delay has influence for the longer time period. With the increase in the multiplication rate and differentiation rate the system response becomes unbounded in nature, while decrease in the apoptotic rate system shows the same behavior. With the reverse condition, systems may tend to

collapse. However, the absolute cell number of any compartment does not have any influence on the qualitative behavior in the system dynamics though the output has an increased number of cells. Change of value at the progenitors has the influence on that particular lineage. Experimentally stem cells number, multiplication rate, apoptosis rate can be measured but realistically, there is no direct way to measure the differentiation rate of cells particularly for *in vivo*. Number of differentiated cells can be calculated by subtracting the sum of number of apoptotic cells, multiplied cells and the quiescent cells from the total number of cells at any time point. However this approach may disrupt the existing system. To minimize the effect we normalize stem cells differentiation rate (*sdr*) with a calibration factor 0.0365. The number of the quiescent cells number can be absorbed with the multiplication rate, differentiation rate and its delay time.

Table 2. Simulation with the random values of *sr* and *sdr*.

Parameter	Mean	SD
<i>sr</i> (0.001)	0.065	0.001
<i>sdr</i> (0.001)	0.033	3.7404×10^{-5}
<i>sr</i> (0.1)	0.0668	0.1025
<i>sdr</i> (0.1)	0.0329	0.0037

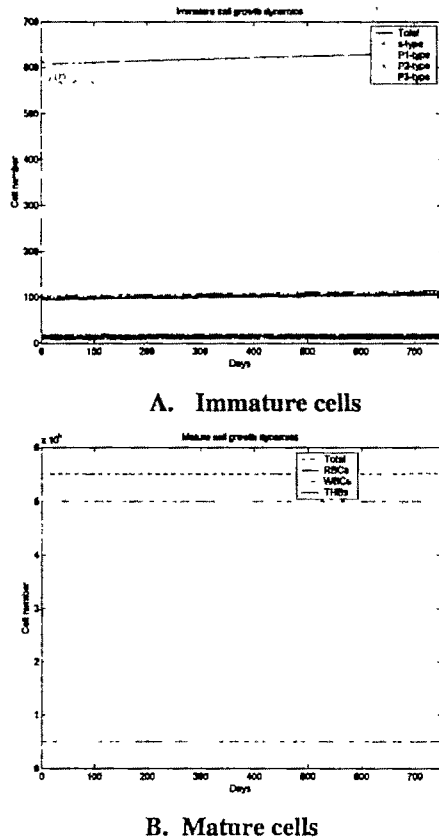


Fig 4. Profile of the dynamics of immature and mature cells with a random value around the mean of value of *sr* = 0.065.

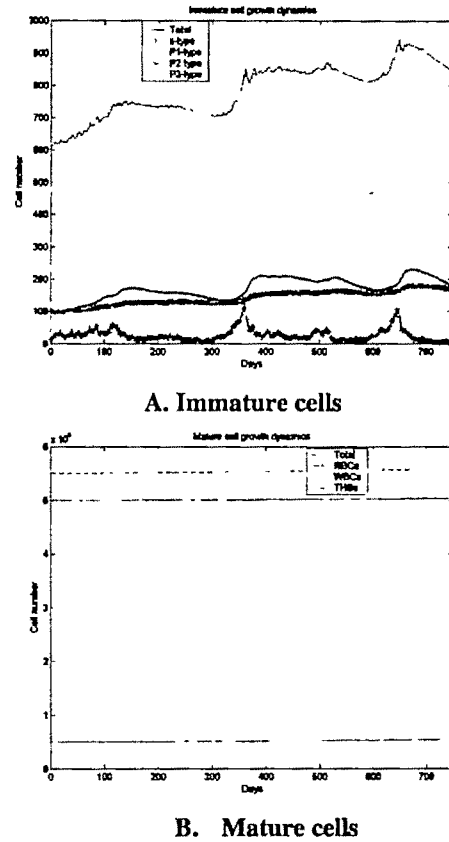


Fig 5 Profile of the dynamics of immature and mature cells with a random value around the mean of value of *sr* = 0.0668.

B. Stochastic perturbation

As depicted in the previous section, change in the parametric value of the peripheral compartment has no qualitative influence in the system dynamics. Hence it is important to study the effect of stochastic perturbation with the parameters of the cells present in the bone marrow compartment. In this study we have only considered the parametric influence of the stem cells. We have studied the system dynamics with a single random value of differentiation rate (*sdr*) at the stem cell level. Simulation study reveals that there is disruption of normal behavior in majority of the cases. Interestingly, with some values (e.g. *sdr*=0.0289), the bone marrow and peripheral blood compartment gets decoupled. With the addition of stochastic component around the mean value of multiplication rate (*sr*) at every time interval (Table 2), a change in the system dynamics is noted. Simulation result shows that with the increase in the standard deviation around the mean value of the multiplication rate (*sr*), there is a more deviation in the system output from the normalized condition within a given interval of time (Fig 4, 5). This is noted particularly in the bone marrow compartment.

V. CONCLUSION

Simulation studies suggest that persistence of one of the parametric values with a minor shift is able to produce pathophysiological shifting in the hematopoietic system. Our

simulation study indicates that occurrence of different hematological disorders may be due to the minor shifting of parametric value particularly at the immature cell stage. In reality, it is not known whether that value may persist for longer interval of time for the manifestation of the disease phenotype. Moreover there is large variation of biological data at the individual level as well as due to instrumental limitation. This may also increase the chance of erroneous prediction about the system dynamics by the conventional way of data collection. Definitely increasing the amount of data collection in a given interval of time can minimize that sort of uncertainty. Together with this, there is a need for the development of instruments having higher sensitivity. However both the approaches may increase the therapeutic cost. Cost can be minimized by observing the data for a shorter period of time and fitting it to the mathematical model with a proper calibration factor to predict the system dynamics.

Our study also indicates the fact that with the available instrumental facility it is very difficult to translate a low level data for prediction at the gross morphological /functionality. Hence this study reinforces the requirements of the expert domain knowledge for the setting of proper calibration factors. In disease cases increment in the subtractive terms or multiplication and /or differentiation terms may produce control. Hence the specific therapeutic drugs which may alter these factors can be tested through this model. Thus, it helps the hematologists to assess any specific mode of therapy after application of that therapy for a shorter interval of time to judge the therapeutic outcome for the long run. Incorporation of controllability and stability criteria would enhance this sort of judgment.

ACKNOWLEDGMENT

All authors are thankful to Bengal Engineering & Science University, Shibpur for supporting this work.

REFERENCES

- [1] S.H. Orkin, "Hematopoiesis. how does it happen?" *Curr. Opin. Cell Biol.*, Vol. 7, pp 870-807, Dec 1995.
- [2] D. Kaplan and L. Glass, "One dimensional differential equations," In: *Understanding Nonlinear Dynamics*, New York-Berlin-London. Springer-Verlag, 1995, pp. 147-207.
- [3] J. Adamson, "The relationship of erythropoietin and non metabolism to red blood cell production in humans," *Semin. Oncol.*, Vol. 21, pp.9-15, 1974.
- [4] M. Silva, D. Grillo, A. Benito, C. Richard, G. Nunez, J. Fernandez, "Erythropoietin can promote erythroid progenitor survival by repressing apoptosis through bcl-1 and bcl-2," *Blood*, Vol. 88, pp 1576-1582, 1996
- [5] T.H. Price, G.S. Chatta, D.C. Dale, "Effect of recombinant granulocyte colony stimulating factor on neutrophil kinetics in normal young and elderly humans," *Blood*, Vol. 88, pp. 335-340, 1996.
- [6] D. J. Kuter, "Megakaryopoiesis and thrombopoiesis (Chapter 110)" In: *Williams Hematology*, 6th ed, E. Beutler, A.M. Lichtman, B.S. Coller, T.J. Kipps, U. Seligsohn, Ed., USA: The McGraw Hill Company, 2001, pp 1339-1356
- [7] M. Ratajczak, J. Ratajczak, W. Marlicz, C. Pletcher, B. Machalinski, J. Moore, H. Huang, A. Gewirtz, "Recombinant human thrombopoietin (TPO) stimulates erythropoiesis by inhibiting erythroid progenitor cell apoptosis," *Br J. Hematol.*, Vol. 98, pp 8-17, 1997
- [8] S. Tanimukai, T. Kimura, H. Sakabe, Y. Ohmizono, T. Kato, H. Miyazaki, H. Yamagishi, Y. Sonoda, "Recombinant human c-Mpl ligand (thrombopoietin) not only acts on megakaryocyte progenitors, but also on erythroid and multipotential progenitors in vivo," *Exp. Hematol.*, Vol. 25, pp 1025-1033, 1997.
- [9] M. Ogawa, "Differentiation and proliferation of hematopoietic stem cells," *Blood*, Vol. 81, pp. 2844-2853, 1993
- [10] I.R. Lemishka, D.H. Raulet, R.C. Mulligan, "Developmental potential and dynamic behavior of hematopoietic stem cells," *Cell*, Vol. 45, pp 917-927, 1986.
- [11] C. Hauwie, M. Mackey, "Modeling complex neutrophil dynamics in grey collie," *J. Theor. Biol.*, Vol. 204, pp. 504-519, 2000.
- [12] P. Fortin, and M.C. Mackey, "Periodic chronic myelogenous leukemia: Spectral analysis of blood cell counts and etiological implications," *Br. J. Haematol.*, Vol. 104, pp 336-345, 1999.
- [13] C. Colijn and M.C. Mackey, "A mathematical model of hematopoiesis--I. Periodic chronic myelogenous leukemia," *J. Theor. Biol.*, Vol. 237, pp 117-132, 2005.
- [14] C. Colijn and M.C. Mackey, "A mathematical model of hematopoiesis. II. Cyclical neutropenia," *J. Theor. Biol.*, Vol. 237, pp. 133-146, 2005.
- [15] C. Colijn, A.C. Fowler, M.C. Mackey, "High frequency spikes in long period blood cell oscillations," *J. Math. Biol.*, Vol. 53, pp. 499-519, 2006.
- [16] J. Le, M.C. Mackey, "Stochastic differential delay equation, moment stability, and application to hematopoietic stem cell regulation system," *SIAM J. Appl. Math.*, Vol. 67, pp. 387-407, 2007.
- [17] F. Michor, T.P. Hughes, Y. Iwasa, S. Branford, N.P. Shah, C.L. Sawyer, M.A. Nowak, "Dynamics of chronic myeloid leukaemia," *Nature*, Vol. 435, pp. 1267-1270, 2005.
- [18] Bustun, S A , and Nolan, T.. 'Pitfalls of quantitative real time reverse transcription polymerase chain reaction'. *J. Biomol. Tech.*, Vol. 15, pp. 155-166, 2004.
- [19] C. Gottinger, B. Mechtold, A. Radbruch "Operation of a flow cytometry," Chapter 1, In: *Flow cytometry and cell sorting*, 2nd Edition, Radbruch A (Ed), Berlin, Heidelberg, New York: Springer Lab Manual, 2000, pp.3-26.
- [20] L.D. Hartle and A.G. Clark, "Random genetic drift," (Chapter 7) In: *Principles of population genetics*, 3rd ed., Sunderland, Massachusetts: Sinauer Associates, 1997, pp. 267-313.

Design and Simulation of Signal Generator for a new Noninvasive RF Heartbeat Detection System

S.Shabu¹, Roshna.R²

¹ College of Engineering, Trivandrum, INDIA e-mail: shabusurendran@hotmail.com

² College of Engineering, Trivandrum, INDIA e-mail: roshnar83@gmail.com

Abstract—Nowadays cardiovascular diseases are one of the leading causes of death and noninvasive measurements for assessing these diseases would be highly valuable. The objective of this work is to design a signal generator that provides 400 mW power to the antenna. The operating frequency is chosen as 1.15GHz.

Key words—Circulator, Directional coupler, RF oscillator.

I. INTRODUCTION

THE term noninvasive implies a medical procedure which will not penetrate or break the skin or a body cavity. Remote measurement of breath and heartbeat is desirable in many situations, such as detection of people and parameters of their movement inside the building in process of law enforcement and antiterrorist operations, at the airports as a remote lie detector, touch less measurement of heartbeat and breathing of patients when a contact sensor for some reasons cannot be used.

The study about wireless detection of breath and heart rate has been started from 1975 and almost all the earlier works is based on Doppler Effect [1], [7] - [10], but found to be less sensitive. The proposed work is based on scattering principle and is more sensitive than the system based on Doppler Effect.

In order for the RF beam to have enough penetration the frequency of the wave found to be in L or S band. For this reason frequency of operation is selected as 1.15 GHz and the power is optimized as 400mw. The system will provide a range of 10 feet.

II. BLOCK DIAGRAM DESCRIPTION

The system consists of

1) *Signal generator*: The signal generator will provide 400mw power to the transmitting antenna and 40mW power to the null balance system.

2) *Transmitter and Receiver section*: This section consists of two separate antennas for transmitting and receiving. Patch antennas can be used for this purpose.

3) *Null Balance System*: The Null balance system is for removing the clutter present in the received signal. It consists of Digital Phase shifter, Digital attenuator, and an interface control. This interface control will produce a signal to cancelling out the clutter present in the received signal, after analyzing it. This signal is used for controlling the power output from the signal generator circuit.

4) *Signal Extractor*: The signal extractor includes a mixer circuit, RF amplifier circuit and a low pass filter to extract the heartbeat signal.

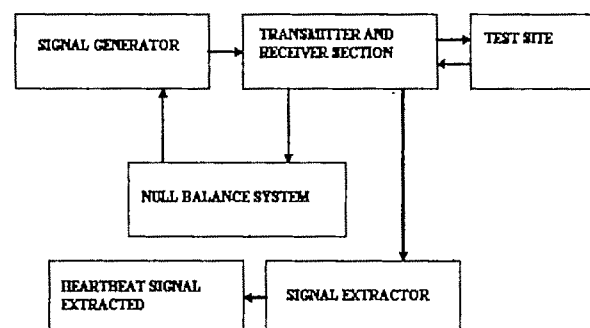


Fig.1

III. THEORETICAL BACKGROUND

The basic principle of the system is to illuminate the human subject with a low intensity RF signal and then the

scattered signal is collected using receiving antenna. Heartbeats or respiration affect the amplitude and phase of the scattering field. So the received signal consists of amplitude and phase modulation of the heart movement to the scattering field. From this heartbeat signal is extracted. All the above phenomena can be explained consistently by combining the Amplitude Modulation (A.M.) and Phase Modulation (P.M.) theory, instead of Doppler Effect or only a simple phase modulation. In physics, Doppler effect denote the apparent variation in frequency of any emitted wave, such as a wave of light or sound, as the source of the wave approaches or moves away, relative to an observer, as well as the wave reflected by a moving object, just like the speed meter shows. Quantificational, for the reflective case, the shift of frequency should be speed-dependent. For the periodical movement, the velocity covers a wide range and the final waveform must occupy a continuous spectrum everybody knows, any periodical function can be decomposed to its base component and high-order harmonics. Heartbeats or respiration affect the amplitude and phase of the scattering field just in this manner. The AM and PM to the scattering electric field can be expressed by the well-known Fourier series as,

$$Es = \left[\sum_{n=0}^{\infty} An \cos(n\Omega t) + \sum_{n=1}^{\infty} Bn \sin(n\Omega t) \right] \cos \left[\omega t + \sum_{n=0}^{\infty} Cn \cos(n\Omega t) + \sum_{n=1}^{\infty} Dn \sin(n\Omega t) \right] \quad (1)$$

Where ω is the frequency of the source and Ω is the frequency of heartbeats.

IV. DESIGN ENVIRONMENT AND CHALLENGES

RF circuits cannot be designed as low frequency devices. These circuits include one or more distributed elements. So the Maxwell Equations cannot be simplified as for the low frequency circuits. At low frequencies, the length of the circuit is generally much smaller than the operating wavelengths. But at RF frequencies, circuits will have considerable electrical length i.e., the physical length of the circuit is comparable to the wavelength of the signals propagating in the circuit. When characterizing a device in the RF frequencies, the various effects to be considered are presence of stray capacitance, stray inductance, Skin effect and radiation. At RF, measurement of currents and voltages in different parts of a circuit are not easy and useful as in low frequencies. So, instead of current and voltage parameters, RF circuits are specified in terms of S parameters, which deal with power flows in and out of ports. Due of these effects, special care is to be taken in RF designs. The design procedure becomes extremely tedious if all these factors are considered. Computer Aided Design packages specially built for RF circuit designs can be a very useful tool for the design. The simulations tools used in this work are Microwave Office

2004 (MWO) and Visual System Simulator 2004 (VSS). These powerful tools are fully integrated in the AWR Design Environment and allow to incorporate circuit designs into system designs without leaving the AWR Design Environment.

IV. SIGNAL GENERATOR CIRCUIT

The signal generator consists of an RF oscillator, a 10 dB directional coupler and a 30 dB circulator.

A. RF Oscillator

The procedure is to design an RF oscillator using Y parameters[2] ,[5],[6].The first step is biasing a transistor to find the Y parameters.The biasing circuit is given in Fig. 2.Y Parameters are given in the fig. 3.These Y parameters are used for rest of the design.Active biasing is preferred to provide the temperature stability. RFC connected to base and collector terminals of the transistor serve the purpose to isolate the RF signal from DC power source.

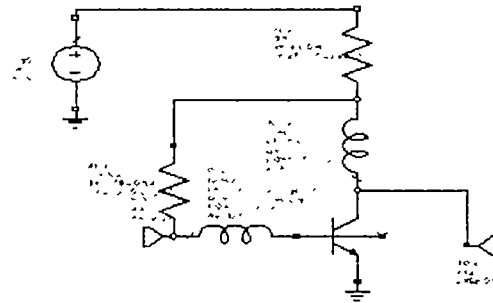


Fig. 2

The biasing is done at 1.15 GHz frequency for a supply voltage of 5 Volts and a current of 10mA.A beta controlled transistor is used for the design.

Frequency	Real	Imaginary
1.15 GHz		
Y11	6.5122	-5.6741
Y21	130.82	-21.266
Y12	-0.71646	5.9422
Y22	0.78811	-6.5364

Fig. 3

At RF and low microwave frequencies four oscillator configurations are used namely, clapp, colpitts, Hartley and Armstrong. This design includes a Hartley configuration.

Oscillator should generate a 26.5 dBm power at 1.15 GHz frequency. The feedback elements are designed as $L_2=52.76\text{mH}$, $C_2=43\text{nF}$ and $L_3=0.03\text{nH}$.DC analysis is performed to design the biasing resistors.

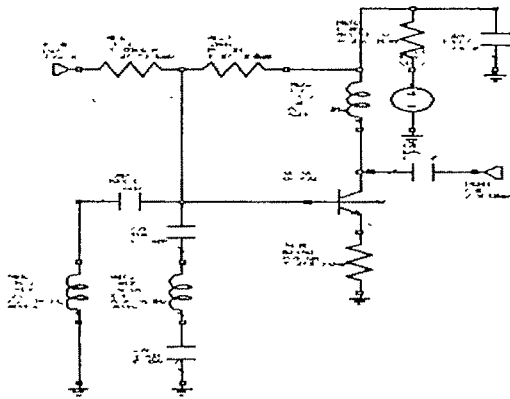


Fig. 4

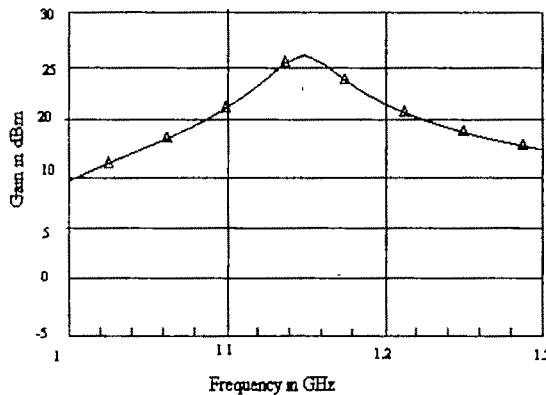


Fig.5

B.10 dB Directional coupler.

Directional Couplers and power dividers are passive devices used in the field of radio technology. They couple part of the transmission power in a transmission line by a desired amount through another port. It can be used for both power division and power combining. In power division, an input signal is divided by the coupler into two or (or more) signals of lesser power. The coupler may be a three port or a four port component with or without loss. Three port network take the form of T junctions. The basic properties of the three and four port network is described by scattering matrix theory.

Basic Wilkinson Coupler

A Wilkinson coupler is a three port network that divides input power (at port1) between port2 and port 3 [3] [4]. The Wilkinson coupler can be made for any arbitrary power division. It has a useful property of being lossless when the output ports are matched. It consists of two quarter wave sections with characteristic impedance Z_2 and Z_3 connected in parallel with the input line, which has a characteristic

impedance Z_c . If we want to split the input power P_1 into output P_2 so that

$$P_3 = K^2 P_2 \quad (2)$$

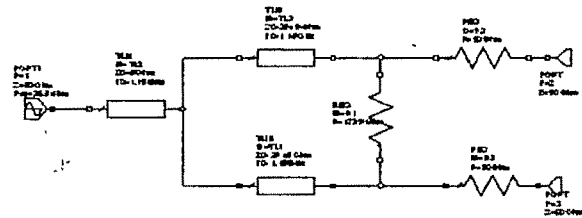


Fig.6

Coupling Factor

Directional couplers are specified in terms of the coupling accuracy at the frequency band center. Coupling factor is given as

$$CP_{12} = -20 \log |S_{21}| \quad (3)$$

Isolation

Isolation of a directional coupler can be defined as the difference in signal levels in dB between the input port and the isolated port when the two output ports are terminated by matched loads. Isolation factor between port 2 & port 3

$$IL_{23} = -20 \log |S_{23}| \quad (4)$$

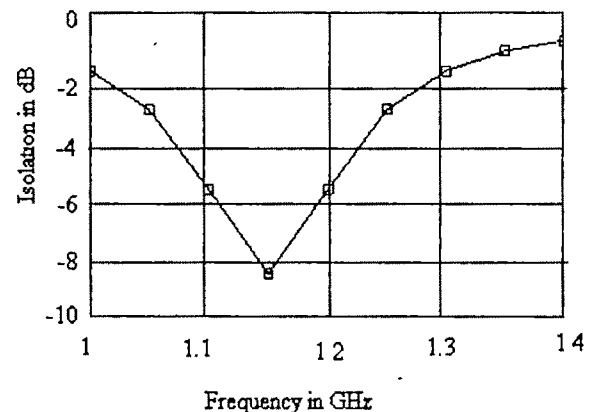


Fig.7

C.Circulator

Circulators are used to route outgoing and incoming signals between the antenna, the transmitter and the receiver [4]. In a simple system, this function could be performed by a switch that alternates connecting the antenna to the transmitter and the receiver. The use of chirped pulses and a high dynamic range may lead to temporal overlap of the sent and received pulse, however, requiring a circulator for this function. A

circulator is a non reciprocal ferrite device with usually three ports. That is, energy into port 1 predominantly exits port 2, energy into port 2 exits port 3, and energy into port 3 exits port 1. In a reciprocal device the same fraction of energy that flows from port 1 to port 2 would occur to energy flowing the opposite direction, from port 2 to port 1. The insertion loss of the circulator is the loss from port 1 to 2, while the loss from port 1 to 3 is referred to as isolation. A typical circulator will have a zero dB insertion loss from port 1 to 2 and 30 dB of isolation from port 1 to 3. The selection of ports is arbitrary, and circulators can be made to "circulate" either clockwise (CW) or counterclockwise.

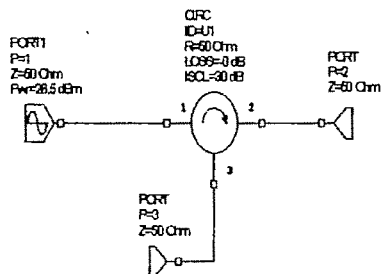


Fig.8

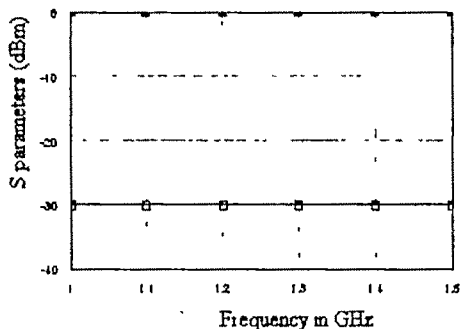


Fig.9

D.Signal Generation Circuit

Fig.10 shows the signal generation circuit. An oscillator generates electromagnetic waves of 1.15 GHz with an output power of 400 mw (26.5 dBm). The 10 dB directional coupler branches out one-tenth of the wave (40 mW) using directional couplers (10 db), and one part is given to the null balance system as a reference signal and the major part is fed to the antenna Fig.11 shows the power to the transmitting antenna and fig .12 shows power to the null balance system.

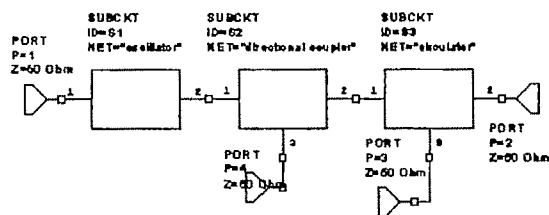


Fig.10

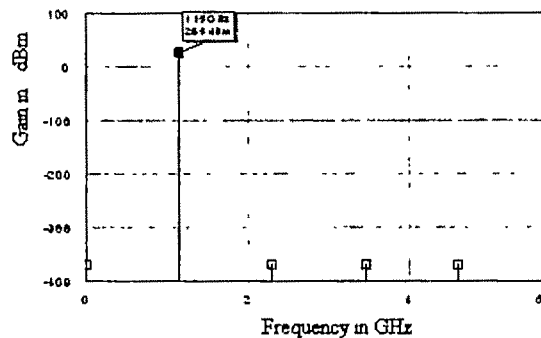


Fig. 11

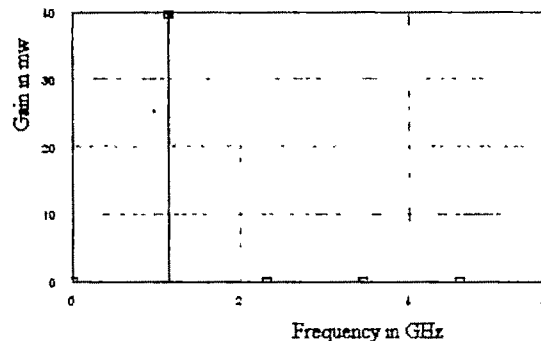


Fig.12

V.CONCLUSION

One of the world's recent medical trends is to pursuit remote healthcare system. In RF circuit design after the development of an initial design including specific components, if it does not meet the specifications, the design needs to be revised. The design process would require the construction and measurement of a laboratory prototype at each iteration, which would be expensive and time-consuming. Computer aided design can greatly decrease the time and cost of a design, while enhancing its quality. As a part of life detection system, a 1.15 GHz signal is generated. Circuits for oscillator, coupler and circulator are designed and the simulation results are verified. Now it is ready for field test.

REFERENCES

- [1]Yanming Xiao1, Jenshan Lin, Olga Boric-Lubecke, Victor M. Lubecke "A Ka-Band Low Power Doppler Radar System for Remote Detection of Cardiopulmonary Motion" , *IEEE Proceedings in Medicine and Biology 27th annual conference*,2005.
- [2] George D Vendelin, Pavo Microwave circuit design using linear and nonlinear Techniques, PP 723-725.

- [3] Collin Foundation for Microwave Engineering", 2ndEd McGraw Hill, Inc. PP 289-312
- [4] Microwave Engineering by David M Pozar, 2ndEd. Wiley PP 351-440, PP 537-543.
- [5] Matthew M Radmanesh, "Radio Frequency and microwave Illustrated", Pearson Education, Asia, Chapter 15.
- [6] R. Ludwig, P Bretchko, "RF Circuit Design, Theory and Applications" Chapter 9, Pearson education, PP 463-529.
- [7] Kun-Mu Chen, Yong Huang, Jianping Zhang, Adam Norman "Microwave Life-Detection Systems for Searching Human Subjects Under Earthquake Rubble or Behind Barrier", *IEEE Transactions on Biomedical Engineering*, January 2000
- [8] K M. Chen, D Misra, H. Wang, H. R. Chuang, and E. Postow, "An X-band microwave life-detection system," *IEEE Trans. Biomed. Eng.*, vol. BME-33, pp. 697-702, July 1986.
- [9] H. R Chuang, Y F. Chen, and K. M Chen, "Automatic clutter canceller for microwave life-detection system," *IEEE Trans Instrum. Meas.*, vol 40, pp. 747-750, Aug. 1991.
- [10] K. M Chen, J Kallis, Y. Huang, J. T. Sheu, A Norman, C. S. Lai, And A. Halac, "EM wave life-detection system for post-earthquake rescue operation." presented at the 1994 URSI Radio Science Meeting, Seattle, WA, June 19-24, 1994.

A Methodology for Studying the Characteristics of Expansion of Stent Like Structures in a Hyper Elastic Artery Model

Naveen Kumar KU^{*1}, Sujesh Sreedaharan², Nandakumar CG³, Muraleedharan CV⁴

^{1,3} Dept. of Ship Technology, Cochin University of Science & Technology, Cochin, India, email: naveenkulnt@rediffmail.com

^{2,4} Division of Artificial Organs, Biomedical Technology Wmg, Sree Chitra Thirunal Institute for Medical Sciences and Technology, Trivandrum, India, email: muralicv@sctimst.ac.in

Abstract— A stent is a device used for keeping the natural blood vessels (arteries) patent by supporting them from inside. The modeling of expansion behaviour of stent vessel couplet using any analytical or finite element techniques is extremely challenging due to many reasons. This paper describes a technique for the analysis of stent artery couplet using finite element techniques for studying the characteristics of expansion. The stent is modeled using isotropic work hardening elements described by a series of piece wise linear material model and the artery is modeled using hyperelastic elements. The stent expansion is simulated by applying internal pressure on the inner surfaces of the stent elements. As this internal pressure increases, the stent elements undergo plastic deformation and radial expansion. Eventually they contact the artery elements and subsequently becomes a typical contact analysis problem. At the end of the expansion period, the load is removed and the balloon is allowed to deflate. This results in certain quantum of recoil in the stent elements. The modeling of the system was done in Pro Engineer Wildfire and the analysis using ANSYS. The analysis could be used for studying the possible areas of vessel injury due to lateral shear during stent deployment and areas of non uniform contact pressures on the vessel wall. Typical stent characteristics like elastic recoil and foreshortening could also be studied using this model.

Key words—contact analysis, finite element techniques, foreshortening, stent

I. INTRODUCTION

A VASCULAR stent is a device used for keeping cardiovascular arteries patent by supporting them from inside. It consists of a metallic cylindrical grid which is deployed in position using by plastic expansion using balloon catheters percutaneously. Expanding stent pushes the inner lumen of the artery radially by deforming the plaque which has been blocking the artery against the vessel wall. The stent is introduced in a crimped state allowing it to pass into the site of the constriction or blockage via the femoral or brachial

arteries. The expansion of the stent is achieved by expanding a balloon on which the stent is mounted during delivery procedure. The expanding stent pushes the inner lumen radially outward to restore patency. In the case of a vascular stent, a stenosis which is the material causing the blockage is deformed and “scaffolded” against the vessel wall. In the vast majority of cases, the deployment of a stent restores an unimpeded blood flow in the direct post-intervention period. However post-stenting narrowing of the vessel may occur due to various reasons

Narrowing of a stented vessel subsequent to the stenting procedure is termed in-stent restenosis and it involves the formation of Intimal Hyperplasia though a complex cascade of cellular events post-stenting [1]. Stent design is a major factor influencing in-stent restenosis post-stenting

But it is well known that stents cannot completely negate the phenomenon of restenosis, it has been a well established fact that in-stent restenosis rates are in the range of 20 – 50 % for different stent designs [2]. The available experimental studies clearly indicate the stent – artery mechanical interaction as significant causes for the activation of restenosis mechanism [3]. This calls for a better understanding of the stent – artery biomechanics. The main limitation of the previous study on the “Simulation and Analysis of Coronary Stent Expansion” was that the artery and the plaque were not modeled.

Some research have already been carried out in this regard; Rogers et al. [3] used finite element method to carry out a 2D analysis to investigate balloon artery interaction during stent placement. A study of the arterial tissue within repeating units of some of the commercially available stent designs has been reported by Lally et al [4]. 3D model of the artery and the stent was developed by Auricchio et al [5]. Many of these studies clearly indicate that the stresses induced by the stent on the artery vary with stent designs, and these stresses are responsible for the restenosis [6].

The major difficulties encountered in the study of stent artery interaction stress can be attributed to

- the constitutive modeling of soft tissues

- nonlinearity arising from the large deformations of the stent and artery
- the interaction of the stent, and artery

II. MATERIALS AND METHODS

Finite-element analysis requires the geometry, material properties and the appropriate loading conditions to simulate the stenting procedure. Pro-Engineer [7] was used to model the stent geometry and ANSYS [8] was used for the finite element analysis

A. Geometric Modeling

The 3D geometry of the stent was modeled in Pro-Engineer. The stent in its unexpanded configuration is shown in Fig.1 and Fig.2. Due to symmetry in the radial and longitudinal directions only a quarter of the cross-section with half the total length is modeled. The quarter symmetry model with planes of symmetry is shown in Fig.3.

The artery is modeled as a cylinder and the symmetry conditions are made use of effectively.

The meshing capabilities of ANSYS have been made use of to refine meshes at the contact points and at stent strut junctions. A finer mesh has been allowed for more accurate stress and strain evaluation at critical regions

The geometric approximation of the stent was performed with SOLID45 brick elements which could account for large deformation and material nonlinearities. The coronary artery on the other hand was meshed with SOLID185 hyperelastic elements. Fig.4 and Fig.5 shows the meshing of the stent and artery respectively

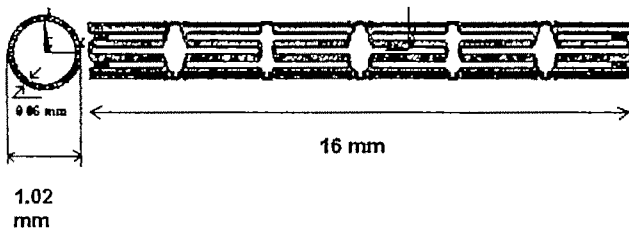


Fig. 1 Stent geometry in the unexpanded configuration

B. Material properties

The material model for the artery wall and arterial tissue, was selected as a 5-parameter third-order Mooney–Rivlin hyperelastic constitutive equation [9]. Which has been found to be adequate to describe the non-linear stress-strain relationship of these arterial tissues. The formulation can be stated as (1)

$$W = C_{10}(I_1 - 3) + C_{01}(I_2 - 3) + C_{20}(I_1 - 3)^2 + C_{11}(I_1 - 3)(I_2 - 3) + C_{02}(I_1 - 3)^2 + (J - 1)^2 / d \quad (1)$$

Where W is the strain-energy density function of the hyperelastic material, I_1 , I_2 and I_3 are the strain invariants; C_{ij}

are the hyperelastic constants and d is the material incompressibility parameter. The values of C_{ij} are obtained from published data on human femoral artery [10].

The stent is assumed to be made up of SS316LN stainless steel and the plastic constitutive response is described through a von Mises – Hill plasticity model with isotropic hardening [11]. The material model adopted in this analysis is a piecewise linear hardening model, described through a sequence of stress – strain couples, after yielding and up to a limit point.

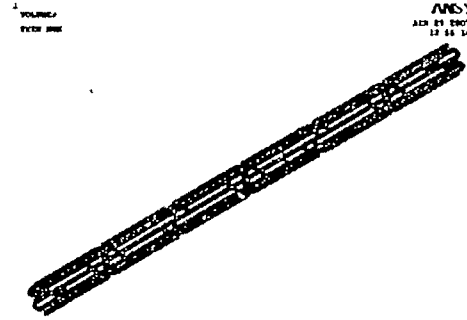


Fig. 2 Stent in the unexpanded configuration

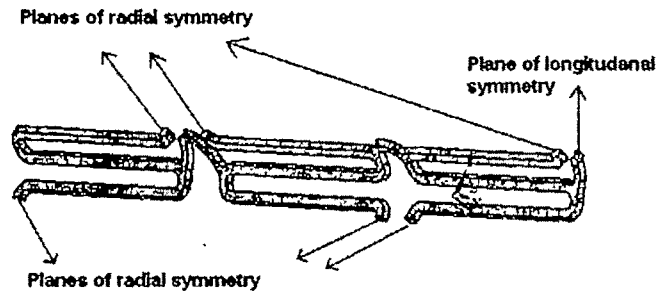


Fig. 3 Planes of symmetry of the stent

C. Boundary conditions

Symmetric boundary conditions were applied to the planes of symmetry for both the stent and artery. The artery was restrained at one end in the axial direction, to restrain the rigid body motions

The finite element model of the stent consists of 8251 elements. The stent was discretized using 500 elements along the length and 27 elements along the circumference with 2 elements across the thickness of the modeled geometry. The element size was 0.03 mm

The finite element model of the artery consists of 8251 elements. The artery was discretized using 459 elements along the length and 9 elements along the circumference with two elements across the thickness of the modeled geometry

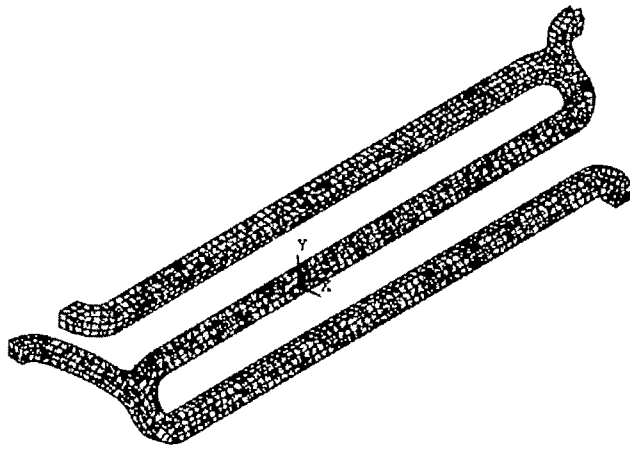


Fig. 4 Discretisation of the stent

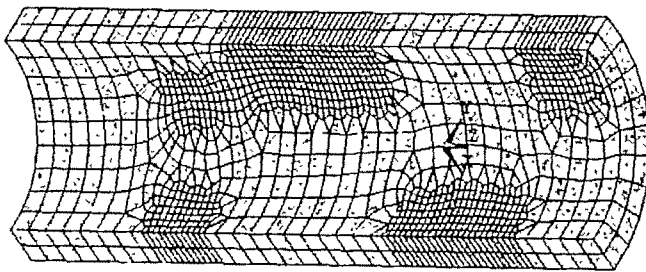


Fig. 5 Discretisation of model of the artery

D. Loading

The pressure 0.6 N/mm^2 (6 atm) has been applied to the inner portion of the stent. A total of 87 time steps have been applied as pressure load. The stent has been unloaded to zero pressure in 27 steps

III. RESULTS

The finite-element models predicted that the stent restored patency to the stenosed vessel, a 60 % stenosis was assumed, i.e. the lumen area was 60 % blocked by the stenotic plaque deposit. The plaque was not modeled here. Fig.6 and Fig.7 show the stent and artery before and after expansion, a half symmetry model in the radial direction has been shown. The finite element analysis outputs have shown that the stent restores the patency to the stenosed vessel.

The finite element analysis output have shown that the stent expands the artery with it, opening up the lumen diameter to a diameter larger than the initial diameter of the non – stenosed artery. During the unloading phase there is significant elastic recoil of the artery and hence the lumen diameter decreases. This continues until equilibrium is reached between the stent and the artery, the final diameter of the artery is still larger than the non – stenosed artery. Hence it can be safely

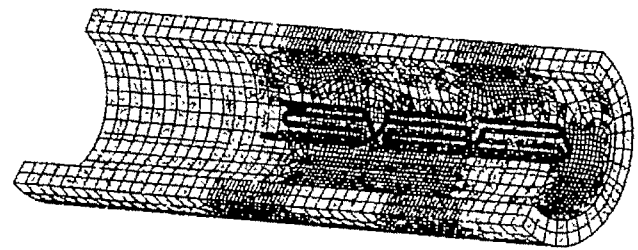


Fig. 6 Stent and the Artery in the unexpanded configuration

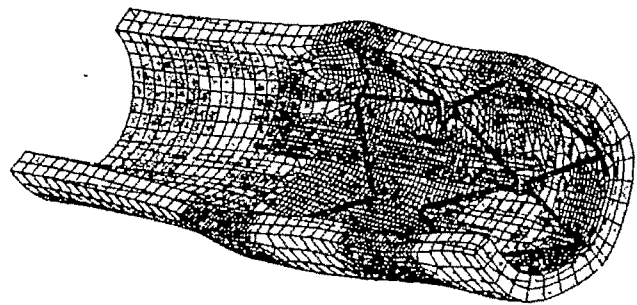


Fig. 7 Stent and the artery in the expanded configuration

concluded that the original shape of the artery is maintained by the procedure of stenting.

The deformed artery after loading is shown in Fig. 8. The major portion of the artery deforms in the range of 0.350 mm to 0.450 mm. This means that on loading the artery diameter increases by 17 – 23 % of the initial outside diameter. The maximum radial dilation of the artery occurs at the point of contact of the stent and the minimum is at locations far away from the stent struts. Radial retraction was observed in the stents as a result of the radial compressive forces exerted by the artery on the stent. This radial retraction was due to bending of the stent struts and it continued until equilibrium has been reached between the radial strength of the stents and the radial compressive forces exerted by the artery. The final diameter of the artery is about 5 – 10 % of the initial outside diameter

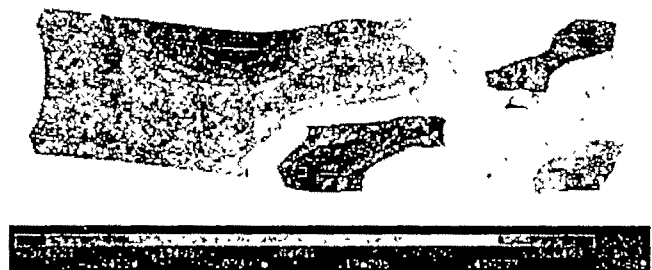


Fig. 8 Radial deformation profile of the artery (mm)

Draping of the arterial tissue between the stent struts is a matter of concern. The region of draping may be devoid of intimal hyperplasia making them potential sites of restenosis. As shown in Fig. 9 the tissue drapes between the repeating

units of the stents. The maximum draping is found to be 0.033 mm which is lesser than the permissible design value

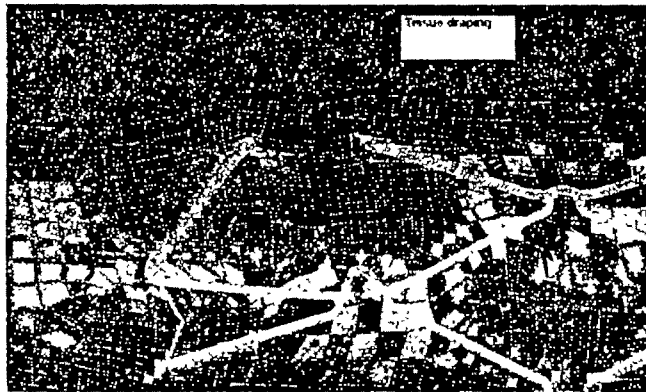


Fig. 9 Draping of tissue between the stent struts

The Principal Stress distribution in the artery has been obtained which shows a maximum of 0.67862 N/mm^2 at node no. 10375. These localized regions are hotspots since the artery is in direct contact with the stent. At other regions the stress is between $0.3 - 0.377 \text{ N/mm}^2$. The principal stresses are the direct indications to tissue injury and vascular lesions. The maximum principal stress in the final configuration of the artery has been 0.126 N/mm^2 at node no. 10340. Hence the artery would remain with this prestress in the future. The influence of magnitude of stress/prestress which may initiate a restenosis is not very clear even from the literature and this issue is not addressed in this paper. But the stress/prestress can be effectively quantified and their distribution can be clearly studied.

The plot between the principal stress and principal strain is shown in Fig.10. The curve obtained was similar to that obtained through experimental and numerical modeling

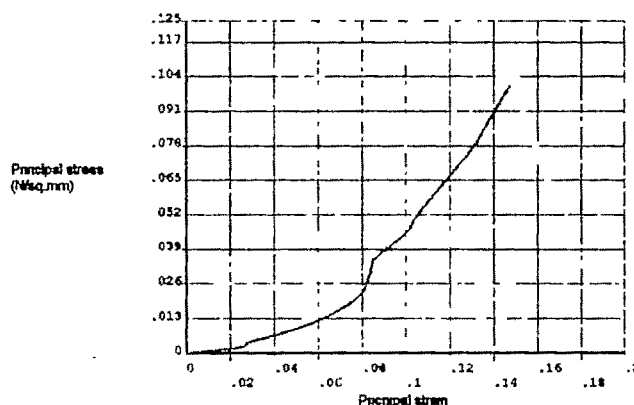


Fig. 10 Stress vs Strain curve for the hyperelastic Artery

The radial deformation of the stent has been obtained for the loading and unloading phase. The maximum value of radial deformation has been found to be 1.705 mm, at node no. 5958. The maximum value of final deformation has been found to be 1.445 mm. at the same node. This gives the maximum recoil value of 0.26 mm. A radial stiffener has been included in the

stent design to prevent the flaring of the free end. The free end could flare up initially, which could cause it to contact the artery wall earlier, causing deep vascular lesions. The major portion of the stent expands by 1.5 to 1.55 mm and settles down to 1.2 to 1.25 mm on unloading.

Fig. 11 shows the plot between radial deformation and time for node no. 5958. The curve indicates the sudden increase in the radial deformation in the very early loading phase. Later the deformation of the stent stabilizes mainly due to the presence of artery. The contact of the stent with the artery occurs within 20-21 % of the normalized time (the normalized time is 1 for loading and 1 for unloading). The abrupt decrease in the deformation during the unloading within 6% of the normalized time is noticeable. Later the deformation becomes permanent set. Typical variation of radial deformation with time has been shown in Fig. 11

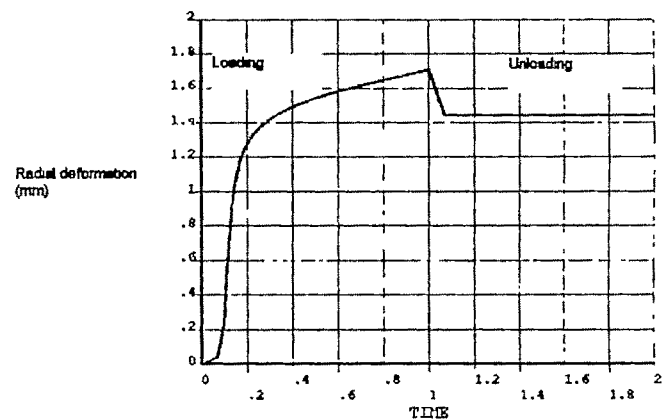


Fig. 11 Radial deformation of the Stent(node 5958) vs normalized time

Fig. 12 shows the distribution of von Mises stress on the stent during loading and maximum value is 416.313 N/mm^2 at node no. 6281

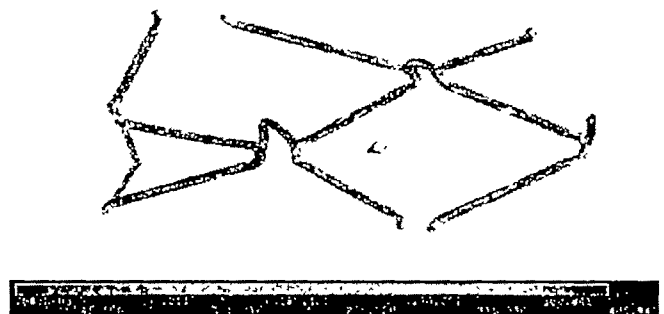


Fig. 12 von Mises stress distribution across the Stent

The stress values in the stent are the highest at the junctions of the stent struts, resulting in the plastic deformation of these points. It can be seen that the stress is more across the thickness than at the surface of the stent. However the subsequent stress is well within the plastic limit. The regions of high stresses are concentrated at the corners of the ring and

not at the middle, this was because the struts pull apart from each other during expansion causing foreshortening of the stent

Fig. 13 shows the principal stress vs principal strain plot of node no. 6181. It can be observed that the plastic deformation sets in at stress of 200 N/mm^2 . At this point the curve ceases to be linear, and the work hardening of the material can be seen in the non-linear region and the unloading path follows the elastic slope.

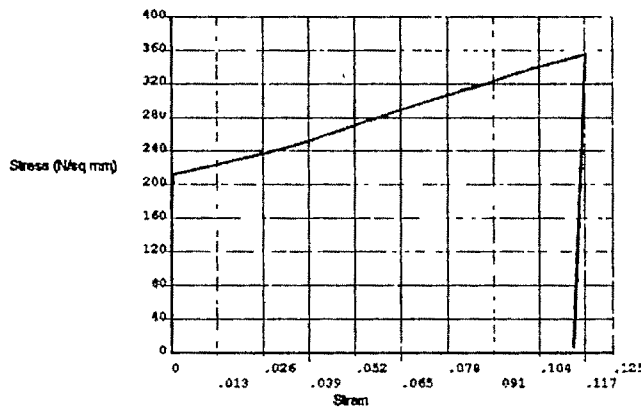


Fig. 13 Stress vs Strain curve for the Stent

IV. CONCLUSION

The coupling between the stresses imposed on the vessel wall and the radial retraction of the stent has been clearly illustrated in the present study.

A three-dimensional model for studying the revascularization of a stenotic artery through the insertion of a balloon-expandable stent has been constructed. Large deformation analysis of stent and artery has been carried out using the capabilities of the commercial code ANSYS. The stent artery interaction has been studied using the contact analysis. The study shows the ability of accurate bio-mechanical investigations to help and improve actual methodologies.

The methodology described in this study has been proposed as a method to compare and analyze existing stent designs and can now be used to develop new stent designs. Since this study shows that the correlation between stress predictions and in-stent restenosis, it would be worthwhile to develop finite-element models of realistic vessel geometries, which can be obtained from Intravascular Ultrasound (IVUS) imaging. By determining 3D patient specific geometries pre-stenting it may be possible to choose a stent design based on the patient's specific coronary artery stenosis geometry and thereby optimize the outcome of stenting procedures.

REFERENCES

- [1] Grewe P H, Deneke T, Machraoui A., Barmeyer J, Muller K.M., "Acute and chronic tissue response to coronary stent implantation pathologic findings in human specimen", *Journal of the American College of Cardiology*, Vol. 35, pp 157-163 (2000)
- [2] Freed M., Grines C, Safian R D., "The New Manual of Interventional Cardiology", Physician Press, (1997)
- [3] Campbell Rogers, David Y. Tseng, James C. Squire, Elazer R. Edelman, "Balloon-Artery Interactions During Stent Placement A Finite Element Analysis Approach to Pressure, Compliance, and Stent Design as Contributors to Vascular Injury", *Circulation Research*, Vol. 84, pp 378-383 (1999)
- [4] Lally C., Dolan F., Prendergast P.J., "Cardiovascular stent design and vessel stresses:a finite element analysis", *Journal of Biomechanics*, Vol. 38, pp 1574-1581 (2005)
- [5] Auricchio F., Di Loreto M., E. Sacco, "Finite-element Analysis of a Stenotic Artery Revascularization through a Stent Insertion", *Computer Methods in Biomechanics and Biomedical Engineering*, Vol. 00, pp. 1+15
- [6] Schwartz R., Holmes D.R., "Pigs, dogs, baboons, and man; lessons in stenting from animal studies", *Journal of Interventional Cardiology*, Vol. 7, pp 355-368 (1994)
- [7] Pro-Engineer Wildfire reference manual
- [8] ANSYS, Inc. Theory Reference
- [9] Mooney M., "A theory of large elastic deformation", *Journal of Applied Physics*, Vol. 11, pp 582-592 (1940)
- [10] Lally C., Dolan F., Prendergast P J., "Cardiovascular stent design and vessel stresses:a finite element analysis", *Journal of Biomechanics*, Vol. 38, pp 1574-1581 (2005)
- [11] Chaboche J. L. and Lemaitre J., "Mechanics of Solid Materials", John Wiley & Sons, (1987).

Technical Session 4C

Electric Drives

ANN - Based Current Control of A Voltage Source PWM Inverter

R.Arulmozhiyal¹, K.Baskaran²

¹Electrical Engineering Department, Sona college of Technology, Salem e-mail:arulmozhiyal_08@yahoo.com

²Computer Science Engineering Department, Government college of Technology, Coimbatore e-mail:baskaran_101@yahoo.com

Abstract - Current controlled voltage source PWM Inverter plays the most important role in such high performance application of VSI as A.C motor drives and motion controllers, A.C power supplies and active power filters. The main task of the control system in current control PWM Inverter is to force the current vector in the three phase load according to the reference trajectory. Two types of current controller are used. Sub harmonic PWM, Hysteresis controlled PWM. Hysteresis controller has two types: a) Fixed band b) Sinusoidal band. Fixed band hysteresis controller has disadvantages, first, that switching frequency changes according to operating condition of motor. Second, the ripple current is large so load current contain harmonics that causes additional machines heating. Sinusoidal band hysteresis current controller where the hysteresis band vary sinusoidally over a fundamental period rather than being fixed. The sub harmonic PWM has no problem associated with the switching frequency, but the steady state phase lag is a problem for high frequency operation.

The schematic of a current controlled voltage source PWM Inverter supplying a three phase induction motor. The reference current I_{ref} is compared to actual stator current I_s . The current error $e_a = I_s - I_{ref}$ is the input to the current controller which generates the command voltage. The appropriate inverter switches are turned on and off by using the signal obtained from the comparator output. The current controller can be a linear PI controller. The use of PI controller makes it possible, in a definite frequency band, to minimize the amplitude and phase errors in the three stator currents.

Artificial neural network technology has the potential to provide an improved method over conventional techniques. This paper develops a Neural network based current control voltage source inverter. The main advantages of neural network controller are fast signal processing, learning and generalization abilities, robustness and insensitivity to the load parameter changes. The modes and learning techniques have been investigated by simulation.

Keywords- Artificial neural network, Current controlled voltage source inverter, Hysteresis control, Neural network Inverter control.

I. INTRODUCTION

THE current-control technique has a most important role in current-regulated PWM inverters which are widely used in AC motor drives, A.C power Supplies and active power filters. A variety of current control methods have been studied and reported in the literature [1]. Among the various current control methods, hysteresis current control is the simplest method and the capability to limit the peak current. But the switching frequency of this method is not fixed. As a result, the load current contains harmonics that cause additional machine heating.

Artificial neural network technology has the potential to provide an improved method of deriving non-linear models which is complementary to conventional techniques. Neural networks are intrinsically non-linear and the actual algorithmic relevant set of training examples is required which can be derived from operating plant data. In contrast to other machine learning techniques, neural networks can modify their behavior in response to the environment, have the flexibility of easily handling different problem sizes, and have the potential for hardware implementation.

II. DESCRIPTION OF CURRENT CONTROLLER

A. Hysteresis controller:

The control for one inverter leg is shown in Figure 1.

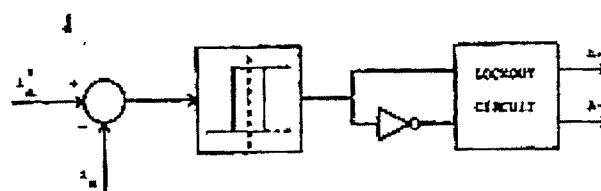


Figure 1. Hysteresis control for one phase

When the line current becomes greater (less) than the current reference by the hysteresis band, the inverter leg is switched in the negative (positive) direction, which provides an instantaneous current limit if the neural is connected to the dc bus midpoint. In a system without a neural connection, the actual current error can reach double the hysteresis band

assuming the three phase current reference sums to zero.

B. Ramp comparison controller:

A Ramp comparison control for one inverter leg is shown in Figure 2.

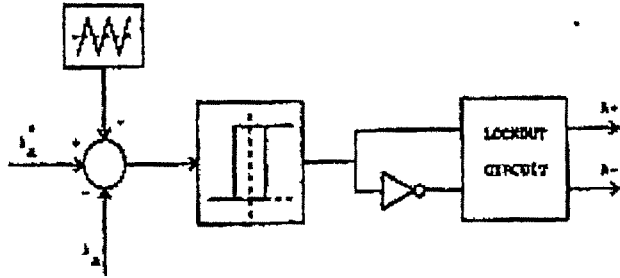


Figure 2. Ramp comparison controller for one phase

The controller can be thought of as producing asynchronous sine - triangle PWM with the current error considered to be the modulating function. The current error is compared to a triangle wave form and if the current error is greater (less) than the triangle waveform, then the inverter leg is switched in the positive (negative) direction. With sine triangle PWM, the inverter switches at the frequency of the triangle wave and produces well define harmonics. Multiple crossings of the ramp by the current error may become a problem when the time rate of change of the current error becomes greater than that of the ramp. The error can be reduced by increasing the controller can be adjusted by either adjusting the triangle amplitude or amplifying the current error.

III. NEURAL NETWORK CONCEPT

There are many artificial neural-network architectures that have been proposed. [14] One architecture has been predominant; that is the feed forward neural network (FNN). The standard neuron structure, illustrated in Figure 3 is adopted which is comprised of a summer and a logistic function $f(net_{p,i})$ that can be either a sigmoid or a linear function. The equation for the i -th neuron of the p -th layer structure is

$$net_{p,i} = \sum_{k=1}^n w_{p,i,k} O_{p-1,k} + \theta_{p,i} \quad (1)$$

$$O_{p,i} = f(net_{p,i}) \quad (2)$$

where $O_{p,i}$ is the output

$O_{p-1,k}$ is the k -th output at the $(p-1)$ -th layer

$w_{p,i,k}$ is the weight from the k -th input of $(p-1)$ -th layer to the i -th output of the p -th layer.

$\theta_{p,i}$ is the bias.

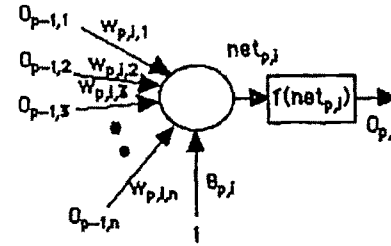


Figure 3. Structure of an elementary neuron

These neurons are organised in layers, as shown in Figure 4.

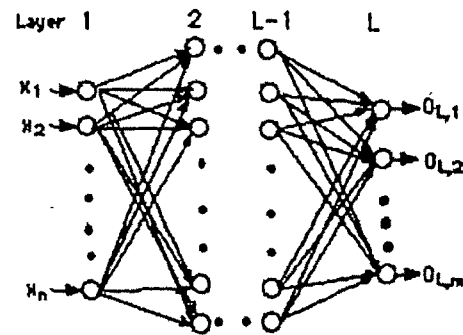
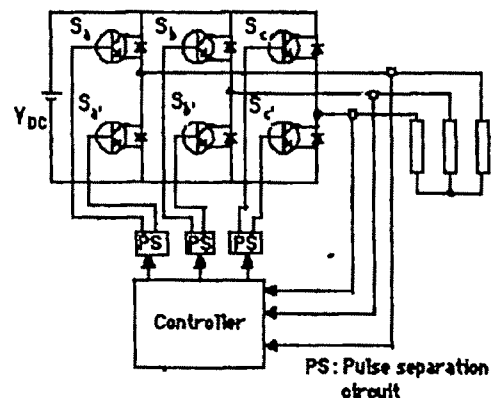


Figure 4. Feedforward neural network architecture

Scaled data enters the network at neurons of the input layer, and is propagated to the output through intermediate layers. Each connection has associated with it a weighting, which modifies the signal strength. There are various techniques for optimizing criterion functions to train the neural network. One important characteristic of neural network classifiers is that their training usually requires iterative techniques. The back propagation classifier is the most popular technique trained by using the gradient descent method.

IV. NERUAL NETWORK INVERTER CONTROL

The voltage source inverter (VSI) is illustrated in Figure 5.



The input signal to the inverter is an analog signal such as current error or voltage error. The output signal of the inverter is a binary signal. Therefore, the controller has the properties of a nonlinear function to map the analog input into binary output. [8],[9] Neural network architectures have the capacity to learn nonlinear system models. They can perform collective processing and learning and provide powerful processing capabilities with great potential for highly parallel computation.

The hysteresis and neural network controls both have to find an algorithm for the nonlinear mapping function. In the neural network method, training is required to learn something about the plant behavior. The input to the neural network are three phase current errors and the outputs are the voltage vectors. Current errors can be randomly generated at the neural network input and the back propagation method is used to update the weights so as to decrease the current errors. Since the hysteresis current control for the VSI is known, the neural network must learn the dynamic behavior of the hysteresis current control. It can be on line or off-line learning.

Figure 6 shows the neural network inverter control.

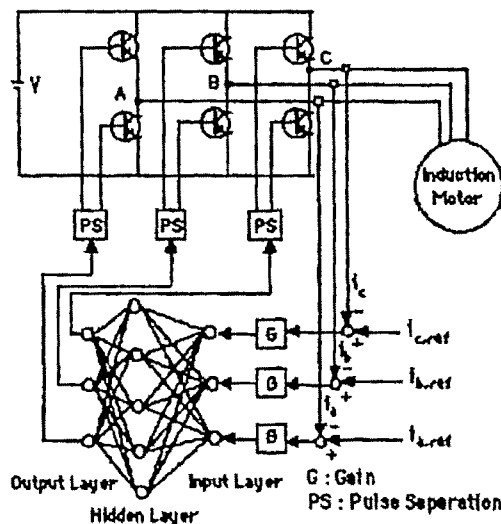


Figure 6. Neural network inverter control

The three sinusoidal reference currents are $i_{a,ref}$, $i_{b,ref}$, $i_{c,ref}$. Reference current $i_{b,ref}$ and $i_{c,ref}$ phase shifted 120° and 240° respectively from $i_{a,ref}$. First the three phase currents from voltage source inverter are measured and compared with the three reference currents. The error signals are multiplied by given coefficient G and then input to the neural network. The neural network is trained to have minimum output error.

The training rule is

$$\begin{aligned} \text{If } |i_{m,ref} - i_m| < \varepsilon &\Rightarrow \text{keep } O_m \text{ at the same state} \\ \text{If } |i_{m,ref} - i_m| > \varepsilon &\Rightarrow \text{keep } O_m = 1 \\ \text{If } |i_{m,ref} - i_m| < -\varepsilon &\Rightarrow O_m = 0 \end{aligned} \quad (3)$$

where ε is small error, $m = a, b, c$ phases O_m is the output of

the neural network. Pulse separation circuit that will keep two output waveforms from overlapping. If the two output waveforms from Pulse separation circuit overlap, the upper and lower transistors in one inverter leg will conduct at the time, which will damage the transistors.

V. SIMULATION RESULT

The simulation model for neural network inverter control is developed. The system parameters in Figure 6 are

DC bus voltage $V = 75\text{V}$

Inductance $L = 0.01\text{mH}$

Resistance $R = 2\text{ohms}$

Switching frequency = 19.8KHZ .

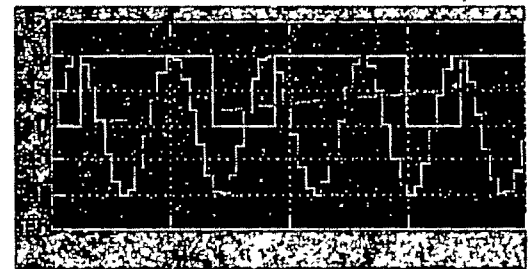


Figure 7. Space vector PWM

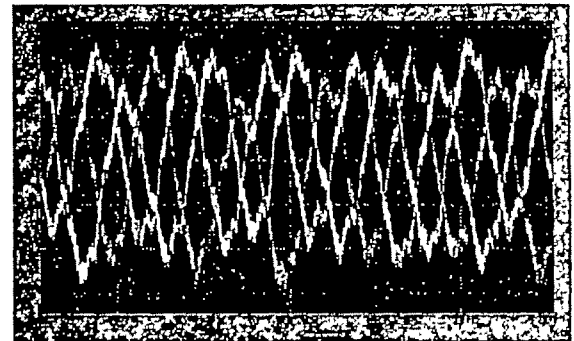


Figure 8. Inverter output current waveform without neural network

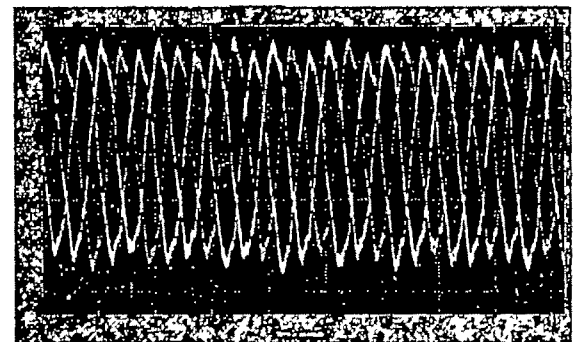


Figure 9. Inverter output current waveform with neural network

VI. CONCLUSION

Neural network control of a sinusoidal current controlled

VSI is presented in this report. Three different controller structures are considered. First, Hysteresis controller, Ramp comparison controller and a neural network controller. Simulation results are presented for the neural network controller. The neural network also has fast processing speed and fault tolerance. The fault tolerance property will allow the neural network to work well even if one of three current sensors failed. Thus, neural networks appear to have significant advantages in power electronic applications.

REFERENCES

- [1] D.M Brod and D.E.Novotony, "Current Control of VSI-PWM Inverters", IEEE/IAS 1984 Annual meeting.
- [2] B.K.Bose, "An Adaptive hysteresis band current control techniques of a voltage fed PWM Inverter for machine Drive system", IECON 1988.
- [3] M.Bhul and R.D.Lorenz, "Design and Implementation of neural networks for digital current regulation of inverter drives", in IEEE-IAS, Annual conference 1991.
- [4] M.A.Dzieniakowski and M.P.Kazmierkowski, "Microprocessor based novel current regulator for VSI-PWM inverters", in IEEE-PESC, 1992.
- [5] M.A.Dzieniakowski, M.P.Kazmierkowski, "Novel space vector based current controller for PWM inverters", IEEE Trans on Power Electronics, vol 6, 1991.
- [6] D.Driankov, "Introduction to fuzzy control", Narosa publication.
- [7] R.G.Hoft, "Intelligent control-Power Electronics systems", Oxford university press
- [8] B.R.Lin and R.G.Hoft, "Power Electronics inverter control with neural networks", APEC 1993.
- [9] B.R.Lin, "Analysis of neural and fuzzy power electronic control", IEEE proceedings, Measurement Technology, vol, 144, No:1, January 1997.
- [10] B.R.Lin and R.G.Hoft, "Power Electronics converter control based on neural network and fuzzy logic methods", in Proc.IEEE-PESC, 1993.
- [11] R.J.Liou and M.R.Azimi-sadjade, "Fast Learning process of multiplayer Neural networks using recursive Least squares methods", IEEE Trans.on signal processing Feb 1992.
- [12] Malesani.L, and Tenti.P, "A Novel hysteresis control method for current controlled VSI PWM inverters with constant modulation frequency", Proceeding of IAS Conference 1987.
- [13] Mohan.N, Undeland.T and Robbins.W, "Power electronics converters, applications and design", John Wiley & sons, Newyork 1989.
- [14] S.N.Sivanandam, "Introduction to Artificial Neural networks", Vikas publication
- [15] A.M.Trzynadlowski and S.Legowski, "Application of neural networks to the optimal control of three phase voltage controlled inverters", IEEE Tran on Power Electronics vol 9, no.4, July 1994

A Simulink Based Dynamic Modeling and Analysis of High Performance Induction Motor Drive

Rajesh Kumar¹, R.A. Gupta², S.V. Bhangale³

^{1,2,3}Malaviya National Institute of Technology, JLN Marg, Jaipur, India
e-mail ¹rkumar_mnit@rediffmail.com, ³bhangale_sv@yahoo.com

Abstract—This paper presents a dynamic modeling and simulation of Induction Motor Drive using the MATLAB / Simulink. The model is described by the simple equations. This proposed method has been successfully implemented in Simulink environment. The model is tested under steady state and transient conditions using the example of three phase squirrel cage Induction motor. This model can be use for the different control of Induction motor drive. Although traditional per phase equivalent circuit has been widely used in steady state analysis and design of induction motor it is not appropriate to predict dynamic performance of the motor. In order to understand and analyzed vector control of induction motor, dynamic model is necessary. Unfortunately the dynamic model equations are complex and there are many different forms of the model depending on the choice of reference frame. It is the objective to explain the model form in a concise way to understand clearly. The dynamic curves of the motor phase current, speed, electromagnetic torque are obtained from the simulation result.

Keywords — Dynamic modeling, Induction Machine, Matlab/ Simulink

I. INTRODUCTION

THE induction motor which is the most widely used in the industry has been favored because of its good self started capability; simple and rugged structure low cost and reliability. There have been numbers books and paper presented detailing, modeling and simulation of various induction machines drive system [3]-[7]. The analog computer was used for the simulation of induction motor, the mathematical model was implemented using the electronic operational amplifiers capable of performing basic mathematical operation like integration ,addition multiplication and division [1]-[2]. The dynamic model equations can develop by using the different references frames and the selection of the frame is depending on the purpose of control [8]-[9].

The mutual inductances between the rotor and stator coils will change because the angle between the axes of the rotor and stator changes. To eliminate the time varying inductances, the equations are frequently transformed to d-q variable in the arbitrary reference frame. The simulation of the induction motor is conveniently accomplished by solving for the flux

linkage per second in terms of the voltage applied to the machine.

The electrical machine is simulated using the different circuit simulators under the steady state conditions. The control of the electrical machine under the transient behavior is important and this is done in the Simulink. . In this paper the model is develop in synchronous rotating frame and transfer in to stationary reference frame, which has a advantage of eliminating some terms from the voltage equations and easy to simulate. Most of the drive control schemes uses the stationary reference model.

II. DYNAMIC INDUCTION MOTOR MODEL

The Induction Motor model is developed by using the circuit coupled approach. An ideal three phase induction motor is used with the assumptions no magnetic saturation, uniform air gap, neglecting hysteresis and eddy current losses, sinusoidal distribution of air gap flux. The magnetically coupled rotor and stator circuits are shown in Fig. 1. and from this, the equations of voltage for rotor and stator windings are given by the following expressions. The axis of a rotor phase is displaced by an angle θ_2 from the axis of the corresponding stator phase.

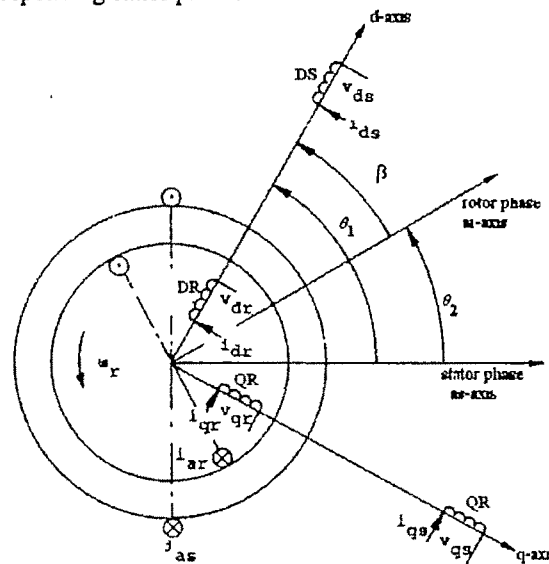


Fig.1. Three phase Induction motor with superimposed d-q-axis

As rotor rotates the angle θ_2 varies with time and is given by,

$$p\theta_2 = \omega_r \quad (1)$$

Where ω_r is the angular speed of the rotor in electrical radian per second and p is differential operator.

If ω_0 is the synchronous speed in electrical radian per second, the slip is given by

$$s = (\omega_0 - \omega_r) / \omega_0 \quad (2)$$

The d-q reference frame is considered to be rotating synchronously with respect to the stator. Thus, considering the d-axis to be coincident with phase 'as' axis of stator at time $t=0$, it will advance by an angle θ_1 such that $p\theta_1 = \omega_0$ (3)

The angle between the d-axis and the rotor phase 'ar' axis is given by

$$\beta = \theta_1 - \theta_2 \quad (4)$$

The voltage and current relations for the stator and rotor windings are given by the following expressions.

For stator	For Rotor
$v_{as} = R_s i_{as} + p\psi_{as}$	$v_{ar} = R_r i_{ar} + p\psi_{ar}$
$v_{bs} = R_s i_{bs} + p\psi_{bs}$	$v_{br} = R_r i_{br} + p\psi_{br}$
$v_{cs} = R_s i_{cs} + p\psi_{cs}$	$v_{cr} = R_r i_{cr} + p\psi_{cr}$

(5)

The self inductances of the stator and rotor phases, mutual inductances between stator winding and mutual inductance between rotor winding are constant because of smooth rotor construction, the mutual inductance between the stator phase and rotor phase is depend on the position of rotor, the instantaneous values between them proportional to the cosine of the angle between stator and rotor axes at instant. The flux linkage equations for stator and rotor windings are given as the fallows:

For stator winding

$$\psi_{as} = L_{ss} i_{as} + L_{sm} (i_{bs} + i_{cs}) + L_{sr} [i_{ar} \cos \theta_2 + i_{br} \cos(\theta_2 + 2\pi/3) + i_{cr} \cos(\theta_2 - 2\pi/3)]$$

$$\psi_{bs} = L_{ss} i_{bs} + L_{sm} (i_{as} + i_{cs}) + L_{sr} [i_{ar} \cos(\theta_2 - 2\pi/3) + i_{br} \cos \theta_2 + i_{cr} \cos(\theta_2 + 2\pi/3)]$$

$$\psi_{cs} = L_{ss} i_{cs} + L_{sm} (i_{as} + i_{bs}) + L_{sr} [i_{ar} \cos(\theta_2 + 2\pi/3) + i_{br} \cos(\theta_2 - 2\pi/3) + i_{cr} \cos \theta_2] \quad (6)$$

For rotor winding

$$\psi_{ar} = L_{rr} i_{ar} + L_{rm} (i_{br} + i_{cr}) + L_{sr} [i_{as} \cos \theta_2 + i_{bs} \cos(\theta_2 - 2\pi/3) + i_{cs} \cos(\theta_2 + 2\pi/3)]$$

$$\psi_{br} = L_{rr} i_{br} + L_{rm} (i_{ar} + i_{cr}) + L_{sr} [i_{as} \cos(\theta_2 + 2\pi/3) + i_{bs} \cos \theta_2 + i_{cs} \cos(\theta_2 - 2\pi/3)]$$

$$\psi_{cr} = L_{rr} i_{cr} + L_{rm} (i_{ar} + i_{br}) + L_{sr} [i_{as} \cos(\theta_2 - 2\pi/3) + i_{bs} \cos(\theta_2 + 2\pi/3) + i_{cs} \cos \theta_2] \quad (7)$$

Where

L_{ss} = Self inductance of a stator phase winding.

L_{rr} = Self inductance of a rotor phase winding.

L_{sm} = Mutual inductance between stator phase windings.

L_{rm} = Mutual inductance between rotor phase windings.

L_{sr} = Mutual inductance between stator and rotor phase windings.

Consider the three phase system is balanced.

$$i_{as} + i_{bs} + i_{cs} = 0 \quad i_{ar} + i_{br} + i_{cr} = 0 \quad (8)$$

$$i_{as} + i_{bs} = -i_{cs} \quad i_{bs} + i_{cs} = -i_{as} \quad i_{as} + i_{cs} = -i_{bs} \quad (9)$$

$$i_{ar} + i_{br} = -i_{cr} \quad i_{br} + i_{cr} = -i_{ar} \quad i_{ar} + i_{cr} = -i_{br}$$

Substituting the value of equation (9) in equation (6) to (7) the following flux linkage equations are obtained.

$$\begin{aligned} \psi_{as} &= L_{ss} i_{as} + L_{sm} (-i_{as}) \\ &+ L_{sr} [i_{ar} \cos \theta_2 + i_{br} \cos(\theta_2 + 2\pi/3) + i_{cr} \cos(\theta_2 - 2\pi/3)] \\ &= i_{as} L_{ss} + i_{ar} L_{sr} \cos \theta_2 + i_{br} L_{sr} \cos(\theta_2 + 2\pi/3) \\ &+ i_{cr} L_{sr} \cos(\theta_2 - 2\pi/3) \end{aligned} \quad (10)$$

Or

$$\psi_{as} = L_s i_{as} + L_1 i_{ar} + L_3 i_{br} + L_2 i_{cr}$$

Where

$$L_s = L_{ss} - L_{sm} \quad L_1 = L_{sr} \cos \theta_2$$

$$L_2 = L_{sr} \cos(\theta_2 - 2\pi/3) \quad L_3 = L_{sr} \cos(\theta_2 + 2\pi/3)$$

Similarly we can write the expression for ψ_{bs} , ψ_{cs} , ψ_{ar} , ψ_{br} and it can be expressed in matrix form as follows.

$$\begin{bmatrix} \psi_{as} \\ \psi_{bs} \\ \psi_{cs} \\ \psi_{ar} \\ \psi_{br} \\ \psi_{cr} \end{bmatrix} = \begin{bmatrix} L_s & 0 & 0 & L_1 & L_3 & L_2 \\ 0 & L_s & 0 & L_2 & L_1 & L_3 \\ 0 & 0 & L_s & L_3 & L_2 & L_1 \\ L_1 & L_2 & L_3 & L_r & 0 & 0 \\ L_3 & L_1 & L_2 & 0 & L_r & 0 \\ L_2 & L_3 & L_1 & 0 & 0 & L_r \end{bmatrix} \begin{bmatrix} i_{as} \\ i_{bs} \\ i_{cs} \\ i_{ar} \\ i_{br} \\ i_{cr} \end{bmatrix} \quad (11)$$

Where $L_r = L_{rr} - L_{rm}$

A. Transformation in to synchronously rotating reference frame.

Substitution of equation (11) into the equations (5) get a set of nonlinear differential equations, the nonlinearity is due the trigonometric terms as θ_2 is the function of time. These equation can be transform in to set of linear equations using the mathematical transformation like the dq or $\alpha\beta$. By doing

so the trigonometric time varying coefficients are eliminated, the variables and parameters are expressed in mutually decoupled direct and quadrature axes. The d-q equations of induction motor can be expressed either in stationary or rotating reference frame. The use of a reference frame that rotates at synchronous speed yields an advantage that with sinusoidal excitation the variables appear as dc quantities in steady state condition. The transformation to d-q axes reference frame rotating at synchronous speed, ω_0 radian /sec, is given by the Fig. 1 and d-q axis stator and rotor voltage equations are as follows.

For stator

$$\begin{aligned} v_{ds} &= 2/3 [v_{as} \cos \theta_1 + v_{bs} \cos(\theta_1 - 2\pi/3) + v_{cs} \cos(\theta_1 + 2\pi/3)] \\ v_{qs} &= -2/3 [v_{as} \sin \theta_1 + v_{bs} \sin(\theta_1 - 2\pi/3) + v_{cs} \sin(\theta_1 + 2\pi/3)] \end{aligned} \quad (12)$$

For rotor

$$\begin{aligned} v_{dr} &= 2/3 [v_{ar} \cos \beta + v_{br} \cos(\beta - 2\pi/3) + v_{cr} \cos(\beta + 2\pi/3)] \\ v_{qr} &= -2/3 [v_{ar} \sin \beta + v_{br} \sin(\beta - 2\pi/3) + v_{cr} \sin(\beta + 2\pi/3)] \end{aligned} \quad (13)$$

Where

$$v_{ds}, v_{qs} = \text{d-q voltages of stator.}$$

$$v_{dr}, v_{qr} = \text{d-q voltages of rotor.}$$

The same transformations are defined for the currents and flux linkages of stator and rotor windings.

B. Basic Machine Relation in Synchronously Rotating reference Frame.

The final voltage equations obtained by expressing d-q component of flux in terms of d-q currents. The procedure adopted is to write down the transformation for flux linkages similar to equations (12) and (13). Then θ_2 is replaced by $(\theta_1 - \beta)$ in equation (11).

Substituting equations (11) in the transformation equations for flux linkages and simplifying the result by using trigonometric reduction form the following flux linkages relations are obtained

$$\psi_{ds} = L_s i_{ds} + L_{12} i_{dr} \quad \text{Where } L_{12} = 3/2 L_{sr}$$

The parameter of the induction motor is measurement with respect to stator windings. It is more convenient to refer all quantities to stator windings. Hence in this paper referring to stator windings.

$$\psi_{ds} = L_s i_{ds} + (a L_{12}) (i_{dr} / a) \quad \text{or} \quad \psi_{ds} = L_s i_{ds} + L_m i_{dr}$$

Where a = the turns ratio.

$$L_m = a L_{12} \quad \text{and} \quad i_{dr} \text{ is now the referred value.}$$

Self inductance L_s may be express as

$$L_s = L_{ls} + L_m$$

Where L_s = stator leakage inductance, L_m = magnetizing inductance.

Therefore the flux linkage equations in terms of leakage and magnetizing inductances are as:

For stator

$$\begin{aligned} \psi_{ds} &= (L_{ls} + L_m) i_{ds} + L_m i_{dr} \\ \psi_{qs} &= (L_{ls} + L_m) i_{qs} + L_m i_{qr} \end{aligned} \quad (14)$$

For Rotor

$$\begin{aligned} \psi_{dr} &= (L_{lr} + L_m) i_{dr} + L_m i_{ds} \\ \psi_{qr} &= (L_{lr} + L_m) i_{qr} + L_m i_{qs} \end{aligned} \quad (15)$$

Where

$$\psi_{ds}, \psi_{qs} = \text{d-q components of stator flux linkage.}$$

$$\psi_{dr}, \psi_{qr} = \text{d-q components of rotor flux linkage.}$$

$$i_{ds}, i_{qs} = \text{d-q currents components of stator.}$$

$$i_{dr}, i_{qr} = \text{d-q currents components of rotor.}$$

$$L_{lr} = \text{rotor leakage inductance.}$$

Expression of dq component voltages in terms of flux linkages are obtained by substituting equations (5) into equations (12) to (13) and sampling the result by making use of transformations for dq components linkages. The resulting expressions are

For stator

$$v_{ds} = R_s i_{ds} + p \psi_{ds} - \omega_0 \psi_{qs}, \quad v_{qs} = R_s i_{qs} + p \psi_{qs} + \omega_0 \psi_{ds} \quad (16)$$

For rotor

$$v_{dr} = R_r i_{dr} + p \psi_{dr} - s \omega_0 \psi_{qr}, \quad v_{qr} = R_r i_{qr} + p \psi_{qr} + s \omega_0 \psi_{dr} \quad (17)$$

Substituting equations (14) and (15) into equations (16) and (17) the voltage and current equations can be written in matrix form as:

$$\begin{bmatrix} v_{ds} \\ v_{qs} \\ v_{dr} \\ v_{qr} \end{bmatrix} = \begin{bmatrix} R_s + L_{sm} p - \omega_0 L_{sm} & L_m p & -\omega_0 L_m \\ \omega_0 L_{sm} & R_s + L_{sm} p & \omega_0 L_m & L_m p \\ L_m p & -s \omega_0 L_m & R_r + L_{rm} p & -s \omega_0 L_{rm} \\ s \omega_0 L_m & L_m p & s \omega_0 L_{rm} & R_r + L_{rm} p \end{bmatrix} \begin{bmatrix} i_{ds} \\ i_{qs} \\ i_{dr} \\ i_{qr} \end{bmatrix} \quad (18)$$

$$\text{Where } L_{sm} = (L_{ls} + L_m), \quad L_{rm} = (L_{lr} + L_m)$$

For squirrel cage induction motor v_{dr} and $v_{qr} = 0$

The instantaneous power input to stator is given by

$$P_t = v_{as} i_{as} + v_{bs} i_{bs} + v_{cs} i_{cs} \quad (19)$$

The input power expressed in terms of d-q components as

$$P_t = 3/2 (v_{ds} i_{ds} + v_{qs} i_{qs}) \quad (20)$$

The instantaneous power input to rotor is given by

$$P_r = 3/2 (v_{dr} i_{dr} + v_{qr} i_{qr}) \quad (21)$$

The electromagnetic torque can be obtained as the rotor power divided by the rotor angular speed in mechanical radian/sec. Power associated with rotor speed voltage, from equations (18).

$$\begin{aligned} P_{\omega r} &= 3/2 \{ [-s\omega_0 L_m i_{qr} - s\omega_0 L_{lm} i_{qr}] i_{dr} + [s\omega_0 L_m i_{ds} + s\omega_0 L_{lm} i_{dr}] i_{qr} \} \\ P_{\omega r} &= 3/2 [-s\omega_0 L_m i_{qr} i_{dr} + s\omega_0 L_m i_{ds} i_{qr}] \\ P_{\omega r} &= 3/2 (-s\omega_0 L_m) [i_{qr} i_{dr} - i_{ds} i_{qr}] \end{aligned} \quad (22)$$

Since the angle (β) between d-axis and rotor phase 'ar' axis advancing with time, $p(\beta)$ is positive. The rotor moves opposite with respect to d-q frame at a speed $-p(\beta)$.

$$\begin{aligned} \omega_{rm} &= -p(\beta) / 2 \text{ POLES} \quad \text{Speed in mechanical radian/sec} \\ \omega_{rm} &= -s \omega_0 / 2 \text{ POLES} \end{aligned}$$

The electromagnetic torque for motoring action is

$$\begin{aligned} T_e &= P_{\omega r} / \omega_{rm} \\ &= 3/2 (-s\omega_0 L_m) [i_{qr} i_{dr} - i_{ds} i_{qr}] / (-2s \omega_0 / \text{POLES}) \\ &= (3/2) (\text{POLES} / 2) L_m [i_{qr} i_{dr} - i_{ds} i_{qr}] \end{aligned} \quad (23)$$

The equations (18) and (23) represent the d-q axes model of ideal induction motor in synchronously rotating frame.

The above equations (16), (17) and (18) of the voltages express in a stationary reference frame by setting the phase displacement between the d-axis and stator phase 'as' will zero.

When $\theta_1 = 0$, $p\theta_1 = \omega_0$, $\omega_0 = 0$

For stator For rotor

$$\begin{aligned} v_{ds} &= R_s i_{ds} + p\psi_{ds} & v_{dr} &= R_r i_{dr} + p\psi_{dr} + \omega_1 \psi_{qr} \\ v_{qs} &= R_s i_{qs} + p\psi_{qs} & v_{qr} &= R_r i_{qr} + p\psi_{qr} - \omega_1 \psi_{dr} \end{aligned} \quad (25)$$

$$\begin{bmatrix} v_{ds} \\ v_{qs} \\ v_{dr} \\ v_{qr} \end{bmatrix} = \begin{bmatrix} R_s + L_{sm} p & 0 & L_m p & 0 \\ 0 & R_s + L_{sm} p & 0 & L_m p \\ L_m p & \omega_1 L_m & R_r + L_{lm} p & \omega_1 L_{lm} \\ \omega_1 L_m & L_m p & \omega_1 L_{lm} & R_r + L_{lm} p \end{bmatrix} \begin{bmatrix} i_{ds} \\ i_{qs} \\ i_{dr} \\ i_{qr} \end{bmatrix} \quad (26)$$

The equations (24) and (26) represent the d-q axes model of ideal induction motor in stationary reference frame.

III. INDUCTION MOTOR SIMULATION

MATLAB/ SIMULINK is powerful software tool for modeling and simulation and accepted globally. In this paper the mathematical model are present in both reference frame synchronously and stationary reference frame. The equations (14) - (17) and (23)-(25) have been implemented in MATLAB SIMULINK to obtain the dynamic model of induction motor model in stationary reference frame. The simulation block diagram consist of the transformation blocks, electrical model blocks i.e. dq axis fluxes and currents and mechanical model block. The complete simulation diagram is depicted in Fig. 4.

IV. RESULT AND DISCUSSION

The dynamic model presented in this paper has accurate simulation results under steady state and transient conditions. The simulation on the induction motor is carried out and results are shown in Fig. 3(a)-(d). The motor run at the different conditions i.e. no load, load and speed reversal, and the performance is shown in Fig.3. (a)-Fig.3.(d). At the start torque is raised and get stable at the time 0.25 sec, when a load of 2.4 N-m and 4.5 N-m is applied due to its impact the torque and stator current get increased during these instants. The speed reversal is applied at period of 0.8 sec. Fig.3. (b) and Fig.3. (c) shows the response of stator current and torque of machine under the speed reversal case. The response of the machine during the different conditions shows that the machine is dynamic which support verification of model in simulation environment.

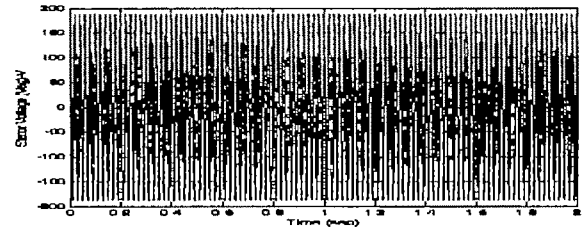


Fig.3 (a) Stator phase voltage (volt)

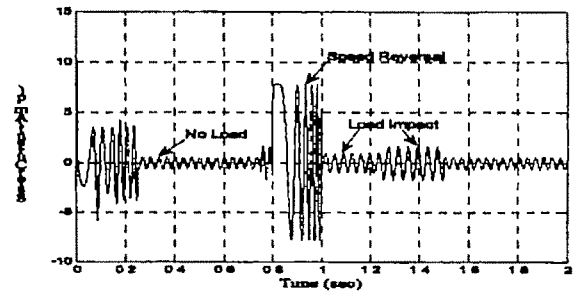


Fig 3 (b) Stator Current (Amp)

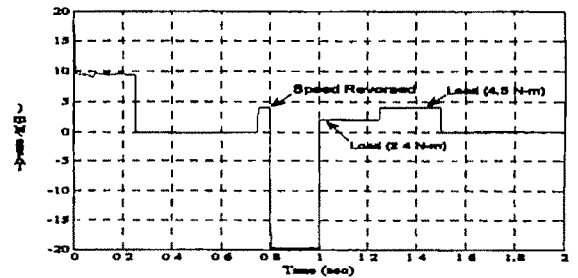


Fig.3 (c) Torque Response (N-m)

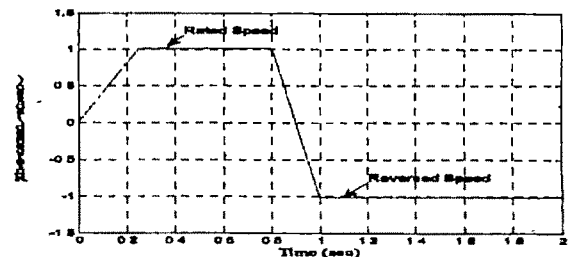


Fig.3 (d) Speed Response (rad/sec)

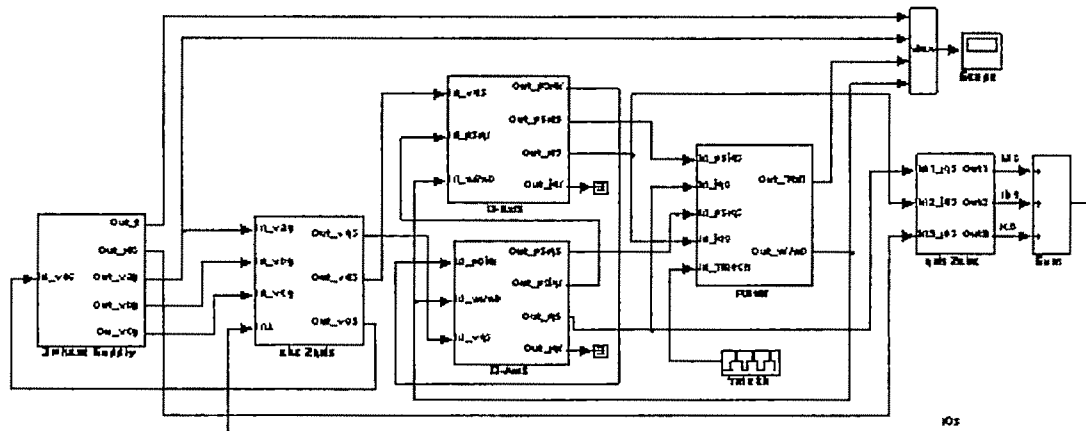


Fig.4. Simulink Induction motor model in stationary reference frame.

V. APPENDIX

Three phase 1 HP, 414V, 50 Hz, 4 pole star connected Squirrel cage Induction motor. The motor parameters are
 $R_s = 3.35 \Omega$, $R_r = 1.99 \Omega$, $L_s = 6.94 \text{ mH}$
 $L_r = 6.94 \text{ mH}$, $L_m = 163 \text{ mH}$, $J = 0.012 \text{ Kg-m}^2$

VI. CONCLUSION

This paper demonstrates that the detailed mathematical model of induction machine and using MATLAB/SIMULINK it simulate under the dynamic condition. The main variables encountered in induction machine drive, such as torque, speed, currents, voltage and flux and main advantage of using the proposed simulation environment is that these quantities can be conveniently observed, and parameters can be changed to investigate their effect to control performance. The simulation results demonstrate the versatility of the presented induction motor model.

VII REFERENCES

- [1] P C Krause and C H Thomas "Simulation of symmetrical Induction Machinery" *IEEE Trans. on power apparatus and system*. Vol. pas 84 No.11 pp-1038-1053 Nov-1965
- [2] Cheung, R W. Y.; Jin, H., Wu, B; Lavers, J D. "A generalized computer aided formulation for the dynamic and steady state analysis of induction machine inverter drive systems" *IEEE Trans. Energy Conversion EC-5* (1990) pp. 337-343
- [3] Chee-Mun Ong "Dynamic Simulation of Electric Machinery using Matlab/Simulink" Publication *Prentice Hall PTR New Jersey*
- [4] R. Krishnan "Electric Motors Drives Modeling Analysis and control" Publication *Prentice Hall of India 2002*
- [5] H.Le-Huy, "Modeling and simulation of electrical drives using Matlab/Simulink and Power System Block set," *The 27th Annual Conf. of the IEEE Int Electr. soci (IECON'01), Denver /Colorado*, pp. 1603-1611.
- [6] A Dumitrescu, D. fodor, T. Jokinen, M. Rosu and S. Bucurenciu "Modeling and Simulation of Electric Drive Systems Using Matlab/Simulink Environments" *Electric Machines and Drives, 1999. International Conf IEMD '99* 9-12 May 1999 pp 451 - 453
- [7] G R. Slemon, "Modelling Induction Machines for Electric Drives," *IEEE Trans. on Ind Applications*, Vol 25, No 6, pp 1126-1131, Nov. 1989.
- [8] R. J. Lee, P Pillay and R. G Harley "D,Q Reference Frames for the Simulation of Induction Motors" *Electric Power Systems Research*, 8 (1984/85) 15-26 Department of Elect. Engg University of Natal, King George V Avenue, Durban (South Africa) (Received April 9, 1984)

- [9] S. N. Ghani and R. Champaneri, "Dynamic models of two phase induction machines along physically existing holonomic two phase reference frame $\alpha\beta$ ", in *Proc. of Int AMSE Conf. on Modeling and Simulation*, July 1-3, 1982, Paris-Sud, vol. 6, no 6, pp. 64-86.

A PFC Based High Performance Induction Motor Drive

¹Rajesh Kumar, ²R. A. Gupta, ³S.V. Bhangale

^{1,2,3}Malaviya National Institute of Technology JLN Marg, Jaipur, INDIA

email: rkumar_mnit@rediffmail.com, Bhangale_sv@yahoo.com

Abstract— This paper presents a comprehensive analysis of vector controlled induction motor with Power Factor Corrector (PFC) circuit. In this paper, a simulink implementation of induction motor model for its vector control along with controller and PWM inverter is described. The proposed scheme also provides PFC circuit in order to improved supply power factor. Simulation results obtained show the power factor of machine becomes unity even at low speed.

Index Terms— Induction motor, Vector Control, Power Quality, THD, THC, Power factor

I. INTRODUCTION

INDUCTION motor for many years has been regarded as a workhouse in industrial application. In last decades, the induction motor has evolved from being a constant speed motor to a variable speed variable torque machine. Its evolution was challenged by the easiness of controlled dc motor at low power applications. When application required large amount of power and torque the induction motor becomes more efficient to use. With the invention of variable voltage variable frequency drives (VVVF), the use of an induction motor has increased [2].

For better understanding of implementation of vector control, a systematic modeling of induction motor drive is required which includes PID controllers, PWM inverters, Hysteresis current controller etc. The best-known controllers used in industrial control process are PID controllers because of their simple structure and robust performance over wide range of operating conditions. Design of controller depends on the proportional, integral & derivative gains [7]. The Hysteresis current regulated voltage source inverter is considered for feeding power to the Induction motor. The close loop vector control of the Induction motor is achieved through PID speed controller. The machine is operated at the desired operating conditions and the currents in the motor windings are regulated within Hysteresis band around the reference currents. The rotor speed is used as the feedback signal for the controller. In order to achieve four-quadrant operation, field oriented control or vector control is used for Induction Drive. Torque control, which forms inner loop maps directly into current loop. Speed control can conveniently achieve by closing a feedback loop around inner loop. One major disadvantage of induction motor is that it offer low power factor. At low speed power factor is even very low. In order to improve power factor a power factor correction (PFC) circuit is added to scheme

II. VECTOR CONTROL OF INDUCTION MOTOR

Induction motor is simulated in Matlab/ simulink using machine equations. Vector control also known as Field oriented control (FOC) enables the induction motor to be controlled in a method similar to a dc motor [2]. The conversion of three stator currents into two dc current enables the speed torque of the motor to be calculated in a manner similar to that in a dc motor. In FOC, there are two transformations, the first transformations convert the three-stator currents into two components and the second transformation allows the stationary reference frame to rotate synchronously with the stator flux vector. The torque is controlled by torque production current, which is the q-component of stator current space vector. At the same time, the flux is controlled by flux production current, which is the d-component of the stator current space vector. In the direct field oriented control, both the instantaneous magnitude and position of the rotor flux are supposed to be precisely known i.e. directly measured or estimated using nonlinear state observer. Theoretical study of investing the performance of induction motor driven by direct vector controller is simulated in software Matlab/simulink [3],[4],[10],[12].

III. DRIVE SCHEME

In proposed scheme as shown in Fig.1, supply voltage is rectified and is passed through power factor corrector (PFC) block. PFC block generate required dc voltage for inverter and also control power factor [2]. Inverter switching is obtained as follows motor speed is compared with reference speed and is fed through PID controller to get I_q^* and stator flux is compared with reference flux and fed to PID controller in order to generate I_d^* . These I_d^* and I_q^* are then converted in to three phase I_{abc}^* using d-q to abc transformation. Now stator current I_{abc} is compared with reference current (I_{abc}^*) and error signal is fed to Hysteresis current controller. This current controller generates firing pluses for VSI, which is used to feed supply to Induction Motor. [6], [9]

A. Modeling of Machine

An Induction Motor model can be represented with differential equations as given in [14]. By using the d-q equivalent circuit and the equations [13] the simulink model of Induction machine is shown in Fig.2

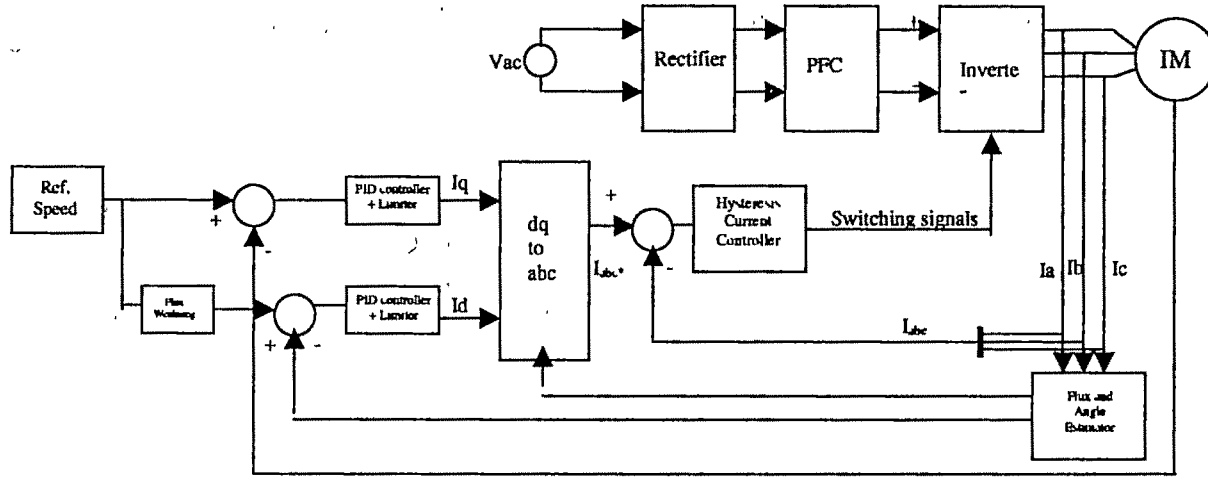


Fig 1 Drive Scheme

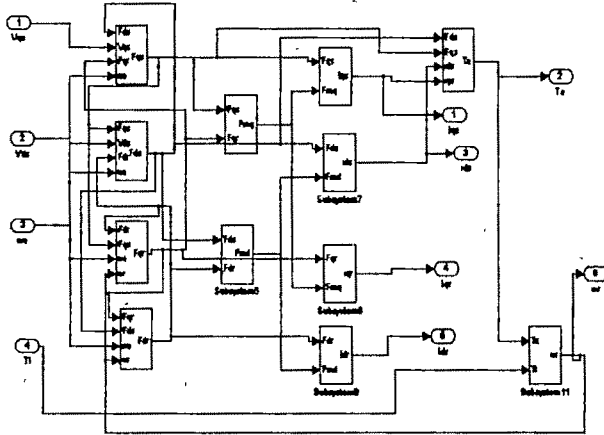


Fig 2. Simulink model of induction machine

B. Flux linkage calculation block

$$\text{Flux} = L_m * I_d / (1 + T_r * s) \quad (1)$$

$$T_r = L_r / R_r, L_r = L_l' + L_m \quad (2)$$

Theta is calculated by using below equations

$$\text{Theta} = \int (\omega_r + \omega_m) dt \quad (3)$$

$$\omega_r = L_m * I_q / (T_r * \text{flux}) \quad (4)$$

Where L_m = mutual induction, Theta = Electrical angle, ω_m = Rotor mechanical speed (rad/s), I_d = d component of stator current, T_r = Time constant, L_r = Inductance of Rotor, R_r = Resistance of Rotor

C. Hysteresis current controller and PWM Inverter

Basically a current controller is usually preferred to follow the current command in some apparatus. The current control technique plays an important role in PWM inverters. Various techniques for current controller have been proposed in recent

year. Considering easy implementation, quick response, maximum current limit and insensitivity to load parameter variation, the Hysteresis controller is a popular option [6]. Following equations are used for firing the inverter for one phase. Similar equations can be obtained for other phases.

$$\text{If } (i_a^* - i_a) > -h \text{ then } s_1 = 1 \quad (5)$$

$$\text{If } (i_a^* - i_a) \leq -h \text{ then } s_1 = 0 \quad (6)$$

Where h is width of hysteresis band.

The Hysteresis current controller contributes to the generation of switching pattern for inverter. Following equations represent the output of inverter.

$$V_{as} = V_{dc}/3(2s_1 - s_2 - s_3) \quad (7)$$

$$V_{bs} = V_{dc}/3(-s_1 + 2s_2 - s_3) \quad (8)$$

$$V_{cs} = V_{dc}/3(-s_1 - s_2 + 2s_3) \quad (9)$$

Where V_{as} , V_{bs} , and V_{cs} are three phase stator voltages.

IV. POWER FACTOR CORRECTION (PFC) CIRCUIT

The converter is controlled using a proportional-integral-derivative (PID) controller to regulate its output DC link voltage [4]. DC link voltage is compared with reference voltage and error is fed to PID controller. The output of the PID controller is passed through a limiter to produce peak amplitude of inductor reference current (I_{ln}^*). This amplitude is then multiplied by a rectified unit sinusoidal template (obtained from AC mains) to derive the rectified sinusoidal reference current (i_l^*). A hysteresis current controller is used to derive the gating signal for a switch of the converter. Inductor current is compared with inductor reference current and according to error of these to current HCC generates the switching for switch S.

In response to the gating signal of the switch, the converter regulates the DC link voltage even under nonlinear load of an inverter fed Induction Motor drive and in face of fluctuations in supply voltage. It also ensures that the converter draws unity power factor sinusoidal current from the AC mains.

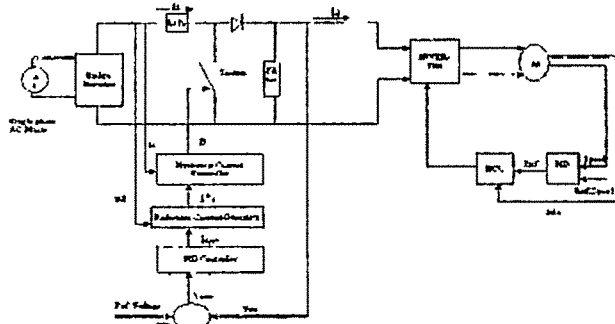


Fig 3 Power Factor Correction Circuit

A. Modeling of PID controller

The transfer function of a PID controller has the following form

$$G(s) = K_p + \frac{K_i}{s} + K_d s \quad (11)$$

In the time domain equation of PID controller can be written as

$$U(t) = K_p(t) \times e(t) + K_i(t) \int e(t) dt + K_d \frac{de(t)}{dt} \quad (12)$$

Where K_p , K_i and K_d are the proportional, integral and derivative gains respectively

B. Voltage Controller for dc Link Reference Inductor Current

The error between reference (V_{dc}^*) and sensed value of (V_{dc}) of dc link voltage acts as an input to the PID voltage controller [4].

The error in the dc link voltage at n^{th} instant is given by:

$$V_{dce(n)} = V_{dc}^* - V_{dc(n)} \quad (13)$$

The reference inductor current is estimated as:

$$i_i^* = I_{im} U_d \quad (14)$$

Where $U_d = \frac{v_d}{V_{sm}}$, $v_d = |v_s|$

$$v_s = V_{sm} \sin(\omega t), \omega = \text{Supply frequency in rad/sec.}$$

C. Hysteresis Current Controller of PFC Converter

The switching signal of the MOSFET of a PFC converter is generated using hysteresis current control as:

$$\text{If } k(i_i^* - i_i) > -h \text{ then } S=1 \quad (15)$$

$$\text{If } k(i_i^* - i_i) \leq -h \text{ then } S=0 \quad (16)$$

Where i_i = Inductor current, k = Gain factor for a amplifying the current error

D. The PFC Converter

The PFC converter is represented by two first order differential equations of inductor current and dc link capacitor voltage as:

$$\frac{di_i}{dt} = \frac{(v_d - V_{dc}(1-s) - R_i i_i)}{L} \quad (17)$$

$$\frac{dV_{dc}}{dt} = \frac{(i_i(1-s) - i_d)}{C} \quad (18)$$

Where R_i = Resistance of the inductor coil.

C = dc link capacitance.

i_d = dc link load current (chopper input current)

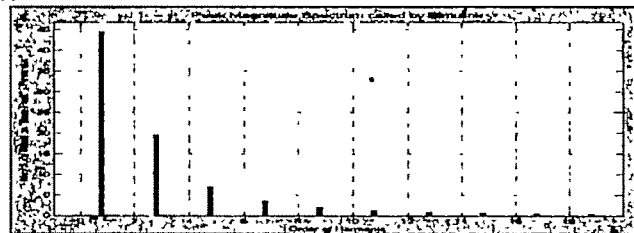
V. RESULTS AND DISCUSSIONS

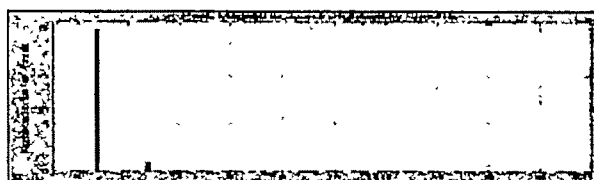
Performance of drive is examined with PFC (WPFC) and without PFC (WOPFC) converter under full load condition. Table-I shows the variations of various parameters WPFC and WOPFC.

TABLE I

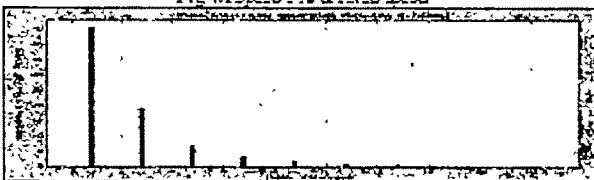
Speed % Of Rated	WPFC/ WOPFC	PF	THD	Crest factor	RMS	Peak
100	WOPFC	0.81	0.31	1.645	44.36	73.0
	W PFC	1	0.09	1.477	25.05	37.0
80	WOPFC	0.78	0.34	1.654	41.58	68.8
	WPFC	1	0.08	1.483	21.71	32.2
50	WOPFC	0.72	0.41	1.642	38.25	62.8
	WPFC	1	0.08	1.488	17.0	25.3
30	WOPFC	0.67	0.46	1.619	36.55	59.2
	W PFC	1	0.08	1.4265	14.02	20
15	WOPFC	0.63	0.5	1.60	35.49	56.8
	WPFC	1	0.08	1.4966	11.96	17.9
5	WOPFC	0.60	0.52	1.5825	34.88	55.2
	WPFC	1	0.09	1.51	10.6	16

Fig. 4.1-4.6 shows the harmonics pattern of supply current at different speed as percentage of rated with and without PFC circuit. The comparison is carried out in terms of Crest factor, which is ratio of peak current and rms current. From graph we can easily conclude that there is reduction in harmonics. This is also shown in tabular form in Table 1. Power factor of machine reduced from 0.81 at rated speed to 0.5 at 5% of rated speed but by using PFC power factor remains unity. Variations of various Supply Current parameters with Speed are shown in Fig 5. Variations of machine parameter are also shown in Fig 6.

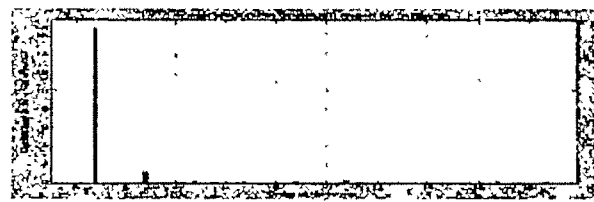




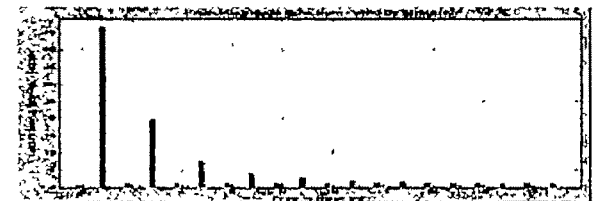
(b) Supply current harmonic spectrum with PFC
Fig 4.1 Speed 5% of rated speed



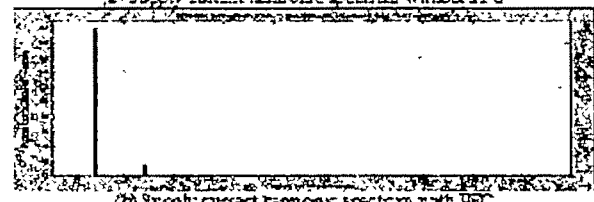
(a) Supply current harmonic spectrum without PFC



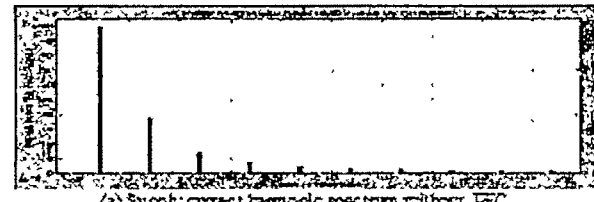
(b) Supply current harmonic spectrum with PFC
Fig 4.2 Speed 15% of rated speed



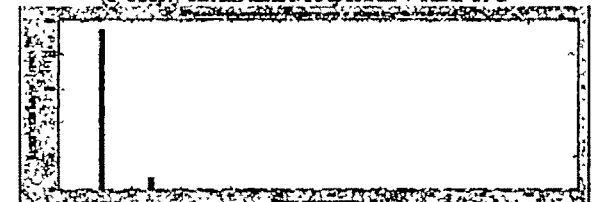
(a) Supply current harmonic spectrum without PFC



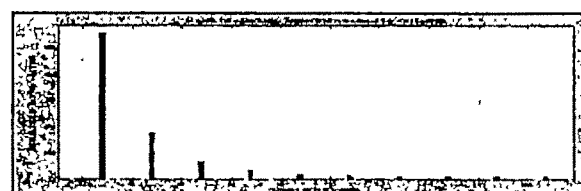
(b) Supply current harmonic spectrum with PFC
Fig 4.3 Speed 30% of rated speed



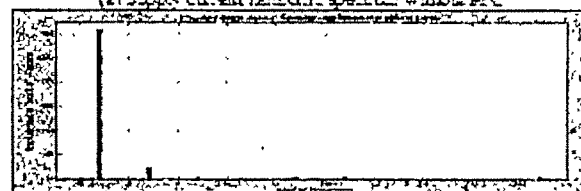
(a) Supply current harmonic spectrum without PFC



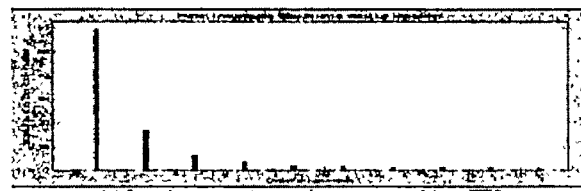
(b) Supply current harmonic spectrum with PFC
Fig 4.4 Speed 50% of rated speed



(a) Supply current harmonic spectrum without PFC



(b) Supply current harmonic spectrum with PFC
Fig 4.5 Speed 80% of rated speed



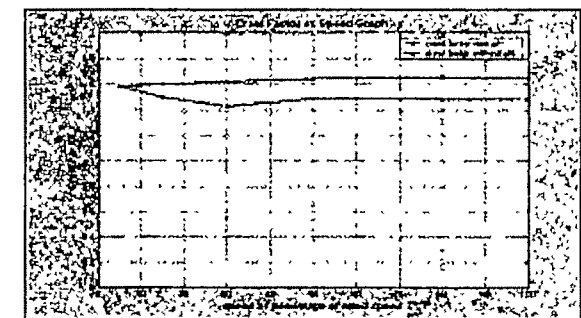
(a) Supply current harmonic spectrum without PFC



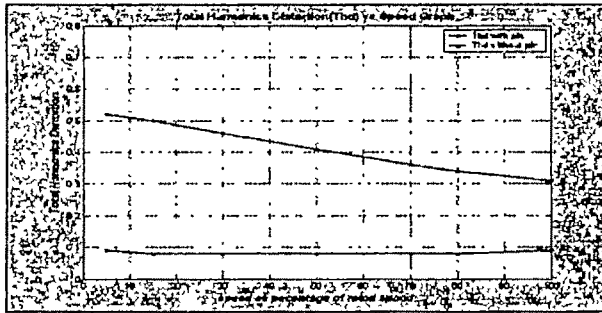
(b) Supply current harmonic spectrum with PFC
Fig 4.6 Speed 100% of rated speed



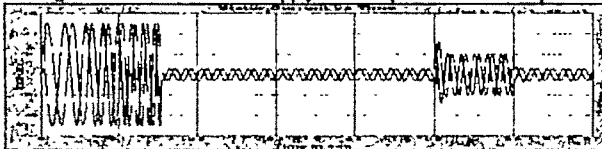
(a) Power factor vs Speed Graph



(b) Crest Factor vs Speed Graph



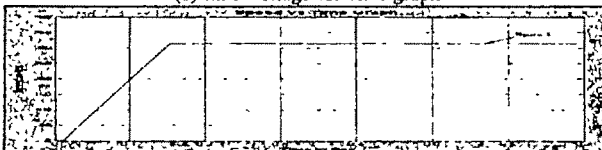
(c) Total Harmonics distortion vs Speed Graph
Fig 5 Variations of various Supply Current parameters with Speed



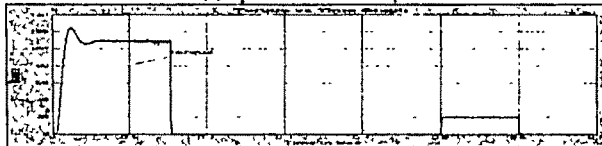
(a) Line Voltage vs. Time graph



(b) Line Voltage vs. Time graph



(c) Speed vs. Time Graph



(d) Torque vs. Time Graph

Fig 6 Variations of various parameter of machine when speed is 314 rps

VI. APPENDIX

Motor Parameters refer to stator side: Rated power 30 hp, Rated Voltage 230v, $r_s=1.106$, $r_r=0.332$, $x_l=1.106$, $x_r=0.464$, $x_m=26.3$, $J=0.01$, $f_b=100$, $f_r=50$, $p=2$

VII. REFERENCES

- [1] L-Tang, M F Rahman, "A New direct torque control strategy for flux and torque ripple reduction for induction motor drive- a matlab/simulink model", IEEE international electrical machine and drive conference 2001 pp 884-890
- [2] Bimal K Bose, "Modern Power electronics and ac drives", Prentice Hall, 2002
- [3] H Le-Huy, " Modeling and simulation of electrical drives using matlab/simulink and power system blockset," The 27th annual conference of the IEEE industrial electronic society (IECON'01), Denver/colorado pp1603-1611
- [4] M.L Deaguar, M M .Cad, "The concept of complex transfer function applied to the modeling of induction motor," Power engineering society winter meeting 2000 pp 387-391
- [5] M A. Ouhranche, "Simulation of a direct field oriented controller for an induction motor using matlab/simulink software package", Proceeding of the IASTED international conference may 15-17, 2000
- [6] Zabanch, Ehab, "Field oriented control of a multilevel pwm inverter fed induction motor", Curtin University, western Australia 2002
- [7] B.C. Kuo, "Automatic controls system, 5th ed. Englewood cliffs NJ: Prentice- Hall, 1987.
- [8] Y. Takahansi, M.J. Rabins and D.M. Auslander, control and dynamic systems Menlo park NJ Addison-Wesley, 1970.
- [9] Z. Tan, Y. Li and M. Li, "A Direct torque control of induction motor based on three level inverter", in conf Rec IEEE PESC'2001, 2001 vol 2 pp 1435-1439
- [10] M. Depenbrock, "Direct self- control of inverter fed-machine", IEEE trans. power electronics vol 3 no. 4 pp 420-429 oct 1988
- [11] Y.S. Lai and J.H. Chen , "A new approach to direct torque control of induction motor drive for constant inverter switching frequency and torque ripple reduction," IEEE trans energy conversion vol 16 no 3 pp220-227 sept. 2001
- [12] P. Vas, "Vector control of ac machines," Oxford University Press 1990
- [13] Ozpineci B., "Simulink Implementation of Induction Modular a modular approach".IEEE 2003.pp 728-734.
- [14] P.C.Krause, Analysis of Electric Machinery, McGraw Hill Book company, 1986
- [15] Bhim Singh, B.P.Singh, M.Kumar, "PFC converter fed PMBLDC Motor Drive for Air Conditioning", IE Journal, Vol84, June 2003, pp 22-27
- [16] R.S.Rajawat, Rajesh Kumar, R.A.Gupta, "Simulation and Analysis of vector control PWM fed induction motor, IEE National conf on PEPFEM'05 ,India, Jan 28-29 ,pp 91-94

Constant v/f Control of Combined Inverter-Induction Motor Drive

S. P. Muley¹ and M. V. Aware²

¹Department of Electrical Engineering, PCE, Nagpur, shubhada_muley@rediffmail.com

²Department of Electrical Engineering, VNIT, Nagpur, mv_a_w@yaho.com

Abstract - This paper gives the analysis and simulation of a combined inverter and induction motor drive system. The overall d-q model of a voltage stiff inverter and an induction motor synchronously rotating reference frame is obtained in Matlab Simulink. The circuit represents a complete dynamic model in which a inverter voltage v_i can be any independent time function and the inverter switching is completely modeled including all harmonics. Open loop and closed loop operation is studied.

Keywords: Inverter, Induction motor, VSI, Volts/Hz control

I. INTRODUCTION

INVERTER - Fed induction motors are taking an increasing share of the variable speed drive market. There are applications for reduced dynamic requirements such as standard industrial drives, or pump and fan drives operating at a maximum efficiency point. These are mainly low cost solutions based on constant volts/hertz control.

For inverter fed drive systems requiring high dynamic performance, induction machines are modeled using d-q (Park's) transformation in arbitrary reference frame [1]-[2]. For analysis of motor drives, it is useful to model the inverter in the same reference frame as the induction motor, i.e. in terms of d,q,o components. This type of modeling is particularly useful when combined performance of the motor with the inverter [1]-[3] is required. This paper presents the analysis of constant volts/Hz controlled drive using combined inverter and induction motor model in synchronously rotating reference frame.

II. V/f controlled Induction Motor Drive

A simplified diagram of the system studied is as shown in the figure 1. It consists of a dc source, an inverter and an induction motor. Closed loop speed control by slip regulation of combined inverter – induction machine improves the dynamic performance [12]. The speed loop error generates the slip command ω_s through a proportional-integral (P-I) controller and limiter. The slip is added to the speed feedback speed signal to generate the slip frequency command. The frequency command ω_c also generates the voltage command through a volts/Hz generator

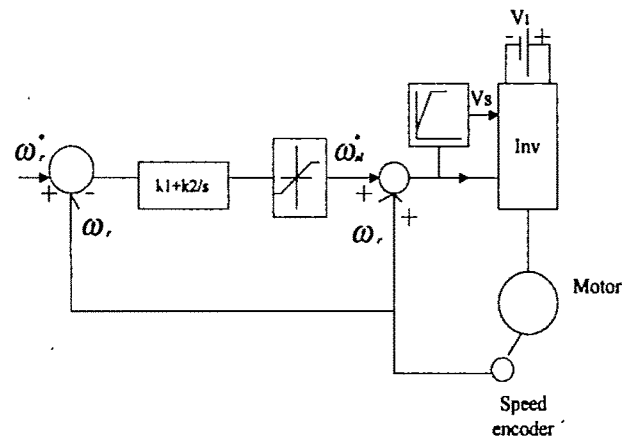


Fig. 1 System studied

III. Modeling of Inverter

The d, q model for a voltage source inverter (VSI) inverter is obtained by simply applying the d,q transformation to the inverter equations on a mode by mode basis. The d-q equations for the six modes of a voltage source inverter can be obtained as shown in equations given below (1-4). The d-q voltages for different switch positions can be expressed as space vectors. The synchronous reference frame is more useful for induction motor-inverter simulation. The switching functions in the synchronous reference frame can be derived as shown in fig.2.

$$g_{qs}^* = 1 + \frac{2}{35} \cos 6\omega_e t - \frac{2}{143} \cos 12\omega_e t + \dots \quad (1)$$

$$g_{ds}^* = \frac{12}{35} \sin 6\omega_e t - \frac{24}{143} \sin 12\omega_e t + \dots \quad (2)$$

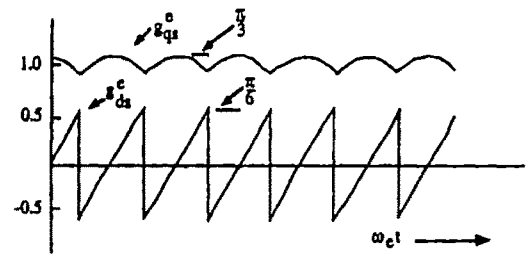


Fig. 2 The synchronous frame VSI switching function formulation

Therefore the d,q relations for the VSI inverter can be conveniently described with the two switching functions

$$v_q^* = \frac{2}{\pi} v_i g_q^* \quad \dots\dots\dots 3$$

$$\frac{\pi}{3} i_i = i_q^* g_q^* + i_d^* g_d^* \quad \dots\dots\dots 4$$

Where v_i & i_i are the dc link voltage & current respectively.

IV. Combined Inverter –Induction Motor Model.

A very useful and compact form of the machine equations for uniform air-gap machines in freely rotating reference frame is obtained as given. In majority of cases the machine is connected in delta or wye [11]. The currents i_{ω} and $i_{\omega'}$ are identically zero & the equations can be written in matrix form as

$$\begin{bmatrix} v_d \\ v_q \\ v_d' \\ v_q' \end{bmatrix} = \begin{bmatrix} r_s + L_s p & -\omega L_m & L_m p & -\omega L_m \\ -\omega L_m & r_s + L_s p & -\omega L_m & L_m p \\ L_m p & (\omega - \omega_r) L_m & r_r' + L_r' p & (\omega - \omega_r) L_r' \\ -(\omega - \omega_r) L_m & L_m p & -(\omega - \omega_r) L_r' & r_r' + L_r' p \end{bmatrix} \begin{bmatrix} i_d \\ i_q \\ i_d' \\ i_q' \end{bmatrix}$$

where

$$\begin{aligned} L_r' &= L_r + L_m \\ L_s &= L_s + L_m \end{aligned} \quad \dots\dots\dots 5$$

$$T_e = T_L + \frac{2}{p} J \frac{d\omega_r}{dt} \quad \dots\dots\dots 6$$

Where p is the operator d/dt , r_s is the stator resistance, r_r' is the rotor resistance (referred to the stator winding) and L_s , L_r' & L_m are the stator & rotor leakage reactances & magnetizing reactance respectively. T_L is the per unit load torque. J is the moment of inertia. P is the no of pole pairs.

ω_r is the rotor speed & ω is the speed of the synchronously rotating reference frame.

However, this model proves inadequate when applied to dynamic conditions as encountered in a variable frequency drive. The over all d-q model of a voltage source inverter and an induction motor is obtained. The circuit represents a complete dynamic model in which a inverter voltage (V_i) can be any independent time function and the inverter switching is completely modeled including all harmonics. The model of the machine and the switching functions can be represented in synchronously rotating reference frame.

The inverter d-q model thus obtained can be combined with induction motor model. The Fig.3 shows the model of the machine and the switching function in the synchronous frame.

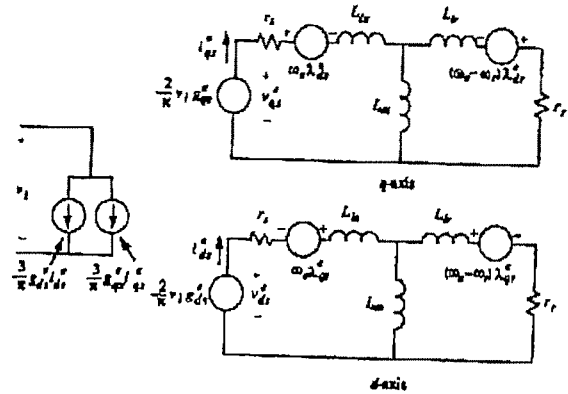


Fig. 3 Synchronous frame d,q model of a VSI driven induction machine

V. Analysis of d-q model

Analysis of combined inverter- induction motor d-q model in synchronous reference frame in open loop as well as in closed loop (V/f control) is carried out in Matlab Simulink using 5 hp induction machine with parameters given in Table-2. The open loop operation is studied. The inverter switching function formulation gives the d-q voltages, which is applied to the induction machine. The closed loop V/f control of inverter – IM model simulations are obtained. A closed loop V/f control with simplified d-q model of VSI driven IM in synchronously rotating reference frame is simulated as shown in fig.4. The performance is tested for a change in reference frequency from 5 Hz to 50Hz

TABLE-1: IM Parameters

3 phase, 230V, 60 Hz, 4 pole, 5 hp induction machine

Rr=0.408	Rs=0.531
Llr=0.00252	Lls=0.00252
Lm=.00847	J=0.1

The switching function formulation of the inverter in synchronously rotating reference frame described by equations 1 & 2 is shown in figure 5. The d-q voltages obtained is applied to the combined model of the inverter and induction motor and is simulated in Matlab Simulink in open loop & in closed loop. The stator currents for the closed loop constant v/f operation of the induction machine and inverter is presented in figure 6. The rotor speed and electromagnetic torque for the same machine is shown in figure 7 & 8. The dynamic test is carried out on the by applying the step change in frequency as shown in fig.9.

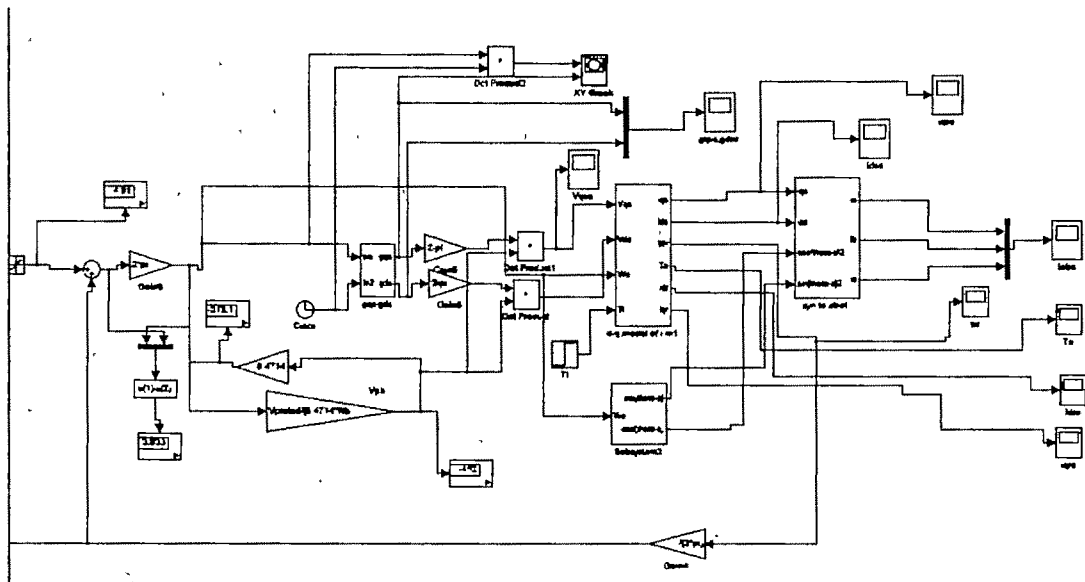


Fig. 4 Closed loop V/F control of induction motor with d-q model of inverter in synchronously rotating reference frame

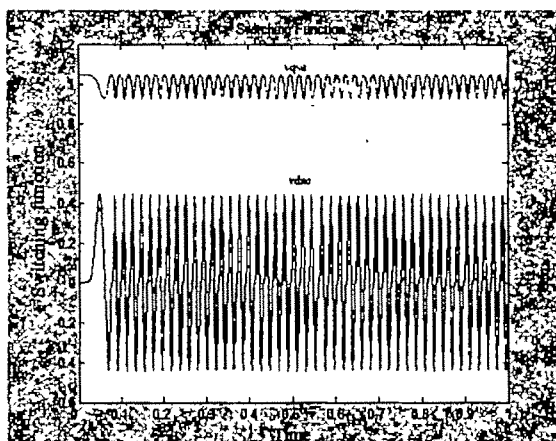


Fig 5 Inverter switching function formulation in synchronously rotating reference frame

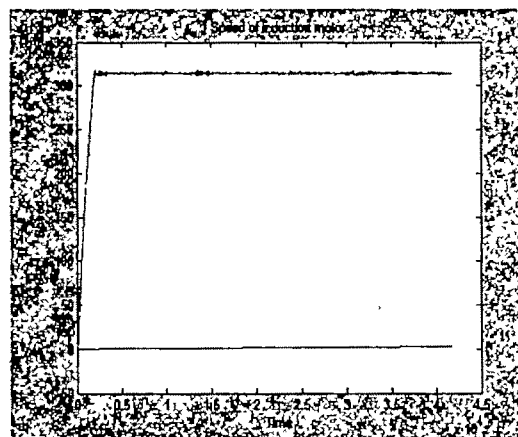


Fig 7 Rotor speed of combined inverter – induction motor d-q model in synchronous reference frame using closed loop v/f control.

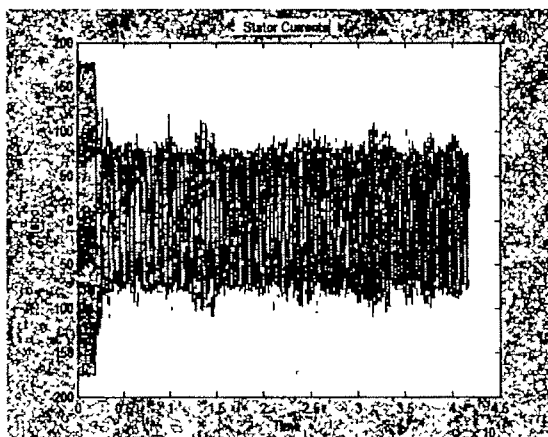


Fig 6 Stator currents of combined inverter – induction motor d-q model in synchronous reference frame using closed loop v/f control

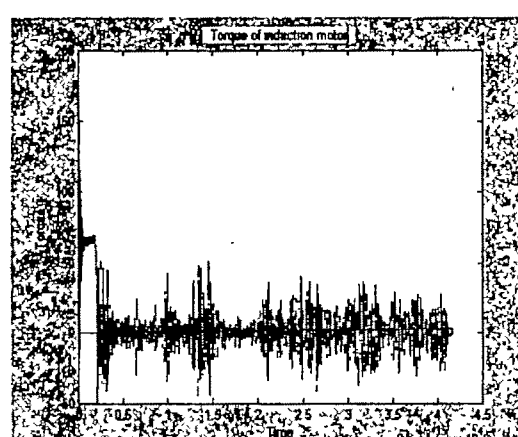


Fig 8 Electromagnetic torque of combined inverter – induction motor d-q model in synchronous reference frame using closed loop v/f control.

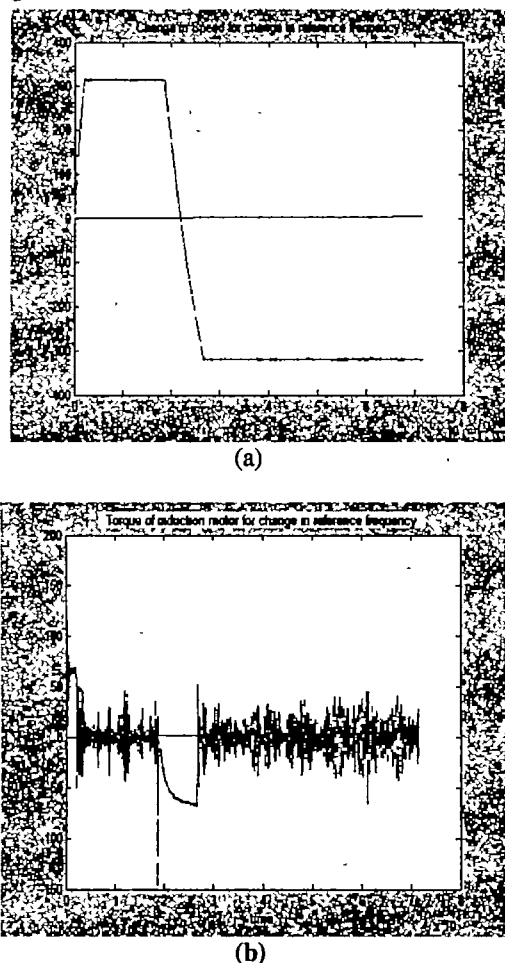


Fig.9 Closed loop V/f control with simplified d-q model of VSI driven IM in synchronously rotating reference frame for a change in reference frequency from 50 Hz to -50Hz (a) Rotor speed (b) Electromagnetic torque

VI. CONCLUSION

In this method of analysis the equations which describe the induction machine in synchronously rotating reference frame are related to the equations which express the average value of the converter variables. Performance of the induction motor is carried under dynamic condition which is satisfactory and hence the model presented was satisfactory. Open loop and closed loop operation is studied. Combined model of the inverter and induction motor, simulated in Matlab Simulink gives better dynamic performance.

REFERENCES

1. T.A. Lipo & P.C. Krause, "Stability analysis of a Rectifier-Inverter Induction Motor Drive", IEEE Trans. On Power Apparatus and systems, vol. PAS-88, no.1, Jan 1969.
2. T.A. Lipo & P. C. Krause, "Stability analysis of a Symmetrical Induction Machine", IEEE Trans. On Power Apparatus and systems, vol. PAS-88, no.11, Jan 1969.
3. H. S. Chikwanda, H. R. Bolton, "Analysis of the naturally commutated, converter fed Induction motor drive system using a flux vector method", IEE proceedings-B, VOL.140, No. 6, Nov.1993.
4. Scott D. Sudoff, D. C. Aliprantis, B. T. Kuhn, P. I. Chapman, "An Induction machine model for predicting inverter machine

- interaction", IEEE Trans. On Energy Conversions, vol.17, no.2, June 2002.
5. G. R. Slemon, "Modelling of Induction machines for Electric Drives", 0093-9994/1989 IEEE
6. R. J. Kerkman, B. J. Siebel, "A Simplified Inverter model for online control and simulation", 0093-9994/91 @ 1991 IEEE
7. T. A. Lipo and P. C. Krause, "Stability analysis of a reluctance synchronous machine," IEEE Trans. Power Apparatus and Systems, vol. PAS-86, pp. 825-834, July 1967.
8. R. G. Hoft, "Liapunov stability analysis of reluctance motors," IEEE Trans. Power Apparatus and Systems, vol. PAS-87, pp.1485-1491, June 1968.
9. T. A. Lipo and P. C. Krause, "Stability analysis for variable frequency operation of synchronous machines," IEEE Trans. Power Apparatus and Systems, vol. PAS-87, pp. 227-234, January 1968.
10. G. J. Rogers, "Linearised analysis of induction-motor transients," Proc. IEE (London), vol. 112, pp. 1917-1926, October 1965.
11. P. C. Krause and C. H. Thomas, "Simulation of symmetrical induction machinery," IEEE Trans. Power Apparatus and Systems, vol. PAS-84, pp. 1038-1053, November 1965.
12. Jee-Hoon Jung, Gang-Youl Jeong, Bong-Hwan Kwon, "Stability improvement of V/f controlled Induction motor drive system by a dynamic current compensator", IEEE Transactions on Industrial Electronics, vol. 51 no. 4, August 2004.

Observer-Based Sensorless Control of A Vector Controlled Five-Phase Induction Motor Drive

M. Rizwan Khan, Atif Iqbal, Mukhtar Ahmad

Department of Electrical Engineering, Aligarh Muslim University, Aligarh, 202002, India
rizwan_ee@rediffmail.com, atif_iqbal1@rediffmail.com

Abstract: Multi-phase ac motor drives are nowadays considered for various applications, due to numerous advantages that they offer when compared to their three-phase counterparts. In principle, control methods for multi-phase machines are the same as for three-phase machines. Variable speed induction motor drives without mechanical speed sensors at the motor shaft have the attractions of low cost and high reliability. To replace the sensor, information of the rotor speed is extracted from measured stator currents and voltages at motor terminals. Vector-controlled drives require estimating the magnitude and spatial orientation of the fundamental magnetic flux waves in the stator or in the rotor. Open-loop estimators or closed-loop observers are used for this purpose. They differ with respect to accuracy, robustness, and sensitivity against model parameter variations. This paper analyses operation of an observer-based sensorless control of vector controlled five-phase induction machine with current control in the stationary reference frame. The observer-based sensorless operation of a three-phase induction machine is well established and the same principle is extended in this paper for a five-phase induction machine. Performance, obtainable with hysteresis current control, is illustrated for a number of operating conditions on the basis of simulation results. Full decoupling of rotor flux control and torque control is realised. Dynamics, achievable with a five-phase vector controlled induction machine, are shown to be essentially identical to those obtainable with a three-phase induction machine.

Keywords: Multi-phase, Full Order Observer, Vector control, Sensorless control

I INTRODUCTION

Variable speed electric drives predominately utilise the three-phase machines. However, since the variable speed ac drives require a power electronic converter for their supply (in vast majority of cases an inverter with a dc link), the number of machine phases is essentially unlimited. This has led to an increase in the interest in multiphase ac drive applications, since multiphase machines offer some inherent advantages over their three-phase counterparts. A number of interesting research results have been published over the years and detailed reviews are available in [1-7].

Major advantages of using a multi-phase machine instead of a three-phase machine are detailed in [1-7] and are higher torque density, greater efficiency, reduced torque pulsations, greater fault tolerance, and reduction in the required rating per

inverter leg (and therefore simpler and more reliable power conditioning equipment). Additionally, noise characteristics of the drive improve as well.

Sensorless vector control of three-phase induction machine has attracted wide attention in recent years [8-11]. Several attempts have been made in the past to extract the speed signal of the induction machine from measured stator currents and voltages. Initially, the sensorless techniques were restricted to techniques which are only valid in the steady-state and can only be used in low cost drive applications, not requiring high dynamic performance. Different, more sophisticated techniques are required for high performance applications in vector controlled drives [11]. In a sensorless drive, speed information and control should be provided with an accuracy of 0.5% or better, from zero to the highest speed, for all operating conditions and independent of saturation levels and parameter variations. In order to achieve good performance of sensorless vector control, different speed estimation schemes have been proposed and a variety of speed estimators exist nowadays.

Sensorless operation of a vector controlled three-phase induction machine drive is extensively discussed in the literature [12,13], but the same is not true for multi-phase induction machine. Only few application specific sensorless operation of multi-phase machine is elaborated in the literature. The problem of using the position sensor in 'more-electric' aircraft fuel pump fault tolerant drive is highlighted in [14]. The drive utilises a 16 kW, 13000 rpm six-phase permanent magnet motor with six independent single-phase inverters supplying each of the six-phases. The authors proposed an alternative sensorless drive scheme. The proposed technique makes use of flux linkage-current-angle model to estimate the rotor position.

Although several schemes are available for sensorless operation of a vector controlled drive, but the most popular is the MRAS because of ease of their implementation [15,16]. An attempt is made in this paper to extend the MRAS-based technique of a three-phase machine to an indirect field oriented five-phase induction motor drive.

It has been shown in [17] that multi-phase machine models can be transformed into a system of decoupled equations in orthogonal reference frames. The d - q axis reference frame currents contribute towards torque and flux production, whereas the remaining x - y components plus the zero sequence component do not. This allows a simple extension of the RFOC principle in that the rotor flux linkage is maintained entirely in the d -axis, resulting in the q -axis component of rotor flux being maintained at zero. This reduces the electromagnetic torque equation to the

same form as that of a dc machine or a rotor flux oriented three-phase machine. Thus the electromagnetic torque and the rotor flux can be controlled independently, by controlling the d and q components of stator current independently. The decoupled control of torque and flux using rotor flux oriented control for a five-phase induction machine is illustrated in [6].

An observer can be classified according to the type of representation used for the plant to be observed. If the plant is considered to be deterministic, then the observer is a deterministic observer; otherwise it is a stochastic observer. The most commonly used observers are *Luenberger* and *Kalman* types. The *Luenberger* observer (LO) is of the deterministic type and the Kalman filter (KF) is of the stochastic type. The basic Kalman filter is only applicable to linear stochastic systems, and for non-linear systems the extended Kalman filter (EKF) can be used, which can provide estimates of the states of a system or of both the states and parameters (joint state and parameter estimation). The EKF is a recursive filter, which can be applied to a non-linear time-varying stochastic system. The basic Luenberger observer is only applicable to a linear, time-invariant deterministic system. The extended Luenberger observer (ELO) is applicable to a non-linear, time-varying deterministic system. In summary it can be seen that both the EKF and ELO are non-linear estimators and the EKF is applicable to stochastic systems and the ELO to deterministic systems. The extended Luenberger observer (ELO) is an alternative solution for real-time implementation in industrial drive systems. The simple algorithm and the ease of tuning of the ELO may give some advantages over the conventional EKF. A full-order (fourth-order) adaptive state observer (Luenberger observer) which is constructed by using the equations of the induction machine in the stationary reference frame by adding an error compensator. In the full-order adaptive state observer the rotor speed is considered as a parameter, but in the EKF and ELO the rotor speed is considered as a state variable. It is shown that [20-22] when the appropriate observers are used in high-performance speed sensorless torque controlled induction motor drive (vector controlled drives, direct controlled drives), stable operation can be obtained over a wide speed range, including very low speeds.

A simulation study is performed for speed mode of operation, for a number of transients, and the results are reported in the paper.

II MODELLING OF A FIVE-PHASE INDUCTION MACHINE

Standard assumptions of general theory of electrical machines apply to the modelling described in what follows, including the one related to the sinusoidal spatial distribution of the field in the machine. Spatial displacement between any two consecutive phases in a five-phase machine is $\alpha = 2\pi/5$. For the sake of generality, both stator and rotor windings are assumed to be five-phase. The model of the machine, given in terms of phase variables, is transformed into a common reference frame, rotating at an arbitrary angular speed.

Model Transformation in arbitrary reference frame

Correlation between original phase variables and new variables in the arbitrary rotating reference frame is given with

$$\begin{aligned} \underline{v}_{dq}^s &= \underline{A}_s \underline{v}_{abcde}^s & \dot{\underline{i}}_{dq}^s &= \underline{A}_s \dot{\underline{i}}_{abcde}^s & \underline{\psi}_{dq}^s &= \underline{A}_s \underline{\psi}_{abcde}^s \\ \underline{v}_{dq}^r &= \underline{A}_r \underline{v}_{abcde}^r & \dot{\underline{i}}_{dq}^r &= \underline{A}_r \dot{\underline{i}}_{abcde}^r & \underline{\psi}_{dq}^r &= \underline{A}_r \underline{\psi}_{abcde}^r \end{aligned} \quad (1)$$

where the transformation matrices for stator and rotor, are given by equation (12).

$$\underline{A}_s = \sqrt{\frac{2}{5}} \begin{bmatrix} \cos \theta_s & \cos(\theta_s - \alpha) & \cos(\theta_s - 2\alpha) & \cos(\theta_s + 2\alpha) & \cos(\theta_s + \alpha) \\ -\sin \theta_s & -\sin(\theta_s - \alpha) & -\sin(\theta_s - 2\alpha) & -\sin(\theta_s + 2\alpha) & -\sin(\theta_s + \alpha) \\ 1 & \cos(2\alpha) & \cos(4\alpha) & \cos(4\alpha) & \cos(2\alpha) \\ 0 & \sin(2\alpha) & \sin(4\alpha) & -\sin(4\alpha) & -\sin(2\alpha) \\ \frac{1}{\sqrt{2}} & \frac{1}{\sqrt{2}} & \frac{1}{\sqrt{2}} & \frac{1}{\sqrt{2}} & \frac{1}{\sqrt{2}} \end{bmatrix}$$

$$\underline{A}_r = \sqrt{\frac{2}{5}} \begin{bmatrix} \cos \beta & \cos(\beta - \alpha) & \cos(\beta - 2\alpha) & \cos(\beta + 2\alpha) & \cos(\beta + \alpha) \\ -\sin \beta & -\sin(\beta - \alpha) & -\sin(\beta - 2\alpha) & -\sin(\beta + 2\alpha) & -\sin(\beta + \alpha) \\ 1 & \cos(2\alpha) & \cos(4\alpha) & \cos(4\alpha) & \cos(2\alpha) \\ 0 & \sin(2\alpha) & \sin(4\alpha) & -\sin(4\alpha) & -\sin(2\alpha) \\ \frac{1}{\sqrt{2}} & \frac{1}{\sqrt{2}} & \frac{1}{\sqrt{2}} & \frac{1}{\sqrt{2}} & \frac{1}{\sqrt{2}} \end{bmatrix} \quad (2)$$

The angles of transformation for stator quantities and for rotor quantities are related to the arbitrary speed of the selected common reference frame ω_d through:

$$\begin{aligned} \theta_s &= \int \omega_d dt \\ \beta &= \theta_r - \theta = \int (\omega_r - \omega) dt \end{aligned} \quad (3)$$

where ω and θ are rotor angular (electrical) speed and instantaneous rotor position, respectively. Application of (2) in conjunction with (1) and the phase-domain model (1-10) of a five-phase induction machine leads to the following set of equations in the arbitrary common reference frame (symbol p stands for $p = d/dt$):

$$\begin{aligned} v_{ds} &= R_s i_{ds} - \omega_d \psi_{qs} + p \psi_{ds} & v_{dr} &= R_r i_{dr} - (\omega_d - \omega) \psi_{qr} + p \psi_{dr} \\ v_{qs} &= R_s i_{qs} + \omega_d \psi_{ds} + p \psi_{qs} & v_{qr} &= R_r i_{qr} + (\omega_d - \omega) \psi_{dr} + p \psi_{qr} \\ v_{\alpha s} &= R_s i_{\alpha s} + p \psi_{\alpha s} & v_{\alpha r} &= R_r i_{\alpha r} + p \psi_{\alpha r} \\ v_{\beta s} &= R_s i_{\beta s} + p \psi_{\beta s} & v_{\beta r} &= R_r i_{\beta r} + p \psi_{\beta r} \\ v_{0s} &= R_s i_{0s} + p \psi_{0s} & v_{0r} &= R_r i_{0r} + p \psi_{0r} \end{aligned} \quad (4)$$

$$\begin{aligned} \psi_{ds} &= (L_s + L_m) i_{ds} + L_m i_{dr} & \psi_{dr} &= (L_r + L_m) i_{dr} + L_m i_{ds} \\ \psi_{qs} &= (L_s + L_m) i_{qs} + L_m i_{qr} & \psi_{qr} &= (L_r + L_m) i_{qr} + L_m i_{qs} \\ \psi_{\alpha s} &= L_s i_{\alpha s} & \psi_{\alpha r} &= L_r i_{\alpha r} \\ \psi_{\beta s} &= L_s i_{\beta s} & \psi_{\beta r} &= L_r i_{\beta r} \\ \psi_{0s} &= L_s i_{0s} & \psi_{0r} &= L_r i_{0r} \end{aligned} \quad (5)$$

$$T_e = p L_m [i_{dr} i_{qs} - i_{ds} i_{qr}] \quad (6)$$

The only difference between the five-phase machine model, given with (4)-(6), and the corresponding three-phase machine

model is the presence of x-y component equations in (4) and (5). Rotor x-y components are fully decoupled from d-q components and one from the other. Since rotor winding is short-circuited, x-y components cannot appear in the rotor winding. Zero sequence component equations for both stator and rotor can be omitted from further consideration due to short-circuited rotor winding and star connection of the stator winding. Finally, since stator x-y components are fully decoupled from d-q components and one from the other and vector control is applied (i.e. only d-q axis current components are generated), the equations for x-y components can be omitted from further consideration as well. This means that the model of the five-phase induction machine in an arbitrary reference frame becomes identical to the model of a three-phase induction machine. Hence the same principles of RFOC can be utilised, as for a three-phase induction machine.

III. VECTOR CONTROL OF A FIVE-PHASE INDUCTION MACHINE

Indirect rotor flux oriented control, with current control in stationary reference frame, is studied further on. The indirect rotor flux oriented controller is shown in Fig. 1.

Operation in the base speed region only is assumed, so that the rotor flux reference (and consequently stator d-axis current reference) is constant at all times.

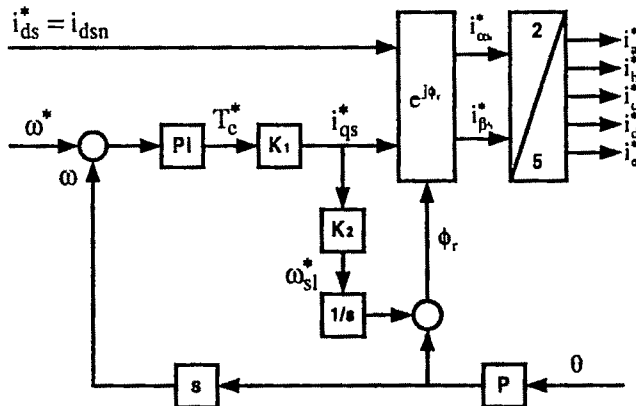


Fig. 1 Indirect rotor flux oriented controller for a five-phase induction machine (symbol * denotes references and parameters of the controller).

The two constants of Fig. 1 are determined with machine parameters and are equal to:

$$\begin{aligned} i_{q^*}^* &= K_1 T_e^* \Rightarrow K_1 = i_{q^*}^* / T_e^* = \frac{1}{P} \frac{L_r}{L_m} \frac{1}{\psi_r^*} = \frac{1}{P} \frac{L_r}{L_m^2} \frac{1}{i_d^*} \\ \omega_{sl}^* &= K_2 i_{q^*}^* \Rightarrow K_2 = \omega_{sl}^* / i_{q^*}^* = \frac{L_m}{T_r \psi_r^*} = \frac{1}{T_r i_d^*} \end{aligned} \quad (7)$$

The five-phase voltage source inverter is controlled using hysteresis current control and closed-loop speed control is investigated. The relationship between the star connected machine phase-to-neutral voltages and inverter leg voltages is given with

$$\begin{aligned} v_a &= (4/5)v_A - (1/5)(v_B + v_C + v_D + v_E) \\ v_b &= (4/5)v_B - (1/5)(v_A + v_C + v_D + v_E) \\ v_c &= (4/5)v_C - (1/5)(v_A + v_B + v_D + v_E) \\ v_d &= (4/5)v_D - (1/5)(v_A + v_B + v_C + v_E) \\ v_e &= (4/5)v_E - (1/5)(v_A + v_B + v_C + v_D) \end{aligned} \quad (8)$$

where capital letters denote inverter leg voltages (which take the value of either dc link voltage or zero) and lower case indices denote phase-to-neutral voltages of the machine.

IV. SENSORLESS OPERATION OF FIVE-PHASE INDUCTION MACHINES

The developed model of a five-phase induction motor indicates that an observer used for three-phase machines can be easily extended to multi-phase machines. For multi-phase machines observer-based speed estimator requires only d and q components of stator voltages and currents. The model of a five-phase induction machine (4-6), it has been shown that the stator and rotor d and q axis flux linkages are function of magnetising inductance L_m and stator and rotor d and q axis currents, where as the x and y axis flux linkages are function of only their respective currents. Therefore in speed estimation for multi-phase machine the x and y components of voltages and currents are not required. The speed can be estimated using only d and q components of stator voltages and currents.

The proposed full order observer-based five-phase vector controlled induction motor drive structure with current control in the stationary reference frame is shown in Fig. 2.

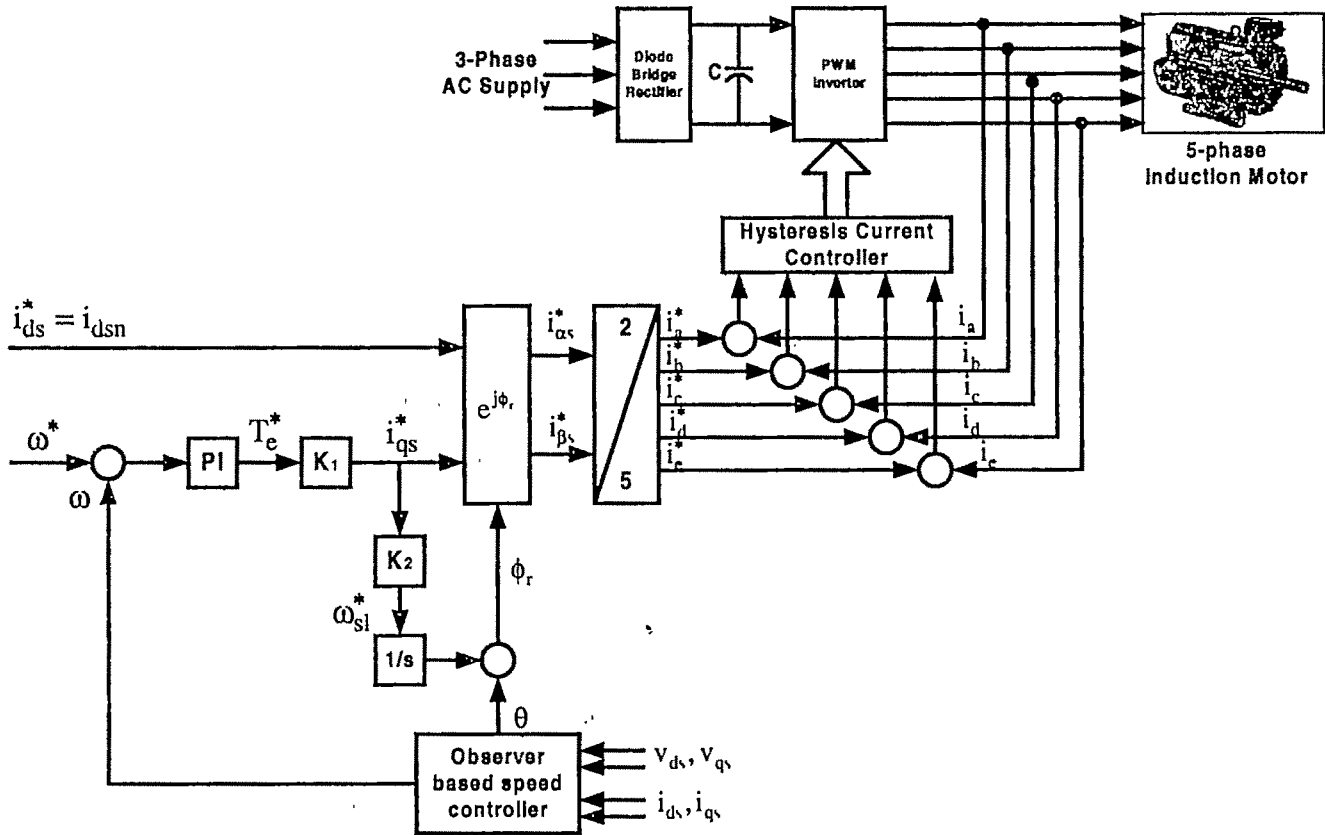


Fig. 2 Observer-based five-phase induction motor drive structure with current control in the stationary reference frame.

V. OBSERVER-BASED SPEED ESTIMATOR

A state observer is a model-based state estimator which can be used for the state and/or parameter estimation of a non-linear dynamic system in real time. In the calculations, the states are predicted by using a mathematical model ; but the predicted states are continuously corrected by using a feed back correction scheme. The actual measured states are denoted by x and the estimated states by \hat{x} . The correction term contains the weighted difference of some of the measured and estimated outputs signals (the difference is multiplied by the observer feedback gain, G). The accuracy of the state observer also depends on the model parameters used. The state observer is simpler than the Kalman observer, since no attempt is made to minimize a stochastic cost criterion.

To obtain the full-order non-linear speed observer, first the model of the induction machine is considered in the stationary reference frame, which can be described as follows:

$$\frac{dx}{dt} = Ax + Bv \quad (9)$$

and the output vector is

$$\dot{i}_s = Cx \quad (10)$$

By using the derived mathematical model of the induction machine, e.g. if the component form of the equations(9), is used, since this is required in an actual implementation and adding the correction term, which contains the difference of actual and estimated states, a full-order state observer, which estimates the stator currents and rotor flux linkages, can be described as follows:

$$\frac{d\hat{\mathbf{x}}}{dt} = \mathbf{A}\hat{\mathbf{x}} + \mathbf{B}\mathbf{v} + \mathbf{G}(\mathbf{i}_s - \hat{\mathbf{i}}_s) \quad (11)$$

and the output vector is

$$\hat{\mathbf{i}}_s = \mathbf{C}\hat{\mathbf{x}} \quad (12)$$

where A is a state matrix, B is the input matrix, G is the observer gain matrix, C is the output matrix, x is the state vector, v is the input vector, i , stator current vector.

Also the state matrix of the observer (\hat{A}) is a function of the rotor speed, and in a speed –sensorless drive, the rotor speed must be estimated. The estimated rotor speed is denoted by $\hat{\omega}_r$, and in general \hat{A} is a function of $\hat{\omega}_r$. The estimated speed is considered as a parameter in \hat{A} , however in extended Kalman filter considered as a state variable. In eqns (9) and (10) the different terms are explained as follows:

$$\begin{aligned}
\hat{A} &= \begin{bmatrix} -[1/T'_s + (1-\sigma)/T'_r]I_2 & [L_m/(L'_s L_r)]I_2/T_r - \hat{\omega}_r J \\ L_m I_2/T_r & -I_2/T_r + \hat{\omega}_r J \end{bmatrix} \\
B &= [I_2/L'_s, O_2]^T \\
C &= [I_2, O_2]^T \\
v &= v_s = [v_{ds}, v_{qs}]^T \\
\hat{x} &= [\hat{i}_s, \hat{\psi}_r]^T \\
i_s &= [i_{ds}, i_{qs}]^T, \quad \hat{i}_s = [\hat{i}_{ds}, \hat{i}_{qs}]^T \\
J &= \begin{bmatrix} 0 & -1 \\ 1 & 0 \end{bmatrix}
\end{aligned} \tag{13}$$

$I_2 = \text{diag}(1,1)$, is a second order identity matrix.

O_2 , is a 2x2 zero matrix.

In state matrix \hat{A} , the different terms are as follows:

L_m and L_r are the magnetising inductance and rotor self-inductance respectively, L'_s is the stator transient inductance, $T'_s = L'_s/R_s$ and $T'_r = L'_r/R_r$ are the stator and rotor transient time constants respectively, and $\sigma = 1 - L_m^2/(L_s L_r)$ is the leakage factor.

The observer gain matrix is defined as

$$G = -\begin{bmatrix} g_1 I_2 + g_2 J \\ g_3 I_2 + g_4 J \end{bmatrix}$$

which yields a 2x4 matrix. The four gains in G can be obtained from the eigen-values of the induction motor as follows:

$$\begin{aligned}
g_1 &= -(k-1)\left(\frac{1}{T'_s} + \frac{1}{T'_r}\right) \\
g_2 &= (k-1)\hat{\omega}_r \\
g_3 &= (k^2 - 1)\left\{-\left[\frac{1}{T'_s} + \frac{(1-\sigma)}{T'_r}\right]\frac{L'_s L_m}{L_r} + \frac{L_m}{T_r}\right\} \\
&\quad + \frac{L'_s L_m}{L_r}(k-1)\left(\frac{1}{T'_s} + \frac{1}{T'_r}\right) \\
g_4 &= -(k-1)\hat{\omega}_r \frac{L'_s L_m}{L_r}
\end{aligned} \tag{14}$$

It follows that the four gains depend on the estimated speed, $\hat{\omega}_r$. By using eqns (9) and (10) it is possible to implement a speed estimator which estimates the rotor speed of an induction machine by using the adaptive state observer shown in Fig. 3.

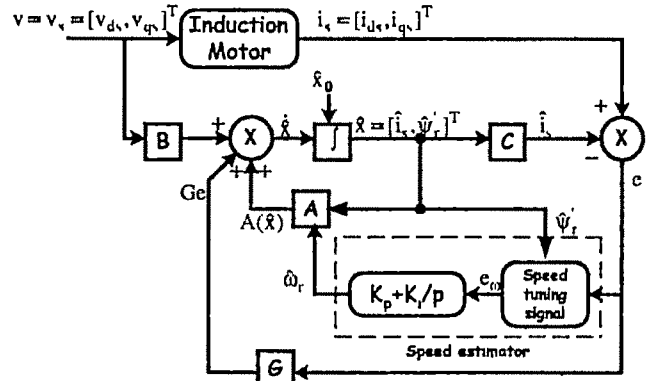


Fig. 3 Adaptive speed observer (speed-adaptive flux observer)

In Fig. 3 the estimated rotor flux-linkage components and the stator current error components are used to obtain the error speed tuning signal and given by equations:

$\hat{\psi}_r = \hat{\psi}_{dr} + j\hat{\psi}_{qr}$ and $e = e_{ds} + je_{qs}$. The estimated speed is obtained from the speed tuning signal by using a PI controller thus,

$$\hat{\omega}_r = K_p(\hat{\psi}_{qr}e_{ds} - \hat{\psi}_{dr}e_{qs}) + K_i \int (\hat{\psi}_{qr}e_{ds} - \hat{\psi}_{dr}e_{qs})dt \tag{15}$$

where K_p and K_i are proportional and integral gain constants respectively, $e_{ds} = i_{ds} - \hat{i}_{ds}$ and $e_{qs} = i_{qs} - \hat{i}_{qs}$ are the direct and quadrature axis stator current errors respectively. The adaptation mechanism is similar to that as used in the MRAS-based speed estimators, where the speed adaptation has been obtained by using the state-error equations of the system considered.

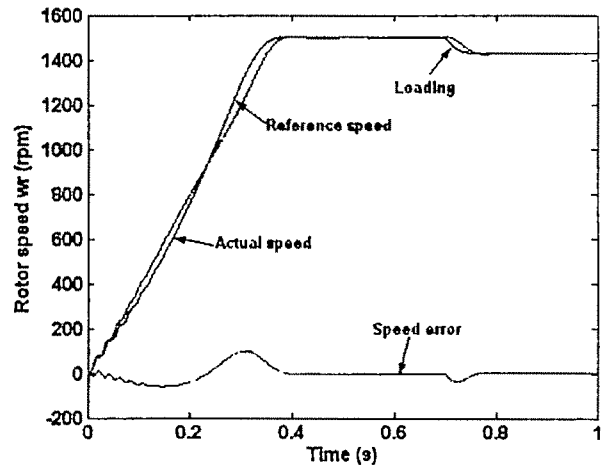


Fig. 4 Induction motor speed characteristics for direct mains fed

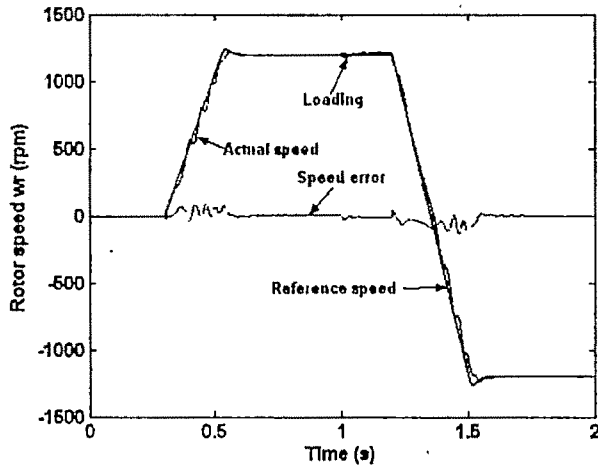


Fig. 5 Induction motor speed characteristics

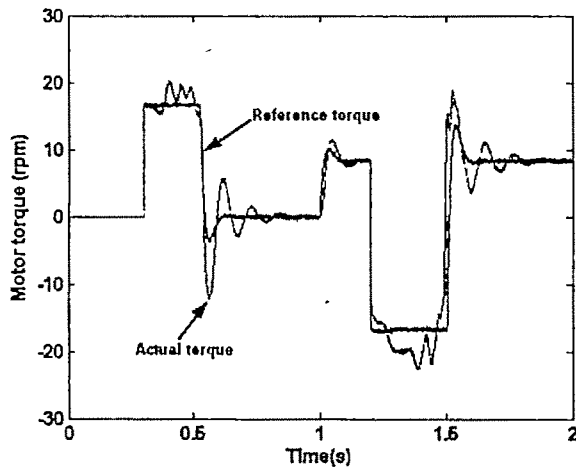


Fig. 6 Induction motor torque characteristics

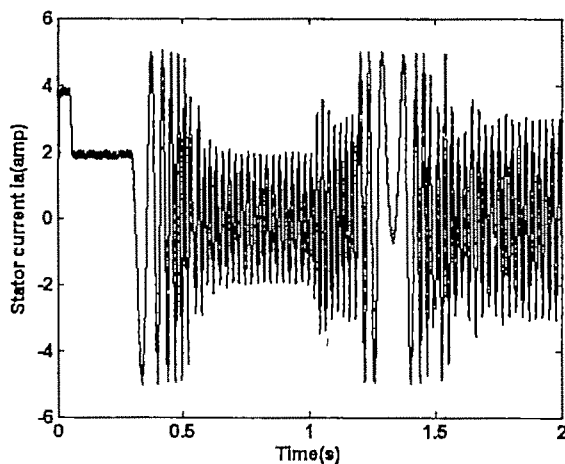


Fig. 7 Induction motor current characteristics

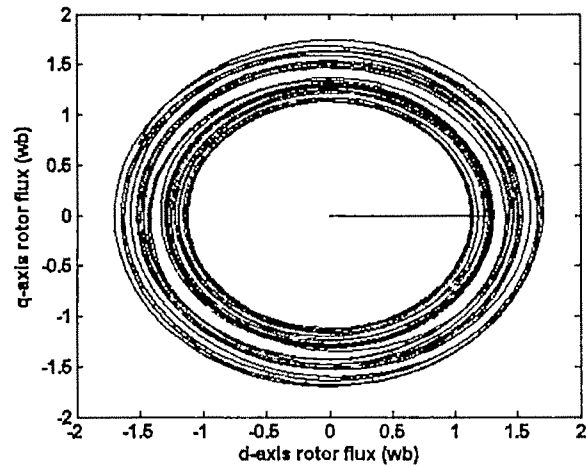


Fig. 8 Locus of d and q-axis fluxes

VI. SIMULATION RESULTS

Per-phase equivalent circuit parameters of the 50 Hz five-phase induction machine, used in the work, are $R_s = 10\Omega$, $R_r = 6.3\Omega$, $L_s = L_r = 0.04\text{ H}$, $L_m = 0.42\text{ H}$. Inertia and the number of pole pairs are equal to 0.03 kgm^2 and 2, respectively. Rated phase current, phase-to-neutral voltage and per-phase torque are 2.1 A, 220 V and 1.67 Nm, respectively. Rated (rms) rotor flux is 0.5683 Wb. Hysteresis band is set to $\pm 2.5\%$ of the rated peak phase current (i.e. $\pm 0.07425\text{ A}$). Torque limit is at all times equal to twice the rated motor torque (i.e. 16.67 Nm). Dc link voltage equals 587 V ($= \sqrt{2} \times 415\text{ V}$) and provides approximately 10% voltage reserve at rated frequency. The drive is operated in speed mode with speed feedback is taken from full order speed estimator.

Figure 4 displays the results for speed characteristics of the induction motor when motor is directly fed to the mains.

The total simulation time is 2.0s. Speed command of 1200 rpm is applied at $t=0.3\text{ s}$ in a ramp wise manner from $t = 0.3$ to $t = 0.35\text{ s}$ and is further kept unchanged. Operation takes place under no-load conditions.

Disturbance rejection properties of the drive are investigated next. A load torque equal to the motor rated torque is applied in a step-wise manner at $t = 1\text{ s}$.

Finally, reversing transient is examined as well. The command for speed reversal is given at $t = 1.2\text{ s}$.

The responses, obtained for these periods, are shown in Fig. 5,6,7. It is concluded from the responses that the actual speed and torque closely follows the reference.

Fig. 8 displays the results for the locus of rotor fluxes.

VII. CONCLUSION

The paper deals with full order observer-based sensorless vector control of a five-phase induction machine, utilising an indirect machine is at first reviewed and it is shown that the resulting model is the same as for a three-phase machine rotor

flux oriented controller and current control in the stationary reference frame. Hence the same vector control principles and speed estimation technique are applicable. Operation in the speed mode is further studied, utilising the hysteresis current control. The speed feedback signal is the estimated one obtained from observer-based speed estimator. The attainable performance is examined by simulation. It is shown that the dynamic behaviour, obtainable with the indirect vector control, is the same as it would have been had a three-phase machine been used. Rotor flux and torque control are fully decoupled, enabling the fastest possible accelerations and decelerations with the given torque limit.

REFERENCES

- [1] G.K.Singh, "Multi-phase induction machine drive research – a survey", *Electric Power System Research*, vol. 61, 2002, pp. 139-147.
- [2] M.Jones and E.Levi, "A literature survey of state-of-the-art in multiphase ac drives", *Proc. 37th Int Universities Power Eng. Conf. UPEC*, Stafford, UK, 2002, pp. 505-510.
- [3] H.A. Toliyat and H.Xu, "DSP-based direct torque control (DTC) for five-phase induction machines", *Proc. Int. Power Elec. Conf. IPEC*, Tokyo, Japan, (2000), pp. 1195-1199.
- [4] H.Xu, H.A. Toliyat and L.J. Petersen, "Five-phase induction motors drives with DSP-based control system", *IEEE Trans. On Power Electronics*, vol. 17, no. 4, (2002), pp. 524-533.
- [5] H.Xu, H.A. Toliyat and L.J. Petersen, "Resilient current control of five-phase induction motor under asymmetrical fault conditions", *Proc. IEEE Applied power Elec. Conf. APEC*, Dallas, Texas, (2002), pp. 64-71.
- [6] A.Iqbal, S.N. Vukosavi and E.Levi, "Vector control of a five-phase induction motor drive", *Proc. 38th UPEC*, Thessaloniki, Greece, 2003, CD-ROM paper No. EMD11, pp.57-60.
- [7] Leila Parsa, "On Advantages of Multiphase Machines" *IECON 2005*
- [8] L. Parsa and H. Toliyat, "Sensorless Direct Torque Control of Five-Phase Interior Permanent Magnet Motor Drives", *IEEE Industry Applications Conference, IEEE-IAS 2004, Annual Meeting*, Oct 3-7, 2004.
- [9] F. Terrien, S Siala and P.Noy, "Multiphase Induction Motor Sensorless Control for Electric ship Propulsion", *Proc. PEMD 2004*.
- [10] J. Holtz, "Sensorless Control of Induction Machines —With or Without Signal Injection?," *IEEE Transactions on Industrial Electronics*, vol. 53, no. 1, Feb 2006.
- [11] J. Holtz, "Sensorless control of induction motors," *Proc. IEEE*, vol. 90, no. 8, pp. 1358-1394, Aug. 2002.
- [12] Peter Vas, "Sensorless Vector and Direct Torque Control", Oxford University Press, 1998.
- [13] K. Rajashekara, A. Kawamura, and K. Matsuse, "Sensorless Control of AC Motors", Eds. Piscataway, NJ: IEEE Press, 1996.
- [14] S.Green, A.G.Atkinson, B.C.Mecrow and A.King, "Sensorless Operation of a Fault Tolerant PM Drives", *IEE Proc. Elect. Power application*, vol.150, No.2, pp.117-125.
- [15] M. E. Elbuluk, L. Tong and I. Husain, "Neural Network based Model Reference Adaptive systems for high performance motor drives and motion controls," *IEEE Trans. Ind. Applcat.* Vol. 38, May/June 2002.
- [16] K. H. Kim, S. M. Chung, G. W. Moon, I.C. Baik and M.J. Youn, "Parameter estimation and control for PMSM drive using MRAS," *Proc. of 21st IEEE IECON* vol. 1, pp. 387-392, 1995.
- [17] D.C. White, H.H. Woodson, "Electromechanical Energy Conversion", New York, John Wiley & Sons, 1959.
- [18] P. L. Jansen and R. D. Lorenz, "A physically insightful approach to the design and accuracy assessment of flux observers for field oriented induction machine drives," *IEEE Trans. Ind. Appl.*, vol. 30, no. 1, pp. 101-110, Jan/Feb. 1994.
- [19] P. Vas, *Sensorless Vector and Direct Torque Control*. Oxford, U.K.. Oxford Science, 1998
- [20] Profumo, F., Griva, G., Tenconi, A., Abrate, M., and Ferraris, L. "Stability analysis of Luenberger observers for speed sensorless high performance spindle drives" *European Conf. on Power Electronics and Applications, EPE'99*, Lausanne, Switzerland, 1999, CD-ROM Paper No. 604
- [21] J. Hu and B. Wu, "New integration algorithms for estimating motor flux over a wide speed range," *IEEE Trans. Power Electron.*, vol. 13, no. 5, pp. 969-977, Sep. 1998.
- [22] H. Kubota, I. Sato, Y. Tamura, K. Matsuse, H. Ohta, and Y. Hori, "Stable operation of adaptive observer based sensorless induction motor drives in regenerating mode at low speeds," in *Conf. Rec. IEEE-IAS Annu. Meeting*, Chicago, IL, Oct. 2001, pp. 469-474.
- [23] Matlab/Simulink reference guide www.mathworks.co.uk.

Simulation of Space Vector Theory Based Variable Speed Operation of a PMSM Drive System Using Predictive Current Control

A. Lekshmi¹, R. Sankaran², and S. Ushakumari³

¹ Lecturer, Dept. of Electrical Engg., College of Engg., Trivandrum, India, email: alekshni@rediffmail.com

² Professor, Dept of EEE, SASTRA University, Thanjavur, India email: r_shankaran43@yahoo.com

³ Asst Professor, Dept. of Electrical Engg., College of Engg, Trivandrum, India, email: ushalal2002@yahoo.com

Abstract- A closed loop system consisting of a permanent magnet synchronous motor [PMSM] drive and a 6-pulse inverter is simulated for variable speed operation. The controller uses the concept of predictive current control for pulse width modulation. Simulation results cover the startup behavior and response following a step change in reference speed, load torque and dc link voltage during running. Issues concerning the functional design of subsystems and their overall integration are discussed.

Key words- Closed loop control, PMSM, Predictive current control, Space vector, Variable speed operation.

1. INTRODUCTION

Though expensive, synchronous motor drives do compete with their induction motor counterparts in applications requiring high efficiency and reduced life cycle cost [1].

Synchronous motors using permanent magnets yield a drive with higher power to weight ratio, high torque to current ratio and fast dynamic response [2]. The higher cost of such a drive is expected to come down in future due to the availability of high energy low cost permanent magnets [3].

A common configuration of PMSM drive system consists of a PMSM fed from a variable frequency PWM voltage source inverter and control circuits [4]. Here the current in each stator phase is forced to follow a reference waveform derived from the speed error. Two of the major techniques of current control of PWM inverters are hysteresis control and predictive current control. On-off control with hysteresis is characterized by a fast response but the current ripple is usually large [4]. In predictive current control scheme, the switching instants of the power semiconductor devices are determined by calculating the required voltage to force the motor currents to follow the reference [4].

Space vector modulation of the three phase inverter has major advantages in machine control [5], [6]. Space Vector PWM [SVPWM] refers to a special technique of determining the switching sequence of the inverter power switches for obtaining variable output voltage. It generates less harmonic distortion in the voltage and current waveforms of the motor

windings. It also provides more efficient use of the dc bus voltage in comparison with the direct sinusoidal modulation technique [1]. This paper deals with the simulation of a closed loop PMSM drive system by combining the predictive current control and SVPWM techniques.

2. THEORY OF BRUSHLESS SYNCHRONOUS MOTOR

In a brushless synchronous motor, the conventional field excitation in the rotor is replaced by permanent magnets, thus eliminating the slip ring and brush assembly [3], [7]. With the advent of power semiconductor switching devices, the replacement of mechanical commutators in the form of an inverter has been achieved. The above two innovations have contributed to the development of the permanent magnet synchronous and brushless dc machines. PM ac motors are classified on the basis of the wave shape of their induced emf, i.e. sinusoidal and trapezoidal. The sinusoidal type is known as PM brushless synchronous motor and trapezoidal type goes under the name of PM Brushless DC [PMBLDC] motor [3], [8].

Fig.1 shows the equivalent two pole model of the PMSM in rotor frame. The equations are [3]

$$\frac{d}{dt} i_d = \frac{1}{L_d} v_d - \frac{R}{L_d} i_d + \frac{L_q}{L_d} \frac{P}{2} \omega_r i_q \quad (1)$$

$$\frac{d}{dt} i_q = \frac{1}{L_q} v_q - \frac{R}{L_q} i_q - \frac{L_d}{L_q} \frac{P}{2} \omega_r i_d - \lambda \frac{P}{2} \frac{\omega_r}{L_q} \quad (2)$$

$$T_e = 1.5 \frac{P}{2} [\lambda i_q + (L_d - L_q) i_d i_q] \quad (3)$$

where i_d , i_q , v_d , v_q , L_d and L_q are the d and q axis currents, voltages and inductances respectively. R is the stator resistance, P is the number of poles, λ is the flux induced by rotor on stator windings, T_e is the electromagnetic torque and ω_r is the angular velocity of the rotor.

Equations (1) – (3) are adequate for modeling the electromagnetic and electromechanical phenomena where saturation of the magnetic circuit is neglected and rotor currents are negligible in view of the high resistivity of the permanent magnet rotor poles. Accordingly there is no equation involving rotor currents [3].

Mechanical system equations are

$$\frac{d}{dt} \omega_r = \frac{1}{J} [T_e - F\omega_r - T_m] \quad (4)$$

$$\frac{d}{dt} \theta_r = \omega_r \quad (5)$$

where J is the inertia of rotor and load, F is the viscous friction of motor and load, T_m is the mechanical torque and θ_r is the rotor angular position.

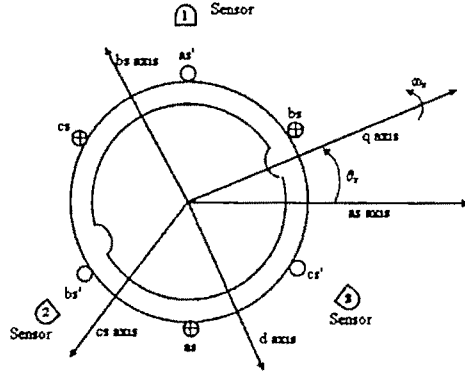


Fig. 1. Two pole model of the PMSM

The fundamental amplitude of the voltage applied to the stator windings may be changed by PWM of the inverter. The turning on and off of the six numbers of IGBT's are governed by logic, sequence and timing considerations for maintaining unidirectional torque.

3. MODEL EQUATIONS USING SPACE VECTOR

Space vector theory is very much related to the generalized two-axis theory of electrical machines [5]. It is valid for the analysis of any arbitrary variation of instantaneous voltage and current as generated by a voltage source inverter.

A two pole, three phase machine, whose stator windings are supplied by a system of three phase currents $i_a(t)$, $i_b(t)$ and $i_c(t)$ which vary arbitrarily with time is considered. With the neutral point isolated, there will be no zero sequence stator currents. Resultant mmf produced by the stator currents as a function of the orientation θ of the space vector is given by [5]

$$f_s(\theta, t) = N_s [i_{sa}(t) \cos \theta + i_{sb}(t) \cos(\theta - 2\pi/3) + i_{sc}(t) \cos(\theta - 4\pi/3)] \quad (6)$$

where N_s is the number of stator turns.

Equation (6) can be rewritten as

$$f_s(\theta, t) = \frac{3}{2} N_s \operatorname{Re} \left\{ \frac{2}{3} [i_{sa}(t) + a i_{sb}(t) + a^2 i_{sc}(t)] e^{-j\theta} \right\} \quad (7)$$

where a and a^2 are space operators equal to $e^{j\frac{2\pi}{3}}$ and $e^{j\frac{4\pi}{3}}$ respectively.

$$\text{Hence } f_s(\theta, t) = \frac{3}{2} N_s \operatorname{Re} \{ \bar{i}_s(\theta, t) \}, \quad (8)$$

where $\bar{i}_s(\theta, t)$ is the stator current space vector. Similarly the stator voltage space vector is given as

$$\bar{v}_s(\theta, t) = \frac{2}{3} [v_{sa} + a v_{sb} + a^2 v_{sc}] \quad (9)$$

Park transformation leads to the derivation of stator voltages in terms of the direct and quadrature axes variables. Accordingly stator voltage space vector equation referred to rotor reference frame is obtained as [5]

$$\bar{v}_s = \bar{i}_s R_s + \frac{d\bar{\psi}_s}{dt} + j\omega_r \bar{\psi}_s \quad (10)$$

4. IMPLEMENTATION OF SPACE VECTOR USING PWM

A typical three phase voltage source inverter is shown in Fig.2, where v_a , v_b and v_c are the phase voltages of the motor. Considering 120° conduction mode of operation for the inverter switches, there are 15 possible combinations of on and off states. Among this, only 6 combinations are active for power transfer, which are shown in Table I. The sector-wise voltage vectors \bar{V}_1 to \bar{V}_6 , each one having a length of $(1/\sqrt{3})V_{dc}$ form a hexagon as shown in Fig. 3.

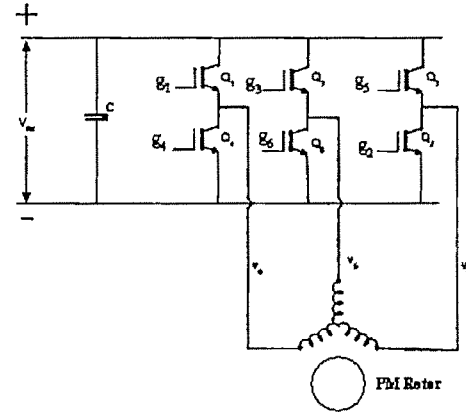


Fig. 2 Three phase 6-pulse inverter

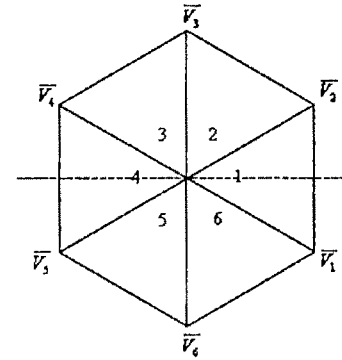


Fig. 3 Primary Voltage Space Vectors

Table I: Space vector switching table

State	v_a	v_b	v_c	$\frac{2}{3}[v_a + a v_b + a^2 v_c]$	Voltage Vector
1.	$\frac{V_{dc}}{2}$	$-\frac{V_{dc}}{2}$	0	$\frac{1}{\sqrt{3}} V_{dc} \angle 330^\circ$	\bar{V}_1
2.	$\frac{V_{dc}}{2}$	0	$-\frac{V_{dc}}{2}$	$\frac{1}{\sqrt{3}} V_{dc} \angle 30^\circ$	\bar{V}_2
3.	0	$\frac{V_{dc}}{2}$	$-\frac{V_{dc}}{2}$	$\frac{1}{\sqrt{3}} V_{dc} \angle 90^\circ$	\bar{V}_3
4.	$-\frac{V_{dc}}{2}$	$\frac{V_{dc}}{2}$	0	$\frac{1}{\sqrt{3}} V_{dc} \angle 150^\circ$	\bar{V}_4
5.	$-\frac{V_{dc}}{2}$	0	$\frac{V_{dc}}{2}$	$\frac{1}{\sqrt{3}} V_{dc} \angle 210^\circ$	\bar{V}_5
6.	0	$-\frac{V_{dc}}{2}$	$\frac{V_{dc}}{2}$	$\frac{1}{\sqrt{3}} V_{dc} \angle 270^\circ$	\bar{V}_6

5. PREDICTIVE CURRENT CONTROL SCHEME

In Predictive current control method, the motor current is measured at a fixed sampling rate [2]. The current reference is calculated as a sequence of discrete samples from speed error and dynamic torque-speed characteristic of the drive system. The error in current space vector is computed as the difference between the reference and actual current space vectors. Using the principle of predictive current control, the required value of the voltage space vector at the next sampling instant is computed as follows so as to minimize this current error.

The required voltage vector at the k^{th} sampling instant is given by

$$v(k) = e(k) + L \frac{di(k)}{dt} + Ri(k) \quad (11)$$

$e(k)$ is the emf space vector, $i(k)$ is the current space vector, L is the stator inductance per phase and R is the stator resistance per phase.

Equation (11) can be rewritten for calculating $v(k)$ as

$$v(k) = e(k) + \frac{L}{T} [i^*(k+1) - i(k)] + Ri(k) \quad (12)$$

where $i^*(k+1)$ is the desired value of current at the next sampling instant. Space vector modulation is used to generate the vector $v(k)$ as shown in Fig. 4. Here $v(k)$ is obtained in sector I from the adjacent vectors \bar{V}_1 and \bar{V}_2 with appropriate duty ratios t_1/T and t_2/T where T is the period of the high frequency modulating signal.

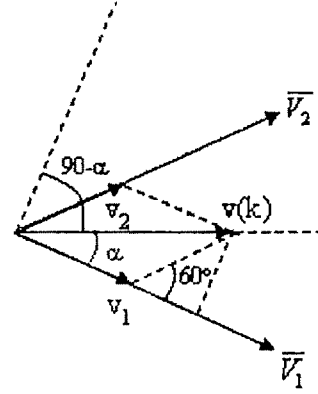


Fig. 4 Generation of space vector in sector 1

Resolving the vector $v(k)$ along \bar{V}_2 and \bar{V}_1 ,

$$v_2(k) = \frac{2}{\sqrt{3}} v(k) \sin \alpha \quad (13)$$

$$v_1(k) = v(k) \cos \alpha - 0.5 v_2(k) \quad (14)$$

where α is the modulation angle.

The duration t_1 and t_2 of the states 1 and 2 are given by

$$t_1 = \frac{v_1}{1/\sqrt{3} V_{dc}} T \quad (15)$$

$$t_2 = \frac{v_2}{1/\sqrt{3} V_{dc}} T \quad (16)$$

$$T = t_1 + t_2 + t_0 \quad (17)$$

where t_0 is the zero state or inactive state.

6. SIMULATION BLOCKS

The simulation of the drive system is done using Matlab-Simulink software. The blocks in the Simulink model is broadly grouped as shown in Fig.5.

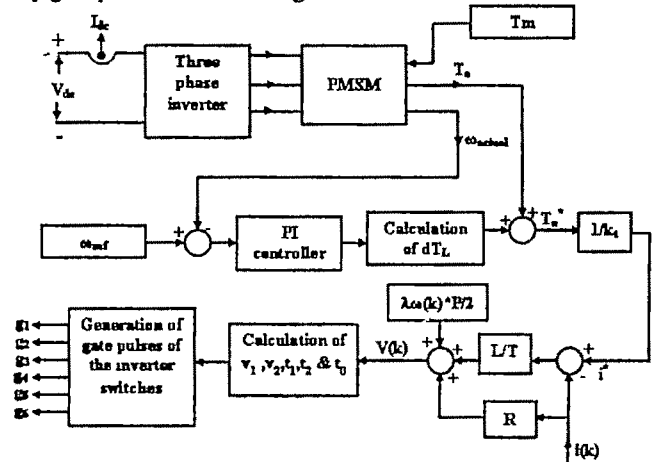


Fig. 5 Overall Block Diagram of PMSM Drive System

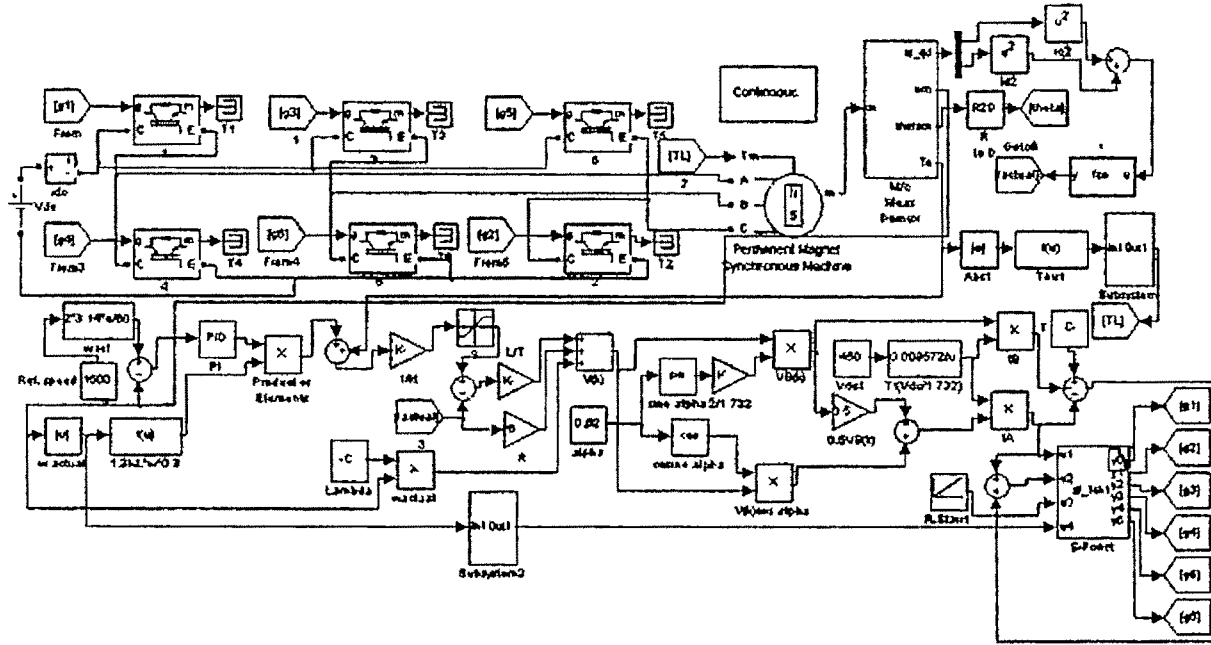


Fig 6 Simulink Block Diagram of the closed loop drive system

The inverter block comprises six numbers of IGBT's in bridge configuration and is fed from a constant dc supply. The stator windings of the PMSM are fed from the variable frequency variable voltage inverter. The electromagnetic torque, T_e and the actual speed of the machine, ω_{actual} are obtained from the machine model. The actual speed is compared with the reference speed to get the speed error, $d\omega$ which is fed to a PI controller. Assuming a typical mechanical load characteristic in the form $T_L = K_L \omega_{actual}^{1.3}$, the processed speed error can be related to the additional torque as

$$dT_L = 1.3K_L \omega_{actual}^{0.3} d\omega \quad (18)$$

K_L is the load torque constant.

Now the torque reference $T_e^* = T_e + dT_L$ and the reference current i^* is computed as $i^* = T_e^* / k_t$ where k_t is the torque constant. After obtaining the actual space vector current $i(k) = \sqrt{i_d^2(k) + i_q^2(k)}$, current error is used for computing the required space vector $v(k)$. Using a constant value of 30° for modulation angle, α , corresponding to the middle of a sector, the vector $v(k)$ is resolved along the sector boundaries as $v_1(k)$ and $v_2(k)$. The timings t_1 and t_2 are calculated from equations (15) and (16). The switching waveform with parameters t_1 , t_2 and t_0 is periodic with period T and is used to modulate the space vector in each sector. The Simulink model is shown in Fig.6.

7. CONSIDERATIONS AND ISSUES IN SIMULATION

Many issues have to be addressed in the simulation of the above scheme, consisting of an outer speed control loop and

an inner loop, where the stator currents and hence the torque are defined and controlled. The foremost is synchronizing of the stator space vector frequency with rotor angular velocity, to be achieved by correctly timing the cyclic switching of the inverter IGBT's. In addition, the desired magnitude of the stator currents, dependent on the rotor speed has to be realized by pulse width modulation defined by the parameters t_1 , t_2 and t_0 in a predictive manner. In essence, minimization of the speed error calls for matching of the electromagnetic torque with load torque under different operating conditions. It is seen while preparing the simulation schematic, that the above functional requirements cannot be directly implemented with the available blocks in Simulink. Hence a S function is written in C language which acquires the switching parameters t_1 , t_2 and t_0 and generates repeating sequences for each of the 6 gate trigger signals g_1, g_2, \dots, g_6 . This is then converted to a CMEX file to link with other Simulink blocks. In effect, this S function in conjunction with another S function for counter operation on sampling instants determines the duration of the generated voltage space vector in a particular sector corresponding to the present value of the rotor speed.

8. SIMULATION RESULTS

After entering the machine data, properties of various functional block and simulation parameters including sampling time and run time, the schematic shown in Fig.6 is simulated first for the start up behavior for a set of selected reference speed settings. A speed range of 500 rpm to 1500 rpm is covered in the runs. A typical transient start up

behavior for reference speed, $N_{ref} = 1100$ rpm is shown in Fig.7.

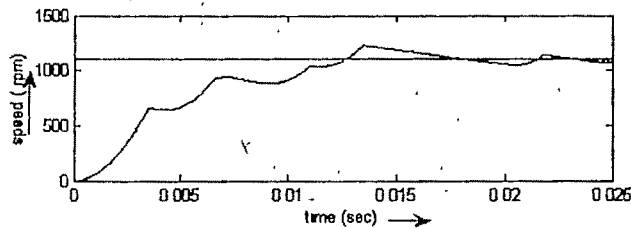


Fig.7 Start up transient response ($N_{ref} = 1100$ rpm)

Further a set of problems covering disturbances while running, in the form of step change in reference speed setting, load torque and dc link voltage are simulated. The transient behavior for a step change of reference speed from 1300 rpm to 1500 rpm is shown in Fig.8. Fig.9 shows the transient response following an additional braking torque of 0.05 Nm at 30 ms. Similarly the time response due to a step change in the dc link voltage from 450 V to 400 V at 20 ms is depicted in Fig.10.

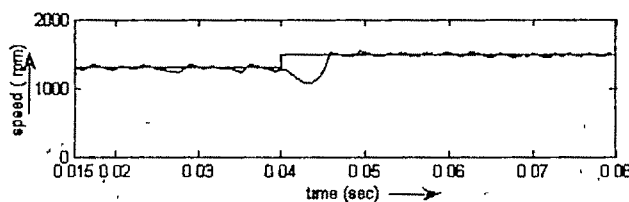


Fig.8 Transient response after step change in N_{ref}

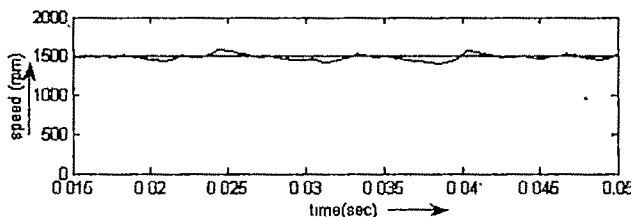


Fig.9 Transient response after step change in load torque

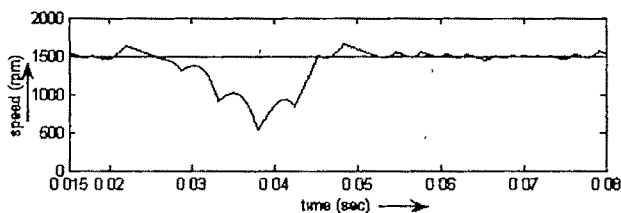


Fig.10 Transient response after step change in V_{dc}

The patterns of transient response obtained indicate the effectiveness of the control strategy for retaining the desired reference speed after a very short transient interval of the order of 0.05 ms.

APPENDIX I

MACHINE DETAILS

380 V, 3 phase, 2.4 A

$R = 6$ ohms, $L = 0.0778$ H, $J = 1.24 \times 10^{-4}$ kg. m²

ACKNOWLEDGMENT

The authors would like to acknowledge the whole hearted support given by The Principal, The Head of the Department and technical staff of the Department of Electrical Engineering, College of Engineering, Thiruvananthapuram for availing the facilities in the college.

REFERENCES

- [1] Bimal K. Bose, Modern power electronics and ac drives, Pearson Education, India, 2003.
- [2] Jawad Faiz, M. R. Azizian, M. Aboulghasemian Azami, "Simulation and analysis of brushless DC motor drives using hysteresis, ramp comparison and predictive current control techniques", *Simulation Practice and Theory* 3(1996), Elsevier, pp. 347 -363.
- [3] R. Krishnan, Electric Motor Drives – Modeling, Analysis and control, Pearson Education, India, 2003.
- [4] Hoang Le-Huy, Louis A. Dessaint, "An adaptive current control scheme for PWM Synchronous motor drives. Analysis and simulation", *IEEE Transactions on Power Electronics*, vol.4, No 4, October 1989, pp.486-495.
- [5] S.K. Pillai, Analysis of thyristor power-conditioned motors, Universities Press.
- [6] Mohamed M. Negm, Mohamed F. Salem, Osamia S. Ebrahim, "Design and Implementation of a SVPWM Technique using Low cost Multifunction Data Acquisition Card", *2004 International conference on Power System Technology. POWERCON 2004*, Singapore, 21- 24 November 2004, pp 1816 – 1821.
- [7] Pragasen Pillay, Ramu Krishnan, "Modeling, Simulation and Analysis of Permanent-Magnet Motor Drives, Part I. The Permanent Magnet Synchronous Motor Drive", *IEEE Transactions on Industry Applications*, vol 25, No.2, March/April 1989, pp. 265-273.
- [8] Paul C. Krause, Oleg Wasynczuk, Electromechanical motion devices, Mc Graw Hill Book Company, Singapore, 1989

New Current Control of PMSM Drives in Synchronously Rotor Reference Frame

M. Kadjoudj¹, M.E. Benbouzid², and C. Ghennai³

¹ Batna University, 05000 Algeria, e-mail: kadjoudj_m@yahoo.fr

² Brest University, French e-mail: m.benbouzid@ieee.org

³ Gizan University KSA, ghennai_chawki@Lycos.com

Abstract— Hysteresis current controllers are not optimal with respect to switching frequency, but exhibits very good dynamical properties characterized by unconditioned stability, fast response, robustness and good accuracy. Predictive and ramp comparator controllers performs some optimisation on the switching frequency at the expense of the dynamical response. The conventional current control, based on the hysteresis comparators, is one of the simplest and more popular types, although it exhibits several undesirable features, such as high switching frequency and heavy interference among the phases in case of systems with isolated neutral. In order to eliminate these limitations, several methods of improvement have been proposed. This paper addresses the problems of torque ripple minimisation and current phases interferences in PMSM drives. The key point of the proposed control technique is the regulation of both the direct and transversal current components formulated in the synchronously rotating reference frame. In addition, an extra second error current zone is introduced to overcome the imprecision in the direct current component control.

Key words— PMSM, rotor synchronously reference frame, hysteresis control, torque ripple minimization.

I. INTRODUCTION

RECENT developments in power electronics, magnetic materials and motion control provide an excellent opportunity to use synchronous and induction motors in high performance drive applications. Among various types of AC motors, the PMSM is becoming popular due to some of its advantageous features such high torque to current ratio, as well as high power to weight ratio, high power factor, low noise and robustness [1][2].

The hysteresis current control technique has proven to be the most suitable solution for all the applications of current controlled voltage source inverter (VSI). The ramp comparison method is the most commonly used one for various kinds of power electronic systems. Its switching frequency and thus output harmonic spectrum are fixed. However, the PWM switching behaviour and performance depends on the load and motor parameters [3][4].

Moreover, an inherent current tracking error exists. The hysteresis current controlled PWM scheme is very simple, provides good current amplitude control against load and source parameter changes. However, the resulting output voltage inverter is irregular and depends on the load variation and phase current interferences leading to analysis problem and switching performance degradation [5][6][7].

In this paper, effective method to eliminate the inconveniences has been demonstrated to be a viable way to obtain robust and high performance control. The structure shown in figure 1 is investigated in order to simplify computation. Two controllers of modulating DC variables can be obtained through the coordinate transformation of three phase current. The novel strategy employs two independent hysteresis regulators in the rotor dq-axis synchronously reference frame.

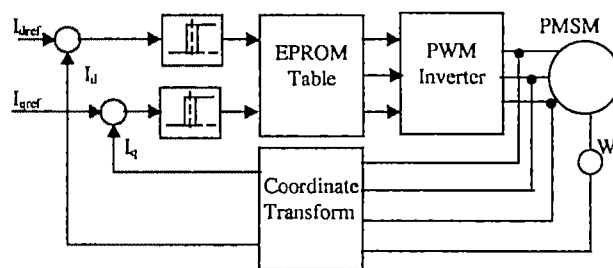


Figure 1. PWM inverter with two current loops

Furthermore, because of the limitation number of the voltage vectors, the control strategy may be optimal only for the inverse current component, but not for the current longitudinal component. A second hysteresis zone, that contributes to improve the control of the d-axis current component.

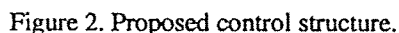
II. Proposed Control Strategy

In order to maximize the torque/current ratio, the real current vector must be oriented along the resulted counter EMF vector E. This may be achieved by using hysteresis

For convenient presentation of the theoretical basis of the proposed current controller, it is assumed that the change rate can be considered as constant, and the parasitic resistance can be neglected. The maximum value of the current derivative in (1) becomes,

As illustrated by equation (1), the deviation of the current vector is proportional to the difference vector ΔV . The control strategy is based on the selection of the next voltage state that must satisfy the following criteria :

- The block diagram of the proposed control structure is shown in Figure 2. The current references I_{dref} and I_{qref} are obtained respectively by the speed loop and the weakening block. The real current components I_d and I_q as well as the rotor position are deduced from the machine model. The d-axis position block determines the sector number of the d-axis. The digital output signals of the band hysteresis controllers, together with the d-axis position sector select the state of the inverter switches (S_A , S_B , S_C) using the switching table.



the sector $k=2$, which is bounded by the voltage vectors V_2 and V_3 . Hence, the difference vector in this case can be defined as,

In general, if the d-axis is in the sector k , the difference vector expressions will be as follows:

$$\Delta V_{k+1} = V_{k+1} - E \text{ or } \Delta V_{k+2} = V_{k+2} - E \quad (4)$$



III. Control of the direct and inverse components

When the direct reference component of the current reference is set to zero ($I_{dref}=0$), the direct component of the real current will be very close to the width of the band hysteresis ΔI_d . Whenever the current vector crosses the borders of the band hysteresis i.e., $|I_d| > \Delta I_d$, the control process acts to force it back to the interior of the band hysteresis. Assuming the d-axis is located in the sector k , two possible cases are distinguished:

Case one: If $|I_d| > \Delta I_d$ with $I_d > 0$, the application of the vector V_{k+2} leads to ΔV_{k+2} with opposite direction to the direct current. As the current deviation vector is proportional to ΔV , the current component I_d will be reduced.

Case two: If $|I_d| > \Delta I_d$ with $I_d < 0$, the real current is therefore in advance with respect to the q-axis, the quadrature component in this case will be negative. The vector V_{k+1} is to be selected. This latter gives a difference vector ΔV_{k+1} in concordance with d-axis forcing I_d back to the interior of the band hysteresis.

It is always possible at any instant, to choose either mode V_{k+1} or V_{k+2} to reduce the magnitude of the current error for sector k . In other words, the conventional two-mode hysteresis controller does not have stability problem.

However, one can see that mode V_{k+1} can be applied only when the condition $I_q < 0$ is satisfied. Otherwise, the magnitude of the current error will increase.

When the upper border of the band is reached i.e., $I_q > I_{qref} + \Delta I_q$, one of the zero vectors should be selected. The choice of either the state voltage V_0 or V_7 which should be done must insure a soft switching of inverter components. However, in order to insure this condition, the following sequences have to be respected,

- Select the state voltage vector V_0 at the instant preceding either V_1 , V_3 or V_5 [10][11].
- Select the state voltage vector V_7 at the instant preceding either, V_2 , V_4 or V_6 .

Suppose the output voltage is zero and the actual current crosses lower band. In this case, the output voltage has to be increased by selecting V_{k+1} and V_{k+2} in order to increase the load current.

Figures 4 and 5 show the simulation results for the above control algorithm. Despite the current I_q is not imposed, for the reason of DC-bus reduction, the pulsations of the current are minimal. This proposed control structure ensures the self-piloting of the machine under several conditions.

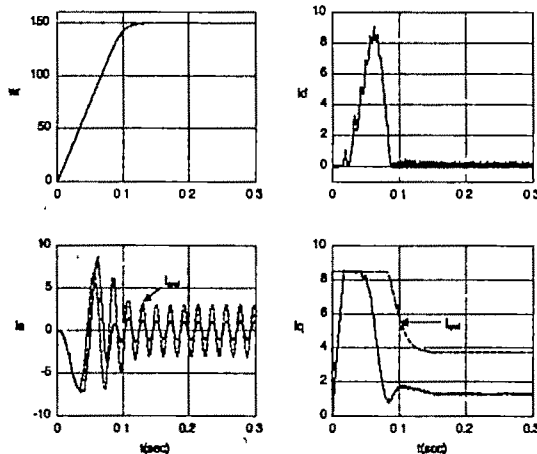


Figure 4. Control of the direct current component..

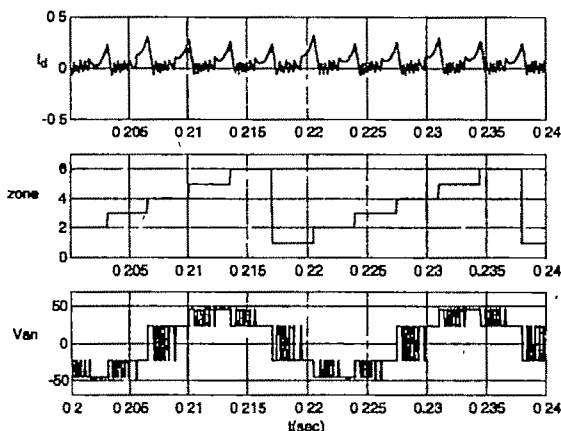


Figure 5. Steady state waveforms.

The overshooting in the direct current waveform at the crossing moments from one sector to another can be explained as follows: The d-axis rotates in the opposite direction of the vectors V_{k+1} and V_{k+2} that are applied to control the current I_d . At the beginning of each sector, the difference vector ΔV_{k+1} has usually a small component, this leads to a slow increase of the current. Whereas, at the end of each sector, the component of the difference vector ΔV_{k+2} is significant and reduce rapidly the current towards the admissible limits.

In figures 6 and 7, when sufficiently high DC-bus is applied, the I_q controller will get into the control process together with the direct current controller I_d . Once the current I_q loop is active, the same voltage vectors selected in the previous controller will be imposed if the current reaches the lower border of the hysteresis band. The zero vectors V_0 and V_7 are applied when the upper border of the hysteresis band is achieved ΔI_q .

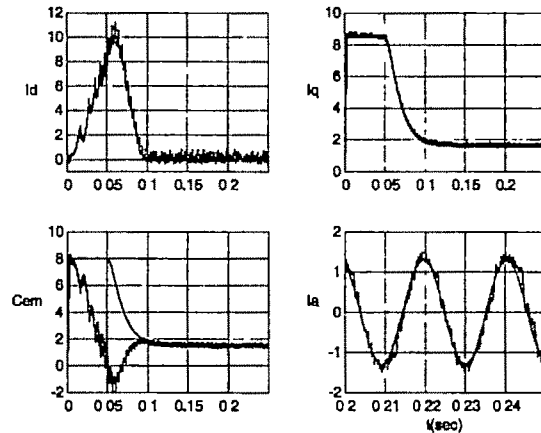


Figure 6. Simultaneous control of I_d and I_q .

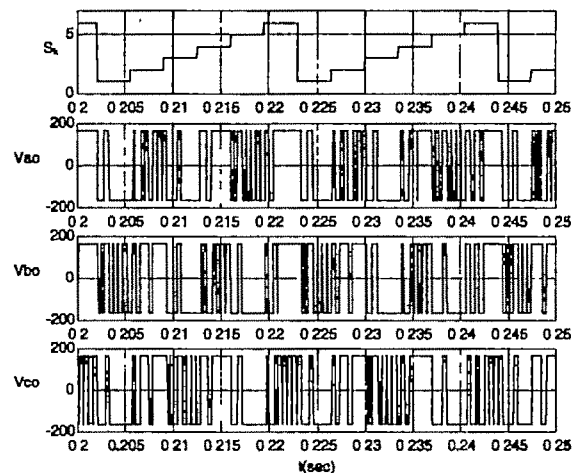


Figure 7. Switching states of the power devices

Figure 8 and 9 illustrate the effect of the widths of the hysteresis band of the stator current components on the performances of the control strategy. A choice of a band for the quadrature current leads to a reduced oscillations ratio. A comparative study shows that the switching frequency of the upper switch of the first leg of the inverter is very important for the case $\Delta I_q = 0.02A$ (1% of the permanent

current). In the sector 5, the maximum switching frequency is 4.4 kHz, whereas it is 2.3 kHz in the same sector for $\Delta I_q=0.08A$. However, increasing the width of the hysteresis band of the quadrature current regulator, has an almost increased effect on the overshooting phenomena of the limits of the band ΔI_d . Although the action of I_q regulator is less important than the I_d regulator, the direct current varies between $\pm 0.1A$ and $\pm 0.14A$ respectively for $\Delta I_q=0.02A$ and $\Delta I_q=0.08A$ at the crossing instants from one sector to another.

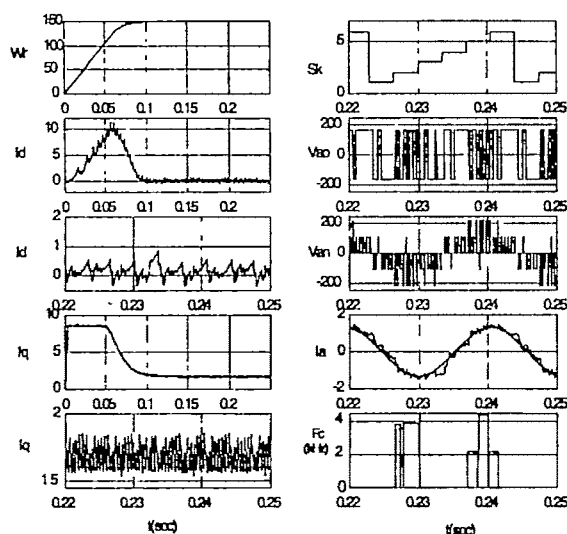


Figure 8. Effect of the hysteresis band width $\Delta I_q=0.02A$
 $\Delta I_d=0.02A$

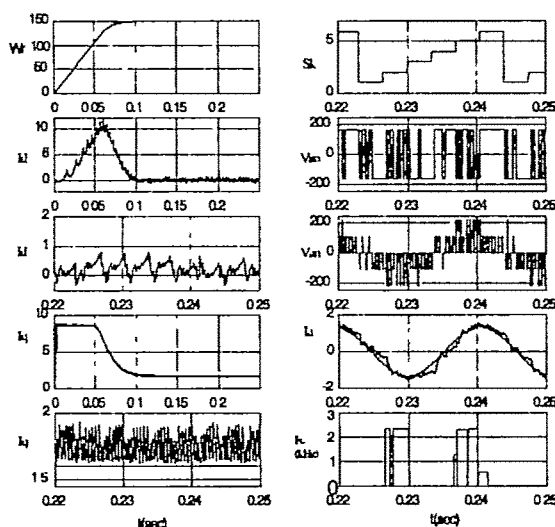


Figure 9. Effect of the hysteresis band width $\Delta I_q=0.08A$
 $\Delta I_d=0.02A$

For a fixed width of the hysteresis band of I_q , an excessive increase of ΔI_d leads to a less precise control of the direct current component. This may affect the phase angle of the line current. The requesting time of the I_d regulator is inherently reduced. As results, the pulsation frequency of the I_q current will be increased. The direct current reference is null, the impact of the direct current regulator on this control structure is fully limited.

Because of the difficulties of the operation conditions, the deviation current dI/dt varies very rapidly. The consequence of such variation is shown clearly by equations 1 and 2. In fact, the counter E.M.F. vector E is brought to the indirect axis that is liable to the rotor inertia. This axis may spend extra time in the sector limited by the vectors V_{k+1} and V_{k+2} , while the reference current moves immediately to the next sector S_{k+3} .

In order to avoid the current control losses, a control band is required. This increases the number of vectors that are able to be applied. When the direct axis lies in the sector S_k , the vectors V_{k+1} and V_{k+2} are already applied beyond the first band. Beyond the second band control and in order to limit the rapid variations of the current, additional voltage vectors have to be selected. Concerning the sector S_k , the new vectors of the second hysteresis band are V_k and V_{k+3} . Thus, the problems of the beginning and end of the sector are solved by the adoption of the second width of the hysteresis band ΔI_{d2} .

Indeed, each band zone is associated with a specific voltage vectors in the process of tracking the reference. In contrast to the two voltage vectors V_{k+1} and V_{k+2} , the new control in the additional zone has to efficiently utilize several voltage vectors with adjacency. Figures 10, 11 and 12 show the performance analysis of the new current controllers in the synchronously reference frame in case of second zone current control introduced.

Table 1 illustrates the different possibilities required for new algorithm of the control strategy.

	ROTOR POSITION (SECTORS S_k)					
	S_1	S_2	S_3	S_4	S_5	S_6
Positive direction						
First zone	V_2-V_1	V_3-V_4	V_4-V_5	V_5-V_6	V_6-V_1	V_1-V_2
2 nd zone	V_1-V_4	V_2-V_5	V_3-V_6	V_4-V_1	V_5-V_2	V_6-V_3
Negative direction						
First zone	V_6-V_3	V_5-V_2	V_4-V_1	V_3-V_4	V_2-V_5	V_1-V_6
2 nd zone	V_5-V_1	V_4-V_2	V_3-V_3	V_2-V_4	V_1-V_5	V_6-V_6

Table 1. Introduction of second hysteresis zone.

Additionally the following remarks have to noticed:

- The second hysteresis band of I_q is not designed to bring down the current limits as the real current is less than the lower limit $-\Delta I_{q2}$.
- The vectors V_{k+1} and V_{k+2} , selected to increase the current I_q during the simple switching, are the only recourse of the second band control to increase the current.
- At the beginning and the end of the sectors, the control of I_d by the vectors V_k and V_{k+3} may increase, even slightly, the current I_q .

With the use of the second band control of the current I_q , the control becomes very effective and reliable even at highly redoubtable dynamic changes. The voltage waveforms show that the switching frequency is perfectly

reduced. The I_d and I_q oscillate closely around their references. To improve the performances of the control structure, the pulsations of the current I_d have to be reduced, by consequence those in the line current. Reducing the width of hysteresis band has a side effect on the switching frequency, hence this solution is not recommended.

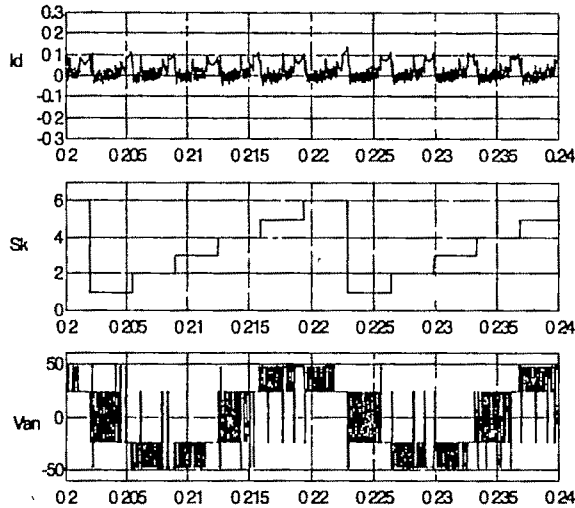


Figure 10 Direct current control with second zone.

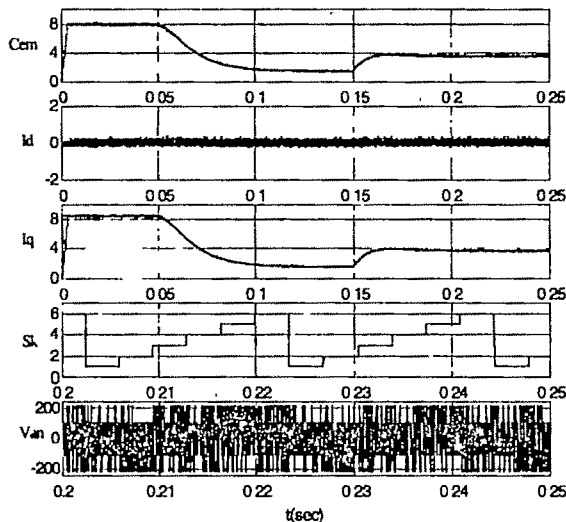


Figure 11 Regulation of direct and inverse currents.

V. Conclusion.

In contrast to the conventional hysteresis control where the switching frequency is independent of the three phases, the new proposed control structure is based on the vector aspect characterized by advantages such as:

- Performances stability insured by the use of a second hysteresis band, even at severe dynamic regimes.
- Improved characteristics by damping the torque pulsations and the current battements
- Reduction of the switching frequency by the use of two vectors that delimit the transversal axis and the zero vectors.
- Soft switching of the inverter.

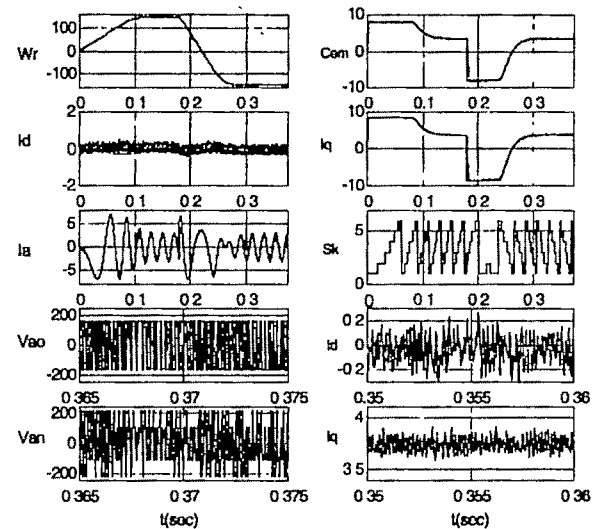


Figure 12 Performance analysis with speed inversion test.

REFERENCES

- [1] V.Petrovic, R.Ortega, M.Stankovic, G.Tadmor, "Design and implementation of an adaptive controller for torque ripple minimization in PMSM drives," *IEEE trans. Power electronics*, vol. 15, pp.871-880; Sept.2000.
- [2] T.W. Chun, K.Choi, "Development of adaptive hysteresis band control strategy of PWM inverter with constant switching frequency," in *Proc. of the IEEE APEC'96*, vol. 1, pp. 194-199, 1996.
- [3] B.K.Bose, "An adaptive hysteresis band current control technique of a voltage fed PWM inverter for machine drive system," *IEEE trans. Ind. Electron.* vol 37, pp. 402-407, Oct. 1990.
- [4] M. Kadjoudj, M.E. Benbouzid, C. Ghennai, D.Diallo, "A Robust hybrid current control for PMSM drives," *IEEE trans. on energy conv.*, vol 19 No 1, pp. 109-115, 2004.
- [5] L.Malesani, P.Mattavelli, P. Tomasin, "Improved constant frequency hysteresis current control of VSI inverter with simple feedforward bandwidth prediction," *IEEE trans. Ind. Applications*, vol. 33, pp. 1194-1202, Sept/Oct. 1997.
- [6] S. Buso, L. Malesani, P. Mattavelli, "Comparison of current control techniques for active filter applications," *IEEE trans. on industry electronics*, vol. 45, No. 5, pp. 722-729, October 1998.
- [7] M.P. Kazmierowski, L. Malesani, "Current control techniques for three phases voltage source PWM converters : A survey," *IEEE trans. on Indus. electronics*, vol. 45, No. 5, pp. 691-703, October 1998.
- [8] W.Qian, S.K.Panda, J.X Xu, "Torque ripple minimization in PM Synchronous motors using iterative learning control," *IEEE trans. on power electronics*, vol. 19, No. 2, pp. 272-279, March 2004.
- [9] G.Tadmor, "Control of a combined GTO/IGBT drive system for low torque ripple in a large PMSM," *IEEE trans. on Control systems technology*, vol. 12, No. 1, pp. 21-26, January 2004.
- [10] W.C.Gan, L.Qin, "Torque and velocity ripple elimination of AC PM motor control systems using the internal model principle," *IEEE trans. on Mechatronics* Vol. 9, No 2, pp 436-441, June 2004.
- [11] B.J.Kang, C.M.Liaw, "A robust hysteresis current controlled PWM inverter for linear PMSM driven magnetic suspended positioning system," *IEEE trans. on Indus. electronics*, vol. 48, No. 5, pp. 956-966, October 2001.

Modeling of PWM-Inverter fed Induction Motor Drive and Simulation Analysis of Motor Terminal Overvoltages

B.Basavaraja¹ and D.V.S.S.Siva Sarma²

¹ National Institute of Technology, Warangal, e-mail: banakara_36@rediffmail.com.

² National Institute of Technology, Warangal, e-mail: sivasarma@gmail.com.

Abstract— An increasing part of low voltage standard induction motors operates with PWM voltage source inverters using IGBTs and they are applied to a wide range of power 0.1 kW up to some MW. The PWM (Pulse Width Modulation) inverter mode of control generates a large frequency spectrum of overvoltages. The resulting undesired overvoltages at the motor terminals stress the motor insulation. Usual standards applied to the induction motors recommend to limit the value of rate of rise of voltage to be less than $(dv/dt) < 500\text{--}600\text{V}/\mu\text{s}$ for the motor insulation to be healthy condition. This value is suitable for a motor fed directly by the AC power supply, but when the motor is fed by an inverter without any filtering device, the dv/dt may reach up to $6000\text{--}7000\text{V}/\mu\text{s}$ or even more depending on the installation. In the recent past many authors have presented their investigations on various issues associated with the motor failure due to over-voltage that appears at the motor terminals due to the impedance mismatch between the power cable and the motor as well as non-uniform distribution of voltage in stator winding. This paper describes the modeling of the system consist of PWM Inverter, Cable, induction motor and their interaction. The system is simulated in MATLAB and experimental study is carried out for validating the modeling and simulation of the drive system. At the end Sensitivity analysis is made to study the influence of system parameters Viz cable length, motor rating and rise time on motor terminal overvoltage. Finally simulated are compared with experimental results and found to be in good agreement.

Key words—cable length, mismatch impedance, insulation failure, modeling, overvoltages.

I. INTRODUCTION

THE growing use of induction motors for high power adjustable speed applications is essentially due to the quick technological evolution of fast switching electronic devices, such as the insulated gate bipolar transistors (IGBT), which are nowadays widely adopted in medium voltage, medium power converters, for their performances in terms of driving, switching behavior, etc.

While the high switching speeds and advanced PWM schemes significantly improve the performance of the PWM-

inverter-fed induction motors, the high rate of voltage rise (dv/dt) of $0\text{--}650\text{ V}$ in less than $0.1\mu\text{s}$ has adverse effects on the motor insulation. These steep rising and falling pulses lead to an uneven distribution of voltages within the motor, especially during switching transitions. This contributes to insulation deterioration and subsequent failure of the motor. In addition, the dv/dt contributes to damaging bearing currents and electromagnetic interference (EMI). If a long cable is employed between the inverter and the motor, damped high frequency ringing at the motor terminals occurs resulting in excessive over voltage, which further stresses the motor insulation. Also, the motor impedance, which is dominated by the winding inductance, presents an effective open circuit at high frequencies at the end of the long cable. This produces a reflected voltage at the end of the cable approximately equal in magnitude and with the same sign, resulting in twice the magnitude of the incident voltage at the motor terminals as shown in Fig 2(b). Hence the problems associated with PWM fed A.C Drives are

1. Terminal over voltages due to PWM Inverter and cables
2. Surge propagation within winding
3. Bearing currents
4. EMI

This paper describes the representation of mode of the system consist of PWM Inverter, Cable, induction motor and their interaction. The system is simulated in MATLAB and experimental study is carried out for validating the modeling and simulation of the drive system. At the end Sensitivity analysis is made to study the influence of system parameters Viz cable length, motor rating and rise time on motor terminal overvoltage. Finally simulated are compared with experimental results and found to be in good agreement.

II. SYSTEM REPRESENTATION

The Fig.1 shows the system representation consisting of PWM inverter, power cable and induction motor. Transmission line representation of the power cable, high frequency model of the power cable, high frequency model of the induction motor and PWM inverter model are designed which are used for terminal over voltage analysis.

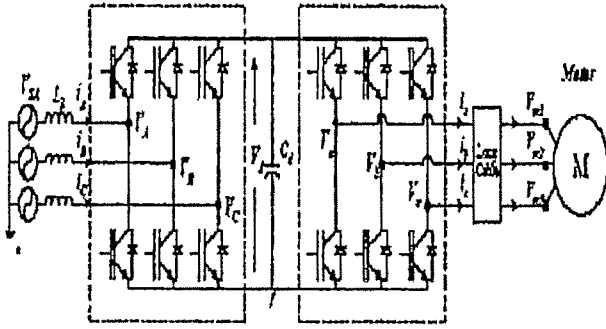


Fig 1 PWM inverter driving an induction motor using long cable leads

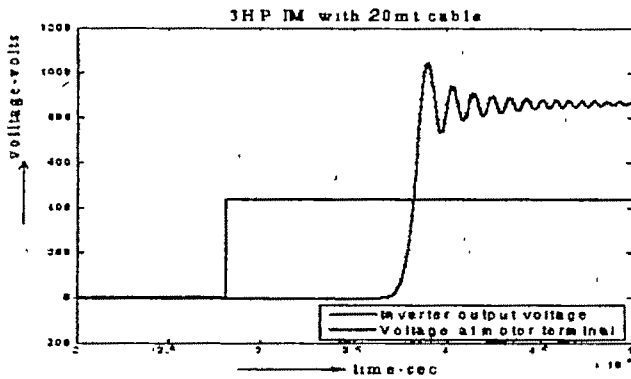


Fig.2. Simulated waveform of at inverter terminal and overvoltages waveform at motor terminal

Fig.1.shows schematic of the PWM inverter (ASD) driving an induction motor using long cable. An adjustable speed drive basically consists of a rectifier and an inverter section, which converts the dc to ac of a selected frequency.

Fig.2 shows the simulated results of inverter output voltage and motor terminal voltage waveform.

Difference in impedances of the cable and motor leads to voltage reflection and hence over voltage appears at motor terminal [1].

III. COMPLETE SYSTEM MODELLING IN MATLAB

Modelling of inverter, cable and motor has been developed and the MATLAB simulation circuits are shown in Fig.3 for low and high frequency applications. All the three models are combined together to represent the complete PWM inverter fed ASD system. The total simulation model of the ASD used in MATLAB is shown in Fig. 3. In this model a certain length of cable is connected between the inverter and the motor of 3HP, and a 420V pulse voltage is applied to the motor through cable. The pulse initiated at the cable will be reflected at the motor terminal due to impedance mismatch between the cable and the motor. The effect of voltage reflection causes overvoltages at the motor terminal. The simulation results showing the overvoltages at motor terminal for different cable length and HP ratings is shown in next section.

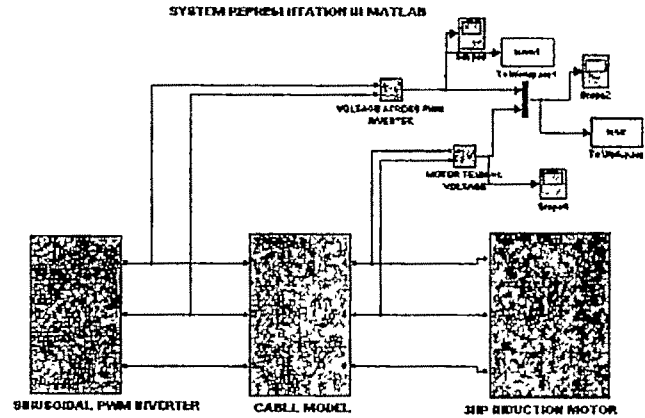


Fig.3 System representation in MATLAB

IV. SIMULATION AND EXPERIMENTAL ANALYSIS OF TERMINAL OVERVOLTAGES

The DC supply to the inverter is 420V and the inverter switches at a frequency of 2 kHz. Fig 4 shows the line to line voltage output of the PWM inverter for a simulation time of 20ms. The waveform appears clean and free from overvoltages; this is from the source reflection coefficient equalling -1. A closer inspection of the output can be made in Fig.5, which is zoomed in to show only six pulses of the output waveform [2].

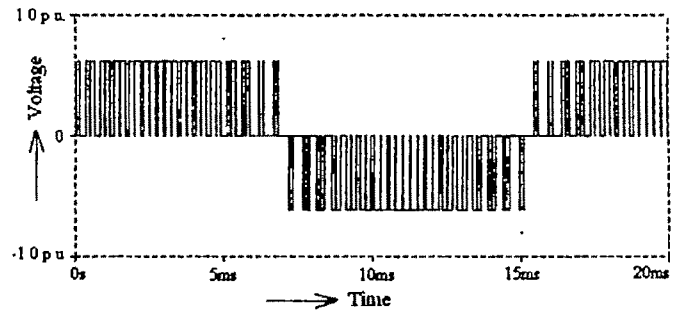


Fig. 4 Line voltage at source

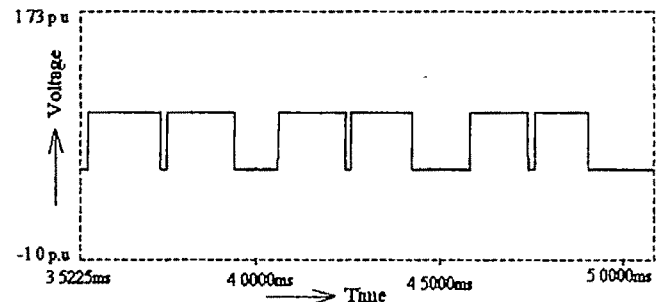


Fig. 5 Line voltage at source zoomed

Fig.6, the line to line voltage waveform at the motor terminals, shows that there are overvoltages occurring at every pulse generated by the source. The majority of the overvoltages are less than or equal to 2pu, but a few exceed 2pu (these will be discussed further on). Fig. 7 shows the voltage waveform zoomed into six pulses of Fig 6.

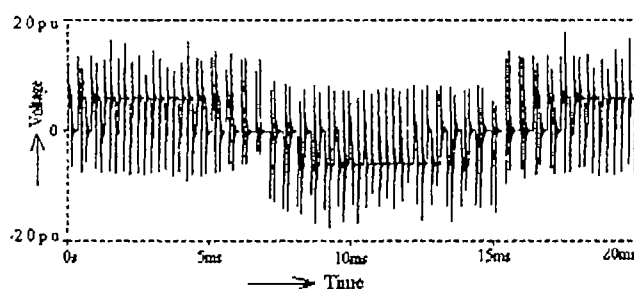


Fig. 6 Line to line voltage at motor terminals with 100m cable

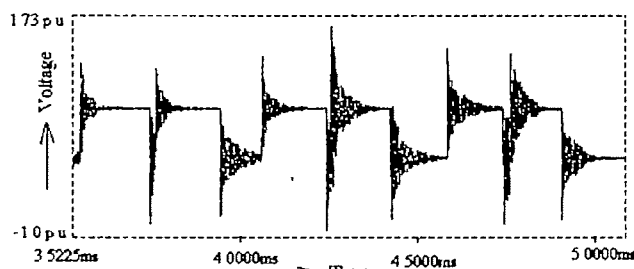


Fig.7 Zoomed line voltage of Fig. 6 at the motor terminals with 100m cable

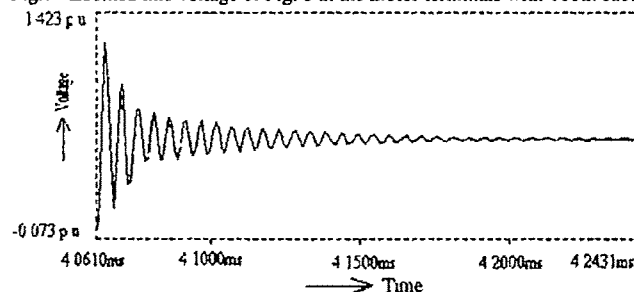


Fig. 8 Zoomed line voltage of Fig. 3.29 at the motor terminals with 100m cable

Fig 7 shows the overvoltages occurring both at the rising edges and the falling edges of the pulses. Fig 8 is zoomed in on one rising edge pulse showing a 2pu (900V) peak overvoltage and its subsequent decay.

Thus overvoltages are dependant on cable to motor surge impedance mismatch, cable length and magnitude and rise time of ASD output. Cable length affects the impedance, oscillation frequency and damping of overvoltages. However, with cables longer than the 2pu critical length of 50-200m for IGBT devices, overvoltages can become much larger than 2pu, on the order of 3-4pu. It has been determined that overvoltages >2pu are dependant on drive modulation technique, carrier frequency, cable natural frequency (f_0) of oscillation, cable high frequency damping losses and inverter output rise time. If the carrier frequency is fast enough and the damping is low enough a residual overvoltage will remain while the next ASD pulse arrives at the motor terminals. Now not only is there a 2pu overvoltage as the incident pulse is reflected but there is also the oscillation overvoltage and its reflection. The new overvoltage is the sum of the pulse, the overvoltage oscillation, and two reflections, this peak can be as high as 4pu. An example of this type of >2pu overvoltage can be seen in Fig. 9, from the results of the above simulation.

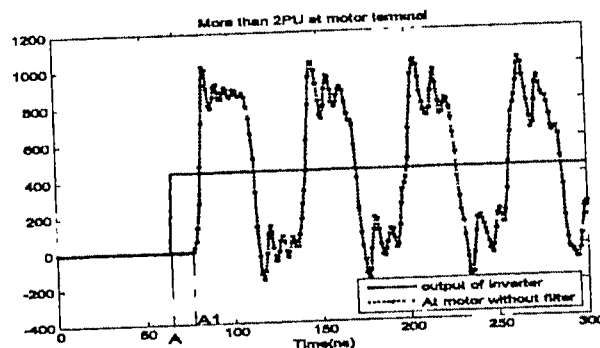


Fig. 9 Overvoltage greater than 2pu as two oscillations double up

In the left side of the figure a falling edge overvoltage can be seen, but before the transient has time to decay the next pulse has arrived causing another overvoltage and transient, the two waves and the pulse sum to form the new overvoltage. The highest of these overvoltages reaches 1100 volts almost 3pu.

There are other causes of >2pu overvoltages as given in some papers [3]. They are termed as double pulsing and polarity reversals. Double pulsing is similar to that mentioned above, where a pulse and a reflected wave meet the motor terminals at the same time. A double pulse is additionally dependant on the dwell time of the ASD pulse, the longer the dwell time the more likely double pulsing will occur. With longer dwell times the reflected oscillation remains in the cable longer, as compared to the time of the next pulse, allowing the next pulse to arrive at the motor terminals and double up with the existing oscillation.

Polarity reversals occur when modulating signals are transitioning in and out of over modulation or at the point of intersection of two modulation waveforms [4]. When the transition occurs the pulse will change from a positive value to a negative value, essentially a pulse of magnitude twice what it would normally be. This large pulse, like the others, travels to the motor terminal and is reflected, but this reflection is much larger than the others as the pulse is larger. This is an extreme overvoltages greater than 3pu. Fig.10 shows the 2-dimentional plot of variation of peak voltages vs cable length.

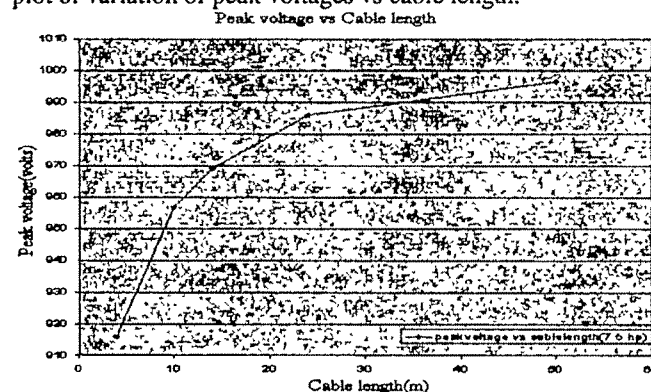


Fig.10. 2-D plot for cable length vs peak voltage

The Fig. 11, the voltage waveforms obtained during the experimental analysis with 3HP induction motor, verifies that

overvoltages occur at the motor terminals.

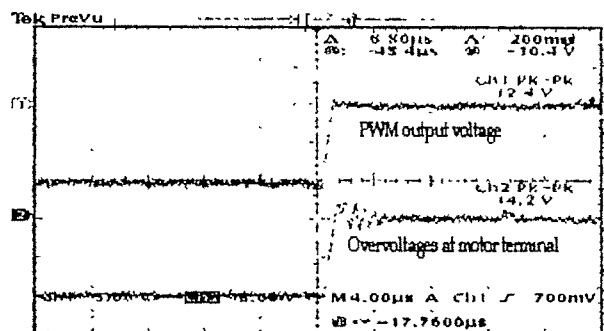


Fig 11 PWM inverter output voltage and motor terminal voltage waveforms for 3HP with 14m cable

TABLE-I

15HP MOTOR FOR DIFFERENT CABLE LENGTHS

Cable length (m)	Motor terminal voltage (volts)	Motor terminal voltage (p.u.)
4	917.5	2.186
10	956.5	2.280
14	969.024	2.307
24	986.03	2.348
50	996.4625	2.373

Observing Fig.10, 11 and Table-I, overvoltages at motor terminal increases due to increase in cable length connected between motor and inverter.

Motor rating is also the region for occurrence of overvoltages at the motor terminal. The Fig.12 shows the effect of HP rating on overvoltages.

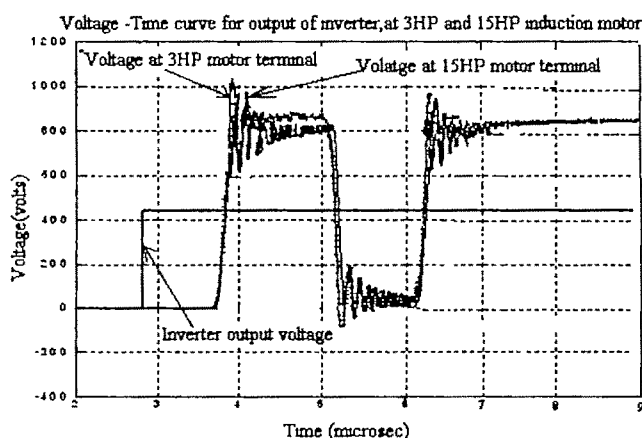


Fig 12 Line to line voltage at motor and inverter terminals for 3HP, 15HP motors for a cable length 14m

TABLE-II

EFFECT OF MOTOR RATING FOR A CABLE LENGTH=60M; RISE TIME=20ns, APPLIED VOLTAGE OF 420VOLTS

Rating of the Motor	Over Voltage (in Volts)
3 HP	1075
15 HP	925

Observing from Fig. 12 and Table-II, the higher rated motors experience less peak voltage magnitude as compared with lower rated motor.

Since the machine will be damaged by large overvoltages, it is necessary to find a solution. There are passive filters and line terminators are the two methods to date that deal with overvoltages on induction machines with respect to long cables and PWM.

V. CONCLUSIONS

This paper represents modelling of the set-up consists of PWM inverter-cable-induction motor and overvoltages analysis. The overvoltages are dependant on cable to motor surge impedance mismatch, cable length and magnitude and rise time of PWM inverter output. Cable length affects the impedance, oscillation frequency and damping of overvoltages. These overvoltages may go upto 2 p.u. However, with cable lengths greater than the critical length,, the overvoltages can become much larger than 2 p.u. of the order of 3-4 p.u.

VI. REFERENCES

- [1] G Skibinski, R. Kerkman, D. Leggate, J. Pankau and D. Schlegel, "Reflected Wave Modelling Techniques for PWM AC Motor Drives" *Applied Power Electronics Conference and Exposition 1998*, Vol 2, pp 1021-1029
- [2] Erik Persson, "Fast switching adjustable speed drives an overview" *Power Engineering Journal*, August 2000, pp 148-157.
- [3] G Skibinski, D Leggate and R. Kerkman, "Cable Characteristics and Their Influence on Motor Over-Voltages" *Applied Power Electronics and Exposition, APEC-97 Twelfth Annual Conference Proceedings 1997*, 23-27 Feb 1997, Vol 1, pp 114-121.
- [4] Russel J. Kerkman, David Leggate, Dave Schlegel and Gary Skibinski "PWM Inverters and Their Influence on Motor Over-Voltages" *Applied Power Electronics Conference and Exposition 1997*, Vol 1, pp 103-130
- [5] J.A Oliver and G.C. Stone, "Implications for the Application of Adjustable Speed Drive Electronics to Motor Stator Winding Insulation" *IEEE Electrical insulation Magazine 1995*, pp 32-36.
- [6] Austin H. Bonnett, "Analysis of the Impact of Pulse-Width Modulated Inverter Voltage Waveforms on AC Induction Motors" *IEEE Transactions on Industry Applications*, Vol.32, No.2, March/April 1996, pp 386-392
- [7] Austin H. Bonnett, "A Comparison between Insulation Systems Available for PWM Inverter Fed Motors" *IEEE Transactions on Industry Applications*, Volume: 33, Issue 5, Publication on Date: Sept/Oct 1997, pp 1331-1341.
- [8] John M Bentley and Patrick J. Link, "Evaluation of Motor Power Cables for PWM AC Drives" *IEEE Transactions on industry applications*, Vol.33, No 2, Mar/Apr 1997, pp 342-358.
- [9] Mike Melfi, Jason Sung, Sid Bell and Gary Skibinski, "Effect of Surge Voltage Rise time on the Insulation of Low Voltage Machines Fed by PWM Converters" *IEEE Transactions on Industry Applications*, Vol.34, No.4, July/Aug1998 pp 766-775.

Speed Control of DC Drives for Controlling Tension of Steel Strips in Steel Strip Manufacturing Industries

S.K. Sen¹, B.R. Das², S. Banerjee³, S.K. Basak³ and S.K. Mondal³

¹ Professor, Department of Applied Physics, Univ. of Calcutta, Kolkata, e-mail: sunitksen@yahoo.co.in

² Scientific Officer, USIC, Univ. of Calcutta, Kolkata

³ Associate System Engineer, IBM India Pvt. Ltd., e-mail: sbanerjee2007@gmail.com

Abstract— In the steel strip manufacturing industries, the steel clothes go through various processes (such as slitting, heat treatment, oil quenching etc.) before being delivered to the market with the desired quality. This needs a controlled speed of the strips which initially come out of a spool driven by a dc drive called the decoiler and are finally wound back on another spool driven by another dc drive called the coiler. Thus the speed of the decoiler increases while that of the coiler decreases. This disparity in the speeds of the two drives may change the quality of the final product.

This paper describes a method to be employed to overcome the above mentioned problem. The proposed feedback control system is based on an 8051 microcontroller. Opto-interrupters are used to measure the speeds of the two drives and a Linear Variable Differential Transformer (LVDT) is used to measure the sag of the steel strip for producing the feedback signals. A prototype of the model has been developed in the laboratory to carry out the above experiment and the results are discussed below.

Key words—DC drives, sag, speed control, tension.

I. INTRODUCTION

The quality of steel as a product from a steel strip manufacturing industry depends on how well the different processes are controlled which it has been taken through one after the other. The material properties of steel do not meet the requirements even if any one of the control parameters of these processes varies during the operation. One such important parameter is the time duration of each process which must be controlled to perfection. Since in the steel strip manufacturing industries, a long strip passes through the processes (e.g. slitting, heat treatment etc.) at a stretch, it is

basically the speed of the strip which has to be controlled. Now, the strip is initially wound on a spool and is unloaded by a dc drive (decoiler) and after going through the processes, it is wound on another spool driven by another dc drive (coiler). So the speeds of the two dc drives have to be controlled [1]-[4]. Also, there must not be any sag of the strip so that its tension control becomes the other criterion.

The method that has been employed to address the above stated problem is that the speed of the decoiler drive is controlled according to the set points from a look-up table for which the speed of the strip coming out of the decoiler spool is maintained at the desired value. The speed of the coiler drive is controlled by examining the sag of the strip in order to minimize the sag. An 8051 microcontroller [5]-[10] is used as the controller unit.

II. THEORY

If 'v' cm/s be the speed at which the strip traverses during the process, 'r' cm be the radius of the decoiler spool without any strip wound on it, 'm' be the number of the turns of strip initially wound on the decoiler and 't' cm be the average thickness of the strip, then after 'n' revolutions of decoiling, the number of pulses per second to be obtained from the corresponding opto-interrupter is given by

$$P_d = 60v / [2 \times 3.141 \times \{r + (m-n)t\}] \dots\dots\dots (1)$$

The constant value '60' belongs to the number of pulses that is obtained from the opto-interrupter for one revolution of the corresponding spool in our model (Figure 1).

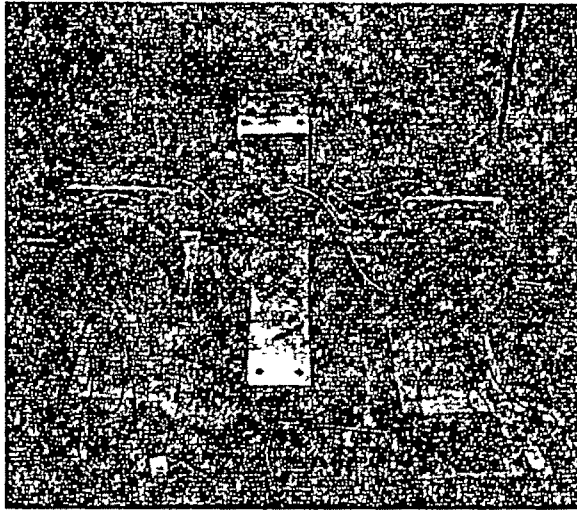
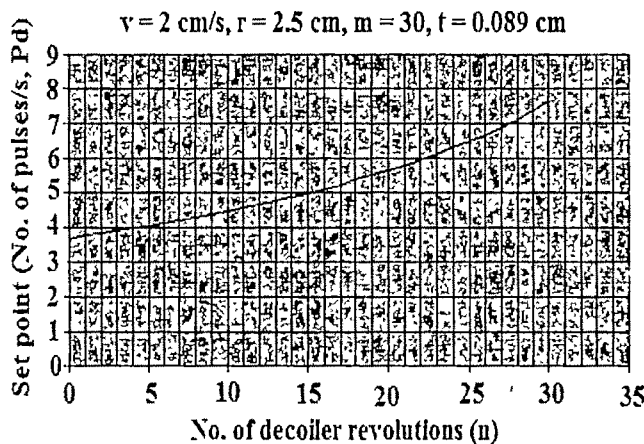


Figure 1: The model of the Decoiler-Coiler system.

Equation (1) shows that throughout the operation, the pulse rate from decoiler should increase as the number of turns of strip on it decreases. The nature of this increment, i.e., the number of pulses to be obtained per second from the corresponding opto-interrupter versus the number of revolutions of the decoiler spool is shown in graph 1.

Substituting the values of the different parameters used in equation (1) for our system, the look-up table of set points for the decoiler drive is developed.



Graph 1: Change of decoiler set point with number of revolutions.

The speed of the coiler drive, on the other hand, is controlled by comparing the output of the Linear Variable Differential Transformer, which is used to measure the sag of the strip, with the set point corresponding to no sag.

Out of the numerous standard control actions, proportional control action is chosen to control the speeds of both the drives, which is given by

$$m = K_p e + M \quad \dots\dots\dots (2)$$

Where m is the manipulated variable, K_p is the proportional sensitivity and e is the error signal given by

$$e = (\text{set point} - \text{feedback signal})$$

M being the manipulated variable at zero deviation.

Tuning of controllers: Proportional control is used to control speeds of both the decoiler and coiler drives in our system. Hence the tuning parameters must include the proportional sensitivities (K_p) of both the control actions.

Also, to take care of the variation of load variable throughout the process (the decoiler load decreases whereas the coiler load increases with time), provision for changing the proportional sensitivities for both the decoiler and coiler control actions were taken care of during the process by following another look-up table in the software. Since the motors are identical in electrical specifications, it is assumed that the nature of decrement of K_p for decoiler is identical to that of the increment of K_p for coiler. Hence, same look-up table for both the drives are used.

III. BLOCK DIAGRAM

The block diagram of the system is shown in Figure 2. It reveals that the LVDT is used to measure the sag of the strip. Its output is signal conditioned, converted to an 8 bit digital word with the help of an analog to digital converter [5] and is finally fed to 8255#1 which is one of the two available 8255 programmable peripheral interfaces (PPIs) [11]. Opto-interrupters (MOC 7811) are used to measure the speeds of the two spools. Port C of the other PPI (8255#2) monitors the output voltages of the opto-interrupters and accordingly produces the clock pulses for counter 1 and counter 2 of programmable counter 8253 [11]. Ports A and B of 8255#2 are used to send the control action signals to the two DC drives. Each of these control action signals is an 8-bit digital word and thus they are first converted into analog voltages using digital to analog converters. After signal conditioning, each of these analog voltages is used to produce a rectangular waveform having a proportional duty cycle. These waveforms are amplified using motor controller circuits [12] and are finally fed to the two motors.

IV. DEVELOPMENT OF THE SOFTWARE ALGORITHMS

The software is developed on a DYNA-51 system development kit provided by Dynalog India Private Limited. It uses an 8051 microcontroller as its Central Processing Unit. To develop the software, the following are considered: (1) The pulses from opto-interrupters are counted by the programmable counter 8253, (2) The on-chip timer T1 [6]-[7] of 8051 is used to produce a delay of 1s, (3) The numbers of pulses obtained per second from both the opto-interrupters are written in two separate portions of the RAM.

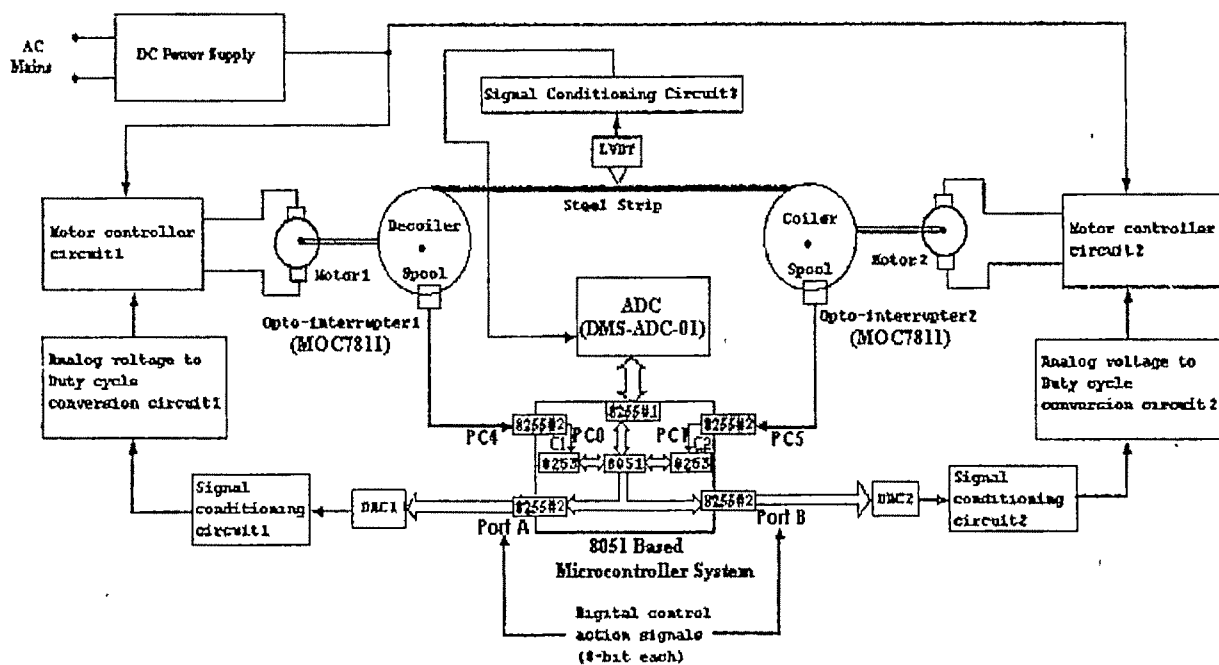


Figure 2: Block diagram of the system

V. CONCLUSION

Assembly language [6]-[7] is used to write the software. The algorithms for the main program and different subroutines are given in appendix in detail. The decoiler-coiler system responds satisfactorily when the software is executed. The look-up table for the proportional sensitivities of both the control actions is having all identical values as trial runs. Development of the theory to find out the nature of change of the proportional sensitivities and to tune the control system remains as the tasks to be carried out in future.

APPENDIX

Algorithm 1: The main program

(Look up tables for set points of decoiler and proportional sensitivities of both the controllers are initially included before the instructions of main program.)

Steps:

1. Clear timer 1 start bit.
2. Initialize 8255#1 ports as follows: Port A and Port B as input, Port C as output.
3. Initialize 8255#2 ports as follows: Port A, Port B and Port CL as output, Port CH as input.
4. Reset PC0 of 8255#2.
5. Reset PC1 of 8255#2.
6. Initialize counter 1 of 8253 as a 16 bit binary counter in Mode 0.
7. Load both the lower and upper bytes of the counter 1 with FFH.

8. Initialize counter 2 of 8253 as a 16 bit binary counter in Mode 0.
9. Load both the lower and upper bytes of the counter 2 with FFH.
10. Load R0, R1, R2 and R3 registers of bank 0 with count values for level sensitive counting.
11. Load R4 of bank 0 with initial number of seconds' value 00H.
12. Load R5 of bank 0 with count value for producing 1 second delay.
13. Load R6, R7, R3 and R5 of bank 2 with initial values.
14. Load R1, R2 and R3 of bank 3 with initial values.
15. Enable timer T1 interrupt.
16. Initialize timer T1 in Mode 1.
17. Load T1 lower and upper bytes with the initial values for producing 1s delay.
18. Read Port C of 8255#2.
19. Wait until PC7 of 8255#2 is set to logic 1.
20. Send initial control action words to Port A and Port B of 8255#2.
21. Start timer T1.
22. Enable oscillator of ADC and send Start of Conversion (SOC) pulse through 8255#1.
23. Read Port C of 8255#1.
24. Call the coiler subroutine if the ADC has set End of Conversion (EOC) bit.
25. Read Port C of 8255#2.
26. Jump to step 32 if bit PC4 is in logic 1.
27. Otherwise reload counter R1.
28. Decrease counter R0 and jump to step 25 until R0 contains 0.
29. Reset PC0 of 8255#2.
30. Reload counter R0.

31. Jump to step 36.
32. Reload counter R0.
33. Decrease counter R1 and jump to step 25 until R1 contains 0.
34. Set PC0 of 8255#2.
35. Reload counter R1.
36. Read Port C of 8255#1.
37. Call the coiler subroutine if the ADC has set End of Conversion (EOC) bit.
38. Read Port C of 8255#2.
39. Jump to step 45 if bit PC5 is in logic 1.
40. Otherwise reload counter R3.
41. Decrease counter R2 and jump to step 38 until R2 contains 0.
42. Reset PC1 of 8255#2.
43. Reload counter R2.
44. Jump to step 49.
45. Reload counter R2.
46. Decrease counter R3 and jump to step 38 until R3 contains 0.
47. Set PC1 of 8255#2.
48. Reload counter R3.
49. Jump to step 23.

Algorithm 2: The coiler subroutine

Steps:

1. Send logic state 1 to Output Enable (OE) pin of ADC.
2. Read ADC output.
3. Move output of ADC to R7 register of bank 3.
4. Read set point of LVDI.
5. Clear carry.
6. Subtract content of R7 register of bank 3 from content of accumulator.
7. Jump to step 16 if carry flag is set.
8. Move content of accumulator (A) to register B.
9. Load A with the content of memory location pointed by register R1 of bank 3.
10. Multiply A with content of register B.
11. Move content of A to register R7 of bank 3.
12. Load A with data 80H.
13. Clear carry.
14. Subtract content of R7 register of bank 3 from content of A.
15. Jump to step 27.
16. Move content of A to register R7 of bank 3.
17. Load A with data FFH.
18. Clear carry.
19. Subtract content of R7 register of bank 3 from content of A.
20. Increase content of A by 1.
21. Move content of A to register B.
22. Load A with the content of memory location pointed by register R1 of bank 3.
23. Multiply A with content of register B.
24. Add data 80H to A.
25. Jump to step 27 if carry flag is not set.
26. Load A with data FFH.

27. Send the content of A to port B of 8255#2.
28. Enable oscillator of ADC and send Start of Conversion (SOC) pulse through 8255#1.
29. Return.

Algorithm 3: Interrupt service routine for internal timer 1 (T1)

Steps:

1. Clear TFI flag.
2. Decrease content of R5 by 1.
3. Move content of R5 to accumulator (A).
4. Jump to step 8 if zero flag is set.
5. Load T1 lower and upper bytes with the initial values for producing 1s delay.
6. Set TR1 bit.
7. Return.
8. Increase content of R4 by 1.
9. Load R5 of bank 0 with count value for producing 1s delay.
10. Load T1 lower and upper bytes with the initial values for producing 1s delay.
11. Set TR1 bit.
12. Move content of R4 to R6.
13. Move content of R4 to R7.
14. Read counter 1 of 8253.
15. Select memory bank 2.
16. Move content of A to R2 (bank 2).
17. Read counter 2 of 8253.
18. Move content of A to R4 (bank 2).
19. Move content of R6 (bank 2) to A.
20. Clear carry.
21. Subtract content of R2 (bank 2) from content of A.
22. Move content of location 12H to 16H.
23. Initialize external RAM location C000H.
24. Increase the initialized external RAM location by 1.
25. Decrease the content of R6 (bank 0) and jump to step 24 until the content becomes zero.
26. Send content of A to location pointed by DPTR.
27. Move content of A to location 20H.
28. Exchange content of A with that of R3 (bank 2).
29. Add content of R3 (bank 2) to that of A.
30. Load register B with value 3CH.
31. Divide A by B.
32. Compare content of A with value 01H and jump to step 40 if not equal.
33. Increase content of 1AH.
34. Select memory bank 3.
35. Compare content of R2 (bank 3) with value 1EH and jump to step 37 if not equal.
36. Jump to the stop subroutine.
37. Come back to memory bank 2.
38. Move content of 1AH to 1CH.
39. Increase content of 1CH by 1.
40. Move content of B to 13H.
41. Move content of R7 (bank 2) to A.
42. Move content of 14H to 17H.
43. Initialize external RAM location E000H.
44. Increase the initialized external RAM location by 1.

45. Decrease the content of R7 (bank 0) and jump to step 44 until the content becomes zero.
46. Send content of A to location pointed by DPTR.
47. Move content of A to location 21H.
48. Exchange content of A with that of R3 (bank 2).
49. Add content of R5 (bank 2) to that of A.
50. Load register B with value 3C1H.
51. Divide A by B.
52. Compare content of A with value 011H and jump to step 56 if not equal.
53. Increase content of 1BH.
54. Move content of 1B1H to 1DH.
55. Increase content of 1DH.
56. Move content of B to 15H.
57. Load R0 (bank 2) with value 7EH.
58. Load 18H with value 40H.
59. Decrease content of R0 (bank 2) by 1.
60. Decrease content of 181H by 1.
61. Decrease the content of 1CH and jump to step 59 until the content becomes zero.
62. Load A with the content of memory location pointed by R0 (bank 2).
63. Clear carry.
64. Subtract the content of 20H from that of A.
65. Jump to step 76 if carry flag is set.
66. Move content of A to B.
67. Select memory bank 3.
68. Load A with the content of memory location pointed by R0 (bank 3).
69. Come back to memory bank 2.
70. Multiply A by B.
71. Add value 80H to A.
72. Jump to step 74 if carry flag is not set.
73. Load A with value FFH.
74. Send content of A to port A of 8255#2.
75. Jump to step 93.
76. Move content of A to 1EH.
77. Load A with value FFH.
78. Clear carry.
79. Subtract content of 1EH from A.
80. Increase content of A by 1.
81. Move content of A to B.
82. Select bank 3.
83. Load A with the content of memory location pointed by R0 (bank 3).
84. Come back to bank 2.
85. Multiply A with B.
86. Move content of A to 1EH.
87. Load A with value 80H.
88. Clear carry.
89. Subtract content of 1EH from A.
90. Jump to step 92 if carry flag is not set.
91. Load A with value 00H.
92. Send content of A to port A of 8255#2.
93. Move content of 21H to 19H.
94. Increase content of 19H.
95. Decrease content of 1DH by 1 and jump to step 94 until the content becomes zero.
96. Come back to bank 0.
97. Return.

Algorithm 4: The stop subroutine

Steps:

1. Load A with value 00H.
2. Send the content of A to ports A and B of 8255#2.
3. Repeat step 3.

REFERENCES

- [1] Y. S. E. Ali, S. B. M. Noor, S. M. Bashi and M. K. Hassan, "Microcontroller performance for DC motor speed control system," Power Engineering Conference PECon 2003 National Proceedings, pp. 104 – 109, Dec. 2003.
- [2] G. Sen Gupta, S. Mukhopadhyay and Chew Moi Tin, "A project based approach to teach mixed-signal embedded microcontroller for DC motor control," Electronic Design Test and Applications DELTA 2006, Third IEEE International Workshop, pp. 6, Jan. 2006.
- [3] R. Krishnan and A. S. Bharadwaj, "Single chip microcontroller implementation of an induct vector controlled induction motor drive system," Power Electronics Specialists Conference PESC 1989, 20th Annual IEEE Record, vol. 1, pp. 265 – 270, June 1989.
- [4] J. C. Kim, S. H. Lee, D. Y. Lee, J. H. Lee, W. C. Jeong, H. J. Park and I. S. Mok, "Single-chip implementation of a 32-bit microcontroller for motor drive," ASIC Conference 1998, 11th Annual IEEE International Proceedings, pp. 3-6, Sept. 1998.
- [5] M. K. Mayes and W. Chin Sing, "A 200 mW, 1 Msample/s, 16-b pipelined A/D converter with on-chip 32-b microcontroller," IEEE J. Solid-State Circuits, vol. 31, issue 12, pp. 1862-1872, Dec 1996.
- [6] M. A. Mazidi and J. G. Mazidi, "The 8051 microcontroller and embedded systems, Pearson Education, Delhi, 1st edition, 2002, 435p.
- [7] K. J. Ayala, "The 8051 microcontroller: architecture, programming and applications," Penram International Pub., Mumbai, 2nd edition, 1997 (2005 printing).
- [8] R. Bannatyne and G. Viot, "Introduction to microcontrollers," WESCON/97 Conference Proceedings, pp. 564-574, Nov 1997.
- [9] D. Beetner, H. Pottinger and K. Mitchell, "Laboratories teaching concepts in microcontrollers and hardware-software co-design," Frontiers in Education Conference FIE 2000, 30th Annual IEEE, vol. 2, pp. SIC/1 – SIC/5, Oct. 2000.
- [10] R. Bannatyne and G. Viot, "Introduction to microcontrollers. I," WESCON/98, pp. 350-360, Sept. 1998.
- [11] R. S. Gaonkar, "Microprocessor architecture, programming and applications with the 8085/8085A," Penram International Publishing (India) Private Limited, Mumbai, 3rd edition, 1997, 735p.
- [12] A. Bertacchini, P. Pavan, L. Tamagnini and L. Feignani, "Control of brushless motor with hybrid redundancy for force feedback in steer-by-wire applications," Industrial Electronics Society IECON 2005, 32nd Annual IEEE Conference, pp. 6, Nov 2005.

Technical Session 5A

Power System

Power Vector Coordinated Multilateral Trades

Sudha Balagopalan¹, S Ashok² and KP Mohandas³

¹ National Institute of Technology, Calicut, India e-mail: sudhabalagopalan@yahoo.com

² National Institute of Technology, Calicut, India e-mail: ashoks@nitc.ac.in

³ National Institute of Technology, Calicut, India e-mail: kprmdas@nitc.ac.in

Abstract--A new procedural algorithm, for coordinating multilateral trade, in a restructured electricity market, is presented in this paper. Transmission Service Providers iterate load flow to least loss formulation and through transmission charges guide injections towards optimum. Power vectors coordinate coalition formation.

Key words —Co-operative Game theory, Electricity Market Restructuring, Graph Theory Applications, Graph Theoretic Allocations

I. INTRODUCTION

IN a power system, with many generator and load buses, graph theoretic allocation [1] of loads to generators provides interesting study. On computation, it is seen that at any bus, for a particular load, allocation from a generator to that load varies as the total generation at any bus varies. Table I (Appendix) illustrates a five bus case. The table shows that actual power that flows to a load is different from what is contracted by the agent at that bus and depends on deals struck by other agents at other buses. Clearly, what is paid for is different from what an agent gets. Restructuring of the power sector must address this issue. Here, a *coalitional k-lateral trade* is proposed to obtain justifiable allocations.

Electricity market restructuring has several models [2] [3] [4] and all implementations have as yet not addressed all the challenges [5]. Persistent gaps [6] are reported in the interface between engineering aspects of system operations and economic aspects of market operation. The distributed electricity market, envisaged by coordinated multilateral trade [7] to [11] assures autonomy of end-users and hence economic efficiency. Sufficiency of network, the concern of Transmission System Provider (TSP), is attained through curtailment or adjustment bids. Since the concept of electricity market originated from the need for reduced prices and reliability of network, coordinated multilateral trade is the model on which developments are proposed.

When conflicting motives exist coordination is of utmost importance and the role of the coordinator can be fulfilled best

by the TSP. Coordination by the Power System Operator (PSO), through curtailment measures [7], [11] may be viewed with suspicion by the end-users. Also, curtailment schemes being unilateral will not be acceptable to all without misgivings. If a solution is not obtained within time sub-optimal operation results. Trade volume reduces. *Moreover in third world countries like India line loss is the issue and not congestion.* Hence, Transmission Service Charges (TSC) is proposed as instruments of coordination to lead the power system towards *least loss performance*. An efficient design of transmission policies and tariffs makes TSP active decision makers unlike in [7] and guide the transaction towards a coordinated least loss multilateral trade.

The proposal for coordinating energy and transmission trade, using transmission pricing signals derived from net node injections [12] accords this flexibility to TSP. However usage, losses and congestion are flow dependant. Graph theory [1] when used to calculate contributions of loads and generators to line flows indicate that larger loads or generators do not imply larger loss. Clearly, node injections are not useful for transmission pricing. Three ideas emerge at this juncture. TSC design must be transmission line flow based. The tariff for transmission should penalize deviations from least loss flow along each and every line. End users must have incentive to self-curtail or to contract additional trades such that larger amount of power is forced along lines with lower resistances. Line flow dependant TSC is proposed here for coordinating trades. Penalizing trades which cause deviation from least loss formulation is proposed to be included in the design for guidelines for tariff. To reduce the impact of penalties the market participants need to co-operate, negotiate with other agents and form socially stable core [13], [14] to derive maximum benefit. The power vector [15] is another instrument that is proposed here to initiate negotiations (and designed to be released by the TSP corresponding to least loss formulation) for forming stable coalitions i.e. which achieve maximum social welfare.

A. Co-operative Game Theory (CGT)

Unlike non-co-operative game theory which is a detailed model of all the moves available to the players, CGT abstracts away from this level of detail and describes only the outcomes that result when players come together in different

combinations. Hence it could also be termed combinatorial game theory and is more suitable in electricity market structure because it embodies co-operation among players and also competition in a particularly strong and unfettered way.

B. Socially Stable Core

A situation in which a finite set of players can obtain certain payoffs by co-operation is described as a co-operative game with transferred utility. Also, for a given social structure e.g. a network, a hierarchical ordering or some dominance relation exists in any subset of players. For every coalition, such an underlying social structure is defined by a power vector whose components reflect the strengths of individual members of the coalition within the social structure. More powerful players are able to increase their payoffs at the expense of the lesser powerful players unless they move to alternative internal organizations. For a payoff vector to be in the socially stable core there should be neither incentives to deviate from an economic point of view, nor from a social one. A payoff vector is economically stable if it is feasible and non-dominated. If there is a weighted sum of these power vectors that gives all individuals the same power, then individuals are equally powerful at the proposed payoff and the payoff vector is called socially stable.

C. Digraph and power vectors

Power vector of a coalition is completely determined by the social structure along which the coalition is organized. In electricity markets the social structure is given by a directed graph on the set of players. A directed graph consists of nodes and directed edges. The nodes now are either predecessors or successors and if every node is neither its own predecessor nor successor, a graph with such nodes is irreflexive and called a digraph. Here the method used to measure power of nodes (players) consists of a node, deriving power, from both the number as also power of its successors [15] as given below.

Let A be the collection of irreflexive digraphs on the vertex set $N = \{1, 2, \dots, n\}$ with $(i, j) \in N \times N$ denoting the arc \vec{ij} . The positional power function is the function $f^p : A \rightarrow \mathbb{R}^n$ which maps each $A \in A$ to

$$f^p(A) = \frac{1}{n} \left(I - \frac{1}{n} T^A \right)^{-1} s^A \quad (1)$$

Here T^A is the adjacency matrix of A , with the ij^{th} entry $t_{ij}^A = 1$ if (i, j) is an arc of A and 0 otherwise, and s^A is the score vector giving the number of successors of each node.

This paper proposes a two level computational framework for multilateral trade coordinated through flow based transmission signals coalitions, derived from power vectors. In section II a basic outline of the method is described with underlying assumptions. The method of using demand data of the agents for obtaining least transmission loss condition and application of power vectors for guiding the transaction towards least loss formulation are also explained. In section III the algorithm procedure is illustrated, through a five bus model. Conclusions, including scope for future research are dealt with in Section IV.

II. SOCIALLY STABLE COORDINATED MULTILATERAL TRADE MODEL

A. Model outline

The cost-benefit figures of the profit motivated end users are not readily available and if released are not reliable. On the other side there is the TSP which has access to network configuration data and is concerned with network reliability. Thus there are two premises for information derivation and so two levels of computations. Thereafter co-operation is suggested for undertaking the transactions, which while maximizing benefits to the end users, minimizes the social welfare cost. Pricing signal that can be used to implement the latter is derived from transmission line flows; and cooperation is effected through negotiated collaborations based on individual power vectors.

B. Procedural Algorithm steps

The steps are outlined below:

- 1) The system operator announces the network data (available transmission line configuration, impedances and limits), tariff policies (for line usage- e.g. MW-Mile, loss and congestion allocation to trade, ancillary service).
- 2) Brokers arrange trades, perform load flow and submit bus injections and line flows with directions in the form of power vectors for k-lateral trade.
- 3) TSP performs load flow analysis and least loss iterations, computes transmission charges (penalizing deviations from least loss formulation) and power vectors and publishes these, which help the agents to start negotiating.
- 4) Brokers find mutually beneficial trades that reduce cost of transmission and form socially stable coalitions. Reliability is improved and additional trades are shopped.
- 5) Final demand is conveyed and scheduled and TSP is obligated to implement this agreement honoring the charges already communicated.
- 6) Anomalies from the committed schedules can be compensated by the TSP if practicable.

Assumptions in the model are

- 1) Approximate line flow is used with relevant assumptions
- 2) All assumptions associated with rational behavior of agents in co-operative game theory environment are considered valid.
- 3) Only one agent is associated with each node/bus.

C. Least loss Formulation & Use of power vectors

Once k-lateral agreements are made by end users, they communicate to TSP the amount of power at the point of intended injection but keep their cost-benefit data private. TSP collects data for all n nodes performs load flow analysis and arrives at the total loss on the transmission line using the following equations.

For a network with N nodes, l lines, M reduced incidence matrix (size $l \times N - 1$), z net injected power at $N-l$ nodes y_j net power injected at node j , z vector of line flows, z_i flow through line i , R primitive resistance matrix ($N \times N$)

$$z = R^{-1} M (M^T R^{-1} M)^{-1} y \quad (\text{line flow eq.}) \quad (2)$$

$$P_i = z^T R z \quad (\text{transmission loss eq.}) \quad (3)$$

$$\sum_{j=1}^N y_j - P_i = 0 \quad (\text{energy balance eq.}) \quad (4)$$

The differential of the loss function with respect to power at each bus when set to zero while keeping injections at all other buses constant gives the generation at that bus for least loss for such a schedule. Of the schedules, one formulation with power loss on lines least, amongst all schedules gives the least loss formulation. Allocation of losses or derivation of TSC will be based on deviation of line flow in this schedule and individual line flows already submitted. Calculations are shown below.

$$P_i = z^T R z$$

$$= (R^{-1} M (M^T R^{-1} M)^{-1} y)^T R R^{-1} M (M^T R^{-1} M)^{-1} y \quad (5)$$

$$= y (R_{bus}^{-1})^T y$$

where $R_{bus} = (M^T R^{-1} M)$

$$\text{Solve for } \frac{\partial P_i}{\partial y_i} = 0 = \sum_{j=1}^n 2g_{ij} y_j \quad (6)$$

where $i \in N$ and g_{ij} is the ij^{th} element of $(R_{bus}^{-1})^T$

Power vectors are derived for the most desirable transaction(s). The agents now arrange or re-arrange trades to reduce the impact of TSC i.e. to maximize their profit and are guided by the power vector released by the TSP for lowest transmission charges and negotiate with other agents for achieving this. Final demand functions are communicated or if necessary iterated with the co-operation of the TSP till all end users are satisfied.

III. DEMONSTRATION ON A FIVE BUS POWER SYSTEM

A. Case Study - 5 Bus Power Systems

A 5 bus power system example with two suppliers and four consumers is taken. (Fig.1. & Table II & III)

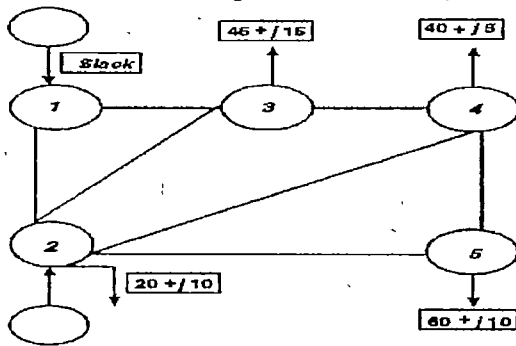


Fig. 1. Five bus power system

TABLE II
BUS DATA FOR FIVE BUS POWER SYSTEM

BUS	1	2	3	4	5
Gen (MW)	Slack	40, 30	-	-	-
Load(MW)	Slack	20, 10	45, 15	40, 5	60, 10

So using the frame-work given for load flow analysis, total power shuttling over the lines, consequent losses and power vectors (all including ground bus) are computed and analyzed.

TABLE III
LINE AND FLOW DATA USING APPROX. AND EXACT METHOD

Line	R+jX	B/2	Line flow	Line flow
1-2	.02+j.06	.03	88.47	85.43
1-3	.08+j.24	.025	41.08	39.57
2-3	.06+j.18	.02	24.8	24.29
2-4	.06+j.18	.02	27.99	27.43
2-5	.04+j.12	.015	55.	53.71
3-4	.01+j.03	.01	18.78	18.86
4-5	.08+j.24	.025	6.46	6.29
Sum	Total power shuttling		262.6	255.6
PI	(in MW)		4.77	4.73

Analysis: Approximate method and load flow analysis results correspond. A total load of 165MW causes shuttling of a total 255.6MW and line loss of 4.77MW. Each possible trade i.e. each load alternatively met by generators at all other buses is considered and computations submitted as in Table IV

TABLE IV
LOAD ON ONE BUS AND GENERATORS ON ALL OTHER BUSES

Bus(i,j)	(2,1)	(2,3)	(2,4)	(2,5)	(5,1)	(5,2)	(5,3)	(5,4)
Sum	25.4	35.7	36.2	29.7	25.4	88.	139.3	117.
PI	6.7	8.6	8.7	11.6	6.7	104.7	140.7	130.
Power Vector of ground and 5 buses	.24	.27	.27	.24	.24	.30	.27	.27
	.44	.20	.20	.20	.46	.20	.20	.20
	.21	.21	.21	.21	.60	.80	.20	.20
	.43	.64	.40	.40	.20	.20	.63	.40
	.40	.40	.64	.43	.20	.20	.40	.64
Bus(i,j)	(3,1)	(3,2)	(3,4)	(3,5)	(4,1)	(4,2)	(4,3)	(4,5)
Sum	93.9	80.4	53.8	104.5	94.7	72.4	47.	78.6
PI	60.2	43.4	17.9	79.1	50.7	34.7	14.2	58.1
Power Vector of ground and 5 buses	.24	.30	.27	.24	.24	.30	.27	.27
	.47	.20	.20	.20	.47	.20	.20	.20
	.60	.80	.40	.60	.60	.80	.20	.20
	.21	.22	.21	.21	.20	.20	.63	.40
	.20	.20	.64	.20	.21	.22	.40	.64
5 buses	.20	.20	.23	.47	.20	.20	.21	.21

Analysis: Load at bus 2 and 5 are best met by generators at bus 1 for least loss and minimum power shuttling over the network. Similarly load at bus 3 when met by generators on bus 4 and vice-versa lead to optimal network usage.

Computations at second level, at TSP premises is conducted as a load flow by treating injection at all buses as a collection of trades or as a k-lateral trade. There are four possible trade schedules- generators on bus 1 and on every alternate bus i.e. bus 2(Type1), bus 5(Type2), bus 4(Type3) and bus 3(Type4) meeting total load requirements. There are eight such combinations as the ratio of allocation of generation is varied with the second generator's share, increasing from 0 to 165MW. The impact is given in the different columns of Table V including power vectors. There is a reduction of total power shuttling through the lines and a corresponding reduction of total loss (Fig. 2 to 5), a least value, and thereafter an upward trend. The loss on line is plotted with generators on slack bus taking on loads from 165 to 0MW of power.

B. Inferences

1) For all the 4 types of load schedule transmission loss and total power shuttled converge to a minimum. If line loading can be controlled, network security can be ensured. The overall effect of all trades, on the lines, can be computed by the TSP but control has to be effected by the end-users. This interface can be provided by transmission price signals. All

the three components of transmission service charge- usage, congestion and loss on lines should come from such a monitoring of line loading in the design of the TSC.

2) The least loss formulation corresponds to type 3 trade, where 82.5 MW is dispatched from bus-4, line loss is the least and equal to 1.6 MW and total line loading is 160.05 MW. Both TSC and generation expansion signals can be derived as functions of the differences from these optimal values.

3) Corresponding to loss/loading variation, there is also a transition in the power vector values. This transition is an identification of reversal of flow through particular lines and provides an approach route for end users to negotiate a transaction that minimizes their TSC. It is suggested that TSP coordinate negotiations such that coalitions are formed to reduce line flows, with agents adjacent to buses with maximum power and with appropriate agents for achieving these through particular lines.

4) The TSC minimization is at the expense of TSP benefits. However by acting as agents at selective bus(es), or using ancillary services the benefit can be regained, by causing counter-flows without affecting the social cost.

5) The power vectors provide interesting perspectives for analysis. The optimal point of operation is recurrently gives a power nearest to 0.5 for the ground bus. It is unique if it is a transition point. It provides an intuitional understanding of the flow direction for least loss; especially in terms of which line should carry more power at the expense of which lines.

IV. CONCLUSION

A socially stable coordinated least loss multilateral electricity market has been modeled. An application to a 5 bus power system indicates that power vectors guide the agents towards coalitions sharing the responsibility of maintaining security of the system. Least loss formulation is effected through TSC. Also transmission expansion can be substituted, an advantage associated with the integrated system. The non- relevance of financial instruments is a note-worthy advantage. No curtailment of load, only a rescheduling of power flow directions and amounts, through a negotiated change in injections is needed; the scope for deriving generation expansion signals is also implied. Further research is an efficient TSC design, an algorithm for power vector based synchronized negotiation and derivation of generation expansion signals.

APPENDIX

TABLE I
LOAD ALLOCATION TO GENERATORS

Gen-1 129.7MW -P1 Gen-2- 40MW - P2 Loss- 4.74	13.6	39.5	30.5	41.4
	6.4	5.5	9.5	18.6
Gen-1 26.5MW -P1 Gen-2 141.5MW -P2 Loss- 3MW	0	19.2	4	0
	20	25.8	36	60
Gen-1 43.9MW -P1 Gen-4 122.7MW - P4 Loss- 1.6MW	13.85	5	0	23.45
	6.15	40	40	36.55
Gen-1 43.35MW -P1 Gen-3 122.7MW - P3 Loss- 1.85MW	14.2	0	0	27.3
	5.8	15	40	32.7
Gen-1 64MW -P1 Gen-5 102.75MW - P5 Loss- 1.77MW	13.34	37.14	11.77	0
	6.66	7.86	28.33	60
LOAD	Bus-2	Bus-3	Bus-4	Bus-5

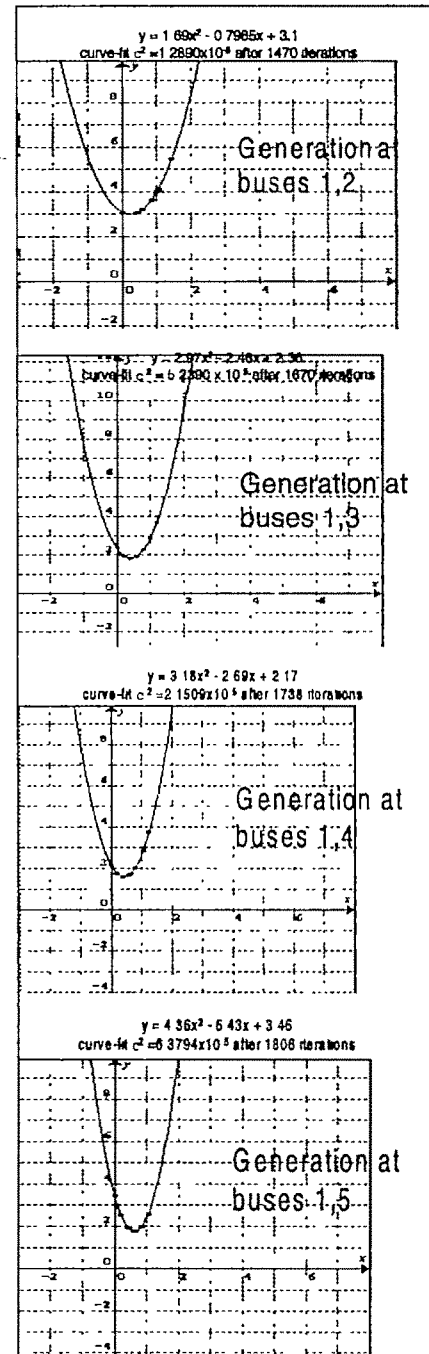


Fig. 2 Power loss verses Generation at bus 1 (160 to 0MW load) with bus,2,3,4 and 5 taking more load

TABLE V GENERATORS ON ALTERNATE BUSES AS PER 4 TYPES OF TRADE

Type 1	3,4,5 at 1	3,5 -1/4-2	3-2;4,5-1	3,4-1;5-2	3,4-2; 5-1	3-1, 4,5-2	3,5-2; 4-1	3,4,5-2	
Sum	274.71	236.43	231.64	217.29	193.36	179	174.21	175.79	158.66
PI	548.97	412.28	398.99	364.17	322.99	308.4	305.2	310.1	300.71
Ref	.2534	.5397	.5397	.5397	.5397	.5397	.5397	.3151	.4913
bus	.5202	.5342	.5342	.5342	.5342	.5342	.5342	.2428	.2486
Power	.6772	.7040	.7040	.7040	.7040	.7040	.7040	.8902	.6995
Vector	.444	.5010	.5010	.5010	.5010	.5010	.5010	.4562	.4913
Of all	.4104	.4661	.4661	.4661	.4661	.4661	.4661	.4224	.4566
5 bus	.2089	.2567	.2567	.2567	.2567	.2567	.2567	.2192	.2486
Type-2	2,3,4 at 1	2-5; 3,4-1	2,3-1; 4-5	2,4-1; 3-5	2,4-5; 3-1	2,3-5; 4-1	3,4-5; 2-1	2,3,4,- 5	
Sum	175.67	147.83	144.36	145.12	147.38	148.14	151.15	175.17	144.78
PI	256.4	199.19	176.91	176.79	189.54	198.16	254.44	345.65	176.57
Ref	.2572	.5032	.5032	.5032	.5032	.5032	.5032	.2572	.5032
bus	.543	.5269	.4921	.4921	.4921	.4921	.4921	.2016	.4921
Power	.8467	.7022	.7022	.7022	.7022	.7022	.7022	.8467	.7022
Vector	.4111	.4589	.2506	.2506	.2506	.2506	.2506	.2096	.2506
Of all	.2096	.2506	.4589	.4589	.4589	.4589	.4589	.4111	.4589
5 bus	.2016	.4921	.5269	.5269	.5269	.5269	.5269	.5430	.5269
Type 3	2,3,5 at 1	3,5 -1; 2-4	3-4, 2,5-1	2,3-1; 5-4	2,3-4; 5-1	3-1; 2,5 -4	3,5-4; 2-1	2,3,5- 4	
Sum	211.38	190.71	167.83	162.33	162.64	163.57	168.69	183.07	163.73
PI	376.97	284.74	205.14	176.4	169.99	160.285	175.82	216.79	160.054
Ref	.2572	.4902	.5309	.5190	.5329	.5329	.4962	.2858	.4904
bus	.5427	.5248	.4881	.4525	.4941	.4941	.243	.2362	.2428
Power	.8464	.9006	.6736	.462	.4647	.4647	.4576	.4167	.4565
Vector	.4098	.2484	.2552	.2532	.4996	.4996	.6995	.6565	.4911
Of all	.2016	.4161	.6974	.6614	.7034	.7034	.7345	.7146	.6994
5 bus	.2096	.2484	.2552	.2532	.2555	.2555	.2494	.2143	.2484
Type4	2,4,5 at 1	4,5 -1; 2-3	4-3; 2,5-1	2,4-1; 5-3	2,4-3; 5-1	4-1; 2,5-3	4,5-3; 2-1	2,4,5- 3	
Sum	241.09	217.71	200	188	188	184	196	208	183.077
PI	367.54	286.17	228.57	194.74	194.74	184.69	198.4	235.89	184.61
Ref	.2524	.4609	.5110	.5110	.5110	.4961	.4961	.2863	.4961
bus	.5144	.5236	.5386	.5386	.5386	.2430	.2430	.2362	.4906
Power	.8512	.8996	.7039	.7039	.7039	.4576	.4576	.4168	.4576
Vector	.2351	.2418	.5274	.5274	.5274	.7336	.7336	.7177	.4859
Of all	.4102	.4507	.4605	.4605	.4605	.7006	.7006	.6530	.4576
5 bus	.2082	.2435	.2519	.2519	.2519	.2494	.2494	.2144	.2494

References

1. Felix F Wu, Yixin Ni and Ping Wei "Power Transfer Allocation for Open Access Using Graph Theory- Fundamentals and Applications in Systems without Loop flow" IEEE Transactions on Power Systems Vol. 15 No:3 Aug 2000 pp
2. A.K David "Dispatch methodologies for open access Transmission system" IEEE Transactions on Power Systems, Vol. 13, No. 1, Feb '98 pp.46-53
3. RS Fang & David "Optimal dispatch under Transmission contracts" IEEE Transactions on Power Systems, Vol. 14, No. 2, May' 99 pp 732-737
4. Dr. Loi Lei Lai "Power System Restructuring and Deregulation" John Wiley Publications
5. AF Vojdani, CF Imperato, NK Saini, BF Wollenburg and HJ Happ Transmission Access Issues IEEE, Transactions on PS Vol. 11/1, Feb' 96, pp. 41-51
6. Hung-Po Chao, Shmuel S Oren, Alex Papalexopoulos, Dejan Sobajic & Robert Wilson " Interface Between Engineering and Market Operations in Restructured Electricity Systems" (Invited paper) Proceedings of IEEE Vol. 93, No 11, 2005, pp.1984-97
7. Pravin Varaiya and Felix Wu "Coordinated Multilateral Trades for Electric Power Networks: Theory and Implementation" IEEE Transactions on Electric Power and Energy Systems Vol 21 1999 pp 75- 102
8. Shmuel S Oren, Pablo T Spiller, Pravin Varaiya and Felix Wu " Folk Theorems: Proofs and Counterexamples" Journal of Regulatory Economics 10 2996 Kluwer Academic Publishers pp 5-26
9. Shmuel S Oren, Pablo T Spiller, Pravin Varaiya and Felix Wu " Nodal Prices and Transmission Rights: A Critical Appraisal
10. Chris SK Yeung, Ada SY Poon, FF Wu "Game Theoretical Multi-Agent Modeling of Coalition Formation for Multilateral Trades" IEEE Transactions on Power Systems, Vol. 14, No:3, August 1999 pp.929-934
11. X Wang ,YH Song & Q Lu "A coordinated Real-Time Optimal Dispatch Method for Unbundled Electricity Markets" IEEE Transactions on Power Systems, Vol. 17, No. 2, May 2000 pp. 482-90
12. Marija Ilic, Eric Hsieh and Prasad Ramanan "Transmission Pricing of Distributed Multilateral Energy Transactions to Ensure System Security and Guide Economic Dispatch" IEEE Transactions on Electric Power Systems Special publication on tools for managing restructured energy systems -submitted in May 2003 7 pages
13. P Jean-Jacques Herings, Gerard van der Laan , Dolf Talman "The Socially Stable Core in Structured Transferable Utility Games" submitted for publication to International Journal of Game Theory on 12.4 2006 (29 page)
14. P Jean Jacques Herings, Gerard van der Laan and Dolf Talman "Measuring the power of Nodes in Digraphs" Tinbergen Institute Discussion paper 2001-096/1 16 pages
15. Jean Derks, Gerard van der Laan, Valery Vasil'ev " On the Harsanyi payoff vectors and Harsanyi imputations" submitted for publication to International Journal of Game Theory on 12.8.2005 (14 pages)

High Speed Fault Identification in A HVDC System Using Wavelet Modulus Maxima

M. Sushama¹, Ch.Prasanth Babu¹, A.Jaya Lakshmi¹, G.Tulasi Ram Das¹
Department of Electrical and Electronics Engineering, J.N.T.U College of Engineering, Hyderabad, India.
¹E-Mail : m73sushama@yahoo.com

Abstract – This paper presents a high speed fault identification technique based on wavelet transformation. The main aim of the paper is to understand the wavelet technique analysis of different kinds of faults using wavelet transforms. In this paper, different HVDC system faults are considered. The simulation results are analysed and shown that the application of wavelet technique leads to faster and reliable solution for fault identification. The results prove that the Wavelet transform technique is superior compared to the Time-Amplitude technique.

1. INTRODUCTION

The safety of a HVDC system depends on the fast detection and clearance of faults. The traveling wave theory is used to provide the fastest protection. Long HVDC lines are hence modeled as distributed elements as they cannot be analyzed with concentrated parameters.

According to traveling wave theory, voltage and current traveling waves appear on the line when fault occurs. The fault generated traveling waves contain sufficient fault information that can be used for high-speed fault identification and line protection. In AC transmission lines, the amplitude of fault generated traveling waves changes with the voltage angles. There is a problem for the traveling wave protection when faults occur near voltage zero crossing. However, there is no such problem for DC transmission lines so that traveling wave protection is ideally suited for HVDC lines.

In HVDC systems, commutation failures in the converter station and single-phase short circuit faults at the AC side are similar to HVDC line faults. It is an important requirement of HVDC line protection that different fault types be identified and the correct decision be made as fast as possible.

However, a fast and reliable fault identification is still a big challenge. It is not easy to identify HVDC faults by using pure frequency domain based methods or pure time domain based methods. The pure frequency domain based methods are not suitable for the time-varying transients and the pure time domain based methods are very easily influenced by noise.

The wavelet transform provides a new approach for analyzing time-varying transients. It has the capability of analyzing signals simultaneously in time and frequency domain. Moreover, it can adjust analysis windows

automatically according to frequency, namely, shorter windows for higher frequency and vice versa. Hence it is suitable for characteristic identification and traveling wave protection [1-4]. However, wavelet based fast identification and protection in HVDC systems is a relatively new field.

In this paper, the behavior of different faults in HVDC power systems will be analyzed through wavelet transform and the identification criteria based on wavelet techniques will be proposed. Based on the above investigations, the high-speed HVDC line protection will be developed. The simulations are carried out with MATLAB. The results show that the wavelet techniques lead to a new way for the fault identification and the protection in HVDC systems.

2. FAULTS IN HVDC SYSTEMS

For the analysis and the identification of HVDC system faults, different cases are studied. A standard model of 12-pulse HVDC system under the MATLAB environment is used for the simulation. Figure.1 shows the simulation model in which a 1000 MW (500 kV, 2kA) DC line is used to transmit power from a 500 kV, 5000 MVA, 60 Hz network to a 345 kV, 10 000 MVA, 50 Hz network. The DC line is 300 km long and the speed of the traveling wave is 296112 km/s.

Figure.2 shows the voltages and currents of DC line at the rectifier terminal when (a) DC line short circuit, (b) commutation failure at the inverter station, (c) singlephase short circuit on the AC side of inverter station, and (d) normal operation condition as a reference case.

From Figure. 2, we can see that different types of faults lead to similar transient processes. It is not easy to identify the faults and to make correct protection decision fast within 3-5ms by using traditional methods.

3. WAVELET TRANSFORMS

The Wavelet transform transfers a time varying signal into a time-scale plane and thus can represent the original signal with time as well as frequency information. Each scale in wavelet transform corresponds to a certain frequency band and the time window widths are changed with scale or frequency automatically. Such multiresolution property is particularly suitable for analyzing transient signals. Another important reason why wavelet transform is attractive for engineers is because there are fast calculation algorithms based on filter bank structure.

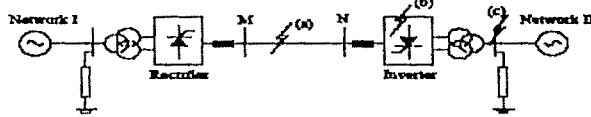


Figure 1. Simulation model

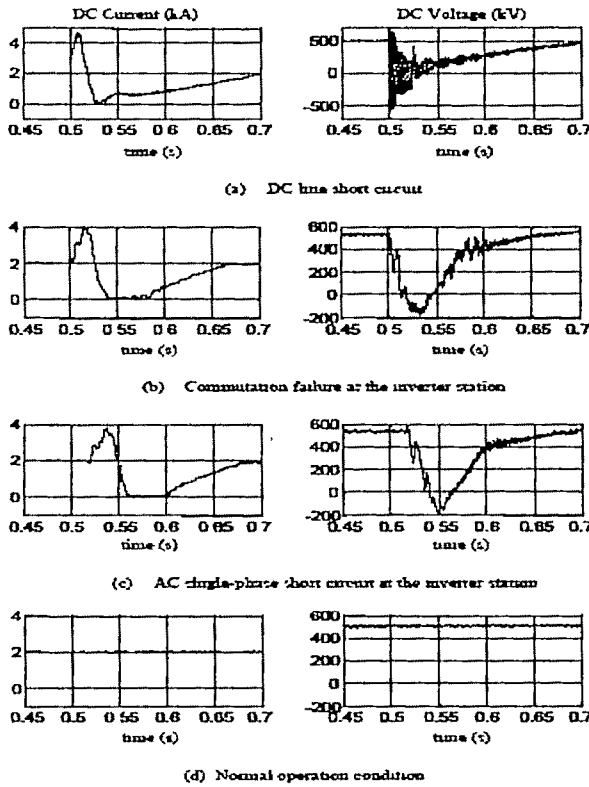


Figure 2. Faults in HVDC systems

There are different algorithm structures for the wavelet transform. Considering a better time location and a better information keeping, we use the a'trous structure but without down-sampling blocks following the high pass filters. Figure 3 shows our filter bank where H0 and H1 are low-pass filters and high-pass filters respectively. The outputs of high-pass filters are the wavelet transform of the original signal, called as **Wavelet coefficients**.

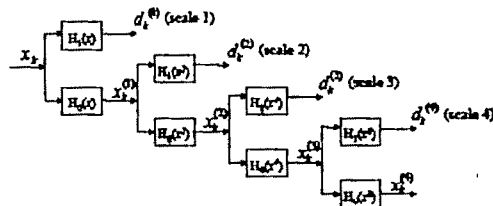


Figure 3. Wavelet filter bank

The absolute local maximum values of wavelet coefficients are called **wavelet modulus maxima**. If the mother wavelet is the first derivative of a smooth function, the edge of a signal can be represented well by its wavelet modulus maxima. Under above condition, the wavelet modulus maxima occur at an edge point, the polarity of the

maxima shows the change direction of the edge, and the amplitude represents the changing intensity of the edge. It is proved that the wavelet modulus maxima satisfy the following relation.

$$\left| \frac{W_{\max} x(t)}{W_{\max} x(t)} \right| \leq A s^{\alpha} \quad (1)$$

Where, $W_{\max} x(t)$ is the wavelet modulus maxima of signal $x(t)$, A is a constant, s is scale and α is Lipschitz exponent. This relation means that the wavelet modulus maxima of an edge ($\alpha=0$ or $\alpha>0$) remain unchanged or increase in value while the wavelet modulus maxima caused by white noise ($\alpha<0$) decrease in value when scale increases. Additionally, the number of wavelet modulus maxima caused by white noise decrease sharply when scale increase [6]. This makes a strong denoising function possible. The simulation results show that the wavelet modulus maxima represent the edges well even when signals are mixed with noise around 20% [7].

4. WAVELET ANALYSIS OF HVDC SYSTEM FAULTS

The transients of the study cases above will be analyzed through wavelet transform. Each case is sampled at 80 kHz and 512 samples are taken for wavelet transform in 4 scales. The Haar wavelet is used as the mother wavelet. HVDC line currents, HVDC line voltages and corresponding reverse voltage travelling waves are used as the input signals of the wavelet filter bank. Reverse voltage travelling waves are calculated with equation 2

$$u_r = (u_{DC} - Z_c i_{DC}) / 2 \quad (2)$$

Where u_r is reverse voltage travelling wave, u_{DC} and i_{DC} are the DC voltage and DC current respectively, and Z_c is the surge impedance of the HVDC line.

4.1 Normal operations

The DC current and DC voltage are steady with small changes around the rated values during the normal operation conditions. Figure 4 and Figure 5 display seventh level decomposition of fault current in case of AC single phase and DC line fault respectively.

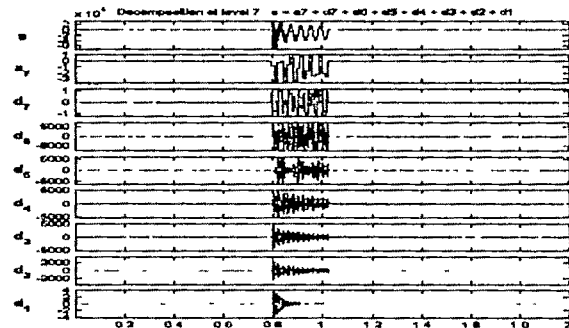


Fig.4 Seventh level decomposition of fault current in case of AC single phase faults using Haar wavelet.

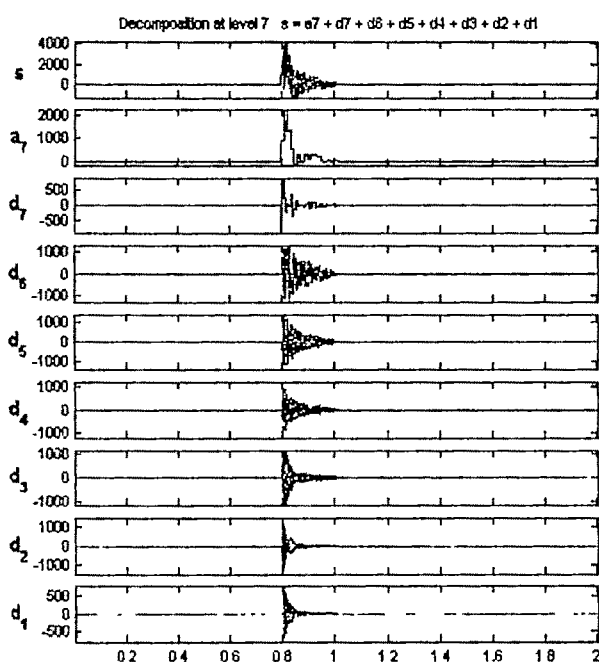


Figure.5 Seventh level decomposition of fault current in case of DC line fault using Haar wavelet.

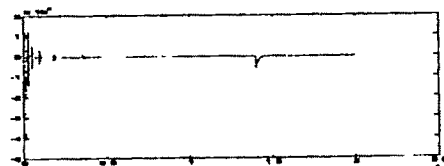


Fig 6.Coefficients plot of AC single phase plot

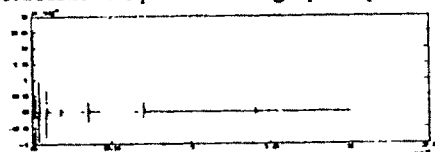


Fig.7 Coefficients plot of DC line current faults. modulus maxima occur regularly and with small values: less than 0.04 for DC current, less than 40 for DC voltage and less than 20 for reverse voltage traveling wave.

3.2 HVDC LINE FAULTS :

HVDC line faults at different locations with different fault resistances are simulated. One of the HVDC line faults occurs at 135 km from terminal M and with zero fault resistance. Figure 8 shows the DC current at the terminal M and its wavelet modulus maxima in four scales. Figure 8 and Figure 9 display the DC voltage and the reverse voltage travelling wave at the terminal M and their wavelet modulus maxima in four scales.

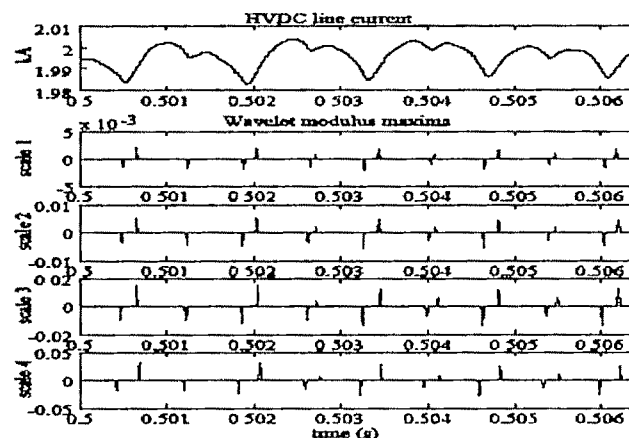


Fig.8 DCcurrent during normal &Wavelet Modulus Maxima.

It can be seen that:

- The wavelet modulus maxima occur at every arriving and reflection instant of the traveling waves. The polarities appear regularly: positive and negative in turns. The values of the wavelet modulus maxima are much larger than ones during the normal operation conditions.

4.3 AC SINGLE-PHASE FAULTS

Figure 9 shows the wavelet modulus maxima of the reverse voltage travelling wave at the terminal M during an AC single-phase fault at the inverter station. Similar to the commutation failure, all wavelet modulus maxima in AC single-phase fault are less than 40, the polarities of modulus maxima remain the same for 3ms. Therefore, the AC fault can also be identified surely from the HVDC line fault and the normal operation with the setting (e.g. 100) value and the polarity change.

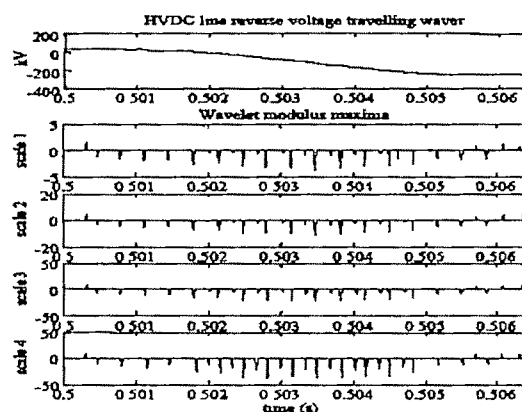


Fig 9 Revers voltage travelling wave & its WMM during AC single phase fault

Unlike the commutation failure, the wavelet modulus maxima in AC single-phase fault occur with more density and relative larger value specially 3ms after the disturbance arrives at terminal M, and the polarities become positive and negative in turns after the unified polarity changes. Considering a fast identification in 3ms, the difference of the wavelet modulus maxima can be better used. Figure 12 shows the energy during 3ms on each scale. It can be seen that the difference between a

commutation failure and an AC fault can be discriminated with the energy.

5 wavelet identification of HVDC system faults

With the help of the above analysis of HVDC faults through wavelet transform, the criteria for the identification can be obtained.

• For HVDC line fault identification, the amplitude of the first wavelet modulus maxima of reverse voltage traveling wave, denoted as

$$|W_{\max} U_r| \dots\dots\dots(3)$$

should be larger than the setting value setting K. The setting can be taken as 100 for 500 kV HVDC lines.

$$W_{\max} U_r > K_{\text{setting}} \dots\dots\dots(4)$$

• For identifying commutation failures and AC faults from the normal operation condition, the pattern of polarity change is used. During the normal operations, the polarities regularly change positive and negative in turns. It will be a commutation failure or an AC fault if the polarities remain the same for 3ms.

For differentiation between a commutation failure and an AC fault, the energy of the wavelet modulus maxima on the scale 7 during 3ms are used. The energy, denoted as

$$E(W_{\max} U_r) \dots\dots\dots(5)$$

should be larger than the setting value. The setting can be taken as 40 for 500 kV HVDC lines.

$$E(W_{\max} U_r) > E_{\text{setting}} \dots\dots\dots(6)$$

Based on the identification of HVDC faults, a new high-speed HVDC line protection can be developed. In this protection, the fault location can be also obtained at the same time as the fault identification. The fault location is calculated according to Equation 7. The key here is the measurement of the time delay Δt . Considering that the reflection from the fault location (reflection factor is negative) is different than the reflection from the line terminal (reflection factor is positive), we measure the time delay between the first two opposite polarity wavelet modulus maxima. Namely, if the first is negative, the next one should be taken with positive polarity.

$$L = \frac{v \times \Delta t}{2} \dots\dots\dots(7)$$

Where L is fault distance in km from the measuring point, Δt is the time delay in s, v is travelling wave speed in km/s.

6 Conclusion

For high-speed HVDC line protection based on travelling waves, methods for transient signal analysis are necessary. Particularly, the identification with similar HVDC transients caused by faults is decisive. The wavelet transform provides a new possibility for this. In this paper, the different HVDC system faults are analysed and the criteria for the identification and the line protection are proposed. The simulation results show that the proposed approach based on the wavelet modulus maxima can make

a definite identification of HVDC line faults, commutation failures and AC single phase faults. The application of wavelet techniques leads to a faster, easier and more reliable solution for the identification of HVDC system faults and the development of new high-speed protection of HVDC lines.

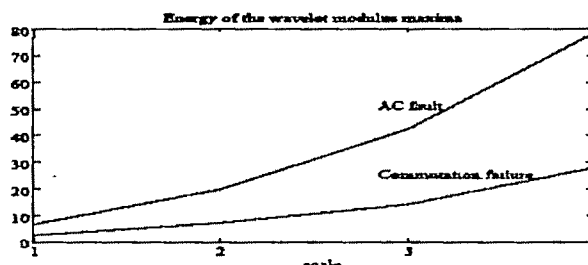


Fig10 Energy of the Wavelet modulus maxima

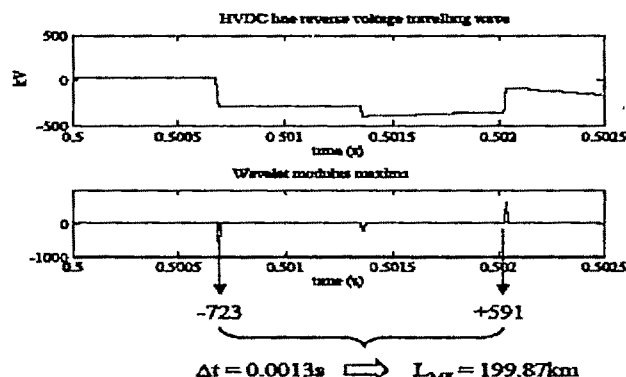


Fig 11 .DC line Fault · 200km from terminal m

References

- [1] L.Shang, G.herold, "Analysis and identification of system faults using wavelet modulus maxima", IEEE transaction.
- [2] Magnago, F.H. and Abur, A., 1998, "Fault location using wavelets", IEEE Trans. on Power Delivery, 13-4, 1475-1480.
- [3] Dong, X. Zh., Ge, Y. Zh. and Xu, B. y., 2000, "Fault position relay based on current travelling waves and wavelets", IEEE PES 2000 Winter Meeting, 23-27.
- [4] L.Shang, J.Herold, "High speed fault identification and protection for hvdc line using wavelet technique", IEEE transaction
- [5] Shang, L., Herold, G. and Jaeger, J., 2000, "A new approach to high-speed protection for transmission line using wavelet technique", PSP 2000, 85-90.
- [6] Mallat, S. and Hwang, W. L., 1992, "Singularity detection and processing", IEEE Trans. On Information Theory, 38-2, 617-643.
- [7] Shang, L., Herold, G. and Jaeger, J., 2001, "High speed protection for transmission line based on transient signal analysis using wavelets", IEEDPSP 2001, 173-176.

Design of an Optimum Controller for DVR to Compensate Unbalanced Voltage Sag

M.R. Shakarmai¹, A. Kazemi², and B. Mahdian¹

¹ Electrical Engineering Department, Islamic Azad University of Khorramabad, Iran, e-mail: mr_shakarami@yahoo.com

² Electrical Engineering Department, Iran University of Science & Technology, Iran, e-mail: kazemi@iust.ac.ir

Abstract— Dynamic Voltage Restorer (DVR) installed between a source and sensitive loads can restore the load voltage to its pre-fault value. To achieve this, it is necessary to transfer the energy and real power of a DVR to a distribution system. Due to the fact that the capability of stored energy is limited as a result of DC capacitors, it is essential to optimize the injected energy of a DVR when it is needed to approach the load voltage to its pre-fault value. Generally it is not necessary to achieve the exact value of pre-fault voltage and when the voltage falls behind a desired interval, the control is acceptable. In this paper, in order to minimize the produced power of a DVR, a characteristic function with some constraints is presented, and the voltage of the load is considered as a variable. Besides, a proper phase locked loop (PLL) to generate the reference signals is proposed in which harmonics and negative sequence voltage (if any) are eliminated and therefore will not appear in the injected voltages. Regarding to these specifications, a PWM controller is proposed and its perfect performance in unbalanced voltage sag cases depicted in simulation results.

Index Terms— Power Quality, DVR, Compensation, Voltage Sag, Optimization.

I. INTRODUCTION

DUE to the vast application of electronic switches in distribution systems, power quality problems such as sag and swell voltages, harmonics and unbalanced voltages have extremely increased. Besides, these problems have a great effect on Hi-Tech. equipment associated to communication, modern controller, automation and etc., and it is possible to lead a noticeable investment to be wasted. One of the most important aspects of power quality is reduction of dynamic voltage which means short-time decreasing in voltage amplitude in the interval of 10 to 90% of its nominal value that is known as the Sag or Dip. Under this circumstance, a new technology, known as the Custom Power, has emerged in order to improve power quality and reliability. Parallel and series compensators are categorized in this group. Basically, Parallel compensators such as distribution static compensator (DSTATCOM) are utilized in order to clear the effects of harmonics on the sources [2]. Series compensators such as DVR are mainly used to improve voltage quality [3]. DVR is placed between sources and loads, depicted in Fig.1, and compensates the voltage value. Ideally, the desired voltage value can be acquired where the stored energy of DVR

is unlimited. But as a result of inherent constraints of DC capacity of DVR, full compensation of the voltage is impossible. Therefore, it is needed to optimize injected energy [4]-[6]. Additionally, an important issue in controller design is generation of reference signals. Otherwise, the controller will not create positive effect on improving system performance. In most loads, it is not necessary that the voltage be exactly equal to its pre-fault value. Therefore, in this paper we consider the voltage as a variable with an allowable tolerance and a performance function is defined. After optimization, the phase and the post-fault value of the load voltage are calculated in order to minimize generated power of a DVR. In this paper, also a new approach for generating reference signals for controller is proposed. Therefore the controller is designed and the result of simulation shows the effectiveness of this design in the case of lack of voltage even in unbalanced situations.

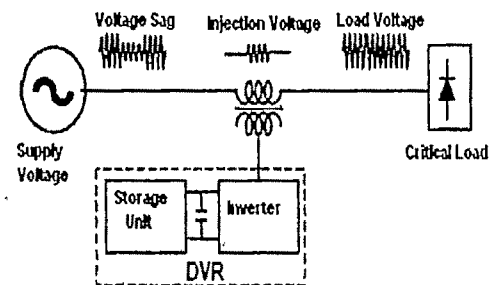


Fig. 1 DVR structure

II. OPTIMIZING THE INJECTED POWER OF DVR

Generally it is not necessary that the magnitude and the angle of compensated voltage be exactly equal to their pre-fault values. Therefore, an allowable tolerance for voltage is considered which depends on nature of the load. Usually, the interval of 90 to 110% for magnitude variations and 5 to 10% for angle variations are acceptable and they do not cause to trip loads. In Fig. 2, a vector diagram of compensated voltage is shown in which, V_{DVR} and I are amplitude of the load voltage, injected voltage of DVR and the load current respectively, and V_y and δ_j are amplitude and angle variations for each phase ($j=a, b, c$) in the event of fault in the network.

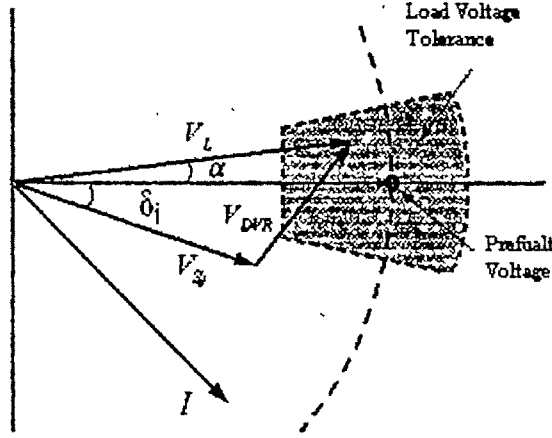


Fig. 2. Vector diagram of current and voltage in DVR

If we consider P_{in} , P_{out} and P_{DVR} as input power of supply, consumed power of the load and generated power of DVR respectively, then the equations related to these powers are as follows:

$$P_{in} = \sum V_{ij} I \cos(\phi - \alpha + \delta_j) = 3V_L I \cos(\phi) \quad (1)$$

$$P_{out} = \sum V_L I \cos(\phi) \quad (2)$$

$$P_{DVR} = P_{out} - P_{in} \quad (3)$$

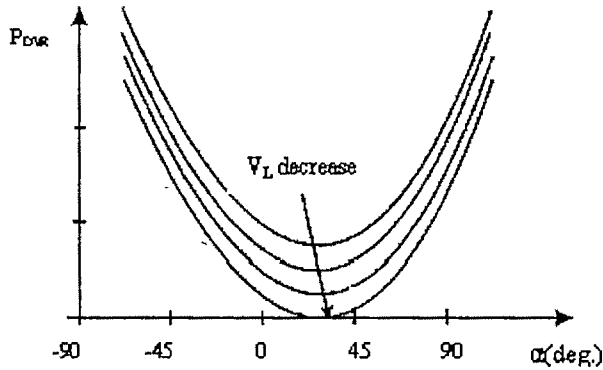


Fig. 3. Generated power of DVR versus two controlling parameters of α and V_L

According to (3) it is obvious that generated power of DVR depends on two parameters α and V_L .

Fig. 3 shows the effect of these two parameters on the generated power of DVR in extreme voltage sag situations. Therefore it is possible to noticeably decrease generated power of DVR. To decrease P_{DVR} to zero, (4) shall be maintained. Meanwhile, α and V_L have to be in voltage tolerance interval in such a way that (5) be maintained. To attain (4) by considering (5), a target function such as (6) is presented to minimize the variations of the load voltage amplitude in the fault time compared to its amplitude of pre-fault.

$$3V_L I \cos(\phi) - \sum V_{ij} I \cos(\phi - \alpha + \delta_j) = 0 \quad (4)$$

$$V_{min} \leq V_L \leq V_{max} \quad (5)$$

$$\alpha_{min} \leq \alpha \leq \alpha_{max}$$

$$J = (V_{prefault} - V_L)^2 \quad (6)$$

Therefore the generated power of DVR is minimized using this approach. Also, the load voltage has minimum variations.

III. BASIC REFERENCE SIGNALS

One of the most important aspects in PWM controller design for DVR is the generation of suitable reference voltages. In this paper, the structure shown in Fig. 4 has been utilized [7].

In this approach, wherever the supply includes harmonics or negative sequences, they will be eliminated in reference wave and therefore will not appear in injected voltage of DVR.

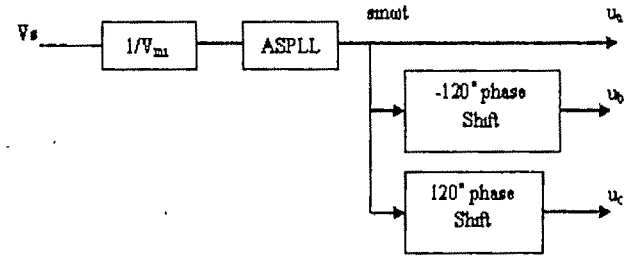


Fig. 4. Block diagram of generating circuit of reference signals

In this structure, according to Fig. 5 a feed backed loop which is suitable for ASPLL (adapted soft phase locked loop) is used in which there exists a filter with a constant time T to clear harmonics and negative sequences [8].

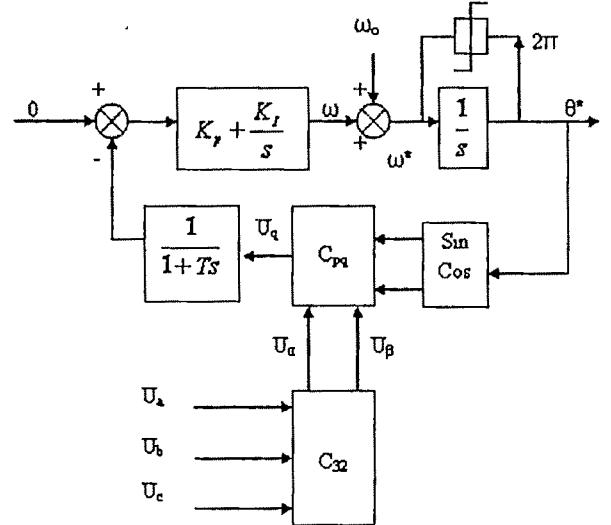


Fig. 5. Structure of ASPLL

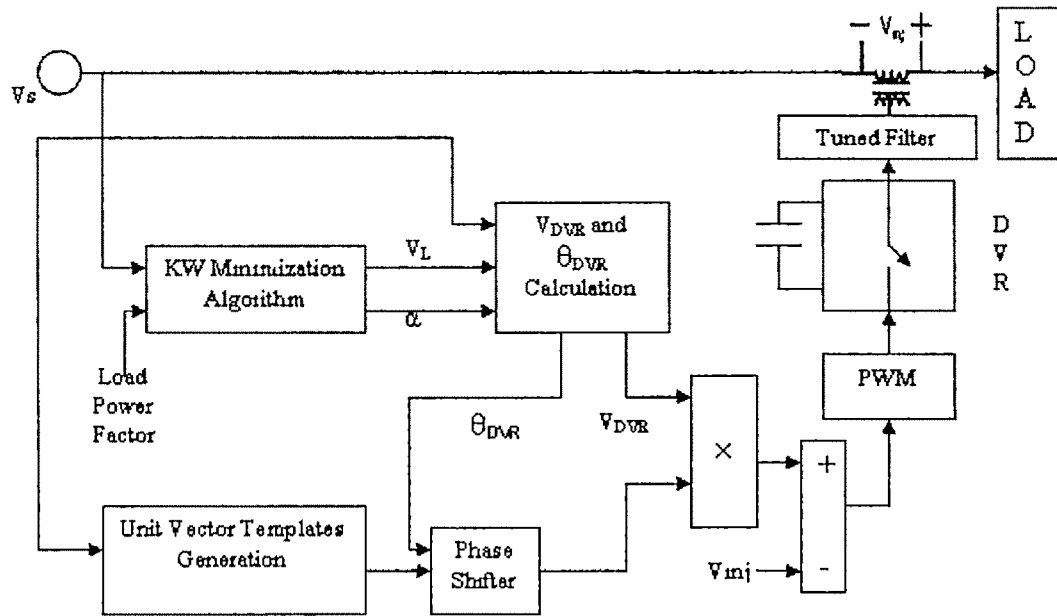


Fig. 6. Block diagram of closed loop control for DVR

IV. PROPOSED CONTROL STRATEGY

Block diagram closed loop of a DVR is shown in Fig. 6. In this diagram, for simplicity, MATLAB software functions are used to optimize injected power which yields optimized parameters of α and V_L . Applying these parameters and input voltage, magnitude and phase of voltage V_{DVR} and θ_{DVR} will be calculated using vector equations. The unit reference vectors are shifted to be equal to θ_{DVR} plus filter phase angle of DVR and the reference signal will be generated when this vector is multiplied to V_{DVR} . This signal is compared to the real value of injected voltage and finally is considered as PWM input. The output of PWM is used for firing elements of inverter in DVR. Then output of DVR is passed through a filter and is added to the line voltage by a series transformer.

V. SIMULATION RESULTS

To check the validity of the proposed controller, it is supposed that $0.975 \leq V_L \leq 1.025$ p.u. and $-45^\circ \leq \alpha \leq 45^\circ$.

Table I. Current and voltage of the source in sag condition and in unbalanced state (state 1)

$V_{Lref} = 310.26$ v	$I = 24$ A
$V_{sa} = 217.188$ v	$\delta_a = -20^\circ$
$V_{sb} = 279.241$ v	$\delta_b = -10^\circ$
$V_{sc} = 263.728$ v	$\delta_c = -15^\circ$
Power angle = 26.56°	

The supply has an unbalanced condition as shown in Table I. Injected voltages and the load voltages are shown in Table II. In this state the result of the controller is shown in Table III in which it is seen that the generated power of DVR is

decreased by 35.4% compared to the un-optimized state.

Table II. Load voltages and injected voltages by DVR (state 1)

Injection voltages	Load voltages
$V_a = 177.9 \angle 59.2^\circ$	$V_L = 304.05 \angle 4.94^\circ$
$V_b = 128.63 \angle -38.52^\circ$	$V_m = 304.05 \angle -105^\circ$
$V_c = 152.4 \angle 192.67^\circ$	$V_L = 304.05 \angle 134.94^\circ$

Table III. Optimization results by proposed method (state 1)

	α (deg)	V_L (p.u.)	P_{DVR} (kW)
Pre-sag compensation	0	1	1.092
Phase advance method	14.62	1	0.895
Proposed method	14.94	0.98	0.7054

Table IV. Current and voltage of the source in sag condition and in unbalanced state (state 2)

$V_{Lref} = 310.26$ v	$I = 24$ A
$V_{sa} = 232.695$ v	$\delta_a = -1.5^\circ$
$V_{sb} = 279.234$ v	$\delta_b = -15^\circ$
$V_{sc} = 310.26$ v	$\delta_c = 0^\circ$
Power angle = 26.56°	

Regarding to status of voltages in fault situations, it is possible that the generated power of a DVR decreases noticeably. For instance, when voltage decreases according to Table IV, the result of the controller is in the form of Table V. In this status, the generated power of DVR effectively decreases compared to the state 1.

Fig. 7 shows source voltages for duration of 10 cycles starting with fault at $t_f=0.3$ and ending with $t_r=0.5$ second for state1 (according to Table I). In Fig. 8, injected voltages of DVR are shown and Fig. 9 shows the load voltages. These figures show that this method compensates the voltage Sag, while minimizing generated power of DVR.

Table V. Optimization results by the proposed method (state2)

	$\alpha(\text{deg})$	$V_f(\text{pu})$	$P_{\text{DVR}}(\text{kW})$
Pre-sag compensation	0	1	0.87596
Proposed method	21.32	1	0.192
Proposed method	21.067	0.983	0.02443

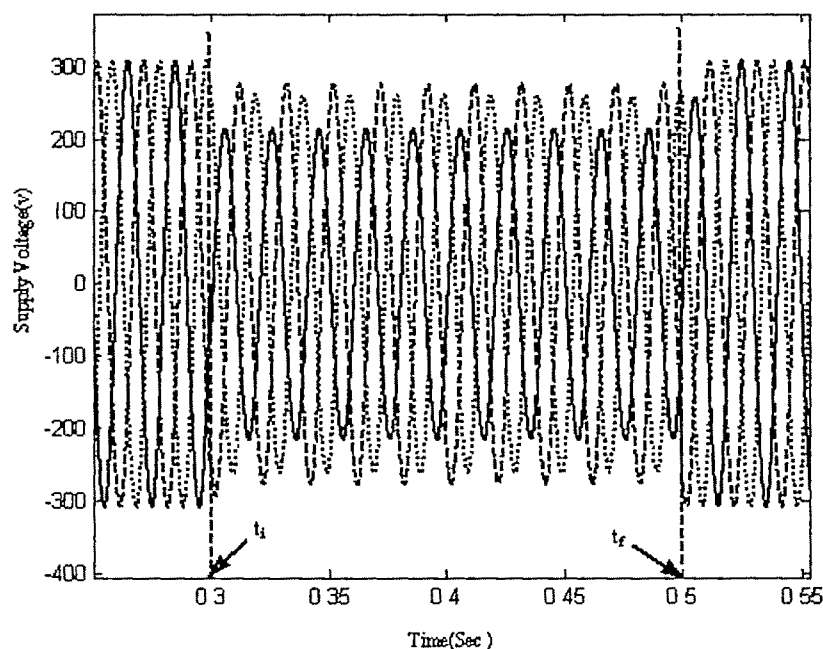


Fig. 7. Phase voltages of a source during the fault

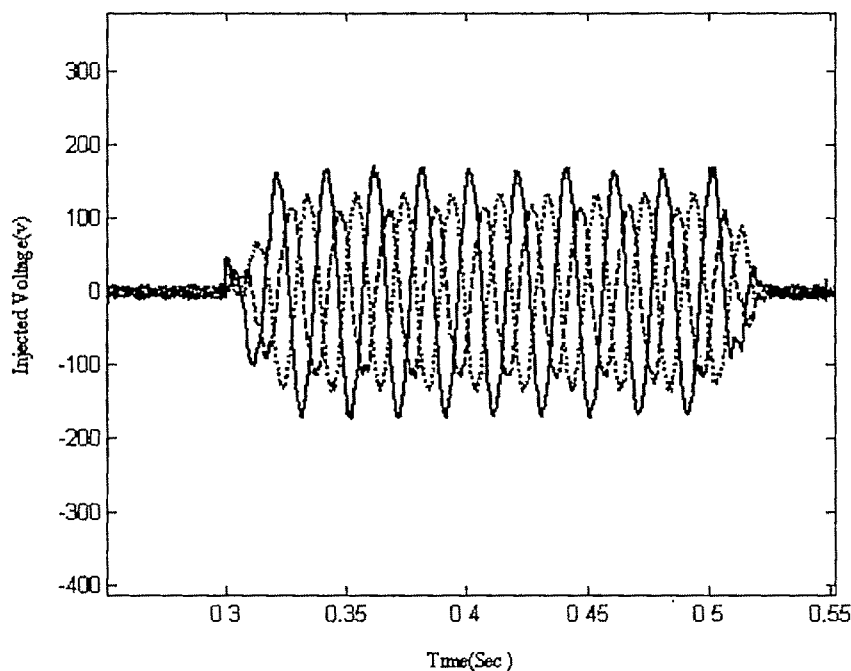


Fig. 8. Injected voltages by DVR

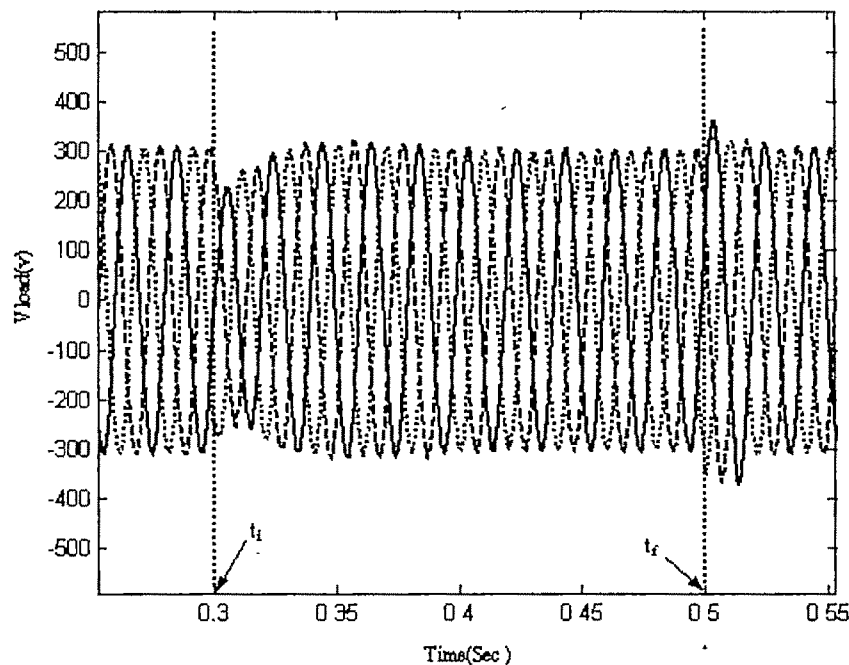


Fig. 9. Load Voltages during the fault

VI. CONCLUSION

DVR can inject a voltage series with a line and restore the load voltages to pre-fault values during the voltage sag. DVR cannot restore the load voltage constantly during the deep voltage sag because the stored energy in DC link is limited, therefore generated power by DVR must be minimized. In other hand, generally it is not necessary that the value and the phase angle of the compensated voltage be exactly equal to its pre-fault values and allowable tolerance for voltage suffices. This paper has proposed a method for minimizing the injected power of DVR to the system considering the above mentioned states. Also to generate reference signals for PWM controller a suitable PLL has been proposed. Simulation results show that this method is effective even during unbalanced voltage sag.

REFERENCES

- [1] N. G. Hingorani, "Introducing custom power," *IEEE, Spectrum*, vol. 32, no. 6, pp. 41-48, June 1995.
- [2] P. W. Lehn and M. R. Irvani, "Experimental evaluation of STATCOM closed loop dynamics," *IEEE Trans. Power Del.*, vol. 13, no. 4, pp. 1378-1384, Oct. 1998.
- [3] T. Wunderlin, O. Dahler and H. Guning, "Power supply quality improvement with dynamic voltage restorer (DVR)," in *Proc. EMPD'98, Energy Management and Power Delivery*, Singapore, vol. 2, 1998, pp. 518-525.
- [4] S. Choi, B. Li and D. Vilathgamuwa, "Dynamic voltage restoration with minimum energy injection," *IEEE Trans. Power Syst.* vol. 15, no. 1, pp. 51-57, Feb. 2000.
- [5] Y. Y. Kolhatkar and S. P. Das, "An optimum UPQC with minimum VA requirement and mitigation of unbalanced voltage sag," *International Journal of Emerging Electric. Power Systems*, vol. 2, no. 2, pp. 1-13, 2005.
- [6] I. Y. Chung, D. J. Won, S. Y. Park, S. I. Moon and J. K. Park, "The DC link energy control method in dynamic voltage restorer system," *Elect. Power Energy Syst.*, vol. 25, pp. 525-531, 2003.
- [7] V. Khadkikar, P. Agarwal, A. Chandra, A. O. Barry and T. D. Nguyen, "A simple new control technique for unified power quality conditioner (UPQC)," in *Proc. 11th Int. IEEE Conf. Harmonic and Quality of Power*, 2004, pp. 289-293.
- [8] K. Wang, F. Zhuo, Y. Li, X. Yang and Z. Wang, "Three-phase four-wire dynamic voltage restorer based on new SVPWM algorithm," in *Proc. 35th Int. IEEE Conf. Power Electronics Specialists*, 2004, pp. 3877-3882.

On Line Three Phase Power Factor Estimation under Nonsinusoidal Unbalanced and Time Varying Condition

Arghya Sarkar¹, K. K. Mazumdar² and S. Sengupta²

¹ MCKV Institute of Engineering, 243 G.T.Road (N), Liluah, Howrah -711204, India, e-mail - sarkararghya@yahoo.co.in .

² Department of Applied Physics, University of Calcutta, 92, A. P. C. Road, Kolkata - 700009, India, e-mail - samasgp@vsnl.net.

Abstract—This paper presents the design and implementation of a novel on line three phase power factor measurement technique under unbalanced, time varying and nonsinusoidal environment. The computational load at real time realization has been reduced by modifying IEEE Std. 1459-2000 recommended three phase power factor definition under certain significant facts. The conventional Goertzel filter bank interpreted fast Fourier transform (FFT) algorithm has been extended in the field of discrete short time Fourier transform (DSTFT), to get the spectrum of each finite short time section of the power signals at arbitrarily located specified frequencies; which further decreases the calculation complexity. The fundamental component of power factor and root mean square values of current and voltage signals have been defined from the perspective of this newly characterized DSTFT with nonuniform frequency distribution, called non-uniform discrete short time Fourier transform (NDSTFT). The method is illustrated and evaluated in real time by means of a Texas Instruments (TI) TMS320VC5416 digital signal processor. Illustrative laboratory test results confirm the validity and accurate performance of the proposed method.

Key words— Active power, digital signal processor, harmonics, Goertzel filter bank, measurement, nonuniform discrete short time Fourier transform.

I. INTRODUCTION

DURING recent years, registration of three phase power factor under nonsinusoidal, unbalance and time varying condition takes a great challenge. Conventional electromechanical three phase power factor meters [1] are based on rms measurement and precisely inaccurate in the presence of harmonics [2]. With the advent of digital signal processors, attempt has been taken to include harmonic impact. Fast Fourier transform (FFT) based algorithm [3], short-time Fourier transform (STFT) based algorithm [4], Discrete Wavelet Transform (DWT) [5] based approach, and adaptive linear neural network (ADALINE) [6] based algorithm are examples of some well known approach. The accuracy of these methods have been influenced by one or more of the following factors: superimposed noise, non-linear static characteristic, computational complexity and slow response.

In this paper a simple but computationally efficient three

phase power factor measurement technique has been proposed for nonsinusoidal, unbalanced and time varying power systems. The main contributions of this paper are as follows:

- Conventional definition of three phase power factor has been modified in such a fashion that only current harmonic information is required for accurate assessment of power factor.
- The concept of Goertzel filter bank interpreted discrete Fourier transform (DFT) has been extended to acquire a new approach for real time implementation of discrete Short Time Fourier Transform (DSTFT), in which the spectrum of each finite short time section of the signal is estimated by realizing the DFT through a bank of IIR Goertzel filters, centered at randomly placed selected frequencies. The new approach has been termed as “nonuniform discrete short time Fourier transform” (NDSTFT).
- The fundamental component of power factor and rms value of current and voltage signals has been expressed in terms of newly proposed NDSTFT.

The algorithm is implemented in real time with a Texas Instruments (TI) TMS320VC5416 digital signal processor. Fast and accurate measurement of three phase power factor has been observed utilizing the developed scheme. The results have been presented in the text.

II. THREE PHASE POWER FACTOR EXPRESSION UNDER NONSINUSOIDAL AND UNBALANCED CONDITION

The definition of three phase power factor in nonsinusoidal and unbalanced situations is still heavily debated. At present, IEEE Std. 1459-2000, approved on September 2002 [7], is the only available document that gives some guidelines for designing instrumentation under these environments. For nonsinusoidal and unbalanced system, it provides a set of definitions that are related to an equivalent virtual balanced system, with the same losses as that of the real unbalanced system.

At the presence of harmonics, periodic voltages and current signals with fundamental time period T , may be represented by Fourier series of the form

$$v(t) = \sum_{k=1}^{\infty} V_k \sin(\omega_k t + \alpha_k) \quad (1)$$

where $v(t)$ is the instantaneous voltage, V_k are peak values of

voltage harmonic k , ω_k are the k^{th} angular frequency component and α_k are the phase angles of voltage harmonic k .

$$i(t) = \sum_{k=1}^{\infty} I_k \sin(k\omega_k t + \beta_k) \quad (2)$$

where I_k are peak values of current harmonic k and β_k are the phase angles of current harmonic k .

The rms voltages and currents can be written as

$$V_{rms} = \sqrt{\sum_{k=1}^{\infty} V_{rms,k}^2} = \sqrt{\frac{1}{2} \sum_{k=1}^{\infty} V_{max,k}^2} \quad (3)$$

$$I_{rms} = \sqrt{\sum_{k=1}^{\infty} I_{rms,k}^2} = \sqrt{\frac{1}{2} \sum_{k=1}^{\infty} I_{max,k}^2} \quad (4)$$

The active power can be shown to be

$$\begin{aligned} P_{avg} &= \sum_{k=1}^{\infty} V_{rms,k} I_{rms,k} \cos(\alpha_k - \beta_k) \\ &= \frac{1}{2} \left[\sum_{k=1}^{\infty} V_{max,k} I_{max,k} \cos(\alpha_k - \beta_k) \right] \end{aligned} \quad (5)$$

For three phase three wire power system RST, starting from the rms line currents and the line to line rms voltages, the effective current I_e , effective voltage V_e and effective apparent power S_e has been defined [7] as follows:

$$I_e = \sqrt{\frac{I_{R_{rms}}^2 + I_{S_{rms}}^2 + I_{T_{rms}}^2}{3}} \quad (6)$$

$$V_e = \sqrt{\frac{V_{RS_{rms}}^2 + V_{ST_{rms}}^2 + V_{TR_{rms}}^2}{9}} \quad (7)$$

$$S_e = 3V_e I_e \quad (8)$$

Hence using (3) - (8), the effective three phase power factor can be expressed as

$$\begin{aligned} PF_e &= \frac{P_e}{S_e} \\ &= \frac{\left[\sum_{k=1}^{\infty} V_{RT_{rms,k}} I_{R_{rms,k}} \cos \theta_{RT_{R_k}} + \sum_{k=1}^{\infty} V_{ST_{rms,k}} I_{T_{rms,k}} \cos \theta_{ST_{T_k}} \right]}{\sqrt{\left(\sum_{k=1}^{\infty} V_{RS_{rms,k}}^2 + \sum_{k=1}^{\infty} V_{ST_{rms,k}}^2 + \sum_{k=1}^{\infty} V_{TR_{rms,k}}^2 \right)}} \\ &\quad \times \frac{\sqrt{3}}{\left(\sum_{k=1}^{\infty} I_{R_{rms,k}}^2 + \sum_{k=1}^{\infty} I_{S_{rms,k}}^2 + \sum_{k=1}^{\infty} I_{T_{rms,k}}^2 \right)} \end{aligned} \quad (9)$$

where P_e is the effective active power, $\theta_{RT_{R_k}}$ and $\theta_{ST_{T_k}}$ are the phase angles between fundamental components of $V_{RT_{rms,k}}$ and $I_{R_{rms,k}}$; and $V_{ST_{rms,k}}$ and $I_{T_{rms,k}}$ respectively, at k^{th} harmonic.

In most cases, the contributions of harmonics above the fundamental to average power are small (less than 1%) [8] and voltage harmonics are usually less than 3% [8]. Incorporating these two assumptions into (9) yields the following

approximate form for true power factor:

$$\begin{aligned} PF_e &\approx \sqrt{3} \left[\frac{1}{m_1} \times \cos \theta_{RT_{R_1}} \times \frac{I_{R_{rms,1}}^2}{\sum_{k=1}^{\infty} I_{R_{rms,k}}^2 + \sum_{k=1}^{\infty} I_{S_{rms,k}}^2 + \sum_{k=1}^{\infty} I_{T_{rms,k}}^2} \right. \\ &\quad \left. + \frac{1}{m_2} \times \cos \theta_{ST_{T_1}} \times \frac{I_{T_{rms,1}}^2}{\sum_{k=1}^{\infty} I_{R_{rms,k}}^2 + \sum_{k=1}^{\infty} I_{S_{rms,k}}^2 + \sum_{k=1}^{\infty} I_{T_{rms,k}}^2} \right] \end{aligned} \quad (10)$$

$$\text{where } m_1 = \sqrt{\frac{V_{RS_{rms,1}}^2}{V_{RT_{rms,1}}^2} + \frac{V_{ST_{rms,1}}^2}{V_{RT_{rms,1}}^2} + 1} \quad (11)$$

$$\text{and } m_2 = \sqrt{\frac{V_{RS_{rms,1}}^2}{V_{ST_{rms,1}}^2} + 1 + \frac{V_{TR_{rms,1}}^2}{V_{ST_{rms,1}}^2}} \quad (12)$$

III. GOERTZEL FILTER BANK INTERPRETED NON-UNIFORM DISCRETE SHORT TIME FOURIER TRANSFORM

Although the Discrete Fourier transform (DFT) works well for the infinite time case of a stationary signal, it is unable to resolve any temporal information associated with time varying power signals. In this context discrete Short Time Fourier Transform (DSTFT) can be considered from the perspective of a DFT taken over short time sections of the signal (the window is fixed). A major disadvantage of the DFT technique is that all of the data points must be available before the spectra can be computed. In real time measurement procedure it is not desirable to wait for an entire window of data before beginning the DSTFT calculations.

In this paper a novel approach has been proposed for real time implementation of DSTFT where the spectrum of each finite short time section of the signal is estimated by realizing the DFT through a bank of IIR Goertzel Filters centered at randomly placed selected frequencies. The technique has all the advantages inherent to the IIR Goertzel filters, including the capacity of doing sample by sample processing, and can estimate the spectrum at the exact frequencies of interest, thus avoiding unnecessary calculations. Since DSTFT has been performed on selected frequencies, nonuniformly located in z plane, the approach is termed as "non-uniform discrete short time Fourier transform" (NDSTFT).

A. Definition of NDSTFT

In most signals, the energy is distributed nonuniformly in the frequency domain. This observation has the motivation for developing the concept of NDSTFT of a finite length "snapshot" sequence as samples of its z -transform evaluated at arbitrarily chosen points in the z -plane. This concept is basically a generalization of the conventional DSTFT. The NDSTFT of discrete time signal $x[n]$ has been defined at a

characterized by the narrowest main lobe (the best resolution among tones close in frequency) and the highest and most slowly decaying side lobes (the worst interference caused by a strong tone on a weaker tone not close in frequency).

IV. POWER FACTOR AND RMS MEASUREMENT USING NDSTFT

Although input voltage and current signals are real sequences, the outputs of NDSTFT are complex in nature. If, voltage and current signals contain a finite number of arbitrarily spaced harmonics with maximum order M and uniformly sampled at frequency $\omega_s = 2\pi N/T$, where $N = 2M$ is chosen according to the sampling theorem, then from (3), (4) and (13), it can be proved that at time index, n ,

$$I_{rms} = \sqrt{\frac{2}{N^2} \left\{ \text{Re}[I_{NDSTFT}[z_i, n]]^2 + \text{Im}[I_{NDSTFT}[z_i, n]]^2 \right\}} \quad (23)$$

$$V_{rms} = \sqrt{\frac{2}{N^2} \left\{ \text{Re}[V_{NDSTFT}[z_i, n]]^2 + \text{Im}[V_{NDSTFT}[z_i, n]]^2 \right\}} \quad (24)$$

Since input current and voltage signals are real sequences and the square magnitude of the NDSTFT samples are of interest in rms computations as shown in (23) and (24), the complex multiplication at every sample estimation, can be completely avoided using following form of (22)

$$|y_k[N]|^2 = q_k^2[N] + q_k^2[N-1] - 2 \cos \omega_k q_k[N] q_k[N-1] \quad (25)$$

The fundamental component of power factor can be defined from (1) and (2), as

$$\cos \theta_1 = \frac{1}{\sqrt{1 + \tan^2 \left(\tan^{-1}(\alpha_1) - \tan^{-1}(\beta_1) \right)}} \quad (26)$$

After rigorous calculation it can be shown that at time index, n ,

$$\cos \theta_1 = \frac{(\text{Re}[V_1] \text{Re}[I_1] + \text{Im}[V_1] \text{Im}[I_1])^2}{\left(\text{Re}[V_1]^2 + \text{Im}[V_1]^2 \right) \left(\text{Re}[I_1]^2 + \text{Im}[I_1]^2 \right)} \quad (27)$$

$$\text{where } V_1 = V_{NDSTFT}[z_i, n] \quad (28)$$

$$\text{and } I_1 = I_{NDSTFT}[z_i, n] \quad (29)$$

V. PROPOSED SCHEME

The block diagram of proposed three phase power factor meter has been presented in Fig. 3, in which the potential transformers (PT_1 , PT_2 and PT_3) and current transformers (CT_1 , CT_2 and CT_3) have been used for scaling down the line voltages (V_{RS} , V_{ST} and V_{RT}) and line currents (I_R , I_S and I_T), respectively. The voltage drops across the burdens (1Ω) of CT's give the voltages corresponding to the line currents. All these signals are passed through instrumentation amplifiers to prevent noise problem. The outputs of instrument amplifiers are further attenuated by potentiometric arrangement so that the maximum signal values are less than 1 volt. The reduced signals are then digitized by analog to digital converter (ADC) and fed to the Texas Instruments (TI) TMS320VC5416 digital

signal processor (DSP) which after executing the developed software calculates and displays the three phase power factor of the system.

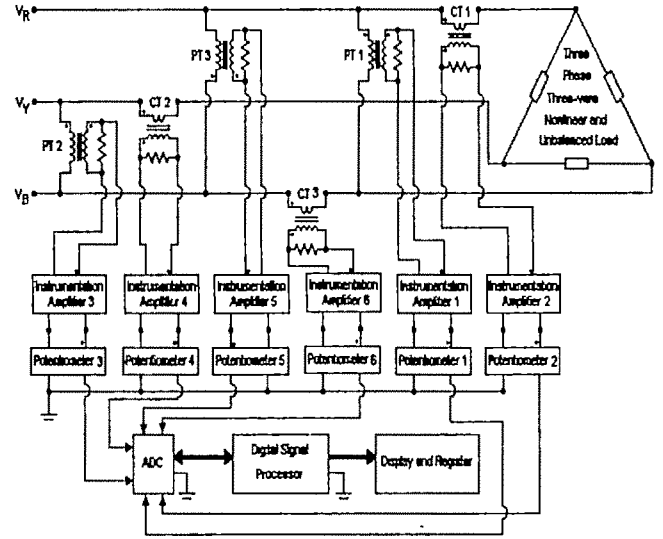


Fig. 3. Block diagram of proposed scheme.

VI. EXPERIMENTATION, RESULTS AND DISCUSSION

The validity and performance of the prototype three phase power factor meter as shown in Fig. 3 have been observed by applying this method to measure the three phase power factor of a delta connected three phase ac full wave voltage regulator with three phase unbalanced RL load. The circuit diagram of experimental set-up has been shown in Fig. 4, in which the full wave voltage regulator is fed from a 400 V, 3 phase, 50 Hz balanced ac system with source inductance and source resistance. The resistance and inductance values corresponding to three phase unbalanced load have been presented in diagram. Since the fundamental frequency is 50 Hz, the sampling frequency is kept at 6.4 kHz to calculate the harmonic pollution accurately up to the 64th harmonics.

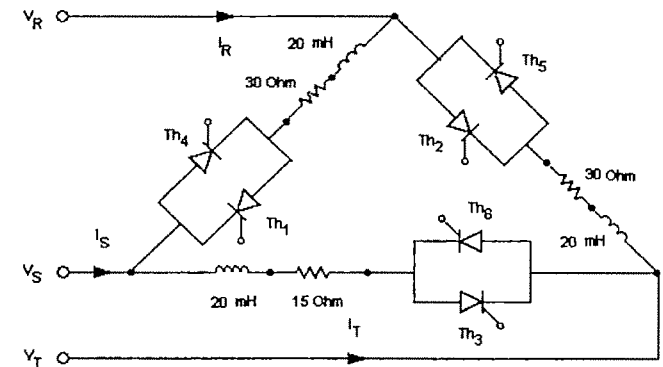


Fig. 4. Circuit diagram of the experimental setup at steady state.

The waveform of line currents I_R , I_S and I_T at triggering angle 60° and corresponding percent harmonics amplitude vs. harmonic number plots have been presented in Fig. 5 and

Fig. 6, respectively.

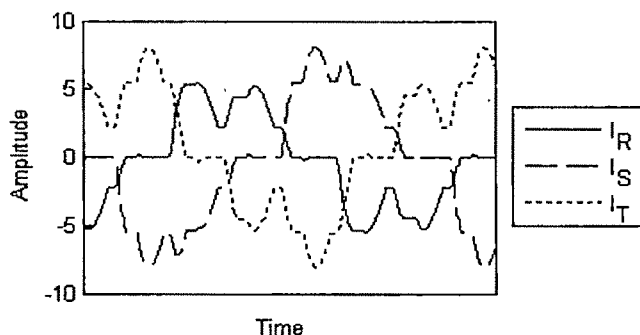


Fig. 5. Current wave forms of full wave voltage regulators with unbalanced load at 60° triggering angle.

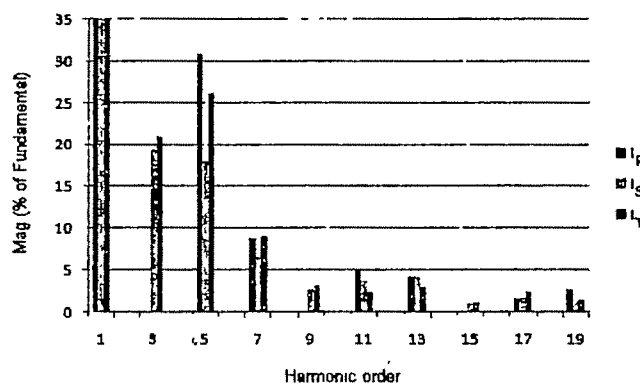


Fig. 6. Harmonic number vs. percent amplitude of current harmonics at 60° triggering angle..

From harmonic analysis curve it has been observed that 3rd, 5th, 7th and 11th harmonics can be considered as dominant current harmonics as there amplitudes are greater than 5% of fundamental amplitude.

To extract harmonic information using NDSTFT approach with modified mathematical model as derived in (10) – (12), five band pass IIR Goertzel filter have been adopted to design efficient filter bank where pass bands are centered at frequencies, corresponding to 1st, 3rd, 5th, 7th, and 11th harmonics.

A computer based measurement technique has been considered as standard method, in which the attenuated system data are digitized with sampling frequency 6.4 kHz and fed to a computer through a PCI-02 Data Acquisition System (DAS) card. At off-line, a personal computer (PC) with P-IV, 3.1GHz processor is used to process all the voltage and current samples using a software program written in C language. The results obtained from the PC based method using (9) have been set as a reference and compared with the results of the proposed three phase power factor measurement technique, as shown in Table I.

The results show that the Gortzel filter bank implemented NDSTFT provides fast and accurate tracking of power factor with less mathematical operation. The modulus of experimental error is around 1%. The sources of errors in the above experiments have been identified as: (1) Quantization error in analog to digital conversion and (2) Truncation error

and round off noise in the calculation part of the system.

TABLE I

THREE PHASE POWER FACTOR OF FULL WAVE VOLTAGE REGULATOR WITH UNBALANCED LOAD AT STEADY STATE

Triggering Angle (Degree)	Total Harmonic Distortion			Three Phase Power Factor (Proposed)	Three Phase Power Factor (Standard)	% Error
	%I _{THD} R phase	%I _{THD} S phase	%I _{THD} T phase			
15°	12.65	12.92	16.12	0.7367	0.7294	0.99
30°	14.22	16.94	17.59	0.6423	0.6491	1.05
45°	20.41	21.81	23.03	0.5267	0.5321	1.02
60°	33.01	28.58	35.39	0.3965	0.4005	1.00

VII. CONCLUSION

The paper presents a new approach for real time estimation of three phase power factor under unbalance, nonsinusoidal and timevarying condition. The theoretical basis of Goertzel filter bank interpreted NDSTFT has been established which provides a very pragmatic and promising approach for fast estimation of power signal parameters, corrupted by a small number of arbitrarily located harmonics. The modification of conventional expression of three phase power factor and application of Goertzel filter bank interpreted NDSTFT reduces the computational complexity and makes the approach suitable for uniprocessor implementation. The real time laboratory test reveals the accurate performance of the proposed algorithm. The developed scheme is cheap, highly reliable and provides enough flexibility to suit the requirements of different systems.

REFERENCES

- [1] E. W. Golding, and F. C. Widdies, "Electrical Measurements and Measuring Instruments" *Wheeler Publishing*, 5th edition, 1991.
- [2] D. Slomovitz, "Behaviour of power-factor meters under non-sinusoidal current and voltage," *Int. Jour. Electronics*, vol. 01.70, no 4, pp. 827-838, 1991.
- [3] J.-C. Montano, A. Lopez, M. Castilla, and J. Gutierrez, "DSP-based algorithm for electric power measurement," *IEE Proc. Sci. Meas. Technol.*, vol 140, no 6, pp. 485-490, Nov. 1993.
- [4] A. Ozdemir, and A. Ferikoglu, "Low cost mixed-signal microcontroller based power measurement technique," *IEE Proc. Sci. Meas. Technol.*, vol. 151, no. 4, pp. 253-258, July 2004.
- [5] E. Y. Hamid, and Z.-I. Kawasaki, "Instrument for the quality analysis of power systems based on the wavelet packet transform", *IEEE Power Engineering Review*, vol. 22, issue 3, pp. 52 - 54, Mar 2002.
- [6] P. K. Dash, S. K. Panda, A.C. Liew, B. Mishra, and R. K. Jena, "A new approach to monitoring electric power quality", *Electric Power Systems Research*, vol. 46, no 1, pp. 11-20(10), July 1998.
- [7] IEEE Std. 1459-2000, "IEEE Trial-use standard definitions for the measurement of electric power quantities under sinusoidal, non sinusoidal, balanced or unbalanced conditions" – *IEEE Standard*, September 2002.
- [8] IEEE Working Group on Nonsinusoidal Situations: Effects on Meter Performance and Definitions of Power, "Practical definitions for powers in systems with nonsinusoidal waveforms and unbalanced loads: A discussion," *IEEE Trans. Power Delivery*, vol. 11, no. 1, pp 79-101, 1996.
- [9] S. Bagechi and S. K. Mitra, "The Nonuniform Discrete Fourier Transform and its applications in signal processing", *Kluwer Academic Publishers*, Norwell Massachusetts, 1999.

Power Factor Control of Distribution System by Using DSTATCOM

J. Ramanjaneya Reddy¹, S. Jagadish Kumar², and CH. Siva Kumar³

¹ Department of Electrical Engineering, Osmania University, Hyderabad, INDIA, e-mail: jinreddy.85@gmail.com

² Department of Electrical Engineering, Osmania University, Hyderabad, INDIA, e-mail: jagadishkumar1@yahoo.com.

³ Department of Electrical Engineering, Osmania University, Hyderabad, INDIA, e-mail: ch_siva_kumar@rediffmail.com.

Abstract—Electricity suppliers are nowadays concerned about the quality of the power delivered to customers. With the development of power electronics, several solutions have been proposed on distribution networks in order to ensure highest possible power quality for the customers. In this paper the performance of Distribution Static Compensator (DSTATCOM) is analyzed for the power factor control in a radial distribution system. The power factor control is performed using the detailed model of the DSTATCOM. Then a simplified model using the power factor controller is developed and its performance is verified by comparing with that of the detailed model.

Key words— Custom Power, DSTATCOM, Flexible AC Transmission Systems (FACTS), Power Quality.

I. INTRODUCTION

THE concept of Flexible AC Transmission Systems (FACTS), as the name implies, was originally developed for Transmission networks but similar ideas are applied in Distribution systems. The new high power electronic systems applied to distribution systems owe something to the ideas of FACTS but also use concepts and techniques developed for power electronic systems with lower voltage and current ratings. In both cases, voltage source converters are used as the main component of the system. To date, the main applications for power electronics on the distribution system have been to improve two aspects of power quality voltage dips and harmonic distortion [1]. The new technologies known as Custom Power, using power electronics-based concepts, have been developed to provide protection from power quality problems in distribution systems. FACTS use Power electronic devices and methods to control the high-voltage side of the network for improving the power flow. Custom Power is for low-voltage distribution, and improving the poor power quality and reliability. At present, a wide range of flexible controllers, which capitalize on newly available power electronics

components, are emerging for custom power applications [2].

II. DSTATCOM CONTROLLERS

A DSTATCOM, which is schematically depicted in Fig. 1, consists of a three-phase voltage source converter shunt connected to the distribution network through a coupling transformer [2]–[5]. It is simply an alternating, synchronous voltage source connected in shunt to the distribution three-phase feeder circuit via a coupling transformer. It is a fast response, inverter based power controller that provides flexible voltage control at the point of connection for improving the power quality in distribution systems. It can also provide instantaneous power factor correction to improve line utilization and minimize energy losses. It can exchange reactive power with the distribution system by varying the amplitude and phase angle of an internal voltage source with respect to the line terminal voltage, resulting in controlled current flow through the coupling transformer.

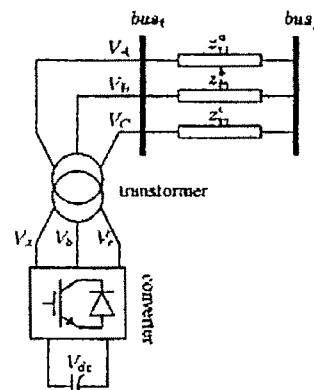


Fig. 1. DSTATCOM structure.

The power factor controller is shown in Fig.2. Here reactive power reference Q^* is set to zero in order to minimize the reactive power drawn from the supply i.e., unity power factor operation [6].

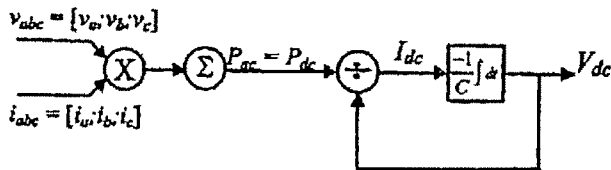


Fig. 5 DC link model.

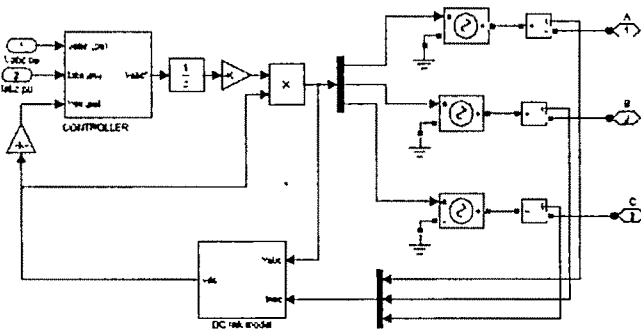


Fig. 6. DSTATCOM simplified model implementation.

IV. SIMULATION RESULTS

A test system is comprised of a 25-kV, 100-MVA, 60-Hz substation which is represented by a Thévenin equivalent seen towards the source side while the equivalent load is the impedance looking toward the right into the network, at bus 2. This substation is feeding a distribution network, where there is a DSTATCOM connected at bus 2 through a 25/2-kV Y/Δ transformer. Since the DSTATCOM is connected at this bus, it is called the *Point of Common Coupling (PCC)*. The test system is shown in Fig. 7 [3]-[5]. Initially there is no load connected at bus 2; at $t=0.2$ sec, Load L_1 and at $t=0.5$ sec, Load L_2 is applied.

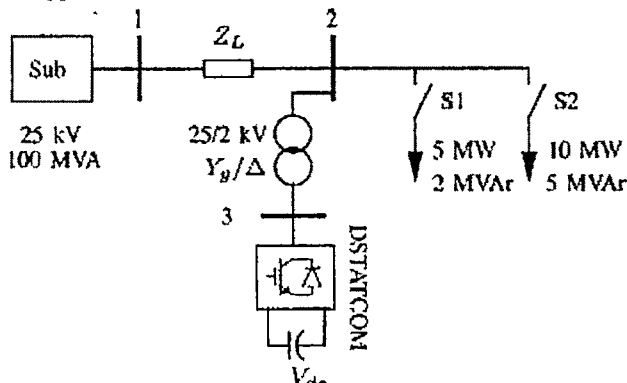


Fig. 7. Single-line diagram of the test system.

Initially when there no DSTATCOM at PCC, the reactive power drawn from the supply is 0.566 p.u at $t = 0.2$ sec and 1.078 p.u at $t = 0.5$ sec, terminal voltage is 0.971 p.u at $t = 0.2$ sec and 0.907 p.u at $t = 0.5$ sec and power factor is 0.928 at $t = 0.2$ sec and 0.906 at $t = 0.5$ sec.

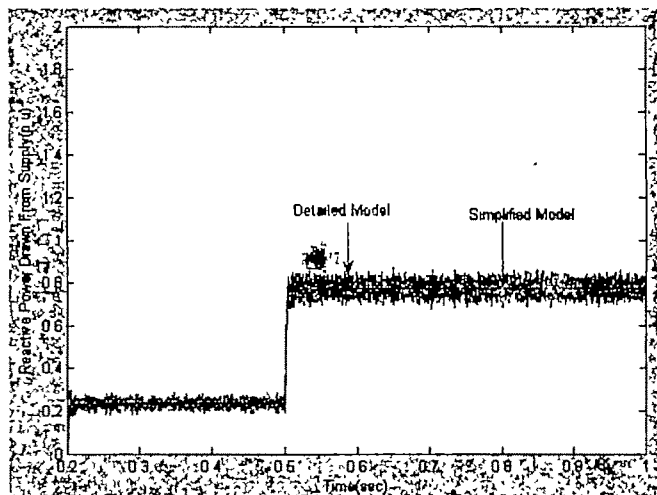


Fig. 8. Reactive power drawn from supply with different models of DSTATCOM.

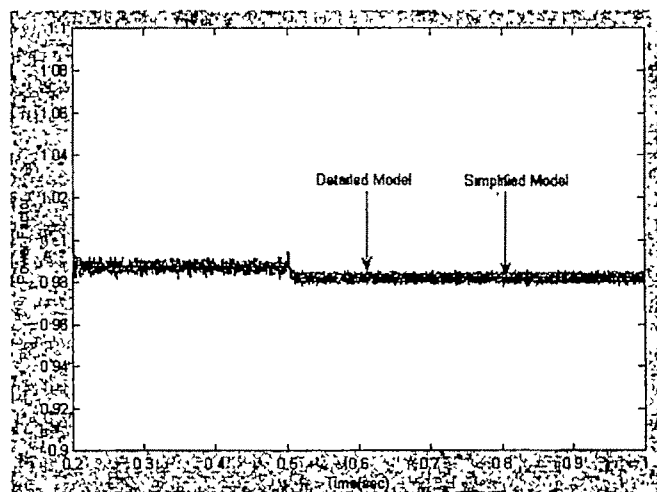


Fig. 9. Improved power factor with different models of DSTATCOM.

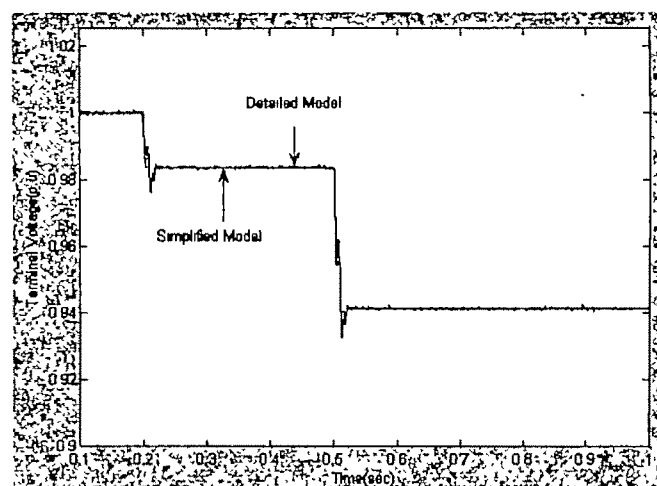


Fig. 10. Improved terminal voltage with different models of DSTATCOM.

The simulation results are used to compare the detailed and simplified models of the DSTATCOM power factor controller.

The figures from Fig. 8 to Fig. 10 show the reactive power drawn from the supply, improved power factor and improved terminal voltage for different models of DSTATCOM power factor controller.

The reactive power, power factor and the terminal voltage without DSTATCOM, with detailed model as well as simplified model of DSTATCOM power factor controller are depicted for comparison in the tables from Table I – III.

TABLE I. COMPARISON OF REACTIVE POWER DRAWN FROM THE SUPPLY (P.U)

Time	Without DSTATCOM	With Detailed Model of DSTATCOM	With Simplified Model of DSTATCOM
t=0.2sec	0.566	0.22	0.22
t=0.5sec	1.0782	0.79	0.79

TABLE II. COMPARISON OF TERMINAL VOLTAGE (P.U)

Time	Without DSTATCOM	With Detailed Model of DSTATCOM	With Simplified Model of DSTATCOM
t=0.2sec	0.971	0.985	0.985
t=0.5sec	0.907	0.94	0.94

TABLE III. COMPARISON OF POWER FACTOR

Time	Without DSTATCOM	With Detailed Model of DSTATCOM	With Simplified Model of DSTATCOM
t=0.2sec	0.928	0.985	0.985
t=0.5sec	0.906	0.981	0.981

V. CONCLUSIONS

In this paper DSTATCOM, which is one of the custom power devices is used to control the power factor. To verify the performance of the DSTATCOM, a variable load is connected at bus 2. From the simulation results it is observed that the detailed model of the DSTATCOM power factor controller significantly minimizes the reactive power drawn from 0.566p.u to 0.22p.u at $t = 0.2$ sec and from 1.782 p.u to 0.79 p.u at $t = 0.5$ sec. With the minimized reactive power drawn from the supply, the terminal voltage is also improved and improves the power factor from 0.928 to 0.985 at $t = 0.2$ sec and from 0.906 to 0.981 at $t = 0.5$ sec respectively. It is observed that both simplified model and detailed model of DSTATCOM are equivalent when operated as power factor controller and they can effectively control the power factor of the system.

REFERENCES

- [1] N Jenkins, "Power Electronics Applied to Distribution Systems", *Manchester Centre for Electrical Energy*, UMIST.
- [2] O. Anaya-Lara and E. Acha, "Modeling and analysis of custom power systems by PSCAD/EMTDC," *IEEE Trans. Power Del.*, vol. 17, no. 1, pp. 266–272, Jan. 2002.
- [3] N. G. Hingorani, "Introducing custom power," *IEEE Spectr.*, vol. 31, no.6, pp. 41–48, Jun. 1995.
- [4] Y. H. Song and A. T. Johns, *Flexible AC Transmission Systems (FACTS)*, 1st ed: Inst. Elect. Eng., 1999.
- [5] E. Acha, V. Agelidis, O. Anaya-Lara, and T. Miller, *Power Electronic Control in Electrical Systems*, 1st ed. Oxford, U.K.: Newnes, 2002.
- [6] Walimir Freitas, Andre Morelato, Wilsun Xu, and Fujio Sato, "Impacts of AC Generators and DSTATCOM Devices on the Dynamic Performance of Distribution Systems," *IEEE transactions on power delivery*, vol. 20, no. 2, April 2005.

- [7] Walimir Freitas, Edurato Asada, Andre Morelato, and Wilsun Xu, "Dynamic Improvement of Induction Generators Connected in Distribution Systems Using a DSTATCOM".

A PC Based Simulated Frequency Relay for Real Time Protection of Power System

T. K. Sengupta¹, A.Das², A.K.Mukhopadhyaya³

¹ Associate Professor, Academy of technology, West Bengal, India, Pin 712121 (e-mail:tksg1948@yahoo.co.in)

² Reader, Electrical Engineering Department, Jadavpur University, Kolkata-700032, India

³ Former Professor of Electrical Engineering, Department of Applied Physics, University of Calcutta, India

Abstract—While the basic functions of the conventional frequency protection relay satisfies all the protection needs which the present day power system requires, we need some added advantages such as precise frequency measurement, power system control etc. along with the protection scheme. This can be achieved by the computerized and simulated relay.

The developed relay consists of $\langle f \rangle$, $\langle f+t \rangle$, $\langle f+df/dt \rangle$, $\langle f+\Delta f/\Delta t \rangle$, $\langle df/dt+t \rangle$, $\langle \Delta f/\Delta t+t \rangle$ independent elements and simulation of these elements has been done using Simulink blocks. These elements are utilized for designing the frequency protection relay for real time on-line application in power system.

This relay has also the facility of interfacing with the field equipments for physical signal at input and output of the PC. Also it has the facility of generating process signal at output for tripping etc. through DAC 0804 and amplifier. The newly developed relay generates signal which can further be utilized for control of power system such as two-area network, dampening of frequency oscillations, etc.

Key words—Frequency protection, Interfacing, Signal conditioning, Simulink software.

I. INTRODUCTION

THE frequency protection relay for power system has been developed with dedicated elements of a universal frequency relay. The relay also sends the final tripping signal for necessary protection and control of power system.

Considering the frequency protection need, simulation for frequency measurement along with generation of proportional signal has been developed. This has also been done for other frequency functions like f , Δf , $\Delta f/\Delta t$, df/dt etc. As measurement of frequency does not solve problems and it is also required to measure f , $(f+t)$, $(f+\Delta f/\Delta t)$, $(f+df/dt)$, $(\Delta f/\Delta t+t)$ and $(df/dt+t)$. Interfacing hardware and software application for protection against frequency deviation have been developed.

Application of SVC for dampening the wide fluctuation of frequency has also been developed. Development of software based simulated digital relay for the application in power system protection has been finally made.

SIMULINK (MATLAB™) — A RIGHT CHOICE FOR FREQUENCY MEASUREMENT

Accurate measurement of frequency and its variation is an important issue in today's power system. Other than the basic frequency, we require also to measure $(f+t)$, $(f+\Delta f/\Delta t)$, $(f+df/dt)$, $(\Delta f/\Delta t+t)$ and $(df/dt+t)$ for the purpose of power system control and protection. But measurement of these values will give rise to computational difficulties, require more hardware, will generate software complications, will develop measurement inaccuracy etc. Consequently, we have no other options but to opt for simulation. In this paper we have utilized Simulink (Matlab™) software for all computational problems. It further includes hardware for interfacing at input and output of the computer, sending input signal and generating output signal to and from the PC. So this hybrid system has very less hardware with more flexibility.

By using Simulink (Matlab™) software [9], we have generated the output signal and interfaced the same with the physical power system, incorporating the program for control, protection and monitoring of the power system.

simulink model OF FREQUENCY measurement

By using Simulink blocks, development has been made for six numbers of models consisting of different frequency parameters presented in Fig.1- 6. These are f , Δf , $\Delta f/\Delta t$, df/dt , $[f+t]$, $[f+\Delta f/\Delta t]$, $[f+df/dt]$, $[\Delta f/\Delta t+t]$ and $[df/dt+t]$. All these models [2] have been experimented and verified in the respective oscilloscope and counters. Values of the output verified from the input variable frequency of the sinusoidal wave from the Simulink block.

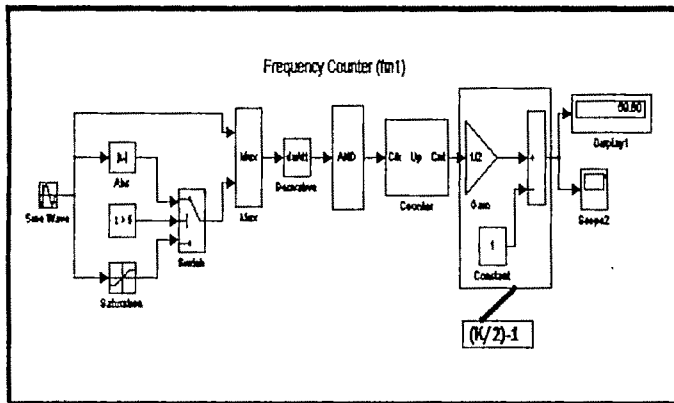


Fig.1: Frequency counters (fm1)

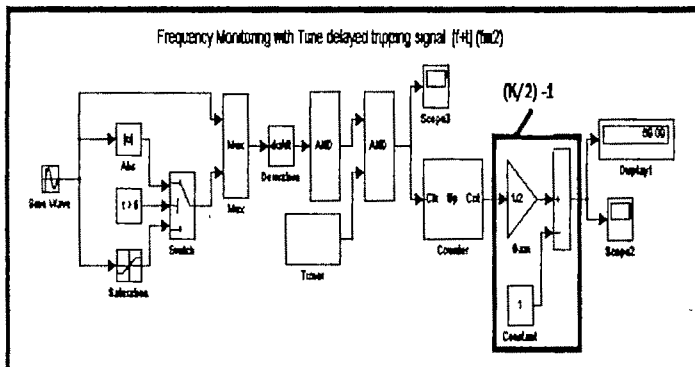


Fig. 2: Frequency with time delayed tripping signal (f+i)(fm2)

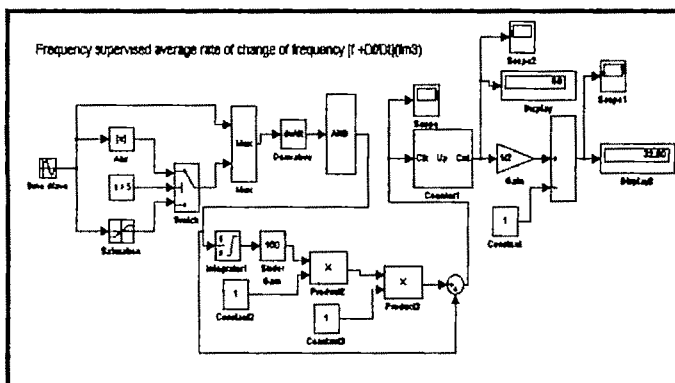


Fig.3.: Frequency supervised average rate of change of frequency (f+ $\Delta f / \Delta t$)(fm3)

SIMULATED PROTECTIVE RELAY

Development of methods for measuring and generating signal proportional to f , Δf , $\Delta f / \Delta t$, df/dt , $[f+t]$, $[f+\Delta f / \Delta t]$, $[f+df/dt]$, $[\Delta f / \Delta t + t]$, $[df/dt + t]$ have been experimented.

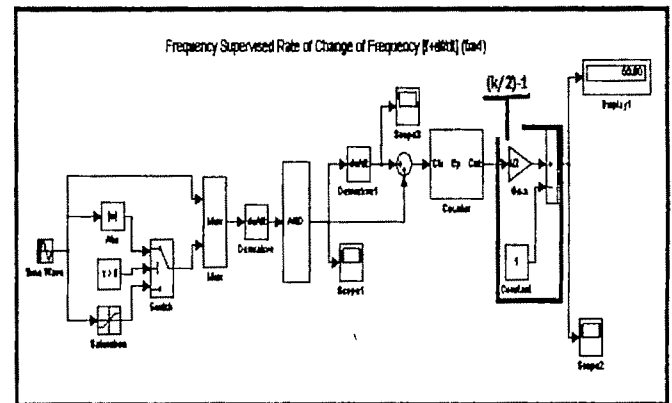


Fig. 4: Frequency Supervised Rate of Change of Frequency $<f+df/dt>$ (fm4)

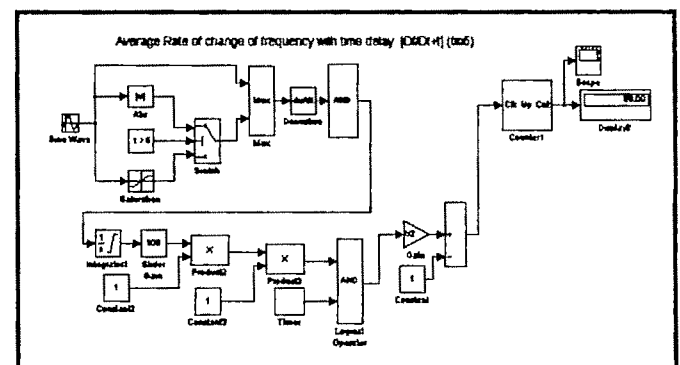


Fig.5: Average Rate of change of frequency with time delay for tripping signal $[\Delta f / \Delta t + t]$ (fm5)

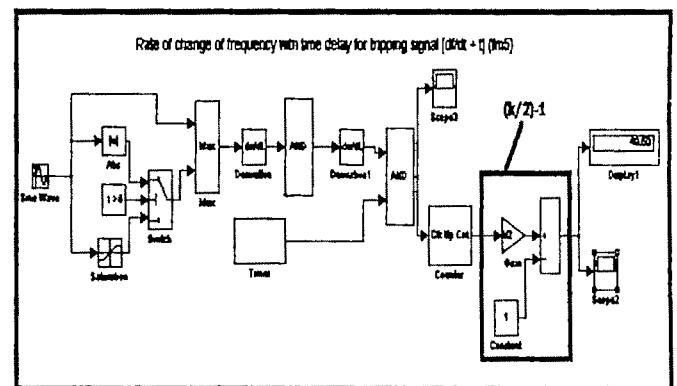


Fig.6: Rate of change of frequency with time delay tripping signal $[df/dt + t]$ (fm 6)

Further development of PC based methods have also been taken up to design a simulated numerical relay. The relay signal trips the system beyond healthy zone of frequency This deals with different protection functions and also generates trip

signals under different conditions for operation of the final tripping in power system.

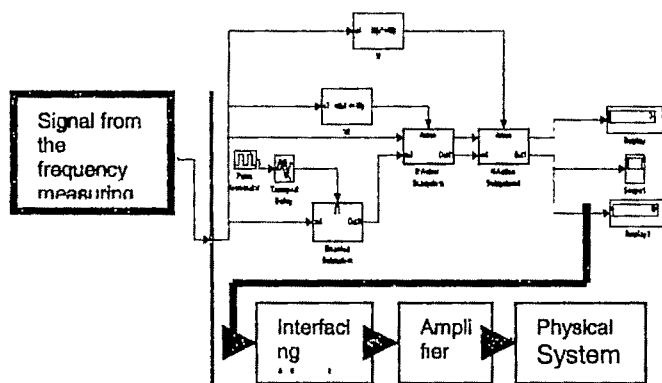


Fig. 7: Schematic arrangement for the simulated relay.

Scheme has been made for frequency protection and tested for an integrated simulated relay [3] which has total nine elements. The elements are i) f , ii) Δf , iii) $\Delta f/\Delta t$, iv) df/dt , v) $[f+t]$, vi) $[f+\Delta f/\Delta t]$, vii) $[f+df/dt]$, viii) $[\Delta f/\Delta t+t]$, ix) $[df/dt+t]$. This has been presented in Fig.7-12. Now, formation of the simulation blocks for each of these elements are presented below. Also, the stage settings for element $<f+df/dt>$ has been fixed, tested and recommended (Table 2) Similar to this setting, settings for other elements have also been tested.

The condition at which the under/over frequency [4] relay has been designed (Fig.8), and tested is as per the following Table 1. This is the outcome of the simulation of the numerical relay with the element $<f+t>$ (Fig.8).

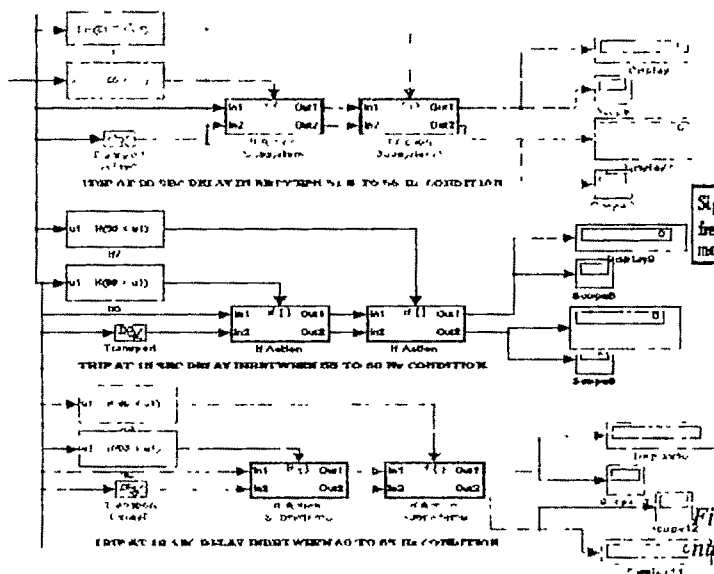


Fig. 8: Over/Under frequency simulated numerical relay.

Serial No.	Frequency (Hz.)	Delay (Second)	time
1	$f < 48.5$	0	
2	$48.5 < f < 49.5$	10	
3	$49.5 < f < 50.5$	20	
4	$50.5 < f < 51.5$	10	
5	$51.5 < f$	0	

Table-1 Test frequency allocation example.

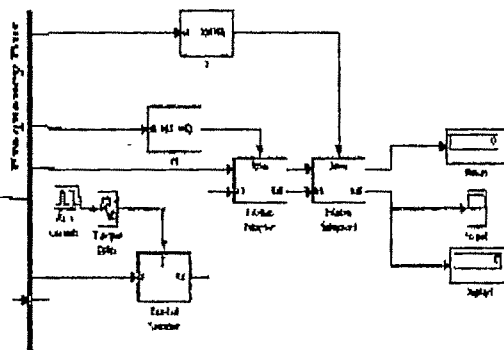


Fig. 9 Simulation of the frequency element $<f+\Delta f/\Delta t>$ for the numerical relay

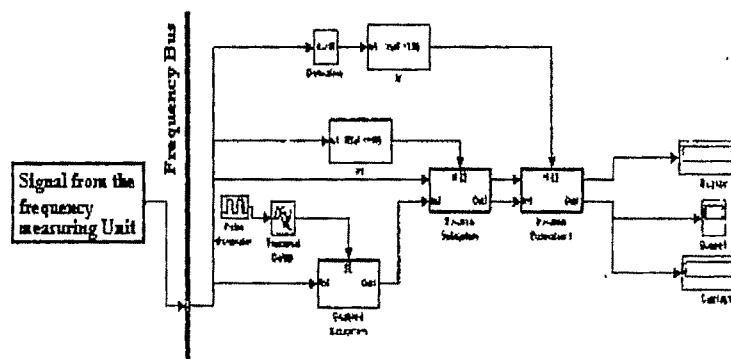


Fig.10: Simulation of the frequency element $<f+df/dt>$

Steps for interfacing of hardware with numerical relay are :

1. Step down from high voltage power to low voltage, low power signal line.
2. Frequency to voltage converter (FVC)
3. Data Accusation System (DAS).
4. Parallel port configuration.
5. Interfacing the frequency measuring unit with the relay simulation unit.
6. Interfacing of the output signal.
7. Amplification of the signal.

APPLICATION OF THE SCHEME AND FINDINGS WITH RESULT

Detail experiment with software has been made for the change of frequency (Δf) due to the power disturbances (ΔP_o) in the power system network. It is observed that such change (fluctuation) of frequency (Δf) is not only due to the characteristic of the load frequency, but also depends on the change of suceptance (ΔB) of Static Var Compensator (SVC) connected at the Generator end.

A combined model of power system along with SVC has been developed. Development of such model in Simulink (MatlabTM) includes "Simulated frequency measuring system" with "the power system" connected with "SVC (FC-TCR type)" [7].

The Simulink based model of power system, SVC, frequency measuring unit, controller for change of ΔB of SVC, feedback control system taken together makes "**new model for frequency dampening**" [5], particularly in case of wide fluctuation time for frequency variation (Δf). The proposed model does not change the Δf value, but helps to improve the dynamic behavior of the power system with respect to the change of frequency (Δf) and the change of power output.

The dynamic response [1] behavior of the frequency has been experimented to evaluate the effect of change of suceptance of the SVC.

It is further experimented after simulation that the change in power and frequency vs. time oscillographs for the two area network using Integral controller, PID controller and Fuzzy Logic controller. Following results observed:

1. Using integral controller, both power and frequency oscillographs initially show oscillations and after some times come to steady state.
2. Using PID controller, the settling time and maximum overshoot decreases i.e. the system becomes more stable.
3. Using Fuzzy Logic controller [6], better steady state error is obtained.

Controller Used	Rise Time	Overshoot	Settling Time	Steady State error
Integral	2.2	0.00019396	18	2.509×10^{-6}
PID	0.074	0.000188855	16.8	-8.364×10^{-6}
Fuzzy Logic	0.56	.0001872	16	-9.9×10^{-6}

Table – 3: Change in Power (pu) vs. time (sec.), Values in pu.

Controller Used	Rise Time	Overshoot	Settling Time	Steady State error
Integral	.2172	0.27005	25	-2.0255
PID	2.068	0.00306	24	-0.4478
Fuzzy Logic	2.22	0.3722	24	-0.0944

Tabl –4: Change in frequenc y(Hz) vs time (Sec.), values in pu Conclusion

A design has been made for a pc based frequency detection and frequency relay for the purpose of monitoring, control and protection of different conditions of frequency in power system. This is for on-line and real-time basis for HV/EHV systems.

Also the method of simulating the frequency in Simulink (MatlabTM) software utilizing different Simulink blocks, has been developed for frequency measurement. The method is software based eliminating all hardware difficulties.

Finally, the design of a relay has been made, not only for under and over frequency protection , but also taking care of $<f>$, $<f+t>$, $<f+df/dt>$, $<f+\Delta f/\Delta t>$, $<df/dt+t>$, $<\Delta f / \Delta t +t>$ etc. which are the critical values for any power system during frequency abnormalities.

REFERENCES

- [1] Aladimir Terzija and Milenko Djuric "A numerical algorithm for real-time estimation of voltage Phasor, Frequency and rate of change, Electrical Machine and power system" Vol.24, No.4, June 1996, Page 417.
- [2] N.C.Pabalawaththa "Frequency estimation method for digital protection of power system". Proc. IPENZ Annu. Conf Manulton, Zealand, 1993, pp 164-175.
- [3] A.A.Girgis, F.M Ham "A new FFT-based digital frequency relay for load shedding" IEEE Trans, PAS-101(2) (1982) 439-443
- [4] C.F.Dalziel and E.W.Stembach "Underfrequency protection of power systems for system relief, load shedding-system splitting" AIEE Trans.(Power Apparatus and Systems), Vol 76, pp.1227-1238, December 1939.
- [5] Wu C.J. and Lee Y.S "Damping of Synchronous generator by static reactive power compensator with digital controller," IEEE Proce , Vol 138, Pt.C, No.5, Pp.427-432, Sep, 1991.
- [6] T.K.Sengupta, Arabinda Das and A.K. Mukhopadhyaya "Application of Fuzzy Logic Controller (FLC) in Two Area Optimal Load Frequency Control systems" Procc. of All India Seminar on Integrated Operation of Power System, Technical Session III, on 06/09/2003 at 3.45-4.30 pm.
- [7] Tapas Kumar Sengupta "Fluctuation of load on alternator along with SVC at its generating end is to be compensated by regulating frequency and reactive power" Procc of Technical Journal of JIS College of Engineering, 2004.
- [8] K.Dutta, S. Chakraborty, S.Pal and T.K.Sengupta "On-Line Measurement of Frequency & Design of Under/Over Frequency Numerical Relay by Simulation" JIS College of Engineering, Kalyani-741235, India
- [9] T K Sengupta, A.Das and A.K.Mukhopadhyay "On-line real-time PC based measurement of power frequency using Taylor's approximation method for HV/EHV power system" Proc of the 20th Engineering Congress, Institute of Engineers (India), Kolkata, December 15-18, 2005.

A Novel Particle Swarm Optimized AGC for Restructured Three Area Power System

Ranjit Roy¹, and S. P. Ghoshal²

¹Electrical Engineering Department, S. V National Institute of Technology, Surat, Gujarat e-mail: rr@eed.svnit.ac.in

²Electrical Engineering Department, National Institute of Technology, Durgapur, West Bengal e-mail: spghoshalniddgp@yahoo.com

Abstract—In this paper, the traditional three-area Automatic Generation Control loop with modifications is incorporated in restructured power system. There are various types of ancillary services present in power system. One of these ancillary services is load following with frequency control which comes broadly under Automatic Generation Control in restructured power system. The prime emphasis of the paper is to propose a novel particle swarm based algorithm namely, Craziness based Particle Swarm Optimization (CRPSO) which is applied to obtain optimal gain parameters for optimal transient performances. In restructured power system, a DISCO can contract individually and multilaterally with a GENCO for power and these transactions are done under the supervision of the ISO. In this paper, the concept of DISCO participation matrix is used to simulate the bilateral contracts in the three area diagram. The proposed algorithm yields true optimal transient response under various operating conditions.

In this paper two different test cases have been studied. First case is the three area radial system and the second case deals with the three area ring system. Results show that in first case the computed values of generators' participations, tie-line exchanges match with the actual values obtained by MATLAB-SIMULINK. But in test case 2, though generators' participations are matching with the actual values, but computed values of tie-line exchanges are differing from the MATLAB-SIMULINK based values. The loop power flow is the cause of the discrepancy in case of ring system.

Keywords—Automatic Generation Control, Bilateral Contracts, CRPSO, Restructured Power System.

NOMENCLATURE

ACE _i	area control error of <i>i</i> th area
<i>b_i</i>	frequency bias coefficient of <i>i</i> th area
Δf_i	frequency error of <i>i</i> th area
$\Delta P_{tie_{ij}}$	tie-line power flow error between <i>i</i> th area and <i>j</i> th area
<i>K_p</i>	proportional gain of PID controller
<i>K_i</i>	integral gain of PID controller
<i>K_D</i>	derivative gain of PID controller
<i>t_p</i>	area time constant
<i>t₁₂</i>	tie-line synchronizing coefficient
<i>b</i>	frequency bias coefficient

<i>apf</i>	ACE participation factor
$\bullet_{12}, \bullet_{13}, \text{ and } \bullet_{23}$	Ratios of areas'
power ratings	
<i>R</i>	Governor regulation
<i>T_g</i>	Governor time constant
<i>T₁</i>	Non-reheat time constant
<i>T_r</i>	Reheat time constant
<i>c</i>	Reheat parameter
<i>K_p</i>	Power System gain constant

I. INTRODUCTION

THE dynamic behavior of many industrial plants is heavily influenced by disturbances and, in particular, by changes in the operating point. This is typically the case for restructured [1], [2] power systems. Automatic Generation Control (AGC) is a very important issue in power system operation and control for supplying sufficient and reliable electric power with good quality. AGC is treated as an ancillary service that is essential for maintaining the electrical system reliability at an adequate level. The main goal of the AGC is to maintain zero steady state errors for frequency deviation and good tracking load demands in a multi-area restructured power system. In addition, the power system should fulfill the requested dispatch conditions.

In an open energy market, generation companies (GENCOs) may or may not participate in the AGC task. On the other hand, a distribution company (DISCOs) may contract individually with a GENCO or independent power producers (IPPs) for power in its area or other areas. Currently these transactions are done under the supervision of the independent system operator (ISO).

This paper introduces a novel PSO namely Craziness based Particle Swarm Optimization (CRPSO) which is applied to obtain optimal gain parameters for optimal transient responses.

II. AGC IN RESTRUCTURED POWER SYSTEM

The traditional electric industry is vertically integrated with all the generation, transmission and distribution under its control with interlinking with the neighboring areas. The main objective of AGC is

(a) to maintain frequency at or very close to the specified nominal value, (b) to maintain power flow on the interlinking tie lines between the areas closer to their scheduled levels and (c) to maintain each unit's generation at most economic value. The AGC is implemented at a centralized location where all the information about the system operation is available like, area generation & demand, frequency and tie line flows. The information is further transmitted to participating generating units for meeting the above objectives. In the restructured environment, GENCOs sell power to various DISCOs at competitive prices. Thus, DISCOs have the liberty to choose the GENCOs for contracts. They may or may not have contracts with the GENCOs in their own area. This makes various combinations of GENCO-DISCO contracts possible in practice. Consider a three-area system in which let GENCO1, GENCO2, DISCO1 and DISCO2 are in area I, GENCO3, DISCO3 and DISCO4 are in area 2 and GENCO4, GENCO5, GENCO6, DISCO5 and DISCO6 are in area 3 as shown in Fig. 1. The full MATLAB-Simulink based block diagram for three-area AGC in a deregulated power market is shown in Fig. 2. Fig. 3 shows the MATLAB-Simulink based diagram for Area2. Similarly the diagrams for Area1 and Area3 are drawn, not shown in the paper.

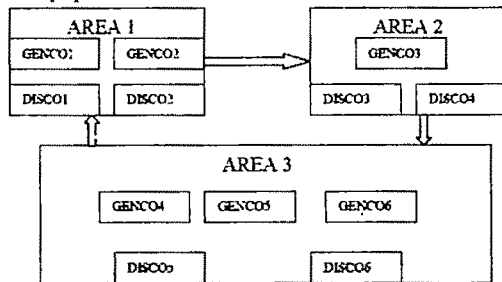


Fig. 1. Schematic diagram of a three-area system in restructured environment

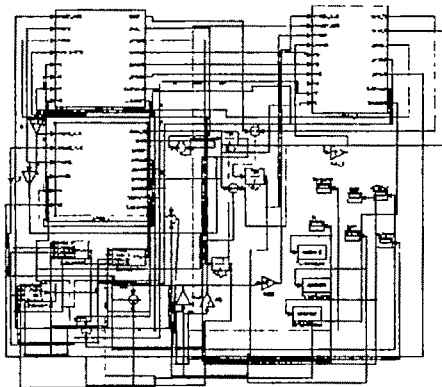


Fig. 2. Three-area AGC simulator block diagram in restructured power market.

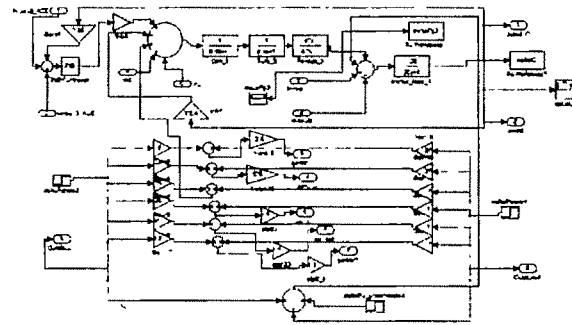


Fig. 3. MATLAB-SIMULINK based diagram of Area 2.

The authors have simulated the individual generation of Gencos and scheduled tie-line power flow in an unequal rating scenario. The concept of contract participation factor matrix (cpf_matrix) makes the visualization of contracts easier. This matrix is having the number of rows equal to the number of GENCOs and the number of columns equal to the number of DISCOs in the system. Here, the ij th entry corresponds to the fraction of the total load power contracted by DISCO j from a GENCO i . The sum of all the entries in a column in this matrix is unity. Coefficients that distribute Area Control Error (ACE) to several GENCOs are termed as ACE participation factors (apfs). Note that

$$\sum_{j=1}^m apf_j = 1. \quad \text{ACE participation factors of } m$$

different GENCOs of i th area are shown by apf_matrix . The contracted scheduled loads in DISCOs in area1 are $delPdisco1$ and $delPdisco2$, in area2 are $delPdisco3$ and $delPdisco4$, in area3 are $delPdisco5$ and $delPdisco6$. The uncontracted local loads in areas 1, 2 and 3 are denoted by $delPuncot1$, $delPuncot2$ and $delPuncot3$ respectively. Ratios of areas' ratings, α_{12} , α_{13} , and α_{23} are given by the following expressions

$$\alpha_{12} = -\frac{P_{r1}}{P_{r2}}, \alpha_{13} = -\frac{P_{r1}}{P_{r3}} \text{ and } \alpha_{23} = -\frac{P_{r2}}{P_{r3}}$$

where P_{r1} , P_{r2} and P_{r3} are the rated powers of areas 1, 2 and 3 respectively.

cpf_matrix=

	DISCOS					
	1	2	3	4	5	6
GENCOS	1	cpf11	cpf12	cpf13	cpf14	cpf15
	2	cpf21	cpf22	cpf23	cpf24	cpf25
	3	cpf31	cpf32	cpf33	cpf34	cpf35
	4	cpf41	cpf42	cpf43	cpf44	cpf45
	5	cpf51	cpf52	cpf53	cpf54	cpf55
	6	cpf61	cpf62	cpf63	cpf64	cpf65

apf_matrix=

apf1	0	0	0	0	0
0	apf2	0	0	0	0
0	0	apf3	0	0	0
0	0	0	apf4	0	0
0	0	0	0	apf5	0
0	0	0	0	0	apf6

delPdisco=

delP disco1	delP disco2	delP disco3	delP disco4	delP disco5	delP disco6
----------------	----------------	----------------	----------------	----------------	----------------

delPUncontracted=

delP uncot1	delP uncot1	delP uncot2	delP uncot3	delP uncot3	delP uncot3
----------------	----------------	----------------	----------------	----------------	----------------

The total generation required of individual GENCOs can be calculated as:

$$\text{deltaPG_matrix} = \text{cpf_matrix} * \text{delPdisco}' + \text{apf_matrix} * \text{delPUncontracted}' \quad (1)$$

where delPdisco' and delPUncontracted' means transpose of delPdisco and delPUncontracted respectively.

The mutual scheduled Tie line power flows among the areas can be represented by the following formulae:-

$$\text{ScheduledPtie12} = ((\text{cpf13} * \text{delPdisco3} + \text{cpf23} * \text{delPdisco3} + \text{cpf14} * \text{delPdisco4} + \text{cpf24} * \text{delPdisco4}) / \alpha_{12}) - (\text{cpf31} * \text{delPdisco1} + \text{cpf32} * \text{delPdisco2}) \quad (2)$$

$$\text{ScheduledPtie23} = ((\text{cpf35} * \text{delPdisco5} + \text{cpf36} * \text{delPdisco6}) / \alpha_{23}) - (\text{cpf43} * \text{delPdisco3} + \text{cpf53} * \text{delPdisco3} + \text{cpf63} * \text{delPdisco3} + \text{cpf44} * \text{delPdisco4} + \text{cpf54} * \text{delPdisco4} + \text{cpf64} * \text{delPdisco4}) \quad (3)$$

$$\text{ScheduledPtie31} = ((\text{cpf41} * \text{delPdisco1} + \text{cpf51} * \text{delPdisco1} + \text{cpf61} * \text{delPdisco1} + \text{cpf42} * \text{delPdisco2} + \text{cpf52} * \text{delPdisco2} + \text{cpf62} * \text{delPdisco2}) / \alpha_{13}) - (\text{cpf15} * \text{delPdisco5} + \text{cpf25} * \text{delPdisco5} + \text{cpf16} * \text{delPdisco6} + \text{cpf26} * \text{delPdisco6}) \quad (4)$$

The closed loop system in Fig.2 is represented in state space form as

$$\dot{x} = A^cl x + B^cl u \quad (5)$$

where x is the state vector and u is the vector of power demands of the DISCOs. A^cl and B^cl matrices are constructed from Fig. 2. Eigen values are computed from A^cl , which are used for determining transient responses of frequency by modal analysis.

III. CRPSO ALGORITHM

PSO is a flexible, robust population-based stochastic search/optimization algorithm with implicit parallelism, which can easily handle with non-differential objective functions, unlike traditional optimization methods. PSO is less susceptible to getting trapped on local optima unlike GA, SA etc.

Eberhart and Shi [3] developed PSO concept similar to the behavior of a swarm of birds. PSO [4] is developed through simulation of bird flocking in multidimensional space. Each particle's present position is realized by the previous position and present velocity information. In CRPSO [5], a craziness operator is introduced to ensure that the particle would have a predefined craziness probability to maintain the diversity of the particles.

The velocity of the particle can be updated as:-

$$V_{j,i}(\text{iter}) = r_2 * \text{sign}(r_3) * V_{j,i}(\text{iter}-1) + (1-r_2) * C_1 * r_1 * \{x_{j,i}(\text{iter}-1) - x_{j,i}(\text{iter}-1)\} + (1-r_2) * C_2 * (1-r_1) * \{x_{j,i}(\text{iter}-1) - x_{j,i}(\text{iter}-1)\} \quad (6)$$

Where r_1 , r_2 and r_3 are the random parameter uniformly taken from the interval [0,1] and sign is a function defined as

$$\text{sign}(r_3) = -1 \text{ when } r_3 \leq 0.05 \\ = 1 \text{ when } r_3 > 0.05$$

When r_1 is large, $(1-r_1)$ is small and vice versa. Moreover, to control the balance of global and local searches, another parameter r_2 is introduced.

For birds flocking for food, there could be some rare cases that after the position of the particle is changed, due to inertia, fly toward a region at which it thinks is most promising for food. Instead, it may be leading toward a region at which is in opposite direction of what it should fly in order to reach the expected promising region. To reverse the direction of bird's velocity $\text{sign}(r_3)$ is introduced for this purpose. A craziness operator is introduced in proposed algorithm to ensure that the particle would have a predefined craziness probability to maintain the diversity of the particles. So, before updating its position the velocity of the particle is crazied by

$$V_{j,i}(\text{iter}) = V_{j,i}(\text{iter}) + P(r_4) * \text{sign}(r_4) * V_{j,i}^{\text{craziness}} \quad (7)$$

Where r_4 is a random parameter which is chosen uniformly within the interval [0,1]; $V_{j,i}^{\text{craziness}}$ is a random parameter which is uniformly chosen from the interval $[V_{j,i}^{\min}, V_{j,i}^{\max}]$; $P(r_4)$ and $\text{sign}(r_4)$ are defined respectively as:

$$P(r_4) = 1 \text{ when } r_4 \leq P_{cr} \\ = 0 \text{ when } r_4 > P_{cr} \\ \text{sign}(r_4) = -1 \text{ when } r_4 \leq 0.5 \\ = 0 \text{ when } r_4 > 0.5$$

Where P_{cr} is a predefined probability of craziness and iter means iteration cycle number.

IV. INPUT PARAMETERS

- Maximum population pool size, $n_p = 50$, maximum allowed iteration cycles for optimization per loop (L), $N_m = 100$. $C_1 = 2.05$, $C_2 = 2.05$, Predefined probability of craziness, $P_{cr} = 0.3$. $V_{j,i}^{\text{craziness}}$ is decreased linearly from 10 to 1.
- Area participation factors, $\text{apf1} = 0.6$, $\text{apf2} = 0.4$, $\text{apf3} = 1.0$, $\text{apf4} = 0.3$, $\text{apf5} = 0.3$ and $\text{apf6} = 0.4$. The

scheduled load of discos in different areas, $\text{delPdisco1}=0.3$, $\text{delPdisco2}=0.2$, $\text{delPdisco3}=0.2$, $\text{delPdisco4}=0.2$, $\text{delPdisco5}=0.3$, $\text{delPdisco6}=0.2$. The local loads of areas 1, 2 and 3 are $\text{delPuncot1}=0.1$, $\text{delPuncot2}=0.1$ and $\text{delPuncot3}=0.1$ respectively. Ratio of rated powers of area1 and area2, $\alpha_{12}=2.5$, ratio of rated powers of area2 and area3, $\alpha_{23}=1/3$, ratio of rated powers of area3 and area1, $\alpha_{31}=1.2$.

iii) The constant input data of the three unequal thermal generating areas are the following:

Name of the parameter	Area1	Area2	Area3
Governor regulation, R (Hz/p.u)	3.0	2.5	2.4
Governor time constant, T _g (Sec)	0.09	0.2	0.08
Non-reheat time constant, T ₁ (Sec)	0.5	0.4	0.3
Reheat time constant, T ₂ (Sec)	4.1	4.1	4.2
Reheat parameter, c	0.34	0.34	0.35
Power System gain constant, k _p (Hz/p.u)	100	100	120

V. SIMULATED TEST CASES

The following are the test cases:

Test case 1: It consists of area 1, area2 and area3 are connected in radially. The contract participation factor matrix for the test case will be

CPFM1=

0.25	0.30	0.15	0.25	0.00	0.00
0.50	0.40	0.10	0.25	0.00	0.00
0.25	0.30	0.15	0.15	0.30	0.25
0.00	0.00	0.25	0.10	0.30	0.15
0.00	0.00	0.15	0.10	0.15	0.25
0.00	0.00	0.20	0.15	0.25	0.35

Test case 2: It consists of area 1, area2 and area3 are connected in ring system. The contract participation factor matrix for the test case will be

CPFM2=

0.15	0.10	0.15	0.25	0.25	0.20
0.10	0.15	0.10	0.25	0.10	0.15
0.10	0.10	0.15	0.15	0.30	0.25
0.15	0.30	0.25	0.10	0.10	0.15
0.25	0.10	0.15	0.10	0.15	0.10
0.25	0.25	0.20	0.15	0.10	0.15

VI. COMPUTATIONAL RESULTS

Optimum AGC controller gains for CRPSO algorithm are computed for all the above test cases. Table I shows the results of optimum AGC controller parameter obtained by CRPSO algorithm for both the test cases. Similarly, Tables II and III show the results of optimum Generators Participations in generations, Tie-line Exchanges obtained by computed values using formulae of Section II and MATLAB-SIMULINK based results for different test cases. Figs. 4 to 10 show the transient response characteristics of Generators

Participations of generations, Tie-line Exchanges, Frequency deviations, Area Control Errors for test cases 1 and 2.

TABLE I
CRPSO BASED AGC CONTROLLER GAINS FOR AREA
INPUT PARAMETERS $t_p=20$, $t_{12}=0.145$, $b=0.425$

Algorith	Test cases	Optimal PID gains			Minimum Figure of Demerit	Optimizing Time (Sec)
		K _p (-ve)	K _i (-ve)	K _d (-ve)		
CRPSO	1	0.5478	1.6432	0.6935	72.21	51.58
	2	0.6861	1.6734	0.7941	81.52	55.32

TABLE II
COMPUTATIONAL RESULTS FOR TEST CASE 1

	Computed Value	Matlab-Simulink based Results	Error
deltaPG1	0.2270	0.2270	0.0000
deltaPG2	0.2980	0.2980	0.0000
deltaPG3	0.9175	0.9175	0.0000
deltaPG4	0.1733	0.1733	0.0000
deltaPG5	0.1417	0.1417	0.0000
deltaPG6	0.2083	0.2083	0.0000
ScheduledPtie12	-0.0750	-0.0750	0.0000
ScheduledPtie23	0.2300	0.2300	0.0000

TABLE III
COMPUTATIONAL RESULTS FOR TEST CASE 2

	Computed Value	Matlab-Simulink based Results	Error
deltaPG1	0.2950	0.2950	0.0000
deltaPG2	0.2000	0.2000	0.0000
deltaPG3	0.7050	0.7050	0.0000
deltaPG4	0.2008	0.2008	0.0000
deltaPG5	0.1908	0.1908	0.0000
deltaPG6	0.2275	0.2275	0.0000
ScheduledPtie12	0.0100	-0.0675	0.1675
ScheduledPtie23	0.2300	0.0362	0.1938
ScheduledPtie31	0.0958	0.0313	0.0645

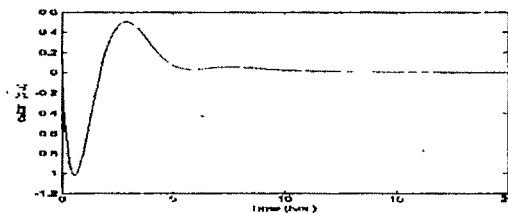


Fig. 4. Plot of deltaf1 versus time for test case 1.

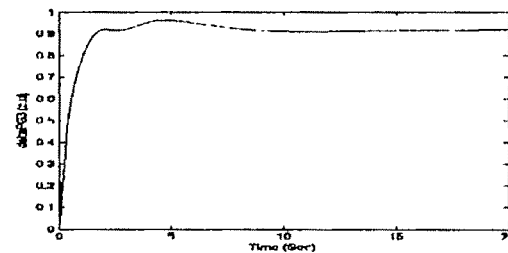


Fig. 5. Plot of deltaPG3 versus time for test case 1

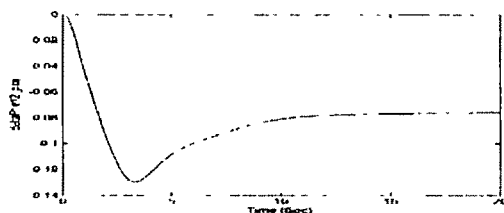


Fig. 6. Plot of deltaPtie12 versus time for test case 1.

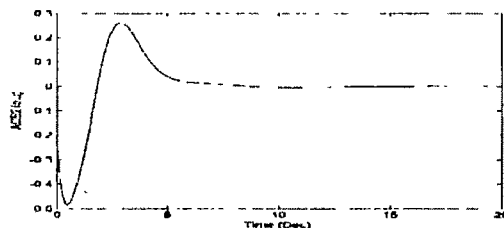


Fig. 7. Plot of Area Control Error, ACE2 versus time for test case 2

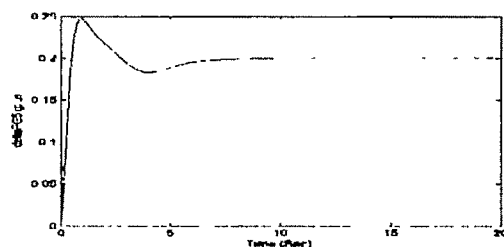


Fig. 8. Plot of deltaPG4 versus time for test case 2.

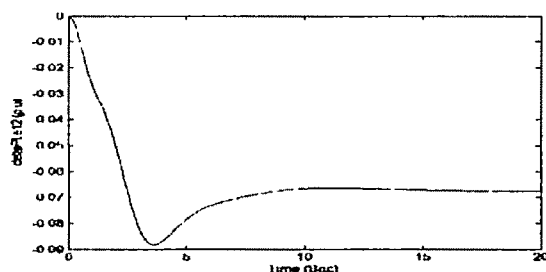


Fig. 9. Plot of deltaPtie12 versus time for test case 2.

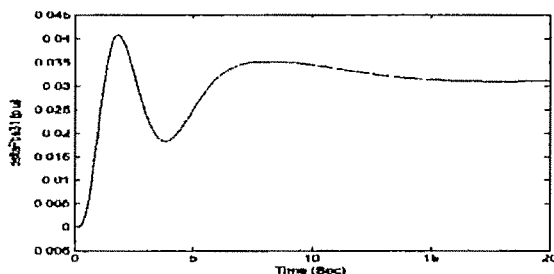


Fig. 10. Plot of deltaPtie31 versus time for test case 2.

VII. DISCUSSIONS

In this paper, one heuristic evolutionary search technique Craziness based Particle Swarm optimization (CRPSO) has been adopted for determination of optimal PID gains suitable for optimal transient responses in automatic generation control in the three area AGC simulator. From Table III, it is clear that in test case 1, the computed values of Generators Participations, Tie-line Exchanges match with the actual values obtained by MATLAB-SIMULINK. But, from Table IV, it is proved in test case 2 that though Generators Participations matching with the actual values, but due to the loop power flow the computed values of Tie-line Exchanges are differing from the MATLAB-SIMULINK based values. This behavior is not reflected in ordinary two area AGC simulator. So, except for the three area ring systems in which tie-line exchanges are not matching with the computed values, our AGC simulator works well in general for AGC in deregulated radial system. Area control errors of the areas finally become zeros. Area optimal frequency responses and tie-line power flow responses exhibit minimum swings i.e., minimum overshoot, minimum undershoot and minimum settling time due to optimal PID gain of the areas.

VIII. REFERENCES

- [1] Kumar, Jayant, Ng, Kah-Hoe, and Sheble, Geraki, "AGC simulator for price-based operation Part 1: A Model", IEEE Trans. On Power Systems, Vol. 12, No.2, pp. 527-532, May 1997
- [2] Donde, Vaibhav, Pal, M.A., and Hiskens, Iran, A., "Simulation and optimization in an AGC system after deregulation", IEEE Trans. On Power Systems, Vol. 16, No.3, pp. 481-488, August 2001
- [3] Eberhart, R.C., Shi, Y., "Particle swarm optimization: developments, applications and resources", Proceedings of the 2001 Congress on Evolutionary Computation, Vol. 1, 27-30 May 2001, pp. 81-86.
- [4] Ghoshal, S.P., "Optimization of PID gains by particle swarm optimization in fuzzy based automatic generation control", Electric Power System Research, vol. 72, issue 3, pp 203-212, May 2004.
- [5] Roy, R., Ghoshal, S.P., "A novel crazy swarm optimized economic load dispatch for various types of cost functions", International Journal of Electric Power and Energy System, accepted for publication.

Development of a Numeric Adaptive Relay For Transformer Overload Protection

Pratap Chandra Karfa, J.K. Das and K. Das (Bhattacharya)

¹ Department of Electrical Engg., Bengal Engineering and Science University, Shibpur, West Bengal, INDIA-711103, e-mail: pratap_karfa@yahoo.co.in.

² Damodar Valley Corporation, DVC Towers, Kolkata, West Bengal, INDIA-700054, e-mail: dasjiban@hotmail.com

³ Department of Electrical Engg., Bengal Engineering and Science University, Shibpur, West Bengal, INDIA-711103, e-mail: poopoolec50@hotmail.com

Abstract— The objective of the work is to develop a numerical adaptive relay for transformer protection using an embedded system based on a digital signal processor chip. Using the signal processing capability of the chip it is possible to implement the Method of Least Square Technique as a Digital Filtering Algorithm which makes it possible to study the Signature Analysis of the current and voltage signals and any other transducer outputs, which may serve as a basis for condition monitoring of the transformer as well as its protection.

The special feature of this relay is that it chooses the appropriate IDMT relay curve for transformer over current protection depending upon the winding temperature to prevent inadvertent tripping of the over current relay during the switching phenomena. In this scheme using adaptive relaying philosophy, it was possible to load the transformer optimally (sensing the temp. condition) and eliminating the any cause of inadvertent tripping. More over, accurate sensing of the fundamental frequency and its minor variation is important. This is done by the Method of Adaptive Sampling which is again a modular algorithm, embedded in the main Relaying Software operational from the DSP. Extraction of second harmonics component with respect to fundamental will give required amount of restraint to the relay and hence inrush blocking will be implemented.

Key words—Adaptive, Numeric, Protection, Transformer.

1. INTRODUCTION

Adaptive relaying by A.G. Phadke et al [1], accepts that relays which protect a power system network may need to change their characteristics to match the changing power system parameters. So during normal and abnormal operating conditions of the power system it may be necessary to change the settings of the protection units to suit the varying configuration of the system. Adaptive relaying considers the fact that the settings of relays will be changed automatically to accommodate the variation of power system parameters [2] and therefore the adaptive relaying requires microprocessor-based intelligent device for efficient and reliable operation.

According to Chen Yunping et al [3], the objective of providing adaptive relay settings is to minimize compromises

in system operation and allow relays to respond to actual system conditions.

Usually the inrush current protection in transformers has been based on the second harmonic blocking method. In most countries this is a generally accepted method with good operational experiences by Bogdan Kasztenny et. al[4]. The waveform blocking criterion is always activated to detect both initial inrush, sympathetic and recovery inrush. This paper utilizes the concept of adaptive relaying to design protection scheme for transformer overloading using the ADSP-2101 Digital Signal Processor (DSP), the signal conditioning of which will be based on The Method of Least Squares.

II. OBJECTIVE AND THE DESIGN LOGIC

The objective is to develop a Numeric Adaptive Relay for Transformer overload protection using an embedded system based on the DSP chip. The sensing of second harmonics wave form is done during initial inrush, sympathetic and recovery inrush, since the second harmonic wave form establishes the blocking criteria for the relay.

Accurate analysis of the second harmonic as well as the fundamental component is possible only after filtering of decaying DC component from the waveform. The decaying DC, predominantly present in the inrush, is very accurately diagnosed by the digital filter with its algorithm based on the method of least square.

Now the over load protection of transformer is based on the IDMT- relay curve and the over current protection acts upon the detection of magnitude of the fundamental component of the current signal. Blocking will be initiated if the second harmonics exceed a preset value of fundamental current or else, if the fundamental is not of alarming magnitude, the relay will follow the IDMT logic.

The **adaptability** is embedded in the Relaying Logic in a two-fold manner.

1. In the Digital filtering algorithm, where detection of fundamental component depends upon the sampling rate and any deviation of the fundamental frequency will entail a

change in sampling rate called the Adaptive Sampling Criterion. This is necessary for accurate filtering of the fundamental and the second harmonic component and decaying DC also.

2. In the relaying algorithm, selection of the IDMT curve depends upon the winding temperature and therefore the overload characteristic of the relay adapts itself to the changing conditions of temperature. This is necessary so that the transformer can be used **optimally** and over load limit can be set depending upon the winding temperature. If the characteristic can be raised, loading will be enhanced and if the characteristic is lowered then loading will be reduced automatically.

The transformer can take care of itself on proper temperature condition monitoring and can filter out necessary harmonics on the proper detection of frequency of the fundamental component in the current signal.

III. DIGITAL FILTERING TECHNIQUE

The Digital filtering is based on the least square method [5] which is taken to get the least sum of error square of the abnormal current signal. This is a non-recursive long data window algorithm and

- a) suppresses noise
- b) fundamental frequency phasors are not affected by the presence of harmonics.

The filtering algorithm is shown in fig.-1

3.1 Adaptive Sampling Criterion

The filtering technique involves working with pseudo-matrices, the elements of which may require alterations with frequency changes. This becomes tedious for the digital filtering algorithm to execute.

Therefore adaptive sampling rate comes into operation. Say, at any instant line frequency was f Hz and we take 12 samples per cycle. So the sampling interval was $\frac{1}{12 \times f}$ sec. When the

line frequency changes to f' Hz then, if we want 12 samples per cycle, the sampling interval is $\frac{1}{12 \times f'}$ sec., not $\frac{1}{12 \times f}$ sec

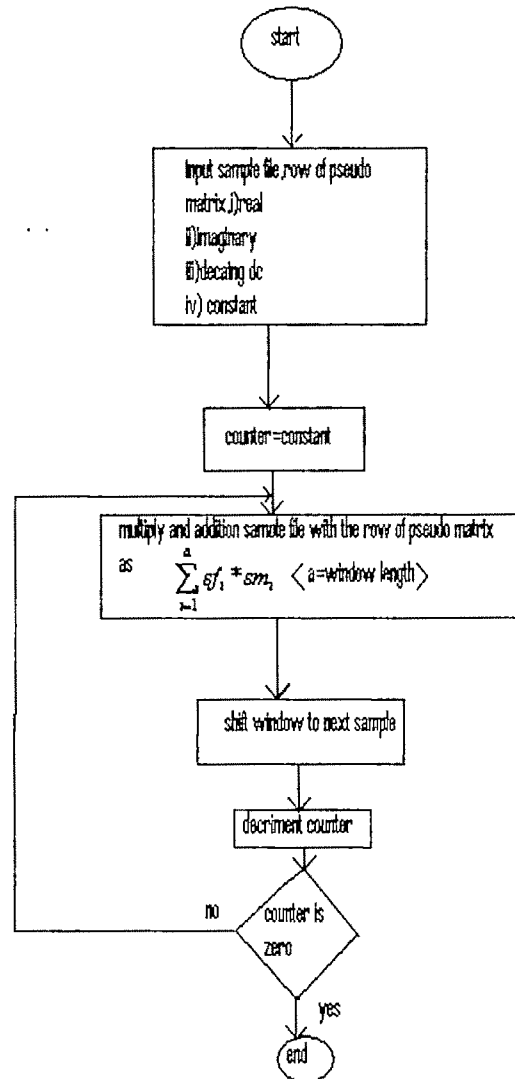


Fig.-1 Flowchart for digital signal processing by the Method of Least Squares

IV. RELAYING LOGIC

The transformer protection is made operational with the ambient temperature as reference and winding temperature is monitored with respect to the ambient temperature. Depending upon the temperature, selection of curve 1,2,3 is shown in figure-2.

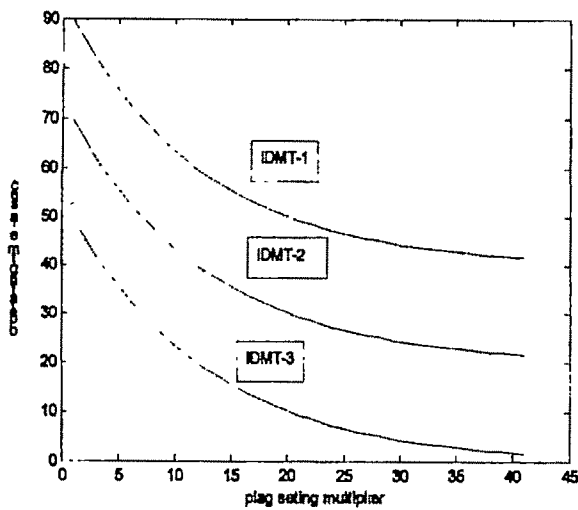


Fig -2 IDMT Curve for Different temperature

The Inverse curve which take less operating time indicate high winding temperature

To take protection against over current during inrush or cold start, the second harmonic component of the signal is calculated and if is significantly present then a delay is executed to wait for the second harmonic to die down. If fault occurs the fundamental value of the current is checked with one and a half times the rated value, and if it is so the trip circuit is enabled instantaneously. It may so happen that for a heavy fault, second harmonics maybe generated due to overfluxing, in that case the fundamental tracking method helps to arrive at trip.

If the fundamental current is not greater than one and a half times of rated value the relay will be tripped as per the IDMT curve chosen.

The mathematical expression of IDMT curve is built inside the numerical relay. The digital signal processor chip (ADSP-2101) enables the execution of the signal conditioning algorithm based on the method of least square. This also facilitates in removal of decaying dc offset from the signal and extraction of the second harmonics and fundamental component is also a result of execution of this algorithm. The relaying algorithm is shown in Fig.3.

Flow chart of relay program :-

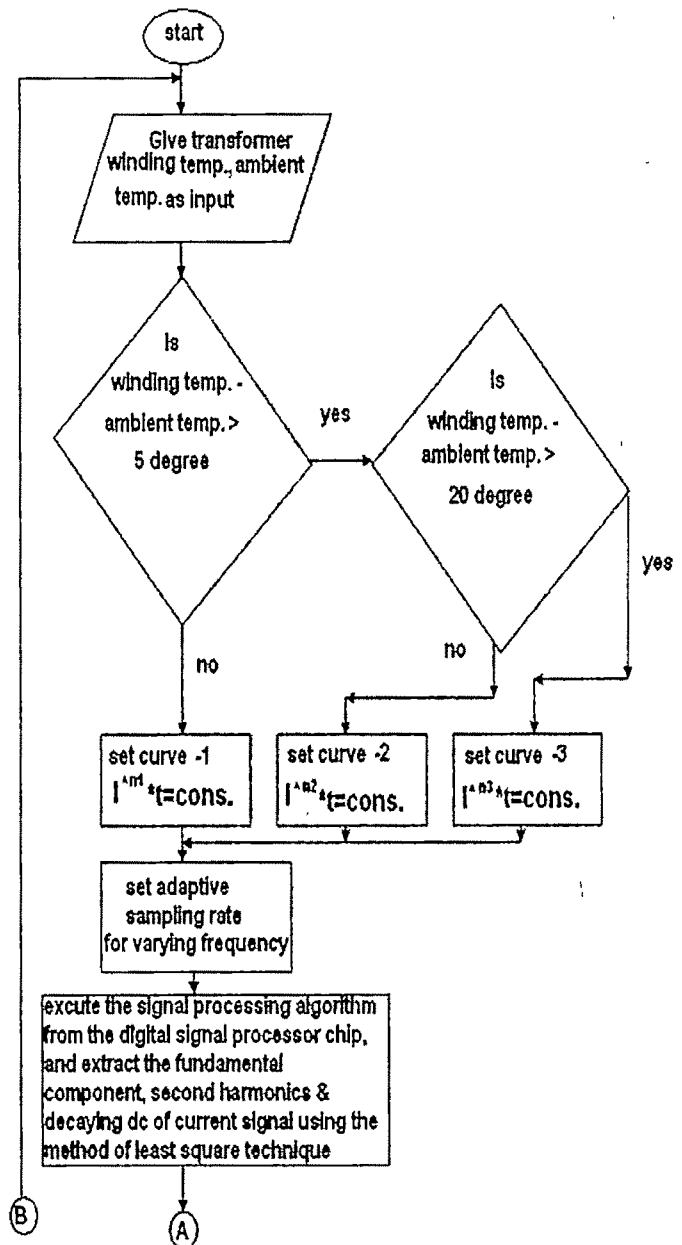


Fig -3. Flow chart for adaptive relaying algorithm

V. RESULTS AND OBSERVATION

The input faulted waveform is shown in figure-4
Now on analysis it was found that if the initial sample I_0 is placed in the middle of the data window then computation of

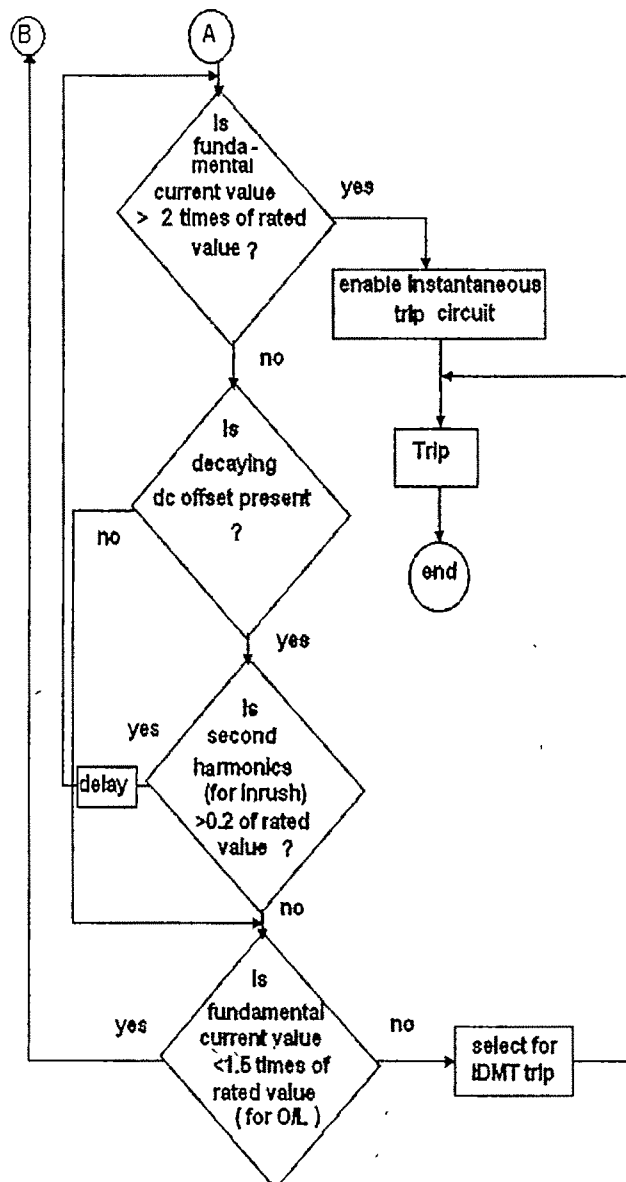


Fig.-3. Flow chart for adaptive relaying algorithm(contd.).

the peak of the decaying d.c is more accurate. Since it is a long data window algorithm appropriate attention and time was taken to be compute no. of samples per window which will be give the nearly exact value of the desired components in the signal. A typical resolution of the faulted waveform into the components of choice are shown in Fig.-5. The results of the relaying algorithm are shown in Table-I.

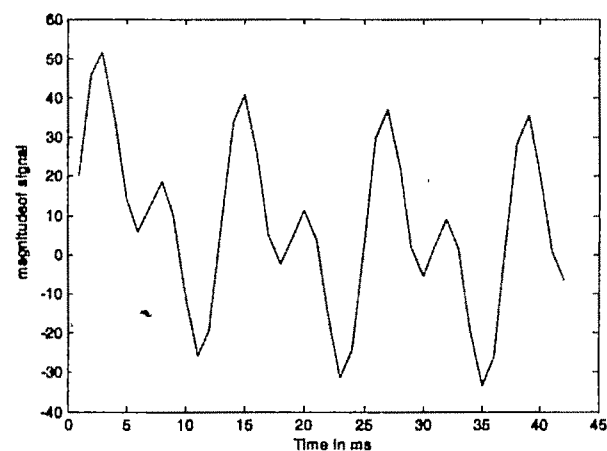


Fig. 4: waveform of the faulted signal

VI. CONCLUSION

In this scheme using adaptive relaying philosophy, it was possible to load the transformer optimally (sensing the temp. condition) and eliminating any cause of inadvertent tripping. This is done automatically choosing the appropriate IDMT curve by the numerical relay. More over sensing the fundamental frequency

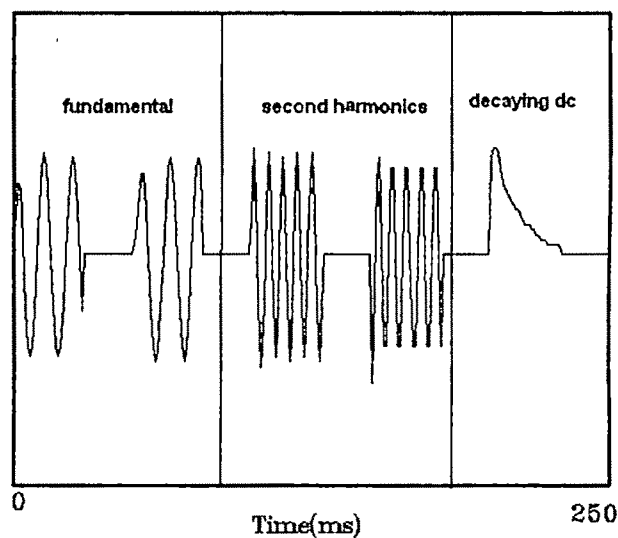


Fig.-5 , Fundamental, Second harmonics and Decaying dc extraction result.

Table -1 Observation of relay output

Sl. No	Fault location		Input on the different components of current				Operating condition of relay	Curve selection for IDMT	Comments
	Amplitude of fault current	Phase angle of fault current	ms of fundamental (50A set value of relay)	ms of second harmonic (6A set value)	Decaying constant				
	25	27	20	21	20	Notrip	I		normal
2	25	31	25	21	15	Notrip	II		Due to restraint
3	25	40	31	21	12	Notrip (Fault)	II		Because fundamental > 1.50%
4	25	50	25	11	6	OL trip	III		Because fundamental > 1.50%
5	25	42	25	5	3	OL trip	II		De
6	25	46	25	5	2	OL trip	II		De
7	25	29	55	5	2	Not trip (Fault)	I		Because fundamental > 1.50%
8	25	40	25	0	0	OL trip	III		Because fundamental > 1.50%

and its minor variation is also important to determine fundamental and second harmonics, no of samples per cycle should be constant. Adaptive relaying utilizes the continuous changing status of the power system as the basis for on-line adjustment of the power system relay settings. Also if the sampling frequency increases, the error level reduces. Such adaptive concept will find a lot of applications in distance protection during feed extension and also to maintain protection co-ordination when the system uses FACTS devices.

REFERENCE

- [1] Phadke A.G, Horowitz, S.H, Throp J. S. "Addaptive Transmission system relaying IEEE transaction on power delivery", vol-3, no.-4 october 1988, pp-1436-1445
- [2] Coding, J.D, House, S.A, Joice J.H., Labhart, Richards, J.R. "Adaptive relaying - a new direction in power system protection" IEEE Potentials, March-1996, pp-28-33
- [3] Chen Yunping, Gong Qingwu, Fu Fengnian, 'An Accurate Fault Location and its data processing by Least Square Method' IEEE, vol. 46, No.4, 2000, pp-1026-1028.
- [4] Bogdan Kasztenny and Ara Kulidjian 'An Improved Transformer Inrush Restraint Algorithm Increases Security while Maintaining Fault Response Performance' annual conference April 11-13, 2000, page(s)-122-125.
- [5] Sachdev, M.S., Tutorial on "Modern Trends in Power System Protection" NPSC, INDIA, IIT Kanpur, Dec-1996

Study For Monitoring And Control Of Power System Parameters Using Geographical Information System

Susmita Dey (Chaudhuri), Anushree Roy, Sumana Chowdhuri, Jitendra Nath Bera

Department of Applied Physics, University of Calcutta,

email: jitendrabera@rediffmail.com, sumana_cu05@rediffmail.com, chaudhuri.susmita@gmail.com, anushreeb4u@rediffmail.com

Abstract— The inherent limitations faced by traditional decentralised system of record keeping and managing different electrical parameters can be replaced by a centralized automated system. This paper describes the development of a centralized automated system for monitoring, analyzing and managing electrical parameters of different sub-stations under normal or various contingencies from a remote location, so as to enhance the overall system performance using state of the art designed Geographical Information System (GIS). The inherent mapping feature of GIS software can be used to locate any sub-station and to retrieve data from the sub-station from a remote place and can accordingly control the power flow under normal and abnormal condition.

Key Words— Geographical information system, Serial communication.

I. INTRODUCTION

Electricity is an aspect of the utility sector that is very essential to the smooth and meaningful development of a society. This involves generation, transmission and distribution of the electric current to consumers. Efficient distribution of the generated power cannot be achieved without proper record keeping and monitoring of the transmission and distribution network system. Electric power utilities worldwide are increasingly adopting the computer aided monitoring, control and management of electric power distribution system to provide better services to electric consumers [1]. So for better utility design and maintenance, the more sophisticated computer based Automated Mapping/Facility Management (AM/FM) or a Geographical Information System (GIS) must be embraced. The GIS provides an environment for building an electric facilities database, which includes graphic information and facility attribute data. The database can be used for engineering analysis, accounting and map production. Facility and network data can be retrieved by searching through the graphic and nongraphic data files. The monitored data can then be used to form input data files for power system applications. With the powerful graphic capability of the system, simulation results can be viewed from the computer screen along with the graphic displays [2].

II. SYSTEM DESCRIPTION

In this work the authors attempted to monitor the power system parameters like instantaneous voltage, Current and instantaneous Power and power factor, frequency and also some equipments' temperature of a distribution system. For this GIS is the front platform where these parameters can be visualized and also some computed parameters like average active power, average reactive VAR etc are monitored. In the background the system actually involves Microcontroller for data collection, serial communication (RS 232) protocol for data fetching from microcontroller to PC and Visual basic for different data retrieving as shown in fig.1.

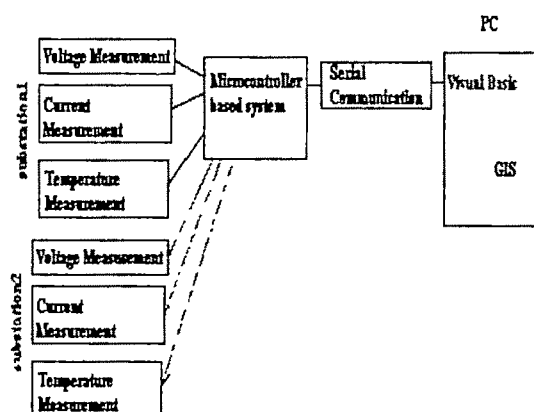


Figure 1: Block diagram of the overall System

GIS Implementation

There is no unique definition for Geographic Information System (GIS) but a commonly accepted one is that it is a system with computer hardware and software functions for the spatial data input, storage, analysis, and output [T. Bernhardsen 1992] [4]. All Geographic Information System (GIS) are computer representations of some aspect of the real world. It is a computer system and a set of tools for capturing, storing, checking, integrating, manipulating, analyzing and displaying data, which are referenced to the earth.

Hagget and Chorley (1967) point out that a spatial model places emphasis on reasoning about the real world by means of translation in space. [3]. A 'well-designed GIS' should be able to provide quick and easy access to large volumes of data and also it should have the ability to select detail by area or theme; link or merge one data set with another; analyze spatial characteristics of data. There are various application areas for GIS like in Defense Agencies for Target site identification, Mobile command modeling and Intelligence data integration; in public Utilities for network management, Service provision and Telecommunications Emergency repair; in Environmental management for Pollution monitoring and Resource management etc.

In this paper Visual Basic Based GIS software JTMAPS2005 has been used. GIS needs to handle two types of data – Graphical or Vector data and Non-spatial or attribute data. Vector data type- Vector data is composed of discrete co-ordinates that can be used as points or connected to created lines and polygons. Points - Discrete location on the surface of the planet, represented by an x-y coordinates pair. Each point on the map is created by latitude and longitude coordinates, and is stored as an individual record in the shape file as shown in fig 2a.

Lines- Formed by connecting two data points. The computer reads this line as straight, and renders the line as a vector connecting two x-y coordinates (X = longitude, Y = latitude). The more points used to create the line, the greater the detail. For lines, this means that the system stores one end of the line as the starting point and the other as the end point, giving the line "direction". as shown in fig 2b.

Polygons- An area fully encompassed by a series of connected lines. Because lines have direction, the system can determine the area that falls within the lines comprising the polygon. Polygons are often an irregular shape fig 2c.



Fig2a. Point Layer



Fig2b. Line Layer



Fig2c. Polygon layer

Serial Communication between GIS S/W and the Microcontroller

A communication method is necessary for creating a link between the outside world and GIS software for monitoring of data. Here RS 232 Protocol is used as the communicating method and data is stored as EXCEL file. In this work asynchronous serial communication is used. Each character is placed in between a start and a stop bit, which is called data framing.

III. SCHEMATIC OF DATA ACQUISITION

The fig. 3 shows the schematic of data acquisition system using microcontroller AT 89C51. For voltage measurement one potential Transformer (PT) is used to step down the system voltage to the input level of analog to digital converter (ADC). Here a potential divider is also used for calibration purpose. Similarly to measure the current a Current Transformer (CT) is used. For Temperature Measurement a temperature sensor is used whose output gives the voltage corresponding to station temperature.

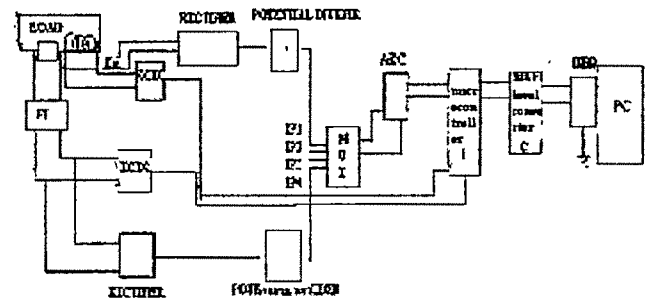


Fig 3: Schematic diagram of project

A four input multiplexer is used to select the proper channel either for voltage or current or temperature. As per software and firmware program when a signal is sent from the computer end for data type selection i.e. current or voltage data or temperature data, microcontroller receives this data through RS 232 serial communication register and send it to the multiplexer for desired channel selection. After selecting the channel multiplexer behaves as an analog switch and the corresponding voltage is then fed to the input of ADC. ADC then converts the voltage level to its digital equivalent data. The micro controller receives these data in the serial communication and transmits it to PC through the level converter for proper level matching. In computer the collected data is stored as an EXCEL file. Using JTMAPS software three rooms are drawn which is represented as three sub-stations.

The measured data are not the actual data. The data is to be calibrated by multiplying the CT and PT ratio.

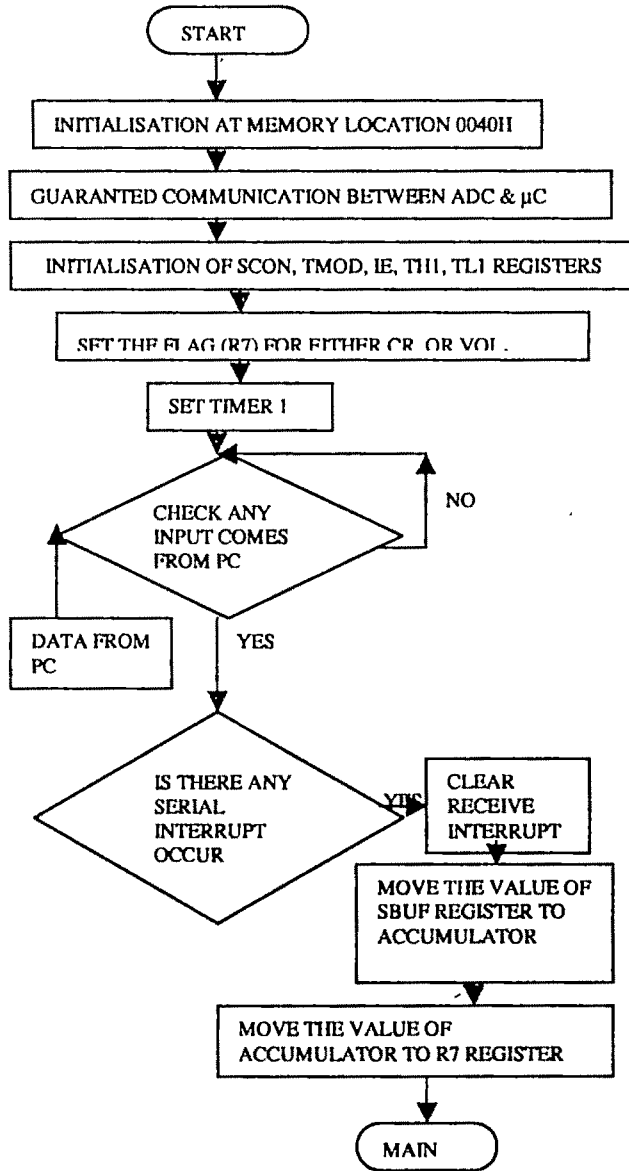
Actual current data= current data X CT ratio.

Actual voltage data = voltage data X PT ratio

IV. FIRMWARE PROGRAM

The program started at memory location 0040H. After receiving a signal from PC the microcontroller set the flag R7 according to type of parameter i.e. voltage or current or temperature. Then the corresponding monitored value is transmitted to the PC.

Flowchart



V. RESULTS

The fig 4 shows the developed GIS View where polygons shown are the representation of Graphical Data where the corners of polygons define the geographical boundaries of different stations. At the right side of this representation, the table shows the attributed data or Non-spatial data, which is the set of information, corresponding to spatial features. Spatial data can be linked with outside relational database in VB.

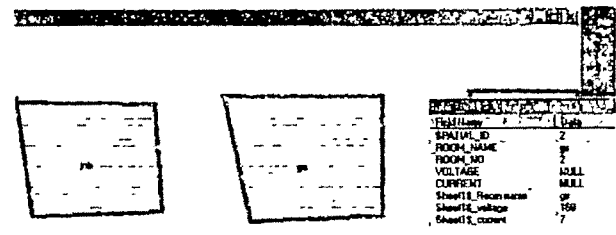


Fig4. Developed spatial and attributed data

Fig5 & fig.6 shows the front-end view in VB of monitoring the voltage data and GIS view after data linking. Here each polygon representing one sub-station.

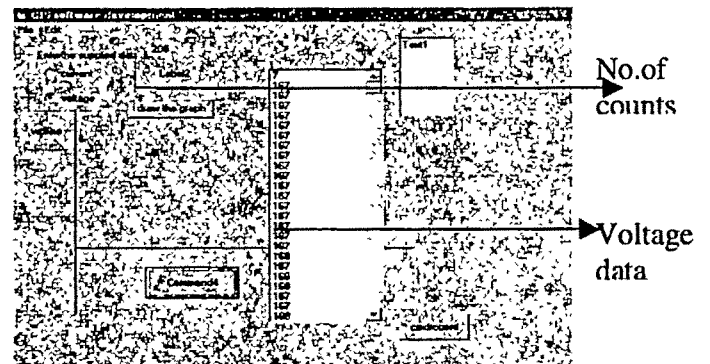


Fig5. Monitoring of voltage data

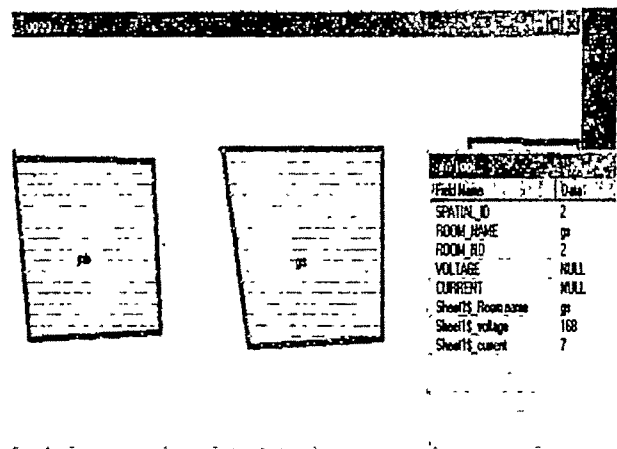


Fig.6. Display of monitored data of a sub-station

VI. CONCLUSION & FUTURE SCOPE

In this project we tried to give a new method for analyzing the power system with a different approach. Visual display of power system parameters of more than one sub-station at a time and monitoring the parameters from a remote centralized area decrease the tedious method of record keeping and saves time of locating problems and as well as can control it in relatively short period of time. At the same time serial communication provide the facility of wireless

communication. So it reduces the cost of wired communication as monitoring of parameters of very remote place without wireless can increase the installation charge and protection charge in a large account.

ACKNOWLEDGEMENT

The authors acknowledge the support provided by the University of Calcutta to carry out this research work.

REFERENCES

- [1] R.P.Gupta, R.K. Varma " Power distribution Automation".
- [2] Tsay, M.T.; Lu, C.N.; Lin, W.M ; Chen, C.S., Power Industry Computer Application Conference, 1993 Conference Proceedings Volume, Issue, 4-7 May 1993 Page(s): 154 – 161, Digital Object Identifier 0 1109/PICA.1993.291022, "Data extraction from a geographic information system for power system applications".
- [3] Davor Skilec, Slavko Krajcar, Sneežing Blagajac, University of Zagreb Faculty of Electrical Engineering . "Application of GIS technology in electrical distribution network optimization
- [4] Ian Heywood, Sarah Cornelius, Steve Carver, "An Introduction to Geographical Information Systems " 2nd Edition.

Technical Session 5B

Transmission and Distribution

Fuzzy System Approach to Power Purchases in A Power Pool of A Deregulated Power System

Ajoy K Chakraborty¹, C. K. Roy², P. B. Duttagupta³

¹ College of Engineering & Management, Kolaghat, India e-mail: akcall@yahoo.co.in

² Jadavpur University, Kolkata, India, e-mail: chinmoy_kanti@hotmail.com

³ Indian Institute of Technology

Abstract— During the past decade the electric power supply industry recreates the electricity markets to improve efficient operation by competition. Deregulation has changed this with the explicit goal of introducing choice to customers, improvement of customer services and reliability. The spot pricing that result in the balance of supply and demand is announced to the customer a priori to plan how much electricity the customer has to buy or sell over and above that of forward contract. The spot pricing can be estimated with degrees of uncertainty and the paper considers cases of cost reduction for quality or quantity of electricity needed by a power pool. The cases considered are – a deterministic model for quality improvement at lower cost and an uncertain model via fuzzy logic for cost reduction by purchase at the market rate.

Key words— Deregulated power system economics, spot pricing, Fuzzy logic based tariffs, purchase demand scheduling.

I. INTRODUCTION

THE reform trends of the 1990s in electricity markets recreates, to some extent, the institutional frame work which was developed a century ago. Pricing of electricity has evolved in the past for a regulated and monopolistic power system on the basis of revenue reconciliation over a period of time related to service life of equipment fixing the marginal cost of installation and production of electricity [1,2,3] and a reasonable amount of profit. Conditional pricing for the time of the day (TOD) use of electricity as well as penalty for low power factor loads were variations available. Thus tariff is a document, approved by the responsible regulatory agency, listing the terms and conditions, including a schedule of prices, under which utility services will be provided. However, power sector has undergone a restructuring in many part of the world and it is observed that the effective economies of the country have relied on price response to match supply and demands of electricity in the dynamic mode. While the restructuring was first undertaken by the developed countries like USA, UK, etc. [3,4], the developing countries like India has also started the restructuring process by setting up a regulatory commission to

regulate tariff based on economic rational to promote healthy competition, private involvement and efficient plant operation. In India since 100% restructuring down to the smallest of distribution consumers is difficult due to unawareness of the new system and the non availability of remote automation in billing and display system, only a few central sector and state boards have started the availability based tariff (ABT). Excess power of Eastern Region is being sold to Northern and Southern regions through power trading corporation through competitive bidding. This paper deals with the details of utilizing the information of pricing structure in a deregulated environment for optimal utility gain. The pricing structure has a nominal set based on past data, forecast of demand and normal availability and is modified by the impact of contingency and involvement of competitively inefficient generation capacity to meet the demand in the dynamic mode. It has been shown that with spot pricing of electricity, the utilities will save expenses by rescheduling the consumption to off peak load demand period and by choosing corresponding sellers that suit the utility most. The strategy for real time pricing (RTP) can be either announcement of pricing rate on hourly basis for twenty four hours a day ahead or announcement of one hourly rate at a time twenty four hours ahead. However, since the loadability of transmission and distribution owned by an agency may not be known to other agencies who do not own them to facilitate power wheeling, an independent system operator (ISO) is required to guide the market operation without the risk of chaotic behaviour or collapse which has actually happened in California [5]. The pricing structure under the changing scenario is a matter of great interest and the uncertainties associated with the forecast and the availability of generation and vendors make the optimal operation a much desired criterion that has been dealt with in this paper for selective guidance.

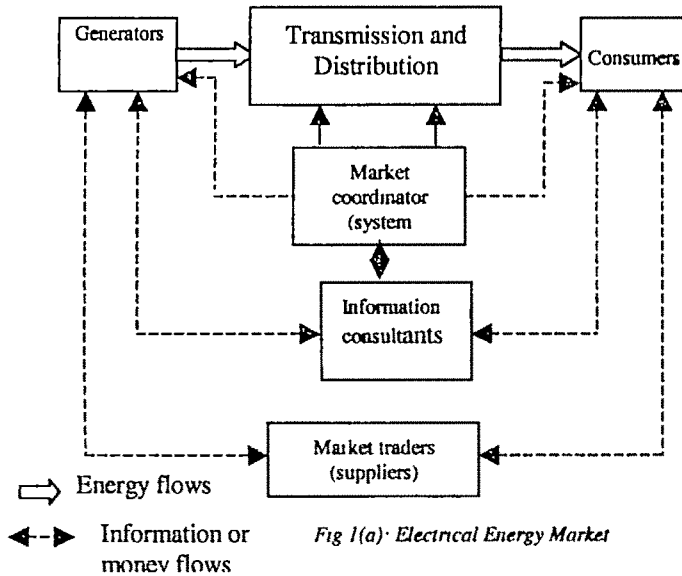


Fig 1(a) Electrical Energy Market

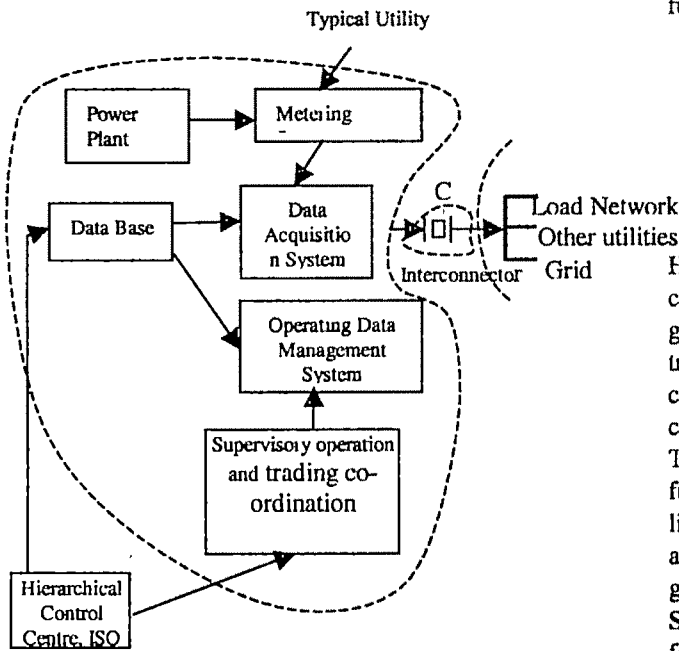


Fig 1(b) Schematic diagram of a typical utility

II. BASIC SYSTEM

The basic case considered is the generation of electricity by various agencies to formulate their own pricing structure for the market. Extreme case is that of captive power generated by utilities and made available to the grid. Transmission and distribution network are under a single regulated body. The alternatives of various vendors of transmission and distribution would be a hierarchical state requiring an ISO. The cost of ancillary and quality of services are accommodated by a suitable model and constraints of energy storage, availability and power wheeling congestion and buy back facility are ignored at the first instance. A first level Electrical Energy Market of deregulated power system is shown in Fig. 1 (a). Fig. 1(b) shows a typical utility connected to loads, other utilities

and the grid through sub transmission, transmission lines and the circuit breakers. However, an utility may have a number of power plants, interconnected via transmission lines and having its own load.

A market place is designated by a forward contract arrangement followed by incidental purchase on designated spot pricing available. The spot pricing as already stated is variations on the normal rate as influenced by competitive demand, contingencies and other restriction on operation. In general it will be non-linear function of energy usage. However, the non-linear function can be split into piece wise linear incremental characteristic for given ranges like

$$\frac{\partial F}{\partial P} = b + 2cP, \quad P_{\min} \leq P \leq P_{\max} \quad (1)$$

where 'F' is the cost function, 'P' the power and 'b' and 'c' are given constants of the spot pricing.

III. SOLUTION METHOD

The problem then boils down to optimal solution of cost function minimization, subject to,

- 1) Equality constraint of power generated = power demand + power loss.
- 2) Inequality constraints of generation, i.e. $P_{\min} \leq P \leq P_{\max}$
- 3) Inequality constraints given by the load ability of transmission lines.
- 4) Cost function minimization by hard limits.

However, in this paper a further dimension has been added by considering the uncertainties of load forecast and that of power generation and transmission. To keep the problem simple the transmission line wheeling congestion is ignored, but the consequence of line loadability limit within the utility is considered both as hard and soft limits.

The uncertainties are specified by a triangular membership function to introduce fuzziness in the character of the variables like forecast and the inequality constraints of power generation and line loading limits. The following stage wise steps are given to bring out the effectiveness of the idea.

Step-1: Optimum Power Flow (OPF) solution is carried out for the internal system with hard bounds for cost evaluation.

Step-2: Optimum Power Flow (OPF) solution is carried out with external buying for given discrete power pricing structure and hard bounds to check for overall cost.

Step-3: Cost reduction on the base case of step-2 by considering soft limits on the basis of fuzziness of variables and evaluating the cost reduction with a particular reliability factor of achieving this target.

For this purpose General Gradient Reduced method has been used with the help of programme package [10].

IV. MATHEMATICAL FORMULAE

In modeling real time electricity rate structure, the objective is to set the spot price of electricity for each consumer equal to the marginal cost of supplying power to the consumer at that instant of time. These are usually determined by Optimal Power Flow (OPF) solution. Since the demand changes in each time interval, for any given demand the operational constraints

consumers for providing power. Since the demand, constraints and unit commitment are not known a priori estimates are used which leads to uncertainty elements to the deterministic model. The mathematical formulation for OPF based deterministic model is as follows:

$$\begin{aligned} \text{Min} \left[\sum F_i(P_{Gi}) \right] \quad \text{Subject to} \\ \Delta P_i \equiv P_{Di} - P_{Gi} + P_i = 0 \end{aligned} \quad (2a)$$

$$\begin{aligned} \Delta Q_i \equiv Q_{Di} - Q_{Gi} + Q_i = 0 \\ \text{for all } i[1, N] \end{aligned} \quad (2b)$$

$$P_{G \min} \leq P_{Gi} \leq P_{G \max} \text{ for } i \in R_G \quad (3a)$$

$$Q_{G \min} \leq Q_{Gi} \leq Q_{G \max} \text{ for } i \in R_G \quad (3b)$$

$$V_{\min} \leq V_i \leq V_{\max} \quad (4)$$

for all $i[1, N]$

$$P_{ij \min} \leq P_{ij} \leq P_{ij \max} \quad (5)$$

for all $i[1, N]$

where,

$$P_i = V_i \sum_{j=1}^N Y_{ij} V_j \cos(\delta_i - \delta_j - \theta_{ij}) \quad (6)$$

$$Q_i = V_i \sum_{j=1}^N Y_{ij} V_j \sin(\delta_i - \delta_j - \theta_{ij}) \quad (7)$$

$$P_{ij} = Y_{ij} \{V_i^2 \cos \theta_{ij} - V_i V_j \cos(\delta_i - \delta_j - \theta_{ij})\} \quad (8)$$

$$F_i(P_{Gi}) = a_i + b_i P_{Gi} + c_i P_{Gi}^2 \quad (9)$$

For which the Lagrangian is,

$$\begin{aligned} F = \sum F_i(P_{Gi}) + \sum \lambda_{Pi} \Delta P_i + \sum \lambda_{Qi} \Delta Q_i + \sum \mu_{Gi} (P_{Gi} - P_{G \min}) + \\ \sum \mu_{Gi} (P_{G \max} - P_{Gi}) + \sum \mu_{Di} (Q_{Di} - Q_{G \min}) + \sum \mu_{Di} (Q_{G \max} - Q_{Di}) \\ + \sum \mu_{ij} (P_{ij} - P_{ij \min}) + \sum \mu_{ij} (P_{ij \max} - P_{ij}) + \sum \mu_{Vi} (V_i - V_{\min}) + \\ \sum \mu_{Vi} (V_{\max} - V_i) \end{aligned} \quad (10)$$

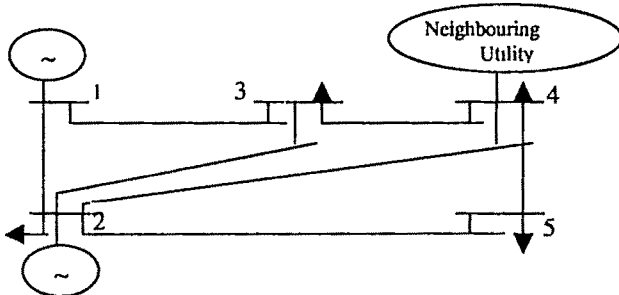


Fig. 2 Single Line Diagram of a 5- Bus Two Generator power system with neighbouring utility at bus 4

with the symbols P, Q for active and reactive power, N the number of buses, G for generation, S for source, $V_i \angle \delta_i$ is the voltage at i^{th} bus and $Y_{ij} \angle \theta_{ij}$ is the admittance of the transmission line ij and R_G is the domain of all the generating units.

For purchasing power from the market, the market price is modeled with triangular fuzzy numbers with linear functions for left and right membership. Therefore if the minimum price is $\bar{\lambda} = (\lambda_0, l_{\lambda 0}, r_{\lambda 0})$ and the offered price to import the maximum power is $\bar{\lambda}_{\max} = (\lambda_{\max}, l_{\lambda \max}, r_{\lambda \max})$

then $\bar{\lambda} = \bar{\lambda}_0 m P_\mu$ which is also a triangular Fuzzy number,

$$\text{where, } m = \left(\frac{\lambda_{\max} - \lambda_0}{P_\mu^{\max}}, \frac{l_{\lambda \max} - l_{\lambda 0}}{P_\mu^{\max}}, \frac{r_{\lambda \max} - r_{\lambda 0}}{P_\mu^{\max}} \right)$$

In contrast to deterministic minimization, utility may try to reduce the cost by a certain percentage with a satisfaction level G which is also a triangular membership function such that $G \geq 0$

Therefore maximize $\sum (\alpha_{PGi}^l l_{PGi} + \alpha_{PGi}^r r_{PGi})$ subject to

$$G - \sum F_i(P_{Gi}) - \delta_1 \left(l_G + \sum \frac{\partial F_i}{\partial P_{Gi}} r_{PGi} \right) \geq 0 \quad (11)$$

and

$$\Delta P_G - (-\sum \Delta P_i + \sum \Delta P_{ij}) - \delta_2 (\sum Y_{\Delta Pi} + \sum r_{Pij} + l_{PG}) \geq 0 \quad (12)$$

$$\Delta P_G - \sum \Delta P_i + \sum P_{ij} - \delta_3 (\sum l_{\Delta Pi} + \sum l_{Pij} + r_{PG}) \geq 0 \quad (13)$$

for each bus

$$P_{ij}^{\max} - P_{ij} - \delta_4 r_{Pij} \geq 0 \quad (14)$$

$$P_{ij} - P_{ij}^{\min} - \delta_4 l_{Pij} \geq 0 \quad (15)$$

for each line

with δ 's as the measures of acceptance, α_{PGi}^l and α_{PGi}^r are the weighting factors of the left and right spreads of the generation of unit I respectively.

V. CASE STUDIES

Three examples are worked out for illustrating the ideas enumerated so far.

A. Example-I

A five bus problem from G.W.Stagg, A.H.Al-Abiad [6, 7] with two internal generations and buying from market at a particular bus. The power system is as shown in fig.2.

B. Example-II

A five bus problem solved through DC load flow with two internal generations and purchase of power from market place at two identified busses of the power system taken from the reference [8].

C. Example-III

A five bus problem solved through DC load flow with two internal generations and purchase of power from market place at one bus which is a modification of problems solved by Shahidepour [9].

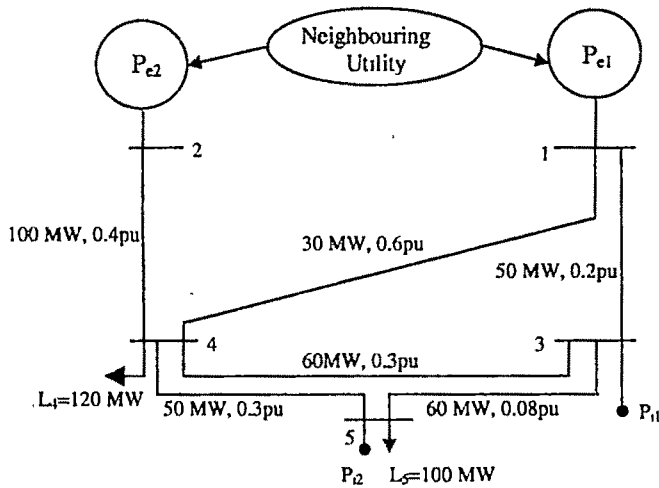


Fig 3(a) A 5- Bus system with two utilities & two local generators

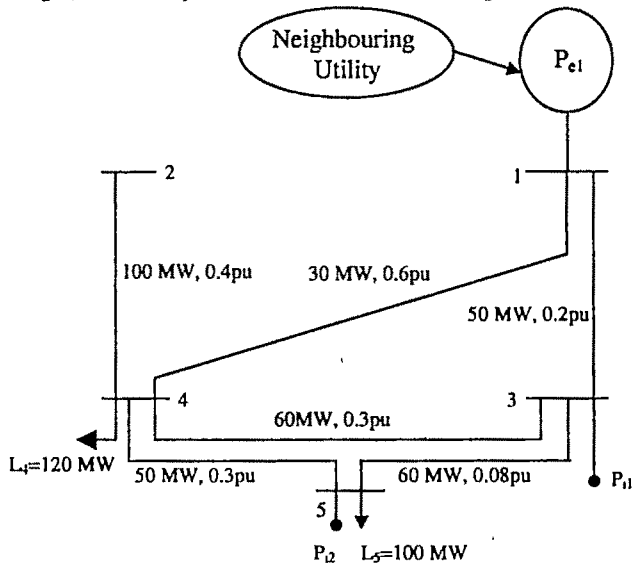


Fig 3(b) A 5- Bus system with one utility & two local generators (Buses 3 & 5)

Case I

It may be observed from Table 1 that though average load that is at L.S.F.1.0 the system operates reasonably well with low transmission line loss and adequate bus voltage, at peak load that is at L.S.F. 1.4 the bus voltage at bus 5 deteriorates under excessive reactive power demand and the transmission line loss also increases dramatically. A solution for this situation is to buy market power at bus 5 as is shown by the last row data in Table 1, if the objective function of optimality is minimum loss and good quality of power by purchasing power at bus 4 from neighbouring utility characterized by constants given at the appendix that gives a higher running cost of \$8127 per hour that would be further escalated if wheeling charges to bus 4 is included. Alternatively, switched reactive power compensation may be considered as in [7] at a fixed cost. Cost of generation also can be minimized if the purchase of power

from neighbouring utility is at a lower rate than the one considered here. This case illustrates reactive power coverage and considers voltage limits but does not consider limits for transfer of power over the transmission lines.

Case II

The base case is the unaided utility with a load of 100 MW at bus 5 and 120 MW at bus 4 and generators with maximum rating of 130 MW at bus 3 and 110 MW at bus 5. The deterministic cost minimization problem with constraints produces a solution of generation level of 130 MW at bus 3 and 90 MW at bus 5 with a over all cost of operation \$ 656.7 per hour. The corresponding line flows are flexible with a margin of 20 MW from the loadability limit. Assuming sub-constraints and fuzziness of the system load the cost of operation can be brought down to \$ 591 per hour in case of purchase from market consisting of two neighbouring systems that is a 10% saving over \$ 656.7 per hour. The levels of generation and line flows are shown in Table-2. It may be observed that the distribution of power line flows is unique without any flexibility and the loadability limits are just maintained. Any uncertainty in the right spread of power demand would require over loading of lines.

Table 1
Estimated performance results of Case I for two specific load demands for optimality conditions of (i) minimum loss and (ii) minimum cost

Load Scaling Factor (LSF)	Loss in pu MW	Cost \$/hr.	P_{g1} in pu MW	P_{g2} in pu MW	Utility in pu MW	Voltage at Bus 5 in pu
1.0	Minimum loss 0.018	6521.7	0.50	0.673	0.00	1.018
1.0	Minimum cost 0.027	6125.1	0.982	0.200	0.00	1.015
1.4	Minimum loss 0.035	8127	1.0	0.35	0.26	1.006
1.4	Minimum cost 0.066	8026	1.0	0.61	0.00	0.98

TABLE-2
GENERATION AND FLOW IN LINES WITH REFERENCE TO FIG (b)

Parameter	Mean value (MW)	Left Spread (MW)	Right Spread (MW)
P_{e1}	60	-	-
P_{e2}	00	-	-
P_{g1}	90	1.00	1.00
P_{g2}	70	1.01	1.00
P_{4-5}	-30	0.00	1.00
P_{3-5}	60	0.00	1.00
P_{3-4}	60	0.00	0.00
P_{1-3}	30	0.00	0.00
P_{1-4}	30	0.00	0.45
P_{2-4}	00	0.00	4.52
Total			

Case III

This case is similar to case II but the only difference is that the power can be purchased from one neighbouring utility at bus I. The generation and the line flows for the fuzzy model are shown in Table-3. The cost reduction is to the tune of 9.5% at \$ 593.3 per hour.

VI. CONCLUSIONS

Two typical case studies (Case I and Case II & III) carried out on well documented power system networks clearly show how quality of supply in terms of voltage and cost reduction corresponding can be achieved by suitable purchase of power from the market. The alternative proposal of selling power to the market from the stock of advanced purchase contract can therefore be also carried out when the spot price goes up. The uncertainty factor of spot pricing and load forecasting has been dealt with fuzzy membership function and cost minimization is carried out on the basis of an acceptance parameter δ near about 1.0. In the case studies of II and III cost reduction of about 10% from the base case has been achieved by loosing margin of safety of line loadability and the flexible nature of line load distribution. Though the investigation reported in this paper has excluded direct evaluation of pricing of the transmission system component including wheeling charges but a recent paper [11] has indicated bilevel transmission cost component evaluation for nodal electricity charges by minimizing a linear combination of right and left spread of soft bound as it has been considered in this paper. Therefore, this investigation has a further potential to include transmission system cost as well.

VII. APPENDIX

The 5-bus system considered is described in details in [6] but the bus loadings are considered to vary over the day. Calculations shown are for a load scaling factor of 1.0 and 1.4 and the generating unit cost characteristics and limits are given in table 4

Corresponding to the generating unit cost

Calculation based on $F(P) = a + bP + cP^2$ with F in \$/hr, a in \$/hr, b in \$/MWhr., c in \$/MW²hr and P in MW.

Power purchased at bus-4 from neighbouring utility was with constants $a = 300$ \$ / hr, $b = 3500$ \$ / MWhr, $c = 600$ \$ / MW²hr.

The corresponding data for case 2 and 3 have been taken from [8] and are shown in Table 4 & 5 with the additional data of right and left uncertainty limits.

Table -4

Generators cost and limit Characteristics (Case -2& 3)

us No.	a \$/hr	b \$/MWhr	c \$/MW ² h	P _{min} MW	P _{max} MW
# 3	0	1	0.008	0	130
# 5	0	3	0.015	0	110
# 1	0	2	0.01	0	250
# 2	0	2	0.03	0	100

Uncertainty Limits:

Bus No.	l_{λ_0} \$/MWhr	r_{λ_0} \$/MWhr	$l_{\lambda_{max}}$ \$/ MWhr	$r_{\lambda_{max}}$ \$/MWhr
# 1	0.3	0.3	0.2	0.2
# 2	0.2	0.2	0.15	0.15

VIII. REFERENCES

- [1] Barrie T. W , Power System Economics, Peter Peregrinus Ltd, London, 1983.
- [2] Wood A. J and Woolenberg B. F, Power Generation, Operation and Control, John Wiley & Sons, INC. N Y.1996.
- [3] Chakraborty A. K., Roy C. K. , Duttagupta P. B. "Choice of Pricing Structure out of a class of alternatives in a Deregulated Power System". Proc. of National Power System Conference-2002, IIT Kharagpur, pages 323 to 326.
- [4] Schweppe F. C., Caramanis M. C., Tabors R. T., Bohn R. E., Spot pricing of Electricity, Kluwer Academic Publs, 1988.
- [5] Klein Barbara, " Federal Regulators Change Course in California" IEEE, Spectrum August,2001, pages- 28-30.
- [6] Stagg G.W, Al-Abiad A.H., -Computer Methods in Power System Analysis, McGraw-Hill Inc., N Y 1968.
- [7] Chottopadhyay D. , Bhattacharya K, Parikh Jyoti "Optimal Reactive Power Planning and Its Spot Pricing: An Integrated Approach" IEEE TRANS. On Power Systems, Vol. 10, No 4 Nov. 1995, pages- 2014—2020
- [8] Shahidehpour S. M., Ferrero R. W "Fuzzy Systems approach to short-term power purchase Considering uncertain Prices" in Electric Power Application of Fuzzy Systems Ed. M E El-Hawary, IEEE Press Piscataway NJ 1998
- [9] Chakraborty Ajoy kr., Roy C.K., Duttagupta P.B. "Cost Reduction of a Power Pool by Purchase of power in a Market Place of a deregulated Power System – A fuzzy Approach". Proc. International Conference on Power Systems (ICPS 2004), Kathmandu. Pg. No. 583-587 2004.
- [10] SOLVER Suite, LINDO Systems Inc. 1415 North Dayton St. Chicago, IL 60622. <http://www.lindo.com>.
- [11] Gill H. A., Galiana Francisco D, Silva Edson L da, "Nodal Price Control: A Mechanism for Transmission Network Cost Allocation" IEEE TRANS. On Power Systems, Vol. 21, No. 1 Feb. 2006, pages- 3—10.

Table -3

Generators cost and limit Characteristics (Case – 1)

Bus No.	a \$/hr	b \$/MWhr	c \$/M W ² hr	P _{min} MW	P _{max} MW	Q _{min} MVAR	Q _{max} MVAR
1	1260	2940	600	50	150	-100	150
. 2	532	4212	600	20	150	-40	50

Feeder Reconfiguration and Capacitor Placement for Loss Reduction of Distribution System Using Genetic Algorithm

P.V.Prasad¹, S.SivaNagaraju², and N.Sreenivasulu³

¹ Chaitanya Bharathi Institute of Technology, Hyderabad, India e-mail: pvp_reddy@yahoo.co.uk

² J.N.T.U College of Engineering, Kakinada, India e-mail: suigin70@yahoo.co.in

³ Madanapalli Institute of Technology & Science, Madanapalli, India

Abstract— This paper presents an efficient approach to feeder reconfiguration and capacitor placement for power loss reduction and voltage profile enhancement in radial distribution systems. Genetic Algorithm (GA) is chosen to solve the network reconfiguration problem and capacitor placement problem. The advantage of this method is that it can provide a global or near global optimum for feeder reconfiguration and capacitor placement. The proposed method is illustrated by employing an IEEE-33 node system.

Key words— Distribution system, reconfiguration, capacitor placement, genetic algorithm, power loss reduction.

I. INTRODUCTION

IN the field of distribution automation, optimal reconfiguration and reactive power compensation allow the attainment of some important goals such as reduction of power losses, voltage profile flattening, improvement of power factor, etc. Feeder reconfiguration is defined as process of altering the topological structures of distribution feeders by changing the open/closed states of the sectionalizing feeders and ties switches. The networks are reconfigured to reduce system real power loss, optimal linking of new loads, relieve overloads and service restoration.

Through the application of reactive power compensation one can reduce power loss, improve the voltage profile and quality of supply. Capacitors have been very commonly used to provide reactive compensation in distribution systems. The benefits of compensation depend greatly on the size of the capacitors added. Using switched capacitors the size of the capacitors installed on feeders can be varied.

The early work on feeder reconfiguration for loss reduction is presented by Aoki et al. [1]. Baran and Wu [2] defined the problem for loss reduction and load balancing as an integer-programming problem. Chiang et al. proposed a solution procedure employed simulated annealing [3,4] to search for an

acceptable non-inferior solution. The other approach to feeder reconfiguration considering the ability of system transformers

and power loss, and voltage profiles had been respectively presented [5-9]. Optimal capacitor placement is a combinatorial optimization problem that is commonly solved by employing mathematical programming techniques. Grainger and Lee [10-12] formulated the problem as a non-linear programming model that can be solved by simple iterative procedures based on gradient search. Su et al. [13] applied fuzzy reasoning approach to optimum capacitor allocation.

Most of the previous studies handled reconfiguration problem without considering the capacitor addition [1-9], or handled capacitor compensation problems without considering feeder reconfiguration [10-14]. They dealt with the feeder reconfiguration and capacitor addition in a separate manner [1-14], which may result in unnecessary losses and cannot yield the minimum loss configuration. However few papers using heuristic techniques for feeder reconfiguration and capacitor placement had been presented [15-17]. In view of this, the Genetic Algorithm method to determine the feeder reconfiguration and capacitor sizing for optimal loss minimization of distribution systems is proposed. The proposed method can attain a global or near global solution for feeder reconfiguration and capacitor setting.

II. PROBLEM DESCRIPTION

In this study, an approach for feeder reconfiguration and capacitor sizing for distribution systems is proposed. The aim is to minimize the power loss of the system, subject to load and operating constraints.

The distribution system reconfiguration problem for loss minimization is to decide the position of sectionalizing switches and tie switches under the current capacity and voltage limit constraints at the same time all loads are to be powered.

The objective of the capacitor placement problem is also to reduce the active power loss of the system, the same as the feeder reconfiguration.

III. FEEDER RECONFIGURATION BASED ON GENETIC ALGORITHM

This problem can be formulated as

$$\text{Min. } f = \sum_{j=1}^{N_b} I_{(j)}^2 r_{(j)} \quad (1)$$

Subject to

$$V_{(i) \min} \leq V_{(i)} \leq V_{(i) \max} \text{ and } I_{(j)} \leq I_{(j) \max}$$

Where f = total active power losses of the system

N_b = total number of branches

$I_{(j)}$ = current flowing through the branch j

$r_{(j)}$ = resistance of the branch j

$V_{(i)}$ = voltage at node i

In addition, feeder reconfiguration has to obey the following rules:

- i) Any load can't be left out of service.
- ii) Network structure must be radial.

A. Chromosome Coding Strategies

Most of available GA applications in power systems are simply employing GA and no special attention has been put on the characteristic of the solved problem, modeling and solving technique [18]. In fact, the most critical problem in applying a genetic algorithm is to find a suitable encoding method for chromosomes in the problem domain.

1) Shorten the Length of Chromosome

To maintain continuous power supply to all the loads, the following set of rules to be adopted for selection of switches. Rule1: All switches those do not belong to any loop are to be closed.

Rule2: All switches connected to the sources are to be closed.

Rule3: Sectionalizing switches, those lie on LV side of the tie switches, are taken as opening options of the initial configuration.

Rule4: Selection of sectionalizing switches to be opened is done by taking any one switch among the available set of switches for a particular tie switch closed.

2) Coding and Genetic Operation Strategies

In this paper, crossover operations are defined as to exchange between the same templates and mutation operations are restricted in one template [20].

B. Implementation of Proposed Algorithm

1) Initialization of population

Initial population is generated randomly with the given population size. By decoding the strings we can get the actual configuration of the system.

2) Fitness

The fitness should be capable of reflecting the objective and directing the search towards optimal solution. Load flow calculation is performed to obtain active power losses. Reciprocal value of active power losses is proposed as fitness function. So fitness function can be written as

$$F = 1/f \quad (2)$$

3) GA operations

In the proposed algorithm, Roulette wheel and Elitist model selection methods are employed. In this way, the diversity of population can be maintained and the best individuals can survive in new generation. In Elitist model selection method, the chromosomes ranked in ascending order according to their

fitness values. The individuals with the best fitness are adopted for the new generation.

4) Terminating rule

The process of generating new trials with the best fitness will be continued based on the difference between best fitness and average fitness is less than specified error.

C. Flow chart of the proposed GA

The flow chart of the network reconfiguration based on GA is given in Fig. 1.

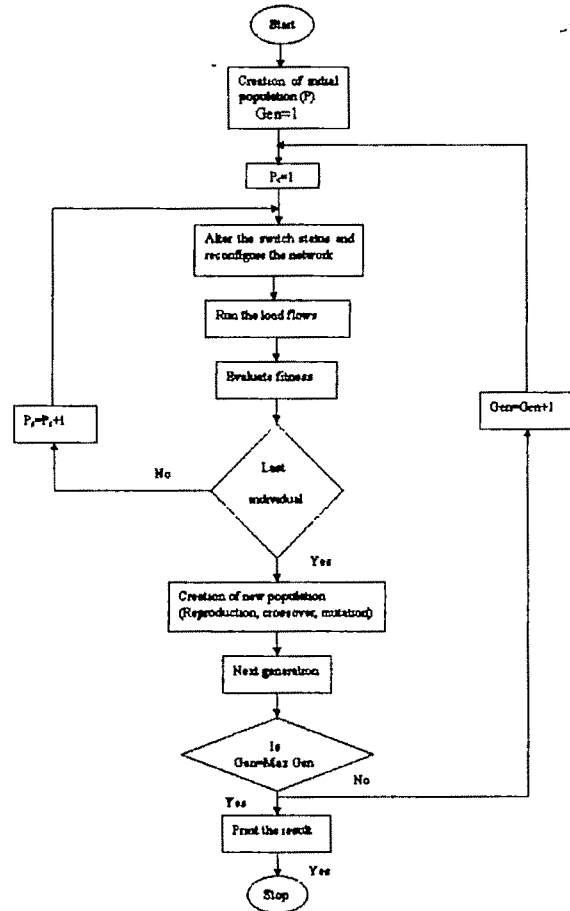


Fig.1 Flow chart of network reconfiguration based on GA

IV. OPTIMAL CAPACITOR PLACEMENT BASED ON GENETIC ALGORITHM

The objective function of the present work is to determine the optimal sizes of the capacitors. The problem can be stated as,

$$\text{Max. } S = KE - KC \quad (3)$$

Where

S = net savings (\$)

KE = benefits due to saving in energy (kWh)

KC = cost of installation of the capacitor

(a) Benefits due to savings in energy loss is given as

$$KE = \Delta KE \times r \quad (4)$$

Where

ΔKE = savings in energy losses
 = (Annual energy losses before installing the capacitor) -
 (Annual energy losses after installing capacitor)
 r = rate of energy in \$/kWh (taken as \$ 0.06/kWh).
 (b) Cost of installation of capacitor is given as

$$KC = Q_C \times ICKC \times IKC \quad (5)$$

Where

Q_C = size of capacitor (kVAR)

$ICKC$ = cost of capacitor/kVAR (\$ 4.0 /kVAR)

IKC = annual rate of cost of capacitor (taken as 0.2)

A. Implementation aspects of GA based capacitor sizing

In this section, GA is applied to calculate the optimum values of capacitors required to be placed on a radial distribution system to maximize the net savings while keeping the voltage at nodes within limit by considering the cost of the capacitors into account. The candidate nodes for the placement of capacitors are found using power loss index and the implementation details are given in [21].

The simulation considers each string as a list of numbers varying from 0 to 3 (assuming 3 capacitor banks). Each digit represents the number of capacitor banks at a node. A maximum of 3 capacitor banks has been placed at a node. The number of digits in a string depends on the number of candidate nodes selected. Binary coding of the string is not implemented because of the large size of the search space for which the execution time is very high. So, integer representation is employed to represent capacitor size. During mutation one of the digits is replaced by another digit, which is randomly generated from the list (0,1,2,3).

The strings are generated such that each element of the string varies from 0 to 3. Even though the initial population is generated randomly, consistent results were obtained. This has been verified by running the program several times with different initial population

1) Evaluation of fitness function

The fitness function should be capable of reflecting the objective and directing the search towards optimal solution. For each population or string size, the calculated capacitors are placed at the candidate nodes and the load flow method [19] is run and the losses, net savings are calculated and these net savings become the fitness function of the GA (as savings are maximized).

2) Algorithm for GA based capacitor sizing

The GA based capacitor sizing algorithm is given below:

1. Generate the random population for size(s) of capacitors for Gen = 1
2. Perform load flows and determine various node voltages, active power losses
3. Obtain the fitness function
4. Select parent strings by roulette wheel production process
5. Perform cross over and mutation on the selected strings and obtain new strings for next generation
6. Repeat steps 2 to 5 until the difference between best fitness and average fitness is less than specified error

7. Stop.

V. COMBINED OPTIMIZATION OF DISTRIBUTION SYSTEM

Feeder reconfiguration and capacitor placement are two important means in reducing the power loss of distribution system. If these two means combined together, it is almost certain that much better result can be obtained. With this idea the program that can perform both the tasks is developed. The flow chart of the proposed method is shown in Fig. 2.

After feeder reconfiguration, the original scheme of capacitor placement is probably not the best one under new network topology, so a new type of feeder reconfiguration and capacitor placement is adopted.

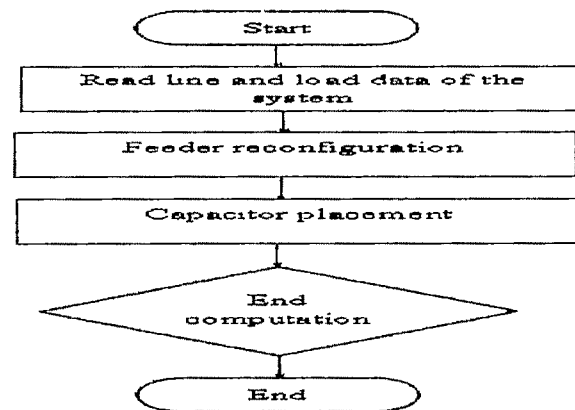


Fig.2. Flow chart for combined optimization problem

A. Illustrative example

The effectiveness of the method is illustrated with IEEE 33-node, 12.66 kV, radial distribution system [2]. This example can be explained with four different cases as follows:

Case1: Only feeder reconfiguration is considered

Case2: Only capacitor placement is considered

Case3: Both capacitor placement and feeder reconfiguration are considered. However, capacitor addition is carried out before feeder reconfiguration.

Case4: Both capacitor placement and feeder reconfiguration are considered and are taken into account simultaneously.

The summary of results for all the four cases is given in Table.1.

VI. CONCLUSION

A useful feeder reconfiguration and capacitor placement problems employing genetic algorithm method for loss reduction of distribution systems has presented. The two important means of reducing the power loss of distribution system are combined together in order to obtain better optimization result. The algorithm has high efficiency in power loss reduction and improvement in voltage regulation. The proposed method has been applied for different systems and the results show that it has a good performance and suitable for online application. From the results, considering both feeders' reconfiguration and setting of capacitor simultaneously can

TABLE I. THE SUMMARY OF RESULTS

Description	Original configuration	Case 1	Case 2	Case 3	Case 4
Switch states altered	—	(33,7), (34,14), (35,9), (36,32)	—	(33,7), (34,14), (35,9), (36,32), (37,28)	(33,7), (34,14), (35,9), (36,32)
Min. voltage (p.u.)	0.9131	0.9378	0.9252	0.9539	0.9633
Total kVAR required	—	—	1200	1200	1125
Voltage regulation (%)	8.69	6.22	7.48	4.61	3.47
Improvement of voltage regulation (%)	—	28.42	13.9	46.9	60.07
Total power loss (kW)	202.4559	139.1180	143.5807	96.4954	71.6473
Power loss reduction (%)	—	31.28	29.08	52.33	64.61

generate more loss reduction than considering them separately. In addition to power loss reduction, the voltage regulation can be improved as well by the proposed method.

REFERENCES

- [1] Aoki,K, Ichimori,T, and Kanezasehi,M, "Normal stage optimal load allocation in distribution system", *IEEE Trans on Power Delivery*, vol.2, pp.147-155, 1987.
- [2] M.E.Baran, F.F.Wu, "Network reconfiguration in distribution systems for loss reduction and load balancing", *IEEE Trans.on Power Delivery*, vol.4, pp.1401-1407, 1989.
- [3] H.D.chiang, J.J.Rene, "Optimal network reconfiguration in distribution systems. part 1: a new formulation and a solution methodology" *IEEE Trans. on Power Delivery*, vol. 5, pp 1902-1908, 1990.
- [4] H.D.chiang, J.J.Rene, "Optimal network reconfiguration in distribution systems: part2. solution algorithms and numerical results", *IEEE Trans. on Power Delivery*, vol. 5, pp.1922-1931, 1992.
- [5] T.P.Wanger A.Y.Chukhani, R.Hackam, "Feeder reconfiguration for loss reduction: an application of distribution automation", *IEEE Trans.on Power Delivery*, vol. 6, pp.1922-1931, 1991.
- [6] R P.Broadwater, A.H.Khan, H.E.Shaalan, R.E.Lee, "Time varying load analysis to reduce distribution losses through reconfiguration", *IEEE Trans. on Power Delivery*, vol. 8, pp 294-300, 1993
- [7] S.K.Goswami, S.K.Basu, "A new algorithm for the reconfiguration of distribution feeders for loss minimization", *IEEE Trans. on Power Delivery*, vol 7, pp 1484-1491, 1992.
- [8] D Shrimohammadi, H W Hing, "Reconfiguration of electric distribution networks for resistive loss reduction", *IEEE Trans on Power Delivery*, vol. 4, pp.1492-1498, 1989
- [9] H C.Cheng, C C.Kou, "Network reconfiguration in distribution systems using simulated annealing", *Electric Power System Research*, vol. 29, pp.227-238, 1994.
- [10] J.J.Grainger and S.H.Lee, "Optimum size and location of shunt capacitors for reduction of losses on distribution feeders", *IEEE Trans on Power Apparatus and Systems*, vol 100, pp.1105-1116, 1982.
- [11] S.H.Lee and J J Grainger, "Optimum placement of fixed and switched capacitors on primary distribution feeders", *IEEE Trans. on Power Apparatus and Systems*, vol. 100, pp. 345-352, 1981.
- [12] J.J.Grainger and S.H.Lee, "Capacity release by shunt capacitor placement on distribution feeders: A new voltage dependent model", *IEEE Trans. on Power Apparatus and Systems*, vol. 100, , pp.1236-1244, 1982.
- [13] S.Sundharajan and A.Pahwa, "Optimal selection of capacitors for radial distribution systems using a genetic algorithm", *IEEE Trans. on Power Systems*, vol. 9, pp.1499-1507, 1994.
- [14] C.T.Su., C.S.Lee., C.S.Ho, "Optimal selection of capacitors in distribution systems", *IEEE Power Tech. '99 conference*, Budapest, BPT99, pp 171042, 1999.
- [15] D.Jiang, R.Baldick, "Optimal electric distribution system switch reconfiguration and capacitor control", *IEEE Trans. Power Systems*, Vol. 11, 1996, pp.890-897
- [16] G.J.Peponis, M.P.Papadopoulos, N.D.Hatziaargyriou, "Distribution network reconfiguration to minimize resistive line losses", *IEEE Trans. on Power Delivery*, vol. 10, pp.1338-1342, 1995
- [17] D.Jiang, R.Baldick, "Optimal electric distribution system switch reconfiguration and capacitor control", *IEEE Trans. Power Systems* vol. 11, pp.890-897, 1996.
- [18] Duan Gang, Yu Yixin, "A Study on global optimization for NP hard problems in power systems", *Automation of Electric Power Systems*, vol.25, pp.14-18, 2001.
- [19] S. Sivanagaraju, M.S.Gridhar, E.Jagadeesh Babu, and Y.Srikanth, "A novel load flow technique for radial distribution system", *National Power System Conference*, NPSC-2, IIT, Chennai, India, pp. 140-144, 2004.
- [20] S. Sivanagaraju, E.Jagadeesh Babu, and Y.Srikanth, "An efficient genetic algorithm for loss minimum distribution system reconfiguration" *Electric Power Components and Systems*, vol.34, pp.249-258, 2006.
- [21] S. Sivanagaraju, N SravanKumar, and V.Ganesh, "Genetic algorithm to reactive power compensation in radial distribution network" conference proceedings of PCID, Chennai, India, pp.565-575, March 2005.

A New Approach to Calculate Frequency Dependent Impedance of Grounding Electrodes

S.M.Shahrtash¹, N.Ramezani²

¹Center of Excellence for Power Systems Automation and Operation
Iran University of Science & Technology, Iran, e-mail: shahrtash@iust.ac.ir

²Center of Excellence for Power Systems Automation and Operation
Iran University of Science & Technology, Iran, e-mail: n_ramezani@iust.ac.ir

Abstract— In this paper, based on the electromagnetic field theory in frequency domain and by using the full set of Maxwell's equations, an exact numerical method is presented to calculate the high frequency characteristics of electrode excited by high frequency sources such as lightning, faults etc. In this method, the effect of ground-reflected waves which exist due to the boundary between earth (lossy medium) and air, have been considered according to the modified image theory that includes a modified reflection coefficient (RC) instead of solving the Sommerfeld integral (S.I) in the high frequency formulation of the Green function.

Keywords— Electromagnetic fields, High frequency performance, Computer modeling, Grounding system.

I INTRODUCTION

OPTIMUM performance of the grounding systems in substations is very important for providing human safety, correct operation of protective device, dissipation of lightning and fault currents, minimization of the flashovers during transients, electromagnetic compatibility in sensitive electrical equipments and insulation coordination of power systems. The steady state behavior of grounding systems (at power frequency) is well understood through many procedures proposed in the literature. Nevertheless, the high frequency analysis of grounding grids under impulse currents excited by lightning discharges, switching and faults are still under research. For investigating the high frequency performance of grounding systems, many researches and studies have been presented, yet [1]-[27].

In general, high frequency modeling of grounding grids can be classified into four categories:

Circuit modeling [1]-[6], which is based on replacing all conductors of grounding system by an equivalent circuit containing lumped capacitors, inductors and resistors with too many approximations.

Electromagnetic field calculation methods [7]-[17], which solve the problem in time and frequency domains by using the

full set of Maxwell's equations. These methods have made the least assumptions and so they are the most accurate procedures.

Hybrid methods [18]-[20], that combine the circuit and electromagnetic field approaches. In these procedures, the analysis is carried out easier than the electromagnetic field method but with lower accuracy.

Equivalent transmission line substitution [21]-[27], which are based on traveling wave calculations. This model neglects the mutual electromagnetic coupling between grounding conductors and its accuracy is not desirable.

In this paper, based on the electromagnetic field theory in frequency domain and by using the full set of Maxwell's equations, an exact numerical method is presented, so-called method of moments (MOM). According to the MOM, a new method to analyze the transient behavior of grounding electrode up to 40 MHz is presented. In this method, the effect of ground-reflected waves which exist due to the boundary between earth (lossy medium) and air, have been considered according to the modified image theory that includes a modified reflection coefficient (RC) instead of solving the Sommerfeld integral in the high frequency formulation of the Green function.

In order to show the accuracy of the proposed method the results of two methods from the literature are also shown, and a discussion is given.

II. FREQUENCY ANALYSIS OF GROUNDING ELECTRODE

The frequency response is a useful approach to introduce a system in terms of its response to inputs with different frequencies. Whereas the frequency response of a system depends on its elements and reveals its natural frequencies, so it can be used to find the output of that system for a given input. Fig.1 shows a horizontal grounding electrode that is a perfectly conducting element, with length L and radius r , buried in a lossy medium with permittivity ϵ_e , permeability μ_e and conductivity σ_e (earth), at depth H that is fed by a high frequency current source (I_f) which corresponds to lightning, faults or etc.

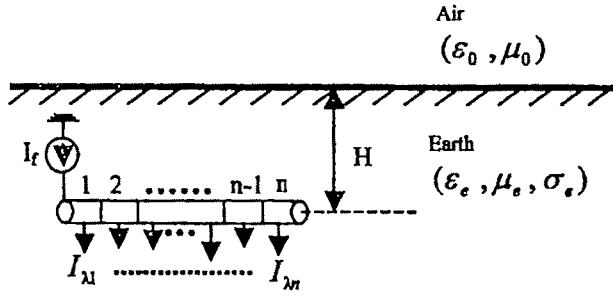


Fig.1. Grounding electrode buried in earth

In sequel, first two published procedures [15],[24] for computing the input impedance and the behavior of grounding electrode in the frequency domain are described for comparison with the proposed method.

A. The boundary element procedure based on RC [15]

This procedure is based on the antenna theory model for the horizontal grounding electrode. In the model, instead of evaluation of Sommerfeld integrals in the Green function (described in section 2.3) for the influence of the two media configuration (earth/air half space), the reflection coefficient (RC) approximation has been used. First step in the modeling of grounding system in frequency domain is segmentation of the electrode and calculation of longitudinal current distribution in each segments. For evaluation of these currents, the following process must be carried out.

According to the horizontal grounding electrode presented in Fig.1 the electric field integral equation for a thin wire buried in a lossy medium is computed by the Pocklington integral equation as:

$$E_x^{inc} = -\frac{1}{j4\pi\omega\epsilon_0} \int_{-L/2}^{L/2} \left[\frac{\partial^2}{\partial x^2} + k_0^2 \right] \left[g_o(x, x') - R_{TM} g_i(x, x') \right] I(x') dx' \quad (1)$$

where E_x^{inc} is tangential component of the incident field, $I(x')$ is the unknown current distribution induced along the electrode axis, $g_o(x, x')$ and $g_i(x, x')$ are the source and image (according to image theory) Green functions for grounding electrode buried in the lossy media, respectively, and are defined by:

$$g_o(x, x') = \frac{e^{-k_2 R_1}}{R_1}, \quad g_i(x, x') = \frac{e^{-k_2 R_2}}{R_2} \quad (2)$$

In addition, k_2 is the propagation coefficient of the earth and R_1, R_2 are the distances from the source and image points to the observation point. The treatment of half space is considered by RC approximation through introducing:

$$R_{TM} = \frac{(1/n)\cos\theta - \sqrt{1/n - \sin^2\theta}}{(1/n)\cos\theta + \sqrt{1/n - \sin^2\theta}} \quad (3)$$

where θ and n are computed by:

$$\theta = \arccos \frac{|x - x'|}{2H}, \quad n = \frac{\epsilon_{eff}}{\epsilon_0}, \quad \epsilon_{eff} = \epsilon_e \epsilon_0 - j \frac{\sigma}{\omega} \quad (4)$$

According to [15], by extension of Eq. (1) for M segments and applying the boundary element scheme, a set of linear equations can be derived as:

$$\sum_{j=1}^M \sum_{i=1}^{N_n} [Z]_{ji} [I]_j = [0] \quad (5)$$

where $[Z]_{ji}$ is the matrix representation for the mutual effect (i.e. mutual impedance) between i th and j th segments and N_n is the total number of basis functions on n th wire.

Then with computing the current distribution along each segment by (5), the electric field and voltage in any point on the grounding electrode can be calculated and consequently the input impedance in frequency domain is computed.

B. Simple Formula for Frequency dependent impedance [24]

This method presents a simple formula based on the transmission line theory for computing the horizontal ground electrodes in high frequency. Corresponding formulas for the characteristic impedance (Z_c) and the propagation coefficient (γ) of the grounding electrode, depicted in Fig. 1, is given by:

$$Z_c = \frac{1}{\sigma_e \pi L} \left(\ln \left(\frac{2L}{\sqrt{2rH}} \right) - 1 \right) \sqrt{\frac{j\omega\sigma_e \mu_0 L^2}{2 \left(1 + \frac{j\omega\epsilon_e}{\sigma_e} \right)}} \quad (6)$$

$$\gamma = \sqrt{\frac{j\omega\mu_0 (\sigma_e + j\omega\epsilon_e)}{2}} \quad (7)$$

The grounding impedance of the electrode, Z , may be obtained by:

$$Z = Z_c \coth(\gamma L) \quad (8)$$

C. The proposed procedure

The proposed method is based on investigating the behavior of grounding electrode in the frequency domain through computing the distribution of dissipated leakage currents from grounding electrode to earth. Derivation of the relations and the whole procedure is described in the following steps:

1) The problem formulation

First, the grounding electrode is divided to n segments. To maintain high accuracy, the length of each segment should be less than one tenth of the minimum wavelength of the considered frequency spectrum.

Fig. 2 shows two segments of the grounding electrode. The normal electric field on the surface of each segment is the sum of \vec{E}_i that is the normal component of incident electric field intensity impressed by the high frequency current point source on the surface of segment and $\vec{E}_s (= \sum_{k=1}^n \vec{E}_{sk})$ is the normal scattered electric field intensity caused by the leakage currents of different segments.

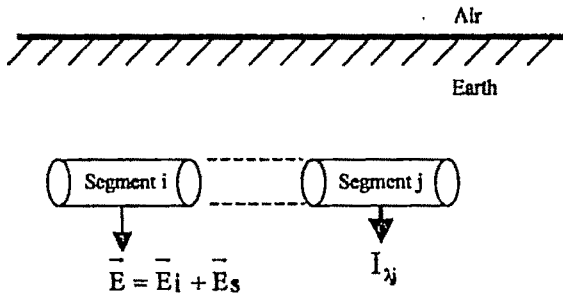


Fig.2. Segments of grounding electrode impressed by electric fields

Given the relations in Appendix I to find the electric field at any point, the potential (U) caused by the electric field (\vec{E}) at any observation point (z) can be written by:

$$U = - \int_{\infty}^z \vec{E} dz \quad (9)$$

For solving this problem, according to Fig.3, it is assumed that the point current source with known current value (I_f) is uniformly leaking current into earth. As is depicted, with assuming perfect conductor performance for the electrode, the induced voltage in each segment is obtained by superimposing two components; the first one is due to the voltages induced by the leakage currents of different segments, named as V_j and is calculated as:

$$V_j = \sum_{k=1}^n V_{jk} = \sum_{k=1}^n Z_{jk} I_{jk} \quad j=1, 2, \dots, n \quad (10)$$

while Z_{jj} is the self-impedance of the j -th segment which is the ratio of the voltage induced on the j -th segment due to the leakage current I_{jj} , and Z_{jk} is the mutual impedance between the j -th and k -th segments which is the ratio of voltage induced on the j -th segment due to the leakage current I_{kk} . The second

component of the voltage, named as V_g (that is equal to V_j), is the voltage induced on the i th segment due to the point current source and is calculated by (18).

Therefore, the basic relation for voltages of different segments can be shown, in matrix form, as:

$$[Z][I_{\lambda}] = [V_g] \quad (11)$$

where the $[Z]$ matrix contains self-impedance of each segments and mutual impedances between segments. The column matrix I_{λ} represents the unknown leakage currents and V_g is the vector containing the second component of the induced voltages on the segments.

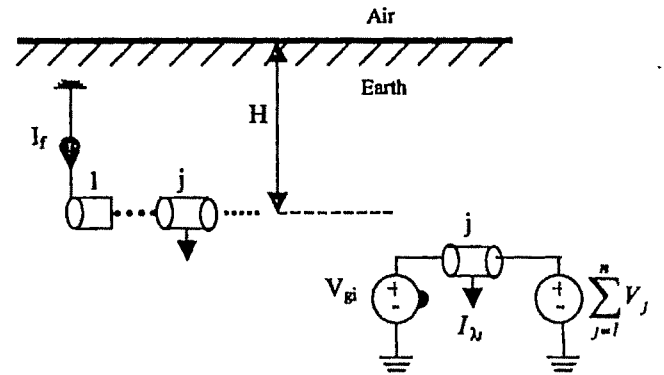


Fig.3. Representation of induced voltage on j th segment

2) The voltage computation at any point

When a buried electrode injects a leakage current in the lossy medium, at any point in its proximity, the leakage current density \vec{J}_{λ} is given, by Ampere-Maxwell law, through the following equation:

$$\vec{J}_{\lambda} = \sigma_e \vec{E}_s + \epsilon_e \frac{\partial \vec{E}_s}{\partial t} \quad (12)$$

where \vec{E}_s is the normal time variable scattered electric field intensity. In the frequency domain (ω is angular frequency), (12) can be written as:

$$\vec{E}_s = \frac{I}{\sigma_e + j\omega\epsilon_e} \vec{J}_{\lambda} \quad (13)$$

In addition, the Faraday-Maxwell law defines the scattered electric field \vec{E}_s at any point by:

$$\vec{E}_s = -j\omega\vec{A} - \nabla\vec{V} \quad (14)$$

where \vec{A} is the vector magnetic potential caused by the leakage

current and V is the scalar electric potential caused by the leakage currents. In (14), the magnetic vector potential, A , can be substituted by:

$$\vec{A} = \mu_e J_\lambda(v) \quad (15)$$

where $J_\lambda(v)$ is the volume density of leakage current as defined by Eq. I.1. By using (13), (14) and (15), the voltage at any point, with the distance r , (in the air or earth) can be expressed as the following (refer to Appendix I):

$$V(r, \omega) = \frac{1}{4\pi} \left(\frac{1}{\sigma_e + j\omega\epsilon_e} + j\omega\mu_e \right) \int_{\lambda} J_\lambda(\lambda) G(r) d\lambda \quad (16)$$

where $G(r)$ is the Green function for half-space conducting medium that is described later.

3) Computation of $[Z]$ matrix

The elements of $[Z]$ matrix are calculated through computing the following relation:

$$Z_{ij}(j\omega) = \frac{V_i}{I_j} = \frac{1}{4\pi} \left(\frac{1}{\sigma_e + j\omega\epsilon_e} + j\omega\mu_e \right) \int_{\lambda_i} J_\lambda(L) \left[\int_{\lambda_j} J_\lambda(\lambda) G(r_{ij}) d\lambda \right] dL \quad (17)$$

For the diagonal elements or the self-impedances, r_{ij} equals to the radius of the conductor.

4) Computation of $[v_g]$ matrix

According to (16) and assuming constant leakage current density, the induced voltage V_{gi} at any point on the surface of the i th segment is computed by:

$$V_{gi}(r_i, j\omega) = \frac{1}{4\pi} \left(\frac{1}{\sigma_e + j\omega\epsilon_e} + j\omega\mu_e \right) \times I_f(j\omega) \times G(r_i) \quad (18)$$

where r_i is the distance of i -th segment from the current source and $I_f(j\omega)$ is the source current representation in frequency domain.

5) The modified method for $G(r)$ computation

As is mentioned, analysis of grounding system in high frequency domain by electromagnetic field theory, in proximity of the interface of two medium, is concerned with calculation of S.I.s. Since the analytical solution of these infinite integrals is very rigorous and rather time-consuming, much attention has been focused to develop numerical and approximate solutions for them. In this section, a rapid and simple formula for the computation of this Green function with existence of air/earth interface is developed.

The proposed formula is based on a modification on the relations presented in [27], which are given in Appendix II. According to Fig II.1, since the grounding electrode is buried into the earth, the source and its image positions are interchanged as shown in Fig. 4.

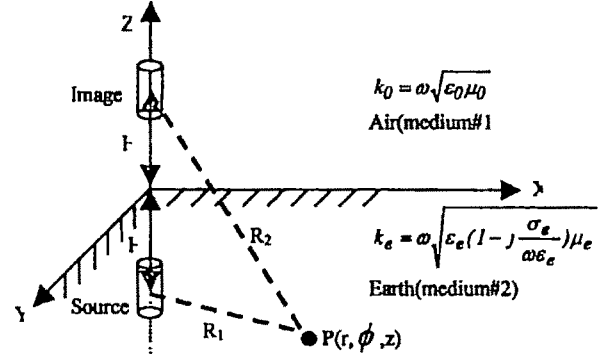


Fig.4. Vertical dipole above the ground

In this case, the Green function in accordance to the image theory is introduced:

$$G(P_m) = \frac{e^{-k_e R_1}}{R_1} + \frac{e^{-k_e R_2}}{R_2} + \Delta G_e \quad (19)$$

where:

$$R_1 = \sqrt{r^2 + (z - H)^2}, R_2 = \sqrt{r^2 + (z + H)^2} \quad (20)$$

In addition, the correction term due to existence of air/earth medium interface, ΔG_e is computed through the S.I as following [31]:

$$\Delta G_e = \int_0^\infty \frac{2k_0^2 \lambda}{k_0^2 \sqrt{\lambda^2 - k_0^2} + k_e^2 \sqrt{\lambda^2 - k_e^2}} J_0(\lambda r) e^{-k_e(z+H)} \frac{\lambda d\lambda}{j\sqrt{\lambda^2 - k_e^2}} \quad (21)$$

Instead of solving this integral, which its integrand contains Bessel function and has some singular points, the modified reflection coefficient, given in (22), is proposed that considers the effect of the air/earth interface, as well. The proposed coefficient is found through converting (n) to $(1/n)$ in (II.2), because the source is put in the earth medium. Then for extracting (19) from (II.1), ΔG_e is presented as:

$$\Delta G_e = \frac{-2\sqrt{1/n^2 - \sin^2 \theta}}{(1/n^2) \cos \theta + \sqrt{1/n^2 - \sin^2 \theta}} \frac{e^{-k_e R_2}}{R_2} \quad (22)$$

where:

$$n = \frac{k_e}{k_0} = \sqrt{\frac{\epsilon_e}{\epsilon_0} - \frac{j\sigma_e}{\omega\epsilon_0}}, \quad \tan \theta = \frac{\sqrt{R_2^2 - (2H)^2}}{2H} \quad (23)$$

III. COMPARISON BETWEEN THE RESULTS WITH OTHER METHODS

To evaluate the results achieved by the proposed method in this paper, it is compared with two approximate models [15] and [24].

It is assumed that a horizontal electrode, with length $L=1m$, radius $r=5mm$, has been buried in the depth $H=1m$, where $\sigma_e=0.01$ or $0.001s/m$, $\epsilon_e=8.85 \times 10^{-11}$ and $\mu_e=4\pi \times 10^{-7}$. In addition, a double exponential current pulse source that equals to $I_f=1.1043 \times (e^{-0.07924 \times 10^6 t} - e^{-4.0011 \times 10^6 t})$, is injected to the left end of this electrode.

The frequency variations of the input impedance for the mentioned horizontal grounding electrode are shown in Figs. 5 and 6, which represents the comparison among the results of the proposed method and the mentioned references. As is shown, in lower frequencies (less than 13MHz) the results obtained with the methodology presented in this paper are in agreement with the others. But the results have a considerable differences in upper frequencies. These differences are due to that in the presented method, the modified coefficient has been found directly from the full set of Maxwell's equations.

Also, by applying the proposed formula, the input impedance spectrum of grounding electrode with various earth conductivity is shown in Fig. 7. It can be seen that in low frequencies the magnitude of input impedance decreases with the increase of σ_e , while in higher frequencies no such relation exists.

IV. CONCLUSION

In this paper, a novel, accurate and simple approach based on EMF theory to analyze the high frequency behavior of the grounding system, is presented. This numerical procedure computes the leakage currents injected in the earth by each segments of grounding electrode with the method of moments (MOM).

The proposed modified formula for computing Green function is a closed-form formula that is substituted for the rigorous solutions of S.Is in order to consider the influence of half-space configuration (air/earth), and is valid for a wide range of frequency and parameters.

Finally, the frequency spectrum of input impedance for the grounding electrode is obtained and compared with some of the published approximation procedures, where shows the agreement in low frequencies and the deficiencies through those procedures in high frequencies.

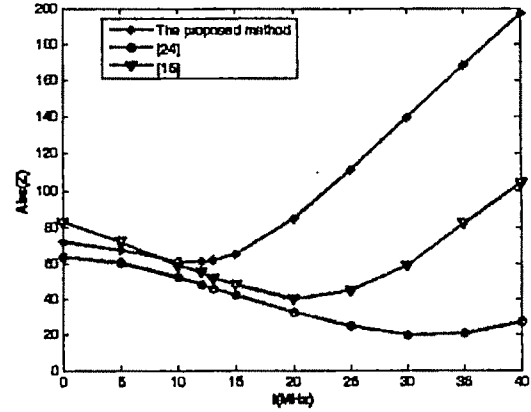


Fig.5. Input impedance of grounding electrode ($\sigma_e = 0.01 s/m$)

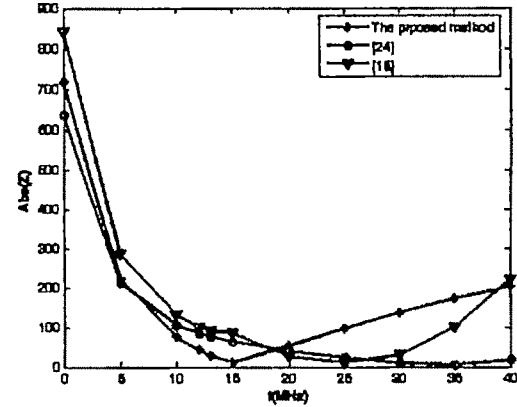


Fig. 6. Input impedance of grounding electrode ($\sigma_e = 0.001 s/m$)

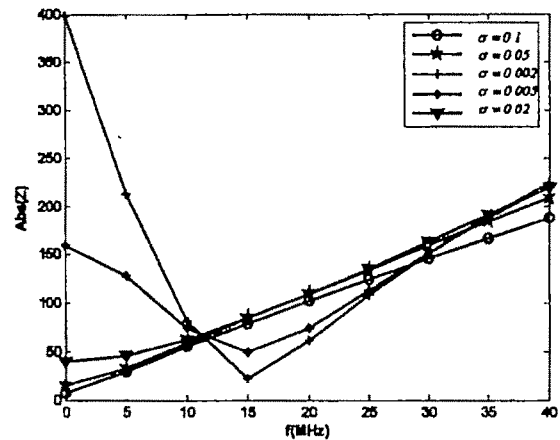


Fig. 7. Input impedance of grounding electrode with various earth conductivity

APPENDIX I

With assuming that the point source drains the leakage current, I , into soil, the volume leakage current density, \vec{J} , is computed with image theory by:

$$\vec{J} = \frac{I}{4\pi} \left(\frac{1}{r^2} \vec{r} + \frac{1}{r'^2} \vec{r}' \right) \quad (I.1)$$

where r, r' are distance between point source and its image from observation point:

The scattered field is obtained by using (I.1) and (13) as the following:

$$E_s(r, j\omega) = \frac{I}{4\pi(\sigma_e + j\omega\epsilon_e)} \left(\frac{1}{r^2} \vec{r} + \frac{1}{r'^2} \vec{r}' \right) \quad (I.2)$$

Also, according to (15) for a point source, the vector potential in any point can be calculated by:

$$\vec{A}(r) = \frac{\mu_e I}{4\pi} \left(\frac{1}{r^2} \vec{r} + \frac{1}{r'^2} \vec{r}' \right) \quad (I.3)$$

Then, the induced voltage in any observation point, P, at space is calculated by (14) as the following relation:

$$\nabla V = -(E_s + j\omega A) \quad (I.4)$$

Therefore, for a point source can be written:

$$V_P(r, j\omega) = \int_r^\infty E_s(r, j\omega) + j\omega \int_r^\infty A(r) dr = \frac{I}{4\pi} \left(\frac{1}{\sigma_e + j\omega\epsilon_e} + j\omega\mu_e \right) \left(\frac{1}{r} + \frac{1}{r'} \right) \quad (I.5)$$

As is shown in Fig. (I.1), whereas a linear grounding conductor contains a numerous of above point source (k), by superposing law and image theory, the induced voltage in P is obtained by:

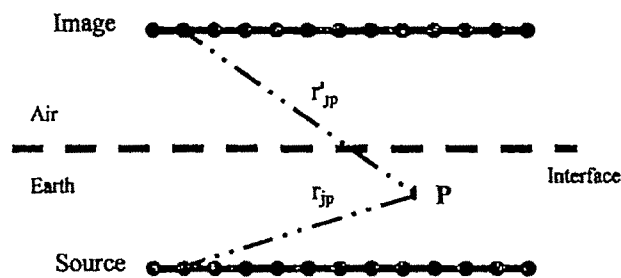


Fig I.1. A linear grounding conductor

$$V_P(r, j\omega) = \frac{I}{4\pi} \left(\frac{1}{\sigma_e + j\omega\epsilon_e} + j\omega\mu_e \right) \sum_{j=1}^k \left(\frac{I_j}{r_{jp}} + \frac{I'_j}{r'_{jp}} \right) \quad (I.6)$$

Assuming that the leakage current into soil is equal on the surface of a conductor segment with length of L, and also any

point source is a segment with length of Δx , so:

$$\frac{I_j}{\Delta x} = \frac{I}{L} = J_\lambda \quad (I.7)$$

Then Eq. (I.6) can be substituted by:

$$V_P(r, j\omega) = \frac{I}{4\pi} \left(\frac{1}{\sigma_e + j\omega\epsilon_e} + j\omega\mu_e \right) \int_0^L J_\lambda \left(\frac{1}{r_{jp}} + \frac{1}{r'_{jp}} \right) dx \quad (I.8)$$

In high frequency analysis, the (I.8) relation can be replaced by:

$$V_P(r, j\omega) = \frac{I}{4\pi} \left(\frac{1}{\sigma_e + j\omega\epsilon_e} + j\omega\mu_e \right) \int_{\lambda} J_\lambda(\lambda) G(r) d\lambda \quad (I.9)$$

where $G(r)$ is the Green function.

APPENDIX II

As shown in Fig.II.1, the [27] proposed the Green function computation when a vertical dipole is located over the lossy half-space as the following:

$$G(r) = \frac{e^{-jk_0 R_1}}{R_1} + R(\theta) \frac{e^{-jk_0 R_2}}{R_2} \quad (II.1)$$

where the reflection coefficient is obtained by:

$$R(\theta) = \frac{n^2 \cos \theta - \sqrt{n^2 - \sin^2 \theta}}{n^2 \cos \theta + \sqrt{n^2 - \sin^2 \theta}} \quad (II.2)$$

while:

$$n = \frac{k_e}{k_0} = \sqrt{\frac{\epsilon_e}{\epsilon_0} - \frac{j\sigma_e}{\omega\epsilon_0}} \quad (II.3)$$

and

$$\tan \theta = \frac{\sqrt{R_2^2 - (2H)^2}}{2H} \quad (II.4)$$

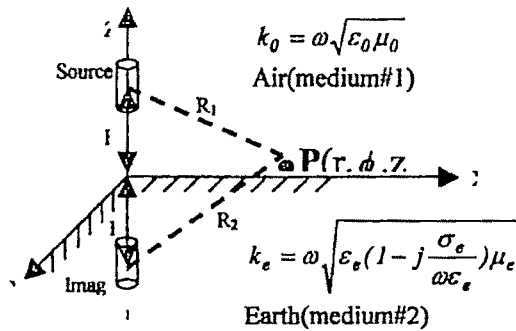


Fig. II.1. Vertical dipole above the ground

REFERENCES

- [1]. A.P.Meliopoulos, M.G.Moharam, "Transient Analysis of Grounding Systems", IEEE Trans. On Power Apparatus and Systems, vol. PAS-102, no.2, February 1983, pp. 389-399
- [2]. M.Ramamoorthy, and etal, "Transient Performance of Grounding Grids", IEEE Trans. On Power Delivery, vol. 4, Oct. 1989, pp.2053 - 2059
- [3]. A. Geri, and etal, "Non-linear Behavior of Ground Electrodes Under Lightning Surge Currents: Computer Modeling and Comparison with Experimental Results", IEEE Trans. On Magnetics, vol. 28, March 1992, pp.1442 - 1445
- [4]. A. Geri, "Behavior of Ground Systems Excited by High Impulse Currents: The Model and its Validation", IEEE Trans. Power Delivery, vol.14, no.3, July 1999, pp.1008-1017
- [5]. A.F.Otero, and etal, "Frequency- Dependence Grounding System Calculation by Means of a Conventional Nodal Analysis Technique", IEEE Trans. On Power Delivery, vol.14, no. 3, July 1999, pp.873-878.
- [6]. Jose Cidras, and etal, "Nodal Frequency Analysis of Grounding Systems Considering the Soil Ionization Effect", IEEE Trans. On Power Delivery, vol 5, no.1, Jan 2000, pp.103-107.
- [7]. L.Greev, F.Dawalibi, "An Electromagnetic Model for Transients in Grounding Systems", IEEE Trans. On Power Delivery, vol. 5, Oct. 1990, pp. 1773 - 1781
- [8]. W.Xiong, and etal, "Transient Performance of Substation Grounding Systems Subjected to Lightning and Similar Surge Currents", IEEE Trans. On Power Delivery, vol. 9, July 1994, pp.1412 - 1420
- [9]. B.Nekhoui, and etal, "Calculating the Impedance of a Grounding System", IEEE Trans. on Magnetics, vol.32, no 3, May 1996, pp.1509-1512.
- [10]. R.G.Olsen, and etal, "A Comparison of Exact and Quasi-static Methods for Evaluating Grounding Systems at High Frequencies", IEEE Trans. On Power Delivery, vol.11, April 1996, pp.1071 - 1081.
- [11]. L. Greev, M. Heimbach, "Frequency Dependent and Transient Characteristics of Substation Grounding Systems", IEEE Trans. On Power Delivery, vol. 12, Jan. 1997, PP.172 - 178.
- [12]. I.F. Gonos, et al, "Behavior of A Grounding System Under Impulse Lightning Current", Proceedings of the 6th International Conference on Optimization of Electrical and Electronic Equipment (OPTIM '98) , vol. 1, May 1998, pp. 171 - 174.
- [13]. L.Greev, "Modeling of Grounding Systems for Better Protection of Communication Installations Against Effects from Electric Power System and Lightning", Twenty-Third International Telecommunications Energy Conference (INTELEC 2001), Oct. 2001, pp. 461 - 468.
- [14]. L.Greev, and etal, "Grounding Systems Modeling for High Frequencies and Transient: some Fundamental Considerations", IEEE Proceedings of Power Tech Conference, vol. 3, June 2003, pp.1020-1026.
- [15]. V.Doric, et al, "Transient Analysis of the Grounding Electrode Based on the Wire Antenna Theory", Engineering Analysis with Boundary Elements, Elsevier, 2004, pp. 801-807.
- [16]. L. Greev, "Calculation of the Transient Impedance of Grounding Systems", DSc Thesis, University of Zagreb (Croatian), 1986.
- [17]. Vesna A.Toseva, L.Greev, "Electromagnetic Analysis of Horizontal Wire in Two- Layered Soil", Elsevier, 2004, pp.21-29
- [18]. C.Portela, "Frequency and Transient Behavior of Grounding Systems, I. Physical and Methodological Aspects", IEEE 1997 International Symposium on Electromagnetic Compatibility, Aug. 1997, pp.379 - 384.
- [19]. M.Heimbach, L. Greev, "Grounding System Analysis in Transients Programs Applying Electromagnetic Field Approach", IEEE Trans. On Power Delivery, vol. 12, no.1, Jan 1997, pp.186-193.
- [20]. Roberto Andolfatal, and etal, "Aerial and Grounding Systems Analysis by the Shifting Complex Images Method", IEEE Trans. On Power Delivery, vol.15, no.3, July 2000, pp.1001-1009.
- [21]. R.Verma, D.Mukhedkar, " Impulse Impedance of Buried Ground Wire", IEEE Trans. On Power Apparatus and Systems, vol. PAS-99, no. 5, Sept/Oct 1980, pp.2003-2007.
- [22]. R.Velazquez, D.Mukhedkar, "Analytical Modeling of Grounding Electrodes Transient Behavior", IEEE Trans. On Power Apparatus and Systems, vol. PAS -103, no.6, June 1984, pp. 1314-1322.
- [23]. F.E. Menter, L.Grev, "EMTP-Based Model for Grounding System Analysis", IEEE Trans. On Power Delivery, vol. 9, Oct. 1994, pp.1838 - 1849.
- [24]. L. Greev, V. Arnaudovski, "Frequency Dependent and Transient Impedance of Grounding Systems: Comparison Between Simulation and Measurement", Proceeding of the Second International Symposium: Lightning and Mountains, Chamonix-Mont-Blanc, France, June 1997, pp.239-244.
- [25]. Yaqing Liu, and etal, "An Improved Transmission - Line Model of Grounding Systems", IEEE Trans. On Electromagnetic Compatibility, vol. 43, no. 3, August 2001, pp. 348-355.
- [26]. GAO Yanqing, and etal, "Impulse Transient Characteristic of Grounding Grid", 3rd International Symposium on Electromagnetic, May 2002, pp. 276-280.
- [27]. M.I. Lorentzou and etal, "Time Domain Analysis of Grounding Electrodes Impulse Response", IEEE Trans. On Power Delivery, vol. 18, April 2003, pp.517 - 524.
- [28]. Akira Ishimaru, "Electromagnetic Wave Propagation, Radiation, and Scattering", Prentice-Hall, Inc., A Division of Simon & Schuster Englewood Cliffs, N.J. 07632, 1991.
- [29]. Peter L. Tokarsky, Vladimir V.Dolzhikov, "Simple Approximate Formulas for Evaluating Sommerfeld Type Integrals", VIIth International Conference on Mathematical Methods in Electromagnetic Theory, 1998, pp 246-248.
- [30]. Raj Mitra, et al., "Solving the Current Element Problem over Lossy Half-space Without Sommerfeld Integrals", IEEE Trans. On Antennas and Propagation, vol. Ap-27, no. 6, November. 1979, pp 778-782.
- [31]. Technical Report, "The Transient Behavior of the Grounding Electrode", ENPSC-155, IUST, 2007.

An offline Simulation Study of Security Analysis of a Multibus Power System Using Load-Flow Based Technique

Sangita Das Biswas¹, Kabir Chakraborty², Tanima Bhattacharya³ and Bishakha Nandi⁴

¹ Department of Electrical Engineering, Tripura University, Tripura, India e-mail: sangitadasbiswas@rediffmail.com

² Department of Electrical Engineering, Tripura University, Tripura, India e-mail: kabir_jishu@rediffmail.com

³ Tripura University, Tripura, India e-mail: bhattacharyatanima@yahoo.co.in

⁴ Tripura University, Tripura, India.

Abstract— Power System stability deals with stable operation of a power system during various operating conditions. Power system security involves practices suitably designed to keep the system in operation when a line or a generator or any other equipment in the system fails. Contingency analysis being a major component of the security function in power system, there are standardized parameters to check system security. In this paper an offline method is presented for security assessment with load flow analysis to obtain the security indicators for power lines of a multi bus power network. Generator loss as well as line trip has been simulated and multiple separate contingencies have been investigated in order to check the security of the assumed systems. Static security analysis has been conducted using two very popular security indicators e.g. the line outage factor (LOF) and voltage security factor (VSF). It has been observed that in any multi bus power system it is possible to check these two indicators following any contingency and subsequently it is possible to rank the lines accordingly as per their security level.

Key words— Contingency, Line outage factor, Security analysis, Stability, Voltage security factor.

I. INTRODUCTION

STABILITY is an important constraint in power system operation. Most system stability problems occur in response to large disturbances under heavy load conditions [1]. One of the major problems associated with such a stressed system is system blackout or system collapse. There are many incidents of system blackout, reported [2]. The term system security means the ability of a system not only to operate stably but also to remain stable following credible contingencies or adverse system changes [2]. If the system is unstable, the system must be insecure [3].

Analysis of the security of power system deals with quasi-static approach and in present day technology this is the only practical approach and computationally feasible.

An important part of security study is that a particular system state is said to be secure only with reference to one or more specific contingencies cases, and a given set of quantities

monitored for violation. Most power systems are operated in such a way that any single contingency will not leave other components heavily over loaded, so that cascading failures are avoided [4]. In scientific literatures, there is strong evidence of investigation of power system security since 80's of the last century [5-19]. Most of these research publications are related with direct investigation in to the security aspect of the power system. In some of these publications attempts have been made secured indicators.

II. LOAD-FLOW PROBLEM

Load-flow solutions are basic tools in most kind of power system analysis studies. In order to ensure the convergence and simplify computation, all buses are classified as PV bus, PQ bus and Slack bus. Load flow techniques provide basic calculation procedure in order to determine the characteristics of power system under steady state operating mode. The effects of uncertainties on the steady-state behavior of power systems can be evaluated by a stochastic or probabilistic load flow (PLF) analysis. Load-flow is an essential tool for the study of radial distribution systems (RDS). The inputs to load-flow solutions are subject to uncertainties due to load and line parameter variations. Usually these techniques are off-line and involve computers for solving steady state load flow equations (SLFE). For SLFE solution, all the state and control variables must lie within specified practical limits, which are dictated by specifications of power system hardware and operating constraints [19].

The load-flow problem is formulated assuming the power system network to be linear, bilateral and balanced and having lumped parameters. However, the power and voltage constraints impose non-linearity in the load-flow formulation and this invites the help of iterative techniques for solution. Load-flow solution techniques solve a set of simultaneous non linear algebraic equations involving trigonometric functions. There are two unknown variables at each node in a system. The iteration cycle is terminated when the bus voltages and angles are such that the specified condition of load and generation are satisfied. Load-flow calculations

usually employ iterative techniques such as Gauss-Seidel, Newton-Raphson and Fast-Decoupled Load Flow (FDLF) methods [20].

III. SECURITY ANALYSIS AND CONTINGENCY EVALUATION

Under normal operating conditions a power system may face the contingencies of: 1. Loss of generating unit, 2. Sudden loss of a load, 3. Sudden change in flow in an intertie, 4. Outage of a transmission line, 5. Outage of a transformer, 6. Outage of a shunt capacitor or reactor, and 7. Single phase or three-phase fault. The outage may be either network outage or power outage. Contingency would reduce the security level. The contingencies in the distribution or sub-transmission levels may also lead the system to another state with lesser security. A system operator has to analyse the effect of such highly probable contingencies so that the operator may take corrective action in the event of their occurrence. The security assessment and its enhancement form an important part of planning and operation of power systems that are continuously expanding. Complete system security involves system prediction, system contingency evaluation, system corrective strategy and automatic control.

IV. CONTINGENCY SELECTION

We would like to get some measure as to how much a particular outage might affect the power system. The idea of a performance index seems to fulfill this need. The definition for the overload performance index (PI) is as follows:

$$PI = \sum_{\text{all branches}} (P_{\text{flow } l} / P^{\text{max}})^{2n}$$

If n is a large number, the PI will be a small if all flows are within limit, and it will be large if one or more lines are overloaded. To complete the security analysis, the PI list is sorted so that the largest PI appears at the top. The security analysis can then start by executing full power flows with the case which is at the top of the list, then solve the case which is second, and so on down the list. This continues until either a fixed number of cases are solved, or until a predetermined number of cases are solved which do not have any alarms.

V. SIMULATION AND RESULT

An offline study has been done for security analysis as well as contingency analysis. Load-flow analysis has been used to obtain the security indicators, Line Outage Factor (LOF) and Voltage Security Factor (VSF), for power lines in a multi bus power network. The power network, which has been used for the analysis, is shown in appendix. The analysis is done by tripping generators and lines. Here generator 3, generator 4, line 1 and line 4 are removed and corresponding LOF and VSF are recorded to check the security of the lines. Results are

shown accordingly in table-I, table-II and table-III.

Table-I

Line No.	Gen.3 removed		Gen. 4 removed	
	Active power	Reactive Power	Active power	Reactive Power
	LOF	LOF	LOF	LOF
1	1.286466	-0.09236	0.99976	0.99957
2	0.4542	-0.287814	1	0.99972
3	0.98059	0.31808	0.99997	0.99966
4	1.0187	0.4116	1.00006	0.99985
5	1.02019	2.42579	1	1.2312
6	0.806944	0.382919	0.99978	0.99976
7	0.372435	0.36915	0.998974	0.99958
8	1.301939	2.16	1	1
43	1.05091	1.0332	0.99924	1
44	1.03769	1.03749	1	1

The order of security level of different lines while active power is concerned for the removal of Generator 3 is given by $L8 < L1 < L43 < L44 < L5 < L4 < L3 < L6 < L2 < L7$. Here Line 8 is least secure and Line 7 is most secure. The security level of Line 1 is slightly better than Line 8. Here Line 8 is most contingent and Line 7 is least contingent. The rank of line 8 is at the bottom position and Line 7 at the top.

The order of security level of different lines while active power is concerned for the removal of Generator 4 is given by $L4 < L2, L5, L44, L8 < L3 < L6 < L1 < L43 < L7$. Here Line 4 is least secure. But the security level according to recorded data of Line 2, Line 5, Line 8 and Line 44 are same. Moreover Line 7 is most secure. Here Line 7 is least contingent. The rank of Line 7 is at the top level.

The effect of removal of generator 3 is most severe for line 8 than the removal of generator 4. But line 2 is much more secure for the removal of generator 3 than the removal of generator 4. The security level of line 7 remains same irrespective of the removal of generator 3 and generator 4.

Security level when reactive power is considered for the removal of Generator 3 is given by

$L5 < L8 < L44 < L43 < L4 < L6 < L7 < L3 < L1 < L2$. Here line 5 is least secure and line 2 is most secure.

Security level when reactive power is considered for the removal of Generator 4 is given by

$L5 < L44, L43, L8 < L4 < L6 < L2 < L7 < L3 < L1$.

Here also the security level of line 8, line 43 & line 44 are same. So line 5 is least secure and line 1 is most secure.

Table-II

Line No.	Line 1 removed		Line No.	Line 4 removed	
	Active power	Reactive Power		Active power	Reactive Power
	LOF	LOF		LOF	LOF
2	1.1560	-0.5387	1	0.7562	0.2800
3	1.0445	1.4431	2	1.444	0.5302
4	0.9119	1.3937	3	1.3957	-0.3423
5	0.9233	0.18304	5	0.0245	2.03
6	1.35	1.37522	6	0.1985	0.6338
7	3.3799	-0.4525	7	1.2633	-0.6924
8	0.7368	0.82	8	0.1052	4.15
43	1.03875	1.0253	43	0.5227	0.6337
44	1.02944	1.0284	44	0.6077	0.6069

While active power is considered, the order of security level of the remaining lines after the removal of line 1 is,
 $L7 < L6 < L2 < L3 < L43 < L44 < L5 < L4 < L8$.

When reactive power is concerned, the order of security level is,

$$L3 < L4 < L6 < L44 < L43 < L8 < L5 < L7 < L2.$$

Line 8 is most secure and Line 7 is least secure when active power is considered. Line 2 is most secure and Line 3 is least secure when reactive power is considered. While active power is concerned Line 8 is least contingent and Line 7 is most contingent. Line 2 is least contingent and Line 3 is most contingent when reactive power is considered.

While line 4 is removed, the order of security level of active power and reactive power flows are,

$$L2 < L3 < L7 < L6 < L1 < L44 < L43 < L5 < L8$$

for active power.

$$L8 < L5 < L6 < L43 < L44 < L2 < L1 < L3 < L7$$

for reactive power.

Line 5 is most secure and Line 2 is least secure when active power is considered. Line 7 is most secure and Line 8 is least secure when active power is considered. Line 5 is least contingent and Line 2 is most contingent when active power is considered. Line 7 is least contingent and Line 8 is most contingent when reactive power is considered. Again the security level of line 2 is poor for the removal of line 1 and line 4 while active power is concerned.

While considering the reactive power, the security level of line 7 is good for the removal of any one of the lines. Line 8 is most secure for the removal of line 1 & 4 while active power is concerned. The security level of line 6 is deteriorating for the removal of line 1 and line 4 respectively while active power flow is concerned.

Table-III

Bus No.	VSF				
	Gen 3 removed	Gen 4 removed	Gen 5 removed	Line 1 removed	Line 4 removed
1	1	1	1	1	1
2	0.9926	1	1.0002	0.9925	1.001
3	0.9804	1	1	1	1
4	0.9980	1	0.9988	0.9991	0.9638
5	0.9970	1	0.9985	0.9975	1.0361
6	0.9967	1	0.9987	0.9966	1.015
7	0.9973	1	0.9954	0.9965	1.0168
10	0.9973	1	0.9944	0.9980	1.029
11	0.9973	1	0.9954	0.9965	1.0168
12	1	1	0.9127	1	1

The order of voltage security level of the buses, when generator 3 is removed, is as follows –

Bus3 < Bus2 < Bus6 < Bus5 < Bus7, Bus10, Bus11 < Bus4 < Bus1, Bus12. Here Bus 3 is the least secure.

If case I and case II are compared then it can be concluded that Bus 3 is comparatively less voltage secure for the removal of generator 3 than the removal of generator 4 but it becomes more contingent for the removal of generator 3.

The orders of voltage security level of the buses, when generator 5 is removed, are as follows –

Bus12 < Bus10 < Bus7, Bus11 < Bus5 < Bus6 < Bus4 < Bus1, Bus3 < Bus2. Here Bus 12 is less secure than the others.

The orders of voltage security level of the buses, when line 1 is removed, are as follows –

Bus2 < Bus7, Bus11 < Bus6 < Bus5 < Bus10 < Bus4 < Bus1, Bus3, Bus12.

Here Bus 2 is less voltage secure than the other buses & Bus 1, Bus 3 & Bus 12 are most voltage securing.

The order of voltage security level of the buses, when line 4 is removed, is as follows –

Bus4 < Bus1, Bus3, Bus12 < Bus2 < Bus6 < Bus7, Bus11 < Bus10 < Bus5

Bus 4 is least voltage secure & Bus 5 is most voltage secure.

If case IV and case V are compared then it can be concluded that Bus 2 is comparatively less voltage secure for the removal of line 1 than the removal of line 4 but it becomes more contingent for the removal of line 1.

VI. CONCLUSION

The objectives of system stability are to monitor and ultimately control the stability during power system operation. Continuity of service in case of contingency affecting the system can only be guaranteed if certain conditions are fulfilled in terms of system structure on the one hand and in terms of organizations of the system on the other. In this paper we have presented an offline simulation study for security analysis of a multi bus power network. Power system stability

as well as security analysis can be precisely and automatically estimated. Security and contingency analysis can be done by finding LOF and VSF, the two commonly used stability indicators. The LOF and VSF can be found for each and every line. The results of this type of analysis allow systems to be operated defensively. So in any power system when instability occurs for the failure of generators or lines or any other

equipment, immediate action can be taken by analyzing system security.

APPENDIX

The power network used by us for the preparation of this paper is given below in Fig. 1.

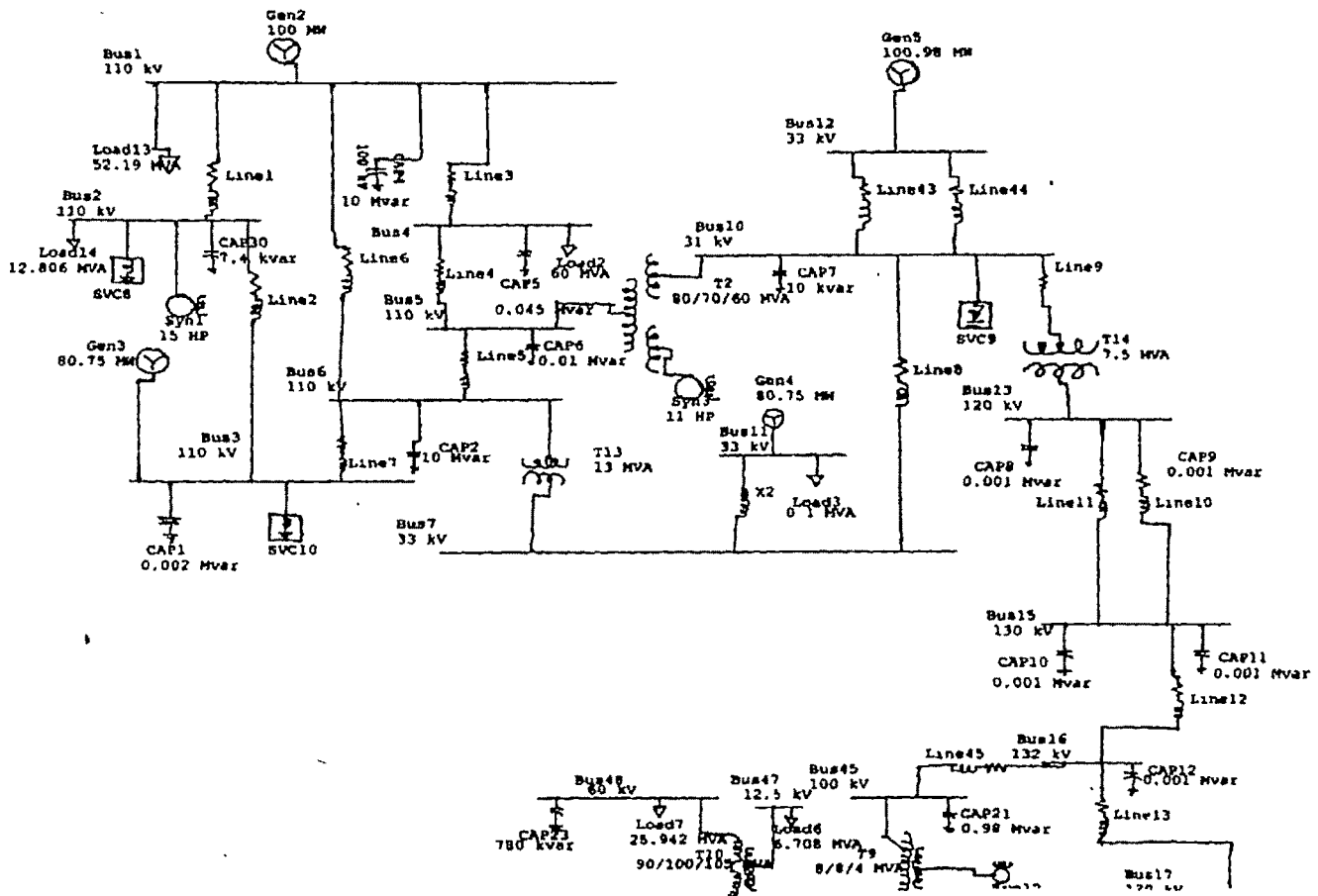


FIG. 1: POWER NETWORK

ACKNOWLEDGMENT

We would like to thank Prof. Abhijit Chakraborti, BESU, WB, for his valuable guidance during the preparation of this paper.

REFERENCES

- [1] S.K.Starrett, W.R. Anis Ibrahim, B.P. Rust, "Wide-Area Fuzzy Logic control of voltage/ Var under simulated on line conditions, Power eng Lett , IEEE Power Eng. Rev., 20(3) March 2000 pp. 45-47.
- [2] IEEE Committee Report, "Voltage Stability of Power Systems.concepts,analytical tools and industrial experiences," IEEE publication No. 90TH10358-2-PWR, New York, 1990.
- [3] Y.Y Hong, Y.L. Yang, "Expert System for enhancing voltage security/stability in power systems, IEE Proc. Gener Transm. Distrib 146(4) (1999) pp 349-354.
- [4] D P Kothari, and L.J.Nagrath, Modern Power System Analysis, Tata McGraw-Hill, New Delhi, 2006.
- [5] B Stott, O.Alsac and A J.Monticelly, "Security Analysis and Optimization", Proc IEEE, Vol 75,NO.12, Dec.1987, pp 1623-1644
- [6] A.A Fouad, "Dynamic Security Assessment Practices in North America", IEEE Trans. On Power Systems, Vol 3, No. 3, 1988, pp 1310- 1321.
- [7] G.C. Ejebe, et al, "Fast Contingency Screening and Evaluation for Voltage Security Analysis", Trans On Power Systems, Vol 3, No. 4, Nov.1988, pp 1582-1590.
- [8] Special issue of Proc. IEEE, February 2000
- [9] P. R. Bijwe, S.M. Kelapure, D.P. Kothari, K K. Saxena, "Oscillatory Stability Limit Enhancement by Adaptive control Rescheduling", Int. J. of Electric Power and Energy Systems, Vol 21, No 7, 1999. pp 507-514

- [10] L.D. Arya, S.C. Chaube and D.P. Kothari, "Line Switching for Alleviating Overloads under Line outage Condition Taking Bus Voltage Limits into account", Int J. of EPES, Vol. 22, No. 3, 2000, pp 213-221.
- [11] P. R. Bijwe, D.P. Kothari, S. Kelapure, "An Effective Approach to Voltage Security and Enhancement", Int J of EPES, Vol. 22, No.7, 2000, pp 483-486
- [12] P.R Bijwe, D P Kothari and L D.Arya, "Over load ranking of line outages with post generation rescheduling", Int. J. of electrical machine and power systems, Vol. 22, No.5, 1994, pp 557-568.
- [13] L.D.Arya, D.P Kothari et al. 'Post Contingency Line Switching for Overload Alleviation or Rotation', Int J. of EMPS, Vol.23, No.3, 1995, pp 345-352.
- [14] P.Kundur, Power system stability and control, Section 2.12, 11.2 and chapter 14, McGraw-Hill, New York 1994.
- [15] A.Chakraborty, D.P.Kothari and A.K.Mukhopadhyay, Performance, Operation and control of EHV Power Transmission System, Wheeler Publishing, New Delhi, 1995.
- [16] A.J.Wood and W.F Wollenburg, Power Generation, Operation and Control, 2nd Edn, John Wiley, New York, 1996.
- [17] John J. Grainger and W.D Stevenson, Power System Analysis, McGraw-Hill, New York 1994 *Letter Symbols for Quantities*, ANSI Standard Y10.5-1968.
- [18] G.L.Kusic, Computr_Aided power System Analysis, Prentice-Hall, New Jersey, 1986.
- [19] I.J.Nagrath and D.P.Kothari, Power System Engineering, Tata McGraw-Hill, New York 1994.
- [20] Abhijit Chakraborti, Sunita Halder, "Power System Analysis Operation & Control", Prentice-Hall of India Private Limited, New Delhi, 2006

Voltage Sag and Unbalance Mitigation in Distribution Systems Using Multi-level UPQC

H. R. Toodeji¹, S. M. Ale Emran², N. Farokhnia³, H. Askarian, S.H. Fathi, G. B. Gharehpetian,

M. Abedi,

Electrical Engineering Department, Amirkabir University of Technology, Tehran, Iran

¹ harnadzeza_toodeji@yahoo.com

² alomran2000@gmail.com

³ naemr_TOM@yahoo.com

Abstract— In this paper, a UPQC (Unified Power Quality Conditioner) with cascaded Multilevel inverters with separated DC source is proposed. In addition, voltage sag, unbalance and load power factor in distribution system is mitigated using proposed multilevel UPQC. This method has some privilege in the elimination of transformer and filter. SPWM (Sinusoidal Natural Pulse Width Modulation) scheme is used for pulse generating to control multilevel inverters.

The results showed the effectiveness of the proposed method.

Key words—Custom Power, UPQC, Cascade Multilevel Inverter, Voltage sag, Unbalance, Distribution Grid

I. INTRODUCTION

INCREASINGLY development of nonlinear loads is deteriorating power quality in distribution systems, causing disturbance in operation of many sensitive loads which, all are very sensitive to the voltage sag, the 85% to 90% voltage sag which last 16ms may lead to the equipments to shut down. Nowadays, in the occident, the concern about voltage sag is far more than that of other power quality problems. Custom power devices, such as DVR (dynamic Voltage Restorer), DSTATCOM (Distribution Static Compensator), and UPQC (Unified Power Quality Conditioner) have been introduced in recent years for power quality improvement in electricity distribution.

Advances in manufacturing of power semiconductor devices have led to better characteristics such as higher voltage and current ratings as well as increased switching frequency. Besides, implementation of multilevel inverters has made high power and high voltage power quality conditioners much feasible. So far, multilevel inverters have been used for DSTATCOM and DVR as reported in some publications in recent years, but the report about the research and design of

cascade multilevel transformer-less topological UPQC project has not been seen on publication yet. The application of a multibridge converter for STATCOM was first proposed in [1] and [2], and the application of a multibridge converter for static synchronous series compensator (SSSC) and unified power-flow controller (UPFC) were described in [3]–[4]. Recently, a dynamic voltage restorer (DVR) with three H-bridge modules was proposed in [5]–[6].

In this paper, A UPQC employing cascaded H-bridge multilevel inverter is studied as a means to compensate voltage sag and unbalance and the simulation results are compared with those of a conventional UPQC. In order to minimize THD, phase shifted multi-carrier based strategy (SPWM) [7] is used to control the multi-level inverter. It is shown that by cascading a few number of H-bridge inverters, UPQC can be directly connected to the distribution grid without any step-down and a series injection transformer. The results show that using a multilevel UPQC provides a satisfactory performance in compensating voltage sag and unbalance with minimized THD, unity power factor and lower switching frequency, therefore lower switching losses in the main switches.

The operation of the proposed UPQC was verified through simulations with MATLAB/Simulink

II. MULTILEVEL INVERTER TOPOLOGIES

It is generally accepted that the performance of an inverter, with any switching strategies, can be related to the harmonic contents of its output voltage. Power electronics researchers have always studied many novel control techniques to reduce harmonics in such waveforms. Up-to-date, there are many techniques, which are applied to inverter topologies. In multilevel technology, there are several well-known topologies as follows: [7];

1. Diode clamped multilevel inverter (DCMI) [8].

2. Flying-capacitor multilevel inverter (FCMI) [9], [10], [11].
3. Cascaded multilevel inverter with separated DC sources [9], [12], [13]. (Fig. 1)

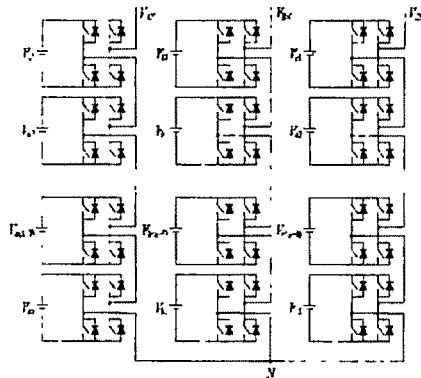


Fig 1 Three phase Cascaded multilevel inverter with separated DC sources

The last multilevel inverter shown in Fig. 1 has many advantages, such as: circuit layout flexibility, there are no extra clamping diodes or voltage balancing capacitor, the number of output voltage levels can be easily adjusted by adding or removing the full-bridge cells, and the least number of components in comparison with other inverters [9].

Due to the great demand for medium-voltage high-power inverters, the cascade inverter has drawn tremendous interest ever since. This configuration recently became very popular in AC power supply and adjustable speed drive applications. In back-to-back inverter applications, however, it is not possible to use multi-level inverter using cascaded-inverters with separate DC source, because a short circuit will be introduced when two back-to-back inverter are not switching synchronously. To overcome such a problem, a transformer having one primary winding and several secondary windings can be used. On the other hand, the structure of separated dc sources is well suited for various renewable energy sources such as fuel cell, photovoltaic, biomass, etc. This multi-level inverter is made of several full-bridge inverters. The AC output of each of the different levels of full-bridge inverters are connected in series such that the synthesized voltage waveform is sum of the inverter outputs. The distance between each level is the same, and equal to V_{dc} .

Each full-bridge inverter product a three level waveform $+V_{dc}, -V_{dc}, 0$; so the number of levels is: $N=2k+1$

Where k is the number of dc sources. However, all of above inverters can produce multi-level voltage or current as shown in Fig. 3.

A. Number of levels

The nominal distribution line to line voltage is 400 volts(rms), and the amplitude of the phase voltage will be:

$$V_{phase} = \frac{400 \times \sqrt{2}}{\sqrt{3}} = 326.6$$

It has been used three levels in the proposed configuration; thus the maximum voltage of switches can be nearly 110 volts, which is acceptable for common MOSFETs.

B. Switching Scheme

A so-called phase-shift sinusoidal pulse width modulation (PS-SPWM) switching scheme is proposed to operate the switches in the system. The scheme is briefly explained with the aid of Figures 2 and 3 obtained by simulation with MATLAB. Fig. 2 shows the typical pulse generated by one cell for the inverter shown in Fig. 1 by comparing a sinusoidal reference with a triangular carrier signal [14].

A number of K -cascaded cells in one phase with their carriers shifted by an angle $\theta_c = 360^\circ / K$ and using the same control voltage produce a load voltage with the smallest distortion as shown as in Fig. 4. The effect of this carrier phase-shifting technique can be clearly observed in Fig. 3. This result has been obtained for the multilevel inverter in a seven-level configuration. The smallest distortion is obtained when the carriers are shifted by an angle of $\theta_c = 360^\circ / 3 = 120^\circ$ [9].

Fig. 4 is frequency spectrum of multilevel SPWM. it shows that, low order harmonics have a negligible amplitude and only high order harmonics between 120-150 (6000 Hz, 7500 Hz) and 250-280 (7500 Hz, 14000 Hz) have rather significant amplitude, therefore in the applications which these harmonics have not any important effect, the filter could be eliminated.

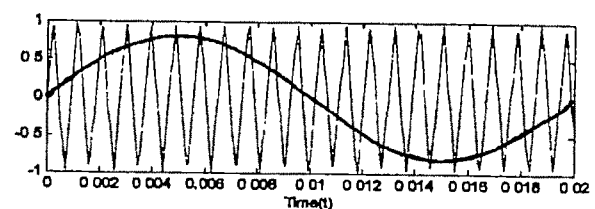
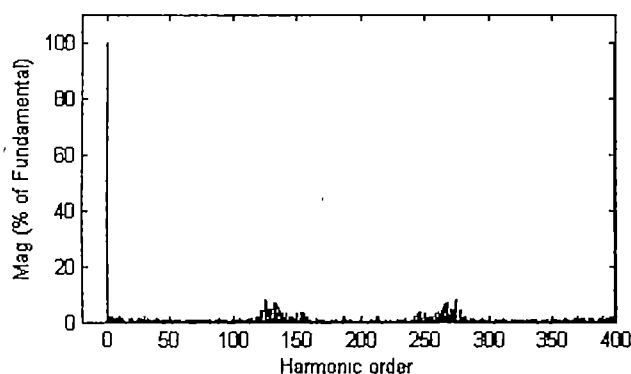
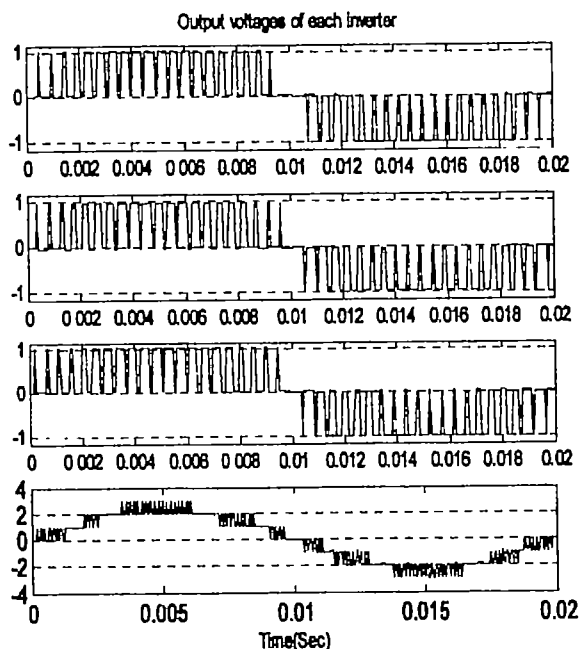


Fig. 2. Comparing carrier and reference voltages



III. MULTILEVEL UPQC

The unified power-quality conditioner (UPQC) has been widely studied by many researchers as an ultimate device to improve power quality. Several configurations were proposed for UPQC such as Fig. 5. This UPQC has two converters that share one dc-link capacitor. It has a bypass function to remove the series and shunt converter from service during the distribution system or load fault [15].

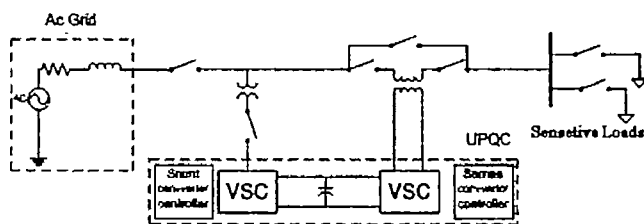
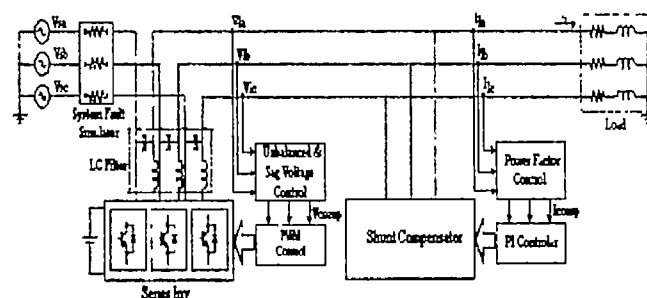


Fig. 6 shows a configuration of the proposed UPOC based on

several pairs of H-bridge modules for each phase. Each pair has two H-bridge modules. The H-bridge module in shunt part is connected in series without any transformer, and the H-bridge in series part also is directly connected in series and inserted in the distribution line.

Two converters have been used in the Multilevel UPQC: 1) Series Multilevel Inverter 2) Shunt Multilevel Inverter (Fig. 6)



The presently developed UPQC can operate in much lower dc-link voltage than the operation voltage of the distribution system. The restriction in dc-link voltage is due to the maximum sustained voltage of the switching element. Series connection of the switching element was developed to increase the dc-link voltage. However, the maximum allowable number of switching elements is limited.

A multilevel converter was proposed to increase the converter operation voltage, avoiding the series connection of switching elements. In high power system, the multilevel inverters can appropriately replace the exist system that use traditional multi-pulse converters without the need for transformers. All three multilevel inverters can be used in reactive power compensation without having the voltage unbalance problem [9].

The proposed UPQC can be directly connected to the distribution system without series and shunt injection transformer, which struggle with core saturation and voltage drop. In order to validate the proposed system, computer simulation using the MATLAB Power System Blockset package is carried out with the main parameters:

$$V_s = 400, f = 50 \text{ Hz}, f_c = 1080 \text{ Hz}.$$

A. Series Inverter

Different main circuit structure will have different compensation effectiveness and cost performance. The practical topological structure that can be used: Three level structure and multilevel structure. Under the circumstances that the same fundamental wave is outputted, compared with the traditional two level structure, three level structure has the advantage of bearing lower switch frequency, device stress, switching losses, and producing less harmonics.

The shortcoming is that, in practical application, the device should still stand large voltage stress, and parameter choice room of the device is relatively small.

It makes the control become very complicated to deal with the unbalance of capacity voltage and the elimination of

narrow pulse. Meanwhile, the redundant design and the expanding of systematic capacity are difficult. For the cascade multilevel structure, the more levels it has the less harmonics it produces, and less loss it generates.

Series compensator on the basis of the topology of multilevel has much comprehensive superiority than other topology in systematic reliability, device type choosing, controlling complexity, and total efficiency.

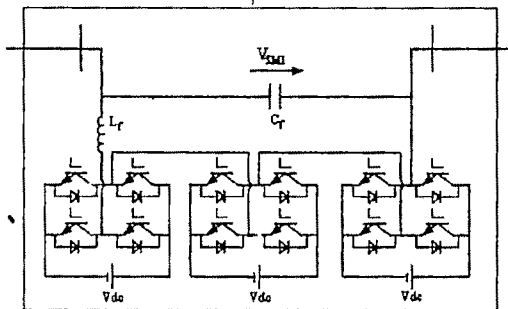


Fig. 7. The main circuit topology of cascade multilevel series inverter

Fig. 7 shows the main circuit topology of cascade multilevel series inverter (single line diagram). The multibridge converter composed of three H-bridge modules for each phase, was proposed to increase the converter operation voltage

In the figure, each cascaded H-bridge inverter unit has its own mutually independent DC source ($V_{dc} = 108\text{V}$). Within one work period, the series converter, formed by several H-bridge inverters that connected in series, outputs voltage waveform of $2k+1$ levels. Because of adoption of cascade structure, the series converter has novel charge modes and need not add charging circuit, also the series injecting transformer. The topology makes it helpful to save the cost, reduce the space occupation and improve systematic reliability, meanwhile, the cascade modules makes it feasible to improve the equivalent switch frequency of the device greatly, simplify filter design and reduce losses without improving switch frequency of the device. Besides, the filter could be eliminated in some cases that harmonics are acceptable.

The function of series inverter is to compensate the voltage disturbance in the source side, which is due to the fault in the distribution line. The control algorithm is made of 2 parts; they are voltage sag detection and SPWM control. The detection of voltage sag compares system voltage with reference voltage and send out sag signal.

Equation (1) shows the state equation of the series inverter.

$$V_C = K_{PI}(V_{ref} - V_S) \quad (1)$$

Fig. 8 shows the configuration of series inverter control, which is based on (2). A PI controller is used in the control algorithm.

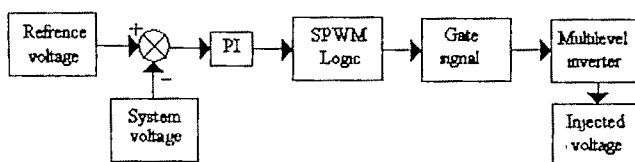


Fig. 8 Series inverter control diagram

The values of PI controller parameters are determined with trial and error. They have an important effect in the response of the voltage control.

Figures 9-10 show the simulation results of voltage control, which confirm the fact that the output voltage of each phase is compensated without large transient and steady-state errors

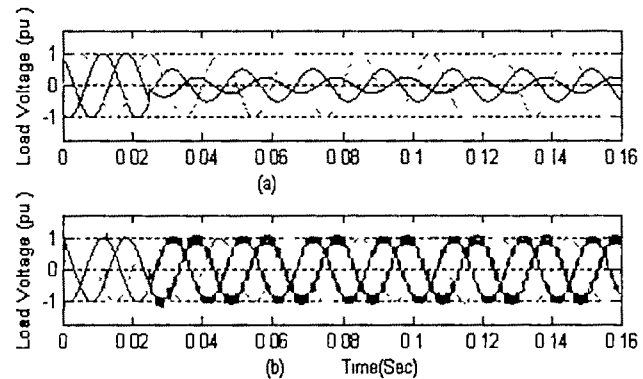


Fig. 9. Unbalance compensation (without filter) : (a) unbalanced voltages (b) compensated voltages

It's worth to be said that since voltage sag is a special mode of unbalanced voltages, the compensation of voltage sag is the same as unbalanced voltage compensation.

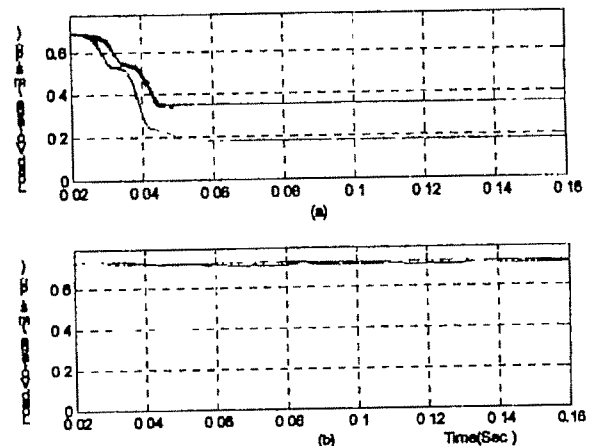


Fig. 10. Unbalance compensation (without filter). (a) RMS values of unbalanced voltages (b) RMS values of compensated voltages

The effect of using LC filter is shown in Fig. 11. One of important advantages of multilevel inverters is reducing harmonics; thus the filter could be eliminated in some cases that harmonics are less than the standard range and it results in decreasing the cost of the system.

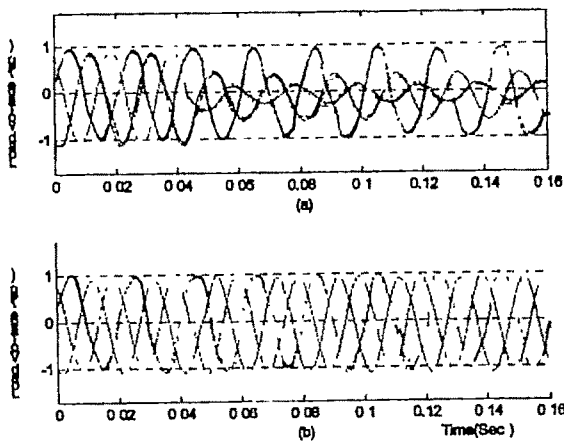


Fig 11. Unbalance compensation (with filter).
(a) unbalanced voltages (b) compensated voltages

A. Shunts Inverter

The reactive power generated or absorbed is directly controlled by adjusted i_q^* . Likewise, the real power exchange can be controlled by adjusted i_d^* . As a result, the reactive power and active power can be separately controlled. Then, i_d^* and i_q^* are the active current component and reactive current component of the shunt compensator: active power flows into the shunt compensator when i_d^* is positive, and flows out when i_d^* is negative. The shunt compensator generates leading reactive power when i_q^* is positive and lagging reactive power when i_q^* is negative. A feedback decoupling control is proposed as shown in Fig. 12 to obtain these performances. A PI controller is used for both active and reactive current control loops. The shunt compensator has been modeled with mathematical equations and a source current. Therefore, in the block diagram, i_d^* is zero. This control method can mitigate load power factor as shown as in Fig. 13.

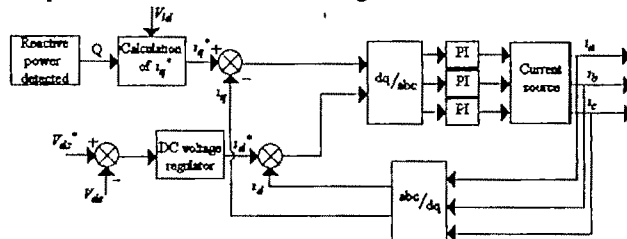


Fig. 12 Shunt inverter control diagram

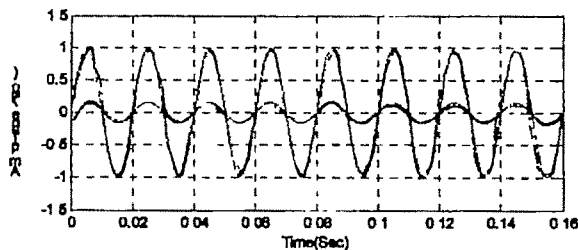


Fig. 13. Power Factor Compensation

The Load output phase voltage and current is shown in Fig.13, Obviously, the difference between load voltage and current phase angles become zero after about 0.01 Sec. That is to say the shunt compensator generates inductance reactive power. The three phase simulated system is based on the control scheme as Fig.12.

IV. CONCLUSION

The problem of voltage sag and unbalance is objective and unavoidable, in order to reduce the losses caused by the voltage sag, to adopt specific custom-built power electronics based installations are great helps. The topology of cascade multilevel is the rational choice of UPQC.

To respond properly, the SPWM switching strategy should be used during unbalanced conditions. Separate DC buses have been used for each phase of inverter.

This paper proposes a configuration of UPQC, in which each phase consists of 3 pairs of H-bridge modules without any transformer.

The proposed UPQC can be directly connected to the distribution system without any injection transformer, which struggles with core saturation and voltage drop.

The effectiveness of the proposed UPQC to compensating unbalanced voltage and power factor was verified through simulations with MATLAB/Simulink.

V. REFERENCES

- [1] H. Fujita and H. Akagi, "The unified power quality conditioner: The integration of series and shunt active filters," IEEE Trans. Power Electron., vol. 13, no. 2, pp. 315-322, Mar. 1998.
- [2] F. Peng, J. McKeever, and D. Adams, "A power line conditioner using cascade multilevel inverters for distribution systems," IEEE Trans. Ind. Appl., vol. 34, no. 6, pp. 1293-1298, Nov/Dec. 1998.
- [3] F. Peng and J. Lai, "A multilevel voltage-source inverter with separate DC source for static var generation," in Proc. IEEE/IAS Annu. Meeting, Orlando, FL, Oct. 8-12, 1995, pp. 2541-2548.
- [4] B. Han, H. Kim, and S. Baek, "Performance analysis of SSSC based on three-level multi-bridge PWM inverter," Elsevier Sci. Elect. Power Syst. Res., vol. 61, no. 3, pp. 195-202, Jun. 2002.
- [5] B. Li, S. Chor, and D. Vilathgamuwa, "Transformerless dynamic voltage restorer," Proc. Inst. Elect. Eng., Gen. Transm. Distrib., vol. 140, no. 3, pp. 263-273, May 2002.
- [6] B. Han, Senior Member, IEEE, B. Bae, Student Member, IEEE, S. Baek, and G. Jang, Member, IEEE, "New Configuration of UPQC for Medium-Voltage Application" IEEE TRANSACTIONS ON POWER DELIVERY 2005
- [7] Jason Lai, Chair Dusan Borjovic Alex Q. Huang, "OPTIMIZED HARMONIC STEPPED-WAVEFORM FOR MULTILEVEL INVERTER", Msc thesis, 1999
- [8] A. Nabae, I. Takahashi, and H. Akagi, "A new neutral-point clamped PWM inverter," IEEE Trans. Ind. Applicat., vol. IA-17, pp. 518-523, Sep/Oct. 1981
- [9] Jose Rodriguez; Jih-Sheng Lai; Fang Zheng Peng; "Multilevel Inverters. A Survey of Topologies, Controls, and Applications" IEEE Transactions on Industrial Electronics, Vol. 49, No.4, August 2002
- [10] T. A. Meynard and H. Foch, "Multi-level choppers for high voltage applications," Eur. Power Electron. Drives J., vol. 2, no. 1, p. 41, Mar. 1992.
- [11] C. Hochgraf, R. Lasseter, D. Divan, and T. A. Lipo, "Comparison of multilevel inverters for static var compensation," in Conf. Rec. IEEE-IAS Annu. Meeting, Oct. 1994, pp. 921-928

- [12] P. Hammond, "A new approach to enhance power quality for medium voltage ac drives," *IEEE Trans Ind. Applicant.*, vol. 33, pp. 202-208, Jan /Feb. 1997.
- [13] R. H Baker and L. H. Bannister, "Electric power converter," U. S. Patent 3867643, Feb. 1975
- [14] Xianglian Xu, Yunping Zou, Kai Ding, and Fei Liu "Cascade multilevel inverter with Phase-Shift SPWM and its application in STATCOM
- [15] Han, B.; Bae, B.; Kim, H.; Back, S., "Combined operation of unified power-quality conditioner with distributed generation" *Power Delivery*, *IEEE Transactions on* Volume 21, Issue 1, Jan. 2006 Page(s) 330 - 338

Electromagnetic Field Effect on Metallic Particle Contamination in a Common Enclosure Gas Insulated Bus duct

G.V.Nagesh Kumar¹, J.Amarnath², B.P.Singh³ and K.D.Srivatsava⁴

¹ Vignan's Institute of Information Technology, Andhra Pradesh, INDIA e-mail: gundavarapu_kumar@yahoo.com

² Jawaharlal Nehru Technological University, Hyderabad, INDIA e-mail: amarnathjinka@yahoo.com

³ BHEL Corporate (R & D), Vikas Nagar, Hyderabad, India

⁴ University of British Columbia, Vancouver, B.C, Canada

Abstract— The superior dielectric properties of Sulphur Hexafluoride (SF₆) have long been recognized. Due to the high reliability of the equipment, Gas Insulated Substation can be used for longer time without any periodical inspections. Conducting contamination could, however, be seriously reduce the dielectric strength of a gas insulated system. These particles can either be free to move in the Gas Insulated Bus (GIB) or they may stick either to an energized electrode or to an insulated surface. If a metallic particle crosses the gap and comes into contact with the inner electrode or if a metallic particle adheres to the inner conductor, the particle will act as a protrusion on the surface of the electrode. Consequently, voltage required for breakdown of the GIS may be significantly decreased. The distance traveled by the particle using appropriate equation, is found to be in good agreement with the published work for a given set of parameters. The purpose of this paper is to develop techniques, which will formulate the basic equations that will govern the movement of metallic particles like aluminum and copper in a bus duct. The simulation also considers the electromagnetic field effect on particle movement and the results have been presented and analyzed.

Key words— Metallic particles, Electromagnetic analysis, Gas Insulated Substations.

I. INTRODUCTION

GAS insulated sub-station systems offer a compact, cost-effective, reliable and maintenance-free alternative to the conventional air insulated sub-station systems. Their compact size offers a practical solution to vertically upgrade the existing sub-station and to meet the ever-increasing power demand in developing countries. Metal-enclosed SF₆ insulated switchgear (GIS) has already a long service experience since it was firstly introduced into the market 1968 with SF₆ also as arc quenching medium as an interesting and economical alternative to conventional air insulated substations. The use of SF₆ within the power energy supply is mainly driven by the gas-insulated switchgear. The state of the art shows single phase and three phase encapsulated designs. For the distribution

voltage level mainly three phase enclosures are used. For higher voltage levels single-phase encapsulation is a standard. In the last years the development of SF₆ insulated switchgear was mainly driven by the aim to reduce the use of material and costs by still extremely high reliability.

In a Gas Insulated Bus duct (GIB), all live parts are enclosed in compressed Sulphur Hexafluoride gas chambers, which are divided into a number of compartments or bays according to the layout or configuration of its several components. Basic components of the GIS bay are circuit breakers, disconnectors, Earthing switches, bus ducts, current and voltage transformers, etc. The inner live parts of GIS are supported by insulators called spacers, which are made of alumina filled epoxy material. The GIS enclosure forms an electrically integrated, grounded enclosure for the entire substation. Even though SF₆ exhibits very high dielectric strength, the withstand voltage of SF₆ within the GIS is drastically reduced due to the presence of particles or defects like:

1. Free particles on the inner surface of the enclosure,
2. Protrusion on the high voltage (HV) bus,
3. Protrusion on the inner surface of the enclosure and
4. Narrow gaps between the spacer and the electrode due to imperfect casting and or imperfect mechanical strength, which may lead to high electrical stress and thus micro discharges.

Free conducting particles are most dangerous to GIS. These free conducting particles may have any shape or size, may be spherical or filamentary (wire like) or in the form of fine dust. Particles may be free to move or may be fixed on to the surfaces. They may be of conducting material or of insulating material. Particles of insulating materials are not so harmful as they have little effect on the insulating properties of gases. So wire like particles made of conducting material is more harmful and their effects are more pronounced at higher gas pressures. The origin of these particles may be from the manufacturing process, from mechanical vibrations or from moving parts of the system like breakers or disconnectors etc.

Several authors conducted experiments on insulating particles [1-3]. However the presence of atmospheric dust containing conducting particles, especially on the cathode, reduces the breakdown voltage. Conducting particles placed in a uniform ac field lift-off at a certain voltage. As the voltage is raised, the particles assume a bouncing state reaching a height determined by the applied voltage. With a further increase in voltage, the bounce height and the corona current increase until break down occurs. The lift off voltage is independent of the pressure of gas. After the onset of bouncing, the offset voltage is approximately 30% lower than the lift-off voltage.

Some of the methods of conducting particle control and de-activation are:

- Electrostatic trapping
- Use of adhesive coatings to immobilize the particles
- Discharging of conducting particles through radiation, and
- Coating conducting particles with insulating films

The work reported in this paper deals with the movement of metallic particle in 3-phase common enclosure Gas Insulated busduct in a common enclosure. In order to determine the axial and radial movement in an enclosure, Monte-Carlo technique has been adopted in conjunction with motion equation. The simulation also considers the particle movement in 3-phase common enclosure GIB with Electromagnetic field effect. Electromagnetic field is considered as the current in the conductor is time varying. The specific work reported deals with the charge acquired by the particle due to macroscopic field at the tip of the particle, the force exerted by the field i.e., both electric and magnetic field on the particle, drag due to viscosity of the gas and random behavior during the movement. Wire like particles of aluminum and copper of a fixed geometry in a 3-phase bus duct have been considered. The movement pattern for higher voltages class has been also obtained [4-5]. In Monte-Carlo technique it has been assumed that at every time step the particle can have a maximum movement 1^0 to 4^0 from vertical.

II. MODELING TECHNIQUE

A typical horizontal three-phase bus duct shown in Figure 1 has been considered for the analysis.

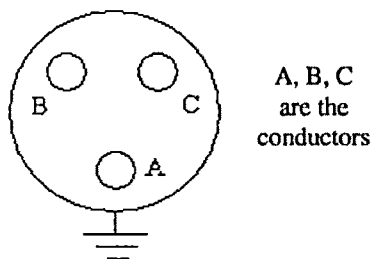


Fig. 1 A typical 3-phase common enclosure Gas insulated bus duct.

Understanding the dynamics of a metallic particle in a coaxial electrode system is of vital importance for determining the effect of metallic contamination in a Gas Insulated System.

If the motion pattern of a metallic particle is known, the probability of particle crossing a coaxial gap and causing a flashover can be estimated. The lift-off field for a particle on the surface of an electrode can be estimated by solving the motion equation.

A conducting particle in motion in an external electromagnetic field will be subjected to a collective influence of several forces. The forces may be divided into:

- Lorentz force (F_{LF})
- Gravitational force (mg)
- Drag force (F_d)

The motion equation is given by

$$m \frac{d^2 y}{dt^2} = F_e - mg - F_d \quad (1)$$

where m = mass of the particle

y = displacement in vertical direction

F_{LF} = Lorentz force (Electric and Magnetic Field)

g = gravitational constant

Figure 1 shows a horizontal three phase bus duct comprising of inner conductors spaced equilaterally in a metal enclosure. The enclosure is filled with SF_6 gas at a high pressure (0.3 MPa). A particle is assumed to be at rest at the enclosure surface, just beneath the bus bar 2, until a voltage sufficient enough to lift the particle and move in the field is applied.

After acquiring an appropriate charge in the field, the particle lifts and begins to move in the direction of field having overcome the forces due to its own weight and drag. The simulation considers several parameters e.g. the macroscopic field at the surface of the particle, its weight, Reynold's number, coefficient of restitution on its impact to both enclosures and viscosity of the gas. During return flight, a new charge on the particle is assigned based on the instantaneous electric field.

The direction of drag force is always opposed to the direction of motion. The expression for drag Force and Lorentz force given in equation (2) and equation (3).

$$F_d = \dot{y} \pi \left(6\mu K_d (\dot{y}) + 2.656 \left[\mu \rho_g l \dot{y} \right]^{0.5} \right) \quad (2)$$

where

\dot{y} is the velocity of the particle

μ is the viscosity of the fluid

r is the particle radius

ρ_g is the gas density

l is the particle length

$K_d (\dot{y})$ is the drag coefficient

The Lorentz Force is given by

$$F_{LF} = \frac{\pi \epsilon_0 l^2 E(t_0)}{\ln\left(\frac{2l}{r}\right) - 1} \times \left[\frac{V_m \sin \omega t}{[r_0 - y(t)] \ln\left(\frac{r_0}{r_1}\right)} + \dot{y} \frac{\mu I}{2\pi[r_0 - y(t)]} \right] \quad (3)$$

The above forces are substituted in equation (1) and it becomes a second order non – linear differential equation. To solve the motion equation Runge-Kutta 4th order method is adopted.

III. SIMULATION OF PARTICLE MOTION

The study of the motion of moving metallic particles in GIS requires a good knowledge of the charge of the particle. Computer simulations of the motion of metallic wire particles were carried out on GIB of 64 mm inner diameter for each enclosure and 500 mm outer diameter with 400 kV applied to inner conductors with 120° phase difference. Aluminum and copper wire like particles were considered to be present on enclosure surface.

In order to determine the random behavior of moving particles, the calculation of movement in axial and radial directions was carried at every time step using rectangular random numbers. The above simulation yields the particle movement in the radial direction only. However, the configuration at the tip of the particle is generally not sufficiently smooth enough to enable the movement unidirectional. This decides the movement of particle in axial direction. The randomness of movement can be adequately simulated by Monte-Carlo method. In order to determine the randomness, it is assumed that the particle emanates from its original site at any angle less than ϕ , where $\phi/2$ is half of the solid angle subtended with the vertical axis. At every step of movement, a new rectangular random number is generated between 0 and 1 and modified to ϕ . The angle thus assigned, fixes the position of particle at the end of every time step, and in turn determines the axial and radial positions. The position in the next step is computed on the basis of equation of motion with new random angles as described above.

IV. RESULTS AND DISCUSSION

Table 1 and Table 2 show the radial and axial movement of the particle with and without magnetic field effect. The results have been presented by using Monte-Carlo Technique also shown in Table 1 and Table 2. Figure 2 to Figure 17 show the movement patterns of copper and aluminum particles with and without magnetic field for a applied voltages of 300 KV and 400KV rms respectively. The radius of the particles in all cases is considered as 0.1 mm and length of the particle as 10mm.

During its movement it makes several impacts with the enclosure. The highest displacement in radial direction during its upward journey is simulated to be 65mm for 400 KV GIS.

As the applied voltage increases the maximum radial movement also increases as given in Table 1. However, it is noticed that even up to a voltage of 100kV, the particle could not bridge the gap.

Further calculations may reveal the limiting voltage to enable the particle to reach the high voltage conductor. A graphical representation of radial movement in relation to axial movement is given by Monte-Carlo technique as shown in Figure 3. The movement of copper particle was determined for 400kV with similar parameters as above and found to have a maximum movement of 18mm in radial direction as shown in Fig. 4. The movements are also calculated for other voltages.

The movement of copper particle is also given in Table 1. It is noticed that the movement of copper particle is far less than aluminum particle of identical size. This is expected due to higher density of copper particle. The axial and radial movement of aluminum and copper particles are calculated using Monte-Carlo technique for two voltages i.e. 300kv and 400kv with a solid angle of 1°.

It is significant to note that for all the cases considered, there is no change in maximum radial movement, even when Monte-Carlo method is applied. A relatively high value of axial movement is achieved with the random angle of 1°. As expected the axial movement of copper particle is lower than the aluminum. The movement of aluminum and copper particles with Electromagnetic Field is shown in Figures 10 to Figure 17. It has been observed that with the Electromagnetic effect a considerable change in the radial movement for all the cases.

Table 1. Axial and Radial Movement of Aluminum and Copper Particles without Magnetic Field

Voltage	Type	Max. Radial Movement (mm)	Monte – Carlo (1°)	
			Radial (mm)	Axial (mm)
300 KV	Al	36	36	536
	Cu	07	07	116
400 KV	Al	65	65	616
	Cu	18	18	312

Table 2. Axial and Radial Movement of Aluminum and Copper Particles with Magnetic Field

Voltage	Type	Max. Radial Movement (mm)	Monte – Carlo (1°)	
			Radial (mm)	Axial (mm)
300 KV	Al	38	38	537.6
	Cu	7.5	7.5	117
400 KV	Al	66.2	66.2	617
	Cu	18.4	18.4	313.7

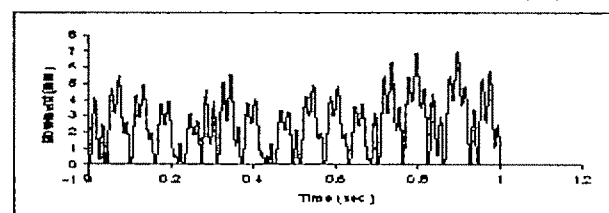


Fig. 2. Particle movement without Magnetic Field in a 3 - phase GIS for 300 KV/ Cu/ 10mm / 0.1radius

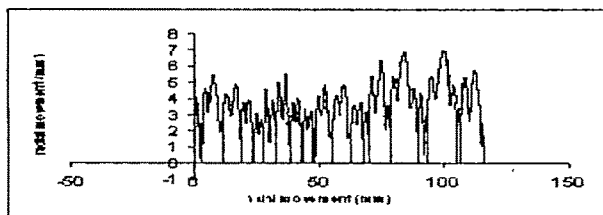


Fig. 3. Axial & Radial movement without Magnetic Field in a 3 - phase GIB for 300 KV/ CU/ 10mm / 0.1radius

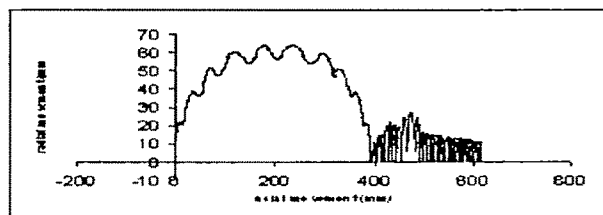


Fig 9. Axial & Radial movement without Magnetic Field in a 3 - phase GIB for 400 KV/ AL/ 10mm / 0.1radius

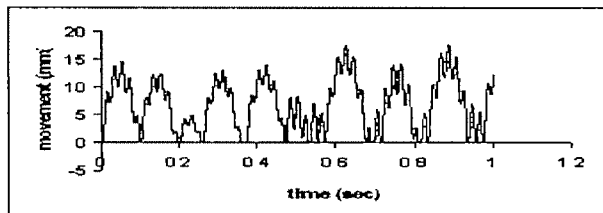


Fig. 4. Particle movement without Magnetic Field in a 3 - phase GIB for 400 KV/ CU/ 10mm / 0.1radius

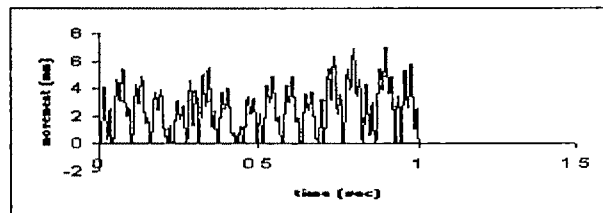


Fig. 10. Particle movement with Magnetic Field in a 3 - phase GIB for 300 KV/ CU/ 10mm / 0.1radius

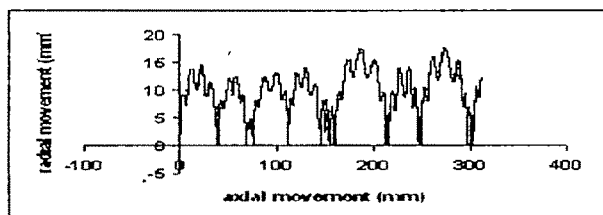


Fig 5. Axial & Radial movement without Magnetic Field in a 3 - phase GIB for 400 KV/ CU/ 10mm / 0.1radius

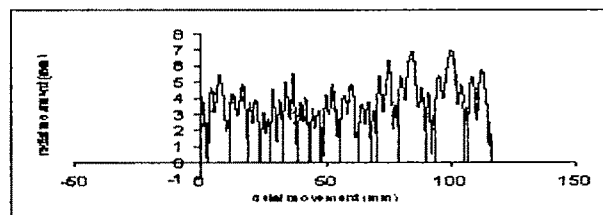


Fig 11. Axial & Radial movement with Magnetic Field in a 3 - phase GIB for 300 KV/ CU/ 10mm / 0.1radius

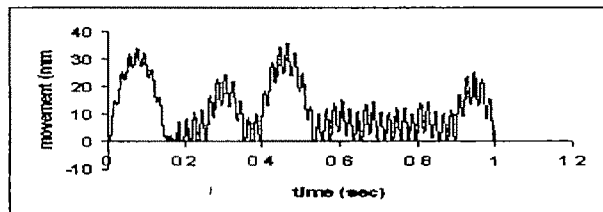


Fig. 6 Particle movement without Magnetic Field in a 3 - phase GIB for 300 KV/ AL/ 10mm / 0.1radius

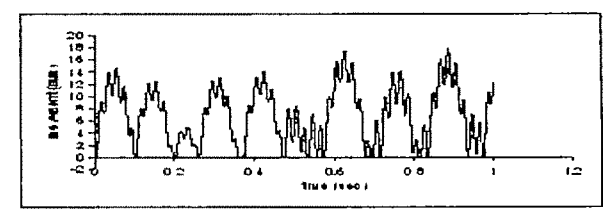


Fig. 12. Particle movement with Magnetic Field in a 3 - phase GIB for 400 KV/ CU/ 10mm / 0.1radius

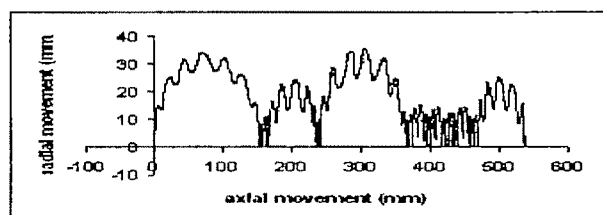


Fig 7 Axial & Radial movement without Magnetic Field in a 3 - phase GIB for 300 KV/ AL/ 10mm / 0.1radius

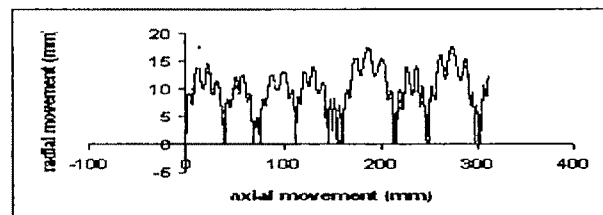


Fig 13. Axial & Radial movement with Magnetic Field in a 3 - phase GIB for 400 KV/ CU/ 10mm / 0.1radius

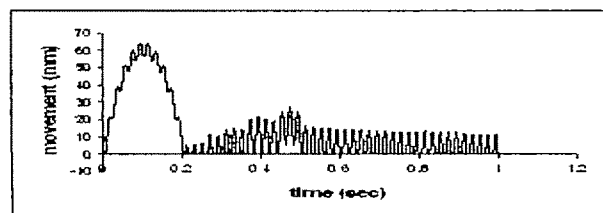


Fig 8 Particle movement without Magnetic Field in a 3 - phase GIB for 400 KV/ AL/ 10mm / 0.1radius

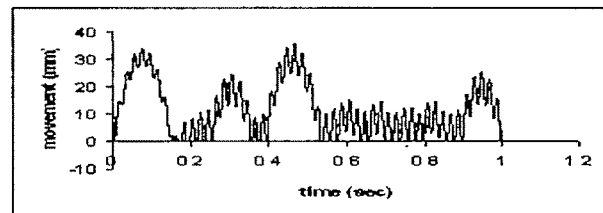


Fig. 14. Particle movement with Magnetic Field in a 3 - phase GIB for 300 KV/ AL/ 10mm / 0.1radius

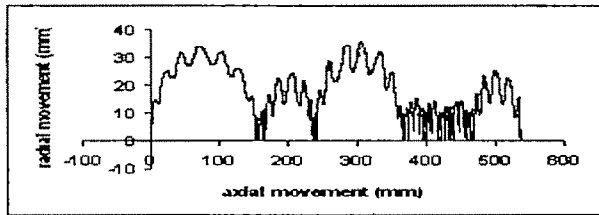


Fig 15. Axial & Radial movement with Magnetic Field in a 3 - phase GIB for 300 KV/ AL/ 10mm / 0.1radius

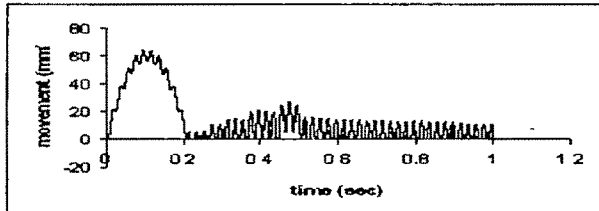


Fig. 16. Particle movement with Magnetic Field in a 3 - phase GIB for 400 KV/ AL/ 10mm / 0.1radius

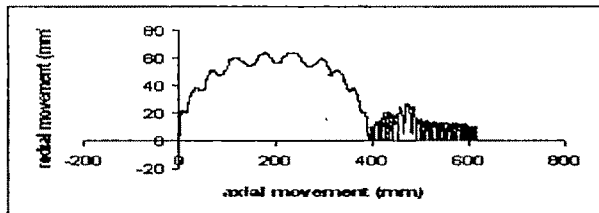


Fig 17. Axial & Radial movement with Magnetic Field in a 3 - phase GIB for 400 KV/ AL/ 10mm / 0.1radius

V. CONCLUSION

A model has been formulated to simulate the movement of wire like particle in 3-phase common enclosure GIB on bare electrode. When Lorentz force exceeds the gravitational and drag forces the particle lifts from its position. A further increase in the applied voltage makes the particle move into the inter electrode gap in the direction of applied field. This increases the probability of a flashover. The influence of increased voltage level on the motion of the particles is also investigated. If the calculations, as described above, are performed at a higher voltage level, the particle will lift higher from the surface and the time between bounces will increase.

The results obtained from the calculations show that additional information about the particle could be obtained when voltage dependence is introduced in the calculations. For instance, it can be noted that aluminum particles are more influenced by the voltage than copper or silver particles due to their lighter mass. This results in the aluminum particle acquiring greater charge-to-mass ratio.

The coefficient of restitution, which denotes the ratio of outgoing to incoming velocities, is of vital importance for determining the maximum movement of particle. As in the case of Lorentz force it is observed that more than 100 KA short circuit current there is an increase in the movement. The results obtained are presented and analyzed. Monte-carlo simulation is also adopted to determine axial as well as radial movements of particle in the busduct. Distance traveled in the

radial direction is found to be same with or without Monte-carlo simulation. All the above investigations have been carried out for various voltages under power frequency.

ACKNOWLEDGMENT

The authors are thankful to management of Vignan's Institute of Information Technology, Visakhapatnam, BHEL Corporate (R&D) and JNT University, Hyderabad, for providing facilities and to publish this work.

REFERENCES

- [1] A.H. Cookson, P.C. Bolin, H.C. Doepken, R.E. Wootton, C.M. Cooke and J.G. Trump, "Recent Research in the United States on the Effect of Particle Contamination Reducing the Breakdown Voltage in Compressed Gas Insulated System", Int. Conf. On Large High Voltage System; Paris, 1976.
- [2] H. Anis and K.D. Srivastava, "Breakdown Characteristics of Dielectric Coated Electrodes in Sulphur Hexafluoride Gas with Particle Contamination", Sixth Intern Sympos High Voltage Engineering, Paper No. 32.06, New Orleans, LA, USA 1989.
- [3] M.M. Morcos, K.D. Srivastava, and S.M. Gubanski, "Dynamics of Metallic particle contamination in GIS with dielectric coating electrodes", IEEE Trans. Power Delivery Vol 15, pp 455-460, 2000.
- [4] J. Amarnath, B. P. Singh, C. Radhakrishna and S. Kamakshiah, "Determination of particle trajectory in a Gas Insulated Busduct predicted by Monte-Carlo technique", IEEE Conf. Electr. Insul. Dielectric Phenomena (CEIDP), Texas, Austin, USA, 1991 Vol. 1, pp. 399-402, 1991.
- [5] G.V. Nagesh Kumar, J. Amarnath, B.P. Singh and K.D. Srivastava, "Electric Field Effect on Metallic Particle Contamination in a Common Enclosure Gas Insulated Bus duct", IEEE Transactions in Dielectrics and Electrical Insulation, April 2007, PP. 334-340.

PD Detection and Location in Cable Networks Based on Traveling Waves Indices

S.M. Shahrtash¹, F. Haghjoo²

¹ Iran University of Science and Technology, Iran e-mail: Shahrtash@iust.ac.ir

Abstract—In this paper, a new method for detection and location of PDs in single core cables has been proposed. The method is based on monitoring two indices composed from forward and backward traveling waves measured in the two cable ends, and combining them to find the PD location. The two indices have been used to investigate the occurrence of internal PDs and discriminating them from external PDs and any other events. Also, in the case of internal single PDs, they have been used to construct the PD current waveform by using the Bergeron model for cable. Through simulating the network by ATP, the results have shown good performance in detection and location.

Key words—Partial Discharge, Location, Traveling wave, cable network.

I. INTRODUCTION

THE most important phenomenon in insulation degradation is Partial Discharge (PD), which if not inspected and remedies actions provided it can make insulation failures. Detection and location of PDs in cable networks, not only makes the maintenance programs more effective and less expensive, but also can increase system reliability.

Although low PDs exist in all of the HV devices and cables, but as the intensity of PDs increases it is an indication showing the system approaches to an emergency condition. Fortunately, in contrast to short circuit faults, there is adequate time for the diagnosis of PDs, because it gradually increases and reduces insulation properties.

Routine testing of the insulation condition is performed in certain periods, through off-line procedures, which need power outage and are somehow destructive. In on-line diagnostic methods of PDs, there is no need for any outages, and if the insulation condition shows that some remedial actions are needed the repairing time may be minimized. On-line diagnostic methods are based on performing signal processing on current and voltage signals, measured in different observation points on the considered system or apparatuses.

For defect detection in embedded cables, electrical signals are only obtainable at the two ends of each section, and the signal processing must be performed based on the measured signals at these points.

In this paper, detection and location of PD in cable

networks have been performed based on Traveling Waves (TW) theory [1-3], using two defined indices, named as ε_s and ε_R . These indices are constructed by combination of forward and backward voltage waves in sending and receiving end of the cable. Also the PDs current wave shape is reconstructed through a simple process.

II. PD LOCATION ALONG THE CABLE BASED ON TRAVELING WAVE COMPONENTS

The famous set of equations for describing cables' voltages and currents in transient regime in distributed model can be shown as:

$$\begin{cases} \frac{\partial^2 v}{\partial x^2} = LC \frac{\partial^2 v}{\partial t^2} \\ \frac{\partial^2 i}{\partial x^2} = CL \frac{\partial^2 i}{\partial t^2} \end{cases} \quad (1)$$

After solving them, the following results will be obtained:

$$\begin{aligned} v(x, t) &= V_F(x - v_c t) + V_B(x + v_c t) \\ i(x, t) &= I_F(x - v_c t) + I_B(x + v_c t) \end{aligned} \quad (2)$$

where F and B subscripts are used for forward (in positive direction of x) and backward (in negative direction of x) waves, respectively. Also the following relations exist between these waves;

$$\begin{aligned} V_F(x - v_c t) &= Z_c I_F(x - v_c t) \\ V_B(x + v_c t) &= -Z_c I_B(x + v_c t) \end{aligned} \quad (3)$$

In the above equations, Z_c is the characteristic impedance of the cable and v_c is traveling wave velocity (which is about 55 percent of c [4], for PE cables).

Based on the above equations, the forward and backward voltage and current are obtainable as in the following:

$$\begin{aligned}
 V_F(x, t) &= \frac{1}{2} [v(x, t) + Z_c i(x, t)] \\
 V_B(x, t) &= \frac{1}{2} [v(x, t) - Z_c i(x, t)] \\
 I_F(x, t) &= \frac{1}{2} [i(x, t) + \frac{1}{Z_c} v(x, t)] \\
 I_B(x, t) &= \frac{1}{2} [i(x, t) - \frac{1}{Z_c} v(x, t)]
 \end{aligned} \quad (4)$$

As effect of The occurrence of *PDs* or any other electrical transient disturbances, two equal signals are generated and started to travel in opposite directions with V_c (according to physical parameters of propagation path).

Assuming that the traveling time along the cable is τ in seconds, then:

-If a traveling voltage wave enters a cable from sending end, that wave will be detected at the sending end as a forward voltage wave, and τ seconds later, at the receiving end as a backward voltage wave, and therefore:

$$[v_R(t_k) - Z_c i_R(t_k)] = [v_S(t_k - \tau) + Z_c i_S(t_k - \tau)] \quad (5)$$

-If a traveling voltage wave enters a cable from receiving end, that wave will be detected at the receiving end as a forward voltage wave, and τ seconds later, at the sending end as a backward voltage wave, and therefore:

$$[v_S(t_k) - Z_c i_S(t_k)] = [v_R(t_k - \tau) + Z_c i_R(t_k - \tau)] \quad (6)$$

-If a traveling voltage wave, as a result of *PD* (or any other problem that generates transient voltage signal), is produced at a point on the cable under consideration, none of the above equations holds. These are the main criteria to detect and locate *PDs* which are explained in the next section.

III. PD LOCATION WITH TW BASED INDICES

As described in the previous section, in the case of external defect, the difference of backward and delayed forward voltage waves measured at the cable ends will be zero. Therefore, according to (5) and (6) the *TW* based indices can be defined as:

$$\begin{aligned}
 \varepsilon_S(t) &= [i_R(t - \tau) + i_S(t)] + \\
 &\quad \frac{1}{Z_c} [v_R(t - \tau) - v_S(t)]
 \end{aligned} \quad (7)$$

$$\begin{aligned}
 \varepsilon_R(t) &= [i_S(t - \tau) + i_R(t)] + \\
 &\quad \frac{1}{Z_c} [v_S(t - \tau) - v_R(t)]
 \end{aligned} \quad (8)$$

By introducing f_s as sampling frequency and $N_\tau = \frac{\tau}{\Delta t} = \tau \cdot f_s$, in digital mode the indices are defined as:

$$\begin{aligned}
 \varepsilon_S(k) &= [i_R(k - N_\tau) + i_S(k)] + \\
 &\quad \frac{1}{Z_c} [v_R(k - N_\tau) - v_S(k)]
 \end{aligned} \quad (9)$$

$$\begin{aligned}
 \varepsilon_R(k) &= [i_S(k - N_\tau) + i_R(k)] + \\
 &\quad \frac{1}{Z_c} [v_S(k - N_\tau) - v_R(k)]
 \end{aligned} \quad (10)$$

If the two indices have zero value in any pre-defined period of time (or any obtained sample), then in the case of detecting *TW*, they are entered from outside of the cable. Otherwise, *PD* is detected along the cable, provided that the time difference between the instants of detecting a backward voltage waves at the two ends becomes not more than τ (or N_τ).

Now, referring to Fig.(1), if a *PD* occurs in point *F* of cable *AB*, for *AF* and *FB* subsections the following relations can be written:

$$\begin{aligned}
 &[\frac{1}{Z_c} v_S(t - \tau_{11}) + i_S(t - \tau_{11})] - \\
 &[\frac{1}{Z_c} v_F(t) - i_{FA}(t)] = 0
 \end{aligned} \quad (11)$$

$$\begin{aligned}
 &[\frac{1}{Z_c} v_R(t) - i_R(t)] - \\
 &[\frac{1}{Z_c} v_F(t - \tau_{12}) + i_{FB}(t - \tau_{12})] = 0
 \end{aligned} \quad (12)$$

where $\tau_{11} = \frac{x}{V_c}$ and $\tau_{12} = \frac{L_1 - x}{V_c}$ are the wave traveling time from *A* to *F* and from *F* to *B*, respectively.

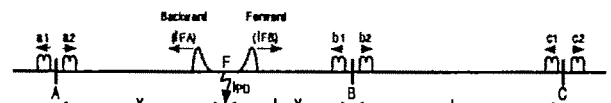


Fig. 1. A section of a cable network with installed V and I sensors

By applying a time shift equal to τ_{12} in (11):

$$\begin{aligned} & \left[\frac{1}{Z_c} v_S(t - \tau_{11} - \tau_{12}) + i_S(t - \tau_{11} - \tau_{12}) \right] \\ & - \left[\frac{1}{Z_c} v_F(t - \tau_{12}) - i_{FA}(t - \tau_{12}) \right] = 0 \end{aligned} \quad (13)$$

Defining $\tau_1 = \tau_{11} + \tau_{12}$, (13) can be rewritten as:

$$\begin{aligned} & \left[\frac{1}{Z_c} v_S(t - \tau_1) + i_S(t - \tau_1) \right] \\ & - \left[\frac{1}{Z_c} v_F(t - \tau_{12}) - i_{FA}(t - \tau_{12}) \right] = 0 \end{aligned} \quad (14)$$

And then by adding (12) and (14):

$$\begin{aligned} & \frac{1}{Z_c} [v_S(t - \tau_1) - v_R(t)] + [i_S(t - \tau_1) + i_R(t)] = \\ & - [i_{FA}(t - \tau_{12}) + i_{FB}(t - \tau_{12})] \end{aligned} \quad (15)$$

The LHS in the above equation is \mathcal{E}_R and by applying KCL at F, the RHS becomes the PD current; therefore (15) can be rewritten as:

$$\mathcal{E}_R(t) = i_{PD}(t - \tau_{12}) \quad (16)$$

Similarly, it can be found:

$$\mathcal{E}_S(t) = i_{PD}(t - \tau_{11}) \quad (17)$$

In the digital mode, by definition of $N_{11} = \tau_{11} \cdot f_s$ and $N_{12} = \tau_{12} \cdot f_s$, (16) and (17) can be changed to:

$$\mathcal{E}_R(k) = i_{PD}(k - N_{12}) \quad (18)$$

$$\mathcal{E}_S(k) = i_{PD}(k - N_{11}) \quad (19)$$

Therefore, if the indices defined by (7) and (8) in analog mode, or (9) and (10) in digital mode, have non-zero values, PD has been occurred in the protected zone and these indices show the shifted PD current signal. The delay time for each index depends on the location of defect point wrt each end of the cable.

The final step to determine the location of PD is to find the time difference between the observation of \mathcal{E}_S and \mathcal{E}_R at the two ends of the cable. In order to perform this calculation, the cross correlation (CC) of them is calculated, in analog mode, according to different time shifting and through the following relation:

$$CC|_{\text{shift}=t_{sh}} = \int_{t_0}^{t_0+t_{DW}} \mathcal{E}_S(t) \mathcal{E}_R(t + t_{sh}) dt \quad (20)$$

The CC value is obtained for time duration

($t_0 \sim t_0 + t_{DW}$) and by considering different shift times, i.e. t_{sh} , in order to find its maximum value. The t_{DW} is the data window (DW), and is described in the next section. Introducing, $N_{DW} = t_{DW} \cdot f_s$ and $N_{sh} = t_{sh} \cdot f_s$, in digital mode, (20) becomes:

$$CC|_{\text{shift}=N_{sh}} = \sum_{k=k_0}^{k_0+N_{DW}} \mathcal{E}_S(k) \mathcal{E}_R(k + N_{sh}) \quad (21)$$

Calculating CC for $N_{sh} = 0, 1, 2, \dots, N_{\tau_1}$ (N_{τ_1} corresponding to τ_1), and finding (N_{sh}^{Max-CC}), i.e. the sample at which CC takes the max. value, the PD location can be determined as:

$$x = \frac{L_1}{2} \left(1 + \frac{N_{sh}^{Max-CC}}{N_{\tau_1}} \right) \quad (22)$$

Obviously, by considering \mathcal{E}_R as stationary signal and \mathcal{E}_S as the shifted one in (21), the distance of the defect point from the receiving end will be obtained.

IV. MODELING AND IMPLEMENTATION

The cable network is modeled in ATP as in Fig. 2, with the following details:

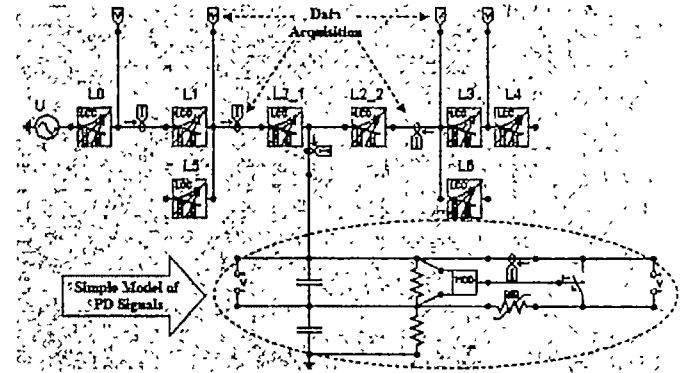


Fig. 2. Cable network with inserted simple PD generator in section L2 (Data are obtained through V and I sensors, installed in the cable ends)

A. Cable Modeling

For this purpose, the Bergeron model [1-3] of single phase cable is used.

B. PD Modeling

The PD signals are generated through a two-capacitors model [5].

In this model:

- The top capacitor is the representative for the

spherical cavity in the insulation layer.

- The bottom one is the equivalent capacitor for the residual insulation in the same column.
- The shunt resistors are the cavity resistance and the insulation resistance.

When voltage across cavity capacitor rises and exceeds the defined breakdown voltage, the T switch will be closed. Then this capacitor will be discharged via non-linear resistance R(i). If cavity voltage decreases to under a determined voltage (i.e. residual voltage), the switch will be opened and again the top capacitor will be charged.

C. Data Window Duration

It is possible to choose a long data window, but the calculation burden becomes large. Decreasing DW may be performed until that it reaches at least half of the PD signal duration (e.g. as the duration of PD signals in this simulation is about 3.5 micro-seconds, selecting DW as 2 ~ 4 micro-seconds is suitable).

In general, DW should have the following properties:

- For reducing the calculation burden, DW should be selected with the lowest possible duration.
- The DW must contain suitable information for PD diagnosis.
- DW starting edge must be determined according to the instant that PD current value exceeds a pre-determined threshold (next sub-section).

D. Selecting Thresholds

In real cases, for external PDs, the introduced indices will be non-zero for the following reasons:

- In spite of available procedures for advanced signal de-noising, some noises with low amplitudes remain.
- A/D converters have errors [6], which make some small pulses to be appeared in the output.

In addition,

- Low intensity PDs that normally exist in HV devices are non-important and should be ignored in the proposed algorithm.
- PD in the new cables should be not exceed 10pc[7-8], but much more than this value is not a reason for any emergency conditions. So the thresholds should be selected as such that only enables the detection of growing PDs.

Consequently, in order to determine a practical threshold, a considerable PD source (e.g. 1 nc) is inserted along the protected cable and near each end of it. The TW indices are calculated and the minimum value of them is chosen as the above-mentioned threshold.

Therefore, PD in-zone detection criterion can be presented as:

$$\varepsilon_s(k_s) > Thr \quad \& \quad \varepsilon_r(k_r) > Thr \\ \Rightarrow PD \text{ DETECTED}$$

V. INDICES MEASUREMENT AND PD DETECTION IN PROTECTED CABLE

The proposed algorithm, in digital mode, is implemented as in the following:

1. On-line sampling of voltage and current at cable ends
2. Filtering power frequency component of the signals in companion with performing signal de-noising
3. Calculation of TW based indices according to the cable length
4. Comparing indices with thresholds
 - i. Saving next $N_t + N_{DW}$ voltage and current samples, if any of the two indices exceeds the threshold.
 - ii. If during the above process, the other index exceeds the threshold before N_t samples from the start, then PD is detected and step '5' will be followed. Otherwise, return to step 1.
5. Calculating CC for each N_{sh} which takes the values from 1 to N_t and finding its maximum and corresponding sample N_{sh}^{Max-CC}
6. Determining PD location based on N_{sh}^{Max-CC}

Fig. (3) shows the flowchart of the above algorithm.

The voltage and current signals of the cable L_2 in Fig. (2), with 10km length are shown in Fig. (4-a). The forward and backward voltage components for two cable ends are shown in Fig. (4-b) and TW based indices and PD current in point F are shown in Fig. (4-c). The defect point F is placed at 500 m far from the sending end. Choosing the sampling frequency as 10MHz, the proposed algorithm determines the PD location at 502.8736 m far from the sending end that shows only 0.575 % error.

Fig.(5) shows the percentage of error in PD location for different sampling frequencies which proves the accuracy of the proposed method.

Although different DW does not affect this accuracy, but, in noisy conditions, it is expected that longer DW raises the accuracy of PD location procedure.

VI. CONCLUSION

In this paper, an integrated and complete approach for detection, location and PD signal reconstruction in HV cables has been proposed, based on TW indices. The results showed that the proposed algorithm has a very dependable accuracy for PD location and reconstruction of PD current signal. By increasing the sampling frequency, this small error is even reduced, while the calculation burden is increased.

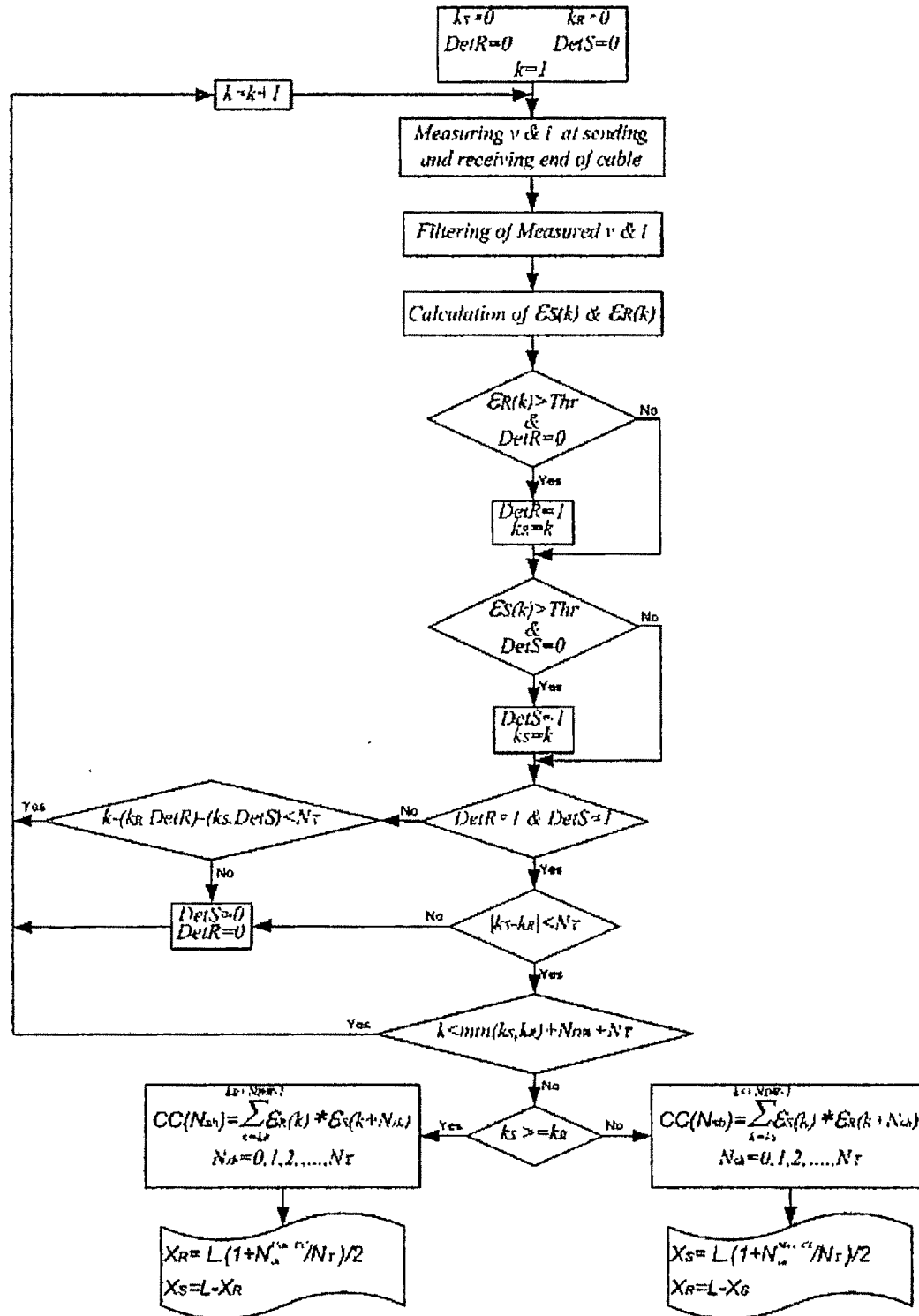


Fig. 3. The flowchart of the proposed method

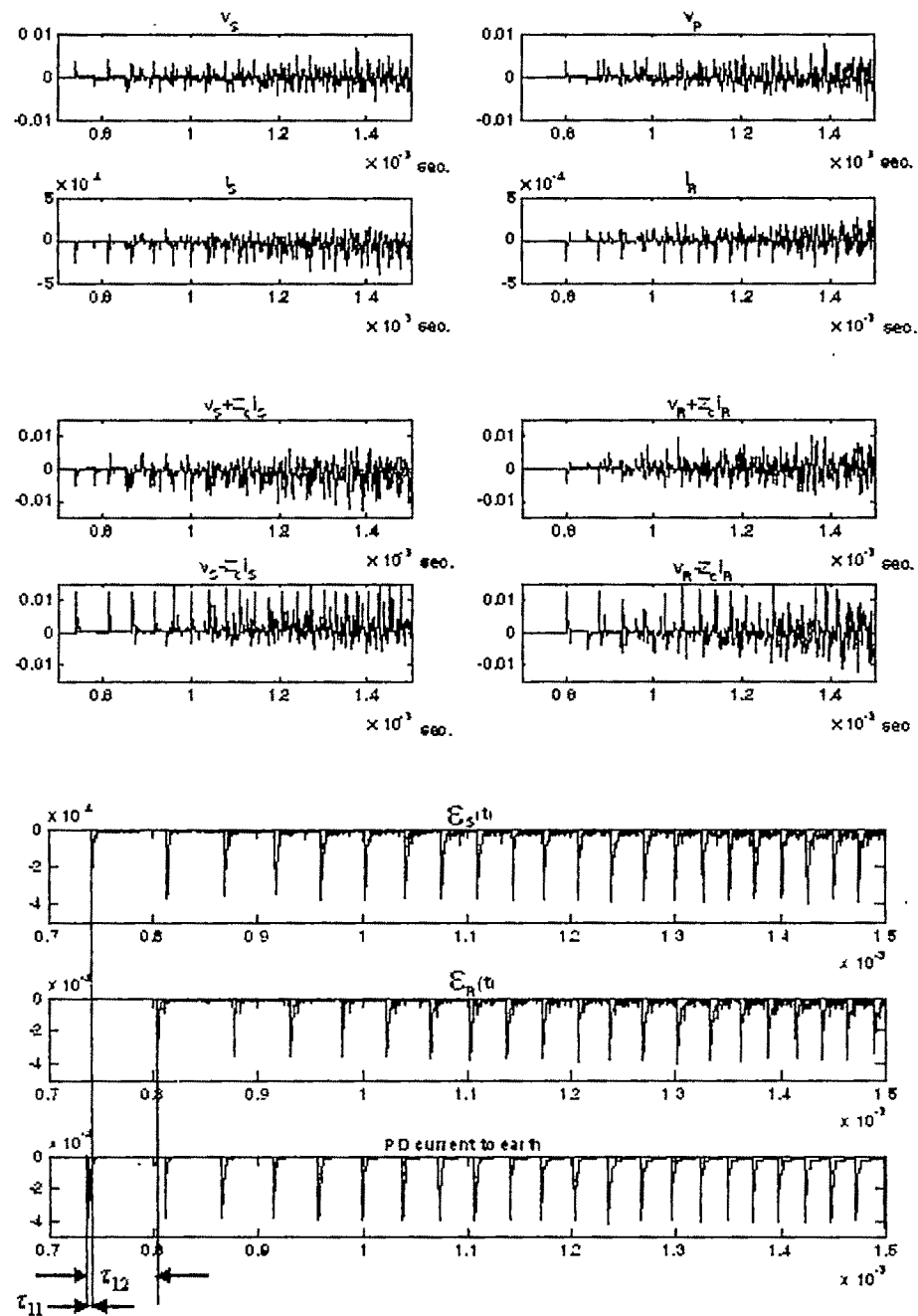


Fig. 4 (a) Voltage and current signals, (b) Forward and backward voltage waves and (c) Indices and PD current

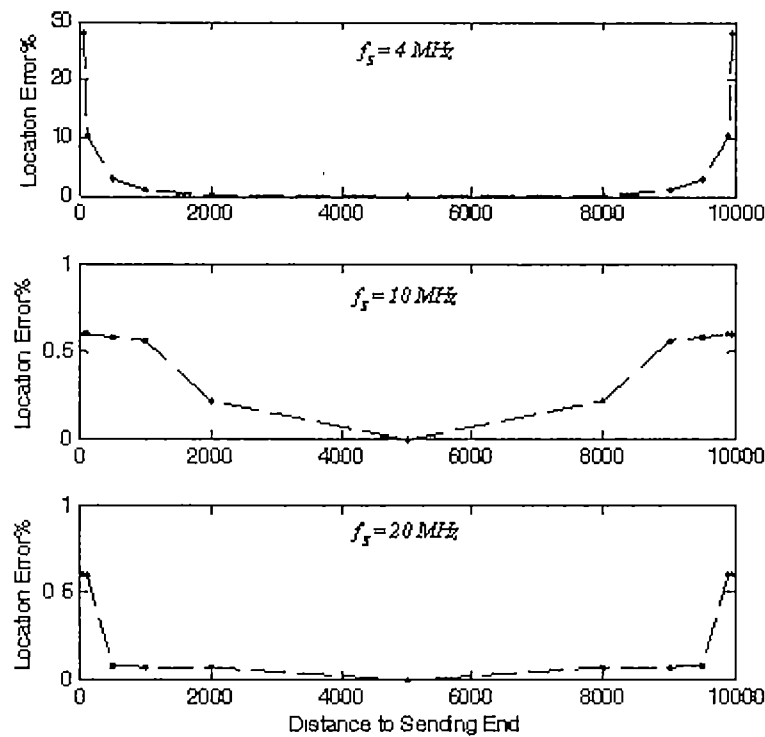


Fig 5 Percentage of error in PD location for different sampling frequencies

REFERENCES

- [1] Allan Greenwood; Book "Electrical Transients in Power Systems", 1991
- [2] J P Bickford, N. Mullineux, J. R. Reed; Book "Computation of Power-System Transients"; 1976.
- [3] Hermann W Dommel, "EMTP Theory Book"
- [4] Steven Boggs, Ash Pathak, Philip Walker, "Partial Discharge XXII: High Frequency Attenuation in Shielded Solid Dielectric Power Cable and Implications Thereof for PD location"; IEEE Electrical Insulation Magazine; Vol. 12, No. 1, pp 9-16, January/February 1996.
- [5] Kolev, N P.; Gadjeva, E D; Danikas, M.G., Gourov, N R.; "An Approach to Develop a Partial Discharge Investigation"; Proceeding of Electrical Insulation Conference and Electrical Manufacturing & Coil Winding; pp. 507-510, 26-28 Oct. 1999.
- [6] Galia D Muginov, Anastasios N Venetsanopoulos; "A New Approach for Estimating High-Speed Analog-to-Digital Converter Error"; IEEE Transactions on Instrumentation and Measurement, Vol 46, No 4, pp. 980-985, August 1997.
- [7] Moh Shew Chong; "Partial Discharge Mapping of Medium Voltage Cables - TNB'S Experience"; CIRED, 16th International Conference and Exhibition on Electricity Distribution (IEE Conf. Publ. No. 482), Vol. 1, 18-21 June 2001.
- [8] Edward Gulski, Frank J Wester, Johan J. Smit, Paul N Seitz, Mark Turner; "PD Detection in Power Cables Using Oscillating Wave Test System", IEEE International Symposium on Electrical Insulation, USA, April 2-5, 2000.

Reduced Order LQG Controller for Distribution Static Compensator used for Load Voltage Control of Distribution System

Rajesh Gupta¹ and Arindam Ghosh²

¹Department of Electrical Engineering, MNNIT, Allahabad, India, e-mail: rajeshgupta@mnnit.ac.in

²School of Engineering Systems, QUT, Brisbane, Qld, Australia., e-mail: a.ghosh@qut.edu.au

Abstract— In this paper, a Linear Quadratic Gaussian (LQG) controller is proposed for the distribution static compensator (DSTATCOM) system. This eliminates the need of full state feedback and also incorporates the effect of random load variations and polluted load voltage conditions. To further reduce the complexity of controller, a reduced order controller is designed for the DSTATCOM that is used for the load voltage control. First, the fourth order model of the DSTATCOM is reduced to the second order using balancing method of model reduction. A second order LQG controller is then designed for the inverter switching control of the DSTATCOM. The use of method of balanced realization indicates that there is a possibility of approximate second order plant model based on a-priori error bound. It is shown that the second order model reduced from the full order plant gives a closely matched frequency response characteristics over a wide range of frequencies. This yields steady state and dynamic performance of the DSTATCOM using reduced order controller to be approximately same as when used with the full order controller. It is shown that the DSTATCOM using proposed reduced order LQG controller regulates the load voltage. The theoretical results are verified for the single-phase control of the DSTATCOM using simulation studies.

Key words—Controller, DSTATCOM, LQG, Reduced-order.

I. INTRODUCTION

THE distribution static compensator (DSTATCOM) is an important device for the control of the load voltage of a distribution system [1]-[4]. The stable operation of the DSTATCOM requires state-feedback control for tracking of the reference load voltage [1], [2]. This requires full state feedback using various variables of the DSTATCOM system. Use of number of sensors and feedback of many variables limits the use of the DSTATCOM as voltage regulating device. Use of dynamic estimator minimizes the number of sensors required for the feedback of the variables. However random load variations and polluted point of common-

-coupling (PCC) voltage makes the control and estimation stochastic in nature. The LQG controller has been a widely used controller for the control of references and estimation of the states under such stochastic conditions of the system.

In this paper, an LQG controller is designed for the DSTATCOM that is regulating the voltage at the PCC of the distribution system. This eliminates the need of full state feedback and also incorporates the effect of random load variations and polluted PCC voltage conditions. Design of LQG controller from full order DSTATCOM model, leads to a higher order controller. This increases the complexity of the controller implementation. A reduced order LQG controller can be designed using balanced method of model reduction [5]. This method has been used in this paper to design a low order LQG controller for the DSTATCOM that is used for the PCC voltage control. First, the fourth order model of the DSTATCOM is reduced to the second order model. A second order LQG controller is then designed for the inverter switching control of the DSTATCOM. The advantage of using balanced realization is that it indicates the possibility of approximate second order plant model based on a-priori error bound. Also the method yield closely matched frequency response characteristics over a wide range of frequencies.

II. DSTATCOM MODEL

Fig. 1 shows a typical DSTATCOM compensated electrical power distribution system. It is desired to use the DSTATCOM in voltage control mode [1]-[4]. In this mode the terminal voltage v_t at the PCC is controlled against the variations in the source voltage v_s and load changes.

Consider the distribution system that consists of a linear load (R_l, L_l) and supplied from the voltage source v_s through a feeder (R, L) as shown in Fig. 1. The DSTATCOM consists of a voltage source inverter (VSI) that is connected to the PCC through a transformer T_1 of voltage ratio 1: n . The VSI constitutes of switches Sw_1 to Sw_4 that is made of a power semiconductor device like IGBT and an anti-parallel diode. The voltage V_{dc} represents the dc link voltage of the VSI. The inductance and resistance in the shunt path referred towards

secondary side of the transformer are L_T and R_{in} respectively. The resistance R_{in} also includes any other loss component such as inverter conduction and switching losses. The filter capacitor C_f is connected across the PCC. The currents flowing through the different branches are: the source current i_s , the load current i_l , the current through the filter capacitor i_{cf} , the inverter output current i_{in} and the current injected in the shunt branch i_{sh} . The net controllable voltage at the output of the VSI is uV_{dc} , where u is defined as the control input and represents the switching logic of the inverter. The parameters of the system shown in Fig. 1 are given in Table 1. The equivalent circuit of the DSTATCOM system of Fig. 1 is shown in Fig. 2.

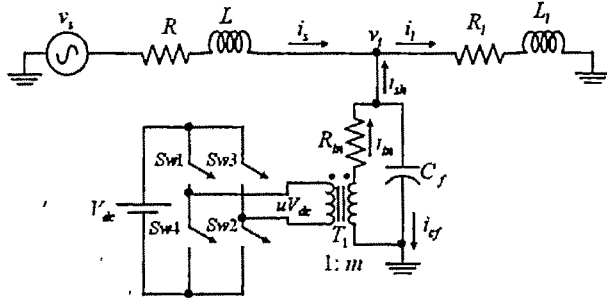


Fig. 1 A DSTATCOM compensated distribution system

Table 1 System parameter

Parameters	Numerical value
Source voltage (v_s)	6.00 kV (rms)
Frequency (f)	50 Hz
Feeder impedance (R, L)	6.05 Ω , 0.1155 H
Filter capacitor (C_f)	77.75 μF
DC bus voltage (V_{dc})	500V
Transformer (T_1)	1MVA, 440V/11KV,
Equivalent shunt impedance (R_{in}, L_T)	6.0 Ω , 38.5 mH,

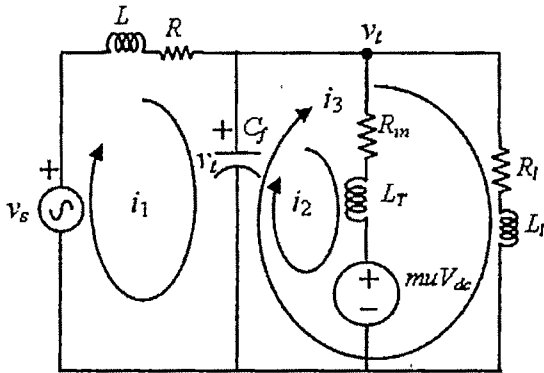


Fig. 2 Equivalent circuit of the system of Fig 1.

Comparing Fig. 1 with Fig. 2 following relations can be written.

$$i_s = i_1; \quad i_l = i_3; \quad i_{cf} = i_1 - i_2 - i_3; \quad i_{sh} = i_3 - i_1 \quad (1)$$

Choosing the state vector $x^T = [i_1 \ i_2 \ i_3 \ v_l]$, the following state space representation is obtained.

$$\dot{x} = Ax + b_1 v_s + b_2 u \quad (2)$$

where,

$$A = \begin{bmatrix} -R/L & 0 & 0 & -1/L \\ 0 & -R_{in}/L_T & 0 & 1/L_T \\ 0 & 0 & -R_l/L_l & 1/L_l \\ 1/C_f & -1/C_f & -1/C_f & 0 \end{bmatrix}, b_1 = \begin{bmatrix} 1/L \\ 0 \\ 0 \\ 0 \end{bmatrix}, b_2 = \begin{bmatrix} 0 \\ -mV_{dc}/L_T \\ 0 \\ 0 \end{bmatrix}$$

In order to have tractable state variables, the following state transformation is performed.

$$z = [i_{sh} \ i_{cf} \ v_l \ i_l]^T = \begin{bmatrix} -1 & 0 & 1 & 0 \\ 1 & -1 & -1 & 0 \\ 0 & 0 & 0 & 1 \\ 0 & 0 & 1 & 0 \end{bmatrix} x = Px \quad (3)$$

The state equation (2) is then transformed into the following new set of state model.

$$\dot{z} = PAP^{-1}z + Pb_1 v_s + Pb_2 u_c = \bar{A}z + \bar{b}_1 v_s + \bar{b}_2 u_c \quad (4)$$

Following output equation is obtained with terminal voltage v_l as output.

$$y = Cz = [0 \ 0 \ 1 \ 0]z \quad (5)$$

In view of designing controller in the discrete-time domain, it is required to first discretized the plant model.. If the sampling period is denoted by t_d then the model (2) and (5) is discretized as [6]

$$z(k+1) = A_d z(k) + b_{1d} v_s(k) + b_{2d} u_c(k) \quad (6a)$$

$$y(k) = C_d z(k) \quad (6b)$$

where,

$$A_d = e^{\bar{A}t_d}; \quad b_{1d} = \int_0^{t_d} e^{\bar{A}\tau} \bar{b}_1 d\tau; \quad b_{2d} = \int_0^{t_d} e^{\bar{A}\tau} \bar{b}_2 d\tau \quad (7)$$

With the choice of parameters given in Table 1 and sampling period t_d of 10 μs , the system matrices of (6) are listed in Appendix A.

III. LQG CONTROL

The state space model of (2) is obtained under the deterministic conditions. However due to random load variations and polluted PCC conditions, the appropriate way to represent the system is through stochastic model. Following is the standard stochastic state space model of the system [7].

$$\text{State equation: } \dot{z} = \bar{A}z + \bar{b}_1 v_s + \bar{b}_2 u + \bar{b}_3 w \quad (8a)$$

$$\text{Measurement equation: } y = C_1 z + v \quad (8b)$$

$$\text{Output equation: } n = C_2 z \quad (8c)$$

where, v , w and the initial condition x_0 are Gaussian stochastic processes and independent of each other. In addition, v and w are zero mean with following covariance matrices

$$E[v(t)v^T(\tau)] = R_v \delta(t-\tau), \quad E[w(t)w^T(\tau)] = R_w \delta(t-\tau) \quad (9a)$$

$$E[x(t_0)] = X_0, E[x(t_0)x^T(t_0)] = \Sigma_0 \quad (9b)$$

It is desired to design a discrete-time linear quadratic infinite-time tracking control and therefore the system of (8) is discretized. Then the following performance index is defined.

$$J = E \left\{ \sum_{k=0}^{\infty} (z(k) - z_{ref}(k))^T Q (z(k) - z_{ref}(k)) + u^T(k) R u(k) \right\} \quad (10)$$

A switching function $u_c(k)$ may be determined using the control law of the following form [1]

$$u_c(k) = -K(z(k) - z_{ref}(k)) \quad (11)$$

where, K is the optimal feedback gain matrix determined after minimization of (10). In case of switching control tracking of DSTATCOM, the control input to the DSTATCOM, i.e., $u(k)$ is determined from the switching function $u_c(k)$ using the relay function $\phi(\cdot)$ [2]. The relay function relates input $u_c(k)$ to the output $u(k)$ as

$$\begin{aligned} u(k) &= +1 \quad \text{for } u_c(k) > 0 \\ u(k) &= -1 \quad \text{for } u_c(k) < 0 \end{aligned} \quad (12)$$

Since $z(k)$ in (11) is not accessible for feedback, it is estimated as $\hat{z}(k)$ using steady state Kalman filter [7]. The filter equation is given by the following form

$$\hat{z}(k+1) = (A_d - b_{2d}K - K_e C_d) \hat{z}(k) + K_e y(k) + b_{2d} K z_{ref}(k) \quad (13)$$

where K_e is the error estimation gain matrix. For the state feedback control (11), the reference z_{ref} for state vector z must be calculated. Suppose it is desired that the inverters inject a current i_{sh} such that the load terminal (PCC) voltage v_l has an rms value of 6.35 kV and lags the source voltage by 20° . Then from Fig. 1 and using the parameters given before, the following reference values are calculated for a frequency $f = 50$ Hz.

$$v_{lref}(t) = 8980 \sin(100\pi t - 20^\circ) \text{ V} \quad (14a)$$

$$i_{shref}(t) = 72.6552 \sin(100\pi t - 160.65^\circ) \text{ A} \quad (14b)$$

$$i_{cfref}(t) = 219.3570 \sin(100\pi t + 70^\circ) \text{ A} \quad (14c)$$

where the subscript 'ref' in (14) denotes the reference values. It is to be noted that the reference for load current is set as zero, i.e., $i_{lref} = 0$. This is because the load changes at any time during the operation and the DSTATCOM must cater to these changes. The random variation of load is modeled through white noise in (9). Fig. 3 shows the full block diagram of LQG based control of the DSTATCOM. The block diagram shows the discretized plant with discrete-time LQG controller.

As stated in [7], the non-linear relay controlled system using LQG design as shown in Fig. 3 has guaranteed robustness when the following two conditions are satisfied.

Condition 1: $\phi(\cdot)$ belongs to the sector $(1/2, \infty)$ such that at the non-linearity insertion point there is a gain margin $(1/2, \infty)$ and a phase margin of 60° .

Condition 2: The design of estimator/controller gains K_e/K are such that the pathway from the control u to the estimator is relatively inconsequential or the estimator output is far more dependent on the plant output y than on the plant input u .

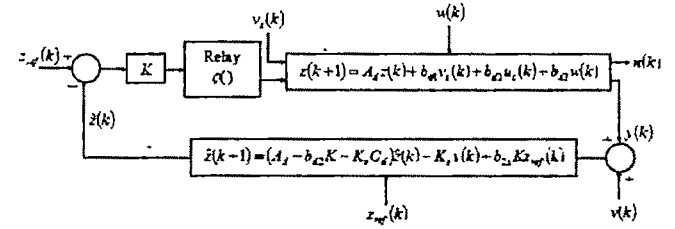


Fig. 3 Discrete-time equivalent of LQG based switching control of DSTATCOM.

IV. REDUCED ORDER CONTROLLER DESIGN

In this section a reduced order LQG controller is designed for the full order system. The full order DSTATCOM model (8) is first discretized. The equivalent discrete model is reduced to a reduced order model. The low order LQG controller is then designed for the reduced order system model. The method of balancing technique is used to reduce the higher order system model.

Let us consider the stochastic model of DSTATCOM compensated distribution system (8). The system is discretized with a sampling period of 10 μ s. Following matrices are defined as, the weighting matrices Q and r , intensity matrices R_w and R_v , and input matrix \bar{b}_3 . The weighting matrices are considered on the basis of priority of the state control and cost in the input respectively for Q and R in (10). The intensities matrices are chosen based on the disturbance effect. The input matrix \bar{b}_3 is chosen depending on the effect of stochastic disturbance on each state. These matrices are defined as

$$\begin{aligned} Q &= \text{diag}[1 \ 0 \ 10 \ 0]^T \quad r = 0.1 \\ R_w &= 1.0 \quad R_v = 0.01 \quad \bar{b}_3 = [10 \ 100 \ 10 \ 100] \end{aligned} \quad (15)$$

Maximum weighting is given to PCC terminal voltage control. The load and filter current is not given any weightage [1], [2]. Random variation of load and switching component in filter current are most disturbed and this appears in disturbance matrix. The PCC polluted terminal voltage is under measurement error. It is assumed that the terminal voltage is the only measurable variable and accessible for feedback. The desired outputs are capacitor filter current i_{cf} , shunt injected current i_{sh} and terminal voltage v_l . Therefore in (8), following are chosen.

$$C_1 = [0 \ 0 \ 1 \ 0], \quad C_2 = \begin{bmatrix} 1 & 0 & 0 & 0 \\ 0 & 1 & 0 & 0 \\ 0 & 0 & 1 & 0 \end{bmatrix}; \quad (16)$$

Under these conditions, it is desired to design a second order reduced discrete-time LQG controller, which estimates the states and tracks the reference variable z_{ref} .

Balanced realization for the full order model given in Appendix A, has been obtained. The Hankel singular values for the model is calculated as $\{2.4146, 1.9702, 0.1392, 0.0034\} \times 10^4$. First two dominant singular values indicate the possibility of reduced second order model with an L_∞ -error norm of 62 db. The full order discrete model given in Appendix A is reduced to a second order model using discrete-time balancing technique [5]. The reduced order model is given in Appendix B. Fig. 4 shows the comparison of the bode plots of the original and reduced models. Figure shows the close approximation of the reduced model to the full model over wide range of frequencies. This indicates that both dynamic and steady state characteristics of the reduced order model will approximate the full order model under closed loop.

A reduced second order LQG controller (11) and (13) has been designed after correspondingly reducing the model (8) and weighting/intensity matrices (8). The reduced controller equation (13) is given in Appendix C.

It may be noted that the gain of the relay nonlinearity is generally very high, which satisfies the Condition 1 in Section III. Furthermore, the gain of the control input to estimator is calculated as 2.08 and the gain from output to the estimator calculated as 77949 at power frequency. This implies that the estimator output is far more dependent on the plant output than the control input. This satisfies the Condition 2. Therefore the LQG design has guaranteed robustness.

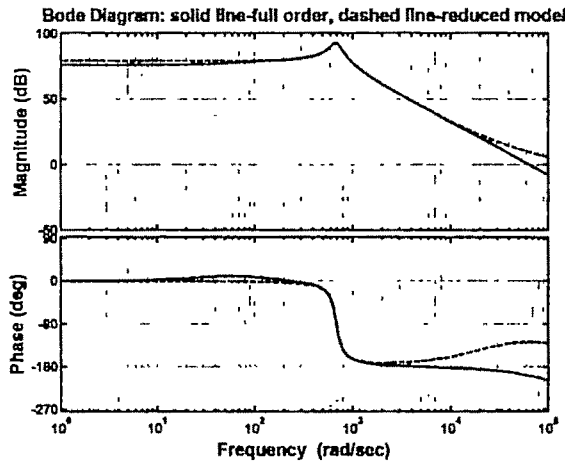


Fig. 4 Bode diagram of full order and reduced order models.

Implementation of ideal relay algorithm (12) will lead to infinitely large switching frequency for the switches used in the VSI shown in Fig.1. In order to avoid this a hysteresis band (h) is introduced with the ideal relay. The modified algorithm of the relay with hysteresis is given by

$$\begin{aligned} u(k) &= +1 \quad \text{for } u_c(k) > +h \\ u(k) &= -1 \quad \text{for } u_c(k) < -h \end{aligned} \quad (17)$$

V. SIMULATION RESULTS

Consider the system parameters given in Table 1 and references defined in (14). Fig. 5 shows the tracking performance of the DSTATCOM using the reduced order LQG controller designed in Appendix C. Figure shows the tracking of the reference terminal voltage v_t , filter capacitor current i_{cf} and shunt current i_{sh} . Fig. 6 shows the tracking error in the corresponding variables. The hysteresis band chosen in (17) for tracking of the reference is $h = 0.0359$. This leads to the switching frequency of 8 kHz for the switches of VSI. The tracking characteristics are found satisfactory with this finite switching frequency. The source voltage and load are considered variable during the simulations. This shows that the DSTATCOM regulates the terminal voltage..

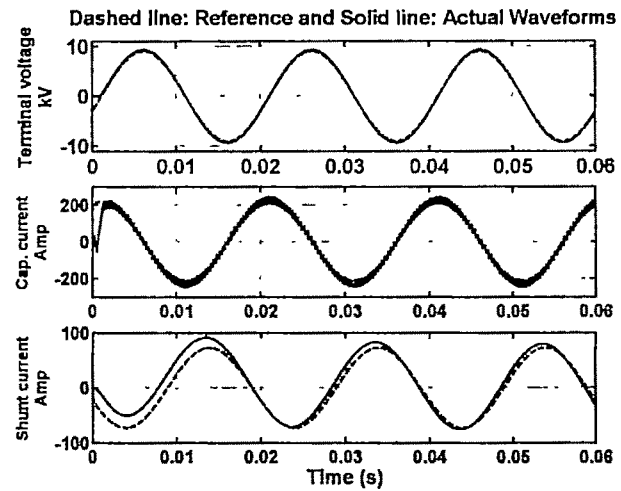


Fig. 5 Tracking of the references for terminal voltage, filter capacitor current and shunt current by DSTATCOM.

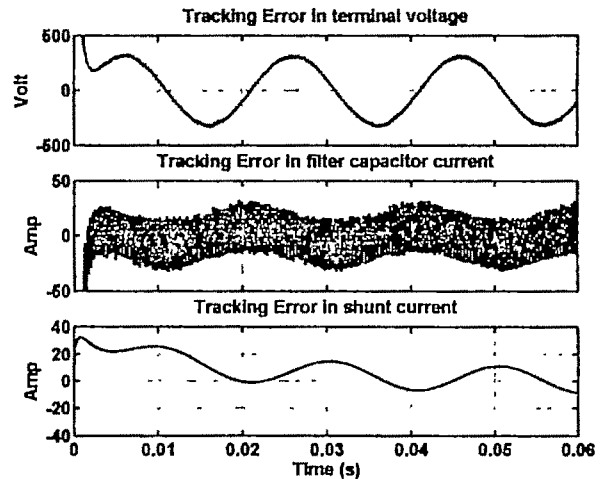


Fig. 6 Tracking error in terminal voltage, filter capacitor current and shunt current.

VI. CONCLUSION

The second order LQG controller designed for the DSTATCOM, controls the voltage at the PCC. The kalman

filter designed for the estimation of the states minimizes the number of sensors required for the state feedback control under stochastic system conditions. The method of balancing technique of model reduction gives close approximation of the reduced order model to the full order model over wide range of frequencies. An a-priori error bound indicated the presence of valid second order model. The use of high gain nonlinear relay ensures the robust performance of the DSTATCOM with the LQG controller.

APPENDIX A

Following system matrices are obtained after discretization.

$$A_d = \begin{bmatrix} 0.999 & 6.67 \times 10^{-6} & 1.03 \times 10^{-4} & -3.65 \times 10^{-3} \\ -1.04 \times 10^{-3} & 0.998 & -3.63 \times 10^{-4} & 3.65 \times 10^{-4} \\ -6.72 \times 10^{-5} & 0.128 & .999 & 2.35 \times 10^{-4} \\ -3.87 \times 10^{-10} & 1.11 \times 10^{-6} & 1.72 \times 10^{-5} & 0.995 \end{bmatrix}$$

$$b_{1d} = \begin{bmatrix} -8.65 \times 10^{-5} \\ 8.65 \times 10^{-5} \\ 5.56 \times 10^{-6} \\ 3.21 \times 10^{-11} \end{bmatrix}; \quad b_{2d} = \begin{bmatrix} 7.22 \times 10^{-6} \\ 3.24 \\ 0.208 \\ 1.20 \times 10^{-6} \end{bmatrix}; \quad C_d = [0 \ 0 \ 1 \ 0]$$

APPENDIX B

System matrices for the reduced order model are given below.

$$A_{red} = \begin{bmatrix} 0.999 & 6.75 \times 10^{-3} \\ -6.75 \times 10^{-3} & 0.999 \end{bmatrix};$$

$$b_{1red} = \begin{bmatrix} 1.34 \times 10^{-4} \\ 1.75 \times 10^{-4} \end{bmatrix}; \quad b_{2red} = \begin{bmatrix} 5.57 \\ 5.39 \end{bmatrix}; \quad b_{3red} = \begin{bmatrix} 1.55 \times 10^{-3} \\ 2.82 \times 10^{-3} \end{bmatrix};$$

$$c_{red} = [5.57 \ -5.39]$$

APPENDIX C

Designed second order controller equation is given below.

$$\hat{z}(k+1) = \begin{bmatrix} -8.51 & 8.19 \\ -9.13 & 8.84 \end{bmatrix} \hat{z}(k) + \begin{bmatrix} 0.026 \\ 0.012 \end{bmatrix} y(k)$$

$$+ \begin{bmatrix} 9.36 & -8.04 & -2.14 & 0.81 \\ 9.06 & -7.78 & -2.07 & 0.78 \end{bmatrix} z_{ref}(k)$$

$$K = [1.68 \ -1.44]$$

REFERENCES

- [1] G. Ledwich and A. Ghosh, "A flexible DSTATCOM operating in voltage or current control mode," *IEE Proc. - Generation, Trans. & Distrib.*, vol. 149, No. 2, pp. 215-224, March 2002.
- [2] A. Ghosh and G. Ledwich, *Power Quality Enhancement using Custom Power Devices*, Kluwer Academic Publisher, Boston, MA, 2002.

- [3] M. K. Mishra, A. Ghosh and A. Joshi, "Operation of a DSTATCOM in voltage control mode", *IEEE Trans. Power Delivery*, vol.18, no.1, pp.258-264, Jan. 2003.
- [4] R. Gupta and A. Ghosh, "Frequency-domain characterization of sliding mode control of an inverter used in DSTATCOM application", *IEEE Trans. Circuits. Sys.- I: Reg. Papers*, vol.53, no.3, pp. 662-676, March 2006.
- [5] L. Pernebo, and L. M. Silverman, "Model Reduction via balanced state-space representation", *IEEE Transaction on Automatic Control*, vol. 27, pp. 382-387, 1982.
- [6] B. C. Kuo, *Digital Control Systems*, Oxford University Press, Inc, Madison Avenue, New York, 1992.
- [7] B. D. O. Anderson and J. B. Moore, *Optimal Control: Linear Quadratic Methods*, Englewood Cliffs, NJ: Prentice-Hall, 1990.

Concept and Benefits of Microgrid System with Modeling and Simulation

Prasenjit Basak¹, S.P. Chowdhury², and S. Chowdhury³

¹ Research Scholar, Jadavpur University, e-mail: prasenjitbasak1@yahoo.co.in

² Reader, Electrical Engg. Deptt Jadavpur University, e-mail: spchowdhury63@yahoo.com

³ Lecturer, Women's Polytechnic, Jodhpur Park, e-mail: suncitra69@yahoo.com

Abstract— The electrical power utility structure is changing the power generation concept worldwide and opening up new challenges in the generation and distribution markets. Restructuring of power markets is helping towards penetration of Distributed Generation (DG) in the electricity networks. Electric utilities are seeking new technologies to provide good quality power and reliability to their customers. Small non-conventional generation option is rapidly becoming attractive to many utilities because these technologies produce electrical power with less environmental impacts, are easy to install, and are highly efficient. As the awareness on environmental issues like global warming increasing, renewable energy source becoming a most significant source of energy. Geographical, Environmental, Political and financial factors of different countries lead to increased use of many renewable energy sources like Wind Electric Conversion System, Photovoltaic (PV) System, Biomass System and Fuel Cell System etc.

Low power generation capacity of individual distributed resources (DRs) ignited the requirement of integration of different types of DRs to enhance the power capacity, reliability and marketability as a whole, and the concept of Microgrid is established as an integrated form of generation, storage and load systems with suitable power electronics based control mechanism capable of working under main grid connected mode and islanded mode. Microgrid system should be well equipped with generation and storage technologies. Photovoltaic Cells, Micro-turbines, Fuel cells, Wind turbines, Reciprocating engines and small Hydro-turbines etc, contribute generation technologies. Batteries, Flywheels, Superconducting magnetic energy storage systems, and Super capacitors etc implement storage technologies. All these distributed generation and storage technologies could be grouped together into Microgrid.

The purpose of this paper is to present the concept and benefits of Microgrid system formed by DRs and the other main purpose is to describe a model of Microgrid system simulated by Matlab software. Many new issues have created a new scenario for the electric power infrastructure such as, deregulation of the electric utility industry, public awareness of the environmental impacts of electric power generation, rapid increases in electric power demand and significant advancement in several generation technologies which are more environment friendly than conventional coal, oil and gas fired plants. An approach to quantify the above points is proposed, results are discussed with necessary diagrams, Matlab model curves etc. In order to represent an appropriate figure of the Microgrid performance.

Key words— DER, Microgrid, Photovoltaic Cell, Simulation.

I. INTRODUCTION

The world is becoming more crowded day by day. The conventional sources of energy will be exhausted by the end of the century or beginning of the next century. Nuclear energy requires skilled technicians and poses the safety as regards to radioactive waste disposal. Solar energy and other non-conventional energy sources are the sources; those are to be utilized in future. Demand for energy will continue to grow even if governments of various countries adopt policies to conserve energy. This growth must increasingly be satisfied by resources. The continued growth of energy demand requires that energy resources be developed with the utmost care. Electricity from nuclear power is capable of making an important contribution to the global energy supply although worldwide acceptances of it, on a sufficiently large scale, yet to be established.

Coal has the potential to contribute substantially to future energy supplies but due to the limitations on availability all the countries are thinking suitable alternative over it. Also, the use of natural gas is constrained by incentives and costly inter continental gas transportation systems. Under this situation, other than hydroelectric power, renewable resources of energy e. g., solar, wind, wave will contribute remarkable quantities of additional energy during the century worldwide.

Now, the integration of individual alternative small power source is rapidly changing the power scenario and interest in Distributed Energy Resources (DER) is being increased rapidly. The uneconomical larger power plants in many regions due to increasing system and fuel costs, and environmental regulations, are not suitable prospective in future power generation stage. In addition, recent technological advances in small generators, Power Electronics, and energy storage devices have provided a new opportunity for distributed energy resources at the distribution level, and especially, the incentive laws to utilize renewable energies has also encouraged a more

decentralized approach to power delivery and energy efficiency improvements. Policies for achieving energy conservation should continue to be the key elements of all future energy strategies.

Few countries in the world have placed as much faith in renewable energy sources as India has. When the world was reeling under the oil price shocks of 1973 and 1979, every nation had made a beeline for renewable energy sources as alternatives to fossil fuels.

ROLE OF INDIA

India has implemented a lot of policies over renewable energy sources and it was reflected in the numerous policy decisions taken by the government at the highest level. India is one of the few countries, which have a full-fledged ministry belong to non-conventional energy sources. There is a renewable energy development agency at the centre and similar agency in most of its states.

II. DISTRIBUTED ENERGY RESOURCES AND MICROGRID CONCEPT

Evolutionary changes in the regulatory and operational climate of traditional electric utilities and the emergence of smaller generating systems such as micro turbines have opened new opportunities for on-site power generation by electricity users. In this context, distributed energy resources (DER) - small power generators typically located at users' sites where the energy (both electric and thermal) they generate is used - have emerged as a promising option to meet growing customer needs for electric power with an emphasis on reliability and power quality. The system of DER includes generators, energy storage, load control, and, for certain classes of systems, advanced power electronic interfaces between the generators and the bulk power provider. It is desired that the significant potential of smaller DER to meet customers' and utilities' needs can be best utilized by combining these resources into MicroGrids.

The main features of DER generating technologies based on Microgrid concept is their interconnection through inverter-like power electronics. The effort is initially focused on micro turbines and fuel cells and other emerging technologies that might ultimately be used in Micro Grids could be larger.

Customers benefit from a Micro Grid because it is designed and operated to meet their local needs for heat and power as well as provide uninterruptible power, enhance local reliability, reduce feeder losses, and support local voltages. The pattern of exchange of energy services between the Micro Grid and the bulk power provider grid is determined by commercial conditions.

III. MICROGRID COMPONENTS

Many small (less than 250-kW) generation and storage technologies are already being used to save peak generation

and provide back-up generation during power system outages. This gives a brief overview of each of the major technologies currently in use or expected to soon become available. These technologies are divided into two major categories: generation and storage. Brief overview of Generation technologies described below.

Micro-turbine: Micro turbines, generally fueled by natural gas, are composed of a generator and small gas turbine mounted on a single shaft. Micro turbines rotate at high speeds, some at nearly 100,000 rpm. A permanent magnet generator spinning at this high shaft speed produces the power in the form of high-frequency AC, which is converted to DC and then to standard 50-Hz AC using an inverter.

Fuel Cells: Generally phosphoric acid fuel cell is used which is available in the 200-kW size range. This fuel cell operates at about 40 percent conversion efficiency. Because this device operates at 400 degrees F, waste heat is available as steam, which boosts the overall fuel conversion efficiency.

Photovoltaic Cells: Photovoltaic (PV) devices have been in existence for many years since their early use in the U.S. space program. They rely on sunlight to produce DC voltage at cell terminals. The amount of voltage and current that PV cells can produce depend on the intensity of sunlight and the design of the cell. PV systems use cell arrays that are either fixed or follow the sun to capture additional energy. Because solar energy takes a large area of PV cells to produce significant power. At a typical cell conversion efficiency of 10 percent, about 10 m² of panels are needed to provide a peak power of 1 kW. To reduce the number of costly PV devices used, mirrors or lenses can be used to concentrate sunlight on to the cells. This increases the PV cell output but requires tracking devices to ensure that the array is aligned with the sun. Photovoltaic, like micro-turbines and fuel cells, generate DC voltage that must pass through an inverter to produce 50-Hz alternating current for distribution on the utility grid.

Solar Thermal: Although there are a number of large-scale (several-megawatt) generation technologies in the solar thermal field, the main technology for small-scale generation is the sterling dish. This technology is being tested in the 10- to 25-kW range. In this system, light is concentrated on a small receiver by a sun-tracking array of mirrors. The heat collected by the receiver is transferred to the hot end of a sterling engine. The sterling engine uses working fluid in a closed cycle to push pistons and generate shaft rotation.

Wind: Wind generation has been commercially available for many years. In large wind farms wind turbines from 700 kW to 1.5 MW are available. Several smaller wind turbines (<250 kW) are available for use in Micro-Grids. These machines typically use an induction generator driven by a rotor with blades. As is true for the solar options, the wind generators' power output is determined by the availability of their energy source. When the turbine is operating in stand-alone mode, any

power requirement in excess of the wind energy available must be supplied by storage systems or other generation.

Small Reciprocating Engines: Reciprocating engines that run on various fuels are available in small sizes and up to several megawatts. These engines, especially the larger ones, have good efficiencies (30 to 40 percent). They operate in stand-alone applications like scaled-down generation plants with synchronous generators capable of controlling voltage and frequency. Waste heat from these units can help boost overall system efficiencies. Reciprocating engine generators are a mature, low-cost, familiar technology with some attractive benefits for Micro-Grids. The most common fuel is diesel, which causes serious emissions problems.

Storage Technologies: Storage is important in the Micro-Grid both because peak loads are expensive to serve with purchased power and because Micro-Grid generation sources may not be able to respond to load changes as needed. Load changes are usually caused by fast transients resulting from starting of motors or turning on/off of equipment. All the storage systems mentioned in the sections below require power electronics to convert the stored power to standard, 50-Hz, AC, utility-grade power.

Batteries: Batteries are the traditional method of storing electrical energy; there is considerable operational experience with battery systems. Lead-acid batteries, available in almost any size, are used in many applications that require back-up power. Batteries store energy in chemical form and are charged/discharged with DC current. This DC current is converted to standard, 50 Hz or 60-Hz, AC electrical power.

Flywheels: These systems incorporate composite rotors, magnetic bearings, and advanced power electronics. Flywheels store energy in high-speed (up to 100,000-rpm) rotating wheel-like rotors or disks connected to motor/generators. High-speed rotation is important because the amount of power stored in the flywheel is proportional to the square of the rotational speed. The flywheel is charged by taking utility power and converting it to drive the flywheel motor, which increases flywheel speed. During a "discharge," power is drawn from the flywheel by the generator, which slows the rotor speed. Because the output of the flywheel generator is variable, an inverter is used to convert power to standard, 50-Hz AC power.

Superconducting Magnetic Energy Storage: Superconductors allow the passage of electrical current without losses. Electrical energy is stored as a circulating current in a superconducting coil of wire. This circulating current establishes a magnetic field in which the energy is stored. The major energy loss in this system results from the need to cool the coil to very low temperatures. Power electronic interfaces charge and discharge the superconducting coil. Superconductor storage technology could be adapted to larger Micro-Grid applications.

Super capacitors: Super capacitors are very-high-capacity electrolytic devices that store energy in the form of electrostatic charge. They are composed of two electrodes with a very thin separator. Energy storage capacity increases as the surface area of the electrodes increases. Energy is stored as a DC field in the super-capacitor, and the system uses power electronics to both charge and discharges the capacitors. Super capacitors can have very high discharge rates and could handle fast load changes in a Microgrid.

Combined Heat and Power (CHP): One important benefit of Microgrid is an expanded opportunity to utilize the waste heat from conversion of primary fuel to electricity. Because typically half to three-quarters of the primary energy consumed in power generation is ultimately released unutilized to the environment, the potential gains from using this heat productively are remarkable.

Unlike electricity, heat, usually in the form of steam or hot water, cannot be easily or economically transported long distances, so CHP systems typically provide heat for industrial processes, on-site space heating, local heating, or for domestic hot water or sterilization. To make CHP systems feasible, a sufficiently large need for heat must exist within a sufficiently dense area that circulation of steam, hot water, or another appropriate medium is feasible and profitable.

IV. INTEGRATION OF DERs: MICROGRID

The Microgrid is the integration of Distributed Energy Resources. Proper control system allows the Microgrid to present itself to the bulk power system as a single controlled unit. Co-ordination on interface, control and protection are required for each DER and voltage control, power flow control, load sharing during islanding, protection, stability, and over all operation are essential. The smooth transition of Microgrid to and from the island mode is another important feature.

- **Micro-source Controller:** The Power and Voltage Controller coupled with the micro source provides fast response to disturbances and load changes independent of communications.
- **Energy Manager:** Provides operational control through the dispatch of power and voltage set points to each Micro-source Controller.
- **Protection.** Protection of a Micro Grid in which the sources are interfaced using power electronic devices to the required functionality.

V. MICROGRID SIMULATION USING MATLAB

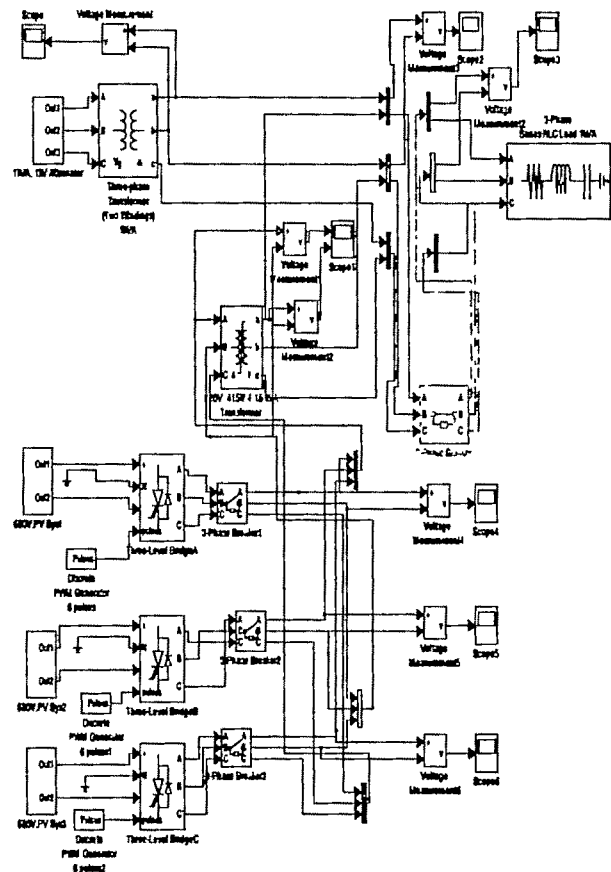
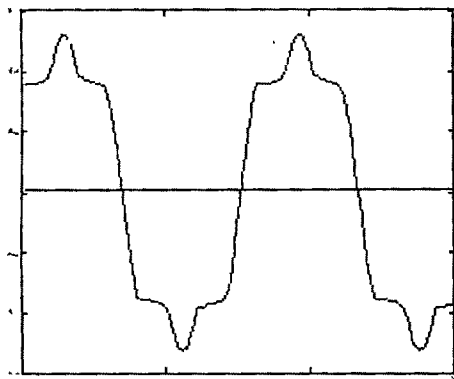
The authors have presented a Microgrid system in Matlab software environment using Simulink Toolbox. The scheme

is shown below. In this system One number 3-phase, 1kVA, 1kV, 50 Hz Alternator is shown as a 3-phase A.C. source, the output of which is connected with busbar through 1kV/415 V, 3-phase transformer. On the other side, there are three numbers of 680V D.C. system representing PV source. For simplicity, constant D.C. voltage source are assumed to represent a composite PV system. The output of each D.C. source are connected with "Three-level bridge inverter" and three inverters are connected in parallel as shown in the figure. The three phase A.C. outputs of inverters are connected through a 3-phase transformer to the busbar of 3-phase A.C. source as shown in the figure. Finally, a three phase, 1kVA , RLC load is connected with the Microgrid system and the nature of voltage wave forms are studied at different points of the system by the simulated scope as available in the Simulink toolbox option.

There are further challenges to obtain better sinusoidal waveforms by simulating proper control environment. However, the basic scheme of integration of Distributed Energy Resources is reflected in this paper.

The successful operation of Distributed Generation depends on the acceptance and participation of local community. The factors like local availability of fuel, conveniently meeting operational requirements, sound maintenance and service support are the most important factors to establish a specific Microgrid system, the most power alternative to future power crisis.

VL MICROGRID SIMULATION DIAGRAM



VII. REFERENCES

- [1] Renewable Energy Sources & Conversion Technology- Bansal, Klemm and Melisa W.-K. Chen, *Linear Networks and Systems* (Book style). Belmont, CA: Wadsworth, 1993, pp 123-135.
- [2] Renewable Energy Sources- Twidell & Weir Renewable Energy Sources- Twidell & Weir
- [3] Distributed Generation and Renewable Energy System - Ramakumar. Fellow IEEE. 2002-37th Intersociety Energy Conversion Engineering Conference.
- [4] "A Model of PV generation suitable for Stability analysis"- Yun Tiam Tan, Student Member IEEE, Nicholas Jenkins, Senior Member, IEEE
- [5] "A New Islanding Detection Algorithm for Distributed Generations Interconnected with Utility Networks"- SI Jang, Seoul National University and Next Generation Power Technology Centre, Rep. Of Korea & KII Kim : Kangwon National University and Next Generation Power Technology Centre, Rep. of Korea

Assessment of Transmission Line Losses through Power Flow Tracing in a Deregulated Multi-Bus Power System

Ashim Kumar Dey¹, Narendra Nath Sinha², J.K.Das³, S. Sengupta⁴

¹Meghnad Saha Institute of Technology, Kolkata, India e-mail: mail2ashim@gmail.com

²Public Works Department, Govt. of West Bengal, Kolkata, India e-mail: nnsinha25@gmail.com

³Damodar Valley Corporation, DVC Towers, Kolkata, India e-mail: dasjiban@hotmail.com

⁴Department of Applied Physics, University of Calcutta, Kolkata, India e-mail: samarsgp@vsnl.net

Abstract- With the introduction of power system reforms, commercial issues related to transmission system has become a major thrust area for the system operators/regulatory bodies particularly in terms of introduction of a transparent methodology for network charging and loss loading. This paper introduces a simple technique based on 'Proportional Sharing Principle' that traces the flow of power in transmission networks. A 'Participation Matrix' is developed whose elements represent the participation factor of the sources towards the loads and to the line losses. Fictitious Loading Methodology is used for distributing the line losses among the network participants. The proposed technique is applied on an IEEE standard 14 bus test system to demonstrate its feasibility. The results obtained are verified with the standard available results.

Key words- Fictitious Loading, Participation Matrix, Power Tracing Technique, Proportional Sharing Principle.

I. INTRODUCTION

ADVENT of open access, has shifted the focus of Attention to commercial issues especially pricing mechanisms for usage cost and loss loading. In order to allocate the transmission cost at actual to the users, it is essential to know, how the customer is utilizing the transmission network. More specifically we can say that it is necessary to know the contributions of the individual participants (generator units, load units, etc.) to the power flows and losses through the transmission network. In a Power Pool operation the constituents are billed monthly for wheeling charges, called as *Transmission Service Charges (TSC)* which are proportional to their total allocated share in the Central Power Pool for that month [3]. This makes the wheeling charge mechanism approximate. An ideal pricing mechanism would have been to find out how much distance a particular generator's power has travelled so as to meet a particular constituent's load and charge accordingly for the amount of power and the distance. But for the exact implementation of this transmission pricing scheme, it is necessary that the mesh structured electrical network should be converted into a simplified model. Again, the complex structure of the

transmission network allows a number of possible paths through which the electricity can flow from generators to the loads. The electricity tracing methodology allows us to trace the flow of power in a meshed electrical network, and yields information regarding what amount of real power and reactive power is being supplied from a particular generator to a particular load and what is the share of each generator towards the transmission line losses. By means of power flow tracing, it is possible to decompose the power flows in a transmission line into the constituent generators and loads. Henceforth, it is possible to recover the transmission charges based on actual usage of the transmission line. There are lots of methodologies already proposed to tackle this problem such as DC Distribution Factors based method, Current based method, Power Flow comparison method and so on. In 1996, J.Bialek [1] proposed a methodology to analyse the amount of real and reactive power flow from a particular generator to a particular load. The 'Proportional Sharing Principle' is used here as a power tracing tool, to obtain the contribution of individual generator units towards meeting up of the individual loads. Sun [2], proposed that graph theory can be used to trace the complex power flows. He has expressed the power flow graph as a directed flow graph based on the bus power allocation and circuit equivalence. The above proposed methods have the shortcomings that nothing has been mentioned about the reactive power loss contribution of the sources and in other case the proposed technique is quite approximate and cannot be generalized for a real system. In this paper, the authors attempt to introduce power flow tracing and loss allocation method, which is both electrically valid and readily justified to the market participants.

II THE TRACING PRINCIPLE

Normally flow of electricity cannot be labelled based on the sources or loads. Hence tracing the flow of power from individual generator to individual loads is a complex process. The main principle used to trace the flow of electricity is the '*Proportional Sharing Principle*'. The

principle is illustrated in Fig.1. The principle basically based on the assumption that all the incoming flows are distributed in a proportional manner among the outflows [6]. The fig shows that a network node N_5 is connected with two incoming flows coming from nodes N_1 and N_2

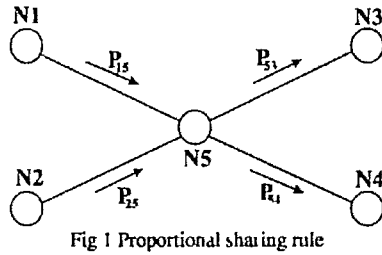


Fig 1 Proportional sharing rule

and two outgoing flows to nodes N_3 and N_4 . The power entering in the node N_5 is denoted by P_{15} and P_{25} respectively whereas the power flowing out of the node is denoted by P_{53} and P_{54} respectively. It is obvious that

$$P_{15} + P_{25} = P_{53} + P_{54} \quad (1)$$

The contributions of the two incoming flows P_{15} and P_{25} towards the outgoing flow P_{53} can be written as:

$$P_{53} = P_{53} \left\{ \frac{P_{15}}{(P_{15} + P_{25})} \right\} + P_{53} \left\{ \frac{P_{25}}{(P_{15} + P_{25})} \right\} \quad (2)$$

and in a similar manner the contributions towards the outflow power P_{54} is:

$$P_{54} = P_{54} \left\{ \frac{P_{15}}{(P_{15} + P_{25})} \right\} + P_{54} \left\{ \frac{P_{25}}{(P_{15} + P_{25})} \right\} \quad (3)$$

The 'Proportional Sharing Principle' explained here can be extended further to all the network nodes that allows to trace the flow of electricity in a meshed network by some recursive calculations.

III. ALLOCATION OF GENERATORS OUTPUT TO LOADS AND LINE LOSSES

A 6-node network with active and reactive power flow is shown in Fig.2. Active power flow is indicated on the top or to the left of the line, while reactive power flow is shown to the right or below the line. For generators and loads similar convention are used.

A. Introduction of Fictitious Node

Power flow is always accompanied with losses, both active and reactive. This creates a difference in flows at the beginning and the end of each line. Fictitious line nodes are introduced to take care of the line losses. Each line is divided into two lines with the introduction of fictitious nodes. Load of a fictitious node is the loss of the corresponding line. For active power flow the line nodes always acts as sinks whereas for reactive power flow the line nodes may act as sinks or sources. Thus, with the introduction of fictitious line nodes the 6-bus, 11-lines system changes to 17-bus, 22-lines system. This is illustrated in Fig.3 and Fig.4 for active and reactive power flow respectively where nodes numbered from 7 to 17 are the fictitious line nodes and number of lines becomes twice the original number i.e. 22. Nodes 7, 10, 14, 16 and 17 acts

as reactive power sources whereas nodes 8, 9, 11, 12, 13 and 15 acts as reactive power sinks.

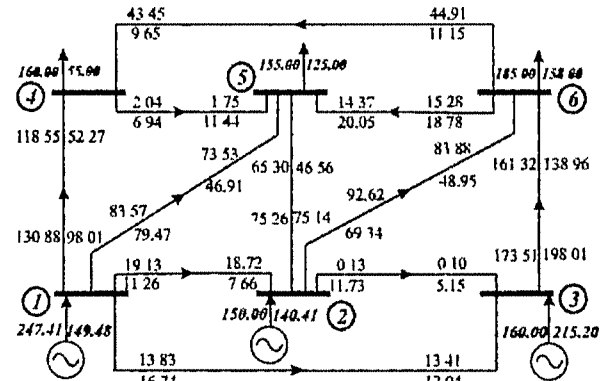


Fig. 2 Active and reactive power flow in 6-bus system.

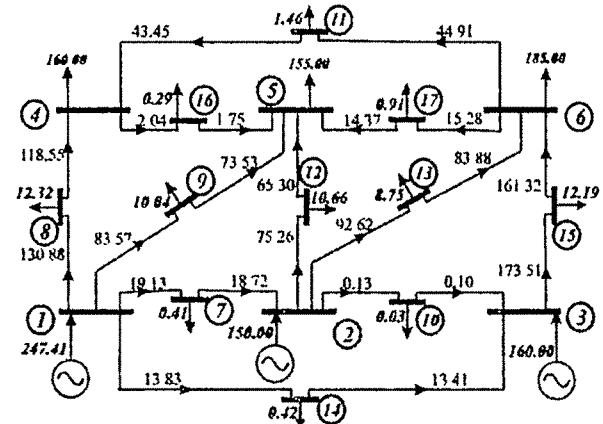


Fig. 3 Active power flow with fictitious nodes

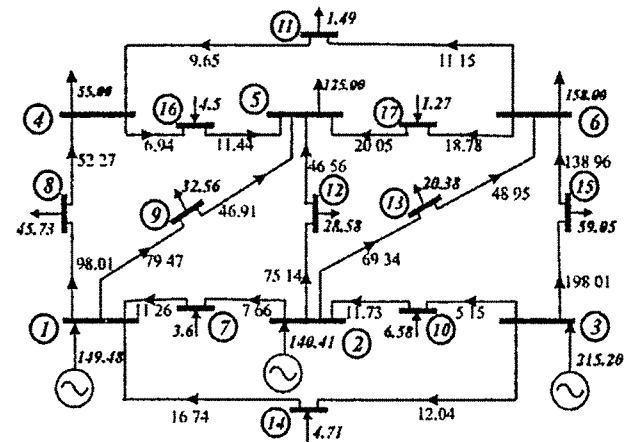


Fig. 4 Reactive power flow with fictitious nodes.

B. Nodal Power Outflow

Power flow through lines can be represented by matrices $[P_f]$ and $[Q_f]$ for active and reactive power flow respectively of dimension $[(n_b + n_L) \times (n_b + n_L)]$, where ' n_b ' and ' n_L ' represent number of nodes and lines of the original system. Rows of these matrices represent the node from which a line started ('from bus') and the column

represent the node to which a line terminates ('to bus'). The non-diagonal element $[P_f]_{ij}$ and $[Q_f]_{ij}$ represent the active and reactive power flow in the line $[P_L]_{ij}$ and $[Q_L]_{ij}$ which started at node i and terminates at node j . The diagonal element, $[P_f]_{ii}$ and $[Q_f]_{ii}$ represents the nodal load $[P_i]_i$ and $[Q_i]_i$ respectively at node i . Mathematically, this is represented as

$$[P_f]_{ij} = \begin{cases} [P_i]_i & \text{if } i = j \\ [P_L]_{ij} & \text{if } i \neq j \end{cases} \text{ and } [Q_f]_{ij} = \begin{cases} [Q_i]_i & \text{if } i = j \\ [Q_L]_{ij} & \text{if } i \neq j \end{cases} \quad (4)$$

for i and $j = 1, 2, \dots, n_b + n_L$

Let, $[P_N]$ and $[Q_N]$ be two column matrices of dimension $[(n_b + n_L) \times 1]$ whose elements $[P_N]_i$ and $[Q_N]_i$ are the total active and reactive power outflow respectively from node i . Mathematically,

$$[P_N]_i = \sum_{j=1}^{n_b+n_L} [P_f]_{ij} \text{ and } [Q_N]_i = \sum_{j=1}^{n_b+n_L} [Q_f]_{ij} \quad (5)$$

for $i = 1, 2, \dots, n_b + n_L$

C. Power Allocation Matrices

Let, $[D_P]$ and $[D_Q]$ be two matrices defined as *active power allocation matrix* and *reactive power allocation matrix* respectively of dimension $[(n_b + n_L) \times (n_b + n_L)]$. Their elements are given by

$$[D_P]_{ij} = \begin{cases} -[P_f]_{ij}/[P_N]_j & \text{if } i \neq j \\ 1 & \text{if } i = j \end{cases} \quad (6a)$$

$$\text{and } [D_Q]_{ij} = \begin{cases} -[Q_f]_{ij}/[Q_N]_j & \text{if } i \neq j \\ 1 & \text{if } i = j \end{cases} \quad (6b)$$

for $i, j = 1, 2, \dots, n_b + n_L$

Referring to (1) and (2) and applying (6b) for Fig.4, power allocation matrix is given in the appendix.

D. Nodal Generation:

The nodal generation is an inflow to the system. Total inflow in a node is equal to the total outflow of the node. By proportional sharing principle, proportion of the inflow from sources or generators in a node may be represented by matrices $[P_G]$ and $[Q_G]$ for active power and reactive power generation respectively having dimension $[(n_b + n_L) \times 1]$. Element of these matrices for node i are given by

$$[P_G]_i = [P_g]_i/[P_N]_i \text{ and } [Q_G]_i = [Q_g]_i/[Q_N]_i \quad (7)$$

where, $[P_g]_i$ and $[Q_g]_i$ are the i^{th} element of active power and reactive power nodal generation matrices and i ranges from 1 to $(n_b + n_L)$.

E. Allocation of Generator Output

The contribution of generator in i^{th} node to the load in j^{th} node are represented by the elements of matrices defined as $[P_{alloc}]$ and $[Q_{alloc}]$ for active and reactive power respectively having dimension of $[(n_b + n_L) \times (n_b + n_L)]$. Rows represent the sources or generators and columns represent the sinks or loads. Elements are given by

$$[P_{alloc}]_{ij} = [P_G]_i [D_P^{-1}]_{ij} [P_i]_j \quad (8a)$$

$$\text{and } [Q_{alloc}]_{ij} = [Q_G]_i [D_Q^{-1}]_{ij} [Q_i]_j \quad (8b)$$

for $i, j = 1, 2, \dots, (n_b + n_L)$

Allocation of generators output to system loads are represented by matrices $[P_{Load}^{(alloc)}]$ and $[Q_{Load}^{(alloc)}]$ whose elements are given by

$$[P_{Load}^{(alloc)}]_{ij} = [P_{alloc}]_{ji} \text{ and } [Q_{Load}^{(alloc)}]_{ij} = [Q_{alloc}]_{ji} \quad (9)$$

for $i = 1, 2, \dots, (n_b + n_L); j = 1, 2, \dots, n_b$

Similarly, allocation of generators output to line losses are represented by matrices $[P_{Loss}^{(alloc)}]$ and $[Q_{Loss}^{(alloc)}]$ whose elements are given by

$$[P_{Loss}^{(alloc)}]_{ij} = [P_{alloc}]_{ji} \text{ and } [Q_{Loss}^{(alloc)}]_{ij} = [Q_{alloc}]_{ji} \quad (10)$$

for $i = 1, 2, \dots, (n_b + n_L)$

$j = n_b, (n_b + 1), \dots, (n_b + n_L)$

Application of these equations to network shown in Fig.3 and Fig.4 are given in Table I to Table IV.

Table I Allocation of active power to loads

Loads in	Sources in			Total (MW)
	Node 1	Node 2	Node 3	
Node 4	120.9	13.1	26	160
Node 5	83.4	62.6	9	155
Node 6	16.5	56.3	112.2	185
Total (MW)	220.8	132	147.2	500

Table II Allocation of reactive power to loads

Loads in	Sources in							Total (MVar)
	Node 1	Node 2	Node 3	Node 7	Node 10	Node 14	Node 17	
Node 4	39.1	3.9	9.6	0.9	0.2	1.2	0	55
Node 5	44.4	49.9	20.1	1.1	2.3	1.4	1.3	125
Node 6	0	38	118.2	0	1.8	0	0	158
Total (MVar)	83.5	91.8	147.9	2	4.3	2.6	1.3	338

Table III Allocation of active power to line losses

Losses in	Sources in			Total (MW)
	Node 1	Node 2	Node 3	
Line 1	0.4	0	0	0.4
Line 2	12.3	0	0	12.3
Line 3	10	0	0	10
Line 4	0	0	0	0
Line 5	0.1	0.4	0.9	1.4
Line 6	1.2	9.5	0	10.7
Line 7	1	7.8	0	8.8
Line 8	0.4	0	0	0.4
Line 9	0.9	0	11.2	12.1
Line 10	0.2	0	0.1	0.3
Line 11	0.1	0.3	0.6	1
Total (MW)	26.6	18	12.8	57.4

Table IV Allocation of reactive power to line losses

Losses in	Sources in							Total (MVar)
	Node 1	Node 2	Node 3	Node 7	Node 10	Node 14	Node 17	
Line 2	38.5	1.8	3.2	0.9	0.1	1.2	0	45.7
Line 3	27.4	1.3	2.3	0.7	0.1	0.9	0	32.7
Line 5	0	0.4	1.1	0	0	0	0	1.5
Line 6	0	26.4	1	0	1.2	0	0	28.6
Line 7	0	18.8	0.7	0	0.9	0	0	20.4
Line 9	0	0	59.1	0	0	0	0	59.1
Total (MVar)	65.9	48.7	67.4	1.6	2.3	2.1	0	188

F. Participation Matrix

Participation Matrix, $[K_{Load}]$ and $[K_{Loss}]$ are defined as matrices whose row represents the nodal loads or line losses and columns represents the generators or sources of the modified system with fictitious line nodes. The elements of these matrices are complex (consisting of both active and reactive part) in nature. Its each element will give the contribution of a generator or source to a nodal load or line losses. Its element $[K_{Load}]_{ij}$ will give the contribution of

generator or source connected to j^{th} node to the load connected to i^{th} node. The real part of an element of the matrices represents the active load or line loss in MW while the imaginary part represents the reactive load or line loss in MVar. Dimension of participation matrix for nodal loads is $[n_b \times (n_b + n_L)]$ and that for line losses are $[n_L \times (n_b + n_L)]$.

IV CASE STUDY AND RESULT ANALYSIS

The algorithm developed above is applied and simulated with IEEE 14-bus standard test system shown in Fig.5. This system with 20-lines and 14-bus is modified to 34-bus and 40-line system with the introduction of fictitious nodes, which takes care of the line losses. The allocation of generators output, both active and reactive power, to system bus loads and line losses are computed using (4) to (8) and are tabulated in Table V to Table VIII.

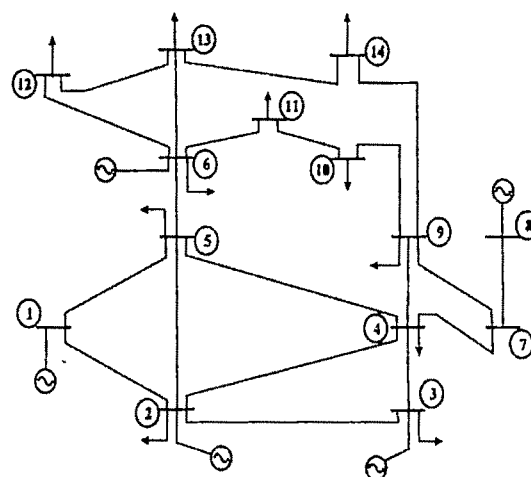


Fig 5 Single-line diagram of IEEE 14-bus system

Table V Allocation of active power to loads

Load in Node No.	Load Shared by (MW)		Total Load (MW)
	Gen. No.1 at Node 1	Gen. No.2 at Node 2	
2	17.19	4.51	21.7
3	76.28	17.92	94.2
4	41.24	6.56	47.8
5	7.03	0.57	7.6
6	10.37	0.83	11.2
9	25.45	4.05	29.5
10	8	1	9
11	3.24	0.26	3.5
12	5.65	0.45	6.1
13	12.5	1	13.5
14	13.21	1.69	14.9
Total (MW)	220.2	38.84	259

Table VI Allocation of reactive power to loads

Load in Node No.	Load Shared by (MVar)							Total Load (MVar)
	Gen. No.1 at Node 2	Gen. No.2 at Node 3	Gen. No.3 at Node 6	Gen. No.4 at Node 8	Gen. No.5 at Node 9	Gen. No.6 at Node 19	Gen. No.7 at Node 20	
2	12.3	0.13	0	0.29	0.01	0	0.01	12.7
3	0	19	0	0	0	0	0	19
4	0	-1.17	0	-2.55	-0.09	0	-0.1	-3.91
5	0.11	0.42	0	0.91	0.03	0.09	0.03	1.59
6	0.2	0.76	4.59	1.66	0.06	0.17	0.06	7.5
9	0	0	0	3.16	13.4	0	0	16.6
10	0.04	0.16	0.99	1.15	3.4	0.04	0.01	5.79
11	0.05	0.18	1.1	0.4	0.01	0.04	0.02	1.8
12	0.04	0.16	0.98	0.35	0.01	0.04	0.01	1.59
13	0.16	0.59	3.55	1.28	0.05	0.13	0.05	5.81
14	0.04	0.17	1	1	2.74	0.04	0.01	5
Total (MVar)	12.9	20.4	12.2	7.65	19.7	0.55	0.1	73.5

Table VII Allocation of active power to line losses

Loss in Line	From bus	To Bus	Line Loss Shared By (MW)		Total Line Loss (MW)
			Gen. No.1 at Node 1	Gen. No.2 at Node 2	
1	1	2	4.3	0	4.3
2	1	5	2.76	0	2.76
3	2	3	1.84	0.48	2.32
4	2	4	1.33	0.35	1.68
5	2	5	0.71	0.19	0.9
6	3	4	0.32	0.05	0.37
7	4	5	0.47	0.04	0.51
11	6	11	0.05	0	0.05
12	6	12	0.07	0.01	0.08
13	6	13	0.2	0.02	0.22
16	9	10	0.01	0	0.01
17	9	14	0.1	0.02	0.12
18	10	11	0.01	0	0.01
19	12	13	0.01	0	0.01
20	13	14	0.05	0	0.05
Total (MW)			12.23	1.16	13.39

Table VIII Allocation of reactive power to line losses

Loss in Line	From bus	To Bus	Line Loss Shared By (MVar)								Total Line Loss (MVar)
			Gen No. 1 at Node 1	Gen No. 2 at Node 2	Gen No. 3 at Node 3	Gen No. 4 at Node 6	Gen No. 5 at Node 8	Gen No. 6 at Node 9	Gen No. 7 at Node 19	Gen No. 8 at Node 20	
1	1	2	0	7.02	0.08	0	0.16	0.01	0	0.01	7.28
2	1	5	-16.55	19.86	0.79	0	1.73	0.06	0.13	0.06	6.08
3	2	3	0	3.44	1.64	0	0.08	0	0	0	5.16
4	2	4	0	0	0.44	0	0.96	0.03	0	0.04	1.47
7	4	5	0	0	0.49	0	1.06	0.04	0	0.03	1.62
8	4	7	0	0	0	0	1.7	0	0	0	1.7
9	4	9	0	0	0	0	0.25	1.05	0	0	1.3
10	5	6	0	0.32	1.16	0	2.5	0.09	0.25	0.1	4.42
11	6	11	0	0	0.01	0.07	0.04	0	0	0	0.12
12	6	12	0	0	0.02	0.09	0.04	0	0	0	0.15
13	6	13	0	0.01	0.04	0.26	0.09	0	0.02	0	0.42
14	7	8	0	0	0	0	0.46	0	0	0	0.46
15	7	9	0	0	0	0	0.8	0	0	0	0.8
16	9	10	0	0	0	0	0.01	0.03	0	0	0.04
17	9	14	0	0	0	0	0.05	0.2	0	0	0.25
18	10	11	0	0	0	0.02	0.01	0	0	0	0.03
20	13	14	0	0	0.01	0.07	0.02	0	0	0	0.1
Total (MVar)			-16.55	30.65	4.68	0.51	9.96	1.51	0.4	0.24	31.4

V. CONCLUSION

The pressure towards unbundling and the deregulation of the transmission services provided by the utilities are increasing throughout the world day by day. The degree of actual utilization of the transmission line by generators and loads should be confirmed promptly and accurately to develop the actual usage based pricing mechanism. In this paper a power tracing methodology based on 'Proportional Sharing Principle' has been developed for a deregulated power market. The method allows assessing the impact of a

particular generator to a particular load on the power system. Contributions of individual generator (or loads) to the transmission line losses have been determined with the help of 'Fictitious Node' method. A Participation Matrix is developed such that the elements of this matrix give the contribution factors of each generator towards the loads and also towards the line losses. The electricity tracing method proposed here may be used as a basis for tariff determination in the Pool system of operation and may be attractive to regulatory bodies to fix up transparent technique for usage based network pricing and loss loading. In bilateral mode of transactions, effective ways must be determined to introduce usage based tariff. This is left for further research as future scope of the work.

APPENDIX

$$[D_{\ell}] =$$

1	0	0	0	0	0	0	0	-1	-1	0	0	0	0	0	0	0	0
0	1	0	0	0	0	0	0	0	0	-0.68	0	0	0	-1	-1	0	0
0	0	1	0	0	0	0	0	0	0	0	0	-0.438	0	0	0	-0.719	-1
0	0	0	1	0	0	0	0	0	0	0	0	0	0	0	0	0	-0.807
0	0	0	0	1	0	0	0	0	0	0	0	0	0	0	0	0	0
0	0	0	0	0	1	0	0	0	0	0	0	0	0	0	0	0	0
-0.003	0	0	0	0	0	0	0	1	0	0	0	0	-1	0	0	0	-0.937
0	0	0	-0.844	0	0	0	0	0	0	0	0	0	0	0	0	0	0
0	0	0	0	-0.375	0	0	0	0	1	0	0	0	0	0	0	0	0
0	-0.077	0	0	0	0	0	0	0	0	1	0	0	0	0	0	0	0
0	0	0	-0.158	0	0	0	0	0	0	0	1	0	0	0	0	0	0
0	0	0	0	-0.372	0	0	0	0	0	0	0	1	0	0	0	0	0
0	0	0	0	0	-0.26	0	0	0	0	0	0	0	1	0	0	0	0
-0.094	0	0	0	0	0	0	0	0	0	0	0	0	0	0	1	0	0
0	0	0	0	0	-0.739	0	0	0	0	0	0	0	0	0	0	1	0
0	0	0	0	-0.082	0	0	0	0	0	0	0	0	0	0	0	0	1
0	0	0	0	0	-0.16	0	0	0	0	0	0	0	0	0	0	0	1

REFERENCES

- [1] Bialek, J. "Tracing the flow of electricity", *IEE Proc. Gener. Transm. Distrib.*, vol.143, no.4, pp. 313-320, 1996.
- [2] Sun, H., Yu, D.C., and Zheng, Q.: "AC power flow tracing in transmission networks", *IEEE Power Engineering Society Winter Meeting*, Jan. 2000, Vol. 3, pp. 1715-1720.
- [3] A. R. Abhyankar, S. A. Khaparde, S. A. Soman, P. Pentayya "A Transmission Pricing Mechanism Based on Power Tracing for Central Transmission Utility in India", *International Journal of Emerging Electric Power Systems*, Volume 2, Issue 1, 2005, Article 1033.
- [4] C.-T. Su, J.-H. Liaw and C.-M. Li, "Power-flow tracing and wheeling costing considering complex power and convection lines" *IEE Proc.-Gener. Transm. Distrib.*, Vol. 153, No. 1, January 2006
- [5] A. R. Abhyankar, S. A. Soman, and S. A. Khaparde, "Optimization Approach to Real Power Tracing: An Application to Transmission Fixed Cost Allocation", *IEEE TRANSACTIONS ON POWER SYSTEMS*, VOL. 21, NO. 3, AUGUST 2006, pp.1350-1361, 2006.
- [6] D. Kirichen, R. Allen, G. Strbac, "Contributions of Individual generators to loads and flows", *IEEE Transactions on Power, Systems*, Vol.12, No.1, pp.52-60, February, 1997.

Technical Session 5C

VHDL and Embedded Systems

Simulation of Random Early Detection Algorithm Using VHDL

Nilay Khare ¹, Kavita Khare ²,

¹HOD CSE & IT Dept., UIT, RGPV, Bhopal, ²Asstt. Prof. EL & Comm. Engg. Dept. MANIT, Bhopal, India

Abstract— The Paper presents Random Early Detection (RED) gateways for congestion avoidance in packet switched networks. The gateway detects incipient congestion by computing the average queue size. When the average queue size exceeds a preset threshold, the gateway drops or *marks* each arriving packet with a certain probability, where the exact probability is a function of the average queue size. RED gateways are designed to accompany a transport-layer congestion control protocol such as TCP. The RED gateway has no bias against bursty traffic and avoids the global synchronization of many connections decreasing their window at the same time.

Key words— RED, Xilinx ISE 5.2i, Model Sim, Virtex.

I. INTRODUCTION

SINCE the growth of the Internet in the last decade is an exponential one. This growth has put pressure on vendors to build high performance Internet Protocol (IP) routers with capacities exceeding 1 Tb/s. Also, the demand for more bandwidth with the advent of network intensive Internet applications has made router buffer management a high priority[1].

In high-speed networks the gateways are likely to be designed with correspondingly large maximum queues to accommodate transient congestion. In TCP transport protocol detects congestion only after a packet has been dropped at the gateway. However, it would clearly be undesirable to have large queues that were full much of the time this would significantly increase the average delay in the network. Therefore, with increasingly high-speed networks, it is important to have mechanisms that keep throughput high but average queue sizes low [9].

RED gateways can be useful in gateways with a range of packet-scheduling and packet-dropping algorithms. RED congestion control mechanisms could be implemented in dropped first when the queue exceeds a certain size.

II. OVERVIEW

In a packet-switched network, a feedback-based congestion control mechanism is essential to provide data transfer services efficiently. Its main objective is to prevent packet losses in the network, and to utilize network resources effectively. The Random Early Detection (RED) algorithm is simply a congestion avoidance technique. It monitors network traffic loads in an effort to anticipate and avoid congestion at common network bottlenecks i.e. the scheme kicks in before any congestion actually occurs.

Moreover, RED uses Active Queue Management techniques currently deployed in large IP networks. It takes advantage of TCP's congestion control mechanism. Packets are dropped probabilistically prior to periods of high congestion [3]. Thus RED is based on two separate algorithms. The algorithm for computing the average queue size determines the degree of burstiness that will be allowed in the queue of the router. The algorithm for calculating the packet marking probability determines how frequently the packets are marked, given the current level of congestion at the router. The router marks packets at fairly evenly spaced intervals, in order to avoid biases and to prevent global synchronization, and also to mark packets sufficiently frequently to control the average queue size. The RED gateway calculates the average queue size. The average queue size is compared to two thresholds, a *minimum* threshold and a *maximum* threshold. When the average queue size is less than the minimum threshold, no packets are marked. When the average queue size is greater than the maximum threshold, every arriving packet is marked. If marked packets are in fact dropped, or if all source nodes are cooperative, this ensures that the average queue size does not significantly exceed the maximum threshold. When the average queue size is between the minimum and the maximum threshold, each arriving packet is marked with probability pa , where pa is a function of the average queue size avg . Each time that a packet is marked, the probability that a packet is marked from a particular connection is roughly proportional to that connection's share of the bandwidth at the gateway.

First the time period for which the router is idle has to be taken into account when the average queue size is computed.

This is done by estimating the number m of small packets that could have been transmitted by the router during the idle period[3,9].

$$avg \leftarrow (1 - w)^m avg,$$

where " m " is equal to the queue idle time i.e. current time – start of the queue idle time, divided by the small packet transmission time, " s "; " w " represents the queue weight.

When there is no idle period before a packet arrival, the average queue size is computed using the following formula,

$$avg \leftarrow avg + (q - avg) w,$$

where " q " denotes the current queue size.[3,9]

Second as avg varies between min_{th} and max_{th} , the initial drop probability, p_b , varies linearly from 0 to max_p , the maximum drop probability:

$$p_b \leftarrow max_p (avg - min_{th}) / (max_{th} - min_{th})$$

The final drop probability, p_a , increases slowly as the count of number of packets increases since the last marked packet:[3,9]

$$p_a \leftarrow p_b / (1 - count \cdot p_b),$$

this ensures that the router does not wait too long before marking a packet. The larger the count, the higher the drop probability. The router marks each packet that arrives at the router when the average queue size exceeds maximum threshold. Another option for the RED router is to measure the queue in bytes rather than in packets. With this option, the average queue size accurately reflects the average delay at the router. When this option is used, the algorithm would be modified to ensure that the probability that a packet is dropped is proportional to the packet size in bytes:

$$pb \leftarrow max_p (avg - min_{th}) / (max_{th} - min_{th})$$

$$p_b \leftarrow p_b \cdot \text{Packet Size} / \text{Maximum Packet Size}$$

$$p_a \leftarrow p_b / (1 - count \cdot p_b)$$

- Therefore in this case a large FTP packet is more likely to be marked than a small Telnet packet. In RED the queue weight w is determined by the size and duration of bursts in queue size that are allowed at the router. The minimum and maximum thresholds are determined by the desired average queue size.

III FUNCTIONAL DESCRIPTION

Figure 1 provides an overview of the system architecture for the RED buffer management scheme. It consists of four main components: Main Controller, Packet Drop Probability Unit (PDPU), Random Packet Drop Unit (RPDU) and the Compute Random Value Unit (CRVU). Input Interface and the Buffer are the other two components. We assume that one cell is equivalent to one packet. Therefore unlike variable packet length systems there is no provision for a Packet Segmentation Unit before the input interface, which is generally used to chop each packet into a number of fixed-length segments (i.e. cells) before sending them to the input interface. Similarly there is no provision for any Packet Reassembly Unit after the input interface, which would reassemble the cells back into a packet before forwarding them to the next processing unit. The input interface has a buffer space to store four cells worth of data.

The buffer on the other hand can hold a maximum of 1024 cells. We define a cell arrival event when the cell has been completely received in the input interface. As the name suggests the Main Controller controls all the components and processes in the system. It sends out control signals to components which respond with acknowledge signals. It determines when and how the other three components operate. The PDPU is the important part of the system. It runs the RED algorithm and computes the packet drop probability. This probability is fed to the RPDU, which determines whether to drop the packet, or not. This decision is based on the random number generated by the CRVU. The next section looks into the four components discussed here in more detail.

Sub-component Design

A. Input Interface : RED is essentially a packet-discard algorithm. However, the algorithm is run on cells rather than packets in this system. The assumption being that every packet is equivalent to a cell. There are four concurrent connections to the input interface as shown in figure 1. Each of the four connections operates at 3.125 Gbps due to 8B10B coding only 80% of that bandwidth is utilized. Thus each input connection operates at 2.5 Gbps providing a total bandwidth of 10 Gbps. One cell arrives at an input connection every four clock cycles i.e. a total of four cells arrive at the interface. Sixteen clock cycles constitute a time slot. Four cells arrive at one input connection every time slot. Thus 16 cells arrive at the input interface every time slot. The length of a clock cycle is 12.8 ns and is computed in the following manner:

- 1 cell is 32 bits in size
- 16 cells arrive at each input connection every time slot which are $16 \times 32 = 512$ bits long
- There are 4 concurrent connections = $512 \times 4 = 2048$ bits wide at the input interface
- Total bandwidth = $2.5 \times 4 = 10$ Gbps
- Therefore length of each time slot = $2048\text{bits}/10\text{Gbps} = 204.8$ ns
- Total number of clock cycles per time slot = 16
- Therefore, length of each clock cycle = $204.8\text{ns}/16 = 12.8$ ns

B. Main Controller :

Figure 2 captures the different states that the Main Controller goes through. There are three states namely, IDLE, PDPU and RPDU. If the input interface is empty i.e. there is no cell arrival, then the *cell_ready* signal is set to '0' and the system stays in the IDLE state. No RED algorithm processing is performed. The Controller also stays in the IDLE state when the reset (*rst*) signal is active.

When a cell is available at the input interface it sends out an active *cell_ready* signal to the Main Controller. The Controller in turn sets the *start_pdrop* signal thus moving from the IDLE to the PDPU state. In this state the PDPU and the CRVU components are activated.

The control stays in the PDPU state as long as a cell is available and the *drop_early* or the *en_q* signals are active. When a cell is available and the *done_pdrop* signal is set but the *drop_early* and the *en_q* ones are inactive the control moves from the PDPU to the RPDU state. While the *done_drop* control is '0' and a cell is available the control stays in the RPDU state itself. On the other hand when *done_drop* is set then the RED algorithm moves to the PDPU state to process the next batch of incoming cells. Moreover if at any state either the *rst* signal is activated or a cell is not available then the control immediately moves back to the IDLE state and stays in this state as long as cells do not arrive at the input interface.

C. Other Components

The other three main components include the Packet Drop Probability Unit, the Compute Random Value Unit and the Random Packet Drop Unit. The PDPU computes the packet drop probability. The CRVU works in parallel with the PDPU.

Both are activated when the Main Controller sets the *start_pdrop* to '1'. CRVU uses a random number generator function to compute a random number. A random number is generated every 2 cycles. This value is ultimately fed to the RPDU, which compares it to the packet drop probability, p_b . If the random value is less than or equal to p_b then the packet is discarded else the packet is sent to the buffer

Figure 2 Different states of the Main Controller.

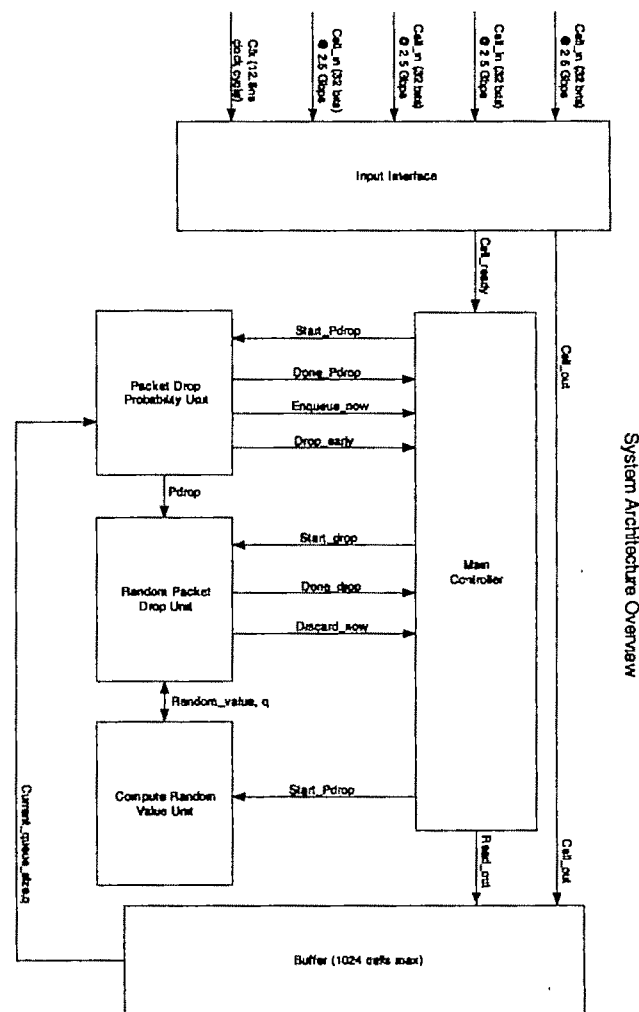
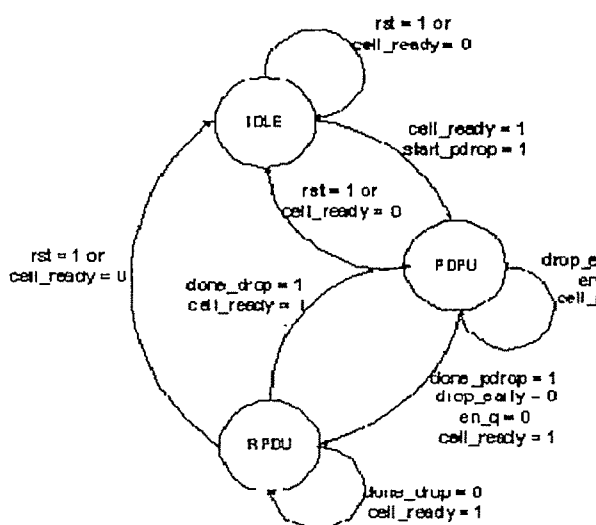


Figure 1: RED System Architecture Overview

IV. DISCUSSION AND CONCLUSION

There are many areas for further research on RED gateways. The foremost open question involves determining the optimum average queue size for maximizing throughput and minimizing delay for various Network configurations. One area for further research concerns traffic dynamics with a mix of Drop Tail and RED gateways, as would result from partial deployment of RED gateways in the current Internet. Another area for further research concerns the behavior of the RED gateway machinery with transport protocols other than TCP, including open- or closed-loop rate-based protocols.

This paper has addressed possible schemes to overcome bottlenecks to the present Internet infrastructure especially the high-speed routers. It investigated implementation architecture for the Random Early Detection (RED) buffer management scheme. Here the system architecture for the RED algorithm is presented. The architecture is divided into four modules: Main Controller, Packet Drop Probability Unit, Random Packet Drop Unit and the Compute Random Value Unit. The Main Controller issues signals that control the other three modules.

The Packet Drop Probability module runs the actual algorithm and if necessary computes the packet drop probability. If you are using *Word*, use either the Microsoft Equation Editor or the *MathType* add-on (<http://www.mathtype.com>) for equations in your paper (Insert | Object | Create New | Microsoft Equation or MathType Equation). "Float over text" should *not* be selected. On other hand the Random Packet Drop Unit uses this drop probability and the random number generated from the Compute Random Value module to decide whether to drop a packet or not. We also looked at simulation results from our VHDL design to verify the appropriate functions of every component.

Table 1 Comparison of Device Utilization between Spartan and Virtex implementation :-

Device	Main Controller		PDPU		RPDU		CRVU	
	Spartan	Virtex	Spartan	Virtex	Spartan	Virtex	Spartan	Virtex
Number of Slices	27 %	6 %	5 %	1 %	5 %	1 %	3 %	0 %
Number of slice Flip Flops	17 %	4 %	2 %	0 %	0 %	0 %	2 %	0 %
Number of 4 inputs LUTs	23 %	5 %	3 %	0 %	4 %	1 %	1 %	0 %
Number of bonded IOBs	46 %	42 %	10 %	9 %	28 %	26 %	10 %	9 %
Number of GCLKs	25 %	25 %	50 %	50 %	25 %	25 %	25 %	25 %

Table 2 Comparison of Timing between Spartan and Virtex implementation :

Timing	Main Controller		PDPU		RPDU		CRVU	
	Spartan	Virtex	Spartan	Virtex	Spartan	Virtex	Spartan	Virtex
Speed Grade	-5	-6	-5	-6	-5	-6	-5	-6
Minimum period	15.8 ns	14.05 ns	5.98 ns	5.37 ns	4.17 ns	3.50 ns	10.1 ns	8.34 ns
Maximum Frequency	63.2 Mhz	71.16 Mhz	167.16 Mhz	185.85 Mhz	239.349 Mhz	285.388 Mhz	98.8 ns	119.870 Mhz
Maximum input arrival time before clock	9.67 ns	9.63 ns	No path	No path	4.85 ns	3.91 ns	4.66 ns	3.68 ns

Maximum output required time after clock	10.5 ns	8.8 ns	8.79 ns	7.5 ns	10.1 ns	8.30 ns	8.45 ns	7.01 ns
Maximum combinational path delay	No path	No path	No path	No path	12.7 ns	10.4 ns	No Path	No Path

REFERENCES

- [1] Jonathan Turner, "Resilient Cell Resequencing in Tera bits routers", proceeding of the Allerton Conference on communication, Control and Computing, 2003
- [2] Mei-ling Shyu, Shu-Ching Chen, Hongli Luo, "Per-Class Management and Adaptive packet drop Mechanism for Multimedia Networking", to be presented at *IEEE INFOCOM 2000*, May/June 2002.
- [3] Hiroyuki Ohsaki, Masayuki Murata and Hideo Miyahara, "Steady state analysis of Random Early Detection Gateway with Controlled Traffic by TCP", presented at *IEEE INFOCOM 2000*, May/June 2001.
- [4] Go Hasegawa and Masayuki Murata, "Analysis of Dynamic Behavior of many TCP connection sharing Tail-Drop/RED Router." to be presented at *IEEE INFOCOM 2000*, May/June 2001.
- [5] S. Athuraliya, S. H. Low, V. H. Li, and Q. Yin, "REM: Active Queue Management," *IEEE Network*, pp. 48-51, May/June 2001.
- [6] C. Diot, and J. L. Boudec, "Control of Best Effort Traffic," *IEEE Network*, pp. 14-15, May/June 2001.
- [7] V. Firoiu, M., Borden, "A Study of Active Queue Management for Congestion Control," *Proc. Infocom*, pp. 397-413, 2000.
- [8] Bernhard Suter, T.V. Lakshman, Abhijit K Choudhary, Dimitrios "Buffer Management Schemes for Supporting TCP in Gigabits Router with Per-Flow Queuing," *IEEE journal*, Vol 17 June 1999.
- [9] W. R. Stevens, *TCP/IP Illustrated, Volume 1: The Protocols*. New York: Addison-Wesley, 1994.
- [10] S. Floyd and V. Jacobson, "Random early detection gateways for congestion avoidance," *IEEE/ACM Transactions* August 1993.

An Efficient Simulator for Power Grid Analysis in VLSI Chips

I. Vishnu Vardhan¹, Sandeep K. Dey², Susmita Sur-Kolay², Debasis Mitra³, Bhargab B. Bhattacharya²

¹ Novell Technologies, India, e-mail: ivishnuvardhan@gmail.com

² Advanced Computing and Microelectronics unit, Indian Statistical Institute, Kolkata e-mail: skd_t, ssk, bhargab@isical.ac.in

³ School of VLSI Technology, Bengal Engineering and Science University, e-mail: debasis mitra@gmail.com

Abstract—Traditional power grid analysis is often focused on resistive, i.e. IR-drop only. Recently, due to the rapidly increasing operating frequency, the transient power fluctuation caused by Ldi/dt has also become significant. Such resistive and inductive drops can cause transient timing failures in the chip. The power grid can be modeled as a distributed RLC circuit. The electrical model that represents the grid can be very large (millions of components and nodes), thus making on-chip power grid analysis a difficult task. Hence, efficient tools for power grid analysis are required for the designers in order to analyze this problem. Further, in deep sub-micron VLSI chips, when several transistors in physical proximity switch simultaneously, a substantial power supply drop, known as droop, may occur because of concurrent load on a via of the power grid. As a result of lower supply voltage, transistors may slow down. Such timing faults are termed as droop faults. Modeling of droop faults and the test vector generation for such faults require an efficient power grid simulator to identify the droop prone vias. In this paper, we propose a new efficient technique called closed form analysis for faster analysis of power grid to identify such vias considering the reduction in supply voltage, increasing frequency and increase in integration of devices. Experimental results show that the proposed method performs better than the traditional power grid simulators such as Modified Nodal Analysis (MNA) and Hierarchical Analysis.

Key words—Closed form, droop, power grid simulator, via.

I. INTRODUCTION

VLSI system performance has increased by orders of magnitude in the last few decades obeying Moore's law. Continued technology scaling and improving transistor performance to increase frequency has made it possible. Increasing integration capacity enabled designers to realize complex architectures, and reducing energy consumed per logic operation to keep power dissipation within limit. The technology treadmill will continue and soon provide integration capacity of billions of transistors and thus, the Number of transistors per unit area of a chip will increase

progressively with each technology generation. Also, the average current per unit area will increase with the increase in transistor density. In nanometer design, where the frequency is in the range of several GHz, today, we cannot ignore the on-chip inductive (Ldi/dt) drop along the multilayer power grid anymore. Moreover, power supply voltage is usually scaled down with technology resulting in decreased noise margin [1], [2]. SPICE simulations show that around 10-15% voltage drop may cause 20-30% increase in gate propagation delay [3]. A change of 1% in power supply voltage may lead to nearly 4% change in delay for most of the 90 nm static CMOS gates [4]. Thus, this increase in number of devices has made power consumption as barrier. So, this has made the power delivery networks in VLSI circuit design a major design challenge. A typical VLSI power grid is composed of alternate metal lines of power (V_{dd}) and ground (GND) nets in each layer. The upper and lower metal layers are connected by vertical vias. Such a power grid with three layers is shown in Fig 1. The V_{dd} and GND terminals of transistors are connected to the tap points at the lower most metal layer.

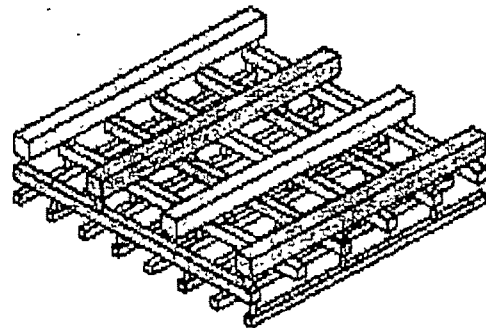


Fig. 1. A typical three layer power grid

Simultaneous switching of transistors connected to the via causes maximum current flow through the via and a droop in voltage. Voltage droop [5] at the via slows the switching of transistors connected to it. If the voltage droop at a via is more than stipulated value, then it makes the circuit faulty. To lower the total power dissipation, there is also reduction in supply voltage and the corresponding reduction in device threshold

voltage. Thus the circuits are more susceptible to noise, including power bus voltage variations. Also, increased density of switching devices and rise in their operating frequency has led to power density problem. The rise in power density with a simultaneous reduction in power supply voltage leads to a large increase in the amount of current that needs to be delivered. The current demand is increasing as specified above but the supply voltage of modern deep sub micron VLSI is decreasing day by day. This results in huge power grids that are required to distribute large amounts of current, at increasingly lower voltages. The resulting voltage drop on the grid reduces noise margin and increases gate delay, having a serious performance impact. Reduced noise margins may lead to false switching at certain logic gates and latches. Higher logic gate delays, on the other hand, may slow down the circuit enough so that timing requirements cannot be met. Some sources of power fluctuation are IR drop, Ldi/dt-drop, and resonance issues. The Ldi/dt-drop is becoming significant with increasing operating frequency. Hence, to accurately model and verify the quality of power delivery, both capacitance [14] and inductance [15] should be considered in the power grid analysis problem.

At present modern VLSI circuit power grids are becoming performance-limiting factors. Hence, efficient analysis of power grids [6-13] is necessary for both predicting the performance and improving the performance if possible. For analysis of power grids traditional circuit simulation techniques are not practical with respect to time and memory complexity. Hence, new efficient techniques for power grid analysis are to be developed keeping into consideration the execution time and memory. In section II we will discuss MNA and Hierarchical techniques and in section III we will discuss our proposed scheme that we called Closed Form Analysis. Experimental results and comparisons are discussed in section IV.

II. BACKGROUND

The method by which circuit equations are formulated is of key importance to a computer-aided circuit analysis and design program for integrated circuits. It affects significantly the set-up time, the programming effort, the storage requirements, and the execution speed of the computer program. The method which one selects needs to be flexible, computationally efficient, and economical with storage. Below we discuss some of the techniques for formulating the circuit equations.

A. Modified Nodal Analysis (MNA)

Modified Nodal Analysis (MNA)[6] is the most efficient way to formulate equations for circuits containing current-dependent, linear or nonlinear network elements. The branch currents are accurately and conveniently obtained as output of MNA. In formulating the circuit equations by using the MNA for a given network, we start with the set of branch currents through the voltage sources and through elements whose currents are controlling variables, and nodal voltages versus a common datum node as variables. Kirchhoff's current law is applied to each node other than the datum node in the circuit such that the summation of currents leaving the node is equal

to zero. The MNA matrix [6] can in general be expressed in the form:

$$\begin{pmatrix} Y_R & B \\ C & D \end{pmatrix} \begin{pmatrix} V \\ I \end{pmatrix} = \begin{pmatrix} J \\ F \end{pmatrix}$$

where Y_R is a reduced form of the nodal matrix excluding the contributions due to voltage sources and the current controlling elements. B contains partial derivatives of the Kirchhoffs current equations with respect to the additional current variables and thus contains +1 or -1 for the elements whose branch relations are introduced. The matrices C and D represent the branch constitutive relations, differentiated with respect to the unknown vector. The vectors J and F are excitations, which include the initial values from previous time steps corresponding to capacitors and inductors.

B. Hierarchical Analysis

The run time and memory requirement for solving a linear system is determined primarily by size and sparsity of the coefficient matrix. If the network is very large (10^7 – 10^8 nodes), the available physical and virtual memory of the system is insufficient even for loading in the data associated with the network. So, the objective of this approach is to reduce the size of the problem. This objective is met by partitioning the given network into sub networks of manageable size, and solving the network by solving the sub-pieces individually. Since the entire network is tightly connected, we cannot ignore the interaction between the various partitions. So, in order to account for the interactions between the partitions, while at the same time not enlarging the size of the problem at hand, models are used for the partitions that capture their behavior as observed at their interface nodes (also called ports). We refer to these models as macromodels [7], [8]. A macromodel is a multi-port linear circuit element that has the same linear relation between the voltages and currents through its ports as the partition itself. With macromodels for partitions available, the original (unpartitioned) network is efficiently solved after replacing the partitions by the respective macromodels, as the macromodels are much smaller in size than the partitions themselves.

III. CLOSED FORM ANALYSIS

An equation is said to be a closed-form solution if it solves a given problem in terms of functions and mathematical operations from a given generally accepted set. Once we formulate the circuit equations using MNA, we can find the nodal voltages and currents in the circuit at different timestamps by iteratively solving them. Usually, in most of the cases, we want the nodal voltages and currents after particular number of time steps say n . For this, we need to iteratively solve the MNA equations n times. But, by the closed form analysis of circuit, we can overcome this problem by directly finding the nodal voltages and currents in the circuit after n time steps. In this section, we present a method to do closed form analysis with some assumptions. Using MNA, we get the circuit equations in the form of $AX = B$ where X is the unknown vector of nodal voltages and currents. Once the matrix A is formed, it is constant through out the iterations. Matrix A depends on the given circuit and the time step. But

vector B depends on the present time point voltage source and current source values and previous time point unknown vector. This can be inferred from the formation of MNA equations. In our power grid simulation, we use the DC voltage source and DC or AC current sources. Let us assume that we have all our current sources in our model as DC. Then, at any time step, vector B depends on the previous time step unknown vector and have some constant added to it that depends on the voltage and current sources. Initially, we obtained matrix A and vector B_1 by using MNA method. On solving $AX_1 = B_1$, we got X_1 . At next time step, matrix A will not be changed but rhs i.e., vector B will be changed. For next time step, rhs can be written as

$$B_2 = K + VX_1 \quad (1)$$

where K is vector that depends on voltage and current sources and V is matrix which depends on capacitors and inductors. It is advantageous to consider the contributions of each circuit element to the V matrix and K vector separately. The element rubber stamps given in table I corresponding to the circuit of a general node shown in Fig. 2 summarize the contributions for each type of element, where BR refers to the additional branch relation. The matrix V and vector K can be generated by using the element stamp table I in a straightforward manner. For a given circuit, the dimension of the matrix V is same as that of the matrix A and the dimension of the vector K is same as that of vector B formed by MNA. The construction of matrix V and vector K can be done along with that of matrix A formed by MNA.

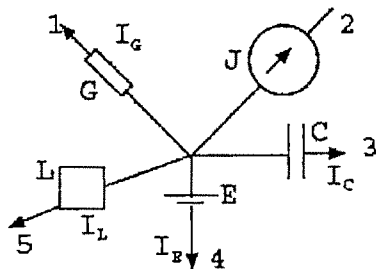


Fig. 2. A general node

For next time step, the unknown vector can be written as

$$X_2 = A^{-1}(K + VX_1) \quad (2)$$

we can write n^{th} time step rhs as

$$B_n = K + VX_{n-1} \quad (3)$$

and unknown vectors at successive time steps as

$$X_3 = A^{-1}(K + VX_2) \quad (4)$$

or, $X_3 = A^{-1}K + A^{-1}VA^{-1}K + A^{-1}VA^{-1}VX_1$ from Eq.(2)

Therefore, $X_3 = (I + A^{-1}V)A^{-1}K + (A^{-1}V)^2X_1$ (4)

where I is the identity matrix of dimension same to that of matrix A .

$$X_4 = A^{-1}(K + VX_3) \quad (5)$$

From 4 and 5, we can write

$$X_4 = (I + A^{-1}V + (A^{-1}V)^2)A^{-1}K + (A^{-1}V)^3X_1 \quad (6)$$

On generalizing the above equations, we can write unknown vector at n^{th} time step as

$$X_n = (I + A^{-1}V + (A^{-1}V)^2 + \dots + (A^{-1}V)^{n-2})A^{-1}K + (A^{-1}V)^{n-1}X_1$$

$$X_n = ((A^{-1}V)^{n-1} - I)(A^{-1}V - I)^{-1}A^{-1}K + (A^{-1}V)^{n-1}X_1 \quad (7)$$

Using above result, we can find n^{th} time step unknown vector without finding the intermediate time point unknown vectors.

TABLE I
STAMP TABLE

	Current not Output			Branch Current Output		
		V_1	V_2		V_1	V_2
For Construction of matrix V	C	i	c.h	-c.h	i	
		3	c.h	-c.h	3	
				BR	c.h	-c.h
	L				V_1	V_2
For Construction of Vector K						I_L
					1	
					5	
					BR	
						$-L.h$
	E				K	
					1	
					4	
			K		BR	E
						K
	J	i	-J		i	
		2	J		2	
					BR	J

IV. EXPERIMENTAL RESULTS

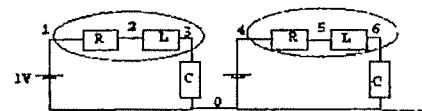


Fig. 3. Partition in a simple electric circuit

A. Modified Nodal Analysis

We have implemented MNA using C. We are able to handle matrices of size up to 15000. The Table II gives the Results of C simulation for different sizes of circuit given in Fig. 3. In Tables II and III, # of elements in column 1 gives the count of each type of circuit element in the circuit. The size of the resulting matrix in column 2 is the total number of MNA equations formed, i.e., the size of matrix to be handled. The column3 reports the time taken to solve the matrix and the column4 reports the number of times the MNA equations are iteratively solved.

TABLE II: Results of MNA

# Elements	Matrix size	Time (min)	# Iterations
1000R, 1000C, 1000L, 1000V	5000	47	4
1400R, 1400C, 1400L, 1400V	7000	127	4
2000R, 2000C, 2000L, 2000V	10000	660	4
3000R, 3000C, 3000L, 3000V	15000	Not handled	

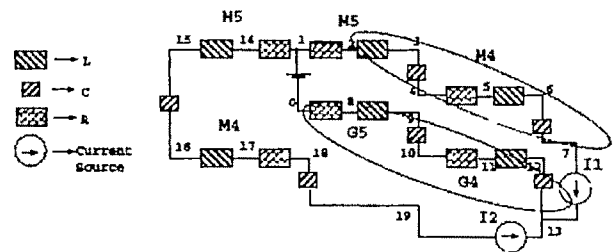


Fig. 4. An equivalent electric circuit of power grid and with hierarchical partition indicated by ellipses

In our simulation with C, we used LU Decomposition with partial pivoting to solve system of linear equations. Efficient methodology of solving linear equations either serially or parallel, keeping accuracy, can decrease the time spent by C simulation. As our purpose is power grid simulation, we simulated the power grid shown in Fig.4 with 3 metal layers for different sizes. Table III gives the results of C simulation for different sizes of our concerned power grid circuit.

TABLE III: Results of MNA for Fig.4

# Elements	Matrix size	Time (min)	# Iterations
1200R, 1200C, 1200L, 200I	5000	86	4
1680R, 1680C, 1680L, 280I	7000	233	4
2400R, 2400C, 2400L, 400I	10000	680	4
3600R, 3600C, 3600L, 600I	15000	Not handled	

B. Hierarchical Analysis

The macromodeling approach in hierarchical technique provides a significant speed-up as the creation of macromodels for the partitions can be performed in parallel. The input to this simulation is MNA format of each partition of the electrical circuit added with some labels. The equivalent circuit of power grid considered for simulating is partitioned as shown in Fig.4. To analyze the circuit shown in Fig.3 using hierarchical method, it has been partitioned as shown by the ellipses. The real time used by hierarchical simulation mainly depends on the maximum size of all the grids. Proper partitioning of circuit will improve the execution time. Simulation results of the circuit shown in Fig.3 are given in the Table IV. Table V gives the real time used by the simulation done using hierarchical technique on the circuit shown in Fig.4.

TABLE IV: Results of Hierarchical Simulation for Fig.3

# Elements	Matrix size Before Reduction	Time (min)	Reduced Matrix Size	Time (Seconds)
1200R, 1200C, 1200L, 200I	5000	86	600	8
2400R, 2400C, 2400L, 400I	10000	680	1200	64
3600R, 3600C, 3600L, 600I	15000	Not Handled	1800	220

TABLE V: Results of Hierarchical Simulation for Fig.4

# Elements	Matrix size Before Reduction	Time (min)	Reduced Matrix Size	Time (Seconds)
1200R, 1200C, 1200L, 200I	5000	86	600	8
2400R, 2400C, 2400L, 400I	10000	680	1200	64
3600R, 3600C, 3600L, 600I	15000	Not Handled	1800	220

In Table IV and V, column 2 reports the matrix size before reduction that is same as the size of matrix formed in case of traditional MNA, the column 4 reports the maximum of the partition sizes in hierarchical analysis on which execution time or storage requirement depends and the column 3 and the column 5 reports the execution time taken by traditional MNA and Hierarchical analysis respectively. Hierarchical simulation can handle any number of elements but the maximum size of the matrices should not cross 15000. As specified in the

algorithm of hierarchical analysis, we use the files and so limit of file size should also be considered. The results shown above are for one iteration. Unlike to traditional MNA, hierarchical takes same time for any successive iteration. So, time required increases linearly with the number of iterations unlike to traditional MNA.

C. Closed Form Analysis

Time complexity of this algorithm is $O(\max((size)^3, (size)^2 \log(n)))$ where $size$ is the size of the matrix A and n is the number of iterations. The time complexity of traditional MNA is $O(\max(size)^3, (size)^{2n})$. So depending on the problem, we can select one of these methods. If we need to perform more number of iterations for smaller matrix sizes, better to use the closed form analysis. So, if matrix size is comparably larger to that of number of iterations, then closed form analysis takes less time compared to that of traditional MNA. The execution time of simulation of closed form technique against MNA simulation on different sizes of network of Fig.3 and of Fig.4 for different iterations is given in the Table VI. The disadvantage of hierarchical method over traditional MNA, i.e., linear increase in time with number of iterations, can be overcome if we combine hierarchical method with closed form analysis. It may be noted that, as the number of iterations increases, the accuracy of the result gets worsened.

TABLE VI: Results of Closed Form Analysis

Matrix size	Time in Seconds(MNA,Closed Form)		# Iterations
	for Fig.3	for Fig.4	
250	(2.8)	(2.14)	1024
250	(22.12)	(33.20)	32768
250	(781.16)	(1025.25)	1000000

D. Comparisons

We have already mentioned that, the method by which circuit equations are formulated affects the storage requirements, execution time of the program and the accuracy of the result. In this section with these parameters we will compare MNA, Hierarchical and Closed form techniques. Hierarchical analysis takes much less space compared to any other simulation, as the storage needs depends on the maximum of the partition sizes. Closed form analysis takes double the storage that needed by the C simulation of traditional MNA, as we need to find matrices $(A^{-1}V - I)^{-1}$ and V , which requires more memory. But as the number of iterations increases, closed form analysis will perform faster. Due to repetitive multiplication of matrices in closed form analysis, it gives accuracy only up to 10^{-2} for 32 iterations.

TABLE VII: Comparison of MNA and Hierarchical Analysis

Circuit Elements	Traditional MNA(size,time,memory)	Hierarchical Analysis
1000R, 1000C, 1000L, 1000V	5000, 47 minutes, 50MB	3000, 10 minutes, 18MB
1400R, 1400C, 1400L, 1400V	7000, 127 minutes, 100MB	4200, 27.2 minutes, 32MB
3000R, 3000C, 3000L, 3000V	Not Handled	9000, 600 minutes, 160MB

The execution time and storage requirement comparison between traditional MNA and hierarchical analysis is given in

Table VII. Each entry in Table VII gives the maximum size of matrix to be handled, time and storage area required to execute networks. Size with the hierarchical analysis depends on the partitioning style of that circuit. Traditional MNA by C simulation and closed form analysis comparison is given in Table VIII.

TABLE VIII: Comparison of MNA and Closed form Analysis

Size	Closed Form Analysis (time in Seconds , memory in KB)	MNA (time in Seconds , memory in KB)	# Iterations
500	(116,500)	(9.250)	1024
250	(14.250)	(2.125)	1024
250	(20.250)	(33.125)	32768
250	(25.250)	(1025.125)	1000000

V. CONCLUSIONS

The problem of power dissipation in the power delivery network is one of the challenges in nanometer technology. The RLC model of power grid has been simulated by various techniques discussed in the previous sections. The MNA approach is the basic method for formulating circuit equations. The hierarchical modeling offers an alternative approach to the traditional nonhierarchical analysis method, capable of handling the increasing size of power grids. Closed form analysis is totally new of its kind, used when the intermediate time points nodal voltages and branch currents are not required. Experimental results show that as the number of iterations increases, the proposed closed form analysis will perform better. Hence, it might be used as a potential tool for the detection of droop prone vias.

VI. ACKNOWLEDGEMENTS

The authors wish to acknowledge the suggestions and comments of Dr. Sandip Kundu and Dr. Sujit Zachariah of Intel Corp., USA.

REFERENCES

- [1] A. Devgan, S. Nassif, "Power Variability and its Impact on Design," *Proc. Intl. Conf. on VLSI Design 2005*, pp. 679-682.
- [2] H. H. Chen, D. D. Ling, "Power Supply Noise Analysis Methodology for Deep-Submicron VLSI Chip Design," *Proc. DAC 1997*, pp. 638-643.
- [3] Y. -M. Jiang, K. -T. Cheng, "Analysis of Performance Impact Caused by Power Supply Noise in Deep Submicron Devices," *Proc. DAC 1999*, pp. 760-765.
- [4] C. Trumurti, S. Kundu, S. Sur-Kolay, Y. -S. Chang, "A Modeling Approach for Addressing Power Supply Switching Noise Related Failures of Integrated circuits," *Proc. DATE 2004*, pp. 1078-1083.
- [5] D. Mitra, S. Bhattacharjee, S. Sur-Kolay, B. B. Bhattacharya, S. T. Zachariah, S. Kundu, "Test Pattern Generation for Power Supply Droop Faults," *Proc. VLSI Design 2006*, pp. 343-348.
- [6] C. -W. Ho, A. E. Ruheli, P. A. Brennan, "The Modified Nodal Approach to Network Analysis," *IEEE Trans. Circuits and System*, Vol. CAS-22, No. 6, pp. 504-509, 1975.

- [7] M. Zhao, R.V. Panda, S. S. Sapatnekar, T. Edwards, R. Chaudhury, D. Blaauw, "Hierarchical Analysis of Power Distribution Networks," *IEEE Trans. Computer-Aided Design of Integrated Circuits and Systems*, Vol. 21, No. 2, pp. 159-168, Feb. 2002.
- [8] J. Singh, S. S. Sapatnekar, "Partition-Based Algorithm for Power Grid Design Using Locality," *IEEE Trans. Computer-Aided Design of Integrated Circuits and Systems*, Vol. 25, No. 4, pp. 664-677, Apr. 2006.
- [9] Q. Zhou, K. Sun, K. Mohanram and D. C. Sorensen, "Large power grid analysis using domain decomposition," *Proc. DATE 2006*, pp. 27-32.
- [10] Y. Tanji, T. Watanabe, H. Kubota and H. Asai, "Large Scale RLC Circuit Analysis Using RLCG-MNA Formulation," *Proc. DATE 2006*, pp. 45-46.
- [11] H. Qian, S. R. Nassif, S. S. Sapatnekar, "Power Grid Analysis using Random Walks," *IEEE TCAD*, Vol. 24, No. 8, pp. 1204-1224, Aug. 2005.
- [12] S. R. Nassif, J. N. Kozhaya, "Fast Power Grid Simulation," *Proc. DAC 2000*, pp. 168-171.
- [13] Y. -M. Lee, C. C. -P. Chan, "Power Grid Transient Simulation in Linear Time Based on Transmission - Line - Modeling Alternating - Direction - Implicit Method," *IEEE TCAD*, Vol. 21, No. 11, pp. 1343-1352, Nov 2002.
- [14] K. Nabors and J. White, "FastCap: A Multipole Accelerated 3-D Capacitance Extraction Program," *IEEE Trans. Computer-Aided Design*, Vol. 10, No. 11, pp. 1447-1459, Nov. 1991.
- [15] M. Kamon, M. J. Tsuk, J. White, "FastHenry: A Multipole Accelerated 3-D Inductance Extraction Program," *IEEE Trans. Microwave Theory Techniques*, Vol. 43, No. 9, pp. 1750-58, Sept. 1994.

VHDL Simulation of A Memory Efficient, High Speed Huffman Decoder: Extension to FPGA Implementation

Bijoy Kumar Upadhyaya¹, P. Venkateswaran², S. K. Sanyal³ and R. Nandi⁴

¹Department of Electronics & Telecommunication Engineering, Tripura Institute Technology, Narsingarh, Tripura (W)

^{2,3,4}Department of Electronics & Telecommunication Engineering, Jadavpur University, Kolkata, India, 700 032.

(email: ¹bku_ju@rediffmail.com, ²pvnw@ieee.org, ³s_sanyal@ieee.org, ⁴robnon@ieee.org)

Abstract— Data compression is always a critical issue in the application areas such as storage and communication. Huffman presented a lossless coding technique to compress data into a smaller form based on the fact that some characters are used more frequently than the others. In this paper a modified Huffman technique which provides solution to the two inherent drawbacks of basic Huffman coding: wastage of memory in Look Up Table (LUT) due to progressive scattering of the Huffman tree and long search time required to determine the symbol from the LUT is described. Very High Speed Integrated Circuit (VHSIC) Hardware Description Language (VHDL) model of the modified Huffman Decoder is presented. Two buffer memory blocks required to model the decoder is done using the embedded RAM (Block RAM) of Xilinx Spartan-3 Field Programmable Gate Array (FPGA) chip. Simulation result of the decoder is obtained using ModelSim XE-III software that endorses the satisfactory functioning of decoder. Finally, the VHDL model is implemented on Xilinx Spartan-3 FPGA kit. Resources of the FPGA chip required to implement the decoder is presented. Estimated power consumption of the design is also computed.

Key words— FPGA, Huffman Coding, LUT, VHDL.

I. INTRODUCTION

DATA compression reduces the space needed for storage of data, and reduces the bandwidth (or amount of time) required for transmitting the data over a communication medium. The Huffman coding [1] creates variable-length codes that are an integral number of bits. Symbols with higher probabilities get shorter codes. It is represented by an inverted root tree called Huffman tree. From implementation point of view the basic Huffman coding scheme suffers from two drawbacks: wastage of memory in Look-Up Table (LUT) due to progressive scattering of the Huffman tree and long search time required to determine the symbol from the LUT. This paper describes a modified Huffman technique [2] which provides solution to the two problems of the basic Huffman coding technique.

Decoding algorithm of the said technique is described in the form of block diagram. The modified Huffman decoder consists of three major operational blocks namely: Buffer RAM, Address Generator and Symbol Generator. In this paper Very High Speed Integrated Circuit (VHSIC) Hardware Description Language (VHDL) [3] model of the modified Huffman Decoder is presented [4]. The VHDL models of the three individual blocks of the decoder are separately described in the form of flow charts. The memory buffer required in the Buffer RAM block is modeled using 1k X 16 bit dual port embedded RAM (Block RAM) and the LUT RAM of Symbol Generator block is modeled using another 1k X 16 bit single port Block RAM (BRAM) of Xilinx Spartan-3 Field Programmable Gate Array (FPGA) chip [5]. Software simulation of each block is accomplished using ModelSim XE-III software. Finally, all the VHDL models are implemented on Xilinx Spartan-3 (Device XC3S400) FPGA kit.

II. MODIFIED HUFFMAN CODING TECHNIQUE

In order to reduce the memory requirement and to make the decoding procedure efficient a special Huffman tree called the Single-Side Growing Huffman Tree (SGH-Tree) [2] is adopted. SGH-Tree is a kind of Huffman trees whose growth is directed toward one side of the tree. To avoid inefficiency in situation when Huffman tree grows, a clustering technique has been adopted. With clustering, an SGH-tree is partitioned every L levels to reduce the memory size. Only with L bits from the coded data stream are used to read the code word table. As a result the method shows better efficiency.

Fig. 1 shows a SGH based Huffman tree, T that is clustered in every 2 level and thus 3 clusters are generated. A table is assigned to each cluster. Each entry in the table provides two pieces of information: MSB specify whether a terminal node in the cluster represents an actual tree terminal node (MSB = 0), or the node is just being cut by a cut line (MSB = 1). In the later case the node is a connecting node between two clusters. The second part of the data in the table provides the information about the location of the node in the memory, assigned to the Huffman LUT.

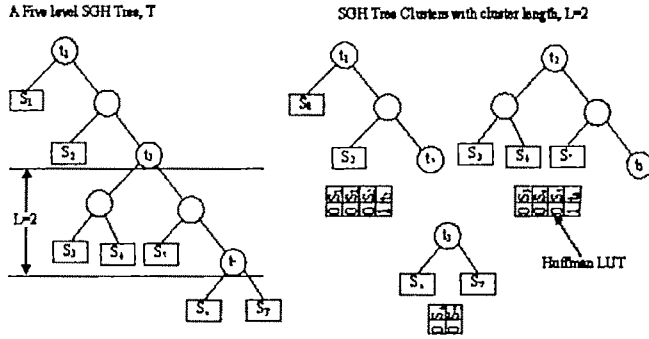


Fig. 1: A SGH based Huffman tree and its clustering.

Table I: Combined Huffman table

0	1	2	3	4	5	6	7
0-01-	0-01-	0-01-	0-01-	0-01-	0-01-	0-01-	0-01-
00	00	00	00	01	01	01	01
0-11-	0-11-	0-11-	0-11-	0-11-	0-11-	1-01-	1-11-
02	02	04	05	06	07	10	14
0-00-	0-00-	0-01-	0-01-	0-01-	0-01-	0-01-	0-01-
03	03	09	0A	0B	0B	0B	0B
0-10-	0-10-	0-10-	0-10-	0-11-	0-11-	0-11-	0-11-
0C	0C	0D	0D	0E	0F	10	11
0-11-	1-00-	1-01-	1-11-	0-00-	0-00-	0-00-	0-00-
12	24	34	3A	13	14	15	15
0-01-	0-01-	0-01-	0-01-	0-01-	0-01-	0-01-	0-01-
16	17	18	18	18	18	19	19
0-01-	0-01-	0-01-	0-01-	0-01-	0-01-	0-11-	0-11-
19	19	1A	1A	1A	1A	1B	1C
0-11-	1-00-	0-00-	0-00-				
1D	3A	1E	1F				

Table I shows a combined Huffman table [6] construed from the small LUTs which are attached to each cluster for maximum code word length up to 13 with cluster length $L=4$. Each entry in Table I consists of three pieces of information: a single (MSB) bit designated as the symbol or no-symbol code. The second piece of information is a two-bit code specifying the length of the relevant codeword or the length of the next associated cluster (plus one). The last piece of information, given as part of each entry in the LUT, is either the source code (Symbol) or the address to the next cluster.

III. OPERATIONAL BLOCKS OF MODIFIED HUFFMAN DECODER

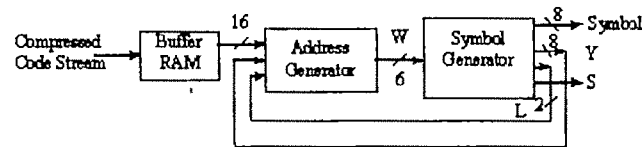


Fig. 2: Block diagram of modified Huffman decoder

Fig. 2 shows the operational blocks of the modified Huffman decoder. The decoder consists of three major operational blocks, namely; the Buffer RAM block, the Address Generator block, and the Symbol Generator Block. The Buffer RAM block receives compressed code stream, converts into a sixteen bit code word called *code part* and then sends to a buffer RAM. The Address Generator is the second and most important operational block in the decoder. This block

receives the 16-bit *code part* from buffer RAM, slices them into partial or full code words, and generates the address for the source code memory (Huffman symbol LUT). Symbol Generator is the third block that consists of a RAM, containing the source codes and their offset (cluster) addresses in a format addressable by the code words and a DeMUX which is used to separate the source codes (Symbol) from the offset cluster addresses (Y).

A. Buffer RAM Block

The Buffer RAM block consists of a 16-bit Serial In Parallel Out (SIPO) shift register that receives the compressed code stream serially from the input and delivers them in 16-bit format, called *code part*, to the Buffer RAM. The address to this RAM is prepared by Input Address Generator block which is basically an 8-bit counter. The counter increments each time a word is written into the memory. The Buffer RAM is used to regulate the data flow and to provide codes for processing without any interruption. This is necessary because while the input data is received in a constant rate, it may not get processed with the same rate. This is due to the fact that the variable length coding scheme, used in the Huffman coding, may consume the code bits in a different rate.

To access the Buffer RAM we need to first read-enable the RAM and then read one 16-bit *code part* slice at a time. The read address of the Buffer RAM is generated by the Output Address Generator Block and it works in similar manner as that of Input Address Generator. The output of this block is a 16-bit *code part*.

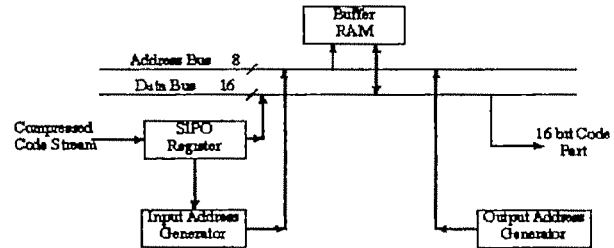


Fig. 3: Detailed view of Buffer RAM block

B. Address Generator Block

The Address Generator block is the heart of the Huffman decoder circuitry. This block, shown in Fig. 4, is aimed to generate the address for the symbols in the LUT, and also to identify the corresponding codewords within the input bit stream. The process of the address generation starts by partitioning the 16-bit *code part* into equal sized groups, with group size $L (= L' - 1)$ and in present case, $L' = 4$. The input data (in the A register) is partitioned into four groups of 4-bits each, and the entire input data is simultaneously transferred into another register B, consisted of four 4-bit registers B_0, B_1, B_2 , and B_3 as shown in Fig. 4. In the next step four parallel 4-to-1 multiplexers are used to select one of the B_i registers, for $i = 0, 1, 2, 3$ and to transfer the data from one B_i into a 7-bit register C. This is done through a barrel shifter. For this purpose a two bit down counter is used which starts from 3 and count down to 0. As a result, B_3 to B_0 are loaded in Register C in descending order. The barrel shifter used for this purpose is

designated as K and the operation is explained with the help of Fig. 5. Depending on how far the code-bits are consumed, Barrel shifter K transfers the data from a B, to C, filling a 4-bit slot within the C register. The filling is done immediately to the right of the last valid bit in C.

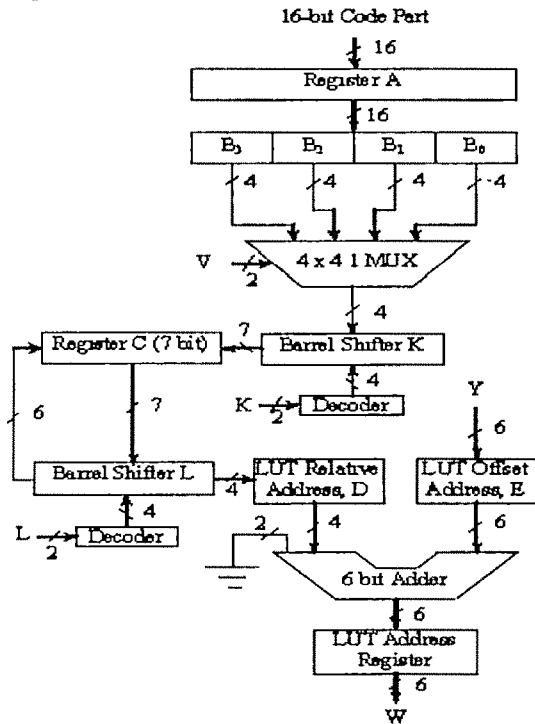


Fig. 4: Detailed view of Address Generator block

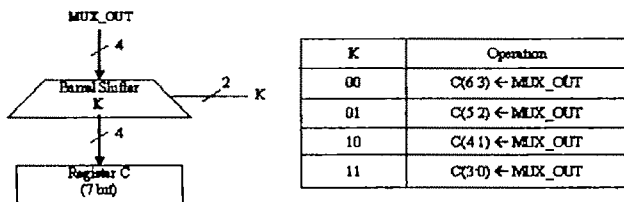


Fig. 5: Barrel Shifter K operation

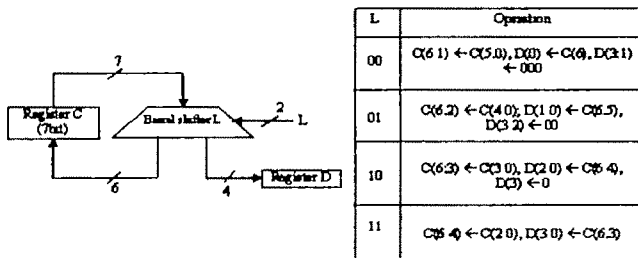


Fig. 6: Barrel Shifter L operation

Now, LUT relative address will be generated. First we recognize that the word-length of the LUT relative address, i.e. L' , is either being given an initial value ($= 4$) for the start, or it is obtained through an earlier process, fed back from the Symbol Generator block. With L specified another barrel shifter, (Fig. 6) is used to transfer the desired code bits from the C register into the D register.

The shift parameter K is determined from L using the relation $K = \text{one's complement of } L$. Now, to generate the actual (absolute) address for the LUT, a 6-bit adder is used which adds the LUT relative address from the D register with the LUT offset address Y from the Symbol Generator block. The output W, resulted from the adder, is stored into the LUT Address Register and is subsequently used to access the LUT RAM, located in the Symbol Generator Block, as shown in Fig. 7.

C. Symbol Generator Block

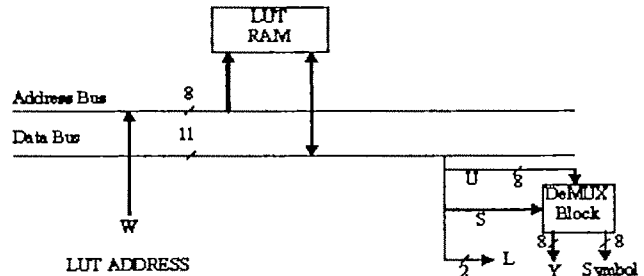


Fig. 7: Detailed view of Symbol Generator block

The Symbol Generator Block is the third operational block that produces either the relevant source code (Symbol) or the address (Y) to a particular cluster (memory block) for next search. The LUT RAM contains the entire Huffman LUT shown in Table I. The processing in this block starts when the address W is received from the Address Generator Block. The address code W is a 6-bit word which fetches an 11-bit data from the LUT RAM to the data bus. This data is the concatenation of three pieces of information as described in Table I. A DeMUX block is used to distinguish the symbol from the cluster address with the help of S.

IV. VHDL MODELING OF MODIFIED HUFFMAN DECODER

The VHDL model of each block is presented in the form of flow chart.

A. Buffer RAM Block

Buffer RAM block utilizes one of the dual port Block RAMs (BRAM) of Xilinx Spartan-3 FPGA as memory buffer. Clock_circuit2 is another VHDL program which is port mapped to buffer_ram program to divide the clock frequency by 16 (i.e. $\text{CLK16} = \text{CLK} \div 16$). RAMB16_S18_S18_inst is the process to access the BRAM.

B. Symbol Generator Block

This block utilizes another single port BRAM of the FPGA to store the Huffman LUT shown in Table I.

C. Address Generator Block

Clock_circuit3 is a VHDL program used to generate $\text{CLK4} = \text{CLK}/4$. YDASH, YDDASH AND YDDDASH are the delayed version of Y used to match with the timing of other parameters like V, L etc.

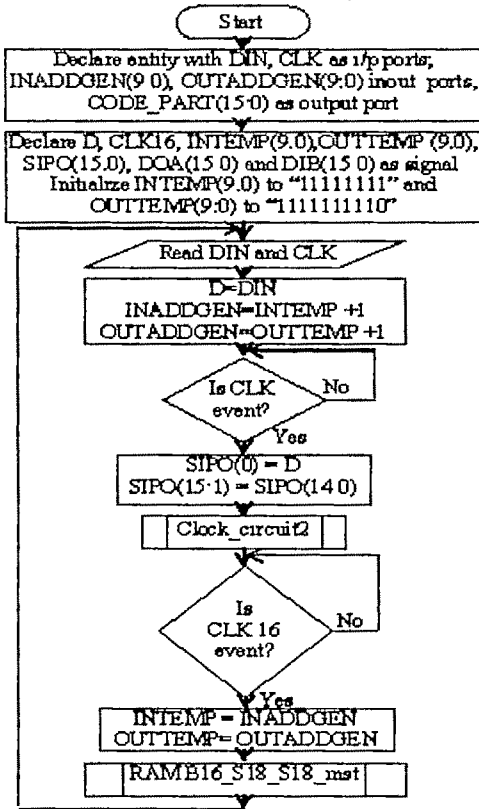


Fig. 8: Flow chart of Buffer RAM block

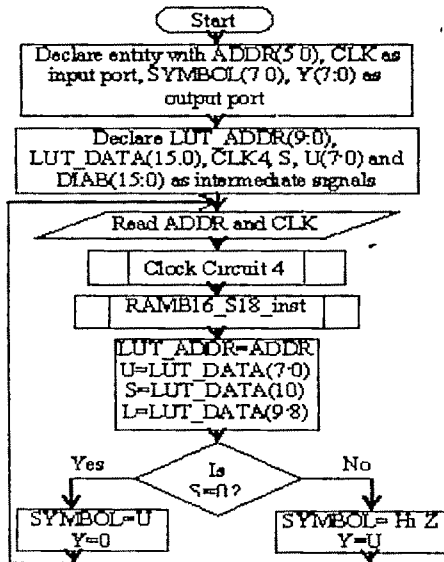


Fig. 9: Flow chart of Symbol Generator block

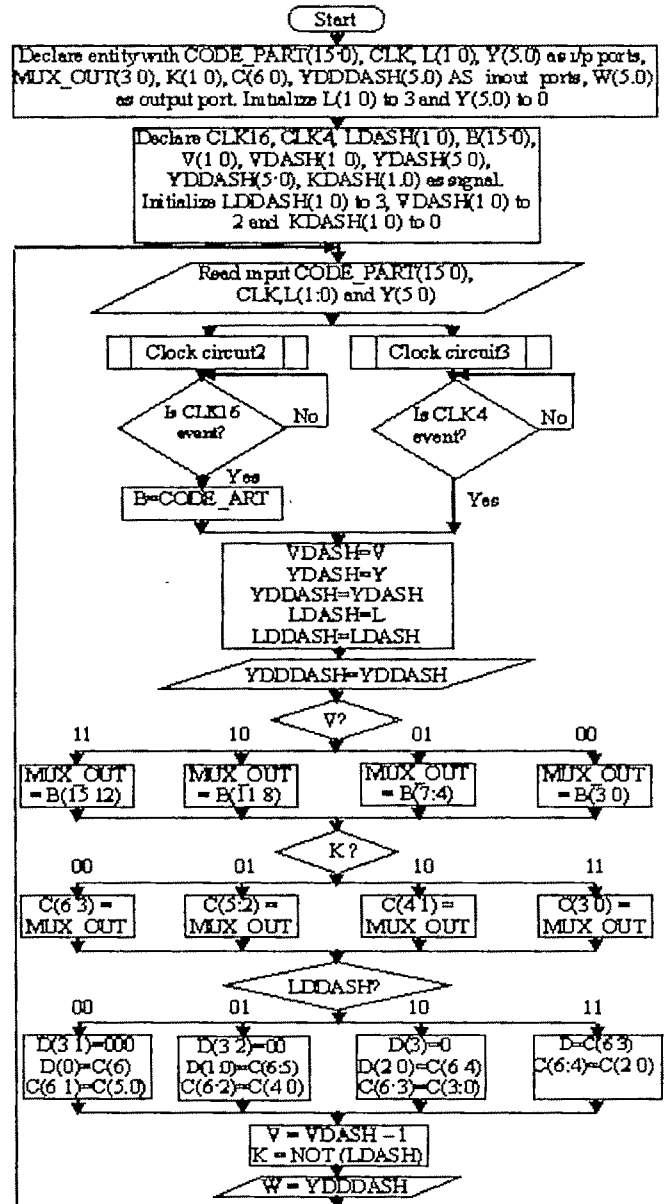


Fig. 10: Flow chart of Address Generator block

V. SIMULATION RESULT OF VHDL MODEL

Simulation result of each of the three blocks of modified Huffman decoder is presented in the form of waveforms obtained using ModelSim XE-III software.

A. Buffer RAM Block

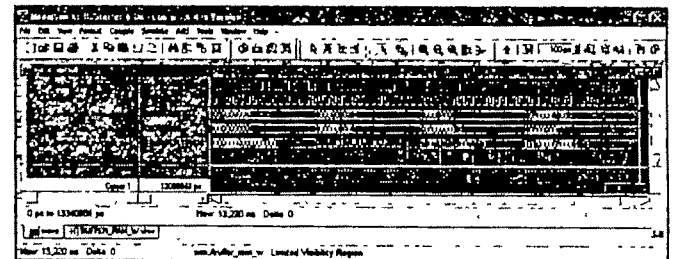


Fig. 11: Simulation waveform of Buffer RAM block.

In Fig. 11, the first code part available at the input is 1001101010001110 and it is stored in the memory location 00000001. Similarly the second code part 1100000000001111 is stored in memory having address 00000010.

B. Address Generator Block

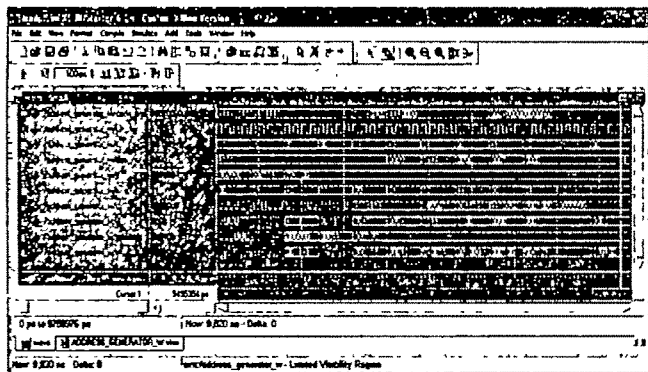


Fig. 12: Simulation waveform of Address Generator block

As shown in Fig. 12, the first 16 bit code part is 1111111111111111. MUX_OUT value is 1111 for the all four CLK4 events. Initially L value is chosen to be 11. So K = 00. With K = 0, C(6:3) are loaded with 1111 in the second CLK4 event. In the 3rd CLK4 event this code part 1111 is loaded in register D. In this same CLK4 event, contents of D are added with (YDDASH) to produce W, (= 1111). Similar observation can be made for other CLK4 events also.

C. Symbol Generator Block

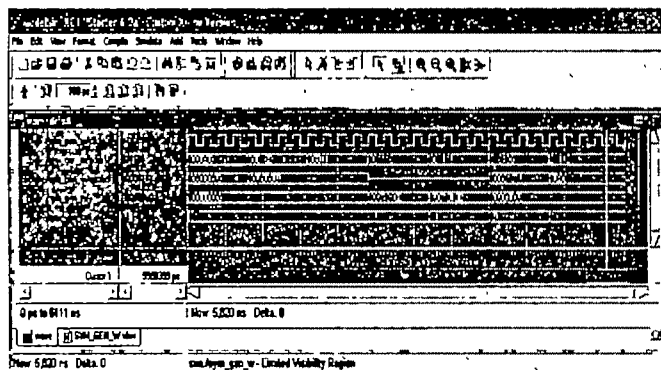


Fig. 13: Simulation waveform of Symbol Generator block

The first address assigned to the block is 000000 as shown in Fig. 13. This address fetches the content of first location from the BRAM which is 0-01-00. Since the first bit 0, this location contains the symbol which is 00H and the length of the code word is 2. As shown in Fig. 13, the symbol line is in High Impedance (Hi Z) when the address is 001110. This is because of the fact that the memory location addressed by 001110 contains the data 1-01-10. Since S = 1, there is no symbol present in this location. Absence of symbol is indicated by Hi-Z condition. The 2nd data 01 indicates that two bits are to be sliced out from the input code part to generate new

relative address. This relative address is added with the previously generated offset i.e. 10H to generate the next physical address.

VI. FPGA IMPLEMENTATION OF VHDL MODEL

VHDL models of the modified Huffman decoder are implemented on Xilinx Spartan-3 (Device XC3S400) FPGA kit. The HDL Synthesis Report and Device Utilization Summary [7] (generated using Xilinx Synthesis Technology, version G. 35, a Xilinx tool that synthesizes HDL designs) of all the three modules are combined and presented in tabular form in Table II.

It is evident from the table that very few resources of the Xilinx Spartan-3 FPGA are required to implement the said decoder thus keeping the provision to implement other circuits of the receiver on the same chip. Large number intermediate signals are used as I/O ports in the model (which consumes bonded IOBs) to verify the internal operations which will not be required in the actual design. The estimated power consumption of the complete decoder is found to be 735 mW (245 mW per block) using XPower Software.

Table II: Combined HDL Synthesis and Device Utilization Report

HDL Synthesis Report		Device Utilization Summary	
# ADDER/SUBTRACTOR		Selected Device: 3e400pq208-5	
10-bit adder	4	Number of Slices	69 out of 3584 2%
6-bit adder	2		
2-bit adder	1		
2-bit adder	1		
# REGISTERS	45	Number of Slice Flip Flops	87 out of 7168 1%
16-bit registers	1		
10-bit registers	2		
2-bit registers	3		
1-bit registers	39	Number of 4 input LUTs	75 out of 7168 1%
# SHIFT REGISTERS	6		
3-bit shift registers	6		
# MULTIPLEXERS	11	Number of bonded IOBs	114 out of 141 80%
1-bit 4-to-1 multiplexer	7		
1-bit 2-to-1 multiplexer	3		
4-bit 4-to-1 multiplexer	1		
# TRI-STATES	1	Number of BRAMs	2 out of 16 12%
8-bit tri-state buffer	1		
		Number of OCLCs	1 out of 3 12%

The successful operation of the circuit is physically verified using input toggle switches and output LEDs attached to the kit. The system clock frequency is lowered from 1MHz to approximately 1Hz for this purpose using another VHDL program for frequency division by 2²⁰.

REFERENCES

- [1] D.A. Huffman, "A method for the construction of minimum redundancy codes," *Proc. IRE*, vol. 40, no. 10, pp. 1098-1101, Sept. 1952.
- [2] R. Hashemian, "High Speed Search and Memory Efficient Huffman Coding," *Proc. 1993 IEEE Inter. Symp. Circuit Syst*, May 3-6, 1993
- [3] Douglas L. Perry, *VHDL: Programming by Example*, 4th ed. New Delhi : Tata McGraw-Hill, 2002, pp. 15-70.
- [4] Bijoy Kumar Upadhyaya, "Studies on the design and simulation of some special circuits using VHDL: extension to FPGA implementations," M. E. Tel. E. Thesis, Dept. of Elec. and Tel Comm. Engg., Jadavpur University, Kolkata, India, 2007.
- [5] S. Brown & J. Rose, "FPGA and CPLD architectures: a tutorial", *IEEE Design & Test of Computers*, pp. 42-57, Summer 1996.
- [6] R. Hashemian, "Design and hardware implementation of a memory efficient Huffman decoding," *IEEE Trans. on Consumer Electronics*, Vol. 40, No. 3, pp 345-352, Aug, 1994.
- [7] *Xilinx Spartan 3 FPGA Trainer (VVS07) User Manual, Version - 1.0*, Vi Microsystems Pvt. Ltd. Chennai.

Hardware/Software Partitioning Problem in Embedded System Design Using Particle Swarm Optimization Technique

Amit Konar¹ and Alakananda Bhattacharya²

¹ Departmental of Electronics and Tele-Communication Engineering, Jadavpur University, Calcutta, India,
e-mail: konaramit@yahoo.co.in

² Departmental of Electronics and Tele-Communication Engineering, Jadavpur University, Calcutta, India,
e-mail: b_alaka2@hotmail.com

Abstract—Hardware/software partitioning is a crucial problem in embedded system design. In this paper, we provide an alternative approach to solve this problem using Particle Swarm Optimization algorithm. Performance analysis of the proposed scheme with Integer Linear Programming, Genetic Algorithm and Ant Colony Optimization technique has been compared using standard benchmark datasets, and the computer simulations reveal that the proposed approach outperforms all the meta-heuristic based existing techniques with respect to cumulative runtimes for several runs of the same program. The Integer Linear Programming has been found to yield the optimal solutions, and the proposed swarm scheme yields sub-optimal solution, sufficiently close to the reported results obtained for integer programming.

Key words—Genetic Algorithm, Hardware/Software Partitioning, Integer Linear Programming, Particle Swarm Optimization

I. INTRODUCTION

AN embedded system is a computing system rather than desktop computers/laptops/palmtops, capable of reacting spontaneously with sensory inputs in real time and designed for dedicated applications. Typical applications that employ embedded systems include fax machines, copiers, printers, scanners, cash registers, alarm systems, card readers, mobile phones, digital cameras, washing machines, DVD players, speech recognizers and many more. Like typical computer systems, embedded systems too include hardware and software components. In other words, it is common to use both application-specific hardware accelerator circuits and general-purpose programmable units with appropriate software for embedded system design. Usually application specific hardware is much faster than software and also more power efficient, but expensive at the same time. Software, on

the other hand, is cheaper, but slow and consumes much power when implemented on a general purpose processor. Hence for faster realization or power-critical situations, hardware based systems are preferred, whereas non-critical modules of embedded systems are realized in software. Consequently a trade-off between cost, power and performance needs to be devised to realize an embedded system on a mixed hardware/software platform.

Among the most crucial steps in embedded system design, partitioning, that is, deciding which components/modules of the system should be realized on hardware and which ones in software is a fundamental problem. This is referred to hardware/software partitioning problem in embedded systems literature [1]. Traditionally hardware/software partitioning was accomplished manually. However, with the increased complexity in embedded systems, researchers currently prefer an automatic approach to handle this problem.

Classically there exist two approaches, exact and heuristic, to handle the hardware/software partitioning problem. The exact algorithms include branch and bound [2], dynamic programming [3], [4] and integer linear programming [1], [5], [6]. Most of the partitioning algorithms in the existing literature, however, are heuristic. This is due to the fact that partitioning is an NP hard problem, and therefore exact solutions tend to be quite slow for bigger dimensions of the problem [2], [7]. Among the well known heuristic based algorithms, Genetic Algorithm (GA) [8-11], simulated annealing [12-14], tabu search algorithm [12], greedy algorithms [15], [16] and Ant Colony Optimization (ACO) [17] are most common.

Besides the heuristic algorithms referred to above, sometimes family of heuristics such as hierarchical clustering [7], [18], [19], [20]. Kernighan-Lin heuristic [21] are equally useful for application in partitioning problem. Scheduling best algorithms, which could be the third variety of partitioning

algorithms, have also been used in the recent literature [6], [9], [15], [22], [23].

In this paper, we propose a meta-heuristic algorithm, which was originated from the sociological behavior of the intelligent creatures such as eagles, bees, ants. These creatures compete for food and thereby follow a dynamics to obtain optimal food from a given pool of resource food-grains. Such algorithms based on the collective behavior of these creatures are referred to as *swarm intelligence algorithm*. Particle Swarm Optimization (PSO) is one such well known swarm intelligence algorithm. In PSO, we define particles to represent agents to search optima of a given non-linear and rough search landscape. Classical optimization techniques that employ derivatives to find optima cannot be used in many engineering problems because of several discontinuities of the search surface. PSO is a possible scheme to determine optima for such engineering optimization problems. Hardware/software partitioning problem can be formulated as an optimization problem, and multi-agent search such as PSO can be invoked to find optimal solution to the partitioning problem. Here each particle position denotes a trial solution to the problem. Trial solutions are iterated using the steps of the PSO algorithm to determine better candidate solution and the process is repeated until no further improvement in solution is detected. The position of the best particles at this stage is considered as the final solution to the problem.

In this paper, we compare PSO with ACO, GA and other heuristic/meta-heuristic algorithms using standard benchmarks available in the literature, and note that PSO outperforms all the existing algorithms.

The paper has been divided into six major sections. Section 2 offers a formal definition to the problem. In section 3 we briefly outline the main steps of the PSO algorithm, and also illustrate the scope of PSO in hardware/software partitioning problem. Computer simulation and comparison with other heuristic/meta-heuristic algorithm are presented in section 4 and conclusions are listed in section 5.

II. FORMAL DEFINITIONS

Arato *et al.* [8] formalized the hardware/software partitioning problem by an undirected graph $G = (V, E)$, where V denotes the set of vertices and E denotes the set of edges. The vertices refer to tasks, and edges refer to communication between the selected pair of vertices. They took an attempt to partition the set of vertices V into V_H and V_S , where V_H denotes the tasks to be realized on a hardware and V_S denotes the tasks to be realized on software. Obviously $V_H \cap V_S = \emptyset$ and $V_H \cup V_S = V$. In this paper, we, however formalize the hardware/software partitioning problem by using a task graph following Marwedel [24].

A task graph is a directed graph consisting of nodes/vertices V and edges E . Thus the task graph $T = \langle V, E \rangle$ where $V = \{V_1, V_2, \dots, V_n\}$ denotes the set of tasks and $E = \{e_{ij}\}$ for $i, j = 1$ to n denotes the set of edges from vertex i to vertex j . The edges here refer to dependencies. In other words, the existence of a directed edge e_{ij} indicates that task representing node i has to be executed prior to execution of the task denoted by node j .

III. HARDWARE/SOFTWARE PARTITIONING BY PARTICLE SWARM OPTIMIZATION ALGORITHM

In this section we first briefly outline the particle swarm optimization (PSO) algorithm, and then demonstrate the scope of the algorithm in the partitioning problem.

A. Classical PSO Algorithm

Motivated by the behavioral and sociological characteristics of bees and flies, Eberhart and Kenedy [25] proposed the PSO algorithm. It has been observed that bees usually identify their food by a collective effort. The dynamics of a bee to move towards the target position (location of food resources) depends on three factors: i) the current direction of its motion, ii) the global best position identified by all its fellow bees until this time, and iii) the local best position that the bee has experienced so far.

Let

$x_{i(t)}$ be the current position of the i th bee at time t ,

$v_{i(t)}$ be the velocity of the i th bee at time t ,

$p_i^l(t)$ be the local best position experienced by the i th bee until time t ,

$p^g(t)$ be the global best position of all the bees at time t ,

the dynamics of the i th bee then can be described by the following two equations:

$$\begin{aligned} v_i(t) &= w v_i(t-1) + \alpha_l^i (p_i^l(t) - x_i(t)) + \alpha_g^i (p^g(t) - x_i(t)) \quad (1) \\ x_i(t) &= x_i(t-1) + v_i(t) \quad (2) \end{aligned}$$

where w , α_l^i and α_g^i denote the inertial velocity, local acceleration coefficient (LAC) and global acceleration coefficient (GAC). The second equation apparently seems to have unmatched dimensions on the two sides of the equality. The confusion regarding dimension can be resolved by considering the following interpretation:

$$x_i(t) = x_i(t-1) + (t - t - 1) v_i(t)$$

The coefficient of the velocity term in the last equation being one is implicitly mentioned by the original equation (1).

The PSO algorithm has been used for solving optimization, search and machine learning problems. In this section, we would like to illustrate the scope of PSO in optimization problems. Classical optimization problems usually require computing partial/total derivatives of the given objective function to be optimized. Unfortunately, in many engineering and scientific optimization problems, the surface of the non linear objective function being discontinuous at several points, derivative based optimization techniques can no longer be employed for such problems. PSO is one such derivative free optimization technique, where given the objective function, we can determine the optima by executing the PSO algorithm. For convenience let us consider a simple two dimensional surface $z = x_1^2 + x_2^2$, which has the minima at the origin; (0, 0). To make the PSO amenable for such optimization problem, we define

$$f = x_1^2 + x_2^2$$

as the fitness function, which will measure the fitness of a particle in the PSO algorithm.

The ants/bees/swaps in PSO algorithm are modeled by particles. Suppose a number of bees are left on a surface $z = x_1^2 + x_2^2$, where they have a food resource at the origin, the minima of the surface. Here, each bee (or the particle) has two dimensions x_1 and x_2 and they can measure their height by evaluating $f = x_1^2 + x_2^2$. Each particle in his trial motions over iterations remembers its local best position so far attained, and reports the local best position to a black board manager who determines the minimum of the local best positions attained by all the particles at the end of a iteration. The particles change their position following the basic PSO dynamics presented in equations (1) and (2). The basic PSO algorithm is outlined below.

Algorithm PSO

Input: Initial position $x_i(0)$ and velocity $v_i(0)$ for each particle i ,

The fitness function $f(\bullet)$;

Output: The global best position attained by the best particle;

Step 1: For each particle i ,

Evaluate $f(x_i)$;

If $f_i(x_i) < p_i^l(t)$,

$p_i^l(t) \leftarrow f_i(x_i)$,

end for;

$p^g(t) \leftarrow \text{Min}(p_i^l(t))$;

$\forall i$

Step 2: Evaluate the particle's next position by executing the basic PSO equations (1) and (2) in order.

Step 3: Repeat steps 1 and 2 until convergence occurs by exhibiting $|x_i(t) - x_i(t-1)| < \delta$, $\forall i$, where δ is a pre-assigned small positive number.

B. PSO in Hardware/Software Partitioning Problem

The PSO can be employed for hardware/software partitioning problem. Here, we consider each particle to be n dimensional, where n denotes the number of tasks on the given task graph.

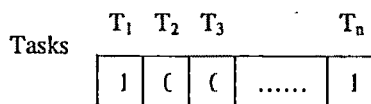


Fig. 1: Representation of a particle by a n -dimensional string

Fig. 1 provides one way of representing a particle by a n -dimensional binary string, where a "1" and a "0" respectively denote hardware and software representation of the task.

Each particle thus attempts to determine the optimal solution for the hardware/software partitioning problem. The fitness function of the i th particle is defined by

$$F_i = \sum_{j=1}^N A_j T_j \quad (3)$$

where A_j denotes the area required for the VLSI implementation of the task and T_j denotes the execution time on that platform. When the task j is realized on software, A_j is considered unity and T_j denotes the execution time of the task on a given software platform.

The particles thus traverse in a N -dimensional space of tasks, and attempt to determine the optimal solution by minimizing the fitness function. The local best position and the global best position here refers to the best position of a particle with respect to smaller fitness function locally and globally respectively until the current iteration. The solution for the classical hardware/software partitioning problem is obtained by identifying the position of the best particle that has the smallest fitness function. Each dimension of the i th particle in the present case being binary (1 for hardware and 0 for software realization), the solution for the best particle is a binary string describing the hardware/software realization of all the n tasks.

IV. COMPUTER SIMULATION

A computer simulation of the PSO, ACO, ILP and GA was performed for the proposed hardware/software partitioning problem using three standard benchmarks, such as IDEA, RC6 and MARS, and the results of the cumulative runtimes and cost of the solutions found by the algorithms are plotted in Fig. 2 and 3 respectively. It is known that ILP always find the optimum [26], so we were interested to examine the performance of the meta-heuristic algorithms: GA, PSO and ACO that can give rise to a near-optimal solution, acceptable to embedded system designers. This is due to the fear that ILP is too costly to realize for its massive computations. An examination of Fig. 2 reveals that PSO outperforms all meta-heuristic algorithms from the point of views of cumulative runtimes.

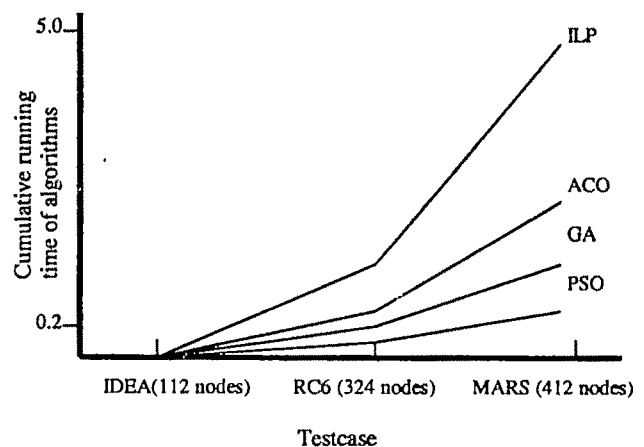


Fig. 2 Results of computer simulations for cumulative running time of the algorithms on benchmark problems.

Cumulative cost of found solutions in each benchmark is given in Fig. 3. A look at Fig. 3 reveals that the cumulative

cost, which gives a measure of the quality of solution, is found to be the best for ILP and next for PSO. So, the role of PSO as a meta-heuristic to the partitioning problem becomes evident from the results of computer simulations.

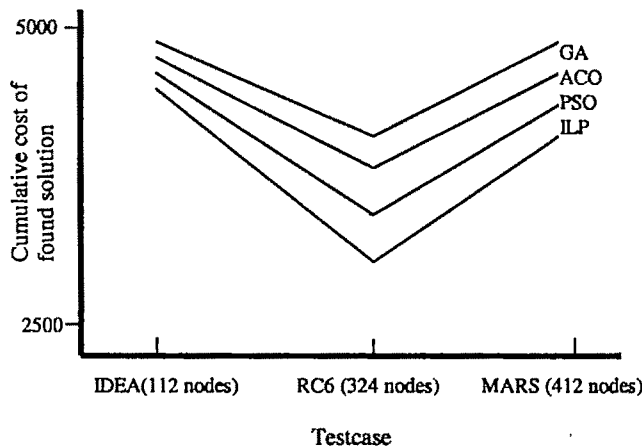


Fig. 3 Results of computer simulation for cumulative cost of found solution of different algorithms on different benchmark problems.

V. CONCLUSIONS

In this paper we introduced a new simplified model for hardware/software partitioning problem. Although it is NP hard in general, we could find an efficient approach to solve the problem using Swarm Intelligence techniques. We compare the performance of the proposed algorithms with already reported results on ILP [8], GA [8] and ACO [27]. The empirical test revealed that ILP-based solution works most efficiently for graphs with as many as few thousand nodes and yields optimal solutions, whereas the PSO gives near optimal solution on an average. It is further observed that the PSO based algorithm outperforms GA, ACO and ILP with respect to runtime requirements for the given partitioning problem.

REFERENCES

- [1] Z. A. Mann and A. Orban, "Optimization problems in system-level synthesis," in *Proc. 3rd Hungarian-Japanese Symposium on Discrete Mathematics and Its Applications*, 2003.
- [2] N. N. Bm, M. Imai, A. Shiom, and N. Hkichi, "A hardware/software partitioning algorithm for designing pipelined ASIPs with least gate counts," in *Proc. 33rd Design Automation Conference*, 1996.
- [3] J. Madsen, J. Grode, P. V. Knudsen, M. E. Petersen, and A. Haxthausen, *LYCOS. The Lynghy co-synthesis system*. *Des. Automat. Embedd. Syst.* 2, 2, 195-236, 1997.
- [4] M. O'Nils, A. Jantsch, A. Hemani, and H. Tenhunen, "Interactive hardware-software partitioning and memory allocation based on data transfer profiling," in *Proc. International conference on Recent Advances in Mechatronics*, 1995.
- [5] R. Niemann, *Hardware/Software Co-Design for Data Flow Dominated Embedded Systems*, Kluwer Academic Publishers, Norwell, MA, 1998.
- [6] R. Niemann and P. Marwedel, "An algorithm for hardware/software partitioning using mixed integer linear programming," *Des. Automat. Embedd. Syst.*, Special issue: Partitioning Methods for Embedded Systems 2, pp. 165-193, 1997.
- [7] F. Vahid and D. Gajski, "Clustering for improved system-level functional partitioning," in *Proc. 8th International Symposium on System Synthesis*, 1995.
- [8] P. Arato, S. Zuhasz, Z. A. Mann, A. Orban, and D. Papp, "Hardware/software partitioning in embedded system design," in *Proc. of the IEEE International Symposium on Intelligent Signal Processing*, 2003.
- [9] R. P. Dick and N. K. Jha, "MOGAC: A multiobjective genetic algorithm for hardware-software co-synthesis of hierarchical heterogeneous distributed embedded systems," *IEEE Trans. Comput.-Aid. Des. Integr. Circ. Syst.* 17, 10, pp. 920-935, 1998.
- [10] G. Quan, X. Hu, and G. Greenwood, "Preference-driven hierarchical hardware/software partitioning," in *Proc. of the IEEE/ACM International Conference on Computer Design*, 1999.
- [11] V. Srinivasan, S. Radhakrishnan, and R. Vemuri, "Hardware software partitioning with integrated hardware design space exploration," in *Proc. of DATE*, 1998.
- [12] P. Eles, Z. Peng, K. Kuchcinski, and A. Doboli, "System level hardware/software partitioning based on simulated annealing and tabu search," *Des. Automat. Embedd. Syst.* 2, 1 (Jan), pp. 5-32, 1997.
- [13] R. Ernst, J. Henkel, and T. Brenner, "Hardware/software cosynthesis for microcontrollers," *IEEE Des. Test Comp.* 10, 4, pp. 64-75, 1993.
- [14] M. Lopez-Vallejo, J. Graza, and J. C. Lopez, "Constraint-driven system partitioning," in *Proc. of DATE*, pp. 411-416, 2000.
- [15] K. S. Chatha and R. Vemuri, "MAGELLAN: Multiway hardware-software partitioning and scheduling for latency minimization of hierarchical control-dataflow task graphs," in *Proc. of CODES 01*, 2001.
- [16] J. Grode, P. V. Knudsen, and J. Madsen, "Hardware resource allocation for hardware/software partitioning in the LYCOS system," in *Proc. of Design Automation and Test in Europe (DATE '98)*, 1998.
- [17] M. Dorigo and T. Stutzle, *Ant Colony Optimization*, MA, MIT Press, 2004.
- [18] T. F. Abdelzaher and K. G. Shin, "Period-based load partitioning and assignment for large real-time applications," in *IEEE Trans. Comput.* 49, 1, pp. 81-87, 2000.
- [19] E. Barros, W. Rosenstiel, and X. Xiong, "Hardware/software partitioning with UNITY," in *Proc. 2nd International Workshop on Hardware-Software Codesign*, 1993.
- [20] F. Vahid, "Partitioning sequential programs for CAD using a three-step approach," *ACM Trans. Des. Automat. Electron. Syst.* 7, 3 (July), pp. 413-429, 2002.
- [21] B. W. Kernighan and S. Lin, "An efficient heuristic procedure for partitioning graphs," *Bell Syst. Techn. J.* 49, 2, pp. 291-307, 1970.
- [22] A. Kalavade and E. A. Lee, "The extended partitioning problem: Hardware/software mapping, scheduling and implementation-bin selection," *Des. Automat. Embedd. Syst.* 2, 2, pp. 125-164, 1997.
- [23] M. Lopez-Vallejo and J. C. Lopez, "On the hardware-software partitioning problem: System modeling and partitioning techniques," *ACM Trans. Des. Automat. Electron. Syst.* 8, 3 (July), pp. 269-297.
- [24] P. Marwedel, *Embedded System Design*, Springer, 2006.
- [25] R. C. Eberhart and J. Kennedy, "A new optimizer using particle swarm theory," in *Proc. 6th Symp. Micro Machine and Human Science*, Nagoya, Japan, 1995, pp. 39-43.
- [26] L. Wolsey, *Integer Programming*, John Wiley & sons, 1998.
- [27] G. Wang, W. Gong and R. Kastner, "Application partitioning on programmable platforms using the ant colony optimization," *J. of Embedded Computing*, vol. 11, no. 19, 2006.

A CPLD Based Gold Code Generator

S.Chattopadhyay and S.K.Sanyal

Department of Electronics & Telecommunication Engineering, Jadavpur University, Kolkata -700032, India
e-mail: sudiptachat@yahoo.com
e-mail: s_sanyal@icee.org

Abstract— The present days of mobile communication symbolize an era of Direct Sequence (DS) Code Division Multiple Access (CDMA) technology that has received considerable attention during last few years. The generation of spreading codes has been an instrumental part in DS-CDMA realization. Among the various spreading codes, Gold code is one of them. This paper describes the generation of Gold codes of length 31 using VHDL simulation and also the CPLD implementation on Xilinx XC95108TQ100 device.

Key words—CPLD, DS-SS-CDMA, Gold code, VHDL.

I. INTRODUCTION

THE Direct Sequence Spread Spectrum Code Division Multiple Access (DS-SS-CDMA) system has now come up as a highly emerging digital technology for 3G and beyond mobile systems. One of the important goals of Spread Spectrum technique used for multiple access system is to find a set of spreading codes, which allows a large number of users to use a band of frequencies with minimum mutual interference. So Spreading Code generation plays an important role in DS-CDMA realization.

Among the various spreading codes, maximal length pn-sequence (m-sequence) & Gold Codes have enormous applications in DS-CDMA & W-CDMA systems. In contrast to simple m-sequences, Gold sequences are suitable for multi-user CDMA systems because they offer a large number of sequence sets with good cross-correlation properties between the single sequences [1]. Since auto-correlation refers to the degree of correspondence between a sequence and a phase-shifted replica of itself, it is used in communication systems in choosing code sequences that give the least probability of false synchronization. So high peak value of auto-correlation will reduce the possibility of false synchronization in CDMA system. The agreement between two different codes is measured by cross-correlation property. So CDMA codes need low peak value of cross-correlation to reduce the interference generated by

other users' signals.

The m-sequence can be generated using Linear Feedback Shift Register (LFSR), provided it is represented by a primitive polynomial. Once the m-sequences of a particular length have been generated, it is necessary to find the preferred pair of m-sequences to generate the gold codes of the same length. For a code length of 31, we get six numbers of m-sequences, whereas Gold code provides us with thirty-three numbers of sequences. That is why Gold codes are widely used in WCDMA for large number of codes available compared to m-sequence for a particular code length. The implementation of the Gold code generator in VLSI area makes it useful in low power communication system design [2].

II. THEORETICAL BACKGROUND OF GOLD CODE GENERATION

A. Maximal Length pn-sequence (m-sequence) generation

Maximal Length pn-sequence can be generated using Linear Feedback Shift Register (LFSR) [3]. Any LFSR can be represented as a polynomial of variable x known as generator polynomial given by

$$G(x) = g_m x^m + g_{m-1} x^{m-1} + g_{m-2} x^{m-2} + \dots + g_2 x^2 + g_1 x + g_0$$

Where g_i are the tap weights either 0 or 1.

The generator polynomial $G(x)$ provides the necessary feedback taps g_i of the LFSR, which are to be combined by modulo-2 addition to get an m-sequence. The necessary condition for generator polynomial $G(x)$ to generate an m-sequence is that $G(x)$ has to be irreducible. But this condition is not sufficient. The irreducible polynomials, which are primitive, can only generate m-sequence. So the necessary and sufficient condition for generation of m-sequence is that the generator polynomial should be primitive [4].

A polynomial $p(x)$ of degree m over $GF(2)$ is irreducible [5] if it can not be factored in to non-trivial polynomials i.e. if $p(x)$ is not divisible by any polynomial over $GF(2)$ of degree less than m but greater than 0. An irreducible polynomial of deg m is said to be primitive [5] if it has order 2^m-1 i.e. if the smallest positive integer n for which $p(x)$ divides x^n+1 is $n=2^m-1$

B. Gold code generation

For generation of Gold sequences it is necessary to find out preferred pair of m-sequences. If 'a' is an m-sequence of degree n of length N generated from a primitive polynomial, it is possible to have another m-sequence $a' = a[q]$, called the decimation of sequence 'a' by sampling every q^{th} symbol of 'a'. $a' = a[q]$ will have period N if and only if $\gcd(N, q) = 1$, where gcd denotes the greatest common divisor.

Two m-sequences 'a' and 'a'' are called the preferred pair [4] if:

- $n \neq 0 \pmod{4}$; i.e. n odd or $n \equiv 2 \pmod{4}$
- $a' = a[q]$, where q is odd and either $q = 2^k + 1$ or $q = 2^{2k} - 2^k + 1$
- $\gcd(n, k) = 1$ for n odd
 $= 2$ for $n \equiv 2 \pmod{4}$

Two m-sequences of length N with a periodic cross correlation function that takes on the possible values $\{-1, -t(n), t(n) - 2\}$ are called preferred sequences [4],[6]. Where $t(n)$ is given by :

$$t(n) = 1 + 2^{(n+1)/2} \quad \text{for } n \text{ odd}$$

$$= 1 + 2^{(n+2)/2} \quad \text{for } n \text{ even}$$

For preferred pair of m-sequences formed by a and a' having period $N = 2^n - 1$, the family of Gold codes is defined by $\{a, a', a + a', a + Da', a + D^2 a', \dots, a + D^{N-1} a'\}$, where D is the delay element [3]. So Gold codes are generated by modulo-2 addition of 'a' with the N cyclically shifted version of 'a' to give $N+2$ numbers of Gold sequences. The generation of Gold codes of length 31 is shown in Fig.1.

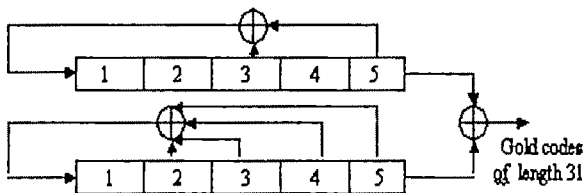


Fig.1: Generation of Gold codes of length 31

Fig-1 shows the generation of gold codes of length 31 by using two shift registers, each consisting of five stages. In fig.1 the upper shift register is represented by the generator polynomial $f_1(D) = 1 + D^3 + D^5$ and the lower one represented by generator polynomial $f_2(D) = 1 + D^2 + D^3 + D^4 + D^5$, where $f_1(D)$ and $f_2(D)$ are two primitive polynomials. Since each of the m-sequences is of length 31, cyclic shifting of $f_2(D)$ and

modulo-2 addition of the shifted version of $f_2(D)$ with $f_1(D)$ will produce 31 numbers of Gold codes. Including the original m-sequences represented by $f_1(D)$ and $f_2(D)$, we get a total of $31 + 2 = 33$ Gold sequences. Among 33 Gold sequences, only two sequences 'a' and 'a'' are represented by primitive polynomials and hence are maximal. The rest 31 numbers of Gold sequences are not maximal.

III. VHDL CODING OF GOLD CODE GENERATOR

The VHDL programming of Gold code generator consists of two parts: first part declares the entity and the second part describes the architecture body of the entity.

The first part of the programme declares the entity gold_seq. Along with this, a set of interface ports have also been declared. Port declaration requires port name, direction and data type declaration [7]. Entity gold_seq uses six ports such as, s(buffer std_logic), enable(in std_logic), clk(in std_logic), count(in std_logic), set(in std_logic) and reset(in std_logic).

The second part of the programme describes the architecture body of the entity gold_seq using structural modeling. The architecture body has been described using two components, sequence1 and sequence2. These two sequences are the m-sequences represented by generator polynomials $f_1(D)$ and $f_2(D)$ and form the preferred pair.

Each of the components sequence1 and sequence2 has been treated as a separate entity. The architecture body of entity sequence1 uses two components dflipflop and dflipflop1. Similarly architecture body of sequence2 has been described by another two components d_ff and d_ff1. Each of the four components, dflipflop, dflipflop1, d_ff & d_ff1 has been regarded as a separate entity and has been described using behavioral model.

IV. VHDL SIMULATION AND CPLD IMPLEMENTATION RESULTS

With the help of our developed program, we have generated 33 numbers of Gold codes and the results have been verified by downloading the program on CPLD board and by observing the on/off status of the LED display.

The CPLD board uses Xilinx XC9500 CPLD series 'XC95108-TQ100' device. These devices are flash based and are aimed at combinational logic intensive applications. These devices have a total of 108 macro cells which provide 2400 usable gates. The pin-to-pin propagation delays are 15.0 ns with 55.6 MHz maximum system frequency.

The RTL schematic of the Gold code generator produced by the VHDL program is shown in Fig.2. It consists of two blocks: Block-1 & Block-2. The RTL Schematic of Block-1 & Block-2 are shown in fig.3 & Fig.4 respectively. RTL schematic of a CPLD design helps us to understand the design schematically.

Resource usage and timing report are available from fitter report and performance summary report of CPLD device. The

resource usage and the timing report of the CPLD device for Gold sequence no. 1, have been shown in Table. I and Table. II respectively. These two reports provide valuable informations related to CPLD design. The generated 31 numbers of Gold codes, excluding two maximal sequences have been listed in Table. III.

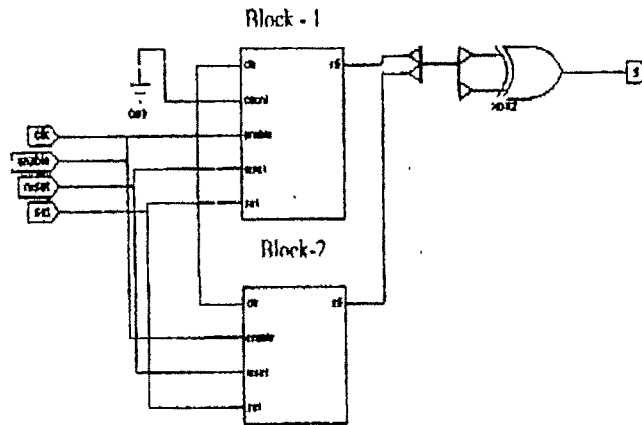


Fig.2: RTL Schematic of Gold code generator

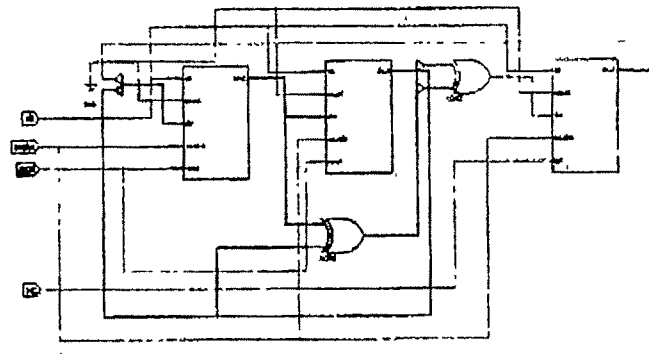


Fig.3: RTL Schematic of Block - 1

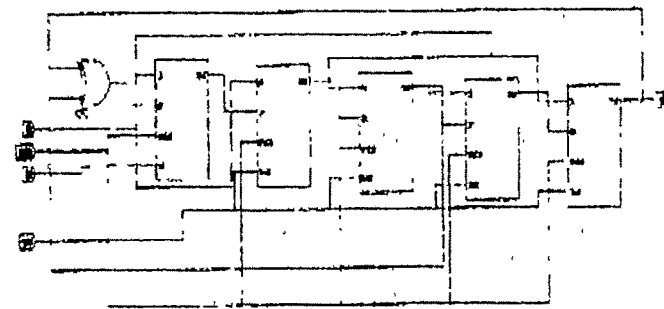


Fig.4: RTL Schematic of Block - 2

Macrocells used	11/108(10%)
Product terms used	30/540(6%)
Registers used	10/108(9%)
Pins used	5/81(6%)
Function block used	13/216(6%)

Table. I: Resource usage of the Gold sequence 1

Clock pad to output pad delay	17.5ns
Clock to set up delay	11.5ns
Set up to clock at the pad delay	9.0ns

Table. II: Timing report of the Gold sequence 1

Seq. No.	Generated gold Sequences
1	0000001000110110000110011100110
2	0001100110011110010100101111001
3	0010111011001110110001001000111
4	01000000110111111010000111011
5	1001110100101101101100011000011
6	0010011110101001000000100110010
7	0101001010100000011001011010001
8	1011100010110010101010100010111
9	0110110010010111001101010011010
10	1100010011011100000010110000001
11	1001010001001010011101110110110
12	0011010101100110100011111011000
13	011101110011111101111110000101
14	1111001110001100100111010111111
15	111101011101011010110111001010
16	111010000100100110101100100000
17	1100110110111011110011011110100
18	1000011010000101111110101011100
19	0001000011111001100101000001100
20	001111000000001010010010101101
21	0110010111110000111100111101111
22	1101011000010011100001101101011
23	1011000111010101011011001100010
24	0111111001011000101110001110000
25	1110000101000011000100001010101
26	1101111101110100010000000011110
27	1010001100011010111000010001000
28	0101101111000111101000110100100
29	1010101001111101001001111111101
30	0100100100001000001011110100110
31	10001111111000100011111000101001

Table. III: Generated Gold sequence of length 31

V. CONCLUSION

Gold codes provide a large number of codes with high peak value of autocorrelation and low peak value of cross correlation. Thus Gold sequence is more suitable in CDMA application than m-Sequence

Emphasis, should to be given for betterment of the design to achieve low power consumption and less delay time with are two important aspects of VLSI design.

Various studies could be made to find the effect of different spreading codes on modulation quality of different digital modulation schemes such as, QPSK, $\pi/4$ -QPSK, $\pi/4$ -DQPSK etc. This study could be treated as useful tool to study the modern digital modulation techniques used in mobile communication system.

REFERENCES

- [1] Dr. K. Feher, *Wireless Digital Communications : Modulation & Spread Spectrum Applications*, Prentice-Hall of India, New Delhi-110 001, 2005, pp. 301.
- [2] Tsung-Hsien Lin, William J. Kaiser, and Gregory J. Pottie, "Integrated Low-Power Communication System Design for Wireless Sensor Networks," *IEEE Communications Magazine*, December 2004, pp. 142.
- [3] Tri T.Ha, *Digital Satellite Communication*, Macmillan Publishing Company, New York, 1986, PP. 531.
- [4] E.H. Dinan and B.Jabbari, "Spreading Codes for Direct Sequence CDMA and Wideband CDMA Cellular Networks", *IEEE Communications Magazine*, September 1998, pp. 48-51
- [5] Shu Lin, Daniel J. Costello Jr, "*Error Control Coding: Fundamentals and Applications*," Prentice-Hall, Inc. Eaglewood Cliffs 07632, New Jersey, 1993, pp 28
- [6] J G Proakis, *Digital Communications*, 4th ed., McGraw-Hill International Edition, 2001, pp. 768-770.
- [7] J. Bhaskar, *A VHDL Primer*, Pearson Education Ltd, India, 2002, pp. 68-69, 125-129.

Protection from Buffer Overflow with External Hardware in an Embedded System

Asim Datta¹ and S. Sengupta²

¹Sikkim Manipal Institute of Technology, Majitar, Sikkim -737132,
e-mail: datta_asim@rediffmail.com

²Department of Applied Physics, University College of Technology,
University of Calcutta, 92 A.P.C. Road, Kolkata-700009, India
e-mail. samarsgp@vsnl.net

Abstract—With more embedded systems networked, it becomes an important research problem to defend embedded systems against buffer overflow attacks. A buffer overflow used an unprotected or unbounded copy with attacker controlled data to overwrite a buffer on the stack. The paper points out deficiencies of the existing approach and sets the requirements for the new approach. This paper presents an efficient solution to the persistent problem of buffer overflow attacks with external hardware only. This external additional hardware monitors overwriting of the frame pointer, and before overwriting exits the process. This overflow checking as in external hardware, actual program processing speed is not affected.

Key words— Security, buffer overflow attack, embedded system, external hardware, protection..

I. INTRODUCTION

BUFFER overflows have been the most common form of security vulnerability in the last ten years. Buffer overflow attacks cause serious damages to general purpose systems as well as to special purpose embedded systems. Because of the growing deployment of networked embedded systems, security becomes one of the most significant issues for embedded systems. The most dominant form of buffer overflow exploitation is *stack smashing* attack [1], simply overwrites the return address of a function on the stack so that, when the function returns, control jumps to a location where the attacker would have inserted malicious code [2]. Other more complex variants attempt to modify locations referenced by function pointers and the global offset table [2] [3].

Traditionally, a buffer overflow used an unprotected or unbounded copy with attacker controlled data to overwrite a buffer on the stack. The attacker's data would be copied down the stack until the return address of the overflowing function was overwritten [5]. At this point, the attacker can gain execution control at a location of his choosing. In order for a buffer overflow attack to succeed, it needs to achieve the following two goals (1) inject the attack code and (2) force the process to execute the injected code [6].

With the increasing complexity of embedded applications, it becomes more attractive and necessary to design an embedded system by integrating as many off-the-shelf components as possible. A serious problem is here to check whether these components have buffer overflow vulnerabilities and to protect an embedded system application from buffer overflow attacks [2].

The related technologies passed through revolutionary changes through ages to ensure reliable operation of an embedded system. A number of researches are going on in this field as mentioned in [1] – [10] to effectively defend embedded systems against buffer overflow attacks. A hardware design is necessary if the software method is unable to achieve some of the requirements.

This paper proposes a technique called External Hardware (E H Technique) Technique that uses hardware to defend a system against buffer overflow attacks even without the knowledge of the source code. The performance overhead is also minimal, so this approach can be easily applied to embedded applications that have real-time constraints.

II. BUFFER OVERFLOW ATTACK

Buffer overflow attack exploits vulnerabilities in programs (most often unchecked buffer on the process runtime stack) to overwrite control information (i.e., function return address) [1] [8]. By overflowing a stack-allocated buffer, the attacker can seize the control of the process and force it to execute arbitrary, malicious code as shown in fig.1.

The overall goal of a buffer overflow attack is to subvert the function of a program so that the attacker can take control of that program [9].

Different way attacker can gain control:

1. The attacker can supply sufficient payload to be injected in a buffer as string input to the program and program stores it. Here the attacker uses the victim program's buffer to store the attack code and the attacker does not have to overflow any buffers to do it. The attacker need only parameterize the code, and then program to jump to it.
2. Each time a function is called, it lays down an activation record on the stack that includes, among other things, the

return address that the program should jump to when the function exits. Any writing past the bound of a data structure will overwrite adjacent data structures and change their values. If the overwritten area contains a function's return address, then when the function returns this new value will be used as the address of the next instruction after the return. So, if a user could inject his/her code into memory and change a return address to point to the injected code. This form of buffer overflow is called a "stack smashing attack" and cause a majority of buffer overflow attacks.

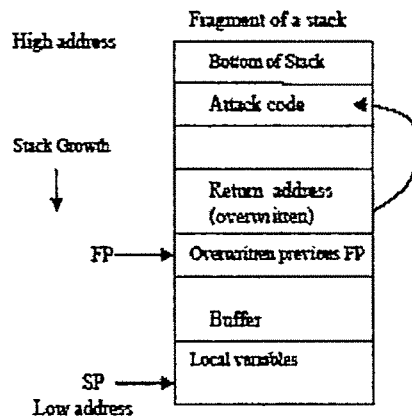


Fig 1: Buffer Overflow Attack

3. Function pointers can be allocated anywhere (stack, heap, static data area) and so the attacker need only find an overflowable buffer adjacent to a function pointer in any of these areas and overflow it to change the function pointer. So, when the program makes a call through this function pointer, it will jump to the attacker's desired location.

If programs don't check the size of the input for a buffer array and the size of the input data is larger than the size of the buffer array, then areas adjacent to the array will be overwritten by the extra data. The (3) way is rare in embedded systems, and this why less emphasis is given on it.

The use of the safe programming languages is effective to defend against buffer overflow attacks. But for embedded system applications, most software is still written in "unsafe" languages such as C or assembly [10] [11]. C compilers allocate space for local variables and the return address of a function in the same stack frame [12].

A common stack smashing attack example is given where arguments, return address, previous frame pointer(FP), and local variables are pushed onto the stack one by one[13][6]. The stack structure of Intel x86 processors is used in these examples because it is easy to explain and understand[2]. This examples for basic buffer overflow attack methods are shown to provide the background for understanding why EHTechnique is necessary and how it works.

A vulnerable program is written in Fig.2(a) such that only one byte overflows from its buffer. Fig.2(b) shows a typical stack structure after function *func()* is called. The arrows in figure 1(b) show the growth directions of stack and memory respectively. Variables are physically padded o the first 4 bytes, so a 255 byte buffer would take up as much space as a 256 byte buffer. This means that the overflowing byte will

overwrite the saved frame pointer, which was pushed into the stack at the beginning of *func()*. Similarly, any function using *strcpy()* may copy more than 256 characters into *buffer[]* as *strcpy()* does not check the size of the inputs. Therefore, the inputs can overflow the return address in the stack and make it point to the attack code injected in *buffer[]* as shown in Figure 2(b). An attack based on heap or BSS uses a similar idea[2].

```

func(char *msg)
{
    char buffer[256];
    int i;
    for (i=0; i<=256; i++)
        buffer[i] = msg[i];
}

main(int argc, char *argv[])
{
    if (argc < 2)
    {
        exit(-1);
    }
    func(argv[1]);
}
    
```

Fig 2. (a) Vulnerable program

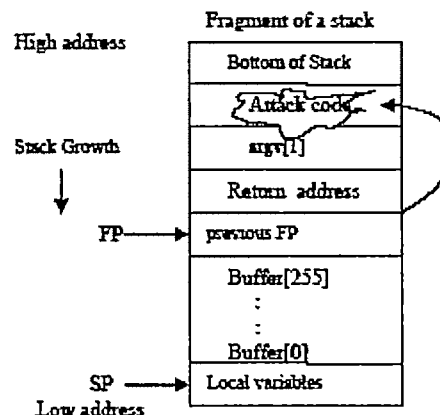


Fig 2: (b) The stack structure and attack

III. RELATED WORKS

There have been several efforts pertinent to the problem of buffer overflow attacks. Not surprisingly, software developers have exerted tremendous effort to avoid coding errors leading to viruses. Some combined hardware/software based approaches are proposed as only the software method is unable to achieve some of the requirements.

There are five basic approaches to defending against buffer overflow vulnerabilities and attacks: Writing Correct Code, Operating Systems Approach, Direct Compiler Approach, Indirect Compiler Approach & Combined Hardware/Software Approach.

Writing Correct Code: In addition to the emphasis on writing secure code, there have been a number of measures developed by software vendors to enhance the security of their products[14]. Writing correct code is a laudable but remarkably expensive proposition [9], especially when writing in a language such as C[28].

Operating Systems Approach: By changing part of the O.S. kernel, it is possible to prevent or detect certain types of

buffer overflow attacks. GCC places executable code on the stack for "trampolines." Kernel patches are available for both Linux and Solaris [16], [17] that make the stack segment of the program's address space non-executable. Attacks exist that bypass this form of defense [19] by pointing a code pointer at code already resident in the program. Other attacks could be constructed that inject attack code into buffers allocated in the heap or static data segments.

Direct Compiler Approach: In an extension to the GNU C compiler, Richard Jones and Paul Kelly have developed a new method to enforce array bounds and pointers checking in the C language [18]. They make the check without changing the representation of pointers, so checked code is compatible with unchecked code. This method solves the buffer overflow attack problem, including those attacks targeting at objects other than return addresses, e.g. function pointers. But the compiler did not appear to be mature; complex programs such as elm failed to execute when compiled with this compiler. Purify[20] is a memory usage debugging tool for C programs. Purify is not actually intended as a production security tool: Purify protection imposes a 3 to 5 times slowdown. The Compaq C compiler for the Alpha CPU "check_bounds" option is used. But only explicit array references are checked, no bounds checking is performed on accesses made by subroutines[28].

Indirect Compiler Approach: The indirect compiler approach is to perform integrity checks on code pointers before dereferencing them[9]. While this technique does not make buffer overflow attacks impossible. Snarskii [21] implemented customized C library for FreeBSD [22]. Libsafe [4] from Bell Labs intercepts function calls to shared C Library and conducts the similar frame-pointer based boundary checking. These approaches fail if a program chooses not to enable frame pointer at compile time (many programs do so for performance optimization) and if the buffer overflow vulnerability is caused by application internal function calls. StackShield [24], StackGuard [23] are medications of gcc. StackShield and StackGuard can only protect a system against a particular type of stack smashing attacks that need to overwrite return addresses. They can't protect frame pointer, function arguments and local variables always. PointGuard [25] is proposed to protect pointers from buffer overflow attacks by encrypting pointer values, which limit its applicability somehow for embedded system protection.

Combined Hardware/Software Approach: The HSDefender [2] [26] technique protects important stack structures, shared function pointers, and local function pointers. However, it is still possible that a variable can be overwritten by a pointer in the heap or BSS. Boundary checking is implemented by a pipeline phase, so not completely performance overhead free. For Function Pointer XOR operation hardware modification of existing processors are suggested. So, new processors should be deployed in the marketplace and becomes standardization issue. The architecture-based split stack approach [6] based on implementing the *split control and data stack, and secure return address stack*, can eliminate the performance overhead. But it requires recompilation in order to provide security benefit and requires changes in the instruction set [27].

IV. PROPOSED EXTERNAL HARDWARE TECHNIQUE

The use of the safe programming languages is effective to defend against buffer overflow attacks. However, it is not realistic to assume that all programmers will follow this good practice or to assume every off-the-shelf software is immune to buffer overflows. It is also impractical to require all software components to use the same language or to be compiled by the same compiler. Therefore, it is very hard for a system integrator to check buffer overflow vulnerabilities of an component based on a pure language-based approach.

The proposed External Hardware technique (E H Technique), shown in figure.3 will be used only for buffer overflow protection purpose to the existing embedded system as an additional circuitry. If this circuitry can be made available in chip form, so that size for the embedded system will not be a discussion issue. In this functional circuitry there are two comparison units. In first unit comparison will be between frame pointer (FP) opcode and opcode of an instruction from system bus if the instruction is memory write related. If result of the comparison unit is zero, latches are hold the address which is the content of frame pointer. Latching of address will be in the T_3 t-state in Intel x86 based processors. Zero comparator output will be strobe signal for FP address hold circuit and it is from system address bus. In case lower order address bus are multiplexed with data bus, lower order input will be from system latches as shown in figure.3. Then increased or decreased address will be stored to be compared with current cycle address depending on processor. The implementation of this hardware on different processors may be different because of different stack structures[2][26]. Whole functional will be activated if only stack indication signal from processor is generated indication stack manipulation operation.

The second unit functional will check, if frame pointer address is going to overwrite or not. In an opcode fetch cycle address latch signal initiates comparison operation and comparison will be in T_1 t-state and holds output upto of initiation write signal. If result is zero, at the instant of initiation of write signal processor will be informed that frame pointer are going to overwrite and processor will exit the process. Sufficiently increasing or decreasing (depending on processor) the FP address, this scheme can defend a system against stack smashing attacks completely.

V. SECURITY & PERFORMANCE ANALYSIS

The advantage of the compiler-based implementation is that it can work on its own without any change in the processor. The disadvantage is of the compiler-based implementation that it requires recompilation in order to provide security benefit. This considerably decreases application program processing speed. There is possibly performance overhead associated with

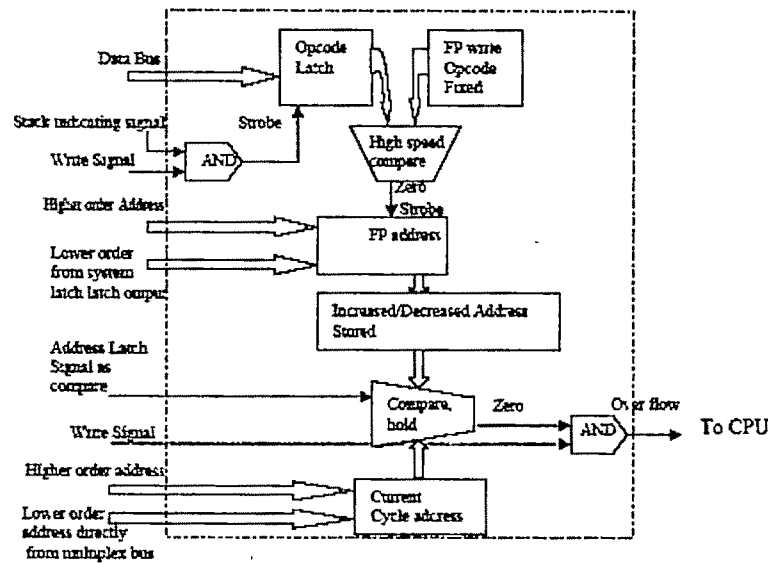


Fig 3: Functional diagram of external hardware

Table 1: Performance comparison with the previous work

Methods	Significant Speed overhead	Modification of Processor/stack structure	Source/Extra code Required	External hardware	Increased Memory size	Hardware Complexity
Operating Systems Approach (Non-Executable stack)	Yes	No	Yes	No	Yes	No
Direct/Indirect Compiler Approach	Yes	No	Yes	No	Yes	No
Combined Hardware/Software Approach	No	Yes	No	Yes	Yes	Yes
External Hardware method	No	No	NO	Yes	No	Yes

any additional register pressure due to the allocation of one's architectural registers as the control stack pointer. GCC register allocator does not model separate functional units well resulting in instable performance. Another source of potential overhead is due to the less efficient use of virtual memory space. The architectural approach does not incur performance overhead and is transparent to application programs, however, the biggest disadvantage is that it requires change in the instruction set[6]. In extra alignment does consume extra stack space, and generally increases code size. Trade-offs are made depending on the size of the programmer's application plus any third party components and libraries. As the program evolves and grows, the allocation decisions are revised in a time-consuming manner. Object files produced using whole program optimization carry intermediate code that serves as input link-time code generation. Linking operations impact performance on embedded processors. Unlike general purpose processors having a single, large memory, embedded processors have many different memories. The layout of the application into various target memories impacts performance. Certain

kinds of fast memory, such as on-chip memory, are limited in space and desired for critical application functions.

As EHTEchnique is an external hardware based solution, program processing speed will not be affected at all the writing and the boundary checking is completely in external hardware in parallel program execution. This is the biggest advantage. Therefore, there is no performance overhead. Source code and extra protection code are not needed. So, there is no new constraints in front of third party software developers. Using our approach to protect a program does not need to modify the source code of the program. Besides, does not change the layout of stack frames, so binary code it generated is compatible with existing libraries and other object files. Using our solution, users can prevent attackers from compromising their systems by changing the return address to execute injected code, which is the most common method performance overhead as function pointers are rarely used in embedded applications. The security comparisons concerning

Table 2: Security comparison with previous approaches

Approaches	Protection of Portion		
	Frame Pointer(FP)	Arguments	Return Address
StackGuard	Yes	No	Yes
StackShield	No	No	Yes
HSDDefender	Yes	Yes/No	Yes
EHTechnique	Yes	Yes	Yes

stack smashing attacks with some previous important are summarized in Table 2.

VI.CONCLUSION

In this paper, the proposed technique is used to defend embedded systems against buffer overflow attacks. It is a hardware based protection with less software modification. This dedicated external hardware can be designed easily as Application Specific Integrated Circuit(ASIC), most suitable form for embedded application. Considering protection it provides a mechanism that can effectively protect embedded systems against buffer overflow attacks and efficiently check if a component has been protected, even without the presence of source code. EHTechnique is more suitable for embedded system integration than the previous approaches.

REFERENCES

- [1] Aleph One, Smashing stack for fun and profit. Phrack, 7(49), November 1996.
- [2] Z. Shao, Q. Zhuge, Y. He, and E.H.-M. Sha, "Security Protection And Checking for Embedded System Integration against Buffer Overflow Attacks via Hardware/Software," IEEE TRANSACTIONS ON COMPUTERS, VOL. 55, NO. 4, APRIL 2006
- [3] H. O'zdoganoglu, T.N. Vijaykumar, C.E. Brodley, and A. Jalote, "Smashguard: A Hardware Solution to Prevent Security Attacks on the Function Return Address," Technical Report TR-ECE 03-13, Purdue Univ., Feb. 2004.
- [4] D. Wagner, J.S. Foster, E. A. Brewer, and A. Aiken, "A First Step towards Automated Detection of Buffer Overrun Vulnerabilities," Proc. Network and Distributed System Security Symp., pp. 3-17, Feb 2000.
- [5] H. Etoh and K. Yoda, Protecting from stack smashing attacks <http://www.tri.ibm.com/projects/security/ssp/main.html>.
- [6] J. Xu, Z. Kalbarczyk, S. Patel, and R.K. Iyer, "Architecture Support For Defending against Buffer Overflow Attacks," Proc. Second Workshop Evaluating and Architecting System Dependability, Oct. 2002.
- [7] K. Skadron, P. S. Ahuja, M. Martonosi, and D.W. Clark, Improving prediction for procedure returns with return address-stack repair mechanisms. In International Symposium on Micro architecture, pages 259-271, 1998.
- [8] A. Baratloo, T. Tsai, and N. Singh, Transparent Run-Time Defense Against Stack Smashing Attacks. In Proceedings of the USENIX Annual Technical Conference, June 2000.
- [9] C. Cowan, P. Wagle, C. Pu, S. Beattie, and J. Walpole, Buffer overflows: Attacks and defenses for vulnerability of the decade. In Proceedings of DARPA Information Survivability Conference and Exposition, pages 119-129, January 2000.
- [10] E. Haugh and M. Bishop, "Testing C Programs for Buffer Overflow Vulnerabilities," Proc. Network and Distributed System Security Symp., Feb. 2003
- [11] H. Brugge, Bounds checking C compiler <http://web.inter.nl.net/hcc/haj.ten.brugge/>.
- [12] R.W.M. Jones and P.H.J. Kelly, "Backwards-Compatible Bounds Checking for Arrays and Pointers in C Programs," Proc. Third Int'l Workshop Automated and Algorithmic Debugging, pp. 13-26, 1997.
- [13] Klog, "The Frame Pointer Overwrite," <http://doc.bughunter.net/buffer-overflow/frame-pointer.html>
- [14] C. Cowan, Calton Pu, and Heather Hinton, Death, Taxes, and Imperfect Software: Surviving the Inevitable. In Proceedings of the New Security Paradigms Workshop, Charlottesville, VA, Sept. 1998.
- [15] Rafel Wojtczuk, Defeating Solar Designer Non-Executable Stack Patch. Bugtraq mailing list, <http://geekgirl.com/bugtraq/>, January 30, 1998.
- [16] "Solar Designer". Non-Executable User Stack. <http://www.openwall.com/linux/>.
- [17] Casper Dik, Non-Executable Stack for Solaris. Posting to comp security.unix, <http://x10.dejanews.com/>, January 2 1997.
- [18] Richard Jones and Paul Kelly, Bounds Checking for C. <http://www-ala.doc.ic.ac.uk/phjk/BoundsChecking.html>, July 1995
- [19] Michele Crabb, Curmudgeon's Executive Summary. In Michele Crabb, editor, The SANS Network Security Digest. SANS, 1997. Contributing Editors: Matt Bishop, Gene Spafford, Steve Bellovin, Gene Schultz, Rob Kolstad, Marcus Ranum, Dorothy Denning, Dan Geer, Peter Neumann, Peter Galvin, David Harley, Jean Chouanard.
- [20] Memory Leaks and Access Errors In Proceedings of the Winter USENIX Conference, 1992. Also available at http://www.rational.com/support/techpapers/fast_detection/
- [21] Alexander Snarskii, Increasing Overall Security. <ftp://ftp.lucky.net/pub/unix/local/libc-letter>, Feb. 1997.
- [22] Alexander Snarskii, FreeBSD Stack Integrity Patch <ftp://ftp.lucky.net/pub/unix/local/libc-letter>, 1997.
- [23] C. Cowan, C. Pu, D. Maier, H. Hinton, J. Walpole, P. Bakke, S. Beattie, A. Gie, P. Wagle, and Q. Zhang, "Stackguard: Automatic Adaptive Detection and Prevention of Buffer-Overflow Attacks," Proc. USENIX Security Symp., Jan. 1998.
- [24] Vendicator, Stack Shield: A stack smashing technique protection tool for Linux, World Wide Web, <http://www.angelfire.com/sk/stackshield/info.html>, 2000.
- [25] C. Cowan, S. Beattie, J. Johansen, and P. Wagle, "Pointguard: Protecting pointers from buffer overflow vulnerabilities," in Proc. of the USENIX Security Symposium, August 2003.
- [26] Z. Shao, Q. Zhuge, Y. He, and E.H.-M. Sha, "Defending Embedded Systems against Buffer Overflow via Hardware/ Software," Proc. IEEE 19th Ann. Computer Security Applications Conf., Dec 2003.
- [27] Pu-Hau Hsu, Tzi-Cker Chiueh, "RAD: A Compile-Time Solution to Buffer Overflow Attacks," Proc. the 21st International Conference on Distributed Computing Systems, IEEE Computer Society, 2001
- [28] E. Haugh and M. Bishop, "Testing C Programs for Buffer Overflow Vulnerabilities," Proc. Network and Distributed System Security Symp., Feb. 2

Transmission of ECG Signal Using Microcontroller Based Wireless Bi-phase Modulation Technique

R.Gupta¹, C.Das², A.Mondal³, J.N.Bera¹, M.Mitra¹, T.K.Mitra¹

¹ Department of Applied Physics, University of Calcutta, India

e-mail: rgaphy@caluniv.ac.in, jitendrabera@rediffmail.com, mmaphy@caluniv.ac.in

²Dr.B.C Roy Engg College, West Bengal, India, e-mail: chandan_0074@yahoo.com

³BCET, Durgapur, West Bengal, India, e-mail: arininstru@rediffmail.com

Abstract— One of the emerging issues in rural health management system in India is to extend the services among the poor population distributed at vast geographical locations with poor connectivity in terms of infrastructure. ECG is considered as one of the prime physiological signal to detect the cardiac condition of a human being. This paper illustrates the development of a wireless transmitter system, aimed to transmit low frequency ECG signals over a remote distance. The chief motivation behind this work is to develop a wireless telecardiology system, which will be developed to aid the rural health-care management. The transmitter will act as a prime component in the 'Portable Telecardiology Kit', which is one component of a wireless telecardiology solution for detecting preliminary level cardiac abnormalities.

Key words— Bi-phase modulation, ECG signal, Microcontroller, Transceiver.

I. INTRODUCTION

WIRELESS data services and systems represent a rapidly growing and increasingly important segment of the communication applications. Wireless systems were initially developed to carry voice data, but with development of technology, different types of data, like image, video, message is now sent over wireless systems. Many types of mobile wireless networks are in use. Main challenges are delay spreads and multipath fading etc. [1].

A successful application of wireless communication

systems is in the field of advanced healthcare services. Transmission of digital and video images has been in use to transfer the medical images using medical image compression technique. Use of wireless systems for emergency services, maintaining electronic patient records, patient monitoring and home care telemedicine applications is reported[2-4].

In a personal area network, a group of wearable medical sensors can be monitored in a telemedical environment. Recent advances in microcontroller and sensor technology including low power consumption and good performance to cost ratio made possible a whole range of new applications using distributed sensor networks. Using Wireless Intelligent Sensor (WISE) some important physiological signals like EEG, ECG, GSR can be tracked for mobile patients in a DSP server in telemedical environment [5-8]. In a multi-tier telemedicine system, a Wireless Body Area Network(WBAN) can be formed using wireless intelligent devices to aid computer-assisted physical rehabilitation applications and ambulatory monitoring. The system performs real-time analysis of sensors' data, provides guidance and feedback to the user, and can generate warnings based on the user's state, level of activity, and environmental conditions. In addition, all recorded information can be transferred to medical servers via the Internet and seamlessly integrated into the user's electronic medical record and research databases [9]. Use of satellite link is demonstrated [10-14] to implement wireless telemedicine, but it requires expensive equipments, dedicated links and skilled operators.

A wireless Telecardiology system can be developed in which a remote patient can be monitored using a microcontroller with a cordless telephone. The ECG signal of the patient is sent to the local health care center, where an automated

cardiac signal processing system analyses the ECG signal and if abnormalities are found, a report is generated to be sent back to the patient [15].

A wireless transmitter using microcontroller is described in the paper. The modulation technique used is BPM (Bi-phase modulation), which has some unique advantages over Pulse Position Modulation (PPM) for low frequency signals [16-18].

II. MATERIALS AND METHODS

A. Development of Bi-phase Modulation Scheme

The block diagram of the transmitter section is given in

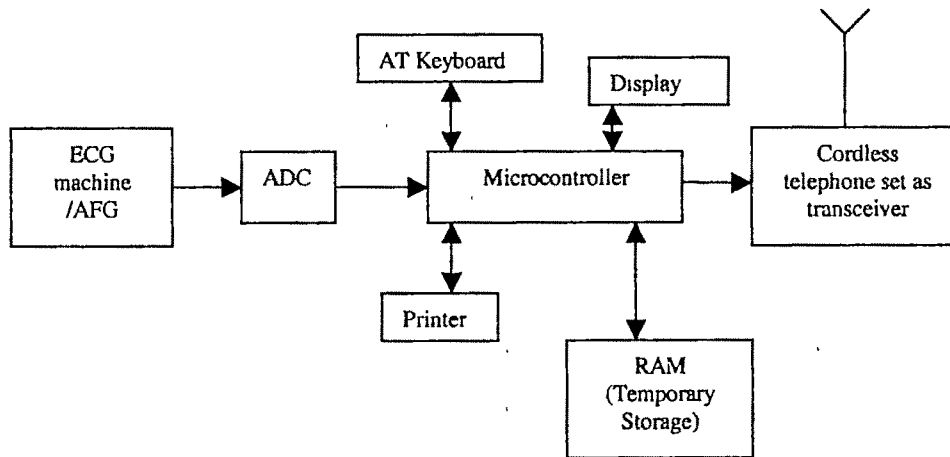


Fig 1: Block diagram of the transmitter using Bi phase modulation

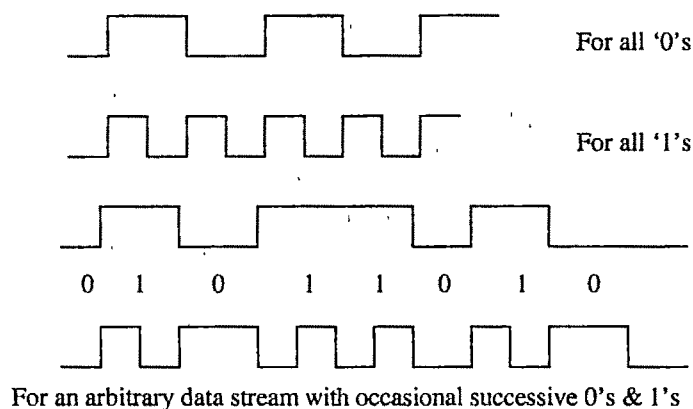


Fig2: Bi-phase Modulation Protocol

'store-and-transmit' basis. The command is generated from an ASCII keyboard interfaced with microcontroller in interrupt mode. An external RAM is used to store the data from ADC upon a chosen keystroke. The same data is then streamed to the transmitter in a bi-phase format using the microcontroller upon a second pre-assigned keystroke from the keyboard. Before final transmission proper data-framing is done for each byte with the inclusion of 'zero' as start bit and 'one' as stop bit. The data packet is formed with 100 such frames with a

Fig1. The ECG signal is received by the microcontroller unit after conversion by an 8-bit ADC. The signal is first stored temporarily in the contiguous memory locations in the external RAM as data. The data is then converted into a bi-phase format using the microcontroller and finally sent by the transmitter of a cordless telephone set. The chief aim is to convert the data [ECG signals of a patient] into a bi-phase format using an 8-bit microcontroller. The ECG signal is simulated using an arbitrary function generator connected with a PC with the help of prerecorded ECG database [12-lead]. The algorithm is developed to transmit the data on

synchronization pattern. The final objective is to transmit the ECG data along with some relevant physiological information (like body mass index, age, sex, etc.) which will be crucial for decision making about the patient's cardiac condition. These information are transmitted in a separate tag page before the actual ECG data in a separate data packet with a distinct separate synchronization pattern, so that the receiver can distinguish between the tag page and actual ECG data.

Since ECG is inherently a low frequency signal. For

transmission of such signals, the Bi-phase modulation is adopted in the developed system. To avoid the occurrence of successive 0's and 1's in the data pattern received in the

transmitter leading to a loss of synchronism, a new family of pulse formats represented by only two levels has been proposed(Fig.2).

A. Transmission of the signal

The data in bi-phase format is transmitted using a wireless communication system in VHF band. The reason of choosing the VHF band is to use a standard available cordless telephone set customizing its modulation circuit. The bi-phase signal from the microcontroller output modulates the VHF oscillator of the telephone set. A frequency modulation scheme is implemented with 117 MHz as carrier frequency.

The final aim is to operate this transceiver in a transmitter mode, while as receiver mode it will receive the report of analysis of the ECG data at the local rural healthcare center.

testing the quality of transmission some standard signals were sent in the preliminary stage. The response of the system is shown in fig 3(a) using sinusoidal and saw-tooth waves. For bandwidth study, suitable amplitude signal (below 4V) with frequency range 250Hz to 3.5 KHz is chosen. The receiver was kept at a distance of about 200 feet and the received signal was analyzed. The result was acceptable. Thereafter some prerecorded database of ECG signals was sent. The outcomes at receiver of the cordless phone are shown at fig 3(b). As the distance is increased, the link tends to fail sometimes due to multipath fading. Suitable mitigation technique is to be used for optimized performance.

III. TESTING

The transmitter system has been designed and run with prerecorded database in the initial stage for pilot study. For

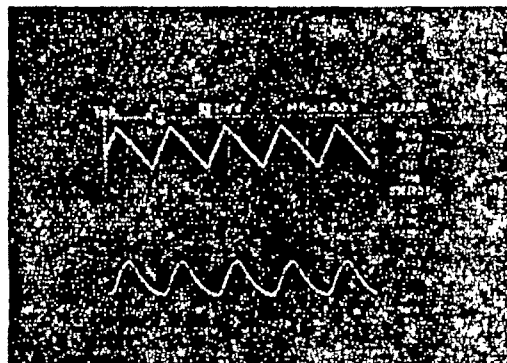
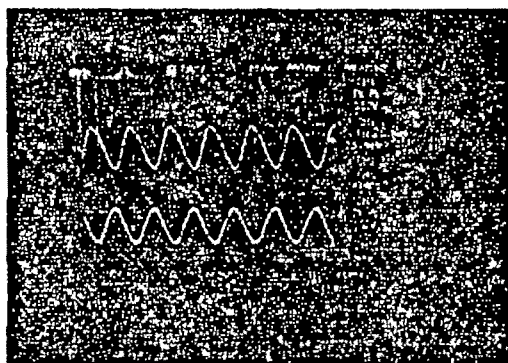


Fig 3(a): Response of the transmitter for test signals
[The upper waveform corresponds to the transmitter and lower one to the receiver]

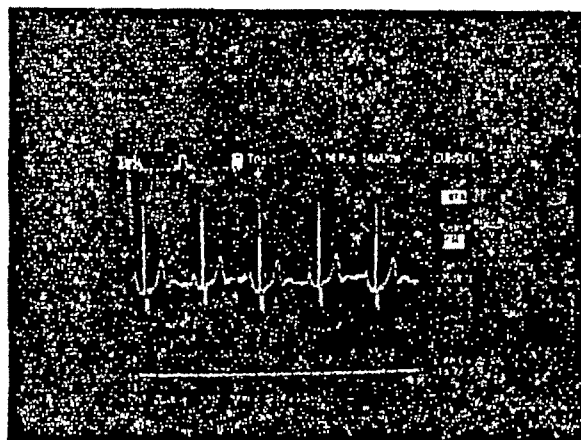


Fig 3(b): ECG waveform at the receiver placed at 200ft
[Transmitter connected with AFG to simulate the ECG signal]

IV. CONCLUSION

The wireless transmitter described in this paper is designed with the objective of developing a total wireless cardiac care system. This unit will establish a wireless link between the patient home and the rural health care center. The unit is required to be carried by a semi-skilled technician to the patient site in response to a chest pain report. A portable ECG machine will be hooked up with this 'kit' to send the signal to the health care center. In the center there will be a PC based automated cardiac signal processing system, which will extract the ECG data from the received signal. Then it will analyze the signal from a knowledge-base. If any abnormalities are found, that will be generated and sent back to the portable telecardiology kit at patient home using a similar duplex communication system, operating at a different frequency.

The system will be a solution to the poor infrastructure in rural health management in India. In certain seasons, the connectivity in remote areas, especially hilly regions become very poor. The rural population of vast geographical locations in India can benefit from using this system, which can be run 24 hours a day and, moreover, requires minimum human intervention for its operation.

REFERENCES

- [1] K.Pahlavan and A.H.Levques, "Wireless Data Communications", *IEEE Pressing*, vol.82, pp. 1398-1430 September 1994.
- [2] C.S.Pattichis, E.Kyriacou, S.Voukarides, M.S.Pattichis, R.Istevanian, C.N. Schizas, "Wireless Telemed Systems: An Overview", *IEEE Antennas and Propagation*, vol. 44, pp.143-153, April 2002.
- [3] J.Bei, Y.Zhang, D.Shen, L.Wen, C.Ding, Z.Cui, F.Tian, B.Ya, B.Dai, J.Zhang, "A Portable ECG and Blood Pressure Telemetry System", *IEEE Engineering in Medicine and Biology Magazine*, vol.18, pp. 63-70, August 1999.
- [4] K.Hung, Yuan-Ting Zhang, "Implementation of a WAP-based telemedicine system for patient monitoring", *IEEE trans on Information Technology in Biomedicine*, vol. 7, pp. 101-107, June 2003.
- [5] E.Jovanov, J.Price, D.Rasovic, K.Kavi, T.Martin, R.Adhami, "Wireless Personal Area Network in Telemedical Environment", in *Proc. 2000 IEEE EBMS conf on Information Technology Applications in Biomedicine*, pp.22-27.
- [6] J.Agre, L.Clare, "An Integrated Architecture for Cooperative Sensing Networks", *IEEE Computer*, pp.106-108, May 2000.
- [7] G. Asada, M. Dong, T.S. Lin, F.Newberg, G.Pottis, W.J.Kaiser, H.O.Maroy, "Wireless Integrated Network Sensors: Low power Systems on a Chip", in *Proc. ESSCIRC '98, Solid State Circuits Conference*, pp.9-16, 1998.
- [8] M.Jiang, "Tele-cardiology Sensor Networks for Remote ECG Monitoring", M.Sc Thesis, Dept. Comp.Engg, Rochester Inst. Of Technology, Rochester, NY, 2006.
- [9] E.Jovanov, A.Milenkovic, C.Otto, P.C.Groen, "A Wireless Body Area Network of Intelligent Motion Sensors for Computer Assisted Physical Rehabilitation", *Journal of NeuroEngineering and Rehabilitation*, 2005.
- [10] P. B. Angood, R. Satava, C. Doorn, and R. Merrell, "Telemedicine at the Top of the World: the 1998 and 1999 Everest Extreme Expeditions," *Telemed. J. e-Health*, vol. 6, pp. 315-323, 2000.
- [11] S. Y. N. Boyd, J. R. Bulgrin, R. Woods, T. Morris, B. J. Rubal, and T. D. Baugh, "Remote Echocardiography via INMARSAT Satellite Telephone," *J. Telemed. Telecare*, vol. 6, pp. 305-307, 2000.
- [12] S. Hwang, J. Lee, H. Kim, and L. Myoungcho, "Development of a Webbased Picture Archiving and Communication System Using Satellite Data Communication," *J. Telemed. Telecare*, vol. 6, pp. 91-96, 2000.
- [13] B. K. Gilbert, M. P. Mitchell, A. R. Bengali, and B. K. Khonduria, "NASA/DARPA Advanced Communications Technology Satellite Project for Evaluation of Telemedicine Outreach Using Next- Generation Communications Satellite Technology: Mayo Foundation Participation," in *Mayo Clinic Proc.*, vol. 74, 1999, pp. 753-757.
- [14] R. Satava, P. B. Angood, B. Harrett, C. Macedonia, and R. Merrell, "The physiologic cipher at altitude: Telemedicine and real-time monitoring of climbers on Mount Everest," *Telemed. J. e-Health*, vol. 6, pp. 303-313, 2000.
- [15] M.Mitra, S.Mitra, J.N.Bera, B.B.Choudhury, "Preliminary Level Cardiac Abnormality Detection Using Wireless Telecardiology System", presented at ICDS'07, Guadeloupe, French Caribbean, Jan 2-6, 2007.
- [16] W.C.Chang, D.S.Ha, "On the Performance of Bi-phase Modulated UWB Signals in a Multipath Channel", *IEEE Semiannual Vehicular Technology Conf 2003*, vol.3, pp.1654-1658, 2003.
- [17] K.Ohno, T.Kobe, T.Ikagami, "A proposal for An Interference Mitigation Technique Facilitating The Coexistence of Biphasic UWB and Other Wideband Systems", Pub. in *International workshop on Ultra Wideband Systems*, pp.50-54, 2004.
- [18] J.Bera, R.Bera, S.Pal, S.K.sarkar, "Multimedia MAC (Medium Access Control) protocols Towards Personal Communication Network", presented at Horizons of Telecommunications 2003, Kolkata, India, February 3-5, 2003.

Technical Session 6A

ANN

Type Identification of Unknown Thermocouple Using Probabilistic Neural Network

Kundu. P¹, and Sarkar. G²

¹Department of Electrical Engineering, Jadavpur University, Kolkata, India (e-mail: kundupalash2004@yahoo.co.in).

²Department of Electrical Engineering, Jadavpur University, Kolkata, India (e-mail: sgautam63@yahoo.com).

Abstract—It is well known that the neural network is the powerful tool for pattern recognition. Here a general method is proposed for type identification (e.g. J, K, S etc.) of unknown thermocouple sensor using suitable artificial neural network (ANN). The input output characteristic of different type thermocouples are trained by a pattern classifier network, which is a probabilistic neural network (PNN). The input (Temperature) – output (thermo e.m.f.) characteristic of different types of thermocouple are characterized by their thermo-coefficients (α, β, γ , etc) within their corresponding full scale operation. In the proposed case, if a PNN is properly trained with the calibration data set of each type of thermocouple along with their class no., it can identify the characteristic pattern of the corresponding type (e.g. J, K, E etc) by producing appropriate class no. already designated. Once their class no. is determined, corresponding thermo coefficients can easily be determined from the calibration of identified type of thermocouple.

Key words— Classification, PNN, radial basis neural network.

I. INTRODUCTION

APPLICATION of Artificial neural network (ANN) in measurement, instrumentation and control is gaining importance for several years, taking the advantage of non-linear modelling, mapping, estimation of errors, and pattern recognition. An artificial neural network is a computational structure that is inspired by observed processes in natural networks of biological neurons in the human brain. It consists of simple computational units, called neurons that are highly interconnected. Depending on the value of weighted sum of the variables, the neuron gives a signal to the neurons in the adjacent layer through a non-linear transfer function (log sigmoid, tan sigmoid function). The choice of the architecture of the network depends on the task to be performed and the architecture of the model is specified by the node

characteristics, network topology and learning algorithm. In standard architecture, neurons are grouped into different layers like input, output and hidden layers. Generally, for modelling of physical systems, multi layered, feed forward network (one layer for input and output, and few hidden layers) is normally used. The basic capability of neural networks is to learn patterns from examples and experiences. This is accomplished by adjusting the weights of given interconnections according to some learning algorithm. In general, the learning can be supervised or unsupervised. In a supervised learning the learning is guided by specifying, for each training input pattern, the class to which the pattern is supposed to belong. That is the desired response of the network to each training input pattern and its comparison with the actual output of the network are used with learning algorithm for appropriate adjustments of the weights. These adjustments, whose purpose is to minimize the difference between the desired and actual outputs, are made incrementally. That is small adjustments in the weights are made in the desired direction for each training pair. This is essential for facilitating a convergence to a solution (specific values of the weights) in which patterns in the training set are recognized with high fidelity. Once a network converges to a solution, it is then capable of classifying each unknown input pattern with other patterns that are close to it in terms of the same distinguishing features. In an unsupervised learning algorithm, the network forms its own classification of patterns. The classification is based on commonalities in certain features of input patterns. This requires that a neural network implementing an unsupervised learning algorithm be able to identify common features across the range of input patterns.

II. GENERAL METHOD FOR PATTERN IDENTIFICATION USING PROBABILISTIC NEURAL NETWORK

If there is k object associated with n numbers of variables (X_1, X_2, \dots, X_n), considering object inputs and outputs, its pattern may be classified with a variables Y of k -dimensions, such that for a subset of real valued variables X_1, X_2, \dots, X_n

falling between the range $[X_{\min} \dots X_{\max}]$. $Y_j = (1, 1, 1, \dots, p \text{ th term})$ and for $j = i$ only and $Y_j = (0, 0, 0, \dots, p \text{ th term})$ for $j \neq i$; Where, j = output designator = 1, 2, 3, ..., k , and i = input designator. Here the neural network serves as non-linear function estimator, whose value lies in the range $[1, 0]$ depending on successful matching of object pattern or not. Thus when $Y_k = f_k(X_1, X_2, X_3, \dots, X_n) = 1$ for a given subset $X_p = (X_1, X_2, X_3, \dots, X_n)$ and $Y_k = f_k(X_1, X_2, X_3, \dots, X_n) = 0$ for other subset $X_q = (X_1, X_2, X_3, \dots, X_n)$ is satisfied, the existence of k th object is identified. The following description clearly explains how a PNN can classify the object pattern.

A. Radial Basis Neural Network (RBNN)

Since the problem of thermocouple type identification can be considered as pattern classification, probabilistic neural networks (PNN) can be used for this problem[3]. Basically the architecture of PNN is a modified version of that of generalized regression neural network (GRNN). However both these architecture belongs to the category of radial basis neural network (RBNN) and are variants of RBNN. The pattern classification problem can be solved using multilayer perception (MLP) feed forward network with most widely used back propagation training algorithm but despite its ubiquity, back propagation has serious training problems with large no. training data set, lack of which may produce false prediction of class.

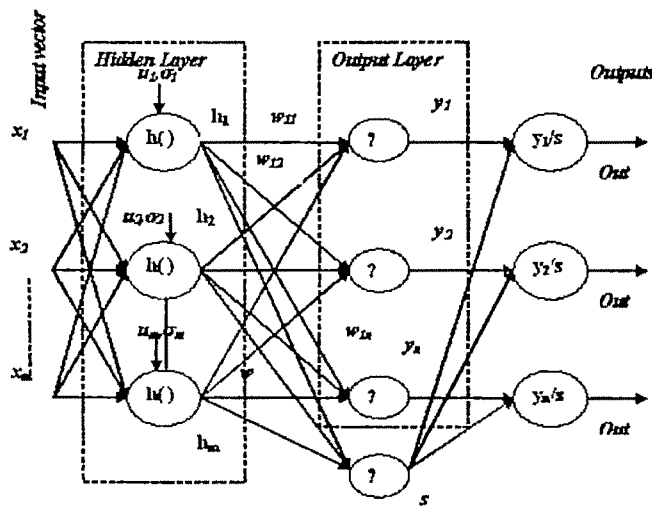


Fig. 1 Radial Basis Neural Network

The radial basis function network, topology of which is shown in Fig. 1. looks much like the common feed forward network used with back propagation training; however its operation is fundamentally different rather than starting with random values, the weights of each hidden layer neuron are set to values that produce the desired response. A maximum output for an input identical to its weights, with a lesser output for dissimilar

inputs. The topology of RBNN is shown in Fig. 1. Here, inputs $x_1, x_2, x_3, \dots, x_n$ comprising an input vector x , are applied to all neurons in the hidden layer. Each hidden layer neuron computes the following exponential function, called Gaussian response functions.

$$h_i = \exp[-D_i^2 / (2\sigma^2)] \quad (1)$$

where x = an input vector, u_i = weight vector of hidden layer neuron i (Note that this equals an input training vector). There must be one hidden layer neuron for each such training vector) and $D_i^2 = (x - u_i)^T (x - u_i)$ = Squared distance between the input vector and training vector.

The weights of each hidden layer neuron are assigned the values of an input training vector. The output neuron produces the linear weighted summation of these as given by:

$$y = \sum_i h_i w_i \quad (2)$$

where w_i = a weight in the output layer.

Sometimes the outputs are optionally normalized according to following formula that divides the output of each neuron in the output layer by the sum of all hidden layer outputs.

$$out_i = \sum_i h_i w_i / \sum_i h_i \quad (3)$$

Thus the output has a significant response to the input x only over a range of values of x , called the receptive field of the neuron, the size of which is determined by the value of σ , sometime called spread parameter.

B. Generalized Regression Neural Network (GRNN)

GRNN or generalized regression neural network belongs to category of RBNN, which has the desirable property of requiring no iterative training. The topology of GRNN is identical as shown in Fig. 1. It approximates any arbitrary function between input and output vectors, drawing the function estimate directly from the training data. Furthermore, it is consistent; that is, as the training set size becomes large, the estimation error approaches zero, with only mild restriction on the function. GRNN is based on nonlinear regression theory, a well established statistical technique for function estimation. By definition, the regression of a dependent variable y on an independent variable x estimates the most probable value for y , given x and training set. The training set consists of values for x , each with a corresponding value for y (x and y are, in general, vectors). GRNN is based upon the following formula from statistics.

$$E(y|x) = \frac{\int_{-\infty}^{\infty} y f(x, y) dy}{\int_{-\infty}^{\infty} f(x, y) dy} \quad (4)$$

where, y = output of the estimator, x = the estimator input vector, $E(y|x)$ the expected value of the output, given the input vector x , $f(x, y)$ = the joint probability density function of x and y .

GRNN is, in essence, a method for estimating $f(x, y)$, given only a training set. Because, the probability density function is derived from the data set without perception about its form, the system is perfectly general. The function value is estimated optimally as follows:

$$y_i = \sum_{l=1}^n h_l w_{ij} / \sum_{l=1}^n h_l \quad (5)$$

where w_{ij} = the target (desired) output corresponding to input training vector x_i and output I , the output of hidden layer neuron $h_i = \exp[-D_i^2 / (2\sigma^2)]$, $D_i^2 = (x - u_i)^T (x - u_i)$ = squared distance between the input vector x and training vector u , x = the input vector, u_i = training vector i , σ = a constant controlling the size of the receptive region.

C. Probabilistic Neural Network (PNN):-

PNN results from modification of GRNN, the topology of which is shown in Fig. 2. Since GRNN can approximate any continuous function; it can easily be made into pattern classifier. In PNN, each output represents the probability of its associated class. This result may appear surprising considering the different theoretical foundation of two paradigms, PNN coming from Bayesian classifier theory and GRNN from regression theory. A classifier has binary target vectors, each of which has a single one indicating the target class. All other components are zero; the GRNN network used as a classifier will have its output layer weights set to ones and zeros. Classification then consists of applying an input vector and determining which output is greatest. The basis for PNN is Bayes theorem, which states:

$$P(y^i | x) = P(x | y^i) P(y^i) / P(x) \quad (6)$$

where $P(y^i | x)$ the probability that input vector x is in class y_i , $P(y^i)$ = the probability of class i occurring, $P(x)$ = the probability of an input vector with values x .

In PNN, the probability distribution function $P(x | y^i)$ is approximated by Parzen windows, typically using the exponential function. By the previous definitions,

$$P(x | y^i) = (K / N^i) \sum_{j=1}^{N^i} \exp[-D_j^2 / (2\sigma^2)] = (K / N^i) \sum_{j=1}^{N^i} h_j^i \quad (7)$$

where $K = 1 / (2\pi^{d/2} \sigma^d)$ = the scaling factor to produce a multidimensional unit Gaussian, $D_j^2 = (x - u_j)^T (x - u_j)$ = the squared Euclidian distance between the current input x and training vector j in class I h_j^i = training vector (hidden layer neuron) output j in class i , d = number of components in the input vector, N^i = number of training vector, N = total number of training vectors (hidden layer neurons).

The hidden layer in PNN is portioned by their classes and

all interleaved weights are unity. The probability of y_i may be estimated by its relative frequency in the training set, as, $P(y^i) = N^i / N$

Applying Bayes theorem to calculate the conditional probability of x for each class, then summing these over all classes yields

$$\begin{aligned} P(x) &= \sum_{i=1}^{N^i} P(x | y^i) P(y^i) \\ &= \sum_{i=1}^{N^i} (K / N^i) \sum_{j=1}^{N^i} \exp[-D_j^2 / (2\sigma^2)] (N^i / N) \\ &= (K / N) \sum_{i=1}^{N^i} \sum_{j=1}^{N^i} h_j^i \end{aligned} \quad (8)$$

where N^i = the number of classes.

Thus, the inner summation adds all hidden layer neuron outputs associated with class i ; the outer summation counts these over all classes. The double summation may be eliminated by simple counting all hidden neuron outputs. Therefore,

$$P(x) = (K / N) \sum_{i=1}^N h_i \quad (9)$$

Substituting,

$$P(y^i | x) = \frac{\sum_{j=1}^{N^i} h_j^i}{\sum_{i=1}^N h_i} \quad (10)$$

where N^i = is the number of hidden layer neurons associated with class j .

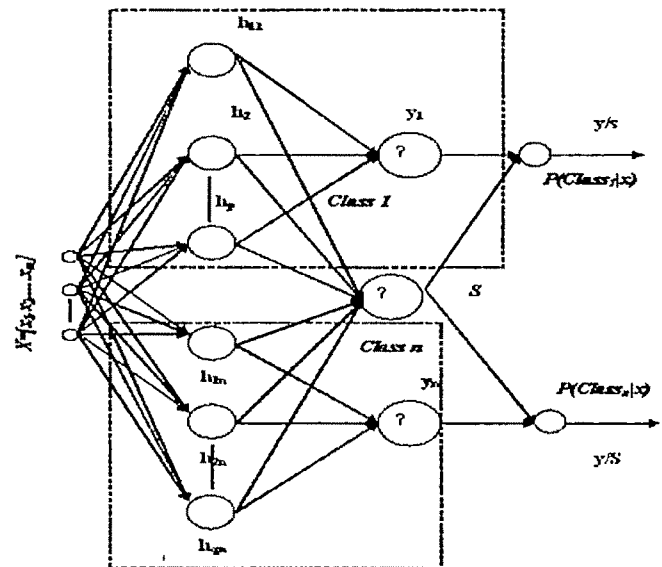


Fig 2. Probabilistic Neural Network.

Thus it can be summarized that in PNN,

- Each output represents the conditional probability of a class, given the current input vector.
- Hidden layer neurons are portioned by class.
- The numerator is summed only over those hidden layer

neurons associated with a given class.

Since PNN is a classifier, the target is either 0 or 1 for a given training vector. Therefore the summation in the numerator is taken only over those hidden layer neurons which are in class i.

III. CASE STUDY

Here the object variables are two, namely X_1 (Thermo e.m.f. in mV) and X_2 (Temperature in °C), which form the input vector P. The object pattern variables is Tc (target class), the values of which are assigned as 1,2,3,4,5,6,7,8 since in the present case eight different types thermocouple sensors (e.g. J, K, S, T, R, N, B and E types) are considered. The composition and range of operating temperature of different thermocouples are shown in Table I. The object variable is input to ANN and target is the output from the ANN. The trained network is tested with testing data set for each type thermocouple. The overall performance of the training and testing the network is also analyzed.

TABLE I
THERMOCOUPLE TYPES

Type	Composition	Temp. range (°C)
B	Pt-30% Rh versus Pt-6% Rh	0 to 1820
E	Ni-Cr alloy versus a Cu-Ni alloy	-270 to 1000
J	Fe versus a Cu-Ni alloy	-210 to 1200
K	Ni-Cr alloy versus Ni-Al alloy	-270 to 1372
N	Ni-Cr-Si alloy versus Ni-Si-Mg alloy	-270 to 1300
R	Pt-13% Rh versus Pt	-50 to 1768
S	Pt-10% Rh versus Pt	-50 to 1768
T	Cu versus a Cu-Ni alloy	-270 to 400

A. Preparation of Thermocouple Data Base

The entire data for different type thermocouples are compiled from internet online ITS-90 thermocouple reference table according to NIST (National Institute of Standard & Technology) standard. The thermocouple object database is arranged in the format shown in Table II. X_1, X_2 are inputs for thermo e.m.f. and temperature. As the ANN input should be in the range of -1 to +1, so all the inputs are normalized by using the formula as follows: $\frac{(e - e_{min})}{(e_{max} - e_{min})}$ and $\frac{(T - T_{min})}{(T_{max} - T_{min})}$.

B. Training & simulating the PNN

When the input vector P{e.m.f. temperature} is presented, the first layer of PNN computes distances from the input vector to the training input vectors and produces a vector whose elements indicate how close the input is to a training input. The 2nd layer sums these contributions for each class of inputs to produce as its output a vector of probabilities. Finally, a suitable transfer function in the second layer picks the maximum of these probabilities, and produces a one for that class and a 0 for the other classes. It is assumed that there are Q input vector/target vector pairs. Each target vector has K

TABLE II
THERMOCOUPLE DATA BASE

Type	Sl. No.	X1 e.m.f. (mV)	X2 Temp. (°C)	Target Class No. (Tc)
J	1	-8.095	-210	1
	2	-8.076	-209	1

	1410	69.496	1199	1
K	1411	69.553	1200	1
	1412	-6.458	-270	2
	...	-6.457	-269	2
	...	-6.456	-268	2

S	3054	54.852	1371	2
	3055	54.886	1372	2
	3056	...	-50	8
	-49	8
	-48	8

T	4874	18.682	1767	8
	4875	18.693	1768	8
	4876	-6.258	-270	5
	4877	-6.256	-269	5

B	5545	20.748	398	5
	5546	20.810	399	5
	5547	20.872	400	5
	5548	0.000	0	7
	5549	0.000	1	7
	...	0.000	2	7
E	...	-0.001	3	7
	...	-0.001	4	7
	...	-0.001	5	7
	...	-0.001	6	7
	...	-0.001	7	...
	...	-0.002	8	...
R

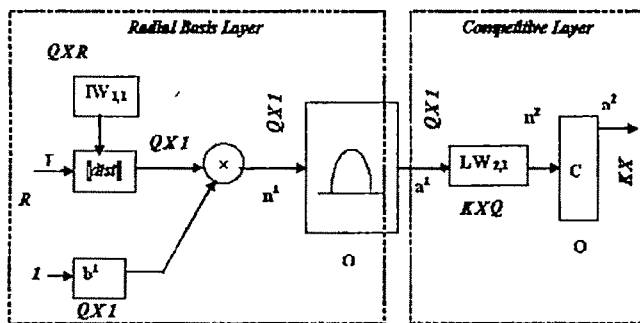
	7368	13.809	1819	7
	7369	13.820	1820	7
	7370	-9.835	-270	6
	7371	-9.833	-269	6
N	7372	...	-268	6

	8640	76.29	999	6
	8641	76.37	1000	6
	8642	-0.226	-50	4
...	8643	-0.223	-49	4
	8644	...	-48	4

	10460	21.08	1767	4
	10461	21.10	1768	4
...	10462	-4.345	-270	3
	10463	-4.345	-269	3
	10464	-4.344	-268	3

	12032	47.47	1299	3
	12033	47.51	1300	3

(in the present case $K=8$) elements. One of these elements is one and the rest is zero because each input vector is associated with one of K classes. The 1st layer input weights, IW are set to the transpose of the matrix formed from the Q training pairs (e.g. P^T). When an input is presented the $\|dist\|$ box produces a vector whose elements indicate how close the input is to the vectors of the training set. These elements are multiplied, element by element, by the bias and sent the radbas transfer function. An input vector close to a training vector will be represented by a number close to one in the output vector a^1 .



$a^1 = \text{radbas}(\|IW_{1,1} - P\|b^1)$; $a^2 = f(LW_{2,1}.a^1)$
 a^1 is i th element of a^1 where, $IW_{1,1}$ is a vector made of the i th row of $IW_{1,1}$
 $Q = \# \text{input/target pairs} = \# \text{of neurons in layer 1}$
 $R = \# \text{elements in input vector; } P = \text{input vector}$
 $K = \# \text{of classes of input data} = \# \text{of neurons in layer 2}$

Fig. 3. Operation of PNN.

If an input is close to several training vectors of a single class, it will be represented by several elements of a^1 that are close to one. The 2nd layer weights LW , are set to the matrix T of target vectors corresponding to target class T_c . Each vector has a one only in the row associated with that particular class on put, and zero elsewhere. The multiplication Ta^1 sums the elements of a^1 due to each of the K input classes. Finally, the second layer transfer function produces a one corresponding to the largest element of n^2 , and zeros elsewhere. Thus, the network has classified the input vector into a specific one of K classes because that class had the maximum probability of being correct.

IV. RESULTS AND DISCUSSIONS

In this investigation, the ANN training and simulations were performed with the programme under MATLAB [5] environment using built in functions, (a) 'newpnn' for creation, configuration and training of the PNN (b) 'sim' for testing the network. (c) 'int2vect' for conversion of target class into target vector (d) 'vec2int' for conversion of target vector into class no. After training the PNN, it has been tested randomly with sample input vector for each type of thermocouple and the results are tabulated as shown in the Table III. The target

class no. are assigned as mentioned in the Table II.

TABLE III
SIMULATION RESULT

Input vector $P = \{e.m.f. \text{ temp}\}$	Identified Class Y_c	Corresponding type
{ 69.439 , 1198 }	1	J
{ 54.852 , 1371 }	2	K
{ 47.477 , 1299 }	3	N
{ 20.748 , 398 }	5	T
{ 21.089 , 1767 }	4	R
{ 76.298 , 999 }	6	E
{ 13.809 , 1819 }	7	B
{ 18.682 , 1767 }	8	S
{ 69.439 , 1198 }	1	J
{ 54.852 , 1371 }	2	K
{ 47.477 , 1299 }	3	N
{ 20.748 , 398 }	5	T

V. CONCLUSION

Here a PNN is proposed to work as pattern classifier in identifying the unknown thermocouple type (e.g. J, K, S.... etc.). However the outputs of the ANN can also be processed with the help of another suitable ANN connected in cascade with the previous network for computing the thermocoefficients $(\alpha, \beta, \gamma, \dots)$ up to appropriate dimensions suitable for different type thermocouples based on piece-wise liberalization with multiple breakpoints. The proposed study is expected to encourage the designer in undertaking the challenging task for implementing the method in real time embedded hardware systems, such as micro controllers with 16 bit resolution or fixed-point digital signal processors (DSP).

REFERENCES

- [1] N. J. Medrano-Marques, B. Martin-del-Brio, "A general method for sensor linearization based on Neural Network," ISCAS 2000 - IEEE International Symposium on Circuits and Systems, May 28-31, 2000, Geneva, Switzerland.
- [2] M. Attari, F. Boudjema, and M. Heniche, "An Artificial Neural Network to linearize a G (Tungsten vs. Tungsten 26% Rhenium) thermocouple characteristic in the range of zero to 1200° C," IEEE Catalog Number:95 TH8081.
- [3] P.D. Wasserman, *Advanced methods in Neural Computing*. Van Nostrand, New York, 1993.
- [4] Duda R. O., and P.E. Hart, *Pattern Classification and Scene Analysis*. Wiley, New York, 1973.
- [5] Neural network toolbox5 user guide, The MathWorks, 2007.

Application of Neuro-Fuzzy Controller in HVAC System

A. K. Pal

Heritage Institute of Technology, Kolkata, India, e-mail: arabinda_k_pal@yahoo.com

Abstract— Linguistic modelling of complex nonlinear systems constitutes the heart of many control and decision-making processes and fuzzy logic represents one of the most effective algorithms to build such linguistic models. In the first part of this paper, only thirty-six fuzzy rules are developed using fuzzy triangular membership function. The objective of using less number of fuzzy rules is leading to a smaller amount of computational time. In the second part few of these rules are used to train a neural network by back propagation neural network (BPNN) to develop a neuro-fuzzy controller (NFC). In the designed three layer neural network, the first layer contains two neurons for two inputs: error (e) and change of error (Δe) respectively, whereas the second layer or the hidden layer contains thirty neurons and the third layer use only one neuron to get the output (u) value. The third part of the paper is used to study the performance of neuro-fuzzy controller for a linear and a nonlinear process respectively. In the pilot study part proposed NFC is applied to the supply air pressure control loop of Heating, Ventilation and Air-conditioning (HVAC) system. Most of the controllers commissioned in HVAC systems are of Proportional-Integral-Derivative (PID) type, due to its relatively simple structure. But the tuning procedure of a HVAC system may take a control engineer up to three days to search for a proper PID controller setting for an air pressure loop. The situation is even worse, if re-tuning is needed and this is true for many large HVAC systems. Therefore, it is highly desirable to develop workable technology for HVAC industries. The tuning procedure of the proposed NFC is very easy. Simulation results show that the Neuro-Fuzzy controller performances are comparable to the other methods under normal conditions.

Key words— Back propagation neural network, fuzzy logic controller, linguistic modeling, neuro-fuzzy controller.

I. INTRODUCTION

VARIATIONS in conventional control loop are known to be made in industrial process control systems [1].

However in starting and shut down stages, parameterization of controllers or even in switching between different control modules need the help of the operator. The knowledge of this 'operator' is usually based on experience and does not lend itself to be expressed in differential equations. It follows a pattern given as 'if the situation is such and such, I should do the following'. This is what is called expert's knowledge and the fuzzy logic control offers a convenient technique of representing and implementing this knowledge. A very important part in the paper is development of the fuzzy logic rules from this knowledge.

The performance of the proportional-integral (PI) and proportional-derivative (PD) type fuzzy logic controllers (FLC) is known to be quite satisfactory for linear systems, however the performance of conventional PI or PD controllers

for higher order systems, integrating systems or large dead time, as well nonlinear systems are not satisfactory. But the performance of PI or PD type fuzzy logic controllers is good for such systems. Fuzzy modeling [2] –[12] uses a natural description language to form a system model based on its fuzzy logic with fuzzy predicates.

Neural networks have a large number of highly interconnected processing elements that discriminate the ability to learn and generalize from training patterns or data. They are like human brain and can perform pattern-matching tasks. Neural networks combined with fuzzy logic can make excellent performance at developing human made systems that can perform the same type of information processing that our brain performs [13]. Distributed representation and learning capabilities are two features of neural networks [14]. Most importantly, neural networks can perform filtering operations that are beyond the capabilities of the conventional linear filtering techniques because of their non-linear nature [15],[16].

The back propagation neural network (BPNN) trained controller takes less processing time compared to other techniques. Neural networks represent massively parallel distributed processing capability which makes a real-time processing of large volume of data more realizable with the potential of improving performance through dynamic learning. The use of back propagation neural network in control application has been found to be very much suitable [17] – [19]. Most of the control applications used a multi layer network as shown in Fig.2. The training of a BPNN involves 3 stages; the feed forward of the input training pattern, the calculation and back propagation of the associated error and the weight adjustments [20]. After the network has been trained, its application involves only the feed forward phase and reversing is not possible.

II. GENERATION OF RULES

The basic function of the fuzzy logic is to represent the rules in a structured way the control policy of an experienced process operator and / or control engineer can do. This is formed in a set of production rules such as

If {process state} then {control output}

For example, consider a set of desired input-output data pairs: $[e^{(1)}, \Delta e^{(1)}; u^{(1)}], [e^{(2)}, \Delta e^{(2)}; u^{(2)}]$ -----(1)

Where error (e) and change of error (Δe) are inputs and u is the output. The simple 2 inputs and 1 output case is chosen in order to explain and clarify the basic ideas of the approach [21]; and extends to generalized multi input-multi output cases. The task here is to generate a set of fuzzy rules from the desired input- output pairs of equation (1). Assumed the domain intervals of e, Δe and u are $[e^-, e^+]$, $[\Delta e^-, \Delta e^+]$ and

$[u^-, u^+]$ respectively. Each domain interval is divided into $2N+1$ regions, where N can be different for different variables, and the lengths of these regions can be equal or unequal. Setting N at 3 the expert defined fuzzy rules are developed and thus total region $[-1, +1]$ is divided into 7 divisions as shown in Table I, denoted by NB (negative big), NM (negative medium), NS (negative small), ZE (zero), PS (positive small), PM (positive medium), PB (positive big) and assign each region a fuzzy membership function. Fig.1 shows that the domain interval of e , Δe and u is divided into seven equal regions. The shape of each membership function is triangular.

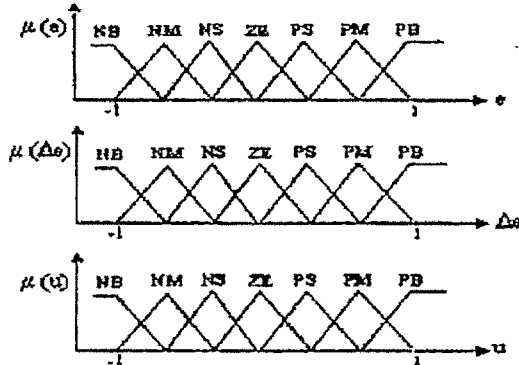


Fig.1: Membership Functions of inputs e , Δe and output u

Suppose now that the term sets of e , Δe , and u all have been chosen equal in size and contain the same linguistic expressions for the magnitude part of the linguistic values, i.e., $LE = \Delta LE = LU = \{NB, NM, NS, ZE, PS, PM, PB\}$ as shown in Fig.1. For example, a cell of Table I represented by the intersection of the first row and the first column, presents a rule such as,

If $e(k)$ is NB and $\Delta e(k)$ is NB then $u(k)$ is NB.

$\Delta e \backslash e$	NB	NM	NS	ZE	PS	PM	PB
NB	NB	NB	NB	NM	NS	NS	ZE
NM	NB	NM	NM	NM	NS	ZE	PS
NS	NB	NM	NS	NS	ZE	PS	PM
ZE	NB	NM	NS	ZE	PS	PM	PB
PS	NM	NS	ZE	PS	PS	PM	PB
PM	NS	ZE	PS	PM	PM	PM	PB
PB	ZE	PS	PS	PM	PB	PB	PB

Table I: Fuzzy rules for computation of u

The 6 discrete values of error (e) and 6 discrete values of change of error (Δe) generate 36 numbers of output (u) values or fuzzy if-then rules by following algorithm.

```

for (i = 0; i <= 5; i++)
{
    for (j = 0; j <= 5; j++)
    {
        e = (-1 + (i * (0.4)));
        Δe = (-1 + (j * (0.4)));
        u = g(e, Δe);
    }
}

```

Those are fed to the back propagation neural network for training to design a Neuro-Fuzzy Controller (NFC).

III. BACK PROPAGATION ALGORITHM

The implementation of back propagation algorithm can be given as follows [22]:

- Initialize the weights to small random values.
- Choose a pattern x_k , $k=1, 2, \dots, n$ and apply it to the input layer.
- Propagate the signal forwards through the network using

$$S_j = \sum_{k=1}^n W_{jk} x_k$$

$$v_j = f(S_j) \quad j=1, 2, \dots, h$$

$$q_i = \sum_{j=1}^h w_{ij} v_j$$

$$y_i = f(q_i) \quad i=1, 2, \dots, m$$

- Compute the deltas for the output layer by comparing the actual outputs y_i with the desired ones y_i^d for the pattern x_k being considered.

$$\delta_i = f(q_i) (y_i^d - y_i)$$

- Compute the deltas for the hidden layers by propagating the errors backwards

$$\Delta_j = f(S_j) \sum_{i=1}^m w_{ij} \delta_i$$

- Use $w_{ij}(t+1) = w_{ij}(t) + \eta \delta_i v_j$

$$W_{jk}(t+1) = W_{jk}(t) + \eta \Delta_j x_k$$

to update all connections.

- Go back to step ii and repeat for the next pattern.

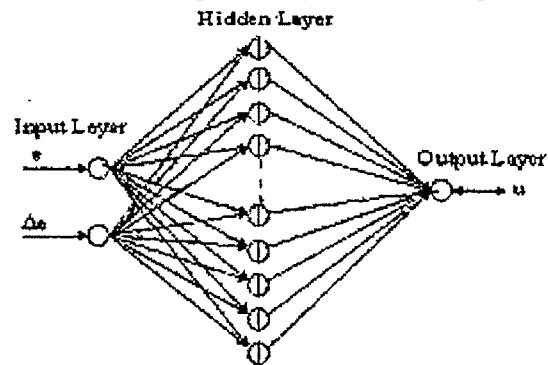


Fig.2: Architectural graph of a three layer perceptron with one hidden layer

A single neuron by itself is not a very useful pattern recognition tool. The real power of neural networks comes when neurons combine into the multi layer structures [23]. In the designed three layer neural network, the first layer contains two neurons for two inputs: error (e) and change of error (Δe) respectively, whereas the second layer or the hidden layer contains thirty neurons and the third layer use only one neuron to get the output (u) value.

The neurons of the first layer receive the inputs, then the linear combiner and the activation function are applied to the inputs to produce the outputs, as shown in Fig.2. These outputs of the first layer then act as the input of the second

layer and in this way calculates the output in the final layer. The function signal appearing at the output neuron is computed, expressing it as a continuous nonlinear function of the input signal and synaptic weights associated with that neuron.

To design a neuro-fuzzy controller from 36 if-then rules, in each epoch calculate the deviation (d); i.e. difference between desired output value and actual value calculated by neural network. Using the equation (2) calculate epoch error in every iteration.

$$E_n = \sum_{j=1}^n d_j^2(n) \dots\dots\dots(2)$$

Where n is the number of iteration and j is the number of rules for each epoch. Changes of synaptic weights are calculated by passing the data sets randomly one by one. Thirty fuzzy rule bases taken from thirty-six fuzzy rule bases randomly to train the network. Epoch error (E_n) is calculated, and it goes on until the difference of epoch error ($\Delta E_n = E_n - E_{n+1}$) reaches to 0.0001.

Once the training is over, the proposed Neuro-Fuzzy Controller is used in a linear and a nonlinear process by proper tuning of the inputs and output to judge the effectiveness of the controller.

NFC can be represented as

$$N_u * u(k) = F(N_e * e(k), N_{\Delta e} * \Delta e(k))$$

Where N_e , $N_{\Delta e}$ and N_u are the scaling factors (gain) for e , Δe and u respectively, and F is a nonlinear function representing the NFC.

IV. RESULTS

In this section, I studied the performance of Neuro-Fuzzy Controller for a second order linear and a nonlinear process. Different performance parameters such as rising time (t_r), settling time (t_s), % peak overshoot (M_p), integral absolute error (IAE) and integral of the time multiplied absolute error (ITAE) are studied to analyze the performance of the controller [1]. The two integral criterion IAE and ITAE are considered because mere visual observations of response curves are not always enough to make a good comparison between different types of controllers. Large errors contribute heavily to IAE; on the other hand ITAE penalizes heavy errors that occur late in time. Thus IAE and ITAE show true characteristics of the control system.

A. Performance analysis of the NFC

Study as well as analysis is made if the performance of NFC as applied to a linear and a nonlinear process with different time lag (δ).

B. Numerical Example:

1. For Second Order Linear Process

$$d^2y/dt^2 + dy/dt + 0.2y = u(t - \delta)$$

The scaling factors are set at $N_e = 0.9$, $N_{\Delta e} = 5$ and $N_u = 3$

2. For Second Order Nonlinear Process

$$d^2y/dt^2 + (dy/dt)^2 + y = u(t - \delta)$$

The scaling factors are set at $N_e = 0.3$, $N_{\Delta e} = 5$ and $N_u = 19.5$

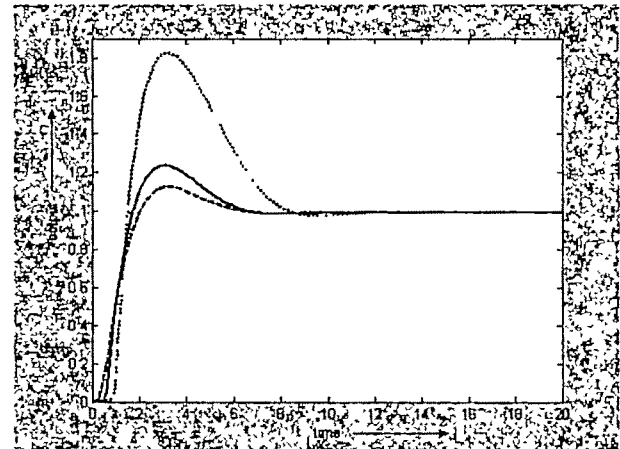


Fig.3: Response characteristics curve of linear model $d^2y/dt^2 + dy/dt + 0.2y = u(t - \delta)$. Here dashed, solid and dotted curves represent $\delta = 0, 0.6$ and 1 value respectively.

δ	%OS	t_r (sec)	t_s (sec)	IAE	ITAE
0	12.62	1.8	5.5	2.33	70.64
0.6	23.92	1.6	5.9	2.68	71.82
1.0	82.60	1.4	7.9	5.20	81.78

Table II: Performance analysis of the linear model $d^2y/dt^2 + dy/dt + 0.2y = u(t - \delta)$

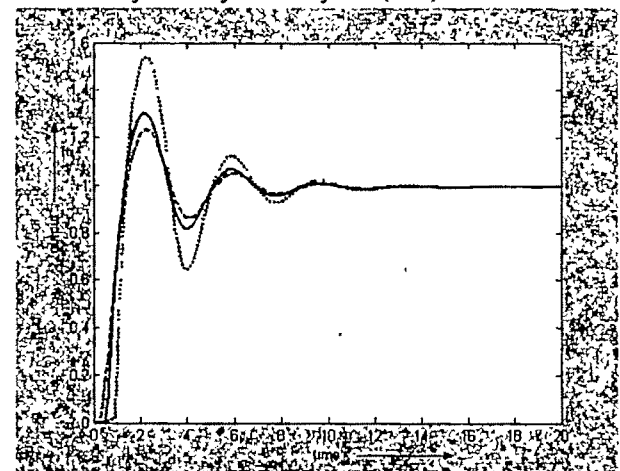


Fig.4: Response characteristics curve of nonlinear model $d^2y/dt^2 + (dy/dt)^2 + y = u(t - \delta)$. Here dashed, solid and dotted curves represent $\delta = 0, 0.6$ and 1 value respectively.

δ	%OS	t_r (sec)	t_s (sec)	IAE	ITAE
0	23.39	4.8	8.3	2.41	76.83
0.6	30.44	4.8	8.4	2.63	77.44
1.0	53.91	8.2	8.5	3.48	79.99

Table III: Performance analysis of the nonlinear model $d^2y/dt^2 + (dy/dt)^2 + y = u(t - \delta)$

The performance of the linear model is shown in Fig.3 and Table II. The performance of the linear model $d^2y/dt^2 + dy/dt + 0.2 y = u(t - \delta)$ is very good in all respects using NFC, specially it gives very low rise time and settling time and variations in time lag (δ) does not hamper the process performances except overshoot. The nonlinear model $d^2y/dt^2 + (dy/dt)^2 + y = u(t - \delta)$ shown in Fig.4 and Table III also gives satisfactory performance for the application of NFC. Especially the models show very fast response while NFC is used.

V. PILOT STUDY

A. HVAC SYSTEM

Heating, Ventilation and Air-Conditioning (HVAC) systems require control of environmental variables such as pressure, temperature, humidity etc. Most of the controllers commissioned in HVAC systems are of Proportional-Integral-Derivative (PID) type, due to its relatively simple structure. But the tuning procedure of a HVAC system may take a control engineer up to three days to search for a proper PID controller setting for an air pressure loop in a building. The situation is even worse, if re-tuning is needed and this is true for many large HVAC systems. It is also realized that many loops in practice are poorly tuned due to lack of process knowledge of control engineers. Therefore, it is highly desirable to develop workable technology for HVAC industries.

A typical cooling only HVAC system is shown in Fig.6. In the system, the outside air is mixed with the building return air. Then the mixed air (supply air) is sucked through the cooling coil via a filter by a supply air fan. The cooled air is then supplied to different zones as shown in the figure. In this HVAC system, the supply air pressure is regulated by the speed of a supply air fan. Increasing the fan speed will increase the supply air pressure, and vice versa. The dynamics of the control signal feeding to the fan Variable Speed Drive to the supply air pressure can be modeled as a second order plus dead time plant.

The transfer function of the supply air pressure loop is obtained as

$$G(s) = 0.81 e^{-2s} / (0.2s+1)(2s+1) \dots\dots (3)$$

Where gain (K) = 0.81, $\tau_1 = 0.2$, $\tau_2 = 2$ and dead time (δ) = 2.

%OS	$t_r(\text{sec.})$	$t_s(\text{sec.})$	IAE	ITAE
0.147	2.6	3.1	2.4	16.3

Table IV: Performance analysis of the supply air pressure loop model $(0.81 e^{-2s}) / (0.2s + 1)(2s + 1)$ in HVAC system using NFC

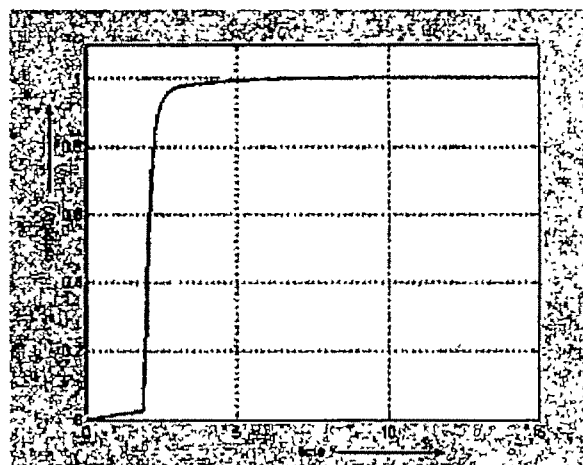


Fig.5: Response characteristic curve of HVAC supply air pressure model $(0.81 e^{-2s}) / (0.2s + 1)(2s + 1)$ using NFC

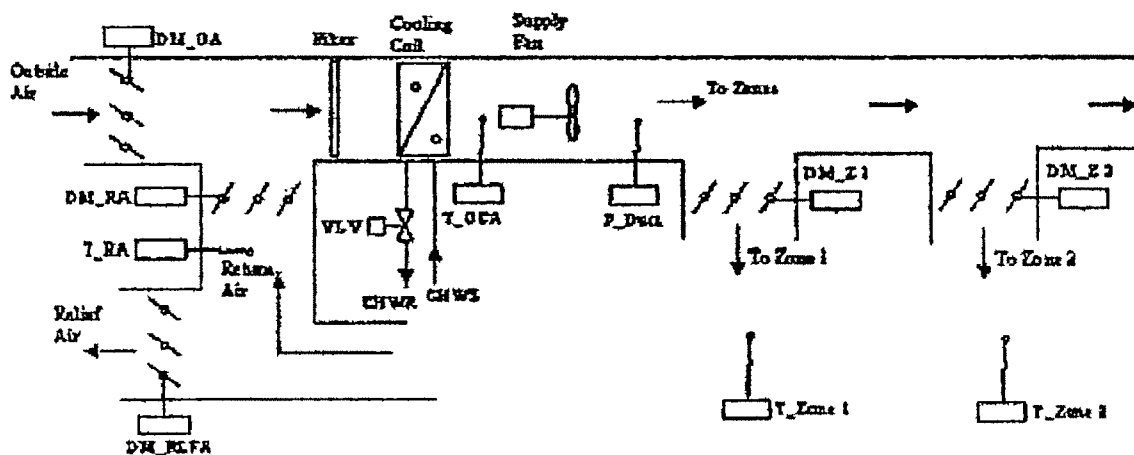


Fig.6: A typical HVAC system

B. Comparison of Practical Performance with Existing Methods

In order to demonstrate the effectiveness and robustness, the performance of the proposed NFC has been compared with those of existing methods, the Bi, Cai's PID controller and Jian, Cai's ANF controller [24] for supply air pressure loop control. The results are provided in Fig. 5 and in Table IV. For the application of NFC, substantial improvements have been observed in settling time and also in peak overshoot for the transfer function of the air supply model $0.81 e^{-2s} / (0.2s+1) (2s+1)$ compare to ANF and PID controller. Compare to 0.147% overshoot by NFC, PID controller and ANF controller shown an overshoot of 17.9% and 0.9% respectively. Similarly NFC shown 3.1 seconds settling time compare to PID controller's 16.2 seconds and ANF controller's 10.6 seconds.

VI. CONCLUSION

The results show that the designed Neuro-Fuzzy Controller does not hamper the process performance. This scheme differs from others as it attempts to use the smaller number of rules during controller design. The objective of using less number of fuzzy rules is leading to a smaller amount of computational time while running a plant. The operators / control engineers can easily tune the controller according to the process requirement. The results show that the NFC does not hamper the HVAC process performance and also works satisfactorily in other linear and nonlinear models. Thus it can be expected to exploit in other loops of HVAC system and other application areas in future.

ACKNOWLEDGMENT

The author would like to thank all referees for their valuable guidance, which helped to improve the quality of this paper.

REFERENCES

- [1] K. Ogata, "Modern Control Engineering," Englewood Cliffs, NJ: Prentice-Hall, 1970.
- [2] C. J. Harris, C. G. Moore, and M. Brown, "Intelligent Control – Aspects of Fuzzy Logic and Neural Nets," Singapore: World Scientific, 1993.
- [3] C. W. Xu and Y. Z. Lu, "Fuzzy model identification and self-learning for dynamic systems," IEEE Trans. Syst., Man, Cyber., vol. 17, pp. 683 – 689, 1987.
- [4] E. H. Mamdani and S. Assilian, "An experiment in linguistic synthesis with a fuzzy logic controller," Int. J. Man – Machine Studies, vol. 7, no. 1, pp. 1-13, 1975.
- [5] L. Wang and R. Langari, "Building Sugeno-type models using fuzzy discrimination and orthogonal parameter estimation techniques," IEEE Trans. Fuzzy Syst., vol. 3, pp. 454 – 458, Nov. 1995.
- [6] L. Wang and R. Langari, "Complex system modeling via fuzzy logic," IEEE Trans. Syst., Man, Cyber., vol. 26, pp. 100 – 106, Feb. 1996.
- [7] M. Sugeno, "Industrial applications of Fuzzy Control," Amsterdam, Netherlands: Elsevier, 1985.
- [8] M. Sugeno and K. Tanaka, "Successive identification of a fuzzy model and its application to prediction of a complex system," Fuzzy Sets Syst., vol. 42, pp. 315 – 334, 1991.
- [9] M. Sugeno and T. Yasukawa, "A fuzzy-logic-based approach to qualitative modeling," IEEE Trans. Fuzzy Syst., vol. 1, pp. 7 – 31, Feb. 1993.
- [10] R. Palm, "Sliding mode fuzzy control", in Proc. Fuzz IEEE, San Diego, CA, 1992, pp. 519-526.
- [11] T. Takagi and M. Sugeno, "Fuzzy identification of systems and its applications to modeling and control," IEEE Trans. Syst., Man, Cyber., vol. 15, 1985.
- [12] W. Pedrycz and J. V. de Oliveira, "Optimization of fuzzy models," IEEE Trans. Syst., Man, Cyber., vol. 26, no. 4, Feb. 1996.
- [13] W. A. Farag, V. H. Quintana and G. L. Lambert-Torres, "A genetic-based neuro-fuzzy approach for modeling and control of dynamical systems," IEEE Trans. on Neu. Net., vol. 9, no. 5, sep 1998.
- [14] G. E. Hinton, J. L. McClelland, and D. E. Rumelhart, "Distributed representation," in Parallel Distributing Processing, vol. 1. Cambridge, MA: M.I.T. Press, 1986, pp. 77- 109.
- [15] A. Amano and T. Arisuka, "On the use of neural networks and fuzzy logic in speech recognition," in Proc. 1989 Int. Joint Conf. Neural Networks, 1989, pp. 301-305.
- [16] Karayiannis, N. B., and A. N. Venetsanopoulos, "Artificial Neural Networks," Kluwer Academic, Boston, 1993.
- [17] B. Kosko, "Adaptive inference in fuzzy knowledge networks," in Proc. 1987 Int. Joint Conf. Neural Networks, 1987, pp. 261-268.
- [18] C. C. Lee and H. R. Berenji, "An intelligent controller based on approximate reasoning and reinforcement learning," Proc. IEEE Intelligent Machine, pp. 200-205, 1989.
- [19] A. K. Pal, "Control of a nonlinear process by modeling PI and PD type fuzzy, self-tuning fuzzy and neuro-fuzzy controller," International Journal of Systemics, Cybernetics and Informatics (ISSN 0973-4864), July 2007.
- [20] C. T. Lin and C. S. G. Lee, "Neural-Network based Fuzzy Logic Control and Decision System," IEEE Trans. on Computers, vol. 40, no. 12, Dec. 1991.
- [21] D. Dirankov, H. Hellendorn and M. Reinfrank, "An introduction to Fuzzy Control," New York: Springer-Verlag, 1993.
- [22] S. N. Sivanandam and M. Paulraj, "Introduction to Artificial Neural Networks," Vikas Publishing, 2004.
- [23] S. Haykin, "Neural Networks," Pearson Education (Singapore), Indian Branch, Sixth reprint 2004.
- [24] W. Jian and C. Wenjian, "Development of an adaptive neuro-fuzzy method for supply air pressure control in HVAC system," Syst., Man, Cyber., IEEE, 2000.

Voltage Stability Evaluation using Artificial Neural Networks

P.Aruna Jeyanthi¹, D. Devaraj² and N. Albert Singh³

¹ Research Scholar, N. I. College of Engineering, Kumaracoil, TamilNadu, India e-mail: arunadarwin@yahoo.com

² Asst. Professor, Kalasalingam University, TamilNadu, India e-mail: deva230@yahoo.com

³ Research Scholar, University of Kerala, Trivandrum India e-mail: albertsingh@rediffmail.com

Abstract— Voltage stability analysis is very important for predicting the potential voltage instability. Load modeling plays a key role in voltage stability assessment. In this paper Leverberg-Marquardt based Neural Network algorithm is used for load modeling. In this paper a general comparison has been made with modal analysis and our proposed approach. The proposed methods are tested either on the IEEE 30 – bus system.

Key words— Artificial Neural Network, Modal Analysis.

I. INTRODUCTION

AS power systems are operated under increasingly stressed conditions, the ability to maintain voltage stability becomes a growing concern. In planning and operating power systems, the analysis of voltage stability for a given system state involves the examination of two aspects;

a) Proximity: how close is the system to voltage instability?

b) Mechanism: when voltage instability occurs, what are the key contributing factors, what are the voltage-weak points, and what areas are involved?

Proximity gives a measure of voltage security whereas mechanism provides information useful in determining system modifications or operating strategies which could be used to prevent voltage instability.

Voltage stability is indeed a dynamic phenomenon and can be studied using extended transient/midterm stability simulations. However, such simulations do not readily provide sensitivity information or the degree of stability. They are also time consuming in terms of CPU and engineering required for analysis of results. Therefore, the application of dynamic simulations is limited to investigation of specific voltage collapse situations, including fast or transient voltage collapse, and for coordination of protection and controls.

Voltage stability analysis often requires examination of a wide range of system conditions and a large number of contingency scenarios. For such applications, the approach based on steady state analysis is more attractive and, if used

properly, can provide much insight into the voltage/reactive power problem.

A number of special algorithms have been proposed in the literature for voltage stability analysis using the static approach. In general these have not found widespread practical application, and utilities tend depend largely on conventional power flow programs to determine voltage collapse level of various points in a network. However, this approach is laborious and does provide sensitivity information useful making design decisions.

The concern for remaining bus voltages' stability has been growing. Many voltage instability incidents have occurred around the world. Some of these incidents even caused partial or complete blackout (voltage collapse).

The power flow based static techniques and quasistatic techniques are still prevailing on voltage stability analysis in many utilities since they are simple, fast, and convenient to use either for estimating the static voltage stability indices or determining the robustness and stability patterns of the test systems. However, the static based voltage stability needs further confirmation by using time-domain simulation. And voltage collapse may occur well before the critical point predicted by steady-state power flow study. More importantly, for dynamic interaction of various loads with different characteristics initiated by heavy load buildup, Line strip, etc., still using steady state or quasi-steady-state analysis may give misleading results. Thus, static techniques and dynamic methods should be coordinated to give accurate and timely results.

Voltage collapse is a dynamic phenomenon in nature, closely associated with overall dynamic characteristics of loads connected to a specific bus (a weak load bus). With complex composition of loads with different dynamics, it may be very difficult, if not impossible, to establish the time-varying dynamic, interaction of all those loads connected to a load bus. However, modeling of each and every load component is not practical. Use of aggregate models describing the overall dynamics might be possible.

Motivated by this fact, the dynamics of all downstream loads and voltage control equipment were modelled as a generic dynamic load model with many factors contributing

to voltage collapse simplified.

Usually the component based load model is used in some utilities. This load modelling approach is very much dependent on the accurate statistics of various power consuming devices. Furthermore, dynamic loading characteristics are too complex to be expressed in a simple form (or analytic form). Neural networks may be an appropriate choice.

In this paper, neural networks will be applied for modeling the static load characteristics and dynamic load flow. This model will be use with the conventional power flow study. The resulting Jacobin will be used for judgment of power system stability. The loading conditions are classified through Levenberg - Marguarat neural networks. In a word, the whole methodology will make use of a neural network model for voltage stability analysis and assessment.

For comparison there is a need for analytical tools capable of predicting voltage collapse in complex networks, accurately quantifying stability margins and power transfer limits identifying voltage-weak points and areas susceptible to voltage instability, and identifying key contributing factors and sensitivities that provide insight into system characteristics to assist in developing remedial actions.

This paper describes a modal analysis approach with the objective of meeting the above requirements. It involves the computation of a small number of eigenvalues and the associated eigenvectors of a reduced Jacobian matrix which retains the Q - V relationships in the network and which includes the appropriate characteristics of generators, loads, reactive power compensating devices, and HVDC converters. This parallels the use of modal analysis for small signal stability studies. However, by using the reduced Jacobian instead of the system state matrix, the focus is on voltage and reactive power characteristics. The eigenvalues of the Jacobian identify different modes through which the system could become unstable. The magnitude of the eigenvalues provides a relative measure of proximity to instability.

The eigenvectors, on the other hand, provide information related to the mechanism of loss of voltage stability. Fast analytical algorithms for selective computation of a specified number of the eigenvalues make the approach suitable for the analysis of large complex power systems. In addition, by appropriate choice of system models, the method can be used to analyze snapshot power flows representing different time.

II. MODAL ANALYSIS FOR VOLTAGE STABILITY EVALUATION

A system is voltage stable at a given operating condition if for every bus in the system, bus voltage magnitude increases as reactive power injection at the same bus is increased. A system is voltage unstable if, for at least one bus in the system, bus voltage magnitude decreases as the reactive power injection at the same bus is increased. In other words a system is voltage stable if V - Q sensitivity is positive for every bus and unstable if V - Q sensitivity is negative for at least one bus.

A. Reduced Jacobian Matrix

The linearized steady state system power voltage equations are given by.

$$\begin{bmatrix} \Delta P \\ \Delta Q \end{bmatrix} = \begin{bmatrix} J_{P\theta} & J_{PV} \\ J_{Q\theta} & J_{QV} \end{bmatrix} \begin{bmatrix} \Delta \theta \\ \Delta V \end{bmatrix} \quad (1)$$

where,

ΔP = incremental change in bus real power.

ΔQ = incremental change in bus reactive power injection.

$\Delta \theta$ = incremental change in bus voltage angle.

ΔV = Incremental change in bus voltage magnitude

If the conventional powerflow model is used for voltage stability analysis, the Jacobian matrix in (1) is the same as the Jacobian matrix used when the powerflow equations are solved using the Newton-Raphson technique. With enhanced device models included, the elements of the Jacobian matrix in (1) are modified.

System voltage stability is affected by both P and Q. However at each operating point we keep P constant and evaluate voltage stability by considering incremental relationship between Q and V. This is analogous to the Q - V curve approach. Although incremental changes in P are neglected in the formulation, the effects of changes in system load or power transfer levels are taken into account by studying the incremental relationship between Q and V at different operating conditions.

To reduce (1), let $\Delta P = 0$, then.

$$\Delta Q = [J_{QV} - J_{Q\theta} J_{P\theta}^{-1} J_{PV}] \Delta V = J_R \Delta V \quad (2)$$

and,

$$\Delta V = J_R^{-1} \Delta Q \quad (3)$$

where,

$$J_R = (J_{QV} - J_{Q\theta} J_{P\theta}^{-1} J_{PV}) \quad (4)$$

J_R is called the reduced Jacobian matrix of the system. J_R is the matrix which directly relates the bus voltage magnitude and bus reactive power injection. Eliminating the real power and angle part from the system steady state equations allows us to focus on the study of the reactive demand and supply problem of the system as well as minimize computational effort.

The program developed also provides the option of performing eigen-analysis of the full Jacobian matrix. If the full Jacobian is used, however the results represent the relationship between $(\Delta \theta, \Delta V)$ and $(\Delta P, \Delta Q)$. Since

$\Delta \theta$ is included in the formulation, it is difficult to discern the relationship between ΔV and $(\Delta P, \Delta Q)$ which is of primary importance for voltage stability analysis. Also modal analysis using the full Jacobian matrix is computationally more expensive than using the reduced Jacobian. For these reasons we have chosen the reduced Jacobian approach.

Modes of Voltage instability :

Let

$$J_R = \xi \wedge \eta \quad (5)$$

where,

ξ = right eigenvector matrix of J_R
 η = left eigenvector matrix of J_R
 Λ = diagonal eigenvalue matrix of J_R
 and

$$J_R^{-1} = \xi \Lambda^{-1} \eta \quad (6)$$

From (3) and (6), we have

$$\Delta V = \xi \Lambda^{-1} \eta \Delta Q \quad (7)$$

or

$$\Delta V = \sum_i \frac{\xi_i \eta_i}{\lambda_i} \Delta Q$$

where ξ_i is the i^{th} column right eigenvector and η_i the i^{th} row left eigenvector of J_R .

Similar to the concept used in linear dynamic system analysis, each eigenvalue λ_i and the corresponding right and left eigenvectors ξ_i and η_i define the i^{th} mode of the system. The i^{th} modal reactive power variation is,

$$\Delta Q_{mi} = K_i \xi_i \quad (9)$$

where,

$$K_i = \sum_j \xi_{ji}^2 - 1 \quad (10)$$

With ξ_{ji} the j^{th} element of ξ_i ,

The corresponding i^{th} modal voltage variation is

$$\Delta V_{mi} = \frac{1}{\lambda_i} \Delta Q_{mi} \quad (11)$$

It is seen that, when the reactive power variation is along the direction of ξ_i the corresponding voltage variation is also along the same direction and magnitude is amplified by a factor which is equal to the magnitude of the inverse of the i^{th} eigenvalue. In this sense, the magnitude of each eigenvalue λ_i determines the weakness of the corresponding modal voltage. The smaller the magnitude of λ_i the weaker the corresponding modal voltage. If $|\lambda_i| \rightarrow 0$ the i^{th} modal voltage will collapse because any change in that modal reactive power will cause infinite modal voltage variation.

In (8), let $\Delta Q = e_k$ where e_k has all its elements zero except the k^{th} one being 1. Then,

$$\Delta V = \sum_i \frac{\eta_{ik} \xi_i}{\lambda_i} \quad (12)$$

where η_{ik} the k^{th} element V - Q sensitivity at bus k

$$\begin{aligned} \frac{\partial V_k}{\partial Q_k} &= \sum_i \frac{\xi_{ki} \eta_{ik}}{\lambda_i} \\ &= \sum_i \frac{P_{ki}}{\lambda_i} \end{aligned} \quad (13)$$

A system is voltage stable if the eigenvalues of the Jacobian are all positive. Those who are used to small signal

stability analysis using eigenvalue techniques may find the requirement for the eigenvalues of the Jacobian to be positive for voltage stability a little confusing because in the study of small signal stability, an eigenvalue with positive real part indicates that the system is unstable. The relationship between system voltage stability and eigenvalues of the Jacobian J_R is best understood by relating the eigenvalues of J_R with the V - Q sensitivities (which must be positive for stability), at each bus.

For practical purposes, J_R can be taken as a symmetric matrix and therefore, the eigenvalues of J_R are close to being purely real. If all the eigenvalues are positive, J_R is positive definite thus V - Q sensitivities are also positive indicating that the system is voltage stable. As the system is stressed, the eigenvalues of J_R become smaller until, at the critical point of system voltage stability, at least one of the eigenvalues of J_R becomes zero.

If some of the eigenvalues of J_R are negative, the system has passed the critical point of voltage stability, because the eigenvalues of J_R change continuously from positive to zero to negative as the system is stressed.

While the magnitude of the eigenvalues can provide a relative measure of the proximity to instability, they do not provide an absolute measure because of the non-linearity of the problem. This is analogous to the damping factor in small signal stability analysis, which is indicative of the degree of damping but is not an absolute measure of stability margin. If a megawatt distance to voltage instability is required, the system is stressed incrementally until it becomes unstable and modal analysis applied at each operating point. The application of modal analysis is to help in determining how stable the system is how much extra load or power transfer level should be added, when the system reaches voltage stability critical point, to determine the voltage stability critical areas and to describe the mechanism of instability by identifying elements which participate in each mode.

B. Bus Participations

The participation factor of bus k to mode i is defined as,

$$P_{ki} = \xi_{ki} \eta_{ik} \quad (14)$$

From (14), P_{ki} indicates the contribution of the i^{th} eigenvalue to the V - Q sensitivity at bus k. The bigger the value of the P_{ki} more λ_i contributes in determining V - Q sensitivity at bus k. For all the small eigenvalues, bus participation factors determine the areas close to voltage instability.

C. Branch and Generator Participations

When the change in reactive power injection is ΔQ_{mi} the resulting voltage variation is ΔV_{mi} and the i^{th} modal angle variation is,

$$\Delta \theta_{mi} = -J_{P\theta}^{-1} J_{Py} \Delta V_{mi} \quad (15)$$

with ΔV and $\Delta \theta$ known, the linearized reactive loss

variation across transmission branch lj , ΔQ_{lj} and the linearized reactive power output variation at generator gk ΔQ_{gk} can be calculated.

D. Calculation of Eigenvalues and Eigenvectors of J_R

It is impractical and unnecessary to calculate all the eigenvalues of a system with several thousand buses. An algorithm for calculating the minimum singular value and the corresponding left and right singular vectors, for both the full Jacobian and the reduced Jacobian, has been developed in [14]. The problem with using the minimum singular value or the minimum eigenvalue as voltage stability index lies in the fact that for a large complex system there is usually more than one weak mode associated with different parts of the system. As a system is stressed, the mode associated with the minimum singular value or the minimum eigenvalue of the base case system may no longer be the most troublesome mode. If the m smallest eigenvalues of J_R are determined, we have obtained the m least stable modes of the system. If the biggest of the m eigenvalues, say mode m , is deemed a strong enough mode, the modes which are not calculated can be neglected because they are known to be stronger than mode m .

E. Load Model

Voltage dependency of load real and reactive power may have large impact on system voltage stability. The load is modelled as the sum of several components, each of which is different exponential function of voltage:

$$P = \sum_i P_{oi} V^{\alpha_i} \quad (16)$$

$$Q = \sum_i Q_{oi} V^{\beta_i} \quad (17)$$

III. NEURAL NETWORKS FOR FUNCTION APPROXIMATIONS.

There are many results about feed-forward neural networks. One of the remarkable results is about its function approximation capability. Back propagation algorithms can be used for training feed-forward neural networks. Since steady-state or quasi-steady-state power systems can be viewed as static processes, the relation between the load demand and voltage magnitude at a specific load bus is static. This static relation can be further viewed as a continuous mapping from voltage magnitude to load real/reactive power. Thus feed-forward neural networks can be applied for steady-state analysis.

Since almost all physical systems are essentially dynamic, their behaviors can no longer be described in terms of a static mapping from the input space to the output space. A way out may be the use of recurrent neural networks which can be state-feedback based, or output feedback based. The complex input-output dynamics can be estimated and approximated by these two kinds of neural networks. A natural choice of the performance criterion for such neural networks would be the weighted summation of the square of the error between the target sequence and the output sequence of the neural networks. The dynamic back-

propagation algorithm is very useful for training a recurrent neural network to follow a pre-specified temporal output sequence if the network is fed the pre-specified input sequence. Power systems are essentially dynamic, but dynamic load flow is too complex to be expressed in a simple form. Recurrent neural networks may be an appropriate option.

Since power systems infrequently experience large instabilities, complete data, and accurate simulation may be limited. Therefore, an indicator is convenient which may show whether dynamic analysis or static analysis is suitable. Since loads are varied randomly with time, an appropriate choice for this indicator would be a back propagation neural network which may capture the probability topology of the loading conditions. The selection of the inputs to this artificial neural network would be very important. Since a specific bus or associated local areas is often the main concern, the loading patterns are very dependent on load demands and voltage magnitudes of such a bus and associated buses.

A. Load Modeling

Static load characteristic can be given by

$$P = F(v, f)$$

$$Q = G(v, f)$$

where P and Q are real power and reactive power at some bus, respectively; v and f are associated voltage and frequency, respectively; $F(\cdot)$ and $G(\cdot)$ are generally nonlinear functions.

We are more concerned about voltage stability than frequency stability since usually voltage decays much faster than frequency does during power system instability. Thus, the above equations may be simplified.

A feed forward neural network can be applied to model these two nonlinear functions. Since sensitivities are useful in power flow study, the calculation of the sensitivity of the output with respect to the input of the neural network should be performed.

Let the input be x , output y .

Then the sensitivity $\frac{\partial y}{\partial x}$ can be computed by applying the chain-rule. For neurons i, j , if neuron j synapses onto neuron i , then $j \rightarrow i$. If $j \rightarrow i, w_{ji}$ and θ_i are the weight from neuron j to i and the threshold of neuron i . Let x_j denote the activity of neuron j . Then activation of neuron i can be given by

$$s_i = \theta_i + \sum_{j \rightarrow i} x_j w_{ji}$$

Inserting the calculated sensitivities into load flow equations, which model the power system networks, yields the linearized form of load flow equations. With the employment of modal analysis, information about relative robustness of load buses can be obtained.

IV. STATIC VOLTAGE STABILITY ANALYSIS

The IEEE 30-bus system is used for simulation. The resulting neural-network load model for bus 7 in the IEEE 30-bus system combined with the Newton-Raphson method is

used in the load flow study and the results are shown in Table-I. It can be observed from the results that if the randomly added loads are ignored, the results may be optimistic; if the random loads are considered to be their average values, the resulted power flow study may be over-simplified, and that the neural networks used present an approximately accurate representation of the nonlinear relation between the random loads and the bus voltage magnitude, and thus give reasonable results. The eigenvalues in Table I are all positive and, through modal analysis, suggest that the power system is still stable.

Table-I

	Original Load	NN Load Model	Modal Load Model
Real Load	4.8	4.8	4.466067
Reactive Load	2.4	2.400122	2.135094
Eigen Values	97.005	97.005	94.675
	86.155	86.154	87.781
	58.209	58.209	53.121
	52.921	52.92	33.009
	32.951	32.951	32.193
	31.628	31.628	26.003
	20.531	20.53	20.683
	18.1	18.1	20.007
	17.548	17.548	17.902
	15.708	15.708	16.271
	13.84	13.84	14.478
	11.956	11.956	12.672
	11.822	11.822	11.799
	9.4446	9.4446	10.741
	8.5568	8.556	0.36661
	7.6468	7.6467	0.83861
	0.096489	0.096562	1.4193
	0.69397	0.69394	3.0658
	1.2607	1.2605	3.5223
	5.3587	5.3583	5.1409
	4.37	4.3697	4.7104
	3.4734	3.4734	6.4733
	2.9704	2.9703	7.6884
	2.8161	2.8157	5.6665

V. CONCLUSION

This paper presents a neural network methodology for dealing with static load modeling. The load patterns are classified by feedforward neural networks. Based on the static load model voltage stability analysis is performed. The sensitivities involved in neural-network models for loads are derived, and are then used in the Jacobian matrix, and further for the modal analysis. The neural-network methodology is tested on both the IEEE-30 bus system. The method includes detailed component models, which may have significant impact on system voltage stability. The results evident that the proposed method is well suited to voltage stability assessment of large complex systems.

REFERENCES

- [1] T. J. Overbye and C. L. Demarco, "Voltage security enhancement using energy based sensitivities," *IEEE Trans. Power Syst.*, vol. 6, pp. 1196-1202, Aug. 1991.
- [2] V. Ajjarapu and C. Christy, "The continuation power flow: A tool for steady state voltage stability analysis," *IEEE Trans. Power Syst.*, vol. 7, pp. 416-423, Feb. 1992.
- [3] B. Gao, G. K. Morison, and P. Kundur, "Voltage stability evaluation using modal analysis," *IEEE Trans. Power Syst.*, vol. 7, pp. 1529-1536, Nov. 1992.
- [4] C. D. Vournas, "Voltage stability and controllability indices for multimachine power systems," *IEEE Trans. Power Syst.*, vol. 10, pp. 1183-1191, May 1995.
- [5] T. V. Cutsem, "An approach to corrective control of voltage instability using simulation and sensitivity," *IEEE Trans. Power Syst.*, vol. 10, pp. 616-622, May 1995.
- [6] G. K. Morison, B. Gao, and P. Kundur, "Voltage stability analysis using static and dynamic approaches," *IEEE Trans. Power Syst.*, vol. 8, pp. 1159-1165, May 1993.
- [7] M. K. Pal, "Voltage stability conditions considering load characteristics," *IEEE Trans. Power Syst.*, vol. 7, pp. 243-249, Feb. 1992.
- [8] G. C. Ejebe *et al.*, "Methods for contingency screening and ranking for voltage stability analysis of power systems," *IEEE Trans. Power Syst.*, vol. 11, pp. 350-356, Feb. 1996.
- [9] T. J. Overbye and C. L. Demarco, "Improved techniques for power system voltage stability assessment using energy methods," *IEEE Trans. Power Syst.*, vol. 6, pp. 1446-1452, Nov. 1991.
- [10] N. Yorino *et al.*, "An investigation of voltage instability problems," *IEEE Trans. Power Syst.*, vol. 7, pp. 600-607, May 1992.
- [11] B. Lee and V. Ajjarapu, "A piecewise global small-disturbance voltage stability analysis of structure-preserving power system models," *IEEE Trans. Power Syst.*, vol. 10, pp. 1963-1968, Nov. 1995.

Electrical Fault Supervision in Induction Motors Using Neural Networks and Multiple Models Approach

ZIDER¹ and B. MENDIL²

^{1,2}Electrical Engineering Department
A. Mira University of Béjaïa
Algeria.

Abstract — The work presented in this paper concerns the use of the multiple models approach for Fault Detection and Accommodation (FDA) of in induction motors. Several analytical models describing the different operating modes of the plant (without and with electrical faults) and a bank of the corresponding controllers are to be managed by a supervision bloc. Artificial Neural Networks (ANNs) have been trained to drive the motor even in the presence of a fault. The obtained results show the effectiveness of the proposed approach.

Key words: Multiple models approach, fault detection and accommodation, induction motors, neural networks.

I. INTRODUCTION

Squirrel Induction Motors, with their robustness and good weight/power ratio, are widely used in industry. Safe and continuous operation requires preventive and corrective maintenance schedule. This allows personal safety, service quality and profit of installations. Unfortunately, the integration of these machines in more and more complex power conversion systems makes the diagnosis more difficult.

In some complex systems, detection and location of faults is insufficient to allow safe operation. Often, this must be associated with an accommodation stage by online modification of the control law. The aim is to stabilize the system and guarantee good performance even after fault occurrence.

In the few last decades, the analytical redundancy approach for the design of fault accommodation structures has received more attention [1,7,8,9]. This, instead of material redundancy, uses only analytical models characterizing different operating modes.

Our aim in this work, initiated in [2,3], is to test this approach for electrical FDA in induction motors. ANNs have been used to construct different blocs. The main advantage of this strategy is the *online* fault detection and decisions-making by reconfiguring the control system. We note that this paper concerns only the electrical faults. Another study on mechanical faults using experimental data has been performed in [2,4].

II. INDUCTION MOTOR MODELS

This section outlines the different models of the squirrel induction motor corresponding to the safe operation and the considered electrical faults. In all models, the following simplifying assumptions have been considered:

- Infinite iron permeability;
- Smooth air gap;
- Sinusoidal distribution of air gap flux density;
- Negligible saturation;
- Rotor cage with regularly distributed non- skewed bars and with no inter-bar currents.

A. Safe Induction Motor

The global Park model of the induction motor without faults with respect to stationary two-axis (dq) frame fixed to rotated field is given by

Electromagnetic Equations:

$$\begin{cases} V_{sd} = R_s \times i_{sd} + L_s \times \frac{di_{sd}}{dt} + M_{sr} \times \frac{di_{rd}}{dt} - L_r \times \omega_r \times i_{sq} - M_s \times \omega_s \times i_{rq} \\ V_{sq} = R_s \times i_{sq} + L_s \times \frac{di_{sq}}{dt} + M_{sr} \times \frac{di_{rq}}{dt} + L_r \times \omega_r \times i_{sd} + M_s \times \omega_s \times i_{rd} \\ 0 = R_r \times i_{rd} + L_r \times \frac{di_{rd}}{dt} + M_{sr} \times \frac{di_{sd}}{dt} - L_r \times \omega_r \times i_{rq} - M_s \times \omega_s \times i_{sq} \\ 0 = R_r \times i_{rq} + L_r \times \frac{di_{rq}}{dt} + M_{sr} \times \frac{di_{sq}}{dt} + \omega_r \times L_r \times i_{rd} + M_s \times \omega_s \times i_{sd} \end{cases} \quad (1)$$

where

$$\omega_s = \omega_r \times \Omega \quad \text{and} \quad \omega_r = p \times \Omega$$

ω_s : pulsation of the stator variables;

ω_r : pulsation of the rotor variables.

Torque Equation:

$$C_e = p \times \frac{M_{sr}}{L_r} \times [\phi_{rd} \times i_{sq} - \phi_{rq} \times i_{sd}] \quad (2)$$

where Ω is the angular velocity and p is the number of the pole pairs.

V_{sd}, V_{sq} : d and q axis stator voltages;

i_{rd}, i_{rq} : d and q axis rotor currents;

ϕ_{rd}, ϕ_{rq} : d and q axis rotor flux;
 R_s, R_r : stator and rotor referred resistor;
 L_s, L_r : Stator and rotor cyclic inductances;
 M_{sr} : stator-rotor mutual inductance.

B. Induction Motor with Electrical Faults

In this work, we have considered three electrical faults:

- Broken bars fault;
- Broken end- ring fault;
- Inter-turn short-circuit in the first stator phase.

1. Motor model with short-circuits in the stator phase SA

A fault in the turns of the stator winding leads to great value of the current in the short-circuited turns, of order of two with respect to that of the locked rotor. This can causes irreversible damages to the core.

An inter-turn short circuit denotes short circuit between two windings in the same stator phase. The electrical circuit of an Y-connected stator is shown on Fig.1. A short-circuit between the star point of the motor and an arbitrary point of the coil is illustrated.

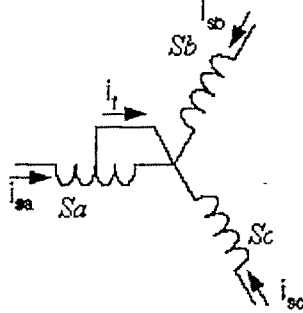


Fig 1 Simplified electrical diagram of a three phase Y-connected stator with an inter-turn short circuit in phase S_a

The short-circuit model into dqo coordinates frame fixed to stator, is given by

$$\begin{cases} V_{sd} = \left(R_s + \frac{M_{sr}^2 R_r}{L_r^2} \right) i_{sd} + L_s \alpha \frac{d i_{sd}}{dt} - \frac{M_{sr}}{L_r} \left(\frac{M_{sr} R_r}{L_r} \phi_{rd} - \omega \phi_{sq} \right) \\ V_{sq} = \left(R_s + \frac{M_{sr}^2 R_r}{L_r^2} \right) i_{sq} + L_s \alpha \frac{d i_{sq}}{dt} - \frac{M_{sr}}{L_r} \left(\frac{M_{sr} R_r}{L_r} \phi_{rd} + \omega \phi_{sq} \right) \end{cases} \quad (3)$$

where

$$\begin{cases} i_{sd} = \left(i_{sd} - \frac{2}{3} \gamma_a i_r \cos \theta \right) \\ i_{sq} = \left(i_{sq} - \frac{2}{3} \gamma_a i_r \sin \theta \right) \end{cases} \quad (4)$$

$$\sigma = \left(1 - \frac{M_{sr}^2}{L_s L_r} \right) : \text{Coefficient of dispersion}$$

γ_a : Amount of turns involved in short- circuit in phase S_a .

Torque Equation:

The electromagnetic torque equation including the fault term is given by

$$C_e = \frac{3}{2} \cdot \frac{P}{2} M_{sr} (i_{sq} i_{rd} - i_{sd} i_{rq}) - \frac{P}{2} M_{sr} \gamma_a i_f i_{rq} \quad (5)$$

2. Modelling Rotor Cage Induction Motors for Fault Detection

In spite of the induction motor reliability, it can present structural faults such as the total or partial rupture of bars and broken end-ring portion. To detect and accommodate these faults, we need models that take into account of the transient behavior corresponding to each situation.

The rotor is viewed as a set of interconnected meshes. Each one is formed of two adjacent bars and the portion of the end-ring which connects them.

The equation to resolve is given by

$$\frac{d[I]}{dt} = [L]^T \cdot \{ [U] - [R] \cdot [I] \} \quad (6)$$

where the inductance and resistor matrices $[L]$ and $[R]$ are defined in *AppedixII*.

The voltage and the current vectors $[U]$ and $[I]$ are given by:

$$\begin{aligned} [U] &= \begin{bmatrix} V_{sd} & V_{sq} & 0 & \dots & \dots & \dots & 0 & 0 \end{bmatrix}^T \\ [I] &= \begin{bmatrix} i_{sd} & i_{sq} & 0 & i_{r0} & \dots & I_{rj} & \dots & i_{r(N_r-1)} & 0 & i_e \end{bmatrix}^T \end{aligned}$$

Torque Equation:

$$C_e = \frac{3}{2} p M_{sr} \left\{ I_{sd} \sum_{k=0}^{N_r-1} i_{rk} \sin k'a - I_{sq} \sum_{k=0}^{N_r-1} i_{rk} \cos k'a \right\} \quad (7)$$

Mechanical Equation:

All the models stated above are characterized by the following mechanical equation

$$J_m \frac{d\Omega}{dt} + F_r \Omega = C_e - C_r \quad (8)$$

where:

C_r is the load torque, Ω is the angular speed, F_r is the friction coefficient, and J_m is the inertia moment.

Simulation

In order to illustrate the effect of a fault on the dynamical behavior of the motor, we have considered, by simulation, the case of the inter-turn short-circuit (100 turns/160). One can see the increase of the speed of the faulty motor. The effect is more apparent on the torque response, leading to great oscillations.

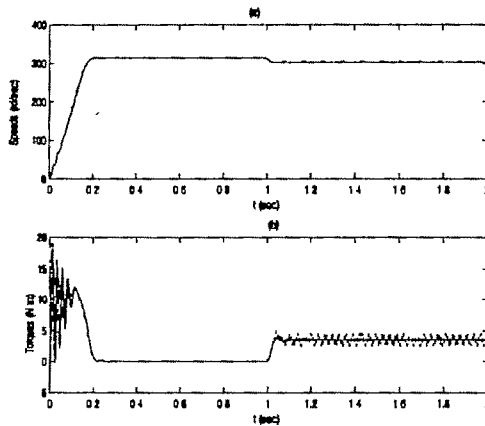


Fig.2. Speed and torque of the induction motor (— safe, —with fault)

III. NEURAL CONTROLLERS DESIGN

It has been demonstrated that neural networks are universal approximators that can model any nonlinear mapping [06]. In particular, a neural network can be used to emulate the dynamical behavior of a plant or to learn how to drive the latter to attain some goal. In this work, neural networks of one hidden layer (of 7 to 10 units with sigmoidal activation functions) and a linear output layer have been used.

Learning control system Structure:

The neural controllers corresponding to the four operating modes (safe and three electrical faults) have been trained using the inverse neural control scheme illustrated by Fig.3. Each controller is trained, based the corresponding model, to implement a control law of the form:

$$U(k) = g^{-1}(Y(k), \dots, Y(k-n_y), U(k-1), \dots, U(k-n_u)) \quad (9)$$

The controllers have been trained, during 2 seconds using a sampling time $T_s=0.1ms$ (20000 samples), to generate the adequate three-phases control voltages. The input vector, of 12 components, consists of reference inputs (angular velocity, torque, and desired current) and the feedback variables (past values of the controller outputs and 02 past values of the plant outputs). Learning has been performed using the *Levenberg-Marquardt algorithm* [05].

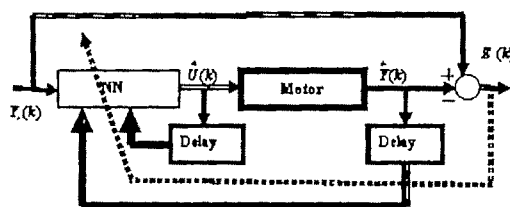


Fig 3. Learning control system structure

Our goal is to allow to the motor to follow the reference speed with steady-state value of 314 rad/sec, even after occurrence of a fault (see Fig.5.). The other reference signals are characterized by the following steady-state values: torque (3.5 N.m) and phase current «Sa» (4A).

From the simulation results (Fig.4 and 5), we can see that:

- Healthy Motor: the outputs follow the reference signals with a slight difference just after load application at time 0.5s (5000 samples).

- Faulty Motor: the outputs follow the references, but with speed oscillations and important torque and current overshoots, after load application at time 0.5s.

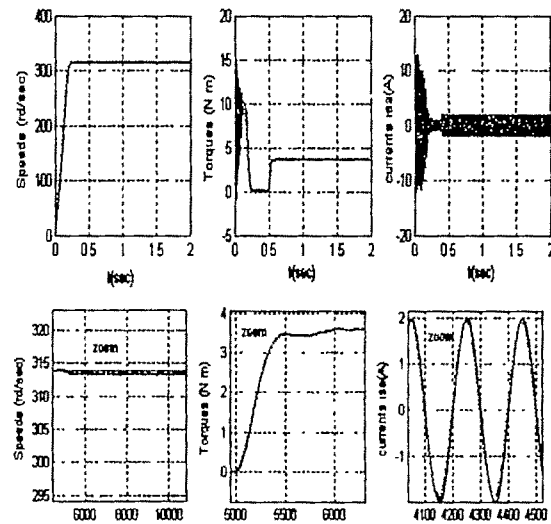


Fig.4. Response of the healthy motor (— references, — response)

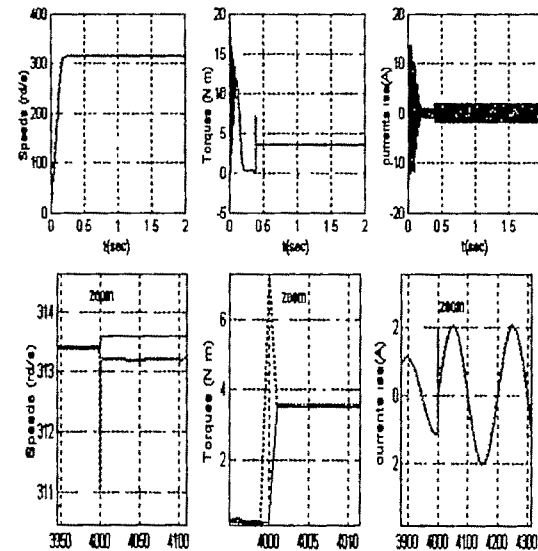


Fig.5. Response of the faulty motor (inter-turn short-circuit) (— references, — response).

IV. ELECTRICAL FAULT DETECTION AND ACCOMMODATION IN INDUCTION MOTOR USING THE MULTIPLE MODELS APPROACH

Traditionally, the design of a control system is based on a fixed model by assuming small changes of the plant and its environment. The adaptive control is the best way to deal with important but slow changes. Nevertheless, it reacts slowly to abrupt changes. This leads to important transient errors or completely unstable plants. Hence, alternative methods are required.

The multiple models approach is a powerful tool to drive complex plants that operate in time variant environments that can present sudden changes from a context to another.

Our work deals with the application of this strategy to ensure good performance of during induction motor operation, even in the presence of a fault. This structure of the system is given by Fig.6.

At each moment, the supervisor detects the current operating mode and selects the corresponding controller. This is based on the dynamic comparison of the plant outputs with those of the models, using performance indices of the form

$$J_{c_i}(k) = \alpha_i \cdot e_n^2(k) + \beta_i \cdot \sum_{m=1}^M e^{-m\lambda_i} \cdot e_n^2(k-m) ; \quad (10)$$

$\alpha \geq 0$ and $\beta, \lambda > 0$

where α and β are free parameters that can be chosen to yield a desired combination of instantaneous and long-term accuracy measures. The forgetting factor λ determines the memory of the index in rapidly switching environments.

The switching scheme consists of monitoring the performance indexes $j_i(k)$ at every instant.

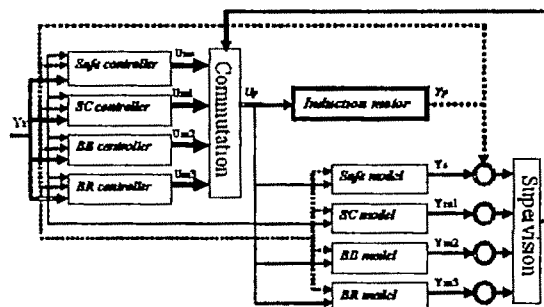


Fig.6: Multiple models control structure for electrical fault detection and accommodation in the induction motor

Simulation:

The plant has been simulated for 02 sec. After safe operation, a fault, randomly selected, has been introduced at $t_1 = 0.1$ sec. For good switching indices, their parameters are empirically adjusted as follows:

Plant-Safe model: $\alpha=0.5, \lambda=0.1, \beta=1$;

Plant- Inter-turn short-circuit model (SC):

$\alpha_1=3, \lambda_1=0.1, \beta_1=3$;

Plant- Broken bars model (BB):

$\alpha_2=1, \lambda_2=0.1, \beta_2=1$;

Plant- Broken end- ring model (BR):

$\alpha_3=3, \lambda_3=0.1, \beta_3=3$.

The Fig.7 illustrates the process of switching between the safe model and the faulty one. We can see several fast commutations between these models and the corresponding controllers. To overcome this problem due to disturbances, a waiting period, T_w , is introduced. After the occurrence of a fault, the supervisor waits for $T_w = 1$ msec and then selects the controller corresponding the minimum index (Fig.8).

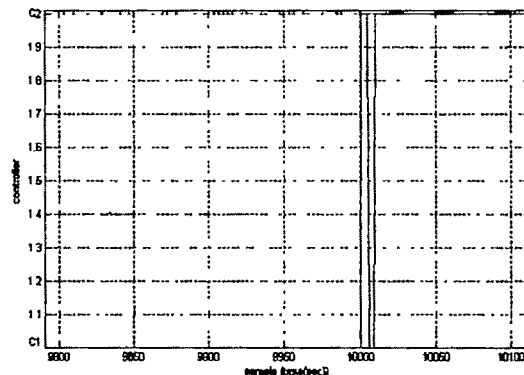


Fig.7. Switching process without waiting time

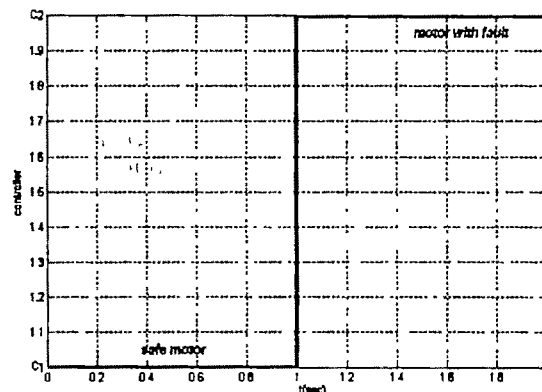


Fig.8. Switching process with waiting time.

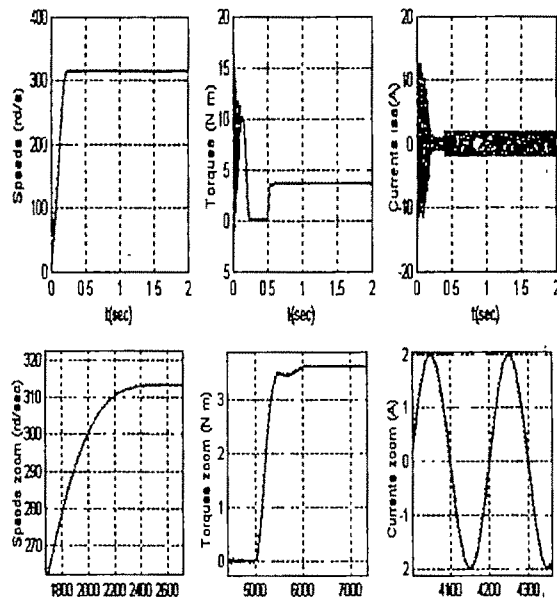


Fig.9. Response of the faulty motor (inter-turn short-circuit case) using the multiple models approach (— references, — response)

From the simulation results of Fig.09, we can see the effectiveness and the good performance of this approach. Beyond the system stabilization, the control system leads to a good response with less overshoots and oscillations, even in the presence of a fault and after load application.

V. CONCLUSION

In this paper, we have presented an efficient approach, based on multiple models strategy, for electrical fault detection and accommodation in induction motors. Our main contributions are:

- Fault detection in *online fashion*;
- *Fault accommodation*, in real time, by reconfiguring the control system.

This allows system stabilization and ensures good performance, during some period of time, after the fault occurrence. This may avoid sudden interruption of production processes, dangerous operation, etc. This is a great advantage compared to off-line techniques (such as signal processing). Our study, even incomplete, opens the door to more investigations in this field.

REFERENCES

- [1] Chen L., Narendra K.S. "Nonlinear adaptive control using neural networks and multiple models". *Automatica* 2001; 37: 1245-1255.
- [2] Ider Z. Détection et accommodation des défauts dans les moteurs à induction Par l'approche multi-modèle *Magister Thesis*, Electrical Eng. Dept, Univ. Béjaia, Algeria, Mai 2006.
- [3] Ider Z., Mendil B. Détection et accommodation des défauts électriques dans le moteur à induction utilisant les

réseaux de neurones et l'approche multi-modèle. *International conference on mechanics and materials (ICMM'06)*, Setif (Algeria); 4-6 Nov. 2006.

- [4] Ider Z., Mendil B. Détection et accommodation des défauts mécaniques dans le moteur à induction par l'approche multi-modèle. *International Meeting on Electronics & Electrical Science and Engineering (IMESE'06)*, Djelfa (Algeria), 3-4 Nov. 2006.
- [5] Marquardt D. An Algorithm for least-squares estimation of nonlinear parameters," *SIAM J. Appl. Math.* 1963; 11:164-168.
- [6] Narendra K.S., Parthasarathy K. Identification and control of dynamical systems using Neural networks. *IEEE Trans. On Neural Networks*, Mar. 1990; Vol. 1, No.1: 4-27.
- [7] Narendra K.S., Balakrishnan J. Adaptive control using multiple models. *IEEE Trans. on Automatic Control*, Feb. 1997; Vol. 42, No. 2:171-187
- [8] Narendra K.S., Xiang C. Adaptive control of discrete-time systems using multiple models. *IEEE Trans. on Automatic Control*, Sep. 2000, Vol. 45, No. 9:1669-1686.
- [9] Polycarpou M. Fault accommodation of class of multivariable nonlinear dynamical systems using the learning approach", *IEEE Trans. on Auto. Cont.*, Feb. 2001; Vol. 46, No. 5: 736- 742.

APPENDIX I

Symbols and machine parameters:

P rated power 1.1 kW
U rated voltage 380 V
I_n rated current 2.6 A
R_s stator resistance 7.58 W
e air-gap length 0.25 mm
R rotor radius 0.03575 m
L rotor length 0.065 m
N_s number of equivalent stator turns/phase 160
N_r number of rotor bars 16
p number of poles pair 1
J inertia momentum 0.0054 kg m²
a₂ friction coefficient 0.006 Nm s
f stator supply frequency *s* slip
w_r rotor speed pulsation
i_{sm} phase *m* stator current
B_{sm} phase *m* stator flux density
q_r electrical angle between the phase *m=0* stator coil and the rotor loop *k=0*
a electrical angle of a rotor loop 0.3927
L_{sp} stator self inductance 0.5711 H
l_{sl} stator leakage inductance 0.0265 H
L_{sc} cyclic stator inductance 0.5976 H
L_{rp} rotor-loop self inductance 4.300 mH
M_{rr} rotor-loop mutual inductance 0.2867 mH
M_{sr} stator - rotor-loop mutual inductance 0.4642 mH
R_e end-ring resistance 100 mW
L_e end-ring leakage inductance 0.1 mH
R_{bk} rotor-bar resistance (healthy) 150 mW

R_{bk} rotor-bar resistance (broken) 30 mW
 L_b rotor-bar leakage inductance 0.1 mH

APPENDIX II

The inductance and resistor matrices $[L]$ and $[R]$ of the rotor cage induction motor are expressed as follows

$$L = \begin{bmatrix} L_d & 0 & \dots & -M_{\alpha} \cos \alpha_d & 0 \\ 0 & L_{\alpha} & \dots & -M_{\alpha} \sin \alpha_d & 0 \\ \vdots & \vdots & \ddots & \vdots & \vdots \\ L_d & M_{\alpha} M_{\alpha} & \dots & M_{\alpha} & \vdots \\ M_{\alpha} L_d M_{\alpha} M_{\alpha} & \dots & M_{\alpha} & \vdots & \vdots \\ \vdots & \vdots & \vdots & \vdots & \vdots \\ 0 & 0 & \dots & M_{\alpha} L_d M_{\alpha} & -\frac{L_{\alpha}}{N_r} \\ \vdots & \vdots & \vdots & \vdots & \vdots \\ 0 & 0 & \dots & -\frac{L_{\alpha}}{N_r} & L_{\alpha} \end{bmatrix}$$

$$R = \begin{bmatrix} R_{\alpha} & -\omega L_{\alpha} & \dots & \dots & M_{\alpha} \omega \sin \alpha_d & \dots & \dots & 0 \\ \omega L_{\alpha} & R_{\alpha} & \dots & \dots & -M_{\alpha} \omega \cos \alpha_d & \dots & \dots & 0 \\ 0 & 0 & R_{d0} & -R_{d0} & 0 & \dots & \dots & -R_{d(N_r-1)} \\ \vdots & \vdots & \vdots & \vdots & \vdots & \ddots & \vdots & \vdots \\ \vdots & \vdots & \vdots & 0 & -R_{d(N_r-1)} & R_{dk} & -R_{dk} & 0 \\ \vdots & \vdots & \vdots & \vdots & \vdots & \vdots & \vdots & \vdots \\ 0 & 0 & \vdots & \vdots & \vdots & \vdots & \vdots & \vdots \\ 0 & 0 & -R_{d(N_r-1)} & 0 & \dots & \dots & 0 & R_{dN_r} \\ 0 & 0 & \frac{R_{\alpha}}{N_r} & \dots & \dots & \dots & \dots & \frac{R_{\alpha}}{N_r} \end{bmatrix}$$

where

R_b, L_b : Resistor and inductance of the rotor bar;
 R_e, L_e : Resistor and inductance of the end-ring;

The terms $L_d, M_{\alpha}, R_{d0}, R_{dk}$, and R_{dN_r} are defined as follows:

$$L_d = L_{\alpha} + \frac{2L_e}{N_r} + 2L_b$$

$$M_{\alpha} = M_{rr} - L_b;$$

$$R_{d0} = R_{\alpha} + \frac{2R_e}{N_r} + R_{b(N_r-1)};$$

$$R_{dk} = R_{bk} + \frac{2R_e}{N_r} + R_{b(k-1)}$$

$$R_{dN_r} = R_{b(N_r-2)} + \frac{2R_e}{N_r} + R_{b(N_r-1)}$$

ANN Application for Identification of Minimal Loss Feeder Reconfiguration

P. L.MuthuKarthik¹, P.S.Venkataramu², T.Ananthapadmanabha³

¹ Vellore Institute of Technology, Vellore, India e-mail:Muthukarthik@gmail.com

² Vellore Institute of Technology, Vellore, India e-mail:venkataramu_ps@yahoo.com

³ National Institute of Engineering, Mysore, India e-mail:apn@yahoo.com

Abstract—Distribution System Automation(DSA) is being carried out very seriously world over to enhance the reliability of the system and to minimize the huge losses that are occurring in the Distribution System. Feeder Reconfiguration(FR) is an important sub-problem of the over all distribution system automation process. Basic concept of feeder reconfiguration is to arrive at the best set of sectionalizing switches to be opened for a given set of tie switch such that the system performance is enhanced. In this paper a novel criterion is developed based on the slope of the curve between the feeder losses verses receiving end voltage. Application of this criterion results in the most minimal loss configuration for any given loading condition. A general MATLAB program is developed to obtain the best switching option. The results have been validated by comparison with the civanlar's loss reduction method. Further in order to incorporate this algorithm in to the DSA switching module, an ANN architecture has been designed which can predict the switching option for any new unseen loading condition.

Keywords--Artificial neural network (ANN), Distribution system, Feeder reconfiguration, sectionalizing switch, Tie switch.

NOTATIONS USED

LOSS_{ij} - Loss in the particular line section.

V_j - Receiving end voltage.

R_{ij} - Sectional resistance.

X_{ij} - Sectional inductance.

α_j - Angle in degrees.

P_{ij} - Sectional real power.

Q_{ij} - Sectional reactive power.

I. INTRODUCTION

The main purpose of electric power system is to efficiently generate, transmit and distribute electrical energy. The need for steady power supply with minimum power interruption and fast supply restoration has also increased. To meet these demands the automation of distribution system is widely adopted. FR is one of the vital operations to be carried out in successful implementation of the DSA. Feeder

configuration can be varied so that the load is supplied at the cost of possible minimal line losses, increased system security and enhanced power quality. Several attempts have been made in the past to obtain an optimal feeder configuration for minimizing losses in distribution systems [1-8]. Civanlar et al. [1] considered one feeder pair at a time for loss reduction and derived a formula to estimate the loss reduction which would result from carrying out a particular switching option. Shirmohammadi et al [2] determined a low-loss configuration by applying an optimal load flow analysis to the system with all switches closed. The system is returned to a radial configuration by opening the branches with the least current, considering one loop at a time. Baran et al.[3] used a branch exchange method and suggested a mechanism to reduce the number of switching options and also developed the approximate power flow method to estimate the loss reduction. Liu et al. [4] developed two loss minimization algorithms in which the authors consider one feeder pair at a time to obtain the optimal solution. Chen et al.[5] presented a method to derive an optimal switching plan to achieve energy loss minimization for short- and long-term operation of distribution systems.. The other approaches to feeder reconfiguration considering the ability of system transformers and feeders, power loss, and voltage profiles have been presented [9-11]. ANN techniques have been widely used for many of the Distribution System problems. ANN's are powerful in solving problems that are inherently non-linear. ANN-based methods are non algorithmic and require no prior knowledge of the functions that relate the problem variables, and do not make any approximation as in the case of most of the mathematical models used.. There are few papers on application of ANN techniques and fuzzy approach for distribution system automation problem [12-20]. Dillon *et al.* [12] applied a single-layer neural network for load forecasting of a power system. ANN's have also been applied to static security and dynamic security assessment. Kim *et al.* [14] utilized ANN's for loss minimization on the Korean distribution system. It was shown that the developed network reconfiguration strategy using ANN can provide the

optimal solution for loss minimization of both constant and sudden load variations, the authors have shown that the method using ANN is more suitable for on-line implementation compared with quadratic programming, simulated annealing and heuristic methods. Kashem et al [15] developed a neural network using FORTRAN and the idea behind grouping of inputs for the network was clearly mentioned. Das [16] used multiple ANN to enhance the accuracy sought in estimating the bus voltages. M A Kashe, et.al[17-18] made use of the daily load curves in training the ANN to predict the switching status. Sahoo,N.C.et.al. [19] proposed a fuzzy based genetic algorithm and the algorithm was tested on a 69 bus system. Salazar,H.et.al.[20] made use of the clustering mechanism in developing the ANN.

In this paper a multi layer perceptron ANN architecture is designed which uses the error back propagation algorithm to predict the switching option for any un seen loading condition. The training data for the ANN architecture are obtained from the repeated simulations using the newly proposed criterion which is based on the slope of the curve between the feeder losses verses receiving end voltage.

II. PROBLEM STATEMENT

A distribution network is reconfigured by opening any sectionalizing switch and closing any tie switch, such that the power from the main station is re-routed. A whole feeder or a part of a feeder may be served from another feeder by closing a tie switch linking the two feeders while an appropriate sectionalizing switch must be opened to maintain the radial structure of the network. So that the resulting Radial distribution system has the desirable performance. Amongst the several criteria considered for optimal network reconfiguration, loss minimization criterion is being widely used. In the context of loss reduction, the problem to be addressed in this paper is to identify the tie/sectionalizing switches that should be closed/opened to achieve the maximum reduction in loss. The change in loss can easily be calculated from the result of two load flow analysis carried out before and after the reconfiguration. But, in real time system, even for a distribution system of moderate size the number of switching options that can be performed is so large that conducting load flow analysis for all switching options is time consuming. In a real system, loading of any bus in turn the feeder to which the bus is connected keeps varying from time to time. So it's not possible to maintain the same reconfigured network for all the loading conditions. It's practically impossible to reconfigure the network for every change in loading condition. So at discrete time intervals the network is reconfigured for a minimal loss network. To achieve this it is necessary to derive a

criterion which eliminates certain switching options and also helps in selecting the best option which improves the system performance. In this paper a criterion based on the slope of the curve plotted between the feeder loss and the receiving end voltage is developed.

III. CRITERION FOR SELECTION OF BEST SWITCHING OPTION

The criterion is based on the slope obtained by differentiating the loss equation with respect to the receiving end voltage. The equation is called the slope equation as it corresponds to the differential equation of first order. To develop the criteria a sample two bus system shown in fig.1 is considered.

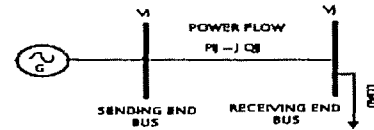


Figure.1. Two bus system

$$I_{ij} = (P_{ij} - j Q_{ij}) / (V_i \angle \alpha_i - V_j \angle \alpha_j) \quad (1)$$

$$LOSS_{ij} = I_{ij}^2 * R_{ij} \quad (2)$$

Substituting 2 in 1 we have

$$LOSS_{ij} = ((P_{ij} - j Q_{ij})^2 / (V_i \angle \alpha_i - V_j \angle \alpha_j)^2) * R_{ij} \quad (3)$$

$$\text{The power flow in that particular section is given by} \\ (P_{ij} - j Q_{ij}) = (V_j \angle \alpha_j)^* (V_i \angle \alpha_i - V_j \angle \alpha_j) / (R_{ij} + j X_{ij}) \quad (4)$$

So substituting 4 in 3 :

$$LOSS_{ij} = V_j^2 (\cos \alpha_j - j \sin \alpha_j)^2 * R_{ij} / (R_{ij} + j X_{ij})^2$$

Upon taking conjugate and eliminating the imaginary term and differentiating the resulting equation :

$$\frac{\partial (LOSS_{ij})}{\partial (V_j)} = \frac{2 * V_j * R_{ij} ((R_{ij}^2 + j X_{ij}^2) * A)}{(R_{ij}^2 + X_{ij}^2)^2} \quad (5)$$

Where $A = (\cos(2 * \alpha_j)) - (4 * R_{ij} * X_{ij} * \cos \alpha_j * \sin \alpha_j)$

Equation 5 is used to compute the slope of each line section for base case (all tie switches open and all the sectionalizing switch closed) and for selected switching options. The best switching option is selected in which the maximum number of line section slopes show a trend of higher rate of increase. This is justified as the slope increase corresponds to decrease in the loss. In implementing the proposed criterion, initial selection of the possible switching options is carried out using the civilnar's criterion [1].

IV. STEP WISE PROCEDURE

Step1 - The base case (all tie switches opened and sectionalizing switches closed) load flow analysis for a particular loading condition is carried out.

Step 2 – The slope of each line section is computed using equation 5.

Step 3 –Civinlar's criterion to eliminate the undesired switching options which would result in an increased loss system is applied to select the best options.

Step 4 – For all the selected switching options the slopes are computed.

Step 5- The number of line sections having increasing slope in comparison with the base case are identified.

Step 6 – The best switching option is selected in which the maximum number of line section slopes show a trend of higher rate of increase. The losses are computed for this switching option and are checked for the reduction in value with the base case.

V. DESIGN OF ANN ARCHITECTURE

ANN architecture is a computer program that is trained to recognize both linear and nonlinear relationships among the input and the output variables in a given data set. Training data sets are generated by carrying out the off-line network reconfiguration simulations for different values of P-Q loads.

Selection of appropriate data set is an important task in ANN architecture design. Based on the relevant literature review and simulations, bus voltages, bus powers and the network connectivity between the buses (represented by '1' for connection and '0' for disconnection) are considered as input variables. The tie-switch position and the sectional switch status (either open or close) is the output of the ANN. All the data are normalized to enable to capture wide range of data sets. Out of the simulated results 13 sets of input and output pairs are used for training the ANN and 5sets are used to test the ANN accuracy in predicting the out put. A multi layer perceptron ANN architecture is designed and the training is carried out using error back propagation algorithm.

The developed neural network architecture is tested for its reliability and accuracy by feeding an unseen loading condition as input data. A program is developed to run the loadflow analysis for the given percentage of loading of the system. The results of the loadflow analysis are given as input to the file containing the weight matrix obtained from the training process. The output from the neural network which provides the status of all the switches is displayed as the output.

VI. CASE STUDY AND RESULTS

Civinlar's sixteen bus system shown in Fig.2 is used as working examples in this paper. Following assumptions are made in implementation of the proposed criterion:

1. The load transferred during the feeder reconfiguration is assumed to be within the thermal rating of the feeder to which the load is transferred.

2. If load on j bus is connected to switch i , then all loads along the path from load j to switch i are assigned to switch i .

3. All the line sections connecting the buses of the same feeder have sectionalizing switches and line sections connecting the buses of different feeder has tie switches.

The system has three feeders connected to a common generator, the transmission lines which connect the generator to the buses are assumed to be of negligible impedance (as the data is not available in the reference paper).

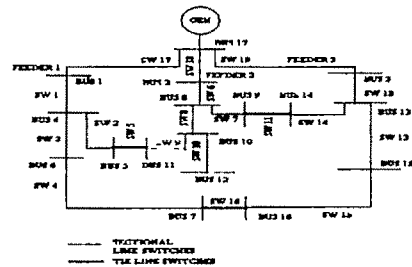


Fig 2: 16 Bus sample system

There are two cases which are considered in simulation and in training the neural network. In case 1 the entire load change of the system in percentage is taken into account and in case 2 the load change in each feeder is taken into account in terms of percentage. This helps to study the system behavior for different loading condition in each feeder and the loading condition on the whole. The training details are mentioned below for these two cases.

	No of input neurons	No of hidden layers	No of hidden layer neurons in each layer	No of output neurons
Case 1	39	2	50	19
Case 2	37	2	50	19

Table 1: Number of neurons in each layer of the neural Network

Due to space constraint only the results of case1 with 100 percent loading condition is displayed here and the decimal values taken while calculating the maximum number of line sections with maximum rate of increase is in the order of 10^{38}

The ANN output for an unseen loading condition, for the same case is displayed in the form of graph. The line section in the X axis of the graph represents the order of

line sections in the same order as shown in Table II for ex. Line section 1 in the graph represents section 1-4.

Similarly for both the cases the criterion was applied and the best reconfigured network was identified. The neural network was also trained for all the cases and tested for unseen loading patterns and the result was found to be satisfactory.

Bus to Bus	Basic case	T.S-16 S.S-3	T.S-16 S.S-4	T.S-11 S.S-7	T.S-5 S.S-8	T.S-5 S.S-8
1-4	-2.56	-2.62	-2.57	-2.56	-2.37	-2.35
4-5	-2.66	-2.66	-2.66	-2.66	-2.65	-2.66
5-6	-2.66	0	-2.66	-2.66	-2.66	-2.66
6-7	0	0	0	0	0	0
7-8	0	0	0	0	0	0
8-9	-2.62	-2.60	-2.64	-2.62	0	-2.62
9-10	0	0	0	0	0	0
10-11	0	0	0	0	0	0
11-12	-2.58	-2.58	-2.58	-2.59	-2.54	-2.58
12-13	0	0	0	0	0	0
13-14	-2.17	-2.17	-2.17	-2.17	-2.16	-2.21
14-15	-2.58	-2.58	-2.58	-2.58	-2.54	-2.58
15-16	0	0	0	0	0	0
No of line sections with increase in slope	---	4	5	6	2	5

T.S – Tie Switch, S.S – Sectional Switch
Table II: No of line sections with increase in slope of all possible switching options for a particular loading condition of a compensated system 100% loading of the system

From Table II we can infer that closing tie switch 11 and opening sectional switch 7 will result in the minimum loss configuration for the given system at a particular loading condition. The real loss of the system before reconfiguration was found to be 0.512 MW and after the reconfiguration the losses were found to be reduced to a considerable amount of 0.485 MW which shows that the system losses have reduced by 5.39 percent. The results obtained were compared with the results proposed by civilnar for the same system and it was found that the proposed method yielded the same results as in civilnar's criteria.

Application of the proposed criterion on a test system has resulted in identification of the best possible switching option as shown in the result. The result obtained is compared with the civilnar's method and found that both are same for most of the system loading conditions. Due to space constraint detailed results are not shown. Further the accuracy of the designed ANN architecture is illustrated with the sample bar graph

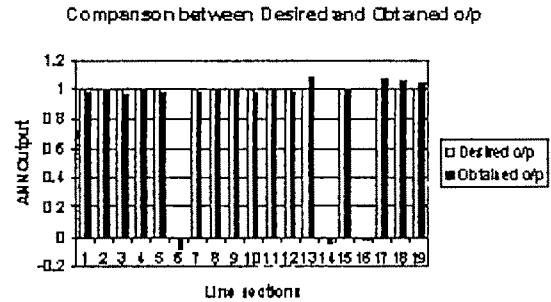


Fig. 2. Comparison between the Desired and Obtained output

VII. CONCLUSION

A novel criterion for reconfiguring the distribution system network for any loading condition is proposed and the effectiveness of the criterion is demonstrated through a case study on a standard distribution network and the results are test evaluated with the other standard methods. An accurate ANN architecture is designed which can predict the switching option for any un seen loading condition. The results are very encouraging and this criterion along with the trained ANN can be very effectively used in real system DSA modules

The following are the major inferences made based on the completed work

1. Altering the topological structure or reconfiguration of the feeder does not always results in a loss reduction configuration. In most of the possible switching options the losses have been reduced significantly but not in all.
2. The proposed ANN approach provides calculation accuracy and good analysis speed. Once the network is trained and evaluated, its method can provide a fast switching status of all the switches. By using 0 and 1 of the switch status as the desired output the network has been trained for the given set of training inputs. Hence the proposed method can be applied to the real system.

APPENDIX

System Data:

Bus to Bus	Section Resistance (PU)	Section Reactance (PU)	End bus Load (MW)	End bus Load (MVAR)	End bus Capacitor (MVAR)
1-4	0.075	0.1	2.0	1.6	---
4-5	0.08	0.11	3.0	1.5	1.1
4-6	0.09	0.18	2.0	0.8	1.2
6-7	0.04	0.04	1.5	1.2	---
2-8	0.11	0.11	4.0	2.7	---
8-9	0.08	0.11	5.0	3.0	1.2
8-10	0.11	0.11	1.0	0.9	---
9-11	0.11	0.11	0.6	0.1	0.6
9-12	0.08	0.11	4.5	2.0	3.7
3-13	0.11	0.11	1.0	0.9	---
13-14	0.09	0.12	1.0	0.7	1.8
13-15	0.08	0.11	1.0	0.9	---
15-16	0.04	0.04	2.1	1.0	1.8
5-11	0.04	0.04	---	---	---
10-14	0.04	0.04	---	---	---
7-16	0.09	0.12	---	---	---

ACKNOWLEDGMENT

The authors acknowledge the support provided by the V.I.T. University to carry out this research work at V.I.T.U.

REFERENCE:

- [1] S Civanlar, J.J. Grainger, H. Yin and S.S.H. Lee, "Distribution feeder reconfiguration for loss reduction," *IEEE Trans. Power Delivery*, 3, 1988, pp. 1217-1223.
- [2] D. Shirmohammadi and H.W. Hong, "Reconfiguration of electric distribution networks for resistive line losses reduction," *IEEE Trans. Power Delivery*, 4, 1989, pp. 1492-1498.
- [3] M.E. Baran and F.F. Wu, "Network reconfiguration in distribution systems for loss reduction and load balancing," *IEEE Trans. Power Delivery*, 4, 1989, pp. 1401-1407.
- [4] C.C. Liu, S.J. Lee and K. Vu, "Loss minimization of distribution feeders: optimality and algorithms," *IEEE Trans. Power Delivery*, 4, 1989, pp. 1281-1289.
- [5] C.S. Chen and M.Y. Cho, "Energy loss reduction by critical switches," *IEEE Trans. Power Delivery*, 8, 1993, pp. 246-253.
- [6] C.C. Liu, S.J. Lee and S.S. Venkata, "An expert system operational aid for restoration and loss reduction of distribution systems," *IEEE Trans. Power Systems*, 3, 1988, pp. 619-626.
- [7] S. Sivanagaraju, N. Visali, V. Sankar, T. Ramana, "Enhancing voltage stability of radial distribution system by network reconfiguration," *Electric Power Components and Systems* 33 (5), 2005, pp. 539-550.
- [8] H. Kim, Y.K. Ko and K.H. Jung, "Artificial neural network based feeder reconfiguration for loss reduction in distribution systems," *IEEE Trans. Power Delivery*, 8, 1993, pp. 1356-1366.
- [9] T.P. Wagner, A.Y. Chikhani, R. Hackam, "Feeder reconfiguration for loss reduction: an application of distribution automation," *IEEE Trans. Power Deliv.* 6 (1991) 1922-1931.
- [10] R.P. Broadwater, A.H. Khan, H.E. Shaalan, R.E. Lee, "Time varying load analysis to reduce distribution losses through reconfiguration," *IEEE Trans. Power Delivery*, 8, 1993, pp. 294-300.
- [11] S.K. Goswami, S.K. Basu, "A new algorithm for the reconfiguration of distribution feeders for loss minimization," *IEEE Trans. Power Delivery*, 7, 1992, pp. 1484-1491.
- [12] T.S. Dillon, "Artificial neural network applications to power systems and their relationship to symbolic methods," *Journal of Electrical Power and Energy Systems*, 13(2), 1991, pp. 66-72.
- [13] D.J. Sobajic, Y. Pao, "Artificial neural-net based dynamic security assessment for electric power systems," *IEEE Transactions on Power Systems*, 4(1), 1989, pp. 220-228.
- [14] H. Kim, Y. Ko, and K. Jung, "Artificial neural-network based feeder reconfiguration for loss reduction in distribution systems," *IEEE Transactions on Power Delivery*, 8(3), 1993, pp. 1356-1366.
- [15] M.A. Kashem, G.B. Jasmon, A. Mohamed and M. Moghavvemi, "Artificial neural network approach to network reconfiguration for loss minimization in distribution networks," *Electrical Power & Energy Systems*, Vol. 20, No. 4, 1998, pp. 247-258.
- [16] B. Das, "Rule based algorithm for meter placement and ANN based bus voltage estimation in radial power distribution system," *Electric Power Components and Systems* 33 (4), 2005, pp. 449-462.
- [17] M.A. Kashem, V. Ganapathy, G.B. Jasmon, "On-line network reconfiguration for enhancement of voltage stability in distribution systems using artificial neural networks," *Electric Power Components and Systems* 29 (4), 2001, pp. 361-373.
- [18] M.A. Kashem, V. Ganapathy, M. Negnevitsky, "Enhancement of load balancing in electrical distribution networks using Artificial Neural Networks," *IPEC 2003 - 6th International Power Engineering Conference*, art. no. P1071, 2003, pp. 907-912.
- [19] N.C. Sahoo, R. Ranjan, K. Prasan, A. Chaturvedi, "A fuzzy-tuned genetic algorithm for optimal reconfigurations of radial distribution network," *European Transactions on Electrical Power* 17 (2), 2007, pp. 97-111.
- [20] H. Salazar, R. Gallego, R. Romero, "Artificial neural networks and clustering techniques applied in the reconfiguration of distribution systems," *IEEE Transactions on Power Delivery* 21 (3), 2006, pp. 1735-1742.

Nonlinear Dynamic Time Series Modeling using Genetically Optimized Evolving Fuzzy Neural Network

Jayashri Vajpai¹ and Arun JB.²

¹ Assistant Professor, Electrical Engg Department, Faculty of Engineering, J.N.V. University, Jodhpur, India, e-mail: jvajpai@gmail.com

² Lecturer, Teacher's Training Centre, Government Polytechnic College Campus, Jodhpur, India, e-mail: arun_jb@rediffmail.com

Abstract—Nonlinear dynamic time series modeling is a generic problem, which permeates all fields of science. It is important for the development of abstract models, particularly when the only information about the system under study is a time series of input-output data pairs, which may exhibit chaotic behavior. The authors have developed a soft computing based methodology for the modeling of systems represented by such series. Fuzzy logic, neural networks and genetic algorithms are considered to be principal constituents of soft computing. Of these, the first component is primarily concerned with imprecision of data and information, the second with learning and the third with optimization. It has been realized that it is advantageous to exploit the synergism of these methods by using them in combination, to develop hybrid models. The proposed model is based on the well-established Evolving Fuzzy Neural Network and employs a genetic algorithm based method for the optimization of the most important parameters that govern the development of its structure. These are the sensitivity threshold, the error threshold and the number of membership functions. An attempt has now been made to adaptively tune these parameters and the centers of the membership functions in the condition layer, using genetic algorithm in on-line mode. The well-examined Box & Jenkins gas furnace modeling problem, for predicting future values of the time series, based on the past history, is used as an illustrative example to demonstrate the potential of the proposed Genetically Optimized Evolving Fuzzy Neural Network model. The proposed methodology may find applications in the areas of signal processing, control, weather forecasting, economic and business planning and several other fields.

Key words— Evolving fuzzy neural network, neuro-fuzzy-genetic system, nonlinear dynamic system, time series modeling.

I. INTRODUCTION

THE recent developments in sensor, communication and computer technologies have made it possible to continuously monitor complex processes in many domains such as industry, environment, medicine, economics, etc. The data hence obtained, is usually in the form of a time series of input-output pairs, often exhibiting nonlinear and dynamic behavior. There is no clear relation between cause and effect in such systems due to the inherent random phenomena. The generate randomness on their own without the need for any external random inputs. This imposes fundamental limits on

prediction. Nonlinear dynamical time series modeling and prediction has, therefore, become an important subject of research. The traditional statistical / mathematical models for nonlinear dynamical processes are inaccurate and difficult to derive with limited a priori data. Hence, adaptive models of these processes are required in order to achieve good online prediction. The soft computing techniques have recently provided an alternative approach to mathematical modeling and are particularly suited to deal with such situations.

Soft computing is a consortium of emerging methodologies; viz., fuzzy logic, neural networks and genetic algorithms. The first is primarily concerned with imprecision of data and information, the second with learning and the third with optimization. The implementation of soft computing is based on the exploitation of the tolerance for imprecision, uncertainty and partial truth to achieve tractability, robustness and low cost solution. In many applications, it is advantageous to exploit the synergism of these methods by using them in combination rather than alone. Examples of combined use include neuro-fuzzy, neuro-genetic, genetic-fuzzy and neuro-fuzzy-genetic systems.

The most significant requirements of soft computing models are tractability (over-coming the curse of dimensionality) and model generalization (expanding the predictive power of the model to previously unseen situations). These are met by the recently developed neuro-fuzzy models to a large extent. Furthermore, such models provide for a qualitative insight into the behavior of the system in the form of easily interpretable fuzzy rules. Their design is often formulated as an optimization problem. The genetic algorithms are well suited for optimization of multi-dimensional, nonlinear and noisy problems. They offer means to systematically and efficiently explore the parameter space of neuro-fuzzy architectures. They allow optimization of the model topology, its parameters, as well as the parameters of the learning algorithm. Thus, soft computing is implemented in the form of a neuro-fuzzy-genetic system that integrates the following techniques:

1. Fuzzy logic for its linguistic nature, tolerance for imprecision and uncertainty in data.
2. Neural network for its inherently parallel architecture

and the ability of abstraction to derive the fuzzy rules. It does not require specification of structural relationships between input-output data for multi-dimensional, multi-domain, and complex data sets.

3. Genetic algorithm for the optimization of the neuro-fuzzy structure.

This paper presents the design of a neuro-fuzzy-genetic system based on Kasabov's Evolving Fuzzy Neural Network (EFuNN) model [1]. The EFuNN is used for modeling and prediction of the output of a nonlinear dynamic process and genetic algorithm for optimizing its parameters. EFuNN is a neuro-fuzzy structure that can evolve to learn the relational mapping existing between the input-output data pairs. It has five layers of neurons, viz., input layer, fuzzy input membership functions layer, rule node layer, fuzzy output membership functions layer and output layer. There are no rule nodes prior to learning and all of them are created during the evolving process. The nodes representing membership functions, the fuzzy rule neurons and connection weights can be modified during learning. Each input variable is represented by a group of spatially arranged fuzzy input layer neurons to represent its fuzzy quantisation, using different types of membership functions. The EFuNN can evolve very fast because it uses one pass training based on unsupervised reinforcement learning [2]. If the corresponding variable values for given input vector values do not belong to any of the existing ones to a degree greater than membership threshold, new fuzzy in-put / output neurons can be created during the adaptation phase of the EFuNN. It is, therefore, necessary to employ some optimization procedure, so that the growth of the structure during online evolution is controlled [3]. The authors hence propose a hybrid model that includes genetic algorithm and EFuNN. The performance of the proposed system is evaluated for the modeling of a chaotic time series, by applying it to the Box & Jenkins furnace data.

II. EVOLVING FUZZY NEURAL NETWORK

The Genetically Optimized Evolving Fuzzy Neural Network model proposed in this paper is based upon the EFuNN proposed by Kasabov [1]. It is, hence, pertinent to briefly present the basic idea of EFuNN before explaining the Genetically Optimized Evolving Fuzzy Neural Network model.

A. EFuNN Architecture

As already introduced, the EFuNN model has a five-layer structure, shown in Fig. 1. Its nodes and connections are created and updated online as data is presented.

The input layer represents input variables. This layer behaves like a simple distribution layer and hence does not require specific connection weights. The second layer of nodes (fuzzy input neurons or fuzzy inputs) represents fuzzy quantization of each in-put variable space. For example, two fuzzy input neurons can be used to represent "small" and "large" fuzzy values for a particular input variable. Different

membership functions can be attached to these neurons. The authors have applied triangular membership functions.

The third layer contains evolving rule nodes representing prototypes of input-output data associations that can be graphically represented as associations of hyper-spheres from the fuzzy input and the fuzzy output spaces. This layer governs the implementation of fuzzy inference system, with the second layer fuzzy neurons interpreted as antecedents of the rules and the fourth layer fuzzy neurons as the consequents. Each rule node is defined by two vectors of connection weights, $W_1(r)$ and $W_2(r)$, the latter being adjusted through supervised learning based on the output error and the former being adjusted through unsupervised learning based on similarity measure within a local area of the problem space. A linear activation function is used for the neurons of this layer.

The fourth layer of neurons represents fuzzy quantization of the output variables. Here, a weighted sum input function and a saturated linear activation function is used for the neurons to calculate the activation level of rules, by evaluating membership degrees to which the output vector associated with the presented input vector belongs to each of the output membership functions. The fifth layer represents the defuzzified crisp values of the output variables. The defuzzified values for the output variables are calculated using Tagaki-Sugeno model.

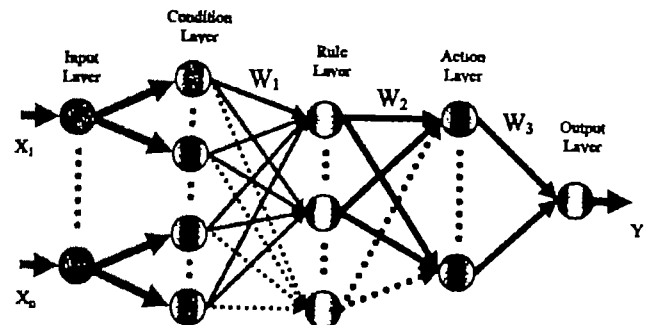


Fig. 1. An Evolving Fuzzy Neural Network Structure

B. EFuNN Algorithm

The basic steps in the EFuNN algorithm are shown below:

1. Propagate the current input vector through the network.
2. Find the highest activated rule node (the winner).
3. IF the maximum activation is less than the sensitivity threshold, add a node.

ELSE evaluate the error between the calculated and the desired outputs.

4. IF the error over the desired output is greater than the error threshold, add a node.

ELSE update the weights of the connections to the winning node.

5. Repeat for each training vector.

The EFuNN has been applied successfully in a large number of applications for modeling and classification of complex relational data. It has been particularly successful for modeling of chaotic time series [4]-[7]. However, it is necessary to make it more adaptive and optimal in structure in order to further enhance its capability.

III. PROPOSED GENETICALLY OPTIMIZED EVOLVING FUZZY NEURAL NETWORK

The Genetically Optimized Evolving Fuzzy Neural Network integrates the powerful global search techniques of genetic algorithm with the neuro-fuzzy model EFuNN described in the section II. This technique, therefore, derives benefits from all major components of soft computing. This has made it successful in modeling of chaotic systems that are characterized by a high degree of uncertainty, nonlinearity and unstable dynamics. It has been made possible by developing the structure of evolving fuzzy neural network on the basis of optimization of the membership functions used for fuzzy inferencing, with the help of genetic algorithm. The changing membership functions have made it possible for EFuNN model to adapt to the drastic changes exhibited by nonlinear dynamic time series.

As already outlined, the potential of EFuNN for modeling of nonlinear dynamical system can be enhanced by optimization of its parameters. Gradient decent algorithm has been applied for changing the shape of membership functions for fuzzy-neural network by Kasabov et al [8]. Similarly another approach for changing membership functions has been suggested by Kim et al, in a model called as HyFIS [6].

Genetic Algorithm (GA) [9] is based on the idea of a population of chromosomes that are elements of high dimensional search space. A chromosome is an arrangement of genes, where each gene takes on values from a suitably defined domain of search space and encodes for a candidate solution. The GA works on a population of such chromosomes, preferentially selecting the ones that encode for high fitness solutions for reproduction. Genetic operators such as mutation, crossover, elitism, etc., are used to introduce variety into the population. Thus, by survival of the fittest over several generations, the population gradually evolves high fitness chromosomes. The authors propose the Genetic algorithm based Optimization of Evolving Fuzzy Neural Net-work. For this purpose, the chromosomes of the GA are formulated as shown in Fig. 2.

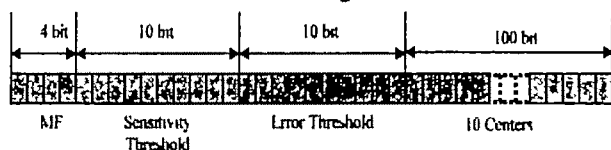


Fig. 2. GA Chromosome

While tuning the EFuNN system for function learning or modeling purposes, the GA objective function aims to minimize the error between the actual data and fuzzy model output. Thus, the fitness function was selected to be:

$$\text{Fitness Function} = \frac{1}{\text{RMSE}} \quad (1)$$

The root mean square of error is estimated through EFuNN. It is customary to use a fitness function given by

$$\text{Fitness Function} = \frac{1}{1 + \text{RMSE}} \quad (2)$$

This fitness function becomes unity as RMSE tends to become zero. But the discrimination in fitness values of chromosomes for small values of RMSE becomes small. It is hence, appropriate to use the function given in equation 1, which offers greater discrimination. It is notable that RMSE never becomes zero for nonlinear dynamic systems and fitness function will therefore always remains finite.

The initial GA populations are randomized, which implies that minimum heuristic control knowledge is used. The appropriate sensitivity threshold, error threshold, number of membership functions and centers of membership functions are evolved and tuned gradually throughout the GA iterations.

The complete algorithm of Genetically Optimized EFuNN is now described.

A. Genetically Optimized EFuNN Algorithm

The optimization by genetic algorithm proceeds along the following seven steps:

1. Initialize the population size, maximum number of generations, the minimum and maximum range of sensitivity threshold, error threshold, number of membership functions, centers of membership functions, number of bits for each center, probability of mutation, percentage of elitism, etc.
2. Randomly formulate the first generation of 200 binary coded chromosomes.
3. Evaluate the fitness of each chromosome in the generation using equation (1).
4. Select fit chromosomes to breed a new generation using Roulette Wheel Selection.
5. Create the next generation chromosomes by multi point crossover (three points) in the present generation.
6. Replace 90% of the parent generation with the child generation. This is known as elitism.
7. Repeat steps 3 - 6 until maximum generations or maximum fitness is reached.

This algorithm calls the EFuNN algorithm as a function in step 3, which, is described in detail in section IIB.

IV. APPLICATION

In this study, Genetically Optimized EFuNN is applied for the prediction of Box & Jenkins gas furnace data (series J), representing the combustion process of a methane air mixture. It is a well known nonlinear dynamical chaotic system and frequently used as a benchmark example for testing modeling and prediction algorithms. The input $u(t)$ is methane concentration in the gas flow into the furnace and the output $y(t)$ is CO_2 concentration in outlet gas. The data set consists of 296 pairs of input output measurements at the sampling interval of 9 sec. [7].

The task of the EFuNN model is to provide an identification for the CO_2 concentration $y(t)$ based on past values of the input and the output. The EFuNN model uses the data set consisting of six inputs, i.e., $u(t-1)$, $u(t-2)$, $u(t-3)$, $y(t-1)$, $y(t-2)$ and $y(t-3)$ with the $y(t)$ as an output. This is done because there is a strong positive correlation up to three

time lags indicating finite memory effect. Thus, the first three pairs of data from the selected time series form the first dataset for EFuNN. The second dataset would then be consecutively formed from second data pair to fourth data pair and so on. Thus, the EFuNN data set has 293 values of input-output variables. The 146 dataset for optimization purpose and remaining 147 dataset are used for testing.

The authors of this paper have found in their previous work [10], that the optimal values of most sensitive parameters for the development of EFuNN model, besides the centers of membership functions, are as follows:

Number of membership functions = 4

Sensitivity Threshold = 0.7944

Error Threshold = 0.2021

In the absence of prior knowledge as above, these parameters can also be readily obtained by applying genetic optimization procedure on training dataset. The evolution of rule nodes is governed directly by error threshold, sensitivity threshold and indirectly by the number of membership functions.

V. RESULTS

For this application, 124 bit chromosomes are formulated for the GA for optimizing the number of membership functions (4 bit), sensitivity threshold (10 bit), error threshold (10 bit) and membership function centers, 10 bits each for representing the ten centers in between the two fixed extreme centers at 0 and 1, as the desired maximum number of membership functions is 12.

The result of optimization of EFuNN parameters using 146 data sets for number of population $N_p = 200$ and number of generations $N_g = 20$ are shown in Fig. 3. The offline optimization procedure finally yields the following optimal values for parameters of EFuNN:

Number of membership functions = 5

Sensitivity threshold = 0.8554

Error threshold = 0.0138

Membership function centers = 0, 0.1008, 0.3510, 0.8742, 1

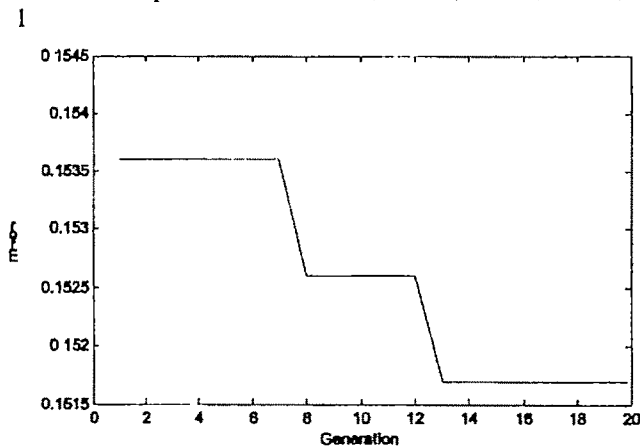


Fig. 3. GA Optimization with Elitism ($N_p=200$, $N_g=20$)

Fig. 4 shows the actual and predicted values, whereas Fig. 5 presents the details of error in prediction. The RMSE for the

predictions is 0.3147. Fig. 6 shows the optimized position of centers of membership functions. Thus, the results obtained by using this approach for Box & Jenkins time series are better than the best available in the literature [10, 11]. The results obtained in this application have been compared with those of Kasabov and our previous attempts in Table I. Ten out of the test data along with their forecasted values are shown in Table II.

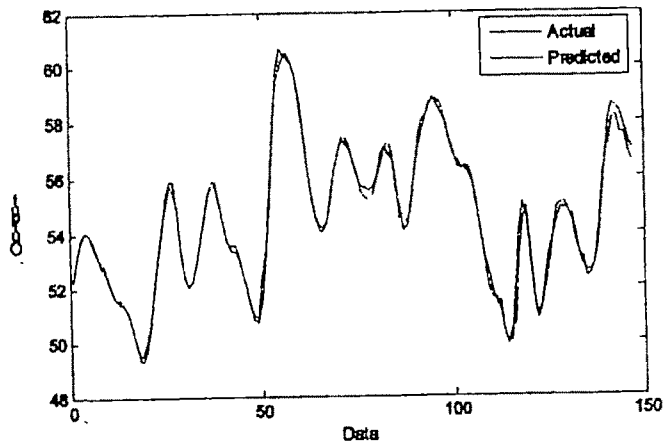


Fig. 4. Actual and Predicted Values of Output for Testing Datasets (RMSE = 0.3147)

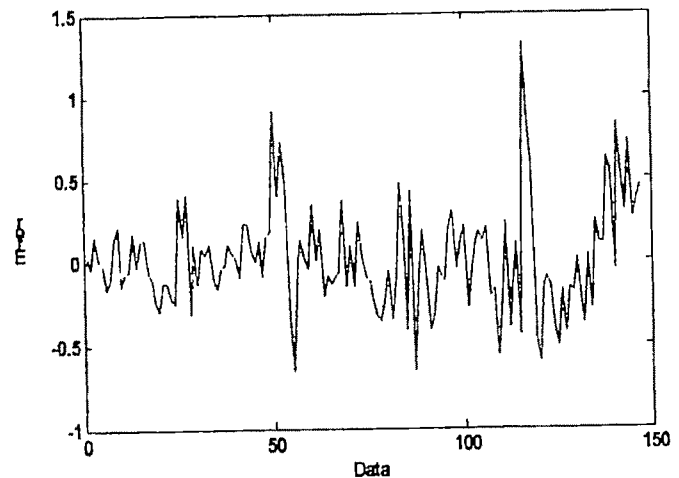


Fig. 5. Prediction Error

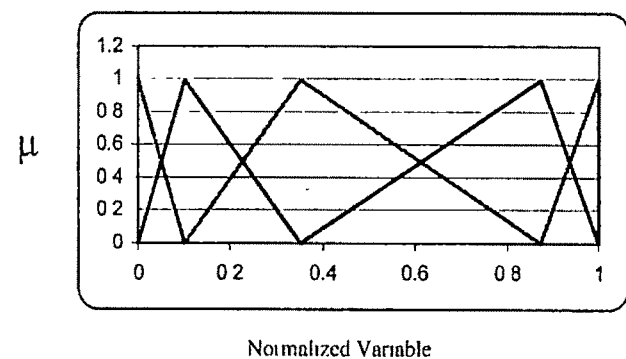


Fig. 6. Optimized Position of Centers of Membership Functions [0 0.1008 0.3510 0.8742 1]

Table I. Results for Box & Jenkins Furnace Time Series Prediction

Parameter	Results obtained with Kasabov's EFuNN [11]	Results obtained with offline Genetically Optimized EFuNN [10]	Results obtained with offline Genetically Optimized EFuNN
No. of Membership Functions (MF)	3	4	5
Maximum Sensitivity Threshold	0.5	0.7944	0.8554
Maximum Error Threshold	0.1	0.2021	0.0138
Interval between MF's centers	Equal	Equal	0, 0.1, 0.35, 0.87, 1
Root Mean Square Error (RMSE)	0.81	0.502	0.3147
Maximum Error for Prediction	—	1.8146	1.328

VI. CONCLUSION

It has been realized from this study that the proposed scheme of modeling of a nonlinear dynamical system by Genetically Optimized EFuNN systems is quite promising. The efficacy of this approach is further enhanced when the optimization of its most sensitive parameters, i.e., number of membership functions, sensitivity threshold, error threshold and membership function centers is done using genetic algorithm. The results obtained by using this approach for Box & Jenkins Furnace time series are better than those available in the literature [10, 11]. This supports our conjecture that the efficacy of EFuNN will be enhanced by genetic optimization of its parameters.

The methodology developed in this study is expected to be useful in applications that demand development of system models from input-output datasets that shows nonlinear, dynamic and chaotic behavior. This includes a wide range of applications such as study of seismically acquired data at

monitoring station in mines, prediction of share prices in financial markets, load forecasting in power systems, forecasting of electricity price in spot market, signal processing in process control, weather forecasting and biomedical applications.

REFERENCES

- [1] N. Kasabov, "Evolving Fuzzy Neural Networks for Supervised / Unsupervised Online, Knowledge-Based Learning", *IEEE Transactions on Systems, Man and Cybernetics, Part B: Cybernetics*, Vol. 31, No. 6, December (2001).
- [2] N. Kasabov, "ECOS: A framework for evolving connectionist systems and the ECO learning paradigm", *Proceedings of the International Conference on Neural Information Processing*, Kitakyushu Japan (1998), pp. 1222-1235
- [3] N. Kasabov and Q. Song, "GA-Optimization of evolving connectionist systems for classification with a case study from bioinformatics", *Proc. of ICONIP'2002*, Singapore (2002)
- [4] A. Ghobakhlou, M. Watts and N. Kasabov, "On-Line Expansion of Output Space in Evolving Fuzzy Neural Networks", *Proceedings ICONIP 2000*, Taejeon Korea (2000).
- [5] J. Vajpal and Arun JB., "Genetic Optimization of Evolving Fuzzy Neural Networks for Chaotic Time Series Modeling", *Proc. of UGC National Conference on Advances in Industrial Automation (NCAIA-04)*, J. N. V. University, Jodhpur (2004), pp. 90-95.
- [6] J. S. Kim and N. Kasabov, "HyFIS: Adaptive neuro-fuzzy systems and their application to nonlinear dynamical systems", *Neural Networks*, Vol. 12 (9) (1999).
- [7] R. Kozma, N. Kasabov, J. Kim, and T. Cohen, "Integration of connectionist methods and chaotic time series analysis for the prediction of process data", *International Journal of Intelligent Systems*, Vol. 13 (6) (1998), pp. 520-538.
- [8] N. Kasabov et al., "FuNN/2-A fuzzy neural network architecture for adaptive learning and knowledge acquisition", *Information Science*, Vol. 101, No. 3-4, (1997), pp. 155-175.
- [9] David E Goldberg, "Genetic Algorithms in Search, Optimization and Machine Learning", Addison-Wesley (2000).
- [10] J. Vajpal and Arun JB., "Genetic Optimization of Evolving Fuzzy Neural Networks for the Modeling of Box Jenkins Furnace Data", *Proc. of UGC National Conf on Advances in Computer Integrated Manufacturing (NCACIM-07)*, J. N. V. University, Jodhpur (2007).
- [11] N. Kasabov, "Online learning, reasoning, rule extraction and aggregation in locally optimized evolving fuzzy neural networks", *Neurocomputing* (2000).

Table II. Input Data, Actual and Predicted Values

S No.	Inputs						Output		Error
	u(t-1)	u(t-2)	u(t-3)	y(t-1)	y(t-2)	y(t-3)	Actual y(t)	Predicted $y_p(t)$	
1	-0.424	-0.603	-0.553	51.2	50.4	50.2	52.3	52.277	0.02282
2	-0.194	-0.424	-0.603	52.3	51.2	50.4	53.2	53.234	-0.034383
3	-0.049	-0.194	-0.424	53.2	52.3	51.2	53.9	53.741	0.15922
4	0.06	-0.049	-0.194	53.9	53.2	52.3	54.1	54.094	0.0064
5	0.161	0.06	-0.049	54.1	53.9	53.2	54	54.014	-0.014421
6	0.301	0.161	0.06	54	54.1	53.9	53.6	53.759	-0.15879
7	0.517	0.301	0.161	53.6	54	54.1	53.2	53.297	-0.096535
8	0.566	0.517	0.301	53.2	53.6	54	53	52.853	0.14654
9	0.56	0.566	0.517	53	53.2	53.6	52.8	52.582	0.21849
10	0.573	0.56	0.566	52.8	53	53.2	52.3	52.44	-0.14013

Technical Session 6B

General Applications-II

Effect of Axial Magnetic Field on Temperature Variation of Self-Gravitating Gas Atmosphere Perturbed by Strong Shock Wave

R.P. Yadav¹, Virendra K. Gangwar¹, Sandeep Bharti², Satyendra Prakash³ and P.S. Rawat⁴

¹Deptt. of Physics, Govt. P.G. College, Bisalpur, Pilibhit (INDIA) - 262201. e-mail : rpyadav93pphysics@yahoo.co.in

²Deptt. of Physics, Govt. P.G. College, Rampur (U.P.)

^{3,4}Deptt. of Physics, Kumaun University, Nainital (U.K.)

Abstract — Neglecting the effect of overtaking disturbances on the motion of strong shock wave, Chester-Chisnell-Whitham method has been applied to study the temperature variation of non-uniform self-gravitating gas atmosphere for two cases viz (i) when shock diverges and (ii) it converges. Analytical relations of shock velocity and shock strength have been derived and used for temperature variation of the medium having density distribution of $\rho \propto r^{-\alpha}$ where α , the density parameter is taken as constant.

It is found that variation of the temperature of the atmosphere is significant and depends on the strength of the shock perturbing the medium.

Keywords — Shock Waves and Fluid Mechanics

I. INTRODUCTION

Extensive work have been done in recent past on theoretical studies of shock wave propagation like Korobeinikov, Melnikova, Ryazanov and Kochina have investigated the problem of self similar flows in non-ideal gases characterized for internal energy (1958-62), Ranga Rao and Purohit discussed it for expanding adiabatic case; whereas Singh and Nayak for isothermal as well as magneto dynamics medium (1975). Sedov and Carrus et al have studied self similar adiabatic flows in self gravitating gas (1959). The propagation of converging shock waves in non ideal gas have studies by Zeldovich, Raizer, Mishkin and Fujimoto, and other (1967).

Singh and J.B. Singh have studied the analysis is non-ideal

gas (1998). Magnetogasdynamics plane shock wave in inhomogeneous medium have been described by Panday and Singh (1998). Self gravitating gas behind shock wave in non-ideal gas explained by Srivastav and Lal (2001) and imploding cylindrical shock wave in non-ideal gas with magnetic field studied by Singh (2002). So in the present paper it have derived the propagation of shock waves in non-uniform self-gravitating gas using Chester-Chisnell-Whitham method and obtained analytical expression for shock velocity, particle velocity, pressure and temperature for converging as well as diverging shock wave,

II. GOVERNING EQUATION

The basic equations for the flow behind the shock front under influence of its own gravitation in presence of magnetic field are written as-

$$\frac{\partial u}{\partial t} + u \frac{\partial u}{\partial r} + \frac{1}{\rho} \frac{\partial p}{\partial r} + \frac{Gm}{r^2} + \frac{\mu}{2\rho} \frac{\partial H^2}{\partial r} = 0 \quad \dots(1.1)$$

$$\frac{\partial p}{\partial t} + u \frac{\partial p}{\partial r} + \rho \left\{ \frac{\partial u}{\partial r} + \alpha \frac{u}{r} \right\} = 0 \quad \dots(1.2)$$

$$\frac{\partial p}{\partial t} + u \frac{\partial p}{\partial r} - a^2 \left\{ \frac{\partial p}{\partial t} + u \frac{\partial p}{\partial r} \right\} = 0 \quad \dots(1.3)$$

$$\frac{\partial H}{\partial t} + u \frac{\partial H}{\partial r} + H \left\{ \frac{\partial u}{\partial r} + \alpha \frac{u}{r} \right\} = 0 \quad \dots(1.4)$$

$$\frac{\partial m}{\partial t} - C_\alpha r^\alpha \rho = 0 \quad \dots(1.5)$$

where r is the radial coordinate, u , p , ρ , H and μ are the particle velocity, the pressure, the density, the axial magnetic field and permeability of gas respectively. m denote the mass inside a sphere of radius r /cylinder of radius r with unit length. $c_\alpha = 2\pi$ or 4π , according to $\alpha=1$ or 2 , respectively for cylindrical or spherical flow and $a^2 = \gamma p / \rho$.

The characteristic form of system of equation (1.1-1.5) is obtained by forming a linear combination of these equations in only one direction in (r, t) plane.

Linear combination of equation (1.1-1.5) can be written as-

$$dp + \rho c_\alpha du + \mu H dH + \frac{\alpha \rho u c^2}{(u+c)} \frac{dr}{r} + \frac{\alpha c G m}{(u+c)} \frac{dr}{r^2} = 0 \quad \dots(2.0)$$

III. BOUNDARY CONDITIONS

The magneto hydrodynamics conditions can be written in terms of a single parameter as-

$$\rho = \rho_0 \xi, \quad H = H_0 \xi, \quad u = (\xi - 1)U / \xi \quad \dots(3.1)$$

$$U^2 = \frac{2\xi}{(\gamma + 1) - (\gamma - 1)\xi} \left[a_0^2 + \frac{b_0^2}{2} \{2 - \gamma\} \xi + \gamma \right] \quad \dots(3.2)$$

$$p = p_0 + \frac{2\rho_0(\xi - 1)}{(\xi + 1) - (\gamma - 1)\xi} \left\{ a_0^2 + \frac{(\gamma - 1)}{4} b_0^2 (\xi - 1)^2 \right\} \quad \dots(3.3)$$

U is the shock velocity, a_0 is the sound speed and b_0 is the Alfvén speed. For strong shock p/p_0 is large.

1. For strong Magnetic Field - ($b_0^2 \gg a_0^2$) under this condition, the boundary condition reduce to-

$$\rho = \rho_0 \xi, \quad H = H_0 \xi, \quad u = (\xi - 1)U / \xi \quad \dots(4.1)$$

$$\frac{p}{p_0} = 1 + x \left(b_0^2 A_1 a_0^2 \right) \frac{U^2}{a_0^2 b_0^2} \quad \dots(4.2)$$

where

$$x = \frac{\gamma(\gamma - 1)(\xi - 1)^3}{2\xi \{ (2 - \gamma)\xi + \gamma \}}$$

and

$$A_1 = \frac{4}{(\gamma - 1)(\xi - 1)^2} - \frac{2}{(2 - \gamma)\xi - \gamma}$$

2. Theory for diverging Shock : Substituting the shock condition 4.1 and 4.2 in equation 2.0 and use $c = U(x/\xi)^{1/2}$, for strong axial magnetic field, i.e. $dH_0 = 0$ and on simplifying we get-

$$dU + \frac{1}{A} \left\{ 1 - \frac{\rho x A}{A_1 \mu_0^2} \right\} \left\{ \frac{x}{\rho_0} \frac{d\rho_0}{d\xi} + \frac{x A d\rho_0}{\mu_0^2} + \frac{2x d\rho_0}{\rho_0} + \frac{2x A d\rho_0}{\mu_0^2} + \frac{\alpha(\xi - 1)}{\{(\xi - 1) + (x/\xi)^2\}} \frac{d\xi}{\xi} \right\} U^2 + \frac{1}{A} \left\{ 1 - \frac{\rho x A}{A_1 \mu_0^2} \right\} \left\{ \frac{d\rho_0}{\rho_0} + \frac{g m \xi (x/\xi)^2}{\{(\xi - 1) + (x/\xi)^2\}} \frac{d\xi}{\xi} \right\} = 0$$

where

$$A_2 = \frac{x}{\xi} + \frac{(\xi - 1)}{2} \left(\frac{x}{\xi} \right)^{1/2} \quad \dots(5.0)$$

the equilibrium state of the gas is assumed to be specified by the condition $\partial/\partial t = 0$, H_0 constant putting this in equation (1.1), we get the equilibrium condition prevailing in front of the shock, as-

$$\frac{1}{\rho_0} \frac{dp_0}{dr} + \frac{Gm}{r^2} = 0 \quad \dots(6.0)$$

Assuming an initial density distribution law as-

$$\rho_0 = \rho r^{-\omega} \quad \dots(7.0)$$

$$dm = c_\alpha \rho_0 r^\alpha dr$$

from equation (1.5) -

$$dm = c_\alpha r' r^{\alpha - \omega} dr \quad m = \frac{c_\alpha \rho' r^{\alpha - \omega + 1}}{(1 + \alpha - \omega)} \quad \dots(8.0)$$

On solving equation 4, 7 and 4.2

$$p_0 = \frac{-c_\alpha \rho^{12} G r^{\rho - 2\omega}}{(\alpha - 2\omega)(1 + \alpha - \omega)} = K_1 r^{\alpha - 2\omega} \quad \dots(9.0)$$

where

$$K_1 = \frac{c_\alpha \rho^{12} G}{(2\omega - \alpha)(1 + \alpha - \omega)}$$

positivity and finiteness of the equilibrium pressure, as defined by (9.0), requires that constant ω should obey the inequality as-

$$\frac{\alpha}{2} < \omega < 2 \quad \dots(10.0)$$

$$a_0^2 = \frac{\gamma p_0}{\rho_0}$$

putting the values of ρ_0 and p_0 from (7) and (9) in above equation we get-

$$a_0 = \left\{ \frac{\gamma K_1}{r_1} \right\}^{(\alpha - \omega)/2} \quad \dots(11.0)$$

Substituting values from 8.0, 9.0, 11.0, in equation 5.0 - and simplifying, we get

$$\frac{dU^2}{dr} + \left\{ \frac{B_1}{r} + B_2 \beta^{-2} r^{\alpha - 2\omega - 1} \right\} U^2$$

$$= -B_3 r^{\alpha-2\omega-1} + B_4 \beta^{-2} r^{2\alpha-3\omega-1} \quad \dots(12.0)$$

where

$$B_1 = -\frac{x\omega}{A_2 \gamma} + \frac{\alpha x(\xi-1)}{A_2 \left\{ (\xi-1) + (x\xi)^{1/2} \right\}}$$

$$B_2 = \frac{x A_1 K_1}{A_2 \rho^{1/2} \alpha^{1/2}} \left\{ (\alpha-3\omega) + \frac{\omega x}{\gamma A_2} - \frac{\alpha x(\xi-1)}{A_2 \left\{ (\xi-1) + (x\xi)^{1/2} \right\}} \right\}$$

$$B_3 = \frac{c_a \rho^{1/2} G}{(1+\alpha-\omega) A_2} \left\{ \frac{x(x\xi)^{1/2}}{\left\{ (\xi-1) + (x\xi)^{1/2} \right\}} - 1 \right\}$$

$$B_4 = \frac{K_1 A_1 x B_3}{A_2 \rho^{1/2} \alpha^{1/2}}$$

where $\gamma p' = \rho' a'^2$

Now solving linear differential equation and neglecting higher terms of β^{-2} , we get -

$$\frac{U}{\sqrt{\rho' G}} = \left[\frac{\frac{K}{\rho' G} \alpha^{-\omega} - \frac{B_3 \alpha^{-\omega}}{(B_1 + \alpha - \omega) \rho' G}}{\frac{B_2 B_3 \beta^{-2} \alpha^{2\alpha-2\omega}}{\rho' G (B_1 + 2\alpha - 3\omega)(\alpha - 2\omega)} + \frac{B_4 \beta^{-2} \alpha^{2\alpha-3\omega}}{(B_1 + 2\alpha - 3\omega) \rho' G}} \right]^{1/2}$$

$$\exp \left\{ \frac{B_2 \beta^{-2} \alpha^{2\alpha-2\omega}}{2(2\omega - \alpha)} \right\} \quad \dots(13.0)$$

where, k is constant of Integration

The expression (13) represents freely propagating shock velocity with strong with strong magnetic field. The expression for freely propagating shock strength can be written as -

$$M = \frac{U}{a_0} = \frac{1}{K_2} \left[\frac{K \alpha^{\alpha-\omega} - \frac{B_3}{(B_1 + \alpha - \omega)}}{\frac{B_2 B_3 \beta^{-2} \alpha^{2\alpha-2\omega}}{(B_1 + 2\alpha - 2\omega)(\alpha - 2\omega)} + \frac{B_4 \beta^{-2} \alpha^{2\alpha-3\omega}}{(B_1 + 2\alpha - 3\omega)}} \right]^{1/2}$$

$$\exp \left\{ \frac{B_2 \beta^{-2} \alpha^{2\alpha-2\omega}}{2(2\omega - \alpha)} \right\} \quad \dots(14.0)$$

3. **For converging shock:-** In the freely propagation

description, the characteristic form of system of equation (1.0-1.5) i.e. the form in which each equation contains derivatives in only one direction in the (r,t) plane is-

$$dp - \rho c du + \mu H dH + \frac{\alpha \rho u c^2}{(u-c)r} \frac{dr}{r} - \frac{\alpha c G m}{(u-c)r^2} \frac{dr}{r} = 0 \quad \dots(15.0)$$

substituting the shock condition (4.1) and (4.2) in equation 2.0 and use $c=U(x/\xi)^{1/2}$, for strong axial magnetic field, i.e. $dH_0=0$ and on simplifying we get -

$$dU^2 + \frac{1}{A_3} \left\{ 1 - \frac{k_1 x A_1 r^{\alpha-2\omega}}{A_3 \mu H_0^2} \right\} \left\{ \frac{x}{r} (\alpha-2\omega) \frac{dr}{r} + \frac{x A_1 k_1 (\alpha-2\omega) r^{\alpha-2\omega-1}}{m H_0^2} \frac{dr}{r} \right. \\ \left. - \frac{2x(\alpha-\omega)}{2\gamma} \frac{dr}{r} - \frac{2A_1 x p_0 \omega}{2\mu H_0^2} \frac{dr}{r} + \frac{\alpha x(\xi-1)}{\left\{ (\xi-1) + (x\xi)^{1/2} \right\} r} \frac{dr}{r} \right\} U^2 \\ + \frac{1}{A_3} \left\{ 1 - \frac{k_1 x A_1 r^{\alpha-2\omega}}{A_3 \mu H_0^2} \right\} \left[\frac{K_1 (\alpha-2\omega) r^{\alpha-\omega-1} dr}{r'} + \frac{G c_a \rho' \xi (x\xi)^{1/2} r^{\alpha-\omega-1}}{(1+\alpha-\omega) \left\{ (\xi-1) + (x\xi)^{1/2} \right\}} dr \right] = 0 \quad \dots(16)$$

Putting and in above equation, after simplification, we get -

$$\frac{dU^2}{dr} + \left\{ \frac{L_1}{r} + L_2 \beta^{-2} r^{\alpha-2\omega-1} \right\} U^2 = -L_3 r^{\alpha-\omega-1} + L_4 \beta^{-2} r^{2\alpha-3\omega-1} \quad \dots(17.0)$$

where

$$L_1 = -\frac{x\omega}{A_3 \gamma} + \frac{\alpha x(\xi-1)}{A_3 \left\{ (\xi-1) + (x\xi)^{1/2} \right\}} \quad L_4 = \frac{K_1 A_1 x L_3}{A_3 \rho' a'^2}$$

$$L_2 = \frac{x A_1 K_1}{A_3 \rho' a'^2} \left\{ (\alpha-3\omega) + \frac{\omega x}{\gamma A_3} - \frac{\alpha x(\xi-1)}{A_3 \left\{ (\xi-1) + (x\xi)^{1/2} \right\}} \right\}$$

$$L_3 = \frac{c_a \rho^{1/2} G}{(1+\alpha-\omega) A_3} \left\{ \frac{\xi (x\xi)^{1/2}}{\left\{ (\xi-1) + (x\xi)^{1/2} \right\}} - 1 \right\}$$

Now solving linear differential Equation (17.0) and neglecting higher terms of β^{-2} , we get-

$$\frac{U}{\sqrt{\rho'G}} = \left[\frac{\frac{K}{\rho'G} \alpha^{-b_1} - \frac{B_3 \alpha^{-2\omega}}{(B_1 + \alpha - \omega) \rho'G}}{\frac{B_2 B_3 \beta^{-2} \alpha^{2\omega-2\omega}}{\rho'G (B_1 + 2\alpha - 3\omega)(\alpha - 2\omega)} + \frac{B_4 \beta^{-2} \alpha^{2\omega-3\omega}}{(B_1 + 2\alpha - 3\omega) \rho'G}} \right]^{1/2} \exp \left\{ \frac{B_2 \beta^{-2} \alpha^{-2\omega}}{2(2\omega - \alpha)} \right\} \quad \dots(18.0)$$

where, k is constant of Integration, the expression (18) represents freely propagating shock velocity with strong with strong magnetic field. The expression for freely propagating shock strength can we written as

$$M = \frac{U}{a_0} = \frac{1}{K_2} \left[K \alpha^{a-B_1-\omega} - \frac{B_3}{(B_1 + \alpha - \omega)} \frac{B_2 B_3 \beta^{-2} \alpha^{2\omega}}{(B_1 + 2\alpha - 2\omega)(\alpha - 2\omega)} + \frac{B_4 \beta^{-2} \alpha^{2\omega}}{(B_1 + 2\alpha - 3\omega)} \right]^{1/2} \quad \dots(19.0)$$

IV. RESULTS AND DISCUSSIONS

Expression (13 & 18) respectively presents shock velocity for diverging and conversion shock. Expression for the particle velocity, the pressure and temperature for diverging shock are given below-

$$u = \frac{\xi - 1}{\xi} U \quad \dots(20.0)$$

$$p = p_0 \left\{ 1 + \chi \left(b_0^2 + A_1 a_0^2 \right) \frac{U^2}{a_0^2 b_0^2} \right\} \quad \dots(21.0)$$

$$\frac{T}{T_0} = \frac{\{2\gamma M^2 - (\gamma - 1)\} \{2 + (\gamma - 1)M^2\}}{(\gamma + 1)^2 M^2} \quad \dots(22.0)$$

Expression for the particle velocity, the pressure and temperature for converging shock are given below -

$$u = \frac{\xi - 1}{\xi} U \quad \dots(23.0)$$

$$p = p_0 \left\{ 1 + \chi \left(b_0^2 + A_1 a_0^2 \right) \frac{U^2}{a_0^2 b_0^2} \right\} \quad \dots(24.0)$$

$$\frac{T}{T_0} = \frac{\{2\gamma M^2 - (\gamma - 1)\} \{2 + (\gamma - 1)M^2\}}{(\gamma + 1)^2 M^2} \quad \dots(25.0)$$

Initially taking $U/a_0 = 10$ at $r=2$ for $\gamma=1.33$ and $\gamma=2.1$ the variation of shock velocity, sock strength, particle velocity, pressure and temperature for diverging and converging shock with propagation distance have been given in table (I, II, III, IV & V), and with χ have been given in table (VI, VII, VIII, IX & X) and table (XI, XII, XIII, XIV & XV) respectively.

For diverging shock, the shock velocity and shock strength both increases with propagation distance R and .But increases in the shock velocity and shock strength both decreases .While for converging shock, the shock velocity and shock strength both increases with propagation r and .But increases in the shock velocity decreases and shock strength increases.

For diverging shock, it is found that the particle velocity, temperature both increases while pressure decreases with propagation distance r and. But an increase in the particle velocity decreases, temperature and pressure both increases.

For converging shock, it is found that the particle velocity, temperature both increases while pressure decreases with propagation distance r .But an increase in the particle velocity and pressure decreases, while temperature increases and an increase in the particle velocity pressure and temperature increases.

TABLE-I

r	U(Diverging)	U(Converging)
2	211.1863	267.0229
2.05	211.2264	268.8879
2.1	211.265	270.722
2.15	211.3023	272.5261
2.2	211.3383	274.3016
2.25	211.3732	276.0494
2.3	211.4089	277.7706
2.35	211.4395	279.4662

TABLE-II

r	M(Diverging)	M(Converging)
2	78.73591	97.02451
2.05	76.94023	97.94374
2.1	77.13998	98.84971
2.15	77.33535	99.74289
2.2	77.52656	100.6238
2.25	77.71378	101.4928
2.3	77.8972	102.3503
2.35	78.07697	103.1968
2.4	78.25325	104.0325

TABLE-III

r	p(Diverging)	p(Converging)
2	58.53456	82.83688
2.05	55.44695	89.12645
2.1	52.59102	85.65031
2.15	49.94446	82.38847
2.2	47.48753	79.32309
2.25	45.2028	76.43816
2.3	43.07474	73.71932
2.35	41.08953	71.15361
2.4	39.23484	68.72937

TABLE-IV

r	u(Diverging)	u(Converging)
2	70.39542	88.00763
2.05	70.40879	89.62932
2.1	70.42167	90.24065
2.15	70.4341	90.84204
2.2	70.44611	91.43387
2.25	70.45772	92.01648
2.3	70.46896	92.59022
2.35	70.47985	93.1554
2.4	70.49041	93.71232

TABLE-V

r	T/T_0 (Div)	T/T_0 (Con)
2	953.0565	1523.072
2.05	958.1335	1552.05
2.1	963.1098	1580.878
2.15	967.9897	1609.558
2.2	972.7774	1638.096
2.25	977.4769	1666.495
2.3	982.0919	1694.759
2.35	986.6256	1722.891

TABLE-VI

ω	U(Diverging)	U(Converging)
1.2	194.6436	318.354
1.3	197.8164	316.244
1.4	200.3809	313.1679
1.5	202.3813	309.7524
1.6	204.5725	306.5462
1.7	206.8619	303.2487
1.8	209.4379	300.1864
1.9	212.904	297.0394

TABLE-VII

ω	M(Diverging)	M(Converging)
1.2	29.8494	48.8209
1.3	37.38032	59.75895
1.4	43.90865	68.63006
1.5	49.70496	76.07535
1.6	55.04743	82.48704
1.7	59.9795	87.92681
1.8	64.57196	92.55071
1.9	69.00904	96.28005

TABLE-VIII

ω	u(Diverging)	u(Converging)
1.2	64.88121	106.118
1.3	65.93879	105.4147
1.4	66.78697	104.3893
1.5	67.46044	103.2508
1.6	68.19083	102.1821
1.7	68.95396	101.0829
1.8	69.81262	100.0621
1.9	70.96798	99.01313

TABLE-IX

ω	w(Diverging)	w(Converging)
1.2	135.2287	339.6051
1.3	124.7711	306.2459
1.4	116.8537	277.3443
1.5	109.8185	251.6343
1.6	103.8098	229.0436
1.7	98.45149	208.5678
1.8	93.75113	190.3212
1.9	90.08616	173.631

TABLE-X

ω	T/T_0 (Diverging)	T/T_0 (Converging)
1.2	174.1917	464.3989
1.3	272.6392	695.3313
1.4	375.8274	916.7943
1.5	481.3356	1126.284
1.6	590.1537	1323.966
1.7	700.4661	1504.218
1.8	811.688	1666.484
1.9	926.937	1803.415

TABLE-XI

γ	U(Diverging)	U(Converging)
1.3	211.3599	259.6574
1.35	211.0453	272.477
1.4	210.5479	288.3214
1.45	209.9223	307.7716
1.5	209.2033	331.6165
1.55	208.4139	360.9255
1.6	207.5686	397.1575
1.65	206.6761	442.3256
1.7	205.7398	499.249

TABLE-XII

γ	M(Diverging)	M(Converging)
1.3	77.68008	95.43065
1.35	76.11454	98.27018
1.4	74.56882	102.1108
1.45	73.0522	107.1034
1.5	71.57837	113.4817
1.55	70.14871	121.4816
1.6	68.76391	131.5714
1.65	67.42285	144.2975
1.7	66.12301	160.4544

TABLE-XIII

γ	u(Diverging)	u(Converging)
1.3	70.4533	86.55
1.35	70.3484	90.82
1.4	70.1828	96.10
1.45	69.9704	102.59
1.5	69.7344	110.53
1.55	69.4700	120.30
1.6	69.1895	132.38
1.65	68.8920	147.44
1.7	68.5799	166.41

TABLE-XIV

γ	p(Diverging)	p(Converging)
1.3	53.07	79.47
1.35	62.16	102.80
1.4	71.28	132.58
1.45	80.42	171.43
1.5	89.57	223.20
1.55	98.75	293.68
1.6	107.94	391.89
1.65	117.15	532.17
1.7	126.373	738.07

TABLE-XV

γ	T/T_0 (Diverging)	T/T_0 (Converging)
1.3	890	1343
1.35	992	1653
1.4	1082	2028
1.45	1161	2494
1.5	1230	3090
1.55	1291	3870
1.6	1343	4917
1.65	1389	6360
1.7	1428	8406

REFERENCES

- [1] Korobeinikov, B.P. Melnikova, N.S. and Rayazanov, EV, The theory of point explosions U.S. Department of commerce (1962).
- [2] Zel'dovich Ya. B. and Rizer, Yu P Physics of shock waves and high temperature hydrodynamic phenomena, vol. 2, Academic Press N.Y. (1967)
- [3] Ranga Rao, M.P. and Purohit, N.K. - Int. J. Eng. Sci., 14 91 (1975).
- [4] Singh, J.B ; Yadav, K.B. and Nayak, G. - Ind. Jour of Theor Phys , 46, 295 (1998)
- [5] R.A. Singh and J.b. Singh Indian Jour. of Theor. Phy Vol. 46, 295, 1998

- [6] S.K. Panday and R.K. Singh Indian Jour. of Theor. Phy. Vol. 47 No. 2, (1996).
- [7] S.K. Shrivastav and A. Lal Ind - Jour. of Theor. Phy. vol. 49 No. 4 (2001).
- [8] S k. Singh ind. Jour of Theor. Phy. Vol. 50, No 3(2002).

Temperature Rise in the Cell Phone User's Head

R. Seetharaman¹

N. Kumaravel¹

¹ Department of Electronics and Communication Engineering,
College of Engineering, Anna University, Chennai-600 025 India
E-mail : rseetharamanece@yahoo.co.in

Abstract—In this paper the thermal analysis has been performed considering the head of a subject exposed to cellular phones and focusing the attention on important organs like the pinna (ear), and skull the maximum temperature increases is obtained in the skull at 0.027°C whereas the maximum temperature increases in the brain, at 0.027°C. The maximum temperature increase in the skull and ear are the same because microwave deposition is assumed to be constant

Key Words— Biological effects of electromagnetic radiations, Cell phone radiation, Temperature rise, Electromagnetic heating.

1. INTRODUCTION

IN recent years there has been increasing public concern about the influence of the electromagnetic wave on the human body. In fact, when a cellular phone is working, the transmitting antenna is placed very close to the user's head where a substantial part of the radiated power is absorbed. The power absorption in any tissue can be called as SAR (specific absorption rate). The SAR is a physical quantity, which causes the tissue heating due to RF exposure. In this work, we computed the temperature rise in a human head for mobile phones using bio-heat equation.

The SAR value of 4 W/kg is accepted worldwide as the threshold for the induction of biological thermal effects. In fact, the tissue heating is strongly influenced not only by the power dissipated in the local tissue volume, but also by the way in which absorption is distributed in the surrounding area. A thermal analysis seems to be necessary, in addition to SAR analysis, to assess the safety of an exposure. From the study of bio electromagnetic interaction, it is interesting to compare the obtained temperature increases with the thresholds for the induction of thermal damages. The threshold temperature increase for neuron damage is about 4.5°C (for more than 30 min).

Radiofrequency (RF) energy has been reported to cause a variety of ocular effects, primarily cataracts but also effects on the retina, cornea, and other ocular systems. The temperature increase necessary to induce thermal damage in the skin is at least 10°C.

In this work, we have evaluated the temperature increases induced in an anatomical model of the human head exposed to the field emitted by a source operating around 500 MHz.

II. CALCULATION METHODS

A. Head Model:

The thermal response as a function of time, until the steady state is reached, has been calculated the head model was created by taking the superimposition of different tissues like skin, skull, bone, gray matter, white matter, fat, humor, cerebro spinal fluid (CSF). All the above tissues have different mass densities and dielectric properties at different frequencies. And also they have different thermal properties. The head model had 500X341 pixels. According to range of pixel values, the different tissues of head are created. Sixteen different types of tissues and organs have been evidenced, and particular attention has been devoted to the modeling of the ear, skin, skull, air and brain simulating its morphology during a phone call.

In some simulations, the hand grasping the phone has been considered. The hand tissue has been assigned electric properties equal to two-thirds of those used for the muscle. The hand is wrapped around the case on three sides, leaving free the side facing the head.

B: Thermal Model:

The temperature increase in the head model has been obtained by

$$K \cdot \nabla^2 T + A_0 + Q_v - B \cdot (T - T_b) = C \cdot \rho \cdot \frac{\partial T}{\partial t} \quad [W/m^3]$$

where K is the thermal conductivity, A₀ and Q_v are volumetric heat sources due to metabolic processes and microwave power deposition, respectively, B is a parameter proportional to the blood perfusion, T_b is the blood temperature, and, finally, C and ρ are the tissue specific heat and density, respectively.

The three dimensional measurement consists mainly of an elevation positioner with head model. For simulating the human interaction with electromagnetic fields different homogenous numerical representations of human body are adopted.

	C [$\text{J/(kg}\cdot^\circ\text{C)}$]	K [$\text{J/(s}\cdot\text{m}\cdot^\circ\text{C)}$]	A_0 [$\text{J/(s}\cdot\text{m}^2)$]	B [$\text{J/(s}\cdot\text{m}^2\cdot^\circ\text{C)}$]
Skin	3500	0.42	1000	9100
Muscle	3600	0.50	690	2700
Bone	1300	0.40	0	1000
Blood	3900	0.00	0	0
Fat	2500	0.25	180	520
Cartilage	3400	0.45	1000	9100
Grey matter	3700	0.57	10000	35000
White matter	3600	0.50	10000	35000
Humor	4000	0.60	0	0
Lens	3000	0.40	0	0
Sclera/Cornea	4200	0.58	0	0
Cerebellum	3700	0.57	10000	35000
Hypophysis	3700	0.57	10000	36000
CSF	4000	0.60	0	0
Parotid	3700	0.57	7000	25000
Tongue	3300	0.42	3700	13000

Table 1: Thermal properties of the head tissues

The thermal parameters used in the above equation have been extrapolated from existing literature [3]–[5] and are reported in the above Table. The most interesting feature to be noted in Table II is that the normal blood perfusion in the brain tissues is about ten times higher than in the other head tissues. This large blood perfusion compensates for the heat production caused by the high basal metabolic rate, maintaining a physiological temperature of about 37.5°C in the inner brain region.

IV. CONCLUSION

The temperature increase has been analysed in the pinna and skull by taking blood temperature as 36.8°C . Figure 1 shows the temperature increase in the skull. Figure 2 shows the temperature increase in the pinna of the ear. The maximum temperature increases is obtained in the skull at 0.027°C whereas the maximum temperature increases in the brain, at 0.027°C . The temperature distribution in the pinna is high compared to remaining parts of the head because of the distance from the source. Figure 3 shows the temperature distribution in head due to microwave power source.

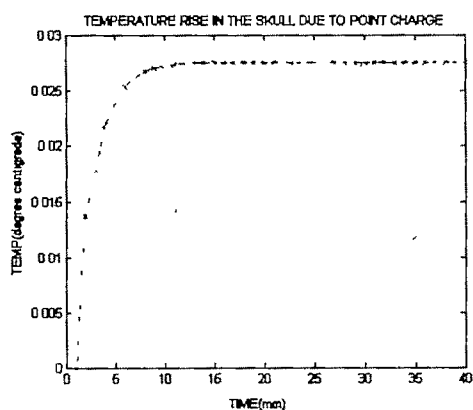


Fig1. Temperature rise in the Skull

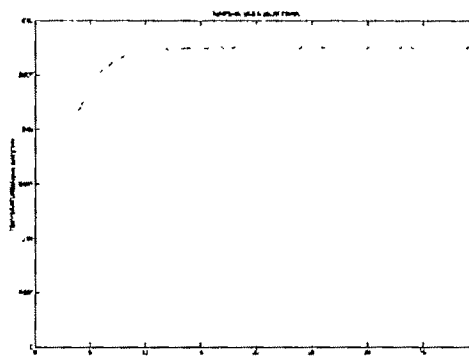


Fig2. Temperature rise in the Pinna(Ear)



Fig3. Temperature Distribution in Head

REFERENCES

- [1] A.Hirata, "Temperature Increase in Human Eyes Due to Near-Field And Far-Field Exposures at 900MHz,1.5GHz,and1.9GHz",IEEE Trans.Electromagn. compat., vol 47, no.1, pp.68-76, Feb.2005
- [2] R. Seetharaman and N. Kumaravel, "Effects on Temperature Rise in Human Eyes due to Cell Phone Radiation - A Review", IEEE National conf on Info and Comm. Convergence, pp 94-96, Dec.2006.
- [3] A. C. Guyton, *Textbook of Medical Physiology* Philadelphia, PA: Saunders, 1991.
- [4] R. G. Gordon, R. B. Roemer, and S. M. Horvath, "A mathematical model of the human temperature regulatory system—Transient cold exposure response," *IEEE Trans Biomed Eng.*, vol. BME-23, pp. 434–444, Nov. 1976.
- [5] R. J. Dickinson, "An ultrasound system for local hypothermia using scanned focused transducers," *IEEE Trans. Biomed. Eng.*, vol. BME-31, pp.120–125,Jan.1984.

Simulation And Analysis Of Micro-Resonators Using Sugar

S.Meenatchisundaram¹, G.Uma², M. Umapathy³, B.S. Sathyanarayana⁴ and P.R.Venkateswaran⁵

¹ Dept of ICE, Manipal Institute of Technology, Manipal, Karnataka, India (e-mail: meenasundar@gmail.com)

² Dept of ICE, National Institute of Technology, Tiruchirappalli, Tamilnadu, India (e-mail: guina@nitt.edu).

³ Dept of ICE, National Institute of Technology, Tiruchirappalli, Tamilnadu, India (e-mail: umapathy@nitt.edu)

⁴ Innovation Center, Manipal Institute of Technology, Manipal, Karnataka, India (e-mail: @satyang1@yahoo.com)

⁵ Dept of ICE, Manipal Institute of Technology, Manipal, Karnataka, India. (e-mail: prvj@yahoo.co.in)

Abstract— The performance of micro-resonators are analyzed in terms of displacement, area and resonant frequency using user friendly MEMS software named as SUGAR. Five different models such as folded flexure beam, fixed – fixed beam, crab leg beam, and meander suspension of microresonator are created in SUGAR and its displacements are analyzed for a constant force applied on the 'x' direction. Various modes of displacement, natural frequency and area of each model are also analyzed. MATLAB is used along with SUGAR to obtain the general characteristics of micro-resonators. The best model is selected using the analysis for minimum area and maximum displacement.

Key words—MEMS, Micro-Resonators, SUGAR, Folded Flexure, Comb-drive actuator.

I. INTRODUCTION

MICRO Electro Mechanical Systems (MEMS) is a rapidly growing technology for miniature devices using fabrication processes similar to those of integrated circuits (ICs) with an application in diverse areas. MEMS technology have been perceived as a breakthrough in the field of inertial navigation, force sensing and motion sensing because of the substantial reduction in cost, size and power as compared to their macroscale counterparts[1].

Resonator is a device with an element vibrating at resonance which changes its output frequency, i.e. mechanical resonance frequency, as a function of a physical or chemical parameter. Silicon integrated-circuit fabrication technology has been used for many years to fabricate identical, small, low-cost, analog sensors with or without integrated electronics on the sensor chip. Resonant sensors in silicon relying on stress changes which change the resonant frequency are more than 100 times as sensitive as standard analog piezo resistive transducers. MEMS based micro-resonators are used in various applications such as to measure force, pressure, flow, acceleration, etc[2].

In the case of mechanical systems, resonance has come to denote the characteristic that large amplitude vibrations will ultimately result from low-power driving at a specific input

frequency. It is especially useful to exploit the phenomenon of resonance at the micromechanical scale as maximum control forces exhibit faster dimensional scaling than spring constants for mechanical beam elements.

In this paper, five different models such as folded flexure beam, fixed – fixed beam, crab leg beam, and meander suspension of microresonator are created in SUGAR and its displacements are analyzed for a constant force applied on the 'x' direction. Various modes of displacement, natural frequency and area of each model are also analyzed. MATLAB is used along with SUGAR to obtain the general characteristics of micro-resonators. The best model is selected using the analysis for minimum area and maximum displacement.

II. MICRORESONATOR STRUCTURES

A. Folded flexure electrostatic combdrive microresonator:

The folded-flexure electrostatic-comb-drive microresonator topology used in this analysis was first introduced by Tang et al.[3] and is now commonly used for MEMS process characterization. The device has applications in oscillators and high-Q filters. The layout of laterally driven folded flexure electrostatic comb-drive microresonator is shown in fig.1.

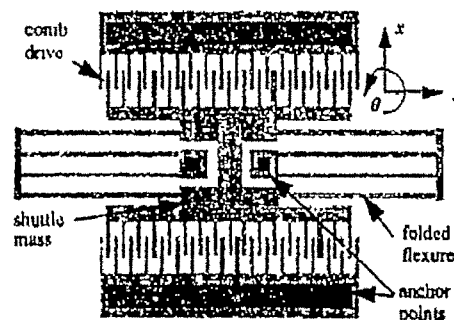


Fig.1 Layout of the lateral folded flexure comb-drive microresonator

The range of design and style variables of this structure is given by Tamal Mukherjee, et al.[4]. The equations for spring constant, effective mass, and electrostatic actuation force can be found from[5], which is also used in[4].

The design equations referred from [5] is given as follows:

$$k_x = \frac{2Et w_b^3}{L_b^3} \frac{L_i^2 + 14\alpha L_i L_b + 36\alpha^2 L_b^2}{4L_i^2 + 4\alpha L_i L_b + 36\alpha^2 L_b^2} \quad (1)$$

where E is the Young's modulus of polysilicon, t is the Polysilicon thickness, and $\alpha = (w_i/w_b)^3$. In the limit of infinitely stiff trusses, approximated by $\alpha \gg (L_i/L_b)$, the effective mass is:

$$m_x = m_s + \frac{1}{4}m_t + \frac{12}{35}m_b \quad (2)$$

where, m_s is the shuttle mass, m_t is the total mass of all truss sections, m_b is the mass of all long beams. The resonant frequencies is given by

$$\omega_x = 2\pi f_x = \sqrt{\frac{k_x}{m_x}} \quad (3)$$

B. Clamped – clamped beam[6]:

A clamped-clamped beam with rectangular cross section is shown in figure 2.

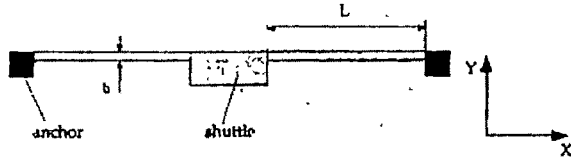


Fig.2 Clamped – clamped beam

The design equations are given by Rob Legtenberg, et al.[6]. The axial displacement along the x-axis can be found directly from Hooke's law and the lateral displacement along the y-axis is obtained from small deflection theory. The spring constants for a concentrated force in the x- and y-directions are given by:

$$k_x = 2Eb h/L \quad (4)$$

$$k_y = 2Eh b^3/L^3 \quad (5)$$

where E is Young's modulus; b is the beam width, h is the beam thickness and L is the length of one beam segment.

C. Crab-leg flexure beam[6]:

A sketch of a crab-leg flexure is shown in figure 3. The thigh segment has a second moment of inertia I_1 and is of length L_1 ; the shin segment has a second moment of inertia I_2 and is of length L_2 .

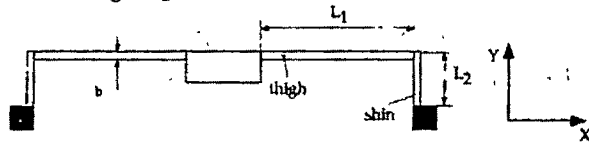


Fig.3 Crab – Leg Flexure beam

The spring constants, as a result of a concentrated force on the shuttle, in the x- and y-directions are given by:

$$k_x = \frac{12E_y I_2}{L_2^3} \left\{ \frac{L_1 I_2 + 2L_2 I_1}{2L_1 I_2 + L_2 I_1} \right\} \quad k_y = \frac{24E I_1}{L_1^3} \left\{ \frac{L_1 I_2 + L_2 I_1}{L_1 I_2 + 4L_2 I_1} \right\} \quad (6)$$

D. Meander Suspension[7]:

A sketch of a Meander Suspension with guided end boundary condition is shown in figure 4.

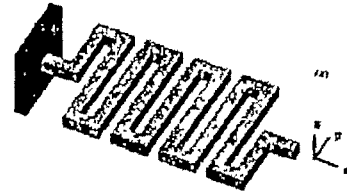


Fig.4 Classic meander Suspension

The spring constants after approximations can be given as:

$$k_x \approx \frac{48EI_b}{a^2(\tilde{a}+b)n^3} \quad k_y \approx \frac{48EI_b}{b^2(3\tilde{a}+b)n} \quad (7)$$

III. SIMULATION

A. SUGAR[8]:

SUGAR is a collection of Matlab routines which implements a nodal analysis approach to MEMS simulation. A wide variety of planar electromechanical systems can be simulated. The user provides a text file describing the geometry and connectivity of the system, and then calls one or more analysis routines to determine static displacement, transient response, etc. Graphical results are displayed using Matlab function calls, and numerical results are available for additional Matlab processing if desired[9].

The user has to provide a .net file that describes the building blocks in terms of geometry, voltage, or applied force. The layer thickness and Young's modulus are defined in a separate process file. Using the information provided by the netlist and process file, SUGAR creates individual stiffness [k], mass [m], and damping [c], matrices for each structural blocks. Since each structure in the netlist may have differing orientations, all local coordinates are transformed into global coordinates. The assemblage of the set of individual matrices into collective system matrices, [K], [M], and [C], where all structures are coupled at common nodes, is accomplished by superposition. Element indices in the system matrix directly correspond to nodal coordinate components. Structures with common nodes have additive contributions to that particular matrix element. Therefore the size of the entire system matrices only depend on the number of distinct nodes.

B. Structures in SUGAR:

The various structures discussed in section 2 are developed in SUGAR by keeping the area as a constant are shown in figures 5 to 8.

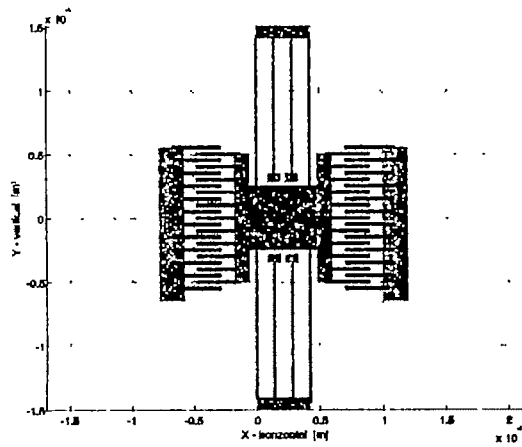


Fig.5 Folded flexure electrostatic combdrive microresonator

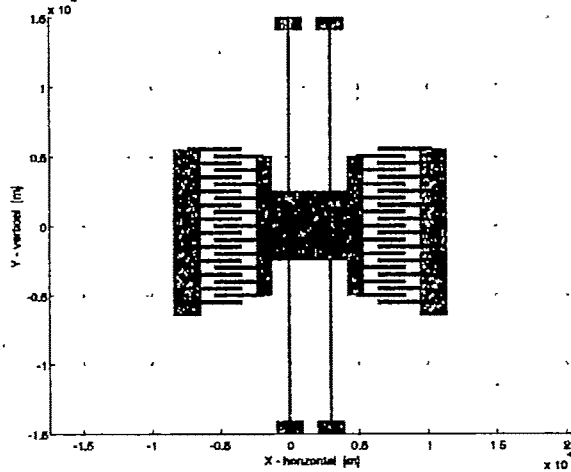


Fig.6 Clamped - Clamped Beam Microresonator

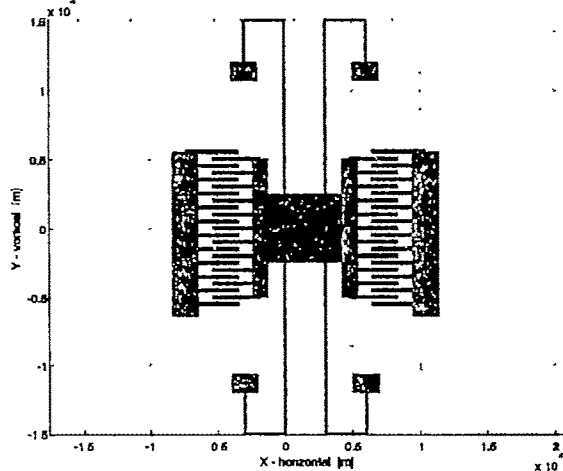


Fig.7 Crab-Leg Flexure Beam Microresonator

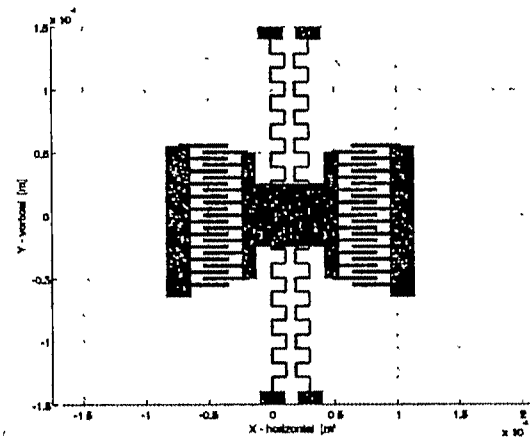


Fig.8.1 Meander Suspension Microresonator

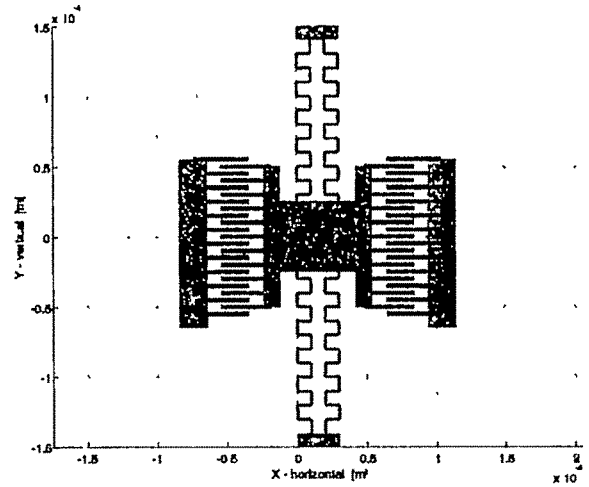


Fig.8.2 Meander Suspension Microresonator with a size reduction of 25% in the springs.

IV. RESULTS AND DISCUSSION

A. Displacement and Resonance Frequency:

The structures are simulated using SUGAR for a $50\mu\text{N}$ force on the x direction and the results are given in table 1.

Table1 Structures Vs Displacement

Structure	Displacement (m)
Folded flexure	10.384e-006
Clamped - Clamped Beam	7.1662e-006
Crab-Leg Flexure Beam	9.7459e-006
Meander Suspension1	9.7191e-006
Meander Suspension2	9.2249e-006

It is observed that the Clamped - Clamped Beam is giving the lowest displacement of 7.1662e-006, i.e providing the highest stiffness. The Crab-Leg Flexure Beam is giving a displacement of 9.7459e-006, which can be altered by altering the length of the crabbed leg. The Folded Flexure is giving a

displacement of $10.384e-006$.

Two structures of Meander suspension are taken into consideration and it is observed that a 25% size reduction in the meander spring is giving a decrease of around 5% in displacement.

The list of structures and its resonating frequency of various modes are given in Table2.

Table2. Resonant Frequencies of Structures

Structures	Mode 1	Mode 2	Mode 3	Mode 4	Mode 5	Mode 6
Folded flexure	40694	53402	78703	196216	201177	204674
Clamped – Clamped	48829	71168	97051	404421	821899	1046586
Crab-Leg	41747	55733	60374	165909	348530	675627
Meander Suspension1	41166	56510	57489	299416	320073	520404
Meander Suspension2	42287	56767	58585	301773	368161	509329

Figure 9 - 13 shows the graphical view of displaced structure with natural frequency.

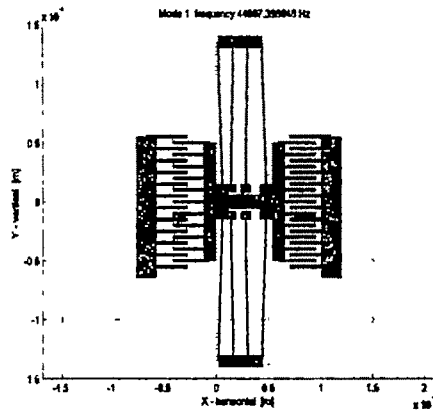


Fig.9 Displaced structure with natural frequency of Folded flexure electrostatic combdrive microresonator

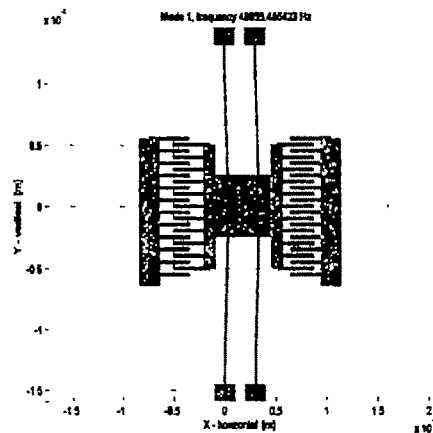


Fig.10 Displaced structure with natural frequency of Clamped – Clamped Beam Microresonator

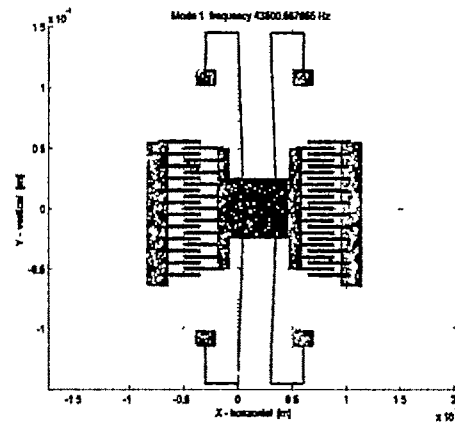


Fig.11 Displaced structure with natural frequency of Crab-Leg Flexure Beam Microresonator

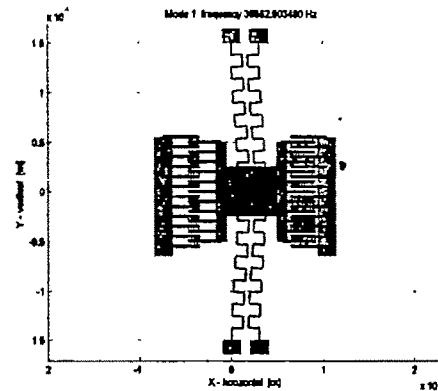


Fig.12 Displaced structure with natural frequency of Meander Suspension Microresonator (1)

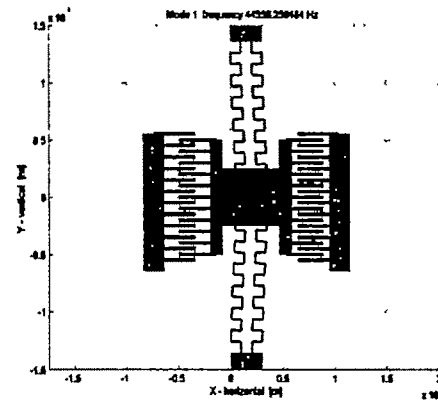


Fig.13 Displaced structure with natural frequency of Meander Suspension Microresonator (2)

B. Area Vs Displacement and Area Vs Resonance Frequency:

Comparison is made between Area Vs Displacement and Area Vs Resonance Frequency is shown in figure 14 and 15.

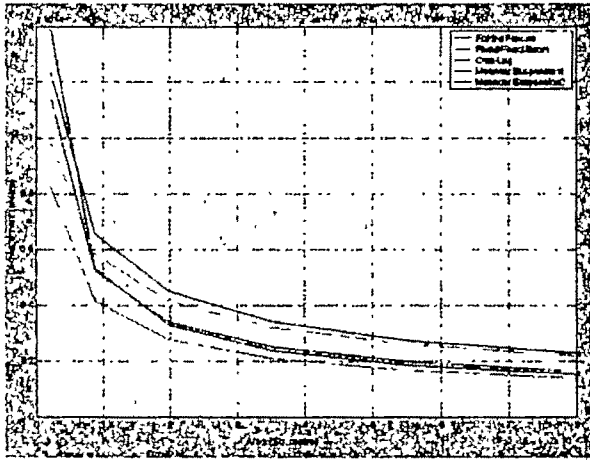


Fig.14 Area Vs Displacement

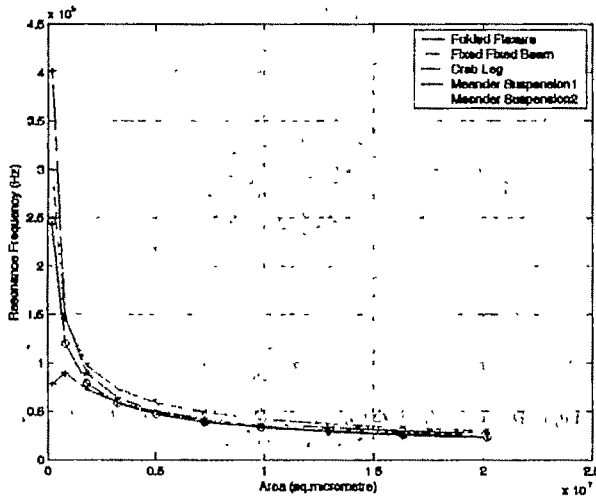


Fig.15 Area Vs Resonance Frequency

V. CONCLUSION AND FUTURE WORK

The simulation result shows that Crab Leg is giving a displacement of $13.9 \times 10^{-6} \text{m}$ and Folded Flexure Microresonator is giving a displacement of 12.4×10^{-6} for an area of $0.25 \times 10^{-7} \text{m}^2$ for a resonant frequency of around 7.5KHz. It can be concluded that Crab Leg is giving higher displacement for smaller area and folded flexure is giving higher displacement for relatively higher area.

The size of the meander springs and the leg of Crab-Leg Microresonator can be chosen in order to get maximum displacement and thus providing the flexibility to design.

SUGAR follows poly MUMPS fabrication procedure and the minimum size of the springs can be designed by considering the fabrication constrain also. There is a flexibility for implementation of optimization is available with SUGAR since it uses Matlab routines, which is not possible using commercial MEMS design softwares like Conventorware and Intellisuite.

Optimization can be done on all the structures by using the optimization algorithms like Genetic Algorithm, stimulated annealing, etc. Further, a comparison can also be made between the commercial tools with SUGAR in terms of resonant frequency and displacement.

REFERENCES

- [1] Ashwin Arunkumar Seshia, "Integrated Micromechanical Resonant Sensors for Inertial Measurement Systems", Ph. D. dissertation, Dept. of Electrical Engineering and Computer Science, Graduate Division of the University of California at Berkeley, 2002.
- [2] Goran Stemme, "Resonant silicon sensors", J. Micromech. Microeng. 1 (1991) 113-125.
- [3] William C. Tang, Tu-Cuong H. Nguyen and Roger T. Howe, "Laterally Driven Polysilicon Resonator", Sensors and Actuators, 20 (1989) 25-32.
- [4] Tamal Mukherjee, Sitaraman Iyer, Gary K. Fedder, "Optimization-based synthesis of microresonators", Sensors and Actuators A 70 (1998) 118-127.
- [5] S. Iyer, T. Mukherjee, G.K. Fedder, "Optimal synthesis of the folded-flexure comb-drive microresonator", Technical Report, Carnegie Mellon University, 1997.
- [6] Rob Legtenberg, A.W. Groeneveld and M. Elwenspoek, "Comb-drive actuators for large displacements", J. Micromech. Microeng. 6 (1996) 320-329.
- [7] G.K. Feeder, K.H. Clark, "Modeling and Simulation of Microresonator with Meander Suspension",
- [8] <http://bsac.berkeley.edu/cadtools/sugar>
- [9] Jason Vaughn Clark, Ningning Zhou, and K.S.J. Pister, "MEMS Simulation Using Sugar V0.5", Berkeley Sensor and Actuator Center, University of California at Berkeley, 497 Cory Hall, Berkeley, CA 9472.

An Analytical Approach to Study Dynamics of Beat-up Mechanism of a Loom

A. Rastgoo¹, A. Mirdehghan²

¹Department of Mechanical Engineering, University of Tehran, e-mail: arastgo@ut.ac.ir.

²Textile Engineering Department, Amir kabir University of Technology, e-mail: sama2@aut.ac.ir.

Abstract— The object of this investigation is to analysis four-bar beat-up mechanism of a weaving loom. This paper deals whit a better way to obtain the differential equation of motion of system. For this purpose we use an analytical method to study the equations of motion. Analytical model has been formulated by *Simulink* using *Lagrange's equation* of type II.

Keywords— Analytical, Beat-up, Dynamic, Mechanism.

I. INTRODUCTION

THE development of high speed weaving machines and requirement to produce better quality fabric necessitate a good fundamental understanding of the whole weaving process. Beat-up is one of the most important functions on weaving machines because it influences the fabric quality [1]. A lay mechanism is shown in Fig.1. It will be seen that the mechanism is in reality a four bar chain in which the loom frame forms the link AD. The link AB is crank, the link BC is the connecting rod and the link CD is the lay sword. As the crank AB rotates, it causes the point C to oscillate and if the reed is attached to link CD, will oscillate as required. The beat-up mechanism together with the shedding mechanism influences the quality of the pick and productivity of a loom and thus forms one of its critical mechanism [2]. It also affects the dynamic characteristics of the machine. Therefore, in designing a loom, much attention is paid to its structure and design [3].

Angular acceleration of crank and linkage has been studied by which the dynamic characteristics formulate by a mathematical model, and the equations are integrated by the *Rung-Kutta* method[4]. The aim of this paper is to find a method by which the same dynamic characteristics as well as relations between crank and linkage can be studied by an analytical model and it formulated by *MATLAB Simulink* using

II. ANALYTICAL MODEL

The use of Newton's second law for formulating the differential equations of motion of a single particle and the use of its extension to the motion of the center of mass of a system of particles and continuum bodies, requires the inclusion of all forces applied to the individual particles of the system. This includes even reaction forces that do not appear in the differential equations of motion. An analytical dynamics is a powerful approach and very easy to use. It is based on work-energy approach, and its fundamental quantities for obtaining the differential equation of motion of dynamical systems are the virtual work done by the force acting on the entire system. Thus, formulation of expressions for acceleration are also avoided. An analytical dynamics views the system in it's entirely, instead of looking at free body diagrams of individual parts. [5]. A real beat-up mechanism differs from an ideal one. An analytical model of this type should always be a compromise between the required accuracy of the result and exactness in representing the real mechanism [4].

The formulated model is based on the following assumption:

- 1-The masses of the elements are concentrated on the joint;
- 2- All the members are perfectly rigid;
- 3-The complete slay with reed is consider as absolutely rigid, joined elastically to the driving draw-bar.

In the analytical model the following *Lagrange's equation* of type II is used:

$$\frac{d}{dt} \left(\frac{\partial T}{\partial \dot{q}_i} \right) - \frac{\partial T}{\partial q_i} = Q_i \quad (1)$$

Where T is the total kinetic energy of the system q_i is any general coordinate, and Q_i is the generalized forces.

Lagrange's Equation of type II.

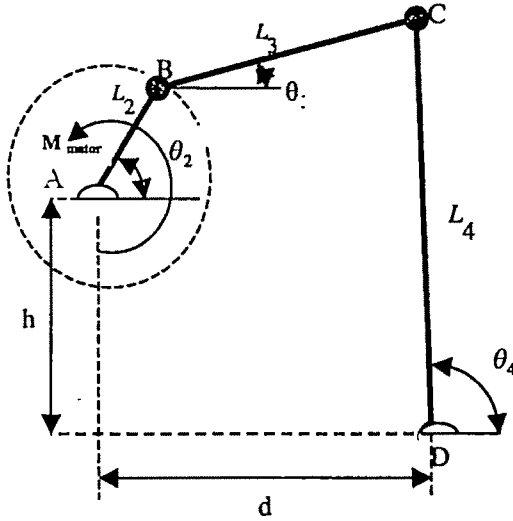


Fig.1. the four bar beat-up mechanism

For the case shown in Fig 1. the kinetic energy and dissipative function for the system can be written as follows:

$$\vec{v}_C = \frac{d}{dt} \vec{DC} + \frac{d}{dt} \vec{C3} = \quad (2)$$

$$\frac{d}{dt} [L_4 (\vec{i} \cos \theta_4 + \vec{j} \sin \theta_4)] + \frac{d}{dt} [\frac{L_3}{2} (-\vec{i} \cos \theta_3 - \vec{j} \sin \theta_3)] =$$

$$(\frac{L_3}{2} \dot{\theta}_3 \sin \theta_3 - L_4 \dot{\theta}_4 \sin \theta_4) \vec{i} + (L_4 \dot{\theta}_4 \cos \theta_4 - \frac{L_3}{2} \dot{\theta}_3 \cos \theta_3) \vec{j}$$

Where \vec{v}_C is the absolute velocity of the center of mass of bar BC. The following expression is then obtained for the kinetic energy of the motion:

$$T = 1/2 I_A \dot{\theta}_2^2 + 1/2 I_D \dot{\theta}_4^2 + 1/2 m_3 \vec{V}_{C3} \cdot \vec{V}_{C3} = \quad (3)$$

$$1/2 I_A \dot{\theta}_2^2 + 1/2 I_D \dot{\theta}_4^2 + 1/2 I_3 \dot{\theta}_3^2 +$$

$$\frac{1}{2} m_3 [(L_4 \dot{\theta}_4 \cos \theta_4 - \frac{L_3}{2} \dot{\theta}_3 \cos \theta_3)^2 +$$

$$(L_4 \dot{\theta}_4 \sin \theta_4 - \frac{L_3}{2} \dot{\theta}_3 \sin \theta_3)^2] =$$

$$\frac{1}{2} I_A \dot{\theta}_2^2 + \frac{1}{2} I_D \dot{\theta}_4^2 + \frac{1}{2} I_3 \dot{\theta}_3^2 +$$

$$\frac{1}{2} m_3 [L_4^2 \dot{\theta}_4^2 + \frac{1}{4} L_3^2 \dot{\theta}_3^2 - L_3 L_4 \dot{\theta}_3 \dot{\theta}_4 \cos(\theta_4 - \theta_3)]$$

where, I_A, I_D, I_3 are the moment of inertia of individual members, $\dot{\theta}_2, \dot{\theta}_3, \dot{\theta}_4$ are the angular velocities;

$$L_2 \cos \theta_2 + L_3 \cos \theta_3 - L_4 \cos \theta_4 - d = 0 \quad (4)$$

$$a_1(\theta_2, \theta_3, \theta_4) = 0$$

$$L_2 \sin \theta_2 + L_3 \sin \theta_3 - L_4 \sin \theta_4 - h = 0 \quad (5)$$

$$a_2(\theta_2, \theta_3, \theta_4) = 0$$

The virtual work δw done by all forces acting on the system is simply:

$$\delta w = M_{\text{motor}} \delta \theta_2 = Q_{\theta_2} \delta \theta_2 \quad (6)$$

M_{motor} is an approximate expression for the torque and is as follows:

$$M_{\text{motor}} = \pi / 6 + \sin(t + 10 * \pi)$$

Generally, it is more convenient to use Lagrange multipliers to handle constraint equation. Since there are two of such equations, two multipliers $\lambda_1(t), \lambda_2(t)$ are needed. For the three variables $\theta_1, \theta_3, \theta_4$ we have:

$$\frac{d}{dt} \frac{\partial T}{\partial \dot{\theta}_2} - \frac{\partial T}{\partial \theta_2} = Q_{\theta_2} + \lambda_1 \frac{\partial a_1}{\partial \theta_2} + \lambda_2 \frac{\partial a_2}{\partial \theta_2} \quad (7)$$

$$\frac{d}{dt} \frac{\partial T}{\partial \dot{\theta}_3} - \frac{\partial T}{\partial \theta_3} = Q_{\theta_3} + \lambda_1 \frac{\partial a_1}{\partial \theta_3} + \lambda_2 \frac{\partial a_2}{\partial \theta_3} \quad (8)$$

$$\frac{d}{dt} \frac{\partial T}{\partial \dot{\theta}_4} - \frac{\partial T}{\partial \theta_4} = Q_{\theta_4} + \lambda_1 \frac{\partial a_1}{\partial \theta_4} + \lambda_2 \frac{\partial a_2}{\partial \theta_4} \quad (9)$$

Where

$$Q_{\theta_2} = M_{\text{motor}}$$

$$Q_{\theta_3} = Q_{\theta_4} = 0$$

Equations (7), (8), (9) yield the following second-order differential equation:

$$\frac{1}{3} m_2 L_2^2 \ddot{\theta}_2 = M_{\text{motor}} - \lambda_1 L_2 \sin \theta_2 + \lambda_2 L_2 \cos \theta_2 \quad (10)$$

$$\frac{1}{3} m_3 L_3^2 \ddot{\theta}_3 - \frac{1}{2} m_3 L_3 L_4 [\ddot{\theta}_4 \cos(\theta_4 - \theta_3) - \dot{\theta}_4^2 \sin(\theta_4 - \theta_3)] =$$

$$- \lambda_1 L_3 \sin \theta_3 + \lambda_2 L_3 \cos \theta_3 \quad (11)$$

$$(\frac{1}{3} m_4 + m_3) L_4^2 \ddot{\theta}_4 - \frac{1}{2} m_3 L_3 L_4 [\ddot{\theta}_3 \cos(\theta_4 - \theta_3) + \dot{\theta}_3^2 \sin(\theta_4 - \theta_3)] =$$

$$\lambda_1 L_4 \sin \theta_4 - \lambda_2 L_4 \cos \theta_4 \quad (12)$$

From the equations (4), (5) we have:

$$L_2 \ddot{\theta}_2 \sin \theta_2 + L_3 \ddot{\theta}_3 \sin \theta_3 - L_4 \ddot{\theta}_4 \sin \theta_4 +$$

$$L_2 \dot{\theta}_2^2 \cos \theta_2 + L_3 \dot{\theta}_3^2 \cos \theta_3 - L_4 \dot{\theta}_4^2 \cos \theta_4 = 0$$

$$L_2 \ddot{\theta}_2 \cos \theta_2 + L_3 \ddot{\theta}_3 \cos \theta_3 - L_4 \ddot{\theta}_4 \cos \theta_4 - L_2 \dot{\theta}_2^2 \sin \theta_2 -$$

$$L_3 \dot{\theta}_3^2 \sin \theta_3 + L_4 \dot{\theta}_4^2 \sin \theta_4 = 0$$

(14)

Which are obtained by taking the second time derivative of the algebraic constraint equations. The five equations are combined into a single matrix which is easily solved numerically by *Simulink* using a *MATLAB Function block* which shown in Fig. 2. The user inputs to the new model are the values for $L_1, L_2, L_3, L_4, m_2, m_3, m_4$ and the expression for

The desired values of a Drapper shuttle weaving loom are the motor torque M .

presented in Table.1.

Table I. Loom setting value

Parameter	Value	Parameter	Value
h (m)	6	L_4 (m)	7
d (m)	4	m_1 (kg)	1
L_1 (m)	0.8	m_2 (kg)	4
L_2 (m)	4	m_3 (kg)	10

Model shown in Fig 2. consists of two integrators for generating $\dot{\theta}_2$ and $\dot{\theta}_3$ using the solution for $\ddot{\theta}_2$ obtained from equation(10).

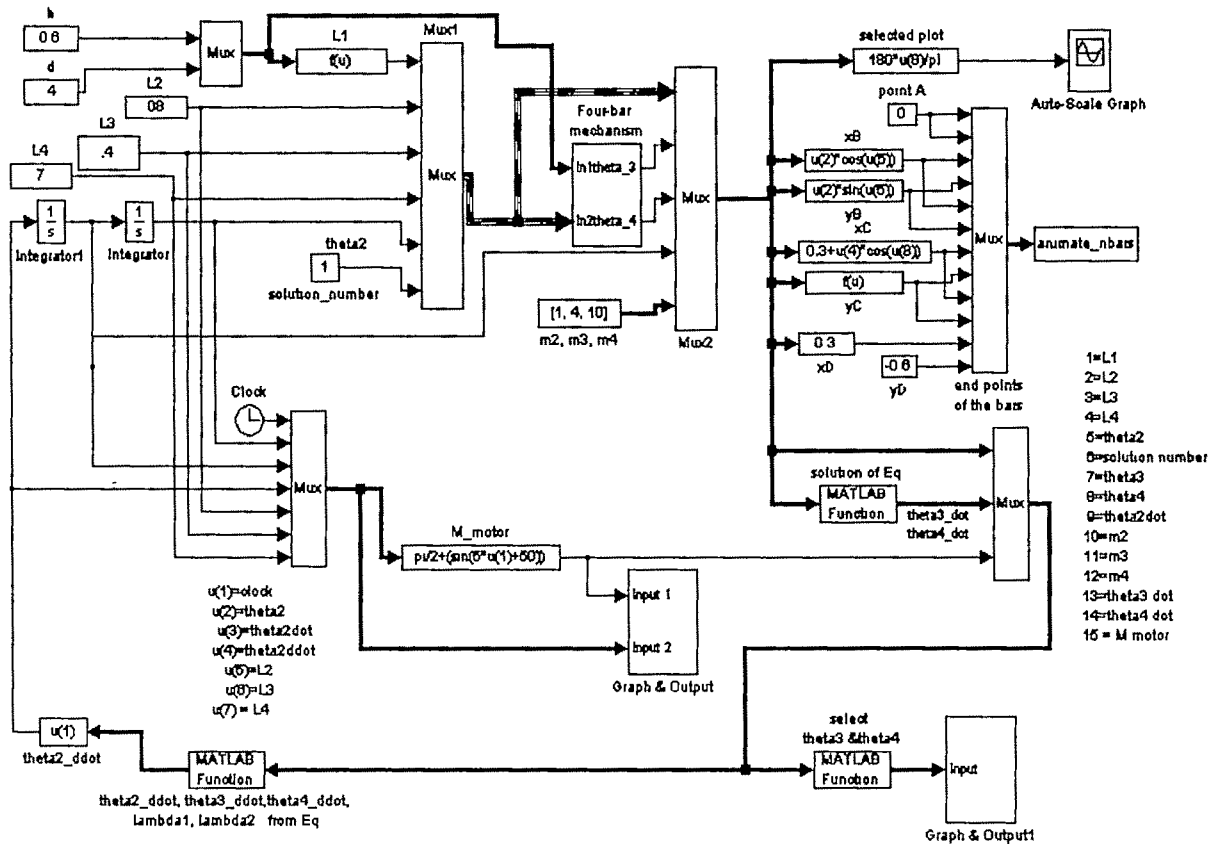


Fig 2. Simulink model

Fig 3-5 shows a solution for $\theta_2, \theta_3, \theta_4$ starting with the configuration defined by solution_ number, with the data specified at the beginning of this example and with $\dot{\theta}_3(0)=0$.

This plots show that θ_1, θ_3 oscillate between two values while θ_2 continually increases. This happens because the average value of the motor torque M_{motor} is non zero and positive.

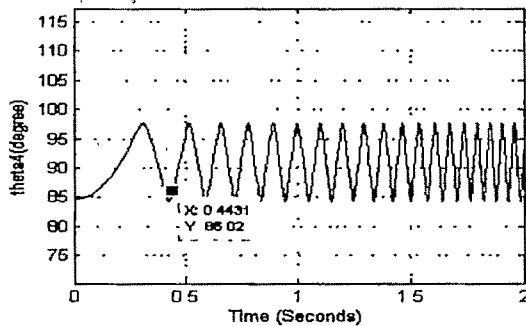


Fig 3. Theta4 generated by the Simulink model of Fig 2.

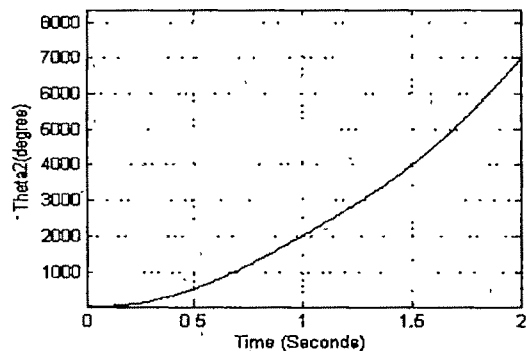


Fig 4. Theta2 generated by the Simulink model of Fig 2.

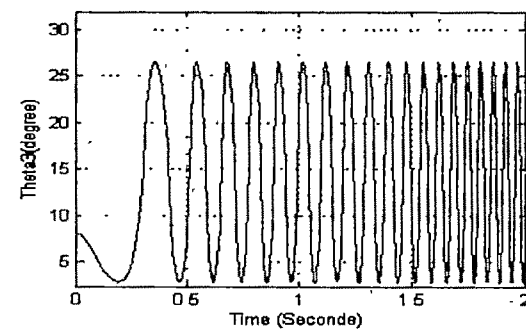


Fig 5. Theta3 generated by the Simulink model of Fig 2.

Fig.6. shows a series of curves for various values of L_3/L_2 (connecting rod /crank). It will be seen that as the connecting rod is made shorter there is an increased deviation from the pure sin wave (the sin wave represents simple harmonic motion). This is another way of saying that the lay fingers in the back position because of the shortness of the connecting rod, and it is this which is used to advantage in the loom. There is a limit to the amount of deviation which can be achieved because as $L_3 \rightarrow L_2$ the mechanism becomes unworkable. The value of L_3/L_2 used in loom depends upon whether a smooth action is required or whether an impulsive jerky type of beat-up is needed; This in turn depends upon the fabric to be woven and the width of the loom. A fine delicate fabric (Fine cotton and Silk) should not be roughly handled, where as a coarse staple yarn (Wollen and Heavy cotton) may require a sharp beat to be effective.

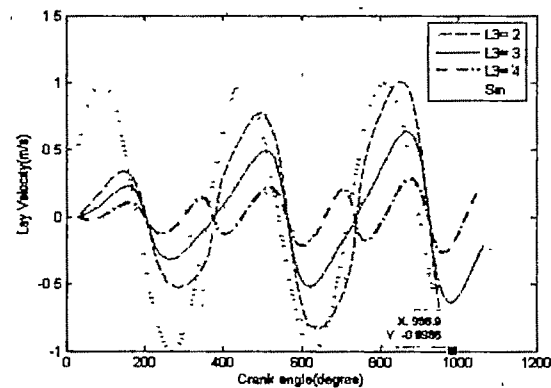


Fig 6. Effect of short connecting rod.

III. CONCLUSION

The aim of this paper is to formulate an analytical model which can easily simulate the dynamic characteristics of the studied beat-up mechanism, with respect to the basic non-linear driving force. The characteristics studied are the dependence of angular displacement, velocity and acceleration of individual members; especially of the slay and the driving moment on the crank. The important criteria are the maximum value of these characteristics and the additional frequency of oscillation, which is induced by the non-linearities in the kinematic chain. by using this simulation we can analyzed the lay motion. It will be seen that as the connecting rod is made shorter there is an increased deviation from the pure sin wave.

IV. REFERENCES

- [1] D. E. A. Plate and k Hepwork, "Beat-up Force in Weaving (Part II)", J Textile Institute, vol 62, no.10, pp 515-531.
- [2] Z Zhonghuai and H Mansour, "Theoretical Investigations of Beat-up", Textile Research Journal, July 1989, pp 395-404.
- [3] H behzadan and Sh Vazir daftari, "Mechanism and Technology of Weaving Machines", 1997, pp. 232-250.
- [4] J Mrazek, "Theoretical Analysis of Dynamics of Four-bar Beat-up Mechanism of a Loom", Mechanism and Machine Theory, Vol 27, No.3, 1992, pp. 331-341.
- [5] R.M. Crespo da Silva, "Intermediate Dynamics", McGraw-Hill, New York, 2004, pp 417-422

Three Dimensional Free Vibration Analysis of Transradially Isotropic Thermoelastic Sphere

J. N. Sharma and N. Sharma

Department of Applied Sciences, National Institute of Technology, Hamirpur – 177005 India

Email: jns@nitham.ac.in, nivi2j@gmail.com

Abstract- Spherically isotropic materials are of particular importance and use because of their application in aerospace and nuclear technology and can be useful as a benchmark to check numerical methods for thermoelastic continuum model analysis. Such materials have their physical properties transversely isotropic about the radius vector drawn from some particular points, fixed with respect to the material. In other words, in these materials, the physical properties are the same for all directions tangent to any sphere with its origin at a certain point. The elastic properties of such materials are described by the five elastic constants. A homogeneous isotropic material with two independent elastic constants is a special case of the spherically isotropic, thermally conducting solid sphere subjected to stress-free and thermally insulated/isothermal boundary conditions. After non-dimensionalizing, the basic governing equations of transradially isotropic thermoelastic sphere are uncoupled and simplified with the help of potential functions by using Helmholtz decomposition theorem. Upon using spherical harmonics wave solution the system of governing partial differential equations is reduced to a coupled system of three ordinary differential equations in radial coordinate. The matrix Frobenius method of extended series is then used to investigate the motion along radial coordinate. The resulting quartic indicial equation is solved by using DesCartes' method to find the characteristic roots. The secular equations for the existence of various types of possible modes of vibrations in the sphere are derived in the compact form after using boundary conditions. The special cases of spheroidal (S-mode) and toroidal (T-mode) vibrations of a solid sphere have also been deduced and discussed. The analysis will be useful in applications involving aerospace, navigation and nuclear technology in addition to check the validity and applicability of finite element method (FEM) and boundary element method (BEM) for thermoelastic continuum model analysis

Key words— Transradially isotropic, Frobenius method, S-Mode, T-Mode.

I. INTRODUCTION

Spherically isotropic materials are of particular importance

and use because of its application in aerospace and nuclear technology [1]. In addition, the latest geophysical results revealed that the earth, in fact, should be modeled as a spherically isotropic in homogenous sphere with liquid nucleus [2]. Chen [3] recently recalled the research history of spherically isotropic bodies. Although great achievements have been made to general solutions [4,5] and vibration theories [6,7], just as it was recently noticed by Schaflaich et.al. [8]. Chen et.al. [9] Obtained the eigen frequencies of an anisotropic sphere in case of elastokinetics.

The purpose of this paper is to present the exact three dimensional vibration analysis of a spherically isotropic sphere with stress free, thermally insulated/isothermal boundary conditions. This analysis can be a benchmark to check numerical methods for thermoelastic continuum modal analysis.

II. FORMULATION AND SOLUTION OF PROBLEM

We consider a homogeneous spherically isotropic, thermally conducting sphere of radius R at uniform temperature T_0 in the undisturbed state initially. In the spherical polar coordinates (r, θ, ϕ, t) , the linear governing equations of motion, and heat conduction and constitutive relations in the absence of body forces and heat sources, are given as:

$$\sigma_{ji,j} = \rho \ddot{u}_i, \quad i, j = r, \theta, \phi \quad (1)$$

$$K_3 \left(T_{rr} + \frac{2}{r} T_r \right) + K_1 \left[\frac{1}{r^2} T_{\theta\theta} + \frac{\cot \theta}{r^2} T_\theta + \frac{1}{r^2} T_{\phi\phi} + \frac{1}{r^2 \sin^2 \theta} T_{\phi\phi} \right] - \rho C_t \dot{T} = T_0 [\beta_1 (\dot{e}_{\theta\theta} + \dot{e}_{\phi\phi}) + \beta_3 \dot{e}_{rr}]$$

where

$$\begin{aligned} \sigma_{\theta\theta} &= c_{11} e_{\theta\theta} + c_{12} e_{\phi\phi} + c_{13} e_{rr} - \beta_1 T \\ \sigma_{\phi\phi} &= c_{12} e_{\theta\theta} + c_{11} e_{\phi\phi} + c_{13} e_{rr} - \beta_1 T \\ \sigma_{rr} &= c_{13} e_{\theta\theta} + c_{11} e_{\phi\phi} + c_{13} e_{rr} - \beta_3 T \end{aligned} \quad (2)$$

$$\sigma_{r0} = 2c_{44}e_{r0}, \sigma_{r\phi} = 2c_{44}e_{r\phi}, \sigma_{0\phi} = 2c_{66}e_{0\phi}$$

$$c_{66} = \frac{(c_{11} - c_{12})}{2}, \beta_1 = (c_{11} + c_{12})\alpha_1 + c\alpha_3,$$

$$\beta_3 = 2c_{13}\alpha_1 + c_{33}\alpha_3.$$

Here c_{ij} , e_{ij} , T , (α_1, α_3) , C_e and ρ are respectively the elastic parameters, strain tensor, temperature change, linear thermal expansions, thermal conductivities, specific heat and density of the medium. The comma notation is used for spatial derivatives and the superposed dot denotes time differentiation. In order to solve the problem we introduce the potential functions G , ψ and w through the relations as:

$$u_\theta = -\frac{1}{\sin\theta} \frac{\partial\psi}{\partial\phi} \frac{\partial G}{\partial\theta}, u_\phi = \frac{\partial\psi}{\partial\theta} - \frac{1}{\sin\theta} \frac{\partial G}{\partial\phi} \quad (3)$$

and assume the solution of the form

$$(\psi, w, G, T) = R \sum_{n=1}^{\infty} (u_n, w_n, v_n, T_n) S_n^m(\theta, \phi) e^{i\omega t}$$

(4.1) where $S_n^m(\theta, \phi)$ are the spherical harmonics; n and m are integers, u_n, w_n, v_n, T_n are functions of $\xi = r/R$ and ω is the circular frequency. Upon using the solution (4) in equation (1) and (2), we obtain

$$\frac{\varepsilon\Omega^2}{\chi^*} \left[\left(\frac{\partial}{\partial\xi} + \frac{2\bar{\beta}}{\xi} \right) v_n + \frac{\bar{\beta}n_1}{\xi} v_n \right] + \left(\nabla_2^2 + \frac{\Omega^2}{\chi^*} - \frac{\bar{K}n_1}{\xi^2} \right) \frac{\beta_3}{c_{44}} T_n = 0 \quad (4.2)$$

$$- \left(\nabla_2^2 + \Omega^2 - \frac{c_1n_1 + 2 - c_1 + c_2}{\xi^2} \right) v_n - \frac{\bar{\beta}\beta_3}{c_{44}\xi} T_n + \left[(1 + c_3) \frac{1}{\xi} \frac{\partial}{\partial\xi} + \frac{3 + c_1 + c_2}{\xi^2} \right] w_n = 0 \quad (4.3)$$

$$\left(c_4 \nabla_2^2 + \Omega^2 - \frac{n_1 + 2C}{\xi^2} \right) w_n - \frac{\beta_3}{c_{44}} \left(\frac{\partial}{\partial\xi} + \frac{2}{\xi} - \frac{2\bar{\beta}}{\xi} \right) T_n + n_1 \left[(1 + c_3) \frac{1}{\xi} \frac{\partial}{\partial\xi} - \frac{1 + C}{\xi^2} \right] v_n = 0 \quad (4.4)$$

$$\left\{ \nabla_2^2 + \Omega^2 - \frac{1}{2\xi^2} [4 + (c_1 - c_2)(n_1 - 2)] \right\} u_n = 0 \quad (5)$$

where

$$\nabla_2^2 = \frac{1}{\xi^2} \frac{d}{d\xi} \left(\xi^2 \frac{d}{d\xi} \right), C = c_1 + c_2 - c_3$$

$$c_1 = \frac{c_{11}}{c_{44}}, c_2 = \frac{c_{12}}{c_{44}}, c_3 = \frac{c_{13}}{c_{44}},$$

$$c_4 = \frac{c_{33}}{c_{44}}, \bar{K} = \frac{K_1}{K_3}, \varepsilon = \frac{T_0 \beta_3^2}{\rho C_e c_{44}}$$

$$\chi^* = \frac{i\omega}{\omega^*}, \Omega^2 = \frac{\rho \omega^2 R^2}{c_{44}}, \bar{\beta} = \frac{\beta_3}{\beta_1}$$

$$\omega^* = \frac{C_e c_{44}}{K_3}, n_1 = n^2 + n$$

III. BOUNDARY CONDITIONS

The surface $\xi = 1$ of the sphere is assumed to be stress free and thermally insulates/ isothermal which leads to

$$\sigma_{rr} = 0, \sigma_{r0} = 0, \sigma_{r\phi} = 0, T_\xi + hT = 0 \quad (6)$$

where h is Biot's heat transfer coefficient. Here $h \rightarrow 0$ refers to thermally insulated and corresponds $h \rightarrow \infty$ to isothermal boundaries.

IV. EXTENDED POWER SERIES SOLUTION

Equation (5) which is spherical Bessel equation has the solution

$$u_n(\xi) = B_{n1} \xi^{\frac{1}{2}} J_n(\Omega\xi), n \geq 1 \quad (7)$$

where

$$\eta^2 = \frac{1}{4} [\theta + 2(n^2 + n - 2)(c_1 - c_2)] > 0$$

J_η is the Bessel function of first kind and B_{n1} are arbitrary constants to be determined from boundary conditions. To solve equations (4) we apply the method of Frobenius in which one looks for solutions in the form of power series

$$(w_n, v_n, T_n) = \sum_{k=0}^{\infty} (A_k(s), B_k(s), D_k(s)) (\Omega\xi)^{s+k} \quad (8)$$

where s is the eigenvalue and coefficients A_k, B_k and D_k are to be determined by boundary conditions. Substitution solutions (8) in equations (4) yields

$$L_1^k(s) A_{k+2} + M_1^k(s) B_{k+2} = P_1^k(s) A_k + R_1^k(s) D_{k+1}$$

$$L_2^k(s) A_{k+2} + M_2^k(s) B_{k+2} = P_2^k(s) A_k + R_2^k(s) D_{k+1}$$

$$R_3^k(s) D_{k+2} = L_3^k(s) A_{k+1} + M_3^k(s) B_{k+1} + P_3^k(s) D_k \quad (9)$$

where L_i^k, M_i^k, P_i^k and $R_i^k, i=1,2,3$ are functions of material properties and k , and are given by

$$L_1^k(s) = \{c_4(s+k+2)^2 - (n_1 + 2C)\}$$

$$\begin{aligned} L_2^k(s) &= \{(1+c_3)(s+k+2) + (3+c_1+c_2)\} \\ L_3^k(s) &= -\varepsilon \Omega^2 (s+k+1) / \chi^* \end{aligned} \quad (10)$$

$$\begin{aligned} M_1^k(s) &= n_1 \{(1+c_3)(s+k+2) - (1+C)\} \\ M_2^k(s) &= \{-(s+k+2)^2 + c_1 n_1 + (2-c_1+c_2)\} \\ M_3^k(s) &= -\varepsilon \Omega^2 \bar{\beta} (n^2 + n) / \chi^* \end{aligned} \quad (11)$$

$$P_1^k(s) = -\Omega^2 = -P_2^k(s), \quad P_3^k(s) = \frac{\Omega^2}{\chi^*} \quad (12)$$

$$\begin{aligned} R_1^k(s) &= \frac{\beta_3}{c_{44}} (s+k+3-2\bar{\beta}), \quad R_2^k(s) = \frac{\bar{\beta}\beta_3}{c_{44}} \\ R_3^k(s) &= -\frac{\beta_3}{c_{44}} \{ (s+k+2)^2 - \bar{K}(n^2+n) \} \end{aligned} \quad (13)$$

Since equations (9) holds for arbitrary k , it must hold for $k=0$. The non-trivial solution requirement for $k=0$ results in the following indicial equations,

$$s^2 - \bar{K}(n^2 + n) = 0 \quad (14.1)$$

$$s^4 + As^2 + Bs + D = 0 \quad (14.2)$$

where

$$\begin{aligned} A &= n_1(1+c_3)^2 - \frac{1}{c_4^2} [c_1 c_4 n_1 + c_4(2-c_1+c_2) - (n_1+2C)] \\ B &= \frac{c_4}{(1+c_3)} [n_1(3+c_1+c_2) - (1+C)] \end{aligned} \quad (15)$$

$$D = -\frac{1}{c_4} [n_1(3+c_1+c_2)(1+C) + n_1 + 2C\{c_1 n_1 + 2 - c_1 + c_2\}]$$

$$C = c_1 + c_2 - c_3, \quad n_1 = n^2 + n$$

The roots of equation (14.2) are denoted by s_j , ($j=1,2,3,4$). The roots of equation (14.1) are denoted by s_j , ($j=5,6$). Moreover, it is also found that any two of the six real roots do not differ by an integer. Therefore, general solution of equations (4) has the form

$$\{w_n, v_n, T_n\} = \sum_{j=1}^3 \sum_{k=0}^{\infty} C_{jk} \{A_k, B_k, D_k\} (\Omega \xi)^{s_j+k} \quad (16)$$

where A_k, B_k, D_k are functions of s_j and are eigenvectors corresponding to eigenvalues s_j and integer k ; C_{jk} are arbitrary constants which can be evaluated by boundary conditions. In case of solid sphere $r=0$ i.e. $\xi=0$, is part of the domain of consideration and hence all the field functions must be bounded at $\xi=0$. Therefore we take those solutions

for s_j which satisfy the condition that $\text{Re}(s_j) \geq 0$. For $k=0$, the eigenvalues s_k and corresponding eigenvector in equations (10) are related by

$$A_2(s_j)=1, B_2(s_j)=Q_B(s_j), D_1(s_j)=0, A_0(s_j)=0 \quad (17)$$

where $Q_B(s_j)$ are given by

$$L_1^0 + M_1^0 Q_B = 0, \quad L_2^0 + M_2^0 Q_B = 0 \quad (18)$$

$$D_0=1, A_3=M_A, B_3=N_B, A_0=0, B_0=0, D_2=1 \quad (19)$$

Also $M_A(s_j)$ and $N_B(s_j)$ can be obtained from

$$L_1^1 M_A + M_1^1 N_B = R_1^1, \quad L_2^1 M_A + M_2^1 N_B = R_2^1 \quad (20)$$

Various quantities in equations (18) to (20) are functions of s_j . When $k \geq 1$, the eigenvectors can be obtained from the recurrence relations (10) in terms of the eigenvectors shown in equations (18) to (20). Thus all the eigenvectors are determined. The six unknowns can be evaluated by six boundary conditions at the outer and inner surfaces.

V. SECULAR EQUATIONS OF SPHEROIDAL AND TOROIDAL VIBRATIONS

Spheroidal mode (S-Mode)

For spherically isotropic thermally conducting solid sphere, the traction-free, thermally isothermal / insulated boundary conditions (6) at the surface $\xi=1$ results in a system of linear algebraic equations which has nontrivial solution if

$$\det(b_{ij}) = 0 \quad (21)$$

Equation represents the frequency equation for flexural wave propagation, spheroidal vibration (s-mode) in a transversally isotropic thermoelastic sphere. The expressions for b_{ij} are given in the Appendix.

Toroidal mode (T-mode)

For longitudinal waves traveling along the axis of sphere, the displacement field is independent of ϕ -coordinate and is of the form $(u_r, u_\theta, 0)$. This mode of wave propagation corresponds to the frequency equation for Toroidal vibrations (T-mode) can be obtained from (21) by setting $m=0$

VI. NUMERICAL RESULTS AND DISCUSSIONS

In order to illustrate the analytical development we propose to carry out numerical calculations to compute lowest frequency of s-mode with radius of the sphere for a transversally isotropic thermoelastic material (zinc crystal). The physical data is given as:

$$c_1 = 4.20, c_2 = 0.89, c_3 = 1.31, c_4 = 1.59, \bar{K} = 1,$$

$$\bar{\beta} = 0.89, \quad \omega^* = 5.01 \times 10^{11}$$

In computer simulation results have been presented graphically in Fig.1 and 2. in case of thermally insulated and isothermal conditions.

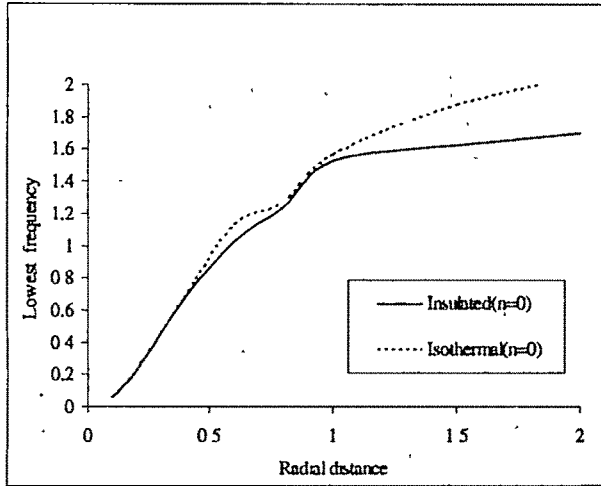


Figure 1: Variation of lowest frequency of S-mode for n=0 with radius of the sphere

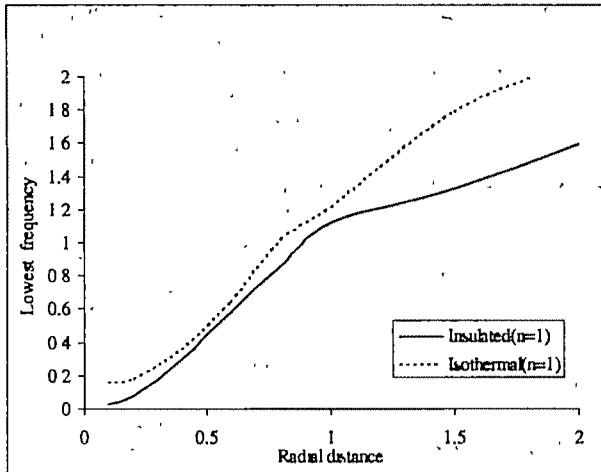


Figure 2: Variation of lowest frequency of S-mode for n=1 with radius of the sphere.

APPENDIX

$$b_{11} = [A' + (c_1 + c_3)(1 + s_1 + k)]A_k P \Omega^{\eta+k}$$

$$b_{12} = [A' + (c_1 + c_3)(1 + s_2 + k)]A_k P \Omega^{\eta_2+k}$$

$$b_{13} = [A' + (c_1 + c_3)(1 + s_3 + k)]A_k P \Omega^{\eta_3+k}$$

$$b_{14} = (c_3 - c_1) \left(P' - (\cos \theta P / \bar{P}^2) \right) m J_\eta(\Omega)$$

$$b_{21} = [-A_k + (s_1 + k - 1)B_k] \bar{P} P' \Omega^{\eta_1+k}$$

$$b_{22} = [-A_k + (s_2 + k - 1)B_k] \bar{P} P' \Omega^{\eta_2+k}$$

$$b_{23} = [-A_k + (s_3 + k - 1)B_k] \bar{P} P' \Omega^{\eta_3+k}$$

$$b_{24} = \Omega \operatorname{im} \left(J_{\eta+1}(\Omega) - \left(\eta - \frac{3}{2} \right) \frac{1}{\Omega} J_\eta(\Omega) \right) P / \bar{P}$$

$$b_{31} = \operatorname{im} [A_k + (1 - s_1 - k)B_k] \Omega^{\eta_1+k} P / \bar{P}$$

$$b_{32} = \operatorname{im} [A_k + (1 - s_2 - k)B_k] \Omega^{\eta_2+k} P / \bar{P}$$

$$b_{33} = \operatorname{im} [A_k + (1 - s_3 - k)B_k] \Omega^{\eta_3+k} P / \bar{P}$$

$$b_{34} = \Omega \left(J_{\eta+1}(\Omega) - \left(\eta - \frac{3}{2} \right) \frac{1}{\Omega} J_\eta(\Omega) \right) P' \bar{P}$$

$$b_{41} = (s_1 + k + h)D_k P \Omega^{\eta_1+k}, b_{42} = (s_2 + k + h)D_k P \Omega^{\eta_2+k}$$

$$b_{43} = (s_3 + k + h)D_k P \Omega^{\eta_3+k}$$

where

$$A' = \left((c_1 m^2 / \bar{P}^2) - n_1 c_3 \right) P + (c_1 + c_3) \cos \theta P' B_k - (D_k / \bar{P}) P$$

$$P = P_n(\cos \theta), \bar{P} = \sin \theta$$

ACKNOWLEDGEMENT

The authors are thankful to the University Grants Commission, New Delhi for providing financial support via project grant no. F. 30-236/2004(SR) to complete this work.

REFERENCES

- [1] M. Maiti, "Stress in anisotropic sphere," J. Eng. Mech, vol. 101, 1975, pp. 101-108
- [2] J. P. Montagner, D. L. Anderson, "Constrained Ref. Mantle Model", Phys. Earth Planet, vol 54, 1989, pp. 205-227.
- [3] W. Q. Chen, "Couple free vibrations of spherically isotropic hollow spheres", Ph. D. Dissertation, Zhejiang University, Hangzhou, China (in Chinese), 1996.
- [4] H. C. Hu, "On the general theory of elasticity for a spherically isotropic medium", Acta Sci. Sin, vol 3, 1954, pp 247-260
- [5] W. T. Chen, "On some problems in spherically isotropic elastic materials", ASME J. Appl. Mech., vol. 33, pp. 539-546.
- [6] Cohen, H., Shah, A. H., Ramakrishnan, C. V., 1972, "Free vibrations of a spherically isotropic hollow sphere", Acoustica, 26, 329-333.
- [7] Ding, H. J., and Chen, W. Q., 1996, "Non axisymmetric symmetric free vibrations of a spherically isotropic spherical shell embedded in an elastic medium", International. J. Solids and Structures, 33, 2575 - 2590.
- [8] Schafbuch, P. J., Rizzo, F. J., Thompson, R. B., 1992, "Eigen frequencies of an elastic sphere with fixed boundary conditions", ASME; J Appl Mech., 59, 458-459
- [9] Ding, H. J., Chen, W. Q., Liu, Z., 1995, "Solutions to equations of vibrations of spherical and cylindrical Shells", Appl. Math. Mech, 16, pp. 1-15.
- [10] Sharma, J. N., Sharma, P. K., 2002. Free vibration analysis of homogeneous transversely isotropic thermoelastic cylindrical panel. J Thermal Stresses 25, 169-182

Direct Simulation of Forced Convection in Porous Media

Mohammad Hassan Rahimian and Abdullah Abasiun

*Mechanical Engineering Dept. Faculty of Engineering
University of Tehran, Tehran, Iran
rahimyan@ut.ac.ir*

Abstract - The objective of this investigation is to obtain physical properties of porous media by using a direct numerical simulation. The porous media is generated in the domain by a random generation program, which distributes the solid rods in the porous media in the desired region. Navier-Stokes equations are solved in fluid region that is filled in the empty cells without any averaging. The continuity, momentum and energy equations are solved in a staggered grid domain with SIMPLE method. No-slip condition is applied in the neighboring of each particle. The physical configuration is a parallel plate channel with adiabatic walls or constant temperature. The energy transport equation is solved in solid particles without invoking the assumption of local thermal equilibrium. The average and local Nusselt numbers and total pressure drop are calculated in steady state flow and are compared with empirical and numerical data.

Key words—Forced Convection – Porous Media – Parallel Plate – Numerical Simulation – Simple Method

I. INTRODUCTION

HEAT and mass transfer in porous media is one of the most important problems in academic investigations and industries. Porous materials increase convective heat transfer and pressure drop in a flow field. First model for pressure drop in porous media was Darcy flow model. This model considers a linear averaged momentum equation. This model is simple and has performed well within the range of its validity [1], but it is not appropriate for fast flows with Reynolds number based on local velocity and pore diameter is greater than $O(1)$. It does not also satisfy no-slip condition on solid boundaries. Some investigators use more complication forms of this model, which have additional nonlinear terms and empirical constants. Poulikakos and Renken [2], [3], Chou and Lien [4], Calmidi and Mahajan [5], Cheng and Hsu [6] used this approach. However, no-slip condition does not

satisfy near any solid particle in their works. Several authors solved details of flow inside of a microscopic periodic structure. Eidsath et al [7], Coulaud et al [8], Fowler and Bejan [9] carried out two-dimensional numerical simulations for flow across banks of circular cylinders. Larson and Higdon [10] analyzed Stokes flow through lattice of spheres. Kuwahara et al [11], [12] assumed a macroscopic uniform flow to pass through a lattice of square rods placed regularly in an infinite space and solved flow in a block constructed from four neighboring square cylinders. Rahimian and Pourshaghghi [13] calculated the fluid flow microscopically in porous media without volumetric averaging. Porous media was generated by random distribution of square cylinders. Navier-Stokes and energy equations were solved considering diffusion and convection terms in fluid region by a point collocated method. The objective of this paper is to solve Navier-Stokes and energy equations in a staggered grid domain. In the staggered grids the velocities at the surface of the filled cells fixed zero while in point collocated methods the velocity of the center of the filled cells were fixed. In a staggered grid domain the points with known velocities are four time of the point collocated. Therefore the investigator should consider more cells in calculation with point collocated method. The results are compared well with experimental and numerical data.

II. PROBLEM DEFINITION

Consider a flow in a channel made of two parallel plates. A uniform grid is generated inside the channel, Fig. 1-a. The region between two plates acts as porous media, if some solid square cylinders are put in selected grids randomly, Fig. 1-b. Random distribution of solid rods is chosen, since there is not any regular distribution of particles in foam material. The size of solid rods is equal to particle size in real porous media; therefore, maximum length between two grids can be equal to the size of particles. More accuracy is achieved if more grids lie in a rod, which implies that more grids must be applied. The main property of this method is random choosing of nodes, which have to be filled. The solid cells are

distinguished from fluid cells by a void fraction parameter F . The value of this parameter is equal to one for solid cells and zero for fluid cells. A random generator program is utilized to fill some percentages of the domain. This program must have two properties. First, it distributes solid rods in the domain monotonously, i.e., it gives equal filling chance to every grid. Second, its porous generation differs in its different runs. The total volume of filled cells must produce desired porosity. Fig. 2 shows a zoomed generated porous domain that flow field is solved inside it. The main configuration in this work is shown in Fig. 3. The channel is divided into three sections I, II, and III. In the sections I and III, channel walls are adiabatic. The section II is filled with porous media which is generated by the method. The governing equations are solved in void regions directly for fluid flow. Solid particles temperature is performed by two different cases. In case (a), the solid temperature varies with time and energy equation is solved for any particle simultaneously with solving energy equation in fluid region. In this case, channel walls in porous section are at constant temperature T_w . In case (b), particles temperature is considered constant and channel walls are adiabatic in all three sections.

III. GOVERNING EQUATIONS

Governing equations that is continuity, Navier-Stokes and conservation of energy including convection and diffusion terms is given as follows

$$\nabla \cdot \vec{V} = 0 \quad (1)$$

$$\frac{\partial \vec{V}}{\partial t} + \vec{V} \cdot \nabla \vec{V} = -\frac{\nabla P}{\rho} + \frac{1}{\text{Re}} \nabla^2 \vec{V} \quad (2)$$

$$\frac{\partial T_f}{\partial t} + \vec{V} \cdot \nabla T_f = \frac{1}{\text{Re} \cdot \text{Pr}} \nabla^2 T_f \quad (\text{in fluid region}) \quad (3)$$

$$\begin{cases} \frac{\partial T_s}{\partial t} = \frac{\alpha_s}{U_r \cdot H} \nabla^2 T_s & (\text{case: a}) \\ T_s = \text{cte.} & (\text{case: b}) \end{cases} \quad (\text{in solid particles}) \quad (4)$$

The nondimensional variables in the above equations have been defined as

$$\begin{aligned} x &= \frac{\tilde{x}}{H}, \quad y = \frac{\tilde{y}}{H}, \quad \vec{V} = \frac{\tilde{\vec{V}}}{U_r}, \quad P = \frac{\tilde{P}}{\rho \cdot U_r^2}, \\ T &= \frac{\tilde{T}}{T_m}, \quad t = \frac{\tilde{t} U_r}{H}, \quad \text{Re} = \frac{\rho \cdot U_r \cdot H}{\mu} \\ \text{Re}_p &= \frac{\varepsilon \cdot \rho \cdot U_r \cdot d}{\mu} \end{aligned} \quad (5)$$

IV. NUMERICAL METHOD

Governing equations should be integrated in space and time using a numerical method. The first step is to choose an appropriate spatial cell network over which flow variables would be evaluated. Two dimensional problems require determination of two components of the velocity vector and pressure at each point in the flow field. To avoid pressure field decoupling between adjacent cells in the grid network, staggered cells are used. Staggered cell system uses three overlapping cells for two components of velocity and pressure. This is done such that for a given pressure cell, pressure is defined at the cell center and the x and y components of velocity are defined at the x and y faces of that cell. This method well known method, SIMPLe, is naturally well suited to the physics of the flow field where over any velocity cell, velocity is driven by the pressure gradient across that cell and pressure should be given at the cell surface.

Flow fields around rigid obstacles are usually transformed from the physical space to a computational space. This transforms the curvilinear, non uniform mesh of the physical space to a rectangular uniform spacing grid, in which the rigid bodies' complex geometrical surfaces become simple surfaces on the boundary of computational space.

V. Results and Discussion

The channel dimensions were chosen $0.5 \times 1.5m$ (height \times length), see Fig. 3. The length of each three sections is equal to $0.5m$. Numerical method was performed using a 300×100 , 600×200 , 900×300 , 1200×400 , 1500×500 and 1800×600 grids for Re_p from 10 to 400. A typical computed flow field is shown in Fig. 4 for $\text{Re}_p=100$ and $\text{Pr}=0.707$ for grid 1200×400 . Particle size is $5mm$ and ε is equal to 0.9. The effect of each particle on the flow is observed well in the zoomed velocity field (Fig. 4-b). These microscopic effects cannot be observed in averaging methods. Temperature contours are plotted in Figs. 5 and 6 for the same flow. In Fig. 5, the solid temperature is assumed constant (case b) at $390K$ and inlet temperature $T_m=300K$. The effect of no thermal equilibrium is observed in this figure. Due to high Re number flow, fluid temperature remains constant before porous domain and solid temperature is not diffused back. Temperature contours in case a are shown in Figs. 6-1 and 6-2 for $\text{Re}_p=5$ and $\text{Re}_p=200$ respectively. Solid material is aluminum with initial temperature equal to inlet flow temperature, $T_m=300K$. Wall temperature in section II is equal to $390K$. As seen, thermal boundary layer thickness decreases with rising in Re_p value near channel walls. Results of \overline{Nu} number in case b are in table 1 for 6 set grids. As seen change of average Nusselt number is negligible for grids more than 900×300 . All of the results in this paper is obtained by 1500×500 grids. In Reference [13] average Nusselt number was calculated by the following relation.

$$\bar{h} = \frac{\dot{m} C_{p,f} (T_{b,out} - T_{b,in})}{A_{p,d} \Delta T_{lm}} \text{ where}$$

$$\Delta T_{lm} = \frac{(T_s - T_{b,in}) - (T_s - T_{b,out})}{\ln \left(\frac{T_s - T_{b,in}}{T_s - T_{b,out}} \right)}$$

In this relation balance of convective heat transfer by total heat transfer was used to obtain average Nusselt number. If the length of porous domain increases heat transfer decreases, because the bulk temperature of fluid tends to surface temperature. Therefore local Nusselt number tends to zero. While in fully developed duct or tube local Nusselt number tends to a non-zero number. In this paper local heat transfer coefficient h_x is calculated as below.

$$h_x = \frac{\dot{m} C_{p,f}}{A_{p,x}} \ln \frac{T_s - T_b(i)}{T_s - T_b(i+1)}$$

Average Nusselt number is calculated by averaging of local convective heat transfer. Results of average Nusselt number versus particle Reynolds number is shown in Fig 7. As shown in low particle Reynolds number the results are compared better with the experimental references.

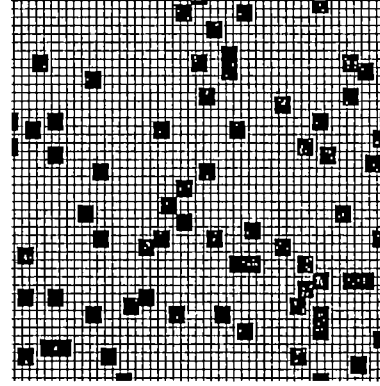


FIG. 2
a porous domain generated randomly with $\epsilon=0.9$

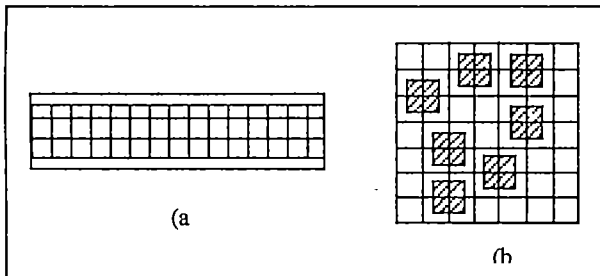


FIG. 1
(a) Uniform grids inside the channel.
(b) Random distribution of solid rods

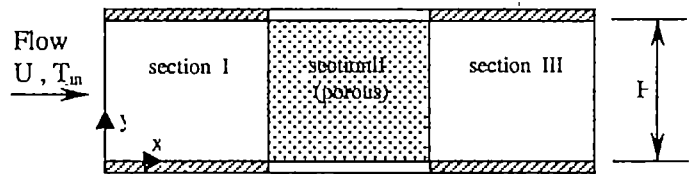


FIG. 3
Schematic of channel geometry

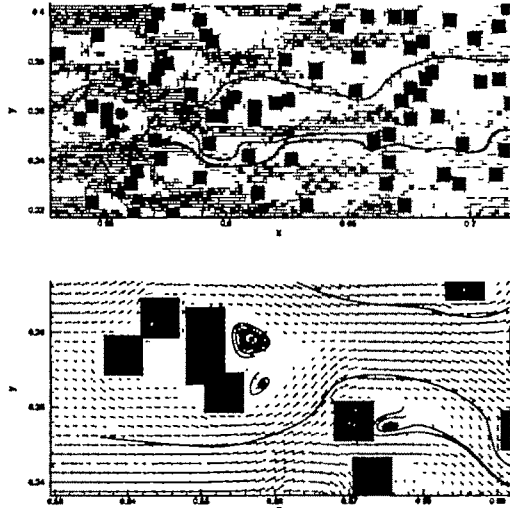


Fig 4- Velocity vectors inside porous domain, $Re_p=100$
each particle contain 4 cells

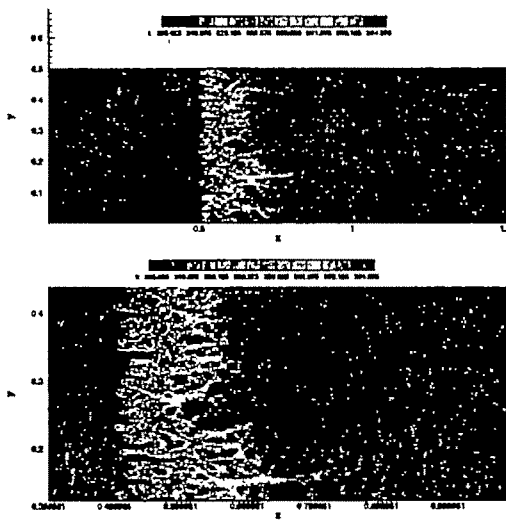
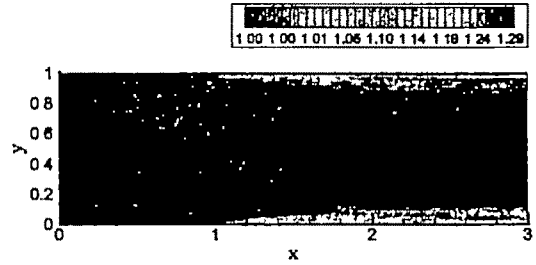


FIG. 5

- (1): Temperature contours in case b , $Re_p=100$, $Pr=0.7$
(2): A zoom of temperature contours in the porous field

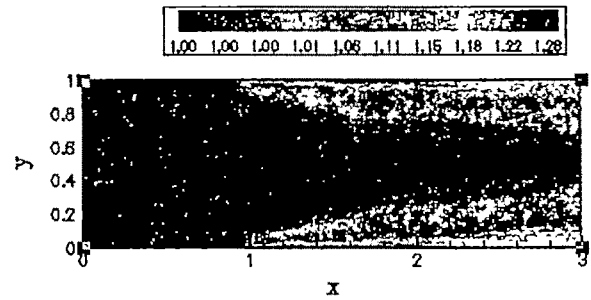


FIG. 6

- Dimensionless temperature field in case a ,
(1) $Re_p=5$, $Pr=0.7$ (2) $Re_p=200$, $Pr=0.7$

Table1- Average Nusselt Number versus Particle Reynolds Number

	cell=1	cell=2	cell=3	cell=4	cell=5	cell=6
Re=10	4.63	5.217	6.92249	6.7059	6	5.873
Re=100	13	19.311	19.3998	19.42	20.06	19.984
Re=400	17.225	19.924	23.537	25.689	27.23	28.788

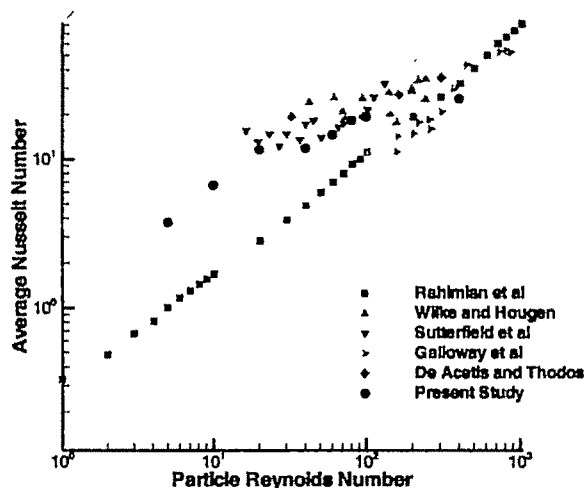


Fig 7- Average Nusselt Number versus Particle Reynolds Number

REFERENCES

- [1] P. Cheng, Heat Transfer in Geothermal Systems, Advances in heat transfer, Vol.14, pp. 1-105 (1979).
- [2] D. Poulikakos, and K. Renken, *ASME J. Heat Transfer*, 109, 880 (1987).
- [3] K.J. Renken, and D. Poulikakos, *Int. J. Heat Mass Transfer*, 31, 1399 (1988).
- [4] F.C. Chou, and W.Y. Lien, Forced Convection in a Parallel Plate Channel Filled with Packed Spheres, *AIChE/ASME Thermo physics and Heat Transfer conference*, HTD-Vol. 139, pp.57-64, ASME, N.Y. (1990).
- [5] V.V. Calmidi, and R.L. Mahajan, *ASME J. Heat Transfer*, 122, 557 (2000).
- [6] P. Cheng, and C.T. Hsu, *Int. J. Heat Mass Transfer*, 29, 1843 (1986).
- [7] A. Eidsath, R.G. Carbonell, S. Whitaker, and L.R. Herman, *Chem. Engng. Sci.*, 38, 1803 (1983).
- [8] O. Coulaud, P. Morel, and J.P. Caltagirone, *J. Fluid Mech.*, 190, 393 (1988).
- [9] A.J. Fowler, and A. Bejan, *Int. J. Heat Fluid Flow*, 15, 90 (1994).
- [10] R.E. Larson, and J.J.L. Higdon, *Physics of Fluids*, A1, 38 (1989).
- [11] F. Kuwahara, A. Nakayama, and H. Koyama, *J. Heat Transfer*, 118, 756 (1996).
- [12] F. Kuwahara, and A. Nakayama, *J. Heat Transfer*, 121, 160 (1999).
- [13] Rahimian M. H., Pourshaghghi A., Direct Simulation of Forced Convection in Parallel Plate Channel Filled with Porous Media, *International Communication of Heat and Mass Transfer*, Vol. 29, No. 6, pp867-878, 2002

Technical Session 6C

Electrical Machines

Damping of Low Frequency Oscillations in Alternators using Neuro Fuzzy Logic Controller

F. Shamila¹, N. Albert Singh², K.A.Muraleedharan³ and K.Gomathy⁴

¹ Research Scholar, University of Kerala, Trivandrum India e-mail: shamisalm@yahoo.com

² Research Scholar, University of Kerala, Trivandrum, India e-mail: albertsingh@rediffmail.com

³ Professor, N. I. College of Engineering, Kumarcoll, TamilNadu, India

⁴ Professor, N. I. College of Engineering, Kumarcoll, TamilNadu, India

Abstract— This paper proposes a novel approach based on Neuro-Fuzzy technique, for the design of an Adaptive Power System Stabilizer (PSS), capable of providing optimal damping characteristics over the entire operating range of synchronous machines in a modern power system. The proposed PSS employs a multilayer network combining the advantages of Artificial Neural Network (ANN) and Fuzzy Logic Control (FLC) schemes. The effectiveness of the proposed Adaptive Neuro-Fuzzy based Power System Stabilizer (ANFPSS) is established by comparing its performance in time domain simulation with that of the conventional PSS.

Key words— Dynamic Stability, Artificial Neural Network (ANN), Fuzzy Logic Control (FLC), Power System Stabilizer (PSS).

I. INTRODUCTION

EXCITATION control is an effective means for enhancing the stability of electric power systems. With the wide spread use of fast-acting high gain excitation systems, the transient stability of a synchronous machine, which is an indication of machine's capability to survive a major disturbance, such as three-phase fault has been significantly improved [1]. However the machine oscillations due to dynamic instability resulting from small disturbances, usually deteriorates with the installation of such excitation systems having fast response and high ceiling voltage [2]. Other major factors that contribute to the dynamic instability are large real power loading of generator or tie line, leading power factor operation of generators and large line reactance. These small frequency oscillations of a system, which is in the range of 0.2-2.5 Hz, are due to the lack of damping of system mechanical mode. The cost effective solution to the problem of oscillatory instability is to provide damping for generator rotor oscillations using Power System Stabilizer (PSS), which are supplementary controllers in the generator excitation system [2].

The conventional PSS employed by the utility is lead-lag stabilizer using the speed as the input [3]. The PSS is useful in compensating the phase lag resulting from voltage regulator, exciter and generator so that a supplementary

damping torque component, which is in phase with rotor speed, is generated. The conventional PSS parameters are determined to ensure the optimal performance at a specific operating point. As power systems are non-linear and also prone to variations in its operating states over a wide range, it becomes necessary for a PSS to adapt situations in real time. Several PSS based on adaptive control techniques have been developed [4,5] and they require model identification in real time, which is a time consuming process.

In recent years fuzzy logic control has emerged as one of the practical solution when the process is too complex and non-linear for analysis by conventional quantitative techniques. However the development of a fuzzy controller has to rely on the experience of the experts for deriving effective fuzzy control rules. Recently there has been an increasing use of artificial neural networks (ANNs) for various applications particularly because of their capability for learning from examples and adaptation.

In the proposed PSS, both the FLC and ANN have been employed together and an Adaptive Neuro-Fuzzy based PSS (ANFPSS) is developed. The generator speed deviation and its derivative are taken as inputs for the controller. The network is trained using the input-output patterns generated through off-line simulation, for various generator-loading conditions. With the property of learning of ANN the fuzzy rules and membership functions of the controller are tuned automatically by the hybrid-learning algorithm. The comparisons of the simulation results of the proposed PSS are done against those with the conventional Power System Stabilizer.

II. SYSTEM MODELLING

For any electric power system dynamic study, a proper mathematical model must be chosen. There are only a limited number of system components important to the dynamic study: the synchronous generator, the governor and the excitation system.

A. Synchronous generator

The three armature phase windings on the stator of the synchronous machine are replaced by two equivalent armature windings, a d-winding on the d-axis and a q-winding on the q-

axis by Park's transformation. The models mainly differ in the number of windings considered along d and q-axis. The third order model [2] represented by the following equations is used for the representation of synchronous generator.

$$\dot{\omega} = 1/M (T_m - T_e - T_d) \quad (1)$$

$$\dot{\delta} = \omega_b (\omega - 1) \quad (2)$$

$$\dot{e}_q = 1/T_{do} [E_{fd} - e_q - (x_d - x'_d)i_d] \quad (3)$$

and the auxiliary equations are

$$T_e \equiv P_e \equiv \frac{e_q V_t}{x_d} \sin \delta + \frac{V_t^2 (x'_d - x_q) \sin 2\delta}{2\pi \lambda_q} \quad (4)$$

$$e'_q = V_t + jx'_d i_d + jx_q * j i_q \quad (5)$$

B. Modeling of Excitation System

The excitation system is considered to be of continuously acting IEEE Type-1 excitation system [3]. The CPSS consists of two phase-lead compensation blocks, a signal washout block, and a gain block. The input signal is the rotor speed deviation $\Delta\omega$ [18]. The block diagram of the CPSS is shown in fig.1

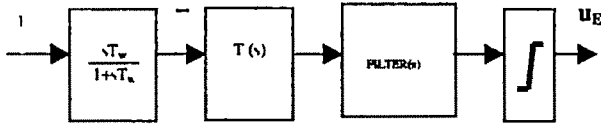


Fig.1 Block Diagram of CPSS

III. ADAPTIVE NEURO-FUZZY PSS

The Adaptive Network Based Fuzzy Logic PSS is designed with two inputs, the generator speed deviation $\Delta\omega$ and its derivative $\Delta\dot{\omega}$, and one control output (u_E). The training data is viewed to be very complex hence seven linguistic variables for each input variable were used to get the desired performance. The linguistic variables are specified by Gaussian membership functions and as a result 49 rules are devised. The rule-base contains the fuzzy IF-THEN rules of sugeno's first order type [7] in which the output of each rule is a linear combination of input variables plus a constant term. The final output is the weighted average of each rule's output. The universe of discourse for the input-output variables is normalized and the gain parameters chosen based on input-output space are $\Delta\omega$ gain=1.0, $\Delta\dot{\omega}$ gain=0.08, u_E gain=0.1

The architecture of the ANFPSS sensing $\Delta\omega$ and $\Delta\dot{\omega}$ is shown in Fig. 2. where node functions in each layer are as described below.

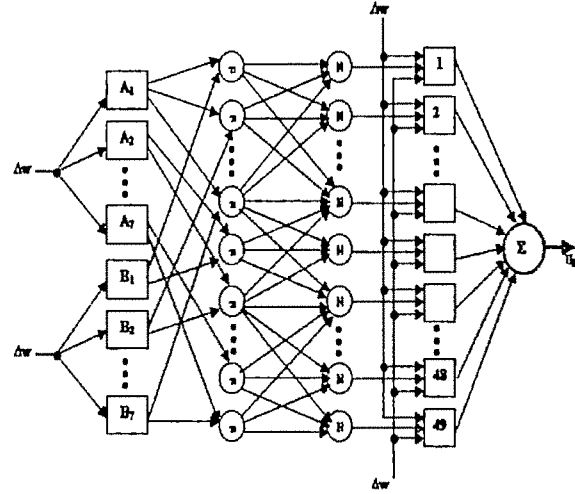


Fig 2. Architecture of ANFPSS

Layer 1:

Each node in this layer is an adaptive node performing Gaussian membership function.

$$o_{1,i} = \mu_{A,i}(x_i) = \exp \left[-\frac{(x_i - c_{ij})^2}{\sigma_j^2} \right] \quad \text{where } i=1, 2, \dots, 7, j=1, 2, \dots, 7$$

x_i is the input to this layer and c_{ij} is the center of the membership function.

Layer 2:

Every node in this layer represents the firing strength of the rule.

$$o_{2,i} = w_i = \mu_{A,i}(x_i) \wedge \mu_{B,i}(y_i) \quad i=1 \dots 7.$$

Eventually the nodes of this layer perform fuzzy AND operation.

Layer 3:

The nodes of this layer calculate the normalized firing strength of each rule.

$$o_{3,i} = \bar{w}_i = \frac{w_i}{\sum w_i} \quad i=1 \dots 49.$$

w_i —firing strength of a rule.

Layer 4:

The nodes in this layer output the weighted consequent part of the rule table.

$$o_{4,i} = \bar{w}_i f_i = \bar{w}_i (p_i x + q_i y + r_i) \quad i=1, \dots, 49$$

where $\{p_i, q_i, r_i\}$ is the parameter set of this node.

Layer 5:

The single node in this layer computes the overall output as the summation of all the incoming signals.

$$O_{5,i} = \sum w_i f_i / \sum w_i \quad i=1 \dots 49.$$

where $O_{5,i}$ denote the output of the 'i'th node in layer

5.

The learning algorithm for the connectionist network structure consists of two separate stages of a learning strategy, which combines unsupervised learning and supervised gradient-descent learning procedure. In phase one a self-organized learning scheme is used to locate initial membership functions and to find the presence of fuzzy logic rules. In phase two a supervised learning scheme is used to optimally adjust the parameters of membership functions for desired output. The back-propagation algorithm is used for the supervised learning. To initiate the learning scheme, training data and the desired or guessed coarse of fuzzy partition (i.e., the size of the term set of each input/output linguistic variable) must be provided from the outside world [6].

The ANFPSS training is done assuming that there is no expert available and the initial values of the membership functions parameters are equally distributed along the universe of discourse and all consequent parts of the rule table set to zero. The ANFPSS starts from zero output and during training it gradually learns the rules and functions as close to the desired controller. Thus during training the network structure update membership functions and rule base parameters according to the gradient descent update procedure.

The ANFPSS was trained by data's created from Power System Stabilizers designed for various operating conditions in which the generator output ranging from 0.2 to 1.0 pu and power factor ranging from 0.85 lead to 0.4 lag. The wide spectrum of possible disturbances used for the training are: reference voltage and infinite bus voltage disturbances in the range of -0.05 pu to 0.05 pu, torque variations from -0.15 pu to 0.15 pu, three phase fault transients, transmission line with different line reactance disturbances, different machine inertia disturbances and one transmission line outage. A total of 2467 input-output data pairs are created for the training of ANFPSS.

IV. TEST SYSTEM & SIMULATION STUDIES

The ANFPSS was designed for a single generating unit connected to a constant voltage bus through two parallel transmission lines. The data related to this system are given in appendix. The nominal operating condition is given by active power=1 pu and pf=0.85 lag.

Load test:

With the generator operating at a power of 0.9 pu and 0.8 pf lag a 0.01 pu step increase in input torque reference was applied at 1s. The disturbance is large enough to cause the system to operate in the non-linear region. System response without PSS and with the CPSS and ANFPSS under these conditions was shown in Fig 3. The system without stabilizer is highly oscillatory. Although the CPSS is effective in damping the oscillations, the ANFPSS settles the oscillations smoothly and quickly.

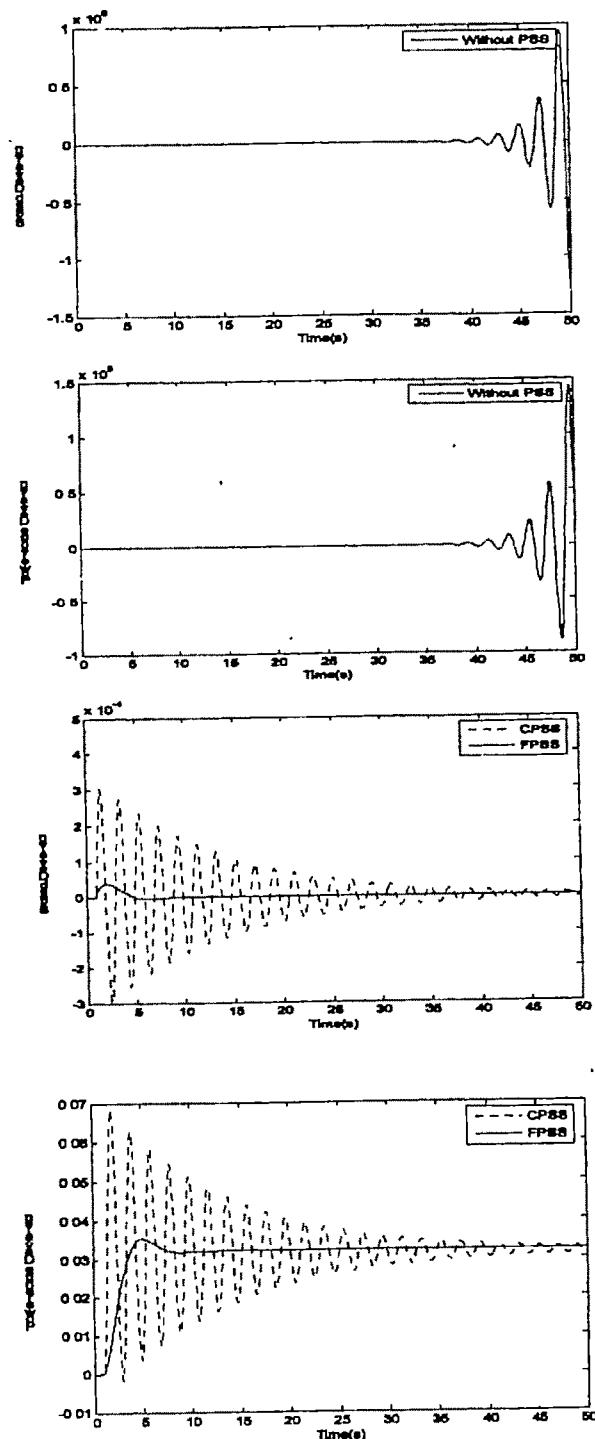


Fig:3 Simulation results for Load Test at a power of 0.9 pu and 0.8 pf lag a 0.01 pu step increase in input torque reference was applied at 1s.

Leading pf Load test:

When the generator is operating at a leading power factor, the situation is much more difficult because the stability margin is reduced. However, in order to absorb the capacitive charging current in a high voltage power system, it may become necessary to operate the generator at a leading power factor. It is therefore desirable that the controller be able to guarantee stable operation of the generator under leading power factor condition.

With the generator operating at a power of 0.4 pu and 0.9 lead, a 0.01 pu step increase in torque reference was applied at 1s. The results given in Fig 4. show that the oscillation of the system is damped out rapidly by the ANFPSS.

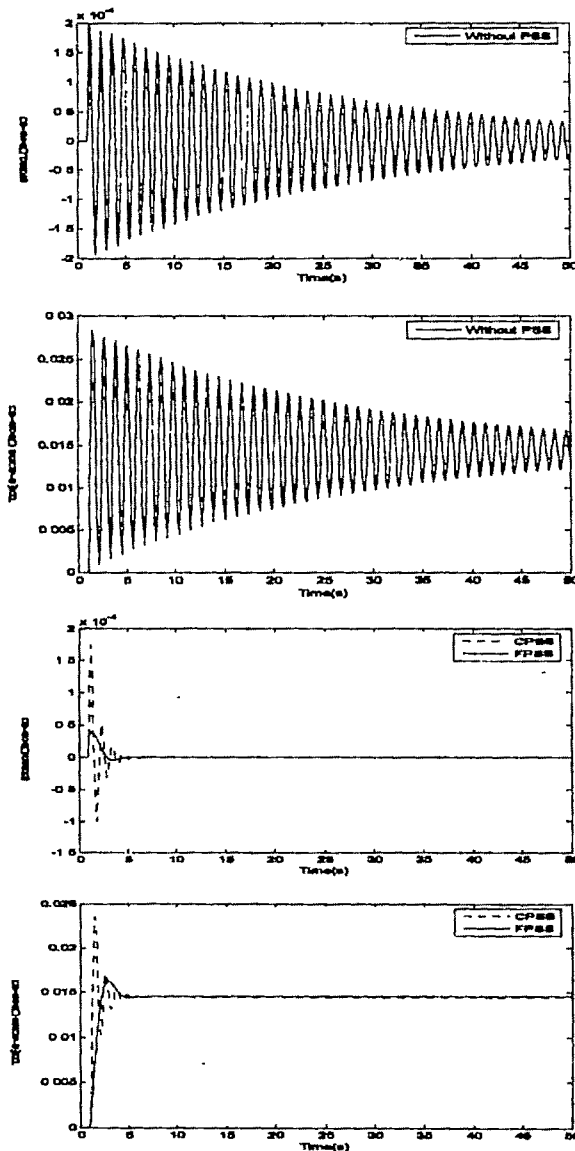


Fig:4 Simulation results for leading pf Load Test at a power of 0.4 pu and 0.9 pf lag a 0.01 pu step increase in input torque reference was applied at 1s.

Switching line Disturbance test:

At an operating point of 0.3 pu power, 0.9 pf lag, one circuit of the double circuit transmission line was switched off at 1s. System response without PSS and with the CPSS and ANFPSS under these conditions was shown in Fig 5. The response with ANFPSS shows less oscillations demonstrating better performance.

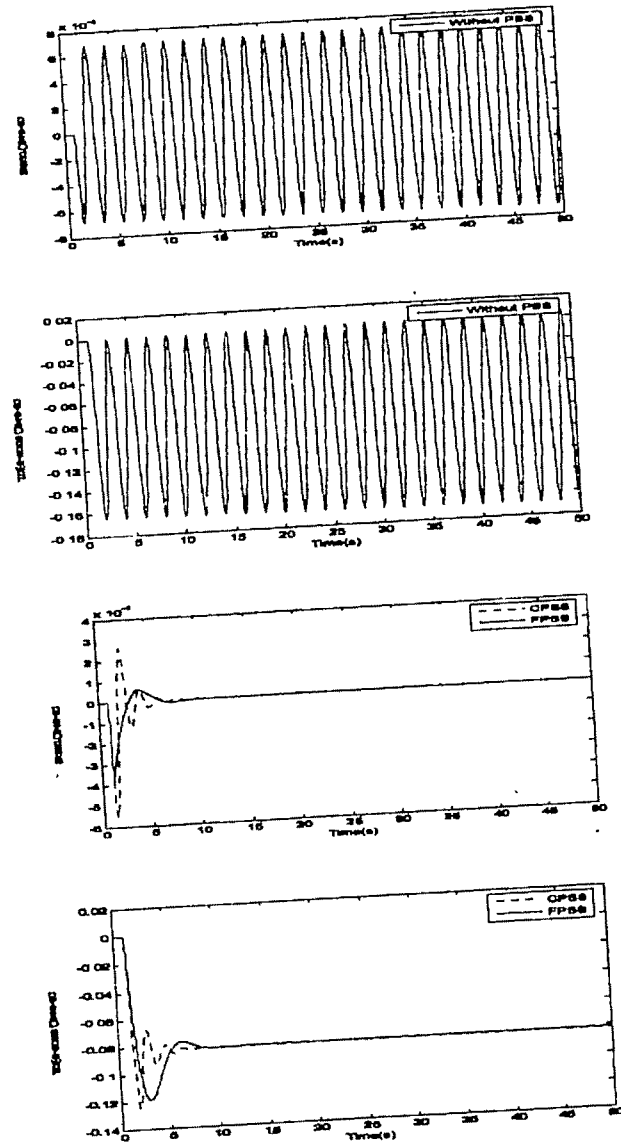


Fig:5 Simulation results for Switching Line disturbance test at a power of 0.3 pu and 0.9 pf lag a 0.02 pu step decrease in input torque reference was applied at 1s.

From these plots, it can be seen that the system becomes stable with the provision of PSS and the oscillations are significantly reduced with the proposed Neuro-Fuzzy based PSS when compared to those with conventional PSS.

V. CONCLUSION

The major contribution of this work has been the application of Neuro-Fuzzy technique in the design of an Adaptive Power System Stabilizer in enhancing the power system damping characteristics for low frequency oscillations. The conclusions drawn from the results of the proposed PSS are

- Lack of online complicated mathematical computations makes it more reliable for real time applications.
- The settling time and the overshoot is greatly reduced compared with conventional PSS.
- The stabilizer is adaptive for various disturbances over a wide range of operating conditions and significantly improves the performance of the system.

APPENDIX

Table .1. Generator Data

(System frequency = 60 Hz, Base MVA=100)

Rated MVA	100
Rated voltage	15 kV
Speed	3600 rpm
R_a	0.001 pu
x_d	0.973 pu
x_d'	0.19 pu
T_{do}'	7.76 s
x_q	1.64 pu
H	4.63 s

Table.2. Excitation system Data

T_R	0 s
T_A	0.05 s
T_E	0.95 s
T_F	1.0 s
K_A	400 pu
K_E	-0.17 pu
K_F	0.025 pu
S_E	0

Table.3. Nominal Load Bus Data.

V_o	1.0 pu
R_c	0.034 pu
X_c	0.997 pu
G	0.242 pu
B	0.262 pu
Active power	1.0 pu
pf	0.85 lag

List of Symbols:

δ	:	Rotor angle.
ω	:	Rotor angular velocity.
E_{fd}	:	Exciter output voltage
M	:	Inertia constant
T_m	:	Mechanical torque
T_e	:	Electrical torque
T_d	:	Damping torque
T_{do}'	:	d-axis open circuit time constant
x_d'	:	d-axis transient reactance
x_d	:	d-axis component of synchronous reactance
x_q	:	q-axis component of synchronous reactance
i_d, i_q	:	d and q axis currents
V_t	:	Generator terminal voltage

REFERENCES

- [1] F.P. Demello and C. Concordia, "Concepts of synchronous machine stability as affected by excitation control", *IEEE Trans. on PAS*, Vol-88, pp.316-329, 1969.
- [2] Y.N.Yu, "Electric Power System Dynamics", *Academic Press, New York*, 1983.
- [3] E.V.Larsen and D.A.Swann, "Applying Power System Stabilizers", *IEEE Trans. on PAS*, Vol.100, pp.3017-3046, 1981.
- [4] Shi-jie Chang, Y.S.Chow, O.P.Malik and G.S.Hope, "An adaptive synchronous machine stabilizer", *IEEE Trans. on PWRs*, Vol.1, pp.101-107, 1986.
- [5] G.P.Chen, O.P.Malik, G.S.Hope, Y.H.Qin, and G.Y.Xu "An adaptive PSS based on the self-optimizing pole shifting control strategy", *IEEE Trans. on Energy Conversion*, Vol.8, pp.639-645, 1993.
- [6] C.T.Lin, C.S.George Lee, "Neural-Network Based Fuzzy Logic Control and Decision system", *IEEE Trans.on Computers*, Vol.40, pp 1320-1336, 1991.
- [7] Sreerama Kumar, R, Rajendran.N, Sunitha.R, Gajendran.F, "On-line tuning of conventional power system stabilizer using Neural Network", *Proceedings of the Int. AMSE Conf.on System Simulation and Communication-CMSC'99*, India, Dec.'99.
- [8] Ned Gulley, J.S.R.Jang, "Fuzzy Logic Tool Box for use with MATLAB, User's Guide", *The MATH WORKS Inc*, Jan.1995.
- [9] Albert Singh.N, "Neuro-Fuzzy Logic Based Power System Stabilizer Design", *M.Tech. Thesis, Dept.of Electrical Engg.College of Engg., Thiruvananthapuram, University of Kerala*, India, April-2000.
- [10] Sreerama Kumar, R, Rajendran.N, Sunitha.R, Gajendran.F, "Power System Stabilizer Design: Recent Developments and future trends", *Third National seminar on modern trends in Power Engg. And development*.Aug.1998, pp.40-44.
- [11] K.A.El-Metwally and O.P.Malik, "Fuzzy Logic Power System Stabilizer", *IEE proc. Generation Transmission and Distribution*, Vol.142, No.3, pp.277-281, May 1995.

Simulation of an Adjustable Speed Synchronous Motor fed from Sinusoidal Currents

Soumya Ray¹, Kaushik Mukherjee², Nikhil Mondal¹ and Sujit K. Biswas¹

¹ Dept. of Electrical Engg., Jadavpur University, Kolkata, India, e-mail : sujit_biswas@hotmail.com

² Dept. of Electrical Engg., Bengal Engg & Science Univ, Howrah, India

Abstract—Three phase synchronous motors conventionally run at the fixed synchronous speed when supplied from a voltage source. However, different methods are available for controlling synchronous motor speed through position feedback. Most of these methods feed rectangular wave currents into the synchronous machine. In this paper a simulation study has been implemented on an adjustable speed, current controlled, auto synchronized synchronous motor, which is fed from sinusoidal currents.

Key words—Synchronous motor drive, Sinusoidal current source, variable speed drive.

I. INTRODUCTION

SOURCING sinusoidal current from an inverter is difficult, especially when the load is a high inductance synchronous motor. Drives, which are used for synchronous motor (SM) speed control, are broadly of two types. One is simple variable voltage, variable frequency type and the other is auto-synchronized type, where actual motor speed dictates the motor input frequency. The second type of drive application makes synchronous motor self-starting.

Current fed drives for auto-synchronized operation of synchronous motor usually controls inverter switching on the basis of instantaneous rotor position of the motor and as a result, the current flowing through the SM stator becomes rectangular wave.

In this paper simulation studies have been conducted on a particular drive scheme where auto-synchronized approach is taken, but switching of inverter is done on the basis of a current feedback technique, so that motor can be fed from sinusoidal currents. Fig.1 shows a block diagram of the proposed scheme.

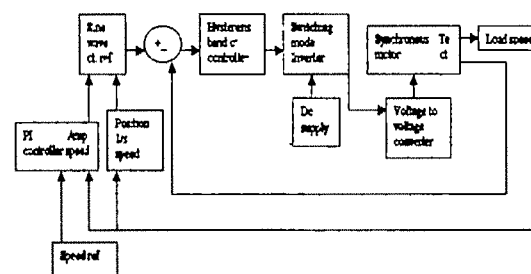


Fig.1: Block diagram of sinusoidal current controlled, auto synchronized, adjustable speed synchronous motor drive.

From fig.1 it can be seen that switching of the inverter is carried out on the basis of a comparison between a reference current and actual stator current. The reference current is an outcome derived from both rotor speed and rotor position.

The technique used in this case for making current sinusoidal is Hysteresis Band PWM. Hysteresis Band PWM is a current feedback technique and in this case, the actual current follows a pre-decided reference current closely. Hysteresis Band current control technique has its own limitations but it can be overcome if used properly and cautiously & obviously it has its own reward as current waveform obtained from this technique is best and very close to the desired sinusoidal shape.

Block diagram shown in fig.1 depicts the operation of the scheme proposed in this paper. As previously stated, current flowing through the motor stator closely follows a reference current which is made sinusoidal in this case. Instantaneous position of rotor dictates the instantaneous magnitude of reference current. Synchronous motor is self-started here and its rotor position as well as speed is used as a feed back. As a result of this, the frequency of reference current varies from zero to a final value. The user decides the final rotational speed of the system which is given as a reference input to the system. Error between actual instantaneous rotor speed and reference speed is processed by a PI-controller and output of the controller is the amplitude of the reference current.

II. HYSTERESIS BAND CURRENT CONTROL PWM

Hysteresis Band Current Control PWM technique is a simple but effective, straightforward switching technique, which uses instantaneous current feedback for the switching logic.

In Hysteresis Band Current Control, the inverter output current is compared with a current reference of desired amplitude & frequency. The difference between instantaneous amplitude of actual & desired current waves is considered as current error. Hysteresis Band control logic compares this current error with a pre-decided hysteresis error band or tolerance band & controls the switching operations of the inverter accordingly. When the output current of the inverter goes below the tolerance limit from the reference current, the upper switch of the inverter is switched on & the load of inverter finds itself connected with $+0.5V_{dc}$ bus. In opposite condition, when the error goes above the upper tolerance band, the hysteresis controller switches the lower switch of the inverter and it connects the load with $-0.5V_{dc}$ bus from the input side.

Thus, the actual output current fluctuates within an error band around the reference current and can be expressed as the superimposition of reference current and a high frequency ripple current with peak to peak magnitude equal to the tolerance band or hysteresis band.

The slope of the ripple current (i.e. di/dt) can be found from the following equations.

When the load is connected with $+0.5V_{dc}$ bus,

$$\frac{di}{dt} = [0.5V_{dc} - V_{cm} \sin \omega t] / L \quad (1)$$

When the load is connected with $-0.5V_{dc}$ bus,

$$\frac{di}{dt} = -[0.5V_{dc} + V_{cm} \sin \omega t] / L \quad (2)$$

where, $V_{cm} \sin \omega t$ is the instantaneous magnitude of the load counter emf and L is the load inductance.

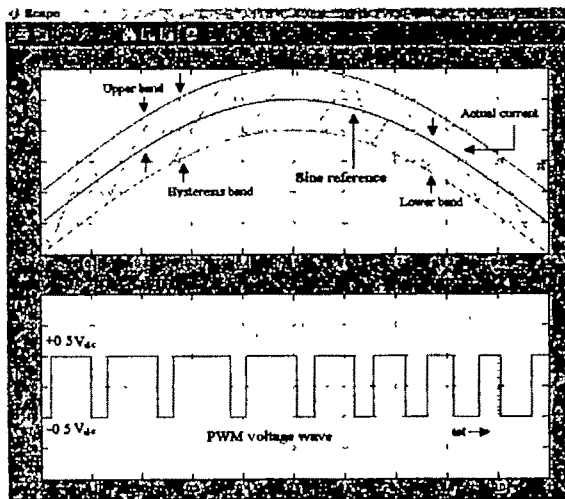


Fig. 2: Principle of hysteresis band current control

Fig.2 shows the above discussion in a visual form and also shows how switching sequence by a hysteresis band controller results in a PWM voltage output from the switch mode inverter. It is clear from the above discussion that if ripple portion of the actual current output is to be reduced, then a near-sinusoidal current waveform will be achievable and that can be done by reducing the hysteresis error band.

As the reference current is tracked forcefully by the output, the actual current hysteresis band actually makes the current controlled switch mode voltage source inverter (VSI) behave as a current source eventually.

In an ideal condition, a hysteresis band controller controls a half bridge inverter (i.e. one inverter leg for one phase) containing two switch-diode pair in series. By controlling the switching instants, the inverter just connects the input bus voltage of any one of the two voltage sources ($+0.5V_{dc}$ or $-0.5V_{dc}$) to the output side load and the single leg inverter mid point potential depends only on upper or lower switch-diode block, which ever is conducting, in an ideal situation (considering zero switch drop). In an ideal condition, only one switch of an inverter leg remains ON, so blanking time is not considered for making the logic. In MATLAB a hysteresis control block is made with a consideration that if output of the logic block is '1' then upper switch will be on, resulting in $+0.5V_{dc}$ at output and '0' will allow $-0.5V_{dc}$ to go out. Fig.3 shows the corresponding MATLAB simulation block. Dead Zone shown in the fig.3 actually contains the hysteresis band magnitude.

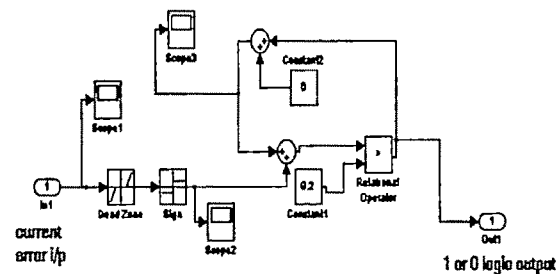


Fig. 3: Hysteresis band logic control

Performance of this control logic is shown in fig.4b with the help of a three phase R-L circuit and the following simulation model data.

$R = 5.5\Omega$, $L = 0.09H$, $A = \text{ref. current magnitude} = 2$, ref. frequency = 20Hz, hysteresis band = $+0.0003A$ to $-0.0003A$, dc voltage = $+280\text{Volts}$ & -280Volts , Fixed step size = 0.0001.

If voltage applied to a R-L circuit is known, then it can be mathematically represented by a differential equation

$$V = iR + L \frac{di}{dt} \text{ or } i = (1/L) \int [V - iR] dt \quad (3)$$

and can be used as a mathematical model for simulation.

Now, for three-phase system three leg inverters are used in normal situation, where the inverter output is never balanced at a given point of time, as the output of a leg could only be $+0.5V_{dc}$ or $-0.5V_{dc}$. To overcome this situation a voltage-to-voltage converter block is required. MATLAB simulation model and the content of the voltage-to-voltage converter block are shown in fig.4a.

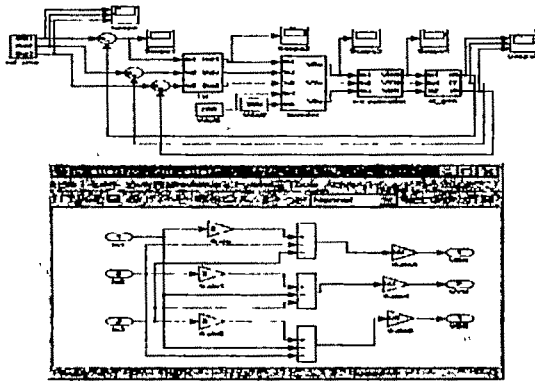


Fig. 4a: Simulation model of three-phase inverter driving three-phase load

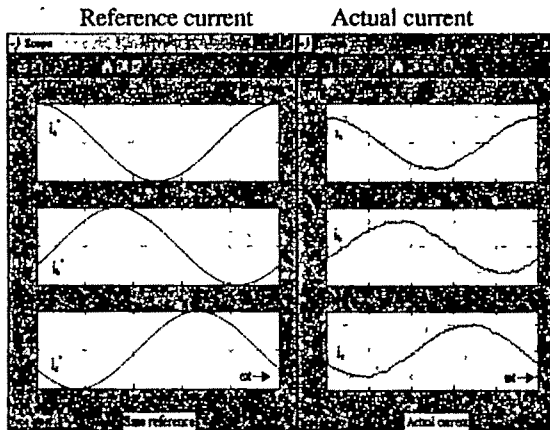


Fig.4b: Reference current & actual current (both y-axis) for three phase R-L load with respect to time (x-axis)

III. SIMULATION MODEL OF SYNCHRONOUS MOTOR

Analysis of synchronous machine can be done easily with the help of its equivalent circuit. As synchronous machines are of two types : one with salient pole rotor and the other with non-salient type, d-q axis equivalent circuit is required for representation of both the types.

From well-known work of R. H. Park in 1920s, the method of referring three-phase stator variable (of synchronous motor) to a reference frame fixed at rotor (i.e. frame rotating at synchronous speed) is well known. Here, Park's

transformation equations are used for referring stator variables to its corresponding d-q frame and extract the output information back.

Fig.5 shows the d-q axis equivalent circuit of synchronous motor with damper windings.

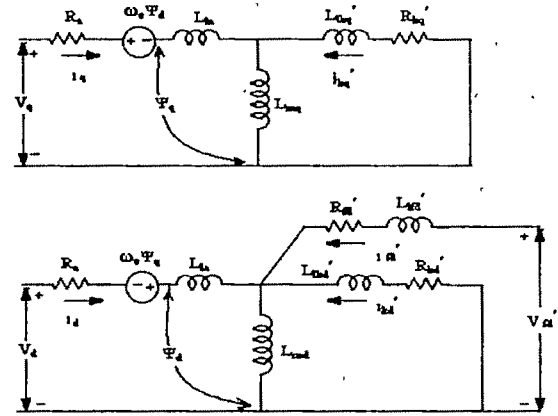


Fig. 5: Equivalent circuit of synchronous motor in d-q axis frame

where

i_d = d-axis current

i_q = q-axis current

i_{fd} = rotor field current refer to stator

i_{kd} = d-axis damper winding current refer to stator

i_{kq} = q-axis damper winding current refer to stator

V_d = d-axis voltage

V_q = q-axis voltage

V_{fd} = rotor field voltage refer to stator

R_a = per phase stator resistance

R_{fd} = rotor field resistance refer to stator

R_{kd} = d-axis damper winding resistance refer to stator

R_{kq} = q-axis damper winding resistance refer to stator

L_{la} = per phase stator leakage reactance

L_{md} = d-axis magnetizing reactance

L_{mq} = q-axis magnetizing reactance

L_{fd} = rotor field resistance refer to stator

L_{kd} = d-axis damper winding resistance refer to stator

L_{kq} = q-axis damper winding leakage reactance refer to stator

Ψ_d = d-axis flux linkage

$\Psi_d = [L_{la}i_d + L_{md}(i_{fd} + i_{kd} + i_d)]$

Ψ_q = q-axis flux linkage

$\Psi_q = [L_{la}i_q + L_{mq}(i_q + i_{kq})]$

ω_e = synchronous speed

($\omega_e \Psi_d$ & $\omega_e \Psi_q$ are speed voltages)

The above equivalent circuit is drawn from stator side, with the rotor variables referred to stator side. The variable

substitutions are shown below.

$$i_r' = (2/3)(N_r/N_s)i_r \quad (4)$$

$$V_r' = (N_s/N_r)V_r \quad (5)$$

$$\Psi_r' = (N_s/N_r)\Psi_r \quad (6)$$

Subscript 'r' refers to rotor. N_s represent the number of turns for stator windings (per phase) and N_r is the number of rotor turns (per phase) related to the respective variable. For example N_{fd} is number of rotor turns of field winding where as N_{kq} is number of rotor turn of q-axis damper winding.

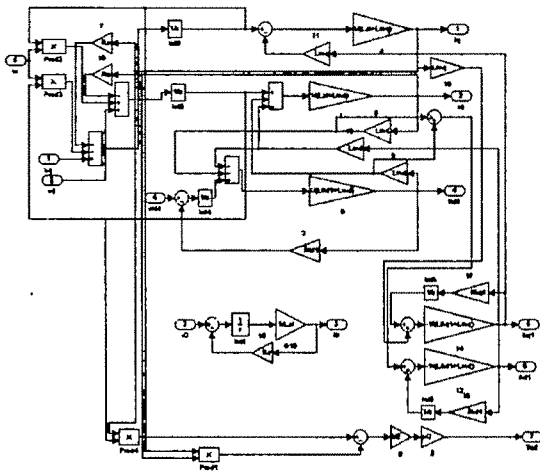


Fig. 6a: Simulation model of synchronous motor in d-q frame with damper winding

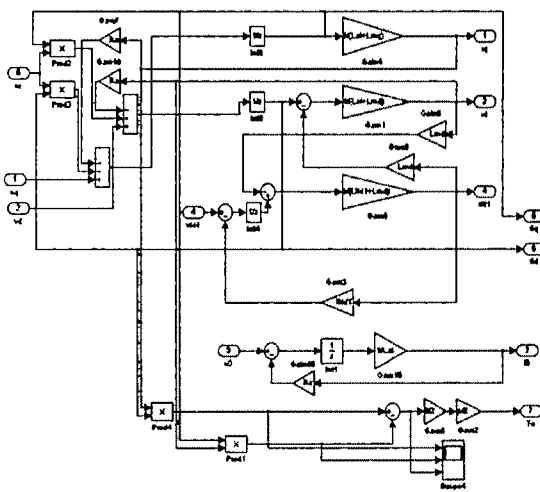


Fig. 6b: Simulation model of synchronous motor in d-q frame without damper winding

From the equivalent circuit shown in fig.5, several equations are derived. With the help of these equations, a simulation model of synchronous motor is made with damper windings (shown in Fig.6a); however as the system runs in auto synchronous mode, damper windings are not required, so a new simpler model is developed and it is shown in fig.6b.

IV. AUTO-SYNCHRONISED SINE WAVE REFERENCE GENERATION

Torque equation of synchronous machines in qd0 frame is given below [1]:

Torque developed is given as :

$$T_e = (3/2)(p/2)*[\Psi_d i_q - \Psi_q i_d] \quad (7)$$

Though electromagnetic torque developed is obtained here through qd0 frame but its magnitude is independent of frame. For simulation, both rotational speed and rotor instantaneous position are derived from mathematical equations and these equations are given below.

$$T_e = T_L + J \frac{d}{dt} \omega_m + f \omega_m \quad (8)$$

where

T_e = Electromagnetic torque

ω_m = Rotational speed

T_L = ω_m independent load torque

J = Moment of inertia of machine & load

f = Proportionality constant for ω dependent load

By integrating angular velocity ω_m , rotor angular position θ_m can be derived

$$\theta_m = \omega_m / s \quad (9)$$

There are only two parameter by which a sine wave can be defined : amplitude and absolute electrical angular position ($\theta_e = \theta_m p/2$). The main consideration of the reference frame used in this paper is that the electrical angular displacement θ_e of a-phase axis is measured from the rotor q-axis & θ_e at time zero is always considered as zero. In the models reference current waves are taken in abc-phase sequence and the current equations are given below.

$$i_a^* = A \cos \theta_e, i_b^* = A \cos(\theta_e - 2\pi/3) \text{ \& } i_c^* = A \cos(\theta_e + 2\pi/3) \quad (10)$$

With a pre-decided current amplitude, an actual synchronous motor data and with the help of equations discussed above, the performance of hysteresis band current controlled drive is tested and its result is shown in fig.7.

Synchronous motor data:

Rating: 3phase, Y-connected, 4-pole, 400Volts, 2.17A, 50Hz, 1.2 Kw, $\cos\Phi = 0.8$, 1500 rpm.

Field Rating: salient pole, 85V, 1.6A, $N_r / N_s = 14.6$, so $V_{fd}' = 85/14.6$

Parameters: $R_a = 5.5\Omega$, $L_{la} = 0.01639H$, $L_{md} = 0.08228H$, $L_{mq} = 0.0477H$, $L_{kld} = 0.06226H$, $L_{kq} = 0.05296H$, $R_{kd} = 16\Omega$, $R_{kq} = 4.167\Omega$, $L_{fd} = 0.01H$, $R_{fd} = 0.3096\Omega$, $J = 0.0581\text{kgm}^2$, $f = 0.00963\text{Nm-s/rad}$ (no load), $T_L = 0.006\text{N-m}$.

Specification for simulation is given below:

Solver option: fixed step, ode4 (Runge-Kutta), Fixed step size: 0.000005, simulation time = 0 to 2.5 sec, hysteresis current band: 0.00005A, dc voltage for inverter: +400V & -400V.

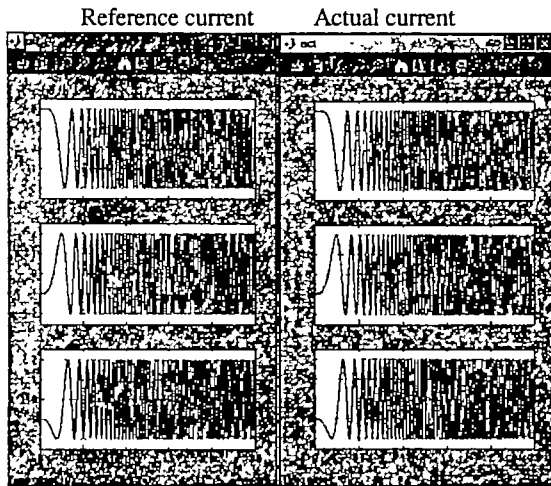


Fig. 7: Auto-synchronized reference current (y-axis) & actual stator current (y-axis) Vs time(x-axis)

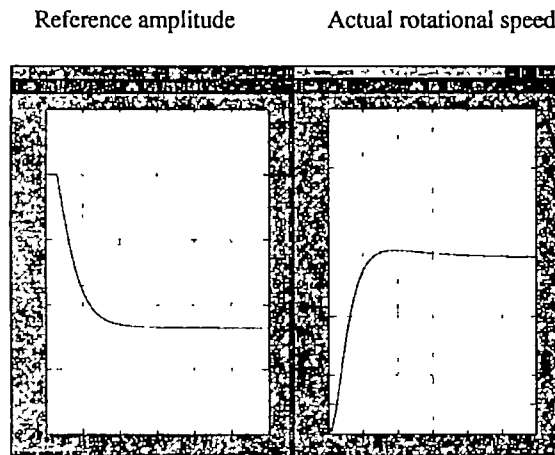


Fig.8: For actual machine simulation, PI controller o/p 'Amp' & actual speed o/p Wm-act (both along y-axis) vs. time (x-axis) for $W_{\text{ref}} = 120 \text{ rad/sec}$ & $f = 0.06 \text{ Nm-s/rad}$

V. SIMULATION RESULTS FOR SPEED CONTROL APPLICATIONS

To achieve the control over the final speed output of the system, the authors have designed a PI controller for a specific

speed range of 160rad/sec (close to 50 Hz electrical) & 94rad/sec (close to 30 Hz electrical). If the controller is considered in form of $K_p*(1+1/sTi)$ then value of K_p is 0.03366 and Ti is 1.0932sec.

One simulation result is shown in this paper (fig.8). The simulation parameters are given below

Solver option: fixed step, ode4 (Runge-Kutta),

Fixed step size = 0.00002, simulation time = 0 to 6 sec,

Other simulation conditions: Voltage i/p = +600V & -600V, Hysteresis current error band = 0.00001A

Speed reference setting: 120 rad/sec.

Proportionality constant for ω_m independent load,

$f = 0.06 \text{ Nm-s/rad}$

VI. CONCLUSION

The simulation study on a sinusoidal current controlled synchronous motor drive has been presented in this paper. The method of rotor position as well as speed feedback has been used to make the scheme self-starting and respond to variable speed commands. This is in contrast to conventional techniques using rectangular current fed synchronous motor drives.

REFERENCES

- [1] Paul C. Krause, 'Analysis of Electrical Machinery', 1986
- [2] Bimal K., Bose, 'Modern Power Electronics & AC Drives', 2002
- [3] Mohan, Undeland & Robbins, 'Power Electronics', 2006
- [4] P. S. Bimbhra, 'Electrical Machinery', 2002
- [5] T. Kenjo & S. Nagamori, 'Permanent-Magnet & Brushless DC Motor', 1985
- [6] L. J. Nagrath & M. Gopal, 'Control System engineering', 2001
- [7] D Roy Choudhury, 'Networks & Systems', 2000

The Superiority of Interleaved Windings in a 25kA Current Injection Transformer

S. M. Pedramrazi and H. Heydari

Iran University of Science and Technology, Electrical Engineering Department
Center of Excellence for Power System Automation and Operation
m_pedram_razi@yahoo.com, heydari@iust.ac.ir

Abstract—The electromagnetic forces, leakage inductances and leakage fluxes are the important parameters to design a high current transformer, so we satisfy to decrease the up parameters in a high current transformer. The leakage flux and other parameters are depending on windings form and because of the interleaved windings form; the pointed parameters will decrease in this form windings. The comparison of important pointed parameters values in the simple concentric form and interleaved form show the advantage of interleaved windings. We use the ansys 8.1 software to get results. The simulation results confirm the interleaved windings advantage.

Key words— Current Injection Transformer (CIT), Leakage Reactance, Leakage Flux, Interleaved windings, Electromagnetic Forces and Finite Element Method.

I. INTRODUCTION

As an electrical utility you have the right to demand that every piece of power equipment installed on your system meets your exact specifications. The reliability and safety of your system depend on all of the components performing as intended. As a manufacturer, the performance and conformance to industry standards of your product are of prime importance. Testing can assure that your product meets or exceeds performance standards. The 25kA CIT is used as a current source [1]. The secondary voltage of this CIT because of type of application is 5V and so the secondary voltage drop is an important design parameter in this CIT. Since the voltage drop is depend on resistance of conductor and leakage inductance, and the resistance in front of leakage inductance is negligible, the value of leakage inductance is a important parameter to design. Leakage inductance is drivable from leakage flux [2, 3]. Various methods have been employed in the past for determining the actual leakage flux distribution, or good approximations to it [4]. Analog methods, for

example, have many desirable virtues, but tend to be of low accuracy and high cost in engineering man hours. For a number of years, Roth's method or one of its many variants has been found adequate for estimating leakage inductance; its drawbacks lie in slow convergence of the Fourier series and in its virtual inability to handle asymmetric problems [5, 6]. In the decade of the 1960s finite difference methods were widely employed. These techniques are capable of dealing with essentially arbitrary geometries with good accuracy, even though computing times occasionally tend to be slow, as a result of the large number of Neumann boundary conditions normally encountered in transformer leakage studies [6]. Their use has probably also been hindered somewhat by the difficulty of producing computer programs which will furnish good results in the hands of appropriate branches of numerical analysis. Now a day the accuracy of the finite element methods is confirmed, and is an appropriate method to field analysis. A much more convenient and efficient method is the incremental energy method, IEM [7, 8, 9]. In fact, energy is the most accurate single quantity provided by the finite element method, FEM [10].

In this paper the comparison between interleaved windings and simple concentric windings is done, and the simulation results on electromagnetic forces, leakage flux and leakage inductance in two cases is investigated and at last the advantage of interleaved windings is confirmed.

II. TRANSFORMER GEOMETRY

A. Design Parameters of the Transformer

We design a 125 kVA single-phase shell type transformer to investigate leakage inductances, leakage flux and electromagnetic forces in two different windings form. The first is simple concentric windings and second is interleaved windings.

Table 1. Design Parameters Of The Transformer

Ratings	Capacity Voltage Current Frequency Phase	125kVA 400/5V 312.5/25000A 50Hz Single-phase
Core	Materials Nominal Flux Density Pure Cross section	M5 Sheets 1.6T 14100mm ²
Windings	Material Cross Section Critical Current Density V/N	Copper 3.2mm×22mm 2.25A/mm ² 5:0V

In the interleaved form the secondary winding is among two divided part of primary winding. In the simple concentric form, first, the primary winding is wound around central leg of core and secondary winding is wound around primary winding. The secondary voltage is 5V and primary voltage is 400V. The main parameters of the transformer are shown in Table 1.

B. Transformer Geometry

The core geometry in the Single-phase CIT transformer is shell type. The top and bottom yokes cross section are only 1/2 of that of the wound limb. The primary and secondary windings have 80 turns and 1 turn, respectively. The primary and secondary windings can be wrapped either concentrically or adjacently to each other around core. However, if the primary and secondary windings are located adjacently to each other, the window height increases nearly double that of the concentric structure. The window height is far too large compared with the window width. As a result, we only consider the concentric situation.

III. LEAKAGE FLUX, LEAKAGE INDUCTANCE & ELECTROMAGNETIC FORCES FORMULATION

A. Leakage Flux Formulation

The flux density B has the components:

$$B_r = -\frac{\partial A}{\partial z} \quad (1)$$

$$B_z = \frac{A}{r} + \frac{\partial A}{\partial r} \quad (2)$$

A is the magnetic vector potential; r and z are radial and axial directions respectively.

The section in which the magnetic field is to be calculated is divided up into small triangular elements. Within one element, the vector potential A is considered to vary linearly.

$$A = \alpha_1 + \alpha_2 r + \alpha_3 z \quad (3)$$

This is equivalent to a constant radial component of flux density within the element.

$$B_r = -\frac{\partial A}{\partial z} = -\alpha_3 \quad (4)$$

However, the axial component varies with the location.

$$B_z = \frac{A}{r} + \frac{\partial A}{\partial r} = \frac{A}{r} + \alpha_2 \quad (5)$$

But in the numerical solution, the triangles are made small enough, so that the axial component B_z at the centroid can be taken as representative for the triangle as a whole.

$$B_z = \frac{A_c}{r_c} + \alpha_2 \quad (6)$$

Because of the linear variation within the element, the vector potential A_c at the centroid is the average of the values at the three vertices.

$$A_c = \frac{1}{3}(A_l + A_m + A_n) \quad (7)$$

Total flux density:

$$B = \sqrt{B_r^2 + B_z^2} \quad (8)$$

From (4), (6) and (8):

$$B = \sqrt{\alpha_2^2 + \alpha_3^2 + \frac{2\alpha_2}{r_c} A_c + \left(\frac{A_c}{r_c}\right)^2} \quad (9)$$

Equation (3) written for each of the three vertices produces three equations, which are solved with respect to the two coefficients α_2 and α_3 (α_1 is not needed).

$$\alpha_2 = \frac{1}{D} [A_l(z_m - z_n) + A_m(z_n - z_l) + A_n(z_l - z_m)] \quad (10)$$

$$\alpha_3 = \frac{1}{D} [A_l(r_n - r_m) + A_m(r_l - r_n) + A_n(r_m - r_l)] \quad (11)$$

where

$$D = (r_m z_n - r_n z_m) + (r_n z_l - r_l z_n) + (r_l z_m - r_m z_l) \quad (12)$$

If l, m and n are assigned in a counter clockwise direction, D is positive, and equal to twice the area of the triangle.

B. Leakage Inductance Formulation

It is assumed that the transformer operates in a two winding connection. This implies that all winding segments carrying negative direction current are connected in series, and that all winding segments carrying positive direction current are connected in series.

The ampere/turns are balanced, and the rating is same for both windings,

$$VA = \sum VA_+ \quad (13)$$

Where the plus sign indicates positive direction current.

The leakage inductance can be calculated from the total magnetic energy, evaluated at peak current:

$$W = \frac{1}{2} L I_{\max}^2 \quad (14)$$

$$X_\Omega = \omega L = \frac{2\omega W}{I_{\max}^2} = \frac{4\pi f W}{I_{\max}^2} \quad (15)$$

In per unit:

$$X_{pu} = x_{\Omega} \frac{I_{rms}}{U} = x_{\Omega} \frac{I_{rms}^2}{VA} = x_{\Omega} \frac{I_{max}^2}{2VA} \quad (16)$$

The magnetic energy can be calculated from the product of current density and vector potential integrated over the volume:

$$W = \frac{1}{2} \iiint J A dv \quad (17)$$

The triple integral is course evaluated numerically:

$$W = \frac{\pi}{2} \sum J A_c r_c D \quad (18)$$

Only those triangular elements belonging to current carrying windings contribute to this sum.

From (4), (3) and (6):

$$x_{pu} = \frac{\pi^2 f}{VA} \sum J A_c r_c D \quad (19)$$

C. Electromagnetic Force Formulation

Electromagnetic forces are calculated as flux density time's density times length times current.

$$F = BLI \quad (20)$$

Because of radial and axial field directions, the forces are divided to two radial and axial components. Radial force due to axial flux tends to separate the two windings. Axial force due to radial flux tends to compress the windings.

The total radial forces give tensile stresses in the outer winding, compressive and bending stresses in the inner winding. Bending stresses can be reduced by increasing the number of axial spacers between the core leg and the winding.

The maximum axial force per unit volume occurs at the winding end. It tends to bend individual disks axially between radial spacers. Axial forces build up down through the winding.

IV. LEAKAGE FLUX AND INDUCTANCE & ELECTROMAGNETIC FORCES

A. Leakage Flux Simulation

In this section, the leakage flux path on windings area is simulated in two different windings Form. In second case the windings form is interleaved and first case is simple concentric windings. Fig.1 shows flux path on primary and secondary windings area in first case. The numbers of elements in this case are 29928 and the numbers of nodes are 59897. The number of element on windings area because of much more variations on field in these areas is more then other areas.

As shown in Fig.1 the flux path in primary and secondary windings are symmetric and the radial fluxes directions are opposite. In this case the total flux density on primary and secondary windings is the same and in same directions. Because of opposite current densities in primary and secondary windings the force directions which apply to windings are in opposite directions. So the primary winding compress to core and secondary winding move to outer direction.

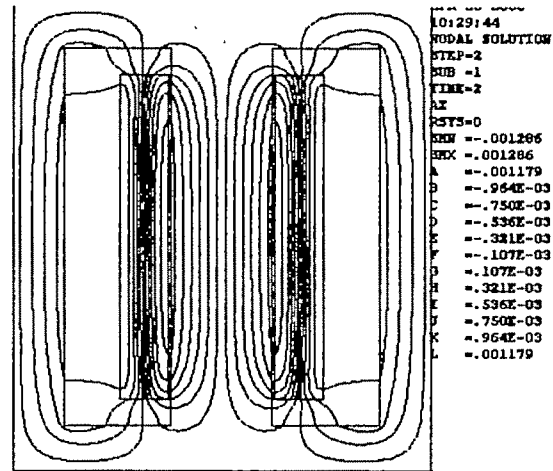


Fig.1. Stray Field in Transformer Windings (case1)

Fig.2 shows the flux leakage in the second case. In this case the windings form is interleaved. The numbers of elements in this case are 28712 and the numbers of nodes are 57283. The number of element on windings area because of much more variations on field in these areas is more then other areas.

In the interleaved windings the leakage flux which results from two part of primary winding on secondary winding are in opposite directions. So the total flux in secondary winding is negligible. In this case the flux directions in two part of primary winding are opposite but the current densities in two winding part has same direction, so the part which is near to core compress to core and other part move to outer direction. The Fig.3 shows the maximum and minimum flux densities on transformer windings in the first case.

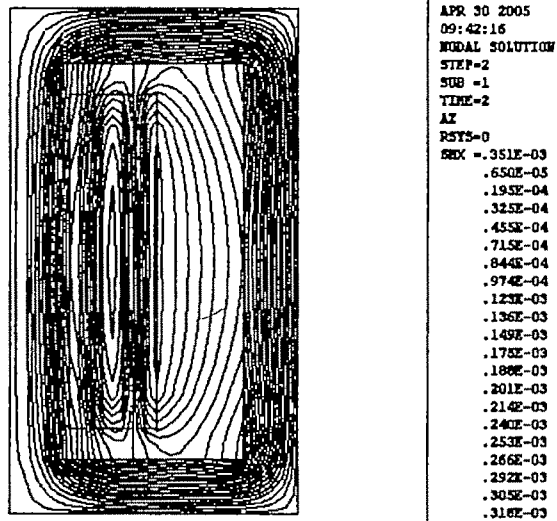
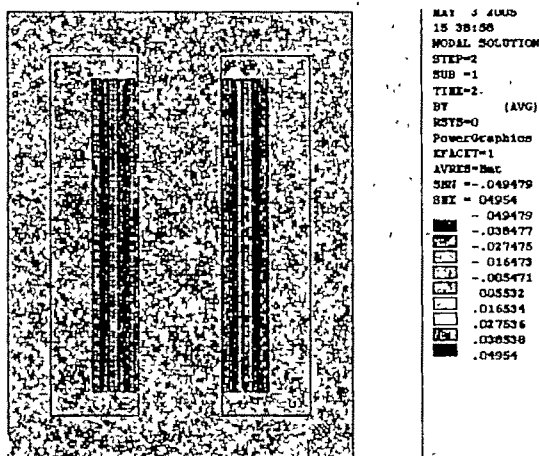
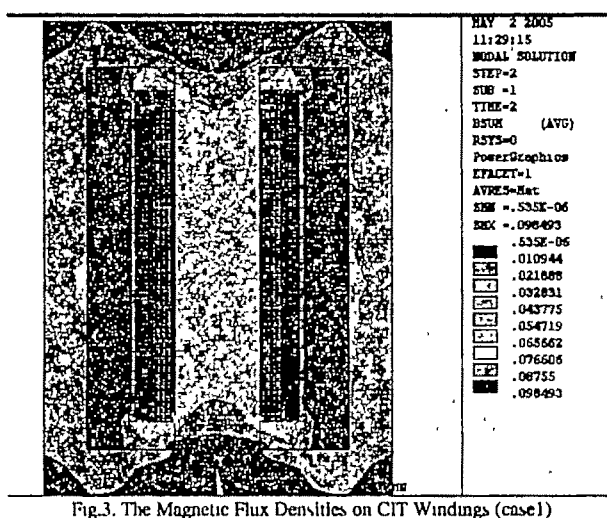


Fig.2. Stray Field in Transformer Windings (case2)

Fig.4 shows the maximum and minimum flux densities on transformer windings in the second case. As shown in the Fig.4 the leakage flux densities on secondary winding are in the opposite direction, so their effects on secondary windings are negligible.



The Table.2 shows the maximum and minimum leakage flux densities on CIT windings in two mention case.

Table.2. The Minimum & Maximum Flux Density In Windings Area (In Two Case)

type	Flux density	
	max	min
First Case	0.096T	0.000000535T
Second Case	0.049T	-0.049T

The comparison between two cases shows that the maximum flux density in the interleaved windings is reduced about %50.

B. Energy & Leakage Inductance Calculation

The stored energy and inductances values in two mention cases are in the Table.3. First the total energy in each winding was gotten from the software and than the leakage inductances was gotten from equation 3.

Table.3. Stored Energy & Leakage Inductances In Cit

Type	Stored Energy		Leakage Inductance	
	Primary (J)	Secondary (J)	Primary $m\Omega$	Secondary $\mu\Omega$
Case 1	13.37	13.08	43.01	6.57
Case 2	3.44	3.5	11.07	1.76

The comparison between two cases shows that in the interleaved windings the total energy and leakage inductance is reduced about %75 in compare to first case.

C. Electromagnetic Force Simulation

The mechanical forces results of 25kA CIT is presented in this section. The validity of the model is checked by negligible axial forces result because of symmetrically coils on the coils as expected. Since the axial stray field almost include whole area of windings the radial force component include whole of windings. In this section the electromagnetic forces on two mention cases was simulated. Table.4 shows the values of radial and axial component of two windings form.

Table 4. Electromagnetic Force Component On Two Windings Form

Windin g	Primary (one turn)		Secondary	
	Axial	Radial	Axial	Radial
Force Compo nent				
First Case	0.0006N	-66N	-6N	1604N
Second case (core part)	0.0003N	-33N	-5.44N	4.52N

The comparison of the electromagnetic forces in two different form winding shows that the interleaved windings will reduce the two axial and radial components of forces. The main component (radial) of forces in secondary winding in the interleaved winding is negligible.

V. CONCLUSION

The windings form is an effective parameter on leakage inductances, leakage fluxes and electromagnetic forces, so the voltage drop in transformer terminals is depended on windings form because of changes of leakage inductances. The energy and leakage inductance is reduced about %75 in interleaved windings. Another parameter is the maximum value of leakage flux that in interleaved windings is reduced about %50 in compare to simple concentric winding. At last the electromagnetic forces which apply to secondary winding in interleaved windings are negligible. So the interleaved windings are preferred to use in the CIT.

In addition different core volume is studied and the results show that the thickness of core isn't effective parameter on mechanical forces. The reason is that the pressures which

apply to windings area is depend on windings length unit. Also the permeability of core isn't effective parameter on mechanical forces but can effect on leakage inductances.

ACKNOWLEDGMENT

The authors gratefully acknowledge the support of the Tehran Regional Electric Company; Energy Ministry, Iran for this research.

REFERENCES

- [1] H. Heydari, M. Ariannejad and F. Faghifan, "Simulation and Analysis of 25kA Current Injection Transformer (CIT) with Finite Element Method", IEEE MELECON 2004, p.p. 909-913, May 2004
- [2] K. Karsai, D. Kerenyi, L. Kiss, "Large Power Transformers". Elsevier Science Publishing Company, Inc. 1987
- [3] M. Kozlowski, and Others, "Selected Short Circuit Strength Problems In Power Transformers", Cigre Report No 12.05, 1979
- [4] Bharat, "Transformers", Heavy Electricals limited Bhopal 1990
- [5] P. Silvester and A. Konrad, "Analysis of Transformer Leakage Phenomena by High Order Finite Element", IEEE Trans. Power Apparatus and Systems Vol.PAS-92 November/December, 1973, pp 1943-1855
- [6] O. W. Anderson, "Transformer Leakage Flux Program Based on the Finite Element Method", IEEE Trans. Power Apparatus and system, Vol.PAS-92 March/April, 1973, pp 682-689.
- [7] N. A. Demerdash, A. A. Arkadan, FEM Modeling of Permanent Magnets", Section # 3, 1981.p.26-7 (17), (19)
- [8] N. A. Demerdash, T. W. Nehl, "Determination of Inductances", IEEE Trans on MAG, Vol.18, pp.1052-54. 1982.
- [9] T. W. Nehl, F. A. Faud, N. A. Demerdash, "Inductances by Energy Perturbation". IEEE Trans on PAS, Vol 101.pp.4441-51, 1982.
- [10] M. Gyimesi and D. Ostergaard, Inductance computation by Incremental Finite Element Analysis", IEEE Trans on Magnetics, Vol.35.NO.3, MAY 1999.

Low Cost Controller for Switched Reluctance Motor

A.K. Dhakar¹, Amitava Das²

¹ Electrical Engineering Department, National Institute of Technology, Durgapur, India e-mail: ajeetdhakar@yahoo.co.in.

² Techno India Group, Salt Lake Kolkata India e-mail: amitavadas_ti@yahoo.co.in

Abstract— This paper present a simple design of an controller of 8/6 Switched Reluctance motor (SRM). It is design to operate minimum number of switching devices. It makes use of a rotor position signal, speed signal and current signal in the closed loop feedback control. The proposed design scheme is applicable for low power rating application. Use of electronic components makes the controller simple, reliable and economical. The test results are presented for 500W, 4- Phase, 3000 RPM motor which has 8 stator poles and 6 rotor poles.

Key words— PI controller, Position sensor, PWM, Switched Reluctance motor.

I. INTRODUCTION

THE switched reluctance machines have been shown to offer high-efficiency, reliable, robust, easy to manufacturer and inexpensive motor which can compete with the more conventional permanent magnet motor, induction motor, in a variety of application. Thus, SR [1] motors can be used in hard surroundings such as in high temperature and in vibration condition, and can be made at low costs. Nevertheless, the primary cost of the switched reluctance motor drive is the power electronic controller. Despite its simple structure, the real-time control of SRM is quite challenging. Various researcher over worldwide use the complicate controller like Bose [4] have used Intel 8751 single chip microcomputer based control for SRM. National Semiconductor in collaboration with SPEED laboratory of Glasgow University developed a control IC LMB1008 [5] for speed control of a three phase SRM. Krishnan et al have described the concept of PC based control [6] of SRM. Various techniques describing the instantaneous torque control and sensorless operation have used analog and digital IC s, 8096 micro-controller [7] of SRM. In this paper an analog controller scheme for speed control of a 500W, 4-phase, 3000 rpm, 8/6 pole switched reluctance motor is developed. The proposed scheme is simple, cost effective and useful for low power application. The control circuits and SRM drive are designed in the laboratory.

II. DESCRIPTION OF THE HARDWARE

The prototype drive comprises Diode bridge rectifier, four phase split link MOSFET inverter, and controller circuit. Controller circuits are used for current sensing, rotor position sensing, PWM current control, and gate drive circuit for MOSFET, power supply unit, speed controller and current limiter. The details of power and control circuits are given here. The motor parameter is given in appendix -II.

A. Power circuit

A MOSFET based inverter is connected in H-bridge split-link configuration and is supplied by a mid-point dc source. The midpoint dc source comprises of a diode bridge rectifier. Besides providing filtering action, another set of two capacitors in series provides three wire dc supplies, such that each winding takes supply from one half of the dc supply and returns the surplus energy to the other half fast recovery diodes during commutation period. Equal valued resistances are connected to balance the voltage. The value of the dc link capacitor is selected to limit the peak-to-peak ripple voltage across the capacitor to less than five percent. Schematic diagram of the inverter circuit is shown in Fig. 1.

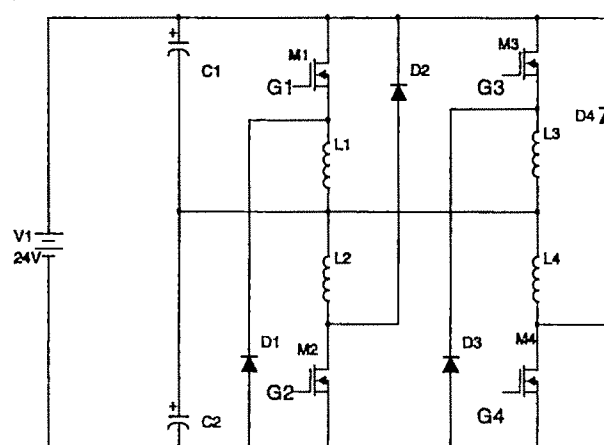


Fig. 1 Inverter circuit of SRM.

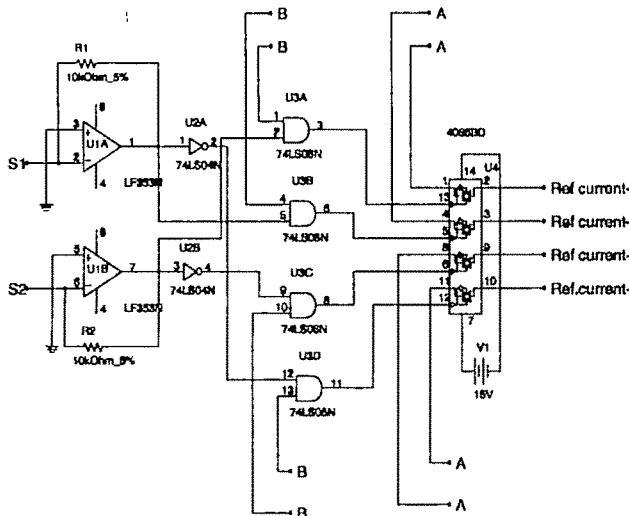


Fig 5. Position sensor conditioning and reference current generation circuit.

E Reference current generation

Now, the reference current magnitude signal I^* from speed controller, and position sensor signal information for forward and reverse motion are available. The position sensor information is latched on to the reference current magnitude I^* using analog multiplexer with S1, S2 as the control inputs to the analog multiplexer. This provides four reference current signals I_1^* , I_2^* , I_3^* and I_4^* for the four phases of SRM winding shown in Fig. 5. The analog multiplexer are shown to provide reference currents for all the four phase windings for forward as well as reverse direction of rotation.

E Triangular waveform generation

Triangular waveform generation is desired for response and frequency with the provision for level shifting, frequency and amplitude scaling. The triangular waveform generated by this circuit has a frequency ranging from 1 to 10 KHz and a magnitude of 5 volt with provision of amplitude scaling. The triangular waveform thus generated is required for PWM current control.

F PWM current control circuit

The winding current is sensed by Hall-effect current sensor and appropriately amplified and scaled by an op-amp based circuit for all the four phases. It provides electrical isolation between power and control stage, and the maximum rating of 25 A of peak current corresponds to 5 volt peak. The winding current is sensed with *allegro micro* make current sensor module, which delivers a proportional and isolated voltage signal. The signal is amplified with a provision for

gain adjustment and magnitude limiting stage towards the current controller. Thus, winding current signals for all the phases are available. This circuit makes use of precision op-amps with fast slew rate. The reference current, winding current and triangular waveform is used in the circuit to generate the gating signal for driving the MOSFET of the particular phase winding. The circuit for all the four channels is shown in Fig.6. The four output signals of the PWM current controller are fed to the four gate drive circuits described in the next section.

G Gate drive circuit

The control signal obtained from the current controller is buffered using AND gate and isolated using fast response optocoupler 6N136. The output signal at the optocoupler is buffered and amplified using a NPN transistor, and the output of this transistor available at the collector is connected to the gate of the, MOSFET module. All the four optocouplers have been biased by the individual power supply so as to provide protection and isolation. The gate driver circuit is shown in Fig.6. A careful design yields the values of the circuit parameters used at various stages. The values of these components are shown in the circuit diagram.

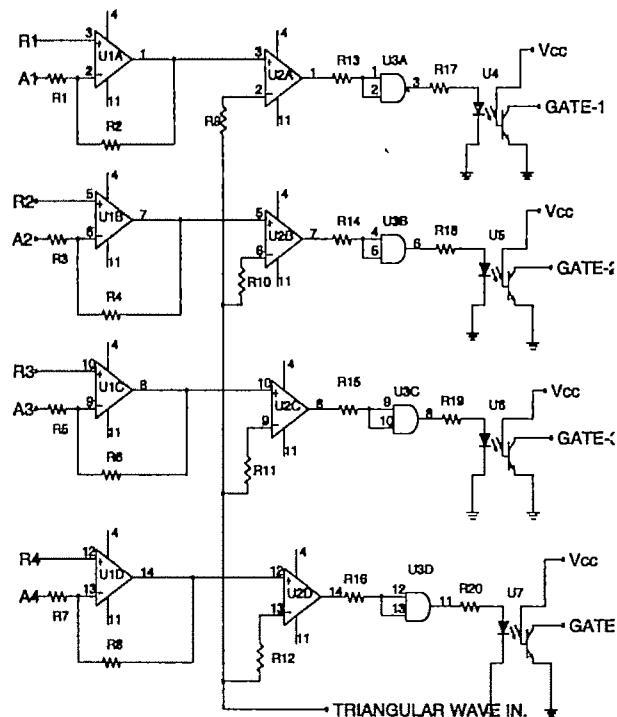


Fig. 6 PWM current control and Gate drive circuit

III. TESTING OF SRM DRIVE

The hardware consisting of power circuit, control circuit and gate drive circuit is tested individually and integrated with the SRM shown in Fig. 7. The drive system is tested for its satisfactory performance, and the response is experimentally recorded. The testing is performed for different operating conditions such as starting, reverse rotation, speed reversal and variable speed response. Experimental results are recorded to evaluate the performance of the drive. These are discussed in the next section.

IV. TEST RESULT AND DISCUSSION

The steady state current in chopping mode during low speed region is shown in Fig. 9. The PWM switching voltage across phase-1 & phase-2 are also shown in Fig. 8. It is observed that an instantaneous control of the motor winding current is accomplished with the help of PWM current controller. The current controller generates fast on and off signals, which control the switching instants of the inverter devices. The system operates at a PWM switching frequency of 7 kHz. Experimental recording of all two-position sensor and voltage signals with the prototype system developed is presented. The relative position of the sensor signals S1 and S2 in forward region is shown in Fig. 10. In this combination of these position sensors signal information along with turn-off and turn-on angle delay that decides the excitation of a particular phase winding. The steady state condition of individual two phase currents while the motor rotating in forward direction is shown in Fig. 9. The graph shows the phase angle displacement between successive phases. The result confirms the ability of the analog controller for satisfactory performance in either direction.

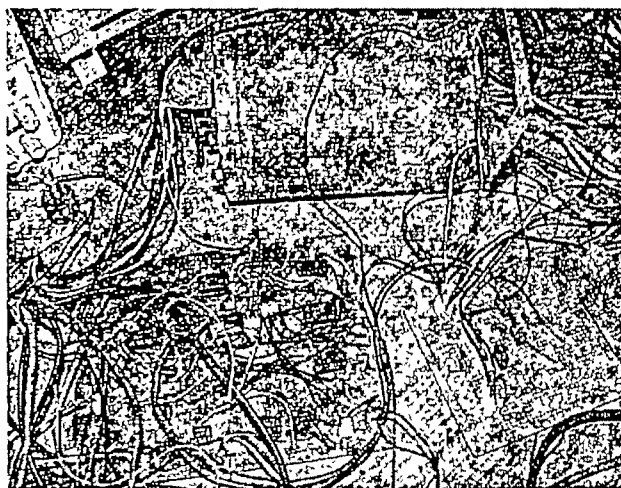


Fig. 7 Controller circuit and SR motor.

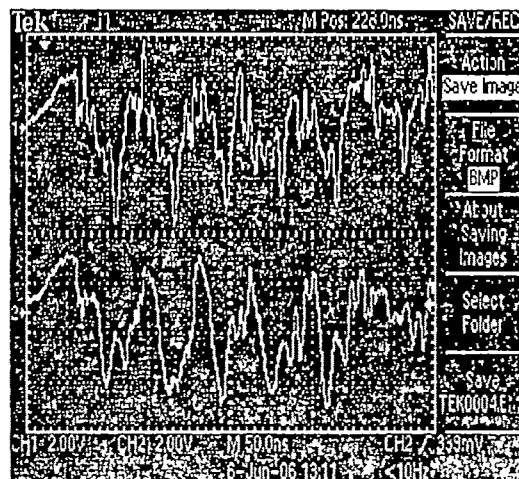


Fig. 8. Voltage waveform in forward direction

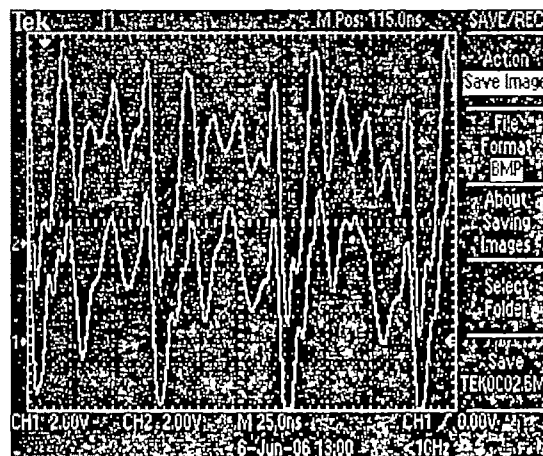


Fig. 9 Current waveform in forward direction

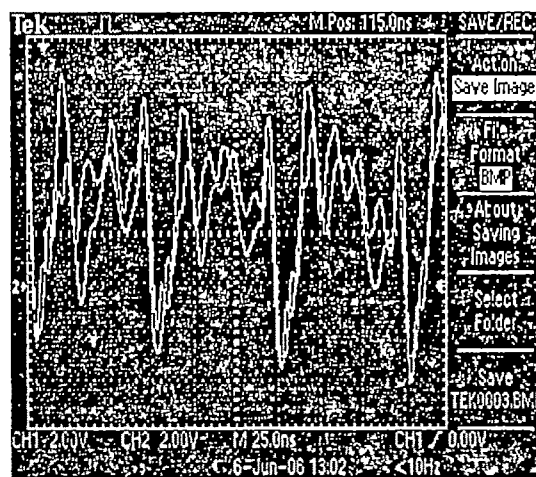


Fig. 10. Position Sensors output in forward direction

V. CONCLUSION

This paper presents a simple analog controller developed for control of switched reluctance motor. The controller is capable of implementing voltage-fed during high speed and low speed region respectively. The hardware developed for speed control of SRM is successfully tested for real time implementation. The results demonstrate that the motor works satisfactorily over a wide range of speed and operating conditions. Experimental results validate the practical design of controller and prove the attractive, features of such a control for industrial applications. Standard off-the-shelf components are used which makes the controller economical. Based on the total cost, in appendix I, it is concluded that the laboratory model is useful for low cost applications such a, washing machine.

REFERENCES

- [1] T.J.E Miller. Switched reluctance motors and their control, Oxford, Magma Physics Publishing and Clarendon Press-Oxford, 1993.
- [2] P.J. Lawrenson, J.M. Stephenson, P.T. Blenkinsop, J. Corda and N.N. Fulton, "Variable-speed switched reluctance motor", *IEE Proceedings Inst. Elect. Eng.*, Vol 127, no 4, pp 253-265, June 1980.
- [3] P.J. Costa Branco, "Influence of Magnetic Non-linearities on Simulation Accuracy of Switched Reluctance Motor Models", In: *Systems and Control: Theory and Applications*, pp. 403-408, World Scientific and Engineering Society Press, Danvers, USA
- [4] B.K. Bose, T.J.E. Miller et P.M. Szczesny, "Microcomputer control of switched reluctance motor", *IEEE Transactions on Industry Applications*, Vol IA-22, no.4, pp 708-715, June 1986.
- [5] T.J.E. Miller, C. Cosar, and D. Anderson, "A new control IC for switched reluctance motor drives", *Proceedings of IEE Fourth International Conference On Power Electronics and Variable Speed Drives*, Conference Publication No. 324, pp 33 1-33, Jul 17-19.1990
- [6] X. Mang, R. Krishnan, S. Dakar, and G. Chandramouli. Personal Computer based controller for switched reluctance motor drive," *Proc. IECON'87* PP. 550-555
- [7] Patrick J. Roche, Michael G. Egan, J.M.D. Murphy. "Intelligent 8096 based multimode control of a variable reluctance motor drive," *Proc. EPE*, 1991, PP. 917-922.
- [8] Hao Chen. Chao Zhang, Xinjun Meng "Variable angle PWM adjustable Speed control of switched reluctance motor drive" *EPE-PEMC 2000*.

APPENDIX-I

COST OF THE CONTROLLER CIRCUIT

NAME OF THE COMPONENT	COSTS IN \$
Op-Amp	5
Current Sensors	10
Mosfet	10
Optocoupler	6
Quad Bilateral Switch	2
Hex Inverter	1
2 Input And Gates	1
Position Sensors	10
Capacitor, Diode, Resistance E.T.C	5
Total (Approximate)	50 \$

APPENDIX-II

PARAMETER OF THE EXPERIMENTAL MOTOR

PARAMETER	SYMBOL	VALUE	UNITS
Stator Diameter	D_s	3.87	inch
Rotor Diameter	D_r	2.012	Inch
Stack Length	L_{stk}	2.012	Inch
Air gap	G	0.01	Inch
No. Of Stator Poles	N_s	8	
No. Of Rotor Poles	N_r	6	
No. Of Phases	M	4	
Stator Pole Arc	β_s	30°	degree
Rotor Pole Arc	β_r	32°	degree
Stator Pole Width	t_s	0.3703	Inch
Rotor Pole Width	t_r	0.401	Inch
Stator Slot Depth	d_s	0.672	Inch
Rotor Slot Depth	d_r	0.2	Inch
Stator Yoke thickness	y_s	0.2469	Inch
Rotor Yoke thickness	y_r	0.1337	Inch
Bore Diameter	D_{sh}	2.032	Inch

PC Based Remote Speed Control and Condition Monitoring of DC Motor

S. Chowdhuri, J. N. Bera, G. Sarkar, S. Phoujdar

Department of Applied Physics, University of Calcutta, India
email: sumana_cu05@rediffmail.com, jletendrabera@rediffmail.com, gaphy@caluniv.ac.in

Abstract— There are number of industries, where DC drive is extensively used due to certain advantages of it over AC drives like the ease of control of speed and torque. The continuous evolution of the control systems with the adoption of various latest technologies makes the control systems very user friendly with much higher degree or level of reliability. The proposed work attempts to make a stand alone close loop controller for DC Machine to work independently in two modes of operation. In one mode i.e. Local Mode, the controller can perform the condition monitoring as well as control of speed, voltage, current, temperature and other machine parameters. In its remote mode of operation, the same can also be monitored and controlled from a remote PC where the controller is connected with the PC through a wireless communication network. So, the state-of-the-art controller is to be made with a networking facility such that no. of machines can be controlled and monitored from a centralized control station with the adoption of embedded technology.

Key Words—PWM, Wireless, SAEC,PIEC

1. INTRODUCTION

From the beginning of this century, electric drives have been replacing the fluid power actuators and Internal Combustion (IC) machines in both high performance and general purpose applications. The growth of electric drives is very high due to the current level of technology both in control aspect and in device aspect. High reliability, long lifetime, relatively low maintenance and short startup times along with ecological compatibility like low emission of pollutants are advantages of electric drives. The quality of electric drives is extended by a high efficiency, low no-load losses, high overload capability, fast dynamic response, the possibility of reversibility. Electric drives are available in a wide range of rated speeds, torques and power; they allow for a continuous speed regulation, reversal capability and they easily adapt to different environment conditions such as the adverse atmosphere or clean room requirements. Unlike the IC engines, electric motors provide for a ripple-free, continuous torque and secure a smooth drive operation. At

present, electric drives absorb more than 70% of all the electric energy produced in an industrial country[1,2, 3,4].

DC Motor though is less used due to some maintenance requirement but there are certain advantages of DC motor like higher degree of control, wider range of speed control and ease of speed control.

Today's civilization is advancing at very faster pace with the adoption of wireless technology. The convergence of wireless technology and the embedded technology makes the wireless systems more reliable, much efficient as well as cost effective one. Moreover, the system can be made mobile one as there is no need of wires for that control system to work. So, modern civilization dreams, based on the successful implementation of wireless communication systems, where every equipment of remote room / office/ factory can be accessed as well as controlled from one's fingertip without the physical presence at that room or office/factory. These advantages can best be utilized towards electrical engineering by having an wireless control and monitoring system of Electrical DC Drives which has tremendous potential in modern Industries

Several works has been sighted which shows the future trend of embedded technology in electrical drives. In [5] implementation of the MC68HC11E9 microcontroller for speed control of DC motor fed by a DC chopper has been investigated. The chopper is driven by a high frequency PWM signal. A simple low cost sensorless control technique for Brush less DC Motor (BLDC) motor drives is proposed in the work [6]. The proposed method utilizes the microcontroller embedded AD converter for terminal voltage measurements. An approach for condition monitoring of an electrical machine is proposed in [7]. The method uses the power leads of the machine itself as the communication link between the sending station located within the machine and the receiving station located remotely outside the machine. The required communication circuit for realizing data transmission for both the ordinary 60-Hz power line and the special pulse-width-modulated (PWM) inverter-fed power line is constructed. A project based approach has been adopted to teach matlab/simulink based controller design, mixed signal embedded microcontroller (SiLab C8051F020) based implementation of the controller for DC motor speed control in [8]. With the advancement of microcontroller technology, it has become possible to control AC drives with complex PWM waveforms generated by using calculating

algorithms while the system is online. Such algorithms allow the manipulation of various parameters within the modulation strategy which can result in changes in the output frequency content in [9]. A hardware board using the Intel 8097 microcontrollers in multiprocessor communication mode with master-slave configuration has been designed.

This work attempts to monitor the parameters like voltage, Current and Speed of a DC Motor as part of the condition monitoring and to control the speed of the motor using microcontroller. The microcontroller[10] based condition monitoring and speed control system is also cost effective solution as it provides a totally system dedicated embedded technology for DC Drives. The state-of-the-art of this work is the introduction of Wireless Technology[11] in the control and monitoring process of Electrical drives.

II. SYSTEM OVERVIEW

The overall schematic diagram is shown in the fig 1. The conditions of DC Motors are to be monitored with the help of the state-of-the-art *Stand Alone Embedded Controller (SAEC)* system. The SAEC will be comprised of a microcontroller unit and with some additional IC chips for condition monitoring. A *Power Converter* based on MOSFET for controlling DC motor speed. A *Wireless Transceiver Unit* is used for conditions transmission to the control room. The measurement of DC supply voltages to the armature and field, the magnitude of dc current flowing through the armature, the running speed of the motor, the temperature of the casing of the motor etc. are the different conditions to be monitored under Motor mode of operations. All these conditions are measured with the help of proper sensors/devices and are continuously scanned by the SAEC. The SAEC will convert these measured parameters into proper data streams and will send the same to PC, remotely placed via the wireless transceiver unit. Apart from the measurement of different parameters, SAEC unit is also capable to control the speed and the starting of the DC machine. To control the speed and starting of the machine, power electronic Converter circuits is absolutely essential. SAEC will be capable to control the converter either in local mode or in remote mode. On the rear end there will be one *PC Interfaced Embedded Controller (PIEC)* and another one *Wireless Transceiver Unit*. Microsoft windows based state-of-the-art software receives the data from PIEC where PIEC receives the machine parameter based data from the wireless transceiver unit in its upward path from machine to PC. The various status of the machine will be displayed as per format of the software and that can also be varied/controlled through the downward path from pc to machine. Thus a database for performance analysis, to study the behavior of the machine under different running conditions as well as different types of fault condition can be formed from which suggestions for different protection schemes, different control action etc. can be speculated. The motor specification is provided in the appendix. The *Power Converter* is basically a chopper circuit based on

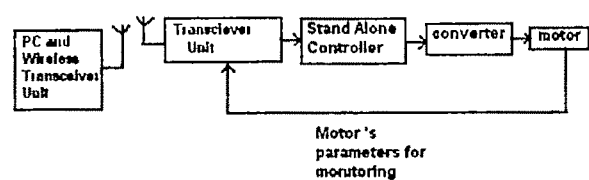


Fig.-1 Basic Schematic for DC motor Speed control and Condition Monitoring

MOSFET whose gate drive signal will come from the SAEC unit. The gate drive signal as generated from controller will be isolated from the power converter by OPTOCOUPLER. The SAEC unit is developed on ATMEL 89C51 microcontroller and the detail firmware is described later.

II. FIRMWARE IMPLEMENTATION

The firmware implemented has several tasks like

- Speed estimation
- Voltage measurement
- Current measurement
- Temperature measurement
- PWM Control signal generation
- SOFTSTART for starting
- Sending measured data for Wireless Transmission
- Receiving the wireless control signals from PC

Speed Control : Here the DC machine's speed is controlled in open loop. Speed control is achieved by the Pulse Width Modulation (PWM) Technique. The voltage level corresponding to speed signal is sent from the PC to Transceiver Unit. The receiver will sense the voltage level and set it to SAEC. The firmware will generate the pulse of required width corresponding to speed demand. This signal is fed to the gate drive circuit of the MOSFET. The frequency for PWM is taken here is 1 KHZ, thus the firmware will generate pulse width ranging from zero to 1mS thereby the duty ratio will vary from 0 to 100%.

Soft start: Another feature of the firmware is soft starting as DC motor can not be started instantaneously from zero speed to full speed due to its drawing of large current and inertia. Hence starter is required and this is implemented in firmware so that machine will change from one speed to other speed with certain softness. The time requirement is dependent on the loading conditions. At no load condition this soft starting requirement will be slower than the loaded condition. Thus the user can remotely set the soft start rate or acceleration rate. Here the machine is tested at light load condition with acceleration rate of one rps/second.

Measurement of speed: For speed measurement proximity sensor is used placed nearer to the rotor shaft. The sensor generates pulses of width proportional to the speed of the motor. The width of the pulse is measured with help of a

counter whose count rate is 500KHz (f_{clk}). Total countvalue (c) with such count rate from one falling edge to another falling edge will give the estimation of speed (n in rpm) as per the equation (1).

$$n = k * 60 * \frac{c}{f_{clk}} \dots \dots \dots (1)$$

Measurement of Voltage: The machine under test is IHP, 220V DC machine, the armature or field voltage measurement requires isolation from the power circuit to control circuit. The isolation is provided with the help of another voltage dependant PWM generator hardware. The task of firmware is to measure this pulse width fed to one of the port pin and accordingly estimate the voltage with proper calibration.

Measurement of current: DC Current is measured with the help of voltage measurement technique as described earlier. The voltage considered here is the drop across a shunt path, proportional to the current.

Measurement of Temperature: Temperature is sensed via temperature sensor. The voltage from sensor is then converted from analog to digital signal by an ADC. The ADC output is read by the microcontroller and is calibrated to the corresponding temperature.

Wireless Communication: For remote access of the measured parameters, a low cost commercially available cordless telephone set is used. The telephone set is customized to transmit the desired data from its base unit while the handheld or mobile unit is used to retrieve the data. The data to be transmitted is first converted to a serial stream with the state-of-the-art frame format using Biphase modulation technique. It is then filtered through a low pass filter and is fed to the input point of the base unit. The base unit transmits this data at ISM band of 900 MHz using inbuilt spread spectrum technique.

On the other hand, the original base band signal i.e. the biphase modulating signal is retrieved back from the handheld unit. It is then fed to the input of PIEC for its biphase demodulation. After the demodulation, the data is fed to the PC through its serial port using standard RS232 protocol.

Results

A PWM signal of frequency 1 KHz with various duty cycle is generated to produce different DC voltage level at the DC motor's terminal. As the motor terminal voltage varies the speed of the motor also varies. Fig2 shows the DC motor Armature voltage for 50% duty cycle at 750 rpm. A particular speed is achieved with a particular duty cycle.

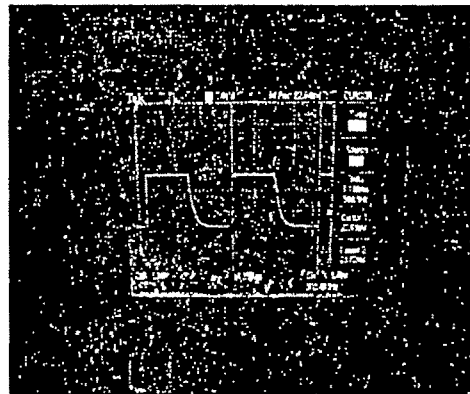


Fig2 : Chopper Output voltage for 750 rpm speed

The duty cycle is adjusted/ altered from a PC. The soft starting facility of the motor is also provided with variable acceleration time. The acceleration time can be adjusted from the PC. So this eliminates the need for a DC machine Starter. This acceleration principle is equally applicable to change to any other speed while the machine is running at another speed steadily. Fig 3 shows the gate drive as generated from the microcontroller. By the process of speed measurement the DC voltage, Current and temperature of the system are also measured with the proper selection of multiplexer input.

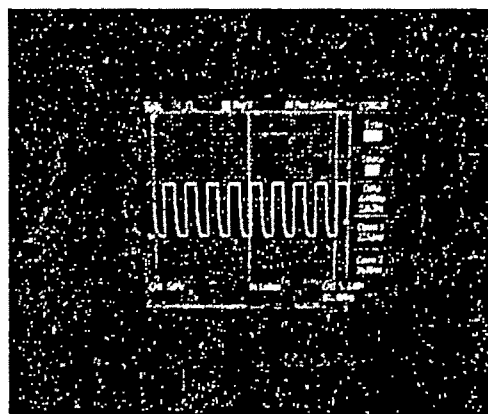


Fig3: 1 KHz pulse stream for gate drive

III. CONCLUSION

The aim of this work is to make a stand alone low cost dedicated embedded speed controller and also motors' condition monitor for any type of motor. The authors attempted in this work to implement the stand alone system for a DC motor, which has still many applications in industries. The same system can also be implemented for other type of motors like Induction motor, synchronous motor, BLDC Motor. The present system described is open loop one with the future objective is to implement in closed loop system with higher accuracy of speed and as well as position control.

REFERENCES

- [1] Power Electronics And Drives, Mohan.Pub: Phi
- [2] Power Electronics, Circuits and Devices, by Rashid,Pub: PHI
- [3] Speed control of DC motor drives based on efficient utilization of energy and optimal performance, Awad, A.S. Mohamed, E.A. Negm, M.M. Said, A.I., Ain Shams Univ., Cairo, Egypt, Electricity Distribution. Part one 14th International Conference and Exhibition on (IEE Conf. Publ. No. 438), Volume. 5, On page(s): 221- 225 vol.5
- [4] Fuzzy logic microcontroller implementation for DC motor speedcontrol Tipsuwan, Y. Mo-Yuen Chow, Industrial Electronics Society, 1999, IECON apov:99 Proceedings. The 25th Annual Conference of the IEEE Volume 3, Issue, 1999 Page(s):1271 - 1276 vol.3
- [5] Microcontroller Performance for DC Motor Sped Control system. Ali Y. Y.S.E. Microcontroller performance for DC motor speed control system, Ali, Y.S.E. Noor, S.B.M. Bashi, S.M. Hassan, M.K. Dept. of Electr. & Electron. Eng., Univ. Putra Malaysia, Selangor, Malaysia Power Engineering Conference, 2003 PECon 2003. Proceedings. National. Publication Date. 15-16 Dec. 2003 On page(s): 104- 109
- [6] A microcontroller embedded AD converter based low cost sensorless technique for brushless DC motor drives, Yongjin Kang; Sang Bin Lee; Jiyeon Yoo, Industry Applications Conference, 2005. Fourtieth IAS Annual Meeting. Conference Record of the 2005, Volume 3, Issue, 2-6 Oct. 2005 Page(s): 2176 - 2181 Vol. 3
- [7] A new approach to motor condition monitoring in induction motordrives, Chen, S.; Zhong, E., Lipo, T.A. Industry Applications Society Annual Meeting, 1993., Conference Record of the 1993 IEEE Volume, Issue, 2-8 Oct 1993 Page(s): 645 - 650 vol.1
- [8] A Project Based Approach to Teach Mixed-Signal Embedded Microcontroller for DC Motor Third IEEE International Workshop on Electronic Design, Test and Applications (DELTA'06) pp. 123-128, Gourab Sen Gupta, Massey University, Palmerston North, New Zealand, Subhas Mukhopadhyay, Massey University, Palmerston North, New Zealand, Chew Moi Tun, Monash University, Malaysia
- [9] PWM strategies for the real-time embedded control and condition monitoring of AC drives, S.K. Sethuraman; M.G. Saravanan, Industrial Electronics, 1993 Conference Proceedings, ISIEapov:93 - Budapest., IEEE International Symposium on Volume, Issue, 1993 Page(s): 219 - 224
- [10] 8051: The Programing, Customising and Applications by Myke Predko, Publ: Pearson
- [11] Multimedia MAC (medium Access Control) protocols towards personal communication network, J.N. Bera, R. Bera, S. Sil., HOT 2003 (Feb 3 5 2003) organised by Institute of Radiophysics & Electronics, Calcutta University

Technical Session 7A

***Electronics and Software Based
Applications***

Amplitude Control in Sinusoidal Oscillator

H. Mechergui¹, A. Haddouk²

¹Institut: Ecole Supérieure des Sciences et Technique de Tunis, Laboratory & Research groups: C.3.S, E-mail: hafidmecher@yahoo.com

²Institut: Ecole Supérieure des Sciences et Technique de Tunis, Laboratory & Research groups: C 3 S, E-mail: wamoin@yahoo.com

Abstract— In this paper we present a new stabilization amplifier with a selected non-linearity which is used to achieve a precise control of the RC oscillator amplitude and distortions.

We determine the transfer function of the stabilization system and using the first harmonic method, we evaluate the oscillator metrological characteristics.

The results of measurements carried out on quadrature oscillator illustrate the behaviour of the presented stabilization amplifier model. The oscillator amplitude is controlled by a precise variable direct current voltage. The new controlled amplifier achieves a good linearity of the amplitude oscillator versus a variable DC voltage. This last can be used to build any harmonic oscillator.

Key words - harmonic oscillators, frequency oscillation, stabilization amplifier, Damping parameter, harmonic linearization method, stabilisation ratio, distortion rate.

I. INTRODUCTION

THE wave form and the metrological qualities of an RC oscillator depend primarily on the amplitude stabilization element [2], [11].

Indeed, to obtain oscillations, the following condition should be satisfied: $\beta(p).G(p)=1$ (1).

With $\beta(p)$ attenuation presented by the network selection and $G(p)$ is the gain of the amplifier used to provide energy for the oscillator.

The analysis of the equation (1) shows that to guarantee oscillations it is necessary that the term $\beta(p).G(p)$ is higher than the unit

i.e: $\beta(p).G(p)=1+\varepsilon_1$.

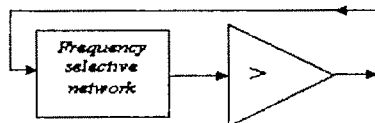


Fig.1: Basic structure of the harmonic oscillator

This condition imposes the instability of the oscillator and its starting will be pseudo oscillating with exponential:

$$u(t)=U_m \sin(\omega t) e^{\alpha_1 \omega t}.$$

To have a stationary regime, it is necessary to introduce an amplitude stabilization element. This last will affect the signal's form and the oscillator becomes a nonlinear system.

The introduction of a nonlinear element inevitably leads to conditions which depend on this last and the metrological parameters of the oscillator are affected by the quality of the stabilization amplifier.

To study the behaviour of the oscillator it is pointed out that since the time when Van Der Pol. proposed his equation:

$$\ddot{y} - \varepsilon \omega \left(1 - \frac{y^2}{y_0^2}\right) \dot{y} + \omega^2 y = 0$$

much of the researches are interested to study oscillators RC [2],[3],[7]. These studies presented mathematical models which where always seeking an optimal solution for a stationary regime providing a signal approaching a sine signal. They also use numerical methods to produce a low frequency sine wave [4],[8].

Unfortunately, the suggested solutions are very expensive to realize because they integrate multipliers, programmable circuits or they use stabilization elements with strongly non linear characteristics [11].

II. PRESENTATION OF THE STABILIZATION AMPLIFIER

In this study we present a precise stabilization amplifier to control the oscillator's behaviour.

The stabilization amplifier model is presented by the figure (2). Indeed, it is composed of operational amplifiers and two variable resistances which select the non linearity of the oscillator.

The oscillation amplitude is referenced to a precise variable direct current voltage.

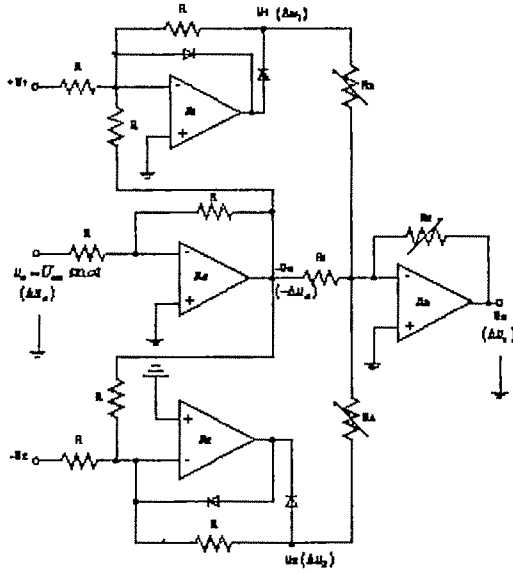


Fig.2: Schematic diagram of the stabilization amplifier

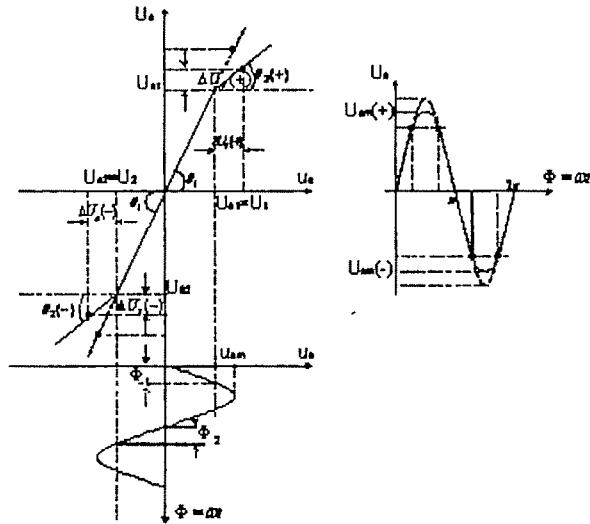


Fig.3: Transfer function of the stabilization amplifier

By associating the stabilization amplifier circuit with a selective filter and a linear amplifier having a gain G and if the system is connected in closed loop, we obtain a harmonic oscillator. This structure is shown in the figure 4.

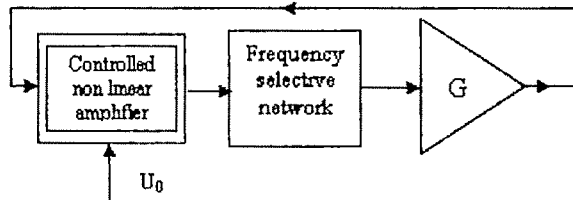


Fig.4: A conceptual model of the oscillator

III. ANALYSIS OF THE STABILIZATION AMPLIFIER

The output signal $u_s(t)$ of the stabilization amplifier to the input signal $u_i(t)$, at the resonant frequency, is necessarily non-linear function of $u_i(t)$ and this will introduce harmonic distortions into the output of the oscillator. Indeed, to analyze the stationary regime of the oscillator we determine the transfer function $u_s(t)$.

function $u_s(t)$.

$$u_s(\phi) = \begin{cases} tg\theta_1 U_m \sin\phi & 0 \leq \phi \leq \phi_1 \\ U_{01}(tg\theta_1 - tg\theta_2) + tg\theta_2 U_m \sin\phi & \pi - \phi_1 \leq \phi \leq \pi + \phi_2 \\ -U_{02}(tg\theta_1 - tg\theta_2) + tg\theta_2 U_m \sin\phi & \pi + \phi_2 \leq \phi \leq 2\pi - \phi_2 \\ tg\theta_1 U_m \sin\phi & 2\pi - \phi_2 \leq \phi \leq 2\pi \end{cases} \quad (2)$$

We put: $u_e = G u_i = G U_m \sin\phi = U_m \sin\phi$,

$u_i = U_m \sin\omega t$ and $\phi = \omega t$.

The non-linear control element system has two zones of operation which are respectively defined by the gains μ_1 and μ_2 ; where $\mu_1 = tg\theta_1$ and $\mu_2 = tg\theta_2$. Its characteristic

makes it possible to write: $\phi_1 = \arcsin \frac{U_1}{U_m}$ (3) and

$\phi_2 = \arcsin \frac{U_2}{U_{1m}}$ (4).

The input voltage u_e of the stabilization amplifier is added with a DC voltage U_{01} or $-U_{02}$ using two inverter amplifiers AO1 and AO2, having unit gain.

When $(U_{01} - u_e) > 0$ or $(-U_{02} - u_e) < 0$, at the input of the AO3 is applied $-u_e$, which is coming from the output of AO4 and at the output of the non-linear control element we find:

$u_s = G \mu_1 u_i$, with: $\mu_1 = \frac{R_2}{R_1} = 1 + \varepsilon_1$ (5) and

$G = \frac{1}{|\beta(j\omega)|}$ (6) where $\varepsilon_1 > 0$ (excitation damping).

Thus the oscillation condition

$|\beta(j\omega)G(j\omega)| > 1$ (7) is carried out.

By examining the equation (7) we note that the increase of u_s

is pseudo periodical with exponential $e^{\alpha_1 \omega_0 t}$. This situation continues until the $u_e(\phi_1) = U_{01}$ or $u_e(\phi_2) = -U_{02}$.

When $(U_{01} - u_e) < 0$ or $|u_e| > |U_{01}|$, the stabilization amplifier gain changes automatically and we obtain a second zone in which the gain is determined by μ_2 . At the output of the amplifier

AO3 we have $\Delta u_s = \frac{R_2}{R_1} \Delta u_e - \frac{R_2}{R_3} \Delta u_i$ (8). Since

$\Delta u_i = -\Delta u_e$ then the equation (7) can be put in the following

form: $\Delta u_s = \frac{R_2}{R_1} \Delta u_e (1 - \frac{R_1}{R_3})$ (9).

From this expression we draw out the gain of the control element: $\mu_{2+} = \frac{R_2}{R_1} (1 - \frac{R_1}{R_3})$ (10), with $\frac{R_1}{R_3} = \varepsilon_2$ (11) (ε_2 : amplitude damping stabilization).

If $(-U_{02} - u_e) > 0$, we apply to the amplifier input AO3: $\Delta u_{e-} + \Delta u_2$ and at its output we have:

$$\Delta u_s = \frac{R_2}{R_1} \Delta u_{e-} - \frac{R_2}{R_4} \Delta u_2. \text{ For the negative zone the gain will be:}$$

$$\mu_{2-} = \frac{\Delta u_{e-}}{u_{e-}} = \frac{R_2}{R_1} (1 - \frac{R_1}{R_4}) \text{ (12) with } u_e < 0.$$

We can vary independently the excitation parameter μ_1 and the amplitude stabilization parameter μ_{2+} and μ_{2-} while adjusting R_2 , R_3 and R_4 , for U_{01} and U_{02} threshold voltage.

In the particular case where $U_{01} = U_{02}$ and $R_3 = R_4$ we have symmetrical stabilization control element with: $\mu_2 = \mu_{2+} = \mu_{2-}$.

If $R_1 = R_3 = R_4$ there will be a saturation zone characterized by $\mu_2 = 0$ which is illustrated by the figure (5).

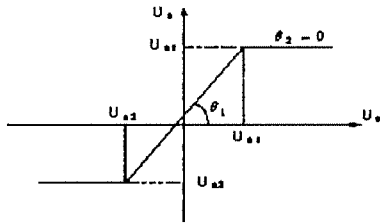


Fig.5: Stabilization amplifier characteristic for $\theta_2=0$

According to expression (12) we notice that the stabilization term intervenes by the ratio of two resistances $\frac{R_1}{R_3}$ or $\frac{R_1}{R_4}$.

The substitution of (5) and (11) in (12) gives: $\mu_{2-} (1 + \varepsilon_1)(1 - \varepsilon_2)$ (13).

While developing (13) we will have

$\mu_2 \equiv (1 + \varepsilon_1 - \varepsilon_2)$. If we put: $\xi = (\varepsilon_1 - \varepsilon_2) < 0$, the gain for the zone two can be written as in the following form $\mu_2 = (1 - \xi_2)$ (14). The equation (14) gives the stabilization condition $\mu_2 < \mu_1$ and the gain of the stabilization amplifier changes automatically. The output signal versus the time will be: $v(t) = U_m \sin(\omega t) e^{-\alpha_2 \omega t}$.

The figure.6 shows the oscillator's behaviour.

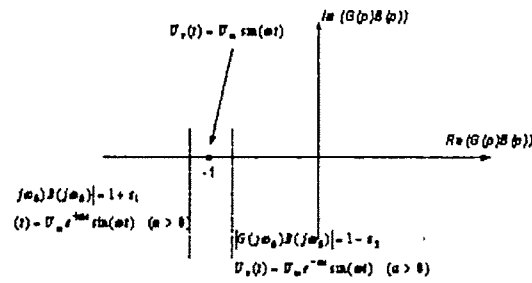


Fig.6. The operating oscillator in the Nyquist plane

IV. OSCILLATOR LINEARISATION

Since the behaviour of the oscillator is nonlinear, then it appears a distortion of the signal, provided by the stabilization nonlinear control element. To analyze the operation of this oscillator we use nonlinear systems specific methods. The simplest is the first harmonic method [1].

At the resonant frequency ($\omega = \omega_0$), the behaviour of the oscillator depends on the first harmonic of the generated signal.

In addition, when the signal is nonlinear, the equivalent gain for the first harmonic decreases. Thus $G(j\omega_0)$ can be replaced by the harmonic gain $Q_h(j\omega_0)$. The equation (1) can be put into the following form: $Q_h(j\omega_0)B(j\omega_0) = 1$ (15).

At first approximation, it is supposed that the selective filter attenuates the harmonics of angular velocity $2\omega_0$, $3\omega_0$... The input voltage of the stabilization amplifier is $u_e = K U_m \sin(\omega_0 t)$. In addition, if we put

$$\lambda(j\omega_0) = \frac{1}{B(j\omega_0)}, \text{ the expression (15) can be written as}$$

$$\text{follows: } \lambda(j\omega_0) - Q_h = 0 \text{ (16).}$$

The harmonic gain is being real, because the amplifier is supposed to be perfect, and working in low frequency. According to [1] the harmonic gain can be determined by the following expression:

$$Q_h = \frac{K}{\pi U_m} \int_0^{2\pi} u_s \sin(\phi) d\phi \text{ (17), with } \phi = \omega t.$$

By substituting the equation (2) into (17) we obtain:

$$Q_h = \frac{1}{\pi U_m} \left[\int_0^{\pi-\phi_1} U_m t g \theta_1 \sin^2 \phi d\phi + \int_{\pi-\phi_1}^{\pi-\phi_2} (U_{01}(t g \theta_1 - t g \theta_2) \sin \phi + U_m t g \theta_2 \sin^2 \phi) d\phi + \int_{\pi-\phi_2}^{2\pi-\phi_2} (-U_{02}(t g \theta_1 - t g \theta_2) \sin \phi + U_m t g \theta_2 \sin^2 \phi) d\phi + \int_{2\pi-\phi_2}^{2\pi} (U_m t g \theta_1 \sin^2 \phi) d\phi \right] \text{ (18)}$$

The resolution of (18) gives the harmonic gain, containing the amplitude of the first harmonic.

$$\begin{aligned}
 Q_h &= \frac{1}{\pi U_m} [U_m t g \theta_1 \left[\frac{1}{2} - \frac{\sin 2\phi}{4} \right]_0^{\pi-\phi_1} + U_{01} (t g \theta_1 - t g \theta_2) \left[-\cos \phi \right]_{\frac{\pi}{2}}^{\pi-\phi_1} \\
 &+ U_m t g \theta_2 \left[\frac{1}{2} - \frac{\sin 2\phi}{4} \right]_{\pi-\phi_1}^{\pi-\phi_2} + U_m t g \theta_1 \left[\frac{1}{2} - \frac{\sin 2\phi}{4} \right]_{\pi-\phi_1}^{\pi+\phi_2} \\
 &- U_{02} (t g \theta_1 - t g \theta_2) \left[-\cos \phi \right]_{\frac{\pi}{2}}^{\pi-\phi_2} + U_m t g \theta_2 \left[\frac{1}{2} - \frac{\sin 2\phi}{4} \right]_{\pi+\phi_1}^{2\pi-\phi_2} + \\
 &+ U_m t g \theta_1 \left[\frac{1}{2} - \frac{\sin 2\phi}{4} \right]_{2\pi-\phi_2}^{2\pi}] \\
 &= \frac{1}{\pi U_m} [U_m t g \theta_1 (\phi_1 + \phi_2 - \frac{1}{2} (\sin 2\phi_1 + \sin 2\phi_2)) + \\
 &(t g \theta_1 - t g \theta_2) (2U_{01} \cos \phi_1 + 2U_{02} \cos \phi_2) + \\
 &U_m t g \theta_2 (\pi - \phi_1 - \phi_2 + \frac{1}{2} (\sin 2\phi_1 + \sin 2\phi_2))] \quad (19).
 \end{aligned}$$

If the amplifier is symmetrical, we have $U_{01} = U_{02} = U_0$ and $\phi_1 = \phi_2 = \phi_0$ and while replacing $t g \theta_1$ and $t g \theta_2$ respectively by μ_1 and μ_2 then the harmonic gain is reduced to

$$\begin{aligned}
 Q_h &= \frac{1}{\pi} [G\mu_1 (2\phi_0 - \sin 2\phi_0) + G\mu_2 (\pi - 2\phi_0 + \sin 2\phi_0) \\
 &+ \frac{U_0}{U_m} (\mu_1 - \mu_2) (4 \cos \phi_0)] \quad (20)
 \end{aligned}$$

Since the amplitude voltage U_m is controlled by a DC voltage U_0 , we can calculate the stabilization ratio: $\delta = \frac{U_0}{U_m}$ (21) and the harmonic gain of the stabilisation element will be:

$$\begin{aligned}
 Q_h &= \frac{1}{\pi} [G(\mu_1 (\arcsin 2\delta - 2\delta \sqrt{1-\delta^2}) + \\
 &\mu_2 (\pi - \arcsin 2\delta + 2\delta \sqrt{1-\delta^2}) + 4\delta (\mu_1 - \mu_2) \sqrt{1-\delta^2})] \quad (22).
 \end{aligned}$$

By replacing $(\mu_1 - \mu_2) = \xi_2$, we obtain:

$$\begin{aligned}
 Q_h &= \frac{1}{\pi} [G(\mu_1 (\arcsin 2\delta - 2\delta \sqrt{1-\delta^2}) + \\
 &\mu_2 (\pi - \arcsin 2\delta + 2\delta \sqrt{1-\delta^2}) + 4\delta \xi_2 \sqrt{1-\delta^2})] \quad (23).
 \end{aligned}$$

The expression (23) gives the harmonic gain Q_h which represents a modelling non linearity of the oscillator.

Indeed, by a judicious choice of ε_1 and while varying the parameter ε_2 of the control element, we can determine the stabilization ratio, which contains the oscillating amplitude U_{1m} . After that, we deduce the selective frequency ω , the harmonic distortions and respectively the static stability of the amplitude $\frac{\Delta U_m}{U_m}$ and that of the angular velocity $\frac{\Delta \omega}{\omega}$.

V. HARMONIC DISTORSIONS CALCULATION

The non linear element of the amplitude stabilization conditions the quality of the signal, provided by the oscillator.

The signal voltage u_1 , being nonlinear, can be expressed in Fourier series as follows: $u_1 = u_{11}(t) + u_{13}(t) + \dots + \dots$.

The harmonic gain for the k^{th} Fourier coefficient is:

$$Q_k = \frac{1}{\pi U_m} \int_0^{2\pi} f(u_e) \sin(k\phi) d\phi \quad (24)$$

Where $k = 2i + 1$ avec $i = 1, 2, 3, \dots$

If we replace $f(u_e)$ by its expression (2) in (24), we obtain

Q_k for the k^{th} harmonic:

$$\begin{aligned}
 Q_k &= \frac{1}{\pi U_m} \left[\int_0^{\phi_1} U_m \mu_1 \sin \phi \sin(k\phi) d\phi + \int_{\phi_1}^{\pi-\phi_1} (\xi_2 U_{01} \sin(k\phi)) d\phi + \right. \\
 &\int_{\pi-\phi_1}^{\pi+\phi_2} U_m \mu_2 \sin \phi \sin(k\phi) d\phi + \int_{\pi+\phi_2}^{2\pi-\phi_2} U_m \mu_1 \sin \phi \sin(k\phi) d\phi + \\
 &\left. \int_{2\pi-\phi_2}^{2\pi} U_m \mu_2 \sin \phi \sin(k\phi) d\phi \right] \quad (25)
 \end{aligned}$$

The equation (25) can be used to derive the amplitude of the various Fourier coefficients and the harmonic distortions.

The resolution of (25) for the third harmonic gives the harmonic gain Q_3 :

$$\begin{aligned}
 Q_3 &= \frac{1}{\pi U_m} [G U_m \mu_1 (\sin 2\phi_1 - \frac{\sin 4\phi_1}{2}) + G U_m (-\sin 2\phi_1 + \frac{\sin 4\phi_1}{2}) \\
 &+ \xi_2 (\frac{2}{3} U_{01} \cos 3\phi_1 + \frac{2}{3} U_{02} \cos 3\phi_2)] \quad \text{For}
 \end{aligned}$$

a symmetrical stabilization amplifier we have:

$$\begin{aligned}
 Q_3 &= \frac{1}{\pi U_m} [G U_m (\mu_1 - \mu_2) (\sin 2\phi_0 - \frac{\sin 4\phi_0}{2}) \\
 &+ \xi_2 (U_{01} \cos 3\phi_0)]
 \end{aligned}$$

By replacing $\xi_2 = \mu_1 - \mu_2$, we obtain the final expression of Q_3 :

$$Q_3 = \frac{\xi_2}{\pi U_m} [G U_m (\sin 2\phi_0 - \frac{\sin 4\phi_0}{2}) + U_m G \sin \phi_0 \cos 3\phi_0] \quad (26).$$

By the substitution of (3), (4) and (22) in (26) and after a trigonometric transformation, we derive the new simplest expression of the third harmonic

$$\text{gain: } Q_3 = \frac{G \xi_2}{\pi} [(1 - \delta^2) (4\delta^2 + \delta (1 - 4\delta^2))] \quad (27)$$

The equation (27) shows that the harmonic distortion depends directly on the stabilization damping ξ_2 . In fact, if the

stabilization parameter $\xi_2 \rightarrow 0$, the harmonic coefficient $Q_3 \rightarrow 0$. Otherwise, if $\xi_2 = 1$, the harmonic distortions will have its maximum value and the equation (27) can be reduced to $Q_3 = \frac{G\delta}{\pi} \gamma$ where $\gamma = (\sqrt{1-\delta^2}) < 1$.

VI. AMPLITUDE AND FREQUENCY RELATIVE INSTABILITY

The development of the equation (15) for the first harmonic, gives the following expression: $X + jY = 0$ (28). The real part of the equation (28) contains the amplitude U_m and can be put in the following form $X = f(y_1, y_2, \dots, U_m)$ (29).

The imaginary part of (28) contains the selective frequency ω_0 , that means $y = f(y_1, y_2, \dots, \omega_0)$ (30).

By developing equation (29) and (30) and according to [7], we can determine respectively the static stability of the amplitude

and that of the selective frequency: $\frac{\Delta U_m}{U_m} = \frac{\Delta U_0}{U_0} + k_0 \frac{\Delta R_{e2}}{R_{e2}}$

and $\frac{\Delta \omega_0}{\omega_0} = \frac{\Delta R}{R} + \frac{\Delta C}{C}$, where k_0 is constant.

We notice that the amplitude stability depends primarily on the reference voltage U_0 . Hence, the frequency stability is related to the oscillator network parameters.

VII. OSCILLATOR SETTING IN EQUATION AND EXPERIMENTAL RESULTS

The validation of these theories is applied on a quadrature oscillator. In fact, this last is used in the LVDT sensor [5], on the phase sensitive detector [9], in biomedical field, and in telecommunication for quadrature mixers.

Thus the stabilization amplifier of figure.3 is inserted upstream with a dual phase-shifting network and an amplifier inverter of phase π . They form together the quadrature oscillator of figure 7 which provides two output signals of identical phase φ_1 and φ_2 equal to $\frac{\pi}{2}$. If the condition $\varphi_1 + \varphi_2 + \pi = 0$ or 2π is carried out, we obtain a quadrature oscillator of a

frequency oscillation $f_0 = \frac{1}{2\pi RC}$.

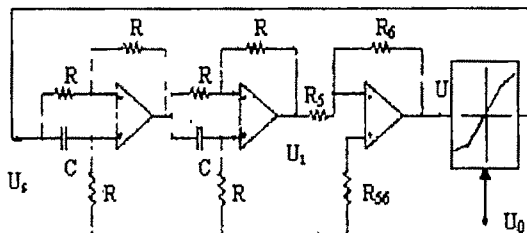


Fig.7 Circuit diagram of the controlled amplitude sine quadrature oscillator

The setting in equation of this oscillator gives:

$$\frac{U_i}{U_s} = \left[\frac{-1 + RC.p}{1 + RC.p} \right]^2 * \frac{-R_6}{R_5}$$

If $u_i = u_e$, we will have:

$$1 = \frac{-(-1 + p.RC)^2.R_6}{(1 + p.RC)^2.R_5} \quad (31)$$

$$\Rightarrow (1 + p.RC)^2.R_5 + (-1 + p.RC)^2.R_6 = 0$$

$$\Rightarrow (R_5 + R_6 - R_5.R^2.C^2.\omega^2 - R_6.R^2.C^2.\omega^2)$$

$$+ j(2.RC.R_5.\omega - 2.RC.R_6.\omega) = 0$$

$$\Rightarrow \{j(R_5 - R_6) = 0 \Rightarrow R_5 = R_6$$

$$\text{and } 1 - R^2.C^2.\omega^2 = 0 \text{ d'où } \omega = \frac{1}{RC}$$

For a frequency oscillation $f_0 = 1000\text{Hz}$ and with ε_1

parameter and $\varepsilon_2 = \frac{R_1}{R_3} = \frac{R_1}{R_4}$ we raise the characteristic

$U_m = f(U_0)$. This result is illustrated by the figure.8a. The least square modelling method gives an estimated linearity of 0.2% for the amplitude U_m versus the reference DC voltage U_0 . Hence, the resulting quadratic error due to the linearity oscillator is $Erq = 3\text{mV}$ for an amplitude range of $U_m = 6\text{V}$.

The amplitude of the sinusoidal signal is controlled by a DC precision voltage. In addition, the non linearity is ordered by a simple resistance. This offers a suitable choice of the oscillator's metrological parameters.

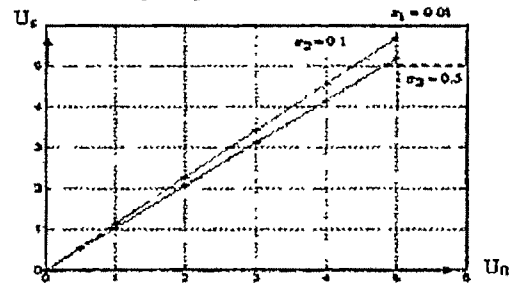


Fig.8a. Variation of the sine wave amplitude U_m versus U_0

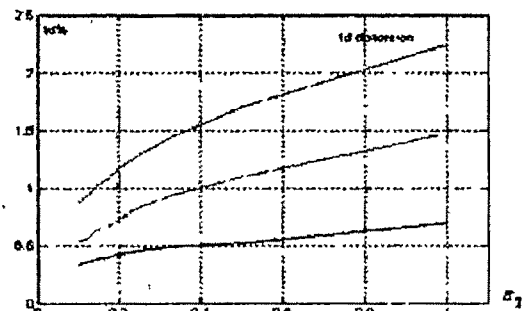


Fig.8b: Dependence of the distortion on the damping coefficient ε_2

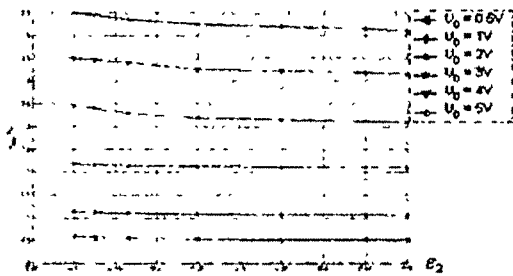


Fig.8c: Oscillator amplitude versus the damping parameter

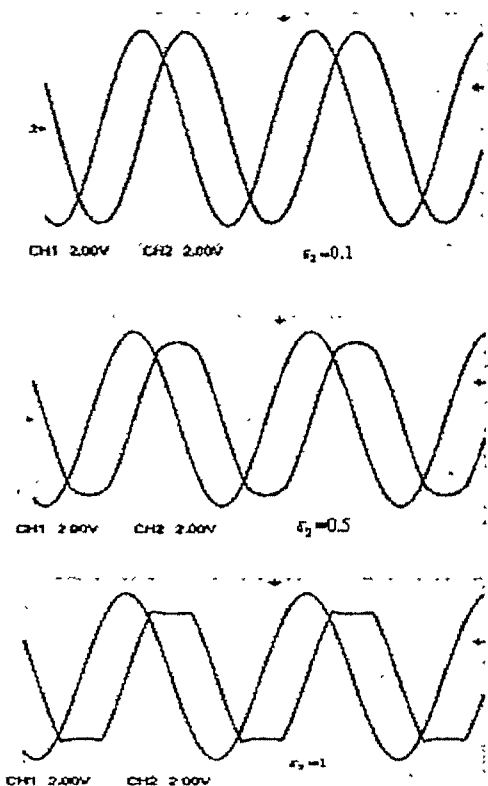


Fig.9: Signal waveforms generated by the quadrature oscillator for different ϵ_2

The variation of U_m depends linearly on U_0 , but it is stabilized by ϵ_2 . Its maximum value exceeds U_0 slightly when ϵ_2 tends towards 1. This result is illustrated by the figure (8.a). The curves of figure 8.b represent the harmonic distortions t_d versus the stabilization damping. Naturally this rate depends on ϵ_2 . If this parameter tightens towards limit 1, the distortions stabilize with their maximum. In addition, if ϵ_2 tends towards 0, the shape of the signal tends towards a

pure sinusoid. Unfortunately the stabilization ratio δ does not contribute, in this case, efficiently to the amplitude stability.

The stabilization ratio δ and the harmonic distortions t_d are antagonistic.

The figure (8.c) represents the variations of U_m according to the parameter of stabilization ϵ_2 . It is noticed that the stabilization ratio $\delta \rightarrow 1$ when $\epsilon_2 \rightarrow 1$ and the amplitude U_m is well controlled.

VIII. CONCLUSIONS

We have presented an amplitude stabilization model to determine the metrological parameters of the RC oscillator. The obtained results are exploited directly for a precise selection of the oscillator's behaviour.

The amplitude of the signal is controlled with a variable DC voltage, which gives a good amplitude static stability.

The experimental validation was made on an oscillator with squaring signal, since this last has a large application in the instrumentation field.

The measurements results, carried out on the quadratic oscillator, illustrate the good behaviour of the presented controlled amplifier model..

The presented nonlinear control element can be used in circuit design of various types of harmonic oscillators (Wien oscillator , shift oscillator.....). It can be put in monolithic integrated circuit. It is enough to associate some external resistances to it, a selective filter and an amplifier, to build finally RC oscillator with a known characteristics.

REFERENCES

- [1] E.P Popov, *Théorie appliquée au processus de contrôle dans les systèmes non linéaire* ISBN: 3314-185-166-73, Publication Nanka, 1973.
- [2] Christian Jaoun, Thèse de 3eme cycle, *contribution à l'étude des oscillateurs non linéaires à deux paramètres*, 1974 Université de Bretagne occidentale, France.
- [3] H. MECHERGUI, *Etude des sources sinusoïdales basses fréquence*, Thèse de 3ème cycle mai 1985 ENSET de Tunis
- [4] H.Mechergui et E. Ben Braiek *Générateur programmable asservie en amplitude JTEA de Sousse 1990* ,
- [5] Moheddine ben Ammar, *Development of instrumentation Incorporating solid state gas sensor Middlesex Polytechnic London. For measurement of oxygen partial*, Thesis for degree of doctor and Philosophy, April 1991
- [6] Raph Holzel, , A Simple Wide Band sine wave quadrature oscillator, *IEEE transactions on instrumentation & measurement*, vol, 42, no 3, June 1993.
- [7] I STANTCHEV, *électroniques analogiques des appareils de mesure*, Université Technique de Sofia, 1994 (ISBN 954-438-094-9) on *instrumentation & measurement*, vol, 42, no 3, June 1993.
- [8] Clay S Turner, *Recursive Discrete -Time Sinusoidal Oscillators*, *IEE Signal Processing Magazine* 1053-5888/03/-May 2003.IEEE.
- [9] A. Haddouk, *Détection synchrone. Application dans l'instrumentation*, maîtrise - ESSTT octobre 2005.
- [10] H. Mechergui, "Operational Amplifier Phase Error on the Wien Bridge Oscillator Behaviour" The 5th WSEAS International Conference on *CIRCUITS, SYSTEMS, ELECTRONICS, CONTROL & SIGNAL PROCESSING*, Miami, Florida, November 1-3, 2006
- [11] K. Aouissa, *Etude des caractéristiques métrologiques des sources de mesures en alternatif*, Mastère - ESSTT Janvier 2007

Quality Control In Distributed Software Systems

Rusakov M.A.

Siberian Federal University, 660074, Russia, Krasnoyarsk, ul. Klenakogo, 26 e-mail: mrusakov@gmail.com

Abstract-This paper views one of the most important aspects of the software quality – the software reliability. It proposes the simplified architectural software reliability model that can be used for measuring the reliability parameters of the software architecture. It uses the well known in Russia distributed software system for business management “Galaxy” as an example.

Key words-Distributed software application, galaxy, software architecture reliability, software quality.

1 INTRODUCTION

THE main characteristic of any software system is quality. However the software quality is a complex value and often it cannot be measured unambiguously.

There are series of characteristics in concept of software quality and reliability, and these series can vary by purposes of using the software system. There are some of them: downtime, transaction reliability, keeping of data integrity, familiar user interface, response time while processing a huge amount of data and many other characteristics [1].

With all these characteristics, some of them, like downtime, can be easily measured, but some of them, like a user friendly level, in most cases, are subjective value.

However, quite often the user unfriendliness causes many human errors¹ and, as an effect, negatively affects the software reliability characteristic and reduces the software quality in general. Since using a certain abstraction level, we can treat software-user as an architectural component, and we can refer human errors to software architectural component errors. All these factors can affect software reliability.

As long as software reliability is an integral part of software quality value, attention will be focused on this characteristic.

In the work it is suggested to estimate the reliability of software architecture (including all architecturally linked components) by the example of well known distributed client-server business management system called “Galaxy” (it has

distributed modular structure and at the same time it uses common global database for the whole business managed by various RDBMS like Pervasive SQL, MS SQL, Oracle) [2], [3].

The typical features of most distributed client-server software systems are remoteness and heterogeneity of software components. And software architects should take into their account series of specific peculiarities. First of all, this is the dependence of software architecture model from series of nonfunctional system requirement such as productivity, protectability, safety, reliability.

In such systems client software and server software are not only installed on different many miles distanced computers connected via local network or Internet, but usually different components work in different operational environment and under various operating systems simultaneously. That is why the subject of software architecture reliability analysis of such software systems has high scientific and practical interest.

The distributed software system architecture analysis is important for data loss prevention in a software system. Data gathering and data storing are very expensive procedures (more often information costs are much higher than a computer system that handles this information). The suggested procedures of software architecture analysis allow preventing excessive data duplicating (for data loss averting due to software system failure in the future) as early as architecture is designed and avoid unnecessary efforts and financial expenditures.

The analysis of the architecture of the distributed business management system “Galaxy” is the one from most important parts while developing software systems of this class. In the source [4] this problem is mentioned as a most critical problem of design and development of such systems.

The architecture of the software system “Galaxy” can be divided into the following layers:

- interface layer (client part of the software);
- business-logic layer (server part of the software);
- database layer (server part of the software).

It is suggested to use the modified model from source [5] for estimating the reliability of the software architecture. In the context of this model for the estimating software

¹ For example unfamiliar or complicated user interface can force user to type data into a wrong field or to forget mark a checkbox.

architecture reliability we use the following parameters and notation (please note that component parameters are used separately for each architecture level).

II.PARAMETERS AND NOTATION

M	number of architecture levels;
F	the total number of architecture components;
N_i	the total number of components on the certain number $i \in \{1, \dots, M\}$;
D_i	non-overlapping set of components on the level i , $i \in \{1, \dots, M\}$;
R_i	the reliability coefficient for component i , $i \in \{1, \dots, F\}$;
PU_i	using probability for component i , $i \in \{1, \dots, F\}$;
PF_i	failure probability for component i , $i \in \{1, \dots, F\}$;
PL_{ij}	conditional probability of failure in component i when component j fails, $i \in \{1, \dots, F\}$, $j \in \{1, \dots, F\}$;
TA_i	comparative access time to the component i , $i \in \{1, \dots, F\}$;
TC_i	comparative failure analysis time for the component i , $i \in \{1, \dots, F\}$;
TE_i	comparative recovery time for component i , $i \in \{1, \dots, F\}$;
TU_i	comparative using time for component i , $i \in \{1, \dots, F\}$;
TR	average system downtime;
MTTF	(mean time to failure) average time to the next failure;
S	readiness coefficient;
R_s	reliability coefficient.

For the described case of the architecture reliability analysis of the distributed software "Galaxy" we have the following parameters:

$M = 3$;
 N_1 – number of components on the first layer;
 N_2 – number of components on the second layer;
 $N_3 = 1$ (DBMS is considered as a single separate component);
 D_1 and D_2 – non-overlapping sets of components on the levels 1 and 2;
 D_3 – consists of a single component – DBMS;
 R_i – reliability coefficients of each architecture component (DBMS reliability coefficient is a part of this set as well);
 TC_i and TE_i – for each i are zero (because failure analysis and failure recovery are not implemented in the system);
 TA_i and TU_i – can vary for different components (these parameters depend on the communication speed).

While analyzing the distributed software architecture reliability it is necessary to take into account interrelationship of various components, i.e. one component failure may cause the failure of another component. Used characteristics allow to estimate faultness and efficiency of distributed client-server software for business management.

The average system downtime (TR) in the software architecture depends on both conditional and unconditional failure probabilities on all architecture levels and on average access time, analysis time and recovery time of failed components [6]. In the suggested model the failure elimination

time on the DBMS level is equal to access, analysis and recovery times. It means that the recovery time is less than failure elimination time.

If a component uses automatic failure elimination and it does not contain a failure, we will treat this component as recovered. At the same time, the newly generated failure of the previous type will be treat as the new failure.

The average system downtime (TR) is calculated for all three architecture levels and for each component on these levels. For each detailed architecture level in the software architecture the using probability of each component is multiplied to the failure probability of the component and then to the sum of average analysis, access and recovery time for the component. In addition, the failed component can cause a failure of dependent components both on the same and different architecture levels. Therefore for each architecture level and for all components the conditional probability of failure multiplies to the sum of comparative access, failure analysis and recovery time of these components. For one level and for each component conditional probability of failure multiplies to the sum of comparative access, failure analysis and recovery time as well.

The comparative analysis and recovery time for the described model are valid only for DBMS level. These time characteristics are considered as equal to zero for the rest components.

One of a series of average system downtime calculation methods is represented in [4]. There is the expression for calculating average time to the next failure (MTTF) in [4] and in [7]. This expression depends both on conditional and unconditional failure possibilities of all components on all architecture layers and on comparative using time of components without failure. The average failure time is calculated for each component on each architecture level. For each software architecture level the using possibility of a component is multiplied to the possibility that each component will work without a failure during the comparative using time of this component. In addition, for each separate architecture layer and for all components the conditional faultless possibility is multiplied to comparative using time of this component. The level without any failure also affects on the average time to the next failure value.

According to [8], the readiness coefficient can be calculated using the following expression:

$$S = MTTF / (MTTF + TR). \quad (1)$$

The reliability coefficient of the distributed software "Galaxy" can be estimated using the following expression:

$$R_s = \sum_{i=1}^F PU_i \times R_i. \quad (2)$$

It is often can be effective for the architecture reliability analysis of real client-server software for business management to use reductive expressions for calculating average system downtime and average time to the next failure. These parameters can be used for measurement and analysis of the software quality. So the expressions will look as the following:

$$\begin{aligned}
 TR = & \sum_{i=1}^F [PU_i \times PF_i \times [TA_i + \\
 & + \sum_{j=1, j \neq i}^F [PL_{ji} \times [TA_j]]]] + \quad ; \quad (3) \\
 & + PU_s \times PF_s \times [(TA_s + TC_s + TE_s) + \\
 & + [PL_{ss} \times [(TA_s + TC_s + TE_s)]]]
 \end{aligned}$$

$$\begin{aligned}
 MTTF = & \sum_{i=1}^F [PU_i \times (1 - PF_i) \times [TU_i + \\
 & + \sum_{j=1, j \neq i}^F [(1 - PL_{ji}) \times TU_j]]] \quad . \quad (4)
 \end{aligned}$$

The expressions above look more rough in compare to the original ones from [7]. However they can be successfully used for express analysis reliability characteristics and quality of the distributed business management software "Galaxy" while estimating certain parameters.

As it was mentioned above, the analysis of the system architecture realized as client-server software and modeled as a distributed set of services, provided by server for client processes is very important for preventing data loss in the complex business management software.

The described set of characteristics used for software reliability and quality measurement may be adjusted because the software architect may determine most suitable parameters and characteristics for the particular software system taking into account system type and area of using. Furthermore, it is possible to use various characteristics for different software systems.

REFERENCES

- [1] Kovalev I.V., Junusov R.V. Multiversion method of developing faultless software architectures for management and control critical technical objects // Science series MIFI-2002 Science-technical conference "Science, innovations and collaboration". Collection of scientific results in 3 parts. Part 2, Moscow, MIFI 2002, pages 151-152
- [2] Oracle Education. "Introduction into Oracle SQL and PL/SQL", volume 1, edition 1.1
- [3] Oracle Education. "Introduction into Oracle: SQL and PL/SQL", volume 2, edition 1.1

- [4] Coulouris G., Dollimore J et al. Distributed Systems: Concepts and Design.- Wokingham: Addison-Wesley, 1994.
- [5] Junusov R.V. Reliability estimation model for guarantor-able software architecture NIISUVPT collection Krasnoyarsk: NIISUVPT, 2001, #7, pages 194-208.
- [6] Sommerville, Ian, Software Engineering, 6th Edition, Russian translation. Moscow: Williams, 2002
- [7] Kovalev I.V., Multiversion method of software reliability increasing of information and telecommunication technologies in corporations / I.V. Kovalev, R.V. Junusov// Telecommunications and informatization of education. #2 (15) March-April. 2003 pages 50-55.
- [8] Cherkesov G.N. The reliability of software-hardware complexes University-book. Saint-Petersburg: Piter, 2005

An Efficient Architecture of Low Density Parity Check Code Decoder

P A Saheeda¹, Preethisree. G²,

¹ ECE Department, College of Engineering Trivandrum, Kerala, e-mail: passaheeda@yahoo.com

² ECE Department, College of Engineering Trivandrum, Kerala, e-mail: preethisree@gmail.com

Abstract— Low Density Parity Check (LDPC) codes have become very popular in recent times due to their capacity approaching performance and are considered in the next generation digital video broadcasting DVB-S2 standard. This paper presents a new architecture for the LDPC Decoder which results in reduced Hardware complexity. In the proposed method, we reduce the computations in the Check node computation unit. The proposed method can achieve same BER performance with a reduction in the Hardware complexity.

Key words— Dual diagonal matrix, Low Density Parity Check Code, Log BP Algorithm, Partly parallel architecture.

I. INTRODUCTION

Low-Density Parity-Check (LDPC) codes are one of the best performing channel codes known today. Invented by Gallager in 1962 [1], they were almost forgotten for nearly 30 years. Rediscovered by MacKay in the mid-90s and enhanced to irregular LDPC codes by Richardson et. al. in 2001, they are now to be used for forward error correction in a vast number of upcoming standards like DVBS2, WiMax IEEE802.16e), and wireless LAN (IEEE 802.11n). Providing very high decoding throughput and outstanding communications performance, they will probably become the channel coding scheme of choice for years to come. Major competitors to LDPC codes are Turbo codes which are already applied in the current UMTS standard.

An LDPC code is typically represented by a bipartite graph, usually called Tanner graph,[2] in which one set of N variable

nodes corresponds to the set of codeword, another set of M check nodes corresponds to the set of parity-check constraints and each edge corresponds to a nonzero entry in the parity-check matrix H . An LDPC code is known as (j, k) -regular LDPC code if each variable node has the degree of j and each check node has the degree of k , or in its parity-check matrix each column and each row have j and k nonzero entries, respectively. The code rate of a (j, k) -regular LDPC code is $1 - j/k$ provided that the parity check matrix has full rank. The construction of LDPC codes is typically random. LDPC codes can be effectively decoded by the iterative belief-propagation (BP) algorithm or the sum product algorithm that, as illustrated in Fig. 1, directly matches the Tanner graph. Decoding messages are iteratively computed on each variable node and check node and exchanged through the edges between the neighboring nodes.

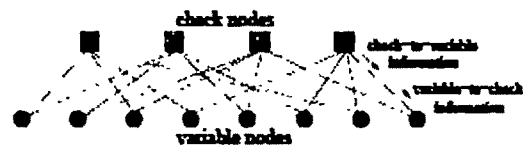


Fig: 1 Tanner Graph Representation of H Matrix and the decoding Message Flow

II. LDPC DECODING ALGORITHM

For hardware implementation, the BP algorithms are often reformulated as the Log-BP algorithms [3] in which multiplication operations are converted to addition operations to decrease the computational complexity. In the following, γ_i represents the log-likelihood ratio (LLR) messages exchanged between variable nodes and check nodes, and stands for intrinsic probability for every bit from a demodulator. The

LDPC decoding algorithm can be summarized in the following four major steps.

1) Initialization

All variables nodes and their outgoing variable messages are initialized to the values of the intrinsic messages. The intrinsic message is defined as

$$\gamma_i = \log \left[\frac{P(x_i = 0 | y_i)}{P(x_i = 1 | y_i)} \right] \quad (1)$$

Here, y_i is the received symbol and x_i is the transmitted symbol.

2) Check-Node Computation

After the incoming messages are gathered in each check node from its connected variable nodes in the Tanner graph, the following check-node computation is performed:

$$\mu_{cv} = \text{sgn} \left(\prod_{j=1}^{d_c-1} \mu_{v,jc} \right) \psi^{-1} \left(\sum_{j=1}^{d_c-1} \psi(\mu_{v,jc}) \right) \quad (2)$$

Here, d_c is the degree of the check node C , $\mu_{v,jc}$ represents the incoming message from neighbor variable node $V_j \neq V$ to check node C , and μ_{cv} is the outgoing message from check node C . Function ψ is equal to ψ^{-1} , and is expressed in the following equation:

$$\psi(x) = \psi^{-1}(x) = \log \left(\frac{1 + \exp(-|x|)}{1 - \exp(-|x|)} \right) \quad (3)$$

After the check-node computation, the outgoing messages are passed to variable nodes along the edges.

3) Variable-Node Computation

The variable-node computation is expressed as follows:

$$\mu_{vc} = \sum_{i=0}^{d_v-1} \mu_{c_i v} \quad (4)$$

where $\mu_{c_i v}$ is the incoming message from the neighbor check node $C_j \neq C$ to variable node V and μ_{vc} is the number of check nodes connected to V , and is the outgoing message from variable node V .

4) Check Stop Criterion

When the variable-node computation is finished, the LLR of every symbol is updated as

$$\lambda_i = \gamma_i + \sum_{i=0}^{d_v-1} \mu_{c_i v} \quad (5)$$

From the updated LLR vector $\lambda = \{\lambda_1, \lambda_2, \dots, \lambda_{i1}, \dots, \lambda_N\}$, a hard decision result $X = \{x_1, x_2, \dots, x_i, \dots, x_N\}$ is calculated as

$$x_i = \begin{cases} 1, & \text{if } \lambda_i \leq 0 \\ 0, & \text{if } \lambda_i > 0 \end{cases}$$

We call μ_{vc} and μ_{cv} in the above algorithm are extrinsic messages, γ_i is the intrinsic message. It is clear that each decoding iteration can be performed in fully parallel by physically mapping each check node to one individual Check Node processing Unit (CNU) and each variable node to one individual Variable Node processing Unit (VNU).

III. PARITY-CHECK MATRIX DESIGN

LDPC codes are linear block codes with sparse parity-check matrices. The H matrix designed consists of two parts Hr and Hd. The Hr part is randomly generated and consists of array of square block matrices, where each block matrix is either a zero matrix or a permuted identity matrix [4]. The Hd part is deterministic and has the form of a dual diagonal matrix as shown in fig 2.

$$\text{Hd} = \begin{bmatrix} 1 & & & & & & \\ & 1 & 1 & & & & \\ & & 1 & 1 & & & \\ & & & 1 & 1 & & \\ & & & & 1 & 1 & \\ & & & & & 1 & 1 \\ & & & & & & 1 & 1 \end{bmatrix}$$

Fig: 2 Dual Diagonal Matrix

Our motivation for choosing the parity-check matrix in this form has three parts.[6] First, it leads to a very practical method of encoding, ie, the parity-check matrix is sufficient to achieve encoding without having to generate a large, non sparse generator matrix with a quadratic encoding complexity. Second, a certain number of bit nodes of degree 2 improve the

code's performance. Grouping those bit nodes in a structured way under the sub matrix makes an easy implementation. Third, the staircase format of the sub matrix guarantees that no short cycle composed of only degree-2 bit nodes exists, which improves the performance.

The Hr matrix is generated by using bit filling algorithm. First a base matrix $M_b \times N_b$ is generated. The base matrix is then expanded by replacing each 0 with $(L \times L)$ zero sub matrix and the 1's with Permuted $(L \times L)$ identity matrix. Let T denote the right cyclic shift operator where $T^u(q)$ right cyclic shifting matrix q by u columns, then the permutation is given by $P_{x,y} = T^u(I)$, where $u = (x-1)y \bmod L$. The matrix generated by the bit filling algorithm has a large girth, which is a standard of good error correcting capability

IV. PARTIALLY PARALLEL DECODER STRUCTURE

Partially parallel decoder structure are originally proposed by Zhang et al. Partially parallel decoder realizes message passing by mapping a certain number of variable nodes or check nodes to a single hardware unit in time-division multiplexed mode. In this paper with this new design methodology we developed a regular LDPC code partly parallel architecture. Since the H matrix consists of cyclically shifted block matrix and dual diagonal matrix it is called a hybrid H matrix. Since we are using partly parallel architecture the number of check node computation unit (CNU) and variable node computation unit (VNU) are M_b and N_b respectively [7].

This decoder performs decoding iteration in $2L$ clock cycles. During the first L clock cycle it works in the check node processing mode and in the second clock cycle it works in the variable node processing mode. All the extrinsic and intrinsic messages are all quantized to 5 bits to optimize for the hardware complexity and are represented in sign magnitude form. Each processing unit consists of RAM blocks to store the Extrinsic and Intrinsic messages.

A. Check Node Computation Unit (CNU)

The CNU performs the computation of all the check nodes and realizes the extrinsic data exchange between all the neighboring nodes. The calculation of the non linear function

$\psi(x) = \ln\left(\frac{1+e^{-|x|}}{1-e^{-|x|}}\right)$ in the log BP algorithm requires the implementation of LUT, which will increase the hardware complexity. The log function can be written as $\ln\left(\frac{1+e^{-|x|}}{1-e^{-|x|}}\right) = -1 * \ln\left(\frac{1-e^{|x|}}{1-e^{-|x|}}\right)$. The function has very small values when x is large as shown in fig 3. The function is affected by the x value with smallest magnitude [4]. But taking only the smallest magnitude will cause performance loss. Therefore in the proposed architecture we take only 'k' smallest LLR values for check node computation..

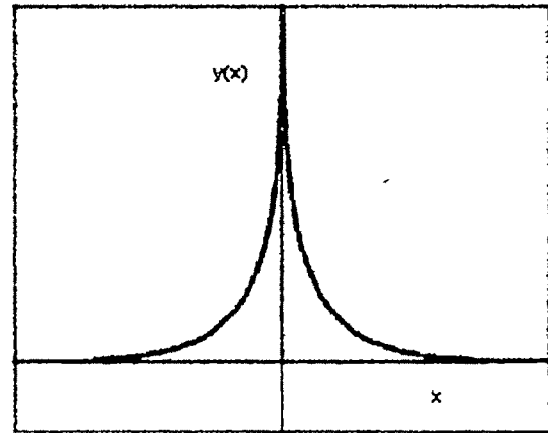


Fig: 3 Plot Of $\psi(x)$

Since each check node is connected to only 6 variable nodes, we take the smallest 3 values. Each CNU reads the extrinsic message from each variable node and finds the smallest values and calculates the check to variable extrinsic message and passed the values to each of the variable nodes. Since all the extrinsic messages are represented in sign magnitude form we take only the magnitude value for finding the smallest values and then for the calculation of the check to variable messages. Here we are taking only half of the messages values for computation which will provide with a very much reduction in the Hardware requirement. The sign value is obtained by XOR-ing all the sign bits of the messages. The check node architecture is shown in fig 4.

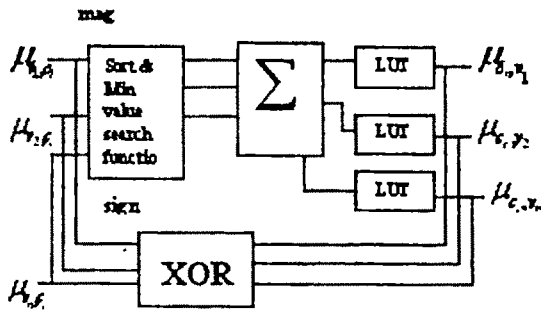


Fig4: Check node unit architecture

B. Variable Node Computation Unit (VNU)

Compared with the check node processing the operations performed in the variable node computation unit is simple, since the decoder only need to carry out all the variable node computation. The VNU reads the check to variable node extrinsic message from the Ram block and calculates the variable to check extrinsic message. Since the extrinsic messages are stored in sign magnitude format it is converted to Two's complement form to perform the addition and then converted back to sign magnitude form. The variable node architecture is shown in fig 5.

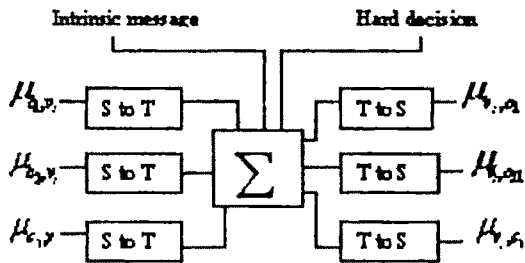


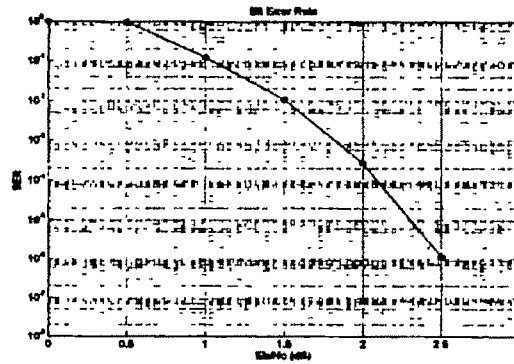
Fig 5: Variable Node Architecture.

S to T – Sign Magnitude to Two's complement

T to S – Two's complement to Sign Magnitude

V. Si

All designs have been described in VHDL. As functional verification and simulation tool, ModelSim has been employed along with Xilinx ISE8.1i. The simulation results shows that no performance loss is incurred due to the reduction in the check node computation



VI. ACKNOWLEDGMENT

Our foremost thanks go to our Head of the department Dr. Sukesh Kumar. We thank him for his patience and encouragement. His insightful suggestions and knowledgeable discussions are always our great help. S. B. Author thanks Dr. M R Baiju, Prof. J David for their valuable feedback. Finally, we thank our parents; their love is always our strength.

REFERENCES

- [1] R.G Gallager " Low Density Parity Check Codes" IRE Trans. Inform. Theory, Jan 1962
- [2] Tong Zhang, Keshab K. Parhi, " An FPGA Implementation of (3,6) regular Low Density Parity Check Code Decoder " EURASIP Journal of Applied Signal Processing 2003.
- [3] Lei Yang, Hui Liu, C. J Richard shi, " code construction and fpga implementation of a Low error floor multi rate Low Density Parity Check Code Decoder" IEEE Transactions on Circuits and Systems, April 2006.
- [4] Chan Ho Lee, " Design of Encoder and Decoder for LDPC Codes Using Hybrid H Matrix". ETRI Journal October 2005.
- [5] M. Girish Chandra, Harihara S. g. B. Adiga, Balamuralidhar, P.S. Subramanian, " Effect of Ckeck Node Processing on the Performance of Message Passing Algorithm in the context of LDPC Decoding for DVB-S2"IEEE 2005.
- [6] Todd K. Moon "Error correction coding - Mathematical Methods and Algorithm"
- [7] Hao Zhong, Tong Zhang " Design of VLSI Implementation oriented LDPC Codes" Ieee vehicular Technology conference 2003[7]
- [8] K.C Chang "Digital Systems design with VHDL and Synthesis"

VLSI Architecture for Implementing Hearing Aid Algorithms

P A Saheeda¹, Reena M Roy²,

¹ ECE Department, College of Engineering Trivandrum, Kerala, e-mail: pasaeeda@yahoo.com

² ECE Department, College of Engineering Trivandrum, Kerala, e-mail: reena_m_roy@yahoo.co.in

Abstract— The design of an effective hearing aid is a challenging problem because of the nature of the impaired ear. The recent development of commercial hearing aids with digital signal processing capabilities has allowed the development of advanced signal processing techniques to aid the hearing impaired. This paper discusses the processing required for digital hearing aids and the architecture suitable for its implementation. The processing includes frequency shaping, adaptive noise reduction and amplitude compression. The basic constraints encountered in the design of hearing aids are low power consumption, small size and programmability of the device to suit the individual requirements. The choice of architecture has a major effect on device power consumption. The biggest gain in power reduction can be achieved by operating the circuitry at the lowest supply voltage, at the lowest possible speed while still meeting system throughput requirements. Thus, on an architecture level, concurrency and parallelism should be used as well as pipelining the data path. Arithmetic operations can be done by choosing a suitable number representation and by selecting an appropriate architecture. The proposed work discusses the design of FPGA based architecture for implementing the algorithms for hearing aid.

Key words— amplitude compression, fpga, frequency shaping, hearing aids.

I. INTRODUCTION

IMPAIRED hearing in most cases is the result of damage to the sensorineural cells of the cochlea. Loss of cell function widens the sharply tuned neural response, which reduces the sensitivity and signal processing capacity of the ear. Conventional aids only compensate for loss of sensitivity and compress the signal to fit within the reduced dynamic range of the impaired ear. Unfortunately, there is a sizable population of the hearing-impaired who cannot benefit from this simple approach. It is clear that to satisfy the needs of this group, new and better designs are required. The goal is to improve users speech understanding and listening comfort and to improve the convenience of device use.

II. WHY FPGA?

The demand for portable and embedded digital signal processing systems has increased dramatically. Hearing aid is an application of such a system with stringent constraints such as area, speed and power consumption. This requires an implementation that meets these constraints with the shortest time to market. The possible implementations that can be used range from an ASIC custom chip, general purpose processor to DSP Processors. The first choice could provide the solution that meets all the hard constraints but it lacks the flexibility that exists in the other two. Also its design cycle is much longer. Using programmable devices (like FPGAs) for DSP applications could narrow the gap between the flexibility of general-purpose processor and programmable DSP processors and the high performance of dedicated hardware using ASIC technology. The availability of hard/soft core processors in modern FPGAs allow moving DSP algorithms written for general purpose processor or DSP processors to FPGAs using the core processors. A more efficient and more complex alternative is to convert the complete algorithm into hardware.

III. SPEECH PROCESSING ALGORITHMS

A. Frequency shaping

Sensorineural loss is characterized by a loss of sensitivity to sounds that varies with signal level and frequency[1]. Speech processing for hearing impaired can be used to separate the high and low frequencies and improve speech comprehension and listening comfort. This requires a gain adjustment that is both level dependant as well as multifrequency dependant. In the frequency shaping algorithm the frequency range with severe hearing loss is applied a high gain and the gain for other frequency bands are given according to the loss in that band.

First the frequency-shaping algorithm is simulated using Matlab. The input signal is split into 16 frequency bands. At a sampling frequency of 16 KHz, the resulting bands are 500Hz wide. To achieve sufficient frequency resolution at low frequencies, a uniform filter bank requires a large number of bands.

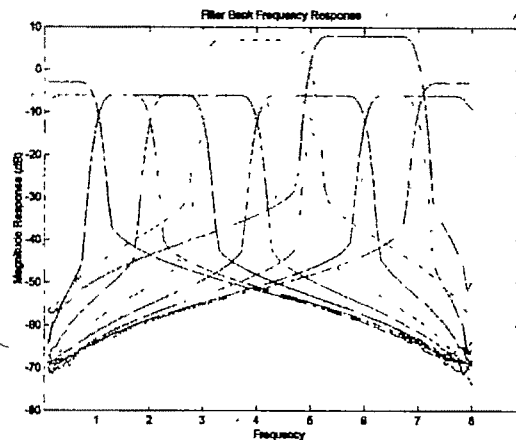


Fig1. The Magnitude response designed to compensate for a subjects hearing loss

The fig 1 shows the magnitude response designed to compensate for a hearing impaired persons hearing loss. This patient has high hearing inability in the frequency range 2 kHz to 2.5 kHz, where a high gain is applied. Similarly a low loss in hearing in the frequency ranges 1.5 kHz to 2 kHz where a low gain is applied.

B. Amplitude Compression

Amplitude compression is also an essential task for a hearing aid. It is used for controlling the overall gain of speech amplification system. It essentially maps the dynamic range of the acoustic environment to the restricted dynamic range of the hearing impaired listener. The threshold level of hearing and the saturation level of speech vary for different frequency bands in the case of hearing impaired persons. Applying the amplitude compression technique in different frequency bands makes the person hear better as in each band the thresholds and saturation levels are considered.

IV. FILTER BANK DESIGN

Assuming that the filter bank consists of high pass and low pass filters (more number of filters can be added) with only the coefficients being different. Here down sampling by a factor two is used. The purpose of the down sampler is to discard every second sample. Through careful design, the down sampler can be removed entirely by the simple means of not calculating the values that would be discarded by the down sampler. This leaves the filter element as the only required element and reduces by one half the total number of multiplications that must occur in each filter. The filter element is made up of some form and number of multipliers, and some form and number of adders that sum the results of the multipliers [3]. In addition, since the full operation cannot be completed in one clock cycle, some type of register or delay element must be used in a practical design, resulting in a pipelined data flow through the filter.

Pipelined FIR filter architecture is shown in fig2, which consists of 6 tap and 6 input samples. S0,S1.....S5 are 18 bit input samples. c1,c2....c6 are 18 bit filter coefficients obtained from mat lab. The circles indicate multipliers. The squares

indicate 36-bit by 36-bit adder units (i, j and k). Each component is designed to complete its operation in one clock cycle. Here single clock multiplier is used. By using the RLOC attribute in VHDL, physical location of input registers relative to the multiplier elements is assigned. Multiplier itself is a dedicated logic device physically located between the configurable logic block (CLB) in FPGA [4]. Adders are invoked in VHDL using a single line code $Sum = I_1 + I_2$. The adder unit i completes its operation in the same clock cycle, j in the next same clock cycle and k in the next same clock cycle. In order to obtain pipelining, registers named Dly are used. The number system used is a variable length fixed point numbering scheme using signed binary arithmetic operations on signed binary values. The design accounts for overflow conditions in multiplication operations but not in the addition operations.

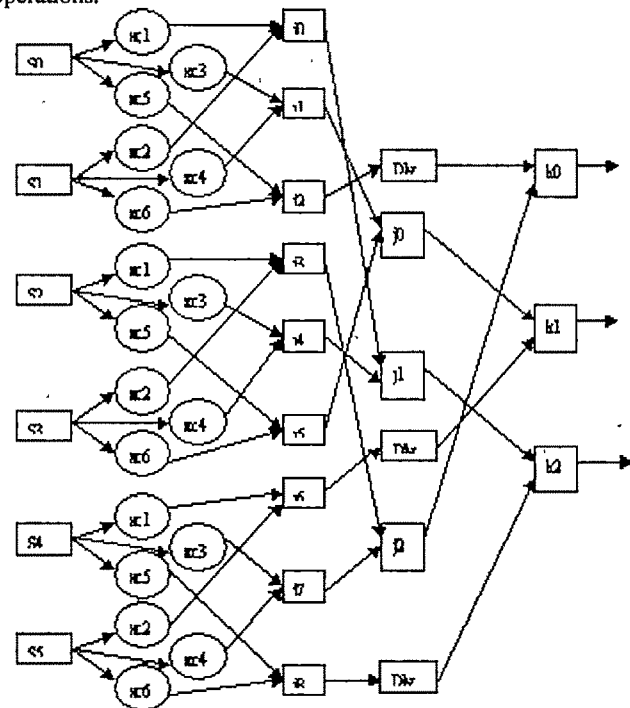


Fig. 2. Pipelined FIR Filter Architecture

V. SYNTHESIS AND SIMULATION

All designs have been coded in VHDL. As functional verification and simulation tool, ModelSim has been employed along with Xilinx ISE8.1i. Device utilization summary for frequency shaping algorithm is shown below.

Selected Device	: 2vp30ff896-6	
Number of Slices	: 2762 out of 13696	20%
Number of Slice Flip Flops	: 1296 out of 27392	4%
Number of 4 input LUTs	: 3564 out of 27392	3%
Number of Shift registers	: 2484	
Number of bonded IOBs	: 97 out of 556	17%
Number of MULT18X18s	: 36 out of 136	26%
Number of GCLKs	: 1 out of 16	6%

(Synthesis and simulation of amplitude compression algorithm is going on progress)

VI. ACKNOWLEDGMENT

Our foremost thanks go to our Head of the department Dr. Suresh Kumar. We thank him for his patience and encouragement. His insightful suggestions and knowledgeable discussions are always our great help. S. B. Author thanks Dr. M R Baiju, Prof. J David for their valuable feedback. Finally, we thank our parents; their love is always our strength.

REFERENCES

- [1] Trudy Stetzler, Neeraj Magotra, Pedro Gelabert, Preethi Kasthuri, Sridevi Bangalore, "Low -Power Real Time Programmable DSP Development Platform for digital Hearing aids.
- [2] Robert Brennan, Todd Schneider, "A Flexible Filter Bank Structure for Extensive Signal Manipulations in Digital Hearing Aids", 1998 IEEE
- [3] V. Pasham, A. Miller, K. Chapman, "Transposed Form FIR Filters," XilinxAPP219, Internet: <http://direct.xilinx.com/bvdocs/appnotes/xapp219.pdf>, October 25, 2001 [September 5, 2006].
- [4] M Adhiwiyogo, "Optimal Pipelining of I/O Ports of the Virtex-II Multiplier," Internet: <http://direct.xilinx.com/bvdocs/appnotes/xapp636.pdf>, March 23, 2005, [September 5, 2006].
- [5] Vaidyanathan, P.P., "Multirate Digital Filters, Filter Banks, Polyphase Networks, and Applications: A Tutorial," *Proc. IEEE*, Vol 78, No. 1, pp. 56-93, January 1990.
- [6] "Using Look-Up Tables as Shift Registers (SRL16) in Spartan-3 Generation FPGAs", Internet: <http://direct.xilinx.com/bvdocs/appnotes/xapp465.pdf>, May 20, 2005.
- [7] Nick Sawyer, "Data to Clock Phase Alignment", Xilinx XAPP225, Internet: <http://direct.xilinx.com/bvdocs/appnotes/xapp225.pdf>, April 19, 2007.

A Soft Computing Paradigm for Handwritten Digit Recognition with Application to Bangla Digits

Nibaran Das¹, Ram Sarkar², Subhadip Basu¹, Mahantapas Kundu¹, Mita Nasipuri¹, Dipak Kumar Basu¹

¹ Computer Sc. & Engg. Dept., Jadavpur University, Kolkata, India

² Computer Sc. & Engg. Dept., MCKV Institute of Engineering, Liluah, Howrah, India e-mail: nasipuri@vsnl.com

Abstract—A soft computing approach combining Genetic Algorithm (GA) and Artificial Neural Networks (ANN) is presented here for selection of an Optimal Combination of windows on the digit image, which when selected for extraction of shadow features produces an optimal recognition performance on samples of handwritten Bangla digits. Out of 16 overlapping windows used during experimentation, the technique selects an optimal combination of 11 windows producing a recognition rate of 93.4% by eliminating rest of the other windows having no significant effect on the recognition performance. The work establishes the excellence of soft computing paradigm in modeling intelligent computation related to automated pattern classification and can be extended to digits as well as characters of other scripts such as English, Hindi, Arabic etc

Keywords— Soft computing, GA, ANN, Intelligent computation, Pattern classification.

I. INTRODUCTION

SOFT computing approach, combining several novel models of computation, such as neural networks, fuzzy sets and systems, and genetic algorithms (GAs), is mainly devised to solve real world ill-defined, imprecisely formulated problems requiring huge computation [1]. Handwritten digit recognition is a typical example of one such problem. Machine recognition of handwritten digits requires modeling perceptual power or *cognitive capabilities* of human beings, at least to some extent, in identifying *handwritten digits* of varying shapes and sizes, caused by different handwriting

styles of different individuals. The problem is also *commercially important* as it is required for automatic pin code identification needed for automatic mail sorting, reading figures from bank cheques and filled in forms and so on.

To deal with the above problem in some of the previous works [2,3], the Multi Layer Perceptron (MLP), i.e., a *feed forward* model of the artificial neural network with *learning* and *generalization* abilities, was used as a *pattern classifier* along with *shadow* and other *features*, extracted after dividing a digit image through a number of *overlapping windows*. This was so as to include *local details* of a digit image in the *feature set* with greater details. Later it is found that all these windows are not required for achieving an optimal *recognition performance*. To find a selective combination of some of these windows so that the shadow features, when extracted from these windows, would produce an *optimal recognition performance* is *computationally intractable*. This motivates the use of Genetic Algorithm (GA) [4], i.e., an intelligent optimization algorithm free from chances of sticking to local minima, is used here for this purpose. More specifically speaking, a simple Genetic Algorithm (SGA) is used. For systematic selection of windows, each digit image is divided through 16 equal size overlapping windows under this work. An *Optimal Combination* of these windows usually does not contain all of them. Overlapping windows are used here to ensure that at least some of the contents of the features extracted from one windows, rejected from the optimal combination is included at the time of recognition with the features extracted from its selected overlapped counterpart.

For implementing the *fitness function* of the SGA, recognition performances are measured through MLP

classifiers trained with features extracted from various combinations of windows, i.e., the candidate combinations of various windows, represented with the *chromosomes* of each *population* of the GA.

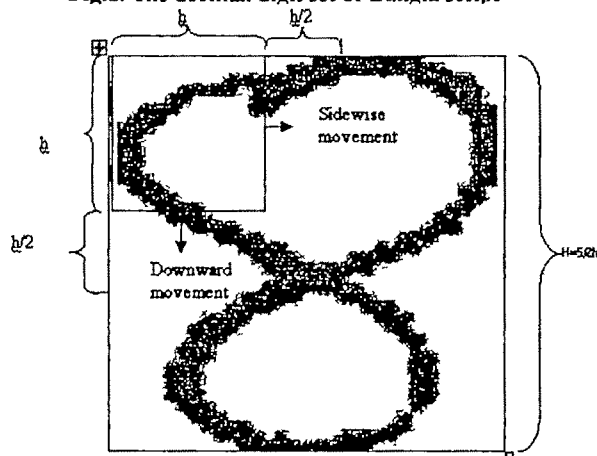
Bangla, digits from which script are used here for experimentation, is the second most popular script in Indian subcontinent. Popularity wise as a language, Bangla stands second in the Indian subcontinent and fifth in the world.

II. BANGLA DIGIT SET AND SHADOW FEATURES

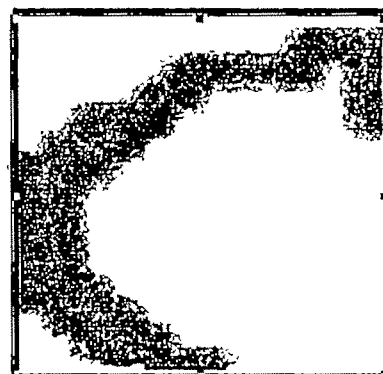
Typical digit patterns of first ten natural numbers (0 to 9) taken from 'Bangla' script are shown in Fig. 1. In this work, each digit image is divided through 16 equal size *overlapping windows*, containing different fragments of the digit image. How these overlapping windows are created is illustrated in Fig2 (a-c). The initially created window of size $h \times h$ is shown at the top left corner of the image frame in the said figure. After extracting features from the window, it is moved *downward* by a length of $h/2$ producing another window, having 50% *overlapping area* with that the previous window. After extracting features from this window, the process is repeated over the entire height of the

0	০	২	৩	৪
০	১	২	৩	৪
৫	৬	৭	৮	৯
৫	৬	৭	৮	৯

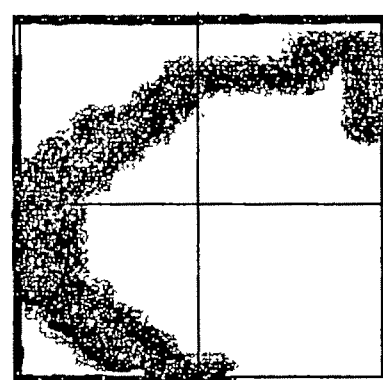
Fig.1. The decimal digit set of Bangla script



a. An illustration for production of overlapping windows on the digit image



b. a single window containing a fragment of a digit image of Fig 2. (a)



c. an illustration for simple shadow features

Fig 2. (a-c) An illustration for extraction of simple shadow features from overlapping windows

image frame resulting into a *vertical scan* of feature extraction. After *completion* of one such vertical scan, the window is moved *sidewise* along the top most horizontal side of the image frame again by a length of $h/2$ before extraction of features from it. Starting from this window again a vertical scan for feature extraction is performed to compute features from various overlapping windows created in this scanning process.

In this way, every vertical scan for feature extraction followed by a horizontal shift of the window along the top most side of the image frame is repeated until the entire image frame is traversed by this process. For the present work the value of h is considered as $2/5$ of the height of the

image frame. Considering digit images of size 32x32 Pixels, 16 overlapping windows are created for the present work. Before extracting shadow features from each such window, it is divided into 4 equal size rectangular regions as shown in Fig 2(c).

So each digit image is divided into 64 equal size overlapping rectangular regions before extraction of shadow features. From each of these rectangular regions, shadow features are computed by considering the lengths of horizontal and vertical projections of the image fragments therein on any two adjacent sides of the encompassing rectangle as shown in Fig 2(c). The shadow features considered here are basically simple shadow features as they are very small in numbers. But by dividing each of overlapping windows into 4 equal size rectangular regions, the total numbers of windows, from where shadow features are computed, is increased here by 4 times increasing the total number of shadow features extracted from a digit image to 128. Use of simple shadow features extracted from a combination of appropriately selected overlapping windows in large numbers may outperform the recognition rate obtained through selection of complex shadow features, i.e., more number of projections considering diagonals and the other two adjacent sides of the rectangles, from the entire image.

III SELECTION OF WINDOWS USING SGA

Selection of a combination of overlapping windows on a digit image, which when used for extraction of shadow features produces an optimal recognition performance, is performed here using SGA. In doing this, each candidate solution or chromosome is encoded with a 16 bit binary string, in which each bit corresponds to one of the 16 overlapping windows on a digit image. Each bit in the chromosome has a value 1 if the corresponding window is selected for feature extraction. Otherwise, it has a value 0. Initially a population of candidate solutions is created by randomly generating 20 chromosomes for SGA. After every iteration of SGA, the population size is kept fixed to 20 chromosomes here.

The fitness of each chromosome of the population thus created is measured by obtaining the recognition rate of an MLP classifier on the test samples, from which shadow features are extracted by considering a combination of overlapping windows, encoded by the chromosome. Prior to that, the MLP classifier is to be trained with the shadow features extracted from the training samples on the basis of the same combination of overlapping windows encoded by the same chromosome. For computing fitness values of all

the chromosomes of a population this process is to be repeated for each chromosome of the population.

After a population is evaluated on the basis of the fitness function, the stopping criterion of SGA is to be tested. In this work, the stopping criterion is reached either after 20 generations have passed or the average fitness value of the current population is greater than or equal to 98% of the maximum fitness value obtained so far.

Failing to reach the stopping criterion, a new population of more promising chromosomes, also called a generation, is to be reproduced from the existing population, in SGA. For this, 20 chromosomes are selected here from the existing population using roulette wheel, weighted proportionally with the fitness values of the chromosomes of the existing population. Once a new population of 20 chromosomes is created in this way, 80% of the chromosomes are selected pair wise randomly from the population for performing crossover operation over them. The crossover point is selected at the middle of each chromosome here.

Once Crossover operation is completed, the current population is left with 16 chromosomes, undergoing crossover, plus 4 chromosomes, selected by roulette wheel method. Half of the chromosomes of this population is again randomly selected for mutation. The exact bit of a chromosome to be mutated is also selected randomly. In this way, a generation of population is reproduced from the old one, which is to be again evaluated to check if the stopping criterion is met. SGA is repeatedly executed in this way until the stopping criteria is reached.

IV. RESULTS AND DISCUSSION

To conduct experiments with the technique described so far, a database of 3000 samples of handwritten Bangla digits is prepared by collecting handwritten samples from people of different age groups, academic levels and sexes. The database consists of image samples of all 10 classes of digits in equal numbers.. By dividing the database in 2:1 ratio, training and test sets are formed. That is, the training set and the test set, used for this work, consist of 2000 samples and 1000 samples respectively.

With this training and test sets, SGA produces an Optimal Combination of 11 overlapping windows giving a recognition rate of 93.4%. The MLP classifiers used here for evaluating the fitness function of SGA by recognizing the test samples are each trained for 2000 iterations of back propagation learning algorithm with a learning rate of 0.8 and a momentum of 0.7.

By following the present technique, it has been possible to eliminate 5 windows having no significant effect on the recognition performance. It establishes the excellence of soft computing paradigm in modeling *intelligent computation* related to *automated pattern classification*. The work can be extended to digits as well as characters of other scripts such as English, Hindi, Arabic etc.

ACKNOWLEDGMENT

Authors are thankful to the "Center for Microprocessor Application for Training Education and Research", "Project on Storage Retrieval and Understanding of Video for Multimedia" of Computer Science & Engineering Department, Jadavpur University, for providing infrastructure facilities during progress of the work. Authors are also thankful to the CVPR Unit, ISI Kolkata, for providing the necessary dataset of handwritten Bengali Numerals. One of the authors, Mr. R Sarkar, is thankful to MCKV Institute of Engineering for kindly permitting him to carry on the research work.

REFERENCES

- [1] Sankar K. Pal, "Soft Computing: Goal, Tools and feasibility", IETE, Vol. 42, No. 4& 5, July-October 1996, p.p.195-204
- [2] S. Basu, C. Chaudhury, M. Kundu, M. Nasipuri, D. K. Basu, "A Two Pass Approach to Pattern Classification," N. R. Pal et.al. (Eds.), Lecture Notes in Computer Science, Vol. 3316, ICONIP, Nov-2004, Kolkata.
- [3] S. Basu, N. Das, R. Sarkar M. Kundu, M. Nasipuri, D. K. Basu, "An MLP based Approach for Recognition of Handwritten 'Bangla' Numerals," accepted for publication in Proc. 2nd Indian International Conference on Artificial Intelligence, Pune.
- [4] M. Srinivas et al., "Genetic algorithms: A Survey", IEEE Computer, p p. 17-26, June 1994

Efficient Nanodevices for Advanced Ultradense VLSI Systems

Subir Kumar Sarkar¹, T. Datta², Ankush Ghosh¹, J. C. Singh¹, G. Prakash³ and Debasis Samanta⁴

¹Dept. of Electronics and Telecommunication Engineering, Jadavpur University, Kolkata, e-mail: skarkar@etce.jdvu.ac.in

² Institute of Engineering and Management, Saltlake ³ Coorg Institute of Technology, South Coorg, Karnataka, ⁴ Indian Institute of Technology, Kharagpur

Abstract— With the emergence of mobile computing and communication devices, design and implementation of low energy VLSI systems have got a significant role to play in VLSI circuit design. The matter of power dissipation was less visible in the early VLSI design issues. But recently power dissipation has become the main design concern in several applications. However, power saving should be achieved without compromising high performance or minimum area, thereby creating a new design culture. As an attempt towards this, in the present work parallel back Propagation artificial neural networks are employed to optimize and predict the various system parameter of a GaN nanodevice so that the relevant device will exhibit better high frequency response and will be power efficient.

Key words— optimization, artificial neural networks, nanodevices, ultradense, scattering mechanism.

I. INTRODUCTION

The first “generation” of computer relied on vacuum tubes. Then came discrete semiconductor devices, followed by integral circuits. The first Small-Scale Integration (SSI) ICs had small number of devices on a single chip- diodes, transistors, resistors and capacitors (but no inductors) making it possible to fabricate one or more logic gates on a single device. The fourth generation consists of LSI i.e. system with at least a thousand logic gates. The natural successor to LSI is VLSI. Current technology has moved far past this mark and today’s microprocessors, which also are fabricated through VLSI, have many millions of individual transistors. During the course of the VLSI design cycle, circuit performance can usually be increased by design improvements, more rapidly in the beginning, then more gradually until the performance finally saturates for the particular design style and technology being used. The level of circuit performance, which can be reached within a certain design time strongly, depends on the

efficiency of the design methodologies, as well as on the design styles. The main objective, however, remains device minimization. Device minimization results in reduced unit cost per function and in improved performance. As a result, the cost per bit of memory chips has almost halved every two years for successive generation of random access memories.

Nanodevices have been the objects of intensive research during the last two decades [1,2]. Some of the devices have matured into commercially useful products and form part of modern electronic circuits. Some requires much further refinement, but have the promise of being useful commercially in the near future [3,4]. In nanodevices the channel length is comparable to the de Broglie wavelength so that a subband structure is developed allowing two-dimensional (sometimes one-dimensional) electronic transport parallel to the interfacial planes. Carrier mobility in such devices is particularly high at low temperatures [4].

In the present work parallel back propagation artificial neural networks (ANNs) are employed to optimize and predict the various system parameter of a GaN nanodevice so that the relevant device will exhibit better high frequency response and will be power efficient. Artificial Neural Networks are a computational tool having Artificial Intelligence origins. They are also called parallel distributed processing systems. They are intended for modeling the organizational principles of the central nervous system, with the hope that the biologically inspired computing capabilities of the ANN will allow the cognitive and tasks to be performed more easily and more satisfactorily than with conventional serial processors.

II. ANALYTICAL MODEL

In the present study we consider square quantum well of GaN of infinite barrier height as the semiconductor nanostructures. This approximation is valid because the band offset between the well and the barrier layers is more than three times the average electron energy in the well for the highest dc electric field considered. The carriers, therefore, are assumed to populate only the lowest sub-band of the square quantum well in the infinite barriers height approximation.

For numerical calculations, electron temperature model has been employed and relevant scattering mechanisms are incorporated in the calculations. Screened scattering rates are considered except for LO phonons, where carrier screening is insignificant in the present condition. Carrier energy and momentum balance equations are solved employing electron temperature model with the help of relevant expressions for various parameters. The expressions for ac mobility, phase angle and cut off frequency (at which the ac mobility drops to 0.707 of its low frequency value) are then obtained for further analysis. As suggested by a growing number of researches, GaN is becoming an important material with regard to the development of opto-electronic devices operating in either the blue region of the visible spectrum or the near ultra violet regime due to its appropriate band gap magnitude [5]. Large peak of GaN electron velocity makes it an important candidate for high frequency application as well [6]. Recently, $1 \mu\text{m}$ AlGaIn/GaN heterostructures field effect transistor [HFET] with the cutoff frequency of 18.3 GHz has been fabricated. It is anticipated that further improvement in device design will yield even faster devices [7,8].

III. SOFT COMPUTING MODEL

An artificial neural network (ANN) is a computational tool having Artificial Intelligence origins containing a number of simple, highly interconnected processing elements, which process information by their dynamic state response to external inputs. ANN offers distinctive advantages in some areas. First, ANN has a better filtering capacity than empirical models. Second, advantage that ANN has over empirical models is the ability to adapt. ANN has specified training algorithms, where we adjust connection weights. With the use of parallel network architecture the training time is much reduced. In a parallel neural network architecture the training data set is divided into equal number of blocks each of which is fed to each network in the parallel architecture, thereby reducing significantly the total training time. Mathematical equation for back-propagation algorithm is written as:

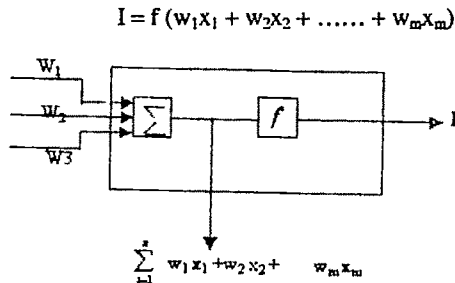


Fig. 1 shows the activation function for back propagation

Fig. 1 shows a back propagation neural networks depicting input layer, hidden layer, output layer and their interactions. The mathematical equations for back propagation algorithm is represented as:

$$I = f\left(\sum_{i=1}^n W_i X_i + W_2 X_2 + \dots + W_m X_m\right)$$

Where x_1, \dots, x_m are the inputs, w_1, \dots, w_m are the corresponding weights.

An important generalization of the perception training rule used in back propagation network is called delta rule. The training equation that following in back propagation network is given by:

$$W_{\text{new}} = W_{\text{old}} + \beta EX / |X|$$

Where W_{new} = the new value of a weight connecting an input component X to the winning neuron. W_{old} = the previous value of this weight. β = a training rate coefficient that may vary during the training process. E = the difference between the desired output and the actual computed output.

There are some specific issues related to backpropagation neural networks (BPNN) which motivate the potential users to use BPNN. Apart from defining the general architecture of a network and perhaps initially seeding it with a random numbers, the user has no other role than to feed it input and watch it train and await the output. The final product of this activity is a trained network that provides no equations or coefficient defining a relationship beyond its own internal mathematics. The network is the final equation of the relationship. BPNN also tend to be slower to train than other types of networks and sometimes require thousands of epochs. If run on a truly parallel computer system this issue is not really a problem, but if the BPNN is being simulated on standard serial machine, training can take some time. This is because the CPU of the machines must compute the function each node and connection separately, which can be problematic in very large networks with a large amount of data. This basically motivated us to use BPNN in the present work.

We restored to use parallel networks to lower down the training time of a particular network and also show how dramatically the training time decreases. It is observed that as the no. of network increases the training time drastically reduces thereby making the system faster.

IV. RESULTS AND DISCUSSIONS

Numerical results are obtained with the material parameters of GaN available in the table 1. The optimized parameters together with the desired ac mobilities are depicted in table 2 and 3. For particular dc biasing field and the frequency of the applied ac field, optimization of the parameters are done to get the desired ac mobility. The dc biasing fields (F_0) are taken as 1×10^5 V/m and 0.5×10^5 V/m and the frequencies of the applied field are 100GHz and 200 GHz which are sufficiently high for a departure from the low frequency behaviour.

From the table 2 and table 3, it is evident that for a frequency of 200GHz and ac mobility of $0.82 \text{ m}^2/\text{v.s}$ (table 2) and $0.73 \text{ m}^2/\text{v.s}$ (table 3) the optimized system parameters are presented by the row 2 of table 2 for a dc biasing field of 1×10^5 V/m

and by the row 3 of table 3 for a dc biasing field of 0.5×10^5 V/m, respectively. This is a soft computing tool based technique and it has the potential of providing on-line prediction of the optimized system parameters and accordingly the system may be fabricated with those optimized parameters. The present model is capable of predicting the better system parameters to meet a desired characteristics of a low dimensional, low power consuming and high frequency nanodevice. It is relevant that high frequency performance is found better when nonequilibrium LO phonons are incorporated into the calculations. Our present model has the special feature that it has the ability of prefixing the device characteristics and accordingly the model can predict the system parameters, biasing field and other relevant parameters. The proposed model has the potentiality of providing the online prediction which will surely save the search time for the technologists involved in fabrication of high frequency nano devices. For extrapolation or interpolation of values, the network is to be retrained including the desired range of parameters.

Table 1: Material parameters of GaN

Parameters	Values
Electron effective mass, m^* (kg)	$0.22 \times 9.1 \times 10^{-31}$
Acoustic deformation potential, E_1 (J)	$8.3 \times 1.602 \times 10^{-19}$
Static dielectric constant, K_s	10.4
Optic dielectric constant, K_a	9.5
LO phonon energy, $\hbar\omega_0$ (eV)	3.216
Background ionized impurity concentration, n_{bi} (m^{-3})	6.0×10^{21}
Longitudinal acoustic velocity, u_l (ms^{-1})	5×10^3
Mass density (kgm^{-3})	6.15×10^3

Table 2: Optimization parameters for dc bias field $F_0 = 1.0 \times 10^5$ V/m, (frequency = 200 GHz)

Ac mobility (m^2/Vs)	Lattice temperature T_L (K)	Channel length, L_z (nm)	Carrier concentration n_{2D} ($10^{15} m^{-2}$)
0.95	77	95	11
0.82	100	90	10
0.76	180	85	9
0.71	280	81	8

Table 3: Optimization parameters for dc bias field $F_0 = 1.0 \times 10^5$ V/m, (frequency = 200 GHz)

Ac mobility (m^2/Vs)	Lattice temperature T_L (K)	Channel length, L_z (nm)	Carrier concentration n_{2D} ($10^{15} m^{-2}$)
0.92	77	100	10
0.80	100	92	9
0.73	280	86	8
0.68	300	82	7

V. CONCLUSION

In conclusion, we have applied the ANN based prediction technique to get the desired small signal ac mobility. For every desired value of ac mobility system parameters are optimized which will surely provide valuable information for the person involved in the technology of device fabrication. Our results will be best understood when they will appear in the real field.

ACKNOWLEDGMENT

Subir Kumar Sarkar thankfully acknowledges the financial support obtained from DRDO, Govt. of India (ERIP/ER/0503561/M/01/905 dt.01/08/2006)

REFERENCES

- [1] S. Aydogu, M. Akavsu and O. Ozbay: Rom Journal. Physics, Vol 50, No 9-10, Page 1047-1053 (2005).
- [2] F. M. S. Lima, A. B. Veloso, A. L. A. Fonseca and O. A. C. Nunes: Brazilian J. of Physics, Vol 36, No 2A, 2006.
- [3] F. M. S. Lima, A. L. A. Fonseca and O. A. C. Nunes and Q. Fanyao: J Appl. Phys., Vol 92, P 5296 (2002).
- [4] S. K. Sarkar, N. R. Bandopadhyay, C. Puttamadappa and A. Mol: "High Frequency ac Transport of Two Dimensional Hot Electrons in GaN Quantum Wells" Journal of the Institution of Engineers, vol. 85, pp56-59(2005).
- [5] J.G. Kim, A.C.Frenkel, H.Lin and R.M.Park: Appl. Phys. 65, 4 (1994).
- [6] M.A Khan et al : IEEE ED Lett.17, 354(1996).
- [7] M.A Khan et al : Electron Lett 32, 357(1996).
- [8] M.A.Khan et al : IEEE ED Lett.17, 584(1996).

Communication Security through Cryptography and Performance Evaluation of Three Encryption/Decryption algorithms

Awadhesh Kumar Singh

Department of Instrumentation and Control Engineering
Netaji Subhas Institute of Technology, New Delhi, INDIA
e-mail: awadeshk2002@yahoo.com

Abstract— This paper has two major purposes, the first, concept behind basic cryptographic methods and types of cryptography. The second, an implementation of three encryption algorithms and a comparison between based on CPU execution time. The selected algorithms are: DES, Triple-DES (T-DES) and blowfish.

Key words— Blowfish, DES, T-DES.

I. INTRODUCTION

THE data protections against an unauthorized access or modification in computer and telecommunication networks is one of the most important challenges at the end of the XX-th century. Cryptography is the way to protect the data over worldwide network. The Cryptography "secure" is "the art of keeping messages secure". A mechanism is needed to assure the security and privacy of information that is sent over the electronic communication media is in need[1],[2]. Whether the communication media is wired or wireless both can be not protected from unauthorized reception or interception of transmission. The paper focuses on the analysis of three types of cryptography and its algorithms: Secret Key Cryptography (SKC): uses single key for both encryption and decryption. Public Key Cryptography (PKC): uses one key for encryption and another for decryption. Hash function: use a mathematical transformation to irreversibly "encrypt" information.

Three symmetric block cipher have been selected for work in this paper: Data Encryption Standard (DES), Triple- DES (T-DES) and Blowfish [1],[5],[6],[8]. These three symmetric block ciphers have been chosen because DES has been a world wide standard for 25 years, it has also been standardized by ANSI and ISO. T-DES resolves the flaws in DES and it is much more complicated version.

The Blowfish is a cipher with a different structure and functionality, and has advantages of low memory requirement and has a simple structure.

II. THE PURPOSE OF CRYPTOGRAPHY

Cryptography is the science of writing in secret code and is an ancient art the first documented use of cryptography in writing dates back to circa 1900 B.C. when an Egyptian scribe used non-standard hieroglyphs in an inscription [7],[10]. Some experts argue that cryptography appeared spontaneously sometime after writing was invented, with applications ranging from diplomatic missives to war-time battle plans. It is no surprise, then, that new forms of cryptography came soon after the widespread development of form of data encryption key.

The most popular data encryption technique is Data Encryption Standard (DES) . The most common SKC scheme today, DES was designed by IBM in 1970s and adopted by the National Bureau of Standards (NSB), Now the National Institute of Standard and Technology (NIST) in 1977 for commercial and unclassified government application. In data and telecommunications, cryptography is necessary when communicating over any untrusted medium, which includes just about *any* network, particularly the Internet.

III. COMMUNICATION SECURITY THROUGH CRYPTOGRAPHY

Communication is an essential part of life, it makes the progress of human being. Traditional media for communication are the sending of letters through the post office, talking over the phone through the telecommunication company or more communally to speak directly with the other person. These traditional media have existed for a long period of time and special provisions have been made so that people can communicate in a secure way , either for personal or business communication. Today the Internet, as a network that interconnects networks of computer around the world is a new

commutation media. Additionally, on the Internet, one can automate the same type of fraud bringing higher gains and a bigger incentive. The law and the technologies to let transparent and secure communication have not been fully defined or set yet.

Cryptography has provided us to security of the world wide network. A fundamental premises in cryptography is that the sets $M, C, K, \{E_e: e \in K\}, \{D_d: d \in K\}$ are public knowledge. When two parties wish to communicate securely using an encryption scheme, the only that they keep secret is the particular key pair (e, d) which they are using, and which they must select. One can gain additional security by keeping the class of encryption and decryption transformations secret but one should not base the security of the entire scheme on this approach. History has shown that maintaining the secrecy of the transformations is very difficult indeed.

Cryptography is the study of mathematical techniques related to aspects of information security such as confidentiality, data integrity, entity authentication, and data origin authentications. Cryptography is about the prevention and detection of cheating and other malicious activities.

Within the context of any application-to-application communication, there are some specific security requirements, including: Authentication: The process of proving one's identity. (The primary forms of host-to-host authentication on the Internet today are name-based or address-based, both of which are notoriously weak.) Privacy/confidentiality: Ensuring that no one can read the message except the intended receiver. Integrity: Assuring the receiver that the received message has not been altered in any way from the original. Non-repudiation: A mechanism to prove that the sender really sent this message.

IV. CRYPTOGRAPHY ALGORITHMS

Cryptography has several differences from pure mathematics. While a mathematician may use A and B to explain an algorithm. A cryptographer may use the fictitious names Alpha and Beta. Suppose Alpha wants to send message to his bank to transfer money. He would like to the message to be private, since it includes information such as his account number and transfer amount. One solution is to use a cryptographic algorithm, a technique that would transfer his message into an encrypted form, unreadable except by those for whom it is intended. When encrypted the message can only be interpreted through the use of the corresponding secret key. Without the key message is useless good cryptography algorithms make it so difficult for intruders to decode the original message that it is not worth their efforts [1],[3],[7]. Some encryption algorithms is shown in the Table.1.

There are several ways of classifying the cryptographic algorithms. For purposes of this paper, they will be categorized based on the number of keys that are employed for encryption and decryption, and further defined by their application and use. Fig.1 shows that the three types of algorithms which discussed in this paper.

Algorithms	Type	Key Size	Features
DES	Block Cipher	56 bits	Most Common, Not strong enough
Triple DES	Block Cipher	168 bits(112 bits effectives)	Modification of DES, Adequate Security
Blowfish	Block Cipher	Variable (up to 448 bits)	Excellent Security

Secret Key Cryptography (SKC): Uses a single key for both encryption and decryption. Secret Key Cryptography also known as Conventional cryptography and symmetric cryptography.

Public Key Cryptography (PKC): Uses one key for encryption and another for decryption. Public Key Cryptography also known as asymmetric cryptography.

Hash Functions: Uses a mathematical transformation to irreversibly "encrypt" information.

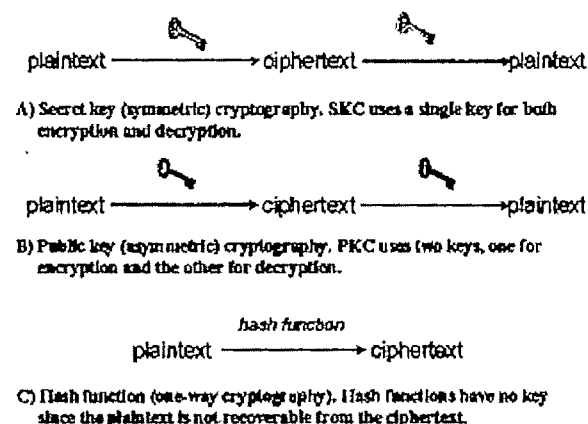


Fig.1 Three types of cryptography: secret-key, public key, and hash function

Block ciphers can operate in one of several modes the following four are the most important:

Electronic Codebook (ECB) mode is the simplest, most obvious application: the secret key is used to encrypt the plaintext block to form a ciphertext block. Two identical plaintext blocks, then, will always generate the same ciphertext block. Although this is the most common mode of block ciphers, it is susceptible to a variety of brute-force attacks.

Cipher Block Chaining (CBC) mode adds a feedback mechanism to the encryption scheme. In CBC, the plaintext is exclusively-ORed (XORed) with the previous ciphertext block prior to encryption. In this mode, two identical blocks of plaintext never encrypt to the same ciphertext.

Cipher Feedback (CFB) mode is a block cipher implementation as a self-synchronizing stream cipher. CFB mode allows data to be encrypted in units smaller than the

block size, which might be useful in some applications such as encrypting interactive terminal input. If we were using 1-byte CFB mode, for example, each incoming character is placed into a shift register the same size as the block, encrypted, and the block transmitted. At the receiving side, the ciphertext is decrypted and the extra bits in the block (that is, everything above and beyond the one byte) are discarded.

Output Feedback (OFB) mode is a block cipher implementation conceptually similar to a synchronous stream cipher. OFB prevents the same plaintext block from generating the same ciphertext block by using an internal feedback mechanism that is independent of both the plaintext and ciphertext bitstreams.

A. DATA ENCRYPTION STANDARD (DES) / TRIPLE DES

Goal of DES is to completely scramble the data and key so that every bit of cipher text depends on every bit of data and every bit of key. It is a block Cipher Algorithm, encodes plaintext in 64 bit chunks. One parity bit for each of the 8 bytes thus it reduces to 56 bits. It is the most used algorithm. DES developed by IBM in the early 1970s. Standard approved by US National Bureau of Standards for Commercial and nonclassified US government use in 1993. DES is an iterated block cipher, iterated means multiple repetitions of a simple encryption algorithm. DES has 16 rounds. Where Block cipher encrypts in fixed-size blocks. DES uses 64-bits blocks. At its simplest level, DES is a combination of the two basic techniques of cryptography: confusion and diffusion. DES follows strict avalanche criteria. Every bit of the key and every bit of the plaintext affects every bit of the ciphertext. It has same keys for encryption and decryption.

DES Encrypt and decrypt data in 64 bits blocks and it is divided into two 32bits halves xL and xR. It has 16 round. Triple DES is same as DES, three key used.

i.e. for $I = 1$ to 16

$\text{buf} = xR \oplus K[I]$ here xR is 48 bit

S-boxes $S[1] - S[8]$

Then go through Permutation.

$xR = xL \oplus \text{result}$

we got new xL and xR

then swapped and merged to get ciphertext

B. BLOWFISH

Blowfish is a symmetric 64-bit block cipher invented by Bruce Schneier; optimized for 32-bit processors with large data caches, it is significantly faster than DES on a Pentium/PowerPC-class machine. Key lengths can vary from 32 to 448 bits in length. The plaintext of 64 bits is divided into two 32-bit halves xL(LEQ) and xR(REQ).

$xL = xL \oplus P_i$

$xR = F(xL) \oplus \text{XOR } xR$

Swap xL and xR

After the sixteenth round, swap xL and xR again to undo the last swap.

Then, $xR = xR \oplus P_{17}$ and

$xL = xL \oplus P_{18}$.

Finally, recombine xL and xR to get the ciphertext.

C. HASH FUNCTION

Hash functions, also called message digests and one-way encryption, are algorithms that, in some sense, use no key (Figure 1C). Instead, a fixed-length hash value is computed based upon the plaintext that makes it impossible for either the contents or length of the plaintext to be recovered. Hash algorithms are typically used to provide a digital fingerprint of a file's contents, often used to ensure that the file has not been altered by an intruder or virus. Hash functions are also commonly employed by many operating systems to encrypt passwords. Hash functions, then, provide a measure of the integrity of a file.

V. PERFORMANCE EVALUATION OF DES, TDES AND BLOWFISH

The program implemented is constructed into three modules. The first module is responsible for generating the Secret Keys and second module is encryption module that would be encrypted the messages. Third module is decryption module that would be decrypted the encrypted messages and got original message. For that the power full portable language, Turbo C is used to develop these modules and implemented on Pentium- IV Processor. It may be proposed to implement in Java and JCA for better result.

The result illustrated that the Key generation operation for all algorithms is the CPU time spent while performing the encryption and decryption operations. It is clear that Blowfish algorithm is a fasted algorithm due to mechanism it follows for ciphering data. The DES algorithm comes in second place followed by the T-DES algorithm. The CPU time for T-DES was the highest due to increased complexity incorporated within the T-DES. This complexity is needed to address the security issues that exist in the DES algorithms.

REFERENCES

- [1] Najib A. Kofahi, Turki Al-Somani and Khalid Al-Zamil " Performance Evaluation of three encryption/ decryption algorithms ", Circuits and Systems Proceedings of the 46th IEEE International Midwest Symposium on Dec, 2003.
- [2] A.S. Tanenbaum, "Modern operating Systems", Prentice Hall, 2003.
- [3] Othman O. Khalifa, MD Rafiqul Islam, S. Khan and Mohammed S. Shebaal " Communications Cryptography ", IEEE RF and Microwave Conference, RFM Proceedings 2004, P 220-223

- [4] M.J.B. Robshaw , " Block Cipher", Technical Report , RSA Laboratories, Number TR-601, July 1994.
- [5] D.R.Frey. Chaotic Digital Encoding, "An Approach to secure Communication", IEE trans. Circuit syst.- II, vol. 40, pp 660-666, Oct. 1993
- [6] William Stallings, " Cryptography and Network Security", Pentice Hall, 2004
- [7] A. Menezes, P. van Oorschot, and S. Vanstone "Handbook of Applied Cryptography" , CRC Press, 1996., www.cacr.math.uwaterloo.ca/hac
- [8] Atul Kahate, " Cryptography and Network Security", Tata Mcgraw-Hill, 2003.
- [9] Bauer, F. L. Decrypted Secrets: method and Maxims of cryptology, 2nd ed. New York: Springer Verlag, 2002.
- [10] D.E.R. Denning, Cryptography and Data Security, Addison-wesley, 1982.

A Novel Design Of Low Power Low Voltage Full Adder Using 14 MOSFETS

Manash Chanda¹, Swapnadip De¹, Amrit Ghosh², Devmalya Banerjee², Pijush Biswas³

¹ Meghnad Saha Institute of Technology, Kolkata

² JIS College of Engineering, Kalyani

³ A. K. Choudhury School of I.T., University of Calcutta, pijush@iccc.org

Abstract: In this paper, 1 bit full adder is built under a new hybrid logic (combination of PTL and CMOS logic) style, using 14 MOSFET. Here we use 6transistor XOR-XNOR circuit to implement the full adder. This full adder offers full voltage swing at every nodes, higher density and high speed than the conventional CMOS design style. TSPICE is the simulator used for the simulation and bsim3v32 technology is used with supply voltage=1v and 10MHz freq. Dual threshold model file (version 49) is used to observe the output.

Keywords: XOR-XNOR, Full Adder, PTL, CMOS.

I. INTRODUCTION

The one bit Full Adder is one of the most widely used building blocks in all data processing (arithmetic) and DSP units. With the growing trend for reducing the power dissipation in VLSI systems and especially in portable applications, reduction (or scaling) of the power supply voltage emerges as one of the most widely practiced measures for low power design. At lower supply voltages, 1 bit full adder circuit with low power dissipation, full voltage swing and high speed becomes important issues. In this paper, a low power and high-speed full adder, based on pass transistor logic (PTL) and static CMOS logic style, is proposed for the embedded system.

II. DESIGN IMPLEMENTATION

The truth table for the full adder circuit is shown in the table,

Table 1: Truth table of full adder

A (\bar{a})	B (\bar{b})	C (\bar{c})	SUM (ϕ)	CARRY (ϕ)
0	0	0	0	0
0	0	1	1	0
0	1	0	1	0
0	1	1	0	1
1	0	0	1	0
1	0	1	0	1
1	1	0	0	1
1	1	1	1	1

From this truth table we can implement the conventional Full Adder circuit, by using CMOS logic style, where

$$\text{SUM} = (A) \text{ XOR } (B) \text{ XOR } (C)$$

$$\text{CARRY} = (AB) + (BC) + (CA)$$

Hence we have used total 28 MOSFET (14 PMOS and 14 NMOS) to implement the conventional circuit. Another design of Full Adder is based on pass transistor logic (PTL) style. The conventional and PTL based design of full adder circuit is shown below,

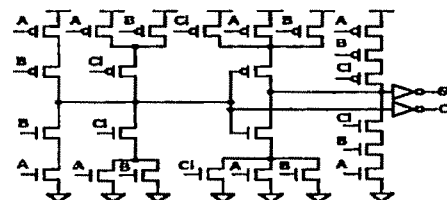


Fig 1: Conventional Full Adder circuit with 28 MOSFET

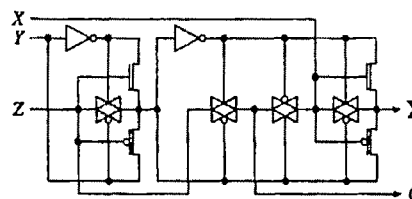


Fig 2: 16 MOSFET Pass transistor logic style

A more efficient design of Full Adder involves the use of CMOS logic and transmission Gate logic. If we observe the above truth table carefully, then we can write;

If $(A \text{ XNOR } B) = 1$ then $\text{SUM} = C$ and $\text{CARRY} = B$ (1)

If $(A \text{ XNOR } B) = 0$ then $\text{SUM} = \text{NOT}(C)$ and $\text{CARRY} = C$ (2)

To implement Full Adder first we have to implement the XNOR function with minimum possible no of transistor. The implementation is shown here.

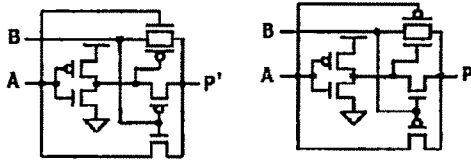


Fig 3(a,b): 6-Transistors XOR & XNOR gate

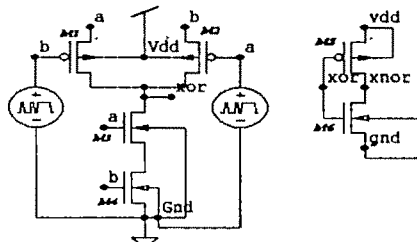


Fig. 3(c): 6 transistor XOR-XNOR (from TSPICE)

Here we use a 6 transistor XOR-XNOR circuit to implement the Adder.[1]The proposed XOR-XNOR circuit is shown above.Hence considering XOR o/p node first,when $A=0/1$ and $B=1/0$ then any one of the PMOS(M1 or M2)will be ON to pass the logic 1 (V_{dd}) to the output port . When $A=B=1$ the both the NMOS(M3 and M4) will be ON to pass the logic 0 (ground) to the output node. When $A = B = 0$, then both PMOS(M1 and M2)will be ON to pass logic 0 to the output node , As PMOS is unable to pass logic 0 smoothly,there may be small logic degradation in XOR node for the $A=B= 0$ input combination. But in XNOR node , as XOR is inverted ,so we will not get any logic degradation .

Now,to implement SUM we have to use the (1) and (2). [2]If $(A \text{ XNOR } B) = 1$ then $SUM = C$ since M1 and M2 will behave like a buffer and the TG pair (M3 and M4) will pass the C to the output node SUM. If $(A \text{ XNOR } B) = 1$ and $(A$

$\text{XOR } B) = 0$ then M1 and M2 will behave like an inverter and pass the complement of C at the output node SUM.If $(A \text{ XNOR } B) = 1$ and $(A \text{ XOR } B) = 0$ then M1 and M2 will behave like an inverter and pass the complement of C at the output node SUM.

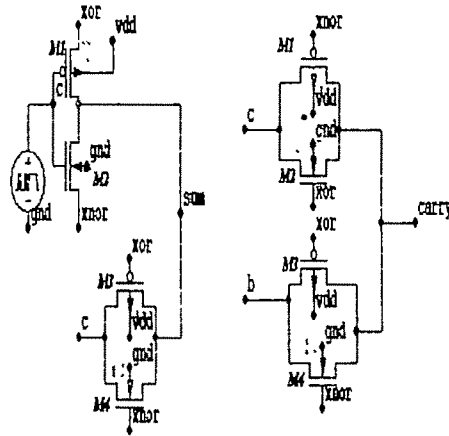


Fig. 4: Implementation of the proposed CARRY and SUM module

For CARRY circuit we can use the same equation . [2]Hence when $(A \text{ XNOR } B) = 1$ and $(A \text{ XOR } B) = 0$ then M1 and M2 both will be ON to pass the signal from node B to the output node CARRY .When $(A \text{ XNOR } B) = 0$ and $(A \text{ XOR } B) = 1$ then M3 and M4 both will be ON to pass the signal from the node C to the output node CARRY .

III. RESULTS and OBSERVATIONS :

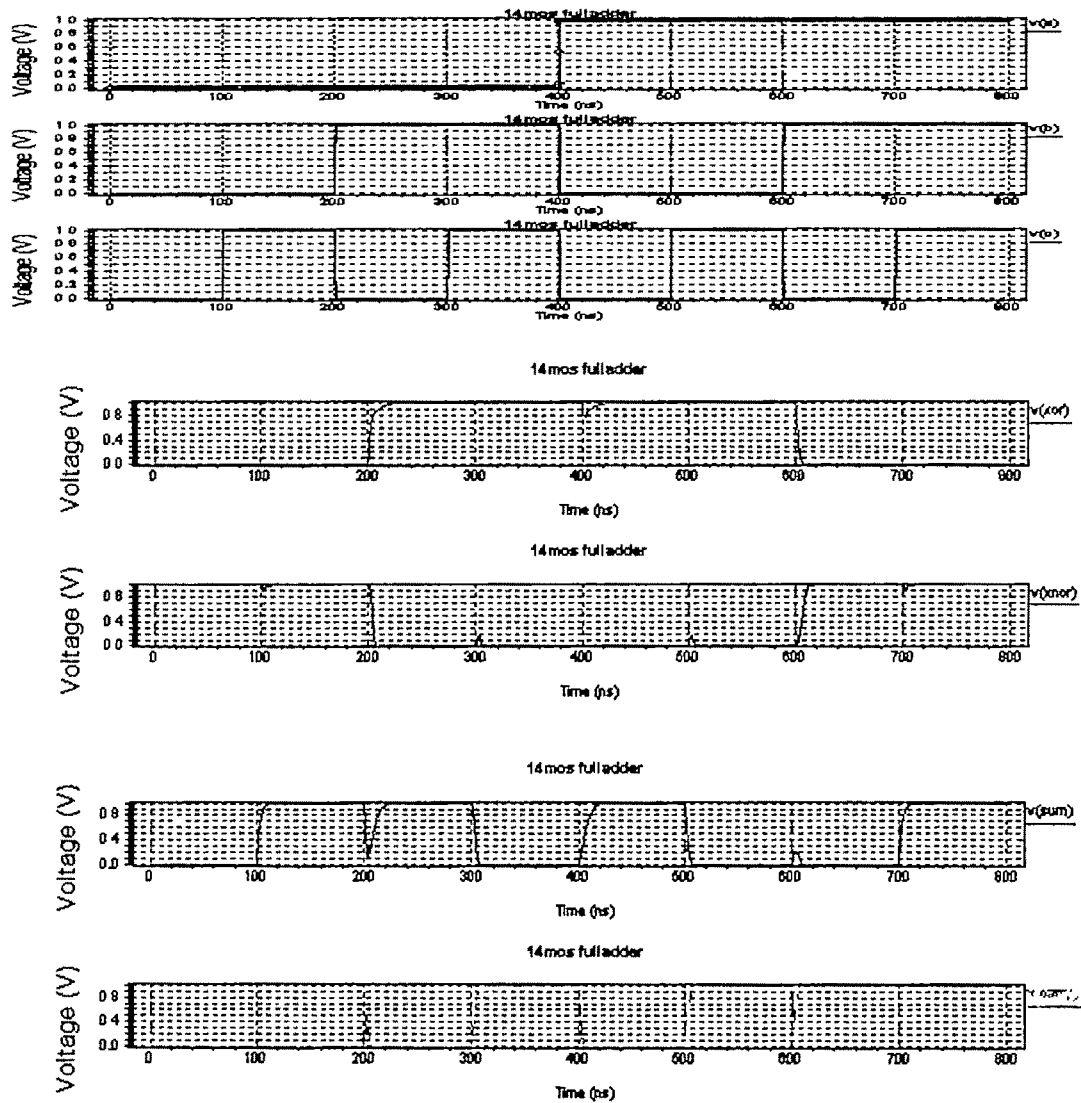


Fig 5: Output waveform of XOR,XNOR,SUM,CARRY with three voltage sources

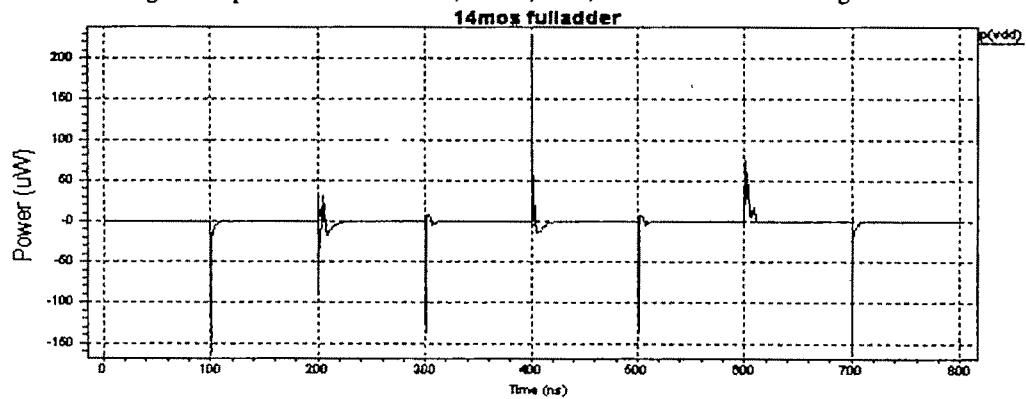


Fig 6 : Power dissipation curve with respect to time

The measured power-delay table for every bit pattern is also shown here;

Table 2: Rise time delay and power measurement (sum and carry as o/p)

i/p	Rise time delay(s)(sum)	Rise time delay(s)(carry)	P(watt) with Vdd = 1V
000	not found	not found	5.16E-10
001	1.45E-09	not found	2.78E-10
010	8.68E-09	1.44E-09	1.63E-10
011	1.93E-09	1.52E-09	1.62E-10
100	9.85E-09	not found	6.44E-10
101	1.78E-09	6.92E-09	2.74E-10
110	not found	9.56E-10	5.01E-10
111	1.43E-09	9.90E-10	2.50E-10

Table 3: Fall time delay and power measurement (sum and carry as o/p)

i/p	Fall time delay(s) (sum)	Fall time delay(s) (carry)	Power (watt) with Vdd = 1V
000	1.17E-09	9.89E-10	1.40E-09
001	not found	not found	2.24E-10
010	1.22E-09	4.34E-09	1.63E-10
011	6.77E-09	not found	1.62E-10
100	1.30E-09	1.04E-09	6.43E-10
101	7.74E-09	1.03E-09	2.76E-10
110	1.16E-09	not found	5.01E-10
111	not found	not found	2.50E-10

IV. CONCLUSION:

A new full adder circuit was proposed by using 14 transistor only., that is possible only due to the use of 6T XOR-XNOR .Though the device count is very low , yet every node offers full voltage swing. Another main advantage is very low power dissipation. So the power delay product is also very low and of the order of 10^{-30} . Hence the limitation is design time since to implement 6 transistor XOR-XNOR circuits; we have to use proper ratioed MOSFET. Here we use the dual threshold model file; we can also use the low threshold model file to get

these data. In case of low voltage file the o/p will be more improved.

REFERENCES

- [1] " A low power bootstrapped CMOS full adder " , Herndez et al , 2nd International conf. on ICEE & 11th International conference on electrical engineering , September , 2005
- [2] " A novel high performance CMOS 1bit full adder cell" , Shams et al , IEEE transactions on circuits and systems , No.-5, May 2000

Technical Session 7B

Image Processing

Statistical-Mechanical Modeling of Digital Halftoning

Jun-ichi Inoue¹, Yohei Saika² and Masato Okada³

¹ Complex Systems Engineering, Graduate School of Information Science and Technology, Hokkaido University, N14-W9, Kita-ku, Sapporo 060-0814, Japan. E-mail: j_inoue@complex.eng.hokudai.ac.jp

² Department of Electrical and Computer Engineering, Wakayama National College of Technology, Nada-cho, Noshiro 77, Gobo-shi, Wakayama 644-0023, Japan. E-mail: saika@wakayama-nct.ac.jp

³ Division of Transdisciplinary Science, Graduate School of Frontier Science, The University of Tokyo, 5-1-5 Kashiwanoha, Kashiwa-shi, Chiba 277-8561, Japan. E-mail: okada@k.u-tokyo.ac.jp

Abstract—A statistical-mechanical modeling of digital halftoning is proposed. The digital halftoning dealt with here is achieved by making use of the threshold mask matrix and for each pixel, the halftoned pixel is determined as black (set to one) if the original grayscale pixel is greater than the mask value and is determined as white (set to zero) vice versa. Basically, our method is a kind of the so-called *model-based digital halftoning technique* and we use the information about the original grayscale image to generate the threshold mask. To determine the optimal value of the mask on each pixel for a given original grayscale image, we first assume that the human eyes might recognize the black and white binary halftoned image as the corresponding grayscale one by a class of linear filters. Then, the energy function is constructed as the distance between the original and the recognized images which is written in terms of the threshold mask. To minimize the energy function with respect to each threshold mask value in the dither array via simulated annealing, we obtain the optimal threshold mask and the resultant halftoned image simultaneously. We also investigate the statistical properties of the threshold mask and the halftoned image by means of the power spectrum analysis.

Key words—Image processing, Model-based digital halftoning technique, Statistical mechanics, Computer simulation, Markov Chain Monte Carlo methods, Simulated annealing, Combinatorial optimization problem, Power spectrum analysis

I. INTRODUCTION

IN the field of digital image processing, digital half-toning which is the process of generating a pattern of pixels with limited number of colors, especially which converts a grayscale image into the binary black and white picture has been widely used in various practical situations in media, such as the printing of newspapers, fax machines and so forth [1][2]. To achieve the digital halftoning, one needs the strategy to arrange the geometrical-combination of the black and white pixels so as to make human eyes to have a kind of *optical illusion*. Namely, the digital halftoning relies on the fact that the human eyes act as a *special low-pass filter*. Actually, to justify the fact, several authors proposed or estimated the so-called the *contrast sensitivity function*, or the *modulation transfer function* of human visual system. For

instance, Analoui and Allebach [3] introduced the contrast sensitivity function having the following form:

$$H(f_p) = k \{ \exp(-2\pi\alpha f_p) - \exp(-2\pi\beta f_p) \} \quad (1)$$

where f_p denotes frequency and α, β are constants setting to

0.012 and 0.046, respectively. They set the scale parameter k to satisfy the condition $\max_{f_p} H(f_p) = 1$.

As another model of the human visual system, Mannos and Sakrison [4] estimated the function as

$$H(f_p) = 2.6(0.0192 + 0.114f_p) \exp[-(0.114f_p)^{11}] \quad (2)$$

We plot the shape of the contrast sensitivity function in FIG.1.

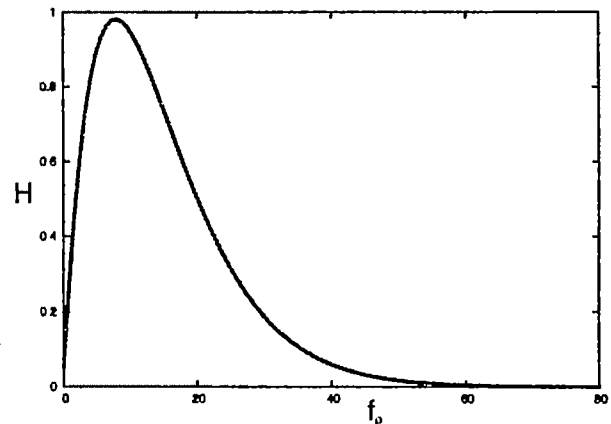


FIG.1. Human-eye modulation transfer function estimated by Mannos and Sakrison [4].

From this figure, we find that in high-frequency regime, the contrast sensitivity function decreases to zero, which means that human eyes cannot recognize high-frequency components in images. In other words, the halftone algorithm should be constructed such that the halftoned binary dots contain relatively high-frequency components to describe the original grayscale levels. This fact is an important guide for us to consider the halftoning algorithms from the view point of physiology. Up to now, to achieve the fine quality of the digital halftoning, a lot of techniques, for instance, the clustered-dot ordered dither method, the threshold mask method [1][2] and the blue noise mask method [5],

error-diffusion method [6] and so on have been proposed and developed by many researchers.

On the other hand, to retrieve the original grayscale image from the halftoned binary image, the so-called *inverse halftoning* has been also developed especially in printer technology. As such an inverse halftoning strategy, not only the conventional smoothing filter but also the Bayesian inference have been used. However, as well-known, in Bayesian inference, we are required to evaluate sums of huge number of ingredients as the so-called Boltzmann factors. Moreover, it is difficult task for us to determine the best possible choice of several parameters, what we call *hyper-parameters*, appearing in the probabilistic model used in the Bayesian inference.

Recently, we proposed a statistical-mechanical approach to analyze the inverse halftoning problem [7]. We introduced a theoretical framework based on several statistical-mechanical techniques or its concepts in order to investigate statistical performance of the inverse digital halftoning. In our recent proceedings [8], we also introduced a *Markov random-fields model* to represent original grayscale image and constructed the inverse halftoning process as a kind of image reconstruction of the grayscale image from a given halftoned binary image. Then, we evaluated the statistical performance by making use of *Markov chain Monte Carlo (MCMC)* simulations and analysis of a solvable Markov random-fields model. Our approach enables us to evaluate or approximate the exponential order of the sum-calculations effectively or approximately.

However, to complete the statistical-mechanical formulation for the digital halftoning, the halftoning procedure besides the inverse halftoning should be also constructed or modeled by means of statistical physics.

In this paper, we propose a statistical-mechanical modeling of the digital halftoning. We first introduce a threshold mask matrix with the same size as the original image. Then, each pixel of the halftoned image is determined as a black pixel if the value of the original grayscale pixel is greater than the component of the threshold mask matrix and is determined as a white pixel vice versa. Then, we assume that human eyes might recognize the original grayscale image by a class of linear filter. By taking into account that the distance between the original and the recognized images is written in terms of the threshold mask, we naturally introduce an energy function to be minimized to determine the optimal threshold mask. For a demonstration of our method to generate the optimal threshold mask, computer simulations of simulated annealing [9][10] is carried out. To investigate the statistics of the threshold mask image and the halftoned image, we evaluate the power spectrum numerically.

The remainder of this paper is organized as follows. In the next section II, we explain our method to generate the optimal threshold mask for a given original grayscale image. In this section, the energy function is introduced as a function of the threshold mask under the assumption that the human eyes might recognize the halftoned image as the corresponding original grayscale version by a linear filter. In section III, we solve the combinatorial optimization problem described by the energy function by making use of the simulated annealing. We

show the resultant halftoned image for a standard grayscale image *lena*. We find that our algorithm generates the binary dots which induce the illusion of a continuous-tone image. In section IV, we investigate the statistics of the threshold mask array and the halftoned image. In the last section is summary.

II. STATISTICAL-MECHANICAL MODELING

We first explain our statistical-mechanical modeling of the digital halftoning. Let us define the original grayscale image located on the square lattice with size $L \times L$ by

$$G = \{g_{x,y} \in 0, 1, \dots, Q-1 \mid x, y = 1, 2, \dots, L\} \quad (3)$$

, where we defined that each pixel $g_{x,y}$ takes Q values.

Then, we introduce the threshold mask matrix with the same size with the above original grayscale image, namely, $L \times L$ as $M = \{m_{x,y} \in 0, 1, \dots, Q-1 \mid x, y = 1, 2, \dots, L\}$ (4)

where each component of the threshold matrix $m_{x,y}$ also takes Q values. The half-toned image is defined by

$$H = \{h_{x,y} \in 0, 1 \mid x, y = 1, 2, \dots, L\} \quad (5)$$

and each pixel in the halftone image H is given by

$$\forall(x, y) \quad h_{x,y} = \Theta(g_{x,y} - m_{x,y}) \quad (6)$$

, where the step function $\Theta(x)$ is defined conventionally as

$$\Theta(x) = \begin{cases} 1 & (x \geq 0) \\ 0 & (x < 0) \end{cases} \quad (7)$$

For this setup of the model system, a pixel of the resulting halftoned binary image is set to one if the pixel of the original grayscale image is greater than or equal to the corresponding pixel of the threshold mask; otherwise the pixel is set to zero.

Our main problem is now to determine the threshold mask M efficiently. For this purpose, we might assume that human eyes might retrieve the grayscale image, let us call, the *recognized image*:

$$S = \{s_{x,y} \in 0, 1, \dots, Q-1 \mid x, y = 1, 2, \dots, L\} \quad (8)$$

from the half-toned image H by making use of the following linear filter:

$$\forall(x, y) \quad s_{x,y} = (\mathbf{K} * \mathbf{h})_{x,y} = \sum_{i,j \in N(x,y)} K(x-i, y-j) h_{i,j} \quad (9)$$

, where $N(x, y)$ denotes the nearest neighboring pixels of a pixel located at (x, y) , including itself (x, y) . Apparently, for our two-dimensional square lattice, the number of the ingredients is $|N(x, y)| = 9$. In this paper, we set the kernel function K appearing in the convolution product $\mathbf{K} * \mathbf{h}$ in equation (9) as $\forall(x, y) \quad K(i, m) = 1$ for simplicity. Of course, the other choice such as the Gaussian-type:

$$K(x-i, y-j) = \frac{1}{2\pi\sigma_x\sigma_y} \exp\left[-\frac{(x-i)^2}{2\sigma_x^2} - \frac{(y-j)^2}{2\sigma_y^2}\right] \quad (10)$$

is possible and as we shall see below, the reconstruction of the energy function is straightforward.

Thus, each pixel in the recognized image calculated by (9) represents 10-grayscale levels, that is, $s_{x,y} = 0, 1, \dots, 9$. Taking into account this limitation, we first reduce 256-grayscale levels to 10 and regard the 10-grayscaled image as the G . Therefore, the choice of the effective grayscale level can be controlled by

choosing the number of the nearest neighboring pixels $|N(x, y)|$.

Then, we might choose a strategy to determine the threshold mask \mathbf{M} that minimizes the distance between the original and the recognized images. Namely, we minimize the following cost

$$\|\mathbf{G} - \mathbf{S}\| = \sum_{x,y} \sum_{i,j} (g_{x,y} - s_{x,y})^2 \quad (11)$$

We should notice that from the relation (4), the above distance $\|\mathbf{G} - \mathbf{S}\|$ is written in terms of the threshold mask \mathbf{M} for a given original image \mathbf{G} . By substituting the equation (4) into the above equation (11) we obtain the energy of the system as a function of the threshold mask \mathbf{M} . Thus, our digital halftoning is now reduced to a combinatorial optimization problem of the following energy function:

$$H(\mathbf{M}|\mathbf{G}) = \sum_{x,y} \left\{ g_{x,y} - \sum_{i,j \in N(x,y)} K(x-i, y-j) \Theta(g_{x,y} - m_{i,j}) \right\}^2 \quad (12)$$

The above energy function $H(\mathbf{M}|\mathbf{G})$ is our starting point of statistical-mechanical modeling of the digital halftoning.

As we have the energy function of the system, one can generate statistical ensembles according to standard statistical mechanics. In its thermal equilibrium, each possible microscopic state \mathbf{M} obeys the following Gibbs distribution:

$$P_{\text{Gibbs}}(\mathbf{M}|\mathbf{G}) = \frac{\exp[-\beta H(\mathbf{M}|\mathbf{G})]}{\sum_{\mathbf{M}} \exp[-\beta H(\mathbf{M}|\mathbf{G})]} \quad (13)$$

One of the simplest uses of the above energy function is to regard its minimum energy state as the optimal threshold mask. Namely, the so-called *MAP (maximum a posteriori) solution*

$$\tilde{\mathbf{M}}_{\text{MAP}} = \arg \min_{\mathbf{M}} H(\mathbf{M}|\mathbf{G}) \quad (14)$$

, which is rewritten in terms of the statistical-mechanical terminology as

$$\tilde{\mathbf{M}}_{\infty} = \lim_{\beta \rightarrow \infty} \text{tr}_{\mathbf{M}} \mathbf{M}_{\infty} P(\mathbf{M}|\mathbf{G}) \quad (15)$$

, is a possible strategy. Calculating the Q^{LCL} sums $\text{tr}_{\mathbf{M}}(\cdot)$ and taking the zero-temperature limit is performed by important sampling of the MCMC method and temperature annealing procedure during the Monte Carlo steps.

The solution might be a good candidate for the suitable threshold mask.

We should comment on the related studies of the model-based digital halftoning to our present work. As a direct binary search in the space of the halftoned binary dots image, Pappas and Neuhoff [11][12][13] introduced the so-called *Least-square model-based halftoning* that attempt to minimize the following energy function (square error):

$$E = \sum_{x,y} (g_{x,y} - s_{x,y})^2 \quad (16)$$

with

$$g_{x,y} = (\mathbf{w} * \mathbf{g})_{x,y} = \sum_{k,l} w(x-k, y-l) g_{k,l} \quad (17)$$

$$s_{x,y} = (\mathbf{w}' * \mathbf{p})_{x,y} = \sum_{k,l} w'(x-k, y-l) p_{k,l} \quad (18)$$

, $p_{k,l} = \delta_{k,l} + (f_1 \alpha + f_2 \beta - f_3 \gamma)(1 - \delta_{k,l})$, where the kernels w, w' in each convolution product denote the human eye filter and $p_{k,l}$ corresponds to some printer model.

The factor f_1 denotes the number of horizontally and vertically neighboring dots that take black, f_2 means the number of diagonally neighboring dots being black, and f_3 is the number of pairs of neighboring dots of black. The coefficients α, β, γ are all positive constants. They looked for the lowest energy state in the space of the binary halftoned image \mathbf{H} by some heuristics (a kind of iterative procedure). On the other hand, by introducing the threshold mask explicitly, we look for the optimal threshold mask in the space of the \mathbf{M} .

When we expand the square of the energy function, we have two terms and each of them is understood in the literature of statistical mechanics of disordered spin system as follows. The first one is the random field term $-g_{x,y} \sum_{i,j \in N(x,y)} \Theta(g_{x,y} - m_{i,j})$ to minimize the total energy on condition that the threshold mask value is greater than the original image for all pixels. The two-body interactions term $\sum_{(i,j) \in N(x,y)} \Theta(g_{x,y} - m_{i,j}) \Theta(g_{x,y} - m_{i,j})$ decreases the total energy when at least one of two pixels in the pairs existing in the region $N(x,y)$ holds the condition that the threshold value is smaller than the corresponding original grayscale pixel. In our system described by the energy function (12), the lowest energy state is determined under the competition between these two conflict effects. Moreover, due to the *quenched* variables (what we call *disorder*) as a given original image \mathbf{G} besides the competition we mentioned above, the lowest energy state in the dynamical variable space of \mathbf{M} might be highly non-trivial and it means that we can use various techniques developed in the field of statistical physics of disordered spin systems to obtain the lowest energy state and to investigate the lowest energy properties. In the next section, we show some demonstrations to make the halftoned image by minimizing the energy (12) via simulated annealing [9][10].

III. NUMERICAL EXPERIMENTS

In this section, we show some demonstrations to generate the optimal threshold mask and the resultant halftoned image for a given standard grayscale image. We test our strategy for one of the well-known standard images, that is *lena* shown in FIG.2. The size of the image is 400×400 and the grayscale level is 256. We first convert the original 256-grayscale image \mathbf{G} to $Q(< 256)$ -grayscale image \mathbf{G} by the following transform:

$$C(x:Q) = \sum_{k=0}^{Q-1} k \left\{ \Theta\left(x - \frac{256}{Q}(k+1)\right) - \Theta\left(x - \frac{256}{Q}k\right) \right\} \quad (19)$$

and make the quenched variables $\forall(x,y) \quad g_{x,y} = C(g'_{x,y}, 10)$ in this paper. For this input data, we construct the energy function and carry out the calculation of the variable (15) via simulated annealing with the annealing schedule $\beta = \sqrt{t+1}/3$. For the solution of the threshold mask, we make the halftoned image according to (6).

In FIG.3, we show the solution of the simulated annealing, namely, the optimal threshold mask that minimizes the energy function. We also show the halftoned binary dots image in FIG. 4. The local structure of the binary dots is shown in FIG.5. From these pictures, we found that globally the resulting

halftoned image looks well, however, locally it contains some curious, undesirable clusters of *vortex configurations*. The similar phenomena are generally observed in the halftoned binary dots image via the *error-diffusion method* [6]. It might be possible to assume that these vortex configurations correspond to locally minimum energy state and might be disappeared when we obtain the globally minimum solution.



FIG.2. Original standard image lena of size 400 x 400. We use this image after reducing the number of the grayscale levels from 256 to 10 by means of the transform (19).

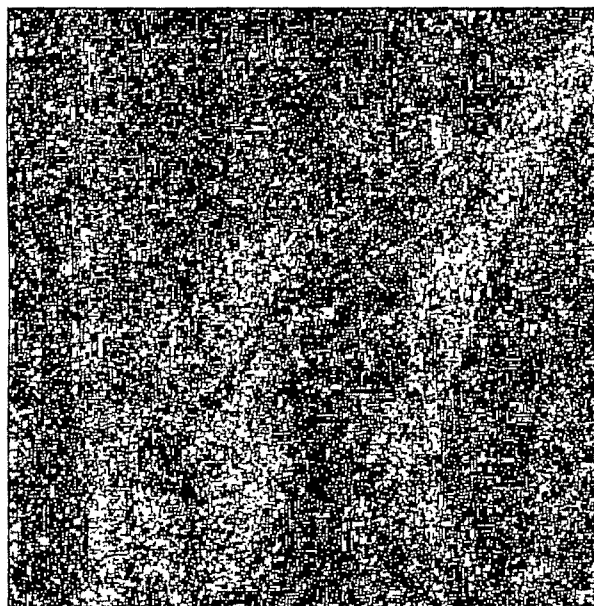


FIG. 3 Generated threshold mask obtained by our algorithm.



FIG.4. The halftoned binary dots image.

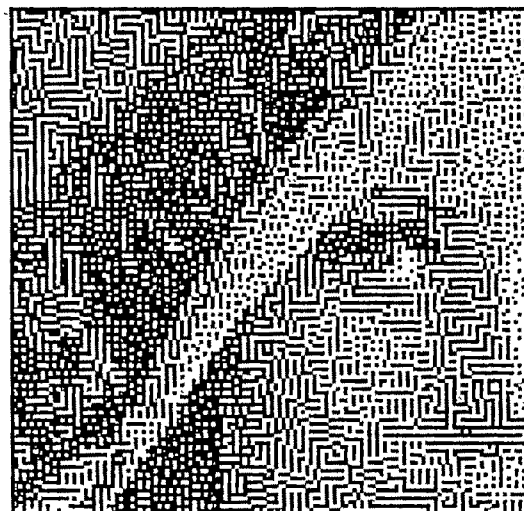


FIG.5. A local structure of binary dots image of FIG. 4. It contains the same kind of vortex configurations as the halftoned binary dots of the error-diffusion algorithm [6].

IV. POWER SPECTRUM STATISTICS

In order to investigate the statistical properties of the model, we first investigate the power spectrum of the threshold mask. As well-known, the so-called blue noise mask, there exists principal frequency and below the value, the power spectrum drops to zero, whereas, the high-frequency components remains finite. On the other hand, the mask generated by our algorithm apparently depends on the structure of the original grayscale image. However, from the power spectrum $P(f_x, f_y)$ shown in FIG.6, we find that the low-frequency components almost disappear and high-frequency components remain finite.

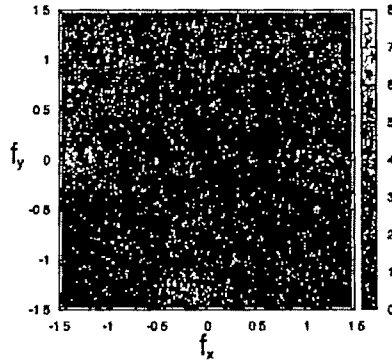


FIG.6. Power spectrum of the resultant binary dots image.

More convenient spectrum statistics is the so-called *radial-averaged power spectrum* [14] defined by

$$P(f_p) = \frac{1}{N(R(f_p))} \sum_{f_x, f_y \in R(f_p)} P(f_x, f_y) \quad (14)$$

where $R(f_p)$ means the region of annual rings in the Fourier space with width Δ_p .

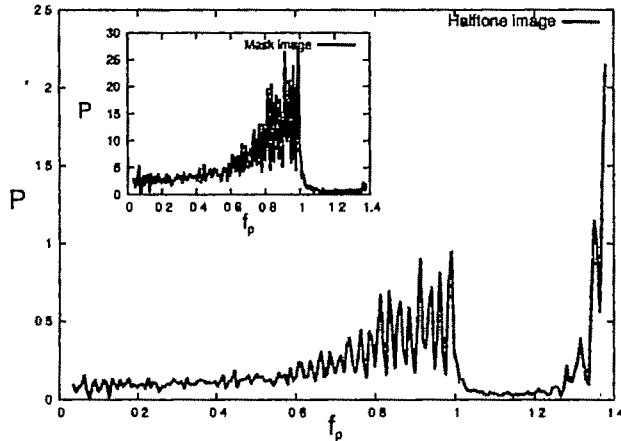


FIG.7. Radial-averaged power spectrum of the halftoned image. Inset is the same statistics for the threshold mask.

In FIG.7, we plot the spectrum statistics for both threshold mask and resulting binary dots of the halftoned image. Inset of FIG. 7 shows the same statistics for the threshold mask image. From this figure, we find that the low-frequency components are not dominant and relatively high-frequency components are larger than the low-frequency counter part. This tendency should be welcomed from the view point of human eyes modulation as we explained in introduction.

V. SUMMARY

In this short paper, we proposed a possibility of modeling for digital halftoning. This formalism helps us to understand the problem as a combinatorial optimization which is described by disordered spin systems. Finding the minimum energy state was

achieved by simulated annealing and we found that the resultant binary dots image looks well. However, in some part of the halftoned image, some vortex structures, which are some times encountered in the error-diffusion algorithm, appear and it might be possible for us to understand the phenomenon by considering the structure of the lowest energy states. Statistical mechanics might help us to and deal with such kind of problems and delete the undesirable local structure.

ACKNOWLEDGEMENT

This work was financially supported by Grant-in-Aid, Scientific Research on Priority Areas *Deepening and Expansion of Statistical Mechanical Informatics (DEX-SMI)* of the Ministry of Education, Culture, Sports, Science and Technology (MEXT) No. 18079001.

REFERENCES

- [1] D.L. Lau and G.R. Ace, "Modern digital halftoning", Marcel Dekker, Ink 2001.
- [2] R. Ulichney, "Digital Halftoning", The MIT Press 1987.
- [3] M. Analoui and J.P. Allebach, "Model based halftoning using direct binary search, *Proceedings SPIE, Human Vision, Visual Processing, and Digital Display III*, vol. 1666, pp. 96-108, August 1992.
- [4] J.L. Mannon and D.J. Sakrison, "The effects of a visual fidelity creation on the encoding of images", *IEEE Trans. Information Theory*, IT-20, pp.525-536, 1974.
- [5] T. Mista and K.J. Parker, "Digital halftoning technique using a blue-noise mask", *J. Opt. Soc. Am. A9*, pp.1920-1929, 1992.
- [6] R.W. Floyd and L. Steinberg, "An adaptive algorithm for special gray-scale", *Proceedings Society Information Display*, vol.17, no.2, pp.75-78, 1976.
- [7] Y. Saika and J. Inoue, "Probabilistic Inference to the Problem of Inverse-Halftoning based on Statistical Mechanics of the Q-Ising model", *Proceedings of the 2007 IEEE symposium on Foundation of Computational Intelligence (FOCI2007)*, pp. 426-430, 2007.
- [8] J. Inoue and Y. Saika and M. Okada, "Statistical-Mechanical Analysis of Inverse Digital Halftoning", *Proceedings of 7th International conference on Intelligent Systems Design and Applications (ISDA07)*, to appear, 2007.
- [9] S. Kirkpatrick, C.D. Gellet and M.P. Vecchi, "Optimization by simulated annealing", *Science*, 220, pp.671-680, 1983.
- [10] S. Geman and D. Geman, "Stochastic relaxation, Gibbs distributions, and the Bayesian restoration of images", *IEEE Transaction on Pattern Analysis and Machine Intelligence*, 6, pp.721-741, 1984.
- [11] T.N. Pappas and D.L. Neuhoff, "Least-squares model-based halftoning", *Proceedings of SPIE, Human Vision, Visual Processing, and Digital Display III*, vol. 1666, pp. 96-108, February 1992.
- [12] T.N. Pappas, "Model-based halftoning of color images", *IS&T's 8th International Congress on Advances in Non-Impact Printing Technologies*, pp. 270-275, 1992.
- [13] T.N. Pappas, "Digital Halftoning: A Model-Based Perspective", *International Journal of Imaging Systems and Technology*, vol. 7, pp.110-120, 1996.
- [14] R.A. Ulichney, "Dithering with blue noise", *Proceedings of the IEEE*, vol. 76, no.1, pp. 56-79, January 1988.

Illumination Normalization Using DCT Coefficients Re-scaling and Adaptive Histogram Equalization for Face Recognition

Virendra P. Vishwakarma¹, Sujata Pandey², and M. N. Gupta¹

¹Department of Computer Science and Engineering, ²Department of Electronics and Communication Engineering
Amity School of Engineering and Technology, Guru Gobind Singh Indraprastha University, New Delhi, India
e-mail: virendravishwa@rediffmail.com

Abstract— In this paper a novel approach for illumination normalization for the application of face recognition is proposed. The input face images for analysis of the proposed system are taken from Yale Face Database B. Our approach for illumination normalization utilizes the fact that low-frequency discrete cosine transform (DCT) coefficients are correlated with illumination variations. We have taken the concept of re-scaling to lower value of the low-frequency DCT coefficients. Initially the contrast of the images from database is stretched to the full range of intensity levels using full image histogram equalization method. Then the low-frequency DCT coefficients are re-scaled to lower value. After this the adaptive histogram equalization is applied on the output of inverse DCT. This results in further enhancement of the output image. The results show better appearance of images as compared to other existing approaches.

Key words— Discrete Cosine Transform, face recognition, histogram equalization, illumination normalization.

I. INTRODUCTION

FACE recognition is one of the most successful applications of image analysis and understanding. This has received significant attention, because of its wide range of commercial and law enforcement applications [1],[2]. Even though current machine recognition systems have reached a certain level of maturity, their success is limited by the conditions imposed by many real applications. For example, recognition of face images acquired in an outdoor environment with changes in illumination and/or pose remains a largely unsolved problem. Ambient lighting changes greatly within and between days and among indoor and outdoor environments. Due to the 3D structure of the face, a direct lighting source can cast strong shadows that accentuate or diminish certain facial features. The illumination problem is basically the variability of an object's appearance from one image to the next with slight changes in lighting conditions and viewpoint. This often results in large changes in the object's appearance [3],[4].

Early work in illumination invariant face recognition focused on image representations that are mostly insensitive to changes in illumination. There were approaches in which the image representations and distance measures were evaluated on a tightly controlled face database that varied the face pose, illumination, and expression. The image representations include edge maps, 2D Gabor-like filters, first and second derivatives of the gray-level image, and the logarithmic transformations of the intensity image along with these representations. However, none of the image representations was found to be sufficient by itself to overcome variations due to illumination changes [4].

The different approaches to solve the problem of illumination variation can be broadly classified into three main categories. The first approach is based on "preprocessing and normalization". The representative methods are histogram equalization (HE), Gamma correction, logarithm transform, etc. for illumination normalization. However, non-uniform illumination variation is still difficult to deal with using these global processing techniques [5]. In the second approach, the systems are exploiting "invariant feature extraction" method. A very renowned method for feature extraction is Fisher-face (based on linear discriminant analysis (LDA)), which maps the image space to a low dimensional subspace to discount variation in lighting etc.[6]. This method is a statistical linear projection method in which the representativeness of the training samples controls the performance of the system. The quotient image is regarded as the illumination invariant signature image, which can be used for face recognition under varying lighting condition [7]. Bootstrap database is required for this method and the performance degrades when dominant features between the bootstrap set and the test set are misaligned. The face modeling methods are under third category (3-D Shape of human faces) [5]. Here the attempt is to construct a generative 3-D face model that can be used to render the face images with different poses and lighting conditions. A generative model called illumination cone was presented in [8]. The main idea of this method is that the set of face images in fixed pose but under different illumination

conditions can be represented using an illumination convex cone, which can be constructed from a number of images acquired under variable lighting conditions and the illumination cone can be approximated in a low-dimensional linear subspace.

In this paper, we propose a novel approach that utilizes the image enhancement capability of DCT. The full image histogram equalization method is applied on the given image for contrast stretching. To suppress illumination variations the DCT is applied on the resultant image. As the low-frequency DCT coefficients correspond to illumination variations, the authors propose a new technique to suppress them. The method involves the re-scaling of these coefficients. Also to achieve further contrast enhancement, the adaptive histogram equalization is applied on the output of inverse DCT. The results show better appearance of images as compared to other existing approaches.

The reminder of this paper is organized as follows. Section II lays out the details of histogram equalization, adaptive histogram equalization, and discrete cosine transform. Experimental results and discussions are given in Section III. Finally, the conclusions are presented in Section IV.

II. BACKGROUND

A. Histogram Equalization

Histogram equalization maps the input image's intensity values so that the histogram of the resulting image will have an approximately uniform distribution [9], [10], [11].

The histogram of a digital image with gray levels in the range $[0, L-1]$ is a discrete function

$$p(r_k) = n_k / n, \quad (1)$$

where r_k is the k^{th} gray level, n_k is the number of pixels in the image with that gray level, n is the total number of pixels in the image, and $k = 0, 1, 2, \dots, L-1$. Basically $p(r_k)$ gives an estimate of the probability of occurrence of gray level r_k .

By histogram equalization, the local contrast of the object in the image is increased, especially when the usable data of the image is represented by close contrast values. Through this adjustment, the intensity can be better distributed on the histogram. This allows for areas of lower local contrast to gain a higher contrast without affecting the global contrast. The histogram equalization for a digital image is defined as a transformation on the input intensity levels (r_k) to obtain output intensity levels (s_k) as

$$s_k = T(r_k) = \sum_{j=1}^k p_r(r_j) = \sum_{j=1}^k \frac{n_j}{n} \quad (2)$$

for $k = 0, 1, 2, \dots, L-1$.

B. Adaptive Histogram Equalization

In histogram equalization, the goal is to obtain a uniform histogram for the output image, so that an "optimal" overall

contrast is perceived. However, the feature of interest in an image might need enhancement locally. Adaptive Histogram Equalization (AHE) computes the histogram of a local window centered at a given pixel to determine the mapping for that pixel, which provides a local contrast enhancement. However, the enhancement is so strong that two major problems can arise: noise amplification in "flat" regions of the image and "ring" artifacts at strong edges [12], [13].

A generalization of AHE, contrast limiting AHE (CLAHE) has more flexibility in choosing the local histogram mapping function. By selecting the clipping level of the histogram, undesired noise amplification can be reduced [14], [15]. CLAHE operates on small regions in the image, called *tiles*, rather than entire image. Each tile's contrast is enhanced, so that the histogram of the output region approximately matches the histogram specified by a distribution parameter, which may be a uniform or a different shape histogram. The neighboring tiles are then combined using bilinear interpolation to eliminate artificially induced boundaries. The contrast, especially in homogeneous areas, can be limited to avoid amplifying any noise that might be present in the image.

C. Discrete Cosine Transform

The DCT is a popular technique in imaging and video compression, which transforms signals in the spatial representation into a frequency representation.

The forward 2D-DCT [5], [16] of a $M \times N$ block image is defined as

$$C(u, v) = \alpha(u)\alpha(v) \sum_{x=0}^{M-1} \sum_{y=0}^{N-1} f(x, y) \times \cos\left[\frac{\pi(2x+1)u}{2M}\right] \cos\left[\frac{\pi(2y+1)v}{2N}\right] \quad (3)$$

The inverse transform is defined as

$$f(x, y) = \sum_{u=0}^{M-1} \sum_{v=0}^{N-1} \alpha(u)\alpha(v)C(u, v) \times \cos\left[\frac{\pi(2x+1)u}{2M}\right] \cos\left[\frac{\pi(2y+1)v}{2N}\right] \quad (4)$$

where

$$\alpha(u) = \begin{cases} \frac{1}{\sqrt{M}}, & u=0 \\ \sqrt{\frac{2}{M}}, & u=1, 2, \dots, M-1 \end{cases} \quad \text{and} \quad \alpha(v) = \begin{cases} \frac{1}{\sqrt{N}}, & v=0 \\ \sqrt{\frac{2}{N}}, & v=1, 2, \dots, N-1 \end{cases}$$

and, x and y are spatial coordinates in the image block, and u and v are coordinates in the DCT coefficients block. Fig.1 shows the properties of the DCT coefficients in $M \times N$ blocks with the zigzag pattern used by JPEG compression to process the DCT coefficients. Although the total energy remains the same in the $M \times N$ blocks, the energy distribution changes with most energy being compacted to the low-frequency

coefficients. In our approach we have taken the DCT coefficients in zigzag pattern as shown in Fig.1.

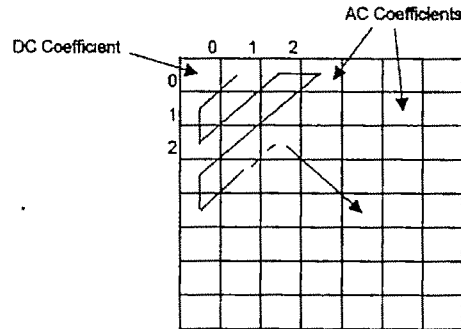


Fig.1 Block feature of DCT coefficients and their selection in zigzag pattern.

The DC coefficient is represented by $C(0,0)$ in the forward 2D-DCT equation. As the cosine of zero is one, the equation is simplified to:

$$C(0,0) = \frac{1}{M \times N} \sum_{x=0}^{M-1} \sum_{y=0}^{N-1} f(x, y) \quad (5)$$

The DC coefficient, which is located at the upper left corner, holds most of the image energy and represents the proportional average of the $M \times N$ blocks. The remaining $((M \times N) - 1)$ coefficients denote the intensity changes among the block images and are referred to as AC coefficients. The DCT is performed on the entire image obtained after processing the input face images by histogram equalization in our approach.

III. EXPERIMENTAL RESULTS AND DISCUSSIONS

A. Face Database

The experiments are carried out on the Yale Face Database B which contains 5760 single light source images of 10 subjects each seen under 576 viewing conditions (9 poses x 64 illumination conditions) [17]. For every subject in a particular pose, an image with ambient (background) illumination was also captured. We concentrated on the images with illumination variations. Some sample images are given in Fig.2.

B. Histogram Equalization

After applying histogram equalization on the images of face database, the contrast of the processed images is stretched to full range of intensity levels. Fig.3(a) shows one of the images taken from database and its corresponding histogram is shown in Fig.3(c). Fig.3(b) shows the processed image after applying histogram equalization on the image of Fig.3(a). The histogram of processed image is shown in Fig.3(d). The histogram of original image, as shown in Fig.3(b), depicts that the probability of occurrence of intensity levels is below the mid of gray scale.

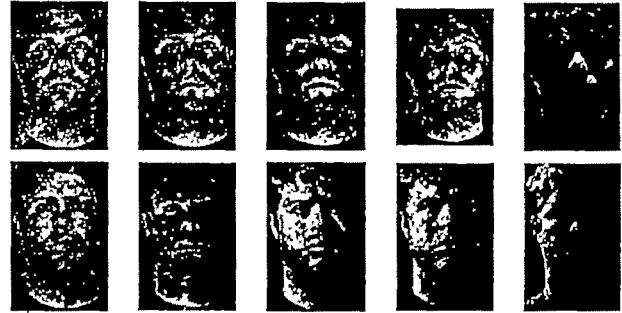


Fig. 2 Sample Images of an individual under different illumination

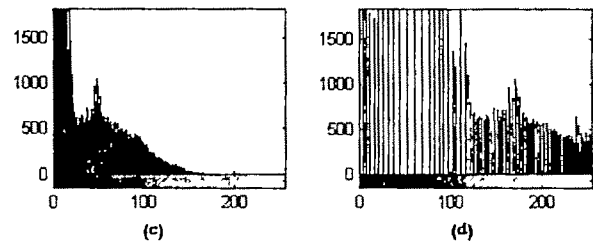
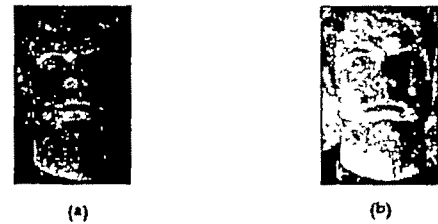


Fig 3 (a) Original Image; (b) Image after histogram equalization; (c) Histogram of image in (a); (d) Histogram of image in (b).

After histogram equalization, we obtain approximately uniform intensity distribution and we get a high contrast image as shown in Fig.3(b). But it is also visible from Fig.3(a) and Fig.3(b) that the illumination variations are not affected, these remain in the images, although illumination variations are shifted to the upward in the gray scale. This problem is solved by the method described in the next sub-section.

C. Illumination Normalization using Re-scaling of Low-Frequency DCT Coefficients

Our approach for illumination normalization utilizes the fact that low-frequency DCT coefficients are correlated with illumination variations. As mentioned in Fig.1 the DCT coefficients are selected in zig-zag pattern, if we select DCT coefficients from upper diagonal elements of top-left corner of Fig.1, the DCT coefficients will be in increasing order of frequency (C_{resc}). For the images taken in analysis (Fig.2), the total number of DCT coefficients are $385 \times 256 = 98560$, out of these the coefficients corresponding to low frequencies are selected for re-scaling. Fig.4 shows the variation of appearance with the number of coefficients selected (C_{resc}). The Fig.4 (a) shows the original image, Fig.4(b) corresponds to image after histogram equalization only, Fig.4(c)-(j) show

the effect on illumination with variation of the number of DCT coefficients selected. It is evident from the Fig.4, that the optimal range of C_{rec} is between 20 to 54 (Fig.4 (e) to (g)). We have taken the lower value of C_{rec} as 20, to increase the computational efficiency of the system.

In the approach given by W. Chen et. al., [5], the low-frequency DCT coefficients are discarded. This results in loss of some information related with low-frequency DCT coefficients, which will be discussed in the next sub-section. In the proposed approach, we are dividing the low-frequency DCT coefficients by a constant 50. This value is taken by considering the ratio of mean in DCT domain of a properly illuminated image with that of a badly illuminated image (considered the last image of the samples in Fig.2).

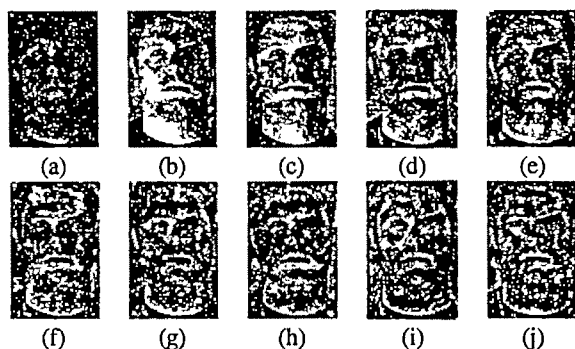


Fig.4 Normalized images with different C_{rec} : (a) original image; (b) only histogram equalization, $C_{rec} = 0$; (c) $C_{rec} = 2$; (d) $C_{rec} = 9$; (e) $C_{rec} = 20$; (f) $C_{rec} = 35$; (g) $C_{rec} = 54$; (h) $C_{rec} = 77$; (i) $C_{rec} = 104$; (j) $C_{rec} = 135$.

D. Adaptive Histogram Equalization

After illumination normalization using re-scaling of low-frequency DCT Coefficients, the adaptive histogram equalization is applied. As for optimal result, we divide the first 20 low-frequency DCT coefficients by a constant (50 as explained in the previous subsection), when we apply the inverse DCT, the contrast of the image obtained is lower. To overcome this problem, after applying inverse DCT, we apply adaptive histogram equalization on the output of inverse DCT. This results in further contrast enhancement of the output image. The numbers of tiles is used 4×4 block for adaptive histogram equalization and we have taken flat histogram shape for the image tiles with contrast limiting to reduce noise amplification.

Fig.5 shows the images after applying the proposed approach on the images of Fig.2 after applying histogram equalization. We have taken the concept of re-scaling to lower value of the low-frequency DCT coefficients, which is done by dividing these coefficients by the constant discussed above. Because the illumination variations are directly related with the low-frequency DCT coefficients. But there are some facial features which correspond to the low-frequency DCT coefficients, so we can not completely discard them (as done by W. Chen et. al., [5]). That is why we re-scale these coefficients and better results are obtained as evident in Fig.6.

E. Comparison with other approach

In Fig.6 the comparative study of the approach given by W. Chen et. al., [5] is done with the proposed approach. The Fig 6(a) shows the original images with illumination variation. The result of discarding first 20 low-frequency DCT coefficients for respective input images are shown in Fig.6(b). The fading effect of images in Fig.6(b) is also visible. The Fig.6(c) shows the output of applying the proposed approach for respective input images taken in Fig.6(a). It is evident from these figures that the performance of the proposed approach is quite better for different illumination variation. Another advantage of our approach is that for different illuminated images, the same approach is applicable and comparable results even in different illumination are obtained.

IV. CONCLUSIONS

In this paper, we propose a novel approach for illumination normalization. The input image contrast is stretched using full image histogram equalization. The low-frequency DCT coefficients are re-scaled to suppress the illumination variations. The appearance of output images of the proposed approach compared to that of the other approaches is better. Hence the proposed technique can be implemented in real time face recognition system. The present research shows that the effect of shadowing is not eliminated. In our future work we will focus on the elimination/reduction of shadowing effect.

REFERENCES

- [1] Zhao, W., Chellappa, R., Phillips, P.J. and Rosenfeld, A. "Face Recognition: A Literature Survey", *ACM Computing Surveys*, vol. 35, no. 4, pp 399-458, Dec 2003.
- [2] R. Chellappa, C. L. Wilson, and S. Sirohey, "Human and machine recognition of faces: a survey," *Proc. IEEE*, vol. 83, no. 5, pp. 705-740, May 1995.
- [3] P. N. Belhumeur and D. J. Kriegman, "What is the set of images of an object under all possible illumination conditions," *International Journal of Computer Vision*, vol. 28, no. 3, pp. 245-260, Jul. 1998.
- [4] Stan Z. Li and Anil K. Jain, *Handbook of Face Recognition*, Springer, 2005
- [5] Wellong Chen, Meng Joo and Shiquan Wu, "Illumination Compensation and Normalization For Robust Face Recognition Using Discrete Cosine Transform In Logarithm Domain" *IEEE Transactions on Systems, Man, And Cybernetics—Part B: Cybernetics*, Vol. 36, No. 2, pp 458-466, Apr. 2006.
- [6] Belhumeur P.N., J. P. Hespanha, and D. J. Kriegman, "Eigenfaces versus Fisherfaces: recognition using class specific linear projection," *IEEE Trans. Pattern Anal. Mach. Intell.*, vol. 19, no. 7, pp. 711-720, Jul. 1997.
- [7] A. Shashua and T. Riklin-Raviv, "The quotient image: class-based re-rendering and recognition with varying illuminations," *IEEE Trans. Pattern Anal. Mach. Intell.*, vol. 23, no. 2, pp. 129-139, Feb. 2001.
- [8] A. S. Georghiades, P. N. Belhumeur, and D. W. Jacobs, "From few to many: illumination cone models for face recognition under variable lighting and pose," *IEEE Trans. Pattern Anal. Mach. Intell.*, vol. 23, no. 6, pp. 630-660, Jun. 2001.
- [9] Sos S. Agaian, Blair Silver and Karen A. Panetta "Transform Coefficient Histogram-Based Image Enhancement Algorithms Using Contrast Entropy", *IEEE Trans on Image Processing*, Vol. 16, No 3, Mar. 2007.
- [10] R. C. Gonzalez, R. E. Woods and S. L. Eddins, *Digital Image Processing Using MATLAB*, Pearson Education, 2005.
- [11] A. K. Jain, *Fundamentals of Digital Image Processing*. Pearson Education, 2006.



Fig.5 Output Images after applying the proposed approach



Fig.6 Comparison of output images (a) original images; (b) the output images of the approach given by W. Chen et. al., [5], after applied on the Images of (a), (c) the output images of the proposed approach after applied on the images of (a).

- [12] W. K. Pratt, *Digital Image Processing*. John Wiley & Sons, New York, 2001.
- [13] J. Alex Stark, "Adaptive Image Contrast Enhancement Using Generalizations of Histogram Equalization" *IEEE Trans. On Image Processing*, vol. 9, no 5, pp. 889-896, May 2000.
- [14] Jin, Yinpeng, Fayad, Laura M.; Laine, Andrew F., "Contrast enhancement by multiscale adaptive histogram equalization", *Proc. of Wavelets. Applications In Signal and Image Processing IX*, vol no. 4478, pp. 206-213, Dec. 2001.
- [15] MATLAB reference manual, available [online]: <http://www.mathworks.com/access/helpdesk/help/toolbox/images>.
- [16] Ronny T., Wanquan L., Svetha V. "Application of the DCT Energy Histogram for Face Recognition", in *Proc. of 2nd International Conference on Information Technology for Application (ICITA 2004)* pp 305-310, Jan. 2004.

- [17] Yale University Face Database, available [online]: <http://cvc.yale.edu/projects/yalefacesB/yalefacesB.html>.

Robust Face Recognition with PCA using Cascaded Correlation Neural Networks

J. Dheeba¹, N. Herald Anantha Rufus², and N. Albert Singh³

¹ N.I College of Engineering, Nagercoil, Anna University, TamilNadu India e-mail: dheeba@rediffmail.com.

² Udaya School of Engineering, Nagercoil, Anna University, India e-mail: herfus@yahoo.com

³ University of Kerala, Trivandrum India e-mail: albertsingh@rediffmail.com

Abstract— People in computer vision and pattern recognition have been working on automatic recognition of human faces for the last two decades. Our approach to the face recognition problem is to combine the principal component analysis and neural networks based on cascaded correlation algorithm. Here the faces are vertically oriented frontal view and also slanting with wide expression change. The gabor features are extracted from the images. It will eliminate background influence as much as possible. The face space is described by a set of eigenfaces. Each face is efficiently represented by its projection onto the space expanded by the eigenfaces and has a new descriptor. Neural networks fail to use knowledge in new learning because they begin learning from initially random connection weights. Here, we examine a connectionist algorithm that uses its existing knowledge to learn new problems. Cascaded Correlation Neural networks are used to recognize the face through learning correct classification of these new descriptors. A real-time system has been created which combines the face detection and recognition techniques. A recognition rate of more than 85% has been achieved over real tests. It is also shown that our face database can be easily expanded to accommodate more individuals.

Key words— Face detection, Pattern recognition, Computer vision, Artificial Neural Networks, Machine learning.

I. INTRODUCTION

IN this paper, we present a neural network-based algorithm to detect rotation invariant, frontal views of faces in gray-scale images. The algorithm works by applying one or more neural networks directly to portions of the input image, and arbitrating their results. Each network is trained to output the presence or absence of a face. The algorithms and training methods are designed to be general, with little customization for faces. Many face detection researchers have used the idea that facial images can be characterized directly in terms of pixel intensities. These images can be characterized by probabilistic models of the set of face images [2], or implicitly by neural networks or other mechanisms [3]. The parameters for these models are adjusted either automatically from example images (as in our work) or by hand. A few authors have taken the approach of extracting features and applying either manually or automatically generated rules for evaluating these features [1]. In our observations of face detector demonstrations, we have found that users expect faces to be detected at any angle. Training a neural network for the face detection task is challenging because of the difficulty in

characterizing prototypical “nonface” images. Unlike face recognition, in which the classes to be discriminated are different faces, the two classes to be discriminated in face detection are “images containing faces” and “images not containing faces”. It is easy to get a representative sample of images which contain faces, but much harder to get a representative sample of those which do not. We avoid the problem of using a huge training set for nonfaces by selectively adding images to the training set as training progresses [3].

Unlike similar previous systems [8, 9, 10] which could only detect upright, frontal faces, this system efficiently detects frontal faces which can be arbitrarily rotated within the image plane. Our system directly analyzes image intensities using neural networks, whose parameters are learned automatically from training examples. There are many ways to use neural networks for rotated-face detection. The simplest would be to employ one of the existing frontal, upright, face detection systems.

II. ALGORITHM

The overall algorithm for the proposed approach is given in Figure 1. Initially, a pyramid of images is generated from the original image. Each 140x140 pixel window of each level of the pyramid then goes through several processing steps. First, the window is preprocessed using histogram equalization, and given to the orientation network. The rotation angle returned by the network is then used to rotate the window with the potential face to an upright position. Finally, the derotated window is preprocessed and passed to Identifier network, which decide whether or not the window contains a face. The system as presented so far could easily signal that there are two faces of very different orientations located at adjacent pixel locations in the image. To counter such anomalies, and to reinforce correct detections, some arbitration heuristics are employed. The design of the orientation and identifier networks and the arbitration scheme are presented in the following subsections.

A. The Orientation Network

The first step in processing a window of the input image is to apply the orientation network. This network assumes that its input window contains a face, and is trained to estimate its orientation. The inputs to the network are the intensity values

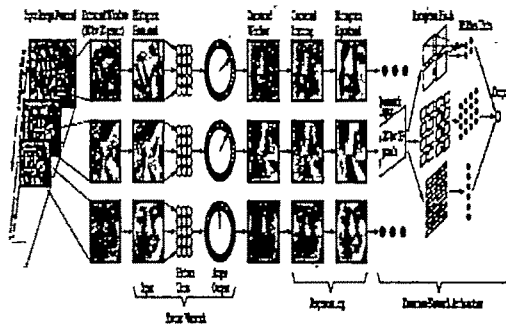


Figure 1: Overview of the Algorithm

in a 140x140 pixel window of the image. The output angle of rotation is represented by an array and affine transformation is used to rotate the image. Examples of the training data are given in Figure 2. The training examples are generated from a set of manually labeled example images containing 75 faces.

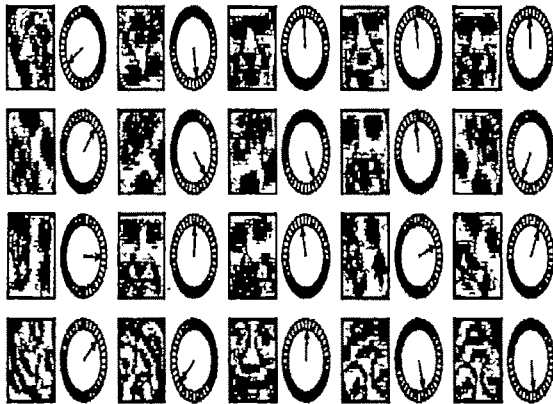


Figure 2: Training Pattern for the Orientation Network

The architecture for the orientation network consists of three layers, an input layer of 2 units, a hidden layer of 70 units, and an output layer of single unit. Each unit uses a hyperbolic tangent activation function, and the network is trained using the standard error back propagation algorithm.

B. The Identifier Network

After the orientation network has been applied to a window of the input, the window is derotated to make any face that may be present upright. The remaining task is to decide whether or not the window contains an upright face. The resampled image, 140x140 pixels, is preprocessed in two steps. First, we resize the image in window of size 18x27. Second, histogram equalization is performed, which expands the range of intensities in the window. The preprocessed window is then given to the identifier network. The identifier network is trained to produce an output of +1 if a face is present and -1 otherwise.

Training a neural network for the face detection task is challenging because of the difficulty in characterizing

prototypical "non-face" images. The two classes to be discriminated in face detection are "images containing faces" and "images not containing faces". It is easy to get a representative sample of images which contain faces, but much harder to get a representative sample of those which do not. The features of the image are a face vector field using Gabor filters [5]. The features are also extracted for the images by flipping and also to the mirror of the image.

The steps followed for training the identifier network are outlined as follows

1. Create an initial set of non-face images by generating 1000 random images.
2. Train the neural network to produce an output of +1 for the face examples, and -1 for the nonface examples. In the first iteration, the network's weights are initialized random. After the first iteration, we use the weights computed by training in the previous iteration as the starting point.
3. Run the system on an image of scenery which contains no faces. Collect sub images in which the network incorrectly identifies a face.

The architecture for the identifier network consists of three layers, an input layer of 2160 units, a hidden layer of 100 units, and an output layer of single unit. Each unit uses a hyperbolic tangent activation function, and the network is trained using the cascade correlation algorithm.

C. The Cascade Correlation Algorithm

Initial configuration:

The algorithm begins with a simple perceptron with N input units [9] and M output units. N and M are chosen on the basis of the problem that the network is to learn as shown in Fig.3.

Initial training:

The perceptron is trained on the entire training set $\{(V_p, T_p) \mid p = 1, \dots, P\}$, until the performance of the network is as good as possible. If the desired performance is obtained, the algorithm stops. Otherwise: Start adding hidden units to the network, one by one.

Training of candidates: A pool of candidates for a new hidden unit is generated. This pool emulates a stochastic search in the weight space, which will decrease the risk of inserting a candidate stranded in a local minimum with high error. Each node in the pool of candidates is connected to all input nodes and all previously inserted hidden units. Each of the candidates is trained with the purpose of maximizing some measure of "goodness" of the candidate.

Inserting a new hidden unit: The candidate with the highest score is inserted "for real" in the network as a new hidden unit. The incoming weights to the new hidden unit are then frozen, i.e. they are not to be changed anymore. The new hidden unit is connected to all output nodes with random weights.

Retraining the network:

All the incoming weights to the output units are retrained in order to adjust the weights from the newly inserted hidden unit. If the performance of the network is satisfying after retraining, the algorithm stops. Otherwise: Go to 3.

Cascade Correlation Neural Network Architecture

A cascade correlation network consists of input units, hidden units, and output units [11]. Input units are connected directly to output units with adjustable weighted connections. Connections from inputs to a hidden unit are trained when the hidden unit is added to the net and are then frozen. Connections from the hidden units to the output units are adjustable consequently.

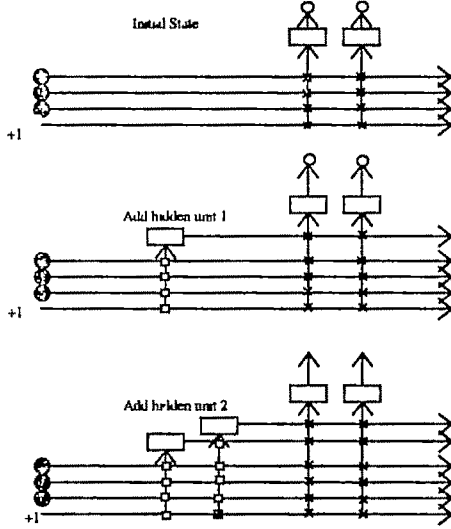


Fig. 3. The Cascade architecture, initial state and after adding two hidden units.

Cascade correlation network starts with a minimal topology, consisting only of the required input and output units (and a bias input that is always equals to 1). This net is trained until no further improvement is obtained. The error for each output unit is then computed (summed over all training patterns). Next, one hidden unit is added to the net in a two-step process. During the first step, a candidate unit is connected to each of the input units, but is not connected to the output units. The weights on the connections from the input units to the candidate unit are adjusted to maximize the correlation between the candidate's output and the residual error at the output units. The residual error is the difference between the target and the computed output, multiplied by the derivative of the output unit's activation function, i.e., the quantity that would be propagated back from the output units in the back propagation algorithm. When this training is completed, the weights are frozen and the candidate unit becomes a hidden unit in the net. The second step in which the new unit is added to the net now begins. The new hidden unit is then connected to the output units, and the weights on the connections being adjustable. Now all connections to the output units are trained. (Here the connections from the input units are trained again, and the new connections from the hidden unit are trained for the first time.) A second hidden unit is then added using the same process. However, this unit

receives an input signal from the both input units and the previous hidden unit. All weights on these connections are adjusted and then frozen. The connections to the output units are then established and trained. The process of adding a new unit, training its weights from the input units and the previously added hidden units, and then freezing the weights, followed by training all connections to the output units, is continued until the error reaches an acceptable level or the maximum number of epochs (or hidden units) is reached.

The purpose of inserting a new unit is to reduce the total error of the network. The way the CCA does this is to train the candidate unit so the correlation between the residual error and the output from the candidate is maximized. Let X and Y be two stochastic variables.

Then the correlation between X and Y is defined as:

$$\text{Corr}[X, Y] = \frac{\text{Cov}[X, Y]}{\sqrt{\text{Var}[X]\text{Var}[Y]}}$$

III. KLT FOR FACE RECOGNITION

Karhunen–Loeve Transform based dimensionality reduction for face images was first proposed by Sirovich and Kirby [6, 7]. Mathematically, the eigenface method tries to represent a face image as a linear combination of orthonormal vectors, called eigenfaces. These eigenfaces are obtained by finding the eigenvectors of the covariance matrix of the training face image set. Let $I_1, I_2, I_3, \dots, I_k$ be a set of k face images, each ordered lexicographically.

The eigenvectors of the matrix

$$C = \sum_{i=1}^K I_i I_i^T \quad (1)$$

that correspond to the largest eigenvalues span a linear subspace that can reconstruct the face images with minimum reconstruction error in the least squares sense. This L -dimensional subspace is called the face space. Assuming is a lexicographically ordered face image and is the matrix that contains the eigenfaces as its columns, we can write

$$x = \phi a + e_x \quad (2)$$

where a is the feature vector that represents the face, and e_x is the subspace representation error for the face image. As a larger training data set is used and the dimensionality of the face space is increased, the representation error gets smaller.

Letting

$$a = [a_1, a_2, \dots, a_L]^T \quad (3)$$

be the feature vector, and

$$\phi = [\phi_1, \phi_2, \dots, \phi_L] \quad (4)$$

be the matrix where are the eigenface vectors, is computed as follows:

$$a_i = \phi_i^T x, \quad (5)$$

IV. EXPERIMENTS

We assessed the feasibility and performance of our novel algorithm on the face recognition task, using a real data set. Specifically we used 75 frontal face images, which were acquired under variable illumination and facial expressions. The database used for evaluating face recognition algorithms displays diversity across gender, ethnicity, and age. The image sets were acquired without any restrictions imposed on facial expression and with at least two frontal images shot at different times during the same photo session. First, the centers of the eyes of an image are manually detected, then rotation and scaling transformations align the centers of the eyes to predefined locations. Finally, the face image is cropped to the size of 18*27 to extract the facial region, which is further normalized to zero mean and unit variance. The corresponding dominant eigen vectors and eigen faces are estimated and using this the face is recognized using Euclidean distance classifier. Figure 4 shows an example of the recognition of a rotated face.

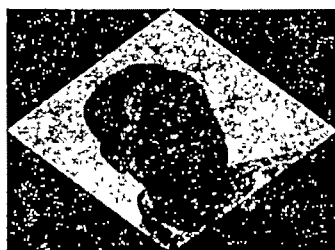


Figure 4: Recognition example from the mixed image.

A. Upright Detection Accuracy

To check the capability, detecting rotated faces has not come at the expense of accuracy in detecting upright faces. In Table 1 we present the result of applying the original identifier networks only and recognition using PCA. As expected, this system does well on the upright test set, but has a poor detection rate on the rotated test set.

Table:1

	Upright test set	Rotated test set
Classification rate	90.2%	15%

B. Proposed Approach Detection Accuracy

To check the capability, rotated and upright faces are applied with both the orientation and identifier networks. In Table 2 we present the result of applying the total image set and recognition using PCA. This system does well on the upright test set, and on the rotated test set.

Table:2

	Upright test set	Rotated test set
Classification rate	90.2%	87.3%

V. CONCLUSION

Face recognition has been an attractive field of research for both neuroscientists and computer vision scientists. Humans are able to identify reliably a large number of faces and neuroscientists are interested in understanding the perceptual and cognitive mechanisms at the base of the face recognition process. In this paper we have designed a feature based pose estimation system and face recognition system using 2D gabor wavelets as local feature information. The system is able to detect 87.3% of faces over two large test sets, with a small number of false positives. The technique is applicable to other template-based object detection schemes.

REFERENCES

- [1] S. H. Lin, S. Y. Kung, and L. J. Lin. "Face recognition/detection by probabilistic decision-based neural network", *IEEE Transactions on Neural Networks, Special Issue on Artificial Neural Networks and Pattern Recognition*, 8(1), January 1997.
- [2] Henry A. Rowley, Shumeet Baluja, and Takeo Kanade. "Neural network based face detection", *IEEE Transactions on Pattern Analysis and Machine Intelligence*, 20(1), January 1998.
- [3] Ming Zhang and John Fulcher. "Face recognition using artificial neural network group-based adaptive tolerance (GAT) trees", *IEEE Transactions on Neural Networks*, 7(3) 555-567, 1996.
- [4] R. Vaillant, C. Monroq, and Y. Le Cun. "Original approach for the localization of objects in images", *IEE Proceedings on Vision, Image, and Signal Processing*, 141(4), August 1994.
- [5] Jianke Zhu, Mang I Vai and Peng Un Mak, "Gabor Wavelets Transform and Extended Nearest Feature Space Classifier for Face Recognition", *Proceedings of the Third IEEE International Conference on Image and Graphics (ICIG'04)*, 2004.
- [6] M. Kirby and L. Sirovich, "Application of the Karhunen-Loeve Procedure for the Characterization of Human Faces," *IEEE Trans. Pattern Analysis and Machine Intelligence*, vol. 12, no. 1, pp. 103-108, Jan. 1990.
- [7] J. Karhunen, E. Oja, L. Wang, R. Vigario, and J. Joutsensalo, "A class of neural networks for independent component analysis," *IEEE Trans. Neural Networks*, vol. 8, pp. 486-504, May 1997.
- [8] E. Osuna, R. Freund, and F. Girosi, "Training support vector machines: An application to face detection," in *Proc. IEEE Conf. Computer Vision and Pattern Recognition*, 1997, pp. 130-136.
- [9] M. Turk and A. Pentland, "Eigenfaces for recognition," *J. Cognitive Neuroscience*, vol. 3, no. 1, pp. 71-86, 1991.
- [10] Xiaoguang Jia and Mark S. Nixon, "Extending the Feature Vector for Automatic Face Recognition", *IEEE Transactions on Pattern Analysis and Machine Intelligence*, 17(12), Dec 1995.
- [11] S. E. Fahlman and C. Lebiere, "The Cascade-Correlation Learning Architecture, in *Neural Information Processing Systems*", Editors D. Touretzky, Morgan Kaufmann Publishers, Inc., Denver, Colorado, 1990, pp. 524-532.

Face Recognition Using Back Propagation Algorithm

V.S. Dixit¹, Shveta Kundra Bhatia²

¹ Department of Computer Science, ARSD College, University of Delhi, Delhi, India, e-mail: veersaindixit@rediffmail.com.

² Department of Computer Science, Swami Shraddhanand College, University of Delhi, Delhi, e-mail: shvetakundra@rediffmail.com

Abstract—An artificial neural network (ANN), often just called a "neural network" (NN), is a group of artificial neurons that are interconnected and use a mathematical model or computational model for information processing based on a connectionist approach to computation. In order to train a neural network to perform some task, each neuron is assigned a weight. This weight is adjusted in such a way that the error between the desired output and the actual output is reduced. This process requires that the neural network computes the error derivative of the weights. In other words, it must calculate how the error changes as each weight is increased or decreased slightly. The back propagation algorithm can be used to tune the weights associated with each neuron. The back propagation algorithm is used in various applications for determining the weights to train the neural network. One of the applications of this methodology is face recognition. Face Recognition involves mapping the face of a person to the identity of that person. It is commonly used in applications such as human-machine interfaces and automatic access control systems. It involves comparing an image with a database of stored faces in order to identify the individual in that input image. The related task of face detection has direct relevance to face recognition because images must be analyzed and faces identified, before they can be recognized. ANN is known to be very effective in pattern recognition applications due to their high reliability.

We shall be creating a neural network package for face recognition, which can match the images to the identity of a single person. It gives us methods and functions for image access, the basic back-propagation functions and utilities for viewing the changes in the percentage correctness and error of the training and test sets. The base for our research is the package developed by Dr. Tom Mitchell which identifies the images to a single person's name "Glickman". The package has been enhanced to identify images of 20 persons in Dr. Tom Mitchell's database. In Dr. Tom Mitchell's database the images are present in the .pgm format with a resolution of 32 X 30 with slight variation in pose, face expression, lighting, whether the person sports sunglasses or not etc.

Keywords—Back Propagation, Face Recognition, Gradient Descent, Neural Networks.

I. INTRODUCTION

THE purpose of the research is to study and implement face recognition using neural networks. The problem is as follows:

Face recognition involves identifying the identity of the person in accordance to the input image (person's face). We have used the back propagation algorithm to train the neural network to identify the image and map it to its identity. Back Propagation is a very popular ANN learning algorithm. It is simple to implement, faster than many other "general" approaches, well-tested, and easy to mold into very specific and efficient algorithms [2]. It is a gradient descent algorithm, which learns the weights of the multilayer network. The gradient descent is employed to minimize the error between the network output values and the target output values for these outputs. A Back Propagation network learns by example. We give the algorithm examples of what we want the network to do and it changes the network's weights so that, when training is finished, it will give us the required output for a particular input. Back Propagation networks [1] are ideal for simple Pattern Recognition and Mapping Tasks.

The number of input nodes in the neural network depends upon the resolution of the image being given as the input to the network. The images in the database have been divided into two sets, the training set that will train the network for identification and test sets that are used for testing of the trained network.

The network used is a three layered fully connected feed forward Neural Network which uses Back Propagation for tuning the weights. The number of input nodes is 960. The number of hidden nodes has been decided by varying the number of nodes as 4, 5, 8, 10, 15 and 20 and testing the performance of the network. The number of output nodes is 20 as images of 20 persons need to be recognized.

We tested for optimal number of hidden nodes, learning rate and number of epochs. The system has been tested extensively by varying every parameter used in the training process.

A number of Neural Network types have been developed over the years. Neural Nets are given many different names such as Artificial Neural Networks (ANNs), Connectionism or Connectionist Models, Multi-layer Perceptrons (MLPs) and Parallel Distributed Processing (PDP). Despite all the different terms and different types, there is a small group of networks which are widely used and on which many others are based. These are: Back Propagation, Hopfield Networks, Competitive Networks and networks using Spiky Neurons. We shall discuss the back propagation network in detail.

Back propagation is a supervised learning technique used for training artificial neural networks. It was first described by Paul Werbos in 1974, and further developed by David E. Rumelhart, Geoffrey E. Hinton and Ronald J. Williams in 1986.

In a single-layer network, each neuron adjusts its weights according to what output was expected of it, and the output the network has given. This is mathematically expressed by the Perceptron Delta Rule:

$$\Delta w_i = x_i \delta$$

$$\text{where } \delta = (\text{desired output}) - (\text{actual output})$$

Where w is the array of weights, x is the array of inputs. The Perceptron Learning Rule is of no use though when we extend the network to multiple layers to account for non-linearly separable problems. When adjusting a weight in the network, we have to be able to tell what effect this will have on the overall effect of the network. To do this, we have to look at the derivative of the error function with respect to that weight. The function used with the back-propagation nets is the Sigmoid (logistic) function. The equation and the graph for it are shown below.

$$y = \frac{1}{1 + e^{-x}}$$

$$y' = x(1 - x)$$

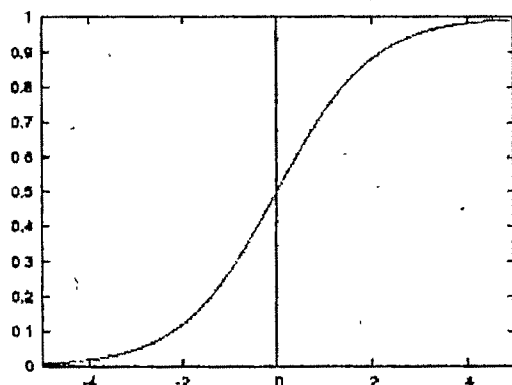


Fig. 1 Graph of Sigmoid Function

In the above graph the function plateaus out at 0 and 1 on the y-axis, and it also crosses the y-axis at 0.5. It differentiates to $f'(x) = x(1-x)$. Therefore now the value of delta is given as follows:

$$\Delta w_i = \eta x_i \delta$$

$$\text{where } \delta_i = f'(net_i)(d_i - y_i)$$

w , x are as above, and η is defined as the learning rate. y_i and d_i are the actual and desired outputs, respectively. Using the Sigmoid activation function, we can rewrite the equation for calculating the deltas for the output layer as follows:

$$\delta_i = y_i(1 - y_i)(d_i - y_i)$$

We now need to calculate delta for the hidden layers. We have to know the effect on the output of the neuron if a weight is to change. Therefore, we need to know the derivative of the error with respect to that weight. For the neuron q in hidden layer p , delta is:

$$\delta_p(q) = x_p(q)[1 - x_p(q)] \sum w_{p+1}(q, i) \delta_{p+1}(i)$$

Each delta value for hidden layers requires that the delta value for the layer after it be calculated. In a 3-layer network, the output-layer delta is first calculated using the delta formula:

$$\delta_i = y_i(1 - y_i)(d_i - y_i)$$

This value is then used to calculate the delta value for all remaining hidden layers using the formula:

$$\delta_p(q) = x_p(q)[1 - x_p(q)] \sum w_{p+1}(q, i) \delta_{p+1}(i)$$

Hence the name 'back-propagation' has been given as the error from the output layer is slowly propagated backwards through the network and hence is known as back-propagation network.

II. PACKAGE DETAILS

The package includes the various files each performing a specific functionality.

pgmimage.c, pgmimage.h: The image package supports reading and writing of .pgm image files and access to the pixel values. An IMAGE data structure is used to define the name of the image, number of rows and columns and the pixel values of the image and an IMAGELIST data structure that defines the number of images in the list and the names of the images.

backprop.c, backprop.h: The Neural Network package. These files provide routines for allocating memory, training by calculating the error and adjusting the weights of the network.

imagenet.c: This file contains the function for loading images into the input nodes of the network, and setting up the target vectors by using the function `load_target()` for training, where the required output for each network is written. For every

output the target varies and the output units change. If the image name and the image of the person match, then the target unit is set to HIGH, otherwise it is set to LOW.

facetrain.c: This is the main program, which uses all the above files to implement the recognizer. There is a performance evaluation module that evaluates the performance of the network for every epoch to find the percentage correctness of recognition.

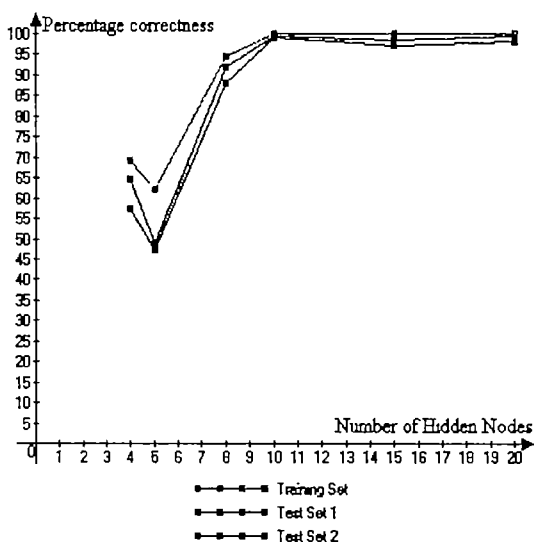
constants.h: The config file called constants.h is used to configure the system and also vary various parameters like learning rate, number of hidden and output nodes.

III. RESULTS AND CONCLUSIONS

The following variations have been made in the database to find the percentage correctness of training and testing the network: Variation in number of hidden nodes (4, 8, 10, 15, 20) with different training cycles or epochs such as 50, 100, 150, 200 and 500. Variation in the learning rate with different training cycles or epochs.

Number of Epochs	Number of Hidden Nodes	Percentage Correctness of the Training Set	Percentage Correctness of the Testing Set 1	Percentage Correctness of the Testing Set 2
50	4	69.3	64.7	57.2
50	5	62	48.9	47.1
50	8	94.5	92	87.9
50	10	100	99.2	99
50	15	100	98.5	97.1
50	20	100	99.2	98

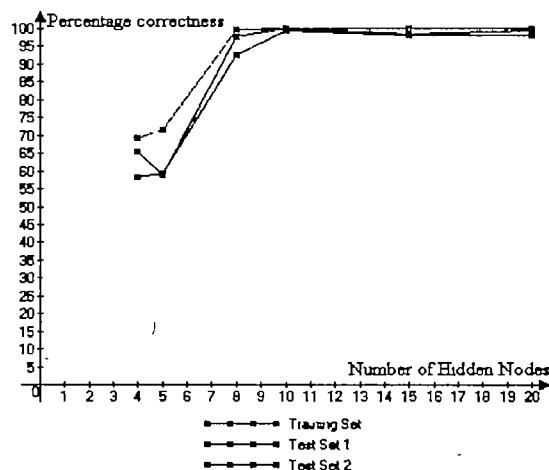
Table 1: Percentage correctness with variation in the number of hidden nodes and number of epochs as 50.



Graph 1: Percentage correctness with variation in the number of hidden nodes with 50 epochs.

Number of Epochs	Number of Hidden Nodes	Percentage Correctness of the Training Set	Percentage Correctness of the Testing Set 1	Percentage Correctness of the Testing Set 2
100	4	69.3	65.4	58.1
100	5	71.4	58.9	59.1
100	8	99.6	97.8	92.7
100	10	100	100	99.5
100	15	100	98.5	98
100	20	100	99.2	98

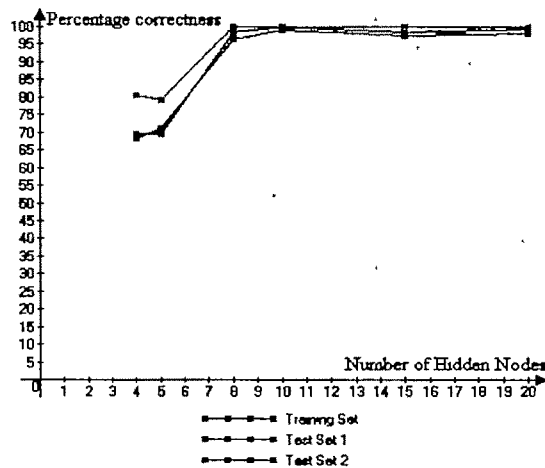
Table 2: Percentage correctness with variation in the number of hidden nodes and number of epochs as 100.



Graph 2: Percentage correctness with variation in the number of hidden nodes with 100 epochs.

Number of Epochs	Number of Hidden Nodes	Percentage Correctness of the Training Set	Percentage Correctness of the Testing Set 1	Percentage Correctness of the Testing Set 2
200	4	80.5	69.7	68.2
200	5	79.4	69.7	71.1
200	8	100	98.5	96.6
200	10	100	100	99
200	15	100	98.5	97.5
200	20	100	99.2	98

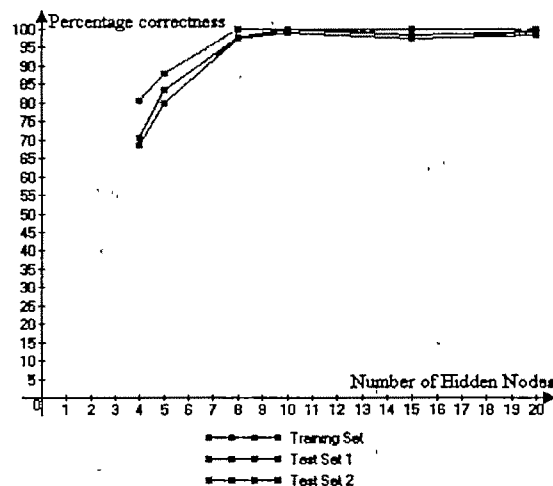
Table 3: Percentage correctness with variation in the number of hidden nodes and number of epochs as 200.



Graph 3: Percentage correctness with variation in the number of hidden nodes with 200 epochs.

Number of Epochs	Number of Hidden Nodes	Percentage Correctness of the Training Set	Percentage Correctness of the Testing Set 1	Percentage Correctness of the Testing Set 2
500	4	80.5	70.5	68.7
500	5	88	83.4	79.8
500	8	100	97.8	97.5
500	10	100	100	99
500	15	100	98.5	97.5
500	20	100	99.2	98.5

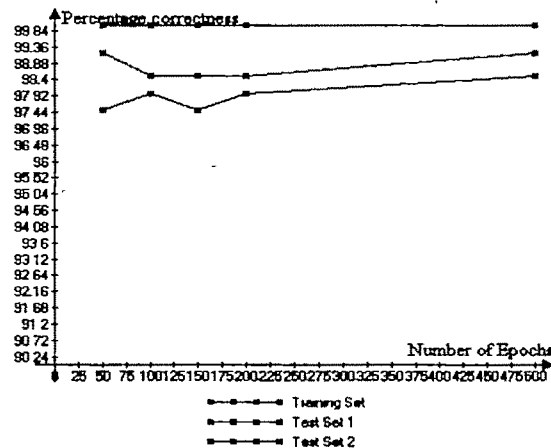
Table 4: Percentage correctness with variation in the number of hidden nodes and number of epochs as 500.



Graph 4: Percentage correctness with variation in the number of hidden nodes with 500 epochs.

Learning Rate	Number of Epochs	Percentage Correctness of the Training Set	Percentage Correctness of the Testing Set 1	Percentage Correctness of the Testing Set 2
0.3	50	100	99.2	97.5
0.3	100	100	98.5	98
0.3	150	100	98.5	97.5
0.3	200	100	98.5	98
0.3	500	100	99.2	98.5

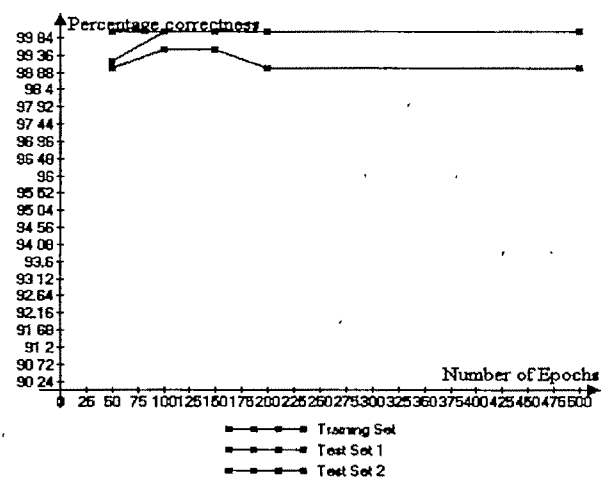
Table 5: Percentage correctness with variation in the number of epochs and the learning rate as 0.3.



Graph 5: Percentage correctness with variation in the number of epochs with 0.3 as the learning rate.

Learning Rate	Number of Epochs	Percentage Correctness of the Training Set	Percentage Correctness of the Testing Set 1	Percentage Correctness of the Testing Set 2
0.5	50	100	99.2	99
0.5	100	100	100	99.5
0.5	150	100	100	99.5
0.5	200	100	100	99
0.5	500	100	100	99

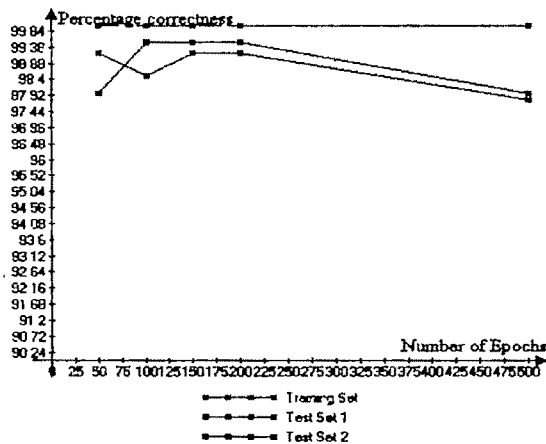
Table 6: Percentage correctness with variation in the number of epochs and the learning rate as 0.5.



Graph 6: Percentage correctness with variation in the number of epochs with 0.5 as the learning rate.

Learning Rate	Number of Epochs	Percentage Correctness of the Training Set	Percentage Correctness of the Testing Set 1	Percentage Correctness of the Testing Set 2
0.7	50	100	99.2	98
0.7	100	100	98.5	99.5
0.7	150	100	99.2	99.5
0.7	200	100	99.2	99.5
0.7	500	100	97.8	98

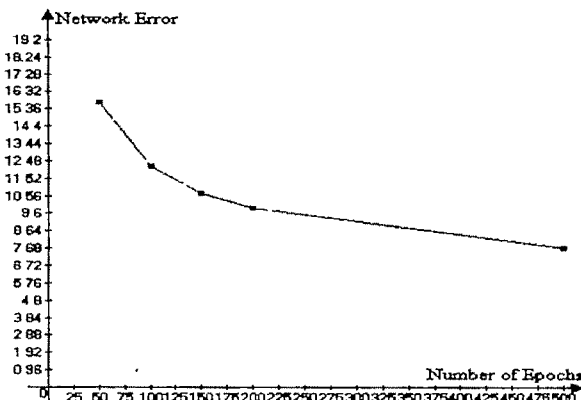
Table 7: Percentage correctness with variation in the number of epochs and the learning rate as 0.7.



Graph 7: Percentage correctness with variation in the number of epochs with 0.7 as the learning rate.

Number of Epochs	Total Error
50	15.7
100	12.2
150	10.7
200	9.9
500	7.7

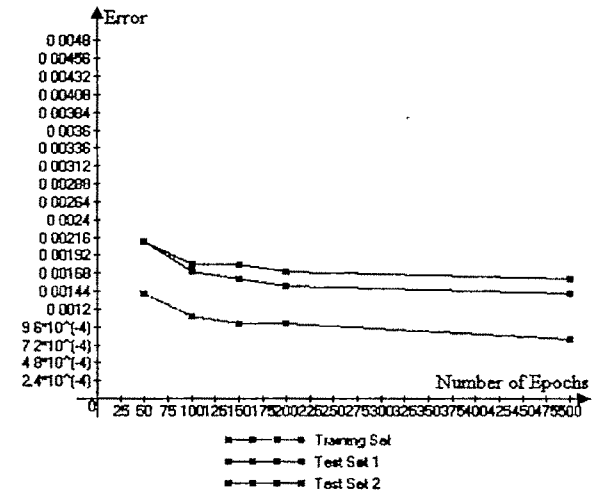
Table 8: Total network error with variation in the number of epochs.



Graph 8: Showing total network error with variation in the number of epochs.

Number of Epochs	Error on Training Set	Error on Test Set 1	Error on Test Set 2
50	0.0014	0.0021	0.0021
100	0.0011	0.0017	0.0018
150	0.0010	0.0016	0.0018
200	0.0017	0.0015	0.0017
500	0.0008	0.0014	0.0016

Table 9: Error on the training set, test set 1 and test set 2 with variation in the number of epochs.



Graph 9: Error on the training set, test set 1 and test set 2 with variation in the number of epochs.

IV. CONCLUSION

The designed Neural Network trained using Back Propagation algorithm behaves the best with the following parameters Learning Rate: 0.5, Number of Hidden Nodes: 10, Number of Epochs: 100. The accuracy of the network decreases with decrease in the number of hidden nodes. The accuracy of the network stabilizes after a certain increase in the number of hidden nodes. The total error of the network decreases with the increase in the number of epochs. In future we are trying to get more optimized results of the said problem using Fuzzy Neural Network in finding the defects in fabrics.

REFERENCES

- [1] Jun Zhang, Yong Yan and Martin Lade Face Recognition, "Eigenface, Elastic Matching and Neural Nets". Proceedings of the IEEE, Vol. 85, No. 9, September 1997.
- [2] John F. Kolen, Jordan B. Pollack Back Propagation Is Sensitive To Initial Conditions Proceedings of the 1990 conference on Advances in neural information processing systems, Pages 860 – 867, Year of Publication: 1990.
- [3] S. Suresh, S.N. Omkar, and V. Man, "Parallel Implementation of Back Propagation Algorithm in Networks of Workstations". January 2005
- [4] Neural Networks A Comprehensive foundation by Simon Haykin.
- [5] An introduction to Neural Networks by James A. Anderson.
- [6] www-cs.cmu.edu/afs/cs.cmu.edu/user/mitchell/rfp/faces.html
- [7] Machine Learning, Tom Mitchell, McGraw Hill, 1997

An Application Module Using Eigenfaces for Face Recognition

S.Tripathi¹, R.Agrawal², M.K.Saini³, A.K.Jain, S.Basu, R.Ramchandani, A.Gupta

¹ Amity School of Engineering and Technology, N.Delhi, e-mail: tripathisudhanshu@gmail.com).

² Amity School of Engineering and Technology, N.Delhi, e-mail: rarun96@yahoo.com

³ Amity School of Engineering and Technology, N.Delhi, e-mail: itsmemanishkumar@rediffmail.com

Abstract— Elgenspace-based face recognition technique has an advantage that faces are normally upright and thus may be described by a small set of 2-D characteristics views. In this paper, an approach to detect and identification of human faces which is real time face recognition system is developed with Graphical User Interface (GUI). This approach takes a snap of a person from the camera and store at a predefined place, which is treated as a two-dimensional (2-D) recognition problem. Face images are then projected on the feature space that encodes the variation among the known face images. The feature space here is defined the eigenfaces which are eigenvectors of the set of faces, they do not necessarily correspond to isolated features. The GUI developed is user friendly and recognizes the image in the unsupervised manner.

Key words—Eigenfaces, Euclidean Distance, Face Recognition, Principal component Analysis (PCA)

I. INTRODUCTION

FACE identification is one of the most remarkable abilities of the human brain. The human brain has immense capacity to store millions of images and to identify and recognize them on the basis of distinct patterns. One can recognize and distinguish thousands of different faces despite distortions brought about by varying facial expressions, intensity levels, ageing, spectacles and changes in facial features like growing of moustache etc.

A computerized face recognition system is a step towards machine implementation of this extraordinary power of the human brain. It may be used in several applications like security systems, criminal identification systems etc. to save a lot of time. It could take hours to scan through the entire data and chances of human error also arise with growing numbers. Best example can be the one in which a face can be isolated among thousands of faces and information related to the concerned person can be obtained within seconds with the help of this software.

Unfortunately, developing a computational model of face recognition is quite difficult because faces are complex, multidimensional and meaningful visual stimuli. The scheme

presented is based on an information theory approach that decomposes face images into a small set of characteristics feature images called "eigenfaces", because they are the eigenvectors (principal components) of the set of faces [1].

II. FACE RECOGNITION SYSTEM

Face recognition is a pattern recognition task performed specially on faces. It can be described as classifying a face either "known" or "unknown" after comparing it with stored known individuals. It is also desirable to have a system that has the ability of learning to recognize unknown faces. Any face processing system is detecting the locations in images where faces are present. However, face detection from a single image is a challenging task because of variability in scale, location, orientation (up-right, rotated) and pose (frontal, profile). Facial expression, occlusion, and lighting conditions also change the overall appearance of faces.

A. Outline of a Face Recognition System

This outline heavily carries the characteristics of a Face recognition System. There are six main functional blocks, whose responsibilities are given below.

The acquisition module is the entry point of the face recognition process. It is the module where the face image under consideration is presented to the system. In other words, the user is asked to present a face image to the face recognition system in this module. An acquisition module can request a face image from several different environments.

In the pre-processing module face images are normalized and if desired, they are enhanced to improve the recognition performance of the system. Some or all of the following pre-processing steps may be implemented in a face recognition system discussed below.

The purpose of image normalization is usually to bring the image or other type of signal, into a range that is more familiar or normal to the senses. Normalization is a linear process. Image size resizing is usually done to change the acquired image size to a default image size such as 256 x 256, on which the face recognition system operates. This is mostly encountered in systems where face images are treated as a whole. Gaussian filtering is used for noisy images especially obtained from a camera or from a frame grabber, Gaussian filtering can clean the image without losing information. Histogram equalization is usually done on too dark or too bright images in order to enhance image quality and to

improve face recognition performance. It modifies the dynamic range of the image and as a result, some important facial features become more apparent.

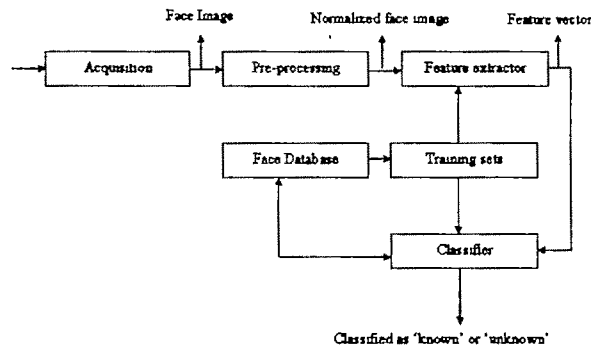


Fig. 1. Typical Face Recognition System

After performing some pre-processing, the normalized face image is presented to the feature extraction module in order to find the key features that are going to be used for classification. In the classification module, with the help of a pattern classifier, extracted features of the face image is compared with the ones stored in a face library (or face database). After doing this comparison, face image is classified as either known or unknown.

Training sets are used during the "learning phase" of the face recognition process. The feature extraction and the classification modules adjust their parameters in order to achieve optimum recognition performance by making use of training sets.

After being classified as "unknown", face images can be added to a library (or to a database) with their feature vectors for later comparisons.

III. EIGENFACES

It is a powerful yet simple technique for face recognition employing the Principal component analysis (PCA) approach. The old techniques focused on particular features of the face [2]. Thus the information used was limited. In the eigenfaces method much more information is used by classifying the faces based on general facial patterns. Hence the whole face is analyzed in totality. Because of the use of greater information, the eigenfaces approach is more effective than the feature based approach.

The main idea for the use of PCA for face recognition is to express the large 1D vector of pixels constructed from 2D facial images with the help of compact principal components of the feature space. This is called eigenspace projection. Eigenspace is calculated by identifying the eigenvectors of the covariance matrix derived from a set of facial images or vectors [1], [3]. PCA is applicable to face recognition because face images are very similar to each other (relative to images of non faces).

In the PCA approach, if the database consists of M images, of N by N matrix each, then the covariance matrix of the images

will give N^2 eigenvectors and eigenvalues as the covariance matrix C has dimensions N^2 by N^2 . However since the number of data points in the image space is less than the dimension of space ($M < N^2$), so instead of solving for the N^2 -dimensional eigenvectors one can solve for M non-trivial eigenvectors by finding the eigenvectors of a different M by M matrix and then performing necessary transformations [4],[5]. These eigenvectors are known as eigenfaces. The pictures in the database as well as the input picture can be expressed as a weighted sum of these eigenfaces (or principal components). However different pictures will have the eigenfaces in different weights or different proportions. Eigenfaces represent the characteristic features of faces which may or may not be present in the face image, may be present to a smaller extent, in which case the weight of that particular eigenface will be very small in that face image. If the feature is present to a higher degree then the corresponding weight of that particular eigenface will be large. Thus the weights are a measure of the degree to which a particular feature is present in the face image.

One may further reduce the number of eigenfaces being considered to a smaller value M_0 by considering only the eigenvectors corresponding to the highest M_0 eigenvalues. The eigenvectors with the highest eigenvalues represent the most variance in the face space. In this case the weighted sum of the M_0 eigenfaces will only be an approximation of the original image. However by choosing the most important eigenvectors one can increase the accuracy of this approximation. With very large databases, omission of less important eigenfaces becomes important in order to conserve computational resources. Also the eigenfaces are all orthonormal. It is not only possible to extract a face given eigenfaces and corresponding weights but one can also extract the weights corresponding to the eigenfaces and a particular face image.

One established fact is that similar pictures will have similar features to similar degrees. This means that the picture of the same person will have similar weights corresponding to each eigenface. An eigenvector of a matrix is a vector such that, if multiplied with the matrix, the result is always an integer multiple of that vector. This integer value is the corresponding eigenvalue of the eigenvector. This relationship can be described by the equation $M \times u = \lambda \times u$, where u is an eigenvector of the matrix M and λ is the corresponding eigenvalue. Eigenvectors possess following properties as they can be determined only for square matrices, there are n eigenvectors (and corresponding eigenvalues) in a n by n matrix., all eigenvectors are orthogonal each other.

IV. OVERVIEW OF THE ALGORITHM

The algorithm for the facial recognition using eigenfaces involves the following procedures. Firstly, the original images of the training set are transformed into a set of eigenfaces E . Afterwards, the weights are calculated for each image of the training set and stored in the set W . Then on getting an unknown image X , the weights are calculated for that particular image and stored in the vector W_x . Afterwards, W_x is compared with the weights of images. One way to do it would be to regard each weight vector as a point in space and

calculate an average distance D between the weight vectors W and the weight vector of the unknown image W_X (the Euclidean distance). If this average distance exceeds some threshold value then the weight vector of the unknown image W_X lies too "far apart" from the weights of the faces. In this case, the unknown X is considered to be not a face. Otherwise (if X is actually a face), its weight vector W_X is stored for later classification. The optimal threshold value has to be determined empirically.

A. Calculation of eigenfaces with PCA

In this section, the original scheme for determination of the eigenfaces using PCA will be presented.

Step 1: Prepare the database

In this step, the faces constituting the training set (Γ_i) should be prepared for processing. Training set is given in Fig. 2.

Step 2: Subtract the mean

The average matrix has to be calculated, subtracted from the original faces (Γ_i) and the result stored in the variable Φ_i . The mean image is Fig. 3.



Fig. 2: Training Set For Processing

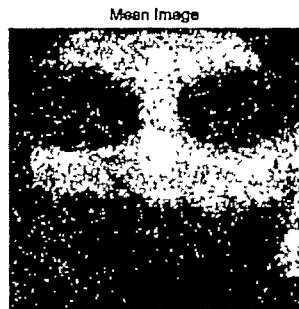


Fig. 3 Mean Image

$$\psi = \frac{1}{M} \sum_{n=1}^M \Gamma_n \quad (1)$$

$$\Phi_i = \Gamma_i - \psi \quad (2)$$

Step 3: Calculate the covariance matrix

In the next step the covariance matrix C is calculated according to

$$C = \frac{1}{M} \sum_{n=1}^M \Phi_n \Phi_n^T \quad (3)$$

Step 4: Calculate the eigenvectors and eigenvalues of the covariance matrix

In this step, the eigenvectors (eigenfaces) u_i and the corresponding eigenvalues λ_i should be calculated. The eigenvectors (eigenfaces) must be normalized so that they are unit vectors, i.e. of length one.

Step 5: Select the principal components

From M eigenvectors (eigenfaces) u_i , only M_0 should be chosen which have the highest eigenvalues. The higher the eigenvalue, the more characteristic features of a face does the particular eigenvector describe. Eigenfaces with low eigenvalues can be omitted, as they explain only a small part of characteristic features of the faces. After M_0 eigenfaces u_i are determined, the "training" phase of the algorithm is finished. The eigenfaces that are generated with the calculated eigenvalues that are not zero is given in Fig. 4.

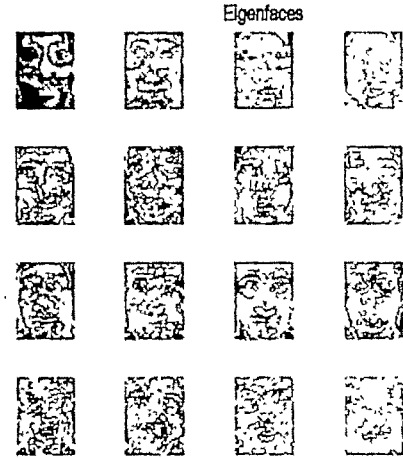


Fig. 4 Generated Eigenfaces

B. Improvement of the Original Algorithm

There is a problem with the algorithm described above. The covariance matrix C in step 3 (equation 3) has a dimensionality of N^2 by N^2 , so one would have N^2 eigenfaces and eigenvalues. For a 256×256 image that means that one must compute a $65,536 \times 65,536$ matrix and calculate 65,536 eigenfaces. Computationally, this is not very efficient as most of those eigenfaces are not useful for this task. So, the step 3 and 4 is replaced by the scheme proposed by Turk and Pentland [1].

$$C = \frac{1}{M} \sum_{n=1}^M \Phi_n \Phi_n^T = AA^T \quad (4)$$

where the matrix $A = [\Phi_1, \Phi_2, \dots, \Phi_M]$. The matrix C however is N^2 by N^2 , and determining the N^2 eigenvectors and eigenvalues is an intractable task for typical image sizes.

$$L = A^T A \quad (5)$$

where $L_{n,m} = \Phi_m^T \Phi_n$

$$u_i = \sum_{k=1}^M v_k \Phi_k \quad (6)$$

where L is a M by M matrix, v_i are M eigenvectors of L and u are eigenfaces. Note that the covariance matrix C is calculated using the formula $C = AA^T$, the original (inefficient) formula is given only for the sake of explanation of A . The advantage of this method is that one has to evaluate only M numbers and not N^2 . Usually, $M \ll N^2$ as only a few principal components (eigenfaces) will be relevant. The amount of calculations to be performed is reduced from the number of pixels ($N^2 \times N^2$) to the number of images in the training set (M). In the step 5, the associated eigenvalues allow one to rank the eigenfaces according to their usefulness and to use only a subset of M eigenfaces, the M_0 eigenfaces with the largest eigenvalues.

C. Classifying the faces

The process of classification of a new (unknown) face Γ_{new} to one of the classes (known faces) proceeds in two steps. First, the new image is transformed into its eigenface components. The resulting weights form the weight vector Ω_{new} .

$$\omega_k = u_k^T (\Gamma_{new} - \psi), \quad k=1,2,\dots,M_0$$

$$\Omega_{new}^T = [w_1, w_2, \dots, w_{M_0}] \quad (7)$$

Euclidean distance between two weight vectors $d(\Omega_i, \Omega_j)$ provides a measure of similarity between the corresponding images i and j . If Euclidean distance between Γ_{new} and other faces exceeds - on average - some threshold value θ , one can assume that Γ_{new} is no face at all. $d(\Omega_i, \Omega_j)$ also allows one to construct "clusters" of faces such that similar faces are assigned to one cluster.

D. The Euclidean Distance

Let an arbitrary instance x be described by the feature vector $x = [a1(x), a2(x), \dots, an(x)]$

where $ar(x)$ denotes the value of the r^{th} attribute of instance x . Then the distance between two instances x_i and x_j is defined to be $d(x_i, x_j)$:

$$d(x_i, x_j) = \text{root of } \left[\sum_{r=1}^n (ar(x_i) - ar(x_j))^2 \right]$$

In a similar manner the Euclidean distances of the test image are calculated with respect to all the eigenfaces and the image corresponds to that image for which the distance is minimum. A certain threshold can be kept over this minimum distance which would determine whether the input image is a face or not. However in this face recognition system, a slight modification is applied, instead of using thresholds, the system provides the five closest matches to the test image. This modification will allow human interface for a final decision on the identity of the face while at the same time fully utilizing the time saving advantage of the eigenfaces technique. The Euclidean distance and weight graph that is created corresponding to an input image is in Fig. 5.

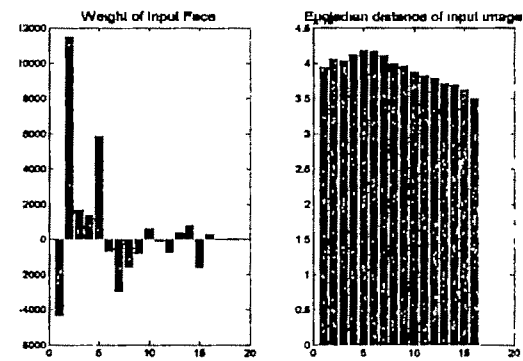


Fig. 5: Euclidean distance and weight graph

E. Authorization of the person

Once the person is recognized then his presence will be done in the file automatically with date and time and if it is the administrator in the database of excel file then parallel port will be enable and present or absent is marked. The reconstructed image to a corresponding input image is given in Fig. 6.

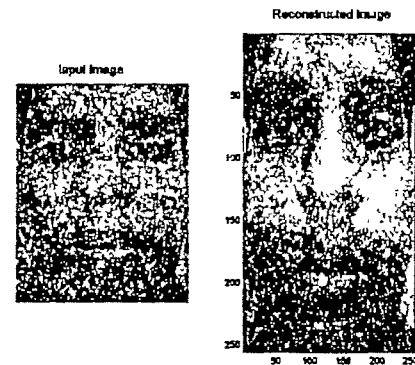


Fig. 6: Input image and Reconstructed Image

V. CONCLUSION

One application of the algorithm presented here can be for automatic attendance system installed on the entrance gate. When the person enters, his/her face is recognized automatically and marked as present in the database. An application module with the help of a small software routine has been developed for recording other details such as entry time, exit time, number of days etc.

REFERENCES

- [1] M.Turk, A.Pentland, "Eigenfaces for Recognition," *Journal of Cognitive Neuroscience*, vol.3 (1), pp. 71-86
- [2] R.Landqvist, A.Mohammed, "Effect of Normalization of Eigenvectors on the Past and RP Algorithm for PCA"
- [3] P. Navarrete and J. Ruiz-del-Solar, "Eigenspace-based Recognition of Faces: Comparisons and a new Approach," *Proc. of the 11th Int. Conf. on Image Analysis and Processing - ICIAP 2001*, pp. 42-47, Sept 26-28, Palermo, Italy, 2001.
- [4] M.Turk, "A Random Walk through Eigenspace," *IECE Trans. Inf & Sys.*, vol. E84-D, No 12 Dec. 2001, pp. 1586-1595
- [5] J. Ruiz-del-Solar and P. Navarrete, "Toward a Generalized Eigenspace-based Face Recognition System," *Lecture Notes in Computer Science* 2396 (Structural, Syntactic, and Statistical Pattern Recognition), Springer, pp 662 - 671, 2002

Equivalence between Two Layout-Variant Document Images *Without* Reading

P.Nagabhushan, Sahana D.Gowda

Dept. of Studies in Computer Science, University of Mysore, Mysore, INDIA, pnagabhushan@hotmail.com, sahanagowda@rediffmail.com

Abstract-Establishing the equivalence of two documents that are content wise similar at the fine level under the geometrical permutation of layout structure of the components at coarse level is the main aim of this research work. Since layout similarity is overlooked, the methods that group the documents based on the similarity in geometrical structure cannot be applied and further since the nature of contents in real life scenario could be complicated and remain apriori unknown, the services of reading mechanisms such as OCR cannot be indented.

It is established in this work that it is sufficient if two document images are compared at two hierarchical levels namely paragraph level (coarse) and word level (fine), since, because of admissible layout variation the equivalence at a medium level such as the line level cannot contribute any extra information in establishing content wise equivalence.

Comparison at paragraph (coarse) level does the preliminary job of establishing the correspondence between the probably matching paragraph components. However the stringent confirmation happens only at the fine (word) level because content wise equivalence demands the existence of these components in both the documents in the same sequence and further the components should display structural equivalence and finally content equivalence between themselves.

Structure similarity is established through the analysis of the extracted Geometrical Span features - Height, Width, Area, Density and Sparsity of the component. The tight boundary contour of the component is plotted on the X-Y plane to extract the Position features - Displacement and Inclination, which are used to analyze the position and sequence of occurrences of the components.

Content equivalence is established through a unique feature called Entropy, which is the measure of energy spots, which occur due to the transition from high pixel to low pixel or vice-versa in a binarized document image. The concept of entropy accomplishes the act of not reading the content of the document images.

Experiments are conducted considering single columned and double columned text document images, with corresponding paragraphs placed in shuffled locations and with adjacent paragraphs merged into one or vice versa.

Keywords - Tight Segmentation, Coarse level, Fine level, Component Structure, Entropy, Text Equivalence.

I. INTRODUCTION

IN the era of modern technology, digital documents predominate. Digital documents are stored and maintained as soft copies within the system. The user would be more cautious in preparing the document and would have generated multiple copies within the system under different file names. If it were articles or technical papers, then they would also be present in different layout structure with same content under different file name. Same content document would be present in different layout structure in different sources on world web as per the publication rules, when retrieving the documents based on layout structure they are recognized as different documents. To avoid or alarm the user of multiple copies of the same document in the system for efficient utilization of memory and retrieval of same document irrespective to its layout structure based on content, a method is required to establish the equivalence between two document images. Conventional approach would be applying an OCR system to understand the document images to establish the equivalence between the document images. This method would be more tedious and complex, as it requires both recognition of characters and the support of contextual grammar for understanding the document images. In the absence of OCR, match between word images [4],[14], match between corner features to rank the word images[6] for retrieval of documents, match between the characters based on the compression ratio[9],[10], detection of duplicates based on the X-base line for each character [8] have been proposed by various authors, but none of the methods speak about the match between components at corresponding levels at different hierarchy such as paragraphs, lines, words and characters between two document images, thereby looking into both visual appearance as well as the content of the document images. The scenario would be more demanding if the documents are of same content with different layout structure than documents of same content with same layout structure: as the visual appearance of the two documents would be different there by establishing the equivalence based on layout structure is not possible. In this paper we have proposed a new method for segmentation for the extraction of components at different levels and content of the components is felt through the information overlay of the components as foreground on the background of the null document image to

establish the equivalence between document images with same content but different layout structure.

Two document images with same content and different layout structure exhibit content and structural equivalence only at word (fine) level since the sequence of occurrence of these components would remain unchanged though at paragraph (coarse) level the components would have undergone geometrical displacement due to differences in layout format. The two document images are compared at two hierarchical levels- paragraph (coarse) level and word (fine) level since the intermediate (line) level components would not fetch any information structurally to measure the equivalence as the intermediate level components would have entirely different structure based on the layout format. The analysis of these components for establishing equivalence between two document images is based on structure and content by extracting the geometrical span features, position features and content feature.

The basic steps involved in establishing the equivalence between two document images are, tight segmentation to extract the components from a document image by enclosing each of them in a rectangular boundary box, followed by feature extraction of each component and the features are matched between components of same hierarchy in sequence between two document images, where geometrical span features are used to compare the area occupied by the components, position features are used to estimate the position of the component on the background of the document image and content feature is used to compare the text content between the components.

Experiments are conducted considering single columned and doubled columned Manhattan document images with paragraphs placed in shuffled locations and with paragraphs split into two adjacent paragraphs and vice versa. The restriction laid down is only that the documents must have font style and size variations at corresponding locations in both the document images because the content feature Entropy- is directly influenced by the change in font style and size.

The paper is organized as follows. In this section 1, the type of documents handled and the steps involved in establishing the equivalence have been stated. In section 2, segmentation procedure for extracting coarse level and fine level component has been presented. In section 3, features extracted from each component at both the levels and comparisons between corresponding components in both the documents are presented. Results have been put in section 4. Conclusions have been summarized in section 5.

II. TIGHT SEGMENTATION AND BOUNDARY CONTOUR OF COMPONENTS ON X-Y PLOT.

Segmentation is a method of extracting the homogeneous regions from the document images. There are different kinds of segmentation techniques based on the applications. To extract the component structure some of the methods existing are connected component analysis [12],[13]-a bottom up approach, Voronoi diagram technique[1],[7],[11]- a geometric approach which is also a bottom up approach etc. These methods obtain the layout structure of the documents at coarse level but do not define the components at different

levels like paragraphs, lines, words and characters. The new approach, known as Tight segmentation [1] is a top down approach, which segments the components at different hierarchical levels such as paragraph (coarse) level, line (medium) level and word (fine) level and encloses them in a tight enclosure. Each component is identified based on the blank space existing between the components at same level. The threshold is automated by calculating the width of the blank space existing between the adjacent components. And also this method extracts the components in a logical sequence without any apriori knowledge.

In this paper we have considered two levels of extraction namely coarse (paragraph) and fine (medium) level, since document images considered would have different layouts but same contents. Due to this the coarse level components would occur at different positions on the background and medium (line) level components would have undergone geometrical changes which could never fetch any information that could be retained for analysis and hence coarse level components would match only with the overall distribution of foreground information pixels to measure the density and the position of the component on the back ground of the document image.

Segmentation is applied on a document image with Manhattan layouts and the procedure of segmentation is as follows.

PROCEDURE: Tight Segmentation -for tight structure extraction of the components and layout plot of the input image.

INPUT: Document Image and Paragraph (coarse component).

OUTPUT: Tight component structure, layouts plot and index of each component.

1. Binarize the input image.
2. Compute the width of the blank space existing in both horizontal and vertical direction from one end of the image to other.
3. Automate the threshold, by sorting the values and the threshold is set to the greatest value.
4. Identify the position of the blank space to obtain the coordinate values of the components.
5. Repeat the procedure in both the directions in horizontal and vertical.
6. Enclose the component through a tight boundary line by considering the coordinates with reference to the background. The enclosing boundary contour of each component is extracted.
7. Enclosing boundary contour is plotted on an X-Y plane.

The components extracted and enclosed in a tight boundary contour through segmentation can be observed in fig.3 of input image in fig. 1 and the structure of the components is plotted on an X-Y plane as shown in fig.5. The new segmentation technique works well on all document images of Manhattan layouts.

III. FEATURE EXTRACTION.

The features extracted from the structure of the components would normally be geometrical features, such as area, density etc for document components representation and various distances such as Euclidean, City Block, Weighted Hausdroff Distance [2] etc to find the structural similarity irrespective to what ever the content could be. Keeping in mind both the aspects - structural as well as text content new features have been extracted such as Content feature- Entropy[5] to measure

the information content of a component and position features-displacement and orientation to analyze the logical sequence among the components of same hierarchy. These features have been explained in detail below.

Given two document images Doc_i and Doc_j are said to be equivalent if both the documents exhibit similar content under the admissible variations in layout structure. The components within the document image are extracted at two hierarchical levels as stated above in section 2. The corresponding components b_{i1} and b_{j1} at coarse (paragraph) level in both the document images Doc_i and Doc_j respectively establish similarity only with respect to density (D)- a geometrical span feature if the two components have the same content followed by the analysis of the position features to match with the location of occurrence in corresponding document images.

Once the blocks b_{i1} and b_{j1} of document images Doc_i and Doc_j respectively, are found to be comparable at coarse level are said to be content wise equivalent if the number of fine level components within them match and also exhibit both structure wise and content wise equivalence with the sequence of occurrences.

Once the document image is subjected to tight segmentation, a component in the document is enclosed in the tight structure. From the X-Y plot of the contour enclosing the tight boundary, the position features- index point (x, y) of every component, its distance from the reference origin ($d = \sqrt{x^2 + y^2}$) and its inclination ($\theta = \tan^{-1}(y/x)$) are extracted for coarse level components.

For an arbitrary component 'b', the POSITION features are shown diagrammatically in figure-1.

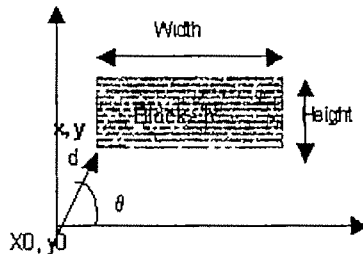


Fig-1: Feature representation and transition points of a component.

In the sequel the GEOMETRICAL features of the component are extracted. These features describe the geometrical SPAN of every component. The suggested span features are (i) Height (H), (ii) Width (W), (iii) Area ($A = H * W$), (iv) Density (D) of the high pixels in the component and (v) Sparsity (S) of the high pixels in the component is the density of null pixels in the component.

The satisfaction of the equivalence between the corresponding components b_{i1} and b_{j1} across the documents Doc_i and Doc_j in terms of POSITION- the sequence of occurrence and the geometrical SPAN feature-density, although necessarily do not guarantee establishing the content equivalence between Doc_i and Doc_j . However the non-satisfaction implies directly that the components b_{i1} and b_{j1} cannot be equivalent. In this context it should be recapitulated that we also accommodate flexibilities in the organization of components at paragraph level to suit certain ground realities such as corresponding paragraphs located in shuffled position, a paragraph in one

document split into two adjacent paragraphs in the other and vice-versa due to change in layout format.

Now comes the major issue of establishing equivalence of text-content or simply CONTENT component wise at hierarchical levels.

It may be recalled that we restrict the documents to contain only text. The text contents as said earlier are interpreted as overlays on the given null document. Hence the overlays cause transition from background (0) to foreground (1). Such a point of transition is referred to as an energy spot since the activity of change in energy takes place at this point. The transition could be from 1 to 0 identified as a negative (-) energy spot or could be from 0 to 1 identified as positive (+) energy spot. These packets of energy could be traced along every horizontal line or row of a component (fine level) and along every vertical line or column of a component (fine level).

The energy parameter is quantified in terms of ENTROPY [5] as given by the following formula.

$$E(t) = p \log(1 + p) + (1 - p) \log(1 + (1 - p))$$

Here t is the transition, $E(t)$ is the entropy. p is calculated based on the number transitions in each row or column divided by the total number of columns or rows respectively. Hence p is the probable occurrence of transition in each row or column and $1-p$ is the probable non-occurrences of transition.

Depending upon the transition as described above $E(t)$ could be $E(t)$ or $E^+(t)$. As said earlier, entropies are computed row wise and column wise. Total entropy of each row ($E_h(t)$) or column ($E_v(t)$) is the summation of $E(t)$ and $E^+(t)$. Total entropy of every component is the summation of entropy of all the rows and columns.

Certain observations can be enunciated at this stage that help in devising the algorithms for equivalence computations.

- Two documents are equivalent if the two corresponding components from the two documents at coarse level display equivalence in terms of POSITION and DENSITY within the scope of permissible flexibilities of structural variations (elongated/stretched) based on the layout format and components could also be shuffled with split and merged paragraphs.
- To establish content equivalence between corresponding comparable coarse level components, the fine level components are subjected to both structure and content analysis of each component in the order of sequence they occur.
- The coarse level components could be split into two components or could be merged into single component, at this case, the components at corresponding document images would exhibit different geometrical span features except the DENSITY feature which would remain same, since the summation of density feature of both the split components would be same as the density of merged single component as illustrated in section 4 and also that the components would only be adjacent if they are split into two components.
- The content-feature ENTROPY is a powerful feature that extracts the content of a component at fine level along with the sequence of occurrences, making it possible to

realize the most significant objective of this research work for establishing the content equivalence without reading the content.

Feature extraction for each component is based on the structure extracted through segmentation with reference to the geometrical aspects and foreground of the component.

PROCEDURE: FEATURE EXTRACTION.

INPUT: Component obtained through segmentation.

OUTPUT: Position, Span and Content features.

1. Extract the vertices of each component.
2. Calculate the Width (W), Height (H), Area (A), Density (D) and Sparsity (S) for each component.
3. Calculate displacement (d) and inclination (θ) considering the index of the component and origin of the plot.
4. Compute the total or overall entropy of each component as stated above.

These features are extracted for every component at coarse and fine level, which helps in establishing the spatial relationship among the same level components, with the sequence of occurrences by labeling them.

The similarity analysis of the components at same level in corresponding document images is established by finding the absolute difference between geometrical span, position and content features.

The algorithm for similarity analysis is summarized below.

PROCEDURE: SIMILARITY ANALYSIS

INPUT: Two components (b_i and b_j) at coarse level.

OUTPUT: Quantitative analysis of two components to estimate similar.

1. Compute the difference between Geometrical span, position and content features of components at coarse level.
2. If the components are similar with respect to density then they are further subjected to segmentation at fine level.
3. Compare the total number of fine level components.
4. If the number of fine level components remains same, then each component in the sequence are correspondingly matched.
5. If the entropy of each fine level component matches in the sequence correspondingly, then they are exactly equivalent with respect to content, font style and size.

The two document images of same content and different layout structure can be directly compared at fine level even without establishing the correspondence at coarse level, but from the coarse level components the reading sequence can be obtained. With in each coarse level component fine level components can also be extracted in the reading sequence so that the comparison becomes one to one match reducing the complexity of searching the sequence order.

IV. EXPERIMENTAL RESULTS.

The cases considered for experimentation are as follows.

1. Document images with same content and layout but coarse level components are shuffled.
At this situation, coarse level components would have same geometric span features and content but the position would be different. The coarse level components would have fine level components at same positions and the same sequence order. Even medium level (line) would also exhibit equivalence correspondingly.

2. Document images with same content, but different layout structure.

Here the coarse level equivalence show correspondence only with the density feature, but also the sequence order could be same. But the medium level could not preserve any kind of resemblance. The fine level components have same content feature-entropy and same sequence of occurrence but the position variations can be observed.

3. Paragraphs could be split or merged due editing or due to different layout structure.

The sequence of fine level components could be same with different positions since the paragraph is split, so some of the words would be in different position, same with the case of merged paragraphs.

Considering documents with same content same layout structure but the paragraphs shuffled have been illustrated below, where coarse level components are extracted and their positions are extracted and labeled as shown in figure 5 and 6 for input image 1 and 2 in figure 1 and 2 respectively.

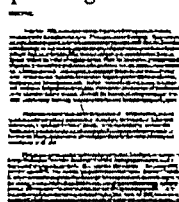


Fig 1: Input Image 1

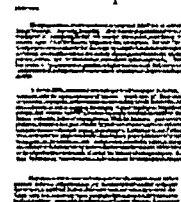


Fig 2: Input Image 2

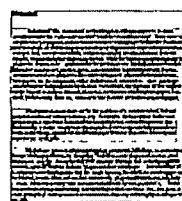


Fig 3: Coarse Level Component

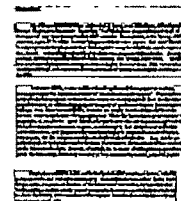


Fig 4: Coarse Level Components

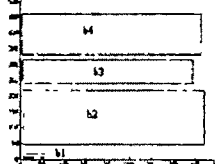


Fig 5

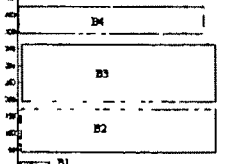


Fig 6

Fig- 5 and Fig- 6 represent the structure of coarse level components. Coarse level components of document image 1 in figure 1 and document image 2 in figure 2, establish corresponds between blocks (b_1 and B_1), (b_2 and B_3), (b_3 and B_4) and (b_4 and B_2) since these components have same geometrical span and content feature but they do not match with position features, therefore the components within the layout are shuffled. Similarly the documents with same content different layout structure as single columned and double columned documents are also compared. The experiments are illustrated with paragraph of same content and different structure that is similar to the comparison between two documents of same content and different layout structure due to page restriction.

Paragraphs with same content in different layout format will have variation in structure, where content equivalence cannot

be established. To establish the content equivalence at fine (word) level components are extracted as shown in fig 7,8 and 9. Experiments are conducted for paragraphs split and merged due to layout format as shown in fig 9. At coarse level the components do not match with geometrical span features, but they are identical with respect to density and the total number of fine level components with in them, which can be considered as comparable and further each fine level components are analyzed with the sequence of occurrence.

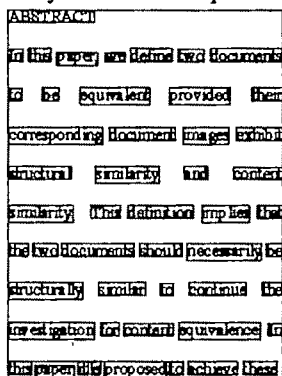


Fig 7: Paragraph vertically aligned

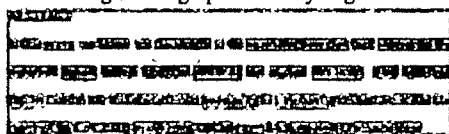


Fig 8: Paragraph horizontally aligned

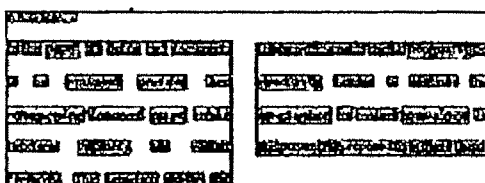


Fig 9: Paragraph split due to doubled columned format

The paragraphs in fig 7, 8 and 9 are identical with respect to content and words arranged in the same sequence, but the position of occurrence of these words are different due to different layout format.

V. CONCLUSION.

Establishing the equivalence between the contents of two document images is one of the important intermediate steps for various applications such as classification, categorization, retrieval etc, where the content match would require an expert or a supervised model to read and understand the document image which would require more time and would become more complex. Avoiding the understanding of document image and to establish a pattern match which could feel the content of the text a new entropy model has been introduced and also a new segmentation technique has been proposed to extract the components in an hierarchical strategy. The segmentation technique works well for documents with Manhattan Layouts. Entropy introduced in this research paper has one major drawback that is, it is variant to font style and size where, it shows different energy for same component of different font and style.

REFERENCES

- [1]. Nagabhushan.P,Sahana.D.Gowda,Bharathi, "Unconstrained Tight Structure Extraction Using Voronoi Tessellation On Document Images", World congress conference MLMTA'06, Los Vegas, Nevada, June 2006.
- [2]. Joost van beusekom, Daniel Keyser, Faival Shafait, Thomas M. Breuel, "Distance Measures for layout-based document image retrieval", DIAL-2006.
- [3]. Sahana.D.Gowda, Nagabhushan.P, "Page Segmentation and Rule Based Identification Method for Technical Journal Pages", International conference on Cognition and recognition, Dec 2005, India.
- [4]. Li.Zhang, Chew Lim Tan, "Word Image Coding Technique and Its Applications In Information Retrieval From Image Documents", IWDA, Kolkata2005.
- [5]. Veronique EGLIN, Stephane BRES, LIRIS-RFV, and INSA de Lyon, "Document image similarity based on layout visual saliency: Application to query by example and documents classification", ICDAR 2003, IEEE Computer society.
- [6]. Jamie Rothfeder, Shaolei feng and Toni M.Rath, "Using corner feature correspondences to rank word images by similarity", proceedings of the Workshop on Document Analysis and Retrieval, Madison, June2003.
- [7]. Kise.K, iwata.M, Matsumoto.K, "On The Applications Of Voronoi Diagrams To Page Segmentation", Computer Vision And Image Understanding, 1998.
- [8]. David Doerman Hupling Li, Omid Kia, Kemal Kilic, "The Detection Of Duplicates In Document Image Databases", MDA, February 1997.
- [9]. Jonathan J.Hull, John F.Cullen, "Document Image similarity and Equivalence Detection", 4th IAPR on ICDAR, Ulm, Germany, Aug 1997.
- [10]. Dar-Shyang lee, Jonathan j.Hull," Duplicate Detection In Symbolically Compressed Documents", ICDAR, Germany, Aug 1997.
- [11]. Kise.K, Sato.A, Matsumoto.K, "Document Image Segmentation As Selection Of Voronoi Edges", Proc. IEEE Workshop On Document Image Analysis, 1997.
- [12]. Ha J, Hatalick R M, Phillips I T, "Document Page Decomposition By The Bounding Box Projection Technique", IEEE, 1995.
- [13]. Ha J. Hatalick J M, Phillips I T, "Recursive X-Y Cut Using Bounding Boxes Of Connected Components", proceedings of the 3rd ICDAR, Canada, 1995, 952-955.
- [14]. Weihua Huang, Chew Lim Tan, Sam Yuan Sung, Yi Xu, "Vertical Bar Detection For Gauging Text Similarity Of Document Images", ICDAR, 1996.

Wavelet and DCT based Image Coding and Reconstruction for Low Resolution Implementation

Swanirbhar Majumder¹, and Md. Anwar Hussain²

¹ Lecturer, e-mail: swanirbhar@gmail.com.

² Asst. Professor, e-mail: bubuli_99@yahoo.com

Electronics and Communication Engineering Department, NERIST (Deemed University), Arunachal Pradesh

Abstract—Compression of data in any form is a large and active field as well as a big business [1] [2]. Image compression is a subset of this huge field of data compression, where we undertake the compression of image data specifically. Present day devices have human machine interactive systems where information is communicated via, text, audio, video or image [5] [6] [9]. So here we propose a methodology for present day display devices where low resolution image may be sufficient [3]. We use discrete cosine transform with masked pixels after discrete wavelet transform of the original image for single or more levels [3] [7]. These results to a hybrid transform which uses the advantages of DWT and DCT both. The received image undergoes filtering and smoothening to cover up the effect of masked pixels. Through this process we achieve a reduction of number of pixels by 73% (with DWT before DCT with masking) to 96% (with DWT with maximum allowable masking after DCT) or in between, for a typical image size of 256X256. This type of hybrid transform can easily be performed with high speed processors available today in the market with appropriate changes in the program [4] [8].

Key words—Discrete Cosine Transforms (DCT), Discrete Wavelet Transform (DWT), image coding, masking.

I. INTRODUCTION

DATA compression has become a necessity for saving bandwidth, power, storage space, etc. Thus it has turned out to be a present day craze as well as source of competition in the race for technology and research with so much manpower, time and money involved for its development [1] [2]. Out of the image compression techniques available, transform coding is the most preferred method [1] [2] [10]. Since energy distribution after transform coding varies with each image, compression in the spatial domain is not an easy task [11]. Images do however tend to compact their energy in the frequency domain making compression in the frequency domain much more effective. Transform coding is simply the compression of the images in the frequency domain [12]. Transform coefficients are used to maximize compression. For lossless compression, the coefficients must not allow for the loss of any information. We have seen that DCT and DWT

have been among the most popular transform coding used. Initially it was DCT which was popularized by the JPEG then came up the JPEG2000 which used the DWT [13] [1] [2]. Based on a comparative study [7] to evaluate the performance difference of the Discrete cosine transform (DCT) and Daubechies-6 wavelet based image coding and reconstruction, it was reported that for still images DWT outperforms DCT typically in terms of compressed output for different quantization levels as well as reconstructed image quality for the same image size. So for less than 64x64 images no DCT algorithm is applied.

As these transforms were popular people started their hardware implementations on FPGAs for faster design of chips. So these transforms were realized on chips for better performance for various high speed processors and embedded systems. Day by day people are coming out with new methods to implement DCT and DWT to even microcoded DWT on chip with various algorithms and implementation [8]. Moreover so much of research has revealed a lot of pros and cons for the various methods, which has been a boon in the technological point of view [14] [15] [16].

We propose a hybrid transform methodology which uses both of these transform coding techniques (DCT and DWT), and is specifically for devices (mobiles, palm tops, video conferencing, etc.) which are of smaller screen size or allow low resolution viewing. We realize very high compression and thus lower the cost of data storage and transfer, at the cost of image resolution. The aforesaid devices may not have the requirement of high resolution of the person or environment, so we go for low resolution image viewing. For hand held devices, normally which are of smaller screen sizes (200x150 or less), be it a 64x64 image or a 1280x1024 full resolution image, when we view it on these devices they appear similar. The smaller sizes though might not give high clarity but convey the required message. Other than that it may be used for low resolution devices like web-cam image or those of video conferencing.

II. IMPLEMENTATION

The first step is thus to extract the image information from input image $X(i,j)$, i.e. to know about its size (number of pixels, RGB or gray scale), type of image (BMP, JPEG, PNG, TIFF, etc.), and the type of device (webcam, mobile, etc.) on which it is to be viewed or the purpose and check whether the device is a low resolution device or has smaller screen. Based on the extraction of aforesaid image information we decide how many level of DWT to apply. As the screen size of these devices are around 200x150 or less, for images in between 256x256 to 64x64 we apply single level DWT. If it is less we do not apply DCT later (as the size 64x64 is small enough so further removal of detail information will make the image unrecognizable). But if it is greater than 256x256 we apply higher levels of DWT. The wavelet we use is Daubechies 6 wavelet because it has emerged to be one of the best for image processing [6]. On applying DWT for single level and keeping the approximate image only we achieve compression about 67-73% (for eg. image of 64x64, 128x128 and 256x256 have approximate image of sizes of 37x37, 69x69 and 133x133 respectively). For two levels of DWT application the approximate image results to about 93% of compression (It is simply the repetition of the single level DWT process of Fig1, on the approximate image to get the second level approximate DWT image).

After DWT we next take Discrete Cosine Transform (DCT) of the approximate image. The 2 dimensional DCT of a discrete image block of 8x8 $P(i,j)$, is defined as $F[i,j]$ as in Equation (1):

$$F[i,j] = \frac{1}{4} C(i) C(j) \sum_{x=0}^7 \sum_{y=0}^7 P(x,y) \dots \dots \cos\left(\frac{(2x+1)i\pi}{16}\right) \cos\left(\frac{(2y+1)j\pi}{16}\right) \quad (1)$$

where x, y, i and j all vary from 0 to 7

$$C(i) \text{ and } C(j) = \begin{cases} \frac{1}{\sqrt{2}} & \text{for } i \text{ and } j = 0 \\ 1 & \text{for all other values of } i \text{ and } j. \end{cases}$$

We then undertake masking of the resultant image where level of masking depends on the type of image (eg. more masking for BMP, less for JPEG, etc.). For high resolution images we can mask up to 54 bits out of 64 bits in each 8x8 block depending on requirement. The maximum achievable compression percentages before entropy coding are shown in Table 1. There we first have the image size limits followed by number of levels of DWT to undergo and the allowable masking. These are followed by the percentage of compression due to DWT, the percentage of compression after applying DCT plus mask on the approximate image and finally the total percentage of compression achieved. The masking is done diagonally, i.e. 0, 1, 3, 6, 10, 15, 21, 28, 36, 43, 49 and 54; as the example masks shown in Fig. 2. This is followed by

quantization and entropy coding. Here we used RLE (Run-Length Encoding) as after reduction of 90% of size, RLE is a better option compared to Huffman encoding as it is less complex. These result to a final output $A(i,j)$ along with B, C and D being quantization levels, size of DCT mask and DWT levels, respectively, as shown in Fig. 3.

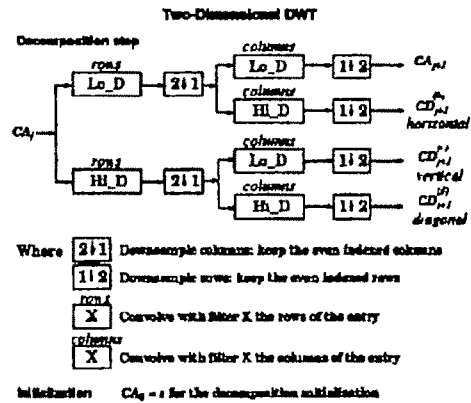


Figure 1: Single level Discrete Wavelet Transform step to extract approximate image

Table 1: Maximum compression before entropy coding for different image sizes of a JPEG2000 image.

Sl No	Image size (less than) in pixels	Db-6 DWT level(s)	8x8 DCT mask	Max % of compression for highest value of DCT mask		
				DWT	DCT	Total
1	64x64	1	0	67	0	67
2	128x128	1	0-43	71	67	90
3	256x256	1	0-54	73	84	96
4	512x512	2	0-36	93	36	97
5	1024x1024	2	0-54	93.5	84	98

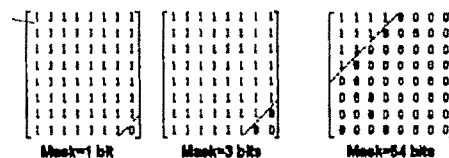


Figure 2: Example Masks to be applied after DCT

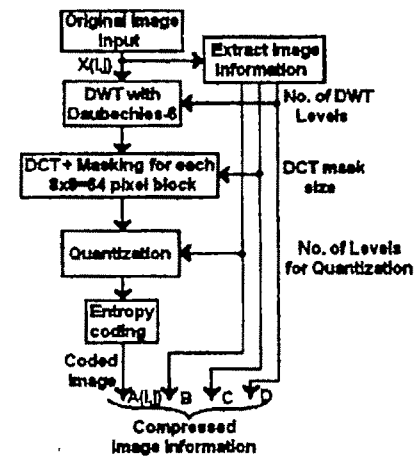


Figure 3: Image compressing algorithm

At the receiver end we have lesser complexity in the decoding process compared to the encoding, and hence it may be implemented on FPGA. We have implemented this methodology only on software (MATLAB® program). Here we need the initial compressed image $A(i,j)$ along with number of quantization levels B ; DCT mask size C ; and number of DWT levels D . These B , C and D values are integrated with $A(i,j)$ (i.e. compressed image data) for transferring as multimedia data. We under take the reverse process, first entropy decoding (reverse RLE or if Huffman coding was used than Huffman decoding); followed by de-quantization based on quantization level information B (along with others information like max value, min value, step size, etc. of the image pixel). Then we proceed for filling up the masked pixels with zero values (zero padding) before IDCT (inverse DCT) using information from C which is followed by IDWT (inverse DWT) with the number of levels specified by D . Lastly we have to under go smoothening & filtering (here we used median filter an inbuilt filter pads the image with zeros on the edges) after IDWT to get $\hat{X}(i,j)$. Here $\hat{X}(i,j) \neq X(i,j)$ but approximately same. The whole algorithm is as described in Fig 4.

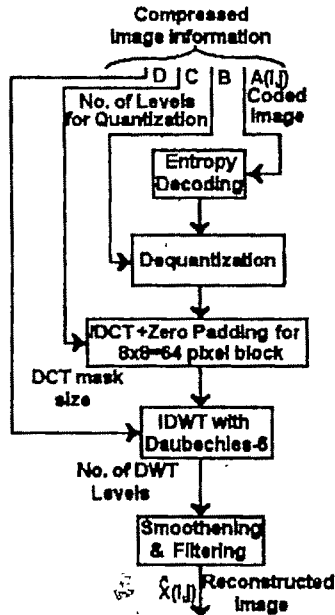


Figure 4: Image decompressing algorithm

III. RESULTS AND DISCUSSION

The original image of size 256x256, shown in Fig 5, is taken and then DWT with Daubechies-6 wavelet was accomplished to get the four blocks in Fig. 6 each of size 133x133. Then we use only the approximate image (resulting 73% compression) to get the DCT and then masking of 54 bits per 8x8 pixel block. We have around 276 numbers of 8x8 blocks in a 133x133 image. Thus removing 14904 (54x276) pixels from 17689 (133x133) pixels resulting to 84% compression by the mask and an overall compression of 95.8%. We have reduced

from 65536 (256x256) pixels to 2785 (17689-14904) pixels (Fig.7). This is followed by 16 level quantization and RLE encoding which further reduces the size. As we achieve finally around 96% compression, the effect of RLE is not much and hence may be avoided if required, for images of smaller size. The coded image along with parameter values $B=16$, $C=54$ and $D=1$ are sent for decompression at the receiver end.

The coded image $A(i,j)$ along with B , C and D values are received by the receiver. Then on computation of entropy decoding and de-quantization, we get the 2785 pixels containing the image data, which may vary slightly from the original sequence due to quantization error. Then we perform IDCT to get the image in Fig 9 from the zero padded image of Fig 8. This image in Fig 9 is of 133x133 i.e. corresponding to the approximate image obtained after DWT at the transmitter side. We then perform single level IDWT on this 133x133 image to get the 256x256 image of Fig 10. This image is then smoothened and filtered to get the image in Fig 11. The output image is sufficiently clear and when we view it in a smaller size screen than its actual size (as in the case of low resolution devices with smaller screens), as in Fig. 12, we can see that the final reconstructed image is very near to the original image in its fidelity.

To compare the reconstructed image with the original image we apply PSNR criterion. The ratio between the maximum possible power of a signal and the power of corrupting noise that affects the fidelity of its representation is called PSNR (peak signal-to-noise ratio). It is commonly used as a measure of quality of reconstruction in image compression etc. Because many signals have a very wide dynamic range, PSNR is usually expressed in terms of the logarithmic decibel scale. The original image $X(i,j)$ and the reconstructed image $\hat{X}(i,j)$ may be compared for evaluation of the effectiveness of the compression technique by calculating the mean squared error (MSE) as given by Eq. (2).

$$MSE = \frac{1}{mn} \sum_{i=0}^{m-1} \sum_{j=0}^{n-1} \|X(i,j) - \hat{X}(i,j)\|^2 \quad (2)$$

The $\hat{X}(i,j)$ is considered as a noisy approximation of the $X(i,j)$. PSNR is expressed by Eq. (3)

$$PSNR = 20 \log_{10} \left(\frac{MAX_I}{\sqrt{MSE}} \right) \quad (3)$$

Here, MAX_I is the maximum pixel value of the image. When the pixels are represented using 8 bits per sample, MAX_I is 255. Typical values for the PSNR in image compression are around 30 dB. But as we are considering great amount of pixel removal so we can not have the luxury of those values but our PSNR lies within 10dB which is considerably good when we are achieving this huge amount of compression for low resolution applications. The PSNR plots for the reconstructed 256x256 $\hat{X}(i,j)$ image with the

original $X(i, j)$ image in Fig. 5 for varying quantization levels and size of mask are plotted in Fig 13 and Fig 14, respectively. It is thus clear that with quantization level more than 16 for any fixed mask size, the PSNR remains approximately constant as is revealed in Fig. 13. While from Fig. 14 we may comment that for increasing mask size PSNR decreases for all quantization levels.



Figure 5: Original Barbara image of size 256x256



Figure 6: Image after DWT with DB-6 (each block size is 133x133)

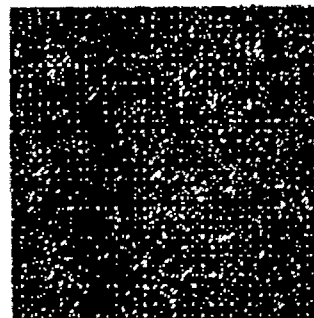


Figure 7: Image after 54 bits masking per 8x8 block after DCT

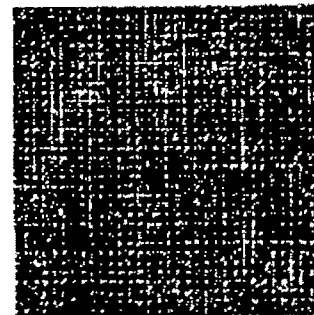


Figure 8: Decoded image after 54 bits zero padding per 8x8 block before IDCT



Figure 9: Decoded image (133x133) after IDCT



Figure 10: Decoded image (256x256) after IDWT

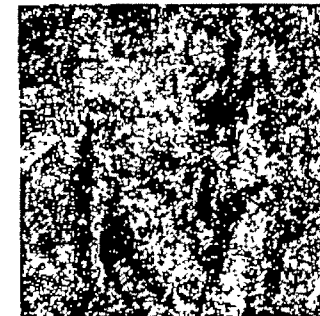


Figure 11: Decoded image (256x256) after unsmoothing and filtering using median filter



Figure 12: Original and reconstructed image viewed at 128x128 size

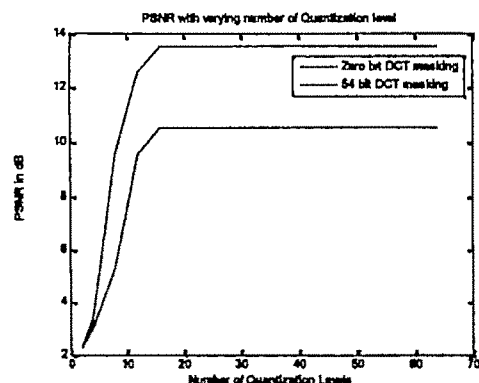


Figure 13: PSNR plot with varying quantization levels for maximum and minimum masking

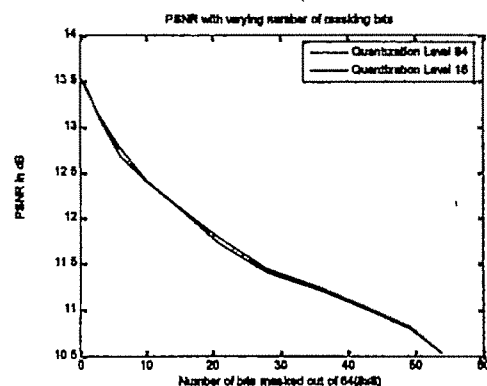


Figure 14: PSNR plot with varying number of masking bits for two quantization levels i.e. 16 and 64

IV. CONCLUSION

Our algorithm has been highly successful in terms of software simulation implementation and has provided results which are satisfactory. Thus we see that this method, if realized on hardware, may be a boon for the huge amount of compression it provides. With quantization level more than 16, there is hardly much difference in the PSNR value. So the only parameter that may be varied is the number of bits to be masked if we fix the quantization level to 16. Thus this further reduces the number of variables from three (B, C and D) to two (C and D) only. Moreover if the smoothing and filtering is improved, better quality picture will be achievable at the same compression ratio. In future our methodology may be further improved for application in the temporal domain and than videos may also be compressed in the similar manner.

We have used median filter for smoothening and filtering to remove the sharp edges at each 5x5 pixel blocks. This may not be quite satisfactory and hence we are also looking to further improve this step. An FPGA implementation of this hybrid compression technique is presently being pursued.

REFERENCES

- [1] Salomon, D., *Data Compression*, 4th Edition. Springer, 2006-07
- [2] Sayood K. *Introduction Data Compression*, 2nd Edition 2000, Morgan Kaufmann
- [3] Wen-Chien Yan, et al, *Compressing discrete cosine transform coefficients by modified set partitioning in hierarchical tree*, November 2005 SPIE and IS&T
- [4] Jiang, W.; Ortega, A., *Lifting factorization-based discrete wavelet transform architecture design*, IEEE Trans. Circuits and Systems for Video Technology, Vol 11, May 2001
- [5] Junejo, N et al, *Speech and Image Compression Using Discrete Wavelet Transform*, IEEE/Sarnoff Symposium on Advances in Wired and Wireless Communication, 2005
- [6] Akintola, A.A. et al, *Evaluation of Discrete Cosine Transform (DCT) for Reconstructing Lost Blocks in Wireless Video Transmission*, Proceeding ACIT - Signal and Image Processing - 2005
- [7] Majumder S.; Hussain A, *A comparative study of DCT and wavelet-based image coding & reconstruction*, Proceedings of SCTII 2007, NIT Rourkela
- [8] Zafarifar, B et al, *Micro-codable Discrete Wavelet Transform*, July 2002
- [9] Andrew, J.P. et al, *Modified discrete wavelet transform for odd length data appropriate for image and video compression applications*, IEEE, 2001
- [10] Henrique S. Malvar, *"Fast Progressive Image Coding without Wavelets"* IEEE Data Compression Conference - Snowbird, Utah, March 2000
- [11] Gerekand, O.N. et al, *"Adaptive polyphase subband decomposition structures for image compression,"* IEEE Trans. Image Processing, vol. 9, pp. 1649-1659, Oct. 2000.
- [12] Wei Jun et al, *Volumetric image compression by 3D Discrete Wavelet Transform (DWT)*, SPIE, The International Society for Optical Engineering, 1995
- [13] Choi J.U. et al, *Watermarking of digital images using wavelet and discrete cosine transforms*, IEEE Trans, 2005
- [14] Watson A.B. et al, *Visibility of Wavelet Quantization Noise*, IEEE Transactions on Image Processing, Vol. 6, No. 8, August 2002
- [15] Servetto S.D. et al, *Multiple Description Wavelet Based Image Coding*, IEEE Trans on Image Processing, vol 9, no. 5, may 2000
- [16] Wahid, K.A. et al, *Error-Free Arithmetic for Discrete Wavelet Transforms Using Algebraic Integers*, 16th IEEE Symposium on Computer Arithmetic (ARITH-16 '03), 2003.

Technical Session 7C

Communication and Microwave

Microstrip Leaky-Wave Antenna With Arbitrary Metallic Strip Radiating Characteristics

Z. Mekkioui¹, H. Baudrand²

¹ Department of Physics, Faculty of Sciences, University of Tlemcen, P.O. Box 119, Tlemcen, Algeria
e-mail: z_mekkioui@mail.univ-tlemcen.dz

² LEN7, ENSEEIHT, 2 RUE CHARLES CAMICHEL,
P.Box 7122 31071 Toulouse Cedex 7, France. Henri.Baudrand@yahoo.fr

Abstract— In this communication, the effects of electronic scanning and radiating patterns are investigated upon the arbitrary shape of the metallic strips. Furthermore, a proposition of a versatile and a flexible method for analyzing complex structures is given. It consists in applying rigorous transverse resonance method combined successfully to least squares technique and the boundary element method.

Key words—Antenna, Leaky-Wave, Radiating, Arbitrary shape.

I. INTRODUCTION

MICROSTRIP leaky-wave antennas (LWAs) have several unique features, which make them attractive candidates for many antenna applications, ranging from mobile communications to phased array radar systems. They have been extensively studied and developed for use in microwave circuit design. Based on planar-layered structures, LWA have been investigated in recent years due to their advantages in terms of low cost and simplicity. They have also attracted profound interest for many decades because of their unique characteristics and their comparative advantages (narrow beam, frequency scanning, non resonant). By properly exciting leaky waves on such structures with a simple feed, narrow-beam radiation patterns may be obtained, which are steered in elevation by varying frequency.

Many works related to microstrip leaky-wave antennas have been given in general for the case of rectangular metallic strips [1]. However, little has been published for any arbitrary shape [2].

In this communication, we present accurately the behavioural features of microwave and millimeter wave of a large 1-D microstrip leaky-wave antenna with non regular

shapes in order to show their effects on radiating characteristics (electronic scanning, radiating patterns...) and consequently their advantage and inconvenient with the regular one. A moment method procedure in space domain is applied to find the vector electric surface current density excited on the metallic parts. The most difficult aspect of the antenna's radiation problem is the generation of the trial functions describing the current on such parts. Thus, the formulated problem is reduced in expressing originally the trial current density upon an orthonormal basis elements generated numerically. Hence, by the least squares technique, an eigen-value problem is set [3].

Then, the computation of the inter-modes inner products matrix is determined and accelerated by reducing the surface integral calculation to a simple one by the boundary elements method [4]. Hence, the method efficiency is showed by Floquet modes number truncation necessary for the convergence of the complex propagation constant.

Otherwise, other challenges which are commonly required in many applications are the possibility to conform the radiating patterns and to perform the characteristics (SLL, beam-width, etc...) by the optimisation of the metallic shape. The reliability of the method is evidently showed by the investigation of new periodic shapes: exponential, sinusoidal, etc...

II THEORY AND BACKGROUND

A. Leaky-Wave Antenna Structure

The geometry of a 1-D microstrip leaky-wave antenna sketched on Fig.1, consists of N printing metallic parts of arbitrary shape, which are periodically etched with d along (Oy) direction. The dielectric substrate of height a and ϵ_r its

relative permittivity is mounted on a ground plane. The structure is assumed too large (infinite) to neglect the edges effects. The excitation of the leaky-wave is realized by a vertical excitation. Horizontal one can also be considered.

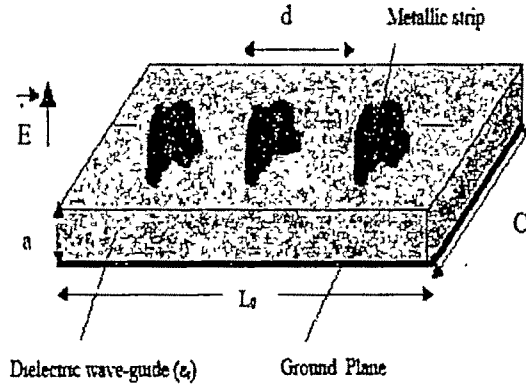


Fig. 1 . Microstrip leaky-wave antenna with metallic strips of arbitrary shape

B. Numerical Trial Basis Construction

In this case, for determining the trial functions basis, no analytical expressions which may reproduce the current density variation in the metallic domain are found. The solution consists to numerically build this basis. The current density J and $\{g_k\}$ functions, chosen as trial functions must be high on metallic parties and vanish on insulation ones. They are expressed in terms of $\{f_{mn}\}$ functions: the periodic walls wave-guide proper modes by:

$$|g_k\rangle = \sum_{m,n} a_{mn} |f_{mn}\rangle \quad k = 1, \dots, N_{fes} \quad (1)$$

N_{fes} : the required trial function number.
 a_{mn} : trial function components.

On Fig.2, the 100 first eigen-values are represented versus the metallic surface (sub-domain: S_M) and the aperture surface (entire-domain: S_T) ratio. So, more values are generated more this ratio has to augment. Also, the number of Floquet modes necessary for computing the complex propagation constant depends on the shape considered and its section. For high

number, spurious solutions may be excited due to the eigen value degeneration.

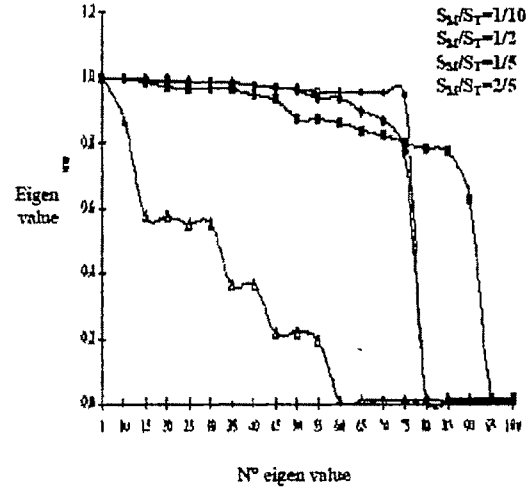


Fig. 2 Eigen-values variation versus S_M/S_T ratio.

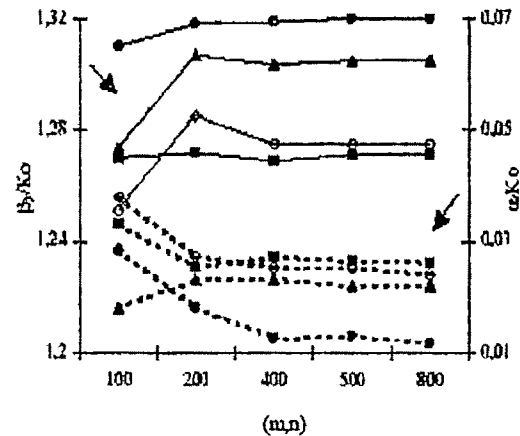


Fig. 3. Complex propagation constant variation for a rectangular metallic strip.
 • 8 seg ▲ 12 seg ◇ 16 seg ■ 20 seg
 — Real Part - - - Imaginary Part

III NUMERICAL RESULTS - INTERPRETATIONS [4]

Many optimal metallic shapes are investigated in order to perform the radiating characteristics of a microstrip leaky-wave antenna.

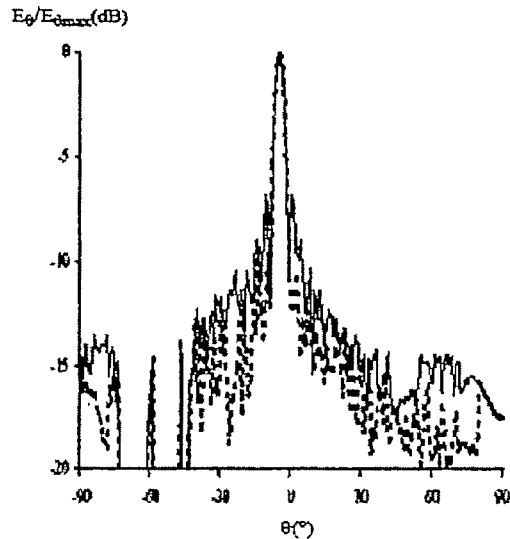
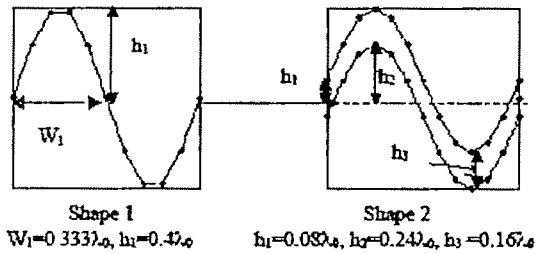


Fig. 4. Radiating patterns E_0/E_{0max} (dB) in E plane for a microstrip leaky-wave antenna loaded with sinusoidal shapes for $L_0=20\lambda_0$ at $f=84\text{GHz}$ (Angular shift at -5°) $\epsilon_r=2.45$, $a=0.387\lambda_0$, $c=0.8\lambda_0$, $d=0.667\lambda_0$ ($\lambda_0=3.75\text{mm}$ at $f=80\text{GHz}$).
 ---- Shape 1 — Shape 2

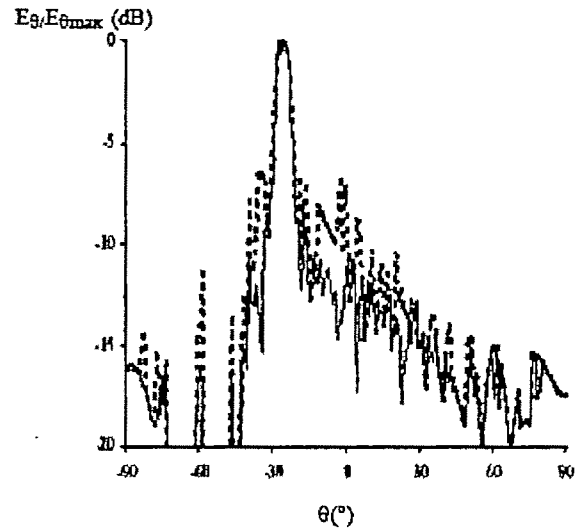
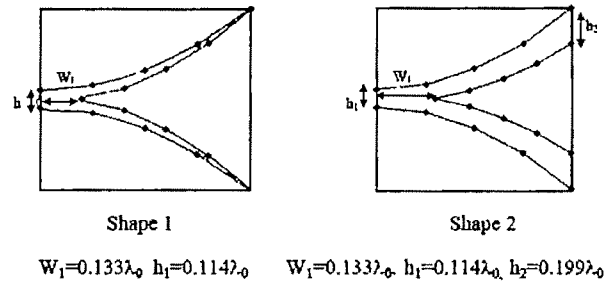


Fig. 5. Radiating patterns E_0/E_{0max} (dB) in E plane for a microstrip leaky-wave antenna loaded with exponential shapes (Vivaldi) for $L_0=15\lambda_0$ at $f=74\text{GHz}$ (Angular shift at -26°) $\epsilon_r=2.45$, $a=0.387\lambda_0$, $c=0.8\lambda_0$, $d=0.667\lambda_0$ ($\lambda_0=3.75\text{mm}$ at $f=80\text{GHz}$).
 ---- Shape 1 — Shape 2

IV. CONCLUSION

This communication addressed the issue of using a uniform 1-D periodic LWA of metallic parts with arbitrary shape to produce a conical scanned beam in elevation plane. By a reduction of the surface integral to a line integral, the inner products are easily computed for more complex shapes. Thus, a convergence check is elaborated for the TE, TM modes and the linear segments numbers required for the contour discretization. Numerical results indicated the ability of the method to accurately model the 1-D LWA. Furthermore, the optimisation and the investigation of new shapes are given for performing the radiating characteristics of such antennas. Then, it will be as indicated above, easy to predetermine the radiating patterns versus the proposed periodic shape. An extension may be done for specific and more complexes forms.

REFERENCES

- [1] M. Ghom, B. Lejay, J.L. Amalric, and H. Baudrand, "Radiation characteristics of uniform and non uniform dielectric leaky-wave antennas," *IEEE Trans Antennas and Propagation*, vol. 41, pp 1177-1186, Sept. 1993.
- [2] I. Ohtera, "Diverging/Focusing of electromagnetic waves by utilizing the curved leaky-wave structure application to broad beam antenna for radiating within specified wide-angle," *IEEE Trans on Antennas and Propagation*, vol. 47, pp. 1470-1475, Sept. 1999.
- [3] Z. Mekkioui, "Contribution to 1-D and 2-D microstrip dielectric leaky-wave antenna analysis with arbitrary metallic shape," *Doct d'Etat Es-Sciences dissertation*, Dept of Phys., Tlemcen Univ., Tlemcen, Algeria, 2004.
- [4] S. Kagami, and I. Fukai, "Application of boundary element method to electromagnetic field problems," *IEEE Trans. Micro-wave Theory and Techniques*, vol. 32, pp 455-461, Apr 1984.

Modeling of Process of Interaction of The Enterprises on The Basis of A Web-Services by Means of Java-Technologies

G. Jumatova¹

¹ Institute of informatics and control problems Ministry of Education and Science of Republic of Kazakhstan, Kazakhstan e-mail: dgujlan@mail.ru).

Abstract— Nowadays the modern commercial enterprise is difficult for presenting without information systems of various purposes - accounting, financial-analytical, industrial, warehouse information systems, etc. The large enterprise uses multipurpose information systems, for example ERP, CRM, SCM and others, and their application can simultaneously occur. Besides there are still suppliers, clients, partners with the complex and specific information systems. All this should be in interaction.

In connection with there is a problem of communication of such diverse data, and also creation of ways, which data in a convenient format for its further processing allow to obtain. The concept a web services creates conditions for the decision of problems of association and integration of diverse systems on the basis of the open standards.

The main purpose of the given work is the description of system engineering of integration of the diverse enterprises for teamwork with use of the concept a web services by means of Java - technologies.

On the basis of developed service probably interaction between the enterprises, centralized use of resources and fast information interchange between them.

Key words— information interchange, interaction of enterprises, modeling, SOAP, Web service, WSDL, XML.

I. INTRODUCTION

MODERN commercial enterprise is difficult for presenting without information systems of various purposes - accounting, financial-analytical, industrial, warehouse information systems, etc. The large enterprises use multipurpose information systems. Besides there are still suppliers, clients, partners with the complex and specific information systems. All this should be in interaction.

The problem is in an effective organization of this interaction to create productive, reliable and safe automated

extra - corporate (i.e. enterprises reaching for limits) chains of those business-processes, which integration is necessary for the enterprise for realization of the business-functions. The basic set of problems of modern information technologies of the enterprises is in the field of integration of extra corporate appendices.

In connection with there is a problem of communication of such diverse data, and also creation of ways, which data in a convenient format for its further processing allow to obtain. The concept a web-services creates conditions for the decision of problems of association and integration of diverse systems on the basis of the open standards.

Efficiency of use a web - services is in the standards; the open protocols of an exchange and the data transmission supported on all platforms Unix and Windows.

II. WEB-SERVICE TECHNOLOGY

A. The basic concepts

At use a web-service to the enterprises it will be absolutely not important, what software is used with the partner for between you there is "a universal translator" - a web-service representing, as a matter of fact, the description of rules on which concrete consumers of the information get access to concrete data. Standard and unified, therefore by means of a web-services it is possible to unite the description rather easily both internal services of the enterprise, and information systems of the whole branch. In the first case "universal translators" facilitate integration diverse software in a local network of the enterprise, in the second - provide transition from automation local business of processes to automation global business of processes.

Service oriented architecture (SOA) and a web-services as its component is not only new way of association of the

isolated programs and the whole information systems [3]. In effect, it is a new way of association of businesses. Destroying traditional corporate barriers, the web-services are provided with a continuity of process of creation of the goods or service, which actually is never limited to frameworks of one enterprise. Closely integrated chains of the enterprises-partners, and - for as much as short term, down to individual contact allow creating the Web-services quickly. By means of web-services coordinate interests and suppliers of raw material and accessories supervise each other, assembly manufactures, transport firms, customs terminals, wholesale and retail sellers, advertising-information services, etc. Due to optimization of costs and selection at each stage of the optimum partner in a prize remain all participants of a chain.

B. Web services architecture

The web services architecture is based on three related standards: SOAP, WSDL, and UDDI.

Generally the three-pronged technologies can be described as follows:

SOAP (Simple Object Access Protocol) defines the mechanism by which a web service is called and how data is returned. SOAP clients can call methods on SOAP services, passing objects in XML format.

WSDL (Web Service Definition Language) describes the external interface of a web service so that developers can create clients capable of using the service.

UDDI (Universal Discovery, Description, and Integration) registries contain information about web services, including the location of WSDL files and the location of the running services, so that a wide community of developers can create clients to access the services and incorporate their functionality into applications.

Related technologies to facilitate web services include HTTP, HTML, XML, WML and URL.

HTTP: The Hypertext Transfer Protocol (HTTP) is an application level protocol with the lightness and speed necessary for distributed, collaborative, hypermedia information systems. Secure HTTP provides a variety of security mechanisms to HTTP clients and servers, providing the security service options appropriate to the wide range of potential end uses possible for the World-Wide Web (WWW).

HTML: Hypertext Markup Language is a markup language used to construct web pages for wired devices.

XML: extensible Markup Language is a markup language used to construct web pages [4].

WML: Wireless markup language is a markup language based on XML for wireless and mobile web communication.

URL: URL is the syntax and semantics for a compact string representation of a resource available via the Internet. For example, we use URL to locate web addresses and FTP site addresses.

C. Interaction principle

JAX-RPC (Java API for XML-Based RPC) provides a tool

that reads WSDL and generates client-side stubs. These stubs are Java classes and interfaces that will be used by our code. The stubs provide a client-side interface to the server-side functionality. For example, if our server offered a Math services with a method called add, the generated stub would also have a method called add. Our client code will call a method on the stub, and the stub implementation code will take the parameters to that method and turn the Java method call into a Web service request. This request will be sent over HTTP to the server and will use SOAP as the RPC protocol.

The client calls the stub, the stub translates the call into a SOAP message, and the stub sends it using RPC. The listening server receives the SOAP message and translates it into a method call at the server. If the server is written in Java, the SOAP message is turned into a Java call. If the server is a .Net server, the call will probably be to a C# or a VB.Net object. The server's return values are translated back to SOAP and then returned to the stub, which translates the returned SOAP message into a Java response.

III. CONCLUSION

Similar techniques are not new, however before technology were others, and afford their application very large enterprises could only. SOA gives an opportunity to use similar technologies to the enterprises of an average level. Many enterprises do not guess at all, that their information system is constructed and functions with use SOA. However they feel, that cost of integration of information systems inside of the enterprise and behind its limits decreases on orders.

At sudden change of a market situation or the purpose of the enterprise, the scheme can be reconstructed business of processes quickly simple modification in rules. Representatives of the enterprise, being on business trip, can get from any computer access to the corporate database and unpack the information necessary for success of negotiations. Crucial messages can act in real time even on a mobile phone or a pocket computer.

REFERENCES

- [1] D. Chappell, T. Jewell, *Java web services*, 2002.
- [2] J. Snell, D. Tidwell, P. Kulchenko, *Programming Web services with SOAP*, 2001.
- [3] R. Englander, *Java and SOAP*, 2001.
- [4] B. McLaughlin, *Java and XML, Second Edition*, 2002.
- [5] G. Jumatova, "Modeling of activity of the enterprises on the basis of the concept a web services by mean of Java-technologies (Conference—Accepted for publication)," *Models and Simulation in engineering, economics and management and general application*, to be published, 2007

Performance Analysis of Neuro-Predictive Controller for Nonlinear Chemical Process

S. Paruya

Department of Chemical Engineering, Haldia Institute of Technology, Haldia, India – 721 657 e-mail. swapanparuya@rediffmail.com

Abstract - Last more than two decades, model predictive controller (MPC) has been proved to be an advanced control strategy to regulate the process with large dead time and lag time. In the present paper, attempts are made to study the performance of neural network based predictive controller for a nonlinear chemical reaction system. The time-delay neural network (TDNN) has been used to simulate the nonlinear time-variant process undergoing the stochastic change in input. The potential advantage of feasible sequential quadratic programming (FSQP) for minimizing the relevant cost function has been utilized to solve for optimum control signal. Performance evaluation of the neuro-predictive controller has been carried out with reference to classical PI controller when both are subjected to set-point changes of stochastic nature. Situations with and without measurement delay have been presented. In both cases, neuro-predictive controller performs better than the PI controller with respect to stability nature, speed of response and ITAE.

Key words – Predictive Control, Neural Network, Advanced Process Control.

I. INTRODUCTION

IMPLEMENTATION of advance process control (APC) strategies and real-time optimization (RTO) in energy-intensive processes has yielded large savings in recent years. They have tremendous potentials and promising futures. Bennett et al. [1] examined the benefits of RTO in energy-intensive processes and reported that 75% of theoretical benefits can lead to the energy savings of 280 trillion BTU per year. Qin and Badgwell [2] reported \$220000 savings per year for energy when MPC was installed in distillation units of a polyvinyl chloride plant. Last more than two decades, MPC has been proved to be an

advanced control strategy to regulate the process with large dead time and lag time. MPC requires solving a sequence of continuous optimization problems that cater to minimization of cost function with equality constraints (process models) and inequality constraints as well. MPC has a series of advantages over classical PID control as illustrated by De Keyser [3]. Many investigators [3-7] have studied model predictive strategies in recent past. In general, MPC algorithm may be described by the steps in sequences – (1) explicit use of a model to predict the process output at future time instants, (2) calculation of a control sequence minimizing a certain objective function and (3) at each instant, the receding horizon is displaced towards the future. Various functionalities in an MPC are shown in Fig. 1. Due to inherent limitations and limited uses of linear MPC, nonlinear MPC (NMPC) has been strongly felt in the most of the situations such as changes in set point during startup. More over, RTO schemes also generate varying set-points (targets) which are plant-economics dependent. Such cases of set-point change are well tackled using NMPC. This is because of the fact that changes in set point sensibly affect the process dynamics. Given the set-point change, processes that were believed to behave linearly shift to the region in which nonlinear dynamics becomes prevalent. One of the major difficulties for formulating NMPC is the identification of nonlinear processes. First-principle based model-identification involves assumptions that may not be valid when the systems undergo changes under severe transient conditions. The regression models may be formulated for nonlinear processes. But for wide operating conditions, a single regression model is not adequate; multiple regression models are required to be developed. In that case, one may encounter the operating conditions for which the empirical models have been formulated. Neural network model (NNM) has the ability to identify nonlinear processes with multiple inputs and outputs very efficiently and quickly compared to the mechanistic models. Control and identifications of various processes based on neural networks are available in literatures [8-11]. Neuro-model

based process optimization has been proved to be more efficient for nonlinear chemical processes [12].

Given the potential advantages of neural network based nonlinear MPC (NNMPC), attempts are made to formulate NNM of a nonlinear chemical reaction system for designing NMPC required for controlling the same. Performance evaluation of NNMPC has been carried out with reference to classical PI controller when both are subjected to set-point changes of stochastic nature. On the other hand, the effect of dead time on their performances has been studied to derive definite conclusions.

II. SYSTEM DESCRIPTIONS

The reaction system is regulation of continuous stirred tank reactor (CSTR) as shown in Fig. 2 and as demonstrated in MATLAB 6.1 as a case study, in which the following reaction takes place under isothermal condition:



For which the reaction rate for B is given by the following kinetics:

$$(-r_B) = \frac{k_1 C_b(t)}{(1 + k_2 C_b(t))^2} \quad (2)$$

In that case study, optimization method for deriving the control law has been modified by using FSQP. The controller has been subjected to stochastic targets (references) at which the product concentrations have to be maintained. Inlet concentration of B_1 and B are C_{b1} and C_{b2} respectively and the corresponding flow rates are W_1 and W_2 . W_1 was kept unchanged ($W_1=1.0$) while W_2 was manipulated to maintain C_b at CSTR outlet at desired value (reference). The reference has been changed stochastically to study its effect on the process and its regulation, which is very much frequent in real-time situations. The inlet concentrations are set to $C_{b2} = 24.9$ and $C_{b1} = 0.1$. The constants associated with the rate of consumption are $k_1 = 1$ and $k_2 = 1$, and these are called reaction rate constants. The stochastic targets are the multiple pulses functions between a minimum value of 22 and a maximum value of 23. The with irregular frequencies were randomly generated.

III. MODEL EQUATION AND SOLUTION SCHEMES

The following cost function has been minimized to solve for optimum control signal (u) which has been considered to be the manipulated variable (W_2). This is because of the fact that the dynamics of the final control element has been incorporated in the present study.

A. Cost function

$$\min J = \frac{1}{2} \int_0^1 [(C_{br} - C_b)^2 + u^2] dt \quad (3)$$

Decision making has been performed by using FSQP for its applicability in nonlinear optimization. The reasons behind choosing are manifold – (1) it minimizes any smooth nonlinear function, (2) it deals with any kind of nonlinear equality and /or inequality constraints, (3) it generates only feasible iterates, (4) the feasibility feature guarantees acceptable values of the manipulated variables, even if they are not quite optimal, and (4) it also helps in speeding up the convergence. We obtain the quadratic programming (QP) subproblem by linearizing the nonlinear constraints using quasi-Newton method because of the fact that QP minimizes a quadratic objective function that is linearly constrained. The sequential steps in FSQP are:

- (1) Updating the Hessian Matrix of the Lagrangian function
- (2) Quadratic programming solution
- (3) Line search and merit function calculation

quadprog routine of MATAB has been used for the optimization in the present investigation.

B. Actual CSTR (Plant)

The CSTR plant caters to the nonlinear dynamics of liquid-holdup in addition to the concentration dynamics of reactant B.

Liquid-holdup dynamics:

$$\frac{dh(t)}{dt} = w_1(t) + w_2(t) - 0.2\sqrt{h(t)} \quad (4)$$

$h(t)$ is height of liquid in CSTR at any instant of time t .

Concentration dynamics of reactant B:

$$\frac{dC_b(t)}{dt} = (C_{b1} - C_b(t)) \frac{w_1(t)}{h(t)} + (C_{b2} - C_b(t)) \frac{w_2(t)}{h(t)} - \frac{k_1 C_b(t)}{(1 + k_2 C_b(t))^2} \quad (5)$$

The plant-state information (C_b) has been determined by solving the above stiff ODEs with the help MATLAB 6.1.

C. CSTR Model - NNM

The use of neural networks for non-linear process modeling and identification is justified by their capacity to approximate the dynamics of non-linear systems including those with high non-linearities or with dead time. In most applications, feedforward neural networks are used, because the training algorithm is less complicated. The problem of obtaining the model of a dynamic system can be solved in two ways: (1) using a static neural network with external dynamics or (2) using a dynamic neural network. Usually, static neural networks are preferred, which requires that filters are applied on the network inputs in order to capture the real system dynamics. The filters usually consist in delaying elements and the network so formed is called a

time delay neural network (TDNN) (Dumitrache et al. [13]). When it comes to non-linear models, the most general model that includes the biggest class of non-linear processes is the NARMAX model (Chen and Billings [14]). The neural NARMAX corresponds to a recurrent neural network, because some of the network inputs are past values of the network output. The structure of a TDNN intended for the present investigation is shown in Fig. 3. The neural network output $C_b(k)$ is a function of the filtered input and output signals (W_2 and C_b). The present TDNN configuration is with input of W_2 and output of C_b . Numbers of delayed inputs and outputs are 2 and 2 respectively while size of hidden layer is seven. *trainlm* function of MATLAB has been used as network training function to update weight and bias values according to Levenberg-Marquardt optimization. The training data have been generated using maximum input of 4 while the output has been limited to a minimum value of 20 and a maximum value of 23.

D. Conventional PID control

To compare performance of NNMPC and conventional PID algorithm, another closed-loop system has been studied, in which NNMPC has been replaced by PID block. It is important to mention that the derivative action has not been introduced because of stochastic nature of set-point variation. The derivation action under this situation amplifies the stochastics. Optimum setting of PI controller has been made using a unit step change. The optimum value of controller gain is set to be 5.0 while the reset rate is 0.9 based on minimizing ITAE by subjecting the system to step change in reference.

IV. RESULTS AND DISCUSSIONS

A. Response of plant without time delay

To study the response, both neuro predictive controller and PI controller have been subjected to stochastic targets. As mentioned earlier, the stochastic targets are the multiple pulse fluctuations between a minimum value of 22 and a maximum value of 23 and they have been randomly generated at irregular frequencies. However, at any time instant, magnitudes of targets are same for both the controller. Figs. 4a and 4b present the plant response with NNMPC and with PI controller respectively. They clearly show the difference in rise time and with NNMPC, rise time becomes less. This establishes the fact that the plant response becomes faster while being regulated with NNMPC. This has been possible due to the facts – with MPC, (1) process model has the ability to predict the process output at future time instants and (2) the future (postulated) control laws can be sequenced called receding horizon strategy and with this sequence, at each instant the horizon is displaced towards the future. This involves the implicit application of the first control signal of the sequence calculated at each step into the real process and process model as well. Fig. 4c shows the variation of

manipulated variable W_2 (control signal in the present investigation) with time with PI controller and with NNMPC and the amplitude of fluctuation is higher with PI controller although the amplitudes of controlled-variable fluctuations with PI controller are not noticeably higher (Figs. 4a and 4b). So, one can anticipate that with increase in range of pulse-fluctuations of targets, stability-quality of the closed-loop system with PI controller degrades. Fig. 4d presents the ITAE ratio (defined by the ratio of ITAE with PI controller to ITAE with NNMPC controller). Initially up to approximately 20.0 s, the performance of PI controller does not look convincing. At the initial instants, the ratio becomes close to 6.0. This indicates that regulations of any startup process or any severe transients with classical PI controller are not economical.

B. Response of plant with time delay

The study of the effect of the time delay on the performance of the controllers has been made based on the understanding that all practical systems suffer from the measurement delay because of the long signal-path between the controller and the sensor. So, the numerical experiment has been carried out by introducing time-delay element on feed-back line. Small time delay of 0.2 s has been considered while the stochastic targets are the multiple pulse fluctuations between a minimum value of 22 and a maximum value of 23. Figs. 5a and 5b show the plant response with NNMPC and with PI controller respectively. The figures indicate that the performance of PI controller in this situation deteriorates by accumulating large amount of error and introducing instability into the system while NNMPC compensates well for the time-delay element and performs well by retaining the stability. Fig. 5c presents the variation of control signal with NNMPC and with PI controller. The fluctuations of the signal with PI controller are more severe than those with NNMPC. The performance comparison with PI control has been also made by plotting the ITAE ratio with time as shown in Fig. 5d. Initially, the ratio becomes close to 120 and at about 13.0 s, it reaches another peak of about 80. Although after 20.0 the ratio starts to decrease, it seems to settle at the value of about 6.0. So, the overall results indicate that the performance of NNMPC in the situation of measurement delay better compared to PI controller and the later can not tackle the situation. It may be explained by the special features of MPC as mentioned in the previous section.

V. CONCLUSIONS

The present investigation attempts to compare the performance of NNMPC and PI controller for the nonlinear chemical in the event of stochastic reference trajectories with and without measure delay. In NNMPC, TDNN has been used and the optimization problem has been solved for control signal using FSQP. Optimum setting of PI controller based on ITAE minimization (by subjecting the system to step change in reference) has been used. In both cases, NNMPC performs better than the PI controller with

respect to stability nature, speed of response and ITAE. Although it is established that neural models better represent nonlinear processes than mechanistic models do, the study in this regard for the process under investigation is required to be made. The analysis may also be made by subjecting the system to other kinds of reference trajectories such as step functions, Impulse functions and sinusoidal functions. As the study shows appreciable changes in dynamics of the closed-loop system by the effect of measurement delay, APC seriously needs intelligent sensors to exploit the full potential of APC [15].

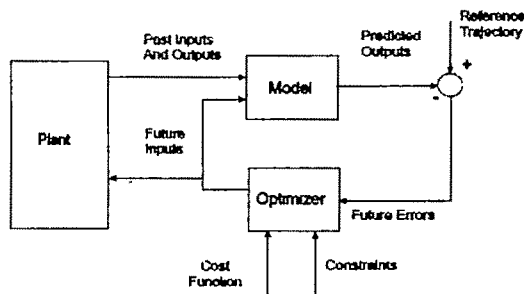


Fig. 1 Various functional blocks in an MPC

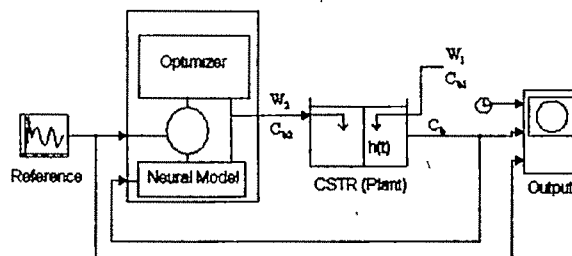


Fig. 2 Control of CSTR outlet concentration

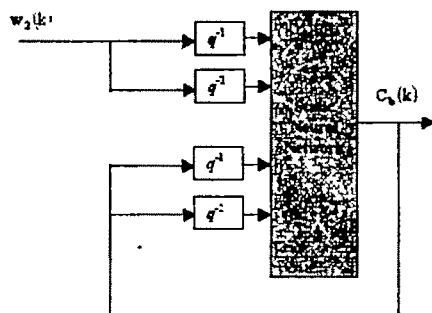


Fig. 3 Structure of a Time Delay Neural Network

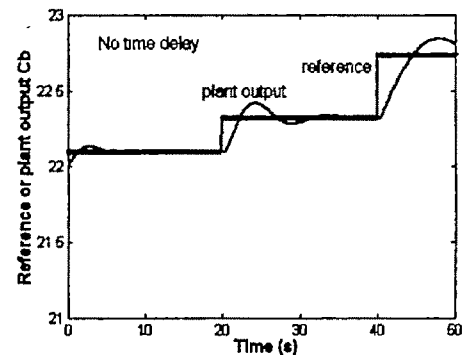


Fig. 4a Plant response with NNMPC

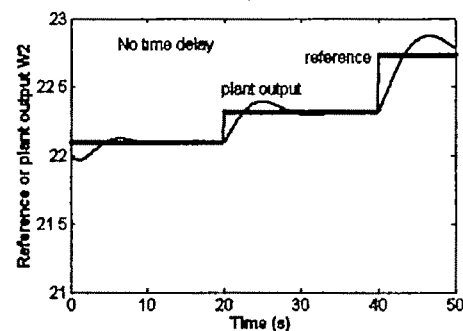


Fig. 4b Plant response with PI controller

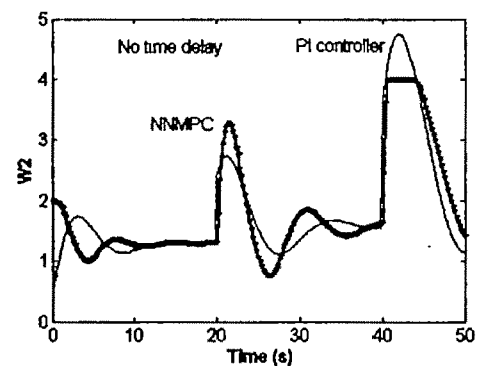


Fig. 4c Variation of control signal (manipulated variable)

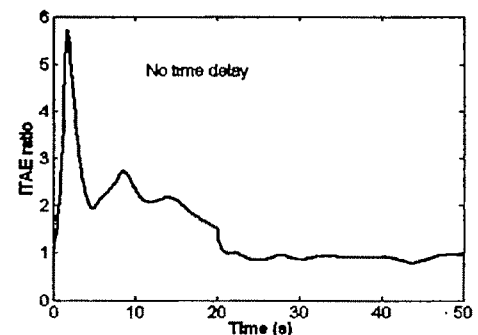


Fig. 4d Comparison of performance of NNMPC and PI

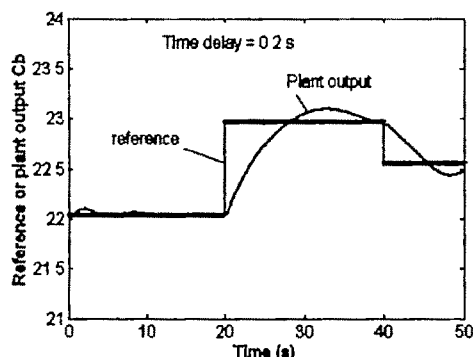


Fig. 5a Plant response with NNMPC

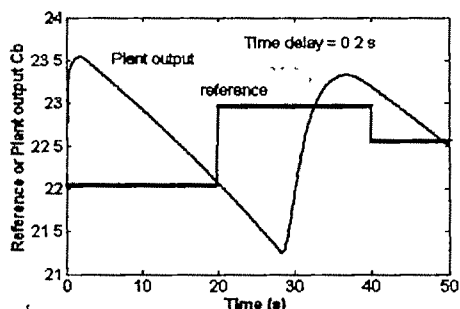


Fig. 5b Plant response with PI controller

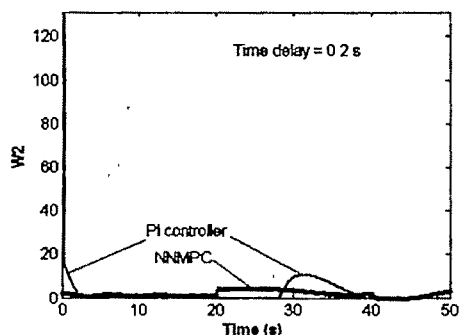


Fig. 5c Variation of control signal (manipulated variable)

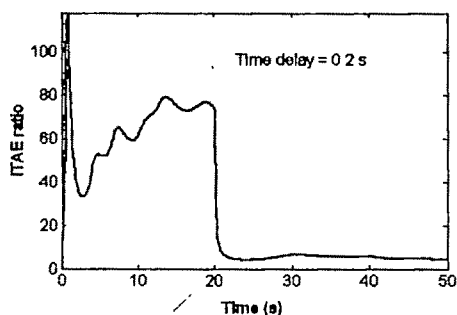


Fig. 5d Comparison of performance of NNMPC and PI

REFERENCES

- [1] J. Qin and T. Badgwell, "A Survey of Industrial Model Predictive Control Technology", *Control Eng. Practice*, vol. 11, pp. 733-764, 2003.
- [2] B.H. Bennet, M.S. Boddy, F. Doyle, M. Jamshidi, and T. Ogunnaike, "Assessment Study on Sensors and Automation in the Industries of the Future: Reports on Industrial Controls, Information Processing, Automation, and Robotics", *US Department of Energy Report*, 2004.
- [3] R.M.C. De Keyser, "Basic Principles of Model Based Predictive Control", *ECC 91 European Control Conference*, Grenoble, France, 1991, pp. 1753-1758.
- [4] R.M.C. De Keyser and A.R. von Cauwenberghe, "Extended prediction self-adaptive control", *IFAC Symp. on Identification and System Parameter Estimation*, York, U.K., 1985, pp. 1225-1260.
- [5] C.E. Garcia, D.M. Prett and M. Morari, "Model Predictive Control: Theory and Practice - a Survey", *Automatica*, Vol. 25, No. 3, pp. 1753-1758, 1989.
- [6] S.J. Qin and T.A. Badgwell, "An overview of industrial model predictive control technology", *In Chemical Process Control-AIChE Symposium Series* (J. Kantor, C. Garcia and B. Carnahan, Eds. New York: AIChE), 1997, pp. 232-256.
- [7] J.B. Rawlings, "Tutorial Overview of Model Predictive Control.", *IEEE Control Systems Magazine*, Vol. 20, No. 3, pp. 38-52, 2000.
- [8] S. Chen, S.A. Billings and P.M. Grant, "Non-linear system identification using neural networks", *Int. J. Control*, Vol. 51, pp. 1191-1214, 1990.
- [9] P. J. Werbos, T. McAvoy and T. Su, "Neural Network, System Identification, and Control in the Chemical Process Industries", D. A. White and D. A., Sofge ed., *Intelligent Control*, Van Nostrand and Reinhold, New York, 1992.
- [10] S. Fabri and V. Kadiramanathan, "Dynamic structure neural networks for stable adaptive control of nonlinear systems", *IEEE Transactions on Neural Networks*, Vol. 7, pp. 1151-1167, 1996.
- [11] G.P. Liu, V. Kadiramanathan and S.A. Billings, "Predictive control for non-linear systems using neural networks", *Int. Journal of Control*, Vol. 71, No. 6, pp. 1119-1132, 1998.
- [12] S. Paruya, "Real-Time Intelligent Optimization Models for Nonlinear Chemical Processes", *Proceedings of National Conference on Applications of Operation Research on Management Science*, Haldia Institute of Technology, 26-27th December, 2006.
- [13] I. N. Constantin Dumitrache and M. Dragolcea, *Neural Networks - Process Identification and Control*. Matrix ROM, Bucuresti (in Romanian), 1999.
- [14] S. Chen and S.A. Billings, "Representations of non-linear systems: the NARMAX model", *Int. J. Control*, Vol. 49, No. 3, pp. 1013-1032, 1999.
- [15] S. Paruya, "Intelligent Sensor - Removing Bottlenecks in Advanced Process Control and Real-Time Optimization of Chemical Processes", *Proceedings of ET & TE 2007*, Haldia Institute of Technology, India, 24-25th February, 2007.

Study of the Microwave Absorption Behaviour of Ceramic Material at X-Band Frequencies

S.K.Srivastava

Department of Physics & Electronics.

Government Post Graduate College Ambikapur (C.G.), INDIA, Email:sk_srisvastava@yahoo.com

Abstract- In the present paper an attempt has been made to develop a theoretical model for calculation of microwave absorption in ceramic materials at X-band frequencies. The microwave absorption coefficients are calculated on the basis of frequency, grain size, concentration of doping as well as sintering temperature. The exposure of microwave on the sample are taken as both for vertical and horizontal polarization. It is found that in case of vertical polarization the microwave absorption coefficients are larger than that of horizontal polarization.

Keywords - Microwave Absorption, Horizontal Polarization, Vertical Polarization ST-Sample Thickness

I. INTRODUCTION

MICROWAVE dielectric in ceramic form has been exploited in application such as filters, resonators, circulators etc. During the past decade material composition have been developed to suit the single crystal system requirements for the HTSC thin film application in the microwave. Microwave dielectric material are widely used for application in the communication market. The advantage of microwave ceramics include high temperature stability, good power handling and the low insertion at higher frequencies. These features in combination with new ideals designs will be basis for continuing success of microwave ceramic in third generation of mobile communication.

The microwave absorption behavior of ceramic materials plays an important for the use of ceramics as phantom materials in cellular mobile phone. The characterization and processing of electronic ceramic at microwave frequency range will be one of the important factor for classified the materials for use in cellular mobile phone.

Therefore In the present paper an attempt has been made to develop a theoretical model for calculation of microwave absorption in ceramic materials at X-band frequencies. The microwave absorption coefficients are calculated on the basis of frequency, grain size, concentration of doping as well as sintering temperature. The exposure of microwave on the sample are taken as both for vertical and horizontal polarization. It is found that in case of vertical polarization the microwave absorption coefficients are larger than that of horizontal polarization.

II. GEOMETRY OF THE PROBLEM

The geometry of the samples are taken as three layered in configuration upper layer, lower layer and middle layer. The upper layer is denoted as layer no.1 middle layer is denoted as layer no.2 and lower layer is denoted as layer no.3 as shown in fig.1.0.

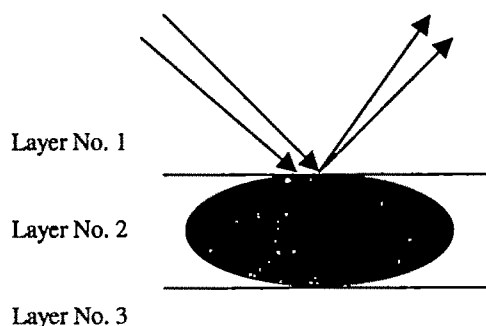


Fig 1.0 : Geometry of the sample.

$\sigma_{\text{ABS}}(1)$ for $0 \leq t \leq t_1$ for Layer 1
 $\sigma_{\text{ABS}}(t) = \sigma_{\text{ABS}}(2)$ for $t_1 \leq t \leq t_2$ for Layer 2
 $\sigma_{\text{ABS}}(3)$ for $t_2 \leq t \leq t_3$ for Layer 3
 Where t is the thickness of the sample.

$\sigma_{\text{ABS}}(1), \sigma_{\text{ABS}}(2), \sigma_{\text{ABS}}(3)$ are the absorption coefficients of the layer 1, Layer2 and Layer 3 of the sample.

III. CALCULATION OF ABSORPTION COEFFICIENTS

The absorption coefficients of doped samples can be calculated using Integral equation model (IEM) developed by Tsang et al (1985)[1]. The absorption coefficients can be written as [1]

$$\sigma_{pq} = (k^2/2) \exp(-2k^2 z) \sigma^{2n} \cup I^{pq} \cup (W^n(-2k_x, 0)/n!) \quad (1)$$

$$\text{where } I^{pq} = \{ (2k_x)^n f_{pq} \exp(-\sigma^2 k_x^2) + k_x^n [F_{pq}(-k_x, 0) + F_{pq}(k_x, 0)]/2 \}$$

$p, q = \text{Vertical (V) or Horizontal (H) polarization.}$
 $f_{pq}, F_{pq} = \text{Kirchoff and Complementary field coefficients, dependent on the dielectric constant through the Fresnel reflection coefficients.}$

The Fresnel reflection coefficients for vertical and horizontal polarization are defined as

$$R_{vv} = 2R_{\text{cos}} / \cos\theta : F_{hh} = 2R_{\text{cos}} / \cos\theta \quad (2)$$

$$F_{vv}(-k_x, 0) + F_{vv}(k_x, 0) = [(2 \sin^2\theta (1 + R_{\text{cos}})^2 / \cos\theta) \{ (1 - \epsilon_r^{-1}) + (\epsilon_r \mu_r \sin^2\theta - \cos^2\theta) / \epsilon_r^2 \cos^2\theta \}] \quad (3)$$

$$F_{hh}(-k_x, 0) + F_{hh}(k_x, 0) = [(2 \sin^2\theta (1 + R_{\text{cos}})^2 / \cos\theta) \{ (1 - \mu_r^{-1}) + (\epsilon_r \mu_r \sin^2\theta - \mu_r \cos^2\theta) / \mu_r^2 \cos^2\theta \}] \quad (4)$$

$$R_{\text{cos}} = \{ \{ \epsilon_r \cos\theta - (\mu_r \epsilon_r - \sin^2\theta)^{1/2} \} / \{ \epsilon_r \cos\theta + (\mu_r \epsilon_r - \sin^2\theta)^{1/2} \} \}$$

$$R_{\text{cos}} = \{ \{ \mu_r \cos\theta - (\mu_r \epsilon_r - \sin^2\theta)^{1/2} \} / \{ \mu_r \cos\theta + (\mu_r \epsilon_r - \sin^2\theta)^{1/2} \} \} \quad (5)$$

where $\epsilon_r = \text{Relative dielectric constant of sample, expressed as a ratio of the complex dielectric constant of upper and lower layer of samples.}$

$\mu_r = \text{Relative permeability of sample. The Scattering Coefficients can be calculated using equation (1), (2), (3), (4) and (5). The absorption coefficients are calculated using both horizontal and vertical polarization.}$

For Horizontal Polarization

$$\sigma_{pq} = (k^2/2) \exp(-2k^2 z) \sigma^{2n} \{ (2k_x)^n f_{pq} \exp(-\sigma^2 k_x^2) + k_x^n [(2 \sin^2\theta$$

$$(1 + [\epsilon_r \cos\theta - (\mu_r \epsilon_r \sin^2\theta)^{1/2}] / \epsilon_r \cos\theta + (\mu_r \epsilon_r \sin^2\theta)^{1/2})^2 / \cos\theta \} \{ (1 - \epsilon_r^{-1}) + (\epsilon_r \mu_r \sin^2\theta - \cos^2\theta) / \epsilon_r^2 \cos^2\theta \} (W^n(-2k_x, 0)/n!) \quad (6)$$

For Vertical Polarization

$$\sigma_{pq} = (k^2/2) \exp(-2k^2 z) \sigma^{2n} \{ (2k_x)^n f_{pq} \exp(-\sigma^2 k_x^2) + k_x^n [(2 \sin^2\theta (1 + [\mu_r \cos\theta - (\mu_r \epsilon_r \sin^2\theta)^{1/2}] / \mu_r \cos\theta + (\mu_r \epsilon_r \sin^2\theta)^{1/2})^2 / \cos\theta) \{ (1 - \epsilon_r^{-1}) + (\epsilon_r \mu_r \sin^2\theta - \cos^2\theta) / \epsilon_r^2 \cos^2\theta \} (W^n(-2k_x, 0)/n!) \} \quad (7)$$

where k is propagation constant depend on frequency $k = 2\pi f / C$

IV. NUMERICAL COMPUTATION

For computation of microwave absorption in ceramic materials at both for vertical and horizontal polarization the complex value of permittivity are taken as for Sample1 and Sample2.

Table 1
 Numerical value of Complex Permittivity for
 (ST= 3mm & 6mm)

S.N	Frequency	Complex Permittivity	
		Sample1	Sample2
1	4.0	13.776-j0.255	14.026-j0.214
2	5.0	13.211-j0.212	13.987-j0.212
3	6.0	12.999-j0.201	13.829-j0.201
4	7.0	12.556-j0.198	12.996-j0.198
5	8.0	12.432-j0.182	12.81-j0.182
6	6.0	12.312-j0.179	12.731-j0.179
7	10.0	12.021-j0.162	12.821-j0.162

V. RESULT AND DISCUSSION

The absorption coefficients of the sample 1, Sample2 and Sample3 are calculated using frequency varying from 4 GHz to 10 GHz and thickness of the sample are taken as 3mm to 6mm. The result obtained are mentioned in table 2 and Table3 for both vertical and horizontal polarization. It is found that at vertical polarization of microwave in sample interface will passes higher value of microwave absorption that for horizontal polarization.

Table 2
Microwave Absorption coefficients
for Horizontal Polarization
(ST= 3mm & 6mm)

S.No.	Frequency in GHZ	Absorption Coefficients	
		Sample1 (10^{-8})m ²	Sample2 (10^{-8})m ²
1.	4.0	0.076	0.90
2.	5.0	0.186	0.220
3.	6.0	0.386	0.457
4.	7.0	0.715	0.846
5.	8.0	1.219	1.444
6.	6.0	1.953	2.313
7.	10.0	2.976	3.523

Table 3
Microwave Absorption coefficients
for Horizontal Polarization
(ST= 3mm & 6mm)

S.No.	Frequency in GHZ	Absorption Coefficients	
		Sample1 (10^{-8})m ²	Sample2 (10^{-8})m ²
1.	4.0	0.096	1.20
2.	5.0	0.193	0.281
3.	6.0	0.402	0.498
4.	7.0	0.816	0.910
5.	8.0	1.721	1.734
6.	6.0	2.310	2.815
7.	10.0	3.296	4.11

REFERENCE

- [1] J.A. Kong and R.T Sin " Theory of Microwave Remote Sensing" Wiley – Inter-science John Wiley And sons , New York, USA, 1985 .
- [2] D Agrawal et al " Studies of microwave processing of ceramic a review" Solid State Materials science Vol.10, Pp 480, 1998.
- [3] Sukhleen Bindra et al " Synthesis of Barium (Cobalt Titanium) Hexaferrite and measurement of its complex permittivity at microwave frequency in X-Band" IETE Journal of research Vol.48.No.1,pp23-26,2002.
- [4] D Clark et al " Microwave processing of materials" Annual Rev. Mater Sci.26,299,1996.
- [5] R.Roy et al " Microwave processing : Triumph of application driven in WC–Composite and Ferroic titanates of composition ferrite materials" Int. Journal of Ceramics Vol.80, pp133, 1997.
- [6] Yonglio et al " Microwave dielectric properties of ZrTiO4 thin films" Journal of Applied Physics Letters Vol.78, No. 16, pp2363-2365. 2001 [7] S.K Srivastava et al " Study of Junction circulation characteristics of Ni-Zn ferrite at microwave frequencies" Proceeding of NAMP Jaipur 2002. pp 236-239 .
- [8] P.K Jain ey al " Microstripo Junction Circulators on LiTiZn Ferrite Substrate" IE(I) Journal-ET Vol.27,1996.

Secure Communication in Power System Using Chaos Masking

Kabir Chakraborty¹, K.S.Sherpa², and S.Sengupta³

¹ Department of Electrical Engineering, Tripura University, Tripura, India, e-mail: kabir_jishu@rediffmail.com.

² Department of electrical & Electronics Engineering, SMIT, Sikkim, India, e-mail: sonam_sp@yahoo.co.in

³ Department of Applied Physics, University of Calcutta, India, e-mail: samarsgp@rediffmail.com

Abstract—The most exciting recent development in nonlinear dynamics is the realization that chaos can be made useful in "Secure Communication". In the present work the phenomenon of secure communication with chaos masking has been investigated experimentally. In this investigation chaos which is generated from two chaos generators (buck converter and boost converter) is masked with the message signal to be transmitted, thus enhancing the security in communication of the signal. This secure communication can also be useful in signal transmission of power system.

Key words— Buck Converter, Boost Converter, Chaotic Signal, Secure communication

I. INTRODUCTION

CHAOS is a periodic long-term behavior in a deterministic system. It exhibits a sensitive dependence of a system's dynamical variable on the initial conditions meaning that no two chaotic systems will evolve in the same way. Trajectories of two perfectly identical chaotic systems starting with nearby initial conditions diverge from each other exponentially. Synchronization of chaos means that the trajectories of two chaotic systems be locked to each other. Hence synchronization seems unlikely for two chaotic systems if trajectories start from initial conditions that differ slightly. Moreover, in practical applications the existence of noise (both internal and external) and system imperfect identification makes the hope of synchronizing two chaotic systems even more complicated. Nonetheless, it has been established that [1], [2], [3] synchronization of chaotic dynamical systems is not only possible but it is believed to have potential applications in communication. The strategy is that when we transmit the message to a friend, we mask it with louder chaos. An outside listener only hears the chaos, which sounds like meaningless noise. But if the friend has a magic receiver that perfectly reproduces the chaos, then he can subtract off the chaotic mask and listen to the message. This synchronization is possible only when a similar chaotic circuit as that of sending end is fabricated. If the configuration circuit

is secret, it is impossible to extract information from the transmitted message.

Hence there has been growing interest in the possibility of synchronizing chaotic signals. This idea has been tested theoretically as well as experimentally in the variety of linear dynamical system including Chua's circuit and Driven Chua circuit [4]. Lai et al [5] demonstrated that applying small temporal parameter perturbation to one of them could synchronize two identical chaotic systems. But in all these methods, synchronization is possible without any message signal. Murli and Lakshmanan [6] investigated the method of transmitting signal using chaos synchronization in Vander Pol-Duffing oscillator. But they transmitted very weak signal with chaotic masking. The synchronization is failed with high strength of message signal. These shortcomings have been overcome by K. Chakraborty et al [7], in their work, the synchronization and faithful recovery of message at the receiving end is independent of message signal strength. In that work, buck converter [7] has been taken as chaos generator.

In the present work, to make communication more secured, buck converter and boost converter are chosen as chaos generator, both chaotic signals are synchronized and masked with message signal.

II. BUCK CONVERTER CIRCUIT

Buck Converter circuit is generally a chopper circuit that modulates input DC to output DC voltage at different levels. The input voltage is connected in series with an inductor and load resistance. There are two switches, (i) S is a controlled

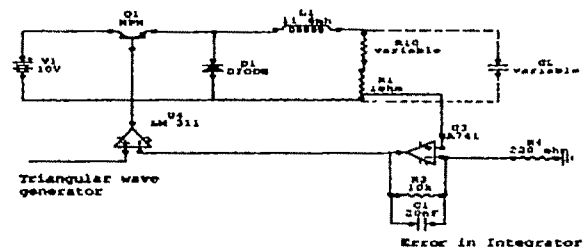


Fig. 1 Buck Converter Circuit

switch (realized by a transistor) and (ii) D is uncontrolled (realized by a diode). The controlled switch is in series with the input voltage and the uncontrolled switch is in parallel with the combination of inductor and load resistor. A capacitor is connected to smoothen the load voltage waveform (shown by the dash line in Fig.1). This is optional, and is not considered in the flowing analysis for the sake of simplicity

When S is in the ON state, the diode is OFF and the current builds up through the inductor and load. When the transistor is OFF the current freewheels through the diode and decays. By properly choosing the switching frequency and inductor value, one achieves continuous current operation and the average output voltage is then given by,

$$V_{out} = V_{in} \frac{T_{on}}{T_{on} + T_{off}} \quad (1)$$

where V_{in} = input voltage, V_{out} = output voltage, T_{on} and T_{off} = on and off times of the controlled switch.

To control the switching through current feedback, the load current is sensed as the voltage across 1 ohm resistance connected in series with the load. The signal is integrated by passing it through a low pass filter. The output of the integrator is compared with a triangular wave voltage. The output of the comparator that compares the triangular wave and error integrator voltage is used to control the on and off period of the switch. When error integrator voltage is less than triangular wave voltage, the controlled switch is turned on, and current flows through the inductor and load. The controlled switch is turned off when error integrator voltage is greater than triangular wave voltage. At this instant the voltage across the inductor reverses its polarity and the current path completes through the diode and load. Consequently the stored energy in the inductor decreases and output voltage falls. When the integrator output voltage drops below the triangular wave voltage, the switch is turned on and the process continues. The choke is designed for linear inductance and a diode with negligible storage is employed.

The system is governed by two sets of linear differential equation pertaining to the ON and OFF states of the controlled switch. The error integrator voltage and load current are taken as state variables.

During the ON period, the equations are:

$$\frac{di}{dt} = \frac{V_{in}}{L} - \frac{R_L}{L} i \quad (2)$$

$$\frac{dv_c}{dt} = i \left(\frac{R_1 + R_2}{CR_1 R_2} - \frac{R_L}{L} \right) - \frac{v_c}{R_1 C} + \frac{V_{in}}{L} \quad (3)$$

During the OFF period, the state equations are

$$\frac{di}{dt} = -\frac{R_L}{L} i \quad (4)$$

$$\frac{dv_c}{dt} = i \left(\frac{R_1 + R_2}{CR_1 R_2} - \frac{R_L}{L} \right) - \frac{v_c}{R_1 C} \quad (5)$$

Though the equations are linear, bifurcation [7] and chaos appear in this circuit because of the switching nonlinearity.

III. BOOST CONVERTER CIRCUIT

Boost converter circuit like the buck converter circuit [Fig.2], is a chopper circuit that steps up the output DC voltage (V_o) level as compared to its input voltage (V_{in}) level, that is,

$$V_o = \frac{k}{1-k} V_{in} \quad (6)$$

where, 'k' is the duty ratio of the switch. In this work, a current controlled boost converter operating in continuous current mode is considered.

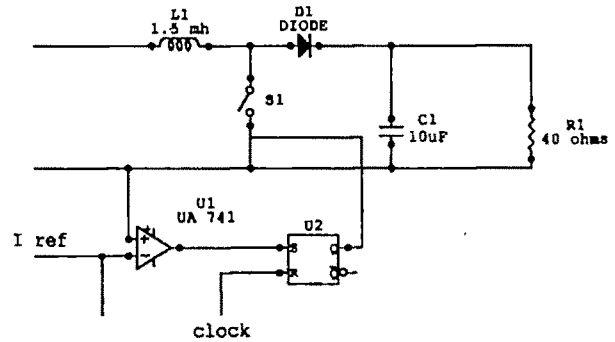


Fig. 2 Boost converter circuit with current control feed back

With this control logic the switch is turned on by the clock pulses that are spaced T seconds apart. When the switch is closed, the current increases until it reaches the specified reference value. The switch opens when $I = I_{ref}$. Any clock pulse arriving during ON period is ignored. Once the switch has opened, the next clock pulse causes it to close.

The evolution of the state variable I and v_c during the ON and OFF periods are described by the differential equations given below

During ON period,

$$\frac{di}{dt} = \frac{V_{in}}{L} \quad (7)$$

$$\frac{dv_c}{dt} = \frac{v_c}{CR} \quad (8)$$

During OFF period,

$$\frac{di}{dt} = \frac{V_{in}}{L} - \frac{v_c}{L} \quad (9)$$

$$\frac{dv_c}{dt} = \frac{I}{C} - \frac{v_c}{CR} \quad (10)$$

These are linear equations but chaos is due to switching nonlinearity.

IV. COMMUNICATION WITH CHAOS MASKING

In Fig.3, the message signal $s(t)$ is to be transmitted is added with output of error integrator and the output of the boost converter and buck converter. The resulting signals $X(1) + X(2) + s(t)$ is used to compare the triangular wave at the transmitter end (Fig3). The same signal is transmitted through the communication channel. Now, the message signal $s(t)$ is masked with chaotic signals $X(1)$ and $X(2)$. If one tries to get the message, he can not extract it because he does not

know for what values of the parameters chaos appears in the buck and boost converters.

At the receiving end (Fig.3), the transmitted signals $X(1) + X(2) + s(t)$ is fed to the inverting input of the comparator. The circuit parameters and configuration of the buck and boost converter are same as those of the transmitter. Due to synchronization the receiver buck converter and boost converter also generates $X(1)$ and $X(2)$ respectively. Now subtracting $X(1)$ and $X(2)$ from $X(1) + X(2) + s(t)$, the message signal $s(t)$ is obtained.

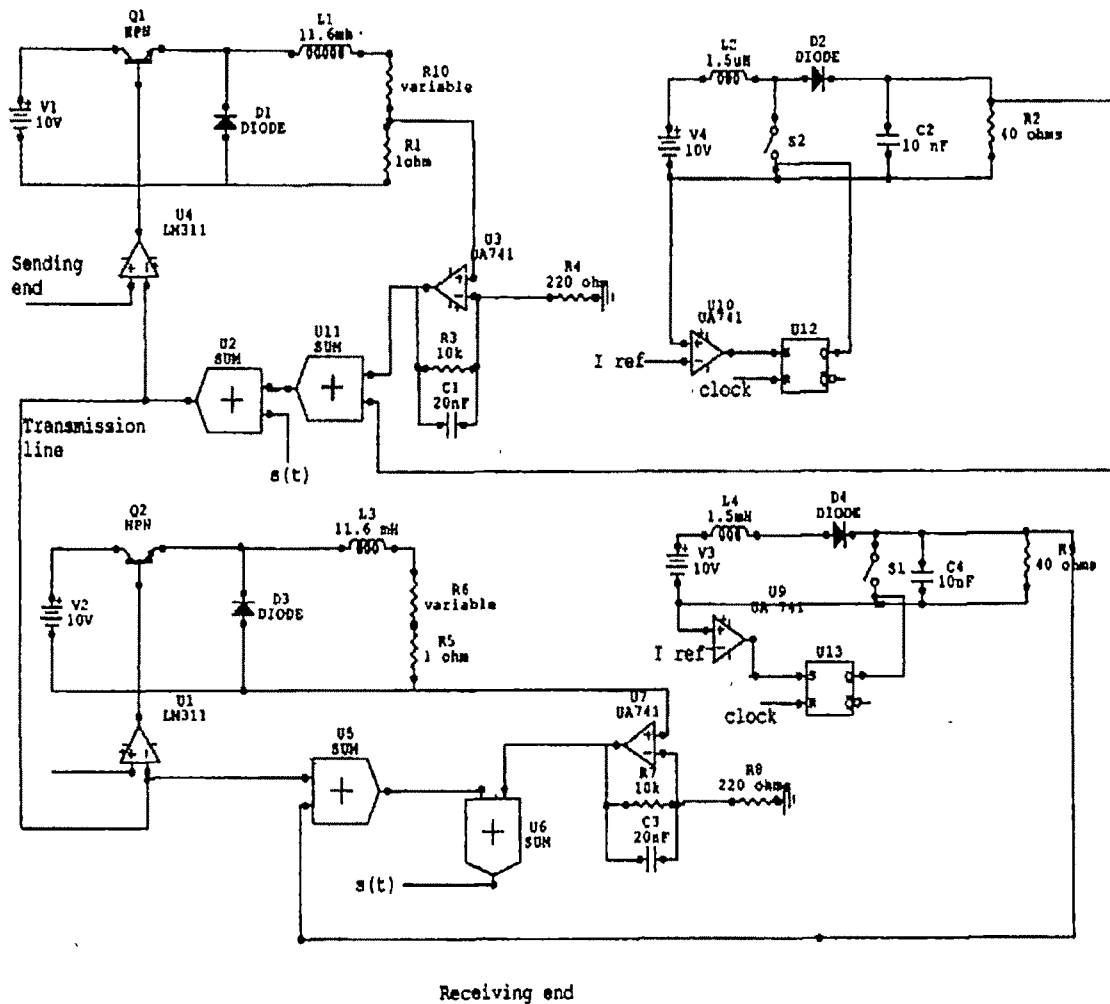


Fig.3 Secure communication Scheme

V. RESULT

The proposed scheme is verified experimentally for sinusoidal wave and triangular wave. The results are shown in figs. 4.1, 4.2, 4.3, and 4.4.

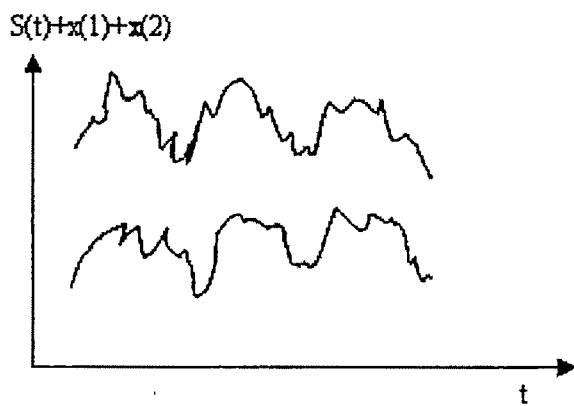


Fig. 4.1 Transmitted masked sine wave.

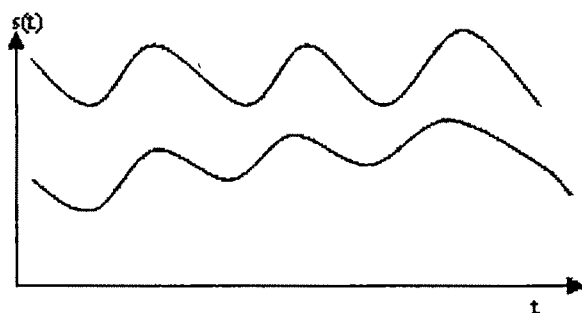


Fig 4.2 Received sine wave

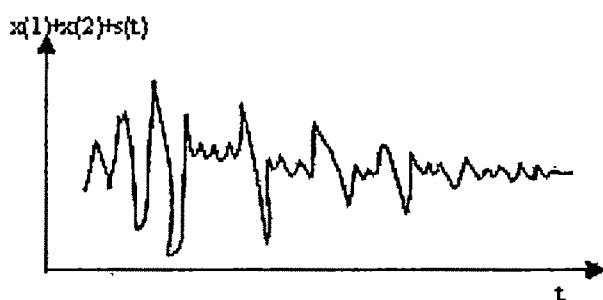


Fig. 4.3 Transmitted masked triangular wave

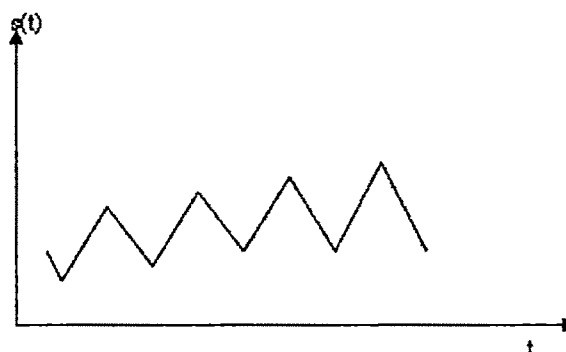


Fig. 4.4 Received triangular wave

VI. CONCLUSION

Earlier it was developed that message can be masked with chaos generated from one circuit i.e. from buck converter. In this investigation the chaotic signal is generated from two circuits i.e. actually more chaotic. So it is impossible to determine the chaotic signal for any person. Thus the communication is said to be "secure". This method of secure communication can be useful in power system, to send some confidential data or signal from one power station to another. Though many methods have been propounded to accomplish the above mentioned task but this method of masking the true signal with the chaotic signal has an edge above all the other methods because a very skilled hand is needed to break open the true signal from the chaotic signal. Separation of true signal can not be achieved by simple jugglery.

ACKNOWLEDGMENT

The authors are thankful to Prof A.K Mukhapadhyay, for his support to this work.

REFERENCES

- [1] L.M. Pecora and T.L. Carroll, Driving system with chaotic signals. Phys. Rev. A, (44):2374-2383, 1991
- [2] A.V. Oppenheim, G.W. Wormell, S.H. Labelle, and K.M. Cuomo Signal processing in the context of chaotic signals. In Proceeding ICASSP 92, 1992.
- [3] Kelvin. M Cuomo and Alan. V Oppenheim. Circuit implementation of synchronized chaos with application to communication. Physical Review Letters, 71(1):65-68, 1993.
- [4] K. Murali and M. Lakshamanan, Synchronizing chaos in driven chua's circuit. Int. journal of bifurcation and chaos, 3(4):1057-1066, 1993.
- [5] Ying Cheng Lai and Celso Grebogi. Synchronization of chaotic trajectories using control. Physical Review E, 47(4):2357-2360, 1993.
- [6] M. Murali and K. Lakshamanan Transmission of signal by synchronization in a chaotic Vander-Pol- Duffing oscillator. Physical Review E. 48(3) :1624-1626, 1993
- [7] Krishnendu Chakrabarty, Gautam Poddar and Soumitro Banerjee. Bifurcation behaviour of the buck converter. IEEE Transaction on Power Electronics, 11(3):439-447, 1996

A New Demodulation Scheme for AM Signals based on Sliding DFT

P.Sumathi¹, P.A.Janakiraman²

¹Electrical Engineering Department, Indian Institute of Technology Madras, Chennai. e-mail: sumichan04@yahoo.co.in.

²Electrical Engineering Department, Indian Institute of Technology Madras, Chennai. e-mail: pajraman@iitm.ac.in

Abstract—This paper presents a new demodulation scheme suitable for extracting the envelope from amplitude-modulated signals in an ultrasonic transmitter-receiver system. The DFT, FFT, Sliding DFT and Goertzel filters are some signal processing algorithms, which can be used for demodulation. In this paper the Sliding DFT based demodulation scheme is proposed, which exhibits smaller computational complexity. The Sliding DFT computes the N point DFT on time samples within a moving window of width N. The SDFT structure has comb filter cascaded with a digital resonator, which resonates at a chosen harmonic frequency. The z-domain SDFT transfer function has N number of zeros and one pole on the unit circle in z-plane. The angular location of the pole within the unit circle sets the resonant frequency. To present the detailed functioning of this demodulator, a carrier signal modulated by a low frequency sine wave with d.c. bias has been used. The demodulator in the receiver, located at the targeted distance is required to reconstruct the envelope, devoid of the d.c. signal. The received signal is to be amplified and rectified prior to demodulation. The Sliding DFT algorithm which is basically a tuned filter can extract the envelope from the rectified signal. In the simulation presented, the 128-point SDFT driven at a sampling frequency of 6.4kHz had been studied to extract a 50Hz envelope from a 40kHz ultrasonic signal. If necessary, the d.c. and the harmonics present in the envelope can also be extracted by additional SDFT blocks. Simulation and Experimental results are presented to show the performance of the SDFT based demodulator. The SDFT scheme was studied in the MATLAB-Simulink environment. Experimentation of the real time performance of the demodulation scheme was studied in a setup built around a Stratix-FPGA device.

Key words—Demodulation, Sliding DFT, AM Signals, SDFT based Demodulator.

I. INTRODUCTION

DIFFERENT techniques are available to extract the envelope from the amplitude modulated (AM) signal, with precision. Processing the Amplitude Modulated (AM) signals of ultrasonic transmitter-receiver systems has been particularly a very difficult task. Envelope detectors used for such AM signals usually consists of a bandpass filter followed by a nonlinear element and a low pass filter. A non-linear envelope detector, termed as the quadratic filter-demodulator,

for band-pass sampled AM signals has been reported, which requires the sampling frequency to be four times the carrier frequency [1]. Simple envelope detectors using a half wave rectifier and filter are used in radio receivers, but fail in some conditions like over modulation and non-sinusoidal envelope. At the worst case, when the message signal is a square wave, this envelope detector shows ripples and negative clipping. Another drawback of the envelope detector is that the input must be band-pass filtered around the desired signal frequency or else the detector will simultaneously detect several signals. It is also very susceptible to noise. Envelope detection can also be done by the squaring and low pass filtering method. The Hilbert transform procedure has been used in speech signal processing. A novel scheme for the transmission of blocks of digital data, based on the SDFT has been proposed for communicating in multi-path acoustic channels and the performance has been evaluated through computer simulation in [2]. The paper being presented, describes a new method for demodulating AM signals using the Sliding DFT algorithm. The Discrete Fourier Transform (DFT), Fast Fourier Transform (FFT), Sliding DFT (SDFT), Goertzel filtering are popular signal processing algorithms used for spectral analysis. The order of computational complexity differs for each algorithm and it is $O(N^2)$ for DFT, $O(N \log_2 N)$ for FFT, and $O(N)$ for SDFT[3]-[5]. Sliding DFT is computationally efficient and computational complexity is low. This paper is organized as follows. Section II describes the Sliding DFT algorithm. The proposed demodulation scheme is discussed in Section III. Numerically Controlled Oscillator (NCO) is described in Section IV. Simulation and Experimental results are presented in Section V and VI. The Conclusions are presented in Section VII.

II. SLIDING DFT

The Sliding DFT computes N point DFT on time samples within a sliding window of width N. The SDFT algorithm can be expressed as,

$$X_k(n) = [X_k(n-1) - x(n-N) + x(n)]e^{j2\pi k/N} \quad (1)$$

where $x(n)$ is input signal, X_k is DFT of $x(n)$, N is window width and k is bin index. The SDFT computes the N point

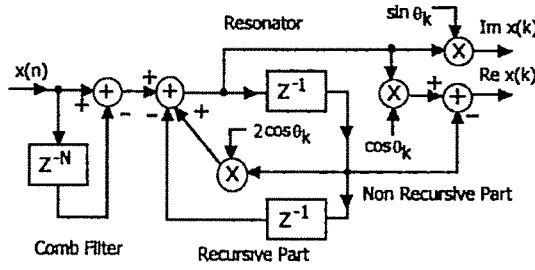


Fig.1 Sliding DFT Structure for the k^{th} bin

DFT for a single bin (k), centered at an angle $\theta_k = 2\pi k/N$ rad, on the unit circle, which also corresponds to the cyclic frequency ($k f_s / N$) Hz. The bin index k is $0 \leq k < N$ and f_s is the sampling frequency. The SDFT procedure is not self-starting. However, a FIFO stack of size N could be filled with phantom-data like zeroes and the DFT set to zero initially. The SDFT transfer function in the z domain,

$$H(z) = \frac{(1-z^{-N})(e^{j2\pi k/N})}{1-e^{j2\pi k/N}z^{-1}} \quad (2)$$

The SDFT transfer function can be split into real and imaginary parts, $\text{Re}[H(z)]$ and $\text{Im}[H(z)]$ and written as,

$$\text{Re}[H(z)] = \frac{(1-z^{-N})(\cos(2\pi k/N) - z^{-1})}{1-2\cos(2\pi k/N)z^{-1} + z^{-2}} \quad (3)$$

$$\text{Im}[H(z)] = \frac{(1-z^{-N})(\sin(2\pi k/N))}{1-2\cos(2\pi k/N)z^{-1} + z^{-2}} \quad (4)$$

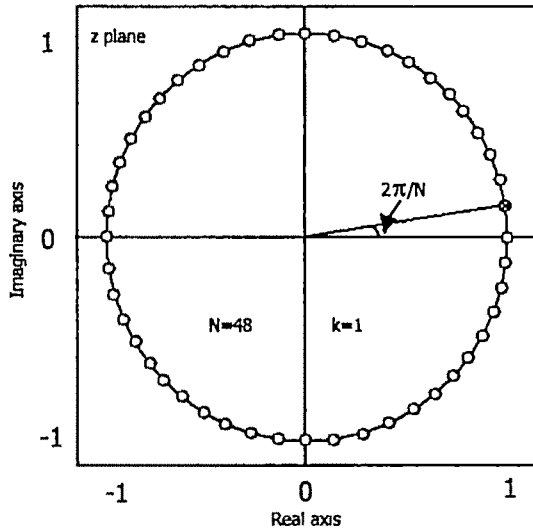


Fig. 2 Pole Zero map of Sliding DFT

The transfer function has N number of zeros and one complex pole. The SDFT structure is a cascade connection of comb filter and digital resonator. The comb filter has N delay elements. The digital resonator contains recursive and non recursive part. Fig.1 shows the Sliding DFT Structure for k^{th} bin. $\text{Re}[H(z)]$ and $\text{Im}[H(z)]$ generates the sine and its orthogonal signal, cosine signal respectively. Fig.2 shows the pole zero map of SDFT in z plane. For example, for the case N

$= 48$, the number of zeros lying on the unit circle is 48; and $k = 1$ shows the complex pole which cancels the zero at an angle of $2\pi/N$ rad. The comb filter delay of N samples forces the SDFT filter's transient response to be $N-1$ samples in length. It will reach steady state only after N samples. Bin index k sets the resonant frequency of the resonator. If $k = 1$, it resonates at the fundamental frequency present in the given input signal. In the z plane, the complex pole cancels the zero at that location thereby tuning to give only the fundamental frequency while rejecting all other frequencies present in the input. This property of SDFT has been used for designing a demodulator to extract the envelope from the AM signals.

III. DEMODULATION SCHEME

A sinusoidal carrier signal $A_c \sin(\omega_c t)$ is generated, where A_c is the amplitude of the carrier signal and ω_c is angular frequency of the carrier. The message signal which is to be transmitted is $A_m \sin(\omega_m t)$, where A_m the amplitude of modulating signal and ω_m is angular frequency of modulating signal. The transmitting signal can be written as,

$$V(t) = [1 + m A_m \sin(\omega_m t)] A_c \sin(\omega_c t) \quad (5)$$

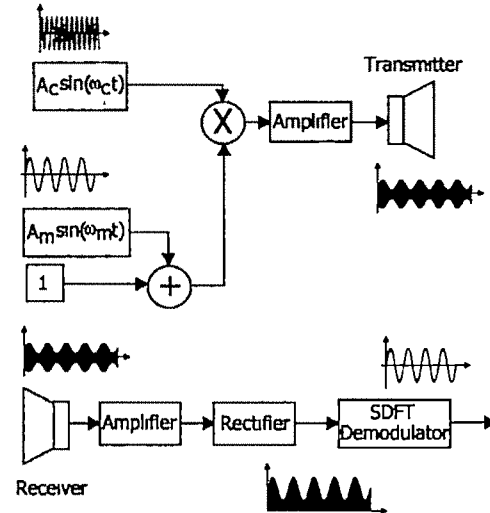


Fig. 3 The Proposed Demodulation Scheme based on SDFT

where m is the modulation index. The detected modulation signal is amplified, rectified and then passed as the input signal to SDFT block, bin-1, which is at the receiver. SDFT block bin-1 extracts the envelope from the AM signal. If we use another SDFT bin 0, for dc ($k = 0$), it can extract d.c. from the AM signal. Fig.3 shows the proposed demodulation scheme based on SDFT. In the case of over-modulation by a sine wave, (modulation index $m > 1$), the envelope gets distorted and its difficult to extract the sine wave using the envelope detector which is a rectifier followed by a low pass filter. However, the SDFT based demodulator can extract the sine-wave envelope from the over-modulated AM signal. At the worst case the

modulating signal may be a square wave, and the SDFT based demodulator can extract the fundamental corresponding to the square wave, from the square wave modulated input signal.

IV. NUMERICALLY CONTROLLED OSCILLATOR

The Numerically Controlled Oscillator (NCO) generates the sampling pulses required for driving the SDFT blocks. The control input to the NCO is α , where, $\alpha = \cos \psi$, $-1 < \alpha < 1$; $\psi = 2\pi f_s / f_{ena}$; f_s is the output pulse frequency of the NCO and f_{ena} is the fixed enabling frequency, 25.6kHz. For the condition, $\psi = \pi/2$, $\alpha = 0$. The enabling frequency $f_{ena} = 4 f_s$. The difference equation obeyed by the NCO is,

$$\begin{bmatrix} x_1(k+1) \\ x_2(k+1) \end{bmatrix} = \begin{bmatrix} \alpha & \alpha-1 \\ \alpha+1 & \alpha \end{bmatrix} \begin{bmatrix} x_1(k) \\ x_2(k) \end{bmatrix} \quad x_1(0) = 1; x_2(0) = 0; \quad (6)$$

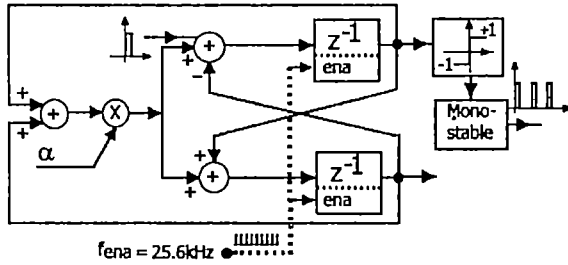


Fig. 4 Numerically Controlled Oscillator

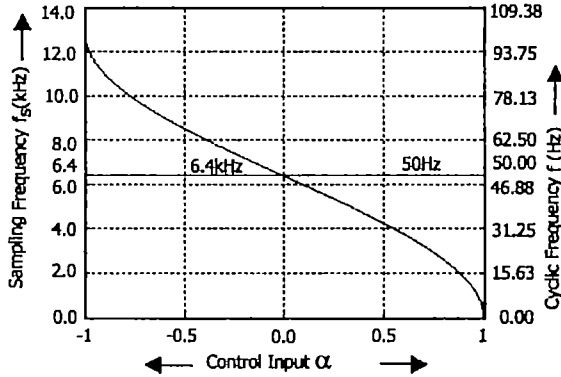


Fig. 5 Characteristics of NCO

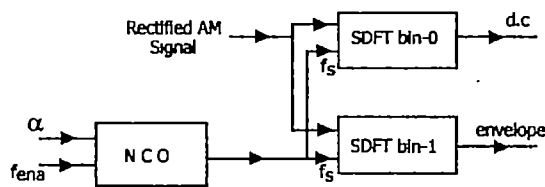


Fig. 6 Block diagram of SDFT Demodulator

The network diagram of numerically controlled oscillator [6] is shown in Fig.4. The I/O characteristic of the NCO is shown in Fig.5. For a 50Hz message signal and a window width $N = 128$, the frequency of the sampling pulses produced by the NCO is 6.4kHz, when it is enabled by 25.6 kHz clock. The maximum output frequency of the NCO is 12.8 kHz, which

corresponds to the absolute input signal-frequency limit of 100Hz. The NCO center frequency can be altered to suit the message signal range. Here NCO is designed to give out pulses corresponding to the center frequency of 50 Hz, $\alpha = 0$, so that the sampling pulse frequency is 6.4 kHz, corresponding to a perfect fit for a 50 Hz signal in a window of width 128. Fig.6 shows the block diagram of SDFT Demodulator. Both the SDFT bin-0 and bin-1, receive their sampling pulses from the same NCO, as shown in Fig.6.

V. SIMULATION RESULTS

A carrier signal of 40 kHz is generated and discretized with a sampling frequency of 256 kHz to avoid aliasing effects. A 50 Hz message signal is generated and discretized at 6.4 kHz. A d.c. bias is added to the message signal and is multiplied with carrier using a conventional multiplier. The received signal is rectified and passed to the SDFT block. This program was developed in DSP Builder MATLAB-Simulink environment. The SDFT bin-0 extracts the d.c. and the bin-1 the fundamental component of the envelope.

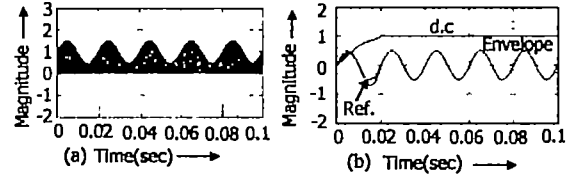


Fig. 7 (a) Rectified AM signal with $m < 1$. (b) Extracted d.c. and Envelope

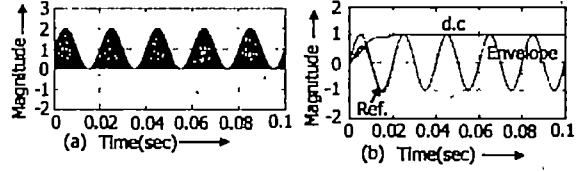


Fig. 8 (a) Rectified AM signal with $m = 1$. (b) Extracted d.c. and Envelope

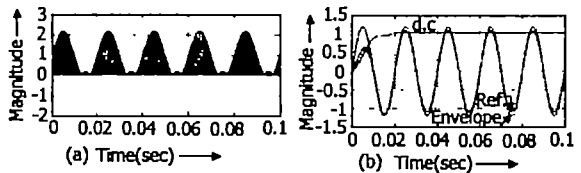


Fig. 9 (a) Rectified AM signal with $m > 1$. (b) Extracted d.c. and Envelope

Fig.7 (a) shows the rectified AM signal with modulation index $m < 1$. Fig.7 (b) shows the extracted d.c., envelope by the proposed SDFT demodulator. It can be seen from Fig.7 (b) that the SDFT Demodulator takes N samples or one complete cycle of the envelope to settle. Fig.8 (a) shows the AM signal with $m = 1$. The extracted d.c., envelope is shown in Fig. 8 (b). The settling time is about 0.02 sec. The AM signal with $m > 1$ is shown in Fig.9 (a). The extracted d.c. and envelope by the SDFT demodulator is shown in Fig.9 (b). It is seen that the proposed scheme works well for over-modulated signal with some magnitude error but the phase coincides with that of the reference signal. The proposed scheme works well for

the worst case of a square-wave message signal, shown in Fig.10 (a). The extracted d.c. and the fundamental corresponding to the square wave are shown in Fig.10 (b). The frequency response of SDFT filter is shown in Fig.11. The magnitude plot shows the rejection of all the frequencies present in the input except the fundamental component.

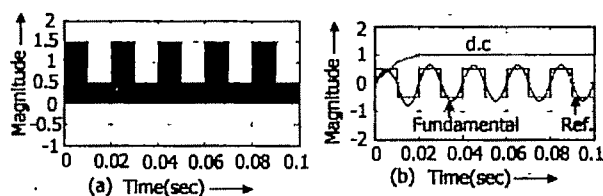


Fig. 10 (a) Rectified Square modulated signal
(b) Extracted d.c, Fundamental Component.

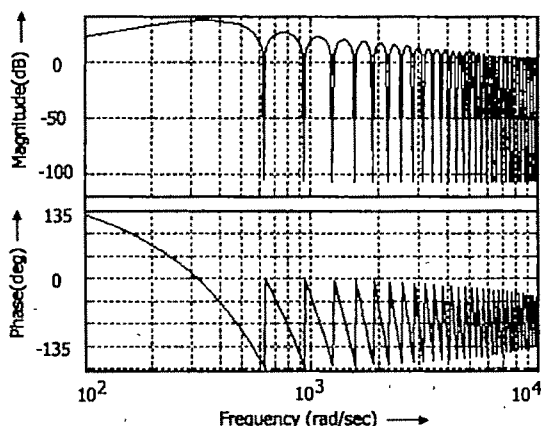


Fig. 11 Bode Plot of SDFT Block

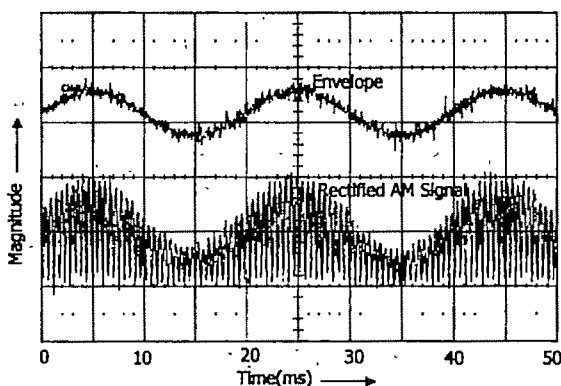


Fig. 12 Rectified AM signal and its Envelope

VI. EXPERIMENTAL RESULTS

A 40kHz-carrier signal was generated and modulated by a message signal of 50 Hz. The Sliding DFT bin-1 ($k=1$) has been designed with window width of $N = 128$, so that the 50Hz signal fits exactly into the window. Therefore, the sampling frequency has been chosen as 6.4 kHz, which is provided by the NCO. The programs were developed in DSP

builder MATLAB-Simulink environment [7]. The program was downloaded into the Stratix FPGA board, running at 80MHz-clock frequency. The rectified signal at the receiver and extracted envelope are shown in Fig.12. The SDFT hardware resource utilization is: five 21-bit gain blocks, two 2-input 20-bit adders, one 3-input 30-bit adder, two 30-bit delay elements, one 20-bit gain element and a 20-bit delay of depth 128.

VII. CONCLUSION

A new demodulation scheme based on SDFT has been proposed. Simulation and Experimental studies were conducted to evaluate the performance of proposed scheme for extracting the envelope of AM signals. The SDFT demodulator acts as a tuned filter for extracting the fundamental component, while rejecting all other harmonic frequencies present in the envelope of the AM signal. This scheme works well for the over-modulated and square wave modulated signals. The demodulation scheme is proposed to be used in extracting the envelope of AM signal in an ultrasonic range measurement system.

REFERENCES

- [1] K.G.Larkin, "Efficient demodulator for bandpass sampled AM signals," *IEE Electronics Letters*, vol. 32, No. 2, pp. 101-102, Jan. 1996.
- [2] Zlelinski and M.Caldera, "Digital acoustic communication in multipath underwater channels," *Oceans*, vol.17, pp.1296-1301, Nov. 1985
- [3] Eric Jacobsen and Richard Lyons, "The Sliding DFT," *IEEE Signal Processing Magazine*, vol.20, No. 2, pp. 74-80, Mar. 2003.
- [4] Eric Jacobsen and Richard Lyons, "An Update to Sliding DFT," *IEEE Signal Processing Magazine*, vol.21, No. 1, pp. 110-111, Jan. 2004.
- [5] Richard Lyons and Amy Bell, "The Swiss Army Knife of Digital Networks," *IEEE Signal Processing Magazine*, vol 21, no.3, pp. 90-100, May 2004.
- [6] Clay S. Turner, "Recursive Discrete-Time Sinusoidal Oscillators," *IEEE Signal Processing Magazine*, vol.20, No.3, pp-103-111, May 2003.
- [7] P.Sumathi and P.A.Janakiraman, "Integrated Phase Locking Scheme for SDFT based Harmonic Analysis of Periodic Signals," *IEEE Trans. on Integrated Circuits and Systems II (to appear)*

Demonstration of Highly Efficient Transmission in Sixty Degree Sharply Bend Waveguide Based on Photonic Crystal at 1.5 μm Wavelength

L. Dekkiche¹, and R. Naoum²

¹ 13, Rue Maarouf Larbi, Sidi Bel Abbes, ALGERIA, 22000 email : ldekkiche_dz@yahoo.com

² Departement of Electronics, Faculty of Engineering of Sidi-Bel-Abbes email : rafah.naoum@caramail.com

Abstract— Photonic crystal waveguides can be used to guide light around sharp bends with little or no loss of energy. This makes them possible candidates as components in optical integrated components which are thought to be the building blocks in future photonic applications. Traditional photonic waveguides are created by making line defects (W1) in the perfect periodic crystals and thereby creating paths in the structure to which the flow of light is confined.

We have investigated the properties of TM polarized light and optimized a 90° waveguide bends that is implemented in planar photonic crystal (PC) with triangular lattice symmetry. The in-plane guiding within the planar PC structures is based on a W1 defect waveguide. The most promising structure was simulated with a 2D-FDTD program (Finite Difference Time Domain), where we achieved transmission efficiency that peaks 100 %. Such propagation has not previously been experimentally confirmed.

Key words— Finite difference Time Domain (FDTD), periodic structures, photonic crystals, waveguide modes.

I. INTRODUCTION

PHOTONIC crystals have inspired great interest recently because of their potential ability to control the propagation of light. They can modify and even eliminate the density of electromagnetic (EM) states inside the crystal [1, 2]. Such periodic dielectric structures with complete band gaps can find many applications, including the fabrication of lossless dielectric mirrors and resonant cavities for optical light [3].

In this paper, we demonstrate a novel method for guiding light around sharp corners, using photonic crystal waveguides. This method is based on the one hand on the

modification in the geometry at the corner and the other hand on the use of the absorbing boundary conditions proposed by [4] which reduce reflection from PBG waveguide ends to under a few percent.

The FDTD method [5] has been widely used to study EM properties of arbitrary dielectric structures.

In this method, one simulates a space of theoretically infinite extent with a finite computational cell. To accomplish this, a number of boundary conditions such as Berenger's Perfectly Matched Layer (PML) [6], have been proposed that absorb outgoing waves at the computational cell boundaries. Applications of the FDTD method are to simulate photonic crystal waveguides, however, pose unique difficulties. While reflection from a PML boundary is minute for a traditional dielectric waveguide substantial reflection from the boundary is observed if a PBG waveguide is terminated so, on the order of 20% - 30% in amplitude [7]. Such reflection introduces unphysical reflected (parasite) pulses which may significantly compromise the accuracy of the simulated response. Reflected waves introduce interference and result in large errors in transmission measurements.

II. FINITE DIFFERENCE TIME DOMAIN METHOD (FDTD)

For a linear isotropic material in a source-free region, the time-dependent Maxwell's equations can be written in the following form:

$$\frac{\partial \mathbf{H}}{\partial t} = -\frac{1}{\mu(\mathbf{r})} \nabla \times \mathbf{E} \quad (1)$$

$$\frac{\partial \mathbf{E}}{\partial t} = \frac{1}{\epsilon(\mathbf{r})} \nabla \times \mathbf{H} - \frac{\sigma(\mathbf{r})}{\epsilon(\mathbf{r})} \mathbf{E} \quad (2)$$

Where $\epsilon(\mathbf{r})$, $\mu(\mathbf{r})$ and $\sigma(\mathbf{r})$ are the position dependent permittivity, permeability, and conductivity of the material, respectively. In the two dimensional case, the fields can be decoupled into two transversely polarized modes, namely, the E polarization and the H polarization. These equations can be discretized in space and time by a so-called Yee-cell technique [8]. The following FDTD time stepping formulas are spatial and time discretizations of equations (1) and (2) on a discrete two-dimensional mesh within the x-y coordinate system for the E polarization [9],

$$H_x|_{i,j+1/2}^{n+1/2} = H_x|_{i,j+1/2}^{n-1/2} - \frac{\Delta t}{\mu_{i,j+1/2}} \frac{E_z|_{i,j+1}^n - E_z|_{i,j}^n}{\Delta y} \quad (3)$$

$$H_y|_{i+1/2,j}^{n+1/2} = H_y|_{i+1/2,j}^{n-1/2} + \frac{\Delta t}{\mu_{i+1/2,j}} \frac{E_z|_{i+1,j}^n - E_z|_{i,j}^n}{\Delta x} \quad (4)$$

$$E_z|_{i,j}^{n+1} = \left(\frac{\epsilon_{i,j} - \sigma_{i,j} \Delta t / 2}{\epsilon_{i,j} + \sigma_{i,j} \Delta t / 2} \right) E_z|_{i,j}^n + \frac{\Delta t}{\epsilon_{i,j} + \sigma_{i,j} \Delta t / 2} \left(\frac{H_y|_{i+1/2,j}^{n+1/2} - H_y|_{i-1/2,j}^{n+1/2}}{\Delta x} - \frac{H_x|_{i,j+1/2}^{n+1/2} - H_x|_{i,j-1/2}^{n+1/2}}{\Delta y} \right) \quad (5)$$

Where the index n denotes the discrete time step, indices i and j denote the discretized grid point in the x-y plane respectively. Δt is the time increment, and Δx and Δy are the intervals between two neighboring grid points along the x and y directions, respectively. Similar equations for the H polarization can be easily obtained.

It can be easily see that for a fixed total number of times steps the computational time is proportional to the number of discretization points in the computation domain, i.e. the FDTD algorithm is of order N. The FDTD time-stepping formulas are stable numerically if the following conditions are satisfied [9].

$$\Delta t \leq \frac{1}{c \sqrt{\Delta x^{-2} + \Delta y^{-2}}} \quad (6)$$

Where c is the fastest speed of the light in all the materials involved in the simulation (In FDTD program, we always choose c be the speed of the light in vacuum). Thus, smaller Δt , this means even longer calculation time.

The number of total time steps should be chosen carefully, too. For pulse propagation, the total time steps should be larger enough, in order to allow the pulse passes the detectors. In particular, when the simulations involve cavities, the number should be sufficiently large.

III. BOUNDARY CONDITIONS

One approach to eliminate errors due to reflected pulses has been to increase the cell size such that the useful and the parasite pulses can be separated [7]. This approach, however significantly increases the computational cost in terms of memory and time. Special care must be taken to separate well the pulses since due to interference the error is proportional to the amplitude, and not to the power, of the reflected pulse. In addition, in the case of steady state simulations, or when a high-Q resonance is involved, it becomes impractical or even impossible to separate the reflected signal amplitude from the useful one. In the previous paper [4], Attila Mekis et al. demonstrate that it is possible to reduce the reflection amplitude from photonic crystal waveguide ends to a few percent by using a k-matched distributed Bragg reflector (DBR) waveguide. This provides a simple means to reduce the computational costs associated with simulating PBG waveguides. In our work, we use this concept of absorbing boundary conditions to obtain an efficient 90° bend structure based on triangular lattice.

IV. DESCRIPTION OF THE PROPOSAL STRUCTURE

The specific structure that we investigated is a 90° sharp bend formed by the intersection of two PC channel waveguides at 90° in an otherwise uniform photonic lattice. We assume a square (figure(1a)) and triangular (figure(2a)) lattices of air holes etched in a dielectric substrate, with refractive index $n = 3.24$, having filling factor of 39 %. Since we want to use this device around 1550 nm we calculate the lattice constant to be 430 nm and obtain therefore a hole radius of 141.9 nm, respectively. The structure is assumed to be bidimensional; i.e., the air holes are infinitely long, the 2DPC (two Dimensional Photonic Crystal) supports a photonic band gap in the region $0.203 < c/a < 0.35$ for TE (Transverse Electric) polarized light.

In the design process, we use 2DFDTD (two Dimensional Finite Difference Time Domain) simulation. This technique is powerful and versatile, and has been introduced and adapted to optical waveguide devices [10, 7]. In FDTD very small time step size must be used because both the carrier and the modulated envelope are included in the wave propagator.

V. RESULTS AND DISCUSSION

The cartography of the magnetic field H_z in the square geometry structure and the transmission and reflection spectra are shown in figure (1b) and (1c) respectively. We note that the transmission reached a value of only 40% (reflection 98%). The reason for this very poor transmission is twofold. First, a large fraction of the power is lost to radiation or reflected backward due to mode mismatch at the corner of the sharp bend. Moreover, the poor

transmission originates from modal mismatch at the junction. In fact, if the incoming mode has space to expand in the junction area, it excites a higher mode with odd parity that is either very lossy or cannot propagate in the output waveguide, so most of the incoming light is reflected and transmission is poor. Therefore, the excitation of modes with odd parity would act as a loss mechanism for the 90° sharp bend. Our conclusion is therefore as follows: the transmission through a junction depends strongly on the relationship between the modes of that may propagate in the PC waveguides and the modes of the junction are not compatible with those of the waveguide, transmission will be poor. The resulting cartography is a mixture of the stationary mode on the level of the bend and propagative wave (figure (1b)).

To improve matters, the obvious choice is to modify the junction region and the geometry lattice. By removing hole at the centre of the junction, we curve the sharp bend, thus eliminating multimode effects.

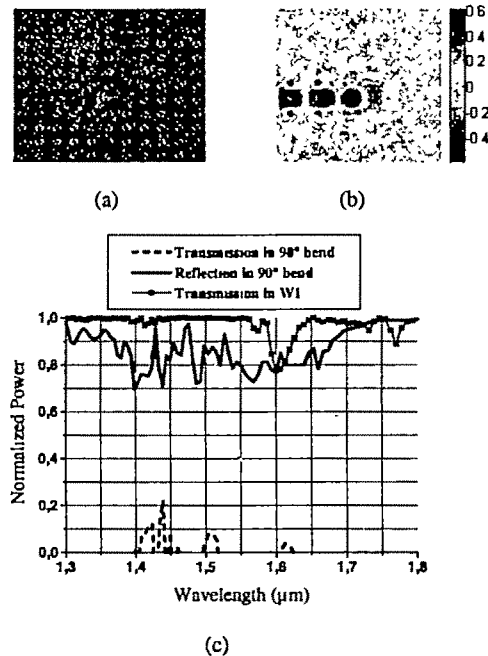


Fig.1. (a): 90° bend structure based on the "square lattice", (b): Magnetic Field amplitude distribution, (c): The transmission spectra.

Using the novel numerical scheme (figure(2a)) for the reduction of spurious reflections from photonic crystal waveguide ends and the reflections induces at the corner of the sharply bend, then clearly increase the bandwidth and power transmission, as directly observed in our, comparative, simulations of a 90° sharp bend in square lattice and triangular one. This solution has been compared to a several previous independent works.

For specific wavelengths we can achieve 100 percent transmission (figure (2c)) efficiency is that the photonic

crystal waveguide be single mode in the frequency range of interest and we see, also, in this figure that the curve of the transmission of the waveguide W1 and the one of the optimized 90° are identical. The figure (2b) shows clearly that the light is confined around the sharp bend, and it can be seen that the radiation has been vanished compared with figure (1b).

The mechanism that explains the good transmission behaviour of this sharply bends is that the factor of the triangular geometry has caused an important shift of the PBG (Photonic Band Gap) towards the big wavelengths compared with the square geometry. This phenomenon is due mainly by the fact that the triangular geometry does not let pass the electromagnetic wave on the one hand, and on the other hand, it has a prohibited frequency bands whatever the polarization of the light. The frequency bands are numerous for the two polarizations TE and TM. Their width reaches the maximum when the diameter of the holes is nearly equal to the distance between two close holes.

Lattice geometry, especially the symmetry of the lattice is a very important factor to determine the band gap. Detailed study needs group theory [11]. The choice of lattice geometry is determined by other factors: the band gap requirement (polarization, band gap width), available material, the difficulty of fabrication, etc. As a general rule, if the first Brillouin zone is close to a circle; then the structure is easier to produce a complete band gap.

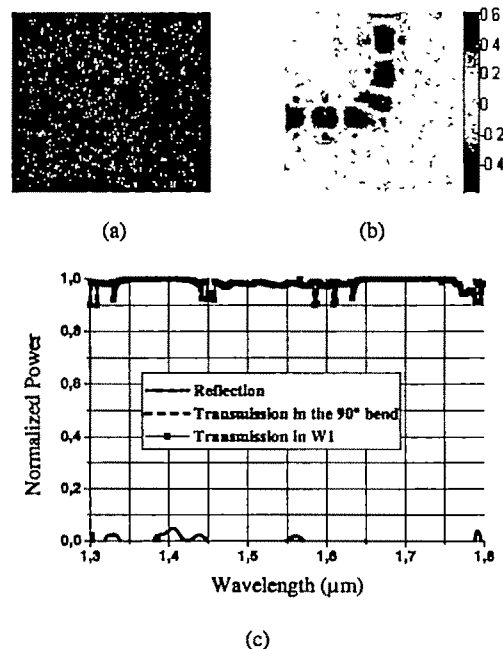


Fig.2. (a): 90° bend structure based on the "triangular lattice", (b): Magnetic Field amplitude distribution, (c): The transmission spectra.

VI. CONCLUSION

While performing a simple sensitivity analysis based on FDTD code, we have obtained an efficient method for improving the frequency response of 2DPC devices. In particular we have applied this technique to a simple 90° sharp bend waveguide emerging from an underlying 2DPC with square lattice symmetry. A single optimization step has already obtained nearly zero reflection over almost the entire PBG. This technique can easily be extended to other 2DPC properties for optimization purposes, because key problem in the design of future integrated optical devices is how to balance ease of fabrication with the reduction of radiation losses.

In conclusion, the triangular lattices photonic crystals are the best candidates and are more suited to realize components in optical integrated with accuracy than the other one. So the large and complete band gap which appears in this kind of lattices leads to the perfect confinement of light in photonic crystal waveguides bends, which can dramatically increase the percentage of transmission that are required for the efficient performance of optical integrated circuits.

REFERENCES

- [1] E. Yablonovich, "Inhibited spontaneous emission in solid state physics and electronics", *Phys. Rev. Lett.* vol. 58, pp. 2059-2062, 1987.
- [2] S. John, "Strong localization of photons in certain disordered dielectric superlattices", *Phys. Rev. Lett.* vol. 58, pp. 2486-2489 1987.
- [3] J. D. Joannopoulos, R. D. Meade, and J. N. Winn, "Photonic Crystals", Princeton Univ. Press, Princeton New-York, 1995.
- [4] A. Mekis, S. Fan, and J. D. Joannopoulos, "Absorbing Boundary Conditions for FDTD Simulations of Photonic Crystal Waveguides". *IEEE microwave and guided wave letters*, vol. 9, no. 12, 1999.
- [5] K. S. Kunz, R. J. Luebbers, "The finite difference time domain method for electromagnetic", Boca Raton, FL: CRC Press, 1993.
- [6] J. P. Berenger, "A perfectly matched layer for the absorption of electromagnetic waves", *J. Computational Physics*, vol. 114, no.2, pp.185-200, 1994.
- [7] A. Mekis, J. C. Chen, I. Kurland, S. Fan, P. R. Villeneuve, and J. D. Joannopoulos, "High transmission through sharp bends in photonic crystal waveguides", *Phys. Rev. Lett.* Vol. 77, pp. 3787-3790, October 1996.
- [8] K. S. Yee, "Numerical solution of initial boundary value problems in isotropic media", *IEEE Trans. Antennas Propagat.* vol. 14, pp.302, 1966.
- [9] M. Qiu, S. He, "Numerical method for computing defect modes in two dimensional photonic crystals with dielectric or metallic inclusions", *Physical Review B*, Vol. 61, No. 19, 15 May 2000.
- [10] Masanori Koshiba, Yasuhide Tsuji and Masafumi Hikari, "Time-Domain Beam Propagation Method and Its Application to Photonic Crystal Circuits", *Journal of Lightwave Technology*, Vol. 18, no.1, January 2000.
- [11] K. Sakoda, "Optical transmittance of a two-dimensional triangular photonic lattice", *Phys. Rev. B*, vol. 51, pp.4672, 1995.

Effect of Demodulator Filter Roll-off Factor on the Quality of QPSK Modulated Mobile Communication System

S.Chattopadhyay and S.K.Sanyal

Department of Electronics and Telecommunication Engineering, Jadavpur University, Kolkata, India
e-mail: sudiptachatt@yahoo.com, e-mail: s_sanyal@ieee.org

Abstract—Quadrature Phase Shift Keying (QPSK) serves as a useful digital modulation technique in various mobile communication systems. The quality of modulation is one of the important factors to govern the performance of the mobile system. In this paper, we have presented the study of different parameters of QPSK modulation, for various roll-off factors of the demodulation filter using Vector Signal Generator, Spectrum Analyzer and Vector Signal Analyzer software.

Key words—CDMA, Eye pattern, Error Vector Magnitude (EVM), Inter Symbol Interference (ISI).

I. INTRODUCTION

QPSK and its different modifications like offset QPSK (O-QPSK), $\pi/4$ -QPSK Differential QPSK (DQPSK), $\pi/4$ -DQPSK etc. serve as useful modulation techniques for IS-95 CDMA, CDMA-2000 and W-CDMA mobile communication system. In-phase and Quadrature (IQ) and QPSK modulations are two important aspects of digital communications because they can perform multi-format modulations [1]. When a modulation technique is used in a mobile communication, the performance of the system depends on the modulation quality of the particular modulation scheme employed.

To assess the modulation quality of a digital modulation technique, we need to study various parameters related to it. Again in a digital transmission system, selection of a proper digital demodulation filter, with a proper value of roll-off factor α is important since it limits bandwidth and reduce Inter Symbol Interference (ISI).

In this paper we have measured different parameters such as, Error Vector Magnitude (EVM), Magnitude Error, Phase Error and Signal to Noise Ratio (SNR) for different values of demodulator filter roll-off factor (α) and shown the variation of each of them with demodulator filter α . Constellation, I-Q and Eye diagram have also been recorded for various values

of demodulator filter α .

II. QPSK MODULATION AND ITS DIFFERENT PERFORMANCE PARAMETERS

A. IQ Modulation and QPSK

In most communication systems, the transmitted signal can in general be represented by

$$s(t) = \sqrt{P} \{ I(t) \cos \omega_c t - Q(t) \sin \omega_c t \} \quad (1)$$

Where P represents the transmitted signal power, $I(t)$ and $Q(t)$ the in-phase and quadrature baseband data modulations, and ω_c the carrier frequency. The $\cos \omega_c t$ term is typically referred to as the in-phase (I) carrier and the $\sin \omega_c t$ as the quadrature (Q) carrier. Antipodal signals are constructed by setting $Q(t) = 0$ and $I(t) = \pm p_I(t)$ for $0 \leq t \leq T$. Alternatively, $I(t)$ can be written as

$$I(t) = \sum_{k=-\infty}^{\infty} a_k p_I(t - kT) \quad (2)$$

Where $a_k = \pm 1$ representing the binary random data and $p_I(t)$ is the base-band in-phase pulse of duration T seconds [2].

In case of QPSK, $I(t) = \pm p_I(t)$ and $Q(t) = \pm p_I(t)$ for $kT \leq t \leq (k+1)T$, independent of each other. Alternatively, QPSK can be represented by (1) with $I(t)$ given by (2) and

$$Q(t) = \sum_{k=-\infty}^{\infty} b_k p_I(t + kT) \quad (3)$$

Where $b_k = \pm 1$ representing an independent binary data stream. For $kT \leq t \leq (k+1)T$, $s(t)$ can be written as

$$s(t) = \sqrt{2P} \cos(\omega_c t + \theta_k) \quad (4)$$

Where $\theta_k = \tan^{-1}(b_k/a_k) = \pi/4, 3\pi/4, 5\pi/4, 7\pi/4$, radians [2]. This is indicated by geometrical representation of QPSK as shown in fig. 1.

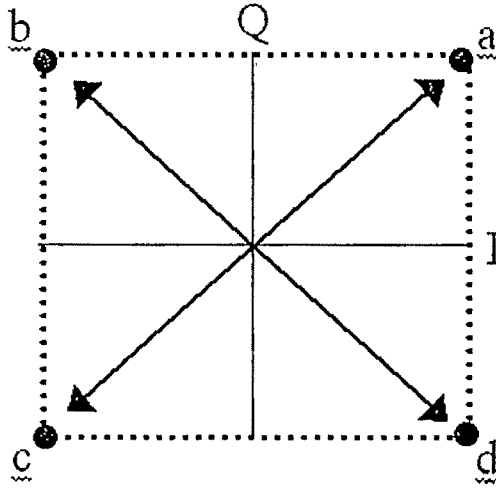


Fig.1: Signal Space Representation of QPSK Signals

In Fig.1, the points in signal space corresponding to each of the four possible transmitted signals are indicated by four 'dots' designated by 'a', 'b', 'c' & 'd'. They correspond to $\pi/4$, $3\pi/4$, $5\pi/4$ and $7\pi/4$ radians of phase angle respectively [3].

B. Band-limited digital transmission and Inter Symbol Interference (ISI)

In digital transmission, when rectangular pulses are passed through a band limited channel, the pulses will spread in time, and the pulse for each symbol will smear into the time intervals of succeeding symbols. This causes Inter Symbol Interference (ISI) and leads to an increased probability of the receiver making an error in detecting a symbol. One obvious way to minimize ISI is to increase the channel bandwidth [4]. In contrast, mobile communication systems operate with minimal bandwidth and need to transmit a greater number of bits per second in a given bandwidth to make the system, bandwidth efficient or spectrally efficient.

Nyquist derived the minimum channel bandwidth requirement for digital transmission. Nyquist's minimum-bandwidth theorem states that if synchronous impulses, having a transmission rate of f_s symbols per second, are applied to an ideal, linear-phase brick-wall low pass channel having a cut-off frequency of $f_N = f_s/2$ Hz, then the responses to these impulses can be observed independently, that is, without ISI [5].

The ideal minimum bandwidth Nyquist channels are not realizable. So to define more practical channel characteristics, Nyquist introduced a theorem on vestigial symmetry in which he added a skew-symmetrical, real-valued transmittance function $Y(\omega)$ to the transmittance of the ideal low-pass filter to maintain the zero-axis crossings of the impulse response. These zero-axis crossings provide the necessary condition for ISI-free transmission [5].

Raised Cosine and Root Raised Cosine filters satisfy the vestigial theorem and thus offer a practical channel with ISI-free transmission [5]. The amplitude response of Raised Cosine filter is given by

$$|H(j\omega)| = \begin{cases} 1 & 0 \leq \omega \leq \frac{\pi}{T_s}(1-\alpha) \\ \cos^2 \left\{ \frac{T_s}{4\alpha} \left[\omega - \frac{\pi(1-\alpha)}{T_s} \right] \right\} & \frac{\pi}{T_s}(1-\alpha) \leq \omega \leq \frac{\pi}{T_s}(1+\alpha) \\ 0 & \omega > \frac{\pi}{T_s}(1+\alpha) \end{cases} \quad (5)$$

Where $\omega = 2\pi f$ and α is the channel roll-off factor. In equation (5) if we replace the term

$$\cos^2 \left\{ \frac{T_s}{4\alpha} \left[\omega - \frac{\pi(1-\alpha)}{T_s} \right] \right\}$$

by its square root, we get the amplitude response of Root Raised Cosine Filter.

Roll-off factor (α) of a filter has an important effect on ISI. For $\alpha = 0$, an unrealizable minimum-bandwidth filter having a bandwidth equal to $f_N = 1/2T_s$ is obtained. For $\alpha = 0.5$, a 50% excess bandwidth is used, whereas for $\alpha = 1$, the transmission bandwidth is twice the theoretical minimum bandwidth [6]. It is obvious that high value of roll-off factor (α) will reduce the effect of ISI. But for a fixed data rate, use of more bandwidth will reduce the bandwidth efficiency and hence the spectral efficiency. So selecting a suitable filter with proper roll-off factor (α) is necessary for efficient digital transmission.

Eye diagrams or eye patterns are frequently used in the evaluation of channel and signal imperfections. Thus Eye patterns could be used as a measure of ISI. As the effect of ISI increases, the Eye opening reduces.

III. MEASUREMENT OF DIFFERENT PARAMETERS OF QPSK MODULATION

In this paper we have presented the study of different parameters of QPSK modulation, which governs the modulation quality of the system. To achieve this, we have used Agilent E4438C 250KHz-3GHz ESG Vector Signal Generator, Agilent E4405B 9KHz-13.2GHz ESA-E series Spectrum Analyzer, together with Agilent 89600 Vector Signal Analyzer (VSA) version 5.30 software.

To generate the QPSK modulated signal, we have selected following parameters in Vector Signal Generator: pn-sequence of length 63 with symbol rate 25 Ksps as the base-band signal, Root Nyquist filter as the pulse shaping transmitter filter with α value of 0.2 and 10MHz frequency with 0dBm amplitude as carrier.

For digital demodulation, we have used Agilent E4405B 9KHz-13.2GHz ESA-E series Spectrum Analyzer, together with Agilent 89600 Vector Signal Analyzer (VSA) software, where Raised Cosine and Root Raised Cosine filters have been selected as Reference filter & Measurement filter respectively in VSA software.

We have measured different performance parameters such as, EVM, Magnitude error, Phase error and Signal to Noise Ratio (SNR) with the variation of demodulator filter alpha (α), keeping the transmitter filter alpha at a fixed value of 0.2. Constellation, I-Q and Eye diagram have also been recorded for various values of demodulator filter alpha. The whole measurement has been repeated for another two fixed values of transmitter filter alpha as 0.35 and 0.5.

IV. MEASUREMENT RESULTS

Variation of EVM, Magnitude error, phase error and SNR with demodulator filter alpha are shown in Fig.2, Fig.3, Fig.4 and Fig.5 respectively. In each Fig., curve-I is plotted for transmitter filter alpha of 0.2, whereas curve-II and curve-III correspond to curves for transmitter filter alpha of 0.35 & 0.5 respectively.

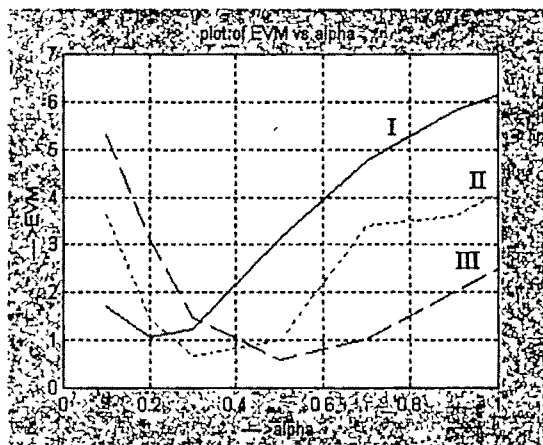


Fig.2: Variation of EVM with demodulator filter alpha.

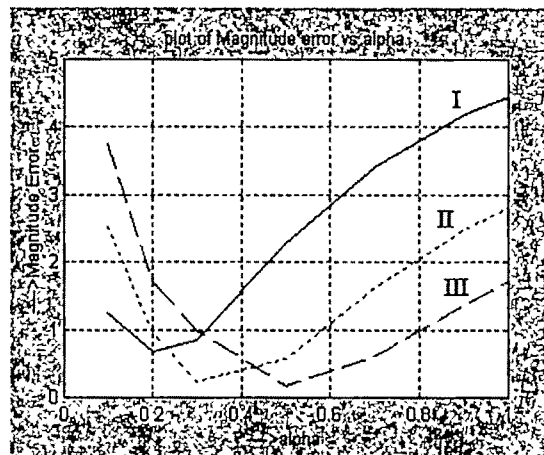


Fig.3: Variation of Magnitude Error with demodulator filter alpha.

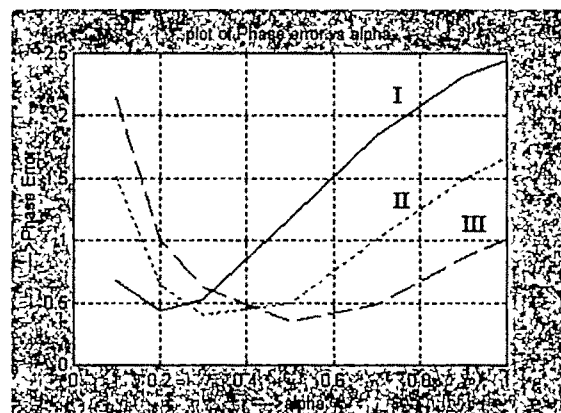


Fig.4: Variation of Phase Error with demodulator filter alpha.

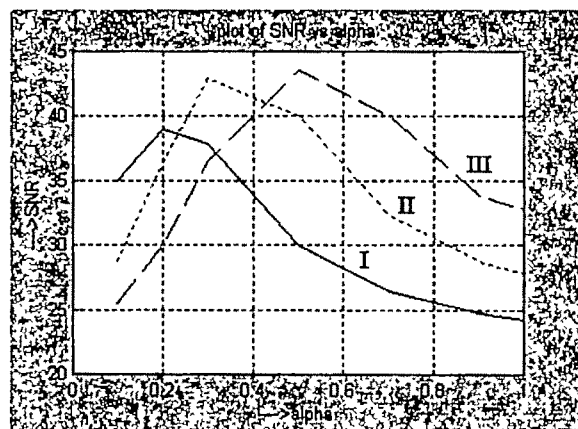


Fig.5: Variation of SNR with demodulator filter alpha.

Fig. 2, Fig.3 and Fig.4 show that minimum values of EVM, Magnitude Error and Phase Error occur for the values of demodulator filter alpha of 0.2, 0.35, and 0.5 for curve-I, curve-II and curve-III respectively, as it is expected theoretically. In Fig.5, we get maximum value of SNR for the value of demodulator filter alpha of 0.2, 0.35, and 0.5 for curve-I, curve-II and curve-III respectively. These figures also guide us to select a suitable demodulator filter with a proper value of alpha, which require minimum values of EVM, Magnitude Error, Phase Error and maximum value of SNR for better digital transmission.

Fig.6, Fig.7 and Fig.8 show the I-Eye diagrams for demodulator filter alpha of 0.2, 0.5 and 0.9 respectively for transmitter alpha of 0.35. Fig.9, Fig.10 and Fig.11 show the I-Q diagrams for the same.

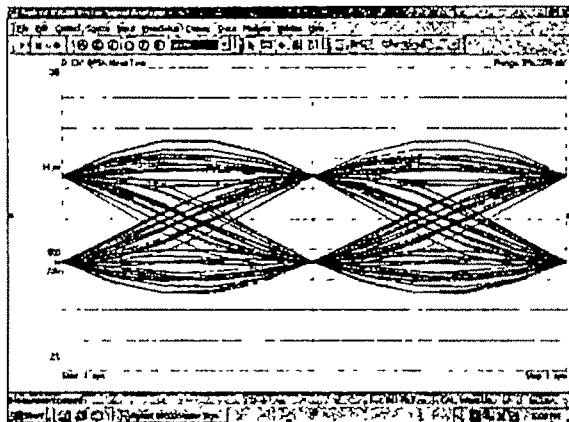


Fig.6: I-Eye diagram for demodulator filter alpha of 0.2

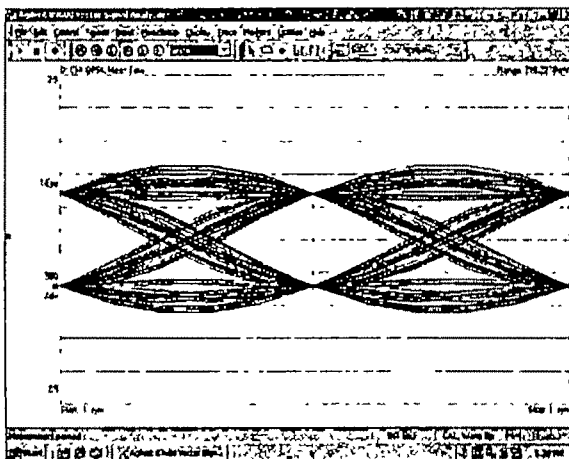


Fig.7: I-Eye diagram for demodulator filter alpha of 0.5

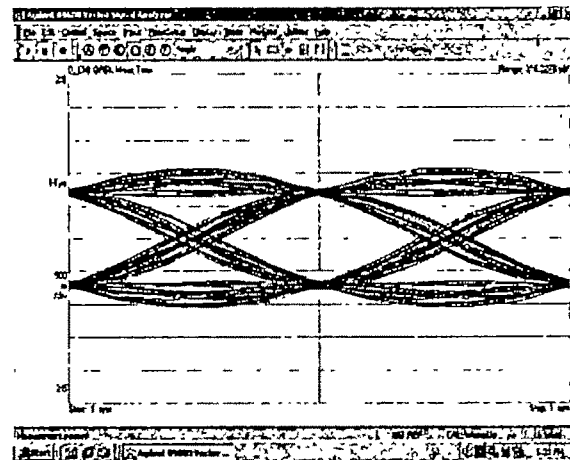


Fig.8: I-Eye diagram for demodulator filter alpha of 0.9

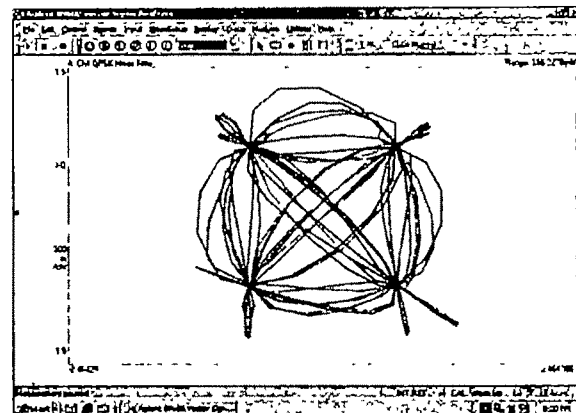


Fig.9: I-Q diagram for demodulator filter alpha of 0.2

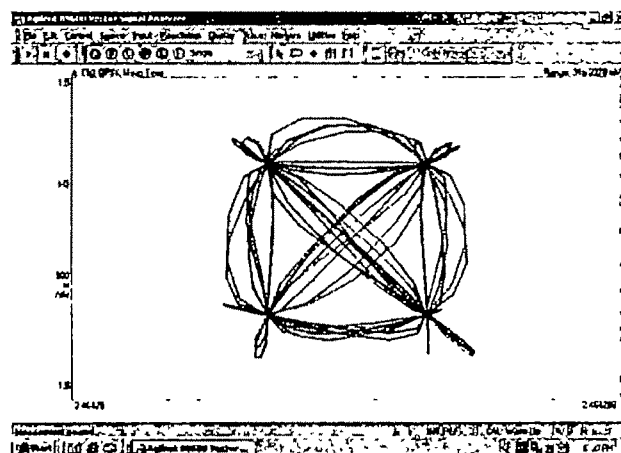


Fig.10: I-Q diagram for demodulator filter alpha of 0.5

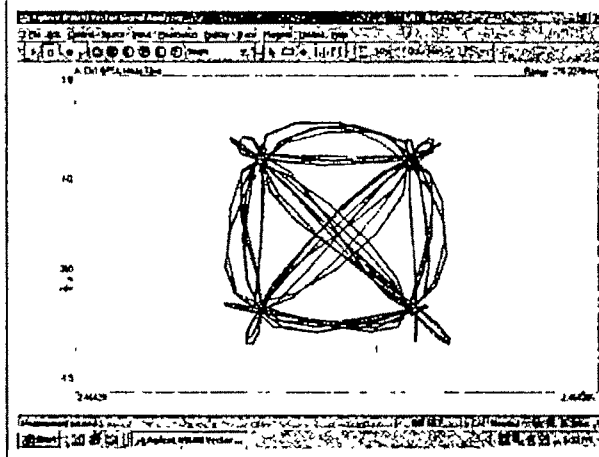


Fig.11: I-Q diagram for demodulator filter alpha of 0.9

Fig.6, Fig.7 and Fig.8 show the effect of demodulator filter alpha on I-Eye diagrams. They show that as demodulator filter alpha increases, eye patterns become better and effect of ISI reduces. The results of Fig.9, Fig.10 and Fig.11 show that as demodulator filter alpha is increased, there are smaller overshoots in the trajectories between the symbol points. This limits the required peak power and reduces the transmitter power requirement

V. CONCLUSION

This paper provides the detailed study of different performance parameters like, EVM, Magnitude Error, Phase Error, SNR, Eye diagram and I-Q diagram. All these parameters can be treated as the useful performance criteria to govern the modulation quality of QPSK transmission. This study can also be used as a powerful tool for the performance analysis of a mobile system in which QPSK modulation is used.

Our work can also be extended in future to study the effect of transmitter pulse shaping filter roll-off factor on the quality of QPSK modulated mobile communication system. Study on different types of transmitter pulse shaping filter would help us to select a proper transmitter filter with a proper value of roll-off factor for effective digital transmission in mobile communication system.

ACKNOWLEDGMENT

The authors wish to place on record their sincere thanks and gratitude to the authorities of Centre for Mobile Computing & Communications, Jadavpur University, Kolkata-700 032, India for providing the necessary facilities to carry out this work through the UGC-Scheme University with the Potential

for Excellence.

REFERENCES

- [1] H-Yeh Chang, T-Wei Huang, H. Wang, Y-Chi Wang, P-Chane Chao and C-Hsu Chen, "Broad-Band HBT BPSK and IQ Modulator MMICs and Millimeter-Wave Vector Signal Characterization", *IEEE Transactions on Microwave Theory and Techniques*, vol. 52, No. 3, March 2004, pp. 908, 914-917.
- [2] M.K. Simon, S.M. Hinedi and W.C. Lindsey, "Digital Communication Techniques: Signal Design and Detection", Prentice-Hall of India, New Delhi - 110 001, 1999, pp. 261-262.
- [3] Taub & Schilling, "Principles of Communications systems", 2nd ed., McGraw-Hill International Editions, 1987, pp. 266-267.
- [4] T.S. Rappaport, "Wireless communications: Principles and Practice", 2nd ed., Prentice-Hall of India, New Delhi - 110 001, 2004, pp. 282.
- [5] Dr. K. Feher, "Wireless Digital Communications: Modulation & Spread Spectrum Applications", Prentice-Hall of India, New Delhi - 110 001, 2005, pp. 117-127.
- [6] B.P. Lathi, "Modern Digital and Analog Communication Systems", 3rd Ed., Oxford University Press, 198 Madison Avenue, New York - 10016, 2004, pp. 314-315

Invited Speeches

The Role of Measurement Automation on Accident Prevention and Industrial Safety

T. K. Mitra

Department of Applied Physics, University of Calcutta, Kolkata, India

Abstract— Industrial safety and safety engineering have assumed a very significant role now a days. In the early days of safety engineering it is used as a means of protection against any failure or breakdown of electrical apparatus and systems. So it is used as a tool against accident prevention. The primary task of safety is to perform measurement of a process parameter using suitable sensor. The measured parameter is now compared against set points or a limited range of high and low parameters. Called limit check when unsafe condition is detected the audiovisual alarm is activated. The accident prevention has a great role in saving human life and costly apparatus and also has a great role for better environment. The selection of parameter and its continuous measurement and monitoring is a vital key of success for safety engineering. In the present paper some aspects of intelligent sensors and safety interlocks for better safety have been discussed.

I. INTRODUCTION

THE task of measurement is parameter estimation. The measurement can be carried out by direct method or by indirect method of comparison of the unknown specimen against a known reference standard. The indirect method is widely accepted as a better method with more reliability and accuracy. The output signal from the indirect method of measurement is now made computer compatible through interface and signal conditioning circuit. The control program in the computer will perform the task of measurement. The hardware as well as inclusion of SCADA features in the software will offer considerable flexibility in the configuration of the system. The inclusion of signal processing algorithms has added new dimensions in measurement using intelligent sensors. The transformation of classical measurement into intelligent measurement took many years from conception of ideas upto implementation of the system. The modifications, changes and perfections are going on so that a better working platform is developed. The system has many applications in the safety engineering aspect, which can be considered as a very useful tool to offer a better environment. Some useful application examples are discussed in the following sections.

II. APPLICATION EXAMPLES

One group of safety circuits operates only when there is a breakdown or unsafe condition in the circuit or in the process. For this purpose some safety parameters are chosen or selected which are continuously monitored by the computerized measurement system. The selected parameter may be over current or undercurrent, over voltage or under voltage overheating and / or earth leakage current etc. As an illustrative example temperature monitoring system for safety applications is further discussed. The sensor selected is thermocouple. The sensor is connected to the computer through interface and signal conditioning circuit. The circuit will also have provision for cold junction compensation for ambient temperature. The above system can use temperature and temperature gradient as safety parameters for overheating protection. This system has excellent dynamic characteristics but have poor response in the starting characteristics. The zero millivolt is a valid signal from the thermocouple. Again repeated heating and cooling of the thermocouple may result in broken thermocouple leads. In the event of broken lead the thermocouple output will also be zero millivolt. This is definitely a false signal. A d.c. biasing circuit through the thermocouple is created as a silent watchdog. In the event of broken lead a large bias voltage is automatically transferred to the computer, which will trigger the safety Interlock.

Apart from relay as a sensing device for safety applications interlock circuits also play a very significant role in safety engineering. The interlock circuits have an excellent application in railway signal engineering. Train movements in the station section is protected by safety interlocks. The track occupation by a train is detected by track relay. The railway signal cannot give clear aspect yellow, double yellow or green aspect unless concerned track relays are clear, the points are set and locked, the routes are set and locked. These interlocks ensure safety in train movements not only in the station section but also in the block section. The interlock circuits prevent any unsafe condition of operation where as relays and protection system respond only after a breakdown has taken place and shut down the system to prevent accident.

Another vital area of safety engineering is condition monitoring and diagnostic engineering. The vibration sensors will measure the vibration parameters, viz, acceleration, velocity and displacement of vibration. The time plane as well as frequency plane response are used to detect any deviation of the vibration characteristics from the normalcy. These characteristics play a very significant role in making advance prediction about any forthcoming failure. This branch of safety engineering has also been used as a very vital tool for accident prevention. Sometimes the advance warning about a forthcoming failure gives the opportunity to reschedule the load before the actual shutdown of the machine. Hence user inconvenience may also be minimized.

The relay engineering also has gone through a revolution. The signal processing capability has resulted in calculable relays or intelligent relays. The computer can now take decision based on calculating the performance equation on the real time data or the processed data. In addition back up protection is also sometimes added to act like a second line of defence in case the primary relay fails. This is more expensive and shut down is over more wide area. In biomedical engineering there had been occasions a remote earth fault can produce unsafe conditions for a patient undergoing routine test and measurement in case the measuring instruments are not properly grounded.

III. DISCUSSIONS

Originally role of safety engineering is in between occurrence of breakdown and prevention of accident. The primary task is parameter selection and continuous estimation of the parameter for safety check. Due to addition of computer entire dimension of measurement engineering has changed, as typical application example rise in temperature as well as rate of rise of temperature are very useful parameters for overheating protection. The decision-making job may do by set point or limit check. Similarly vibration parameters are used for advance detection of failure in the rotating machines. Or warning of approaching trains at unmanned level crossing gates. A patient undergoing bio-electric signal recording may be exposed to shock hazard due to a remote earth fault provided the recording and bio-medical instruments are not properly grounded. Similarly in addition to step changes in voltage the change of voltage gradient may be used for better safety against track occupation by a train.

IV. CONCLUSIONS

The IS 18000 group has given us the guidelines of occupational health and safety management systems. The previous concept was allow a breakdown to take place and the relay interlocking will intervene and prevent accident. The better approach will be identify the hazard, assess the risk and

control the risk. The computerized measurement and signal processing is one of the very effective platforms or tools which can identify parameters, monitor the parameters and generate advance predictions about any forthcoming failures. This form of condition monitoring can ensure better standards of industrial safety.

ACKNOWLEDGEMENTS

The present work is part of application on computer application development system created from projects sponsored by AICTE / MHRD.

REFERENCES

- [1] T. K. Mitra - *Role of Measurement in improvement of quality*; 13th World Congress on Total Quality, pp 140 - 142, Institute of Directors, February 14 - 16, Mumbai 2003, India.
- [2] N. P. Kolev, S. T. Yordanova P. M. Tzvetkov - *Computerised Investigation of Robust Measurement System*; IEEE Trans. on Instrumentation and Measurement, vol 51, No 2, pp 207 - 210, April 2002.
- [3] A. Purushotham and G. Thimuna Reddy - *Automated monitoring manufacturing process for on-line quality control*; International Conference on quality engineering and Management, pp 130 - 132, August 4 - 6, 1997 Coimbatore India, Allied Publishers 1997.
- [4] B. Widrow, I. Kollar M. C. Liu - *Statistical theory of Quantization*; IEEE Trans. on Inst and Measurement, vol 45, no 2, pp 353 - 361, April 1996.
- [5] D. D. Sabin and A. Sundaram - *Quality enhances reliability*, IEEE Spectrum, vol 33, no 2, pp 34 - 41, February 1996.
- [6] R. House - *Choosing the right software for Data Acquisition*; IEEE Spectrum, vol 32, no 3, pp 24 - 39, 1995.

The Changing Face of Power Electronics

Sujit K. Biswas

Department of Electrical Engg., Jadavpur University, Kolkata, India
e-mail : sujit_biswas@hotmail.com

Abstract— Power Electronics has become one of the very important areas and is all set to expand its application areas in the near-future. This paper reviews the nature of developments taking place and shows that the involved technologies are changing at a rapid pace from a power device based technology to a control algorithm based technology. Today, significant developments in non-power-electronics areas are catalyzing spontaneous development in power electronic converters for those specific areas, making the future of Power Electronics truly multi-disciplined and multi-solutioned in nature.

- Conversion of electrical energy from one form to another of choice.
- Smooth control of electrical power flow.
- High efficiency involved in the above processes.
- High reliability of the controlling system.
- Compact size of the controlling system.

The above features are also partially available in a system of magnetic control elements, that are static in nature. Thus, they are also included into the area of Power Electronics, more because they are the predecessors of modern day solid state control and have led the way towards development in power electronics.

I. INTRODUCTION

Power Electronics is one of the fastest changing technology today, having gone through dynamic changes in the last several decades. Power Electronics, as the name suggests, can be considered as "The technology associated with the conversion, control and conditioning of electric power from its available form to the desired electrical form, by the application of electronics". However, Power Electronics has a history that is much older than many of us realize today. That is, if the basic aspect of 'conversion, control and conditioning of electric power' is considered, 'Power Electronics' can be traced back decades before the solid-state era. The solid state era, which has accelerated automation in industry, has led to increased R&D in Power Electronics, in order to meet the demands of increased productivity and improved product quality. Thus, the technologies involved have been going through constant change, depending on the demands of its diverse and ever-expanding application area. Today, significant developments in non-power-electronics areas are catalyzing spontaneous development in power electronic converters for those specific areas, making the future of Power Electronics truly multi-disciplined and multi-solutioned in nature.

Power Electronics has been important because of its several features :

II. HISTORY

The earliest recorded events that laid the foundation stone for Power Electronics dates back to 1883, when the Selenium Diode was used by C T. Fritts as a rectifier, followed by the development of the 3-phase bridge rectifier circuit (Graetz circuit) in 1897. The development of vacuum tube diodes came in about the turn of the century, thus it should not be overlooked that semiconductor technology in some form did exist before the era of vacuum tube devices. Peter Cooper Hewitt demonstrated the glass bulb mercury arc rectifier in 1901. The rectification property of the thermionic diode was used for the first time in 1904 by J. A. Fleming for the reception of radio signals. However, the invention of the three-element thermionic vacuum tube in 1907 by L. DeForest paved the way for a venture into controlled conversion.

Another landmark in the history of Power Electronics was created in 1912 when E. F. W. Alexanderson of the General Electric Company, USA, applied for a patent on a method for modulating the current from a high frequency alternator so that it could be used for radio telephony, using the concept of a magnetic amplifier. Through this technique, several tens of kilowatts could be controlled, while vacuum tubes could control only a few tens of watts! Thus, one can say, 'Power' Electronics went into real high power through magnetic amplifier technology.

World War I and the decade of 1920 witnessed a great growth in vacuum tube technology such that they soon dominated the low power application field. The period between 1926 and 1933 saw the introduction of the gas-filled 'Thyratron' and the mercury-arc 'Ignitron', both of which brought in controllability to very high power using gas and vapor-controlled rectifier technology. In both these, an unidirectional current flows with low voltage drop, only after a signal applied to a third electrode allows the gas-discharge to start. In the Thyratron, the grid is used to prevent the initiation of an arc between anode to cathode until a pre-selected time. In the Ignitron, a pulse of current through the third electrode (igniter) initiates a cathode spot on the pool of mercury after the pre-selected delay. Throughout the 1930's and the 1940's, the popularity of tube-controlled rectifiers increased and the term 'Industrial Electronics' was being used to describe the high power application of electronics for purposes other than communication. World War II catalysed research and development in power control on a scale unthinkable earlier and was responsible for creating some of the basic concepts of power conversion used today. The earlier popularity of magnetic amplifiers slowly declined, even though R&D continued on magnetic amplifiers using magnetic cores with non-linear characteristics. Low frequency push-pull inverters were developed using gas-filled tubes. Even electro-mechanical 'Vibrator' technology, using a spring-loaded, magnetic material as contact piece for an electromagnet (using similar principle as of a classical calling bell) was developed for use in inverters needed to step-up battery low voltage to the much needed higher dc voltage for operating valves for field wireless communication systems. Application areas expanded while converter power levels shot up. For example, in 1930, the New York subway installed a 3MW grid-controlled mercury arc rectifier for dc drive. In 1931, German Railways introduce mercury grid-controlled Cycloconverters for traction drive of Universal motors. In 1934, the first variable frequency ac drive was installed at Logan Power Station, USA, for a 400hp synchronous motor used in ID fan drive, using thyratrons.

The era of solid state semiconductor control was theoretically initiated by the invention of the 'Transistor' in 1948, but was really triggered off by the commercial availability of the Silicon Diode in 1956 followed by the Silicon Controlled Rectifier (SCR) (a member of a class of semiconductor devices that was named as 'thyristor') in 1958. After this, technology developed with new enthusiasm using the new tools and came to be known as 'Thyristor Technology'. The SCR revolutionized Power Electronics and led to the development of non-fragile, high voltage, high current, smaller size, smaller weight, efficient equipment for widespread application. Switching times of SCR's was much smaller than gas-filled tubes and thus switching frequency went up to about a kHz, bringing in new switching based concepts like that of PWM inverters.

Accelerated automation in manufacturing, material handling and process industries, demanded improved efficiencies and reduced maintenance. On the other hand, products had a growing demand for portability, compactness and automated features. Thus, most of the technological developments have been triggered off by the development of newer power semiconductor devices, one after another, in the following decades. In spite of its advantages, the application of SCR's to controlled turn-off circuits has the disadvantage of the associated commutation circuit, thus increasing the size and cost of the equipment. Further, the trapped energy in the commutation circuit causes severe problem of voltage stress across the device and reduces circuit efficiency due to additional loss of energy. The feature of its ability to latch with a small energy pulse at its gate is also one of its disadvantage, reducing system immunity to mal-operation due to noise. Thus, considerable R&D efforts were concentrated on the development of better power semiconductor devices. Toshiba Corporation of Japan introduced high power rated 'Giant Transistors' in early 1970's that eliminated the commutation circuit, improved noise immunity and improved efficiency of the converter. Very soon, the 'Power MOSFET's' was released in late 1970's by International Rectifier of USA, which permitted self-commutation at very high frequencies like 100 kHz, something unthinkable earlier, even though the power ratings were small. The Gate Turn Off Thyristor (GTO) was released by Japanese companies in early 1980's, which presented latching device like SCR but with gate controlled turn-off feature that eliminated the commutation circuit. Very soon, the closest-to-ideal device was released in mid 1980's in the form of the Insulated Gate Bipolar Transistor (IGBT) by General Electric of USA. The IGBT needs very low drive power, is self-commutating and can switch at reasonably high frequency. All these new power semiconductor devices, available in a wide range of voltage and current, made Power Electronics an economically attractive option within the next two decades, leading to its widespread acceptance. After the IGBT, hardly any significantly new power semiconductor has made it to widespread commercial market except the Integrated Gate Commutated Thyristor (IGCT) from ABB, Sweden, in mid 1990's. This is mostly because technology can be said to have become saturated, so that new devices with better performance cannot be evolved. However, considerable improvements in the performance of existing devices are evolving at a rapid scale.

One of the largest application of power electronics during the last half century has been in the field of adjustable speed motor drives, which has been a necessary pre-requisite for numerous industrial processes. The easily controlled dc motor has been the most commonly used variable speed power source in this connection. However, its commutator and brushes make it unable to satisfy the demands for reliability and low maintenance, especially in hazardous & corrosive environments and locations where access to motor for

servicing is restricted. Although ac machines with its superior characteristics have been with us for over a century, they were traditionally used as a fixed speed drive along with mechanical or electro-mechanical speed variators.

Some of the complicated methods of speed variation like pole-changing, cascade connection, Scherbius & Kramer drives, were also used. Special motors like Repulsion motor and Schrage motor achieved speed control through easy mechanical movement of a wheel mounted on it that shifted the brush positions of these ac commutator motors. The phase controlled rectifier was used for speed control of dc drives since the end of 1920's and the phase controlled cycloconverter was used to control the speed of ac motors (over limited range) since early 1930's, it was the availability of large power solid state devices that brought in the era of solid state speed control of ac motors in the 1960's. The ac motors used in variable speed drives are normally subjected to non-sinusoidal voltages and currents, which have two additional effects : additional harmonic power loss and torque pulsations. To overcome these problems, the concept of Sinusoidal PWM was evolved in the late 1960's. Since the 1970's, ac motor control technology drew growing interest to researchers, due to the development and application of new control strategies that could yield performances unthinkable before, started by the introduction of Vector Control or Field Oriented Control. These complicated control strategies could be commercially implemented in the 1980's due to the availability of higher switching frequency devices like Bipolar Power Transistors (and later, IGBT's) and the ease of implementation through microprocessor based digital techniques.

The availability of high frequency switching devices since the 1970's brought in a whole lot of controlled power converters into widespread applications, like the Switching Power Converters. They started replacing linear controllers in existing designs simply by virtue of their drastically reduced size and increased efficiency. Soon, they have started replacing phase controlled SCR converters since they offer better power factor on the ac power line. Awareness of the effect of harmonics and poor factor in the ac power line created the need for regulations and guidelines for the consumers in several countries in the late 1980's. This, in itself, has prompted development of improved performance switching power converters that draw almost sinusoidal currents at near-unity power factor from the ac line. For existing converters, another static switching circuit used as a means of correction for the line power factor and/or the current waveshape, have been extensively put to commercial use since the late 1990's.

III. FUTURE TRENDS

Power Electronics converters have gone through several changes in the last few decades, moving towards high frequency switching technology. This was made possible by the availability of power MOSFET's in the lower power range, IGBT's in the higher power range and IGCT's in the extreme high power range, making devices like Bipolar Power

Transistors and Inverter-grade SCR's obsolete and pushing other SCR's towards restricted application in ac line commutation only. No new power semiconductor device is expected to evolve in the near future, but existing device characteristics will go through substantial improvement, which is already started. Although silicon will continue as the major semiconductor material, new material (like silicon carbide) are expected to play a significant role in the future power devices, reducing the on-state voltage drop as well as the switching times. The technology of device packaging will go through further improvements so that still higher power devices will be available without any problem in their thermal management. Soft switching techniques will have increased application, but is not expected to replace the hard switching techniques totally in all applications for still some time to come.

Power Electronic converters have a much wider application area today than earlier, covering products from mobile phone chargers, PCs/Laptops, TV sets, air-conditioners, industrial drives, static VAR compensators, HVDC transmission, etc. This application area is expected to grow immensely, such that by the turn of the decade, it is expected that about 20% of the total electrical energy consumed will be controlled through some form of power electronic converter. On the power rating of an individual converter, compared to the earlier dominance of industrial and traction application, power generation, transmission and distribution will become the largest. Power electronics is finding increasing application in the latter area, being termed as 'FACTS' or Flexible AC Transmission System, 'Power Quality' and 'Custom Power'. The need for efficient power conversion has been appended with the need to prevent power line disturbances, resulting in development in new topologies and techniques. The traditional SCR phase controlled HVDC converters and Static VAR Compensators are being replaced by high frequency switched, high power IGBT based converters. With the growing interest in Renewable Energy sources like wind & solar power as well as the concepts of Distributed Generation, its interconnection to the grid has to depend upon power electronic converters, which have been developed to take care of these application. One major application area of power electronics developed today is Lighting Control, having evolved from the need for higher efficiency ballasts for various types of lamps. Today, development in LED technology has triggered the development of specifically designed power converters for use with LED lamps for a wide range of application from traffic signals to low power lighting. Aircrafts, ships and electric vehicles are today moving towards "More Electric" concepts, where many of the traditional hydraulic systems are expected to be replaced by electrical actuators with power electronic control. Alternators connected to the driving shafts directly need power electronic converters to control its output voltage and frequency in spite of shaft speed variations.

The trend in variable speed motor drive is towards the use of the Induction and Synchronous Machines in various forms.

In this context, the concepts of Space Vector PWM, Multilevel Inverters and Multi-phase motor drives are gaining wider publicity for commercial implementation. Several application areas that used constant speed drives (like air-conditioning) are opting for variable speed drives in the near future for efficient performance. Artificial Intelligence (Expert System, Fuzzy Logic, Artificial Neural Network and Genetic Algorithm) are the control algorithms of the future. Motor drive converters based on phase control will become obsolete and will be replaced by ones with excellent input power factor. Very little change is expected in the design of the motors, but new applications will demand the motors to be built in new shapes. For example, electric vehicle motors designed to drive the wheel directly is needed to be built in the shape of the wheel hub. A torpedo motor is expected to have its rotor on the outside, in the shape of the propeller itself.

Power Electronics will be increasingly controlled through digital technology based on high speed computing, for several reasons other than the ease of implementing complicated algorithms for better performance. Low cost competitive systems will use it for compactness, minimum settings during production and prevent direct duplication by competitors. Industrial power converters will use it for fault diagnostics, data logging and remote control/monitoring over telephone line. Thus, on one hand, single package microcontrollers are fast becoming an integral part of the power electronic controller in simple systems due to their ease of programming and inbuilt A to D converter at input. DSP Controllers are taking over the more complex ones due to their better computational power. However, the future prediction is that digital controllers for power electronics will be mostly based upon gate array technology, more on CPLD technology than of FPGA.

The future will see more of simulation and analytic tool applications in order to understand fully the behavior of a power electronic converter even before it is physically realized. This process speeds up R&D and removes unexpected problems while developing/designing a system. Several methods of analysis are being applied, ranging from Orthogonal Functions, Wavelets and Chaos. Several effective simulation tools are already available commercially, like SIMULINK.

IV. CONCLUSION

Power Electronics has a long history of evolution and has today become a major, multi-disciplined subject. The trend is moving distinctly towards high frequency switching converters, fuelled by the development of high performance semiconductor power devices. The need for efficiently controlled power with good quality in a form not readily available is creating an ever-increasing diversity of its application area. Digital Control is the tool of the future to implement high performance control algorithms in power electronic converters with reliability and ease.

REFERENCES

- [1] T. G. Wilson, "The evolution of power electronics", IEEE Trans. Power Electr., vol-15, no.3, pp439-446, May 2000.
- [2] B. K. Bose, "Power electronics and motor drives – technology advances, trends and applications", Tutorial presentation at ICTT, Hong Kong, 2005.
- [3] S. Smith, "developments in power electronics, machines and drives", IEE Power Engineering Journal, pp13-17, Feb 2002.
- [4] F. Blaabjerg, A. Consoli, J. A. Ferreira and J. D. van Wyk, "The future of electronic power processing and conversion", IEEE Trans. Power Electr., vol-20, no.3, pp715-720, May 2005.
- [5] J. D. Shepard, "Power electronics futures", Proceedings of IEEE APEC 04, pp31-34, 2004.
- [6] F. C. Lee, "The state-of-the-art power electronics technologies and future trends", Proceedings of IEEE Power Engg. Soc. Summer Meet. pp1229-1232, 2000.
- [7] E. I. Carroll, "Power electronics for very high power applications", Proceedings of IEE Conference on Power Electr. & Variable Speed Drives, pp218-223, Sept 1998.

Beyond CMOS: Problems and Prospects of Nanodevices for VLSI Circuits

Subir Kumar Sarkar

Department of Electronics and Telecommunication Engineering,
Jadavpur University, Kolkata, India
e-mail : sksarkar@etce.jdvu.ac.in

Abstract— With the development of semiconductor technology, it has recently become possible to fabricate laterally defined nanostructures, such as quantum well, wires and dots. Properties of electrons in such structures have attracted a wide interest because of their importance both in physics and device applications but nanodevices have some limitations. Again, integrated circuits devices with low power consumption, high operating speed and high integration density equipments are financially indispensable in modern electronics. Single electron device is one such device. Recent advancements in the field of nanotechnology have made it possible to isolate, control and exploit the properties of an electron at single-spin level. This has brought us closer to the realization of single-spin logic where a single electron, placed in a magnetic field, is utilized as binary logic device.

I. INTRODUCTION

Speed of Computers and Communication equipments has been the fascinating feature now-a-days due to development of very fast switching semiconductor devices [1-4]. Since the response of the system depends on the motion of the conduction electrons of the devices used in the device has been found essential in the context of today's growth in the field of electronics [5]. In the childhood of VLSI technology power consumption was not the essential criterion for consideration. In fact power consideration has been the ultimate design criterion in special portable applications such as wristwatch, laptop/notebook computer and space makers for a long time. The objective in these applications is the minimum power for maximum battery lifetime. A major creative challenge facing today circuit and system VLSI designers is to design new generation products, which consume minimum power [6-9].

However power saving must be achieved without compromising high performance or minimum chip area. High-speed operation and designing with minimum area, specially in memories, are the main design constraints. The state of the art scaling is approaching and these are unsolved problems such as the number of electrons in the active region of the devices. If this number is reduced to less than 10 electrons (holes), quantum fluctuation errors will become too small to block quantum mechanical tunneling which may result in unacceptably large leakage currents. On the other hand, the recent evolution of technology may provide opportunities for novel devices, which may solve these problems. As a consequence, the search for the new principle of the small size devices is becoming more and more important.

At present there are two main branches of the proposal on the suitable operation principles, so called "quantum electronics devices" and "single electron devices". It is natural to expect that quantum effect will play an important role in ultra small electronic devices. However, fragility of the quantum effects causes the very serious doubt that they could be used for VLSI of the post CMOS era. There are inherent limitations of quantum devices like: (i) material and process related limitation, (ii) power limitation (iii) wiring limitation, (iv) quantum mechanical limitation and (v) system architecture limitation [10,11].

II. NANODEVICES

Device dimension is an important parameter so far speed of device is concerned. Low dimensional structures, also called nanostructure, provide opportunities to realize high speed, low power consuming devices. System parameter optimization for estimating the better performance of a low dimensional, low power consuming and high frequency devices of desired characteristics is very important during fabrication. Downloading of the minimum feature size of complementary metal-oxide semiconductor (CMOS) transistor is the basis for advancement in the ultra-large scale technology.

The quantization of electron motion in systems of reduced dimensionality brings about different features in the electron kinetics compared with the usual three dimensional electron systems. Material parameters, the external applied field and the lattice temperature play a crucial role in predicting the device performance. The values of the parameters can be optimized to get the desired response from a device. Further, modern sophisticated technologies have made possible the fabrication of a variety of new quantum devices with tailored system parameters. System parameters are optimized for a particular biasing field to get the desired ac mobility in the millimeter wave frequency region and can be used to analyze the experimental data when they appear in the literature. The application of GA will enable the technologists involved in the fabrication to predict directly the system parameters for a device to be operated at a desired frequency with required ac mobility.

The basic intention of this work is to determine the optimized system parameters of GaAs, (In,Ga)As and GaN quantum/nano structures for efficient low power consuming high frequency nanodevices suitable for ultradense VLSI/ULSI circuits. The optimized system parameters presented here, predict the better performance of nanodevices in the microwave and millimeter wave regime and can be used to analyze the experimental data when they will appear in the literature. The optimized system parameters will surely save the search time for the technologists involved in the fabrication of high frequency low dimensional semiconductor nanodevices. It is possible to choose the best parameters for a desired high frequency response of a particular material. The present GA based technique enables the technologists to determine the system parameters directly to get the desired properties and can be utilized during fabrication.

III. SINGLE ELECTRON DEVICES

The generality and the robustness of the effect and the relative simplicity of the device structure make the single electronics the most likely candidate for future ultra dense digital circuits. Single electronics is a newly emerging field of rapidly growing interest both scientifically and from the point of view of applications to modern and future electronics because of their ultra low power consumption, highly dense and high switching speed [10-12]. Single electron devices that allow manipulation of individual electron are ultimate form of the electron devices. Their potential integration level is obviously extremely high due to its small size. Extremely low power operation solves some of the instability and reliability problem. The speed power product is predicted to lie close to the quantum limit set by Heisenberg uncertainty principle. The processing speed of such device will be nearly equal to electronic speed. The exquisite sensitivity is about five orders of magnitude better than conventional solid state MOSFET transistors. The integration density is much higher than available in the existing VLSI/ULSI circuits. Single electron devices hold out the promise of being the successor to present

day technologies due to their unique principle of operation, quantum nature of carrier transport, ultra-small size and low power dissipation. All the logical circuits starting from NOT gate to CPU of a digital computer can be realized using SEDs[13-15]. To substantiate our statement, a SED based sequence generator circuit is designed implemented and verified by computer simulation.

The sequences to be generated [Fig.1] are of two sections labeled present state and next state. The present state designates two states of flip-flops before the occurrence of a clock pulse, whereas the next states of flip-flops after the clock pulse.

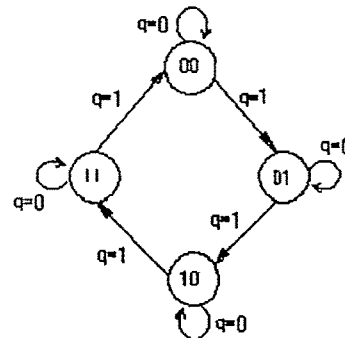


Fig1: Sequence to be generated

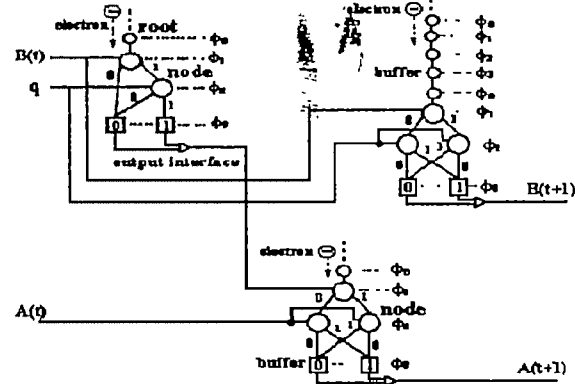


Fig2: Sequential Circuit

The sequence circuit is designed using conventional digital circuit design technique. However, the design steps are not shown for brevity of the paper. The present and next states are shown by $A(t)$, $B(t)$ and $A(t+1)$, $B(t+1)$ respectively. The final designed circuit employing the single electron transistors is shown in Fig. 2 and the timing diagram is shown in the Fig. 3.

$$\text{where } A(t+1) = A(t) \oplus (B(t) \cdot q(t))$$

$$B(t+1) = B(t) \oplus q(t);$$

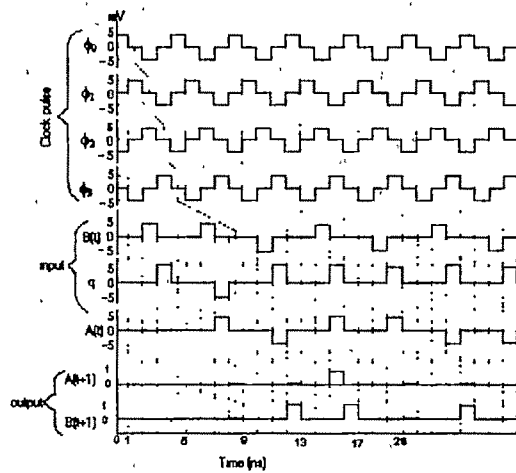


Fig3: Input output waveform of sequence generator circuit

IV. SPINTRONIC DEVICES

Until recently, the spin of electron was ignored in mainstream charge-based electronics. A technology was emerged called Spintronics (Spin transport electronics or spin based electronics), where it is not the electronic charge but the electron spin that carry information, and this offers opportunities for a new generation of devices combining standard microelectronics with Spin-dependent effects that arise from the inversion between spin of the carrier and the magnetic properties of the material [16-18].

Recent advances in nanotechnology have made it possible to isolate, control and exploit the properties of an electron at the single-spin level. This has brought us closer to the realization of 'single-spin logic' where a single electron, placed in a magnetic field, is utilized as a binary logic device. The two non-degenerate orthogonal spin states of the electron (parallel and anti-parallel to the magnetic field) encode the classical bits 0 and 1. The logic signal (or spin state) is communicated between neighboring devices via the exchange interaction between the nearest neighbor spins, without the need for physical wires. The communication is made unidirectional (i.e. the logic signal flows from the input stage to the output stage and not the other way around) by sequentially clocking the successive cells using a three-phase clock.

The advantages of this paradigm are extremely low dynamic power dissipation during switching, ultra-high gate density, and relatively fast processing speed. Spin is also somewhat immune to noise since it does not couple easily to stray electric fields. More over, spin polarization can be relatively long-lived entity in a quantum dot. Spin flip times $> \mu s$ have been measured in InP quantum dots [19-21] and they could be even longer in organic semiconductor quantum dots made of 7F-conjugated polymers [27-28]. This is conducive to fault-tolerant computing. The probability of a random spin flip event occurring in a time T is $1-e^{-TT}$. If this probability is sufficiently small, say less than 3%, than it is possible to correct for bit errors caused by random spin flips using

sophisticated error correcting algorithm [22,23]. Thus the clock period T needs to be $\sim 3\%$ of the spin-flip time, or about 311.5. If we use a clock frequency of 50 GHz, then the error probability during a clock cycle is a miniscule 2×10^{-7} , which is easily handled by error-correction algorithms. Therefore, single-spin logic can yield practical low power and high density computing capability. [24,25].

Hence researchers are in a frame of mind to articulate this technology in every sphere of life. Using single spin logic, we have tried to design and implement a sequence generator circuit and tested it with computer simulation.

The design steps followed in spin-based sequence is the same as done in case of SET based design. The only difference is q is replaced by x in the present design. Figure 4(a) represents the single spin based realization of the designed sequential circuit.

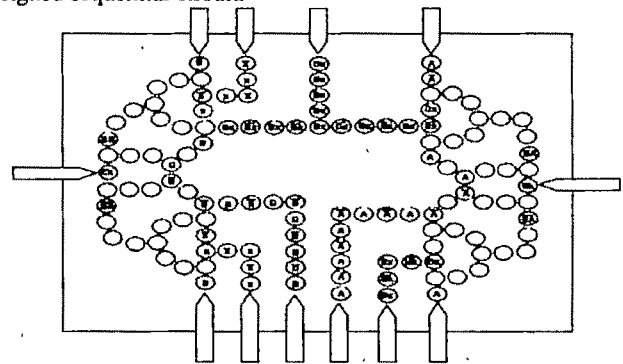


Fig. 4 (a): Single spin realization of the sequential circuit

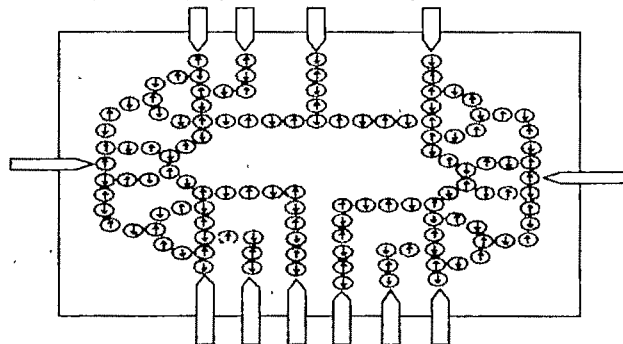


Fig. 4 (b): Spin orientation in each cell when present state is 00 and $x=0$

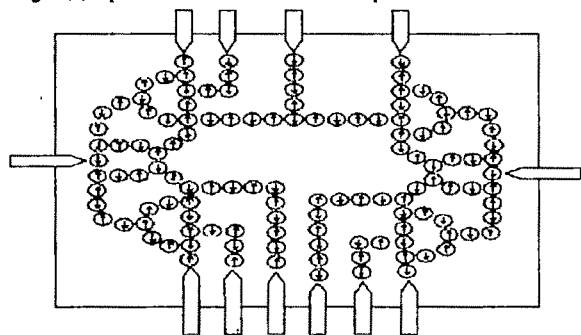


Fig. 4 (c): Spin orientation in each cell when present state is 00 and $x=1$.

Actual functionality of the sequential circuit is verified in figure 4(b) and 4(c) by showing spin orientation of each cell during a change in sequence $00 \rightarrow 01$ subject to application of

input $x=1$. Figure 4(b) depicts the spin orientation of each cell when present state is 00 and applied input $x=0$. In figure 4(c), we have shown that changing x to 1, causes inputs of the DB Flip Flops to become '1', so that in the next clock cycle, the output of the DB Flip Flop becomes '1' and the next state will be 01 as expected.

V. CONCLUSION

Due to the size limitation even with scaling down of the MOSFET technology cannot continue forever. It will hardly go beyond a few nm, even if adequate lithographical technology will be available. As a consequence, the search for the new principles of operation of the small-size devices is becoming more and more important. They possess radically different properties from those of bulk semiconductors. This change in the effective dimensionality offers fascinating changes in electric, magnetic, optical and vibrational properties. The electron mobility is high in those devices. Researches on the (nanodevices) quantum devices continue to be both challenging and exciting as novel structures with different material having different properties are developed. Even with its inherent limitations quantum devices are the most likely candidate for future ultra-dense digital circuits. A single electron is sufficient to store information. The power consumption is drastically reduced. Ultimate form of the electron device. The speed power product is predicted to lie close to the quantum limit. The processing speed of such device will be nearly equal to electronic speed. The integration density is higher than that present in VLSI / ULSI level. The implementations of sequential digital logic circuits using single electron spins in quantum dots is done here also. We point out that these logic circuits are "classical" constructs that do not require global phase coherence unlike "quantum" circuits based on spins in quantum dots. While considerable research and effort have been invested in the search for spintronic quantum computers, very little, if any, investment has been made to realize single spin (classical) logic. This is a paradox since classical logic is easier to implement insofar as one does not have to strive against decoherence."

ACKNOWLEDGMENT

The author thankfully acknowledges the financial support obtained from DRDO, Government of India vide order no:(ERIP/ER/050356/M/01/905 dt. 01/08/2006).

REFERENCES

- [1] S K Sarkar & D Chattopadhyay, Phys Rev B, 62 (2000) 15331
- [2] S Madhvi, V Ventataraman, J C Sturm & Y H Xie, Phys rev B, 61(2000)16807.
- [3] E Bakkers, Z Hens, A Zunger, A Franceschetti, L Kouwenhoven, L Gurevich, D. Vanmarckelbeg : Nanoletter 1, 551, 2001.
- [4] S. Bandyopadhyay and M Cahay, Superlat. Microstruct. 32, 171 (2002).
- [5] G. Allan, Y M. Niquet, C. Delerue : Appl. Phys Lett. 77, 639, 2000.
- [6] S K Sarkar, A Karmakar, & A K De, J. Phys, 75A(2001)367.

- [7] "GA Based Parameter Optimizations for better Millimeter and Sub-millimeter Wave Response Characteristics of GaAs Quantum Wells". Indian J. Phys. 77A (1), pp 23-26, 2003
- [8] S. K. Sarkar: "Multiple Level Optimization for High Frequency ac mobility in GaAs Quantum Wells under Hot-Electron Condition": Computational Material Science (Elsevier) 29, 243-249 (2004).
- [9] M.W.Keller et al: Science 285, 1706(1999).
- [10] A.K Biswas, B Maji, A K De and Subir Kumar Sarkar: Proc. Of the IWPSD 11-15.12.2001. held at SSPL, Delhi.
- [11] A N Korotkov: "Digital-Single-electronics: Problem and possible solutions", Proceed. of SSDM '97, Hamamatsu, Japan, pp 304-305, 1997.
- [12] S. Bandyopadhyay, B. Das and A. E. Miller, "Supercomputing with spin polarized single electrons in a quantum coupled architecture", Nanotechnology, 1994, 5, p. 113.
- [13] Bandyopadhyay, "Computing with spins: from classical to quantum computing", Superlat. Microstruct., 2005, 32, p.171.
- [14] S. Bandyopadhyay, Superlat. Microstruct., 32, 77 (2005).
- [15] D. Rugar, R. Budakian, H. J. Mamin and B. W. Chui, Nature (London), 430, 329 (2004); J. M. Elzerman, et al., Nature (London), 430, 431 (2004); M. Xiao, et al., Nature (London), 430, 435 (2004)
- [16] S. Bandyopadhyay, Phys. Rev. B, 67, 193304 (2003).
- [17] D. Rugar, R. Budakian, H. J. Mamin and B. W. Chui, Nature (London), 430, 329 (2004); J. M. Elzerman, et al., Nature (London), 430, 431 (2004); M. Xiao, et al., Nature (London), 430, 435 (2004).
- [18] S. Bandyopadhyay, Phys. Rev. B, 67, 193304 (2003).
- [19] S. N. Molotkov and S. S. Nazin, JETP Lett., 62, 273 (1995).
- [20] S. N. Molotkov and S. S. Nazin, Zhurnal Eksperimentalnoi i Teoreticheskoi Fiziki, 110, 1439 (1996).
- [21] A. M. Bychkov, L. A. Openov and I. A. Semennhin, JETP Lett., 66, 298 (1997).
- [22] S. Bandyopadhyay, Superlat. Microstruct., 32, 77 (2005).
- [23] S. Bandyopadhyay and V. P. Roychowdhury, Jpn. J. Appl. Phys., 35, Part 1, 3350 (1996).
- [24] S. K. Sarkar, T. Basu and S. Bandyopadhyay: "Single Spin Logic Circuit" Journal of Physics of Low-Dimension Structures, Vol. 2, PP 2-10, 2006.
- [25] S. K. Sarkar, T. Basu and S. Bandyopadhyay: "An arithmetic logic unit of a computer based on spin-polarized single electrons" IET Circuits Device Syst., 1(3), pp.194-199, 2007References.

Mobile GIS, Communication and Concurrent Safety for Intelligent Transport Systems

Rabindranath Bera

Electronics & Communication Engg
Sikkim Manipal Institute of Technology, Sikkim Manipal University
Majitar, Rangpo, East Sikkim, India

Abstract – Motivated by the recent development and success of MIMO technology both in communication and radar files, the author and his group are fully engaged in developing a smart vehicle which will cater for GIS/Communication as well as road safety services. They have formulated the severe problems of multipath, interference at the road and according chosen the design of their system based on COFDM-MIMO. This paper will highlight the details works of their system and also the design.

Key words—Mobile GIS, GPRS, EDGE, 3G wireless, MIMO, RCS, OFDM, CDMA, DSSS, COFDM, Beamformation, MUSIC, ESPRIT

I INTRODUCTION

Mobile GIS is the expansion of a geographic information system (GIS) from the office into the field. A mobile GIS enables field based personnel to capture, store, update, manipulate, analyze, and display geographic information. The integration of GIS, GPS, mobile communication technology and Internet brings us a more convenient spatial information service—mobile GIS. Mobile GIS is based on mobile equipments and transmits spatial information via high performance wireless communication net and Internet. With the developing of GPRS (General Packet Radio Service), EDGE technology and the 3G wireless networks, the transmission ability of wireless network has been enhanced, and the location-based service technology of GIS and wireless network technology are in rapidly developing [1].

With the tremendous success of mobile technology towards voice and low data rate services, scientists are trying globally for the high data rate multimedia services over a fast moving vehicles. Additionally for collision avoidance from the nearby car, the suitable radar technology is to be explored. Therefore, the trend is to develop a smart vehicle which will be embedded with mobile GIS, communication & radar technology.

II. PROBLEMS IN THE PHYSICAL LAYER

The communication and GIS services mentioned above are generally perturbed by the multipath effects due to environments and a fade depth of more than 30 dB are more

common. This restricts data rate and goal of high end multimedia services are perturbed.

For radar based remote sensing case, every target is characterized by its RCS(RADAR Cross Section) function. A target's RCS function represents the amount of energy reflected from the target toward the receiver as a function of the target aspect with respect to the transmitter receiver pair. It is well known that this function is rapidly changing as a function of the target aspect [2]. Both experimental measurements and theoretical results demonstrate that scintillations of 10 dB or more in the reflected energy can occur by changing the target aspect by as little as one milliradian. These RCS scintillations are responsible for signal fading, which can cause large degradations in the system's detection and estimation performances.

The above mentioned problems of SNR fluctuations both in mobile GIS, communication& radar services from the smart vehicle may be solved successfully with the use of MIMO technology. MIMO (multiple input multiple output) is an smart antenna array technology that uses broadband pulses of energy for remote sensing and communication application and may be best suited for such smart vehicle application.

III. DESIGN PHILOSOPHY

To achieve a data rate of 100 MBPS over mobile environment, it relates a total system bandwidth of 100 MHz. MIMO technology alone cannot tackle the problem rather the hybrid technologies to be explored. It is also well accepted that the OFDM (Orthogonal Frequency Division Multiplexing) is the enabler for the MIMO. So Instead of MIMO alone, OFDM may be more useful. And the total spectrum will be subdivided over multiple simultaneous antenna which will be again divided over multiple carriers like 64 OFDM carriers or more.

In this way MIMO-OFDM combination will help tremendously to improve the data throughput by reducing the multipath effects. Also there are tremendous growth in CDMA based DSSS (Direct Sequence Spread Spectrum) technology which is superior in performance in terms of interference rejection. Therefore COFDM-MIMO (Coded OFDM) is the hybrid technology which create a lots of interests to the author and the simplified block is shown in Fig. 1.

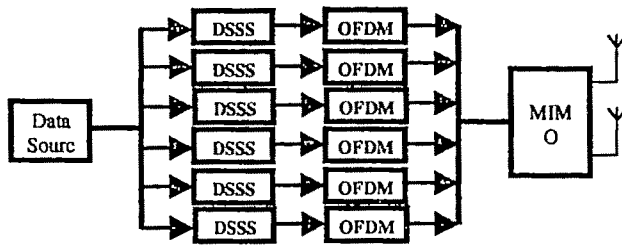


Fig. 1: Simplified Block Diagram of COFDM-MIMO System

IV. THE DSSS SYSTEM

The DSSS system is explored first. The author and his group is successful in sending multimedia data through a IEEE 802.11b adapters using UDP mode of Matlab. Additionally a DSSS Bi-static Radar using the same WiFi b PCI adapter fitted inside a PC is operational at SMIT having the following system parameters.

RF carrier Frequency = 2.4 GHz

Rate = 11 Mbps

RF bandwidth = 20 MHz

Spread with 11 bit Barker Code having sequence = [1; -1; 1; 1; -1; 1; 1; 1; -1; -1; -1; -1]

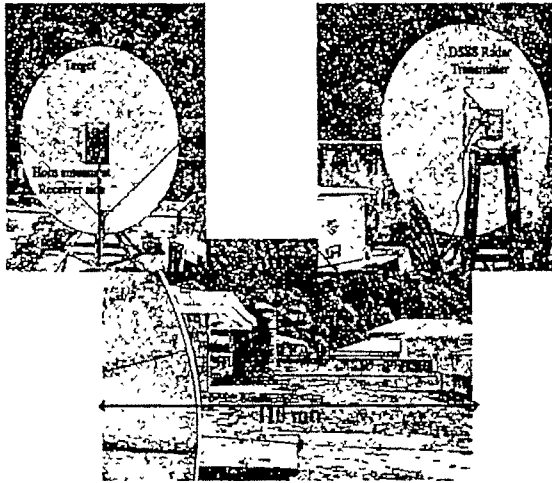


Fig. 2. Photograph of the operational DSSS Radar at SMIT

The total system placement along with the target is as in Fig. 2. The DSSS radar transmitter is placed at a long distance of 110 meter which radiates carrier using a dish antenna of diameter 6 ft with a horn at its focus. The horn is connected to WiFi b adapter fitted inside a PC. At the other end the receiver with another WiFi b adapter and a second horn is placed.

Three big targets of parabolic dishes of diameters 70.5, 72 & 76.5 inches respectively are placed near this receive horn. The targets are fitted on the proper mounting structure and can be rotated manually both in azimuth and in elevation angles which can be read out from the scale mounted at the back. Actually we have modified three commercial parabolic dishes (meant for the satellite reception) with their mounting

structures and utilize them as targets i.e. three vehicles at the road.

A. Experimental Results.

At every position of the targets we are noting down the values of target angular position with received signal strength. The individual results of the targets have been plotted as shown in Fig. 3, 4 and 5 respectively

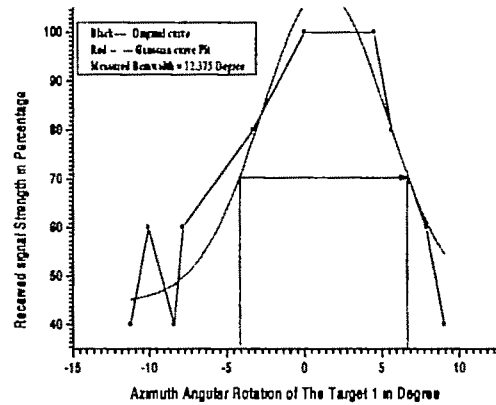


Fig. 3 Plot of Azimuth Angular Rotation of Target 1

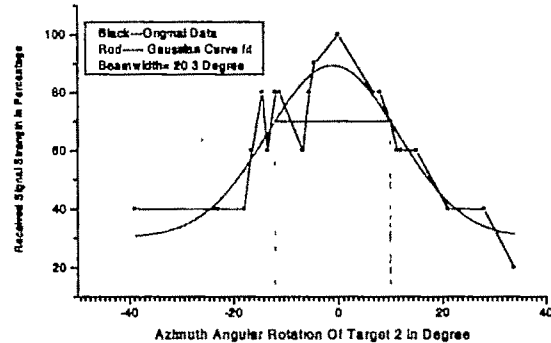


Fig. 4. Plot of Azimuth Angular Rotation of Target 2

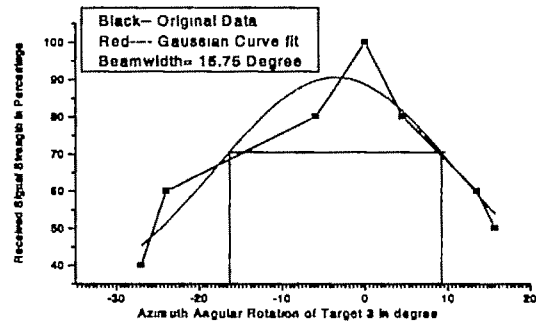


Fig. 5. Plot of Azimuth Angular Rotation of Target 3

The net energy concentration of the incident radiation from the targets will be towards their focus as they are parabolic in

nature. Accordingly the measured received beam patterns are tabulated in the Table 1.

Table 1. Measured Beam Patterns of Three Targets.

Target Name	3 dB Beamwidth in degree (Azimuth)	3 dB Beamwidth in degrees (Elevation)
Target 1	12.375	2.5
Target 2	20.3	27
Target 3	15.75	11

A calibration curve is shown in Fig.6 which can be drawn out of those results and it will be useful in finding any unknown objects RCS of similar kind.

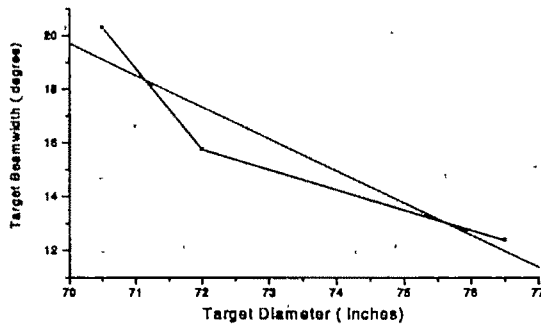


Fig 6. The Calibration Curve for RCS measurement of Azimuth angle.

The DSSS system are explored at the laboratory both for GIS/ Communication and Radar mode. The interference rejection capability of the system are also studied and a processing gain of 100 is achieved. The distance coverage of more than 100 meter is also satisfactory. So putting it to a vehicle, GIS/ communication services can be launched. Additionally, the nearby passing vehicle can be detected comfortably.

V. MIMO-OFDM SYSTEM

Motivated by recent developments in communication theory [3,4], we introduce the concept of multiple-input multiple-output (MIMO) radar. MIMO communication systems overcome the problems caused by fading by transmitting different streams of information from several decorrelated, signals. In MIMO communication systems, the receiver enjoys the average signal to noise ratio (SNR) of the received signal is more or less constant, whereas in conventional systems, which transmits all their energy over a single path, the received SNR varies considerably. The novelty of the MIMO RADAR is that, it capitalizes on target scintillations to improve the RADAR performance.

The performance analysis for the MIMO-OFDM system and Sub-system has been carried out based on MATLAB simulation.

In taking decision about the no of elements of MIMO, we did a lot of simulation where the MIMO elements are varied as desired Fig.7. is showing such a performance curve which

utilizes codes for further processing. Three cases are shown: 1. SISO case, 2X2 & 4X4 MIMO Case. We got stabilized & improved performances which are again desired features from such a system.

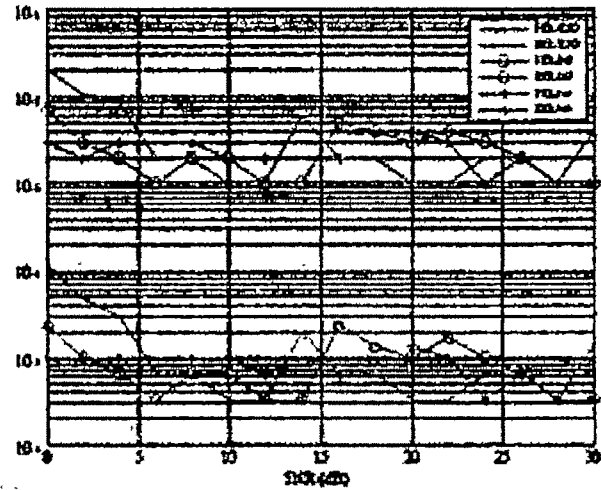


Fig. 7. BER Performance of SISO vs 2x2 vs 4x4.

Parameters: No. of FFT points = 64; Modulation = BPSK; Convolution Code Rate = R1/2; Channel = AWGN.

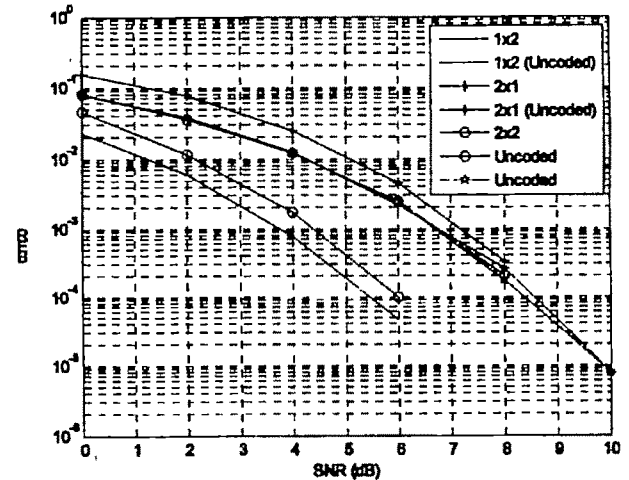


Fig. 8. BER Performance of 1x2 vs 2x1 vs 2x2 vs 4x4 (AWGN)

The variation in the different systems has been depicted in Fig 8 the performance of the uncoded systems seemed to be overlapping. But we can make a clear distinction between the 1X2 (SIMO), 2X1 (MISO) and 2X2 (MIMO) cases. The performance of the MIMO system is more profoundly better over the others. Even the SIMO system performance shows great deal of improvement over other system, which is mainly due to its Receive diversity technique being deployed.

BER Performance comparison between individual subsystem blocks and the total OFDM-MIMO Wi-Fi system is shown in Fig. 9.

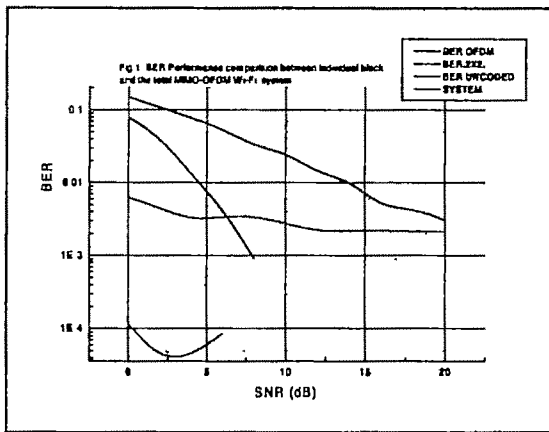


Fig. 9. BER Performance Individual Subsystem and The Overall OFDM-MIMO Wi-Fi system.

Parameters: No. of FFT points = 64; Modulation = BPSK; Convolution Code Rate = $R/2$; Channel = AWGN.

The overall system (OFDM-MIMO) performance is quite interesting having much lower values as compared to individual BER performance as shown in Fig. 8.

The choice of multiple antenna is justified as evident from above simulation. Even the multiple antenna can be utilized for DSSS system also for its better performances in terms of multipath rejection.

V. COMPARISON OF MUSIC AND ESPRIT ALGORITHMS FOR THE ESTIMATION OF DOA WITH BEAMFORMATION

The above systems are able to detect the target (moving vehicle at the road) with higher level of precision as well as efficient communication to passing vehicles and roadside Access points. But the DOA (Direction Of Arrival) cannot be estimated by the system. For this estimation we have simulated two popular algorithm 'MUSIC' (Multiple Signal Classification) & ESPRIT (Estimation of Signal Parameters via Rotational Invariance Technique) and we find some limitation of those estimation which we like to eliminate by some advanced algorithm. By embedding this algorithm for DOA estimation, the system will be able to estimate DOA of the passing vehicles.

A. Direction of Arrival (DOA)

For the beamformer to steer the radiation in a particular direction and to place the nulls in the interfering directions the direction of arrival has to be known beforehand. The DOA algorithms does exactly the same; they work on the signal received at the output of the array and compute the direction of arrivals of all the incoming signals. Once the angle information is known it is fed into the beamforming network to compute the complex weight vectors required for beam steering.

B. Performance Analysis

1. Results of the various pairs of Angles of Arrivals using MUSIC Algorithm

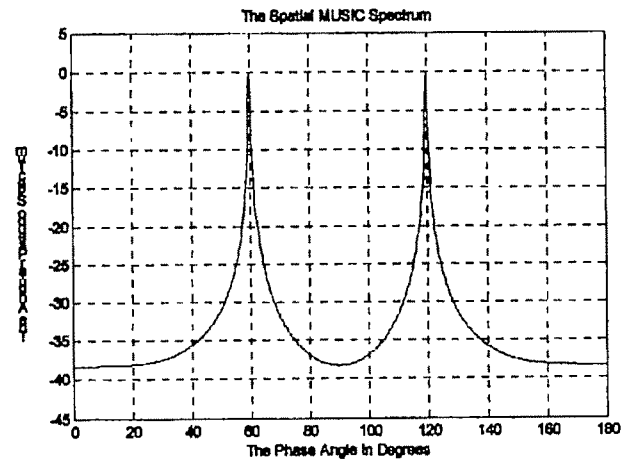


Fig. 10. Spatial MUSIC Spectrum for Angles of arrivals = 60 and 120 degrees.

It is clearly indicated in the Fig. 10 the sensing of two incident radiation by the receiver using MUSIC algorithm. FFT method may not be so good for such high resolution spectral estimation. But the estimation is Gaussian in shape having no problem for well separated radiations but still poor resolution for two nearby radiations. Such a scenario is shown in Fig. 12 where angle of arrivals are very close to each other.

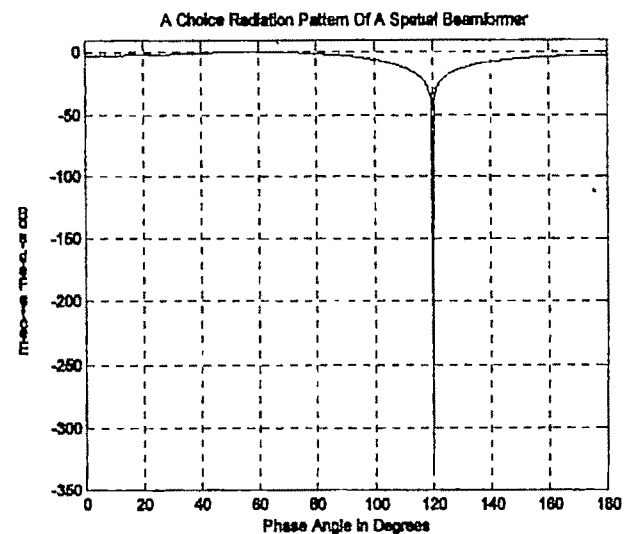


Fig. 11. Null at 120 degree and maxima at 60 degree

The another requirement of DOA is to put nulls towards the unwanted reception. Such a simulation for null at 120 degree with a DOA sensing at 60 degree is shown in Fig. 11. The rejection is more than 300 dB again with a Gaussian shape. Instead of sharp null. Problems of such sharp nulls will be more pronounced for close by radiation of 44 and 45 degrees as in Fig. 13.

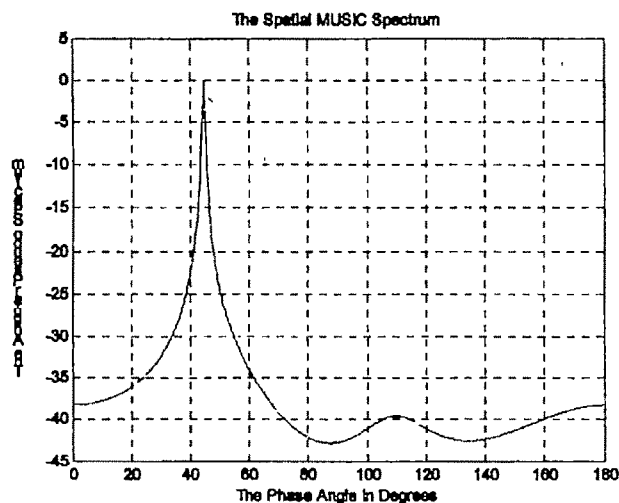


Fig 12. Spatial MUSIC Spectrum for angles of arrivals = 44 and 45 degrees.

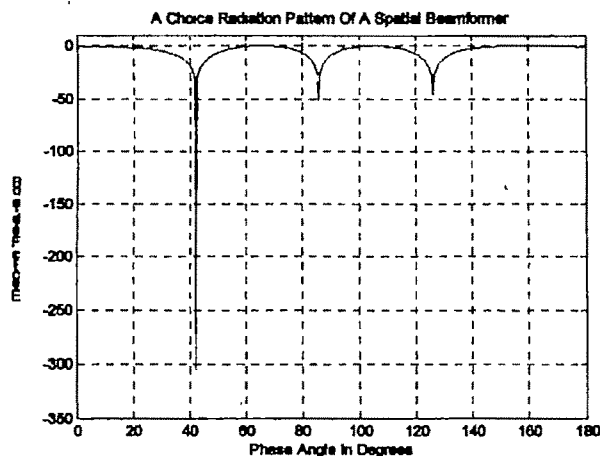


Fig. 13. Plot 4- showing nulls for the two angles of arrivals but with worst resolution at 44 and 45 degrees of signal arrival.

VI CONCLUSION

Both the DSSS system and MIMO -OFDM system are operational at the laboratory of SMIT. The communication and radar modes are also explored for both the systems. The Integration of the systems for COFDM-MIMO is still awaited. Both the systems are able to detect the targets for collision avoidance at the road. The DOA estimation is to be embedded to the systems. Soon we will be exploring the system for the field trial. We may expect lots of further problems during field trials like the Doppler effects due to the motion of the vehicle. The Doppler extraction algorithm to be embedded to the system for determining the speed of the passing vehicles. In summary, the basic level of work has been carried out at the lab, but lots of further efforts to be imparted for actual operation condition.

ACKNOWLEDGMENT

Author is thankful to the staff of E&C Dept. of SMIT and DRDO for providing support both technically and financially in the form of a entitled 'SRS.'

REFERENCES

- [1] Qinghui Suna,b,c, Xiaoli Wangb, Tianhe Chia and Culling Jia,, ' An Integrated System Based on Wireless Communication Technology and Mobile GIS' IEEE transaction on vehicular technology, 2005
- [2] M. Skolnik, *Introduction to Radar System*, McGraw-Hill, 3rd edition, 2002.
- [3] V. Tarokh, N. Seshadri, and A.R. Calderbank, "Spacetime codes for high data rate wireless communication: Performance criterion and code construction," *IEEE Trans on Info. Theory*, vol. 44, no. 2, pp. 744-765, March 1998.
- [4] D. Chizhik, G. J. Foschini, M. J. Gans, and R. A. Valenzuela, "Keyholes, correlations, and capacities of multielement transmit and receive antennas," *IEEE Transactions on Wireless Communications*, vol. 1, no. 2, pp 361-368, April 2002.

HVDC-Link Modeling in OPF using Newton's Method: HDVC-LCC

Enrique Acha

University of Glasgow
Glasgow, Scotland, UK

Abstract— This paper presents a method for incorporating a simple and yet realistic modelling representation of an HVDC-LCC-link into Newton-based power flow algorithms – where all the relevant variables of the DC circuit blend seamlessly with those of the AC circuit for robust iterative solutions. Two distinct but related streams of power flows are addressed in the paper, conventional power flows and the very timely optimal power flow solutions. The paper is tutorial in nature and the HVDC-LCC-link equations are first implemented in a conventional power flow algorithm, to yield an AC-DC power flow using the DC variable elimination method. The Newton-Raphson method is used to solve the reduced set of power flow equations, resulting in an AC-DC power flow algorithm that exhibits quadratic convergence for all the three control modes addressed in the paper. Next, the HVDC-LCC-link power equations are implemented in the optimal power flow algorithm using Newton's method together with the Multipliers method to yield very robust optimal solutions of AC-DC circuits. To show the applicability of the two upgraded AC-DC power systems algorithms, a contrived test network is solved and conclusions are drawn. Moreover, to show the full scale of applicability of the optimal power flow algorithm, a utility size power network is solved – with two different studies presented: the standard network, which is a conventional one, and an upgraded network which includes one HVDC-LCC-link and nineteen FACTS controllers.

Key words— OPF, Newton's method, HVDC, FACTS

I. INTRODUCTION

Point-to-point and back-to-back high voltage direct current (HVDC) transmission links are in operation throughout the world [1]. Furthermore, in large conurbation centers, utility planners are actively considering the viability of reconverting existing AC transmission corridors into

HVDC lines to take advantage of the higher power density achieved with the latter. To make informed decisions power systems application tools with suitable HVDC representation are not only desirable but essential. However, HVDC link representation is often over-simplified or ignored in most power system studies, with Optimal Power Flows (OPF) being a case in point. This applies to both the long established HVDC line commutated current (LCC) and the new breed of HVDC technology based on voltage source converters (VSC) [2], [3].

From the outset, more than six decades ago, the drive for the development of the DC transmission technology was its reduced power loss burden compared to that of a corresponding AC transmission line of equal rating. However, its applicability to other transmission schemes such as submarine transmission and asynchronous inter-connections were quickly realized and these became niches of the HVDC technology. Early DC transmission schemes used mercury arc valves at the converter stations and that limited the appeal of the technology on grounds of transmission availability. The advent of the silicon-controlled rectifier (thyristor) capable of handling large powers and microprocessor-based control techniques made HVDC converters less brittle, vastly increasing their transmission availability and operational control flexibility. The market for thyristor-based HVDC technology has remained firm for many years but new power semiconductors (IGBT and GTO) with improved switching characteristics have reached the power levels which are required for modern power transmission, albeit still at much reduced power ratings than what it is feasible to achieve with thyristor-based technology – Currently, HVDC-VSC systems have a power rating in the range 7-530 MW and DC voltage in the range 10-150 kV whereas HVDC-LCC systems are available in the power range 100-3000 MW and DC voltages up to 600 kV [4].

Nevertheless, the pace of development of the HVDC-VSC

technology is breathtaking [5]. The use of the voltage source converters (VSC) for DC power transmission was only introduced in 1997, with a 3 MW, ± 10 kV DC prototype at Hellsjon, Sweden. The VSC technology includes IGBTs and in order to improve the quality of output voltage, high frequency pulse width modulation (PWM) is used. By increasing the switching frequency, harmonics in the lower frequency range can be reduced or nearly eliminated and the output voltage is a quasi-sinusoidal waveform with a dominant fundamental component, and with the characteristic harmonics shifted to higher orders. Arguably, harmonics in the higher frequency range can be filtered out with less difficulty. However, increasing the switching frequency also increases the power loss. At present, this is the Achilles heel of the high-voltage VSC technology and further design improvements in power semiconductor devices are keenly awaited all the time.

The reason is that the HVDC-VSC technology introduces a wide range of benefits to the AC power network where it is embedded, such as the ability to independently control the reactive power flow at each connecting AC bus, with real potential for improving power quality in both AC sides of the network, and to decouple reactive power flow control from active power flow control. This being a definite advantage of the HVDC-VSC technology over the HVDC-LCC technology when the converter is connected to a weak AC network or to a "dead network", i.e. network with no other voltage source.

In spite of the great many benefits introduced by the HVDC-VSC technology, it is quite clear that until the power IGBT, or any other high-frequency switching valve, does not reach power levels handling closer to those currently achieved by conventional thyristors, bulk power DC transmission will remain the realm of the HVDC-LCC technology. The need for moving extra-large volumes of electrical energy over continental distances is on the increase. The long-distance HVDC transmission schemes in China from the Three Gorges dam to Shanghai, Changzhou and Guangdong, is a case in point. Moreover, renewed interest in laying an 1800 km seafloor DC cable to transport large volumes of geothermal electricity from Iceland to Germany has resurfaced, as a result of a growing market for clean energy. Also, the Trans-Mediterranean Energy Cooperation (TREC) is working on the vision that vast amounts of clean power can be generated in the Saharan desert using Concentrated Solar Power (CSP) technology and transmitted throughout Europe using a grid of HVDC lines.

To keep pace with such unprecedented level of interest in the HVDC transmission technology, both a power flow computer program and an Optimal Power Flow computer program are developed further to encompass comprehensive and reliable models of HVDC-LCC transmission schemes. This would enable thorough assessments of security and economic operation of transmission schemes such as these. The model of the HVDC-LCC-link takes due account of overlapping effects and power transfer control characteristics.

In both application programs the solution algorithms are Newton methods. The equations representing the converter operation are included directly in the Jacobian matrix for the case of conventional power flows, using the so called DC elimination method [6]. In the OPF solution, the converter equations are included directly in matrix W and in the gradient vector of Newton's method [7], with the multipliers method [8] used to handle all inequality constraints to variables. This combination leads to highly efficient solutions of AC-DC power systems, including FACTS controllers. The impact of HVDC links in conventional power flow and OPF studies is illustrated by numerical examples, which includes a contrived five-bus test network and a utility-size network of 2172 buses [9].

II. HVDC-LCC-LINKS

HVDC-links may be configured in a number of ways. In order of increasing complexity, the simplest is the back-to-back link in which the two converters are located in the same site, with no DC line involved. This application is also known as zero-distance HVDC. Next in complexity are point-to-point applications where an actual DC line connects the two converter stations. Other more complex configurations are possible, such as multi-terminal links and series connections.

Without being exhaustive, two variants of the point-to-point HVDC configuration emerge, the mono-polar link and the bipolar link. In the former, the two converters are joined by a single metallic conductor, and earth or the sea is used as the returning path, requiring two full rated electrodes. The latter configuration is shown in Fig. 1 and may be thought as consisting of two symmetric mono-polar links but one operating at positive potential and the other at negative potential, with respect to ground (middle). Notice that the HVDC-LCC converters and DC lines, transformers and other ancillary devices such as tuned filters and capacitor banks and smoothing reactors are also shown in Fig. 1.

The core component of any HVDC-LCC converter is the thyristor valve, used to perform the actual conversion from AC to DC and vice-versa. Such a conversion process is far from ideal and comes accompanied by the generation of harmonic currents in the AC side and harmonic voltages in the DC side of the converter. Assuming perfect valve firing sequences and balanced three-phase voltages and currents in the AC sides of the converters then their periodic steady-state operation will contain only the characteristic harmonics.

To a greater or lesser extent this optimistic operating scenario is not far from what is achieved today with modern power semiconductor valves and control method. Tuned harmonic filters are used to filter out the characteristic harmonics, ensuring sinusoidal voltages and currents in the AC side of the converters. Filters are used in the DC side together with smoothing reactors to ensure a reasonably flat voltage and current profile in the DC side. Further functions of

the smoothing reactor are to prevent resonances in the DC circuit and to limit telephone interference.

The converter stations are connected to the AC buses by means of converter transformers, which scale-down the voltage of the grid to the required entry voltage of the converter. The converter transformers are equipped with an on-load tap-changing mechanism.

The reactive power consumption of an HVDC converter is a function of active power, transformer reactances and control

angles – it increases with increasing active power. Full reactive power compensation is a standard requirement in a converter station, with part of the reactive power produced by filters and the rest by shunt capacitor banks or synchronous condensers if dynamic compensation is deemed necessary.

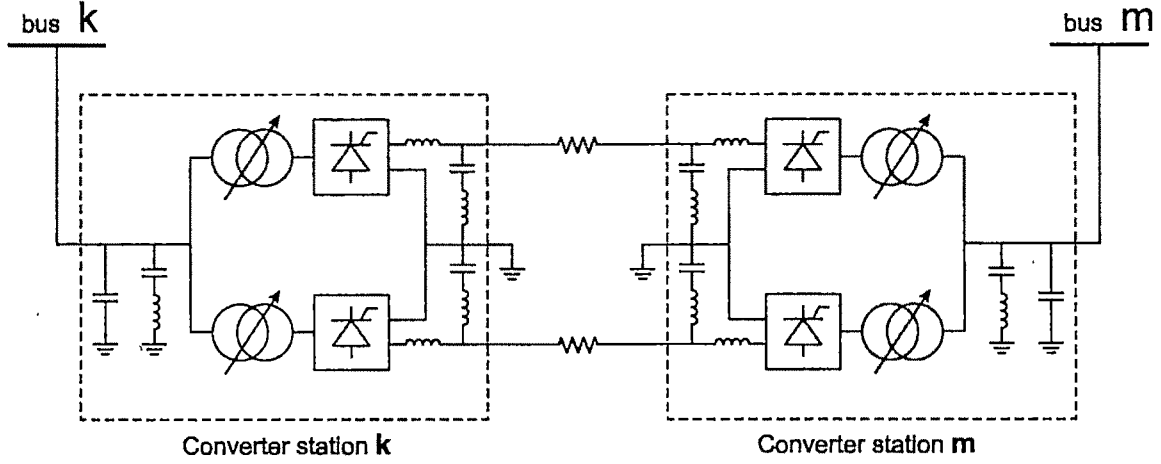


Fig1: HVDC-LCC bipolar transmission scheme

III. HVDC-LINK POWER EQUATIONS

Assuming perfect symmetric conditions in the AC circuit and converter transformers; equidistant converter valve firings and perfect filtering in both the AC and DC circuits, the steady-state, fundamental frequency operation of a mono-polar HVDC link, such as the one operating at positive potential in Fig. 1, may be described by the following set of equations:

$$V_{dR1} - V_{dI1} - R_d I_d = 0 \quad (1)$$

$$V_{dR1} = \left(\frac{3\sqrt{2}}{\pi} a_k V_k \cos \alpha - \frac{3}{\pi} X_{cR} I_d \right) N_R \quad (2)$$

$$V_{dI1} = \left(\frac{3\sqrt{2}}{\pi} a_m V_m \cos \gamma - \frac{3}{\pi} X_{cI} I_d \right) N_I \quad (3)$$

where V_{dR1} and V_{dI1} are the voltage magnitudes at the DC terminals of the rectifier and inverter stations operating at positive potential, respectively. α is the firing angle for rectifier operation and γ is the extinction angle for inverter operation. V_k and V_m are the effective voltage magnitudes at the AC terminals of converter transformers. I_d is the current in the DC circuit. X_{cR} and X_{cI} are the commutation reactances in the rectifier and inverter stations, respectively. N_R and N_I are the number of series connected bridges in the rectifier and converter stations, respectively. Notice that symmetry is assumed in transformer parameters and valve firing which is amenable to a single value of current I_d .

In a six-pulse converter $N_R = N_I = 1$ and the valves fire at 60° intervals. In a twelve-pulse converter $N_R = N_I = 2$ and the interval is 30° . The DC voltage V_{dR1} is made up of two terms, the open-circuit voltage and an equivalent voltage drop due introduced by the commutation effects. The same applies to the DC voltage V_{dI1} . The resistances of the transformer converters are neglected and the transformer short-circuit reactances are taken to be the commutation reactances.

Assuming six-pulse converters ($N_R = N_I = 1$), the powers of the DC link are given by,

$$P_{dR} = P_{dR1} + P_{dR2} = V_{dR} I_d \quad (4)$$

$$P_{dI} = P_{dI1} + P_{dI2} = V_{dI} I_d \quad (5)$$

where $V_{dR} = V_{dR1} + V_{dR2}$ and $V_{dI} = V_{dI1} + V_{dI2}$.

Powers on the AC side, using positive sequence representation, employing the transformation from three-phase to positive sequence with invariant voltages, invariant currents and variant powers, the active powers absorbed from buses k and m are:

$$P_k = \frac{P_{dR}}{3} \quad (6)$$

$$P_m = \frac{P_{dI}}{3} \quad (7)$$

The complex power consumed by the two converter stations, including the transformers, is given by:

$$S_i = \frac{a_i V_i I_{Ri}}{\sqrt{3}} = \frac{a_i V_i k_i I_d}{\sqrt{3}} \quad (8)$$

$$S_m = \frac{a_m V_m I_{Rm}}{\sqrt{3}} = \frac{a_m V_m k_m I_d}{\sqrt{3}} \quad (9)$$

$$Q_i = \sqrt{\frac{(a_i V_i k_i I_d)^2}{3}} - P_i^2 \quad (10)$$

$$Q_m = \sqrt{\frac{(a_m V_m k_m I_d)^2}{3}} - P_m^2 \quad (11)$$

where $k_R = k \frac{\sqrt{6}}{\pi}$; $k_I = k' \frac{\sqrt{6}}{\pi}$ and

$$k = \frac{\sqrt{(\cos 2\alpha - \cos 2(\alpha + \mu))^2 + (2\mu + \sin 2\alpha - \sin 2(\alpha + \mu))^2}}{4(\cos \alpha - \cos(\alpha + \mu))}$$

with k' having the same expression as k but with γ replacing the firing angle α . For most practical power flow situations, both k and k' are very close to 1 and can be assumed to be constant. A recommended value to use is 0.995.

IV. AC-DC POWER FLOWS USING THE NEWTON-RAPHSON METHOD

AC power flows using the Newton-Raphson method

The steady-state operation of a symmetrical, three-phase AC electrical power network comprising n buses is well described by $2(n-1)$ set of non-linear algebraic equations relating nodal powers to nodal voltages:

$$\begin{aligned} P &= f_P(V, \theta) \\ Q &= f_Q(V, \theta) \end{aligned} \quad (12)$$

where P and Q are nodal active and reactive powers, V and θ are nodal voltage magnitudes and phase angles and f_P and f_Q are non-linear functions.

The set of equations (12) is solved very reliably by iteration using the Newton-Raphson method, which involves solving repeatedly the following linearised equation:

$$\begin{bmatrix} \Delta P \\ \Delta Q \end{bmatrix} = \begin{bmatrix} H & N \\ J & L \end{bmatrix} \begin{bmatrix} \Delta \theta \\ \Delta V \end{bmatrix} \quad (13)$$

where $\Delta P = P_G - P_L - P_{cal}$ and $\Delta Q = Q_G - Q_L - Q_{cal}$ are vectors of mismatch active and reactive powers. P_G and Q_G are vectors of specified active and reactive power generations. P_L and Q_L

are vectors of specified active and reactive powers consumed by loads. P_{cal} and Q_{cal} are vectors of calculated active and reactive powers, using eqs. (12). H , N , J , L are matrices of first order partial derivatives of the nodal power equations P and Q in (12) with respect to θ and V . The four matrix elements make up the so called Jacobian matrix.

For an n -bus network, the order of (13) is $n-1$ because the reference bus, i.e. slack bus, does not form part of the iterative solution. Upon convergence of the iterative solution the calculated powers P_{cal} and Q_{cal} match those of the net power ($P_G - P_L$) and ($Q_G - Q_L$) and, hence, the mismatches ΔP and ΔQ become zero, i.e. smaller than a pre-specified tolerance, and the iterative process is terminated.

HVDC operating modes

As indicated by eqs. (4)-(5), the power through the DC link can be regulated by varying the DC voltages, this as a result of varying either the transformers taps or the converters control angles – refer to eqs. (2)-(3). An increase in the control angle is amenable to a decrease in DC voltage, an increase in reactive power consumption (since the current will lag the voltage) and an increase in harmonic generation. Such issues are clearly undesirable and provide an incentive for keeping the control angles at relatively low values.

There are several modes of operation in converter control. In the so called control mode A, the control angles α and γ and V_{di} and P_{di} are specified. The converter transformer taps are varied in order to meet such specifications. In control mode B, γ is kept at its lower value and the transformers taps and P_{di} are specified. The power is regulated by varying the firing angle α . This is a preferred control mode since the tap changer response is far slower than that of the firing angle. In control mode C, α is kept at its minimum value and γ is regulated to maintain constant power. It should be remarked that if the current I_d is kept constant instead of the power P_{di} , three other control modes may be defined

In control mode A, the power and the voltage at the inverter (P_{di} and V_{di}) are held constant with specified control angles enabling the direct calculation of I_d , V_{dR} and P_{dR} :

$$I_d = P_{di} / V_{di}; V_{dR} = V_{di} + R_d I_d; P_{dR} = V_{dR} I_d$$

Using this information in (2) and (3), for the case of a six-pulse bridge, the commutation voltages $a_k V_k$ and $a_m V_m$ can be obtained:

$$c_1 = a_k V_k = \frac{\frac{\pi}{3} V_{dR} + X_c I_d}{\sqrt{2} \cos \alpha} \quad (15)$$

$$c_2 = a_m V_m = \frac{\frac{\pi}{3} V_{di} + X_c I_d}{\sqrt{2} \cos \gamma} \quad (16)$$

It is important to recognize that both c_1 and c_2 are constants which can be computed from system data and specified information – they are not dependent on V_k and V_m . Since the transformers and converter valves are assumed to contain no resistance, the power equations for control mode A, are:

$$P_k = \frac{V_k I_d}{3} \quad (17)$$

$$P_m = -\frac{P_d^{per}}{3} \quad (18)$$

$$Q_k = \sqrt{\frac{(c_1 k I_d)^2}{3} - P_k^2} \quad (19)$$

$$Q_m = \sqrt{\frac{(c_2 k I_d)^2}{3} - P_m^2} \quad (20)$$

The active power carried by the DC link and the reactive powers consumed by the two converters may be interpreted as an equivalent load and generator. In a power flow solution, the equivalent load and generation will remain constant – it will not change as the solution moves from iteration to the next because P_k , Q_k , P_m and Q_m are independent of V_k and V_m . Upon convergence, the transformer taps are calculated:

$$a_k = \frac{c_1}{V_k} \quad \text{and} \quad a_m = \frac{c_2}{V_m} \quad (21)$$

In control mode B, the power at the inverter is kept constant with minimum extinction angle and constant tap changers. An expression for the current I_d may be derived by combining (3) and (5),

$$I_d = c_1 V_m - \sqrt{c_1^2 V_m^2 - c_2 P_d} \quad (22)$$

$$\text{where } c_1 = \frac{a_m \cos \gamma}{\sqrt{2} X_{d1}} \quad \text{and} \quad c_2 = \frac{\pi}{3 X_{d1}}$$

The power equations in control mode B, are:

$$P_k = \frac{P_d^{per} + R_d I_d^2}{3} \quad (23)$$

$$P_m = -\frac{P_d^{per}}{3} \quad (24)$$

$$Q_k = \sqrt{\frac{(a_k V_k k I_d)^2}{3} - P_k^2} \quad (25)$$

$$Q_m = \sqrt{\frac{(a_m V_m k I_d)^2}{3} - P_m^2} \quad (26)$$

In control mode C, the power at the inverter is kept constant with minimum firing angle and constant tap changers. Similarly to control node B, an expression for the current I_d is

derived and then the power equations (23)-(26) will apply with no change. Combining (1), (2) and (5), yields:

$$I_d = c_1 V_k - \sqrt{c_1^2 V_k^2 - c_2 P_d} \quad (27)$$

$$\text{where } c_1 = \frac{a_m \cos \alpha}{\sqrt{2} \left(X_{m1} + \frac{\pi}{3} R_d \right)} \quad \text{and} \quad c_2 = \frac{1}{\frac{3}{\pi} X_{m1} + R_d}$$

AC-DC power flows using the Newton-Raphson method

There are various methods for solving the power flow equations of AC-DC systems. Arguably, the eliminated variables method is the simplest. The basic idea in this method is to treat the converter stations as voltage-dependent loads as seen from the AC bus terminals. The DC equations are solved analytically and the DC variables are eliminated from the power flow equations.

In control mode A, the active and reactive powers consumed by the DC-link are pre-computed whereas in the other two control modes, the powers consumed by the DC-link are re-calculated at each iterative step of the Newton-Raphson algorithm.

If the HVDC link is connected between buses k and m , eq. (13) modifies to the following:

$$\begin{bmatrix} \Delta P \\ \Delta P_k \\ \Delta P_m \\ \Delta Q \\ \Delta Q_k \\ \Delta Q_m \end{bmatrix} = \begin{bmatrix} & & & & & \\ & \text{H} & & \text{N} & & \\ & & & & & \\ & & & & & \\ & & & & & \\ & & \text{J} & & \text{L} & \end{bmatrix} \begin{bmatrix} \Delta \theta \\ \Delta \theta_k \\ \Delta \theta_m \\ \Delta V \\ \Delta V_k \\ \Delta V_m \end{bmatrix} \quad (28)$$

where P , Q , θ and V refer to all network buses but not to those of the converter terminals subscripted k and m , which are shown explicitly. In principle, the following primed elements of the Jacobian change due to the contribution of the DC-link:

$$N_k = N_k + V_k \partial P_k / \partial V_k$$

$$N_m = N_m + V_m \partial P_m / \partial V_m$$

$$N'_k = N_k + V_k \partial P_m / \partial V_k$$

$$N'_m = N_m + V_m \partial P_k / \partial V_m$$

$$L_k = L_k + V_k \partial Q_k / \partial V_k$$

$$L_m = L_m + V_m \partial Q_m / \partial V_m$$

$$L'_k = L_k + V_k \partial Q_m / \partial V_k$$

$$L'_m = L_m + V_m \partial Q_k / \partial V_m$$

with N_k , N_m , N'_k , N'_m , L_k , L_m , L'_k and L'_m referring to the corresponding original components of the Jacobian. The power terms derived in Section 4.2 for P_k , Q_k , P_m and Q_m for control modes A, B and C are used to obtain the modified Jacobian entries described above. Each control mode yields its own set of modified Jacobian entries, several of which take zero values.

V. AC-DC OPTIMAL POWER FLOWS USING NEWTON'S METHOD

Optimal power flows present power systems engineers with a far more powerful solution and analysis tool than that afforded by conventional power flows, for the determination of the equilibrium point of a symmetrical, three-phase AC electrical power network. In contrast to a conventional power flow, the prowess of the optimal power flow solution is its ability to find a set of system operational parameters that minimize a pre-established "cost" function of the system, such as the generator fuel costs, transmission power losses or reactive power production/absorption. Besides, the optimal power solution takes due account of equipment ratings and network operational constraints.

The optimization task selected in this section is the minimization of active power generation cost by the adjustment of suitable control parameters in both the AC and the DC circuits of the network. In general, in this OPF problem, the following formulation applies:

$$\begin{aligned} &\text{Minimize } f(P_G) \\ &\text{subject to } h(P_G, V, \theta, a, \alpha, \gamma, V_{dr}, V_{dl}) = 0 \\ &\quad g(P_G, V, \theta, a, \alpha, \gamma, V_{dr}, V_{dl}) \leq 0 \end{aligned} \quad (29)$$

where P_G , V and θ are the active power generation, node voltage magnitudes and phase angles, respectively. Moreover, a , α , V_{dr} and V_{dl} are associated with the HVDC link and are said to be the DC state variables. They are the tap of the converter transformers, the converters firing and extinction angles, the voltages at the DC buses at each end of the DC line. The function $f(P_G)$ is the objective to be optimized, $h(P_G, V, \theta, a, \alpha, \gamma, V_{dr}, V_{dl})$ represents the power flow equations, including the DC circuit, and $g(P_G, V, \theta, a, \alpha, \gamma, V_{dr}, V_{dl})$ represents the state variable limits as well as functional constraints.

The constrained optimization problem stated in (29) is converted into an unconstrained one by forming an augmented Lagrange function:

$$L(\mathbf{x}, \boldsymbol{\lambda}) = f(P_G) + \boldsymbol{\lambda}^T h(P_G, V, \theta, a, \alpha, \gamma, V_{dr}, V_{dl}) \quad (30)$$

where \mathbf{x} is vector of state variables and $\boldsymbol{\lambda}$ is the Lagrange multiplier vector for equality constraints. The inequality constraints are not incorporated at this stage because they are only included when there are variables outside limits.

A. Lagrange function for the HVDC link

Incorporation of the HVDC equations in the Newton OPF algorithm increases the dimensions of matrix W by eight rows and eight columns per HVDC link in the AC-DC network. Moreover, if the HVDC link is set to regulate active power flow then matrix W is further augmented by one row and one column. Under this operating condition six extra state variables enter in the OPF formulation. Furthermore, three Lagrange multipliers are also used to incorporate the various equality constraints. The solution process satisfies the optimality conditions as given by Kuhn and Tucker.

Eqs. (1)-(8) and (11) are explicitly modeled in the Lagrange function as an equality constraint given by the following equation:

$$\begin{aligned} L_{dc}(\mathbf{x}, \boldsymbol{\lambda}) = & \lambda_r \left[V_{dr} - \left(\frac{3\sqrt{2}}{\pi} a_r V_{dr} \cos \alpha_r - \frac{3}{\pi} X_{tr} \left(\frac{V_{dr} - V_{dl}}{R_{dc}} \right) \right) V_{tr} \right] \\ & + \lambda_l \left[V_{dl} - \left(\frac{3\sqrt{2}}{\pi} a_l V_{dl} \cos \alpha_l - \frac{3}{\pi} X_{tr} \left(\frac{V_{dr} - V_{dl}}{R_{dc}} \right) \right) V_{tr} \right] \\ & + \lambda_{pr} (\Delta P_r) + \lambda_{vr} (\Delta Q_r) + \lambda_{pl} (\Delta P_l) + \lambda_{vl} (\Delta Q_l) \end{aligned} \quad (31)$$

where λ_r , λ_l , λ_{pr} , λ_{vr} , λ_{pl} and λ_{vl} are Lagrange multipliers at the AC nodes where the rectifier and inverter transformers connect, respectively. Also, λ_{pr} , λ_{vr} , λ_{pl} and λ_{vl} are the multipliers of the Lagrange function of the active and reactive power mismatch equations. Vectors \mathbf{x} and $\boldsymbol{\lambda}$ contain the following set of DC variables:

$$\begin{aligned} \mathbf{x} = & [a_r \quad V_{dr} \quad \cos \alpha_r \quad a_l \quad V_{dl} \quad \cos \alpha_l] \\ \boldsymbol{\lambda} = & [\lambda_r \quad \lambda_l] \end{aligned} \quad (32)$$

By way of example, the Lagrange functions at the terminal dR of the rectifier station are given by

$$\begin{aligned} \lambda_{pr} (\Delta P_r) = & \lambda_{pr} (P_r(V, \theta) + P_{lr} - P_{ar} + P_{dr}(x)) \\ \lambda_{vr} (\Delta Q_r) = & \lambda_{vr} (Q_r(V, \theta) + Q_{lr} - Q_{ar} + Q_{dr}(x)) \end{aligned} \quad (33)$$

where $P_r(V, \theta)$ and $Q_r(V, \theta)$ are the calculated active and reactive power injections at node k . P_{lr} and Q_{lr} are active and reactive power loads at node k . P_{ar} and Q_{ar} are scheduled active and reactive power generations at node k , respectively. Also, $P_{dr}(x)$ and $Q_{dr}(x)$ are the active and reactive powers at the DC side of the converter rectifier.

B. HVDC link loading

Line current regulation in the DC line may be represented in OPF formulations by using an equality constraint which remains active throughout the iterative process, unless one expressly wishes to deactivate the constraint. The following equation represents this operating condition:

$$L_{dc}(\mathbf{x}, \boldsymbol{\lambda}) = \lambda_{rl} \left(\frac{V_{dr} - V_{dl}}{R_{dc}} - I_0 \right) \quad (34)$$

where λ_{rl} is the Lagrange multiplier associated with the direct current flowing from the rectifier station to the inverter station. I_0 is the target value of direct current to be maintained across the DC link.

The Lagrange function of the HVDC link comprising the individual contributions presented above is:

$$L_{HVDC}(\mathbf{x}, \boldsymbol{\lambda}) = L_{rl}(\mathbf{x}, \boldsymbol{\lambda}) + L_{rc}(\mathbf{x}, \boldsymbol{\lambda}) \quad (35)$$

C. Linearised system of equations

The linearised equation for minimizing the Lagrange function using Newton's method is:

$$\begin{bmatrix} W_{11} & 0 & W_{13} & W_{14} & 0 \\ 0 & W_{22} & W_{23} & W_{24} & 0 \\ W_{31} & W_{32} & W_{33} & W_{34} & W_{35} \\ W_{41} & W_{42} & W_{43} & W_{44} & W_{45} \\ 0 & 0 & W_{53} & W_{54} & 0 \end{bmatrix} \begin{bmatrix} \Delta z_1 \\ \Delta z_2 \\ \Delta z_3 \\ \Delta z_4 \\ \Delta z_5 \end{bmatrix} = - \begin{bmatrix} g_1 \\ g_2 \\ g_3 \\ g_4 \\ g_5 \end{bmatrix} \quad (36)$$

where matrices W_{ij} contain second partial derivatives of the Lagrange function $L(x, \lambda)$ with respect to state variables x and Lagrange multiplier λ . The terms g_i are vectors of first partial derivatives. The terms Δz_i are vectors of increments obtained at the end of a given iteration. Subscripts i and j take values from 1 to 5, respectively.

D. Handling limits of HVDC link

Limits are enforced using the Multipliers method. The generic function given below for dR is used to handle the HVDC link inequality constraints, where a penalty term, involving the violated limit, is added to the Lagrange function $L(x, \lambda)$. Variables inside limits are ignored. The checking of limits is started at the second iteration.

$$\psi^{(n)}(V_{dc}^{(n)}, \mu^{(n)}) = \begin{cases} \mu^{(n)}(V_{dc}^{(n)} - V_{dc}^{max}) + \frac{c}{2}(V_{dc}^{(n)} - V_{dc}^{max})^2 & \text{if } \mu^{(n)} + c(V_{dc}^{(n)} - V_{dc}^{max}) \geq 0 \\ \mu^{(n)}(V_{dc}^{(n)} - V_{dc}^{min}) + \frac{c}{2}(V_{dc}^{(n)} - V_{dc}^{min})^2 & \text{if } \mu^{(n)} + c(V_{dc}^{(n)} - V_{dc}^{min}) \geq 0 \\ 0 & \text{otherwise} \end{cases} \quad (37)$$

E. Initial conditions of HVDC link

Good initial conditions are required for the HVDC links in order to ensure smooth iterative OPF solutions.

Nodal voltage magnitudes of 1 pu for V_{dr} and V_{di} are selected and used in eqs. (1) and (2) to obtain starting voltage values for V_{dr} and V_{di} . The initial tap positions of the converter transformer are set at 1.

The HVDC Lagrange multipliers λ_R and λ_I are initialized at 0, yielding robust iterative solutions.

It is stated in [2] that rectifier stations have typical firing angles α in the range 14° - 16° and minimum values in the range of 5° - 7° . For the inverter station the range for the extinction angle γ is 15° - 18° and the maximum value will not exceed 22° . In the OPF solution, initial values of $\alpha = 15^\circ$ and $\gamma = 18^\circ$ have been chosen, yielding robust iterative solutions.

VI. HVDC-LCC TEST CASES

To show the applicability of the proposed approaches, the five-bus network shown in Fig.2 is used. All the necessary data to carry out an AC power flow solution is taken from [10].

In this test case the transmission line connected between Lake and Main in Fig. 2, is replaced by a mono-polar HVDC link, with the data given in Table I.

The HVDC link is made to operate in control mode A. The nodal voltage magnitudes and phase angles for the five buses are given in table II while the power flows are shown in Fig. 3.

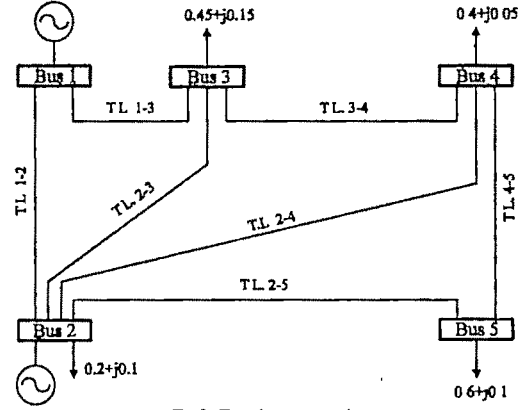


Fig2 Five-bus network

A. Power flow solution for the five-bus test network

Transformer reactances	0.051 pu
DC link resistance	0.10 pu
Rectifier firing angle	15 deg
Inverter extinction angle	18 deg
Transmitted power	0.40 pu

Table 1: HVDC link data.

Name	Voltage (%)	Angle (deg)
North	106	0
South	100	-1.8126
Lake	96.10	-5.5998
Main	96.34	-2.6911
Elm	96.48	-4.8845

Table 2: Bus voltages

Flow results, notice that the DC line has a 1.2 MW power loss and that both converters consume a total of 36.7 MVAR, which are contributed by the generator connected at North since no local provisions were made to supply the required reactive power demanded by the HVDC converters.

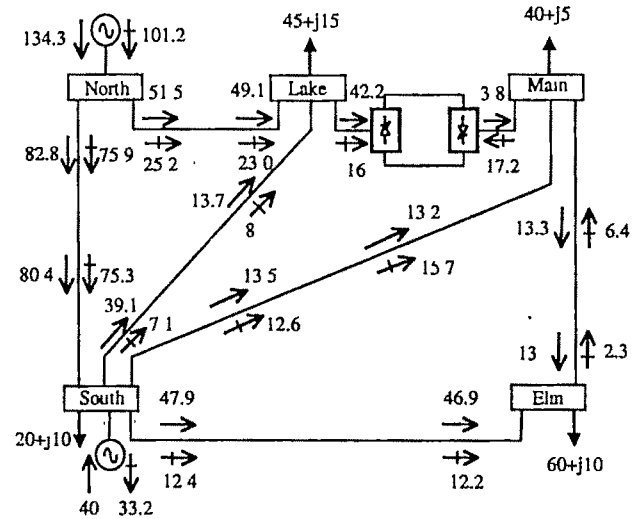


Fig3: Power flow solution of the five-bus network with a mono-polar HVDC link

B. Optimal Power flow solution for the five-bus test network

The five-bus test network is now used to carry out an optimal power flow solution, with minimum generation fuel cost and minimum transmission power loss. The generator fuel costs are taken to be quadratic functions with coefficients given in Table 3.

Bus	Cost Coefficients		
	A (\$/hr)	b (\$/MW-hr)	c (\$/MW ² -hr)
South	60.0	3.40	0.0040
North	60.0	3.40	0.0040

Table 3: Fuel cost coefficients

Upper and lower limits of active and reactive powers of the two generators are given in Table 4, with the DC link impedance values given in Table 5 and the control parameter limits given in Table 6.

Bus	Active Power Limits		Reactive Power Limits	
	Min (MW)	Max (MW)	Min (MVAR)	Max (MVAR)
South	60.0	3.40	-300	300
North	60.0	3.40	-300	300

Table 4: Fuel cost coefficients

	Rectifier (Lake)	Inverter (Main)
Commutation reactance	0.01260 pu	0.00728 pu
DC-link resistance	0.00334 pu	

Table 5: DC-link impedance parameters

DC Variables	Limits	
	Min	Max
V_{dR}	1.0 pu	1.50 pu
a_L	0.90	1.10
α	10°	20°
V_{dI}	1.0 pu	1.50 pu
a_m	0.90	1.10
γ	15°	25°

Table 6: DC-link control parameter limits

The active power flow through the HVDC link is 13.716 MW. The power flow results are shown in Fig. 4, and the active and reactive power at the converters are given in Table 7. The nodal voltages and Lagrange multipliers are given in Table 8.

C. Optimal power flow solution of a large-scale power network

A utility power network consisting of 2172 buses, 2294

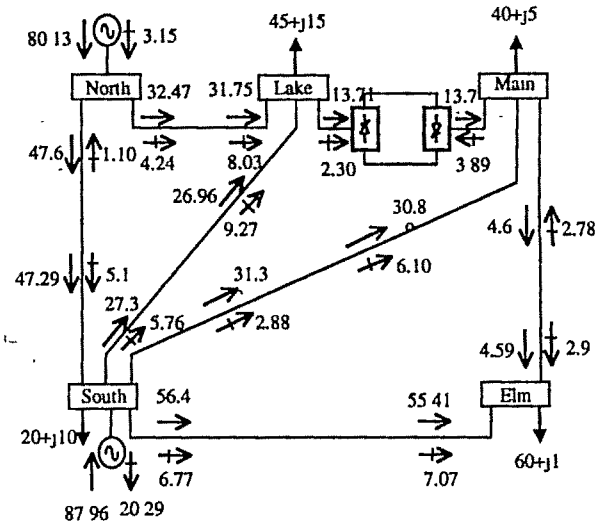


Fig4: Optimal power flow solution of the five-bus network with a monopolar HVDC link.

DC Quantities				
P_{dR} (MW)	Q_{dR} (MVAR)	P_{dI} (MW)	Q_{dI} (MVAR)	I_d (pu)
13.716	2.304	13.712	3.895	0.102

Table 7: DC-link powers and current

Bus	Voltage Magnitude (pu)	Voltage Phase Angle (deg)	λ_p (\$/MW-hr)
Elm	1.071	-4.447	4.2656
Main	1.075	-3.901	4.2378
Lake	1.071	-3.472	4.2225
South	1.100	-1.318	4.1036
North	1.109	0	4.0410

Table 8: Nodal voltages and Lagrange multipliers

transmission lines, 768 transformers, 579 generators, 1259 loads, 208 shunt compensators and 10 series capacitors, is used to carry out an optimal power flow solution. For the purpose of the simulation study, the following assumptions are made on the actual power network: out of the 579 generators, 201 are considered for economic dispatch; twelve of the 768 transformers are assumed to be phase-shifting transformers; and the ten series capacitors are assumed to be Thyristor Controlled Series Compensators (TCSC). Moreover, five Unified Power Flow Controllers (UPFC), one HVDC-link and four additional TCSCs are assumed to exist in the utility power network.

The HVDC-link, five UPFCs and fourteen TCSCs are used to maintain specified active powers along pre-determined transmission paths, increasing the power transfer by more than 10%, with respect to the non-upgraded FACTS network. The shunt converters of the five UPFC are also used to regulate nodal voltage magnitudes at 1 pu at their connecting buses. The FACTS controllers are placed in the high-voltage side of the network, i.e. 230 and 400 kV.

The optimal power flow solution of the non-upgraded FACTS network converges in nine iterations whereas that of the upgraded network does it in 10 iterations. All the various controllable devices uphold their target values. Table 9 summarizes the solutions for this test system.

Results	OPF Solutions	
	Non-upgraded	Upgraded
Active power load (MW)	19718.3	19718.3
Reactive power load (MVAR)	6487.59	6487.59
Active power generation cost (\$/MW-hr)	5179.02	5215.36
Active power losses (MW)	763.654	692.557
Active power generation (MW)	20482	20410.9
Reactive power generation (MVAR)	796.945	728.417

Table 9: Summary of power flow solutions for the 2172-bus system

The FACTS controllers and HVDC-link have an overall positive effect in the operation of this test system – they are amenable to lower transmission losses and, as a consequence, to lower levels of active and reactive power generation. However, it should be noticed that the FACTS upgraded case yields higher generation costs than the base case – the reason is that the UPFCs are being used to regulate voltage magnitudes at 1 pu at their shunt buses and the optimization algorithm has less degrees of freedom to attempt a “better” solution.

VII. CONCLUSIONS

An efficient and versatile AC-DC model, based on expressions derived from the DC-link line commutated control scheme, is used to assess the steady-state response of AC power networks containing HVDC-LCC-links. All the relevant variables of the HVDC-LCC-link are combined with the nodal voltage magnitudes and phase angles of the AC power network in a single frame-of-reference for unified iterative solutions using Newton's method. The DC-link model is suitable for direct implementation in a Newton-Raphson power flow computer algorithm using unified solutions of the AC and DC variables, resulting in iterative solutions with strong convergence. However, this is not an extended variables method since the Jacobian dimensions are not increased and no DC variables are added to the solution vector, leading to overall efficient solutions. Equations are derived for various HVDC control modes and a simple numerical example is presented to illustrate the applicability of the approach.

Moreover, the AC-DC model is also suitable for direct implementation in an optimal power flow algorithm using Newton's method. Contrary to the conventional power flow solution, the HVDC OPF algorithm is not a DC elimination method because matrix W and the gradient vector need to be extended to accommodate explicitly the DC variables, but is it a unified method, leading to very robust optimal solutions. In contrast too to the conventional power flow solution, it is not a pre-condition in the implemented HVDC OPF algorithm to specify the operating control mode of the DC-link in order to determine the optimum set for the control variables. The DC variables are regulated in order to achieve an optimal level of DC current under either condition, constrained or unconstrained current through the DC-link. The usefulness of the OPF HVDC-link algorithm is illustrated by means of numerical examples. The same constrained network used for conventional power flows is used for the optimal power flow solution, enabling comparisons between the two solution approaches. To show a practical application of the OPF algorithm, a utility-size power network is solved for two different cases: the power network with no electronic control; and the power network where an HVDC-link and nineteen FACTS controllers are assumed to have been installed – comparisons between the two optimal solutions are presented.

ACKNOWLEDGMENT

The author gratefully acknowledges the research work on HVDC-LCC-link modelling carried out by his former students: Dr. Hugo Ambriz-Pérez from CFE, México and Mr. Federico Coffele from ABB, Italy.

REFERENCES

- [1] J. Arrillaga et al, *Flexible Power Transmission*, John Wiley & Sons, 2007
- [2] H. Ambriz-Pérez et al, “High Voltage Direct Current Modelling in Optimal Power Flows”, *International Journal of Electrical Power & Energy Systems*, In Press, Corrected Proof, Available online 8 August 2007
- [3] A. Pizano-Martinez et al, “Modelling of VSC-Based HVDC Systems for a Newton-Raphson OPF Algorithm”, *IEEE Trans. on Power Systems*, vol. 22, no. 4, pp. 1794-1803, Nov 2007
- [4] L. Carlsson, “Classical HVDC. Still continuing to evolve”, *Modern Power Systems, MPS Review transmission & Distribution*, pp. 19-21, June 2002
- [5] G. Asplund et al, “DC Transmission Based on Voltage Source Converters”, *CIGRE SC-14*, No 14-302, Paris, 1998
- [6] T. Smed et al, “A New Approach to AC/DC Power Flow”, *IEEE Trans. on Power Systems*, vol. 6, no. 3, pp. 1238-1244, Aug. 1991
- [7] D.I. Sun et al, “Optimal Power Flow By Newton Approach”, *IEEE Trans. on Power Apparatus and Systems*, vol. PAS-103, no. 10, pp. 2864-2880, Oct. 1984
- [8] D.P. Bertsekas, *Constrained Optimization Lagrange Multiplier Methods*, Academic Press, 1992
- [9] F. Aboytes and G. Arroyo, “Security Assessment In the Operation of Longitudinal Power Systems”, *IEEE Trans. on Power Apparatus and Systems*, vol. PWR-1, no. 2, May 1986, pp 225-232
- [10] E. Acha et al, *FACTS, Modelling and Simulation in Power Networks*, John Wiley & Sons, 2004

Indian Electricity Sector

D Sanyal

Energy Auditor and Consultant, Kolkata, India

Abstract—Historically responsibility of the electricity supply in India was shared constitutionally between the central government and the states. The Electricity Act 1910 provided the initial legal framework that governed the operations of licensees. Along with the Electricity Act 1910 the Electricity (Supply) Act of 1948 provided the overall regulatory framework for the sector, which empowered the Central Electricity Authority (CEA) to develop a national power policy that included the responsibility of planning, coordinating and regulating sector development. The 1948 Act also empowered the central government (Ministry of Power) to make rules for carrying out CEA's objectives by means of notification in the official gazette. The 1948 Act created the State Electricity Boards and entrusted them with primary responsibility for public power supply as well as for related state level regulation.

1. INTRODUCTION

The boards were envisioned as largely self-governing entities empowered to set tariffs and monitor licensees. But after the Industrial Policy Resolution of 1956 defined the aspects of generation and distribution that became the exclusive responsibility of the states, consequently the once significant role of private utilities gradually diminished. At the time of independence private utilities and licensed local authorities together provided the major percent of India's public electricity supply. But when their licenses expired, most licensees were taken over by the SEBs, in line with the 1956 Industrial Policy Resolution. Only six of the private utilities originally licensed under the 1910 Electricity Act remained; Bombay Suburban Electric Supply (BSES) and Tata Electric Companies (TEC) in Bombay, Ahmedabad Electric Company (AEC) and Surat Electric Company in Gujarat, Calcutta Electric Supply Company (CESC) and Dishergarh Power Supply Company in West Bengal. Since 1970s the Government of India had been actively involved in power development in India to complement the efforts of the states. The Government owns several generating companies including National Thermal Power Corporation (NTPC) and the National Hydroelectric Power Corporation (NHPC). The Government also owns India's national transmission company and the grid operator, the Power Grid Corporation of India. These utilities were incorporated under the companies Act.

The Ministry of Power (MOP) approved tariff-setting principles for the centrally owned entities. Tariff proposals were received by the Central Electricity Authority, which then sent them to the MOP for notification. Tariffs were determined on a cost of service basis and were subject to basic performance standards. The utilities financial viability was ensured to the extent that their tariff revenues covered operational costs, including debt service. The Government of India also owned and still owns two power sector financial intermediaries, the Power Finance Corporation and Rural Electrification Corporation.

The states owned the SEBs and State Generating Companies, which together generate almost 70 percent of India's electricity, supply and provided most of the distribution to consumers. The 1948 Act explicitly required the SEBs to operate in the most efficient and economical manner and mandated that they adjust their tariffs to achieve a minimum return, after interest, of 3 percent on net fixed assets in operation. The Act, however allowed a state to specify a higher return target for its SEB than statutory minimum return. Further, it specified that interest on loans from the state governments were to be paid by the SEBs only after meeting the minimum return. States were in fact required to provide subsidies to help the SEBs meet the minimum return requirement by compensating the SEBs inter-alia for low tariffs to residential consumers and for using the SEBs as administratively convenient vehicles for agricultural input subsidies. For most SEBs meeting the statutory 3 percent after interest return would cover operating costs and debt service provided state government subsidies were fully paid on time and bill collection were reasonable. Because of their poor operational performance, low tariff and inadequate subsidies however most SEBs did not reach the Act's statutory minimum returns. Their aggregate operating losses were in fact rising at an alarming level. Operating deficits and capital expenditures were financed by borrowing or from state budgetary resources, greatly burdening state government finance across India.

In the year 1991 India reversed its long-standing policy on private investment in the sector. Power was removed from the list of activities reserved for the public sector in the Industrial Policy Resolution and the 1948 Act was amended to lift many of the regulatory disincentives to private investment in the power sector. These changes were fully consistent with the Government of India's objective to tap the financial, technical

and managerial capabilities of the private sector in areas previously restricted to the public sector. India now allowed full local or foreign private ownership of power companies and offered a thirty-year license with the prospect of twenty-year renewals and increased financial returns. Provision was also made in the 1948 Act for private generating companies and captive plants to sell power to SEBs. Additional incentives were introduced in the Government of India's budget for fiscal 1994 reducing the import duty on power projects to 20 percent and offering new private power projects a five-year tax holiday. These changes were expected to result in remarkable business development activity by the private developers.

The Government of India recognized that its economic growth targets would be threatened as long as the country's power supply constrained industrial development and financial losses of the power sector remained a burden on the public sector finances. But with this unsatisfactory state of affairs of the SEBs no private investor would like to invest in the sector and ultimately state government would continue to carry the financial burden of the SEBs. At this point of time the Government of India imposed financial discipline on the SEBs through its central agencies. It also pressed the states to adjust their power tariffs and open the sector to private investment. In addition, the Government of India undertook to support states willing to reform their power sector. Consequently it was decided to reform the sector so that financial burden might reduce on the state government budgetary support and finally private sector participation might be expected in future. Moreover, government was also encouraged by the good performance of the central sector utilities namely Nation Thermal Power Corporation and Power Grid Corporation and expected that reform action would improve the performance of the SEBs.

The word reform as per dictionary means improvement or correction of what is corrupt or defective and government wanted to do exactly the same. SEBs were asked to improve their performance without any structural change rather improve their performance in all activities. However, it was realized that normal reform process has three major drawbacks.

- (a) Most of the SEBs have grown as welfare organization rather than commercial organization.
- (b) All SEBs are conglomeration of three different activities namely generation, transmission and distribution. All these three activities operate through different technology and environment.
- (c) With the existing structure of SEB, it is not possible to attract any private investment. Because, SEBs as an organization are making losses heavily and the structure could not allow any private investment separately for generation, transmission and distribution system.

But the expected improvement could not be ensured.

APDP: The Government of India realized the fundamental problem of the electrical sector in India rested with distribution system. Abnormally high T&D losses and

extremely poor collection efficiency were the root cause of the fast deterioration of the SEBs. Only 55% of total power generated was billed and even less, 41%, was actually paid for. SEBs' average cost recovery through tariffs was only 74% in 1999-2000. In order to reduce these losses large investment was necessary enabling to augment the distribution infrastructure including installation of meters universally. Restructuring along with privatization would not be able to generate that much fund by which required augmentation could be achieved. In order to generate sufficient fund and ascertain the tangible improvement in the performance of the electricity sector in February 2000, the Government of India introduced a new scheme, the Accelerated Power Development Programme (APDP), with the objective of initiating a financial turnaround in the performance of the State owned power sector. The APDP was formulated to finance specific projects relating to:

- (a) Renovation and Modernization, Life extension, Up-rating of old thermal and hydel plants.
- (b) Up gradation & strengthening of sub-transmission and distribution network (below 33kV or 66kV) including energy accounting and metering in the distribution circles.

In line with the APDP 63 distribution circles were identified for up gradation along with old power plants for renovation and modernization. But the financial health of SEBs did not improve due to historically accumulated losses.

APDRP: In the mean time pursuant to one of the resolutions adopted at a meeting of the State Chief Ministers held by the Prime Minister in March 2001, the MoP constituted an Expert Group under Shri Montek Singh Ahluwalia, the then Member (Energy), Planning Commission, to recommend measures for the one-time settlement of outstanding dues of the SEBs towards the Central Public Sector Undertakings and suggest a strategy for capital restructuring of the SEBs. Of the recommendations of this Group, headed subsequently by Shri N. K. Singh, Member (Energy), Planning Commission, the one-time settlement scheme had already been accepted and a start had been made to facilitate reform in the Union Budget 2002-03 as the Accelerated Power Development and Reform Programme (APDRP). Subsequently the Union Budget 2002-03 had re-christened APDP as APDRP, and enhanced the allocation to Rs.3500 crore with the stipulation that "access of the States to the fund would be on the basis of agreed reform programmes, the center piece of which would be the narrowing and ultimate elimination of the gap between unit cost of supply and revenue realization within a specified time frame".

Electricity Act 2003: After the introduction of APDRP it was felt that it would only be effective if a comprehensive restructuring plan with specific targets within reasonable time frame is in place. Moreover, competitive market needs to be created to attract the investors. As a result Electricity Act 2003 was enacted. The Act consolidate the laws relating to generation, transmission, distribution, trading and use of electricity and generally for taking measures conducive to development of electricity industry, promoting competition

therein, protecting interest of the consumers and supply of electricity to all areas, rationalization of electricity tariff, ensuring transparent policies regarding subsidies, promotion of efficient and environmentally benign policies, constitution of Central Electricity Authority, Regulatory Commission and establishment of Appellate Tribunal and for matters connected therewith or incidental thereto. The Act provides an enabling framework for accelerated and more efficient development of the power sector and seeks to encourage competition with appropriate regulatory intervention. Competition is expected to yield efficiency gains and in turn result in availability of quality supply of electricity to consumers at competitive rates. Eventually, no Act can cover every detail of the process and provide performance norms against each activity. Moreover, norms are also dynamic with the change of working environment and technology norms change. As a result after the change of norms or any other functional property the Act need to be amended, which will be a long drawn tedious process. To take care of any ambiguity Electricity Act 2003 authorized the Central Government in consultation with the State Government to prepare National Electricity Policy and Tariff Policy, which can be modified from time to time. Sub-section 1, 2, 3 & 4 of section 3 of the Act states The Central Government shall from time to time, prepare the national electricity policy and tariff policy, in consultation with the State Government and the Central Electricity Authority for development of power system based on optimal utilization of resources such as coal, natural gas, nuclear substances or material, hydro and renewable sources of energy. The Central Government shall publish National Electricity Policy and tariff policy from time to time. The Central Government may, from time to time, in consultation with the State Government and Authority, review or revise, the National Electricity Policy and tariff policy. Accordingly the National Electricity Policy has been prepared and notified on 12th February 2005. Later the tariff policy has been notified on 6th January 2006.

The National Electricity Policy aims at laying guidelines for accelerated development of the power sector, providing supply of electricity to all areas and protecting interests of consumers and other stakeholders keeping in view availability of energy resources, technology available to exploit these resources, economics of generation using different resources, and energy security issues. The National Electricity Policy aims at achieving the following objectives:

- (1) Access to Electricity: Electricity must be available for all households in next five years
- (2) Availability of Power: Demand must be fully met by 2012. Energy and peaking shortages should be overcome and adequate spinning reserve to be available.
- (3) Must be able to supply reliable and quality power of specified standards in an efficient manner and at reasonable rates.
- (4) Per capita availability of electricity should be increased to over 1000 units by 2012.
- (5) Ensure minimum lifeline consumption of 1 unit/household/day as a merit good by year 2012.
- (6) Financial Turnaround and Commercial Viability of Electricity Sector.

(7) Protection of consumers' interests.

It is essential to prepare a plan for implementing any policy. In line with this concept the National Electricity Plan is being prepared by the Central Electricity Authority for implementing the National Electricity Policy.

Introducing competition in different segments of the electricity industry is one of the key features of the Electricity Act, 2003. Competition will lead to significant benefits to consumers through reduction in capital costs and also efficiency of operations. It will also facilitate the price to be determined competitively. The Central Government has already issued detailed guidelines for tariff based bidding process for procurement of electricity by distribution licensees for medium or long-term period vide gazette notification dated 19th January 2005. All future requirement of power should be procured competitively by distribution licensees except in cases of expansion of existing projects or where there is a State controlled/owned company as an identified developer and where regulators will need to resort to tariff determination based on norms provided that expansion of generating capacity by private developers for this purpose would be restricted to one time addition of not more than 50% of the existing capacity. Even for the Public Sector projects, tariff of all new generation and transmission projects should be decided on the basis of competitive bidding after a period of five years or when the Regulatory Commission is satisfied that the situation is ripe to introduce such competition. The real benefits of competition would be available only with the emergence of appropriate market conditions. Shortages of power supply will need to be overcome. Multiple players will enhance the quality of service through competition. All efforts will need to be made to bring power industry to this situation as early as possible in the overall interests of consumers.

In the Electricity Act 2003 open access system has been made mandatory. It is a radical diversion from the conventional method of encouraging competition among the private players. In a conventional system more than one player are given franchise for a specific area and due to competition every one needs to improve their performance to remain in the business. However, transmission and distribution bear a natural monopoly, therefore this type of competition really cannot optimize the benefits. Open access in transmission has been introduced to promote competition amongst the generating companies who can now sell to different distribution licensees across the country. This should lead to availability of cheaper power. The Act mandates non-discriminatory open access in transmission from the very beginning. When open access to distribution network is introduced by the respective State Commission enabling bulk consumers to buy directly from competing generators, competition in the market would increase the availability of cheaper and reliable power supply. Nevertheless, Electricity Act 2003 has not rejected the conventional approach of encouraging competition. It allows distribution licensees to take up generation and generating companies to take up distribution. Section 7 of the Act states "Any generating

company may establish, operate and maintain a generating station without obtaining a license under this Act if it complies with the technical standards relating to connectivity with the grid referred to in clause (b) of section 73." Consequently a generating company may apply for a license to distribute electricity as a distribution licensee in accordance with section 14 (b). Similarly a distribution licensee may take up generation since no license is necessary to undertake generation. Moreover, the Act has also allowed any number of distributing licensees to take up distribution of electricity in the same area. One of the provision of section 14 states "Provided also that the Appropriate Commission may grant a license to two or more person for distribution of electricity through their own distribution system within the same area, subject to the conditions that the applicant for grant of license within the same area shall, without prejudice to the other conditions or requirements under this Act, comply with the additional requirements (including the capital adequacy, credit-worthiness or code of conduct) as may be prescribed by the Central Government and no such applicant who complies with all the requirements for grant of license, shall be refused grant of license on the ground that there already exists a licensee in the same area for the same purpose."

Open access system if properly implemented may improve the performance of electrical sector to a great extent through healthy competition. However, the concept is new thus it requires many clarifications. A few of them are discussed here. Under the open access regulations, there is an urgent need to determine the transmission, charges, wheeling charges and surcharge in order to implement the said regulation. It has been proposed that transmission charges should be calculated on postage stamp system either on per unit basis or on per MW basis. In postage stamp system charges are uniform irrespective of the distance, that means for a 100-meter distance and 500 KM distance charges are same. Many experts opined that the methodology for determination of transmission wheeling charges and surcharges should take into account the capacity available in the system, nature of consumers, consumers who leave the grid and the new consumers who join the grid. It is suggested that transmission charges should be determined on MW basis, since energy based transmission charge may result in under-recording / over recovery of costs and also that the short term open access customers may block the transmission path for others without paying any charges. It was further stated that for calculating transmission charges on MW basis, available capacity should be considered as against the installed capacity. Indian Wind Power Association (IWPA) has suggested postage stamp methodology for determination of transmission charges. However for wind projects relaxation in methodology may be considered wherein the charges may be computed in both distance sensitive and distance neutral methodologies and least cost shall be arrived at based on these methods. It has also been proposed that transmission charges be based on combination of distance sensitive slabs in steps of 25 KM/50

KM with postage stamp based charges in a particular slab. Another group has suggested distance sensitive method should be adopted for transmission charges.

Concerning the transmission losses it has been stated open access customer should justifiably bear the proportionate cost of the transmission loss and also compensate the incremental transmission loss. It has been farther stated that in the present practice, the annual cost of transmission is divided by the unit sold to the ESCOMs, which incidentally covers transmission loss also. It is difficult to determine the incremental line loss, as it is dependant on the location of consumer, location of supplier, hours of usage and season. Hence it is advisable to charge on per unit costs basis for open access customers also as is being followed now.

Utility applications of a RTDS[®] Simulator

Paul Forsyth, Rick Kuffel

RTDS Technologies Inc., Canada

Abstract— The RTDS Simulator is a fully digital, real time power system simulator widely used in the industry. The system provides continuous real time electromagnetic transient simulations based on the Dommel algorithm. The simulator hardware and software have both undergone many improvements since the simulator was first introduced in the early 1990's. The improvements have increased the performance of the simulator and widened its scope of application. In particular, electric power utilities have used the system for closed-loop testing and training on controllers for HVDC, SVC and generators, closed-loop protective relay testing, and large scale real time simulation. The paper describes the simulator design and its utility applications in greater detail.

I. INTRODUCTION

The Real Time Digital Simulator (RTDS[®]) is a fully digital, real time power system simulator developed at the Manitoba HVDC Research Centre in the late 1980's. In 1994, responsibility for the RTDS Simulator was transferred to RTDS Technologies where it has since undergone numerous hardware and software developments. The simulator is now widely used in the electric power industry by utilities, equipment manufacturers and research organizations. The paper describes the simulator design and its utility applications.

II. SIMULATOR DESIGN

A. Hardware

The RTDS Simulator hardware is based on a customized parallel processing architecture designed specifically to solve the electromagnetic transient simulation algorithm developed by Dr. Hermann Dommel [1]. The design is modular so that different size power systems can be accommodated by adding units, referred to as racks, to the simulator. Each rack of hardware includes both communication and processor cards

linked through a common backplane. To divide a large network between different racks, it is split into separate subsystems that are solved on individual racks. Each rack has an InterRack Communication (IRC) card that allows information to be shared between the subsystems. Each rack also contains a Workstation InterFace (WIF) card that synchronizes the simulation calculations and coordinates communication between processor cards as well as communication between racks. Additionally the WIF provides Ethernet communication to and from the graphical user interface during real times simulations.

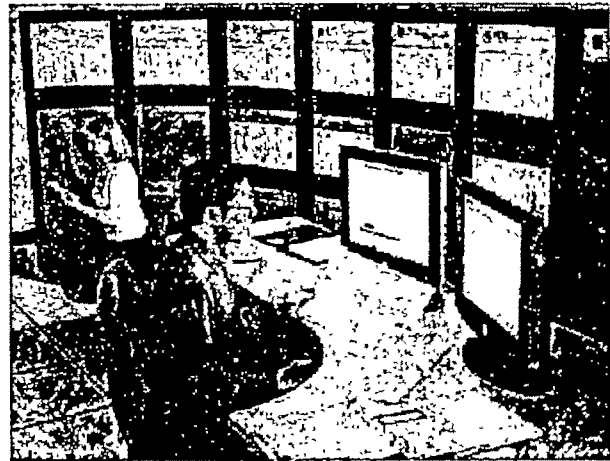


Figure 1: RTDS Simulator Installation

The processor cards are responsible for calculating the overall network behavior. Different components are assigned to different processors so that their contribution to the subsystem response can be calculated in parallel. In general, there are two different types of calculations performed by the processors cards; the network solution (i.e. nodal analysis) and the auxiliary components. The network solution solves the node voltages and branch currents based on the network impedances and the contribution of the auxiliary components. Auxiliary components are lines, transformers, etc. that provide admittance matrix overlays and current injections to the network solution. The combined solution of the network solution and the auxiliary components simulates the overall network response.

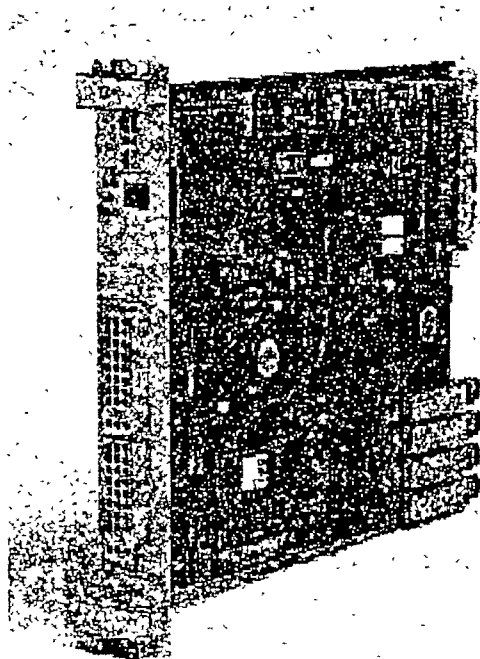


Figure 2: GPC Card

The current RTDS Simulator uses two different processor cards; the Triple Processor Card (3PC) and the Giga Processor Card (GPC). Each 3PC card contains three floating point Digital Signal Processors (DSP) running at 40 MHz, a significant increase over the original Tandem Processor Card (TPC) which had only two DSP's running at 11 MHz. The processors can communicate directly to one another at any time via shared memory, without having to access the backplane, and can therefore be used independently or together to solve more complex component models. The GPC is the most recently developed processor card which contains two RISC processors running at 1 GHz. Due to their computational power, the GPC processors are often used to calculate more than one component model at the same time.

Starting at the concept stage, the RTDS Simulator was intended for testing of physical protection and control equipment, thus making input/output (I/O) a primary design consideration. In some instances, hundreds of signals are passed to and from the simulator to external equipment. Great care was given to ensure that large amounts of I/O could be provided without significantly affecting the simulation timestep. Instead of providing a central communication link, the processor cards and I/O were designed to communicate directly with one another to minimize the communication time.

The GT-I/O cards are a family of I/O developed for the GPC card. The GT-I/O cards connect to the GPC via 2 GHz fiber

optic links and provide complete optical isolation from the simulator. The GT-I/O cards include analogue input and output with 16-bit data converters as well as digital input and output.

Typically the simulation timestep for real time operation of the RTDS Simulator is in the order of 50 μ s. Hard real time is ensured by the WIF card. If any processor cannot complete the calculations and I/O required within the given timestep, the simulation is stopped and an error message issued. The largest simulation ever run in real time provided a full electromagnetic transient representation for a network with over 500 three-phase buses and 90 generators.

Special hardware, algorithms and techniques, introduced later in this paper, have been developed to provide a high degree of accuracy in representing high speed power electronics that typically require a response in the order of 1 μ s.

B. Software

There are several levels of software involved with the RTDS Simulator. At the lower level are the component models (i.e. lines, transformers, generators, etc.) which have been optimized for real time operation. Over the years a comprehensive library of both power system and control components has been developed and refined.

The highest level of software is the graphical user interface known as RSCAD. RSCAD allows simulation circuits to be constructed, run, operated, and results to be recorded and documented.

The RSCAD Draft module allows simulations to be constructed graphically by copying and connecting generic components from the library. The parameters of a particular component can be entered through a data menu. After the network has been constructed, it is compiled to create the simulation code required by the simulator. Once the compile process has been executed, the simulation can be run using RSCAD RunTime.

RunTime, which operates on a PC or workstation, communicates back and forth with the simulator WIF cards via Ethernet. The bidirectional communication allows simulations to be downloaded and run as well as for simulation results to be transferred to the RunTime screen. The network can be operated from RunTime by changing switching states or set points. Slow moving signals such as power, RMS bus voltage, machine speed, etc. can be monitored on a continuous basis to allow transient behavior and state of the network to be observed. Detailed plots of transient events, with a resolution as high as every timestep, can also be recorded by the simulator WIF cards and displayed in RunTime plots.

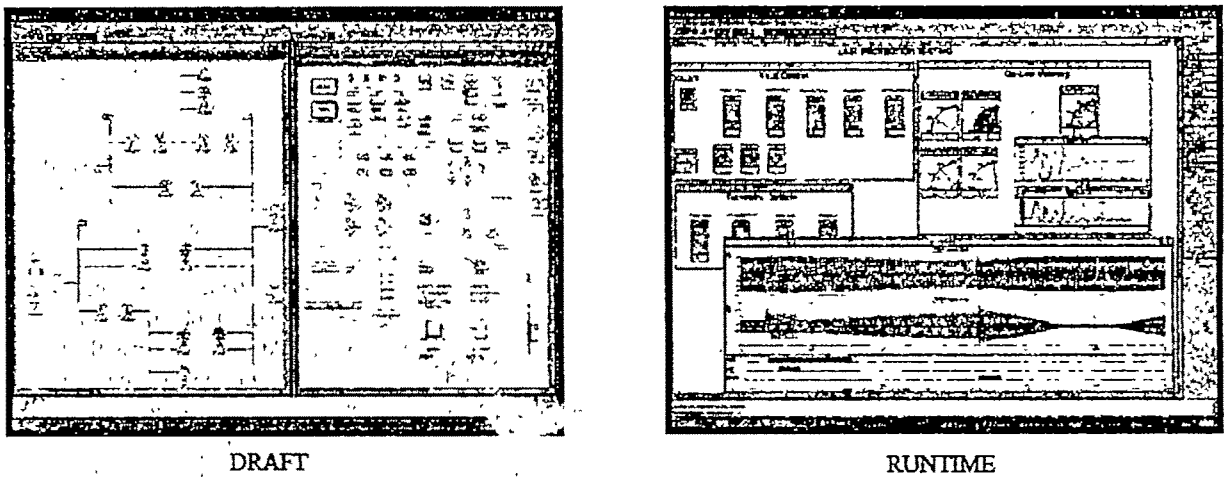


Figure 3: RSCAD Draft and RunTime Screens

III. APPLICATIONS

A. Closed-loop Control System Testing

The simulator has been widely adopted for closed-loop testing of controllers for HVDC, SVC, TCSC, and FACTS devices. Virtually all manufacturers of power electronic systems use the simulator for development, dynamic performance, and factory performance testing. It has also become common practice for utilities purchasing these specialized systems to acquire a real time simulator. The simulator gives the utilities several important advantages that were previously not available:

- a) the facility to perform additional testing of new controllers
- b) the ability to more thoroughly investigate the impact of the new installations on the network considering the true controller response
- c) a chance to provide first hand training for personnel on the operation of the installations and controllers without the danger of impacting network operation
- d) the capability to test control modifications, or updates before going "live" in the network

To provide an accurate simulation of the power electronic schemes mentioned above, the simulator must respond faster than a 50 μ s timestep will allow. For line commutated devices typically used for HVDC, SVC and TCSC, the improved firing algorithm is used to provide a firing pulse resolution in the order of 1 μ s [2]. Before this technique was developed, a firing pulse arriving during the timestep calculation would not fire the valve until the next timestep. Furthermore since the simulation and the controller ran asynchronously, the error observed for a constant alpha order would drift through the timestep. The result was a 50 μ s "gitter" in the firing pulse which produced unrealistic harmonics and limited the ability

of the simulator to test functions that required small adjustments in the firing angle (e.g. SSR damping with HVDC and DC loop control for SVC). The improved firing algorithm uses a Digital Input Times Stamp (DITS) function to measure exactly when during the timestep the firing pulse was issued. The DITS information is then used by the improved firing algorithm to calculate a correction applied to the model in the following timestep.

For force commutated schemes, often used in FACTS devices, a different technique is applied to provide the high speed simulation response required. The technique is referred to as the small timestep Voltage Source Converter (VSC) model and introduces a dual timestep approach [3]. The standard timestep, in the order of 50 μ s, is used to model the larger power system while a small timestep, in the order of 1-3 μ s, is used to represent the VSC model. The two models are numerically interfaced in a manner similar to the technique used to interface state variable models (e.g. dq0 synchronous machine model) to a time-domain simulation. The small timestep approach makes it possible to test firing pulse controllers for 3-level VSC's with Pulse Width Modulation (PWM) frequencies up to approximately 2 kHz. These schemes include STATCOM, wind generators with double fed induction machines, force commutated HVDC, etc.

The RTDS Simulator can also be used to test generator controls such as exciters, power system stabilizers, and governors. Commissioning time can be minimized by using the simulator to pre-tune the controllers and allow personnel to become familiar with the operation and set up of the new equipment, before it is activated in the network. Using the RTDS Simulator for this work also conserves resources since prime-mover energy is not required for the simulator testing. These tests can also be conducted onsite using a portable simulator.

B. Protective Relay Testing

The RTDS Simulator provides the most comprehensive means available for testing protective relays. Both open-loop (i.e. COMTRADE playback) and closed-loop testing can be conducted, but closed-loop testing offers important advantages. Firstly, since closed-loop testing must be and is conducted in real time, less time is needed to perform a sequence of tests compared to using COMTRADE playback. Secondly, real time operation allows multiple protection devices to interact with the simulated network at the same time. Therefore it is the only means to fully test and see the interaction of multiple relays (e.g. double-ended twin circuit line protection involves the interaction of four relays).

When conducting closed-loop protective relay testing, or for that matter any closed-loop testing, the RTDS Simulator acts as the power system. The simulator provides low level (± 10

Since the power system is being simulated, various faults can easily be applied under different network conditions to evaluate the performance of the protection system. The RTDS Simulator also has a script feature to allow a sequence of tests to be run automatically.

Scripts can be created for the simulator using a combination of special simulator commands and C programming. Nested loops allow very extensive and adaptive testing to be conducted and documented automatically.

Recent developments for the RTDS Simulator allow IEC 61850 communication to test devices compliant with the new protocol. The GTNET, which translates the IEC 61850 messaging for the RTDS Simulator, supports bidirectional binary signals (e.g. trips signals from relays as well as status

Vpeak) analogue outputs either directly to the device under test or, as is usually the case for relay testing, via amplifiers. These signals are proportional to the instantaneous value of the signal being represented (e.g. voltage, current, etc). Voltage and current amplifiers are used to bring the simulator's low level analogue outputs up to secondary values normally seen by the relays in service (typical nominal values are 110 Vrms l-l and 1 Arms or 5 Arms). The simulator also has output contacts so that breaker status can be provided to the relays at the auxiliary voltage level. With all of the regular inputs provided to the relays, they behave as if installed in the actual network. If a simulated fault is applied in the protection zone, the relay should trip. To close the test loop, the relay output contacts are connected to the simulator to provide trip and, if applicable, reclose signals. Both single-phase and three-phase tripping schemes can be tested. A basic set up for line protection testing is illustrated in Figure 4.

signals to relays) as well as sampled value signals (i.e. time-stamped voltage and current). Through this facility the RTDS Simulator provides the means to become familiar with and test this new technology.

C. Large Scale Real Time Simulation

Large-scale real time simulations can also be valuable to a utility by providing a more detailed representation of the network behavior than standard transient stability simulations. Among other things, RTDS simulations provide a much better frequency response (DC to ~ 3 kHz), detailed representation of power electronic installations (as opposed to a nominal frequency approximation), real time feedback, and the ability to interconnect with physical devices. The RTDS Simulator is also being used by companies to provide operator training [4].

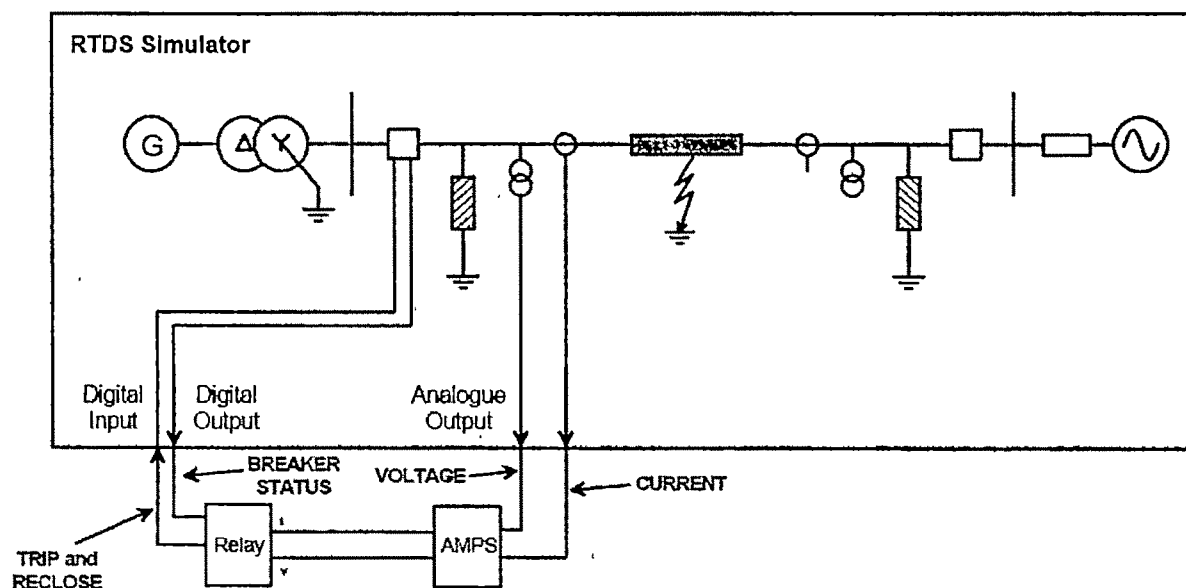


Figure 4: Closed-loop Protective Relay Testing

IV. CONCLUSIONS

Figures Real time digital power system simulators have undergone significant advancements over the last decade and are now widely used in the industry. With advancement and acceptance of the technology, more and more utilities are acquiring real time simulators for closed-loop protection and control system testing as well as for large scale real time simulations.

REFERENCES

- [1] H. W. Dommel, "Digital Computer Solution of Electromagnetic Transients in Single- and Multiphase Networks", *IEEE Trans. On Power Apparatus and Systems*, Vol. PAS-88, No. 4, pp. 388-399, April 1969.
- [2] K. Bergmann, K. Braun, et al., "Advanced Fully Digital TCSC Real-Time Simulation in Comparison with Computer Studies and On-Site Testing", *In Proc. ICDS '99*, Vasterås Sweden, May 1999.
- [3] T. Maguire, J. Giesbrecht, "Small Time-Step ($<2\mu\text{Sec}$) VSC Model for the Real Time Digital Simulator", *In Proc. IPST 2005*, Montreal Canada, June 2005, Paper No. IPST05-168-25c.
- [4] S.T. Cha, T.K. Kim, et. al., "Development of a Training Simulator for Power System Operation", *In Proc. WMSCI 2006*, Orlando USA, July 2006

BIOGRAPHIES

Paul Forsyth graduated from the University of Manitoba with B.Sc.EE in 1988. After graduating he worked for several years in the area of reactive power compensation and HVDC at ABB Power Systems in Switzerland. He also worked for Haefely-Trench in both Germany and Switzerland before returning to Canada in 1995. Since this time he has been employed by RTDS Technologies where he currently holds the title of Marketing Manager / Simulator Specialist.

Rick Kuffel graduated from the University of Manitoba with B.Sc. EE and M.Sc.EE in 1984 and 1986 respectively. After graduating he worked at BBC in Switzerland and Teshmont Consultants in Winnipeg before moving to the Manitoba HVDC Research Centre in 1989. There he worked mainly on the development of the real time simulator and in 1994 became a founding principal of RTDS Technologies.

Modeling the Auditory System: An Interesting Challenge

Christian Berger-Vachon

University of Lyon, France

Abstract— It is well known that hearing aids provide an interesting means to correct auditory disorders, but when we talk to eminent specialists of the subject, they will tell you that we are only at the early stage of making a good correction.

What do we know?

A deaf person has hearing performances, which are worse than a normal hearing subject.

Some differences have been pointed out:

- Brain treatment, voice production and phonation,
- Middle ear function,
- Presbycusis, Recruitment, poor perception of weak sounds,
- Frequency analysis, Ear filters
- Coding strategies in language reconstruction,

...

In fact, everything is open. When a disorder is pointed out, technology tries to build up compensation; it means that there is a close collaboration between physicians and scientists.

In this lecture we recall the main stages of the auditory system, some of the disorders, which are well known so far and how they have been corrected. Also, the main limits are indicated and how new technology tries to improve the auditory performance and how we can restore what is a fundamental right to everybody, the right to communicate.

Pattern Recognition: A Universal Problem Solving Discipline

B.B. Chaudhuri

Computer Vision and Pattern Recognition Unit,
Indian Statistical Institute
203, B T Road, Kolkata 700108, India, e-mail: bbc@isical.ac.in

I. INTRODUCTION

PERCEPTION and Recognition are basic driving units of human intelligence. Man has cherished the idea of developing artificial intelligence so that machine can emulate human behavior and action. One of the earliest attempts can be noted in the three thousand years old Greek temples where the deities used to talk to the worshipers. In reality, the voice was that of the priest which was transmitted through hidden tubes upto the mouth of the deity. More serious attempts are noted in eighteenth century when Christian kratzenstein designed mechanical vowel synthesizer. This was followed by a more advanced work by Wolfgang Von Kempelen. Kempelen's system was further improved by Charles Whitstone in later years. In twentieth century Homer Dudley developed VODER which is an electrical version of speech synthesiser. After the discovery of computer, most attempts for automatic speech synthesis were driven by it and several successful systems were built.

Apart from the examples, of speech recognition, researchers tried to develop systems that can read the books in the manner done by human being. Such attempt is also an example of artificial intelligence. The research on character recognition by machine started as early as in 1870 when Carey invented Retina Scanner for image transmission using mosaic of Photo cells. On the other hand, in 1890, Nipkow invented a sequential scanner for television and Optical Character Recognition (OCR). At the very beginning of twentieth century, Tyurin attempted OCR as reading aid for the blind. In 1929, Tausheck obtained the first OCR patent in Germany. Dr. Shepard from Intelligent Machine Research Company developed a workable OCR in 1950. Another company Solartron Electronics Ltd. made Electronic Reading Automation in 1957. Later, in 1965 IBM OCR system IBM 1287 was exhibited in New York fair. At present, many systems (Scansoft Omnipage, Abby Fine-reader, Charactell Soft writing, Dan Ching Penpower) are available for automatic Optical Character Recognition.

Among Indian Languages a few printed digit recognition systems have been reported, in early 1970's for Hindi, Bangla, Devnagari and Tamil scripts. But in late 1980's first sponsored project on OCR was started in collaboration with C-DAC and IIT Kanpur and in middle of 1990's the first completed OCR systems in Bangla and Hindi were announced by ISI, Kolkata. Around 2001 OCR in Punjabi and Tamil were developed. Online and other offline handwritten character recognition work is now continuing at different places in India.

Apart from pattern recognition, people in earlier days also used various tool for clustering purpose, specially in species determination of animals and plants. Clustering is now considered a major tool in pattern classification. Two other areas enhanced the formation of pattern recognition as new discipline. One is image processing, especially of pictures taken from space mission and need for identifying objects from the pictures. The other is remote sensing, employed for surveying earth by pictures taken by planes and satellites, where land covers needed to be classified. Biomedical image processing is another application that enriched pattern recognition as a discipline.

In pattern recognition problems, the classification or description scheme usually employs one of the following approaches: statistical (or decision theoretic), syntactic (or structural). Statistical pattern recognition is based on statistical characterizations of patterns, assuming that the patterns are generated by a probabilistic system. Syntactical (or structural) pattern recognition is based on the structural interrelationships of non-quantitative features. A wide range of algorithms can be applied for pattern recognition, from very simple Bayesian classifiers to much more powerful neural networks, Hidden Markov Model, Singular value Decomposition.

In this lecture, I shall concentrate on different aspects of Pattern recognition with applications to character recognition, which is one of the most challenging and interesting task, especially for Indian scripts.

II. PATTERN RECOGNITION TECHNIQUES

There are two different types of Pattern Recognition approaches. One is automatic classification, where a set of objects or signal is classified into a few categories. Many recognition tasks can be converted into pattern classification problems. On the other hand, there may be pictorial objects where recognition means fitting an unknown object with a specific description of stored objects of known identity.

To convert the recognition into a classification problem, some distinctive properties or features of the objects are at first measured. These measurements are represented in a multidimensional feature space as points. These points are then classified into groups by unsupervised or supervised manner. The unsupervised approaches fall under the category of automatic clustering. In the supervised scheme, at first the system is trained with known examples of different classes. After the training is over, the system is ready for classifying the unknown data.

Statistical tools have been primarily used in supervised classificatory systems when such a system employs some statistical distribution. The training corresponds to estimating the parameters of the distribution so that various discriminant analysis techniques can be profitably utilized. Such approaches are called parametric approaches. In a non parametric approach, some decision boundary between classes need be demarcated. Then any unknown sample falling within the boundary of a particular class is assigned to that class.

In a parametric situation, quite often Bayes' decision theory is used for classification. Suppose the feature vector x be a d -component vector-valued random variable and let $p(x|\omega_j)$ be the state conditional probability density function for x , with the probability density function for x conditioned on ω_j being the true state of nature. As before, $P(\omega_j)$ describe the prior probability that nature is in state ω_j . Then the posterior probability $P(\omega_j|x)$ can be computed from $p(x|\omega_j)$ by Bayes' formula:

$$P(\omega_j | x) = \frac{p(x | \omega_j)P(\omega_j)}{p(x)} \quad (1)$$

For an unknown sample this posterior probability is computed for all classes. The sample is assigned to the class for which the processor probability is maximum.

Several simplifications can be done when the sample features come from a known distribution e.g., Gaussian distribution. Specially, when the covariance matrix of the training samples is diagonal and equal, this leads to decision surfaces which are linear. In case of two class' problem the discriminate function is of the form :

$$g_i(x) = -\frac{1}{2}(x - \mu_i)' \Sigma^{-1}(x - \mu_i) + \ln P(\omega_i) \quad (2)$$

Where μ stands for mean, Σ stands for covariance matrix and ω_i stands for the i th class.

For discrete features, x can assume only one of m discrete values v_1, \dots, v_m . In such cases the probability density function $p(x|\omega_j)$ becomes singular integrals of the form

$$\int p(x | \omega_j) dx \quad (3)$$

must then be replaced by corresponding sums, such as

$$\sum_x P(x | \omega_j) \quad (4)$$

where we understand that the summation is over all values of x in the discrete distribution. Bayes' formula then involves probabilities, rather than probability densities:

$$P(\omega_j | x) = \frac{P(x | \omega_j)P(\omega_j)}{P(x)} \quad (5)$$

There are certain situations, where the class labels are not very clear and hence the decision boundary cannot be distinctly drawn. If there is a continuous transition of the objects from class to non-class with respect to a set of features, we can call it a fuzzy set. Several clustering and classificatory analysis have been proposed with fuzzy model. Another approach of handling uncertainty in class label is the rough set approach. Here, two bounds are formed on the data with respect to a set of features. If these two bound sets are equal, then it represent a crisp set. If they are different the subset is rough. Several rough set based approaches are also proposed in the literature. For patterns that can not be represented by quantitative features, a different approach called syntactic approach has been proposed. Here, each pattern is partitioned in to a small number of primitives. Rules of generating the patterns using these primitives are generated. In the training phase, an unknown pattern is also segmented into such primitives and subject to the grammar. If the grammar accepts the particular combination of features as belonging to one of the classes, then we assume that the pattern is recognized. Otherwise it is rejected.

III. IMAGE PROCESSING

Quite often the patterns are pictorial in nature. To deal with such patterns, some initial preprocessing and feature measurement are to be done before submitting them to the pattern classifier. The image processing tasks involve tasks like image capture, enhancement and restoration, image

segmentation and feature selection. Various spatial and transform based filtering and other techniques are employed for enhancement and restoration. Also, different optimization approaches and heuristics are used for object segmentation from the background.

We shall give the example of a practical system (OCR) to explain these tasks. The image capture in OCR is normally done using a flatbed scanner at an adequate scanning resolution (normally 300 dpi). The captured image is noise cleaned and enhanced. To separate the relevant information it is converted into a binary image, because text is represented mostly as black over white background. Among various binarization algorithms that of OTSU is one of the most popular. Next, each text line is separated and for each text line the words are segmented. Depending on the script, the characters need be segmented as well.

As an example of multidimensional quantitative features we can subdivide a character image into several squares and compute normalized black pixel density in each of these squares. If the character is partitioned into five by five squares then a twenty-five dimensional feature vector is generated. Now, we can take say, 100 samples of each known class for the training of the classifier. If we take the mean vector and covariance matrix for each class and assume that they belong to normal distribution then the classification phase is completed. Now, for an unknown sample we can compute the feature vector and get posterior probability of belonging to each class. The maximum of these probabilities decide the class level.

We can use fuzzy classifier in this case as well. The above 25 dimensional feature vector can be used to define a fuzzy membership function of a sample belonging to a particular class. When the membership function has been defined for all classes we can use the system for classifying unknown characters.

Syntactic approach has also been tried on OCR problems. Here, each character is partitioned into smaller components like vertical line, convex and concave parts, loops and holes and region of inflection. Then a context free and context sensitive stochastic grammar is trained using known samples for each class. Concatinative rules are also decided to generate and accept a character. An unknown character is accepted if the grammar rules are satisfied by it and it is classified as that character for which the acceptance is the best.

A. Application to Indian script OCR

The problem of Optical Character Recognition (OCR) for Indian script is more difficult compared to Latin scripts because of several reasons. First, The number of characters in alphabet is larger. Second, the vowels take modified shape and sit at difficult position with respect to the consonants, creating many new shapes. Third, there are more than 200 conjunct characters to which the vowel modifiers can also be attached. Thus, the number of shapes to be recognized becomes of the order of 1000. Fourth, the characters touch each other through 'matra' or 'shiro-rekha' and there is a need to segment individual characters before sending them to recognition engine. Fifth, Indian languages are inflectional and agglutinating in nature, so post recognition error correction

becomes a more difficult task than less inflectional languages. Sixth, several shapes of compound characters are undergoing changes over the last 50 years, making several allographs for each character.

The first single font high accuracy OCR has been reported at ISI used some novel innovative techniques for character separation and character classification. Here, the number of classes is reduced by looking at character parts above shiro-rekha separately. Also, the dots below some characters were recognized and removed. Removal of Shiro-rekha from character image easily finds the demarcation line between two neighboring characters. The lower zone is also detected by the abrupt change in crossing count during horizontal run, so that lower modifiers can be separated out. Thus, we have been able to reduce the 1000 class problem into a 400-class problem. Then a binary tree classifier is initially employed to separate this 400 class into smaller subclasses. Stoke based shape features are used in the binary tree classifier. Now, for each small subclass, several quantitative features are computed and a deterministic k-nearest neighbor classifier is designed. This classifier gives character output with ranking. Thus, an unknown charcter can have two tags according to first and second rank. If the word has n characters, then two tags for each create 2**n different strings. The strings are then fed to a dictionary for post-processing. We consider the strings which are valid words and accept the word for which the cumulative classifier score is highest among them. To take care of inflectionality problem of language a clever reverse and forward dictionary employed.

In the current lecture I shall elaborate the above system with pictures and results.

REFERENCES

- [1] R. O. Duda, P.E. Hart, D.G. Stork, "Pattern Classification", John Wiley & sons, 2nd edn., 2001
- [2] B.B. Chaudhuri, D. Datta Majumder, "Two-Tone Image Processing and Recognition", Wiley Eastern Ltd., 1993
- [3] M.Cheriet, N. Khanna, C.L. Liu, C.Y. Suen, "Character Recognition Systems A Guide for Students and Practitioners", John Wiley & sons, 2007
- [4] B.B. Chaudhuri (Ed.), "Digital Document Processing", Springer-verlag, 2007
- [5] R.C. Gonzalez, R.E. Woods, "Digital Image Processing", 3rd edn, Addison Wesley Longman, Inc., 2000
- [6] A. Rosenfeld, A.C. Kak, Digital Picture Processing, Vol 2, Academic Press, New York, 1982.
- [7] T. Pavlidis, Structural Pattern Recognition, Springer-Verlag, Berlin, Heidelberg, New York, 1980.
- [8] K. Fukunaga, "Introduction to Statistical Pattern Recognition", Academic Press, San Diego, 1990.
- [9] J.C. Bezdek, "Pattern recognition with fuzzy objective function algorithms", Plenum Press, 1981
- [10] B. G. Batchelor (ed), "Pattern recognition : ideas in practice", Plenum Press, N Y, 1978
- [11] R. Bernstein (Ed), "Digital image processing for remote sensing", IEEE Press, New York, 1978
- [12] G J Awcock, R Thomas, "Applied image processing", Macmillan, 1995.

Author Index

- A. A. A. Jeddi, 238
 A. Aram, 247
 A. B. Chowdhury, 6
 A. Chakrabarti, 33
 A. Das, 570
 A. De, 33
 A. Gupta, 805
 A. Haddouk, 755
 A. Jaya Lakshmi, 552
 A. K. Chakrabarty, 163
 A. K. Dhakar, 746
 A. K. Dhara, 269
 A. K. Jain, 805
 A. K. M. Nurul Amin, 129
 A. K. Mukhopadhyay, 570
 A. K. Pal, 678
 A. K. Sen, 373
 A. Kazemi, 556
 A. Lekshmi, 528
 A. Mirdehghan, 717
 A. Mondal, 669
 A. Rahmati, 456,461
 A. Rastgo, 124
 A. Rastgoo, 238,247,717
 A. Sarada Devi, 43
 A. Sutradhar, 349
 A. Tadjer, 229
 Abdullah Abasiun, 726
 Abhijit Chakroborti, 6
 Abhik Mukherjee, 488
 Abu Tariq, 412
 Ajay K. Yagati, 471
 Ajoy K Chakraborty, 589
 Akashdeep Agrawal, 167
 Akshay K Rathore, 384
 Alakananda Bhattacharya, 656
 Alireza Rezazade, 110
 Alok Kumar Vishwakarma, 422,427
 Amit Konar, 656
 Amitava Das, 746
 Amrit Ghosh, 782
 Anayet U Patwari, 129
 Anil Ahlawat, 115
 Anil Kumar Bag, 297
 Anindita Senguptaa, 354
 Anish Deb, 265,354
 Ankush Ghosh, 775
 Anushree Roy, 585
 Arghya Sarkar, 561
 Arindam Ghosh, 628
 Arun JB, 699
 Ashim Kumar Dey, 637
 Asim Datta, 664
 Atif Iqbal, 521
 Awadhesh Kumar Singh, 778
 B. B. Chaudhuri, 219,224,883
 B. Basavaraja, 538
 B. Bouhafs, 229
 B. J. J Raju, 43
 B. K. Pandey, 422,427
 B. Kundu, 380
 B. M. Mohan, 293
 B. Mahdian, 556
 B. P. Singh, 417,616
 B. R. Das, 542
 B. S. Sathyanarayana, 712
 B. Sarkar, 373
 B. Chakraborty, 332
 Barwal Shwetla, 449
 Bhargab B. Bhattacharya, 646
 Bijoy K. Mukherjee, 56
 Bijoy Kumar Upadhyaya, 651
 Bipan Tudu, 297,479
 Bishakha Nandi, 605
 C Ghanshyam, 320
 C. Christoher Asir Rajan, 133
 C. Das, 669
 C. Ghennai, 533
 C. K. Chanda, 6
 C. K. Roy, 589
 C. RoyChaudhuri, 324
 CG Nandakumar, 498
 CH. Siva Kumar, 566
 Ch.Prasanth Babu, 552
 Chandhal Dey, 307
 Christian Berger-Vachon, 882
 D Sanyal, 873
 D. Das, 143
 D. Devaraj, 683
 D. Roy Choudhury, 251
 D. S. Karanjkar, 47
 D. V. S. S. Siva Sarma, 538
 David. J, 201
 Debajit Bharali, 471
 Debashis Das, 479
 Debasis Mitra, 646
 Debasis Samanta, 775
 Debasish Mondal, 339
 Deepika Masand, 147
 Devmalya Banerjee, 782
 Dibyendu Bhattacharyya, 297
 Dilip De, 282
 Dilip Dey, 389,393
 Dilip Kumar Mitra, 440
 Dipak Kumar Basu, 206,771
 Dipanwita Gangopadhyay, 80
 Durjoy Majumder, 488
 Enrique Acha, 864
 Epsita Das, 431
 F. Haghjoo, 621
 F. Shamila, 16,731
 Fazilatunnessa, 277
 G Pavan Kumar, 317
 G. B. Gharehpetian, 610
 G. Bandyopadhyay, 380
 G. Jumatova, 822
 G. Prakash, 775
 G. Sarkar, 751
 G. Tulasi Ram Das, 552
 G. Uma, 712
 G. V. Nagesh Kumar, 417
 G. V. Nagesh Kumar, 616
 Gautam Sarkar, 265,673
 Gayatri Agnihotri, 147,407
 H. Askarian, 610
 H. Baudrand, 819
 H. Belhaneche, 255
 H. Heydari, 456,461,741
 H. Mechergui, 755
 H. R. Karimi, 238
 H. R. Toodeji, 610
 H. Saha, 324
 H. Sohanian, 247
 Harsha. A., 201
 IDER Zahir, 688
 Indrajeet Boiragi, 320
 Ishtiyahq M. Hossain, 129
 J. N. Bera, 269,751
 J. Amarnath, 417,616
 J. C. Singh, 775
 J. Dheeba, 796
 J. K. Das, 580,637
 J. N. Bera, 431,669
 J. N. Sharma, 722
 J. P. Tewari, 377
 J. Pal Choudhury, 282
 J. R. P. Gupta, 251
 J. Ramanjaneya Reddy, 566
 J. Sil, 302
 Jayadev Bhat, 273

Jayashri Vajpai, 699
 Jitendra Nath Bera, 585
 Jun-ichi Inoue, 786
 Jyothiraj V. P, 192,483
 K. A. Muraleedharan, 16,731
 K. Baskaran, 503
 K. C. Pradhan, 104
 K. Chaudhary, 384
 K. D. Srivatsava, 616
 K. Das (Bhattacharya), 580
 K. Gomathy, 16,731
 K. K. Mazumdar, 561
 K. S. Sherpa, 832
 K. S. Sumam, 52
 K. Selvajyothi, 80
 K. Thippeswamy, 11
 K. Vaisakh, 21,153
 K. K Garg, 449
 Kabir Chakraborty,
 1,605,832
 Kalyankumar Datta, 368
 Kaushik Mukherjee, 736
 Kavita Khare, 642
 KP Mohandas, 547
 L. Dekkiche, 840
 L. R. Srinivas, 153
 M A Sheikh, 312
 M. Abedi, 610
 M. Ahmadi, 456,461
 M. G. Wani, 453
 M. H. Banna, 277
 M. K. Saini, 805
 M. Kadjoudj, 533
 M. Malki, 255
 M. Mitra, 219,224,399,669
 M. N. Gupta, 791
 M. R. Shakarmai, 556
 M. Raju Hossain, 277
 M. Rizwan Khan, 521
 M. S. Bhowmick, 61,66
 M. S. Jamil Asghar, 412
 M. Shiva Kumar, 476
 M. Siva Kumar, 43
 M. Sukumar, 476
 M. Sushama, 552
 M. Umapathy, 712
 M. V. Aware, 85,517
 M. V. Ramesh, 28,435
 M. Vijaya Kumar, 99
 M. E. Benbouzid, 533
 M. Ksouri, 359
 Madhuchhanda Mitra, 38,216
 Mahantapas Kundu, 206,771
 Mallikarjun S. Holi, 187
 Mallikarjuna Swamy M. S,
 187
 Manas Kumar Bera, 344
 Manash Chanda, 782
 Manjunatha M, 187
 Manoj Pandey, 115
 Masato Okada, 786
 Md. Anwar Hussain, 814
 Mendil Boubekeur, 688
 Mita Nasipuri, 206,771
 Mohammad Hassan
 Rahimian, 726
 Mohandas K P, 211
 Mohsen Modarres, 110
 Monisha Chakraborty, 479
 Mousiki Kar (Deb), 368
 Mukhtar Ahmad, 521
 Muraleedharan CV, 498
 N. Albert Singh,
 16,683,731,796
 N. Farokhnia, 610
 N. Futane, 324
 N. Herald Anantha Rufus,
 796
 N. K. Singh, 177,182
 N. Kumaravel, 710
 N. Mandal, 329,332
 N. Ramezani, 598
 N. Sajikumar, 52
 N. Sreenivasulu, 594
 Nabanita Nath Chowdhury,
 265
 Nabarun Bhattacharyya, 297
 Narendra Nath Sinha, 637
 Naveen Kumar KU, 498
 Naveen Nischal Chava, 377
 Neeraj Verma, 94
 Neila Bédioui, 363
 Nibaran Das, 771
 Nikhil Mondal, 736
 Nilay Khare, 642
 Nitai Pal, 440,444
 Nivedita Sharma, 722
 O. V. Raghava Reddy, 99
 P A Saheeda, 768
 P. A. Janakiraman, 80,836
 P. Aruna Jeyanthi, 683
 P. B. Duttagupta,
 389,393,589
 P. Bera, 143
 P. Chattopadhyay, 380
 P. Das, 243
 P. K. Chattopadhyay, 163
 P. K. Chaturvedi, 104
 P. K. Gujarathi, 85
 P. Kanta Rao, 21
 P. L. MuthuKarthik, 694
 P. Naga Manasa, 43
 P. Nagabhushan, 809
 P. P. Pal, 380
 P. R. Venkateswaran,
 273,712
 P. Ram Mohan, 99
 P. S. Rawat, 704
 P. S. Venkataramu, 694
 P. Sumathi, 836
 P. V. Prasad, 594
 P. Venkateswaran, 651
 Palash Kundu, 673
 Pankaj Chaudhary, 384
 Parikshit Yadav, 75
 Paul Forsyth, 877
 Pijush Biswas, 782
 Piyali Chatterjee, 206
 Prabal Deb, 89
 Pradip Kumar Sadhu,
 440,444
 Prasenjit Basak, 633
 Pratap Chandra Karfa, 580
 Probir Kumar Dhar, 488
 R. A. Gupta, 75,507,512
 R. Agrawal, 805
 R. Arulmozhiyal, 503
 R. Bramhachari, 431
 R. D. Kharadkar, 453
 R. Gupta, 669
 R. K. Pandey, 167,177,182
 R. K. Singh, 377
 R. Kaviani, 124
 R. Nandi, 651
 R. Naoum, 840
 R. P. Yadav, 404,704
 R. Ramchandani, 805
 R. S. Bbajpai, 466
 R. Sankaran, 528
 R. Sarkar, 332
 R. Seetharaman, 710
 Rabindranath Bera, 859
 Rahul Sharma, 119
 Rajani K. Mudi, 307
 Rajesh Babu Kollipara, 104
 Rajesh Gupta, 466,628
 Rajesh Kumar, 75,507,512
 Rajesh Tyagi, 115
 Rajeshwari S, 187
 Rajib Bandhopadhyaya, 297
 Ram Sarkar, 771
 Rambabu. Ch, 158
 Rameshkumar P, 211
 Ramtin Hadidi Ahad Kazemi,
 172

Ranjit Roy, 575
 Ratnesh Kumar, 404
 Reena M Roy, 768
 Rick Kuffel, 877
 Roshna. R, 493
 Rupaban Subadar, 138
 Rupendranath Chakrabarti, 440
 Rupendranath Chakrabarti, 444
 Rusakov M. A., 761
 S Ashok, 547
 S. Banerjee, 542
 S. Basu, 805
 S. C. Bera, 61,66,70,329,332,336
 S. C. Gupta, 407
 S. C. Kar, 269
 S. Chakraborty, 336
 S. Chattopadhyay, 70,660
 S. Chattopadhyay, 844
 S. Chowdhuri, 269,751
 S. Chowdhury, 633
 S. Ekram, 373
 S. G. Hingmire, 47
 S. G. Karad, 47
 S. G. Thampi, 52
 S. H. Fathi, 610
 S. Halder nee Dey, 33
 S. Jagadish Kumar, 566
 S. K. Ahamed, 399
 S. K. Basak, 542
 S. K. Mondal, 542
 S. K. Mukherjee, 282
 S. K. Sanyal, 651,660,844
 S. K. Sen, 542
 S. K. Srivastava, 829
 S. L. Mahmood, 277
 S. Larbi, 255
 S. M. Ale Emran, 610
 S. M. Pedramrazi, 741
 S. M. Shahrtash, 598,621
 S. Meenatchisundaram, 273
 S. Meenatchisundaram, 712
 S. N. Mahendra, 384
 S. P. Bhattacharyya, 119
 S. P. Chowdhury, 633
 S. P. Ghoshal, 56,575
 S. P. Muley, 517
 S. Pal, 70
 S. Paruya, 824
 S. Phoujdar, 751
 S. Saha, 302
 S. Sao, 28,435

S. Sengupta, 269,389,393,399,561, 637, 664,832
 S. Shabu, 493
 S. SivaNagaraju, 594
 S. Tripath, 805
 S. Ushakumari, 528
 S. V. Bhangale, 507,512
 Sahana D. Gowda, 809
 Saheeda P. A., 764
 Salah Salhi, 359,363
 M.Ksouri, 363
 Samarjit Sengupta, 38
 Samir Zaki Mohamed Mehrez, 234
 Sandeep Bharti, 704
 Sandeep K. Dey, 646
 Sandhya Rao, 187
 Sangita Das Biswas, 1,605
 Satyendra Nath Mandal, 282
 Satyendra Prakash, 704
 Saurabh Goyal, 75
 Saurabh Pal, 216,344
 Selma Ben Attia, 359
 Shailendra Jain, 147
 Sharmistha Mandal, 349
 Sheeba O, 196
 Shilpa G. S, 187
 Shilpi Bhattacharya, 89
 Shveta Kundra Bhatia, 800
 Shyamal Kumar Goswami, 368
 Sohini Roy, 471
 Soumya Ray, 736
 Srinivasa Rao. Gorantla, 28,435
 Subhadip Basu, 206,771
 Subir Kumar Sarkar, 775,855
 Subrata Karmakar, 399
 Subrata Majumdar, 163
 Sucharita Mitra, 219,224
 Sudha Balagopalan, 547
 Sudipta Mandal, 354
 Sujata Pandey, 115,791
 Sujesh Sreedharan, 498
 Sujit K. Biswas, 89,736,851
 Sujoy K. Guha, 471
 Sukesh Kumar A, 192, 201,483,196
 Suman Saha, 6
 Sumana Chowdhuri, 585
 Sunil Kumar, 471
 Sunita Mishra, 320
 Surajit Chattopadhyay, 38

Susmita Dey (Chaudhuri), 585
 Susmita Kundu, 431
 Susmita Sur-Kolay, 646
 Swanirbhar Majumder, 138,216,814
 Swapnadip De, 782
 T. Ananthapadmanabha, 694
 T. Benabdesselam, 229
 T. Datta, 775
 T. K. Basu, 143
 T. K. Chatterjee, 444
 T. K. Mitra, 669,849
 T. K. Sengupta, 570
 T. R. Rangaswamy, 288
 Tanimu Bhattacharya, 605
 U. Chakraborty, 70
 U. Kar, 302
 Umalakshmi A, 187
 V. K. Keshavan, 11
 V. K. Sharma, 453
 V. Mukherjee, 56
 V. S. Dixit, 800
 Vertika Singh, 293
 Vineeta Agarwal, 94,422,427
 Vinod Chandra, 317
 Virendra K. Gangwar, 404,704
 Virendra P. Vishwakarma, 791
 Vishnu Vardhan, 646
 Y. Kumar, 407
 Yang Chunyan, 260
 Yogesh V. Hote, 251
 Yohei Saika, 786
 Z. Mekkioui, 819